Springer Aerospace Technology

Martin Grabe
Georgii Oblapenko
Manuel Torrilhon *Editors*

Rarefied Gas Dynamics

Proceedings of the 33rd International Symposium

OPEN ACCESS

Springer

Springer Aerospace Technology

Series Editors

Sergio De Rosa, Department of Industrial Engineering, University of Naples Federico II, Napoli, Italy

Yao Zheng, School of Aeronautics and Astronautics, Zhejiang University, Hangzhou, China

The series explores the technology and the science related to the aircraft and spacecraft including concept, design, assembly, control and maintenance. The topics cover aircraft, missiles, space vehicles, aircraft engines and propulsion units. The volumes of the series present the fundamentals, the applications and the advances in all the fields related to aerospace engineering, including:

- structural analysis,
- aerodynamics,
- aeroelasticity,
- aeroacoustics,
- flight mechanics and dynamics
- orbital maneuvers,
- avionics,
- systems design,
- materials technology,
- launch technology,
- payload and satellite technology,
- space industry, medicine and biology.

The series' scope includes monographs, professional books, advanced textbooks, as well as selected contributions from specialized conferences and workshops.

The volumes of the series are single-blind peer-reviewed.

To submit a proposal or request further information, please contact: Mr. Pierpaolo Riva at pierpaolo.riva@springer.com (Europe and Americas) Mr. Mengchu Huang at mengchu.huang@springer.com (China)

The series is indexed in Scopus and Compendex

Martin Grabe · Georgii Oblapenko ·
Manuel Torrilhon
Editors

Rarefied Gas Dynamics

Proceedings of the 33rd International Symposium

Springer

Editors
Martin Grabe
Institute of Aerodynamics and
Flow Technology
Deutsches Zentrum für Luft- und
Raumfahrt (DLR)
Göttingen, Germany

Manuel Torrilhon
Applied and Computational Mathematics
RWTH Aachen University
Aachen, Germany

Georgii Oblapenko
Applied and Computational Mathematics
RWTH Aachen University
Aachen, Germany

ISSN 1869-1730 ISSN 1869-1749 (electronic)
Springer Aerospace Technology
ISBN 978-3-032-00093-4 ISBN 978-3-032-00094-1 (eBook)
https://doi.org/10.1007/978-3-032-00094-1

This work was supported by Deutsches Zentrum für Luft- und Raumfahrt.

© The Editor(s) (if applicable) and The Author(s) 2026. This book is an open access publication.

Open Access This book is licensed under the terms of the Creative Commons Attribution 4.0 International License (http://creativecommons.org/licenses/by/4.0/), which permits use, sharing, adaptation, distribution and reproduction in any medium or format, as long as you give appropriate credit to the original author(s) and the source, provide a link to the Creative Commons license and indicate if changes were made.
The images or other third party material in this book are included in the book's Creative Commons license, unless indicated otherwise in a credit line to the material. If material is not included in the book's Creative Commons license and your intended use is not permitted by statutory regulation or exceeds the permitted use, you will need to obtain permission directly from the copyright holder.
The use of general descriptive names, registered names, trademarks, service marks, etc. in this publication does not imply, even in the absence of a specific statement, that such names are exempt from the relevant protective laws and regulations and therefore free for general use.
The publisher, the authors and the editors are safe to assume that the advice and information in this book are believed to be true and accurate at the date of publication. Neither the publisher nor the authors or the editors give a warranty, expressed or implied, with respect to the material contained herein or for any errors or omissions that may have been made. The publisher remains neutral with regard to jurisdictional claims in published maps and institutional affiliations.

This Springer imprint is published by the registered company Springer Nature Switzerland AG
The registered company address is: Gewerbestrasse 11, 6330 Cham, Switzerland

If disposing of this product, please recycle the paper.

Preface

The 33rd International Symposium on Rarefied Gas Dynamics (RGD33) was held in Göttingen, Germany, from July 15 to 19, 2024. Since the first meeting in Nice in 1958, venues have changed every two years across countries and continents. This marked only the third time the RGD symposium was held in Germany, returning to Göttingen exactly 50 years after it was first hosted there.

Rarefied gas dynamics is a branch of physics mainly concerned with the study of gas flows in which processes at the molecular level play a role. With its diverse applications ranging from astrophysics to micro-flows, it continues to raise challenging questions that require a multidisciplinary effort of mathematicians, physicists, chemists, computer scientists and engineers.

Still under the impression of the fading COVID-19 pandemic, the RGD33 symposium was deliberately planned as a purely face-to-face event in order to promote direct scientific exchange and strengthen the professional community. The response was overwhelmingly positive. With 243 participants from 30 countries, the attendance exceeded expectations. However, for the first time in its history, the symposium was severely affected by sanctions imposed on Russian universities and research institutions as well as numerous other organizations embargoed by the USA and the European Union. Nevertheless, we remain committed to global scientific cooperation, as we are convinced that it also plays an important role in strengthening civil society against authoritarianism worldwide.

A total of 176 papers were presented in three parallel tracks. In addition, 49 posters were presented and put up for discussion in a dedicated session. The organizers took care to include a balance of contributions from mathematics, natural sciences and engineering in order to promote interdisciplinary exchange. Among the topics discussed during RGD33 were:

Boltzmann and Related Equations,
Granular Flows,
Gas-Surface Interactions,
Quasi-Classical Trajectory Simulation,
Moment Methods,

Electric Propulsion Simulation,
Machine Learning,
Air-breathing Electric Propulsion Simulation,
Spectroscopy,
Micro- and Nanoscale Flows,
Plasma Simulation,
Multi-scale Simulations,
CFD for Rarefied Flows,
Modern DSMC,
Fluid Interfaces,
Multi-scale Simulation Methods,
Particle-based Methods,
High-speed/High-enthalpy Flows,
Flows in Vacuum Systems,
Planetary Science and Exploration,
Jets and Plumes,
Thermochemically Non-equilibrium Flows,
Kinetic Methods,
Plasma Experiments.

Four plenary lectures were delivered at the symposium: the Graeme Bird Lecture was given by Alejandro Garcia. Richard Morgan delivered the Lloyd Thomas Lecture, and Vincent Giovangigli spoke in the Harold Grad Lecture. In addition to the three traditional plenary lectures, the Irving Langmuir Lecture was delivered by Anne Bourdon. The lecture was introduced for this symposium to strengthen connections with the related field of plasma research. Incidentally, Irving Langmuir, earned his PhD in Göttingen. In addition to the four outstanding scientists mentioned above, eight other researchers were invited to highlight their recent work: Alina Alexeenko, Christos Tantos, Eunji Jun, Hossein Gorji, Milana Čolić, Zhenning Cai, Tetsuro Tsuji and Philip Varghese.

The *Proceedings of the 33rd International Symposium on Rarefied Gas Dynamics* comprises of 69 full papers that were accepted for inclusion after having been evaluated by at least two independent professional peers.

The organizers thank the Deutsche Forschungsgemeinschaft (DFG) and the DLR Institute for Aerodynamics and Flow Technology for their generous support. We are also grateful to the many members of our community that served as reviewers and session chairs, as well as for the enthusiastic support we received from our DLR colleagues during all the phases of the symposium. In particular, we are indebted to the DLR Event Management Service (Petra Naoum and Rebecca Bartkowski) for smoothly managing the logistics. Last but not least, we thank the members of the International Advisory Committee, who continue to dedicate their time and effort to

ensure the venerable *International Symposium on Rarefied Gas Dynamics* remains at the scientific forefront of the field.

Göttingen, Germany Martin Grabe
Aachen, Germany Georgii Oblapenko
Aachen, Germany Manuel Torrilhon

Committees

Chair

Martin Grabe, DLR Göttingen

Co-Chair

Manuel Torrilhon, RWTH Aachen University

Local Advisory Committee

Georgii Oblapenko, RWTH Aachen University
Jan Martinez Schramm, DLR Göttingen
Sebastian Karl, DLR Göttingen

Local Organizing Committee

Petra Naoum, DLR Event Management
Rebecca Bartkowski, DLR Event Management
Svetlana Saburova, DLR Event Management
Michaela Welz, DLR Göttingen
Jan Martinez Schramm, DLR Göttingen
Tim Horchler, DLR Göttingen
Tobias Ecker, DLR Göttingen
Sebastian Karl, DLR Göttingen
Divek Surujhlal, DLR Göttingen
Alexander Wagner, DLR Göttingen

International Advisory Committee 2024

Alina A. Alexeenko, USA
Yevgeniy A. Bondar, Russia
Domenico Bruno, Italy
José M. Fernandez, Spain
Michail A. Gallis, USA
Vincent Giovangigli, France
Martin Grabe, Germany
Irina Graur, France
Rakesh Kumar, India
Elena V. Kustova, Russia
Deborah Levin, USA
Thierry Magin, Belgium
Luc Mieussens, France
Rho Shin Myong, South Korea
Sean O'Byrne, Australia
Felix Sharipov, Brazil
Henning Struchtrup, Canada
Quanhua Sun, China
Kojiro Suzuki, Japan
Shigeru Takata, Japan
Vladimir A. Titarev, Russia
Manuel Torrilhon, Germany
Philip Varghese, USA
Kung Xu, China
Yonghao Zhang, China

Prior RGD Symposia

1. Nice, France (1958)
2. Berkeley, USA (1960)
3. Paris, France (1962)
4. Toronto, Canada (1964)
5. Oxford, UK (1966)
6. Cambridge, USA (1968)
7. Pisa, Italy (1970)
8. Stanford, USA (1972)
9. Göttingen, Germany (1974)
10. Aspen, USA (1976)
11. Cannes, France (1978)
12. Charlottesville, USA (1980)
13. Novosibirsk, Russia (1982)
14. Tsukuba, Japan (1984)
15. Grado, Italy (1986)
16. Pasadena, USA (1988)
17. Aachen, Germany (1990)
18. Vancouver, Canada (1992)
19. Oxford, UK (1994)
20. Beijing, China (1996)
21. Marseille, France (1998)
22. Sydney, Australia (2000)
23. Whistler, Canada (2002)
24. Bari, Italy (2004)
25. St. Petersburg, Russia (2006)
26. Kyoto, Japan (2008)
27. Pacific Grove, USA (2010)
28. Zaragoza, Spain (2012)
29. Xi'an, China (2014)
30. Victoria, Canada (2016)
31. Glasgow, UK (2018)
32. Seoul, South Korea (2022)
33. Göttingen, Germany (2024)

Contents

Boltzmann and Related Equations

Variational Solutions to the Coupled Poiseuille and Thermal Creep Problems on the Basis of the Boltzmann Equation for Hard-Sphere Molecules and Cercignani-Lampis Boundary Conditions 3
Silvia Lorenzani

Existence and Regularity of Axisymmetric Weak Solutions to the Spatially Homogeneous Landau Equation 13
Jin Woo Jang and Junha Kim

Maxwell-Stefan Diffusion Model Based on Moment Equations for Gas Mixtures 21
Milana Čolić and Srboljub Simić

Lattice Boltzmann Scheme for Drift Diffusion Equations in Cold Plasma Applications 33
Nathalie Bonamy Parrilla, Stéphane Brull, and François Rogier

Experimental Techniques for Non-equilibrium Flows

Development of Neuromorphic Imaging Spectroscopy for Hypersonic Flight Observation 45
Tamara Sopek, Fabian Zander, Byrenn Birch, and David Buttsworth

Spectroscopic Studies in Non-equilibrium Plasmas 55
Ruairí J. O'Connor and Philip L. Varghese

Initial On-Orbit Cross-Calibration of the Electric Propulsion Electrostatic Analyzer Experiment (ÉPÉÉ) 67
C. A. Maldonado, T. Eddy, P. A. Fernandes, T. K. Kim, J. Derr, A. Barjatya, S. Debchoudhury, G. R. Wilson, A. J. Rogers, M. Dunn, S. M. Klem, B. Weaver, R. Ulrich, K. Potter, K. Moran, L. Castro, J. McGlown, J. D. Williams, R. L. Balthazor, P. Neal, J. Stauffer, and M. G. McHarg

Gas-Surface Interactions

Unsteady Stefan Problem with Kinetic Interface Conditions in Rarefied Gas Phase-Transitions 79
Donat Weniger and Manuel Torrilhon

Molecular Dynamics Study of Scattering of Nitrogen from a Cryogenic Nitrogen Surface 89
Johannes V. Diedrich and Martin Grabe

Investigation of Gas-Surface Interactions in Hyperthermal and Hypersonic Gas Flow 99
Quan Han and Haitao Xia

Hypersonic and Space Vehicle Aerodynamics

DSMC Computations of Intake Performance for Air Breathing Ion Engine 111
Takashi Ozawa, Shunsuke Imamura, Masahito Tagawa, and Kumiko Yokota

Toward a Model for Biological Contaminant Dispersal by Spacecraft Operating and Landing in Near-Vacuum 123
William A. Hoey and John R. Anderson

Comparison Between the Kinetic Fokker-Planck and TAU Navier-Stokes Simulations of Hypersonic Air Flow Around the the RFZ-ST2 Upper Stage 133
Moritz Ertl and Leo Basov

Numerical Analysis of a High Field Magnetic Heat Shield for Re-Entry Applications 141
Vishnu Asokakumar Sreekala, Jakub Glowacki, Tulasi Parashar, Ben Parkinson, Nicholas Strickland, Steve Smart, Joseph Bailey, Xiyong Huang, and Nicholas Long

Effect of Structured Surface on Pressure Measurement in Hypersonic Rarefied Wind Tunnel 151
Ryunosuke Endo, Takashi Ozawa, Masahito Tagawa, and Kumiko Yokota

Identifying the Continuum Breakdown of a Plume Surface Interaction in Near Vacuum Environment for a CFD-DSMC Approach 163
Jannis Petersen, Jonas Göbel, Martin Propst, Bradley Craig, Theodor Heutling, Konstantinos Kontis, Craig White, Martin Tajmar, Jeroen Van den Eynde, and Christian Bach

Modelling Heat Transfer at Low-Density Hypersonic Spacecraft Flight Regimes 173
Vladimir V. Riabov

DSMC Simulation of a Non-axisymmetric Hypersonic Vehicle at 90 km Altitude 183
Angelos Klothakis, Ioannis K. Nikolos, and Vassilis Theofilis

Numerical Simulation of the Flow Field Around a Sounding Rocket for the PMWE Project 193
Miklas Schütte, Igor Hörner, Stefan Löhle, Stefanos Fasoulas, and Marcel Pfeiffer

PICLas-Based Intake Simulation Activities for the Development of an ABEP Specular Intake 203
Nadine Barth, Jonathan Skalden, Konstantinos Papavramidis, Elizabeth Gutierrez, Franziska Tuttas, Marcel Pfeiffer, Raphael Tietz, Philipp Maier, and Georg Herdrich

Effect of Gas-Surface Interactions on Very Low Earth Orbit Mission Operation 213
Sai Sudha Ramesh, Basman Elhadidi, Boo Cheong Khoo, and Wai Lee Chan

Internal Flows in Vacuum Systems

Numerical Analysis of Rarefied Gas Flows Induced by Rotor-Stator Blades 225
Hiroshi Sugimoto, Ayako Miki, and Shogo Sugimoto

Micro-Tapered-Tubes Flow Analysis via DSMC and Experimental Methods 235
Christos Tantos, Foteini Litovoli, Franz Schweizer, Lucien Baldas, Juergen J. Brandner, Jan Gerrit Korvink, Thomas Giegerich, and Marcos Rojas-Cárdenas

Analysis of Propellant Gas Suppression in Shattered Pellet Injector System of the ITER Experiment 247
Ákos Gyenge, Richárd László Csiszár, and Balázs Farkas

Kinetic Theory

From Kinetic Theory to Hyperbolic-Parabolic Fluid Systems of Equations 259
Vincent Giovangigli

Relativistic Equilibrium Distribution of Rapidity: A Kinetic Theory Perspective 273
Guillermo Chacón-Acosta, Ana Laura García-Perciante, and Alma R. Méndez

Classical Trajectories Estimation of Transport Properties of N_2-O_2 Mixtures 283
Domenico Bruno and Aldo Frezzotti

Micro- and Nanoscale Flows

Uniform Flow Past a Circular Disk: Numerical Analysis and Modeling of Thermal Polarization 295
Takuma Tomita, Satoshi Taguchi, and Tetsuro Tsuji

Modeling Transient Slip Behavior from Laminar to Molecular Flow ... 305
Rodion Groll

A Meshless Approach to Study Rarefied Gas Flows in Lid-Driven Square Cavities 315
Himanshi, Anirudh Singh Rana, and Vinay Kumar Gupta

Modelling of the Flow of a Thermal Binary Gas Mixture in a Microchannel with a Sinusoidal Varying Thickness 325
Cédric Croizet

Moment Methods

Spatially Adaptive Moment Model Using Padded Buffer Cell for Linear Hierarchical Moment Equations 337
Rik Verbiest and Julian Koellermeier

Application of Regularized 13-Moment Equations to Continuum–Rarefied Gas Flow Over Aerospike Blunt Body 347
Satyvir Singh and Manuel Torrilhon

Suitability of Moment Methods to Model the Ion Dynamics in a Low-Temperature Plasma 357
Anatole Berger, Nicolas Lequette, Thierry Magin, Anne Bourdon, and Alejandro Alvarez Laguna

A Study on Gramian Closures in Bimodal Phenomena 369
Eda Yilmaz, Georgii Oblapenko, and Manuel Torrilhon

Numerical Study of Grad-14 and 17 Moment Equations for Rarefied Polyatomic Gases 379
Hang Song, Satyvir Singh, and Manuel Torrilhon

Numerical Methods for Kinetic Equations

Adaptation of the Unified Gas-Kinetic Scheme to ES-BGK Models 391
Céline Baranger, Alexis Coëpeau, and Luc Mieussens

Spatially-Parallel Collision Scheme for Implementing Direct Simulation Monte Carlo in Field-Programmable Gate Arrays 401
Saleen Bhattarai, Sean O' Byrne, Edwin Peters, and David Petty

Higher-Order Meshfree Methods for BGK Equations with Moving Boundaries 411
Klaas Willems, Sudarshan Tiwari, and Axel Klar

Comparison of Stochastic BGK and FP Methods for the Simulation of Non-Equilibrium Multi-species Molecular Gas Flows 421
Franziska Tuttas and Marcel Pfeiffer

Molecular-Level Simulations of Turbulent Couette Flow Over Rough Surfaces 431
Ryan M. McMullen, Timothy P. Koehler, and Michael A. Gallis

Simulation of Multi-species Kinetic Instabilities with the Numerical Flow Iteration 441
Rostislav-Paul Wilhelm and Manuel Torrilhon

A Novel Splitting Method for Vlasov-Ampère 451
James A. Rossmanith and Christine Vaughan

Modeling Gap Closure Within Vaporizing Transmission Lines of Pulsed Power Machines Using Particle-in-Cell Direct Simulation Monte Carlo (PIC-DSMC) 461
Grace Kirk, Georgii Oblapenko, David Sirajuddin, Christopher Moore, David Goldstein, and Philip Varghese

Evaporation Simulations in High Pressure Environments with a Multi-species Enskog-Vlasov Solver 471
Raphael Tietz, Rolf Stierle, Stefanos Fasoulas, and Marcel Pfeiffer

Combining Stochastic Particle BGK and Discrete Velocity Method for Efficient Multiscale Simulations 481
Félix Garmirian and Marcel Pfeiffer

An Improved Particle Scheme for Solving Fokker-Planck Models of the Boltzmann Equation 491
Tobias Ott, Hossein Gorji, and Marcel Pfeiffer

Impact of Entropy in Shock Recovery Through Fokker-Planck Kinetics 501
Veronica Montanaro, Lukas Netterdon, Manuel Torrilhon, and Hossein Gorji

A Coupled Semi-Lagrangian/Finite Volume Scheme to Deal with Close-Packing Limit in Thick Sprays 511
Christophe Buet, Bruno Després, and Victor Fournet

Numerical Methods for Non-equilibrium Flows

Effect of Scaled Angle on Unsteadiness Characteristics of Large Separation Bubbles in High Speed Flows 523
Irmak T. Karpuzcu, Deborah A. Levin, and Vassilis Theofilis

Vibronic Modelling in Direct Simulation Monte Carlo 531
Clément H. B. Civrais, Marcel Pfeiffer, Craig White, and René Steijl

A Non-negative Least Squares-Based Approach for Moment-Preserving Particle Merging 541
Georgii Oblapenko

Data-Driven Extraction of 3D Orthogonal Velocity Distribution Modes from 1D DSMC Shocks 551
Robert S. Martin

Numerical Study on the One-Way Flow Between Plates of Different Temperatures with Periodic Distribution of Accommodation Coefficient 561
Ryuichiro Imazu, Hiroshi Sugimoto, and Maika Itou

Simulation of the Neutral Gas Flow Within an Electric Thruster by the Kinetic Fokker-Planck Method and Comparison with Force Balance Measurements 571
Jens Schmidt and Leo Basov

DSMC: A Statistical Mechanics Perspective 581
Alejandro L. Garcia

Ab Initio-Based Collision Model for High-Temperature Molecular Gas Flows 591
Ashirbad Mallick and Tapan K. Mankodi

Impact of Electronic State-Specific Modeling on High-Enthalpy Nitrogen Flows 599
Yuzhe Zhang, Qizhen Hong, Xiaoyong Wang, Chao Yang, and Quanhua Sun

Exploitation of Continuum and Kinetic Theory Approaches for the Simulation of Particle Beam Experiments 609
Surya Kiran Peravali, Amit K. Samanta, Muhamed Amin, Philipp Neumann, Jochen Küpper, and Michael Breuer

Calibration of the Larsen-Borgnakke Model for NO-O Vibrational Relaxation 619
Shubham Thirani, Deborah A. Levin, and Ingrid J. Wysong

Adaptive Particle Discretization Methods for Multiscale Non-equilibrium Flows 629
Simone Lauterbach, Stefanos Fasoulas, and Marcel Pfeiffer

An Effective Temperature Formulation for Predicting State-Specific Reaction Rates and Simulating One-Dimensional Hydrogen-Air Detonations in DSMC 639
Shrey Trivedi, Ahren W. Jasper, John K. Harvey, and Jacqueline H. Chen

Plasma Flows and Processes

Effect of Microwave Coupling and Magnetic Field Topology on Electron Temperature and Thrust on the Example of Two Electric Propulsion Concepts 651
C. E. Schäfer, J. Schmidt, F. Plettenberg, M. Grabe, Y. A. Chan, J. Martinez-Schramm, K. Bräumer, K. Holste, and P. J. Klar

Spatially Resolved Collisional-Radiative Model for a Rarefied Plasma Plume 659
Bruno Fontaine, Federico Bariselli, Pietro Parodi, Pedro Jorge, Damien Le Quang, and Thierry Magin

Evaluation of the Ambipolar Diffusion Approximation Using an Eulerian Boltzmann-Poisson-BGK Solver 669
Marisa Petrusky and Iain D. Boyd

A Structure-Preserving Solver for Particle-Wave Interaction in Non-uniform Magnetized Plasmas 679
Kun Huang, Irene M. Gamba, and Chi-Wang Shu

Potential Fluctuations of Emissive Sheaths in Collisional Boundary Layer Plasmas Using a Kinetic Approach 689
Davut Vatansever and Deborah A. Levin

Challenges Using Rarefied Atmospheric Gases as Propellant for an RAM-EP System 699
Jana Zorn, Ole Forchheim, Kristof Holste, and Peter J. Klar

Astronomical Line Polarization Through Gas Transport 709
Boy Lankhaar

Boltzmann and Related Equations

Variational Solutions to the Coupled Poiseuille and Thermal Creep Problems on the Basis of the Boltzmann Equation for Hard-Sphere Molecules and Cercignani-Lampis Boundary Conditions

Silvia Lorenzani

Abstract In the present paper, we study some mathematical properties of the closed-form solutions to the Poiseuille and thermal-creep problems, obtained on the basis of the Boltzmann equation for hard-sphere molecules and Cercignani-Lampis boundary conditions.

Keywords Variational method · Poiseuille flow · Thermal-creep problem

1 Introduction

An accurate modeling of the gas-surface interaction is crucial in several applications involving the kinetic theory of rarefied gases. This issue can be addressed by choosing suitable boundary conditions for the Boltzmann equation, which describe the relation between the distribution functions of impinging and re-emitted gas molecules at a solid wall. Although different models of gas-surface interaction have been proposed in the literature, research in this direction has not made much progress over the years and most studies still use Maxwell boundary conditions derived in 1879. The Maxwell scattering kernel is characterized by only one free parameter, which represents the accommodation coefficient of all molecular properties. However, this is an oversimplification, since each physical quantity should have its own accommodation coefficient. Indeed, recent experiments have revealed that this model of gas-surface interaction fails to explain several results related to temperature-driven mass flow rates in microchannels [1, 2]. Because of these limitations, in recent years there has been a revival of interest in another more complex model of boundary conditions, the Cercignani-Lampis scattering kernel, which includes two parameters: α_t, representing the accommodation coefficient of the tangential momentum ($\alpha_t \in [0, 2]$) and α_n, being the accommodation of the kinetic energy due to the velocity normal

S. Lorenzani (✉)
Dipartimento di Matematica, Politecnico di Milano, Milano, Italy
e-mail: silvia.lorenzani@polimi.it

© The Author(s) 2026

M. Grabe et al. (eds.), *Rarefied Gas Dynamics*, Springer Aerospace Technology,
https://doi.org/10.1007/978-3-032-00094-1_1

to the bounding walls ($\alpha_n \in [0, 1]$). Despite the growing application of this model of gas-surface interaction to the study of several problems in rarefied gas dynamics, only a few recent papers investigate the mathematical properties of the solution of the Boltzmann equation with Cercignani-Lampis boundary conditions. Indeed, in [3], Chen has proved the local-in-time well-posedness of the Boltzmann equation in bounded domains with Cercignani-Lampis boundary conditions, where the accommodation coefficients can take any value other than zero (specular reflection). But so far, this author was able to construct the steady and global solution only for accommodation coefficients α_t and α_n close to 1 (diffuse boundary condition). In the present paper, we try to get a deeper insight on this issue, relying on the variational formulation of the thermal-creep problem.

2 Variational Formulation of Coupled Poiseuille and Thermal-Creep Problems

Let us consider the flow of a monatomic gas between two infinite parallel plates fixed at $x = \pm d/2$, due to small gradients of pressure and temperature in the z-direction:

$$k = \frac{1}{p}\frac{\partial p}{\partial z}, \quad \tau = \frac{1}{T}\frac{\partial T}{\partial z} \tag{1}$$

where p and T are the local gas pressure and temperature, respectively. Under these conditions, the gas flow is described by the linearized Boltzmann equation:

$$(D - L)h = S \tag{2}$$

where $Dh = c_x \dfrac{\partial h}{\partial x}$ is the differential term, $S = -c_z k - c_z\left(c^2 - \frac{5}{2}\right)\tau$ is the source term and Lh is the linearized collision operator. In Eq. (2), $h(x, \mathbf{c})$ is the small perturbation on the basic equilibrium state and $\mathbf{c}$ is the molecular velocity vector expressed in units of $(2RT)^{1/2}$ (with R being the specific gas constant). In the current investigation, we study the Poiseuille and thermal-creep flows on the basis of the exact linearized collision operator for hard-sphere molecules. Then, the Boltzmann equation (2) can be solved by imposing appropriate boundary conditions on the walls of the channel. In the present work, we will focus on the Cercignani-Lampis scattering kernel:

$$h^+(-(d/2)\mathrm{sgn}c_x, \mathbf{c}) = \int\limits_{c'_x<0} R_{CL}(-\mathbf{c} \to -\mathbf{c}')\, h^-(-(d/2)\mathrm{sgn}c_x, \mathbf{c}')\, d\mathbf{c}', \tag{3}$$

$$R_{CL}(\mathbf{c}' \to \mathbf{c}) = \frac{2c_x}{\pi\alpha_t\alpha_n(2-\alpha_t)} \exp\left\{ - \frac{[\mathbf{c}_t - (1-\alpha_t)\mathbf{c}'_t]^2}{\alpha_t(2-\alpha_t)} \right\} \times \exp\left\{ - \frac{[{c_x}^2 + (1-\alpha_n){c'_x}^2]}{\alpha_n} \right\} I_o\left(\frac{2\sqrt{1-\alpha_n}}{\alpha_n} c_x c'_x \right) \quad (4)$$

with $\mathbf{c}_t = (c_y, c_z)$ being the two-dimensional vector of the tangential molecular velocity and I_o the modified Bessel function of first kind and zeroth order. Equation (3) can be rewritten in symbolic form as follows: $h^+ = Kh^-$, where K is an operator and $h^\pm$ are the restrictions of the function h, defined on the boundary, to positive (negative) values of c_x (that is, h^+ and h^- represent the distribution functions of the reemitted and the impinging molecules on the boundaries, respectively). Since the imposed pressure and temperature gradients give rise to a gas flow and heat transfer in the z-direction, the quantities of physical interest to be computed are the mass $\dot{M}$ and heat flow rate $\dot{Q}$ (per unit time through unit thickness):

$$\dot{M} = \rho \int_{-d/2}^{d/2} v_z(x)dx \quad (5)$$

$$\dot{Q} = \int_{-d/2}^{d/2} q_z(x)dx \quad (6)$$

where ρ is the gas density. In Eqs. (5) and (6), the bulk velocity of the gas $v_z(x)$ and the heat flux $q_z(x)$ are defined as follows:

$$v_z(x) = \pi^{-\frac{3}{2}} \int_{-\infty}^{+\infty}\int_{-\infty}^{+\infty}\int_{-\infty}^{+\infty} e^{-c^2} c_z h(x, \mathbf{c})\, d\mathbf{c} \quad (7)$$

$$q_z(x) = \pi^{-\frac{3}{2}} \int_{-\infty}^{+\infty}\int_{-\infty}^{+\infty}\int_{-\infty}^{+\infty} e^{-c^2} c_z \left(c^2 - \frac{5}{2}\right) h(x, \mathbf{c})\, d\mathbf{c}. \quad (8)$$

In the framework of a linearized analysis, the mass and heat flow rates can be written as the sum of the Poiseuille and thermal-creep contributions:

$$\dot{M} = d^2\, p\, [-G_p\, k + G_T\, \tau] \quad (9)$$

$$\dot{Q} = \frac{d^2}{2}\, p\, [Q_p\, k - Q_T\, \tau] \quad (10)$$

where G_p, G_T, Q_p and Q_T are dimensionless positive coefficients that refer to the Poiseuille flow, the thermal-creep flow, the mechanocaloric effect and the reduced heat flux, respectively. In this paper, we derive approximate closed-form expressions for all these coefficients, taking into account that the Onsager relation holds: $G_T = Q_p$. To this end, we solve the Boltzmann equation by applying the variational technique presented in detail in [1, 2]. In particular, we introduce the following functional J of the test function $\tilde{h}$:

$$J(\tilde{h}) = ((\tilde{h}, P(D\tilde{h} - L\tilde{h}))) - 2((PS, \tilde{h})) + (\tilde{h}^+ - K\tilde{h}^-, P\tilde{h}^-)_B, \tag{11}$$

where P is the parity operator in velocity space, defined by $P[h(\mathbf{c})] = h(-\mathbf{c})$, while $((,))$, $(,)_B$ denote two scalar products reported in [1, 2]. According to the variational principle stated in [1], the functional $J(\tilde{h})$ attains its minimum value when $\tilde{h} = h(x, \mathbf{c})$ solves Eq. (2) with appropriate boundary conditions. Inserting $\tilde{h} = h(x, \mathbf{c})$ in Eq. (11), one gets:

$$J(h) = -((PS, h)) = -k \int_{-d/2}^{d/2} v_z(x)dx - \tau \int_{-d/2}^{d/2} q_z(x)dx = -k\frac{\dot{M}}{\rho} - \tau\dot{Q}. \tag{12}$$

Thus, the stationary value of J has a direct connection with the quantities of physical interest for the problem at hand. Since the details of the variational method of solution are given elsewhere [1, 2], below we report only the main steps undertaken to obtain the analytical formula for the coefficients G_p, G_T and Q_T. Relying on the integral form solution of the Boltzmann equation with the simplified Bhatnagar-Gross-Krook collision model, we derive a test function, which depends on three adjustable constants: A, B and C, to be varied in order to obtain the stationary value of $J(\tilde{h})$. Splitting the constants into two parts, due to the linear superposition of the Poiseuille and thermal-creep effects, and normalizing them in a suitable way, the functional $J(\tilde{h})$ reduces to the sum of three functionals, $J^{(1)}(\tilde{h})$, $J^{(2)}(\tilde{h})$, $J^{(3)}(\tilde{h})$, simply grouping together the terms proportional to $(k\theta)^2$, $(\tau\theta)^2$ and $(k\theta)(\tau\theta)$, respectively. For hard spheres of diameter σ, the length parameter θ is given by $\theta = \sqrt{2}/(\pi^{3/2}\sigma^2 n)$, with n being the gas number density. The stationary value of these functionals is obtained by imposing that their derivatives with respect to the adjustable constants A, B and C vanish. Finally, since Eqs. (12) and (9–10) hold, one can derive the following relationships for the Poiseuille flow G_p, the thermal-creep flow G_T, and the reduced heat flux Q_T:

$$G_p = \frac{2}{\delta^2} \min \frac{J^{(1)}(\tilde{h})}{(k\theta)^2} = \frac{2}{\delta^2} \frac{J^{(1)}(h)}{(k\theta)^2} \tag{13}$$

$$G_T = -\frac{1}{\delta^2}\min\frac{J^{(3)}(\tilde{h})}{(k\theta)(\tau\theta)} = -\frac{1}{\delta^2}\frac{J^{(3)}(h)}{(k\theta)(\tau\theta)} \tag{14}$$

$$Q_T = \frac{2}{\delta^2}\min\frac{J^{(2)}(\tilde{h})}{(\tau\theta)^2} = \frac{2}{\delta^2}\frac{J^{(2)}(h)}{(\tau\theta)^2} \tag{15}$$

where δ is the rarefaction parameter (inverse Knudsen number), $\delta = \frac{d}{\theta}$. By performing an asymptotic expansion of the full variational solution, one can prove that the pressure- and temperature-driven mass flow rates G_p and G_T, respectively, are well approximated, in the range $\delta \geq 3$, by the following closed-form formulas:

$$G_p = \frac{\delta}{\sigma_{0,p}} + \sigma_{1,p} + \frac{\sigma_{2,p}}{\delta} \tag{16}$$

$$G_T = \frac{\sigma_{1,T}}{\delta} + \frac{\sigma_{2,T}}{\delta^2} \tag{17}$$

where the explicit expressions for the coefficients $\sigma_{0,p}$, $\sigma_{1,p}$, $\sigma_{2,p}$ and $\sigma_{1,T}$, $\sigma_{2,T}$ are reported in [2]. On the other hand, the same analysis carried out for the heat flux Q_T did not provide satisfactory results. Therefore, in this case, one should consider the full variational solution, in order to obtain accurate results for $\delta \geq 3$:

$$\begin{aligned} Q_T = {} & (\sqrt{\pi}\,\delta^2)^{-1} \times [c_{11}c_{22}d_{22} - d_{12}^2 c_{22} - c_{11}d_{23}^2 + 2c_{12}d_{12}d_{23} - c_{12}^2 d_{22}]^{-1} \\ & \times [-d_1^2 d_{22}c_{22} - c_{11}d_2^2 c_{22} + 2d_1 d_{12}d_2 c_{22} + d_1^2 d_{23}^2 - 2d_1 c_{12}d_2 d_{23} + c_{12}^2 d_2^2] \end{aligned} \tag{18}$$

where the coefficients are given by:

$$\begin{aligned} c_{11} = {} & -\frac{\delta^4}{4}\alpha_t - \frac{4}{3}\sqrt{\pi}\delta^3 + \sqrt{\pi}\delta^3\alpha_t + 4\delta^2 - 4\delta^2\alpha_t - 4\sqrt{\pi}\delta\alpha_n\alpha_t + 12\sqrt{\pi}\delta\alpha_t \\ & + 4\sqrt{\pi}\delta\alpha_n + 16\alpha_n\alpha_t - 32\alpha_t - 16\alpha_n - \frac{8}{3\pi}\delta^3\hat{J}_1 - \frac{32}{\pi}\delta\hat{J}_2 \\ & + 16\delta^2\mathcal{F}_0\alpha_n(1-\alpha_t) + 16\delta^2\mathcal{F}_1(1-\alpha_t)(1-\alpha_n), \end{aligned} \tag{19}$$

$$c_{12} = -\delta^2\alpha_t + 2\sqrt{\pi}\delta\alpha_t - 8\alpha_t, \quad c_{22} = -4\alpha_t, \tag{20}$$

$$c_1 = \frac{\sqrt{\pi}}{6}\delta^3 - \frac{\delta^2}{2}\alpha_t + 2\sqrt{\pi}\delta + \sqrt{\pi}\delta\alpha_t - 4\alpha_t, \quad c_2 = 2\sqrt{\pi}\delta - 2\alpha_t, \tag{21}$$

$$d_{12} = \frac{\delta^2}{4}\alpha_t + \frac{\sqrt{\pi}}{2}\delta\alpha_n\alpha_t - \sqrt{\pi}\delta\alpha_t - \frac{\sqrt{\pi}}{2}\delta\alpha_n - 4\alpha_n\alpha_t + 6\alpha_t + 4\alpha_n + \frac{8}{\pi}\delta\hat{J}_3, \tag{22}$$

$$d_{22} = -2\alpha_t^3 + 6\alpha_t^2 + \alpha_n\alpha_t - \frac{29}{4}\alpha_t - \alpha_n - \frac{2}{\pi}\delta\hat{J}_4, \tag{23}$$

$$d_1 = 2\sqrt{\pi}\delta, \quad d_2 = -\frac{5}{2}\sqrt{\pi}\delta, \quad d_{23} = \alpha_t, \tag{24}$$

with $\mathcal{F}_0 = 0.196079$ and $\mathcal{F}_1 = 0.247679$, $\hat{J}_1 = -1.4180$, $\hat{J}_2 = 1.8909$, $\hat{J}_3 = 0.9449$, $\hat{J}_4 = 4.7252$.

3 Results and Discussion

Since the Poiseuille flow has been widely considered in the literature and, moreover, it is strongly dependent only on the tangential momentum accommodation coefficient, α_t, in the following we will focus on the quantities of interest for the thermal-creep problem, G_T and Q_T. In order to assess the accuracy of the analytical formulas (17) and (18), derived in Sect. 2, we report in Tables 1 and 2 a comparison between our variational outputs and the numerical results obtained in [4, 5]. These tables show a good agreement (the discrepancy lies, on average, within an error of 10%) for all values of the accommodation coefficients α_t and α_n, as the rarefaction parameter varies in the range $\delta \geq 3$. Indeed, the variational estimates for the temperature-driven mass flow rate G_T exhibit a larger deviation from the numerical findings than those for the heat flux Q_T. This is especially true for $\delta = 3$, thus demonstrating that this value of the rarefaction parameter represents the lower limit of validity of our analytical formulas. The closed-form expressions (17) and (18) allow us to investigate deeper the mathematical properties of the solution to the problem at hand. Indeed, a closer inspection of the dependency of $\sigma_{1,T}$ and $\sigma_{2,T}$, in Eq. (17), on the accommodation coefficients has revealed that there is a continuous set of values for (α_t, α_n) leading to the same estimates for the mass flow rate G_T. This remark holds true also for the heat flux Q_T. As an example, Table 3 shows that, for a pair of different values of the accommodation coefficients (relevant for the comparison with recent experimental measurements [1, 2]), the same estimate for G_T, and also for Q_T, is obtained, in terms of the rarefaction parameter δ. In the specific case of the thermal creep problem, we have found that one can get the same values for the mass flow rate G_T (and also for the heat flux Q_T), when both accommodation coefficients range from 0.1 to 0.9. Further investigation is needed to clarify whether these findings are related to the mathematical result obtained by Chen [3], according to which a well-posed steady and global solution of the Boltzmann equation with Cercignani-Lampis boundary conditions can be constructed only when α_t and α_n are close to 1.

Table 1 Thermal-creep flow rate G_T: comparison between our variational outputs [Var(HS)] and the numerical results reported in [4]

δ	α_t	α_n	0.	0.2	0.4	0.5	0.7	0.9	1.
3.	0.1	Var(HS)	0.2512	0.2490	0.2440	0.2405	0.2312	0.2192	0.2121
		[4]	0.247	0.248	0.249	0.250	0.250	0.251	0.251
	0.2	Var(HS)	0.2537	0.2495	0.2431	0.2391	0.2294	0.2174	0.2106
		[4]	0.238	0.239	0.240	0.240	0.241	0.242	0.242
	0.4	Var(HS)	0.2510	0.2451	0.2378	0.2338	0.2246	0.2143	0.2086
		[4]	0.227	0.228	0.229	0.229	0.230	0.230	0.231
	0.5	Var(HS)	0.2468	0.2408	0.2339	0.2301	0.2219	0.2129	0.2080
		[4]	0.224	0.225	0.226	0.226	0.226	0.227	0.227
	0.8	Var(HS)	0.2260	0.2225	0.2189	0.2171	0.2132	0.2093	0.2073
		[4]	0.222	0.222	0.222	0.223	0.223	0.223	0.223
	1.	Var(HS)	0.2072	0.2072	0.2072	0.2072	0.2072	0.2072	0.2072
		[4]	0.223	0.223	0.223	0.223	0.223	0.223	0.223
	1.2	Var(HS)	0.1849	0.1896	0.1942	0.1965	0.2009	0.2051	0.2072
		[4]	0.224	0.223	0.223	0.223	0.223	0.223	0.222
5.	0.1	Var(HS)	0.1524	0.1570	0.1606	0.1620	0.1641	0.1651	0.1653
		[4]	0.152	0.157	0.161	0.164	0.168	0.172	0.174
	0.2	Var(HS)	0.1563	0.1596	0.1621	0.1630	0.1643	0.1648	0.1648
		[4]	0.149	0.153	0.158	0.160	0.163	0.167	0.169
	0.4	Var(HS)	0.1613	0.1628	0.1638	0.1641	0.1644	0.1643	0.1640
		[4]	0.148	0.151	0.154	0.155	0.158	0.161	0.162
	0.5	Var(HS)	0.1628	0.1636	0.1641	0.1643	0.1643	0.1641	0.1638
		[4]	0.148	0.151	0.153	0.154	0.157	0.159	0.160
	0.8	Var(HS)	0.1643	0.1643	0.1642	0.1641	0.1639	0.1637	0.1636
		[4]	0.153	0.154	0.155	0.155	0.156	0.157	0.158
	1.	Var(HS)	0.1635	0.1635	0.1635	0.1635	0.1635	0.1635	0.1635
		[4]	0.158	0.158	0.158	0.158	0.158	0.158	0.158
	1.2	Var(HS)	0.1615	0.1620	0.1625	0.1627	0.1631	0.1634	0.1635
		[4]	0.162	0.161	0.160	0.160	0.159	0.158	0.157
	1.5	Var(HS)	0.1553	0.1575	0.1594	0.1602	0.1617	0.1628	0.1633
		[4]	0.166	0.164	0.161	0.160	0.158	0.156	0.155
	2.	Var(HS)	0.1286	0.1376	0.1454	0.1488	0.1547	0.1593	0.1611
		[4]	0.158	0.155	0.151	0.149	0.145	0.141	0.139
10.	0.1	Var(HS)	0.0768	0.0813	0.0856	0.0876	0.0915	0.0952	0.0969
		[4]	0.0773	0.0817	0.0859	0.0879	0.0918	0.0955	0.0973
	0.2	Var(HS)	0.0796	0.0835	0.0871	0.0888	0.0922	0.0953	0.0968
		[4]	0.0775	0.0813	0.0849	0.0867	0.0901	0.0934	0.0950
	0.4	Var(HS)	0.0847	0.0873	0.0898	0.0910	0.0933	0.0955	0.0966
		[4]	0.0793	0.0819	0.0845	0.0858	0.0883	0.0908	0.0920
	0.5	Var(HS)	0.0869	0.0890	0.0910	0.0920	0.0939	0.0957	0.0965
		[4]	0.0810	0.0830	0.0850	0.0860	0.0880	0.0900	0.0910
	0.8	Var(HS)	0.0929	0.0937	0.0944	0.0947	0.0954	0.0961	0.0965
		[4]	0.0860	0.0868	0.0876	0.0880	0.0888	0.0896	0.0900
	1.	Var(HS)	0.0965	0.0965	0.0965	0.0965	0.0965	0.0965	0.0965
		[4]	0.0900	0.0899	0.0899	0.0899	0.0899	0.0899	0.0899
	1.2	Var(HS)	0.0997	0.0991	0.0985	0.0981	0.0975	0.0968	0.0965
		[4]	0.0938	0.0930	0.0922	0.0918	0.0911	0.0903	0.0899
	1.5	Var(HS)	0.1038	0.1025	0.1011	0.1003	0.0988	0.0972	0.0964
		[4]	0.0984	0.0965	0.0947	0.0937	0.0917	0.0898	0.0888
	2.	Var(HS)	0.1065	0.1050	0.1032	0.1022	0.0999	0.0973	0.0959
		[4]	0.0992	0.0961	0.0927	0.0908	0.0871	0.0833	0.0814

Table 2 Heat flow rate Q_T: comparison between our variational outputs [Var(HS)] and the numerical results reported in [5]

δ	α_t	α_n	0.	0.2	0.4	0.5	0.7	0.9	1.
3.	0.1	Var(HS)	1.1474	1.1258	1.1052	1.0952	1.0759	1.0574	1.0485
	0.2	Var(HS)	1.0899	1.0721	1.0550	1.0466	1.0305	1.0150	1.0074
	0.4	Var(HS)	1.0155	1.0035	0.9918	0.9861	0.9749	0.9641	0.9588
	0.5	Var(HS)	0.9911	0.9815	0.9721	0.9675	0.9584	0.9496	0.9452
		[5]				0.9789			0.9560
	0.6	Var(HS)	0.9724	0.9649	0.9576	0.9540	0.9469	0.9400	0.9365
	0.8	Var(HS)	0.9461	0.9425	0.9391	0.9373	0.9339	0.9304	0.9287
	1.	Var(HS)	0.9277	0.9277	0.9277	0.9277	0.9277	0.9277	0.9277
		[5]				0.9329			0.9329
	1.2	Var(HS)	0.9101	0.9133	0.9166	0.9182	0.9215	0.9249	0.9266
	1.5	Var(HS)	0.8719	0.8794	0.8871	0.8910	0.8989	0.9070	0.9111
		[5]				0.8897			0.9106
	2.	Var(HS)	0.7518	0.7639	0.7765	0.7830	0.7965	0.8105	0.8178
5.	0.1	Var(HS)	0.7068	0.6991	0.6918	0.6882	0.6812	0.6745	0.6712
	0.2	Var(HS)	0.6844	0.6782	0.6723	0.6693	0.6636	0.6581	0.6554
	0.4	Var(HS)	0.6547	0.6506	0.6467	0.6447	0.6409	0.6371	0.6353
	0.5	Var(HS)	0.6450	0.6418	0.6386	0.6371	0.6340	0.6309	0.6294
		[5]				0.6505			0.6410
	0.6	Var(HS)	0.6377	0.6352	0.6328	0.6316	0.6292	0.6268	0.6256
	0.8	Var(HS)	0.6280	0.6268	0.6256	0.6250	0.6239	0.6227	0.6221
	1.	Var(HS)	0.6217	0.6217	0.6217	0.6217	0.6217	0.6217	0.6217
		[5]				0.6320			0.6320
	1.2	Var(HS)	0.6155	0.6167	0.6178	0.6183	0.6195	0.6206	0.6212
	1.5	Var(HS)	0.6008	0.6034	0.6060	0.6074	0.6100	0.6128	0.6141
		[5]				0.6141			0.6232
	2.	Var(HS)	0.5474	0.5512	0.5552	0.5572	0.5613	0.5655	0.5676
10.	0.1	Var(HS)	0.3606	0.3585	0.3566	0.3556	0.3537	0.3519	0.3510
	0.2	Var(HS)	0.3545	0.3528	0.3511	0.3503	0.3487	0.3471	0.3463
	0.4	Var(HS)	0.3459	0.3447	0.3435	0.3429	0.3418	0.3407	0.3402
	0.5	Var(HS)	0.3430	0.3420	0.3411	0.3406	0.3397	0.3388	0.3383
		[5]				0.3516			0.3491
	0.6	Var(HS)	0.3407	0.3400	0.3392	0.3389	0.3381	0.3374	0.3371
	0.8	Var(HS)	0.3377	0.3374	0.3370	0.3368	0.3365	0.3361	0.3359
	1.	Var(HS)	0.3358	0.3358	0.3358	0.3358	0.3358	0.3358	0.3358
		[5]				0.3468			0.3468
	1.2	Var(HS)	0.3339	0.3342	0.3346	0.3348	0.3351	0.3355	0.3356
	1.5	Var(HS)	0.3292	0.3300	0.3308	0.3312	0.3320	0.3329	0.3333
		[5]				0.3422			0.3446
	2.	Var(HS)	0.3100	0.3113	0.3127	0.3134	0.3148	0.3163	0.3170

Table 3 Variational estimates of the mass flow rate G_T and heat flux Q_T for a pair of different values of α_t and α_n

	$\alpha_t = 0.8$	$\alpha_n = 0.15$	$\alpha_t = 0.83$	$\alpha_n = 0.28$	$\alpha_t = 0.88$	$\alpha_n = 0.33$
	$\alpha_t = 0.63$	$\alpha_n = 0.54$	$\alpha_t = 0.63$	$\alpha_n = 0.67$	$\alpha_t = 0.65$	$\alpha_n = 0.77$
δ	G_T	Q_T	G_T	Q_T	G_T	Q_T
3.	0.223	0.94	0.219	0.94	0.215	0.93
5.	0.164	0.63	0.164	0.63	0.164	0.62
10.	0.0935	0.34	0.0943	0.34	0.0951	0.33

Acknowledgements Silvia Lorenzani is supported by GNFM of INDAM, Italy.

References

1. Nguyen NN, Graur I, Perrier P, Lorenzani S (2020) Variational derivation of thermal slip coefficients on the basis of the Boltzmann equation for hard-sphere molecules and Cercignani-Lampis boundary conditions: comparison with experimental results. Phys Fluids 32:102011
2. Missoni T, Yamaguchi H, Graur I, Lorenzani S (2021) Extraction of tangential momentum and normal energy accommodation coefficients by comparing variational solutions of the Boltzmann equation with experiments on thermal creep gas flow in microchannels. Fluids 6:445
3. Chen H (2020) Cercignani-Lampis boundary in the Boltzmann theory. Kinet Relat Models 13:549
4. Basdanis T, Tatsios G, Valougeorgis D (2022) Gas-surface interaction in rarefied gas flows through long capillaries via the linearized Boltzmann equation with various boundary conditions. Vacuum 202:111152
5. Basdanis T (2024) Private communication

Open Access This chapter is licensed under the terms of the Creative Commons Attribution 4.0 International License (http://creativecommons.org/licenses/by/4.0/), which permits use, sharing, adaptation, distribution and reproduction in any medium or format, as long as you give appropriate credit to the original author(s) and the source, provide a link to the Creative Commons license and indicate if changes were made.

The images or other third party material in this chapter are included in the chapter's Creative Commons license, unless indicated otherwise in a credit line to the material. If material is not included in the chapter's Creative Commons license and your intended use is not permitted by statutory regulation or exceeds the permitted use, you will need to obtain permission directly from the copyright holder.

Existence and Regularity of Axisymmetric Weak Solutions to the Spatially Homogeneous Landau Equation

Jin Woo Jang and Junha Kim

Abstract We provide a concise summary of our recent findings on measure-valued solutions to the spatially homogeneous Landau equation for hard potentials [6]. Specifically, we prove the existence of axisymmetric measure-valued solutions for any axisymmetric initial data in $\mathcal{P}_p(\mathbb{R}^3)$ ($p \geq 2$). Furthermore, we prove that these solutions become instantaneously analytic for $t > 0$, except when the initial data is a single Dirac mass. For soft potentials and Maxwellian molecules, we show that solutions cannot remain confined to a fixed line, even when starting from line-concentrated initial data.

Keywords Landau kinetic equation · Measure-valued solutions · Axisymmetry

1 Introduction

The spatially homogeneous Landau equation serves as a fundamental model in kinetic theory, capturing the dynamics of particle distributions influenced by grazing collisions. This paper aims to announce the recent establishment of the existence of weak solutions in [6] that preserve axisymmetry, provided the initial data is also axisymmetric.

For $t \in [0, T]$ and $v \in \mathbb{R}^3$ with some $T > 0$, the spatially homogeneous Landau kinetic equation is expressed as:

$$\partial_t f(t, v) = Q(f, f) = \partial_i \int_{\mathbb{R}^3} a_{ij}(v - v_*) \left(\partial_j f(v) f(v_*) - \partial_j f(v_*) f(v)\right) dv_*, \tag{1}$$

J. W. Jang
Department of Mathematics, Pohang University of Science and Technology (POSTECH), Pohang, South Korea
e-mail: jangjw@postech.ac.kr

J. Kim (✉)
Department of Mathematics, Ajou University, Suwon, Gyeonggi-do, South Korea
e-mail: junha02@ajou.ac.kr

© The Author(s) 2026

M. Grabe et al. (eds.), *Rarefied Gas Dynamics*, Springer Aerospace Technology,
https://doi.org/10.1007/978-3-032-00094-1_2

where $f(t, v)$ is abbreviated as $f(v)$. The kernel a_{ij} is defined by:

$$a_{ij}(z) = \left(\delta_{ij} - \frac{z_i z_j}{|z|^2}\right)|z|^{\gamma+2}, \quad \gamma \in [-3, 1],$$

with δ_{ij} representing the Kronecker delta ($\delta_{ij} = 1$ if $i = j$, and $\delta_{ij} = 0$ otherwise). The case $\gamma \in (0, 1]$ corresponds to hard potentials, $\gamma = 0$ to Maxwellian molecules, and $\gamma \in [-3, 0)$ to soft potentials.

Defining the following auxiliary quantities:

$$b_i(z) := \partial_j a_{ij}(z) = -2z_i|z|^\gamma, \quad c(z) := \partial_i \partial_j a_{ij}(z) = -2(\gamma + 3)|z|^\gamma, \text{ for } \gamma > -3,$$

$$c(z) := -8\pi\delta(z), \text{ for } \gamma = -3,$$

and their convolutions with f:

$$\overline{a_{ij}(v)} := a_{ij} * f, \quad \overline{b_i(v)} := b_i * f, \quad \overline{c(v)} := c * f,$$

the Landau equation can be reformulated as:

$$\partial_t f = \nabla \cdot (\overline{a}\nabla f - \overline{b} f), \quad \text{or equivalently,} \quad \partial_t f = \overline{a_{ij}}\partial_i \partial_j f - \overline{c} f.$$

It is also noted that the kernel satisfies the bounds:

$$|a_{ij}(z)| \le |z|^{2+\gamma}, \quad |b_i(z)| \le |z|^{1+\gamma}.$$

1.1 Measure-Valued Solutions

In this paper, we focus on measure-valued solutions to the Landau equation. To this end, we begin by introducing the relevant space of probability measures. Let $\mathcal{P}(\mathbb{R}^3)$ denote the set of probability measures on $\mathbb{R}^3$. For $p > 0$, define

$$\mathcal{P}_p(\mathbb{R}^3) := \left\{ f \in \mathcal{P}(\mathbb{R}^3) \, ; \int_{\mathbb{R}^3} |v|^p f(dv) < \infty \right\}.$$

For $p \ge 1$, the space is equipped with the p-Wasserstein distance, given by

$$\mathcal{W}_p(\mu, \nu) := \left(\inf_{\gamma \in \Pi(\mu,\nu)} \int_{\mathbb{R}^3 \times \mathbb{R}^3} \text{dist}(x, y)^p \, d\gamma(x, y) \right)^{\frac{1}{p}},$$

where $\Pi(\mu, \nu)$ denotes the set of all couplings between μ and ν. For $p \in (0, 1)$, $\mathcal{W}_p$ can still be defined by omitting the $1/p$-power in the infimum.

Here, we define the concept of measure-valued weak solutions for the Landau equation in the hard potential case:

Definition 1 **(Measure-Valued Weak Solution)** Let $\gamma \in (0, 1]$. A function $f(t)$ is called a weak solution to the Landau equation if it satisfies the following conditions:

1. Regularity:

$$f \in L^{\infty}_{\text{loc}}((0, \infty); \mathcal{P}_2(\mathbb{R}^3)) \cap L^{1}_{\text{loc}}((0, \infty); \mathcal{P}_{2+\gamma}(\mathbb{R}^3)),$$

   where $\mathcal{P}_p(\mathbb{R}^3)$ denotes the set of probability measures with finite p-th moment.
2. Energy Inequality:

$$\frac{1}{2}\int_{\mathbb{R}^3} |v|^2 f_t(dv) \leq \frac{1}{2}\int_{\mathbb{R}^3} |v|^2 f_0(dv), \quad \forall t \geq 0.$$

3. Weak Formulation: For all test functions $\varphi \in C^2_b(\mathbb{R}^3)$ and $T \geq 0$, the following equality holds:

$$\begin{aligned}\int_{\mathbb{R}^3} \varphi(v) f_T(dv) - \int_{\mathbb{R}^3} \varphi(v) f_0(dv) &= \int_0^T \int_{\mathbb{R}^3}\int_{\mathbb{R}^3} a_{ij}(v - v_*)\partial_i\partial_j\varphi(v) f_t(dv_*) f_t(dv)\,\mathrm{d}t \\ &\quad + 2\int_0^T \int_{\mathbb{R}^3}\int_{\mathbb{R}^3} b_i(v - v_*)\partial_i\varphi(v) f_t(dv_*) f_t(dv)\,\mathrm{d}t.\end{aligned}$$

Here, $a_{ij}(z)$ and $b_i(z)$ are the coefficients defined in terms of the relative velocity $z = v - v_*$, and f_0 denotes the initial measure.

1.2 Main Theorem

The main establishment is as follows:

Theorem 1 (Theorem 1.6 of [6])

Let $\gamma \in (0, 1]$ and suppose the initial profile $f_0 \in \mathcal{P}_p(\mathbb{R}^3)$ for $p \geq 2$ is axisymmetric. Then, there exists an axisymmetric measure-valued weak solution to the Landau equation, satisfying

$$f \in C([0,\infty);\mathcal{P}(\mathbb{R}^3)) \cap L^\infty((0,\infty);\mathcal{P}_p(\mathbb{R}^3)) \cap L^1_{loc}((0,\infty);\mathcal{P}_{p+\gamma}(\mathbb{R}^3)).$$

Furthermore, if f_0 is not a single Dirac mass, the solution f becomes analytic for all $t > 0$.

Remark 1 Several observations regarding the main theorem are as follows:

1. **Uniqueness for $p > 2$:** If $f_0 \in \mathcal{P}_p(\mathbb{R}^3)$ is axisymmetric with $p > 2$, the axisymmetric solution f is unique as a weak solution to the Landau equation, starting from f_0. Uniqueness is established in terms of the optimal transportation cost $\mathcal{T}_p(f, \tilde{f})$; see [4, Theorem 8].
2. **Soft potential case:** For $\gamma \in [-3, 0)$, it is shown that there are no axisymmetric solutions concentrated along a line, even if the initial data is line-concentrated (see Lemma 1). Specifically, for $\gamma \in [-3, -2)$, Golse, Imbert, Ji, and Vasseur [5] proved that axisymmetric weak solutions are smooth away from the axis of symmetry.
3. **Moderately soft potential case:** For $\gamma \in (-2, 0)$, Fournier and Guérin [3, Corollary 4] established the existence of weak solutions.

2 Escape of a Line Support

In this section, we introduce a key lemma that demonstrates the solution escapes a line support instantaneously. Namely we have the following lemma.

Lemma 1 (Lemma 2.1 of *[6]*) *Let $\gamma \in [-3, 1]$. Let $f \in L^1_{loc}((0,\infty);\mathcal{P}_{2+\gamma}(\mathbb{R}^3))$ be any weak solution to the Landau equation which is not a single Dirac mass. Let ℓ be any given line in $\mathbb{R}^3$. Then there is no time interval $[t_1, t_2] \in (0,\infty)$ with $t_1 < t_2$ such that $f(t,\cdot)$ is concentrated on a line $\ell \in \mathbb{R}^3$ for a.e. $t \in [t_1, t_2]$.*

Remark 2 Here are some observations regarding the lemma discussed above:

1. Lemma 1 applies not only to hard potentials where $\gamma \in (0, 1]$, but also extends to soft potentials and Maxwellian molecules with $\gamma \in [-3, 0]$.
2. Lemma 1 pertains to a specific, fixed line ℓ.
3. The proof of this lemma is straightforward and significantly simpler compared to [4, Lemma 16]. Additionally, the constraints $\gamma \in (0, 1]$ and $f_0 \in \mathcal{P}_4(\mathbb{R}^3)$ are not required in this case. For reference, Lemma 16 of [4] states:

Lemma 2 (Lemma 16 of *[4]*) *Let $\gamma \in (0, 1]$, $f_0 \in \mathcal{P}_4(\mathbb{R}^3)$, where f_0 is not a single Dirac mass, and let f be a weak solution of the Landau equation starting from f_0. Then, for any given $t_0 > 0$, there exists $t \in (0, \delta)$ such that $f(t)$ is not concentrated on any line $\ell \subset \mathbb{R}^3$.*

4. Our lemma addresses a fixed line $\ell \subset \mathbb{R}^3$. Even if the support of the solution moves away from the line ℓ instantaneously, it may still lie on a different line

(e.g., a rotating line). This does not necessarily imply that the support contains three non-collinear points. In this respect, Lemma 16 of [4] is more general, as it excludes the possibility of the support being confined to any line, including rotating ones. To ensure the support contains a triangle at any given time, we consider axisymmetric solutions when proving existence.

The proof of our main theorem (Theorem 1) fundamentally relies on a pivotal lemma (Lemma 1), which asserts that the support of the solution instantly escapes confinement to a single line.

3 Ellipticity of $\overline{a_{ij}(v)}$

In the paper [2], it is established that the Landau collision operator has the following elliptic property even for a solution with infinite entropy:

Lemma 3 (Lemma 9 of [2]) *Let $T > 0$ and f be a non-zero non-negative function f in $L^\infty([0,T]; L^1_2(\mathbb{R}^3)) \cap C([0,T]; W^{-2,1}(\mathbb{R}^3))$ with $f_{in} \in L^1_2(\mathbb{R}^3)$. Then, there exist constants $\Delta t \in (0,T]$ and $K > 0$ such that*

$$\overline{a_{ij}(v)}\xi_i\xi_j \geq K(1+|v|^2)^{\frac{\gamma}{2}}|\xi|^2, \qquad v, \xi \in \mathbb{R}^3, \ t \in [0, \Delta t].$$

In [2, Remarks of Lemma 9], it is stated that the proof of the lemma allows in fact the initial condition f_{in} to be a measure, provided that it is not concentrated on a single line. In our case for the proof of Theorem 1, by our key lemma (Lemma 1) we observe that the support of a solution f instantaneously escapes a line support for any $t > 0$. For any $t_0 > 0$, on the time interval $[t_0, \infty)$, the measure f_{t_0} can be treated as the initial profile in Lemma 3, allowing us to establish ellipticity.

4 Gain of Moments

We present a theorem on the gain of moments for the hard potential case.

If the initial profile is in $\mathcal{P}_p(\mathbb{R}^3)$ with $p > 2$, we use the following theorem on the gain-of-moments property:

Theorem 2 (Theorems 3 and 6 of [2]) *Let f be any weak solution of the Landau equation (1) with initial datum $f_{in} \in L^1_2(\mathbb{R}^3)$, satisfying the decay of energy*

$$E(f(t,\cdot)) \leq E(f_{in}(\cdot)), \text{ for } t \geq 0.$$

Then

1. *For all $s > 0$, if $M_s(f_{in}) < +\infty$, then $\sup_{t\geq 0} M_s(f(t,\cdot)) < +\infty$, and for all $T > 0$,*
$$\int_0^T M_{s+\gamma}(f(t,\cdot))dt < +\infty.$$
2. *For all time $t_0 > 0$, and all number $s > 0$, there exists a constant $C_{t_0} > 0$, depending only on M_{in}, E_{in}, and t_0, such that for all time $t \geq t_0$,*
$$M_s(f(t,\cdot)) \leq C_{t_0}.$$
3. *For any $t \geq 0$, $E(f(t,\cdot)) = E_{in}$: the energy is automatically conserved.*
4. *If $f_{in} \in L^1_{2+\delta}$ for some $\delta > 0$, there exists a weak solution starting from f_{in}.*
5. *If $f_{in} \in L^1_{2+\delta}$ for some $\delta > 0$ and f_{in} is not concentrated on a line, there exists a weak solution starting from f_{in} such that for any $t_0 > 0$, $H(f(t)) < \infty$ for all $t > t_0$ and*
$$\sup_{t\geq t_0} \|f(t)\|_{H^k_s} < \infty, \qquad k \in \mathbb{N}, \quad s \geq 0. \tag{2}$$

On the other hand, in the critical case when $p = 2$ and the initial profile is in $\mathcal{P}_2(\mathbb{R}^3)$, we instead argue as follows. If $p = 2$, we apply the de la Vallée Poussin theorem to ensure the existence of a C^2 function $h : [0,\infty) \to [0,\infty)$ satisfying the following properties: $h'' \in [0,1]$, $h'(0) = 1$, $h'(\infty) = \infty$, and $\int_{\mathbb{R}^3} h(|v|^2) f_0(dv) < \infty$. According to [4, Eq. (29)], there exists a finite constant K_T for any $T > 0$ such that for all $n \geq n_0$:

$$\sup_{t\in[0,T]} \int_{\mathbb{R}^3} h(|v|^2) f_t(dv) + \int_0^T \int_{\mathbb{R}^3} |v|^{2+\gamma} h'(|v|^2) f_t(dv)\, dt \leq K_T.$$

These moments estimates will be used to prove the relative compactness of each measure f_t in $\mathcal{P}(\mathbb{R}^3)$.

5 Proof of the Main Theorem

The proof of the main theorem (Theorem 1) has several steps. The first step is to regularize the measure-valued initial condition f_0 as

$$f_0^n := (\alpha_n^{-1} \mathbf{1}_{|v|\leq n} f_0(dv)) * \sigma_n, \qquad n \geq n_0, \tag{3}$$

with the total mass $\alpha_n := \int_{\mathbb{R}^3} \mathbf{1}_{|v|\le n} f_0(dv)$ for some $n_0 \in \mathbb{N}$. In addition, we regularize the equation by adding an additional ellipticity for each $\varepsilon > 0$ as

$$\partial_t f^\varepsilon = Q^\varepsilon(f^\varepsilon, f^\varepsilon) + \varepsilon \Delta_v f^\varepsilon, \tag{4}$$

where Q^ε is a smoothly mollified version of Q such that the coefficients are smooth. The linearized version of (4) has a solution by the standard parabolic theory. Then the solution sequence also has a fixed point f^ε by the Schauder fixed-point theorem with the regularized initial data f_0^n.

Before we pass to the limit $\varepsilon \to 0$ and $n \to \infty$, we can also show that each f^ε is axisymmetric if f_0^n is. This is by showing that $f(Tv)$ satisfies the linear system, where $T = T_\theta$ be a 3×3 rotation matrix such that

$$T := \begin{pmatrix} \cos\theta & -\sin\theta & 0 \\ \sin\theta & \cos\theta & 0 \\ 0 & 0 & 1 \end{pmatrix}, \qquad \theta \in [0, 2\pi).$$

This can be obtained by showing

$$\varepsilon(\Delta f)(Tv) = \varepsilon \Delta(f(Tv)), \text{ for } \theta \in [0, 2\pi),$$

and that

$$Q^\varepsilon(g, f)(Tv) = Q^\varepsilon(g, f(Tv))(v),$$

for a given axisymmetric g.

Then by further obtaining a uniform-in-ε estimate on the energy and the entropy, we have $\{f_t^\varepsilon\}_{\varepsilon>0}$ is weakly compact in $L^1(\mathbb{R}^3_v)$ for each $t \in [0, T]$ by satisfying the Dunford-Pettis compactness criterion. Moreover, using these moment estimates of the previous section, one can show that by the Arzela-Ascoli theorem, there exists a subsequence $\{f^{\varepsilon'}\}_{\varepsilon'>0} \subset \{f^\varepsilon\}_{\varepsilon>0}$ and a limit $f^n \in L^\infty(0, T; L^1_s \cap L\log L(\mathbb{R}^3))$ that serves as a weak solution to (1), corresponding to the initial data f_0^n specified in (3).

Furthermore, we prove that the solution is indeed axisymmetric if the initial profile is axisymmetric. To demonstrate that the solution f^n retains its axisymmetric property, we confirm that the collision operator $Q(f^n, f^n)$ preserves axisymmetry. For an axisymmetric test function $\phi(v) = \phi(T_\theta v)$, the rotational invariance of $a_{ij}(v - v_*)$ ensures that:

$$\int_{\mathbb{R}^3} Q(f^n, f^n)\phi \, dv = \int_{\mathbb{R}^3} Q(f^n(T_\theta v), f^n(T_\theta v))\phi \, dv,$$

where T_θ represents the rotation operator about the symmetry axis. Given that the initial data is axisymmetric, it follows that $f^n(t, v) = f^n(t, T_\theta v)$ for all $t > 0$.

Lastly, we pass to the limit as $n \to \infty$. For $p \ge 2$, we can proceed to show that for each $t \ge 0$, the family $\{f_t^n\}_{n\ge n_0}$ is relatively compact in $\mathcal{P}(\mathbb{R}^3)$. And together with

additional proof on the equicontinuity in time, we use the Arzela-Ascoli theorem to prove that the family $\{f_t^n\}_{n\geq n_0}$ has a limit in $C([0,T];\mathcal{P}(\mathbb{R}^3))$ in the weak sense. This provides the existence of a solution.

Since the support of our solution instantaneously escapes a line support in any time interval $[t_0,\infty)$ for any $t_0>0$, we obtain the ellipticity and the smoothness by the known bootstrap argument $L\log L\to L^2\to H^1\to\mathcal{S}$ as in Desvillettes-Villani [2]. Since the axisymmetric solution is now bounded in H^k for any $k\in\mathbb{N}$, we obtain that the solution is smooth and hence is analytic for any $t>0$ by the result of Chen-Li-Xu in [1].

References

1. Chen H, Li WX, Xu CJ (2010) Analytic smoothness effect of solutions for spatially homogeneous Landau equation. J Different Equat 248(1):77–94. https://doi.org/10.1016/j.jde.2009.08.006
2. Desvillettes L, Villani C (2000) On the spatially homogeneous Landau equation for hard potentials. I. Existence, uniqueness and smoothness. Comm Partial Different Equati 25(1–2):179–259. https://doi.org/10.1080/03605300008821512
3. Fournier N, Guérin H (2009) Well-posedness of the spatially homogeneous Landau equation for soft potentials. J Funct Anal 256(8):2542–2560. https://doi.org/10.1016/j.jfa.2008.11.008
4. Fournier N, Heydecker D (2021) Stability, well-posedness and regularity of the homogeneous Landau equation for hard potentials. Annales de l'Institut Henri Poincaré C, Analyse non linéaire 38(6):1961–1987. https://www.sciencedirect.com/science/article/pii/S0294144921000251
5. Golse F, Imbert C, Ji S, Vasseur AF (2022) Local regularity for the space-homogeneous Landau equation with very soft potentials
6. Jang JW, Kim J (2025) On the axially symmetric solutions to the spatially homogeneous Landau equation

Open Access This chapter is licensed under the terms of the Creative Commons Attribution 4.0 International License (http://creativecommons.org/licenses/by/4.0/), which permits use, sharing, adaptation, distribution and reproduction in any medium or format, as long as you give appropriate credit to the original author(s) and the source, provide a link to the Creative Commons license and indicate if changes were made.

The images or other third party material in this chapter are included in the chapter's Creative Commons license, unless indicated otherwise in a credit line to the material. If material is not included in the chapter's Creative Commons license and your intended use is not permitted by statutory regulation or exceeds the permitted use, you will need to obtain permission directly from the copyright holder.

Maxwell-Stefan Diffusion Model Based on Moment Equations for Gas Mixtures

Milana Čolić and Srboljub Simić

Abstract The aim of this paper is to derive an isothermal Maxwell-Stefan model of diffusion from the moment equations of the Boltzmann system describing a mixture of monatomic and polyatomic gases. A comprehensive diffusion asymptotic analysis of the moment equations, corresponding to an isothermal multi-velocity model of Eulerian fluids, is carried out. In particular, the diffusive scaling of the explicit momentum production term–computed from the Boltzmann collision operator with a cutoff hard-potential-type kernel–enables the explicit determination of Maxwell-Stefan diffusion coefficients in terms of mesoscopic parameters. The model is subsequently validated against the Duncan and Toor experiment as a benchmark, confirming its match with experimental data.

Keywords Gas mixtures · Eulerian fluids · Polyatomic gases · Moment equations · Diffusion limit · Maxwell-stefan model

1 Introduction

A mixture is a medium composed of several identifiable constituents whose interactions–chemical, mechanical, thermal, or electromagnetic–pose significant challenges for modeling, even in simplified settings [11]. For example, considering only mechanical interactions still leaves many open problems [8, 16].

Diffusion is a central phenomenon in mixtures, describing mass transport between components. The classical Fick model represents diffusion as a macroscopic flow from regions of high to low concentration. It combines mass balance equations with

M. Čolić
Institute of Mathematics and Scientific Computing, University of Graz, Graz, Austria

M. Čolić (✉) · S. Simić
Department of Mathematics and Informatics, University of Novi Sad, Novi Sad, Serbia
e-mail: milana.colic@uni-graz.at

S. Simić
e-mail: ssimic@uns.ac.rs

© The Author(s) 2026

M. Grabe et al. (eds.), *Rarefied Gas Dynamics*, Springer Aerospace Technology,
https://doi.org/10.1007/978-3-032-00094-1_3

constitutive relations for diffusion fluxes [8], and can also be derived from the Boltzmann equation via Chapman-Enskog asymptotics, under the assumption of local equilibrium [11]. Although widely used in engineering, Fick's law neglects the fact that molecular motion is inherently random and influenced by interactions among different species. This simplification can lead to inaccurate predictions, particularly when cross-diffusion effects are significant, especially in multicomponent systems.

This study focuses on the Maxwell-Stefan diffusion model, which addresses some of Fick's limitations. It is derived from both mass and momentum balance laws under the assumption that macroscopic velocities are negligible compared to molecular velocities (the speed of sound). In the kinetic theory framework, this justifies the neglect of inertia and enables a systematic derivation from moment equations without assuming local equilibrium [9]. Consequently, the Maxwell-Stefan model provides a more accurate description of diffusion in multicomponent mixtures.

Experimental evidence supports this advantage. The Duncan and Toor experiment revealed non-classical diffusion phenomena–such as reverse diffusion, osmotic diffusion, and diffusion barriers–in three-component systems, which the Fick model fails to predict [21]. These effects are accurately captured by the Maxwell-Stefan model, motivating its further study.

The Maxwell-Stefan model has been derived from the Boltzmann system in various settings. For monatomic mixtures, [9] treats Maxwell molecules, while [10] extends the result to general collision kernels, yielding general diffusion coefficients. A higher-order model retaining inertia appears in [17, 18], and kinetic approaches have been extended to non-isothermal [20] and reactive polyatomic mixtures [3]. These derivations rely on computing moments of the Boltzmann collision operator, a task especially challenging in mixtures [19].

This paper builds on the moment system from [12], derived from the Boltzmann equations for monatomic and polyatomic mixtures. We study the isothermal case under a diffusion asymptotics regime–combining small Knudsen and Mach numbers–following [4]. This yields explicit Maxwell-Stefan diffusion coefficients via the momentum production term.

This work includes several novelties: (i) the mixture may include both monatomic and polyatomic components, with cross-collision operators; (ii) diffusion asymptotics is performed on the explicit momentum production term for relevant collision kernels, both mathematically [1, 2] and physically in the single polyatomic case [14, 23]; (iii) the resulting Maxwell-Stefan diffusion coefficients depend on mesoscopic parameters enabling fit to experimental data, here [15].

The paper is structured as follows: Sect. 2 reviews the isothermal multi-velocity model and production terms from [12]. Section 3 presents the scaling, and Sect. 4 carries out the limit, identifying Maxwell-Stefan coefficients.

2 Isothermal Multi-velocity Model for Eulerian Fluids Based on Kinetic Theory

We consider a mixture of $P \geq 1$ Eulerian fluids–i.e., with diagonal pressure tensors and zero heat flux–in the absence of chemical reactions. In the isothermal case, the evolution of each species' mass density ρ_α and velocity $\mathbf{v}_\alpha$, for each $\alpha = 1, \ldots, P$, is governed by the following balance laws [24],

$$\partial_t \rho_\alpha + \nabla_{\mathbf{x}} \cdot (\rho_\alpha \, \mathbf{v}_\alpha) = 0, \qquad \partial_t \, (\rho_\alpha \, \mathbf{v}_\alpha) + \nabla_{\mathbf{x}} \, (\rho_\alpha \, \mathbf{v}_\alpha \otimes \mathbf{v}_\alpha + p_\alpha \mathbb{I}) = \mathfrak{m}_\alpha, \tag{1}$$

where p_α is a hydrodynamic pressure of the constituent α, while $\mathbb{I}$ is the identity matrix. Since the source term $\mathfrak{m}_\alpha$ corresponding to momentum exchange satisfies $\sum_{\alpha=1}^{P} \mathfrak{m}_\alpha = 0$, summation of (1) over α recovers conservation laws of mass and momentum density of the whole mixture [24],

$$\partial_t \rho + \nabla_{\mathbf{x}} \cdot (\rho \, \mathbf{v}) = 0, \qquad \partial_t \, (\rho \, \mathbf{v}) + \nabla_{\mathbf{x}} \, (\rho \, \mathbf{v} \otimes \mathbf{v} + \mathbf{p}) = 0, \tag{2}$$

after defining the quantities:

$$\rho = \sum_{\alpha=1}^{P} \rho_\alpha; \quad \rho \mathbf{v} = \sum_{\alpha=1}^{P} \rho_\alpha \mathbf{v}_\alpha; \quad \mathbf{p} = \sum_{\alpha=1}^{P} \left(p_\alpha \mathbb{I} + \rho_\alpha (\mathbf{v}_\alpha - \mathbf{v}) \otimes (\mathbf{v}_\alpha - \mathbf{v})\right). \tag{3}$$

An important aspect of the modeling concerns the structure of the momentum production term $\mathfrak{m}_\alpha$. It describes the mutual momentum exchange between the components, but its functional form has to be determined. Initially, heuristic arguments were employed–at least in the context of cross-diffusion processes–assuming a linear dependence on the relative velocities $\mathbf{v}_\alpha - \mathbf{v}_\beta$. Another approach was systematically developed within the framework of extended thermodynamics, a macroscopic theory that uses the entropy principle to close the system of balance equations. However, it shares the limitations of all continuum theories–namely, that the phenomenological coefficients cannot be fully determined within this framework. Finally, the production term $\mathfrak{m}_\alpha$ can also be computed using the moment theory for the Boltzmann equation [12, 22, 25], as will be discussed in the following section.

2.1 Explicit Expression for the Momentum Production Term

The system (1) can be derived from Boltzmann-like equations for a gas mixture, under a specific ansatz for the distribution functions: Maxwellians that, for each species, have their own velocity and temperature. Such a distribution function arises as an *exact* solution of the maximum entropy principle for Eulerian fluids [12], and corresponds to an asymptotic regime in which equilibration within each separate

component runs faster than equalization of species parameters in the gas as a whole [6, 7]. Moreover, for a specific choice of collision kernel, evaluating the multi-species Boltzmann collision operator yields an explicit expression for the production term $\mathfrak{m}_\alpha$ in terms of mesoscopic parameters.

In this paper, we consider the Boltzmann system for mixtures of monatomic gases (indexed by S_{mono}) and polyatomic gases (indexed by S_{poly}), where the modeling of polyatomic species follows the continuous internal energy approach [2, 5]. For the collision kernel used in recent rigorous analyses of the space-homogeneous problem [1, 2]–corresponding to cutoff hard potentials based on the total collisional energy (kinetic plus internal for polyatomic species)–the production term is computed in [12]. In this paper, we refer to Eq. (B6).

$$\mathfrak{m}_\alpha = -\sum_{\substack{\beta=1 \\ \beta\neq\alpha}}^{P} \frac{\rho_\alpha\,\rho_\beta}{m_\alpha m_\beta}(\mathbf{v}_\alpha - \mathbf{v}_\beta)\,\mathcal{K}_{\alpha\beta}\,\mathcal{M}_{\alpha\beta}, \tag{4}$$

where $\mathcal{K}_{\alpha\beta} = \mathcal{K}_{\beta\alpha} > 0$ is a dimension constant (24), and $\mathcal{M}_{\alpha\beta} = \mathcal{M}_{\beta\alpha} > 0$ is a dimensionless constant that depends on all mesoscopic parameters, and on whether α and β consists of monatomic or polyatomic gases. The structure of $\mathcal{M}_{\alpha\beta}$ is given below, while all constants are listed in Sect. 6,

$$\begin{aligned}
&\mathcal{M}_{\alpha\beta} = \mathcal{F}_{\alpha\beta}, \quad \alpha,\beta \in S_{\text{mono}},\\
&\mathcal{M}_{\alpha\beta} = \mathcal{A}_{\alpha\beta}\left(\mathcal{B}_{\alpha\beta}\,\mathcal{F}_{\alpha\beta} + \eta_{\alpha\beta}\,\mathcal{C}_\beta\right), \quad \alpha \in S_{\text{mono}}, \beta \in S_{\text{poly}}\\
&\mathcal{M}_{\alpha\beta} = \mathcal{A}_{\alpha\beta}\left(\mathcal{B}_{\alpha\beta}\,\mathcal{F}_{\alpha\beta} + \eta_{\alpha\beta}\left(\mathcal{C}_\alpha + \mathcal{C}_\beta\right)\right), \quad \alpha,\beta \in S_{\text{poly}}.
\end{aligned} \tag{5}$$

Let us highlight that the term $\mathcal{F}_{\alpha\beta}$ depends non-linearly on $\left|\mathbf{v}_\alpha - \mathbf{v}_\beta\right|^2$, as specified in (25), and originates from the hard potentials in the molecular kinetic energy. Furthermore, the effect of polyatomic species is captured through the constants $\mathcal{A}_{\alpha\beta}$, $\mathcal{B}_{\alpha\beta}$, and $\mathcal{C}_\iota$ ($\iota \in S_{\text{poly}}$), where $\mathcal{C}_\iota$ specifically describes the influence of hard potentials in the molecular internal energy.

In the sequel, various approximations of $\mathcal{F}_{\alpha\beta}$ will be used, motivating the introduction of the following notation in the upcoming remark.

Remark 1 The following shorten notation is used for the coefficients (5),

$$\begin{aligned}
&\mathcal{M}_{\alpha\beta}(x) = x, \quad \alpha,\beta \in S_{\text{mono}},\\
&\mathcal{M}_{\alpha\beta}(x) = \mathcal{A}_{\alpha\beta}\left(\mathcal{B}_{\alpha\beta}\,x + \eta_{\alpha\beta}\,\mathcal{C}_\beta\right), \quad \alpha \in S_{\text{mono}}, \beta \in S_{\text{poly}}\\
&\mathcal{M}_{\alpha\beta}(x) = \mathcal{A}_{\alpha\beta}\left(\mathcal{B}_{\alpha\beta}\,x + \eta_{\alpha\beta}\left(\mathcal{C}_\alpha + \mathcal{C}_\beta\right)\right), \quad \alpha,\beta \in S_{\text{poly}}.
\end{aligned} \tag{6}$$

Obviously, the choice $x = \mathcal{F}_{\alpha\beta}$ gives (5).

3 Diffusive Scaling

To recover the Maxwell-Stefan model of diffusion, one can rely on heuristic arguments and assume that the order of magnitude of inertia terms is smaller than that of the pressure gradient and source term. A more formal approach, based on scaled (dimensionless) balance laws, transforms the system (1) into a dimensionless set of balance laws with a small parameter. To that end, the following dimensionless variables are introduced for any component $\alpha = 1, \ldots, P$:

$$\hat{t} = \frac{t}{\tau}, \quad \hat{\mathbf{x}} = \frac{\mathbf{x}}{L}, \quad \hat{\mathbf{v}}_\alpha = \frac{\mathbf{v}_\alpha}{V}, \quad \hat{\rho}_\alpha = \frac{\rho_\alpha}{\rho_0}, \quad \hat{p}_\alpha = \frac{p_\alpha}{p_0}, \tag{7}$$

where τ, L, V, ρ_0 and p_0 are reference macroscopic variables. Typically for scaled equations of fluid/gas dynamics, the choice of reference pressure determines the final structure of dimensionless equations. Here, we assume $p_0 = \rho_0 C^2$, where C is the Newtonian speed of sound, which is of the same order of magnitude as the mean molecular velocity. Additionally, the reference macroscopic time is assumed to be $\tau = L/V$. The central assumption of the diffusive scaling is

$$V \ll C \quad \Rightarrow \quad \frac{V}{C} = \varepsilon \ll 1. \tag{8}$$

As a consequence, C may be used as universal reference velocity, which implies the following scaling of time and component velocities

$$\hat{t} = \varepsilon \frac{C}{L} t, \quad \varepsilon\, \hat{\mathbf{v}}_\alpha = \frac{\mathbf{v}_\alpha}{C}. \tag{9}$$

To scale the production term $\mathfrak{m}_\alpha$ of the form (1), additionally to (7), we assume

$$\hat{m}_\alpha = \frac{m_\alpha}{m_0}, \quad \hat{\mu}_{\alpha\beta} = \frac{\mu_{\alpha\beta}}{m_0}, \quad \hat{\mathcal{K}}_{\alpha\beta} = \frac{\mathcal{K}_{\alpha\beta}}{m_0 B_0}, \tag{10}$$

where the reference value B_0 for the Boltzmann collision kernel is imposed similarly as in [4], implying the scaling for $\mathcal{K}_{\alpha\beta}$ from (24), and finally for $\mathfrak{m}_\alpha$,

$$B_0 = \frac{1}{\varepsilon} \frac{m_0}{\rho_0} \frac{C}{L} \quad \Rightarrow \; \hat{\mathcal{K}}_{\alpha\beta} = 4\pi (\hat{\mu}_{\alpha\beta})^{1-\frac{\zeta_{\alpha\beta}}{2}} \hat{k}_{\alpha\beta} \quad \text{and} \quad \mathfrak{m}_\alpha = \frac{\rho_0\, C^2}{L}\, \hat{\mathfrak{m}}_\alpha, \tag{11}$$

where ε is the Knudsen number. In conclusion, these scaling assumptions lead to the following scaled balance laws, for any gas component $\alpha = 1, \ldots, P$,

$$\begin{aligned} &\varepsilon \left(\partial_t \rho_\alpha^\varepsilon + \nabla_{\mathbf{x}} \cdot \left(\rho_\alpha^\varepsilon\, \mathbf{v}_\alpha^\varepsilon \right) \right) = 0, \\ &\varepsilon^2\, \partial_t \left(\rho_\alpha^\varepsilon\, \mathbf{v}_\alpha^\varepsilon \right) + \varepsilon^2\, \nabla_{\mathbf{x}} \left(\rho_\alpha^\varepsilon\, \mathbf{v}_\alpha^\varepsilon \otimes \mathbf{v}_\alpha^\varepsilon \right) + \nabla_{\mathbf{x}} p_\alpha^\varepsilon = \mathfrak{m}_\alpha^\varepsilon, \end{aligned} \tag{12}$$

where hats are dropped for the simplicity. The production term (4) in this scaling becomes, in the light of Remark 1,

$$\mathfrak{m}_\alpha^\varepsilon = -\sum_{\substack{\beta=1\\ \beta\neq\alpha}}^{P} \frac{\rho_\alpha^\varepsilon \rho_\beta^\varepsilon}{m_\alpha m_\beta} (\mathbf{v}_\alpha^\varepsilon - \mathbf{v}_\beta^\varepsilon)\, \hat{\mathcal{K}}_{\alpha\beta}\, \mathcal{M}_{\alpha\beta}^\varepsilon, \quad \mathcal{M}_{\alpha\beta}^\varepsilon = \mathcal{M}_{\alpha\beta}(\mathcal{F}_{\alpha\beta}^\varepsilon), \tag{13}$$

since the scaling affects only $\mathcal{F}_{\alpha\beta}^\varepsilon$ given in (27). Note that the equations (12) are *exact* in the sense that no terms are neglected. However, the field variables ρ_α^ε and $\mathbf{v}_\alpha^\varepsilon$ are moments of an approximate (local Maxwellian) distribution function that depends on the small parameter ε, as indicated by the superscript.

A key advantage of the kinetic approach is that it allows for the estimation of $\mathfrak{m}_\alpha^\varepsilon$ with respect to ε. A polynomial expansion around $\varepsilon = 0$ yields

$$\mathcal{M}_{\alpha\beta}^\varepsilon = \mathcal{M}_{\alpha\beta}^{(0)} + \varepsilon^2 \mathcal{M}_{\alpha\beta}^{(2)} + O(\varepsilon^4), \tag{14}$$

where $\mathcal{M}_{\alpha\beta}^{(0)}$ and $\mathcal{M}_{\alpha\beta}^{(2)}$ depend on the nature of the interacting components, in particular on whether species α and β are monatomic or polyatomic. A brief inspection of the momentum balance law $(12)_2$, in light of (13)–(14), shows that the inertia terms on the left-hand side, of order ε^2, are balanced by corresponding terms in $\mathfrak{m}_\alpha^\varepsilon$ of the same order of magnitude. This refined analysis is a particular strength of the kinetic theory framework and cannot be recovered through heuristic macroscopic reasoning.

Moreover, the explicit form of the coefficients $\mathcal{M}_{\alpha\beta}^\varepsilon$ allows for a detailed identification of the terms in the expansion (14). Namely, denoting

$$\bar{\mathcal{F}}_{\alpha\beta} = \lim_{\varepsilon\to 0^+} \mathcal{F}_{\alpha\beta}^\varepsilon = 2^{\frac{\zeta_{\alpha\beta}}{2}} \frac{4}{3\sqrt{\pi}} \Gamma\left(\tfrac{\zeta_{\alpha\beta}+5}{2}\right), \tag{15}$$

the following expansion holds

$$\mathcal{F}_{\alpha\beta}^\varepsilon = \bar{\mathcal{F}}_{\alpha\beta} \left(1 + \varepsilon^2 \frac{\zeta_{\alpha\beta}\, \mu_{\alpha\beta}}{10} \left|\mathbf{v}_\alpha^\varepsilon - \mathbf{v}_\beta^\varepsilon\right|^2 + O(\varepsilon^4)\right). \tag{16}$$

Then, the leading order in ε of (14) is, with the notation of Remark 1,

$$\mathcal{M}_{\alpha\beta}^{(0)} = \mathcal{M}_{\alpha\beta}(\bar{\mathcal{F}}_{\alpha\beta}), \tag{17}$$

while the second order in ε reads

$$\begin{aligned} \mathcal{M}_{\alpha\beta}^{(2)} &= \bar{\mathcal{F}}_{\alpha\beta} \frac{\zeta_{\alpha\beta}\, \mu_{\alpha\beta}}{10} \left|\mathbf{v}_\alpha^\varepsilon - \mathbf{v}_\beta^\varepsilon\right|^2, \quad \alpha, \beta \in S_{\text{mono}}, \\ \mathcal{M}_{\alpha\beta}^{(2)} &= \mathcal{A}_{\alpha\beta}\, \mathcal{B}_{\alpha\beta}\, \bar{\mathcal{F}}_{\alpha\beta} \frac{\zeta_{\alpha\beta}\, \mu_{\alpha\beta}}{10} \left|\mathbf{v}_\alpha^\varepsilon - \mathbf{v}_\beta^\varepsilon\right|^2, \quad \alpha \in S_{\text{mono}} \text{ or } S_{\text{poly}}, \beta \in S_{\text{poly}} \end{aligned} \tag{18}$$

Note that the information on the hard potentials in the molecular internal energy for polyatomic components is suppressed in (18), since the given expressions do not depend on $\mathcal{C}_\iota$, $\iota \in S_{\text{poly}}$.

4 Diffusive Limit Recovering the Maxwell-Stefan Model

To recover the MaxwellâĽ“Stefan model of diffusion, we consider the asymptotic limit $\varepsilon \to 0^+$. In this limit, system (12) formally reduces to:

$$\partial_t \rho_\alpha + \nabla_{\mathbf{x}} \cdot (\rho_\alpha \, \mathbf{v}_\alpha) = 0, \qquad \nabla_{\mathbf{x}} p_\alpha = \mathfrak{m}_\alpha, \tag{19}$$

where:

$$\begin{aligned} &\rho_\alpha = \lim_{\varepsilon \to 0^+} \rho_\alpha^\varepsilon, \quad \mathbf{v}_\alpha = \lim_{\varepsilon \to 0^+} \mathbf{v}_\alpha^\varepsilon, \quad p_\alpha = \lim_{\varepsilon \to 0^+} p_\alpha^\varepsilon, \quad \text{and} \\ &\mathfrak{m}_\alpha = \lim_{\varepsilon \to 0^+} \mathfrak{m}_\alpha^\varepsilon = -\sum_{\substack{\beta=1 \\ \beta \neq \alpha}}^{P} \frac{\rho_\alpha \, \rho_\beta}{m_\alpha m_\beta} (\mathbf{v}_\alpha - \mathbf{v}_\beta) \, \hat{\mathcal{K}}_{\alpha\beta} \, \mathcal{M}_{\alpha\beta}^{(0)}, \end{aligned} \tag{20}$$

with the coefficients in (17). Let us remark that it is *assumed* that solutions of (12) asymptotically converge, in a suitable sense, to solutions of (19).

This asymptotic limit enables to express dimensionless Maxwell-Stefan diffusion coefficients $D_{\alpha\beta}$ in terms of $\mathcal{M}_{\alpha\beta}^{(0)}$, based on the results from [10],

$$D_{\alpha\beta} = \left(\hat{\mathcal{K}}_{\alpha\beta} \mathcal{M}_{\alpha\beta}^{(0)} \right)^{-1}, \tag{21}$$

which provides an insight into possible practical applications of the analytical results derived in this work. In particular, the coefficients $D_{\alpha\beta}$ (21) are expressed in terms of mesoscopic parameters, which can be adjusted to match experimental data, for instance in the context of the Duncan and Toor experiment [15].

4.1 Benchmark Test: Duncan and Toor Experiment

The Duncan and Toor experiment [15], a benchmark example for the Maxwell-Stefan model of diffusion, involves a mixture of H_2, N_2 and CO_2, with the relevant parameters listed in Table 1. Using these parameters, the coefficients $D_{\alpha\beta}$ defined in (21) become functions of $\zeta_{\alpha\beta}$, $\eta_{\alpha\beta}$ and $\hat{k}_{\alpha\beta}$. The key question is whether a combination of these parameters can be found to match the experimental data for $D_{\alpha\beta}$. Since the problem is undetermined, one possible approach is to express $\eta_{\alpha\beta}$ and $\hat{k}_{\alpha\beta}$ as functions of $\zeta_{\alpha\beta}$, so that $\zeta_{\alpha\beta}$ remains the only free parameter. Using (17), (15), $(5)_3$ and (11), equation (21) is then solved for $\eta_{\alpha\beta}$,

Table 1 Parameters (dimensionless) used in Fig. 1

	Component-1 (H_2)	Component-2 (N_2)	Component-3 (CO_2)
m_α [18]	0.0811	1.1351	1.7838
a_α [23]	−0.0304	0.0036	0.9804
	Interaction 1 and 2	Interaction 2 and 3	Interaction 1 and 3
$D_{\alpha\beta}$ [18]	1.4866	0.2998	1.2136
$\mu_{\alpha\beta}$ [18]	0.0757	0.6937	0.0776

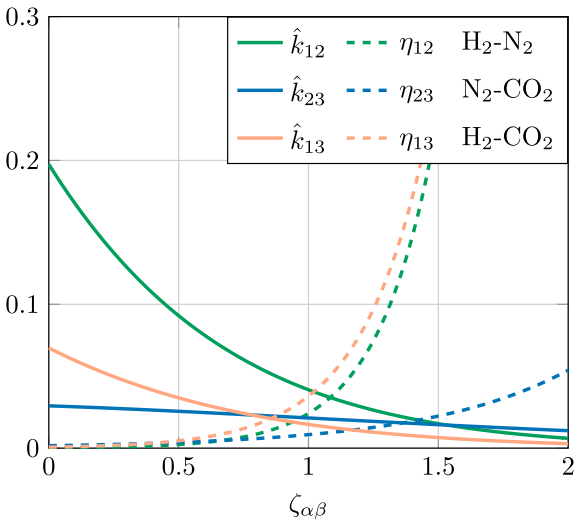

Fig. 1 Parameters $\hat{k}_{\alpha\beta}$ and $\eta_{\alpha\beta}$ as functions of $\zeta_{\alpha\beta}$, adjusted to match the values of $D_{\alpha\beta}$ from the Duncan and Toor experiment through (21)

$$\eta_{\alpha\beta} = \left(\frac{1}{\hat{k}_{\alpha\beta}\, D_{\alpha\beta}\, 4\pi (\hat{\mu}_{\alpha\beta})^{1-\frac{\zeta_{\alpha\beta}}{2}} \mathcal{A}_{\alpha\beta} \mathcal{B}_{\alpha\beta}\, \bar{\mathcal{F}}_{\alpha\beta}} - 1 \right) \frac{\mathcal{B}_{\alpha\beta}\, \bar{\mathcal{F}}_{\alpha\beta}}{(\mathcal{C}_\alpha + \mathcal{C}_\beta)}, \tag{22}$$

where $\hat{k}_{\alpha\beta}$ is chosen to ensure the positivity of $\eta_{\alpha\beta}$ for all $\zeta_{\alpha\beta} \in [0, 2]$,

$$\hat{k}_{\alpha\beta} = \left(D_{\alpha\beta} 4\pi (\hat{\mu}_{\alpha\beta})^{1-\frac{\zeta_{\alpha\beta}}{2}} \mathcal{A}_{\alpha\beta} \mathcal{B}_{\alpha\beta}\, \bar{\mathcal{F}}_{\alpha\beta} \right)^{-1} - 10^{-4}. \tag{23}$$

The dependence of such $\hat{k}_{\alpha\beta}$ and $\eta_{\alpha\beta}$ on $\zeta_{\alpha\beta}$ is illustrated in Fig. 1. These results show that the momentum production term computed in [12] is fully compatible, in the diffusion limit, with the Duncan & Toor experiment [15], while still retaining a free parameter ($\zeta_{\alpha\beta}$) that can be tuned to capture additional flow properties.

5 Conclusion and Outlook

Starting from the multi-velocity model of Eulerian fluids (1) derived as moment equations of the Boltzmann system for monatomic and polyatomic gases with an explicit momentum production term (4), and under scaling assumptions corresponding to small Knudsen and Mach numbers, the scaled macroscopic laws (12) are derived. In the limit, these equations formally lead to the Maxwell-Stefan equations (19). The explicit expression for the momentum production term thus provides Maxwell-Stefan diffusion coefficients (21) that depend on mesoscopic parameters of the collision kernel. The model is validated against the Duncan & Toor experiment. An interesting application of this study is to further identify the free parameters that match experimental data, using a strategy similar to [14], and to develop higher-order moment theory [17].

Acknowledgements Authors acknowledge Grants Nos. 451-03-66/2024-03/200125 and 451-03-65/2024–03/200125 from the Ministry of Science, Technological Development and Innovation of the Republic of Serbia.

6 List of Constants

The mesoscopic parameters are:

- free parameter $\zeta_{\alpha\beta} = \zeta_{\beta\alpha} \geq 0$ is the rate of hard potentials,
- $a_\iota > -1$, $\iota \in S_{\text{poly}}$, is related to the polyatomic molecule number of internal degrees of freedom or the specific heat [12, 23],
- free parameter $\eta_{\alpha\beta} = \eta_{\beta\alpha} \geq 0$ controls an influence of the internal energy,
- $k_{\alpha\beta} = k_{\beta\alpha} \geq 0$ is an appropriate dimensional constant whose value is a free parameter $\hat{k}_{\alpha\beta}$.

Let m_α be the molecular mass and let $\mu_{\alpha\beta} = \frac{m_\alpha m_\beta}{m_\alpha + m_\beta}$ be the reduced mass (both scaled according to (10)). Let k be the Boltzmann constant, and Γ denote the usual Gamma function. The constants involved in (5) read

$$\bullet\ \mathcal{K}_{\alpha\beta} = 4\pi\mu_{\alpha\beta}\left(\frac{kT}{\mu_{\alpha\beta}}\right)^{\frac{\zeta_{\alpha\beta}}{2}} k_{\alpha\beta}, \quad \text{with the scaling } \hat{k}_{\alpha\beta} = \frac{k_{\alpha\beta}}{B_0\, C^{-\zeta_{\alpha\beta}}}, \tag{24}$$

$$\bullet\ \mathcal{F}_{\alpha\beta} = 2^{\frac{\zeta_{\alpha\beta}}{2}}\,\Gamma\left(\tfrac{\zeta_{\alpha\beta}+5}{2}\right) e_1^{-b_{\alpha\beta}}\,\tilde{F}_1\left(\tfrac{\zeta_{\alpha\beta}+5}{2}, \tfrac{5}{2}, b_{\alpha\beta}\right),\ b_{\alpha\beta} = \frac{\mu_{\alpha\beta}}{2kT}\left|\mathbf{v}_\alpha - \mathbf{v}_\beta\right|^2, \tag{25}$$

where ${}_1\tilde{F}_1(a, b, z)$ is the hypergeometric function, defined, for $b > a > 0$, by

$$\Gamma(b-a)\,\Gamma(a)\,{}_1\tilde{F}_1(a, b, z) = \int_0^1 e^{zt} t^{a-1} (1-t)^{b-a-1}\,\mathrm{d}t, \tag{26}$$

which undergoes the following scaling, with all quantities in dimensionless form,

$$\mathcal{F}^{\varepsilon}_{\alpha\beta} = 2^{\frac{\zeta_{\alpha\beta}}{2}}\Gamma\left(\frac{\zeta_{\alpha\beta}+5}{2}\right)e_1^{-b^{\varepsilon}_{\alpha\beta}}\tilde{F}_1\left(\frac{\zeta_{\alpha\beta}+5}{2},\frac{5}{2},b^{\varepsilon}_{\alpha\beta}\right),\ b^{\varepsilon}_{\alpha\beta} = \varepsilon^2\frac{\mu_{\alpha\beta}}{2}\left|\mathbf{v}^{\varepsilon}_{\alpha}-\mathbf{v}^{\varepsilon}_{\beta}\right|^2. \tag{27}$$

$$\begin{aligned}
&\bullet\ \mathcal{A}_{\alpha\beta} = \frac{\Gamma\left(a_\beta+\frac{5}{2}\right)}{\Gamma\left(a_\beta+\frac{\zeta_{\alpha\beta}+5}{2}\right)},\quad \alpha\in S_{\text{mono}},\ \beta\in S_{\text{poly}}\\
&\bullet\ \mathcal{A}_{\alpha\beta} = \frac{\Gamma\left(a_\alpha+a_\beta+\frac{7}{2}\right)}{\Gamma\left(a_\alpha+a_\beta+\frac{\zeta_{\alpha\beta}+7}{2}\right)},\quad \alpha,\beta\in S_{\text{poly}},\\
&\bullet\ \mathcal{B}_{\alpha\beta} = \tfrac{2}{\sqrt{\pi}}\Gamma\left(\tfrac{\zeta_{\alpha\beta}+3}{2}\right),\\
&\bullet\ \mathcal{C}_{\iota} = \frac{\Gamma\left(a_\iota+1+\frac{\zeta_{\alpha\beta}}{2}\right)^2}{\Gamma\left(a_\iota+1\right)^2}\left(\frac{\mu_{\alpha\beta}}{\sum_{\alpha=1}^{P}m_\alpha}\right)^{\zeta_{\alpha\beta}/2}.
\end{aligned} \tag{28}$$

References

1. Alonso RJ, Čolić M (2024) Integrability propagation for a Boltzmann system describing polyatomic gas mixtures. SIAM J Math Anal 56(1):1459–1494. https://doi.org/10.1137/22M1539897
2. Alonso RJ, Čolić M, Gamba IM (2024) The Cauchy problem for Boltzmann bi-linear systems: the mixing of monatomic and polyatomic gases. J Stat Phys 191:9. https://doi.org/10.1007/s10955-023-03221-4
3. Anwasia B, Bisi M, Salvarani F, Soares AJ (2020) On the Maxwell-Stefan diffusion limit for a reactive mixture of polyatomic gases in non-isothermal setting. Kinet Relat Models 13(1):63–95. https://doi.org/10.3934/krm.2020003
4. Anwasia B, Simić S (2022) Maximum entropy principle approach to a non-isothermal Maxwell-Stefan diffusion model. Appl Math Lett 129(9):107949. https://doi.org/10.1016/j.aml.2022.107949
5. Baranger C, Bisi M, Brull S, Desvillettes L (2018) On the Chapman-Enskog asymptotics for a mixture of monoatomic and polyatomic rarefied gases. Kinet Relat Models 11(4):821–858. https://doi.org/10.3934/krm.2018033
6. Bisi M, Martalò G, Spiga G (2012) Multi-temperature hydrodynamic limit from kinetic theory in a mixture of rarefied gases. Acta Appl Math 122:37–51. https://doi.org/10.1007/s10440-012-9724-0
7. Bisi M, Martalò G, Spiga G (2011) Multi-temperature Euler hydrodynamics for a reacting gas from a kinetic approach to rarefied mixtures with resonant collisions. Europhys Lett 95(5):55002. https://doi.org/10.1209/0295-5075/95/55002
8. Bothe D, Dreyer W (2015) Continuum thermodynamics of chemically reacting fluid mixtures. Acta Mech 226(6):1757–1805. https://doi.org/10.1007/s00707-014-1275-1
9. Boudin L, Grec B, Salvarani F (2015) The Maxwell-Stefan diffusion limit for a kinetic model of mixtures. Acta Appl Math 136(1):79–90. https://doi.org/10.1007/s10440-014-9886-z
10. Boudin L, Grec B, Pavan V (2017) The Maxwell-Stefan diffusion limit for a kinetic model of mixtures with general cross sections. Nonlinear Anal 159:40–61. https://doi.org/10.1016/j.na.2017.01.010
11. Chapman S, Cowling TG (1991) The mathematical theory of non-uniform gases. Cambridge University Press, Cambridge, UK

12. Čolić M (2024) Multi-velocity and multi-temperature model of the mixture of polyatomic gases issuing from kinetic theory. Phys Fluids 36:067134. https://doi.org/10.1063/5.0211158
13. Desvillettes L, Monaco R, Salvarani F (2005) A kinetic model allowing to obtain the energy law of Polytropic gases in the presence of chemical reactions. Eur J Mech B Fluids 24:219–236. https://doi.org/10.1016/j.euromechflu.2004.07.004
14. Djordjić V, Oblapenko G, Pavić-Čolić M, Torrilhon M (2023) Boltzmann collision operator for polyatomic gases in agreement with experimental data and DSMC method. Continuum Mech Thermodyn 35:103–119. https://doi.org/10.1007/s00161-022-01167-8
15. Duncan JB, Toor HL (1962) An experimental study of three component gas diffusion. AIChE J 8(1):38–41
16. Giovangigli V (1999) Multicomponent flow modeling. Birkhäuser Boston Inc., Boston, MA
17. Grec B, Simić S (2023) Higher-order Maxwell-Stefan model of diffusion. La Matematica 2:962–991. https://doi.org/10.1007/s44007-023-00071-0
18. Grec B, Simić S (2024) Numerical study of the higher-order Maxwell-Stefan model of diffusion, trends in mathematics, to appear
19. Gupta VK, Torrilhon M (2015) Comparison of relaxation phenomena in binary gas-mixtures of Maxwell molecules and hard spheres. Comput Math with Appl 70(1):73–88. https://doi.org/10.1016/j.camwa.2015.04.028
20. Hutridurga H, Salvarani F (2017) Maxwell-Stefan diffusion Asymptotics for gas mixtures in non-isothermal setting. Nonlinear Anal 159:285–297. https://doi.org/10.1016/j.na.2017.03.019
21. Krishna R, Wesselingh JA (1997) The Maxwell-Stefan approach to mass transfer. Chem Eng Sci 52(6):861–911. https://doi.org/10.1016/S0009-2509(96)00458-7
22. Pavić-Čolić M (2019) Multi-velocity and multi-temperature model of the mixture of polyatomic gases issuing from kinetic theory. Phys Lett A 383(24):2829–2835. https://doi.org/10.1016/j.physleta.2019.06.009
23. Pavić-Čolić M, Simić S (2022) Kinetic description of polyatomic gases with temperature-dependent specific heats. Phys Rev Fluids 7:083401. https://doi.org/10.1103/PhysRevFluids.7.083401
24. Ruggeri T, Simić S (2007) On the hyperbolic system of a mixture of Eulerian fluids: a comparison between single- and multi-temperature models. Math Methods Appl Sci 30(7):827–849. https://doi.org/10.1002/mma.813
25. Torrilhon M (2016) Modeling nonequilibrium gas flow based on moment equations. Annu Rev Fluid Mech 48(1):429–458. https://doi.org/10.1146/annurev-fluid-122414-034259

Open Access This chapter is licensed under the terms of the Creative Commons Attribution 4.0 International License (http://creativecommons.org/licenses/by/4.0/), which permits use, sharing, adaptation, distribution and reproduction in any medium or format, as long as you give appropriate credit to the original author(s) and the source, provide a link to the Creative Commons license and indicate if changes were made.

The images or other third party material in this chapter are included in the chapter's Creative Commons license, unless indicated otherwise in a credit line to the material. If material is not included in the chapter's Creative Commons license and your intended use is not permitted by statutory regulation or exceeds the permitted use, you will need to obtain permission directly from the copyright holder.

Lattice Boltzmann Scheme for Drift Diffusion Equations in Cold Plasma Applications

Nathalie Bonamy Parrilla, Stéphane Brull, and François Rogier

Abstract This paper presents a Lattice Boltzmann Method (LBM) tailored for solving drift-diffusion equations in cold plasma applications. The proposed scheme is aimed to be a first step to address the challenges of simulating cold plasmas, characterized by non-equilibrium conditions and complex interactions among electrons, ions, and electric fields. By employing a parabolic scaling and simplifying assumptions, the method ensures computational efficiency while maintaining accuracy. Validation is performed through numerical test cases. While promising, future work will focus on incorporating energy dynamics and handling variable diffusion coefficients to enhance the method's applicability in diverse plasma scenarios.

Keywords Lattice boltzmann · Drift diffusion · Equivalent equations

1 Introduction

This paper is devoted to the approximation of a drift diffusion equation for cold plasma applications using a Lattice Boltzmann Method (LBM) approach. Cold plasmas are a topic of significant interest due to their numerous industrial applications, ranging from airflow control in aircraft industry to biomedical technologies. Despite their potential, the numerical simulation of cold plasmas poses considerable challenges. Traditional approaches to modeling such systems often rely on finite volumes or similar methods, which, while robust, can be computationally expensive and challenging to implement efficiently. In contrast, the Lattice Boltzmann Method (LBM) offers an attractive alternative due to its inherent simplicity in implementation and natural suitability for parallel computing.

N. B. Parrilla (✉) · S. Brull
Université de Bordeaux, Institut de Mathématiques de Bordeaux UMR 5251, Talence, France
e-mail: nathalie.bonamy-parrilla@math.u-bordeaux.fr

F. Rogier
70 Rue Achille Viadieu, Toulouse, France

© The Author(s) 2026

M. Grabe et al. (eds.), *Rarefied Gas Dynamics*, Springer Aerospace Technology,
https://doi.org/10.1007/978-3-032-00094-1_4

Cold plasmas, which are often weakly ionized, consist of neutral particles, ions, and electrons. The dynamics of the charged particles are governed by their interactions with the electric field and the neutral particles which act as a neutral gas background. They are characterized by non-equilibrium conditions where electron temperatures significantly exceed those of heavy particles. Of particular interest are the behaviors of electrons, which share a structural similarity with ions in the chosen modeling equations. In this work, we consider high-pressure cold plasmas, for which a fluid description is appropriate. The equations used to describe these plasmas are drift-diffusion equation for the electron density, coupled with a mass creation equation for positive ions and a Poisson equation for the electric potential. Negative ions are omitted in the current study; however, the proposed scheme can be readily adapted to handle both negative and positive ions. This model is commonly referred as Local Field Approximation (see [4, 6, 7]). The system under study is the following:

$$\begin{cases} \partial_t \rho + \partial_x(\mu\rho\partial_x\phi - D\partial_x\rho) = \nu\rho, \\ \partial_x^2\phi = \frac{e}{\epsilon_0}(\rho - \rho_{ion}), \\ \partial_t \rho_{ion} = \nu\rho. \end{cases} \tag{1}$$

where ρ is the electron density, ρ_i the positive ions density, ϕ the electric potential, ε_0 the dielectric permittivity and e the electronic charge. The transport coefficients, – namely the mobility coefficient μ, the diffusion coefficient D and the ionization frequency ν – are physical quantities that depend on the reduced electric field $|\partial_x\phi|/N$, where N is the neutral particles density. Given the limitations of LBM for diffusion equations, we will neglect the dependency of D in $\partial_x\phi$, which is acceptable for some discharge regimes where the diffusion is secondary compared to the drift and ionization.

In this work, we propose a Lattice Boltzmann scheme tailored to the drift-diffusion equations with source terms, designed for the simulation of cold plasma dynamics.

Our approach will be validated through a series of numerical test cases, demonstrating the accuracy of the proposed scheme. Finally, we will present an application that compares our LBM-based results against those obtained using a finite volume method, highlighting the advantage of using this method in physical applications.

2 Numerical Scheme for Electron Density

This section presents the numerical scheme employed to simulate the electron density (see (1)). We focus only on 1D case, which can be easily generalized to higher dimensions without significant additional complexity.

2.1 Presentation of the Scheme

2.1.1 Space and Time Discretization

We consider a uniform grid $x \in \Delta x\mathbb{Z}$ with a space step Δx. The parabolic scaling is chosen thus the time discretization is given by:

$$\Delta t = \frac{\Delta x^2}{D}$$

which ensures a constant diffusion coefficient D regardless of the mesh size, contrary to the acoustic scaling (see [1]).

Lattice Structure and Distribution Functions
The chosen lattice structure is the so-called D1Q2 model (see [2]). It consists of two discrete velocities given by

$$\lambda_{1,2} = (-1)^{1,2}\frac{\Delta x}{\Delta t}$$

each associated with a distribution function $f_i, i = 1, 2$. The sum of the distribution functions defines the macroscopic electron density ρ:

$$\rho = f_1 + f_2$$

which is the unknown quantity in the drift-diffusion equation. We will denote $f_j(n\Delta t, i\Delta x)$ by $f^n_{j,i}$ from now, and we will use index in a similar way for all the variables (ρ, ϕ...).

2.1.2 Two-Step Scheme

The numerical scheme consists of two main steps:

1. Collision Step: This step involves relaxation toward an equilibrium state and accounts for ionization effects, which introduce mass generation. It is computed as follows

$$f^{n+1/2}_{1,i} = (1-\omega)f^n_{1,i} + \frac{\omega}{2}(\rho^n_i - \frac{\Delta t}{\Delta x}(\mu\rho\partial_x\phi)^n_i) + \Delta t\,(\nu\rho)^n_i,$$
$$f^{n+1/2}_{2,i} = (1-\omega)f^n_{2,i} + \frac{\omega}{2}(\rho^n_i + \frac{\Delta t}{\Delta x}(\mu\rho\partial_x\phi)^n_i) + \Delta t\,(\nu\rho)^n_i,$$

with ω being the so-called relaxation parameter (see [5]), and where the parameters μ and ν may depend on the modulus of the electric field.

2. Transport Step: In this step, the distribution functions are advected along their corresponding lattice velocities as follows

$$f_{1,i}^{n+1} = f_{1,i+1}^{n+1/2},$$
$$f_{2,i}^{n+1} = f_{2,i-1}^{n+1/2}.$$

The boundary conditions are imposed during the transport step on the boundary cells. Dirichlet boundary conditions on the density are satisfied with the relation:

$$f_{2,0} = \rho_b - f_{1,0},$$
$$f_{1,N} = \rho_b - f_{2,N}.$$

Then the scheme can finally be recast as:

$$f_{1,i}^{n+1} = (1-\omega) f_{1,i+1}^{n} + \frac{\omega}{2}(\rho_{i+1}^{n} - \frac{\Delta t}{\Delta x}(\mu\rho\partial_x\phi)_{i+1}^{n}) + \Delta t\,(\nu\rho)_{i+1}^{n}, \tag{2}$$
$$f_{2,i}^{n+1} = (1-\omega) f_{2,i-1}^{n} + \frac{\omega}{2}(\rho_{i-1}^{n} + \frac{\Delta t}{\Delta x}(\mu\rho\partial_x\phi)_{i-1}^{n}) + \Delta t\,(\nu\rho)_{i-1}^{n}. \tag{3}$$

2.1.3 Coupling with Electric Field and Positive Ions

The LBM is coupled with the electric field through Poisson's equation and the equations on ions (see (1)). The transport coefficients ν and μ are then interpolated from a dataset of physical values, depending on the reduced electric field $|\partial_x\phi|/N$.

2.2 Consistency and Equivalent Equations

The study of consistency for a LB scheme, is an important issue. To address this, two methods are commonly used : derivation of the fluid limit of the lattice Boltzmann equation by using Champan-Enskog expansions (see [5]) or the computation of equivalent equations based on Taylor expansions (see [3]). In this paper, we adopt the latter approach. In the following, we compute the equivalent equations.

We start by summing relations (2)–(3) to obtain the update on the density:

$$\rho_i^{n+1} = (1-\frac{\omega}{2})(f_{1,i+1}^{n} + f_{2,i-1}^{n}) + \frac{\omega}{2}(f_{2,i+1}^{n} + f_{1,i-1}^{n})$$
$$+ \frac{\omega\Delta t}{2\Delta x}((\mu\partial_x\phi)_{i-1}^{n} - (\mu\partial_x\phi)_{i+1}^{n}) + \frac{\Delta t}{2}((\nu\rho)_{i+1}^{n} + (\nu\rho)_{i-1}^{n}),$$

where ρ_{i+1}^n and ρ_{i-1}^n were replaced by their expressions in terms of f. By applying again (2)–(3) to this relation we obtain:

$$\begin{aligned}\rho_i^{n+1} = (1-\frac{\omega}{2})[(1-\frac{\omega}{2})(f_{1,i+2}^{n-1}+f_{2,i-2}^{n-1}) + \frac{\omega}{2}(f_{1,i-2}^{n-1}+f_{2,i+2}^{n-1}) \\ + \frac{\omega\Delta t}{2\Delta x}((\mu\rho\partial_x\phi)_{i-2}^{n-1} - (\mu\rho\partial_x\phi)_{i+2}^{n-1}) + \frac{\Delta t}{2}((\nu\rho)_{i+2}^{n-1} + (\nu\rho)_{i-2}^{n-1})] \\ + \frac{\omega}{2}(\rho_i^{n-1} + \Delta t(\nu\rho)_i^{n-1}) \\ + \frac{\omega\Delta t}{2\Delta x}((\mu\rho\partial_x\phi)_{i-1}^{n} - (\mu\rho\partial_x\phi)_{i+1}^{n}) \\ + \frac{\Delta t}{2}((\nu\rho)_{i+1}^{n} + (\nu\rho)_{i-1}^{n}). \qquad (4)\end{aligned}$$

Now, to rewrite this expression only in terms of ρ and not in terms of f we look at the expression of the density in the neighbour cells:

$$\begin{aligned}\rho_{i+1}^n = (1-\frac{\omega}{2})(f_{1,i+2}^{n-1}+f_{2,i}^{n-1}) + \frac{\omega}{2}(f_{2,i+2}^{n-1}+f_{1,i}^{n-1}) \\ + \frac{\omega\Delta t}{2\Delta x}((\mu\rho\partial_x\phi)_{i}^{n-1} - (\mu\rho\partial_x\phi)_{i+2}^{n-1}) \\ + \frac{\Delta t}{2}((\nu\rho)_{i+2}^{n-1} + (\nu\rho)_{i}^{n-1}),\end{aligned}$$

The sum of this expression with the corresponding one for ρ_{i-1}^n can be identified and replaced in (4):

$$\begin{aligned}\rho_i^{n+1} = (1-\frac{\omega}{2})(\rho_{i+1}^n + \rho_{i-1}^n - \rho_i^{n-1} - \Delta t(\nu\rho)_i^{n-1}) + \frac{\omega}{2}(\rho_i^{n-1} + \Delta t(\nu\rho)_i^{n-1}) \\ + \frac{\omega\Delta t}{2\Delta x}((\mu\rho\partial_x\phi)_{i-1}^{n} - (\mu\rho\partial_x\phi)_{i+1}^{n}) + \frac{\Delta t}{2}((\nu\rho)_{i+1}^{n} + (\nu\rho)_{i-1}^{n}). \qquad (5)\end{aligned}$$

By performing Taylor expansions on (5), we get:

$$\partial_t\rho - (\frac{1}{\omega}-\frac{1}{2})\frac{\Delta x^2}{\Delta t}\partial_x^2\rho + \partial_x(\mu\rho\partial_x\phi) = \nu\rho + \mathcal{O}(\Delta t),$$

where $(\frac{1}{\omega}-\frac{1}{2})\frac{\Delta x^2}{\Delta t} = D$ thanks to the choice of the parameters. The equivalent equation analysis shows that the scheme is in agreement with the fluid model.

3 Numerical Results

In this section we present numerical results obtained with the LB scheme. Two test cases were considered, the first one being academic and considering the dimensionless stationary problem. In the second test case the LBM scheme is directly compared to a finite volumes scheme.

3.1 Results for the Stationary Convection Diffusion Equation

In this subsection we consider the stationary problem as a way to test the stability of the scheme. The equation on the density is coupled with the Poisson equation through the drift velocity:

$$\begin{aligned}
&\rho u - D\partial_x \rho = 0,\\
&u(x) = \mu \partial_x \phi,\\
&\partial_x^2 \phi = \lambda(\rho - \rho_{ion}),\\
&\rho(0) = \rho_{ion},\ \rho(1) = \rho_{ion} + \delta,\\
&\phi(0) = 0,
\end{aligned}$$

on $\Omega = [0, 1]$, where $\rho_{ion} = 1$ and δ to be precised later. The solution for the density is given by:

$$\rho_{sol}(x) = \rho_{ion} \exp\left(\frac{\phi(x)\mu}{D}\right).$$

In order to compute an approximated solution of the Poisson problem, we need an assumption on ϕ. If $|\phi|$ is relatively small, the exponential can be linearized and the Poisson problem then becomes:

$$\partial_x^2 \phi = \frac{\lambda \mu \phi}{D},$$

which then can be solved analytically. This assumption is satisfied if δ is small enough. Finally the quasi analytic solution, taking into account the boundary conditions, is given by:

$$\begin{aligned}
&\phi(x) = ln\left(1 + \frac{\delta}{\rho_{ion}}\right) \frac{D(\exp(-\alpha x) - \exp(\alpha x))}{\mu(\exp(-\alpha x_N) - \exp(\alpha x_N)},\\
&\alpha = \sqrt{\frac{\rho_{ion}\lambda\mu}{D}}.
\end{aligned} \tag{6}$$

The scheme is initialized with a small perturbation of the stationary state

$$\rho(t=0,x) = \rho_{sol}(x) + \beta \sin(k\pi x), \tag{7}$$

where β is small compared to ρ_{sol}. In Fig. 1 are shown the results for $C = 0.3$, $D = 0.4$, $\mu = 0.3$ and $\delta = 0.01$. In Fig. 1a are displayed the initialization of the scheme (see (7)) and its evolution at time $t = 0.2$ with respect to the stationary state ρ_{sol}. In Fig. 1b is plotted the absolute relative error $\frac{|\rho - \rho_{sol}|}{||\rho_{sol}||_{L^\infty}}$. The results are satisfactory with a very small relative error.

3.2 Results for the Instationary Problem

In this subsection we consider the complete system (1). The LB scheme is compared to the results of a finite volume scheme (denoted FV). Both schemes are initialized in the following way :

$$\rho(0,x) = 10^{15}(1 + \exp(-\frac{(x - \frac{L}{2})^2}{L10^{-4}}), \qquad \rho_{ion}(0,x) = \rho(0,x),$$
$$\phi(x) = 0 \, \forall x \in [0, L[, \qquad \phi(L) = 3.10^4 V,$$

where $x \in [0, L]$ and $L = 0.01m$. In Fig. 2 are shown the results for $C = 0.48$, $D = 0.66$, μ and nu depending on the electric field, at final time $1,24.10^{-8}s$. In Fig. 2a are plotted the electron densities computed by the two schemes. The LBM and FV solutions show good agreement, especially in the plateau and peak regions. Both methods capture the shape and height of the density peak well, indicating that the numerical accuracy of LBM is comparable to FV for this case. The green curve

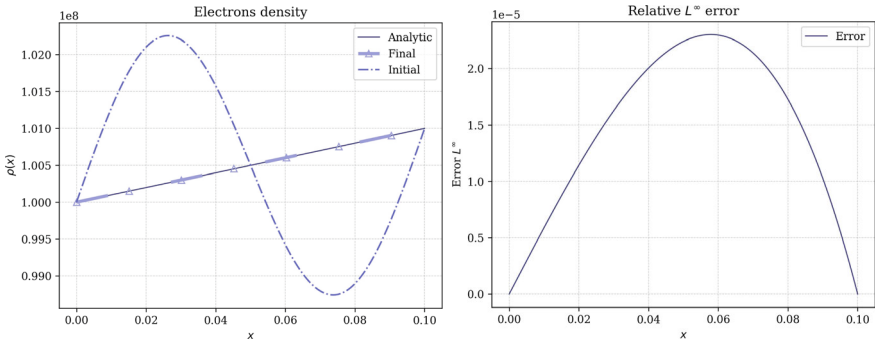

(a) Density (b) Error

Fig. 1 **a** Initial density in blue, analytical density in orange, and numerical density in magenta at time $t = 0.2$. **b** Absolute relative error at $t = 0.2$

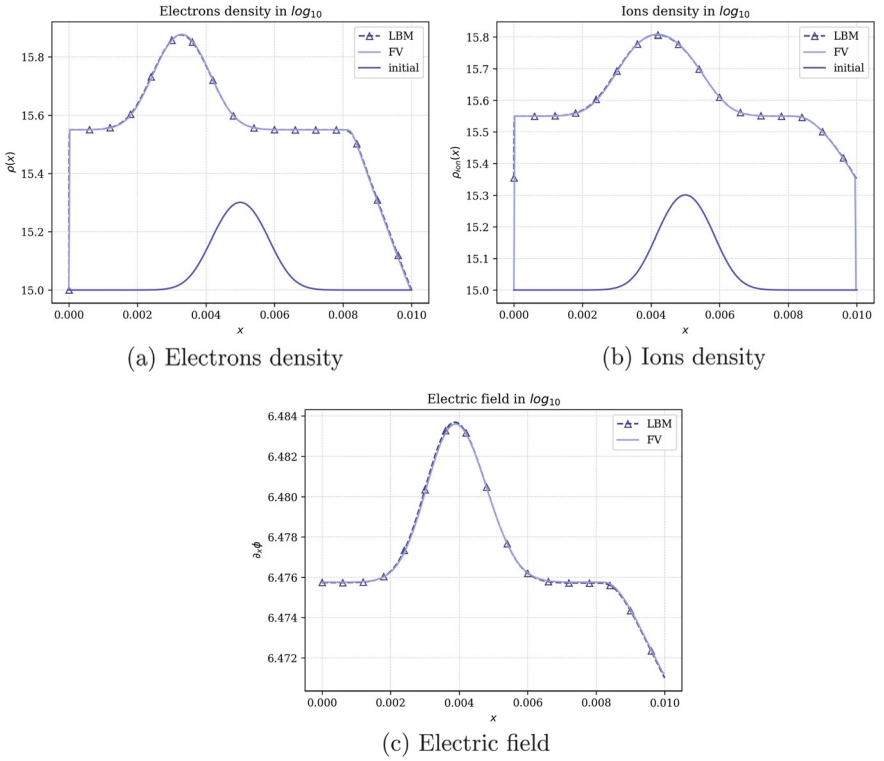

Fig. 2 **a** Logarithm density computed with LB in blue, with FV in orange, at final time. The initial condition for both schemes is displayed in green. **b** Logarithm of ions density computed with LB in blue, with FV in orange, at final time. **c** Logarithm of electric field coupled to LB in blue, to FV in orange, at final time

(initial condition) is significantly smoother and lower in amplitude than the final density profiles. This reflects the effects of ionisation, electron accumulation and redistribution over time due to electric field-driven transport and diffusion.

4 Conclusion

In this work, we introduced a lattice Boltzmann method scheme with a parabolic scaling tailored for drift-diffusion problems with ionization. The analysis demonstrated that the equivalent equation of the scheme corresponds to a drift-diffusion equation with the correct physical parameters, although with a constant diffusion coefficient determined by the choice of the time step. Numerical results were presented to validate the stability of the scheme in stationary cases. Additionally, promising results

were obtained when comparing the scheme with a finite-volume code, highlighting its potential for practical applications. However, there are still several aspects that require improvement. These include the incorporation of a second equation to account for energy dynamics and the development of a strategy to handle variable diffusion coefficients. These enhancements will further extend the applicability and accuracy of the proposed scheme for cold plasma modeling.

References

1. Boghosian B, Dubois F, Graille B, Lallemand P, Tekitek MM (2018) Curious convergence properties of lattice Boltzmann schemes for diffusion with acoustic scaling. Commun Computat Phys 23(4):1263–1278
2. Dellacherie S (2014) Construction and analysis of lattice Boltzmann methods applied to a 1d convection-diffusion equation. Acta Applicandae Mathematicae 131:69–140
3. Dubois F (2008) Equivalent partial differential equations of a lattice Boltzmann scheme. Comput Mathemat Appl 55(7):1441–1449. https://www.sciencedirect.com/science/article/pii/S0898122107006268
4. Hagelaar GJM (2008) Modelling methods for low-temperature plasmas. Ph.D. thesis, Université Toulouse III Paul Sabatier (UT3 Paul Sabatier). https://theses.hal.science/tel-02864696
5. Krüger T, Kusumaatmaja H, Kuzmin A, Shardt O, Silva G, Viggen EM (2016) The Lattice Boltzmann method. Graduate texts in physics, Springer, Cham
6. Markosyan AH, Teunissen J, Dujko S, Ebert U (2015) Comparing plasma fluid models of different order for 1d streamer ionization fronts. Plasma Sources Sci Technol 24(6):065002
7. Matéo-Vélez JC, Degond P, Rogier F, Séraudie A, Thivet F (2008) Modelling wire-to-wire corona discharge action on aerodynamics and comparison with experiment. J Phys D: Appl Phys 41(3):035205. https://doi.org/10.1088/0022-3727/41/3/035205

Open Access This chapter is licensed under the terms of the Creative Commons Attribution 4.0 International License (http://creativecommons.org/licenses/by/4.0/), which permits use, sharing, adaptation, distribution and reproduction in any medium or format, as long as you give appropriate credit to the original author(s) and the source, provide a link to the Creative Commons license and indicate if changes were made.

The images or other third party material in this chapter are included in the chapter's Creative Commons license, unless indicated otherwise in a credit line to the material. If material is not included in the chapter's Creative Commons license and your intended use is not permitted by statutory regulation or exceeds the permitted use, you will need to obtain permission directly from the copyright holder.

Experimental Techniques for Non-equilibrium Flows

Development of Neuromorphic Imaging Spectroscopy for Hypersonic Flight Observation

Tamara Sopek, Fabian Zander, Byrenn Birch, and David Buttsworth

Abstract Enhanced capability to collect hypersonic flight data is required to better understand the flow physics around spacecraft entering Earth's atmosphere. Especially daytime recording, while possible, is challenging, requiring compromises due to saturation and environmental noise. Using event-based cameras will allow spectral measurements to be done equally well during the day and night without modifications to instrumentation, overcoming the current major limitation associated with daytime tests. Combining these cameras with high-resolution spectroscopy enables more reliable collection of critical data, such as the flow temperature and species composition. Measurements were performed using a novel neuromorphic spectroscopy system and a range of light sources, obtaining both broadband and discrete line spectra. Dynamic range and long-range spectroscopy results show performance improvement of the event-based system over the camera typically used for the conditions tested, first-time demonstrating that neuromorphic spectroscopy systems are capable of successfully recording emission spectra.

Keywords Neuromorphic · Spectroscopy · Hypersonic

1 Introduction

Visual, photo- and videographic information of hypersonic/space flight events has for a long time played a crucial role in assessing performance, verifying successes and documenting failures. Forensic analysis of photographic records from rocket failures, including those from the Space Shuttle disasters (Challenger and Columbia), has contributed to improved system design.

A strong incentive exists to better characterize the hypersonic flight conditions. However, the only two options for generating realistic aerothermodynamic conditions

T. Sopek (✉) · B. Birch
University of Queensland, St Lucia, Queensland, Australia
e-mail: t.sopek@uq.edu.au

F. Zander · D. Buttsworth
University of Southern Queensland, Toowoomba, QLD, Australia
© The Author(s) 2026

M. Grabe et al. (eds.), *Rarefied Gas Dynamics*, Springer Aerospace Technology,
https://doi.org/10.1007/978-3-032-00094-1_5

are high-speed ground test facilities and flight experiments. Although the ground test facilities [6] are great at replicating individual aspects of the high-speed flows, they cannot fully replicate the real flight environment. The only way possible is through rare and expensive flight testing. Thus, researchers typically conduct a series of much cheaper testing in the ground test facilities as a first stage, followed by more expensive flight tests. Remote observations of high-speed flight events [4, 5] present the best chance to obtain the prime radiation data, also avoiding embedding sensors and extra hardware onto the vehicle.

But, besides the the rarity of hypersonic flight events, additional challenges in data collection exist related to each observation type. In ground-based observations, a large drawback is a considerable amount of atmospheric absorption of radiation, and many of the relevant events occur over the ocean, eliminating the possibility of such observations. While the issue of atmospheric absorption and transoceanic events can be tackled with airborne observations, removing the issue of clouds and accessibility, the issue of sky background brightness remains present in both observation types. Typically used CCD/CMOS cameras struggle in these conditions, and though they can record objects appearing on a clear blue sky, this is difficult, demanding compromises due to saturation and environment noise. Due to these issues, enhanced by the current technology limitations, highly valuable spectroscopic measurement data is scarce. To maximize the collection of data from every hypersonic flight event, the goal of this study was to explore recent advancements in vision technology and its potential improvements over standard cameras for remote observations of high-speed flight events.

Neuromorphic event-based (EB) vision is a new technology with gain in sensor performance compared to conventional cameras. Standard cameras, with the frame-based output dependent on the exposure, and low temporal resolution, bear issues when imaging moving objects and objects on a bright background. In space imaging, they also deal with high transfer rates due to large amounts of low-importance empty space information. EB cameras are better suited for space-oriented imaging with their continuous data stream featuring high temporal resolution, but low amount of highly relevant data and thus low transfer rates. Due to their high dynamic range measurements with EB cameras can be done equally well during day and night without modifications to instrumentation, enabling easier detection and tracking of targets in space environment [1]. Our proposed instrument is new; coupling of the EB camera with a spectrometer for neuromorphic imaging spectroscopy, which has never been trialed before.

2 Event-Based (EB) Cameras

EB cameras are novel dynamic vision devices based on human retina [3] that record only when there is a light intensity change in the field of view. Instead of measuring the “absolute” brightness all the time, each pixel responds to brightness changes in the scene asynchronously and independently. Due to their advanced method of data

collection, they have been successfully used for a myriad of applications, especially in robotics [2]. The most relevant application here is their use for star tracking and mapping [1]. As they don't continually record data, the problem of vast data amounts created when imaging empty space is avoided. Also, as they only detect light intensity changes, they can cover a wide range of illumination levels.

While standard camera outputs frames at fixed time intervals, an EB camera outputs visual information about the scene as asynchronous events at microsecond resolution, transmitting data with sub-millisecond latency. An event is generated each time a single pixel detects a light intensity change in the FOV—a given pixel's luminosity change reaches a given threshold, it produces a visual event with an x and y address, a timestamp, and a polarity, either "ON" or "OFF" depending on the change in relative luminosity. The output is a stream of digital "events" of variable speed, shown in Fig. 1, each event corresponding to a pixel's preset level of change in log intensity at a certain time, thus a spatio-temporal pattern rather than conventional frames. However, pseudo images can be created by integrating events stream for a chosen length of time. Mathematically, the output of an EB camera is a stream of N events e_i:

$$e_i = [x_i, y_i, t_i, p_i]_{i=1,\ldots,N} \tag{1}$$

where x and y are the spatial coordinates in pixels, t is the timestamp of the event, and $p \in \{-1, 1\}$ is the polarity (the sign of the log intensity change). This visual information encoding is inspired by the spiking nature of biological visual/optic pathways. After the information is transmitted from the sensor, each pixel memorises its last log intensity while monitoring for a change of set magnitude from this memorised value. Once that change has been observed and recorded, the sensor sends another event. This change is defined as:

$$pC = \Delta L(x, y, t) = L(x, y, t) - L(x, y, t - \Delta t) \tag{2}$$

where C is contrast sensitivity, $L(x, y, t)$=log(I) or the logarithmic change of light intensity, t is the timestamp of the event and Δt is the time since the previous event at the same pixel. The logarithmic relationship represents pixels' response to percentage changes in illumination, not the absolute magnitude of the change, resulting in a very wide dynamic range. EB cameras transmit events from the pixel array to periphery and out of the camera via shared digital readout pipeline, with arbiter system determining transfer order. The disadvantages of EB imaging entail the inability to use common image processing algorithms due to asynchronous pixels and no light intensity information. New methods are needed for the spatio-temporal,

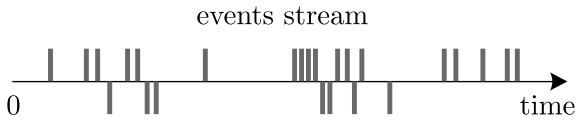

Fig. 1 Events stream output of the EB camera

photometric and stochastic nature of the data, complicating the analysis. With no changes in light intensity (static scene), there is no events creation and the only output is background noise. EB cameras' asynchronous event readout scheme has a limited maximum speed, a potential issue in extremely active scenes. Also, this is new technology, resulting in a few manufacturers, lower sensor resolution, higher cost, and a lean knowledge base.

3 Experimental Setup

An EB camera is paired with a slitless spectrometer to enable collection of spectroscopic data. The slitless spectrometer is a commonly used method to capture spectral emissions of phenomena such as shock layer radiation of a sample return capsule [5]. It typically consists of an order-sorting prism, transmission grating, lens and an optional spectral filter array. The prism refraction angle is mostly chosen to redirect the center wavelength of the observed spectrum back onto the optical axis. Our design was simpler—tilting the recording end of the system at an angle enabled us to eliminate the prism, whilst keeping the image of the spectrum parallel to the focal plane and all colours of the spectrum in focus at the same time. Experiments reported here were done using a Prophesee Gen4 camera (Metavision IMX636 sensor), lens, transmission grating, filter and a light source. The optical arrangement for these experiments was designed to enable the recording of the spectrally and spatially resolved radiation emitted from different light sources. These experiments employed an EB camera and a standard camera system, in the spectral range of approximately 400–900 nm. Three variations of spectrally resolved measurements were performed, using a: (a) Integrating sphere (Labsphere PT-038-PLS), a tunable light source delivers a broadband spectral radiance output, (b) Mercury/argon lamp (Avantes AvaLight-CAL-HgAr), which outputs radiance in the form of discrete spectrum, and (c) streetlight (LED-type and gas-type), readily available light sources for long-range spectroscopy.

Calibration of all spectral data needs to be done to convert the EB camera output into standard light intensity units. This part of the work is ongoing.

4 Results and Analysis

For majority of pseudo images presented in this work integration time was chosen to equal the standard camera exposure time of $\Delta t = 33$ ms except for the dynamic range tests, as described in Sect. 4.2.

4.1 Calibration Light Source Spectra

Broadband Light Source The data reported in Fig. 2 were collected through emission spectroscopy technique using a broadband light source, a tunable LED light source which was used with a 5 mm diameter port, while the output luminance was set to 500 cd/m^2. The recorded broadband spectrum is shown in Fig. 2a, while sections of broadband spectrum are displayed in Fig. 2b. These sections represent spectral regions of the broadband spectrum, obtained using a range of bandpass filters with 10 nm range, which has also helped to determine the bounds of the spectral range achieved. Both figures were created by stitching together pseudo images for different wavelength ranges, to show the full wavelength range achieved with this system. To create light intensity changes with this stationary system, the base plate had to be slightly tapped, also resulting in two spectral lines of different colors and a small spacing between them. The white color in the images corresponds to "ON" events (increase in light intensity), and the blue to "OFF" events (decrease in light intensity). The results shown in this section represent successful demonstration of the basic spectroscopic capability, i.e., ability of the instrument to capture broadband spectrum.

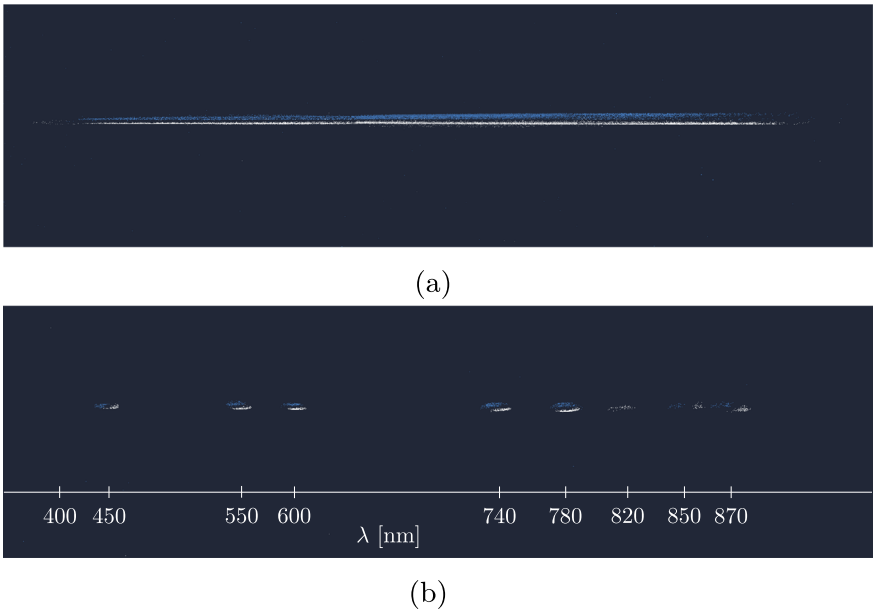

Fig. 2 Example of spectra from a broadband light source: **a** broadband spectrum and **b** sections of broadband spectrum obtained with bandpass filters

Spectral Line Light Source These tests were done using a Mercury-Argon spectral calibration source. The optical power in 600 μm fiber is 1.6 mW. Figure 3a illustrates data obtained with EB camera system; a discrete spectrum, or individual spectral lines, used for wavelength calibration of the EB recordings and corresponding to the light source output, as demonstrated in Sect. 4.1. Figure 3b shows the output of the light source, as provided by the manufacturer. The same calibration light source output was then recorded with a compact spectrometer (Thorlabs CCS175) for a range from 500–1000 nm, shown in Fig. 3c.

4.2 Dynamic Range

EB and standard camera spectrometers were mounted side-by-side and output of the broadband light source (Labsphere PT-038-PLS) recorded at varying luminance levels. These tests were done in a dark room (i.e., lights turned off) with potential sources of light reflection covered. Standard camera spectrometer used settings typically employed in airborne observation missions when recording radiation from a spacecraft re-entering the Earth's atmosphere. Bias values of the EB camera were adjusted, while other were left at default values of the software (Metavision SDK version 4.5.1). The integration time for pseudo images was reduced to $\Delta t = 10$ μs. This time interval was chosen as it corresponds to the average time it takes from when a row of a pixel firing is readout for the first time to the time when the same (or close-by) row of pixel firing is readout again. Since the EB camera records only when there is a change of light intensity in the field of view, an iris was used to block the light source prior to recording and once the recording started, the iris was opened to let the light in. A motorized iris was used for precise and quick control of the aperture. Both camera systems were located at 1 m distance from the light source aperture. The results at specific luminance levels are shown in Fig. 4. The EB data shows a partial spectrum already at the luminance level of 1 cd/m^2, but as not a full spectrum it was not deemed satisfactory. Standard camera images also show spectrum at the lowest luminance setting; but, the SNR is too low for these to be useful. The level of 5 cd/m^2 was determined to be the lower bound for both the EB and the standard camera systems. Images show full spectra at adequate signal-to-noise ratio (SNR) for information extraction. The upper bound of the standard camera system is at 80 cd/m^2, when images become saturated. The upper bound of the EB system is more difficult to find presently as the intensity calibration has not been completed. However, we determined this to be at around 500 cd/m^2, when the shape of the spectrum changes slightly, showing a small bump on the upper side. These results show that while both systems indicate the same lower bound, the standard camera system's upper bound is already at 80 cd/m^2, while the one of the EB system is much higher at 500 cd/m^2. This large difference illustrates the extended dynamic range of the EB camera in the spectroscopy setting. However, the reported values are used

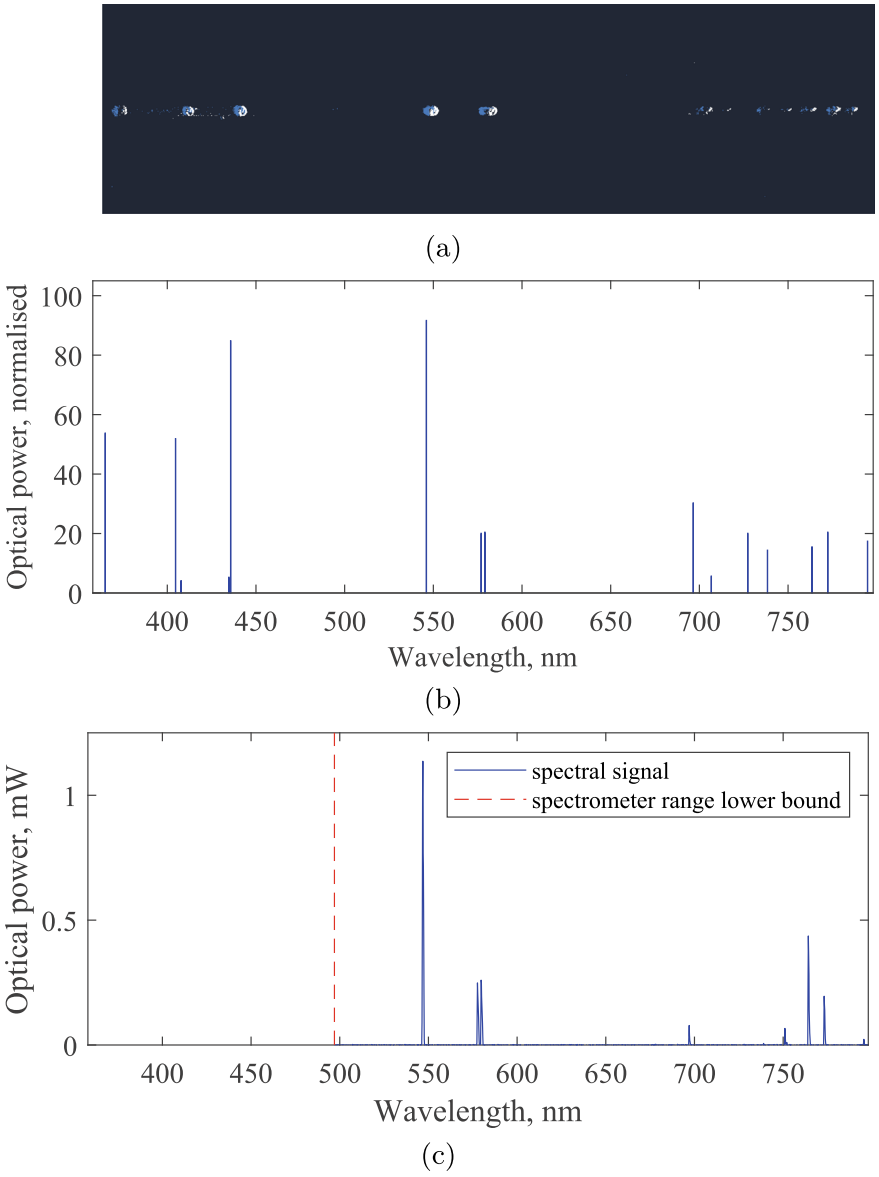

Fig. 3 Comparison of spectra from different sources

here for comparative purposes only, as luminance is a photometric quantity which would need to be converted to its analogue radiometric quantity, radiance, to obtain the amount of light across all wavelengths, and thus a more accurate measurement of the light intensity.

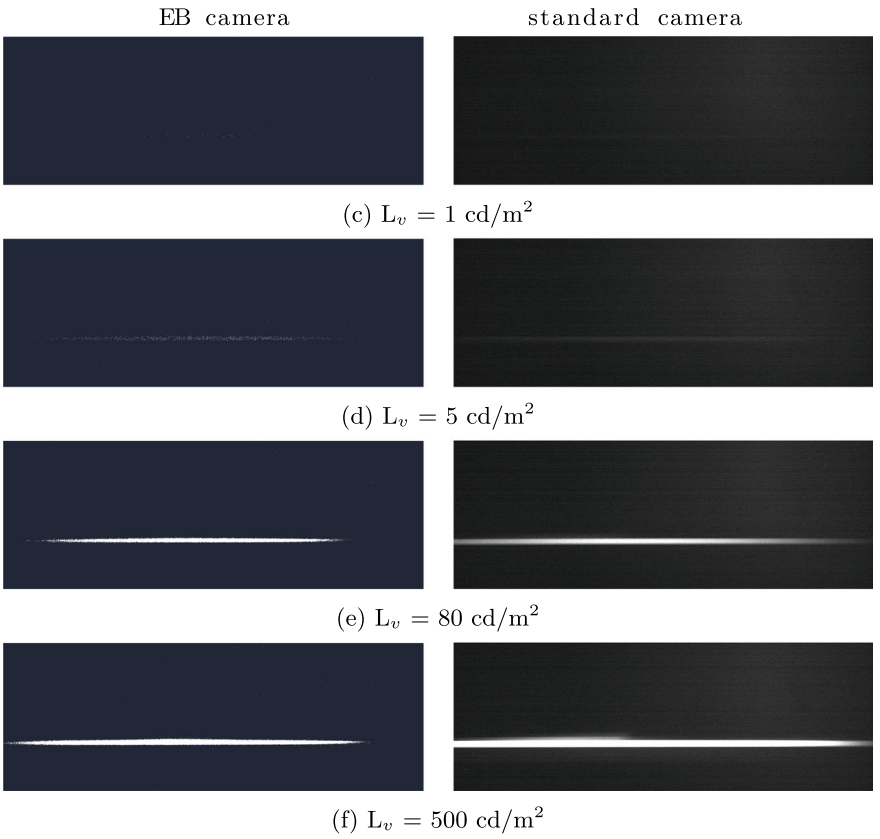

Fig. 4 Demonstration of the dynamic range

4.3 Long-Range Spectroscopy

As objects typically observed during hypersonic flight events are at least many tens of kilometers away from the recording instruments, spectra was imaged from the flagpole beacon light at a distance of approximately 7 km during nighttime. The result is shown in Fig. 5 with another, discrete spectrum consisted of particular spectral lines (observed as bright spots on top of continuous spectrum), thus indicating that it is coming from a gas-type of lamp. The spectral lines locations, originating from the gas-type lamp, were identified and are marked with horizontal lines in the figure. This gas-type lamp with the typical light output color orange-red is most likely a neon lamp, emitting in the range of 600–700 nm. Neon gas discrete spectrum with known spectral line wavelengths has been added for comparison, and the conclusion is that the spectrum of the gas-type lamp is most likely neon spectrum. This also helps us to identify the beacon light spectrum wavelength region as approximately 620–650 nm.

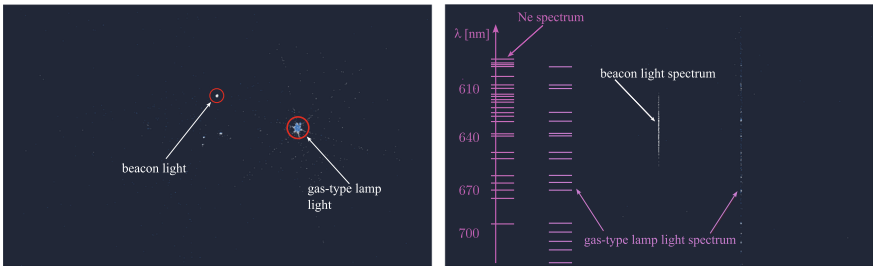

(a) Image (b) Spectra

Fig. 5 Example of spectra from two different lights at over 5 km distance

5 Conclusion

This work demonstrates the viability of pairing EB cameras and a diffraction grating to record spectra. Measurements with this neuromorphic system were done using a range of light sources and conditions, and the results show the system's ability to capture both broadband and line spectra. By comparison with the spectra produced using a known source and manufacturer's data, specific lines of Hg and Ar were identified. Dynamic range and long-range spectroscopy results show improvement in performance of the EB system over the standard camera. Long-range spectroscopy results show the ability of the EB system to capture spectra from several kilometers distance. The reported results provide confidence in using neuromorphic spectroscopy to obtain hypersonic flight data.

References

1. Afshar S, Nicholson AP, van Schaik A, Cohen G (2020) Event-based object detection and tracking for space situational awareness. IEEE Sensors J 20(24):15117-1-5132. https://doi.org/10.1109/JSEN.2020.3009687
2. Delbrück T, Lang M (2013) Robotic goalie with 3ms reaction time at 4% CPU load using event-based dynamic vision sensor. Front Neurosci 7. https://doi.org/10.3389/fnins.2013.00223
3. Gallego G, Delbrück T, Orchard G, Bartolozzi C, Taba B, Censi A, Leutenegger S, Davison A, Conradt J, Daniilidis K, Scaramuzza D (2020) Event-based vision: a survey. IEEE PAMI 44(1):154–180. https://doi.org/10.1109/TPAMI.2020.3008413
4. Jenniskens M, Gural P, Dynneson L, Grigsby B, Newman K, Borden M, Koop M, Holman D (2011) CAMS: cameras for Allsky meteor surveillance to establish minor meteor showers. Icarus 216:40–61. https://doi.org/10.1016/j.icarus.2011.08.012
5. McIntyre TJ, Khan R, Eichmann TN, Upcroft B, Buttsworth D (2014) Visible and near infrared spectroscopy of Hayabusa reentry using semi-autonomous tracking. J Spacecr Rockets 51(1):31–36. https://doi.org/10.2514/1.A32497

6. Sopek T, Glenn A, Clarke J, Di Mare L, Collen P, McGilvray M (2024) Radiative heat transfer measurements of Titan atmospheric entry in a shock tube. J Thermophys Heat Transf Articles in Adv. https://doi.org/10.2514/1.T6918

Open Access This chapter is licensed under the terms of the Creative Commons Attribution 4.0 International License (http://creativecommons.org/licenses/by/4.0/), which permits use, sharing, adaptation, distribution and reproduction in any medium or format, as long as you give appropriate credit to the original author(s) and the source, provide a link to the Creative Commons license and indicate if changes were made.

The images or other third party material in this chapter are included in the chapter's Creative Commons license, unless indicated otherwise in a credit line to the material. If material is not included in the chapter's Creative Commons license and your intended use is not permitted by statutory regulation or exceeds the permitted use, you will need to obtain permission directly from the copyright holder.

Spectroscopic Studies in Non-equilibrium Plasmas

Ruairí J. O'Connor and Philip L. Varghese

Abstract A near-room-temperature capacitively-coupled plasma (CCP) glow discharge cell is used for fundamental studies of low and intermediate pressure Ar plasmas. The cell consists of two cylindrical plate electrodes powered by a 13.56 MHz radio-frequency source, forming a diffuse low-pressure plasma between the electrodes inside a cylindrical glass envelope 10 cm in diameter. The cell is operated at pressures from 0.1 to 10 Torr and electrode voltages up to $\sim$ 2 kV depending on pressure, producing plasmas in which the free electron temperature ranges up to several electron-volts while the gas remains close to ambient temperature ($\sim$ 300K). The emission lines from Ar in the visible and near infra-red (NIR) correspond primarily to transitions from $4p$ states to the metastable and resonant $4s$ Ar states. Calibrated Emission Spectroscopy using Absolute Radiance (CESAR) measurements on these transitions are used to determine population densities of Ar $4p$ states. Tunable laser absorption spectroscopy is used to measure the metastable and resonant Ar $4s$ state populations. These densities are presented in combination with electron density and energy distribution function measurements performed with a Langmuir probe. These measurements enable us to assess the degree of non-equilibrium in the plasma as a function of pressure and electrode voltage. We use Monte Carlo techniques to quantify the uncertainty of all the measurements. The experimental results are used to enhance our understanding of non-equilibrium plasmas and to validate kinetic models of excitation and ionization processes in plasmas.

Keywords Spectroscopy · Non-equilibrium plasma · Emission spectroscopy · Absorption spectroscopy · Langmuir probe

R. J. O'Connor · P. L. Varghese
Department of Aerospace Engineering and Engineering Mechanics, The University of Texas at Austin, Austin, TX, USA

P. L. Varghese (✉)
Oden Institute for Computational Engineering and Sciences, The University of Texas at Austin, Austin, TX, USA
e-mail: varghese@mail.utexas.edu

© The Author(s) 2026

M. Grabe et al. (eds.), *Rarefied Gas Dynamics*, Springer Aerospace Technology,
https://doi.org/10.1007/978-3-032-00094-1_6

1 Introduction

1.1 Background and Motivation

Capacitively coupled plasmas (CCP) are important in many areas of research and industry [2, 4, 8, 17]. Low-temperature glow discharge CCPs present an opportunity for fundamental plasma study with broad applications. The non-equilibrium nature of these plasmas motivates the application of a variety of spectroscopic and probe-based measurements techniques to characterize processes occurring within them.

The basic concept of a CCP is very simple. A plasma is formed in a volume between two capacitively coupled electrodes separated by some gap distance and driven by a radio frequency (RF) oscillating power supply. The bench-top nature of glow discharge devices makes them an attractive target for researchers. Optical and probe access can be readily achieved and a variety of diagnostics applied.

The motivation for this work is to generate data which may be useful to study and validate electron kinetic models and collision cross-sections to be used in advanced plasma simulations. This paper provides an overview of the glow discharge plasma facility and diagnostics currently implemented at UT Austin. The work outlined here, including detailed analysis of the results beyond the scope possible in this paper, will be published in a series of planned, upcoming publications. Optical emission spectroscopy (OES), laser absorption spectroscopy (LAS), and Langmuir probe techniques are applied to a range of low-temperature, low-pressure Ar plasmas. The optical diagnostics were chosen due to their non-intrusive nature and ability to access electronically excited states in the plasma. Results from the OES measurements can be used to correct for stimulated emission in the LAS diagnostic, although this effect is found to be quite small in the observed plasmas. The Langmuir probe allows detailed measurement of the electron energy distribution function (EEDF). Excited state population densities, characteristic temperatures, EEDF and electron density are measured. These results represent a rich set of inputs and validation targets for future non-equilbrium plasma models.

1.2 Glow Discharge Facility

The glow discharge facility at UT Austin consists of the plasma chamber itself as well as the associated control and diagnostic devices. The overall facility is shown schematically in Fig. 1. The plasma volume is formed by two 10 cm diameter parallel plate aluminum electrodes separated by 20 mm and contained within a cylindrical glass chamber. A power supply provides up to 2 kV RF signal at 13.56 MHz via a matching network to the top electrode while the bottom electrode is grounded. Peak-to-peak voltage amplitude is measured using an Impedans Octiv Suite device [10]. Peak-to-peak current amplitude, the phase between voltage and current as well as the RMS power are also recorded. A vacuum pump is used to achieve pressures

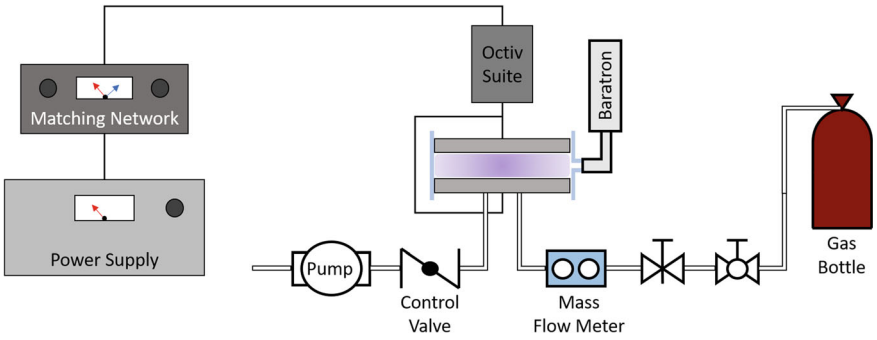

Fig. 1 Schematic diagram of the glow discharge facility

of 0.1 Torr to 10 in the chamber. Ar gas is supplied from lab bottles and regulated using needle valves and a vacuum control valve. Pressure is measured using an MKS Baratron capacitive manometer which is also used in the feedback system for pressure control.

The facility features three diagnostic capabilities, shown in Fig. 2: optical emission spectroscopy (OES), laser absorption spectroscopy (LAS) and a Langmuir probe. These diagnostics are configured to measure time-averaged plasma properties at the center of the plasma volume. Each of these diagnostic techniques are described further in the subsequent sections.

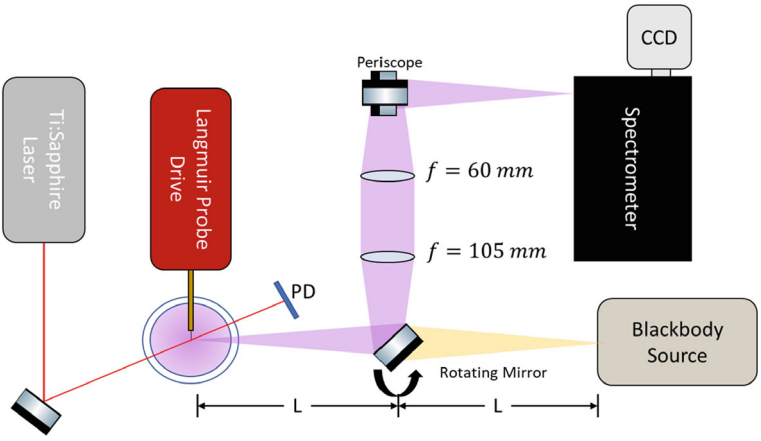

Fig. 2 Schematic diagram of the diagnostics in the glow discharge facility

2 Argon Spectroscopy

2.1 Optical Emission Spectroscopy

OES can be used to measure transitions between electronically excited states of the Ar atom. (Transitions to the ground electronic state are in the vacuum ultraviolet and are not easily measured.) These transitions create a spectrum like the one shown in Fig. 3a. Spectra which are calibrated in both wavelength and absolute spectral radiance can be used to infer the absolute population density of each upper state of the observed transitions. The spectral radiance calibration is performed by measuring a blackbody source at a known temperature of 1473K, as shown in Fig. 2, and comparing the recorded signal to the known spectral radiance of a blackbody given by Planck's equation:

$$B_\lambda(\lambda, T) = \frac{2hc^2}{\lambda^5} \frac{1}{e^{hc/\lambda k_B T} - 1}. \tag{1}$$

Since Ar is a monatomic gas, only electronic energy modes can be excited. The electronic excited states of Ar can be visualized using the Grotrian diagram in Fig. 3 [13]. This diagram emphasizes two excited state groupings of importance to this work. The Ar($4p$) group consists of ten individual states which radiatively decay to the four states in the Ar($4s$) group, emitting light in the visible and near-infra-red and is the basis for our OES measurements. The reverse process, stimulated absorption, is exploited in the LAS measurements discussed in the next section.

In an equilibrium plasma the states should follow a Boltzmann distribution described by Eq. 2:

$$\frac{N_i}{N_j} = \frac{g_i}{g_j} \exp\left(\frac{E_j - E_i}{k_B T}\right), \tag{2}$$

where N_k is the population density, E_k is the energy, and g_k is the degeneracy of state k, where subscript $k = i, j$ refers to the lower and upper states of the transition, respectively. Low-temperature CCPs are known to be in non-equilibrium states, but Eq. 2 provides a useful reference for quantifying the departure from equilibrium in these plasmas. Here B_λ is the spectral radiance of the plasma, λ is the wavelength, T is the temperature, and h, k_B and c are Planck's constant, Boltzmann's constant and the speed of light, respectively.

In order to infer the absolute population density of the upper Ar($4p$) state in each of the observable transitions the following model is used [9]. Assuming uniform conditions along the measurement line-of-sight, a cylindrical measurement volume and an optically thin plasma, the integrated signal intensity of each transition can be related to the upper state population density through

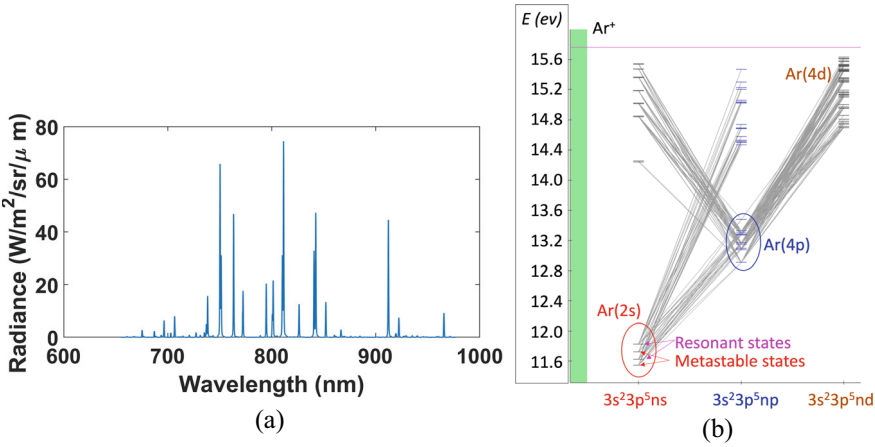

Fig. 3 **a** Spectrum of an Ar plasma at 100 mTorr and 150 V (0.34 W) **b** Grotrian diagram of Ar excited states (reproduced from NIST Atomic Spectra Database [13])

$$I_{ji} = \int_{\lambda_1}^{\lambda_2} \frac{S_{ji}(\lambda)}{C_\lambda} d\lambda = \int_{\lambda_1}^{\lambda_2} n_j \frac{A_{ji}}{4\pi} \frac{hc}{\lambda_{ji}} \Delta L \phi(\lambda, \lambda_{ji}) d\lambda = n_j \frac{A_{ji}}{4\pi} \frac{hc}{\lambda_{ji}} \Delta L. \quad (3)$$

Here A_{ji} is the Einstein spontaneous emission coefficient taken from [13], I_{ji} is the integrated line strength or emission coefficient, ΔL is the depth of field of the imaging system, and ϕ is the line shape function. In this work, ϕ is assumed to be a Gaussian and each measured transition is fit with this function in order to integrate the line profiles analytically.

When this model is applied to each observable transition, the populations of each Ar($4p$) state can be inferred and their distribution visualized in a Boltzmann plot, such as those shown in Fig. 4a and b. The uncertainty bars in these plots are derived from a Bayesian estimate accounting for detector noise as well as the uncertainty in the Einstein A-coefficients [13] and the experimentally determined depth of field. If the states were Boltzmann distributed per Eq. 2, their degeneracy-weighted populations would fall along a straight line in a logarithmic plot against state energy. From Fig. 4 it is clear that this is not the case. The state populations are highly non-equilibrium. The population distributions also change with the plasma conditions indicating that kinetic effects on the excited state populations are important. This type of detailed plasma study using OES can provide a rich dataset for understanding the kinetic processes in the plasma and how those processes change with both pressure and applied voltage.

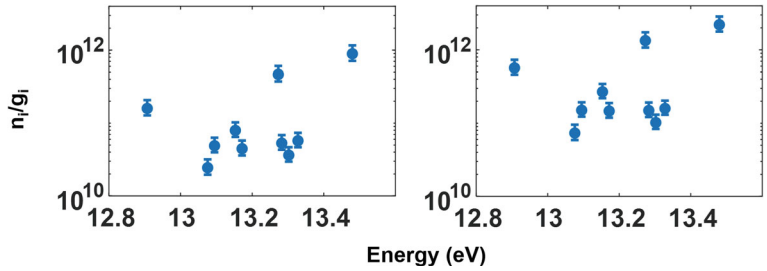

Fig. 4 Boltzmann plots of Ar $4p$ population densities in plasma discharges at 500 mTorr (left) and 1 Torr (right) at 200 V discharge voltage (2.0 and 3.9 W, respectively)

2.2 *Laser Absorption Spectroscopy*

The same transitions which are studied in emission in Sect. 2.1 can be studied in absorption using tunable laser absorption spectroscopy. As seen in Fig. 3, laser absorption spectroscopy targets transitions from the Ar($4s$) to the Ar($4p$) states. The measurement is achieved by passing a widely tunable Titanium:Sapphire laser through the plasma volume and onto a photodetector as shown in Fig. 1. Some of the laser light is split and passed through an air-spaced etalon of known length and onto a second photodetector to provide a relative wavelength calibration from the fringe pattern. As the laser wavelength is scanned across a transition, the absorption signal is measured and an absolute population density of the lower state in the transition (Ar($4s$) in this case) can be obtained using:

$$\frac{\mathrm{d}P_\nu}{P_\nu} = -(n_i B_{ij} - n_j B_{ji}) h\nu\phi(\nu)\mathrm{d}z, \tag{4}$$

where P_ν is the laser power to the detector, B_{ij} and B_{ji} are the Einstein B-coefficients, ν is the laser frequency and z is in the direction of propagation of the laser beam. The Einstein A- and B-coefficients are related [15] by:

$$g_i B_{ij} = g_j B_{ji} = g_j \frac{c^2}{2h\nu^3} A_{ji}. \tag{5}$$

If conditions are assumed to be uniform along the line of sight the integration is over the plasma slab depth, taken to be the diameter of the discharge D, and gives the transmissivity $\tau(\nu)$:

$$\ln(\tau(\nu)) = -(n_i B_{ij} - n_j B_{ji}) h\nu\phi(\nu) D. \tag{6}$$

The population of the upper state in the transition is needed in this equation in order to correct for stimulated emission from the Ar($4p$) states. We cannot use the equilibrium correction for stimulated emission and the population density from the

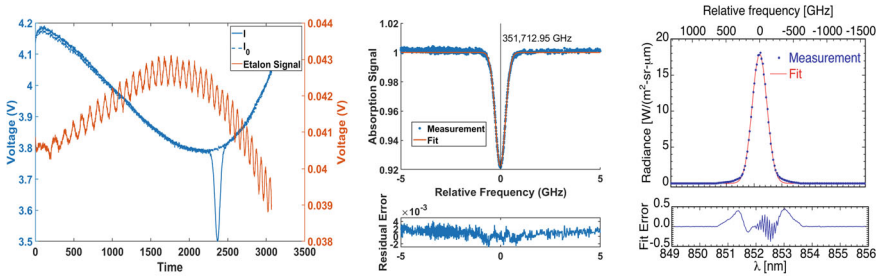

Fig. 5 **a** Raw LAS measurement of Ar $4p \leftarrow 4s$ transition at 852.144 nm recorded in a 1 Torr discharge with 150 V (1.4 W) excitation showing incident I_o, and transmitted I, signals and simultaneously recorded etalon fringe pattern. **b** Calibrated transmissivity plotted as a function of frequency detuning from line center **c** Corresponding emission line under the same conditions. Note the much larger linewidth of the recorded emission line (FWHM $\approx$ 258 GHz) compared to the absorption line (FWHM $<$ 1 GHz.)

OES measurements is used to make this correction. The correction is very small ($< 1\%$) for our experimental conditions. Figure 5 shows a representative measurement of the unabsorbed laser signal (incident intensity recorded with the cell evacuated) and absorbed (transmitted through the cell with discharge operating), as well as the etalon fringe pattern used for the relative frequency calibration. The transmissivity as a function of relative frequency is shown in the second panel. Figure 5 also compares the extremely high spectral resolution of the LAS measurement compared to the OES measurement of the same line at the same plasma condition (852nm, 1Torr, 150V, 1.4W). The absorption line (full width $<$ 1 GHz) is much narrower than the emission line (full width 258 GHz) showing that the recorded emission line broadening is almost entirely due to instrument broadening effects of the spectrometer.

Some representative results from the LAS measurements are shown in Fig. 6 for one plasma condition. It can be seen that the Ar($4s$) states are much closer to Boltzmann distributed than the Ar($4p$) states. From the plot we infer that an approximate

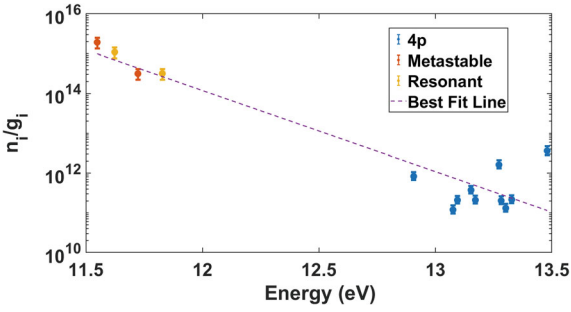

Fig. 6 Boltzmann plot showing $4s$ states measured with LAS as well as $4p$ states measured in OES. Condition shown is 1 Torr, 150 V (1.4 W)

electronic temperature of 0.44 eV describes the relative populations of the Ar($4s$) and Ar($4p$) states, with some of the $4p$ states showing significant non-equilibrium. A detailed comparison of these results with a collisional-radiative model has been submitted for publication [16].

3 Langmuir Probe

A Langmuir probe system from Impedans [12] has been used to measure the EEDF and the electron density and temperature via the moments of the EEDF. The basic concept of the diagnostic is to introduce a thin wire probe tip (∼1mm in diameter) into the plasma volume and bias it relative to the plasma potential [1, 14]. As the bias potential (voltage) is swept the current drawn to the probe tip is measured. At strongly negative biases the current is dominated by ion flux to the probe and at strongly positive biases the current is dominated by electron flux. The total measured current is the sum of the electron and ion current contributions. The variation of electron current drawn by the probe as a function of the bias voltage can be related to the EEDF via the Druyvesteyn model [3] (Eq. 7) assuming (1) an isotropic EEDF. and (2) that the electrons experience no collisions in the sheath around the probe tip. The Impedans probe incorporates RF and DC compensation electronics to minimize well-known perturbative effects of the probe measurement [7, 11]. These consist of self-resonant inductors tuned to the RF driving frequency and its harmonics as well as additional compensation electrodes which capacitively couple to the probe tip to reduce the sheath impedance. A DC reference probe tip is also used to account for local perturbations caused by the probe voltage sweep. The probe geometry is designed to taper down using several steps to contract from the 10mm probe support to the 1mm probe tip to minimize perturbations near the tip.

$$I_e(V - V_p) = \frac{-A_p q_e}{2} \int_{-q_e(V-V_p)}^{\infty} \left(1 + \frac{q_e(V_p - V)}{W}\right) \sqrt{\frac{W}{2m_e}} F(W) dW \tag{7}$$

Here I_e is the electron current to the probe, V is the bias voltage, V_p is the plasma potential, A_p is the probe tip area, q_e is the electron charge, m_e is the electron mass, W is the electron kinetic energy and $F(W)$ is the EEDF. When the distribution function is found, the electron density, n_e, and mean energy, E_{avg} can be found via Eq. 8.

$$n_e = \int_0^{\infty} F(W) dW \tag{8a}$$

$$E_{avg} = \frac{1}{n_e} \int_0^\infty W F(W) dW \tag{8b}$$

In practice the Druyvesteyn model is typically inverted so that the EEDF can be inferred directly from a measured probe I-V trace, shown in Eq. 9. The presence of a second derivative operator on the measured current introduces the complication of noise amplification. Direct derivatives of the measurement can lead to extremely noisy results. To remedy this, we use a Savitzky-Golay filter to smooth and differentiate the probe trace. The resulting smoothed curves and derivatives are shown for a representative measurement in Fig. 7. Also shown is an inferred EEDF. The plasma potential is found as the zero-crossing of the second derivative of the measurement. The results are promising although the use of the Savitzky-Golay filter may introduce artificial features in the distribution function. Measurement uncertainties were not computed for this technique and are assumed to be large (only reliable for order of magnitude estimates of electron density). A more sophisticated model specifically designed for rigorous uncertainty quantification, discussed below, is being developed. Also worth noting, while the Druyvesteyn model is only strictly valid for the component of the measured current coming from electron flux (the measured current is the sum of contributions from both electrons and ions), the second derivative of the ion current is negligible and thus the second derivative of the measured current is considered equal to the second derivative of just the electron component [5–7].

$$\frac{d^2 I_e}{dV^2} = \frac{q_e^2 A_p}{4} \sqrt{\frac{2q_e}{m_e W}} F(W) \tag{9}$$

Some results are shown in Fig. 8 where it can be seen that the electron density increases with both pressure and voltage. At 2.5Torr the assumption of collisionless sheaths for the electrons is suspect, and these results are only illustrative of rough trends in the plasma.

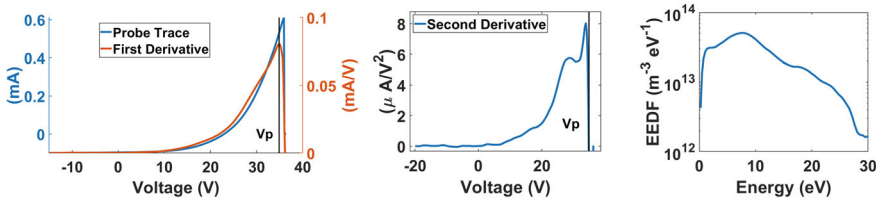

(a) (b) (c)

Fig. 7 **a** Electron current measurement for 500mTorr and 100V (0.25W) and Savitzky-Golay filtered first derivative. The ion current has been subtracted using a straight line fit to the ion dominated portion of the probe trace. **b** Savitzky-Golay derived second derivative. **c** The resulting EEDF (n_e: $6.8 \times 10^{14} m^{-3}$, E_{avg}: $7.4eV$)

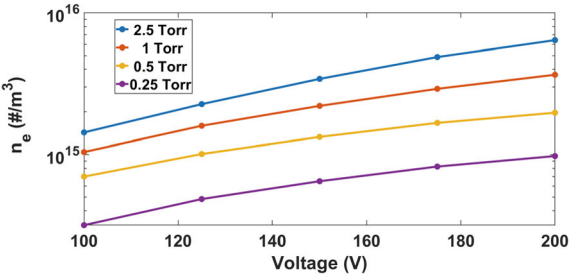

Fig. 8 Trends in electron density for Ar plasmas inferred from Savitzky-Golay filtered Langmuir probe measurements. While the trends are quite accurate, there is an order of magnitude uncertainty in the absolute values due to the derivative analysis technique

The Langmuir probe analysis can be improved by avoiding the differentiation and fitting process entirely. One approach is to fit the Druyvesteyn model directly by representing the EEDF with a set of basis functions and finding the coefficients which best reproduce the experimentally observed current as shown in Eq. 10.

$$I_j = \int_{-qe(V_j - V_p)}^{\infty} G(V_j - V_p, W) \sum_{k=1}^{m} F_k \varphi_k(W) dW + e_j = \mathcal{L}_{jk}(V_p) F_k + e_j \quad (10)$$

Here $\varphi_k(W)$ is the kth basis function, F_k is the kth basis coefficient, G is a function containing the Druyvesteyn model, e is an assumed additive error and j refers to the jth measurement point. A least-squares minimization approach can be used to infer the basis coefficients, with the plasma potential estimated simultaneously. This approach has been tested on analytical test data with a small amount of added noise $O(10^{-5} I_{probe})$. The results are shown in Fig. 9.

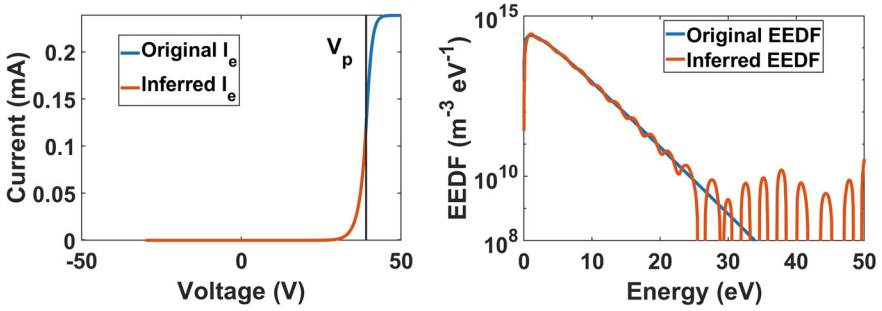

Fig. 9 Initial results of least-squares fitting approach on simulated Langmuir probe measurements. The effect of added noise is clearly seen in the EEDF retrieved

The results are promising, and this approach is being developed further and expanded to a Bayesian uncertainty quantification framework. Page restrictions preclude additional description and full details of this model and the Bayesian inference approach will be discussed in an upcoming publication. Rigorous measurements of EEDFs and electron densities with properly quantified uncertainty will be of immense help in the development and validation of plasma kinetic models under a range of conditions.

4 Conclusion

A pair of non-intrusive optical diagnostics, optical emission spectroscopy and tunable laser absorption spectroscopy, as well as an intrusive probe-based Langmuir probe diagnostic have been applied to Ar plasmas at medium vacuum pressures. Absolute population densities of excited Ar($4p$) and Ar($4s$) states have been measured using optical techniques. The electron energy distribution function and resulting moments have also been measured with the Langmuir probe. This suite of measurements can provide a rich dataset for validation of plasma models such as collisional-radiative models and reduced-order plasma chemistry models. Their application to non-equilibrium plasmas introduces some diagnostic challenges but provides valuable insight into the kinetics which govern the plasma behavior.

Continued work in this area will lead to improvements in non-equilibrium diagnostic techniques and a greater understanding of this important class of plasmas. Evaluation of non-equilibrium spectra continues to be a challenge. We will extend the optical and probe measurements to low pressure nitrogen plasmas in future work. Langmuir probe models that are valid for a wider range of plasma conditions, as well as techniques to evaluate probe measurements in the context of experimental noise and uncertainty, should be developed. The rarefied gas dynamics community can contribute to the extension of the analysis of probes with collisional sheaths.

Acknowledgements This work is supported by the Department of Energy, National Nuclear Security Administration under Award Number DE-NA0003969. PSAAP III grant: *"Exascale Predictive Simulation of Inductively Coupled Plasma Torches"*

References

1. Chen FF (2012) Lecture notes on Langmuir probe diagnostics. Contribut Plasma Phys 52(4):295–308
2. Crose M, Sang-Il Kwon J, Nayhouse M, Ni D, Christofides PD (2015) Multiscale modeling and operation of pecvd of thin film solar cells. Chem Eng Sci 136:50–61; Control and optimization of smart plant operations https://www.sciencedirect.com/science/article/pii/S0009250915001426
3. Druyvesteyn M (1930) Der Niedervoltbogen. Zeitschrift für Physik 64(11–12):781–798

4. Fang M, Zhang C, Chen Q (2016) Tuning the ito work function by capacitively coupled plasma and its application in inverted organic solar cells. Appl Surf Sci 385:28–33. https://www.sciencedirect.com/science/article/pii/S0169433216310856
5. Godyak VA (1990) Measuring EEDF in gas discharge plasmas
6. Godyak VA, Alexandrovich BM (2015) Comparative analyses of plasma probe diagnostics techniques. J Appl Phys 118(23). https://doi.org/10.1063/1.4937446
7. Godyak V, Alexandrovich B (2002) Electron energy distribution function measurements and plasma parameters in inductively coupled argon plasma. Plasma Sources Sci Technol
8. Horváth B, Derzsi A, Schulze J, Korolov I, Hartmann P, Donkó Z (2020) Experimental and kinetic simulation study of electron power absorption mode transitions in capacitive radiofrequency discharges in neon. Plasma Sources Sci Technol 29(5):055002. https://dx.doi.org/10.1088/1361-6595/ab8176
9. Huddlestone RH, Leonard SL (1965) In: Plasma diagnostic techniques. Academic Press
10. Impedans: Octiv suite [apparatus and software]. https://www.impedans.com (2007)
11. Impedans: Impedans langmuir probe installation and user guide v2.17 (2017)
12. Impedans: Langmuir probe [apparatus and software]. https://www.impedans.com (nd)
13. Kramida A, Ralchenko Y, Reader J, NIST ASD team: NIST atomic spectra database (ver. 5.11), December, National Institute of Standards and Technology, Gaithersburg, MD. [Online]. Available: https://physics.nist.gov/asd
14. Mott-Smith H, Langmuir I (1926) Theory of collectors in. Phys Rev 28:727–763
15. Oxenius J (1986) In: Kinetic theory of particles and photons. Springer
16. Tsagkaridis M, Oliver T, Fries D, O'Connor R, Barberena-Valencia J, Raja L, Varghese P, Moser R (2025) Modeling of low-temperature argon plasma in capacitively-coupled glow discharges with a collisional-radiative model. Manuscript submitted for publication
17. Vass M, Wilczek S, Derzsi A, Horváth B, Hartmann P, Donkó Z (2022) Evolution of the bulk electric field in capacitively coupled argon plasmas at intermediate pressures. Plasma Sources Sci Technol 31(4):045017. https://doi.org/10.1088/1361-6595/ac6361

Open Access This chapter is licensed under the terms of the Creative Commons Attribution 4.0 International License (http://creativecommons.org/licenses/by/4.0/), which permits use, sharing, adaptation, distribution and reproduction in any medium or format, as long as you give appropriate credit to the original author(s) and the source, provide a link to the Creative Commons license and indicate if changes were made.

The images or other third party material in this chapter are included in the chapter's Creative Commons license, unless indicated otherwise in a credit line to the material. If material is not included in the chapter's Creative Commons license and your intended use is not permitted by statutory regulation or exceeds the permitted use, you will need to obtain permission directly from the copyright holder.

Initial On-Orbit Cross-Calibration of the Electric Propulsion Electrostatic Analyzer Experiment (ÉPÉÉ)

C. A. Maldonado, T. Eddy, P. A. Fernandes, T. K. Kim, J. Derr, A. Barjatya, S. Debchoudhury, G. R. Wilson, A. J. Rogers, M. Dunn, S. M. Klem, B. Weaver, R. Ulrich, K. Potter, K. Moran, L. Castro, J. McGlown, J. D. Williams, R. L. Balthazor, P. Neal, J. Stauffer, and M. G. McHarg

Abstract The Electric Propulsion Electrostatic Analyzer Experiment is the most recent iteration in a series of laminated electrostatic analyzers that have flown in space. The sensor functions as an ion energy bandpass filter for space plasma, from which the ambient ion density, temperature, and subsequent spacecraft frame charge can be obtained. We present the ÉPÉÉ instrument design and initial on-orbit cross-calibration with the Floating Potential Measurement Unit. The calibrated data are then used to provide observations of the mid-latitude ionosphere during the geomagnetic storms that occurred on November 4th and 5th in 2023.

Keywords Ionosphere · Spacecraft charge · Geomagnetic storm

1 Introduction

The Electric Propulsion Electrostatic Analyzer Experiment (ÉPÉÉ) payload operated on-board the International Space Station (ISS) as a manifested payload on the Space Test Program—Houston 9 (STP-H9) platform from March 15th, 2023, to April 24th,

C. A. Maldonado (✉) · T. Eddy · P. A. Fernandes · T. K. Kim · J. Derr · G. R. Wilson · A. J. Rogers · M. Dunn · S. M. Klem · B. Weaver · R. Ulrich · K. Potter · K. Moran · L. Castro · J. McGlown
ISR-1, Los Alamos National Lab, Los Alamos, NM, USA
e-mail: cmaldonado@lanl.gov

T. K. Kim · A. Barjatya · S. Debchoudhury
Embry-Riddle Aeronautical University, Prescott, AZ, USA

J. D. Williams · R. L. Balthazor · J. Stauffer
i2 Strategic Services, Colorado Springs, CO, USA

P. Neal · M. G. McHarg
US Air Force Academy Department of Physics, Colorado Springs, CO, USA

© The Author(s) 2026

M. Grabe et al. (eds.), *Rarefied Gas Dynamics*, Springer Aerospace Technology,
https://doi.org/10.1007/978-3-032-00094-1_7

2024. The ÉPÉÉ is a fourth-generation iteration of the family of laminated electrostatic analyzers [1, 2]. The ÉPÉÉ payload is a collaborative effort between the Los Alamos National Laboratory (LANL) and the United States Air Force Academy (USAFA). The sensor provides in-situ energy distribution, density, temperature, and spacecraft charge measurements of the local ionospheric plasma. The operational lifetime of the ÉPÉÉ payload aligns with the ascension towards the solar maximum of Solar Cycle 25, allowing for science observations during a period with frequent and sizeable geomagnetic storms.

2 Instrument Description

The laminated design of ÉPÉÉ is based on previous laminated analyzer designs that have flown in space such as the Flat Plasma Spectrometer (FlaPS), Canary, integrated Miniaturized Electrostatic Analyzer (iMESA) [1, 3], and Automated Plums Sentry (APS) [4] instruments. The ÉPÉÉ laminated analyzer design uses geometry coupled with an electric field to act as an energy band pass filter for charged particle populations. The laminated sensor head is composed of stacked conducting electrode layers with patterns of holes and slots machined in each layer to create any number of analyzer elements [4]. Each element consists of a laminated collimator front-end to set the field-of-view (FOV) and prevent unwanted photons from entering the analyzer. The collimator section is implemented to reduce scatter and prevent off-angle incident ions from entering the detector in addition to preventing photons from entering the analyzer and creating contaminating background signal [5–7]. The collimator is also effective at reducing the effects of spacecraft potential due spacecraft sheath focusing [8]. The front-end collimator is then followed by a laminated ESA cavity where ions are separated based on *E/q*. The ESA section consists of (1) an entrance aperture, (2) ESA cavity, and (3) an exit aperture. As ions enter the ESA cavity, they are subjected to an electric field created by biasing created by applying a bias to the discriminator plate, V_1, while holding the opposite plate, V_2, at the host vehicle ground. The combination of the applied electric field and analyzer geometry allow ions within a narrow range of a specified bandpass energy to successfully travel through the entrance aperture, become deflected by the transverse electric field in the ESA cavity, and exit the cavity to be counted as signal current on the anode as shown in Fig. 1. A full energy measurement of the plasma is derived by stepping the applied voltage over a range that matches the targeted plasma energies.

3 Initial On-Orbit Cross Calibration with FPMU

The Floating Potential Measurement Unit (FPMU) is a multiprobe payload designed and developed by Utah State University's Space Dynamics Laboratory to measure the floating potential of the ISS in addition to the density and temperature of the local

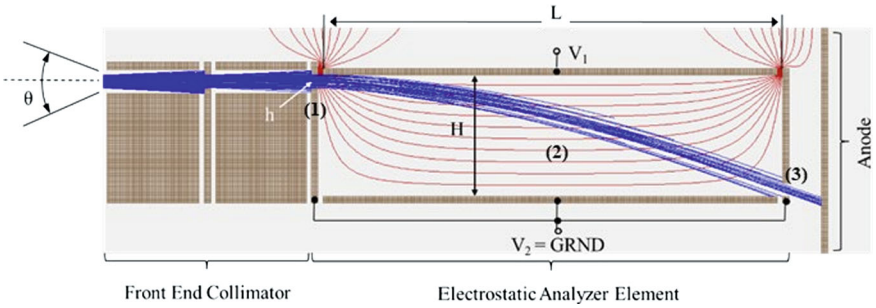

Fig. 1 Magnified cross-sectional view from SIMION for a single laminated electrostatic analyzer element showing the collimator, (1) the entrance aperture plate, (2) electrostatic analyzer cavity, and (3) exit aperture plate

ionospheric plasma environment [9, 10]. The ISS travels at a hyperthermal velocity relative to the ambient ionospheric plasma and the instrument has a very narrow field-of-view. Therefore, the particle flux to the surface of the sensor face can be approximated by a simplified 1-D drifted Maxwellian distribution of the form

$$\phi = nvA \tag{1}$$

where A is the cross-sectional area of the surface. This allows for determination of the signal current measured by the ÉPÉÉ detector

$$I_{\text{meas}} = nu_0 A_{\text{det}} \varepsilon q \tag{2}$$

where A_{det} is the surface area of the ÉPÉÉ detector and ε is a cross-calibration correction factor. Rearranging to solve for the cross-calibration correction factor (ε) between FPMU and ÉPÉÉ yields

$$\varepsilon = \frac{I_{\text{meas}}}{n_{\text{FPMU}} u_0 A_{\text{det}} q} \tag{3}$$

where n_{FPMU} is the number density obtained from FPMU. Assuming plasma quasi-neutrality and FPMU accuracy, ε was calculated to determine the ÉPÉÉ total ion density using data for September 28th and 29th of 2023. The calibration factor was assumed to have a linear response to spacecraft charging; however, off-nominal periods were identified at low and high spacecraft frame potentials. The off-nominal data are removed based on the assumptions that: (1) the ÉPÉÉ data have higher noise at low energies and (2) the higher voltage off-nominal behavior is due to engineering controls used by the ISS to minimize and control higher levels of spacecraft frame charging [11]. The calibration factor as a function of spacecraft charge is generated as shown in Fig. 2.

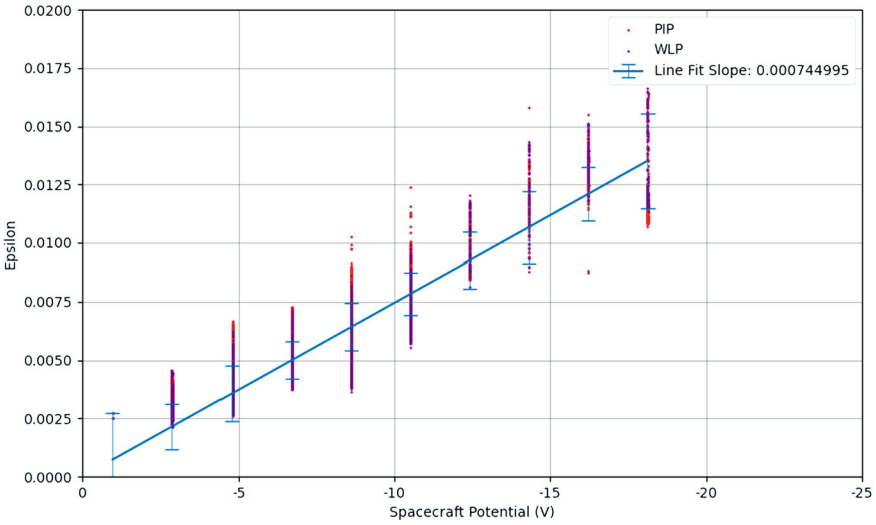

Fig. 2 Linear fit for the cross-calibration correction factor, ε, as a function of ISS frame charge

The ÉPÉÉ analyzer measures the total energy, E_0, of incident ions, which is the sum of the kinetic and potential energy. The potential energy is the electrostatic potential difference between the ambient plasma and the spacecraft frame, ubiquitously referred to as the spacecraft charge. The spacecraft charge is obtained by subtracting the relative kinetic energy of the ISS with respect to the ambient ionospheric plasma from the total ion energy as measured by ÉPÉÉ. The magnitude of the spacecraft charge is due to the net flux of charged particles to and from the spacecraft. The calibrated ÉPÉÉ ion density and spacecraft charge data are shown in Fig. 3. The data are plotted against the FPMU data as a function of orbital time and eclipse conditions. The velocity, altitude, and eclipse conditions are obtained using System Tool Kit.

4 On-Orbit Observations of the 4–5 November 2023 Storms

The ÉPÉÉ data are now used to observe the ionospheric response to two geomagnetic storms which occurred on 4 and 5 November 2023. Figure 4 presents geomagnetic indices and solar wind parameters from 2 to 13 November to provide context for the phases of the geomagnetic storms. An initial minor geomagnetic storm with a magnitude of G1 (on the NOAA scale where $K_p = 5$ [12]) occurred on 4 November 2023. Figure 4a shows meridional component of solar wind induced interplanetary

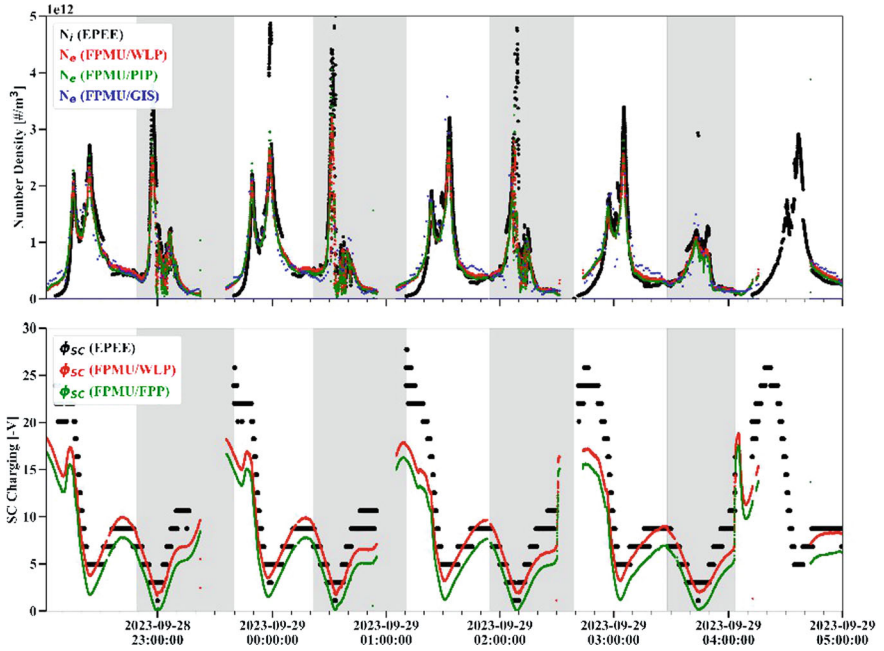

Fig. 3 Comparison of density and spacecraft potential observations as a function of eclipse/sunlight

magnetic field (IMF) in Geocentric Solar Magnetospheric (GSM) coordinate system (B_Z) observed by Advanced Composition Explorer (ACE). As shown in Fig. 4a the main phase of the G1 storm began at ~ 1304 UT on November 4 with a southward turning of the IMF *Bz* reaching -11.7 nT. The Kp index shown in Fig. 4d increases to a maximum of 4.7 at ~ 1800 UT and the Dst index shown in Fig. 4e reaches -54 nT at ~ 2258 UT [13].

During the recovery phase of the minor storm a full halo CME originating from an M1.8 solar class flare observed on 3 November 2023 hit the Earth's magnetic field on 5 November 2023 at 0905 UT [13]. The G3 (strong) storm commenced on 5 November with a southward turn of the *BZ*, reaching a minimum value of − 23.3 nT at 0957 UT and then turned northward reaching a maximum value of 25.5 nT. The *BZ* component continued to fluctuate between northward and southward through the main phase of the storm [13]. The Kp index reached a maximum value of 7.3 at ~ 1500 UT. After reaching a maximum D_{st} magnitude of − 162.6 nT the storm had a long five-day recovery phase as seen in Fig. 4e.

The ÉPÉÉ data are shown in the panels of Fig. 5 for the period of 3–9 November. This time period was selected to provide observations of the mid-latitude region monitored by ÉPÉÉ (mounted on the ISS) from − 51.2 to 51.2 degrees latitude at approximately 400 km. The Equatorial Ionization Anomaly (EIA) is a set of peaks (crests) in plasma density bounding an equatorial trough in plasma density due to electric fields and neutral winds that push plasma away from the equator towards

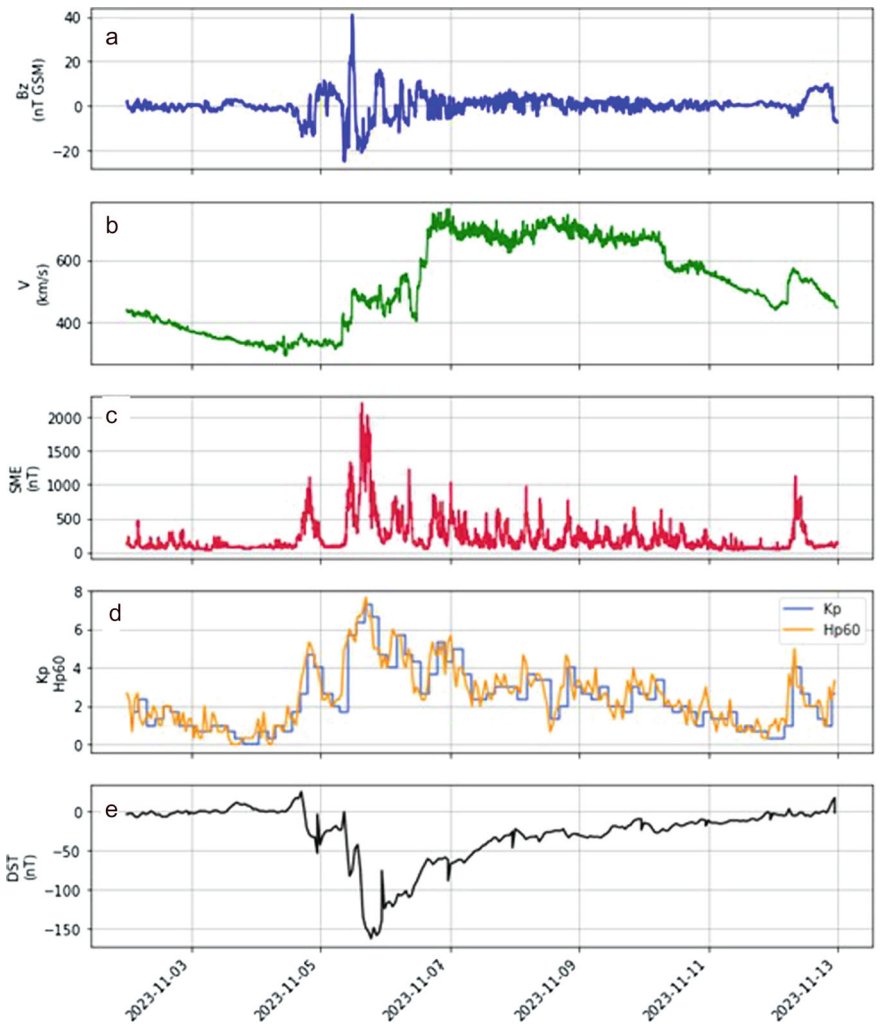

Fig. 4 Solar wind plasma and IMF during the storms of 4–5 November 2023. From top to bottom the panel shows **a** IMF magnitude (B_Z), **b** solar wind proton density, **c** solar wind flow speed, **d** the geomagnetic SME index, **e** the K_p index, and **f** the Dst index

higher and lower geomagnetic latitudes. The panels in Fig. 5 illustrate the (a) average EIA density over this period in addition to the (b) daily density as a function of latitude and longitude. Figure 5c shows plots of the ion density for each day. The data show an enhancement of the EIA crests during the main and recovery phase of the storm on 6 November and 7 November. This increase in ionospheric density is known as a positive ionospheric response to the geomagnetic storm. These positive ionospheric storms are related to an eastward prompt penetration of the electric field (PPEF) that uplifts the F region to higher altitudes, where recombination rates are lower,

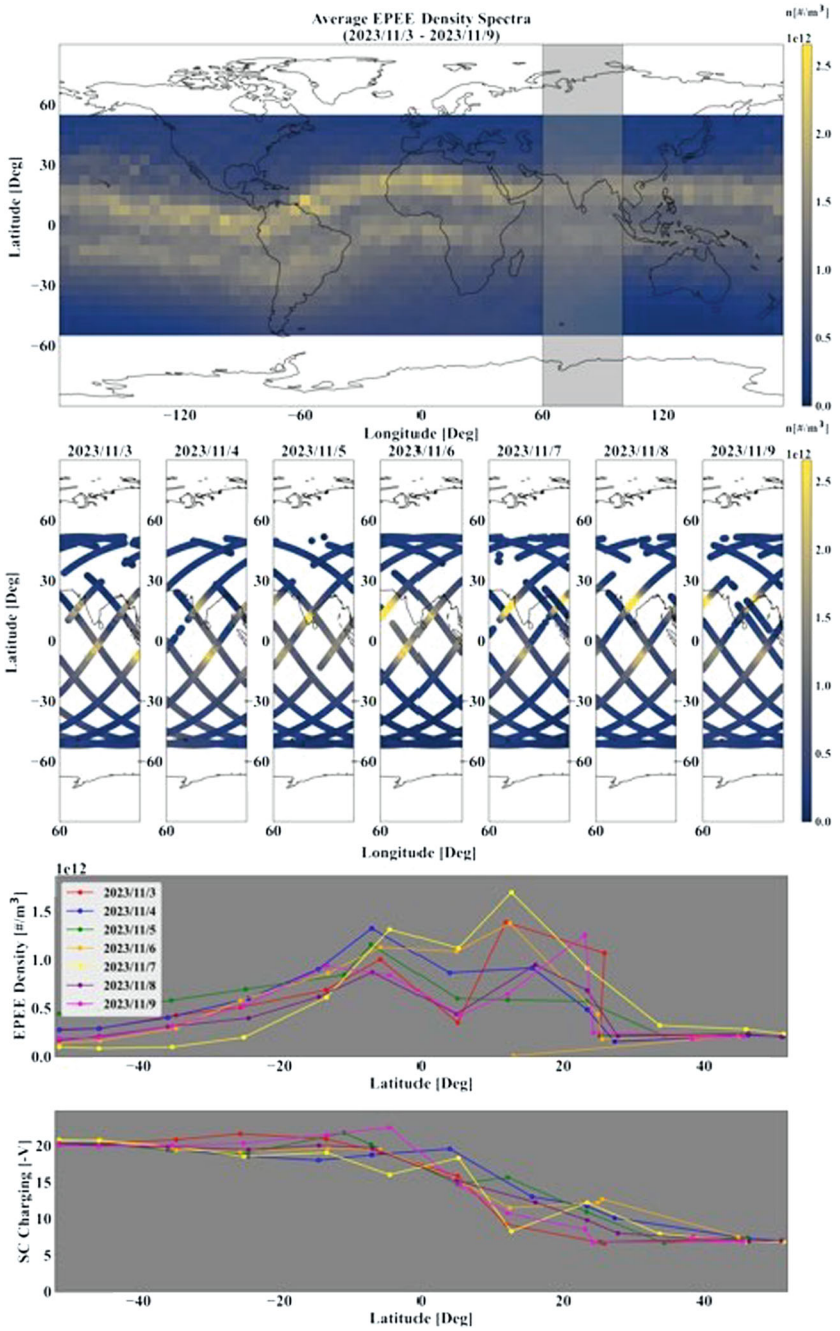

Fig. 5 ÉPÉÉ data over 3–9 November 2023 showing **a** average density and **b** daily density as a function of latitude and longitude. **c** Density and **d** spacecraft charge as a function of day and latitude

thus leading to an enhanced ion density [13]. Figure 5d shows spacecraft charge as a function of day and latitude. The ISS spacecraft charge does not appear to demonstrate an immediate correlation to the November storms however an in-depth investigation of both the density and spacecraft charge will be the subjective of future work.

5 Conclusion

We present initial results from the ÉPÉÉ payload, an ultra-low SWaP plasma spectrometer. The ÉPÉÉ data are cross-calibrated on-orbit using the FPMU WLP and PIP data sets over September 28th and 29th in 2023. The ÉPÉÉ data are then used to observe ISS frame charging and ionospheric density during the peak of Solar Cycle 25, specifically during the G1 and G3 storms in November 4–5, 2023. Future work will include cross-correlation studies using ground-based and Swarm satellite derived total electron content (TEC) data sets. Additionally, the implementation of GUVI data to assess the O/N2 ratio during the November 4–5, 2023, storms will be conducted. This will allow the team to assess the impact of the neutral thermospheric environment on the ionospheric storm morphology.

Acknowledgements Work at Los Alamos National Laboratory is conducted under the auspices of the United States Department of Energy. The authors acknowledge the support of the DoD Space Test Program which provides mission design, spacecraft acquisition, integration, launch and on-orbit operations support for DoD's science and technology (S&T) experiments, and manages all DoD payloads on the International Space Station.

References

1. Maldonado C, McHarg M, Balthazor R, Osiander R (2019) Undergraduate research and science mission opportunities with microtechnology enabled particle detectors. In: Proceedings SPIE 10982, Micro-and nanotechnology sensors, systems, and applications XI, 109820I, Baltimore
2. Balthazor R, Gaefke X, Williams J, Wilcox Z, McHarg M, Neal P, Maldonado CA, Wilson G, Yates W (2024) Anomalous ISS charging observed with Falcon EPEE—early observations. In: Proceedings of the 17th spacecraft charging technology conference, Palais des Papes, Avignon, France
3. Maldonado C, Cress R, Gresham P, Armstrong J, Wilson G, Reisenfeld D, Larsen B, Balthazor R, Harley J, McHarg M (2020) Space radiation dosimetry using the integrated miniaturized electrostatic analyzer—Reflight (iMESA-R). Space Weather
4. Maldonado CA, Ketsdever AD, Balthazor RBNPC, Wilson GR, McHarg MG, Osiander R, Adams RJ (2022) Automated plume sentry observations during international space station thermal control system venting. J Spacecraft Rockets
5. Maldonado C, Wilson G, McGlown J, Morning H, Arnold, D Reisenfeld D, Holloway M (2021) An ultra-low resource ion mass spectrometer for cubesat platforms.In: Proceedings of the 36th annual small satellite conference, Logan, UT

6. Maldonado CA, Wilson G, McGlown J, Morning H, Arnold D, Kim T, Espinoza T, Miller M, Rogers AJ, Reisenfeld D, Holloway M (2022) An ultra-low resource ion mass spectrometer for observation of planetary atmospheres. In: Proceedings of the 37th AIAA/USU small sat conference, Logan, UT
7. Hooks DE, Carpenter B, Hickethier M, Clark C, Brown N, McBride M, Loza-Hernandez I, Stull JA, Maldonado CA (2024) Ultra-black coatings for space instruments: a comparison of traditional Ebonol C processes and a method for future repeatability. J Manuf Process 113(15):230–237
8. Maldonado CA, Reisenfeld D, Fernandes P, Larsen B, Wilson G, Balthazor RL, McHarg MG (2020) The effects of spacecraft potential on ionospheric plasma measurements. J Spacecraft Rockets (submitted)
9. Debchoudhury S, Barjatya A, Minow JI, Coffey VN, Chandler MO (2021) Observations and validation of plasma density, temperature, and abundance from a langmuir probe onboard the international space station. J Geophys Res: Space Phys 126:e2021JA029393
10. Barjatya A, Swenson CM, Thompson DC, Wright KH (2009) Data analysis of the floating potential measurement unit aboard the international space station. Rev Sci Instrum 80:041301
11. Minow JI, Wright KH, Chandler MO, Coffey VN, Craven PD, Schneider TA, Parker LN, Ferguson DC, Koontz SL, Alred JW (2010) Summary of 2006 to 2010 FPMU measurements of international space station frame potential variations. In: 11th Spacecraft charging technology conference, Albuquerque, New Mexico
12. N./.N.S.W.P. Center (2024) NOAA space weather scales. [Online]. Available: https://www.swpc.noaa.gov/sites/default/files/images/NOAAscales.pdf. (Accessed 30 Dec 2024)
13. Agyei-Yeboah E, Fagundes P, Tardelli A, Pillat V, Vieira F, Alves Bolzan M (2025) Global ionospheric response to a G2 and a G3 geomagnetic storms of November 4 and 5 2023. Adv Space Res

Open Access This chapter is licensed under the terms of the Creative Commons Attribution 4.0 International License (http://creativecommons.org/licenses/by/4.0/), which permits use, sharing, adaptation, distribution and reproduction in any medium or format, as long as you give appropriate credit to the original author(s) and the source, provide a link to the Creative Commons license and indicate if changes were made.

The images or other third party material in this chapter are included in the chapter's Creative Commons license, unless indicated otherwise in a credit line to the material. If material is not included in the chapter's Creative Commons license and your intended use is not permitted by statutory regulation or exceeds the permitted use, you will need to obtain permission directly from the copyright holder.

Gas-Surface Interactions

Unsteady Stefan Problem with Kinetic Interface Conditions in Rarefied Gas Phase-Transitions

Donat Weniger and Manuel Torrilhon

Abstract We investigate the unsteady phase transition problem with kinetic interface conditions in rarefied gas deposition and sublimation. We couple the R13 equations of macroscopic gas transport with the heat equation to model the interaction between the gas and the solid phase. The kinetic interface conditions are derived from thermodynamic principles and provide an accurate description of the phase transition process. We employ the Finite Element method with a remeshing approach to solve the coupled system and track the moving interface. Our numerical results demonstrate the effectiveness of the proposed method in capturing the complex dynamics of the phase transition process, including the effects of kinetic interface conditions.

Keywords Stefan problem · Kinetic interface conditions · Rarefied gas deposition · Finite element method · Remeshing

1 Introduction

Kinetic effects in phase transition problems are of high importance in research on microelectromechanical devices (MEMS) [5] and in pharmaceutical freeze drying [3]. Those processes are characterized by a rarefied gas phase which undergoes a phase transition. Accurately capturing all relevant kinetic effects is crucial for understanding the system and designing the devices.

The Stefan problem [8], the classical phase transition model, becomes more complex when kinetic interface conditions are considered [11]. In this work, we tackle this problem for a rarefied gas deposition and sublimation process. We couple the R13 equations [9] with the heat equation to model the interaction between the gas and the solid phase. Thermodynamically admissible kinetic interface conditions [1] close the system. We present high-fidelity numerical results based on the classical Finite Element method and a remeshing approach.

D. Weniger (✉) · M. Torrilhon
Applied and Computational Mathematics, RWTH Aachen University, Aachen, Germany
e-mail: weniger@acom.rwth-aachen.de

© The Author(s) 2026

M. Grabe et al. (eds.), *Rarefied Gas Dynamics*, Springer Aerospace Technology,
https://doi.org/10.1007/978-3-032-00094-1_8

2 Physical Model and Governing Equations

We solve the gas and solid field equations in domains $\Omega_g(t)$ and $\Omega_s(t)$, respectively. The interface $I(t)$ separates the two domains and moves over time with velocity v_n^I. External boundaries $\Gamma_{g/s}$ are fixed. For a general sketch, see Fig. 1.

We assume a monatomic and ideal gas. The R13 equations and the interface conditions for phase transitions are derived for a variety of molecule models, such as Hard-Sphere or Maxwell molecules [1]. They only influence factors of certain coefficients in the final model equations. We therefore do not expect significant influence on the phase transition numerics and will hence restrict ourselves to the simple case of Maxwell molecules.

All equations are non-dimensionalized and linearized around a constant equilibrium state (ρ_0, T_0). Simultaneously, this state is considered to be the saturation condition of the system. Small perturbations from equilibrium by boundary or source terms initiate the phase transition process.

The dimensionless form introduces key parameters into the equations, such as the Knudsen number or the temporal coupling scale between the solid and the gas phase. Analysis of these dimensionless numbers is crucial for gaining insights into the system and choosing appropriate numerical methods.

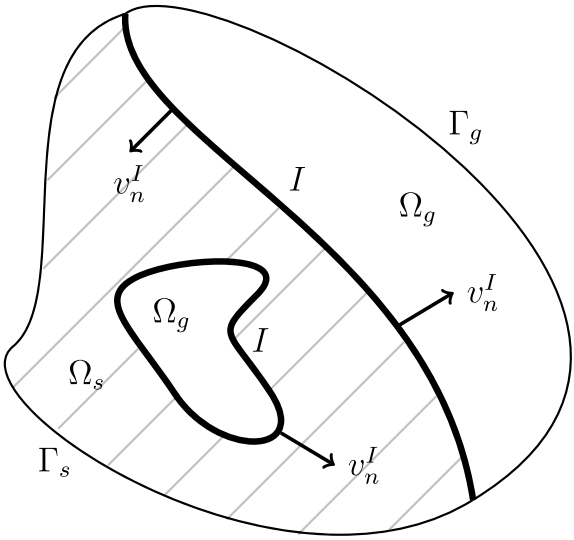

Fig. 1 General two-phase problem with interfaces separating the two subdomains

Einstein summation convention is used throughout the paper for the indices i, j, and k. The corresponding unsteady, linearized, and dimensionless R13 equations are given by [9]

$$\begin{aligned}
\partial_t \rho + \partial_{x_j} v_j &= 0 \\
\partial_t v_i + \partial_{x_i} \rho + \partial_{x_i} T + \partial_{x_j} \sigma_{ij} &= b_i \\
\frac{3}{2}\partial_t T + \partial_{x_j} v_j + \partial_{x_j} q_j &= r \\
\partial_t \sigma_{ij} + \frac{4}{5}\partial_{x_{\langle j}} q_{i\rangle} + \partial_{x_k} m_{ijk} + 2\partial_{x_{\langle j}} v_{i\rangle} &= -\frac{1}{Kn}\sigma_{ij} \\
\partial_t q_i + \partial_{x_k} \sigma_{ik} + \frac{1}{2}\partial_{x_k} R_{ik} + \frac{1}{6}\partial_{x_i}\Delta + \frac{5}{2}\partial_{x_i} T &= -\frac{2}{3Kn} q_i
\end{aligned} \tag{1}$$

with the (dimensionless) closure relations

$$\begin{aligned}
m_{ijk} &= -2Kn\partial_{x_{\langle k}}\sigma_{ij\rangle} \\
R_{ij} &= -\frac{24Kn}{5}\partial_{x_{\langle j}} q_{i\rangle} \\
\Delta &= -12Kn\partial_{x_k} q_k .
\end{aligned} \tag{2}$$

The heat equation [2] is presented and used in mixed form, i.e., energy balance and Fourier's law of heat conduction. It reads

$$\begin{aligned}
\tau\partial_t T + \partial_{x_j} q_j &= r \\
q_j + \partial_{x_j} T &= 0.
\end{aligned} \tag{3}$$

The variables are the density ρ, velocity v_i, temperature T, stress deviator σ_{ij}, and heat flux q_i. An external force term b_i or a heat source term r can be added to the system. The higher-order moments m_{ijk}, R_{ij}, and Δ close the system.

Each phase carries its own set of variables and equations. As a consequence, there are two temperatures, T^g and T^s, and two heat fluxes, q_i^g and q_i^s, at the interface. This allows for physical interface conditions that will produce a temperature jump otherwise not possible. Coupling at the interface therefore requires six equations for the R13 equations, one equation for the heat equation, and one more equation for the unknown interface velocity, for a total of eight interface conditions. The phenomenological R13 conditions for phase transitions are given in [1] by

$$
\begin{aligned}
v_n - v_n^I &= \tilde{\vartheta}\left((T+\rho) - HT^s - \frac{1}{2}(T-T^s) + \frac{1}{2}\sigma_{nn} - \frac{1}{30}\Delta - \frac{1}{10}R_{nn}\right)\\
q_n &= \xi\left(2(T-T^s) + \frac{1}{2}\sigma_{nn} + \frac{2}{15}\Delta + \frac{2}{5}R_{nn}\right) - \frac{1}{2}(v_n - v_n^I)\\
m_{nnn} &= \xi\left(\frac{2}{5}(T^s - T) + \frac{7}{5}\sigma_{nn} - \frac{2}{75}\Delta - \frac{2}{25}R_{nn}\right) - \frac{2}{5}(v_n - v_n^I)\\
\sigma_{nt} &= \xi\left(v_t - v_t^W + \frac{1}{5}q_t + m_{nnt}\right)\\
R_{nt} &= \xi\left(v_t^W - v_t + \frac{11}{5}q_t - m_{nnt}\right)\\
\frac{1}{2}m_{nnn} &= \xi\left(\frac{1}{2}\sigma_{nn} + \sigma_{tt}\right) - m_{ntt},
\end{aligned}
\tag{4}
$$

assuming that the normal vector n_i points from the gas to the solid phase (i.e., the outward normal considering the gas). Subscripts n and t denote the normal and tangential components, respectively. All quantities are evaluated at the interface on the gas side, except for the solid temperature T^s which introduces coupling between solid and gas. Here, $\tilde{\vartheta} = \sqrt{\frac{2}{\pi}}\frac{\vartheta}{2-\vartheta}$ and $\xi = \sqrt{\frac{2}{\pi}}\frac{\vartheta+\chi(1-\vartheta)}{2-\vartheta-\chi(1-\vartheta)}$ are abbreviations for the classical interface parameters. $\chi \in [0, 1]$ is the accommodation coefficient, and $\vartheta \in [0, 1]$ is the deposition or sublimation coefficient. These are empirical coefficients, potentially dependent on the state of the system, which we do not discuss further in this work. The relative latent heat H enters the system through the Clausius-Clapeyron relation. The interface conditions collapse to the default R13 boundary conditions for $\vartheta = 0$ (i.e. no phase transition), see [6]. The first equation is of Hertz-Knudsen-Schrage type [7], extended to the R13 equations.

The remaining two equations are the Rankine-Hugoniot conditions for the mass balance (mass flux across the interface) and energy balance (Stefan condition). In dimensionless and linearized form, and assuming an external observer, they read

$$-v_n^I = \eta(v_n - v_n^I) \tag{5a}$$

$$v_n^I H = \eta q_n^g - \frac{1}{\tau\gamma}q_n^s. \tag{5b}$$

Here, we assumed that the solid phase is at rest.

The set of dimensionless numbers describing the system is

$$\tau = \frac{t_{0,s}}{t_{0,g}} \qquad \text{(time scale ratio)} \tag{6a}$$

$$Kn = \frac{\mu\sqrt{RT_0}}{\rho_0 R T_0 x_0} \qquad \text{(Knudsen number)} \tag{6b}$$

$$\eta = \frac{\rho_0}{\rho_s} \qquad \text{(density fraction)} \tag{6c}$$

$$H = \frac{H_{\text{latent}}}{RT_0} \qquad \text{(relative latent heat)} \tag{6d}$$

$$\gamma = \frac{R}{c_s} \qquad \text{(heat capacity fraction).} \tag{6e}$$

The Knudsen number defines the gas regime and is responsible for potential kinetic effects. The time scale ratio τ is a common parameter in multiscale simulations. If $\tau \approx 1$, the dynamics of the solid and the gas are similar. If $\tau \gg 1$, the gas dynamics are much faster than the solid dynamics, and we need a much smaller time step to resolve the gas scale accurately. We will assume $\tau = 1$ for the sake of simplicity, which is usually given only for microscale systems. The density fraction η mainly controls the mass flux across the interface and is small for a solid and a rarefied gas. Effects like porosity can increase η significantly. The relative latent heat H and the heat capacity fraction γ are abbreviations and naturally occur in the Stefan problem. They control the energy flux across the interface but are of less importance to the general dynamics of the system.

The coupled system is solved by the Finite Element method. The discretization is performed as in [10], with an added implicit Euler scheme for the time integration. The moving interface is tracked by the Level-Set method [4], and a remeshing method is used to adapt the mesh to the moving interface. This way, the physical interface always aligns with edges of the computational mesh and all relevant kinetic effects can be captured.

3 Numerical Results

Pharmaceutical freeze-drying aims to remove water from a frozen substrate in a low-pressure environment [3]. One stage of this process involves the slow heating of the substrate to sublimate the water, followed by the deposition of the water vapor on a condenser in a near-vacuum regime with Knudsen numbers $10^{-4} < Kn < 1$. Minimizing the time until the desired drying level is reached is crucial for applications. Simulations are key in understanding and subsequently controlling the process and designing the devices. This scenario motivates our example.

As discussed in Sect. 2, the physical model is only valid for small perturbations around an equilibrium state. This is, for example, given for slow processes, which is the case in freeze-drying. We therefore expect to capture the relevant kinetic effects despite using a linearized model.

We initialize the domain as a square with a solid substrate in the top-right corner, which is to be dried. The condenser is modeled as another block of solid at the bottom. The remaining domain is filled with a gas at $Kn = 0.1$ and is treated as an enclosed container with adiabatic boundary conditions ($\chi \to 0$). The process is initialized with the substrate at $T = 0.01$, the condenser at $T = -0.01$, and the gas at $T = 0$. The gas density and velocity fields are initialized to zero. Dirichlet temperature boundary conditions are applied to the substrate and the condenser to maintain the process.

We let the simulation run for $t \in [0, 1000]$ using 1000 time steps and a triangular mesh with characteristic lengths from 0.01 (close to the interface) to 0.05. For visible growth and decay of the interface, we choose $\eta = 0.01$. The interface parameters are set to $\vartheta = 0.5$ and $\chi = 0.9$ and there are no heat sources or external force terms.

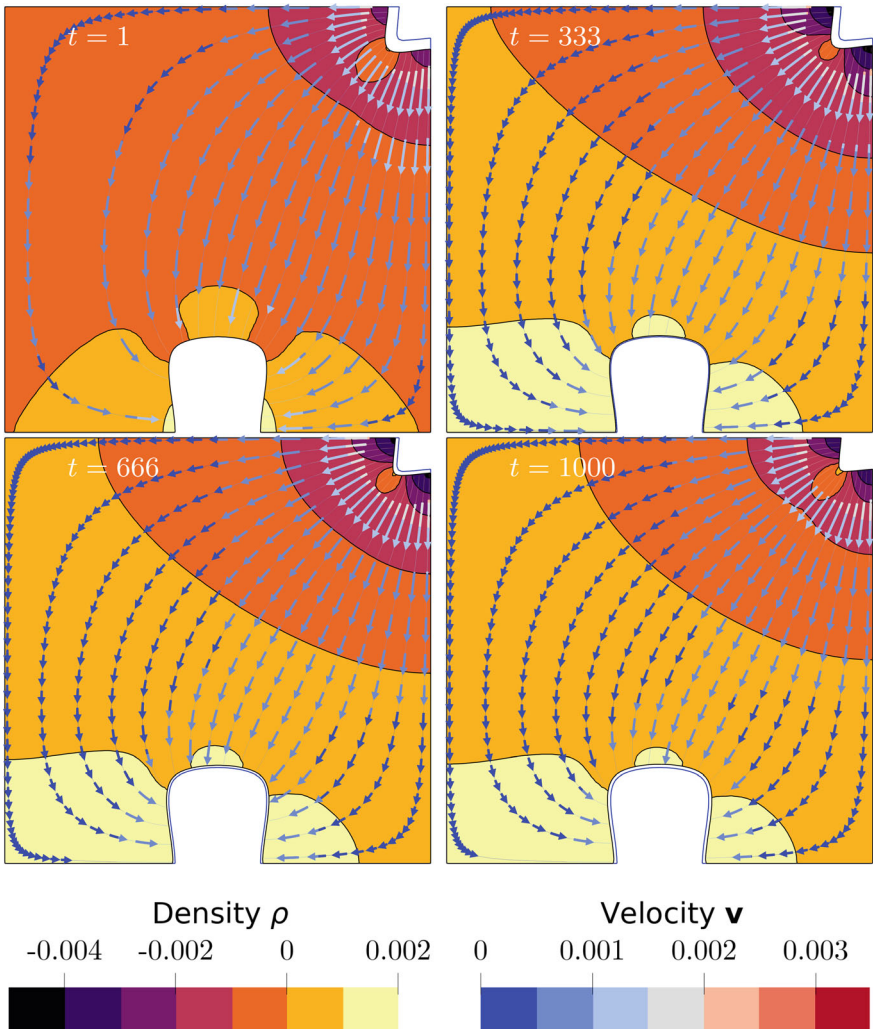

Fig. 2 Combined sublimation and deposition cycle: density contours with velocity streamlines. The four images show the system's state at different times. The top-left after the first time step, the top-right after one-third of all time steps, the bottom-left after two-thirds, and the bottom-right after all time steps. In the top-right corner and on the bottom middle, the initial and final interfaces in blue highlight the total growth and shrinkage

The remaining dimensionless parameters are set to $\tau = H = \gamma = 1$. We present the time evolution after the first time step, after $1/3$, after $2/3$, and at the final time step.

Figure 2 illustrates the density and velocity fields in the gas phase. The gas is sublimated from the substrate due to the heating. It moves towards the condenser and is deposited there. We observe a denser region around the condenser and a more

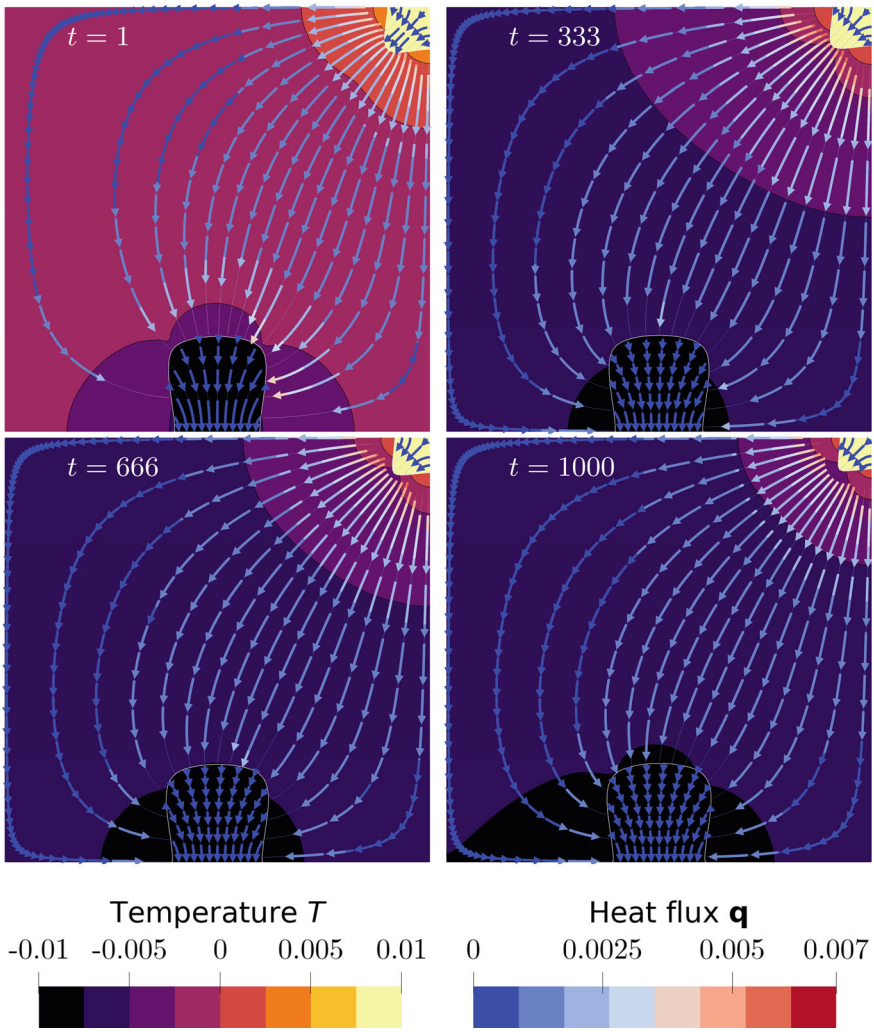

Fig. 3 Combined sublimation and deposition cycle: temperature contours with heat flux streamlines. The four images show the system's state at different times. The top-left after the first time step, the top-right after one-third of all time steps, the bottom-left after two-thirds, and the bottom-right after all time steps

rarefied one near the substrate, resulting in a clear gradient in the density field. Note the shrinkage and growth of the solid regions over time, which is captured by the numerical method. The total degree of movement is highlighted by the blue lines representing the initial and final interfaces.

Figure 3 shows the corresponding temperature and heat flux fields. A clear temperature jump between the substrate and the gas is visible. This jump arises from the kinetic interface conditions and is accurately resolved thanks to the exact remeshing approach.

4 Conclusion and Outlook

We presented a numerical study of the unsteady Stefan problem with kinetic interface conditions in rarefied gas deposition and sublimation. By coupling the transient R13 equations with the heat equation, we modeled the interaction between the gas and solid phases, capturing kinetic effects that are not accounted for in classical models. The kinetic interface conditions allowed for an accurate description of the phase transition process, including phenomena such as temperature jumps at the interface.

Our computational approach employed the finite element method with a remeshing strategy to effectively handle the moving interface. This method ensured that the physical interface aligned with the computational mesh, enabling precise resolution of the kinetic interface conditions. The numerical results demonstrated the capability of the method to capture the complex dynamics of the phase transition process, validating its effectiveness in modeling rarefied gas flows with phase transitions.

The novelty of this work lies in the integration of transient R13 equations with kinetic interface conditions in a unified framework, providing insights into the non-equilibrium effects during phase transitions. By accurately capturing these kinetic effects, our model advances the understanding of processes such as sublimation and deposition in microscale systems.

Future work will focus on exploring the impact of different interface parameters on the phase transition dynamics, such as varying the accommodation coefficient and the deposition or sublimation coefficient, to study their influence on kinetic effects. Additionally, we aim to improve the computational efficiency of the method to enable simulations of larger and more realistic systems. Extending the framework to three-dimensional simulations is a key goal, which will open possibilities for studying complex geometries and more intricate physical phenomena.

References

1. Beckmann A, Rana A, Torrilhon M, Struchtrup H (2018) Evaporation boundary conditions for the linear r13 equations based on the onsager theory. Entropy 20(9). https://www.mdpi.com/1099-4300/20/9/680
2. Donea J, Huerta A (2003) In: Finite element methods for flow problems. Wiley. https://doi.org/10.1002/0470013826
3. Ganguly A, Nail S, Alexeenko A (2012) Rarefied gas dynamics aspects of pharmaceutical freeze-drying. Vacuum Gas Dynam Theory Experim Pract Applications 86(11):1739–1747. https://www.sciencedirect.com/science/article/pii/S0042207X12001716
4. Gibou F, Fedkiw R, Osher S (2018) A review of level-set methods and some recent applications. J Comput Phys 353:82–109. https://www.sciencedirect.com/science/article/pii/S0021999117307441
5. Karniadakis G, Beskok A, Aluru N (2005) In: Microflows and nanoflows—fundamentals and simulation. Springer. https://doi.org/10.1007/0-387-28676-4
6. Rana AS, Struchtrup H (2016) Thermodynamically admissible boundary conditions for the regularized 13 moment equations. Phys Fluids 28(2):027105. https://doi.org/10.1063/1.4941293

7. Schrage RW (1953) In: A theoretical study of interphase mass transfer. Columbia University Press, New York Chichester, West Sussex. https://doi.org/10.7312/schr90162
8. Stefan J (1891) Ueber die Theorie der Eisbildung, insbesondere über die Eisbildung im Polarmeere. Annalen der Physik 278(2):269–286. https://doi.org/10.1002/andp.18912780206
9. Struchtrup H, Torrilhon M (2003) Regularization of Grad's 13 moment equations: derivation and linear analysis. Phys Fluids 15(9):2668–2680. https://doi.org/10.1063/1.1597472
10. Theisen L, Torrilhon M (2021) fenicsr13: a tensorial mixed finite element solver for the linear r13 equations using the Fenics computing platform. ACM Trans Math Softw 47(2). https://doi.org/10.1145/3442378
11. Weniger D, Varghese P, Kowalski J, Torrilhon M (2023) Unsteady Stefan problem with kinetic interface conditions for rarefied gas deposition. Int J Heat Mass Transf 217:124696. https://www.sciencedirect.com/science/article/pii/S0017931023008414

Open Access This chapter is licensed under the terms of the Creative Commons Attribution 4.0 International License (http://creativecommons.org/licenses/by/4.0/), which permits use, sharing, adaptation, distribution and reproduction in any medium or format, as long as you give appropriate credit to the original author(s) and the source, provide a link to the Creative Commons license and indicate if changes were made.

The images or other third party material in this chapter are included in the chapter's Creative Commons license, unless indicated otherwise in a credit line to the material. If material is not included in the chapter's Creative Commons license and your intended use is not permitted by statutory regulation or exceeds the permitted use, you will need to obtain permission directly from the copyright holder.

Molecular Dynamics Study of Scattering of Nitrogen from a Cryogenic Nitrogen Surface

Johannes V. Diedrich and Martin Grabe

Abstract The non-equilibrium gas-surface interactions (GSI) between hot nitrogen gas and 4.3 K nitrogen ice were investigated. For this, Molecular Dynamics scattering simulations were carried out, comparing a flat and a rough aggregated surface model. The sticking probability and accommodation coefficients were determined for use in direct simulation Monte Carlo (DSMC) simulations. It was found that the sticking probability is similar for both models, but not unity despite the low wall temperature of 4.3 K. The accommodation coefficients do not indicate diffuse scattering.

Keywords Molecular dynamics · Scattering · Cryopumps

1 Introduction

Little is known about the scattering of reaction control thruster plumes from cryopump surfaces. This unusual system attracted research interest due to its occurrence in the large scale research facility STG-CT (DLR, "High-Vacuum Plume Test Facility for Chemical Thrusters") [1]. In this testing facility for small sattelite thrusters, the dynamics of rarefied gas flows with high velocities can be observed in high vacuum conditions. This is of interest in the field of plume contamination, which is concerned with the assessment of rocket motor plume effects on their environment. To provide the pumping speeds necessary to keep the vacuum during thruster firing, the entire chamber wall is cooled to 4.2–4.8 K with liquid He. The equilibrium vapor pressure of H_2 at wall temperature determines the chamber pressure. It is assumed that all other plume components except He freeze out completely upon first impact.

As the adsorption and scattering processes on the cryopump surface can currently not be studied experimentally in STG-CT, the system is modeled with molecular

J. V. Diedrich (✉)
Georg-August-Universität Göttingen, Institute of Physical Chemistry, Göttingen, Germany
e-mail: johannes.diedrich@chemie.uni-goettingen.de

M. Grabe
German Aerospace Center, Institute of Aerodynamics and Flow Technology, Spacecraft Department, Göttingen, Germany

© The Author(s) 2026

M. Grabe et al. (eds.), *Rarefied Gas Dynamics*, Springer Aerospace Technology,
https://doi.org/10.1007/978-3-032-00094-1_9

dynamics (MD) scattering simulations. The main objectives are to test the assumption of total freeze-out and—if scattering is a non-negligible process—characterize it parametrically. Hydrazine monopropellant thruster plumes were considered a simple test case with the decomposition products H_2, N_2 and NH_3.

The interaction of rarefied gas flows with surfaces can be modeled using the Direct Simulation Monte Carlo (DSMC) method, using MD to parametrize the scattering kernels [2, 3, 5]. For this purpose, accommodation coefficients are determined as a measure of how much energy the scattering particle loses to or gains from the surface. In this work, the surface is assumed to be fully covered by the plume ice. The system under study is thus the interaction of the plume with its own frozen-out ice. Initially, only one plume species is considered, starting with the heaviest decomposition product, N_2. With the structure of the ice unknown a-priori, the surfaces are built using deposition simulations.

The purpose of this paper is to introduce the problem and document the first approach. The theoretical background and simulation details are discussed in 2, the main results of the deposition and scattering simulations are presented in 3 and finally, conclusions are drawn in 4.

2 Methods and Theory

2.1 Property Sampling

The plume ensemble was discretized by randomly sampling projectile properties from relevant distributions. Representative values for small thrusters in the test environment were chosen for thermodynamic quantities. The speed of the projectile

$$v_{\text{projectile}} = v_{\text{stream}} + v_T. \tag{1}$$

follows the constant stream velocity of the beam $v_{\text{stream}} = 1259\,\text{m}\,\text{s}^{-1}$, modified by a random component v_T drawn from the Maxwell-Boltzmann distribution for one degree of freedom, $f(T)$. This translational temperature was assumed to be $T_{\text{trans}} = 122\,\text{K}$. The rotational temperature was assumed as $T_{\text{trans}} = 159\,\text{K}$, while the direction of rotation was uniformly randomized.

The polar and azimuth angles of the impinging molecule trajectories were drawn from uniform distributions between 0°–75° and 0°–360°, respectively. The impact positions were likewise uniformly randomized over the whole surface. Both the molecule starting orientation and rotation axis were randomized as well, although the latter was constrained to only allow axes of maximum rotational inertia.

The practice of depositing and scattering particles by sampling random angles and velocities to estimate an ensemble with a defined temperature (c.f. Sect. 2.1) is common practice in the literature (c.f. [3, 5]). The clear advantage is the ease of implementation. Looking at the incident surface-normal and surface-tangential energy

components sampled this way, the distributions that result from this procedure show features that may not be expected intuitively from a simple Maxwell-Boltzmann distribution, c.f. Fig. 1. They are likely artifacts introduced by simultaneously drawing from angular and velocity distributions.

2.2 Simulation Details

All MD simulations were performed using LAMMPS [9]. Molecules were treated as rigid rotors within the `fix rigid/nve/small` style in LAMMPS. Time steps were 1 fs in scattering simulations and up to 5 fs in minimization simulations. Simulations were performed with full periodic boundary conditions. The box size in vertical (z) direction was chosen in such a way that, at minimum, the projectile was more than the Lennard-Jones interaction range ($r_{\mathrm{LJ}} = 8\,\text{Å}$) away from a surface in any direction. The nitrogen unit cell was derived from the experimental structure by R. W. G. Wyckoff [10]. Following this structure, molecules following the PHAST-N_2 force field ([11]) were constructed with their corresponding pseudo atoms and atomic distances. The unit cells were then scaled to a cell parameter of $a = 5.6\,\text{Å}$. This value lies in-between the experiment ($a = 5.644\,\text{Å}$) and the one found for PHAST-N_2 ($a = 5.485\,\text{Å}$), to allow for relaxation rather than expansion during minimization. The force field used for H_2 [13] was of the same family as PHAST-N_2, the whole family being design to be expandable to other small molecules.

Three types of surfaces were simulated. First, a flat single crystal of N_2 at 4.3 K with dimensions of $10 \times 10 \times 8$ unit cells (approx. $56 \times 56 \times 45\,\text{Å}$) as a simple reference system. The flat surface was constructing by simulating the system in the NPT ensemble to relax the lattice parameter and in NPT at 4.3 K to assume the desired temperature. Secondly, deposition simulations were performed to incrementally build N_2 surfaces using the same projectile property distributions as in the scattering simulations. Starting from the flat model, the surface was truncated, the bottom-most layer was fixed in place and three layers above were thermostatted using a Nosé-Hoover thermostat chain [12]. Molecules were deposited individually by sampling their properties randomly from the distributions described in 2.1, aborting the simulation if they

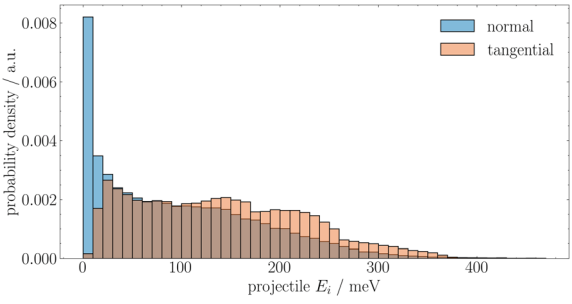

Fig. 1 Distribution of surface-tangential and surface-normal initial projectile energy components, as sampled 5×10^4 times via Eq. 1 and the angular and thermodynamic distributions as described in 2.1

scattered. After any trajectory ending in sticking, the system was cooled using the until the 2 ps average temperature of the accumulated aggregate was reduced below 4.5 K again. This was repeated until the aggregate consisted of the same number of molecules as the flat surface, 3200.

The scattering simulations were performed in the NVE ensemble after a 10 ps thermalization period. 10^4 individual simulations were performed per surface. To randomize the position in phase space of the surface, a random pre-run length of 0–50 ps was added to the thermalization. Trajectories were counted as scattered if the projectile receded from the surface beyond 8 Å. Sticking was defined as the projectile either not leaving the surface within 50 ps. To save computational effort, a stopping criterion for sticking is added, inspired by the study of Bolton et al. [14]. The kinetic plus potential energy of the projectile was averaged over a 1 ps window. Once The simulation was aborted once it dropped below the desorption energy of α-phase nitrogen ice, 69 meV [6]. Such aborted trajectories were counted as sticking, assuming the projectile has not had enough energy to emerge from the potential well for a considerable time. The sticking probability s was defined as the percentage of trajectories classified as sticking. The accommodation coefficients were defined as

$$\alpha = \frac{E_i - E_f}{E_i - E_s}. \tag{2}$$

where E_i and E_f are the initial and final energy of the projectile in any energy component, where α_n, α_t and α_r are defined for surface-normal, surface-tangential and rotational energy, respectively. E_s is a constant equal to the kinetic energy of the most probable velocity in the Maxwell-Boltzmann distribution at surface temperature.

2.3 Uncertainty Estimation

The sticking probability was sampled using Bayesian bootstrapping [15]. For each sample b, given a set of N trajectories, random weights are drawn from the Dirichlet $(0_1, ..., 0_N)$ distribution for each trajectory. New sets of trajectory results (sticking of scattering) are drawn using these weights until B sets of length N exist. In this way, any statistic that can be calculated for the original set of data can be described as a distribution of that statistic over B bootstrapped sets with a mean and standard deviation. The uncertainty given above is the 95% (1.96σ) confidence interval.

The same procedure can be used for the accommodation coefficients, if they are calculated for every individual trajectory. With distributions of initial and final energy in translational and rotational components, the accommodation coefficients were calculated for $B = 10^4$ samples, resulting in AC distributions over which a standard deviation could be calculated.

3 Results and Discussion

The method described in 2.2 was used to build four deposited surfaces to avoid randomization artifacts of a single rough surface. The obtained surfaces are depicted in Fig. 2 and were rendered using Ovito [4]. No defects like vacancies, dislocations or amorphous regions were found in the deposited structures. Only surface roughness from incomplete layers and few vacancies per surface were observed. The extent of the surface roughness was not substantial.

3.1 Scattering Results

The results of performing 10^4 scattering simulations per surface are shown in Table 1. The four deposited surfaces were averaged, reducing statistical errors and uncertainty due to the larger sample size. The sticking probabilities were high ($> 95\%$) for all investigated surfaces. With the approximations taken in the presented simulations (limited species, ice-only surface) we expect the resulting sticking probabilities to be upper limits. This result refutes the assumption of total freeze-out. Compared to previous work on 20 K methane ice ([5]) and the experimentally determined lower limit of s for N_2 on N_2 at 14 K ([6]), the values match expectations and approximately follow the surface temperature.

All α_n and α_t are relatively high, indicating that during scattering a significant amount of energy is exchanged with the wall. The α_t results are qualitatively lower than α_n, in accordance with results by [3]. This finding indicates that the scattering is not entirely diffuse, although surface roughness on length scales beyond the 56 Å simulated in this work may influence this result. The differences in s and ACs between the flat and rough surfaces are minimal and covered by the confidence interval, both for s and the accommodation coefficients. Uncertainties between deposited and flat surface are not quantitatively comparable due to different sample sizes, but

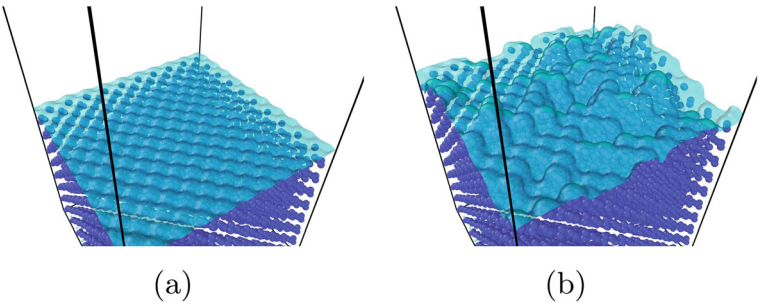

Fig. 2 Images of the surfaces. An isosurface mesh is rendered to highlight the three-dimensional structure. From left to right, the flat surface model **a** and one of the deposited surfaces **b**

Table 1 Summary of the sticking probabilities and accommodation coefficients determined in this work

System	T_s / K	s	α_n	α_t	α_r
This work, flat	4.3	0.984(3)	0.92(15)	0.63(29)	0(11)
This work, deposited	4.3	0.982(2)	0.88(26)	0.71(37)	0(47)
N_2 on N_2 [6]	14	≥ 0.85	–	–	–
CH_4 on D_2O [7]	33.5	0.90	–	–	–
CH_4 on CH_4 experiment [5]	20	0.97	–	–	–
CH_4 on CH_4 MD [5]	20	0.91	0.89[b]		11[a]
N_2 on graphene [3][c]	300	0.3	1.06	0.87	–

Results of other, similar systems from literature are listed for comparison
The most applicable system or condition was chosen for comparison when several were available
Uncertainty estimates follow the bootstrapped distributions, c.f. Sect. 2.3
a Inferred from reported E_i and E_f. $\alpha_r = 11$ is due to them setting $E_{i,r} = 0$
b Only combined translational AC reported
c Values for different impact angles reported, the mean is given here. The sticking probability was reported for their 1100 m s^{-1} data set and the ACs for their 750 m s^{-1} data set

qualitatively, uncertainty decreases with sample size. It is therefore notable that the uncertainty of the deposited surface AC results is higher, indicating a broader spread of scattering results. Regarding the rotational AC, the mean zero and very large uncertainty do not allow meaningful comparison between surfaces. The result that rotational energy is gained on the cold surface is in agreement with the result from [5].

3.2 *Individual Accommodation Coefficient Distributions*

Finding α_r values near or below zero, the underlying distributions were investigated. For this, the ACs were calculated individually for each trajectory. The resulting distributions are shown in Fig. 3. Generally, the distributions range over the entire range 0–1 that the AC is classically defined in. Values outside this range are possible since individual energy components are considered. Such outliers are observed if energy is transferred between modes, like in a molecule gaining more rotational energy in the scattering than it had before. Especially prominent were the high negative values in α_r. The accommodation coefficient has a singularity at $E_i = E_s$, causing extreme outliers when the sampled rotational energy approaches the surface thermal energy (omitted in Fig. 3). Similarly, if the initial energy is zero, the AC loses its meaning except relating the energy gain to the surface energy. This is demonstrated by expressing the rotational energy gain reported by [5] in terms of α_r (c.f. Table 1).

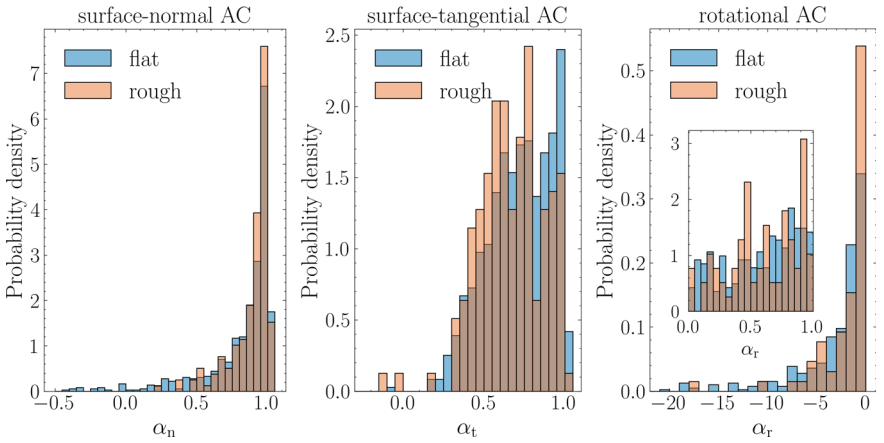

Fig. 3 The distributions of individual accommodation coefficients, in units of probability density, where the bin area corresponds to the fraction of the dataset that falls within the respective bin boundaries. Due to the outliers, only the central 2–98% quantiles of α_r are shown, while the inset zoom shows the 0–1 range for comparison to α_n and α_t. Similarly, in α_t, distant outliers are omitted

The high uncertainty estimates of α_r are in part caused by these mathematical artifacts. However, even in the $0 \leq \alpha_r \leq 1$ region (Fig. 3, inset zoom) it becomes apparent that the distributions of α_r are much broader than of α_n and α_t, ranging far into the negative. As seen in Table 1, the mean α_r values are zero, which in a classical interpretation would indicate no energy change instead of a broad distribution that peaks near $\alpha_r = 1$. The α_t distributions are very broad over the range of 0.4–1, indicating that a single average value in DSMC could be an insufficient representation.

While various other statistical methods for uncertainty estimation are interesting to apply here, many of which result in less extreme values, the bootstrap was chosen here to highlight the broad underlying distributions.

4 Conclusions

The common practice of sampling projectile properties from velocity and angular distributions, it was shown that artifacts occur in the resulting energy component distributions. Further work could investigate how accurately they represent the true energy components of a rocket motor plume impinging on a surface. The proposed deposition scheme might not be necessary for pure species as it produced nearly perfect single crystals. Instead, it is intended and better suited for deposition of mixed ices. The comparison of a flat versus a rough deposited surface showed no significant difference in scattering behaviour. In future work, the deposition method

could be used to deposit mixed ices with different concentrations of H_2 and NH_3 and compare their influence on sticking and scattering.

The question of total plume freeze-out, which initially inspired this study, could be addressed with reasonable certainty. At least approx. 1% of the directly impinging molecules scatter at least once. Regarding the scattering parameters, accommodation coefficients were calculated for surface-normal, surface-tangential and rotational energy components, suitable for use in scattering kernels in simulation methods like DSMC. The distributions of especially the rotational AC were found to be very broad. Instead of a singular parameter, incorporating the different distribution shapes might be necessary.

References

1. Grabe M (2016) STG-CT: high-vacuum plume test facility for chemical thrusters. J Large-Scale Res Facil JLSRF 2:A86–A86. https://doi.org/10.17815/jlsrf-2-139
2. Pham TT, To QD, Lauriat G, Léonard C, Hoang VV (2012) Effects of surface morphology and anisotropy on the tangential-momentum accommodation coefficient between Pt(100) and Ar. Phys Rev E 86:051201. https://doi.org/10.1103/PhysRevE.86.051201
3. Mehta NA, Levin DA (2017) Molecular-dynamics-derived gas-surface models for use in direct-simulation Monte Carlo. J Thermophys Heat Transf 31:757–771. https://doi.org/10.2514/1.T4934
4. Stukowski A (2010) Visualization and analysis of atomistic simulation data with OVITO—the open visualization tool. Modell Simul Mater Sci Eng 18:015012. https://doi.org/10.1088/0965-0393/18/1/015012
5. Brann MR, Ma X, Sibener SJ (2023) Isotopic enrichment resulting from differential condensation of methane isotopologues involving non-equilibrium gas–surface collisions modeled with molecular dynamics simulations. J Phys Chem C 127:13286–13294. https://doi.org/10.1021/acs.jpcc.3c02386
6. Bisschop SE, Fraser HJ, Öberg KI, van Dishoeck EF, Schlemmer S (2006) Desorption rates and sticking coefficients for CO and N2 interstellar ices. Astron Astrophys 449:1297–1309. https://doi.org/10.1051/0004-6361:20054051
7. Thompson RS, Brann MR, Sibener SJ (2019) Sticking probability of high-energy methane on crystalline, amorphous, and porous amorphous ice films. J Phys Chem C 123:17855–17863. https://doi.org/10.1021/acs.jpcc.9b03900
8. Price TW, Evans DD (1968) The status of monopropellant hydrazine technology. Contractor Report JPL-TR-32-1227, NASA, Jet Propulsion Lab
9. Thompson AP, Aktulga HM, Berger R, Bolintineanu et al (2022) LAMMPS—a flexible simulation tool for particle-based materials modeling at the atomic, Meso, and continuum scales. Comput Phys Commun 271:108171. https://doi.org/10.1016/j.cpc.2021.108171
10. Wyckoff RWG (1963) Nitrogen, sample at T = 4.2 K. Crystal Struct 1:7–83
11. Cioce CR, McLaughlin K, Belof JL, Space B (2013) A polarizable and transferable PHAST N2 potential for use in materials simulation. J Chem Theory Comput 9:5550–5557. https://doi.org/10.1021/ct400526a
12. Martyna GJ, Klein ML, Tuckerman M (1992) Nosé-Hoover chains: the canonical ensemble via continuous dynamics. J Chem Phys 97:2635–2643. https://doi.org/10.1063/1.463940
13. McLaughlin K, Cioce CR, Belof JL, Space B (2012) A molecular H2 potential for heterogeneous simulations including polarization and many-body van der Waals interactions. J Chem Phys 136:194501. https://doi.org/10.1063/1.4717705

14. Bolton K, Svanberg M, Pettersson JBC (1999) Classical trajectory study of argon-ice collision dynamics. J Chem Phys 110:5380–5391. https://doi.org/10.1063/1.478433
15. Rubin DB (1981) The Bayesian bootstrap. Ann Stat 9:130–134. https://doi.org/10.1214/aos/1176345338

Open Access This chapter is licensed under the terms of the Creative Commons Attribution 4.0 International License (http://creativecommons.org/licenses/by/4.0/), which permits use, sharing, adaptation, distribution and reproduction in any medium or format, as long as you give appropriate credit to the original author(s) and the source, provide a link to the Creative Commons license and indicate if changes were made.

The images or other third party material in this chapter are included in the chapter's Creative Commons license, unless indicated otherwise in a credit line to the material. If material is not included in the chapter's Creative Commons license and your intended use is not permitted by statutory regulation or exceeds the permitted use, you will need to obtain permission directly from the copyright holder.

Investigation of Gas-Surface Interactions in Hyperthermal and Hypersonic Gas Flow

Quan Han and Haitao Xia

Abstract This study utilizes molecular dynamics simulations to investigate the interaction between silicon carbide surfaces and argon atoms, focusing on the effects of gas temperature and normal velocity on the energy accommodation coefficient (EAC). The results demonstrate a decrease-increase variation of EAC as gas temperature increases from 600 to 12,000 K, driven by the interplay of different collision types and their respective partial EACs. When the normal velocity of argon atom increases from 400 to 3000 m/s, a decreasing trend in EAC is observed in the low incident energy range, which mirrors the effect of changing gas temperature. However, in the high incident energy range, EAC exhibits a fluctuating increase with rising incident energy, showing clear periodic peaks and valleys. This suggests that while both increasing incident energy, the mechanisms governing gas-surface interactions differ. Specifically, the change in normal velocity results in the lower degree of the energy exchange at the interface. Effectively leveraging this characteristic can provide valuable insights for the aerodynamic and aeroheating design of high-altitude vehicles.

Keywords Gas surface interaction · Hypersonic flow · Energy accommodation coefficient

1 Introduction

Accurately predicting aerodynamic heating in hypersonic vehicles requires a thorough understanding of the energy transfer mechanisms at gas-surface interactions, particularly under high rarefied flow conditions, where the energy accommodation

Q. Han (✉) · H. Xia
School of Mechanical and Electronic Engineering, Nanjing Forestry University, Nanjing, China
e-mail: quanhan@njfu.edu.cn

Q. Han
Jiangsu Key Laboratory for Design and Fabrication of Micro-Nano Biomedical Instruments, School of Mechanical Engineering, Southeast University, Nanjing, China

© The Author(s) 2026

M. Grabe et al. (eds.), *Rarefied Gas Dynamics*, Springer Aerospace Technology,
https://doi.org/10.1007/978-3-032-00094-1_10

coefficient (EAC) governs the efficiency of energy exchange [1, 2]. Despite advancements, significant uncertainties persist due to the complex interplay of factors such as incident energy (including both kinetic energy from hypersonic velocity and internal energy from hyperthermal excitation), surface roughness, and gas–gas interactions [3–6]. These challenges are amplified in hypersonic flows, where extreme velocities and temperatures induce unique gas-surface interaction (GSI) phenomena, including high-energy molecule dynamics and transient adsorption–desorption behaviors.

In 1980, Goodman's theoretical model predicted a qualitative decrease-increase trend in EAC with rising incident energy including the incident velocity and gas temperature [7]. In the later molecular dynamics (MD) studies, various trends in EAC changing with incident energy have been reported [8–16]. For example, Tao and Wang [8] demonstrated that gas–gas intermolecular collisions in "continuous scattering" simulations reduce EAC at lower Knudsen numbers, while high incident velocities limit adsorption time, suppressing energy transfer to surfaces. Han et al. [9] showed that EAC decreases with increasing flight velocity due to reduced gas-surface interaction time but rebounds at hypersonic velocities as interaction depth becomes dominant. Chirita et al. [10]emphasized the role of surface temperature, noting that EAC's sensitivity to thermal fluctuations diminishes at incident energies above 500 meV, where a limiting energy transfer regime emerges.

Regarding the influence of gas temperature, which also increases the incident energy, Sipkens et al. [12] observed through molecular dynamics simulations that EAC increases with rising gas temperature under low-temperature conditions. Similarly, Mane et al. [13] found that EAC between aluminum and inert gases (e.g., helium, argon, xenon) increases with temperature, though the rate of increase is smaller, indicating that solid surface properties may mitigate the temperature effect. However, studies by Peddakotla et al. [14] and Sartori et al. [15] found that the EAC of Pt-Ar and Cu-H_2 systems decreases with increasing gas temperature. This study systematically investigates how variations in incident energy—spanning both kinetic energy (through velocity modulation) and internal energy (via gas temperature)—influence EAC under hypersonic conditions.

2 Methodology

2.1 Setup of the Gas-Surface Interaction Model

The gas surface interaction model between cubic silicon carbide (3C-SiC) and argon molecules was constructed using the molecular dynamics software LAMMPS [17], as shown in Fig. 1. Argon atoms were launched from a fixed position above the SiC surface with velocities sampled from a Maxwell–Boltzmann distribution. The SiC slab measures $30 \times 30 \times 18$ Å3 and exposes its (001) face to the incoming atoms. The surface temperature is 300 K and periodic boundary conditions is applied in the *xy*-plane. The interactions between SiC atoms are modeled using the Tersoff potential,

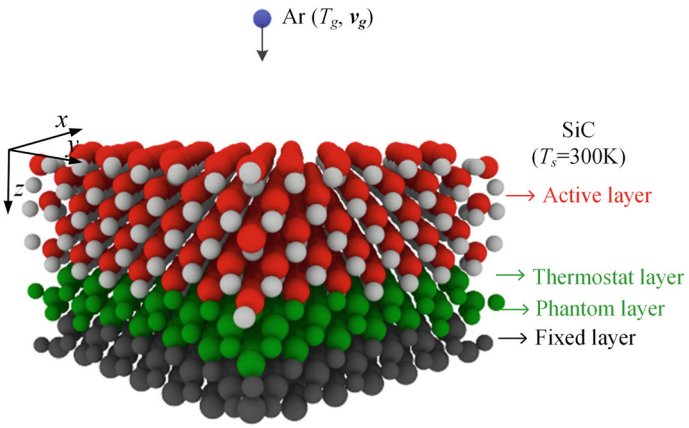

Fig. 1 Schematic diagram of the Ar-SiC interaction model

while the interactions between argon atoms and the C and Si atoms are described using the Lennard–Jones 12–6 potential [18]. All Lennard–Jones interactions have a cutoff radius set to 10 Å (>2.5σ) to balance computational accuracy and efficiency. Ensemble settings were NVE, with a time step of 1 fs and simulation duration of 40 ps, where adsorption is considered if particles remain within the cutoff radius for more than 40 ps.

2.2 *Construction of Incident Velocities of Argon Atom*

In this study, the construction of incident velocities of argon atom uses sampling methods, performing 10,000 independent simulations per calculation case. The velocity distribution is decomposed into thermal velocities and macroscopic flow velocities (v_g), where the thermal velocity components in the *xy*-direction follow the Maxwell–Boltzmann equilibrium distribution, with probability density functions as follows:

$$f(v_{x/y}) = \sqrt{\frac{m}{2\pi kT}} e^{-\frac{mv_{x/y}^2}{2kT}} \tag{1}$$

where m is the mass of gas atoms, T is the gas temperature, and k is the Boltzmann constant. The normal velocity (z-direction) adopts a half-normal distribution superimposed with macroscopic flow velocity:

$$f(v_z) = \sqrt{\frac{2m}{\pi kT}} v_z e^{-\frac{m(v_z - v_g)^2}{2kT}} \tag{2}$$

Two sets of conditions were examined: the first set fixed the gas temperature T_g = 300 K and varying the normal flow velocity v_g from 400 m/s to 3000 m/s. In the second set, the gas temperature was increased from 600 K to 12,000 K with v_g = 0 m/s.

2.3 Collision Types During the Gas-Surface Interactions

As shown in Fig. 2, based on trajectory characteristics of gas atoms interacting with the solid surface, collision behaviors can be classified into three types: Immediate Reflection (IR) with single collision with z-direction trajectory reversal, Trapping-Desorption (TD) with multiple collisions, and Permanent Adsorption (PA) with continuous oscillation within cutoff radius for the full simulation duration. In the classical formula for calculating the EAC, the ratio of adsorption ε is introduced to the formula:

$$\mathrm{EAC}_{\mathrm{classic}} = (1-\varepsilon)\mathrm{EAC}_{\mathrm{collision}} + \varepsilon \tag{3}$$

where $\mathrm{EAC}_{\mathrm{collision}}$ is calculated from the collision events without adsorption. In this study, a modified formula incorporating collision-type contributions is derived[19]:

$$EAC_{\mathrm{modified}} = \sum \beta_k \cdot EAC_k \cdot \gamma_k \tag{4}$$

where β_k is the ratio of collision type, k indicates the IR, TD, and PA collisions. EAC_k is the partial EAC of three collision types, and γ_k is the incident energy correction factor:

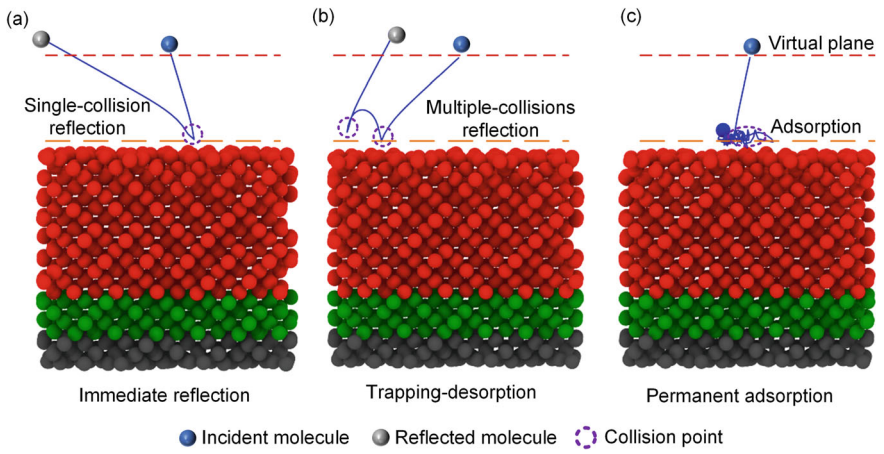

Fig. 2 Collision types during the gas-surface interactions

$$\begin{cases} EAC_k = \dfrac{\langle E_i \rangle_k - \langle E_r \rangle_k}{\langle E_i \rangle_k - \langle E_w \rangle} \\ \gamma_k = \dfrac{\langle E_i \rangle_k - \langle E_w \rangle}{\langle E_i \rangle - \langle E_w \rangle} \end{cases} \tag{5}$$

where $< E_i >$ is the average energy of the incident molecules, and $< E_r >$ is the average energy carried away by the reflected molecules. $< E_w >$ is the reflected energy if the gas has enough time to reach thermal equilibrium with the surface, which is determined to be $2k_BT$ for the monatomic gases investigated in this study.

3 Results and Discussion

3.1 Impact of Gas Temperature on EAC

The EAC shows a clear dependence on incident energy (gas temperature), as illustrated in Fig. 3a. As the gas temperature increases from 600 K to 12,000 K (corresponding to incident energies ranging from 0.10 to 2.08 eV), the EAC initially decreases by 16.7%, from 0.24 to a minimum of 0.2 at 1800 K, and then gradually recovers to 0.32 at 12,000 K. This non-monotonic behavior results from competing collision mechanisms: dominance of IR collisions at high energies versus contributions from TD and PA collisions at lower incident energies. Specifically, the modified formula predicts systematically lower EAC values compared to classical calculations below 0.5 eV, due to the negative correction coefficients ($\gamma_{PA} < 0$) for PA collisions. As shown in Fig. 3b, as the incident energy increases, the ratio of IR collisions rises sharply from 59 to 96%, while the ratio of TD collisions decreases from 33 to 4%, and the ratio of PA collisions drops from 8% to nearly zero. This indicates that, as the gas temperature increases, the thermal velocity of the gas atoms increases, making them more likely to undergo IR collisions, in which they reflect off the surface after a single bounce. Figure 3c displays the trend of partial EAC for the three collision types as a function of incident energy. For PA collisions, the partial EAC is assumed to be in a fully diffusive scattering state, with a value of 1. The partial EAC for IR collisions fluctuates initially and increases with incident energy. In contrast, the EAC for TD collisions decreases rapidly with increasing incident energy before stabilizing. Figure 3d illustrates the variation of the partial incident energy correction factor for the three collision types. In the low incident energy region, the correction factor for IR collisions decreases from 1.4 to 1.1, the correction factor for TD fluctuates around 0.6, and the correction factor for PA collisions is negative, indicating that PA collisions contribute to reducing the overall EAC.

Figure 3e and f show the changes in the average interaction depth and time with incident energy. For the IR collisions, when the incident energy is less than 0.5 eV, the interaction depth increases slightly, while the interaction time decreases significantly. Both effects contribute to fluctuations in the partial EAC for the IR collisions.

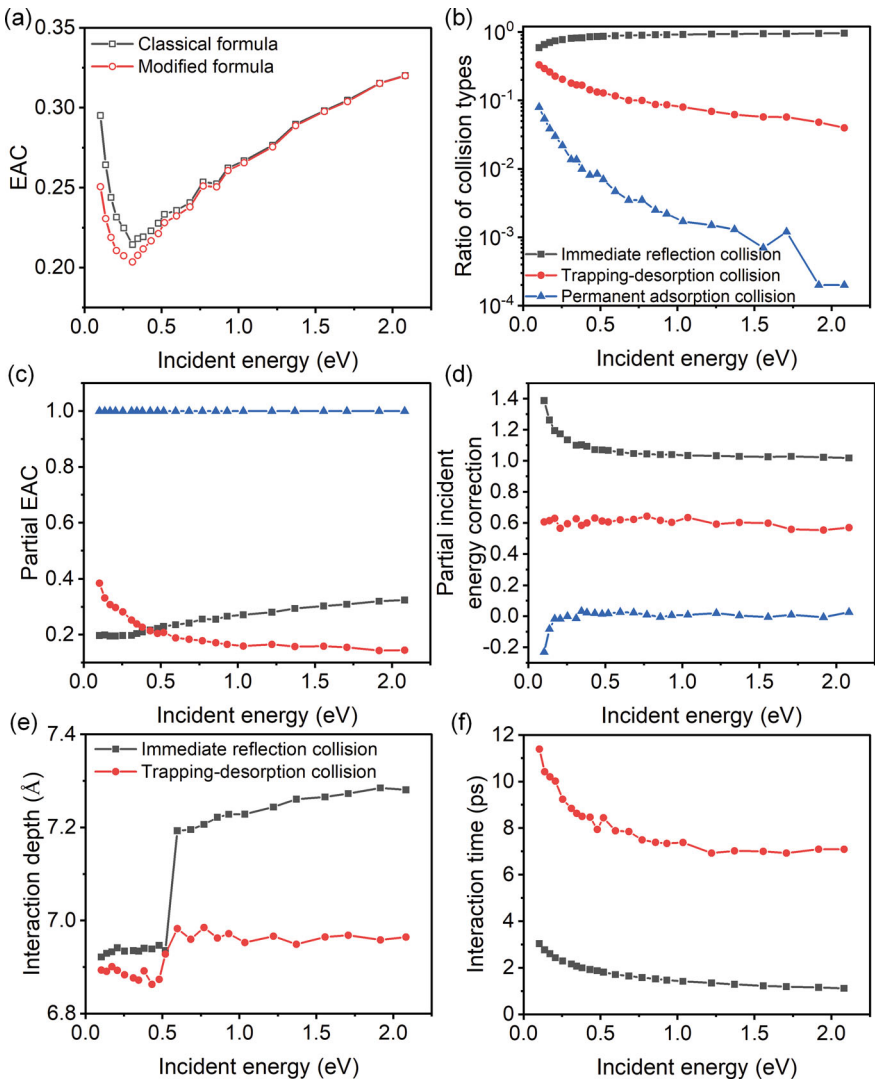

Fig. 3 Effects of temperature-induced changes in incident energy on the EAC and collision details. **a** Overall EAC, **b** Ratio of collision types, **c** Variation of partial EAC for different collision types, **d** Variation of correction factors, **e** Interaction depth, **f** Interaction time

When the incident energy exceeds 0.5 eV, the interaction depth increases sharply and continues to rise with increasing energy, while the interaction time decreases slowly, leading to an increase in the partial EAC for the IR collisions. For the TD collisions, at low incident energies, both the interaction depth and time decrease, causing a rapid decrease in the partial EAC. As the incident energy increases to a

higher value, the interaction depth increases sharply and stabilizes, while the interaction time decreases and stabilizes, resulting in a decrease in the partial EAC for the TD collisions to a stable value.

3.2 Impact of Normal Flow Velocity on EAC

When a vehicle travels at hypersonic speeds, the gas molecules at the gas–solid interface acquire a normal velocity, which increases the incident energy as the normal velocity rises. As shown in Fig. 4a, the EAC values calculated using both formulas are in good agreement. As the incident energy increases with normal velocity, the EAC also exhibits a non-monotonic increase. In the low incident energy range (0.14–0.39 eV, corresponding to a speed range of 400–1000 m/s), the EAC decreases monotonically, reaching a minimum value of 0.2 at 0.44 eV. Afterward, as the incident energy increases, the EAC gradually rises and reaches a local maximum of 0.39 at 1.04 eV. The EAC then decreases as the incident energy increases and reaches a local minimum of 0.32 at 1.44 eV. Finally, the EAC increases again to a local maximum of 0.45 at 2.04 eV.

Figure 4b displays the variation in collision type proportions with incident energy. As the incident energy increases, the ratio of IR collisions rises significantly from 82 to 100%, the ratio of TD collisions decreases from 16.6% to almost zero, and the ratio of PA collisions decreases to zero. This demonstrates the significant effect of increasing normal velocity on collision type, making the collisions almost entirely IR. Figure 4c shows the trend of partial EAC for the three collision types with incident energy. The partial EAC for IR collisions increases with fluctuation but follows the overall EAC. The EAC for TD collisions decreases rapidly with incident energy. Figure 4d shows the variation of the incident energy correction factor for the three collision types. In the low incident energy region, the correction factor for IR collisions decreases from 1.06 to 1, the correction factor for TD collisions increases from 0.75 to 0.88, and the correction factor for PA increases from 0.3 to 0.57. As incident energy increases, only IR collisions remain, and their correction factor stabilizes at 1.0.

Figure 4e and f show the changes in average interaction depth and time with incident energy. For IR collisions, when the incident energy is less than 0.5 eV, the interaction depth decreases slightly, while the interaction time decreases significantly. Both factors contribute to the reduction in partial EAC for the IR collisions. When the incident energy exceeds 0.5 eV, the interaction depth increases sharply, while the interaction time decreases more slowly, causing the partial EAC for the IR collisions to rise with increasing incident energy.

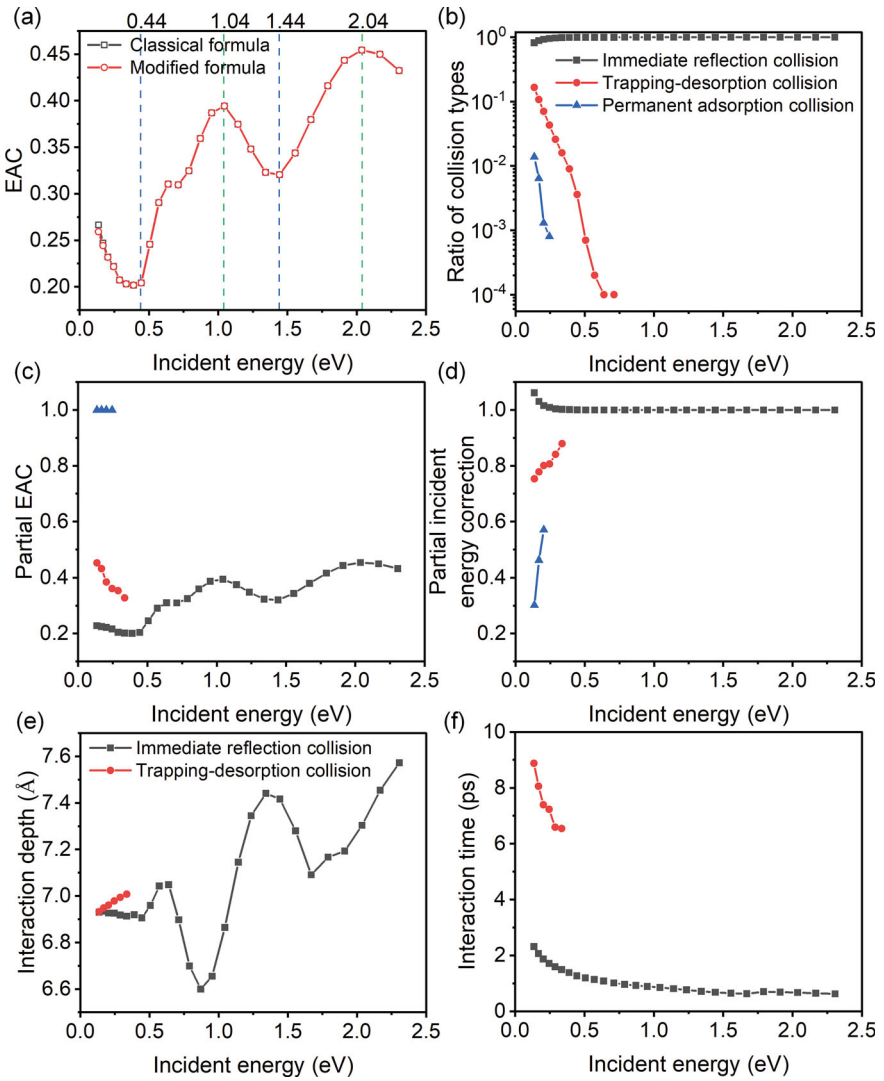

Fig. 4 EAC and collision details varying with normal velocity. **a** Overall EAC, **b** Ratio of collision types, **c** Variation of partial EAC for different collision types, **d** Variation of correction factors, **e** Interaction depth, **f** Interaction time

Acknowledgements This study was supported by the Natural Science Foundation of Jiangsu Province (No. BK20242031), and the China Postdoctoral Science Foundation (2023M740593).

References

1. Liu W, Zhang J, Jiang Y, Chen L, Lee C-H (2021) DSMC study of hypersonic rarefied flow using the Cercignani–Lampis–Lord model and a molecular-dynamics-based scattering database. Phys Fluids 33:072003
2. Mohammad Nejad S, Nedea S, Frijns A, Smeulders D (2022) Development of a scattering model for diatomic gas–solid surface interactions by an unsupervised machine learning approach. Phys Fluids 34:117122
3. Cao B-Y, Sun J, Chen M, Guo Z-Y (2009) Molecular momentum transport at fluid-solid interfaces in MEMS/NEMS: a review. Int J Mol Sci 10:4638–4706
4. Anderson JD (2019) In: Hypersonic and high-temperature gas dynamics. 3rd edn. Aiaa
5. Chen Y, Gibelli L, Li J, Borg MK (2023) Impact of surface physisorption on gas scattering dynamics. J Fluid Mech 968:A4
6. Chen Y, Gibelli L, Borg MK (2024) Impact of random nanoscale roughness on gas-scattering dynamics. Phys Rev E 109:065308
7. Goodman FO (1980) Thermal accommodation coefficients. J Phys Chem 84:1431–1445
8. Ruiling T, Zhihui W (2024) Gas-surface interaction features under effects of gas-gas molecules interaction in high-speed flows. Chin J Aeronaut 37:228–242
9. Han Q, Liu Y, Li Z, Zhang Y, Chen Y (2022) Investigation of energy accommodation coefficient at gas-solid interface of a hypersonic flying vehicle. Aerosp Sci Technol 126:107585
10. Chirita V, Pailthorpe BA, Collins RE (1997) Non-equilibrium energy and momentum accommodation coefficients of Ar atoms scattered from Ni(001) in the thermal regime: a molecular dynamics study. Nucl Instrum Methods Phys Res 129:465–473
11. Prabha SK, Sathian SP (2014) Velocity distribution and velocity correlation of mixture of gases in a nanochannel. Int J Therm Sci 81:52–58
12. Sipkens T, Daun K (2018) Effect of surface interatomic potential on thermal accommodation coefficients derived from molecular dynamics. J Phys Chem C 122:20431–20443
13. Mane T, Bhat P, Yang V, Sundaram DS (2018) Energy accommodation under non-equilibrium conditions for aluminum-inert gas systems. Surf Sci 677:135–148
14. Peddakotla SA, Kammara KK, Kumar R (2019) Molecular dynamics simulation of particle trajectory for the evaluation of surface accommodation coefficients. Microfluid Nanofluid 23:79
15. Sartori E, Brescaccin L, Serianni G (2015) Simulation of diatomic gas-wall interaction and accommodation coefficients for negative ion sources and accelerators. Rev Scient Instrum 87
16. Yamaguchi H, Matsuda Y, Niimi T (2017) Molecular-dynamics study on characteristics of energy and tangential momentum accommodation coefficients. Phys Rev E 96:013116
17. Thompson AP, Aktulga HM, Berger R, Bolintineanu DS, Brown WM, Crozier PS, in 't Veld PJ, Kohlmeyer A, Moore SG, Nguyen TD, Shan R, Stevens MJ, Tranchida J, Trott C, Plimpton SJ (2022) LAMMPS—a flexible simulation tool for particle-based materials modeling at the atomic, meso, and continuum scales. Comput Phys Commun 271:108171
18. Rappe AK, Casewit CJ, Colwell KS, Goddard WA III, Skiff WM (1992) UFF, a full periodic table force field for molecular mechanics and molecular dynamics simulations. J Am Chem Soc 114:10024–10035
19. Han Q, Ma C, Chen W, Wei Z, Zhang Y (2024) Influence of gas-surface and gas-gas interactions on the energy accommodation coefficient in non-equilibrium hypersonic gas flows. Appl Surf Sci 657:159812

Open Access This chapter is licensed under the terms of the Creative Commons Attribution 4.0 International License (http://creativecommons.org/licenses/by/4.0/), which permits use, sharing, adaptation, distribution and reproduction in any medium or format, as long as you give appropriate credit to the original author(s) and the source, provide a link to the Creative Commons license and indicate if changes were made.

The images or other third party material in this chapter are included in the chapter's Creative Commons license, unless indicated otherwise in a credit line to the material. If material is not included in the chapter's Creative Commons license and your intended use is not permitted by statutory regulation or exceeds the permitted use, you will need to obtain permission directly from the copyright holder.

Hypersonic and Space Vehicle Aerodynamics

DSMC Computations of Intake Performance for Air Breathing Ion Engine

Takashi Ozawa, Shunsuke Imamura, Masahito Tagawa, and Kumiko Yokota

Abstract At Japan Aerospace Exploration Agency (JAXA), a study of air breathing ion engine (ABIE) has been carried out for future missions in order to improve the duration of satellites in very low earth orbits (VLEO). For the improvement of the ABIE feasibility, intake performance is one of the important factors. In this work, intake configurations with a utilization of a μ10 ion engine have been investigated for ABIE by conducting direct simulation Monte Carlo (DSMC) simulations, and intake performance at an operational altitude (268 km) has been analyzed. We found that the intake performance can be improved along with the increase of an aspect ratio and a ratio of inflow to outflow cross sections. Several intake configurations were proposed, which can be capable of utilizing the μ10 ion engine for accelerating satellites in VLEO.

Keywords Rarefied gas dynamics · Hypersonic flows · Aerodynamics · DSMC · Air breathing ion engine

1 Introduction

At Japan Aerospace Exploration Agency (JAXA), a feasibility study of air breathing ion engine (ABIE) [1] has been carried out for future missions in order to improve the duration of satellites in very low earth orbits (VLEO) [2, 3]. In order to improve the ABIE feasibility in VLEO, both ion engine performance with air and intake performance are crucial. Intake performances for air breathing electric propulsion (ABEP) have been studied by several research groups over the last decades [4, 5].

T. Ozawa (✉) · S. Imamura
Japan Aerospace Exploration Agency, Sagamihara Kanagawa, Japan
e-mail: ozawa.takashi@jaxa.jp

M. Tagawa · K. Yokota
Kobe University, Kobe Hyogo, Japan

© The Author(s) 2026

M. Grabe et al. (eds.), *Rarefied Gas Dynamics*, Springer Aerospace Technology,
https://doi.org/10.1007/978-3-032-00094-1_11

At JAXA, an ABIE system with a utilization of a μ10 ion engine has been proposed for a demonstration of ABIE at VLEO. In this work, we focus on the intake performance analyses by carrying out direct simulation Monte Carlo (DSMC) [6] simulations. From the interface of the μ10 ion engine, we determine prerequisites of intake development, and carry out a parametric study for intake efficiency with respect to configuration (aspect ratio, ratio of inflow to outflow cross sections, etc.) [7] and use of a collimator. The purpose of intake analyses in this work for ABIE is the ignition capability of the μ10 ion engine and operation at 268 km, where the Super Low Altitude Test Satellite (SLATS) [2] had been operated. The corresponding intake performance requirements at 268 km are (1) compression ratio higher than 70 ($P >= 3 \times 10^{-4}$ Pa, based on conservative ignition requirement for the μ10 ion engine), and (2) intake efficiency higher than 0.15.

2 Prerequisites of Intake for ABIE

In order to utilize the μ10 ion engine, our ABIE intake configuration should meet requirements from the interface of the ion engine and the ABIE system. Figure 1 shows an image of intake configuration with the μ10 ion engine. Freestream molecules are inflowed from the outer region of a core body, reflected by a reflector, and collected inside the μ10 waveguide to be accelerated by the ion engine. The prerequisites of the intake configuration in this work are listed in Table 1. A waveguide length, a waveguide radius, and an exit radius are fixed to fulfill the interface with the μ10 ion engine. Molecule transmittances at an exit screen grid (p_{t1}) and at waveguide surfaces (p_{t2}) are set to 0.12 and 0.26 in this work based on the μ10 ion engine information from Nishiyama et al. Also, the system requirement of a maximum diameter of 340 mm, a maximum length of 900 mm, and an inner radius of 120 mm, has been applied. In this work, we do not consider the attitude uncertainty, and thus, both angle of attack and sideslip angle are set to zero in DSMC.

Figure 2 shows a schematic view of the intake configuration with these prerequisites. The inner body cross section, $S_1 = \pi {R_1}^2 = 0.045$ m^2, and the cross section for ion beam, $A = \pi {R_3}^2 = 0.01$ m^2, are fixed in this work. In order to investigate intake configuration dependence, we first change a ratio of inflow to outflow cross sections ($\alpha = B/A$) from 2 to 4, where B is a cross section of the intake inlet, defined as $B = \pi({R_2}^2\text{-}{R_1}^2)$ [7]. An intake aspect ratio is defined as $\chi = L_1/(R_2\text{-}R_1)$, and χ is changed from 10 to 15. Also, at $\chi = 10$, we compare cases with and without a collimator. The outer radius, R_2, depends on α with the limitation of 170 mm or less, and the intake length, L_1, depends on χ. Nine types of intake configurations (see Table 2) are proposed in this work and shown in Fig. 3. For Types A2, B2, and C2, a ring collimator is located inside the intake tube with a radius of $(R_2\text{-}R_1)/2$ and a length of L_1.

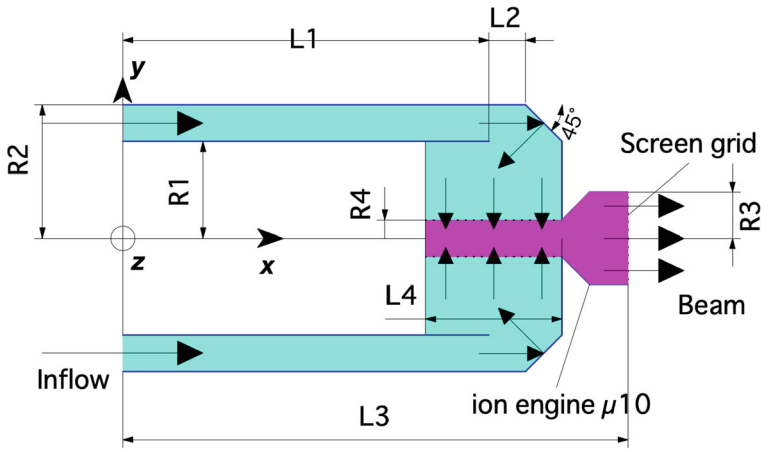

Fig. 1 A proposed intake configuration with a μ10 ion engine

Table 1 Prerequisites of intake parameters in this work

Parameter	Symbol	Value	Unit
Waveguide length	L_4	170	mm
Waveguide radius	R_4	22.5	mm
Exit radius	R_3	57	mm
Transmittance of the exit grid	p_{t1}	0.12	–
Transmittance of the waveguide surface	p_{t2}	0.26	–
Angle of attack	*AoA*	0	deg
Sideslip angle	*Beta*	0	deg
Maximum diameter	D_{max}	340	mm
Maximum length	L_{max}	900	mm
Inner radius	R_1	120	mm

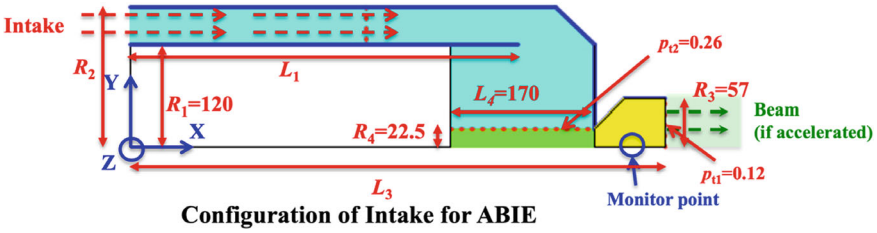

Fig. 2 An image of intake configuration with prerequisites for ABIE

Table 2 Types of intake configurations

	Type 0	Type 1	Type 2
Type A ($\alpha = 2$)	$\chi = 10$	$\chi = 15$	$\chi = 10$ (with a collimator)
Type B ($\alpha = 3$)	$\chi = 10$	$\chi = 15$	$\chi = 10$ (with a collimator)
Type C ($\alpha = 4$)	$\chi = 10$	$\chi = 15$	$\chi = 10$ (with a collimator)

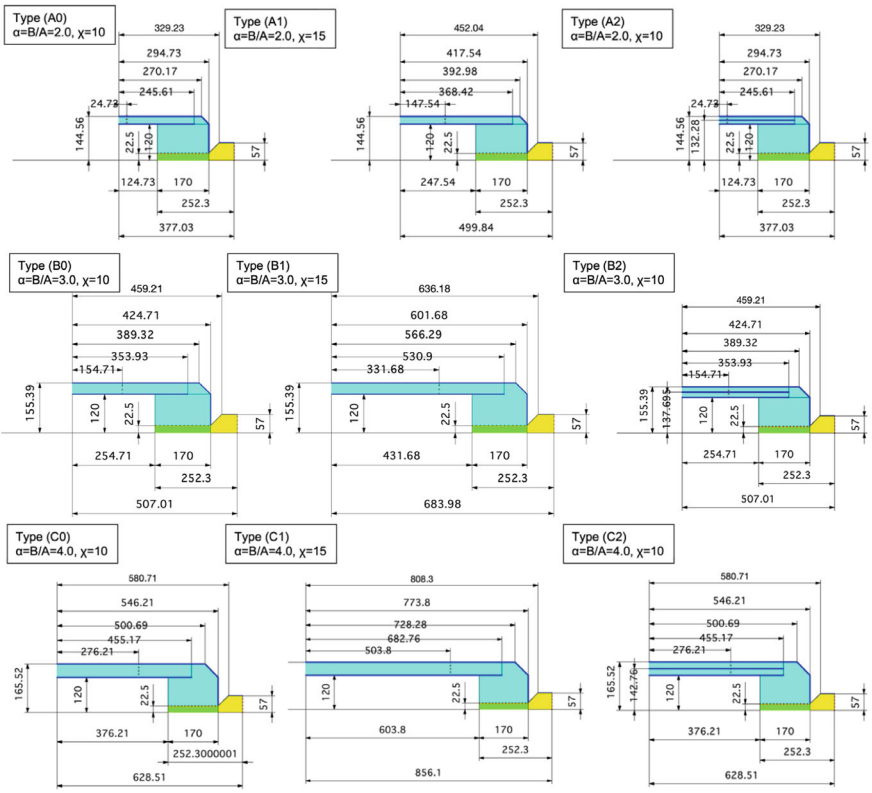

Fig. 3 Comparison of proposed intake configurations for ABIE

3 Computational Modeling

Numerically, we carry out DSMC simulations for hypersonic flows at 268 km around and inside the ABIE intake models. We use a DSMC code, named Modeling Of Transitional-Ionized Flows (MOTIF). General DSMC modeling is employed in the MOTIF code, and details can be found in Refs [8, 9]. In order to apply for ABIE intake analyses, we use the following specific modeling in this work.

(1) For geometry segments at the exit grid, a uniform transmittance (p_{t1}) is employed.
(2) For geometry segments for waveguide surfaces, a uniform transmittance (p_{t2}) is employed.
(3) Neutral particles in the waveguide (green-shaded section in Fig. 2) and discharge chamber (yellow-shaded section in Fig. 2) can be removed based on a ratio of releasing ions to neutral particles (R_{in}).

Note that R_{in} is set to 4 to demonstrate ion acceleration cases with the μ10 ion engine (based on personal communication with Nishiyama et al.). The transmittance parameters determine the ratio of passing the surfaces without collisions to reflection of the surfaces. A dataset of 7 chemical species (N, O, Ar, He, H, N_2, O_2) is used with a freestream condition at 268 km. The freestream speed (V_∞), temperature (T_∞), and number density (n_∞) at 268 km are 7.744 km/s, 921 K, and 1.23×10^{15} m^{-3}, respectively. The mole fractions for N, O, Ar, He, H, N_2, and O_2 are 9.96×10^{-3}, 0.719, 1.21×10^{-4}, 6.05×10^{-3}, 1.59×10^{-4}, 0.256, 9.34×10^{-3}, respectively. No chemical reactions were activated since the impact of chemical reactions is negligible at this altitude. For gas-surface interactions, the Maxwell model is used with a wall temperature (T_w) of 300 K. The surface accommodation coefficient, γ, is basically varied between 0.8 and 1.0 (fully diffuse condition).

We evaluate intake performance using the following 4 output parameters.

(1) Compression ratio: $G = \rho_{ch}$ (density inside discharge chamber) / ρ_∞ (freestream density)
(2) Intake efficiency 1 [5]: $\eta_{i1} = 1\text{-}\Gamma_1/\Gamma_0$

Γ_0: particle inflow flux at the inlet,
Γ_1: particle outflow flux at the inlet.

(3) Intake efficiency 2: $\eta_{i2} = \Gamma_{2i}/\Gamma_0$

Γ_2: outflow particle flux at the exit (Γ_{2n}: neutral, Γ_{2i}: ion).
$R_{in} = \Gamma_{2i}/\Gamma_{2n}$.

(4) Ratio of mass flow rate (J [kg/s]) to drag coefficient (CDS [m^2]): J/CDS [kg/s-m^2]

S: representative cross section ($S = \pi {R_2}^2$).

4 Results and Discussions

4.1 Dependence on α and χ Without Ion Acceleration

First, we conducted DSMC computations with the condition of γ of 1.0 and Rin of 0 for all 9 types of intake configurations. The contour plots of the compression ratio (G) are compared among types A, B, and C in Fig. 4.

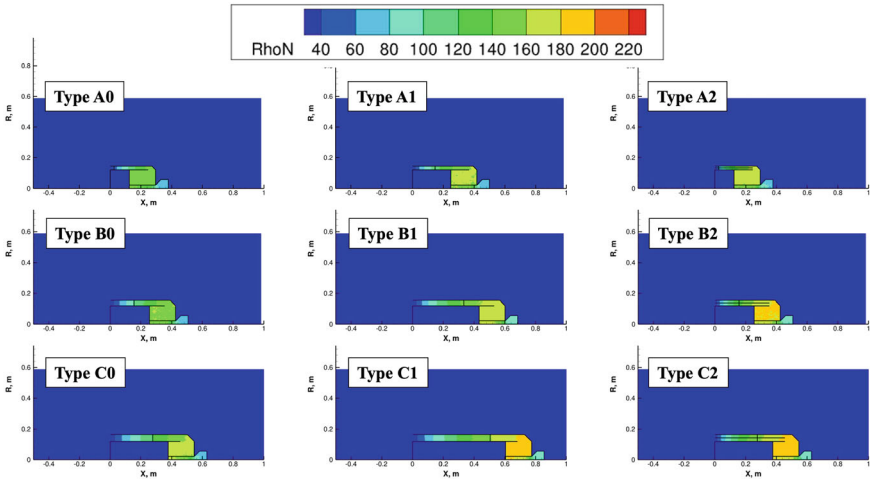

Fig. 4 Comparison of compression ratio contours among 9 intake configurations

Freestream particles entering the intake from the outer region of a core body are reflected by a reflector and collected inside the μ 10 waveguide. The density increases from the inlet to outlet and the density is the highest in the reflected region (outside of the waveguide). The density keeps decreasing from the region outside the waveguide to the region inside the discharge chamber. It can be seen that along with the increase of α and χ, the compression ratio, G, increases inside the waveguide and discharge region. With a collimator, the compression ratio also increases inside the waveguide and discharge region.

The compression ratio inside the discharge chamber is compared in Fig. 5. We found that the compression ratio increases approximately 10–15% along with the increase of α from 2 to 4. Among the types 0, 1, and 2, the type 2(χ = 10 with a collimator) shows better compression ratio. Figure 6 shows the dependence of compression ratio and intake efficiency on χ with α of 4. As the intake aspect ratio increases from 10 to 20, both G and ηi1 increases. However, the effect of α is not significant in terms of *J/CDS* since both the drag and the mass flow rate increases along with the increase of α as you can see in Fig. 7.

4.2 Intake Performance with Ion Acceleration

In this section, we investigate the effect of ion acceleration. Numerically, we demonstrate ion acceleration in the discharge chamber by introducing a ratio of ion outflow flux to neutral outflow flux. According to the study of Nishiyama et al., R_{in} ($=\Gamma_{2i}/\Gamma_{2n}$) is approximately 4 during the μ10 ion engine operation. Therefore, in this study, we compare R_{in} of 0 and 4 cases to figure out the effect of ion acceleration. Figures 8

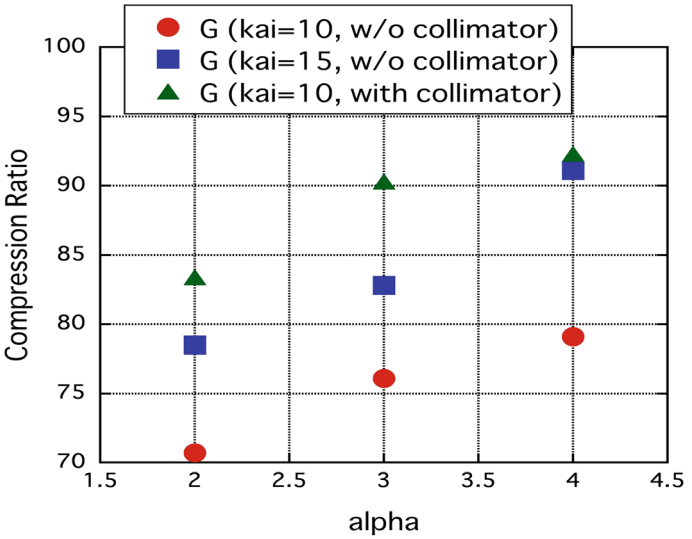

Fig. 5 Dependence of compression ratio (G) on α [$\gamma = 1.0$, $R_{\text{in}} = 0$]

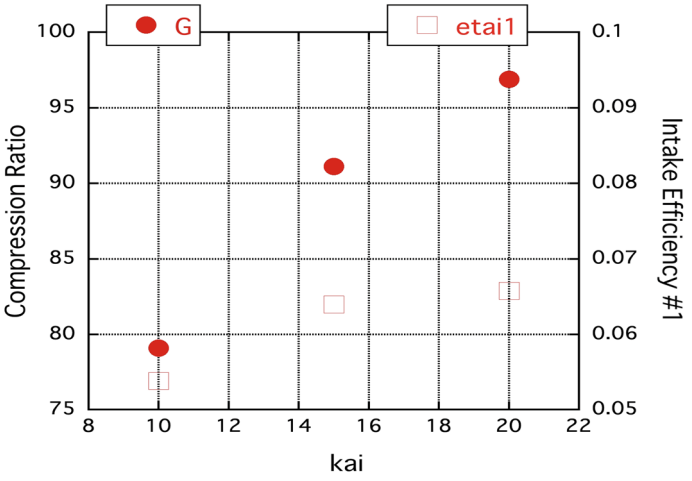

Fig. 6 Dependence of compression ratio (G) on χ [$\gamma = 1.0$, $R_{\text{in}} = 0$, $\alpha = 4$]

and 9 show comparisons of the compression ratio and intake efficiency between R_{in} of 0 and 4. We assumed aluminum surfaces for the intakes, whose surface accommodation coefficient is estimated to be 0.8. For both cases, compression ratio increases along with the increase of α. On the other hand, the intake efficiency decreases along with the increase of α. For instance, the intake efficiency is lower than 0.11 for $\alpha = 4$. With the activation of ion acceleration ($R_{\text{in}} = 4$ cases), compression ratio

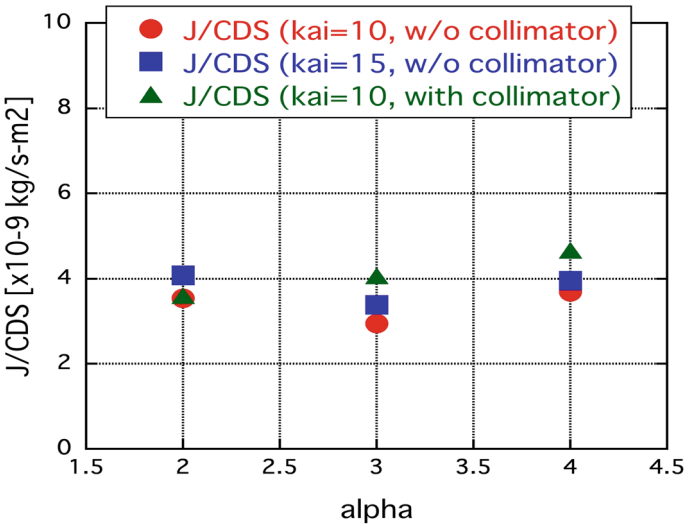

Fig. 7 Dependence of *J/CDS* on α [$\gamma = 1.0$, $R_{\text{in}} = 0$]

decreases. Although the compression ratio for $\alpha = 4$ is higher than 175 without the ion acceleration ($R_{\text{in}} = 0$), the value becomes lower than 80 for the ion acceleration demonstration cases ($R_{\text{in}} = 4$). On the other hand, the intake efficiency increases and is higher than 0.15 for $\alpha = 4$ and $R_{\text{in}} = 4$. In order to fulfill the compression ratio requirement of $G \geq 70$ at 268 km, α should be 4 or higher for the ion acceleration demonstration cases.

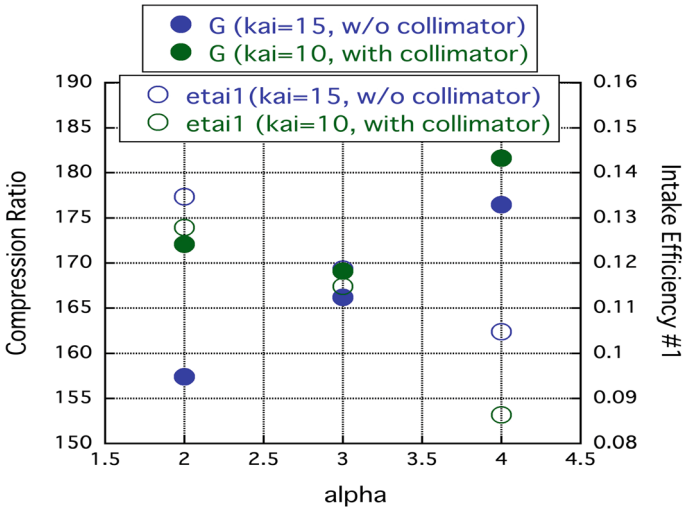

Fig. 8 Comparison of G and η_{i1} with $\gamma = 0.8$, $R_{\text{in}} = 0$ (without ion acceleration)

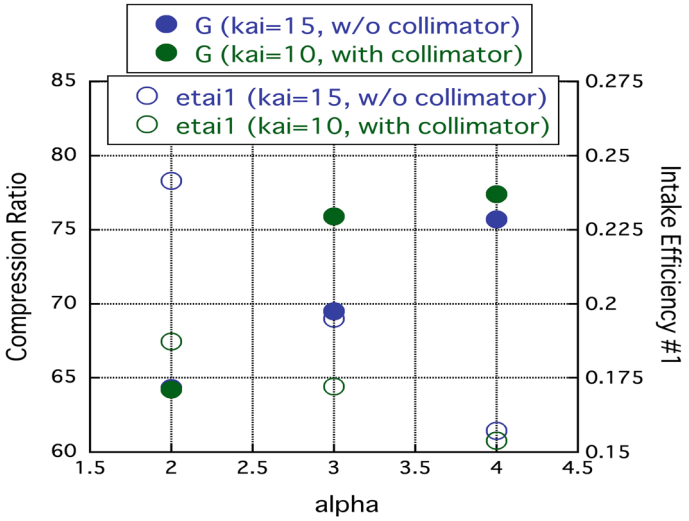

Fig. 9 Comparison of G and η_{i1} with $\gamma = 0.8$, $R_{in} = 4$ (with ion acceleration demonstration)

Figure 10 shows a comparison of η_{i1} and η_{i2} for the ion acceleration demonstration cases. Basically, η_{i2} has similar tendency to η_{i1}. η_{i2} decreases along with the increase of α. Among 6 types, the type A1 ($\alpha = 2, \chi = 15$) has the highest intake efficiency of 0.24 while the compression ratio is the lowest. Figure 11 shows a comparison of *J/CDS* with $\gamma = 0.8$, and $R_{in} = 4$. Similar to the cases without ion acceleration ($R_{in} = 0$), the effect of α is not significant in terms of *J/CDS*. Note that although *J/CDS* is not sensitive to α, α should be 4 among the test configurations from the viewpoint of the compression ratio requirement. The types C1 and C2 show similar intake performances, and the selection may depend on length and manufacturing limitations.

Finally, we show the dependence on the aspect ratio in Figs. 12 and 13. α was set to 4, and χ was changed from 10 to 20 (without collimators) with the condition of $\gamma = 0.8$ and $R_{in} = 4$. Both intake efficiencies, η_{i1} and η_{i2}, increase along with the increase of χ, and η_{i1} becomes higher than 0.15 if χ is greater than 14. *J/CDS* also increases along with the increase of χ.

5 Conclusions

In this work, we have investigated intake performance for ABIE with a utilization of the μ10 ion engine. Under the prerequisites of interfaces and size limitations, dependence on α (ratio of inflow to outflow cross sections) and χ (intake aspect ratio) have been studied. Along with the increase of α, the compression ratio also increased. On the other hand, intake efficiencies decreased, and *J/CDS* was not sensitive to α.

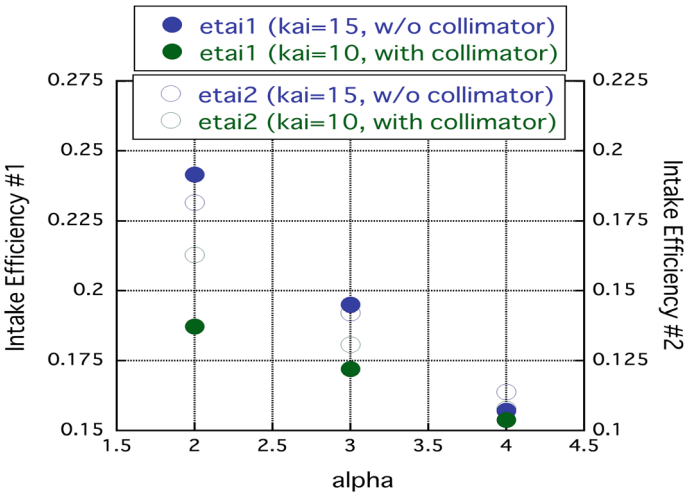

Fig. 10 Comparison of η_{i1} and η_{i2} with $\gamma = 0.8$, $R_{in} = 4$

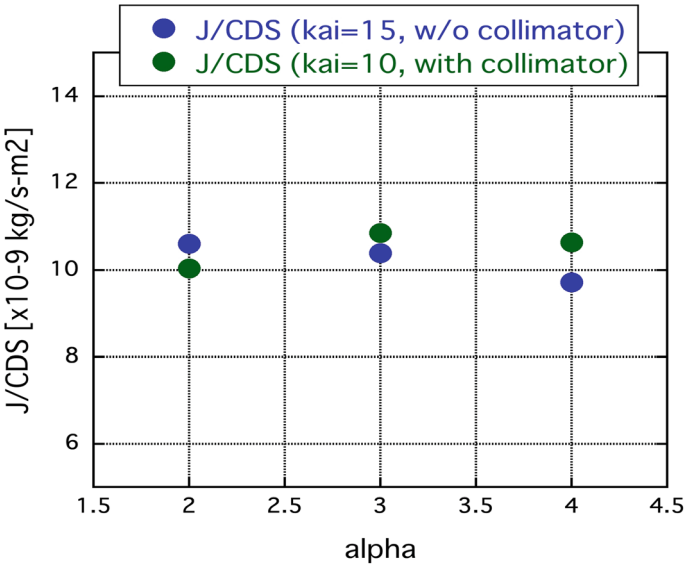

Fig. 11 Comparison of *J/CDS* with $\gamma = 0.8$, $R_{in} = 4$

Along with the increase of χ, both the compression ratio and intake efficiencies increased, which resulted in the *J/CDS* improvement. In addition, with a collimator, both the compression ratio and intake efficiencies became higher. In summary, the following three configurations can be suggested for the ABIE intake under the μ10 ion engine prerequisites in this work.

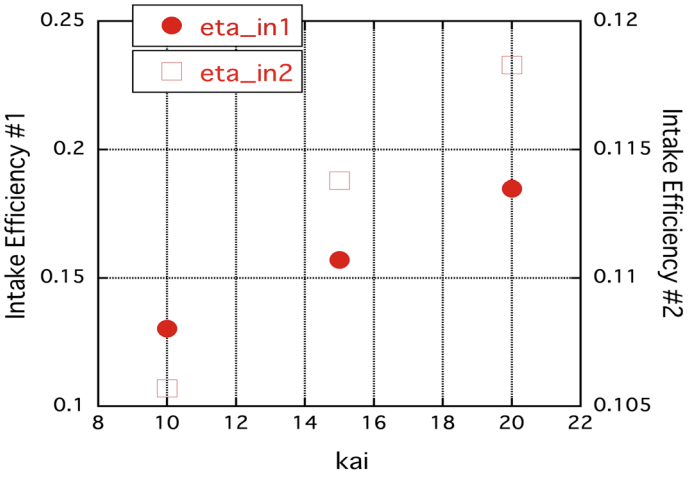

Fig. 12 Comparison of η_{i1} and η_{i2} with $\alpha = 4$, $\gamma = 0.8$, $R_{in} = 4$

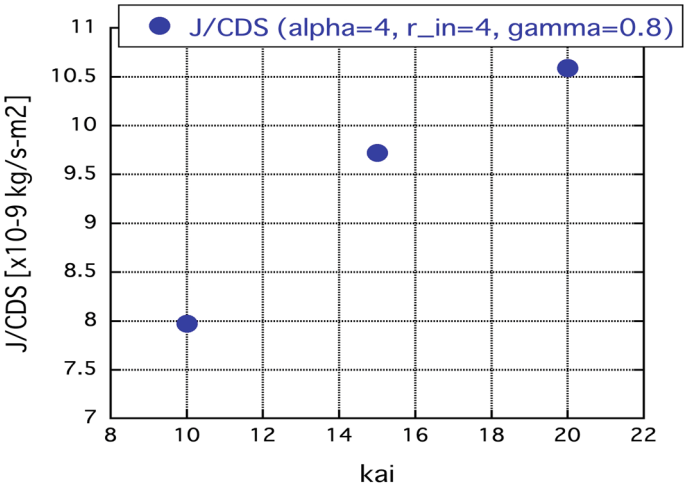

Fig. 13 Comparison of *J/CDS* with $\alpha = 4$, $\gamma = 0.8$, $R_{in} = 4$

(1) Length limitation of 500 mm class: Type B2 ($\alpha = 3$, $\chi = 10$ with a collimator)
(2) Length limitation of 600 mm class: Type C2 ($\alpha = 4$, $\chi = 10$ with a collimator)
(3) Manufacturing limitation (no collimators): Type C1 ($\alpha = 4$, $\chi = 15$ without collimators).

Note that these results are dependent on size and interface requirements.

As our future works, we will first study surface accommodation dependence, such as gold-plating, ITO (Indium Tin Oxide), and POSS-Polyimides coatings. Second, we will study the effect of micro-structured surfaces. Third, we will verify intake

performance using wind tunnel models in the Hypersonic Rarefied Wind Tunnel (HRWT) at JAXA and in the Laser Detonation Wind Tunnel at Kobe University.

Acknowledgements The research performed at JAXA was partly supported by the Grant-in-Aid for Scientific Research (C), No. 24K07893 from Japan Society for the Promotion of Science (JSPS) whose support is gratefully acknowledged. I would like to acknowledge Prof. Nishiyama of ISAS and the ABIE team at JAXA for useful advice of μ10 ion engine interfaces and specifications.

References

1. Nishiyama K (2003) Air breathing ion engine concept. In; Proceedings of the 54th international astronautical congress, IAC-03-S4-02
2. Sasaki M (2017) Mission for super-low earth orbit, SLATS. Space Res Today 198:10–18
3. Imamura S, Utashima M, Ozawa T, Akiyama K, Sasaki M (2018) Current status of the on-going orbit transfer of Super Low Altitude Test Satellite (SLATS). In: Proceedings of the 69th international astronautical congress, IAC-18-C1.8.1
4. Binder T, Boldini PC, Romano F, Herdrich G, Fasoulas S (2016) Transmission probabilities of rarefied flows in the application of atmosphere-breathing electric propulsion. AIP Conf Proc 1786(1):190011
5. Romano F et al (2021) Intake design for an atmosphere-breathing electric propulsion system (ABEP). Acta Astronaut 187:225–235
6. Bird GA (1994) Molecular gas dynamics and the direct simulation of gas flows. Clarendon, Oxford, England, U.K.
7. Fujita K (2004) Air intake performance of air breathing ion engines. J Jpn Soc Aeronaut Space Sci 52(610):514–521 (in Japanese)
8. Ozawa T, Suzuki T, Takayanagi H, Fujita K (2011) Analysis of non-continuum hypersonic flows for the Hayabusa reentry. In: AIAA Paper 2011-3311, 42nd AIAA thermophysics conference, Honolulu, Hawaii
9. Ozawa T, Zhong J, Levin DA (2008) Development of kinetic-based energy exchange models for noncontinuum, ionized hypersonic flows. Phys Fluids 20:046102

Open Access This chapter is licensed under the terms of the Creative Commons Attribution 4.0 International License (http://creativecommons.org/licenses/by/4.0/), which permits use, sharing, adaptation, distribution and reproduction in any medium or format, as long as you give appropriate credit to the original author(s) and the source, provide a link to the Creative Commons license and indicate if changes were made.

The images or other third party material in this chapter are included in the chapter's Creative Commons license, unless indicated otherwise in a credit line to the material. If material is not included in the chapter's Creative Commons license and your intended use is not permitted by statutory regulation or exceeds the permitted use, you will need to obtain permission directly from the copyright holder.

Toward a Model for Biological Contaminant Dispersal by Spacecraft Operating and Landing in Near-Vacuum

William A. Hoey and John R. Anderson

Abstract When spacecraft operate and land in near-vacuum, as for Earth's Moon or icy moons like Enceladus, they introduce *contaminant* into their environments that may impact mission science at local and global scales. The rarefied gas dynamic plume flows generated by chemical propulsion systems may remove and disperse terrestrial particles borne on such spacecraft, including microbes and spores. These high-speed flows provide a unique vector for transport of *biological contaminant* far from a spacecraft in near-vacuum, i.e. in the absence of atmospheric drag. This paper describes the initial development of gas dynamic and orbital mechanics models for spacecraft-generated plume flows and induced particle transport, and an investigation of necessary boundary conditions to address two key questions: how can plume flows remove and disperse microorganism-laden particles or independent microorganisms borne on a spacecraft? And how can biological contaminants redeposit both locally (to the spacecraft, its instruments, and landing site) and globally (i.e. to regions of scientific interest)?

Keywords Plumes · Planetary protection · Chemical propulsion · Rarefied gas

1 Introduction

Spacecraft that would operate near, or land onto, solar system bodies may carry *biological contaminant* including microbes and spores. The characterization and mitigation of this material is a core responsibility of NASA's Planetary Protection (PP) discipline, which is chartered in part with the protection of solar system bodies from contamination by Earth life [1]. Inadvertent contaminant dispersal during spacecraft operation and landing poses a *forward contamination threat* both locally—to a spacecraft's own instrumentation, its sampling systems, or landing site—and globally to distant regions of high scientific value including pristine sites intended for

W. A. Hoey (✉) · J. R. Anderson
NASA Jet Propulsion Laboratory, California Institute of Technology, Pasadena, CA, USA
e-mail: william.a.hoey@jpl.nasa.gov

© The Author(s) 2026

M. Grabe et al. (eds.), *Rarefied Gas Dynamics*, Springer Aerospace Technology,
https://doi.org/10.1007/978-3-032-00094-1_12

sampling, for instance the open cryovolcanic water vents of Saturn's icy moon Enceladus. Forward contamination could make in situ or returned-sample detection of extraterrestrial biosignatures ambiguous or compromise the integrity of extraterrestrial environments that could harbor life, and is therefore rigorously controlled in spacecraft design, assembly, and operations.

In any powered landing with a chemical propulsion system—whether in atmosphere as for Mars or in near-vacuum as for Earth's Moon or the icy moons—engine plume flows that wash over a spacecraft and its landing site can remove, entrain and disperse biological contaminant of terrestrial origin. The nominal operation of chemical propulsion systems in attitude control, orbital adjustment, descent, and landing exposes portions of a spacecraft to direct and indirect high-speed plumes that can exceed 2000 m/s in core flow. Rarefied gas dynamic plume flows may provide a unique and significant vector for long-distance particle dispersal in near-vacuum environments, where no appreciable atmospheric drag would act to limit transport.

1.1 Toward a Model for Biological Contaminant Dispersal in Plumes

Consider the Europa Lander mission concept, which proposed the use of a Sky Crane landing system derived from Mars Science Laboratory Curiosity (MSL) and Mars 2020 Perseverance (M2020) rover heritage, as shown in Fig. 1, for a landing onto Jupiter's icy moon Europa. This landing would expose a vehicle in bridled descent to a complex plume flowfield produced by four monopropellant hydrazine engines [2, 3]. Comparable Mars operations with the Sky Crane generated dust clouds that partially obscured landing sites and led to particulate deposition onto their rovers [4], showing that even in a continuum atmosphere[1] landing plume flows can directly impact a vehicle payload.

Several important questions of forward contamination are presented by such plume-vehicle interactions at Mars, Europa, or for other solar system bodies, including:

- How can engine plume flows *remove and disperse* biological contaminant (microorganism-laden particles or independent microorganisms) borne by a spacecraft?
- How could these plumes *redeposit* biological contaminant locally to a spacecraft, its instrumentation, and landing site, and globally to surfaces far from its landing site?

[1] Plume flow fields in Mars atmosphere will differ substantially from those at Europa given the vast difference in pressure between bodies; at Mars surface (~ 640 Pa) engine plumes remain collimated and continuum, whereas Europa's near-vacuum surface condition (<< 1 μPa) would permit broad expansion through the rarefied and into the free-molecular regime [3].

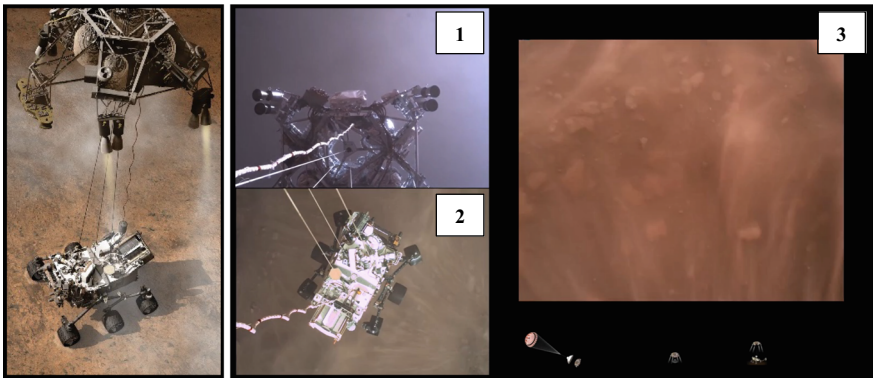

Fig. 1 Sky Crane Mars landings. *Left:* an artist's concept of the Mars Science Laboratory Curiosity rover's landing. *Right:* images from Mars 2020 Perseverance's Sky Crane landing video including *(1)* views upward from the rover's top deck; *(2)* downwards from the Sky Crane; and *(3)* downward from the rover's bottom deck [4]. Surface obscuration is due to the erosion and transport of Mars dusts in the engine plume flow field. *Image credits NASA/JPL-Caltech*

This paper describes the development of an integrated model to answer such questions by delivering information about the distances and angles to which biological contaminant particles will transport as functions of spacecraft configuration (e.g. geometry and engine operation); of initial loadings of contaminant (e.g. shapes, sizes, strains, and associations between microbiology and larger inert particles); and of landing environment (e.g. atmospheric or airless condition, local gravity and rotational reference frame, etc.) Fig. 2 documents the model's intended workflow including key inputs and deliverable results, which derive from similar engineering models developed for the dispersal of lunar regolith in landing plume-surface interactions [5]. The paper proceeds through the columns of Fig. 2; Sect. 2 will address inputs to the framework and the preliminary status of their collection for representative spacecraft in near-vacuum; Sect. 3 will address plume gas dynamic and particle orbital trajectory models under development, and will exhibit results of rarefied gas dynamic plume simulations relevant to the dispersal model. More detailed methodological descriptions and examples of the authors' CFD-DSMC[2] approach can be found in Hoey et al. [3, 5].

[2] CFD: computational fluid dynamics; DSMC: direct simulation Monte Carlo.

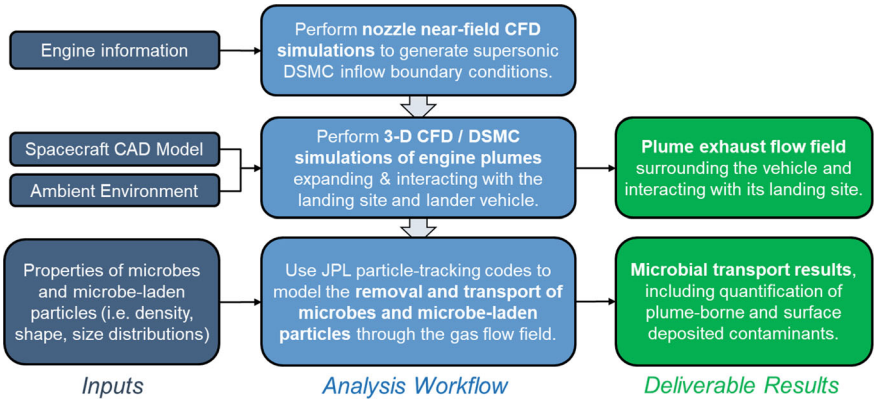

Fig. 2 Model workflow for transport analyses of spacecraft-borne microbes and microbe-laden particles mobilized by chemical propulsion plume flows

2 Model Inputs

2.1 Chemical Propulsion Systems for Mars, Lunar and Icy Moon Cases

Spacecraft chemical propulsion systems intended for attitude control, orbital adjustments, and even primary thrust for probes or landing vehicles often employ monopropellant (N_2H_4) or bipropellant (e.g. MMH/NTO)[3] hydrazine for their stability and performance as detailed by Grabe and Soares [6]. For example, MSL and M2020 Sky Crane architectures used eight monopropellant hydrazine engines to hover and four during bridled descent; the Europa Lander concept proposed a similar design [2, 3]. Other NASA Mars landers to use monopropellant hydrazine systems included Viking, Phoenix, and Insight. Recent mission concepts have studied monopropellant hydrazine in applications including orbiter and lander concepts to Saturn's icy moon Enceladus [7]. Bipropellant hydrazine systems are used both for primary thrust and attitude control on NASA's Europa Clipper mission; see common use on ISS visiting vehicles and similar planned vehicles for NASA's Lunar Gateway space station; and have been proposed for future spacecraft including CLPS (Commercial Lunar Payload Services) uncrewed lunar landers. Other cryogenic propellant mixtures planned for future crewed lunar landers are liquid oxygen / liquid hydrogen and liquid oxygen / liquid methane.

Any propulsion system planned for use in near-surface operations or landings onto solar system bodies could expose these bodies to biological contaminant dispersed

[3] MMH: monomethylhydrazine, fuel, CH_6N_2; NTO: dinitrogen tetroxide, oxidizer, N_2O_4.

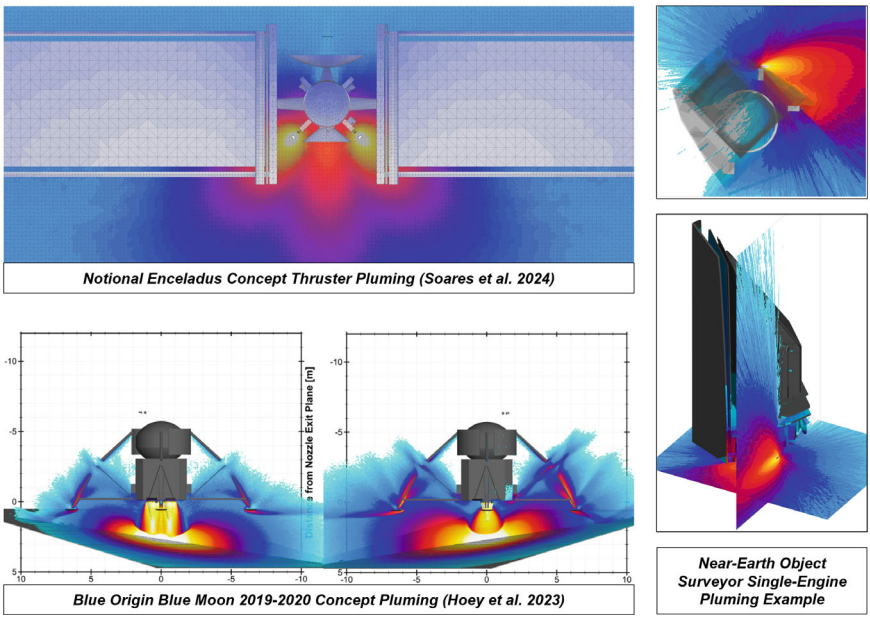

Fig. 3 JPL investigations of self-pluming for space and landing applications with CFD-DSMC methods; models for inert particle transport in such environments are being extended to study microorganism transport in near-vacuum. Representative contours show pressure on log-scales

in plumes, and is therefore of potential interest to NASA's planetary protection discipline. Rarefied gas dynamic plume simulations in near-vacuum conditions will typically require inputs including nozzle contours from throat to exit plane and sonic throat thermodynamic conditions like pressure, temperature, and species mole fraction (alternately, equivalent conditions at the nozzle exit); as well as engine positions, orientations, and firing histories for single- and multiple-engine firings [5]. The authors have performed CFD-DSMC simulations for a range of fuels and thrust levels that already inform the particle dispersal framework; these are introduced in Sects. 3.1 and Fig. 3.

2.2 *Spacecraft Geometries and Environments*

Any study of particle dispersal by spacecraft-generated plume flows must predict the forces applied to various vehicle surfaces by single- and multiple-engine firings, which will be dependent on the specific configuration both of the spacecraft and its engines. Therefore, spacecraft geometric models and derived meshes of sufficient detail to represent *significant features* are necessary—i.e. both (1) features of interest to a dispersal simulation and onto which loads must be queried and (2) all

other features that influence plume flow fields onto, and particle dispersal, from the former—as are rarefied gas dynamic solvers that can treat meshes and multi-plume firings in 3-D. Fortunately, several DSMC solvers are available for 3-D simulations onto spacecraft meshes; the authors apply both NASA JSC's DAC (DSMC Analysis Code) and Sandia's open-source SPARTA (Stochastic PArallel Rarefied-gas Time-accurate Analyzer) [8, 9]. The authors have developed an internal library of relevant spacecraft meshes for NASA and commercial missions including for prior plume simulations; the process of developing a suitable mesh is described in detail by publications including Hoey et al. [5].

In near-vacuum, spacecraft often experience inadvertent plume loading by gas-phase expansion into the backflow region behind a nozzle during single-engine firings, even when engines are oriented to prevent 'direct' plume impingement. In some cases, spacecraft experience 'direct' plume impingement in their nominal operation as plume core flows impinge onto exposed vehicle surfaces within ~ 30° of nozzle centerline (as for Europa Clipper's magnetometer boom and as would occur in bridled descent for a Sky Crane Europa Lander concept); this is also a primary and well-studied mode of plume loading for space stations during the approach and departure of visiting vehicles. Multiple simultaneous firings can produce complex flow fields that impinge and impose appreciable loads onto surfaces not in the direct line-of-sight of nozzle centerlines. Solar array plume impingement can be difficult to avoid, particularly when multi-plume interactions occur—and for icy moon probe and orbiter missions, solar arrays will have exceptionally large surface areas given their distance from the Sun (~ 5.2 AU for Jupiter and Europa; ~ 9.5 AU for Saturn and Enceladus) [7]. During spacecraft landings, plume-surface interactions add additional complexity to the plume-plume and plume-vehicle interactions that occur in orbit, including potential recirculation between the vehicle and landing site and surface erosion / deformation that can influence plume flows [3, 5]. In any case, the system of plume-plume, -vehicle, and -surface interactions for spacecraft operating near, or landing onto, solar system bodies creates many opportunities to impose loads that could remove laden biological contaminant.

Spacecraft atmospheric and exospheric environments may also be significant inputs to models for plume flows and particle transport; e.g. plume simulations at Mars must represent that body's continuum atmosphere. This paper focuses primarily on 'near-vacuum' applications to Earth's Moon and the icy moons of Europa and Enceladus, for which ambient surface-level exospheres are many orders-of-magnitude less dense than any spacecraft-generated plume flows and may therefore be neglected.

2.3 Properties of Relevant Microorganisms and Inert Particles

The shapes, sizes, quantities, and attachment properties of microorganisms to spacecraft surfaces are another key input to a dispersal model. The properties of certain individual microorganisms may be known and their quantities measured on spacecraft surfaces and in assembly cleanrooms. However, relatively few such microorganisms are *standalone*, i.e. not attached to larger, inert particulate. This adds complexity to dispersal analyses: particle removal is strongly influenced by shape and size and so larger inert particles may be relatively easier to remove from surfaces under spacecraft gas dynamic, gravitational, and vibrational loads than standalone microbes. Mikellides et al. (2018) reported on models developed for the removal and transport of biological contaminant from the Mars 2020 Perseverance rover under gravitational acceleration and aerodynamic loads, although not necessarily plume-induced loads, and studied the association between *viable organisms* (VO) and inert particles sampled in cleanroom environments. They found VOs frequently attached to smaller inert particles, at between 0.1–1 per particle of size 1–50 μm diameter, but with no VOs found attached to particles larger than 50 μm [10]. Related work by Malli Mohan et al. [11] expands the study of biological-to-inert-particle attachment to identify chemical composition of inert particles, visualizations of standalone biological contaminant, and results from cultivations of identified VOs. During the Europa Clipper Assembly, Test and Launch Operations (ATLO) campaign, which concluded with a successful launch in October of 2024, tape-lift particle samples were collected by spacecraft contamination control (CC) engineers and analyzed for size distributions and quantities with respect to mission CC requirements. Spacecraft planetary protection (PP) engineers isolated and grew cultures from particle samples taken at similar locations and times, providing information about types and quantities of sampled microorganisms. Future work in support of the particle dispersal model framework described in this paper, already underway, will compare the archived samples and analysis results collected between Europa Clipper's CC and PP teams to augment the Mars-2020-era models of [10, 11].

3 Modeling Approaches

3.1 CFD-DSMC Simulations of Plume Flows

The authors have performed rarefied gas dynamic pluming simulations of relevant thrusters and engines with CFD-DSMC techniques. Monopropellant hydrazine applications feature in support to Europa Lander [2, 3] and Enceladus orbiter [7] mission concepts; a 2022 joint JPL-DLR vacuum chamber thruster test campaign; and in NASA flight project applications including to the upcoming Near-Earth Object Surveyor mission. Bipropellant hydrazine engines feature in support to a NASA

CLPS lander and in pending work related to a 2024 JPL-JSC-DLR test campaign (which provided pressure and heat flux data critical to validating DSMC plume models), while other propellant mixtures have been studied e.g. in validation cases for the Apollo Lunar Module Descent Engine [2] and in collaboration with Blue Origin for a Blue Moon lander concept [5]. More information on the methodology of these simulations can be found in publications like [3, 5]. Example results are demonstrated in Fig. 3.

Future work will integrate these and comparable pluming simulations with biological contaminant properties (Sect. 2.3) and an orbital trajectory model under development for arbitrary solar system bodies (Sect. 3.2) to study long-distance particle dispersal.

3.2 Development of an Orbital Trajectory Model for Biological Contaminant

A particle dispersal model is in development for the biological contaminant dispersal task to generate number density, column density, and body-surface deposition results for 3-D particle fields dispersed by plume firings. The authors apply a model system with a spherical gravitational body (i.e. no surface topography) and, initially, an inertial three-dimensional reference system (neglecting non-inertial effects at first-order). The origin of a right-handed reference system is placed at the center of the spherical body as shown in Fig. 4. Particle trajectories in a gravitational force field are determined using Newton's laws of gravity and motion. The authors have implemented a detailed mathematical formulation for long-distance biological particle transport along orbital trajectories in Mathematica. Future work will document this framework, move it to a compiled language, and link it to source terms for pluming and biological contaminant.

4 Conclusions and Discussion

Spacecraft alter their environments and may compromise their engineering or science objectives as they generate and disperse contaminant (inert or biological). NASA's planetary protection discipline is concerned with limiting the *forward contamination* of solar system bodies with uncontrolled, spacecraft-borne biological contaminant. The action of chemical propulsion system plumes is a mechanism for the removal and long-distance transport of biological contaminant (as particulate, e.g. microbes), particularly for operations and landing in near-vacuum environments. The authors have proposed, and are developing, a framework to model the dispersal of biological contaminant by plumes intended to inform planetary protection requirements and

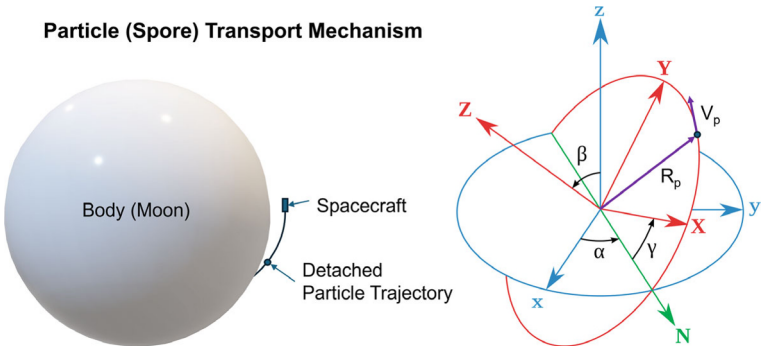

Fig. 4 Particle transport schematic and body-centered (in blue) vs. orbit-plane (in red) coordinate frame references. R_p is the vector from origin to the particle orbital location; V_p, particle velocity. In the body inertial reference frame $R_p = (x_p, y_p, z_p)$ and $V_p = (V_{xp}, V_{yp}, V_{zp})$. The normal vector to the orbit plane is $R_p \times V_p$, the X vector is toward periapsis, and the Y vector orthogonal to $Z \times X$

policy for future missions. This framework builds on established engineering capability for the rarefied gas dynamic simulation of gaseous plumes [2, 3, 7] and plumes carrying particulate [5], and on lessons-learned from the design and assembly of prior spacecraft [4, 6, 10, 11].

Acknowledgements © 2025. California Institute of Technology. Government sponsorship acknowledged. This work was performed at the Jet Propulsion Laboratory, California Institute of Technology, under a contract with NASA. Research was primarily funded by ROSES grant 22-PPR22-0007, PI Dr. W.A. Hoey. High performance computing resources were provided by funding from the JPL Information and Technology Solutions Directorate.

References

1. NASA Office of Safety & Mission Assurance, Planetary Protection Discipline Homepage, https://sma.nasa.gov/sma-disciplines/planetary-protection. Accessed 20 Dec 2024
2. Lam R, Maghsoudi E, Hoey W (2019) Numerical study of lander engine plume impingement on the surface of Europa. In: Proc. 66th JANNAF Propulsion Mtg., 37th exhaust plume and signatures Mtg., Dayton, OH, USA. 2014/46431
3. Hoey W, Lam R, Wong A, Soares C (2020) Europa lander engine plume interactions with the surface and vehicle. In: Proceedings of 2020 IEEE aerospace conference, big sky, MT, USA. https://doi.org/10.1109/AERO47225.2020.9172679
4. NASA Scientific Visualization Studio, Perseverance Rover's Descent and Touchdown on Mars, https://svs.gsfc.nasa.gov/31250. Accessed 20 Dec 2024
5. Hoey W, Martin M, Alred J, Soares C, Ababneh M (2023) Analyses of Blue origin blue moon lunar landing descent engine plume effects. In: Proceedings of 52nd international conference on environmental systems, no. 42, Calgary, Alberta, Canada. 2346/94493
6. Grabe M, Soares C (2019) Status and future of research on plume induced contamination. In: Proceedings of 70th international astronautical congress, IAC-19-D5.3.11, Washington DC, USA

7. Soares C et al (2024) Experimental characterization of spacecraft thruster plume contaminant composition for Enceladus orbiter and lander mission concepts. In: 55th Lunar and planetary science conference, no. 2215, The Woodlands, TX, USA
8. LeBeau G, Lumpkin F (2001) Application highlights of the DSMC Analysis Code (DAC) software for simulating rarefied flows. Comput Methods Appl Mech Eng 191:595–609. https://doi.org/10.1016/S0045-7825(01)00304-8
9. Gallis M, Torczynski J, Plimpton S, Rader D, Koehler T (2014) Direct simulation monte Carlo: the quest for speed. In: Proceedings 29th international symposium rarefied gas dynamics, AIP Conf. Proc. 1628, pp 27–35, Xi'an, China. https://doi.org/10.1063/1.4902571
10. Mikellides I et al (2018) Modelling and laboratory testing of particle resuspension and transport for the assessment of terrestrial-borne biological contamination of the samples on the Mars 2020 mission. In: Proceedings of 14th International Symposium Materials in the Space Environment, Biarritz, France. 2014/48799
11. Malli Mohan G, Cooper M, Venkateswaran K (2019) Microscopic characterization of biological and inert particle associated with spacecraft assembly cleanroom. Nat Sci Rep 9:14251. https://doi.org/10.1038/s41598-019-50782-0

Open Access This chapter is licensed under the terms of the Creative Commons Attribution 4.0 International License (http://creativecommons.org/licenses/by/4.0/), which permits use, sharing, adaptation, distribution and reproduction in any medium or format, as long as you give appropriate credit to the original author(s) and the source, provide a link to the Creative Commons license and indicate if changes were made.

The images or other third party material in this chapter are included in the chapter's Creative Commons license, unless indicated otherwise in a credit line to the material. If material is not included in the chapter's Creative Commons license and your intended use is not permitted by statutory regulation or exceeds the permitted use, you will need to obtain permission directly from the copyright holder.

Comparison Between the Kinetic Fokker-Planck and TAU Navier-Stokes Simulations of Hypersonic Air Flow Around the the RFZ-ST2 Upper Stage

Moritz Ertl and Leo Basov

Abstract We are developing a kinetic Fokker-Planck (FP) method to complement our existing computational fluid dynamics (CFD) code for aerodynamic and aerothermal simulations of space applications. The FP method is capable of simulating problems at low atmospheric densities, where the continuum assumptions of the CFD lose their validity. The FP method solves the Boltzmann equation and has the additional benefit of being computationally effective for low Knudsen numbers when compared to the Direct Simulation Monte Carlo method (DSMC). The FP method has been extended to model internal degrees of freedom using the Master Equation Ansatz for diatomic molecules as well as mixtures. In order to validate the new FP implementations and to better understand the limits of CFD and FP, we are simulating an upper stage, as a large test case. In this work we continue previous investigation with CFD and FP of upper stages, by expanding the modelling from single species diatomic N_2 gas to representing air as a gas mixture. We introduce the underlying simulation methods and explain the relevant differences. We compare the resulting flow fields.

Keywords CFD · Particle method · Fokker-Planck · Aerodynamics · Aerothermodynamics · Hypersonic flow · Upper stage

1 Introduction

Predictions of the flow around a vehicle play an important role in the development of space applications. Simulations can support the design process in many ways, from performance analysis, over load predictions to control system design. Computational fluid dynamics (CFD) are well established and well suited for applications in denser atmospheres, such as airplanes or first stages or reusable vertical takeoff

M. Ertl (✉) · L. Basov
Deutsches Zentrum für Luft- und Raumfahrt, Göttingen, Germany
e-mail: moritz.ertl@dlr.de

L. Basov
Applied and Computational Mathematics, RWTH Aachen, Aachen, Germany

© The Author(s) 2026

M. Grabe et al. (eds.), *Rarefied Gas Dynamics*, Springer Aerospace Technology,
https://doi.org/10.1007/978-3-032-00094-1_13

landing (VTVL) stages [8]. However, the underlying continuum assumptions lose their validity for higher Knudsen numbers, which are the typical regime for upper stages at higher altitudes and lower atmospheric densities. In these higher Knudsen (Kn) number regimes the flow can be described by the Boltzmann equation. Our approach is to numerically solve the Boltzmann equation using the kinetic Fokker-Planck (FP) method [9]. It fulfills our requirement of being computationally efficient both for high Knudsen numbers and when approaching the continuum limit.

In order to validate the new FP implementations, to better understand the limits of CFD and FP and to investigate the differences, our team is currently looking into several test cases. One of the more applied and large cases we selected is the simulation of an upper stage. The aim is to validate the methodologies, to gain insights into their limitations and to establish best practices on where and how to apply each method for large scale engineering applications. For the CFD simulations the DLR TAU code is used. It is well established for the simulation of space applications [10]. For the FP simulations a DLR in-house development of the method has been implemented using the DSMC code SPARTA [16] developed at the Sandia National laboratories. The FP method has been extended to model internal degrees of freedom using the Master Equation Ansatz for diatomic [13] and polyatomic molecules [2] as well as mixtures [12, 13]. For the upper stage simulation, the second stage of the RFZ model was selected. The RFZ model is an initiative of the Spacecraft department of the Institute of Aerodynamics and Flow Technology at the German Aerospace Center in Göttingen, and aims to to provide an open source, common research model for reusable launch vehicles [6]. The specifics of the upper stage are presented in ref [7]. In this work we continue our previous investigation with CFD and FP of the upper stage[1], by expanding the modelling from considering only single species diatomic N_2 gas to representing air as a gas mixture. First we shortly introduce the underlying simulation methods and explain the relevant differences. We then compare the resulting flow fields and pressure distribution and discuss relevant differences.

2 Numerical Methods

The governing equation used to describe flows in a wide range range of regimes is the Boltzmann equation:

$$\frac{\mathrm{D}f}{\mathrm{D}t} = S_{\mathrm{Boltz}}, \tag{1}$$

where f is the scalar velocity distribution function, t is time, and S_{Boltz} is the Boltzmann collision integral. A common approach to numerically solve Eq. (1) is the DSMC method proposed by Bird [3] which is a stochastic model that solves the spatial and temporal evolution of simulation particles, each of which represents a large number of real molecules. The interactions between particles are assumed to be binary collisions with instantaneous changes of velocity. These assumptions require grouping of particles in cells with a size in the order of the mean free path and time

steps in the order of the collision frequency. The DSMC method has become very mature over the last decades and was shown to be applicable for complex problems with thermal and chemical non-equilibrium. However, applying the model in a flow regime close to continuum makes it prohibitively expensive due the aforementioned resolution criteria (see [4, 14] and references therein).

One approach to make Eq. (1) more manageable is to approximate the collision operator S_{Boltz} by a Fokker-Planck collision operator S_{FP}:

$$S_{\mathrm{Boltz}} \approx S_{\mathrm{FP}} = -\frac{\partial}{\partial V_i}(A_i f) + \frac{\partial^2}{\partial V_j \partial V_j}\left(\frac{D^2}{2} f\right) \tag{2}$$

where V is the molecule velocity with indices given in the Einstein notation. Equation (2) can be reformulated as stochastic differential equation which in turn can be solved using a particle method similar to the DSMC approach. The collision step is then replaced by a velocity update of the particles which does not rely on the building of collision pairs making the computational cost of the FP method become independent of the Kn number. The drift coefficient A_i and the diffusion coefficient D of Eq. (2) are model parameters chosen in such a way that production terms calculated using the Boltzmann collision operator are reproduced by the production terms using the FP collision operator [15] with the extension for diatomic gas mixtures based on the master equation ansatz [11]. For the simulations presented in this paper we use the FP cubic model [9].

The CFD simulations are done using the well established DLR TAU code [17] with the spacecraft extensions [10]. TAU solves the compressible Navier-Stokes equations on finite volumes. We use a AUSMDV upwinding with a with a carbuncle fix combined with least squares gradient reconstruction and a 3-stage explicit Runge-Kutta scheme to achieve second order accuracy in space and time.

3 Numerical Setup and Geometry

3.1 Definition of the Rocket Geometry and the Simulation Grids

The RFZ-ST2 model is a generic model of an upper stage for a VTVL reusable launch vehicle which is shown in Fig. 1. It is part of the RFZ model suite of open source rocket models created to provide a common research geometry for simulating VTVL reusable launch vehicles. The geometry sources and trajectory data are freely available at [5].

Both simulations are exploiting the rotational symmetry of the configuration by reducing the computational domain to a 2D axi-symmetric mesh. The CFD mesh is a body fitted triangular mesh with rectangular sublayer. The FP uses a cartesian hirachichaly refine mesh with the geometry represented as per cell surface elements.

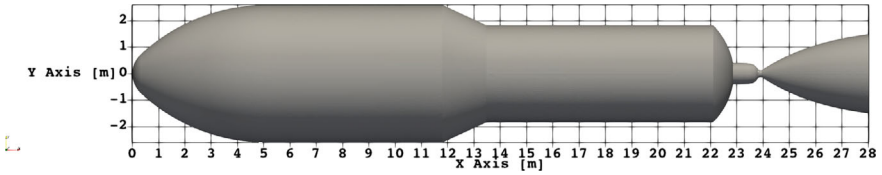

Fig. 1 Visualisation of the RFZ-ST2 upper stage geometry

The mesh refinement functionality of TAU and SPARTA are used to obtain well resolved grids. The final mesh used in this work consists of 1.15×10^6 grid points. The FP simulation domain is a rectangular box with dimensions $L_x = 41\,\text{m}$, $L_y = 12\,\text{m}$, and $L_z = 1\,\text{m}$ in x, y, and z direction respectively. The volume grid was generated containing $820 \times 240 \times 1$ cells and was locally adapted during a pre-run using SPARTA's build in grid adaptation method until each cell contained at least 10 numerical particles for a total of 21×10^6 volume cells. The surface mesh contains 3192 faces.

3.2 Settings and Boundary Conditions

A trajectory point within the applicable region of the CFD method is selected from [5] for an altitude of $h = 70\,\text{km}$. The trajectory point is used to define the farfield boundary condition for both simulations with a velocity in x-direction $v_\infty = 2249.72\,\text{m s}^{-1}$, a density $\rho_\infty = 1.2 \times 10^{-4}\text{kgm}^{-3}$ and a temperature $T_\infty = 226.9\,\text{K}$. The gas is a mixture of diatomic nitrogen N_2 and oxygen O_2 with a mass fraction ratio of $x_{N_2} : x_{O_2} = 0.767 : 0.233$. A Knudsen number of $Kn = 2.0 \times 10^{-4}$ was calculated for this flight regime using the largest diameter of the rocket $L_{ref} = D_{fairing} = 2.6\,\text{m}$ as the reference length with the mean free path being calculated using the VHS model with parameters taken from [3].

For the CFD the boundary condition for surfaces of the upper stage are set as isothermal viscous walls. The FP simulation uses a diffuse boundary condition for the surface with an accommodation coefficient of 1.0. Both simulations use a wall temperature $T_w = 300\,\text{K}$. The FP simulation was performed using a time step of $\Delta t = 1 \times 10^{-6}\,\text{s}$ with a particle weight of $w = 2 \times 10^{15}$. The particle weight was chosen so that a minimum of 8 particles are present in each FP cell.

4 Results

The comparison of the flow fields is visualised as a x-y-slice with the FP results displayed in the upper half and the CFD in the lower half. The density distribution is given in Fig. 2 with a logarithmic scale and the Mach number distribution show in Fig. 3.

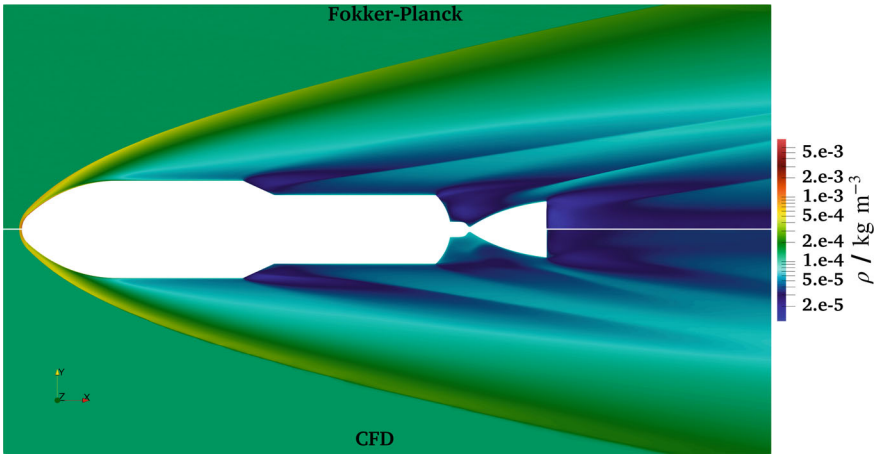

Fig. 2 Comparative visualisation of the RFZ-ST2 upper stage density ρ distribution on a logarithmic scale for the Fokker-Planck simulation (upper half) and the CFD simulation (lower half)

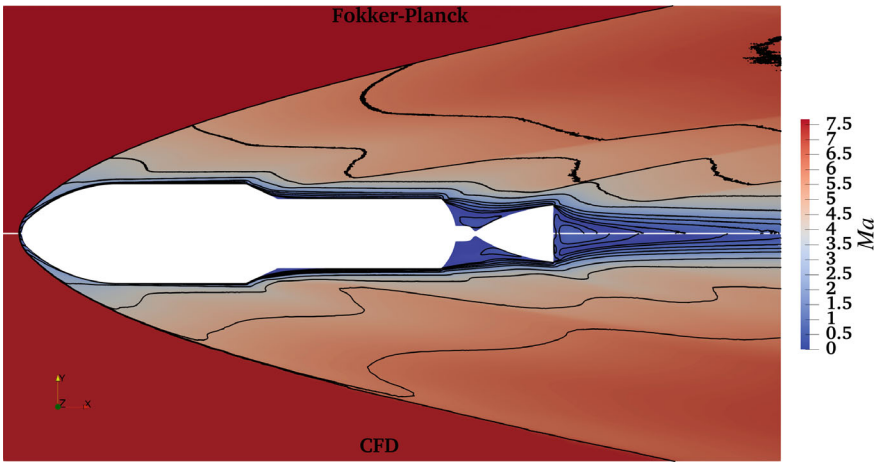

Fig. 3 Comparative visualisation of the RFZ-ST2 upper stage velocity Ma distribution for the Fokker-Planck simulation (upper half) and the CFD simulation (lower half)

The flow field visualisations exhibit a good agreement between the two methods. The structures and angles of shocks in the density visualisation show a good match, as do the the boundary layers and wake regions in the Mach number visualisation. The contour lines in the Mach plot reveal some differences especially in the wake region behind the vehicle. Here, the CFD struggles to resolve the weak shocks in the rarefied regions as sharply as the FP simulation. A difference can be observed in the shock stand-off distance and in the density behind the base plate. A plot of the translational temperature for the mixture and of the vibrational temperatures for both

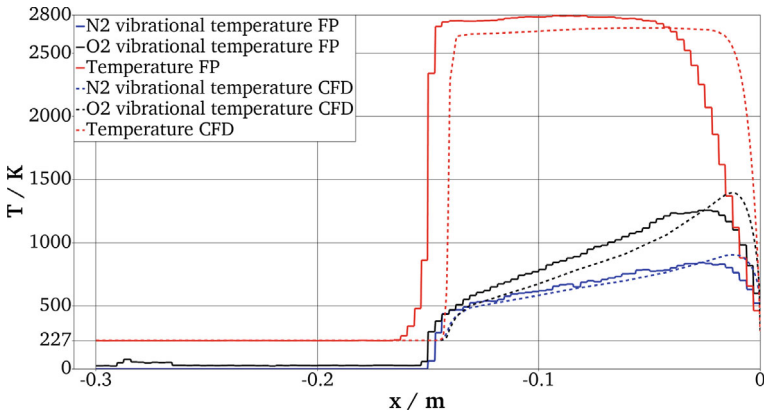

Fig. 4 Comparative Plot of the RFZ-ST2 upper stage temperature T distribution along a center line to the stagnation point for the Fokker-Planck simulation and the CFD simulation

N_2 and O_2 over a center line along the x-axis into the stagnation point is provided in Fig. 4. The steps in the FP results are due to the grid.

The vibrational temperatures of the CFD converge by methodical construction towards an equilibrium with the translational temperature, leading to a value of $T_{trans} = T_{vib} = T_\infty = 227\,\mathrm{K}$ in the free stream. In the FP model the vibrational energies are modeled as discrete level. The probability of a particle changing its vibrational energy level is a function of the translational temperature. Hence the vibrational temperatures tends towards zero in the free stream, due to the low probability of a vibrational mode being excited. The difference in shock stand-off distance is visible in the translational temperature jump with FP predicting the shock at $x_{S,\mathrm{FP}} \approx 0.15\,\mathrm{m}$ and CFD predicting it at $x_{S,\mathrm{CFD}} \approx 0.14\,\mathrm{m}$. This difference is assumed to be due to the modelling of the species mixtures in the FP method. The shock prediction of the DLR TAU is well established and validated and the authors have shown in [1] that the shock stand-off distance matches very well for FP and CFD for a single species free stream. The maximum temperatures of both translational and vibrational temperatures compare well. The relaxation also starts slightly sooner in the FP simulations.

5 Conclusions

We compared simulations of the open source generic upper stage RFZ-ST2 with a N_2 and O_2 species mixture free stream for a trajectory point at 70 km altitude. We simulated using the DLR CFD code TAU and our implementation of the kinetic Fokker-Planck particle method in the open source code SPARTA. The goal is to validate our FP method for use with industrial size cases of space vehicles at high

altitudes. Our results showed a general good agreement between the flow fields, with shock positions and angles comparing very well. Small differences were observed in the shock stand-off distance, which we attribute to the difference in Prandtl number from the current FP implementation. Other possible sources for the differences are the resolution in time and space as given by the cell size and the time step size, as well as the number of simulation particles given by the particle weight. Over all the study shows, that we have a first working implementation of a usable tool for simulating real scale upper stages in high atmospheres, while also pointing out some areas of possible improvements. One of our next steps is the development of a polyatomic model for FP which reproduces a correct Prandtl number for single species gases as well as mixtures. Additionally we are looking into increasing the complexity of our simulations by investigating upper stages with engine plumes.

Acknowledgements The authors gratefully acknowledge the scientific support and HPC resources provided by the German Aerospace Center (DLR). The HPC system CARO is partially funded by "Ministry of Science and Culture of Lower Saxony" and "Federal Ministry for Economic Affairs and Climate Action".

References

1. Basov L, Ertl M, Bykerk T (2024) Comparison of Focker-Planck and CFD simulations of the rfz-st2 upper stage. In: HiSST: 3rd international conference on high-speed vehicle science and technology, 14–19 April 2024, Busan, Korea
2. Basov L, Grabe M (2024) Modeling of polyatomic gases in the kinetic Fokker-Planck method by extension of the master equation approach. In: AIP Conference proceedings. vol 2996. AIP Publishing, p 060004. https://doi.org/10.1063/5.0187658. https://pubs.aip.org/aip/acp/article-lookup/doi/10.1063/5.0187658
3. Bird GA (1994) Molecular gas dynamics and the direct simulation of gas flows. Oxford University Press, New York
4. Bird GA (1998) Recent advances and current challenges for DSMC. Comput Math Appl 35(1):1–14. https://doi.org/10.1016/S0898-1221(97)00254-X. https://linkinghub.elsevier.com/retrieve/pii/S089812219700254X
5. Bykerk T (2023) The rfz model - a standard model for the investigation of aerodynamic and aerothermal loads on a re-usable launch vehicle. https://zenodo.org/communities/rfz-model. Accessed 16 Sept 2023
6. Bykerk T (2023) A standard model for the investigation of aerodynamic and aerothermal loads on a re-usable launch vehicle. In: Aerospace Europe conference 2023—10th EUCASS—9th CEAS, Lausanne, Switzerland
7. Ertl M, Bykerk T (2024) A standard model for the investigation of aerodynamic and aerothermal loads on a re-usable launch vehicle—second stage geometry. In: HiSST: 3rd international conference on high-speed vehicle science and technology, 14–19 April 2024, Busan, Korea. Busan, Korea
8. Ertl M, Ecker T, Klevanski J, Krummen S, Dumont E (2022) Aerothermal analysis of plume interaction with deployed landing legs of the Callisto vehicle. In: 9th European conference for aeronautics and space sciences
9. Gorji MH, Torrilhon M, Jenny P (2011) Fokker–Planck model for computational studies of monatomic rarefied gas flows. J Fluid Mech 680:574–601. https://doi.org/10.1017/

jfm.2011.188. https://www.cambridge.org/core/product/identifier/S0022112011001881/type/journal_article
10. Hannemann K, Martinez Schramm J, Wagner A, Karl S, Hannemann V (2010) A closely coupled experimental and numerical approach for hypersonic and high enthalpy flow investigations utilising the HEG shock tunnel and the DIR tau code. Tech. rep, DLR
11. Hepp C (2022) A kinetic Fokker-Planck algorithm for simulating multiscale gas flows
12. Hepp C, Grabe M, Hannemann K (2020) A kinetic Fokker–Planck approach for modeling variable hard-sphere gas mixtures. AIP Adv 10(8):085219. http://aip.scitation.org/doi/10.1063/5.0017289
13. Hepp C, Grabe M, Hannemann K (2020) Master equation approach for modeling diatomic gas flows with a kinetic Fokker-Planck algorithm. J Comput Phys 418:109638. https://doi.org/10.1063/5.0017289. https://linkinghub.elsevier.com/retrieve/pii/S0021999120304125
14. Ivanov MS (2003) Current status and prospects of the DSMC modeling of near-continuum flows of non-reacting and reacting gases. In: AIP Conference proceedings. vol 663. AIP, pp 339–348. https://doi.org/10.1063/1.1581568. https://pubs.aip.org/aip/acp/article/663/1/339-348/1010897. ISSN: 0094243X
15. Jenny, P., Torrilhon, M., Heinz, S.: A solution algorithm for the fluid dynamic equations based on a stochastic model for molecular motion. J Comput Phys 229(4):1077–1098. https://doi.org/10.1016/j.jcp.2020.109638. https://linkinghub.elsevier.com/retrieve/pii/S0021999109005531
16. Plimpton SJ, Moore SG, Borner A, Stagg AK, Koehler TP, Torczynski JR, Gallis MA (2019) Direct simulation Monte Carlo on petaflop supercomputers and beyond. Phys Fluids 31(8):086101. https://doi.org/10.1063/1.5108534. https://pubs.aip.org/aip/pof/article/1059035
17. Schwamborn D, Gerhold T, Heinrich R (2006) The dlr tau-code: recent applications in research and industry. In: ECCOMAS CFD 2006 CONFERENCE

Open Access This chapter is licensed under the terms of the Creative Commons Attribution 4.0 International License (http://creativecommons.org/licenses/by/4.0/), which permits use, sharing, adaptation, distribution and reproduction in any medium or format, as long as you give appropriate credit to the original author(s) and the source, provide a link to the Creative Commons license and indicate if changes were made.

The images or other third party material in this chapter are included in the chapter's Creative Commons license, unless indicated otherwise in a credit line to the material. If material is not included in the chapter's Creative Commons license and your intended use is not permitted by statutory regulation or exceeds the permitted use, you will need to obtain permission directly from the copyright holder.

Numerical Analysis of a High Field Magnetic Heat Shield for Re-Entry Applications

Vishnu Asokakumar Sreekala, Jakub Glowacki, Tulasi Parashar, Ben Parkinson, Nicholas Strickland, Steve Smart, Joseph Bailey, Xiyong Huang, and Nicholas Long

Abstract Hypersonic flight is important for both military and civilian purposes. A major challenge at these high speeds is the extreme heat threatening the safety and performance of the vehicle. Recent advances in high temperature super conducting magnets (HTS) and high performance computing have renewed interest in this subject. We simulate an upcoming experiment to place an HTS magnet in the Gottingen shock tunnel. We show that the 2 T HTS magnet can increase the shock standoff distance by 1.5 cm (a 60% increase) and reduce the heat flux on the front surface by up to 12%.

Keywords Hypersonics flow · Lorentz force · Magnetic heat shield

1 Introduction

Hypersonic flight technology is gaining significance for its potential to revolutionize defense and commercial sectors with unprecedented speeds and capabilities. However, intense aerodynamic heating at hypersonic speeds is a major challenge. During flight, weakly ionized plasma forms behind the bow shock. The conducting nature of the plasma enables flow control via an external magnetic field. In the 1950s, Resler and Sears introduced magnetohydrodynamic (MHD) flow control, applying a magnetic field to generate a Lorentz force within the plasma [1]. This force slows the flow and pushes the shock away from the surface, potentially reducing heat load and providing thermal protection [2].

With advancements in hypersonic vehicle design and superconducting materials in the 1990s, interest in MHD as a thermal protection technology renewed. Early studies

home page: https://www.wgtn.ac.nz/.

V. A. Sreekala (✉) · T. Parashar
SCPS, Victoria University of Wellington, Wellington, New Zealand
e-mail: vishnu.asokakumarsreekala@vuw.ac.nz

J. Glowacki · B. Parkinson · N. Strickland · S. Smart · J. Bailey · X. Huang · N. Long
Robinson Research Institute, Lower Hutt, New Zealand

© The Author(s) 2026

M. Grabe et al. (eds.), *Rarefied Gas Dynamics*, Springer Aerospace Technology,
https://doi.org/10.1007/978-3-032-00094-1_14

by Bush [3] used simplified models, suggesting that an external magnetic field could reduce aerodynamic heating. Experiments by Gülhan et al. [4] in high-enthalpy wind tunnels confirmed that an external magnetic field could lower surface heat flux at stagnation point. Shock tubes have long been utilized in MHD experiments, starting with Zeimer [5] pioneering demonstration of enhanced shock stand-off in an arc-driven shock tube. Martinez Schramm and Hannemann [6, 7] achieved a fivefold increase in shock stand-off using a 4.5 T pulsed magnetic field in a 22 MJ/kg air test flow. Recent advancements in steady state HTS magnets have enabled the exploration for such applications [8].

This paper aims to numerically investigate the effect of high magnetic fields in hypersonic flows, focusing on a blunt body in an upcoming experimental campaign at DLR-HEG [9]. This preliminary study explores flow dynamics responsible for variations in shock stand off distance as well as aerodynamic heating and provides a systematic understanding of heat flux mitigation in the presence of an external high-field HTS magnet. In Sect. 2 we describe the experimental design as well as the computational method, Sect. 3 described our results, and in Sect. 4 we discuss our conclusions and future directions.

2 Methodology

2.1 Magnet Design and Assembly

The HTS magnet has been custom designed and constructed specifically for the partially-ionized flow experiments at the DLR-HEG(Deutsches Zentrum für Luft- und Raumfahrt High Enthalpy Shock Tunnel Göttingen.). The main magnet housing forms the pre-specified rounded-cylinder blunt-body profile, aiming to maximize the magnetic field at the front surface with constraints on a total length of 600 m of HTS tape and thermal isolation of the cryogenic coils. The magnet is placed at the radial center of the HE chamber and conductively cooled by a cryocooler at the periphery, requiring an extended thermal bus and current leads. A high-vacuum cryostat is used to house the assembly, as the HEG chamber pressure exceeds the experimental requirements. The Fig. 1 shows the experimental test section for the current campaign.The flow field is facing the HTS coil casing in x direction. The final magnet design consists of two symmetrical double pancake coils, each with a conductor inner diameter of 30 mm and outer diameter of 122 mm, made from 4 mm wide HTS tape. A short section of tape was tested for the critical current as a function of temperature, field magnitude, and orientation. Each coil has approximately 600 turns and is cooled by a copper thermal bus connected to a Sumitomo CH208L cryocooler, capable of extracting 10 W of heat at 20 K. The current leads are HTS tapes, with the warm end anchored to the cryocooler's first stage and copper leads extending to room temperature, carrying up to 350 A. In testing, the coils could be cooled to 15 K. The field distribution model is a 2D axisymmetric model with

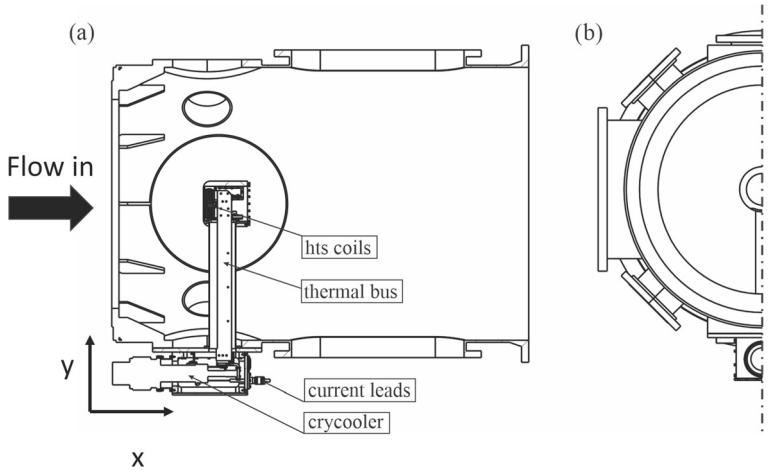

Fig. 1 Experimental test section with the proposed HTS magnet: **a** Side view of the chamber and test cross-section. **b** Front view of the chamber and magnet probe. The flow is in x direction

conductors only, where the field is proportional to the current and does not change with field magnitude. The field map, calculated using finite-element software or the Biot-Savart law, shows a field of 2.0 T at the magnet housing surface for 100 A. Based on the critical current measurements, the magnet could maintain over 300 A at 15 K, but magnetic forces might induce coil degradation at higher currents. A current of 100–200 A is expected to be supported, with higher currents requiring more sophisticated mechanical support.

2.2 Numerical Methods

The influence of magnetic field on bow shock formation was analyzed using the Finite Volume Method in the OpenFOAM framework. This simulation involves two stages: first, calculating the magnetic flux density vector, and second, assessing how the magnetic field affects the flow field and bow shock stand-off distance. The initial magnetic field profile is computed in a custom tool written in OpenFoam that solves the Helmholtz equation for the vector potential.

$$\nabla^2 \mathbf{A} = -\mathbf{J}_\mu \tag{1}$$

The initial magnetic field profile is then computed as the curl of the vector potential $\mathbf{B} = \nabla \times \mathbf{A}$. where $\mathbf{J}$ is the current density (for a 100 A operational current) and μ is the magnetic permeability of free space.

The next step utilizes a two-temperature, density-based solver “hy2Foam" to perform the flow simulation over the magnet assembly [10], specifically developed for

modeling hypersonic reactive flows typical of reentry scenarios. The solver is built upon the extended Navier-Stokes-Fourier framework, enabling it to incorporate magnetic field effects. In the current numerical simulations, the inviscid flux vectors are discretized using the Kurganov scheme to achieve second-order accuracy. For the viscous flux vectors, a second-order central-difference scheme is utilized. Time integration is performed using the implicit Euler method. These effects are accounted for by including the Lorentz force as a source term in the momentum equation. The electric current density J within the plasma is derived using Ohm's law, under the assumption that the contribution of the electric field is negligible, and expressed as follows.

$$F_{\text{em}} = J \times B \tag{2}$$

$$J = \sigma \left(U \times B\right) \tag{3}$$

where U is the velocity field and σ the electrical conductivity expressed using Bush's formulation . In the Bush model [3], the electrical conductivity field, denoted by σ, is given by:

$$\sigma = \sigma_0 \cdot \left(\frac{T_t}{T_0}\right)^n \tag{4}$$

where: σ_0 is the reference electrical conductivity in S/m taken as 5600 S/m, T_0 is the reference temperature in K, taken as 10000 and n is the temperature exponent, taken as 2 in this study, T_t is the local trans-rotational temperature in K.

The high-temperature air's chemical kinetic model features a two-temperature chemical non-equilibrium approach involving seven species (N_2, O_2, NO, N, O, NO^+, e^-) and 11 elementary reactions. Detailed thermodynamic parameters for each species and the rate constants for the reactions are provided by Gupta et al. [11]. Furthermore, the equation for Y_i is discretized with a second-order implicit Euler scheme and solved using the successive over-relaxation method. Additionally, the species reactions are governed by an irreversible Arrhenius reaction mechanism [12] . This approach models the rate of chemical reactions as a function of temperature, enabling a realistic simulation of high-temperature reaction kinetics within the flow field.

2.3 Computational Domain

The flow domain and magnetic field distribution are shown in Fig. 2a. The blunt body features a 100mm cylindrical radius (r_a) with 30mm rounded edges (r_b). A 3D mesh was generated by rotating a 2D gMsh-generated mesh 5^o about the stagnation line (L_A), creating 4500 structured cells with wall/shock refinements. As shown in Fig. 2b, the geometry follows Bush et al. [3] with axial symmetry, featuring a dipole field (2T at body surface, positioned 2 cm from stagnation) aligned with flow. Field mapping used linear interpolation across three cross-sections: axial line L_A, L_1 (3 cm

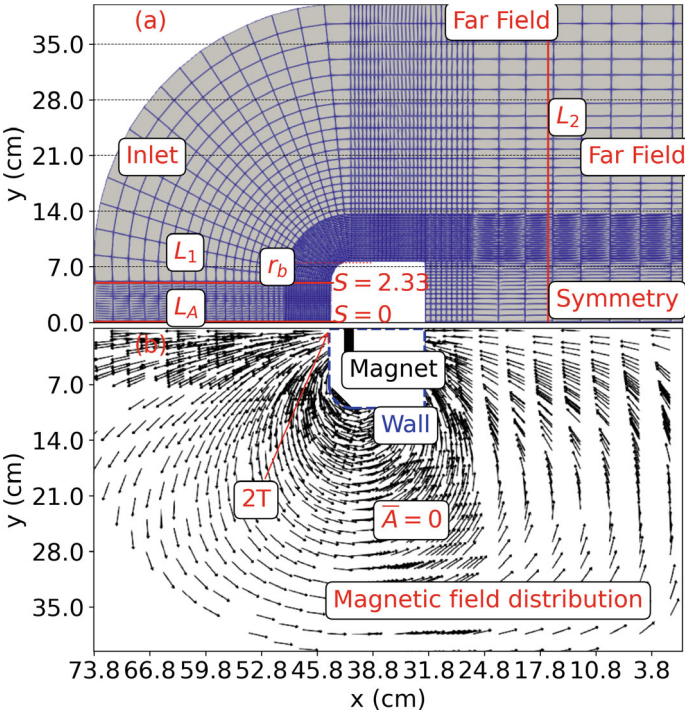

Fig. 2 **a** Computational domain showing the mesh, boundaries, and annotated dimensions. **b** Magnetic field distribution, where the magnetic field strength is calculated to achieve a 2T stagnation point

above L_A), and shoulder line L_{sh} (7 cm above L_A). Surface distance S is measured from stagnation.

2.4 Boundary Conditions and Initialization

The boundary conditions applied for the computational domain is given below in Table 1. The inlet boundary condition is set to be Dirichlet conditions. The farfield, wall and symmetry follow a Neumann conditions.

The initial conditions are set to be the same as the expected experimental values in the DLR-HEG shock tunnel experiment. The inlet velocity is $U = 5994$ m/s,the inlet density of$\rho = 2\,\text{g/m}^3$ and the chemical composition defined by mass fractions: $Y_N = 10^{-10}$, $Y_{N_2} = 0.756$, $Y_{NO} = 0.0221$, $Y_O = 0.1973$, and $Y_{O_2} = 0.0238$ [13]. The inlet translational and vibrational temperatures are set to (following Dirichlet boundary conditions), $T_t = 1187$ K and $T_v = 100$ K, respectively. The post shock region reaches an ionization close to 10^{-4}. The surface temperature of the magnet

Table 1 Boundary conditions used in the simulation

Boundary	Type	Condition
Inlet	Dirichlet	ϕ = Specified
Farfield	Neumann	$\frac{\partial \phi}{\partial n} = 0$
Symmetry	Neumann	$\frac{\partial \phi}{\partial n} = 0$
Fixed wall	Neumann	$\frac{\partial \phi}{\partial n} = 0$

ϕ = is the flux crossing the cells

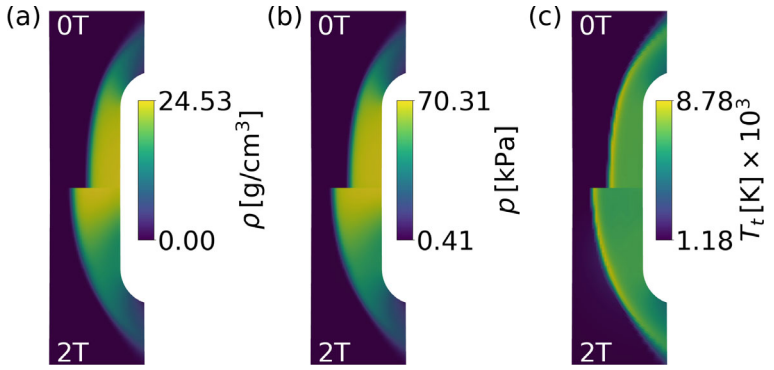

Fig. 3 2D plot for **a** density **b** pressure, **c** translational temperature for $0T$ (top) and $2T$ (bottom)

chamber was computed with a Neumann boundary condition, assuming non-catalytic behavior. The boundary conditions are modified with a slip velocity proportional to the gradient of velocity at the wall, adjusting for the Knudsen layer effects. The slip velocity

$$u_s = \frac{2-\alpha}{\alpha} \cdot \frac{\lambda}{u} \cdot \left(\frac{\partial u}{\partial y}\right)_{\text{wall}} \tag{5}$$

where α is the accommodation coefficient, which represents the fraction of momentum accommodated by the wall. λ is the mean free path of the gas molecules and $\frac{\partial u}{\partial y}$ is velocity gradient of boundary layer. Hence, Velocity along the walls was modeled with a slip boundary condition, while species mass fractions followed a Neumann boundary condition. The chemical reaction mechanism employed in the model uses to the scheme outlined in [12].

3 Result

Figure 3a shows a zoomed in view of density distribution near the body. The top half shows the no-magnetic field case while the bottom half shows the case with 2T magnetic field at the surface of the body. The presence of the magnetic field pushes

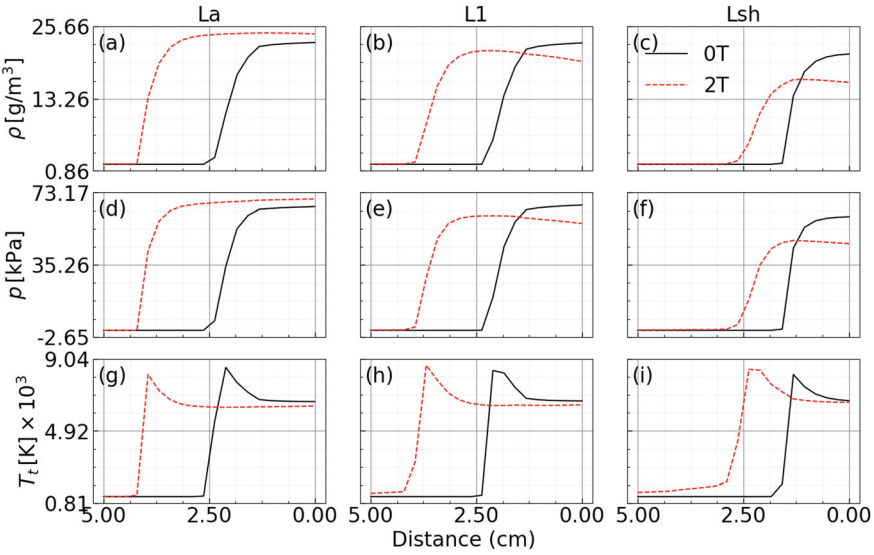

Fig. 4 1D plot of density, pressure and translational temperature along L_A, L_1, L_{sh} for 0T and 2T

the shock significantly further, showing a measurable impact. Figure 3b, c show total pressure and the translational temperature. Both show similar, extended pattern to the density profile. The temperature shows a peak at the shock before the deceleration layer. This feature moves away from the body with the shock in the presence of the magnetic field.

Figure 4 shows the impact of a magnetic field on hypersonic flow properties cross-sectional cuts across the simulation domain. The black lines represent the case without a magnetic field (0T), and the red dashed lines indicate the (2T) case. The plots compare density ρ, pressure p, and translational temperature T_t at different spatial locations (L_A, L_1, L_{sh}). The magnetic field significantly alters the flow dynamics, compressing the flow and affecting shock structure. In the 2T case Fig. 4a, along L_A post-shock density increases from 23.2 g/m^3 (0T) to 24.5 g/m^3(2T), while pressure rises from 66 KPa (0T) to 70 kPa(2T) as shown in Fig. 4d. Translational temperature peaks at 8107 K (0T) and 8000 K (2T) as shown in Fig. 4g. Along L_1, the 2T case shows reduced density (19.1 g/m^3) near the body , with T_t behaving similarly to L_A as shown in Fig. 4b, e, h respectively. At L_{sh}, density and pressure further decrease, with a 0.5 cm reduction in shock stand-off distance compared to L_A. The lowering of the density and pressure away from the symmetry axis likely happens because of the "funneling" effect introduced by the magnetic field. The curving of the magnetic field lines near the magnetic poles create a pathway for the plasma created at the shock to easily flow into the polar region. This funnel can be appreciated in the density and pressure plots shown in Fig. 3.

Figure 5 shows a comparison of the heat flux along the wall. In the 0T case, heat flux reaches close to its peak at the stagnation point along the symmetry, then remain

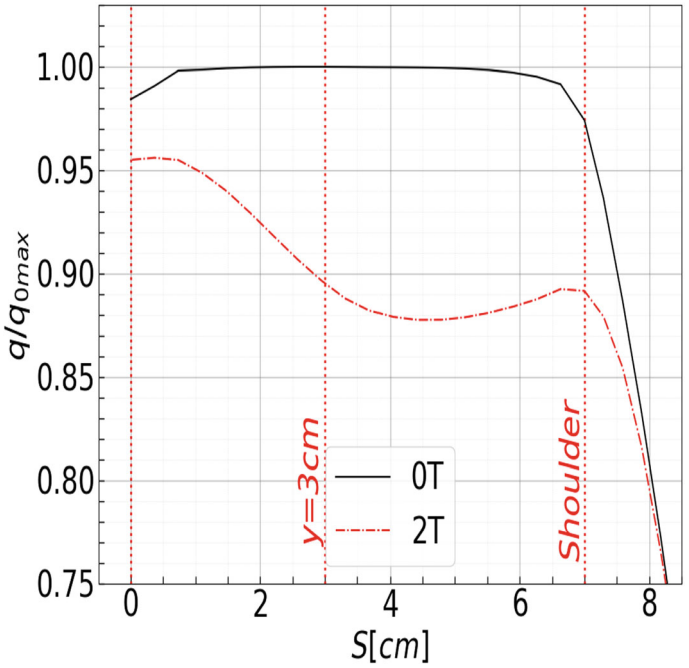

Fig. 5 Wall heat flux comparison for for 0T and 2T. The distance S is measured along the surface of the body, with 0 at the stagnation point

constant as the distance from this point increases. A drop in heat flux is observed before L_{sh}.At stagnation (S = 0), near-isentropic flow thickens the boundary layer, reducing heat flux. A $2T$ field's Lorentz force pushes the shock, diverting plasma (reducing convective heating) and funneling ions poleward. Combined with non-catalytic wall effects suppressing recombination, this creates the observed heat flux dip. As the magnetic field is introduced, the heat flux at the stagnation point initially reduces by up to 5%. Further from the stagnation point the heat flux reduced by roughly 12%.

4 Conclusion

This preliminary study supports an upcoming experimental campaign by Robinson Research Institute and HEG-DLR, examining a 2T HTS magnet in a blunt body configuration. Numerical results show significant flow-field changes under a strong axial magnetic field, with increased shock stand-off distance at higher fields. Although the flow remains isenthalpic from L_A to L_{sh}, post-shock thermal pressure reduction lowers density in the 2T case. A 15 % heat load reduction occurs till L_{sh}, likely due

to decreased pressure and density balancing the stronger field. The altered sheath structure modifies the flow field, potentially affecting heat-load redistribution and vorticity. Such ionized flows are also relevant for interplanetary travel, where the magnet could shield against energetic particles.

References

1. Sears WR, Resler JR (1964) Magneto-aerodynamic flow past bodies. Adv Appl Mech 8:1–68
2. Meyer RX (1959) Magnetohydrodynamics and aerodynamic heating. ARS Journal 29(3):187–192
3. Bush WB (1958) Magnetohydrodynamic-hypersonic flow past a blunt body. J Aerospace Sci 25(11):685–690
4. Gulhan A, Esser B, Koch U, Siebe F, Riehmer J, Giordano D, Königorski D (2009) Experiments on heat-flux mitigation by electromagnetic fields in ionized flows. In: 40th AIAA plasmadynamics and lasers conference, p 3725
5. Ziemer RW, Bush WB (1958) Magnetic field effects on bow shock stand-off distance. Phys Rev Lett 1(2):58
6. Martinez Schramm J, Hannemann K (2019) Study of MHD effects in the high-enthalpy shock tunnel Göttingen (HEG) using a 30 T-pulsed magnet system. In: 31st international symposium on shock waves 2: applications, vol 31. Springer International Publishing, pp 617–623
7. La Rosa Betancourt MA, Collier-Wright MR, Herdrich G (2021) A superconductor-based magnetohydrodynamic shielding system for hypersonic re-entry: MEESST. In: AIAA Scitech 2021 Forum, AIAA 2021–4138, published online
8. Huang X, Parkinson B, Strickland N, Smart S, Bailey J, Sreekala VA, Parashar T, Glowacki J, Long N, Weijers H (2024) Investigation of magnetic heat shielding during spacecraft re-entry using hts magnet–preliminary experimental design. IEEE Trans Appl Superconductivity
9. Hannemann K, Martinez Schramm J, Wagner A, Ponchio Camillo G (2018) The high enthalpy shock tunnel Göttingen of the German aerospace center (DLR). J Large-Scale Res Facilities JLSRF 4(A133):1–14
10. Casseau V (2022) Github repository of the hyStrath platform. *Release Fleming, Commit 984e300*. Retrieved from (https://github.com/hystrath/hyStrath/)
11. Gupta RN, Yos JM, Thompson RA, Lee KP (1990) A review of reaction rates and thermodynamic and transport properties for an 11-species air model. In: NASA Technical Memorandum 101528. NASA, pp 1–50
12. Park C (1993) Review of Chemical-Kinetic Problems of Future NASA Missions, I: Earth Entries. J Thermophys Heat Transfer 7(3):1–50
13. Share RX (2018) The high enthalpy shock tunnel Göttingen of the German Aerospace Center (DLR), J Large-Scale Res Facilities (JLSRF) 4:133. https://doi.org/10.17815/jlsrf-4-168. License: CC BY 4.0
14. Lani C (2023) Magnetohydrodynamic flow control: recent developments and applications. Elsevier
15. Poggie J (2000) Magnetic field effects on fluid flow: theoretical and experimental studies. Springer
16. Geuzaine C, Remacle JF (2009) Gmsh: A 3-D finite element mesh generator with built-in pre- and post-processing facilities. Int J Num Methods Eng 79(11):1309–1331
17. Casseau V, Espinoza DE, Scanlon TJ, Brown RE (2016) A two-temperature open-source cfd model for hypersonic reacting flows. part two: multi-dimensional analysis. Aerospace 3(4):45
18. Bityurin A, Bocharov A, Lineberry J (2004) Results of experiments on mhd hypersonic flow control

Open Access This chapter is licensed under the terms of the Creative Commons Attribution 4.0 International License (http://creativecommons.org/licenses/by/4.0/), which permits use, sharing, adaptation, distribution and reproduction in any medium or format, as long as you give appropriate credit to the original author(s) and the source, provide a link to the Creative Commons license and indicate if changes were made.

The images or other third party material in this chapter are included in the chapter's Creative Commons license, unless indicated otherwise in a credit line to the material. If material is not included in the chapter's Creative Commons license and your intended use is not permitted by statutory regulation or exceeds the permitted use, you will need to obtain permission directly from the copyright holder.

Effect of Structured Surface on Pressure Measurement in Hypersonic Rarefied Wind Tunnel

Ryunosuke Endo, Takashi Ozawa, Masahito Tagawa, and Kumiko Yokota

Abstract Research at the Japan Aerospace Exploration Agency (JAXA) on the Air-Breathing Ion Engine (ABIE) aims to extend satellite operational duration in very-low Earth orbit (VLEO). This study evaluates the impact of micro-structured surfaces on the intake performance using Hypersonic Rarefied Wind Tunnel (HRWT) experiments and computational analyses. We have developed numerical schemes for micro-structured surfaces in DSMC, and our numerical results were consistent with experimental results in HRWT.

Keywords Rarefied gas dynamics · Hypersonic flows · Aerodynamics · DSMC · Air breathing ion engine · Surface treatment

1 Introduction

At the Japan Aerospace Exploration Agency (JAXA), the Air-Breathing Ion Engine (ABIE) [1] has been proposed as a propulsion system for operations in very-low Earth orbit (VLEO) [2]. The ABIE system intakes atmospheric molecules, ionizes them in a discharge chamber, and generates thrust. The performance of the intake section is critical for maintaining pressure in the discharge chamber and preventing molecular backflow, which significantly impacts the overall system efficiency. To improve intake performance, Shoda et al. [3] proposed micro-structured surfaces on the intake internal surface.

The configuration and flow conditions where micro-structured surfaces are effective in rarefied flow regime is not well-known. In order to validate the improvement

R. Endo (✉)
Waseda University, Shinjuku-Ku, Tokyo, Japan
e-mail: ryukitokito@akane.waseda.jp

T. Ozawa
Japan Aerospace Exploration Agency, Sagamihara, Kanagawa, Japan

M. Tagawa · K. Yokota
Graduate School of Engineering, Kobe University, Kobe, Hyogo, Japan

© The Author(s) 2026

M. Grabe et al. (eds.), *Rarefied Gas Dynamics*, Springer Aerospace Technology,
https://doi.org/10.1007/978-3-032-00094-1_15

of intake performance with micro-structured surfaces, it is necessary to compare pressure increase with micro-structured surfaces between numerical results with measured results.

The objectives of this study are as follows. First, we develop numerical schemes for micro-structured surfaces in direct simulation Monte Carlo (DSMC) [4]. The increase in number of micro-structured surface segments results in increase of computational cost. Thus, we develop a simplified analytical surface reflection model for micro-structured surfaces to improve computational efficiency. Second, we evaluate the effect of micro-structured surfaces on pressure in wind tunnel models under hypervelocity rarefied wind tunnel (HRWT) conditions by carrying out DSMC computations. Note that flow conditions are different between HRWT and ABIE flight conditions in terms of speed ratio, rarefaction level, and so forth. Thus, we need to investigate suitable model configuration to evaluate the micro-structured surface effect under HRWT flow conditions.

Intake performance is determined by downstream pressure. However, due to the experimental environment, which differs from the real environment, the difference in results with and without micro-structured surfaces will be checked, rather than specific target values. In previous studies, the analysis suggested that the pitch dependence of micro structured surfaces may be small and the surface coefficient dependence may be large. In the latter part of this study, a simplified smooth geometry model is used, which also made the analysis cost efficient.

2 Experimental Setup

2.1 Model with Micro-Structured Surfaces

The micro-structured surface proposed by Shoda et al. [3] is shown in Fig. 1. It consisted of micro-structured walls of 20 and 74°. This geometry is designed to control the direction of molecular reflection and promote the movement of molecules downstream in the intake section. As shown in Fig. 2, the average reflected angle from the overall wall surface with an assumption of inflow uniform angular distribution is approximately − 77°. This indicates that without molecular collisions, micro-structured surfaces may improve pressure in downstream regions even in thermally equilibrium conditions. Laser etching technology was used to manufacture experimental models of micro-structured surfaces. The experiments involved preliminary test models with micro-structured surfaces of varying pitch widths (50, 100, 500 μm) and a smooth surface model (see Fig. 3). The model is made of aluminum and α is about 0.9–1.0.

Figure 4 shows the intake model used in the experiment and the analysis. Molecules flow in from the left side. The pressure at 45 mm from the inlet, the same point as the measurement section of the wind tunnel test, is summarized as a

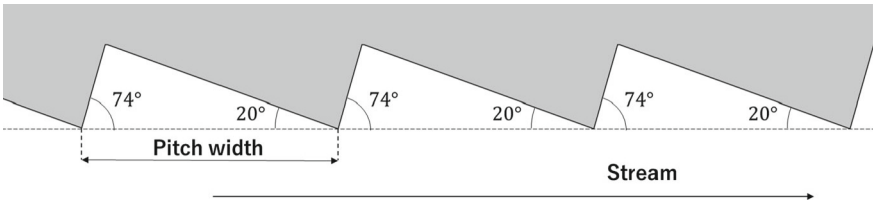

Fig. 1 Schematic of the micro-structured surfaces

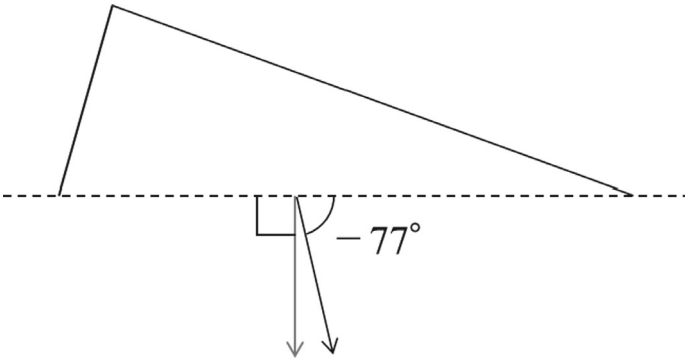

Fig. 2 The image of the average overall reflected angle

Fig. 3 Photograph of experiment model

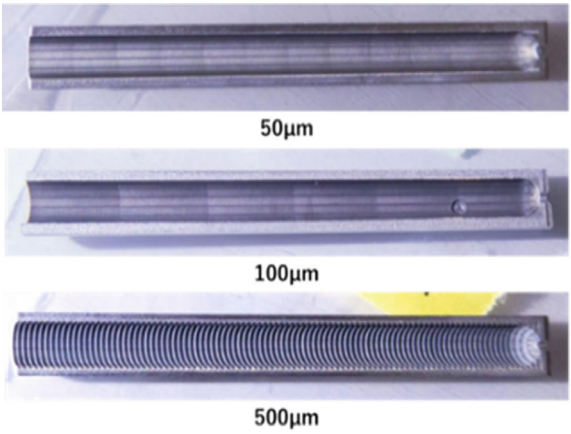

result. For analyses that vary the Knudsen number, the pressure ratio at 45 mm to the inlet pressure is used as the result.

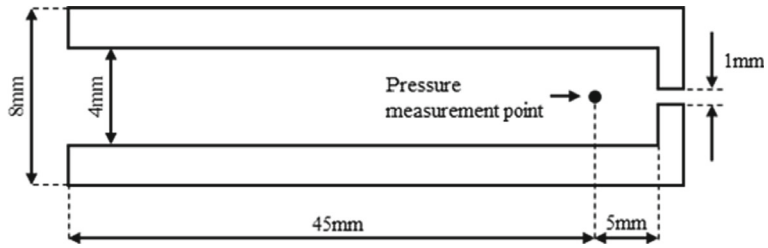

Fig. 4 Image of analytical model for DSMC

Table 1 The DSMC flow field conditions

Parameter	Value	Unit
Speed	750	m/s
Temperature	11	K
Number density	1.1×10^{21}	m^{-3}
Wall temperature	290	K

2.2 *Hypersonic Rarefied Wind Tunnel*

The HRWT (Hypersonic Rarefied Wind Tunnel) has been developed at JAXA Chofu, designed to generate hypersonic rarefied flows [5, 6]. The HRWT consists of a vacuum chamber, air supply system, heating system, nozzle section, model support section, and measurement devices. In this work, pure nitrogen (N_2) is used as the test gas, and rarefied flow is generated through a 45° conical nozzle. The main test conditions for HRWT (17 mm from the nozzle exit on centerline with stagnation pressure of 16.2 kPa and stagnation temperature of 280 K) are listed in Table 1. Details of HRWT can be found in Ref. [4]. Figure 5 shows a photograph of the model (described in Sec. 2.1) mounting. Note that the Knudsen number range of the HRWT is lower than that of expected ABIE flight conditions. Taking the inner diameter of the model shown in Fig. 4 as the representative length, the Knudsen number in HRWT is approximately 0.08 with a mass flow rate of 0.08 g/s.

2.3 *DSMC Analyses*

In our previous work, HRWT nozzle flows were investigated [5] and the flow conditions in the HRWT test section were obtained as shown in Table 1. Using these inflow conditions, we performed DSMC calculations for flows inside and outside the models. The test gas was 100% nitrogen (N_2). The chemical reaction and electronic excitation models were not activated in the MOTIF DSMC code [7] as the temperature was below 1000 K. The Maxwell reflection model was used for gas-surface interactions, with the surface accommodation coefficient (α) used to represent the ratio of

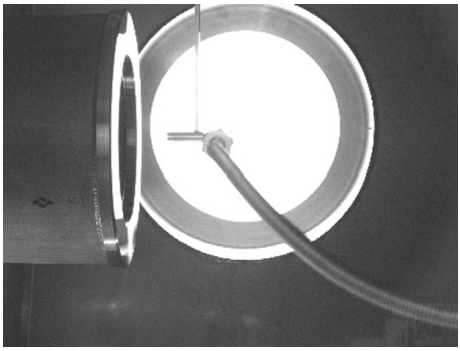

Fig. 5 Photograph of model mounting in HRWT

diffuse to specular reflection. The nitrogen molecule diameter was set to 5.1 Å, and the wall temperature in the simulations was assumed to be 290 K, consistent with the experimental conditions. The mean free path (mfp) of the freestream is 0.3 mm and the number density is 1.1×10^{21} m^{-3} at 0.08 g/s. The Knudsen number was varied by changing the value of the number density. Typical computational parameters are as follows. The system was assumed to reach thermal equilibrium within 3 ms. The computational domain was discretized into 50,000 cells, with a resolution of 2 cells per mfp to ensure accurate results. The distance from the pressure measurement point to the pressure sensor is approximately 10 cm, and this study does not consider rarefaction effects in this area.

3 Results and Discussion

3.1 Evaluation of the Impact of Micro-Structured Surfaces in the HRWT Environment

In this study, the effects of micro-structured surfaces on the pressure distribution in the intake models were evaluated using the HRWT. The test conditions were set with a gas flow rate of 0.08 g/s, using pure nitrogen (N_2) gas. Table 2 shows the pressure measurement results under nominal mass flow rate conditions.

The wind tunnel test results revealed that the micro-structured surfaces did not show a significant impact on pressure distribution in the preliminary test models. No significant differences in pressure values were observed across any of the flow

Table 2 Experimental results at HRWT

mdot(g/s)	Pressure [Pa]			
	Pitch = 50 μm	Pitch = 100 μm	Pitch = 500 μm	NP
0.08	22.2 ± 1	22.6 ± 1	22.1 ± 1	22.7 ± 1

rates, and no trends related to pitch width were found. Additionally, while pressure increased with higher flow rates, this is consistent with the general relationship between flow rate and pressure in rarefied flow environments, independent of the presence of micro-structured surfaces. This result suggests that, in the HRWT environments, the control of reflection direction due to the micro-structure surfaces is not sufficiently effective due to intermolecular collisions. However, these results are specific to the conditions of the HRWT, and different reflection behaviors may occur under actual very-low Earth orbit (VLEO) conditions or in environments with higher Knudsen numbers. Therefore, to complement the wind tunnel results and more thoroughly investigate the effects of micro-structured surfaces, we further carry out DSMC computational analyses.

3.2 Analyses of Actual Geometry Model

The dependence of pressure variations on surface coefficient and Knudsen number was verified by analyses using an actually simulated model of the micro-structured surfaces of the intake section. The inflow conditions were obtained from the HRWT wind tunnel test conditions. For the analytical conditions for the validation of the surface accommodation coefficient dependence, the surface coefficient varied from 0 to 1 in steps of 0.2. Figure 6 shows a comparison of the pressure analysis results for a pitch width of 100 μm at 45 mm when the surface accommodation coefficient was varied.

The analysis results showed that in the range of surface coefficients from 0.8 to 1.0, the pressure values from the actual geometry model were close to the wind tunnel test results from the HRWT (see Table 2). This indicates that the actual geometry model is an effective tool for accurately reproducing wind tunnel test results. Overall,

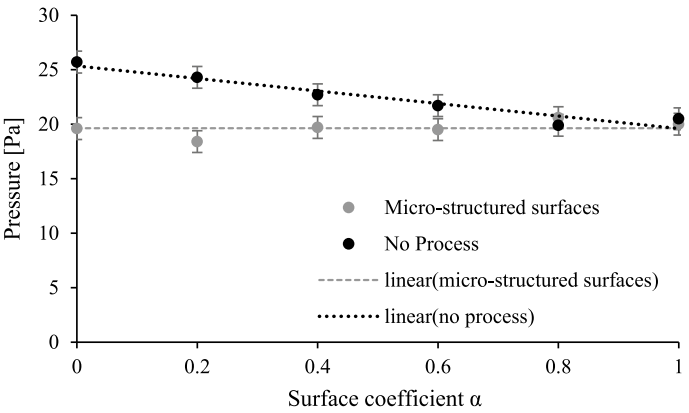

Fig. 6 The pressure dependence on the surface coefficient by analyzing

without micro-structured surfaces, the pressure increases as the α decreases. On the other hand, with micro-structured surfaces, no significant change in pressure was observed when the α was changed. The results without surface processes indicate that specular reflection increases the pressure in the downstream region. On the other hand, with the micro-structured surfaces, results are basically similar to the diffuse case ($\alpha = 1.0$) for all surface accommodation cases. This is because in the near-continuum flow condition, micro-structured surfaces increase intermolecular collisions inside the intake model, and this results in higher pressure gradient from inlet to outlet similar to the full diffuse reflection condition. Considering that realistic surface coefficients are greater than 0.5, it is suggested that a material with $\alpha = 0.6$ could be used to evaluate the influence of micro-structured surfaces in wind tunnel experiments.

The analytical conditions for the Knudsen number dependence study were carried out by varying the Knudsen number from 0.08 to 80 with a surface accommodation coefficient of unity (full diffuse reflection condition).

We analyzed the change in the pressure ratio as the Knudsen number is varied. The pressure ratio is the ratio of the pressure at the measurement point to the freestream pressure. Figure 7 shows the results and it was found that the higher the Knudsen number, the higher the pressure ratio. Comparing the results with and without micro-structured surfaces from, it is observed that the difference in pressure ratio increases as the Knudsen number increases. The reason for this is that the higher Knudsen number allows the molecules to flow without intermolecular collisions. Molecular motion at high Knudsen number is dominated by wall collisions, and the effect of micro-structured surfaces is expected to be more significant. Note that the development of a simplified smooth model and dependence of computational models are presented in Sect. 4.

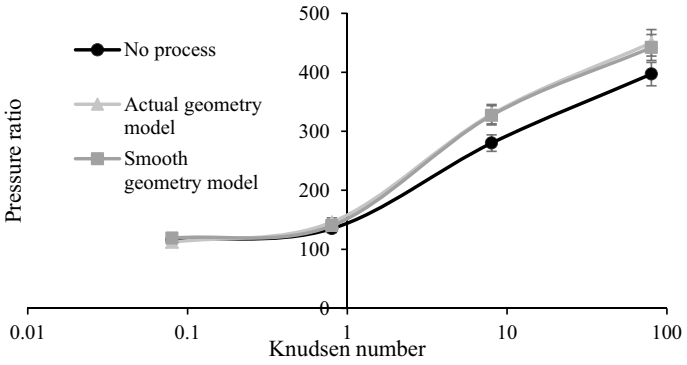

Fig. 7 Increased influence of micro-structured surfaces when Knudsen number is increased by analyzing

4 Comparative Verification of Actual and Smooth Geometry Models

4.1 Simplified Smooth Geometry Model

The actual geometry model faces the challenge that the computational cost becomes higher along with the increase of the number of micro-structured surface segments. Thus, in this section, we develop a simplified smooth model for micro-structured surfaces to improve computational efficiency. A simplified smooth model reproduces the effect of micro-structured surfaces on a flat surface. For this purpose, it provides information on the angle of the reflecting wall according to the angle of incidence of the molecule. Considering a single unit of the micro-structured surfaces, the behavior of molecules can be classified into four types as shown in Fig. 8. Assuming type 1 as "20° wall-reflecting molecules," type 4 as "74° wall-reflecting molecules," and the sum of type 2 and 3 as "iterated molecules," these distributions vary with the angle of incidence of the molecules. The simplified smooth model uses a flux ratio database to determine which wall surface is reflected by the angle of incidence. To generate a database of flux ratios, the type 1–type 4 ratios in Fig. 8 were calculated geometrically from the average path of particles assumed to reflect equally and completely diffusely at each point on the wall surface. For iteration particles, an average angle of $-70°$ was applied, which is the average angle of particles reflecting out of the region from the two wall surfaces (see Fig. 9.).

Figure 10 shows the database of the wall flux ratio to the angle of incidence for perfect diffuse reflection($\alpha = 1$). These distributions are calculated geometrically.

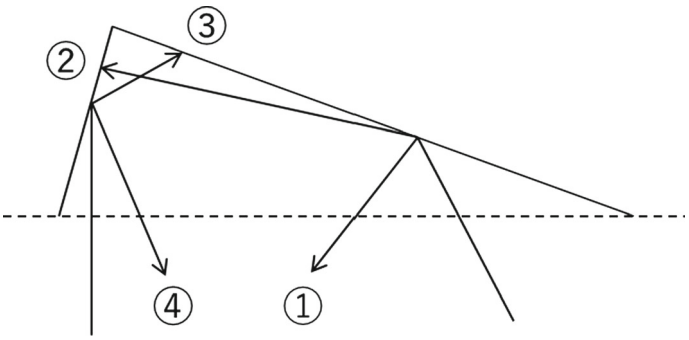

Fig. 8 Classification of molecular reflection

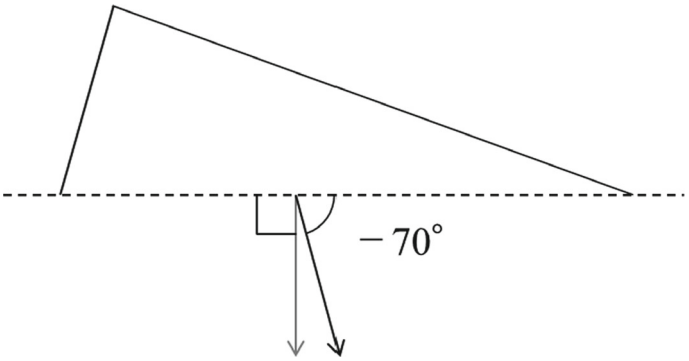

Fig. 9 Wall normal direction for iteration molecules

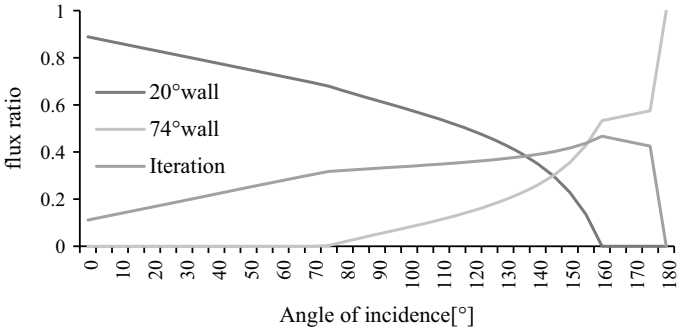

Fig. 10 Flux ratio database at $\alpha = 1.0$

4.2 Comparison of Actual and Smooth Geometry Models

A comparison of the Actual geometry model with a simplified smooth model using the database in Fig. 10 was performed. The Knudsen number varied from 0.08 to 80 and the pitch width of the micro-structured surfaces was set to 100 μm. Figure 7 shows the comparison of pressure ratio at 45 mm among models. The results show that the simplified smooth model agrees well with the actual geometry model at each Knudsen number. In addition, the simplified smooth model reduced the computation time by approximately 90% compared to the actual geometry model. Therefore, the simplified smooth model is considered to be useful for improving the efficiency of future research to investigate the effect of micro-structured surfaces for various conditions.

5 Conclusion

In this study, the effect of the micro-structured surfaces applied to the preliminary intake models was evaluated through wind tunnel tests in HRWT and computational analyses. The measured results showed that no significant increase in pressure due to the micro-structured surfaces was observed, and no clear effect of pitch width change was detected. This indicates that the Knudsen number was not sufficiently high to confirm the surface effect in the wind tunnel environments. To complement this, actual geometry model analyses were performed. The numerical results with the surface accommodation coefficient (α) in the range of 0.8 to 1.0 are basically consistent with the measured pressure. Namely, the actual geometry model has potential to simulate molecular reflection behaviors. Investigation of the Knudsen number dependence also showed that the effect of the micro-structured surfaces increases as the Knudsen number increases. This indicates the potential advantage of micro-structured surfaces in rarefied environments. In the latter part of this paper, we developed a simplified smooth model to improve the efficiency of the analysis. Consequently, the simplified smooth model predicts similar pressure results to the actual geometry model in approximately 90% less time. In our future work, we will investigate the applicability and accuracy of the simplified smooth model for other surface accommodation coefficient cases and flow conditions. We will also optimize wind tunnel model configurations to verify the effect of micro-structured surfaces in HRWT.

References

1. Nishiyama K (2003) Proceedings of the 54th international astronautical congress, IAC-03-S4-02
2. Sasaki M (2017) Space Res Today 198:10–18
3. Shoda K et al (2023) CEAS Space J 15:403–411
4. Bird GA (1994) Molecular gas dynamics and the direct simulation of gas flows. Clarendon, Oxford, England, U.K.
5. Ozawa T, Fujita K, Suzuki T (2015) Development of an aerodynamic measurement system for hypersonic rarefied flows. Rev Sci Instrum 86(1):015105
6. Ozawa T, Suzuki T, Fujita K (2015) Aerodynamic measurements and computational analyses in hypersonic rarefied flows. AIAA J 53(11):3327–3337. https://doi.org/10.2514/1.J053889
7. Ozawa T et al (2011) AIAA Paper 2011-3311. In: 42nd AIAA thermo-physics conference, Honolulu, Hawaii, June 27–30

Open Access This chapter is licensed under the terms of the Creative Commons Attribution 4.0 International License (http://creativecommons.org/licenses/by/4.0/), which permits use, sharing, adaptation, distribution and reproduction in any medium or format, as long as you give appropriate credit to the original author(s) and the source, provide a link to the Creative Commons license and indicate if changes were made.

The images or other third party material in this chapter are included in the chapter's Creative Commons license, unless indicated otherwise in a credit line to the material. If material is not included in the chapter's Creative Commons license and your intended use is not permitted by statutory regulation or exceeds the permitted use, you will need to obtain permission directly from the copyright holder.

Identifying the Continuum Breakdown of a Plume Surface Interaction in Near Vacuum Environment for a CFD-DSMC Approach

Jannis Petersen, Jonas Göbel, Martin Propst, Bradley Craig, Theodor Heutling, Konstantinos Kontis, Craig White, Martin Tajmar, Jeroen Van den Eynde, and Christian Bach

Abstract Within the ESA-funded activity, LUNAR In-Situ LANding Structures (LUNAR ISLANDS), the feasibility of in-situ manufactured structures is explored. These aim to decrease the exposure of surrounding infrastructure and personnel to high-velocity particles of lunar regolith, which result from the interaction of the exhaust plume of the lander and the surface, which is covered by loose regolith. For the numerical investigation of Plume Surface Interaction (PSI), a hybrid modelling strategy is employed, combining a Navier-Stokes (NS)-based Computational Fluid Dynamics (CFD) solver for the continuum regions of the nozzle and plume with a Direct Simulation Monte Carlo (DSMC) solver for the rarefied regions. This contribution describes the automated identification of the breakdown interface and necessary division of the mesh based on that interface to allow for the use of a single mesh.

Keywords Plume surface interaction · DSMC · CFD · Continuum breakdown

1 Introduction

During the Apollo missions, regolith particles released due to PSI caused various issues, including clogging mechanical parts, instrument interference, radiator overheating, and visibility problems [13, 23]. With future lunar missions planned, strategies to mitigate these effects are being developed to ensure safe landings and operations on the lunar surface [1, 6].

J. Petersen (✉) · J. Göbel · M. Propst · T. Heutling · M. Tajmar · C. Bach
Technische Universität Dresden, Chair of Space Systems, Dresden, Germany
e-mail: jannis.petersen@tu-dresden.de

B. Craig · K. Kontis · C. White
University of Glasgow, School of Engineering, Glasgow, UK

J. Van den Eynde
ESTEC European Space Agency, AZ Noordwijk, The Netherlands

© The Author(s) 2026

M. Grabe et al. (eds.), *Rarefied Gas Dynamics*, Springer Aerospace Technology,
https://doi.org/10.1007/978-3-032-00094-1_16

One proposed solution is the construction of lunar landing pads [5, 19]. Solid, low-erodibility surfaces can significantly reduce the particle release during descent [15, 25]. Given the high costs and logistical challenges of transporting materials to the Moon, In Situ Resource Utilisation (ISRU) methods using regolith with additive manufacturing are preferred [11, 12].

Within the LUNAR ISLANDS project, potential manufacturing techniques for such structures are being tested, supported by numerical simulations to complement experimental data [10].

Roberts [20] proposed an erosion theory based on the key assumption that the erosion rate is proportional to the shear stress, making viscous erosion a central mechanism. More recent studies have shown that other regimes–such as deep cratering, diffuse fluidisation, and non-viscous momentum transfer–also play a significant role [14]. These mechanisms are expected to differ in relevance for landing pads, where particles may be bonded through sintering or binders, or where molten surfaces eliminate permeability. Nonetheless, plume flow properties such as velocity, pressure, and temperature are expected to remain critical for predicting regolith response. For a landing pad, this requires resolving the flow features of a supersonic jet impacting a flat surface. A schematic of the PSI is shown in Fig. 1.

In a lunar PSI scenario, the jet plume expands into a near-vacuum, transitioning from a continuum regime to a rarefied gas flow as the mean free path between particles increases. Once this rarefaction exceeds a threshold, the continuum hypothesis underlying the Navier-Stokes equations becomes invalid, reducing accuracy and potentially causing solver divergence or breakdown [9].

Under lunar vacuum conditions, conventional NS-based CFD solvers struggle to resolve regions beyond continuum flow, necessitating the use of stochastic methods like DSMC for plume analysis.

The DSMC method, a stochastic particle-based approach, is widely used for simulating rarefied gas flows in non-equilibrium Knudsen number regimes [18, 26]. It

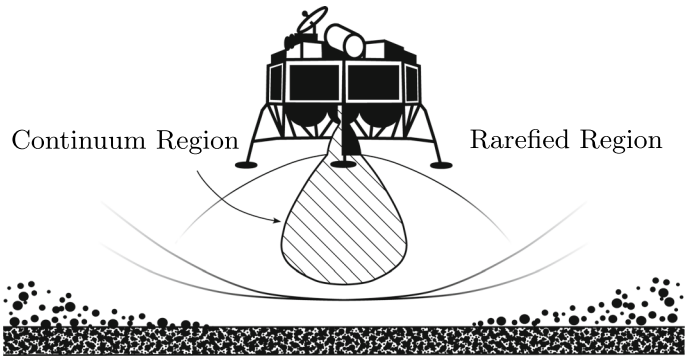

Fig. 1 Schematic illustration of the Plume-Surface Interaction in rarefied conditions

models particles representing many real molecules, significantly reducing computational costs compared to fully deterministic methods like Molecular Dynamics, while effectively capturing gas behaviour.

However, due to the high computational demand of DSMC for dense flows [9], hybrid approaches combining CFD and DSMC have proven valuable for scenarios involving both continuum and rarefied conditions. These approaches leverage the strengths of both methods, enabling detailed simulations across multiple pressure scales or in supersonic and hypersonic flows. Hybrid methods have also been applied successfully to PSI flows, demonstrating their efficiency in these contexts [4, 7, 16, 27].

For hybrid simulations, an interface must be defined to transfer data between NS-CFD and DSMC domains. One option is to position the interface within the continuum region, ensuring all rarefied regions are handled by DSMC. Alternatively, a breakdown criterion for the continuum assumption can define the interface, optimising the division of computational effort by maximising the region handled by the CFD solver.

2 CFD-Setup

The NS-CFD case utilised as a basis for the development of a hybrid approach consists of a conical nozzle, whose jet is impinging a flat wall. The geometric domain and boundary conditions are chosen in a way, that they are in line with a test setup at the University of Glasgow [28]. There, a number of tests for the PSI are run, to gain insight into the interaction of an impinging jet, with loose regolith simulant and sintered regolith samples. For a flat plate, ground pressure measurements are performed, which will be used to compare the numeric results.

The domain is depicted in Fig. 2. The used conical nozzle has a throat diameter of 1mm and an exit diameter d_e of 8.94mm. The Stand-off height (SOH) is set to 8.95 d_e, which is in line with one of the experimental cases.

The total pressure p_T and temperature T_T are set to 1MPa and 780K respectively. The pressure at the outlets is set to 1Pa, as this is the lowest pressure the vacuum chamber can reach. The working gas is pure nitrogen. As the flow is highly compressible, non-reflective boundary conditions were chosen for the inlet and outlet, to prevent compression waves to be reflected and propagate through the domain.

The solver selected for this calculation is OpenFOAM's rhoPimpleFoam. This choice is motivated by the project's parallel development of a coupling procedure between the NS-CFD solver and a Discrete Element Method, aimed at capturing the interaction between the gas flow and regolith particles for the continuum region and therefore for low SOHs. An existing interface for this coupling is already available for rhoPimpleFoam, making it the practical choice. rhoPimpleFoam is a pressure-based, density-variable solver suitable for compressible flows at low to moderate Mach numbers, employing a segregated solution algorithm based on the PIMPLE (merged PISO-SIMPLE) algorithm. In contrast, rhoCentralFoam is a density-based solver

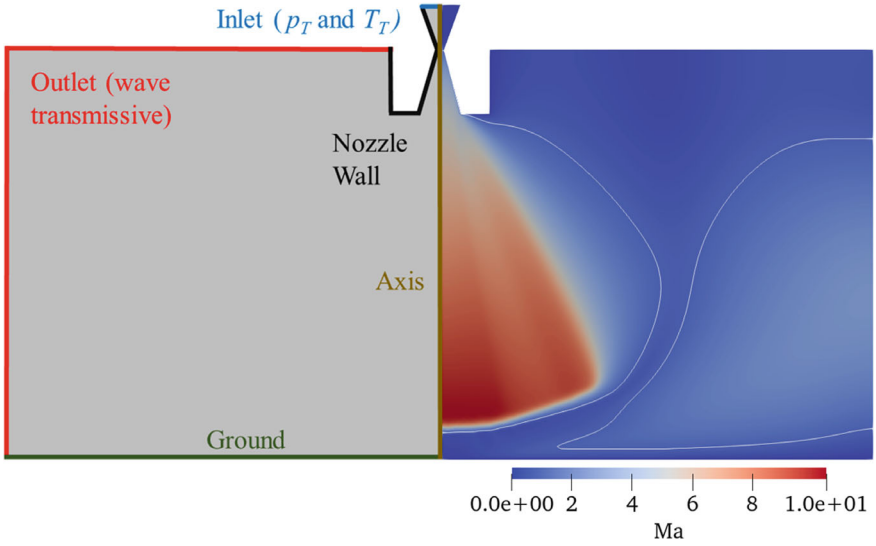

Fig. 2 Domain and boundary conditions used for the NS-CFD approach (left) and Mach contour of the steady-state NS-CFD solution, with $Ma = 1$ isoline highlighted in white (right)

that uses central-upwind schemes designed for high-speed compressible flows, offering better shock-capturing capabilities due to its conservative formulation and low numerical dissipation. Although rhoCentralFoam may yield more accurate results in terms of shock resolution, the chosen methodology, as outlined in Sect. 3, remains compatible with either solver.

Fig. 2 shows the Mach number distribution of the case once it has reached a steady-state. The general flow structure is in line with what would be expected. After the flow expansion through the nozzle, an underexpanded plume forms. The flow is stagnated on the ground at the centre, leading to a redirection in radial direction. Under the formed bow shock the radial flow expands to supersonic speeds, due to the divergent shape of the shock.

3 Breakdown Identification

In fluid dynamics, various semi-empirical parameters have been developed to identify the transition from continuous flow to free molecular flow. When higher-order terms in the distribution function become significant—indicating that translational temperatures and internal energy modes cannot equilibrate quickly due to infrequent particle collisions—the Navier-Stokes equations lose their validity. This validity can be evaluated by examining the magnitude of the coefficients in the first-order solution. The continuum equations fail physically when the velocity distribution function deviates

substantially from equilibrium. However, there is no theory that precisely defines the permissible size of higher-order terms in the power series or the extent of deviation from equilibrium before the Navier-Stokes equations become invalid [17, 21].

The Bird's parameter P is one of the most extensively investigated breakdown parameters in the literature. It was initially defined using the density and its gradient along the streamline s as flow property [2, 24]. Nevertheless, it is believed that for more complex flows, flow properties Q, such as the temperature and velocity, should also be taken into account [24]. Equation 1 shows the generalized version, where any of those flow properties can be set for Q. Additionally, the Mach number Ma, the ratio of heats γ and the mean free path λ are taken into account by the equation.

$$P_Q = Ma\sqrt{\frac{\pi\gamma}{8}}\frac{\lambda}{Q}\left|\frac{dQ}{ds}\right| \tag{1}$$

The value for the Bird's continuum breakdown parameter P of about 0.02 can be employed for the breakdown identification of steadily expanding flows [2]. In general, the Bird's parameter has been frequently utilised for the identification of the flow transition in cases of supersonic expansion into vacuum [17].

Another frequently employed breakdown parameter is the gradient-length local Knudsen number, whose definition can be seen in Eq. 2. This formulation also utilises Q for any flow parameter that can be used, the mean free path λ of the molecules and l, the distance between two points in the flow domain.

$$Kn_{GLL} = \frac{\lambda}{Q}\left|\frac{dQ}{dl}\right| \tag{2}$$

Boyd et al. [3] found that the Gradient-Length Local (GLL)-Knudsen number provides more accurate breakdown interface identification than Bird's parameter P for compressible, hypersonic flows. They demonstrated that placing l along the steepest property gradients yields the best results. In addition to commonly used breakdown parameters, Sun mentions the Tiwari's criterion $\|\phi\|$ [22] and Garcia's parameter B [8], both derived from coefficients in the first-order Chapman-Enskog solution. Another approach, a non-equilibrium quantifier N_δ, has been applied by Rahimi et al. [19].

Defining a cut-off value for breakdown parameters remains challenging. Some researchers use a resolution parameter where discrepancies between continuum and kinetic solutions exceed 5%, while others simply assume small values. The cut-off is typically determined through numerical tests and depends on the tolerance for hybrid-to-kinetic solution differences, which may vary by flow configuration. A conservative limit is often advisable [21].

Wang et al. [24] proposed modified parameters Kn_{max} and P_{max}, based on Boyd's Kn_{GLL} and Bird's P_Q, shown in Eqs. 3 and 4. Although still experimental, these parameters have shown that the best prediction of breakdown occurs when $Kn_{\max}$ exceeds 0.05.

$$Kn_{\max} \equiv \max(Kn_{\rho}, Kn_{T}, Kn_{U}) \tag{3}$$

$$P_{\max} \equiv \max(P_{\rho}, P_{T}, P_{U}) \tag{4}$$

The footnotes of $Kn_{\max}$ and $P_{\max}$ indicate the various flow properties that are included. As the breakdown is also dependent on viscosity and heat transfer, these are taken into account by using the density ρ, the velocity magnitude U and the translational temperature T [24].

For the above-mentioned reasons, the $Kn_{\max}$ with a value of 0.05 is chosen for the following approach, as it is widely used in the literature. However, the selection of the breakdown criterion only affects the location of the interface, not the coupling procedure itself. This ensures that the approach can be applied to a wide variety of flows or with different parameters and values, once comparisons are made and an optimal choice is determined.

The approach is aimed to enable a one-way coupling of the solvers. Meaning, that after reaching a steady-state solution of the CFD, the DSMC calculation gets initialised using those results. After the DSMC calculation reached a steady-state, the solution can be assembled by the two domains. The DSMC solver used in this case is dsmcFoam+ [26], yet the breakdown identification is not tied to the solvers used. One mesh shall be used for the calculation, to make the coupling automatable. By means of mesh-refinement, the requirements to the mesh can be complied with.

Based on the location of this initial breakdown, the mesh is split into three different regions: the CFD-domain, the DSMC-domain and the interface-domain. The CFD-domain consists of all the cells whose $Kn_{\max}$-value is below the threshold, the DSMC-domain of those whose value is above. The interface domain consists of those cells, which are cut by the $Kn_{max} = 0.05$ contour, as shown in Fig. 3. The interface-domain is used to initialise the DSMC calculation based on the results of the CFD calculation.

Fig. 3 Divided mesh with CFD-domain (blue), DSMC-domain (red), interface-domain (white) and the $Kn_{\max} = 0.05$ contour (green)

4 Conclusion

A NS-based CFD case was set up for a PSI scenario in near-vacuum conditions using the OpenFOAM environment. Several semi-empirical parameters for identifying the breakdown of the continuum region were discussed, and one was selected and applied to the aforementioned simulation.

Based on a $Kn_{\max} = 0.05$ threshold, the mesh was divided into regions, enabling the calculation of rarefied areas with a DSMC solver for more accurate predictions of the flow field where the continuum assumption fails. This approach, which divides a single mesh into regions, allows for automation, as no new mesh is required after the initial CFD simulation. The interface location is recalculated for each case, ensuring computational effort remains low and the DSMC method is applied on a smaller region.

It needs to be noted that the approach is limited to capture the initial continuum breakdown. Due to a recompression of the flow on ground, some of the radial flow is in the continuum region as well. This however will be analysed via the DSMC approach as well.

Acknowledgements We gratefully acknowledge funding for this project from ESA (Modelling and Testing of Plume/Regolith Interaction on Lunar Landing Pads and Berms, ESA Contract No. 4000139663/22/NL/MG) and also want to thank all the students involved.

References

1. ASI, CSA, ESA, JAXA, NASA (206) Dust mitigation gap assessment report
2. Bird GA (1970) Breakdown of translational and rotational equilibrium in gaseous expansions 8(11):1998–2003
3. Boyd ID, Chen G, Candler GV (1995) Predicting failure of the continuum fluid equations in transitional hypersonic flows 7(1):210–219
4. Cai G, Liu L, He B, Ling G, Weng H, Wang W (2022) A review of research on the vacuum plume 9(11):706, pII: aerospace9110706
5. Campbell AI, Carson HC, de Soto M, English K, Fiske MR, Martin L, Murai VR, Ramirez F, Romo E, Schang KE, Smith K (2021) Lunar pad - on the development of a unique isru-based planetary landing pad for cratering and dust mitigation. In: AIAA Scitech 2021 Forum. American Institute of Aeronautics and Astronautics
6. Cannon KM, Dreyer CB, Sowers GF, Schmit J, Nguyen T, Sanny K, Schertz J (2022) Working with lunar surface materials: Review and analysis of dust mitigation and regolith conveyance technologies 196:259–274, pII: S0094576522001965
7. Espinoza D (2018) An open-source hybrid CFD-DSMC solver for high-speed flows. Dissertation
8. Garcia AL, Bell JB, Crutchfield WY, Alder BJ (1999) Adaptive mesh and algorithm refinement using direct simulation monte Carlo 154(1):134–155, pII: S0021999199963052
9. Ghazanfari V, Akbar Salehi A, Reza Keshtkar A, Mahdi Shadman M, Hossein Askari M (2021) Investigation of the continuum-rarefied flow and isotope separation using a hybrid cfd-dsmc simulation for uf6 in a gas centrifuge 152:107985, pII: S0306454920306812

10. Heutling T, Propst M, Petersen J, Tajmar M, Patzwald JJ, Stoll E, Schilde C, Lamping T, Kostas K, White C, Craig B, Hijlkema J, van den Eynde J, Bach C (2023) In-situ manufactured landing pads and berms to enable sustainable operations on the lunar surface
11. Imhof B, Urbina DA, Weiss P, Sperl M, Hoheneder W, Waclavicek R, Madakashira HK, Salini J, Govindaraj S, Gancet J, Mohamed MP, Gobert T, Fateri M, Meurisse A, Lopez O, Preisinger C (2017) Advancing solar sintering for building a base on the moon
12. Isachenkov M, Chugunov S, Akhatov I, Shishkovsky I (2021) Regolith-based additive manufacturing for sustainable development of lunar infrastructure—an overview 180:650–678, pII: S0094576521000060
13. Jaffe LD (1971) Blowing of lunar soil by apollo 12: surveyor 3 evidence. SCIENCE 171:4
14. Metzger PT (2024) Erosion rate of lunar soil under a landing rocket, part 1: identifying the rate-limiting physics 417:116136. https://www.sciencedirect.com/science/article/pii/S0019103524001969, pII: S0019103524001969
15. Metzger PT, Autry GW (2022) The cost of lunar landing pads with a trade study of construction methods. http://arxiv.org/pdf/2205.00378.pdf, 50 pages, 15 figures
16. Morris AB, Goldstein DB, Varghese PL, Trafton LM (2016) Lunar dust transport resulting from single- and four-engine plume impingement 54(4):1339–1349
17. Morris AB (2012) Simulation of rocket plume impingement and dust dispersal on the lunar surface. Dissertation
18. Pellicani F (2016) Atmosphere re-entry simulation using direct simulation Monte Carleo (DSMC) method. Master thesis
19. Rahimi A, Ejtehadi O, Lee KH, Myong RS (2020) Near-field plume-surface interaction and regolith erosion and dispersal during the lunar landing 175:308–326, pII: S0094576520303258
20. Roberts L (1963) The action of a hypersonic jet on a dust layer
21. Sun Q, Boyd ID, Candler GV (2004) A hybrid continuum/particle approach for modeling subsonic, rarefied gas flows 194(1):256–277, pII: S0021999103004698
22. Tiwari S (1998) Coupling of the Boltzmann and Euler equations with automatic domain decomposition 144(2):710–726, pII: S0021999198960119
23. Wagner SA (2006) The apollo experience lessons learned for constellation lunar dust management
24. Wang WL, Boyd ID (2003) Predicting continuum breakdown in hypersonic viscous flows 15(1):91–100
25. Watkins RN, Metzger PT, Mehta M, Han D, Prem P, Sibille L, Dove A, Jolliff B, III DPM, Barker DC, Patrick E, Kuhns M, Laine M, Radley CF (2021) Understanding and mitigating plume effects during powered descents on the moon and mars 53(4)
26. White C, Borg MK, Scanlon TJ, Longshaw SM, John B, Emerson DR, Reese JM (2018) dsmcfoam+: An openfoam based direct simulation Monte Carlo solver 224:22–43
27. White C, Scanlon TJ, Merrifield JA, Kontis K, Langener T, Alves J (2016) Numerical and experimental capabilities for studying rocket plume-regolith interactions. In: AIP conference proceedings
28. White C, Zare-Behtash H, Kontis K, Ukai T, Merrifield J, Evans D, Coxhill I, Langener T, van den Eynde J (2019) Test facility to investigate plume-regolith interactions. In: International conference on flight vehicles, aerothermodynamics and re-entry missions and engineering

Open Access This chapter is licensed under the terms of the Creative Commons Attribution 4.0 International License (http://creativecommons.org/licenses/by/4.0/), which permits use, sharing, adaptation, distribution and reproduction in any medium or format, as long as you give appropriate credit to the original author(s) and the source, provide a link to the Creative Commons license and indicate if changes were made.

The images or other third party material in this chapter are included in the chapter's Creative Commons license, unless indicated otherwise in a credit line to the material. If material is not included in the chapter's Creative Commons license and your intended use is not permitted by statutory regulation or exceeds the permitted use, you will need to obtain permission directly from the copyright holder.

Modelling Heat Transfer at Low-Density Hypersonic Spacecraft Flight Regimes

Vladimir V. Riabov

Abstract The effects of rarefaction and nonequilibrium processes on hypersonic rarefied-gas flows over blunt bodies are studied by the Direct Simulation Monte-Carlo technique (DSMC) and by solving the full Navier–Stokes equations and the equations of a thin viscous shock layer (TVSL) under the conditions of wind-tunnel experiments and hypersonic-vehicle flights in the Earth atmosphere at altitudes from 60 to 110 km. The nonequilibrium, equilibrium and "frozen" flow regimes are examined for various physical and chemical processes in air and hydrogen. The influence of similarity parameters (Reynolds number, temperature factor, catalysis parameters, and gas injection rates) on the flow structure near the blunt bodies (a sphere and a cylinder) and on their heat transfer characteristics in hypersonic streams of ionizing air is studied.

Keywords Hypersonic flow · Chemical nonequilibrium · Heat · Gas injection

1 Introduction

The areas of aerodynamic heating and protecting techniques have brought renewed interests in the design of modern hypersonic vehicles [1]. Conservation equations and various physical models are used in the analyses of the structure of the flows of a chemical nonequilibrium multicomponent gas (air, carbon dioxide, hydrogen) near a blunt body [2–8]. In this paper, the flows near spherical and cylindrical bodies under the hypersonic re-entry conditions at altitudes from 110 to 60 km are studied by using the Direct Simulation Monte Carlo (DSMC) technique [6] and numerical solutions of the full Navier–Stokes equations [8] and their approximation, a model of a thin viscous shock layer (TVSL) with the generalized Rankine-Hugoniot conditions [9–11].

The flow characteristics are calculated for different degrees of catalytic activity on the probe surface. It is found that the size of the catalytically influenced zone

V. V. Riabov (✉)
Rivier University, Nashua, NH, USA
e-mail: vriabov@rivier.edu

© The Author(s) 2026

M. Grabe et al. (eds.), *Rarefied Gas Dynamics*, Springer Aerospace Technology,
https://doi.org/10.1007/978-3-032-00094-1_17

of the flow near the body surface depends on the values of rarefaction parameters (the Knudsen and Reynolds numbers), mechanisms of chemical reactions, relaxation rates and diffusion characteristics [11–14]. Calculations of the Stanton number in the stagnation point of the spherical one-meter-radius body, with dependency on the Reynolds number along the Space Shuttle trajectory, agree with flight data [15]. In addition to catalysis, other methods of the heat flux reduction are briefly examined in this paper: the injections of inert gases (helium and nitrogen) [6, 16] and hydrogen from the cylindrical surface to the hypersonic airflow [4].

2 Validation of Computational Results

The fast numerical procedure developed in [11, 12, 14, 16] was used for solving the TVSL equations using Keller's two-point second-order scheme [11, 14]. Calculations were made in the whole range of chemical reaction rates up to the equilibrium values. The iteration process demonstrates a rapid convergence of the second order towards the solution. This property of the numerical algorithm is important when the influence of recombination processes on the flow structure is essential.

The Stanton numbers St at the stagnation point of a sphere were calculated under wind-tunnel conditions at various Re_{of}, Mach number $M_\infty = 15$, and temperature factor $t_\text{w} = 0.15$. The comparison between TVSL results (triangles) and solutions of the Navier–Stokes equations [8] with slip (filled squares) and non-slip (empty squares) boundary conditions is shown in Fig. 1 (*left*). The results correlate well with experimental data [13, 17, 18] (circles) and DSMC data [6] (gradients). The TVSL results (triangles) for a cylinder also correlate well with experimental data [13] (circles) (see Fig. 1, *right*). A comparison between the TVSL results, experimental data [18] and DSMC data [6] along the spherical surface is shown in Fig. 2 (*left*).

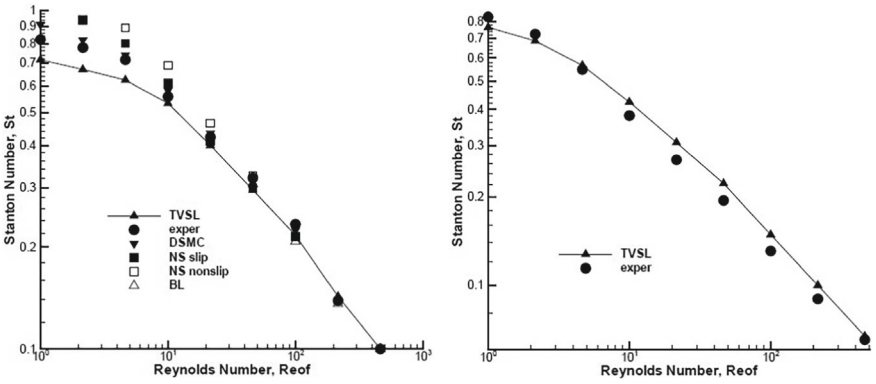

Fig. 1 Stanton numbers *St* versus Reynolds numbers Re_{of} for different medium models and various wind-tunnel experimental conditions [13, 17, 18] for a sphere (*left*) and a cylinder (*right*)

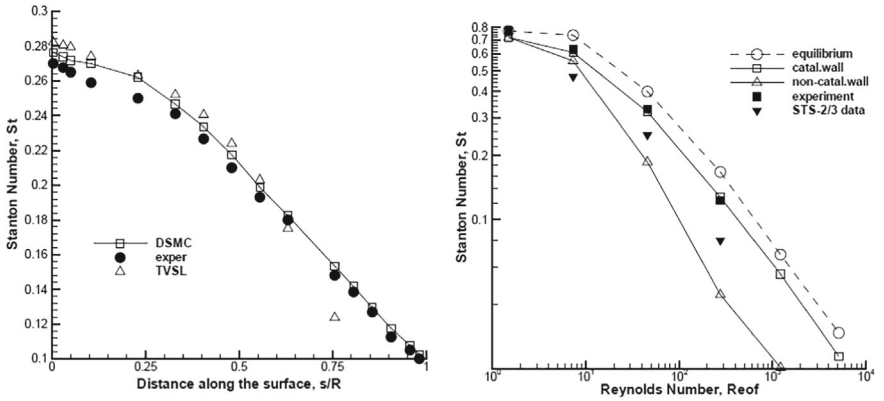

Fig. 2 Left: Stanton numbers *St* along the spherical surface coordinate *s*/*R* at $Re_{of} = 46.38$, $M_\infty = 6.5$, $t_w = 0.31$, $\gamma = 1.4$. *Right*: Stanton numbers *St* versus Reynolds numbers Re_{of} for a sphere of radius $R = 1$ m along the Space Shuttle trajectory and different medium models

3 Computational Results for the Flight Conditions

Calculations were carried out for descent flight conditions of a blunt body in the Earth atmosphere at altitudes $h = 110$, 100, 90, 80, 70, and 60 km and Reynolds numbers (at stagnation conditions) $Re_{of} = 1.49$, 6.97, 47.3, 230, 1220, and 5130 per 1 m, correspondingly. The values of the Stanton number $St = q/(\rho_\infty U_\infty (H_o - H_w))$ in the critical point of a sphere along the Space Shuttle trajectory [15] are shown in Fig. 2 (*right*).

The surface catalysis significantly influences heat flux q. The values of q under the flight conditions at 80 km ($Re_{of} = 230$, $U_\infty = 7.9$ km/s, $R = 1$ m) differ by factor of three for various catalytic surfaces due to the nonequilibrium character of physical and chemical processes in the VSL. This fact is confirmed by the STS-2/3 flight data [15] (filled triangles, Fig. 2, *right*). At the altitude $h = 67.5$ km this difference reaches 240 percent. The effect is less pronounced for catalytic surfaces [11, 14]. The nonequilibrium TVSL results near catalytic surfaces correlate with the data (circles) [11] obtained for equilibrium VSL (see Fig. 2, *right*).

The catalysis does not noticeably influence pressure, VSL thickness, and coefficient of friction at $1.49 \leq Re_{of} \leq 5130$. The calculated values of heat flux and species distributions for flight conditions at $h = 60$–110 km are displayed in Figs. 3 and 4.

The degree of catalysis significantly influences distributions of mass concentrations $\alpha_i = \rho_i/\rho$ in the VSL (see Fig. 3, *left*). The measure of this influence is the width of the catalytically influenced zone d, which is characterized by the difference in distributions α_i for two extreme cases: ideally catalytic and absolutely noncatalytic surfaces. The flight conditions fully define the degree of dissociation of O_2, NO, N_2, concentrations of O and N atoms, and the size of the zone d.

The calculations of α_i on the external boundary of the TVSL at $1.49 \leq Re_{of} \leq 5130$ indicate that the catalysis influences the full width of the VSL at altitudes above

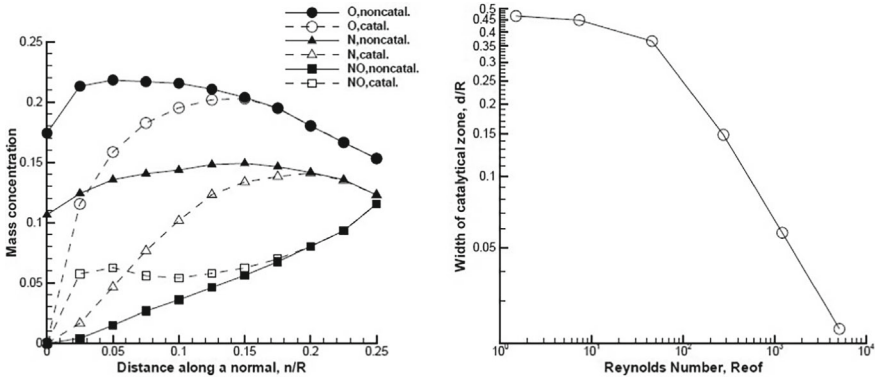

Fig. 3 Left: Mass concentrations αi of air components in the TVSL at $Re_{of} = 230$. *Right*: The width of the catalytically influenced zone d versus Reynolds number Re_{of}

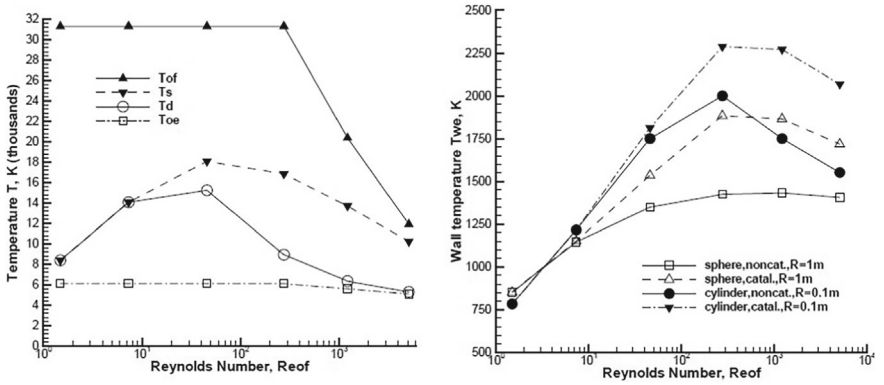

Fig. 4 Left: The values of temperatures T_s, T_d, T_{of}, and T_{oe} versus Reynolds number Re_{of}. *Right*: Equilibrium temperature T_{we} of spherical ($R = 1$ m) and cylindrical ($R = 0.1$ m) surfaces

85 km. At the lower altitudes, species concentrations on the external boundary of the layer reach their values in upstream equilibrium flow [10, 11]. It is found that under the flight conditions at $h = 60$ km, instead of the generalized Rankine-Hugoniot relations, it is possible to use standard boundary conditions [9, 10] at the shock wave. The estimated values d are shown in Fig. 3 (*right*).

Temperature values T_s at the external boundary of TVSL (gradients), stagnation temperature T_{of} (triangles), and values T_d (circles) on the catalytically influenced zone boundary d are shown in Fig. 4 (*left*). At $h \leq 90$ km, a decrease of T_d is observed and its values merge with the temperature T_{oe} (squares) estimated at the equilibrium dissociated-air state behind the shock wave. As Re_{of} increases, T_s rises at h from 110 to 90 km. As the altitude falls below 80 km, due to the vehicle deceleration [15, 17], a monotonous decrease of T_s and T_{of} is observed.

4 Equilibrium Temperature of the Vehicle Surface

Large values of the heat flux towards the body surface led to high level of equilibrium surface temperature $T_{we} = (q/\varepsilon\sigma)^{1/4}$, where ε is emissivity, and σ is the Stephan-Boltzmann's constant. The values T_{we} with $\varepsilon = 0.85$ are shown in Fig. 4 (*right*), for the critical point of a sphere ($R = 1$ m) and on the critical line of a cylinder ($R = 0.1$ m) for two extreme cases of surface catalysis. Using noncatalytic materials (solid lines) leads to a significant decrease in T_{we}. The calculations also indicate that values T_{we} on the cylindrical surface monotonously decrease as the swept angle increases and only slightly depends on the mechanism of catalysis [11, 14].

5 The Binary-Scaling Similitude Law

Numerical results [12] show that parameters in the TVSL are frozen at $Re_{of} < 20$; recombination processes are negligible, and the binary-scaling similitude law [12], $\rho_\infty R = const$, can be applied at $U_\infty = const$. Calculations performed for the critical streamline assuming $U_\infty = 7.8$ km/s, $\rho_\infty R = 5.35 \times 10^{-7}$ kg/m^2 ($Re_{of} = 7.33$), and nose radii $R = 1$ m and 0.005 m show that distributions of flow parameters for these cases correlate satisfactorily. The temperature and electron concentration N_e profiles near a noncatalytic surface are shown in Figs. 5 (*left*) and (*right*), correspondingly.

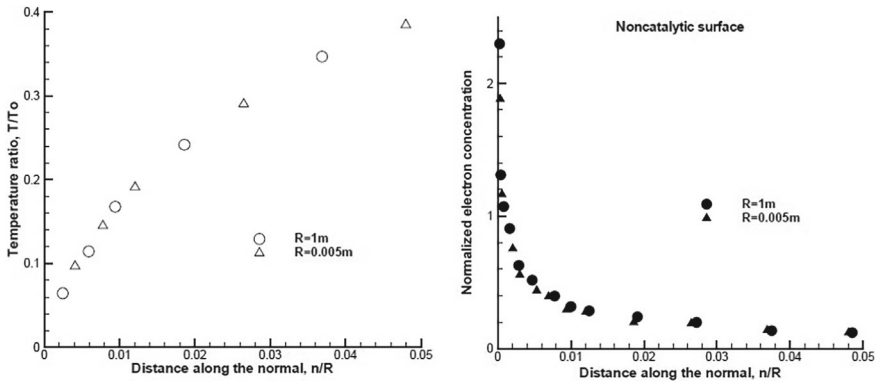

Fig. 5 Temperature T/T_o (*left*) and normalized electron concentration $N_e \times R \times 10^{-14}$ m^{-2} (*right*) at the stagnation streamline of the sphere at $Re_{of} = 7.33$, $U_\infty = 7.8$ km/s, $\rho_\infty R = 5.35 \times 10^{-7}$ kg/m^2

6 Gas Injection Effects

6.1 *Influence of the Air Blowing Factor* G_w

The flow pattern over sphere is significantly sensitive to the blowing parameter G_w, which is the ratio of counterflow outgas mass flux to upstream mass flux. The influence of G_w on the flow structure is studied for hypersonic flow of air at $M_\infty = 6.5$ and $Kn_{\infty,R} = 0.0163$ ($Re_{o,R} = 92.8$), and the temperature factor is equal to 0.31. The flow conditions are the same as suggested by Botin [18] for experiments with air blowing in a vacuum chamber at stagnation temperature $T_s = 1000$ K. The sphere radius is $R = 0.015$ m. Air is blowing diffusively from the orifice with the diameter of 0.002 m, which is in the front critical point of the sphere. The factor G_w varies from 0 to 1.5.

In the case of the strong blowing ($G_w > 0.3$), the temperature field is significantly disturbed in the vicinity of the orifice in the subsonic area [6]. The distributions of the Stanton number St along the spherical surface at various blowing factors are shown in Fig. 6. For the considered transitional flow regime conditions, when the mass injection rate equals 0.7 of the freestream mass flux, the viscous layer is blown completely off the surface, and the heat transfer is zero. The displacement effect spreads both in the upstream direction and along the surface. The width of the displacement zone can be characterized by the normalized surface coordinate $(s/R)_{max}$, where the local heat transfer is maximum St_{max} (see Fig. 6). At the same value of the factor G_w, this effect is more pronounced for injections of light inert gases (e.g., He), as shown in Fig. 6.

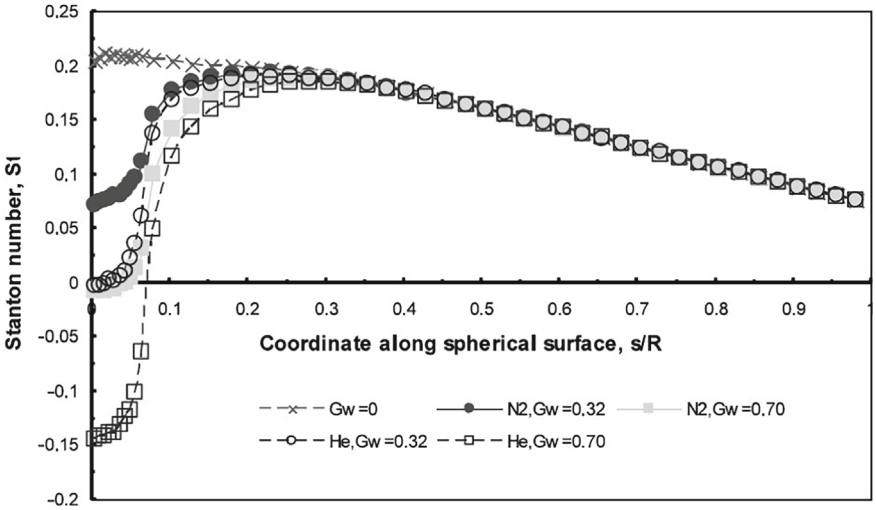

Fig. 6 Stanton number along the spherical surface at $Kn_{\infty,R} = 0.0163$ ($Re_{o,R} = 92.8$) and various air-to-air and helium-to-air mass blowing factors G_w [6]

6.2 Combustion in Hypersonic Air Flows with H_2 Injection

The recent analysis of nonequilibrium processes of hydrogen combustion in hypersonic airflows inside the scramjet engine is based on the numerical solutions of TVSL equations and boundary conditions [4], modeling the flow in the viscous shock layer near a parabolic cylinder at slot and uniform injections. Mathematical description of the nonequilibrium process of hydrogen combustion considered 11 gas components (O_2, N_2, NO, H_2O_2, HO_2, H_2O, OH, H_2, H, O, N) and 35 chemical reactions [19].

The slot injection from the body surface was simulated by using the injection parameter $G = G_0\exp(-\alpha_w/X)$, where G_0 is the value of the parameter at the critical cylinder line, $\alpha_w = 30$, and X is marching coordinate along the surface. The computational results indicate the presence of significant amounts of nonreacting molecular hydrogen near the body. For $Re_0 > 100$, the diffusion of the "hot" reaction products (water and *OH*) occurs from the reaction zone to the surface. This phenomenon leads to the increase of heat flux values at the surface, $Q = 2q/(\rho_\infty {U_\infty}^2)$ towards the body surface along the coordinate X (see Fig. 7, *left*). The heat from combustion reactions does not prevail over the cooling effect of injection at the considered Reynolds number, $Re_0 = 628$. The heat flux is significantly lower than Q at $G_0 = 0$ near the injection zone at moderate injections ($0.02 \le G_0 \le 0.05$). A large quantity of injected hydrogen leads to effective cooling of the surface at a large distance from the injection zone at a high injection level (see diamonds in Fig. 7, *left*). The combustion zone moves from the surface towards the TVSL external boundary as the injection intensity increases.

Cooling the porous surface of the parabolic cylinder was modelled at $Re_{of} = 628$ and the constant intensity of hydrogen injection, $G = G_0 = const$ along the surface. More significant decrease of the heat flux is found at the entire body surface (see Fig. 7, right), compared to the case of slot injection. For the weak injections (squares in Fig. 7, right), the heat flux at the entire computational region is less than Q in the absence of the injection ($G_0 = 0$). The distribution of the heat flux becomes noticeably distinct at moderate (triangles, $G_0 = 0.02$) and strong (circles, $G_0 = 0.03$)

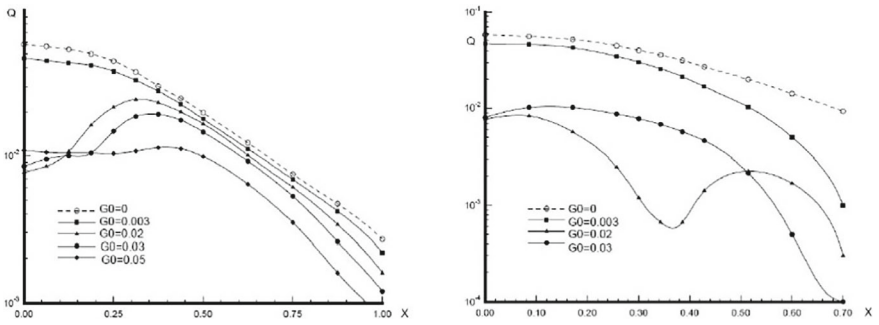

Fig. 7 Heat flux on parabolic cylinder (radius $R = 0.015$ m) at slot (*left*) and uniform (*right*) injections of H_2 to air at $Re_{of} = 628$, velocity $U_\infty = 2933$ m/s, and $T_\infty = 230$ K

injections, as the result of mutual influence of thermophysical properties of hydrogen, high enthalpy values of upstream flow, and the presence of combustion zone in the shock layer.

7 Conclusions

The computational tests were conducted as a model problem for preliminary design of heat protection systems of hypersonic vehicles. The results validate the TVSL model for calculating complex nonequilibrium multicomponent gas flow near blunt bodies under low-density flight and wind-tunnel test conditions. The study of characteristics of the catalytically influenced zone can be used in developing approximation methods of predicting heat fluxes at a catalytic surface of a vehicle. The binary similitude law ($\rho_\infty R = const$) [12] can be applied in the studies of the nonequilibrium flows at small values of the Reynolds number, $Re_{of} < 20$. Gas injections of N_2, air, He, or H_2 can significantly reduce the heat fluxes on the hypersonic-probe surfaces. Strong influences of the blowing factor G_w (the ratio of outgas mass flux to upstream mass flux) and the rarefaction criterion (the Knudsen number or the Reynolds number) on the flow structure around a sphere and a cylinder (temperature fields, the configuration of mixing flow zones) and on heat-flux distributions along the surface have been found.

References

1. Cheng H (1993) Perspectives on hypersonic viscous flow research. Annu Rev Fluid Mech 25:455–484
2. Gnoffo PA, Gupta RN, Shinn JL (1989) Conservation equations and physical models for hypersonic air flows in thermal and chemical nonequilibrium. NASA TP-2867
3. Gupta R, Yos J, Thompson R, Lee K (1990) A review of reaction rates and thermodynamic and transport properties for an 11-species air model for chemical and thermal nonequilibrium calculations to 30,000K. NASA Reference Publication No. 1232
4. Riabov VV, Botin AV (1995) Hypersonic hydrogen combustion in the thin viscous shock layer. J Thermophys Heat Transfer 9(2):233–239
5. Moss JN, Bird GA (1984) Direct simulation of transitional flow for hypersonic reentry conditions. AIAA Paper 84–0223
6. Riabov VV (2004) Heat transfer on a hypersonic sphere with diffuse rarefied-gas injection. J Spacecr Rocket 41(4):698–703
7. Gupta R, Simmonds A (1986) Hypersonic low-density solutions of the Navier-Stokes equations with chemical nonequilibrium and multicomponent surface slip. AIAA Paper 86–1349
8. Ryabov VV (1980) Numerical investigation of the flow of nitrogen past a sphere with allowance for rotational relaxation. Fluid Dyn 15(2):320–324
9. Cheng HK (1963) The blunt-body problem in hypersonic flow at low Reynolds number. IAS Paper 63–92
10. Moss JN (1974) Reacting viscous-shock-layer solutions with multicomponent diffusion and mass injection. NASA TR 411

11. Provotorov VP, Riabov VV (1983) Effect of chemical reactions on the flow of air in a viscous shock layer. Fluid Mech Soviet Res 12(6):17–25
12. Gusev VN, Provotorov VP, Riabov VV (1981) Effect of physical and chemical nonequilibrium on simulation of hypersonic rarefied gas flows. Fluid Mech Soviet Res 10(5):123–135
13. Botin AV, Gusev VN, Provotorov VN, Riabov VV, Chernikova LG (1990) Study of the influence of physical processes on heat transfer toward the blunt bodies in flows with small Reynolds numbers. Trudy TsAGI 2436:134–144
14. Riabov VV, Provotorov VP (1994) The structure of multicomponent nonequilibrium viscous shock layers. AIAA Paper 94–2054
15. Throckmorton D (1982) Benchmark aeroheating data from the first flights of the Space Shuttle Orbiter. AIAA Paper 82–0003
16. Riabov VV, Provotorov VP (1996) Exponential box schemes for boundary-layer flows with blowing. J Thermophys Heat Transfer 10(1):126–130
17. Nomura S (1983) Correlation of hypersonic stagnation point heat transfer at low Reynolds number. AIAA J 21(11):1598–1600
18. Botin AV (1987) A study of local heat transfer to the spherical surface with gas injection at small Reynolds numbers. Uchenyye Zapiski TsAGI 18(5):41–47
19. Dimitrov V (1982) Simple kinetics. Nauka, Moscow

Open Access This chapter is licensed under the terms of the Creative Commons Attribution 4.0 International License (http://creativecommons.org/licenses/by/4.0/), which permits use, sharing, adaptation, distribution and reproduction in any medium or format, as long as you give appropriate credit to the original author(s) and the source, provide a link to the Creative Commons license and indicate if changes were made.

The images or other third party material in this chapter are included in the chapter's Creative Commons license, unless indicated otherwise in a credit line to the material. If material is not included in the chapter's Creative Commons license and your intended use is not permitted by statutory regulation or exceeds the permitted use, you will need to obtain permission directly from the copyright holder.

DSMC Simulation of a Non-axisymmetric Hypersonic Vehicle at 90 km Altitude

Angelos Klothakis, Ioannis K. Nikolos, and Vassilis Theofilis

Abstract This study presents the numerical investigation of a non-axisymmetric hypersonic vehicle, modeled after the X-51 concept, flying at an altitude of 90 km. Due to the low atmospheric density at this altitude and the transitional flow regime, the Direct Simulation Monte Carlo (DSMC) method is employed to accurately capture rarefied effects and molecular collisions. The vehicle's geometry, specifically its inlet design, is examined for its ability to ensure sufficient mass flow and pressure required for scramjet operation under at that altitude. Key outputs include the shock structures and positions and local flow field properties, which elucidate the influence of non-axisymmetric design on the inlet's performance. Results indicate that inlet efficiency, characterized by uniform flow distribution and total pressure increase.

Keywords Hypersonic flows · Hypersonic vehicle · High-altitude flight

1 Introduction

Hypersonic flight, defined as speeds exceeding Mach 5, has long represented a frontier in aerospace engineering. Landmark programs such as the X-15, X-43A, and X-51A have successively advanced our understanding of hypersonic aerodynamics, thermal protection, and propulsion. Among these, scramjet engines (supersonic combustion ramjets) have emerged as a promising solution for sustained high-speed flight at high altitudes. Unlike traditional engines, scramjets maintain supersonic airflow throughout the engine, using the vehicle's forward motion for air compression and enabling efficient combustion at extreme velocities [1–4]. The X-43A's record-setting Mach 9.6 flight and subsequent tests of the X-51A Waverider have validated key elements of scramjet propulsion. These efforts, largely driven by NASA and

A. Klothakis (✉) · I. K. Nikolos
Technical University of Crete, Chania, Crete, Greece
e-mail: aklothakis@gmail.com

V. Theofilis
Technion Israel Institute of Technology, Haifa, Israel

© The Author(s) 2026

M. Grabe et al. (eds.), *Rarefied Gas Dynamics*, Springer Aerospace Technology,
https://doi.org/10.1007/978-3-032-00094-1_18

the U.S. Air Force, have shaped modern hypersonic research by bridging theoretical models with flight-demonstrated performance [5–7].

Recent computational studies have advanced simulation methods for hypersonic vehicles, employing techniques such as direct numerical simulation (DNS) and Direct Simulation Monte Carlo (DSMC) to resolve non-equilibrium and rarefied effects. Qi et al. [8] examined boundary layer transition via DNS, Li et al. [9] evaluated multi-regime aerodynamics of reentry vehicles, and Reji and Lal [10] used DSMC to model rarefied hypersonic flow over capsule geometries.

Building upon this foundation, the present study applies the DSMC method to simulate a three-dimensional, non-axisymmetric vehicle inspired by the X-51A Waverider at 90 km altitude. A geometry was reconstructed from open-source technical drawings [11], allowing detailed investigation of oblique shocks, density gradients, and vortex interactions in a high-altitude regime where continuum approaches become inadequate. This work contributes to the growing body of knowledge on rarefied hypersonic aerothermodynamics.

2 Geometry Definition

Two-dimensional schematics of an X-51A-like configuration were sourced from publicly available materials [11], serving as a reference for constructing the three-dimensional model. In developing this geometry, particular care was taken to account for features that critically affect performance in the hypersonic regime. Figure 1 provides a perspective view of the resulting vehicle design, showcasing how the overall shape of the original X-51A concept recognized for its effective hypersonic aerodynamic characteristics has been preserved. In addition, a simplified representation of the scramjet inlet, located beneath the vehicle, was incorporated to capture the complex flow phenomena typical of hypersonic inlets.

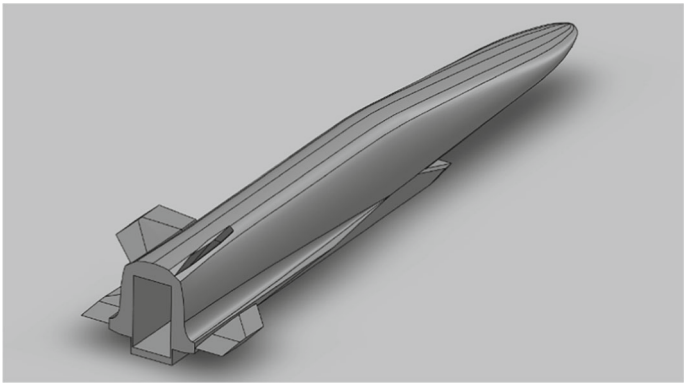

Fig. 1 Overview of the three-dimensional model

Taking all previous considerations into account, the final design is a hypersonic vehicle measuring slightly over 4 m in length and up to 0.86 m in width when including the horizontal fins. Situated beneath the fuselage, the engine extends approximately 2.7 m and features an intake opening of 0.23 m. As illustrated in the plans [11], this engine incorporates a diverging exhaust nozzle, an essential component for achieving optimal performance under the extreme temperatures and pressures characteristic of hypersonic flight. The engine is integrated into the vehicle's structure, with the forward underside acting as a compression ramp to support scramjet functionality. Furthermore, the operating conditions used in the simulations are derived from the U.S. Standard Atmosphere for an altitude of 90 km [12], ensuring realistic environmental parameters for high-altitude hypersonic analysis.

3 Results

The simulation was conducted using the Direct Simulation Monte Carlo (DSMC) method as implemented in the open-source SPARTA solver [13]. The vehicle was assumed to fly at Mach 9 and an altitude of 90 km, where rarefied gas effects are non-negligible. At these conditions, the Knudsen number computed using the relation $Kn = \lambda/L$ where λ is the mean free path and L is the vehicle's length, was found to be 0.00359, placing the flow in the slip regime. This justifies the use of DSMC for accurately resolving velocity slip, temperature jump, and shock structure. The freestream parameters corresponding to this flight point are summarized in Table 2.

The simulation parameters are summarized in Table 1 while the free-stream conditions can be seen in Table 2. Because of the intricate nature of the hypersonic flow surrounding this vehicle, a carefully designed grid refinement scheme was essential. Areas featuring steep gradients particularly near shock waves and within the engine's interior demanded a high-density mesh to capture swift variations in flow properties. As indicated in Table 1, the simulation employed over five billion particles, illustrating the necessity of fine resolution in regions where temperature and pressure can vary substantially. Shocks, expansion waves, and other complex phenomena inside the engine required an even more refined approach than that used for the external flow.

The grid refinement method was guided by local mean free path, ensuring that each cell did not exceed two times the mean free path. To accurately model particle collisions, the near-neighbor scheme [14] was applied, where collision partners were

Table 1 DSMC computational parameters

Number density, ($\#m^3$)	Timestep (s)	Transient period	Sampling period	Number of particles	Number of cells	CPU hours
2.00×10^2	3.00×10^7	50,000	50,000	5.8×10^9	~ 114,500,000	165,888

Table 2 Free-stream conditions

Velocity (m/s)	Temperature (K)	Number density (#/m^3)	Wall temperature (K)	Mach
2530	196	2.00×10^{20}	300	9.0

selected within a sphere whose radius equaled the distance a particle travel in a single timestep. Although cell sizes can exceed one mean free path, prior work has demonstrated that this approach remains accurate up to four mean free paths [15] given that a large number of particles per cell is used. Collisions were simulated using the Variable Soft Sphere (VSS) model [16] and molecular nitrogen (N_2) was selected as the simulation gas. The vehicle wall was modeled as isothermal at 300 K with full thermal accommodation. The computational domain used in this work, measured 18 m in the streamwise direction, 12 m normal to the flow, and 8 m in the spanwise direction. The timestep was set to 0.3 μs which is significantly smaller than the mean collision time. On average after refinement a particle needs about 10 timesteps to cross one cell ensuring smooth properties transport. The flow initially was given a transient period of 50,000 timesteps to evolve; an additional 50,000 samples were then recorded to reduce statistical noise.

Figure 2 shows the final adapted grid, focusing on shock regions, the engine inlet, and the combustion chamber. The pressure in the combustion chamber increases by approximately a factor of 40 relative to the freestream, indicating a compression level consistent with typical scramjet inlet design expectations [3], even though combustion is not modeled in the present study. The Mach number contours in Fig. 3 reveal the external flow structures and confirm that the flow remains supersonic around the engine inlet, aligning with scramjet requirements. Along the fuselage, Mach number progressively decreases as successive oblique shocks interact with the boundary layer. At the scramjet inlet, these contours demonstrate the vehicle's effectiveness in capturing and compressing high-speed flow for combustion even at high altitude highlighting the design's efficiency.

Furthermore, Fig. 4 depicts the pressure contours around the vehicle, illustrating the significant flow compression that occurs behind the nose as a result of oblique

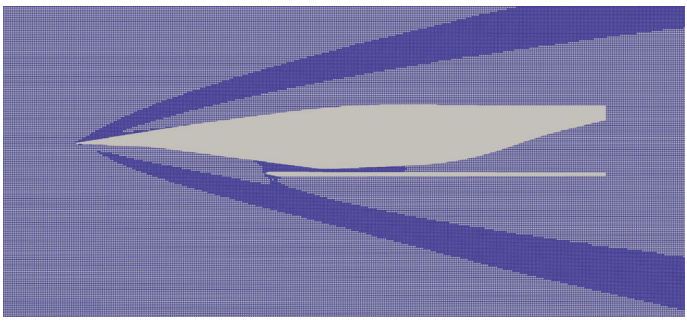

Fig. 2 Flow domain adapted grid

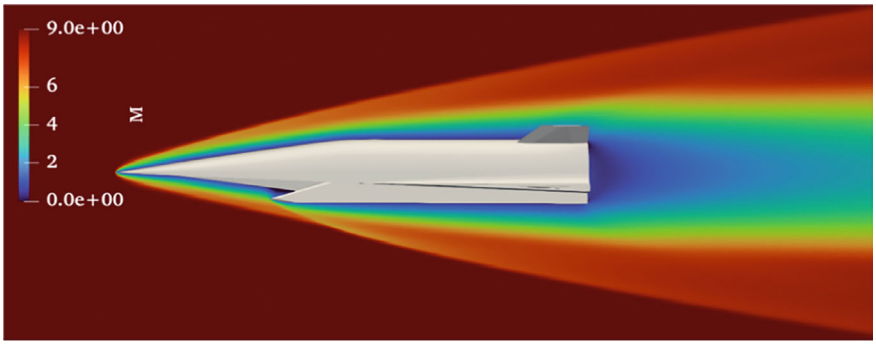

Fig. 3 Mach number contours on the symmetry plane

shock formation. Additional oblique shocks develop at the sharply defined engine inlet edge, elevating local pressures to nearly two orders of magnitude above free-stream conditions, an essential characteristic for scramjet performance. Such pressure increases not only facilitate efficient air compression necessary for high-speed combustion but also introduce complex thermal and mechanical loads on the vehicle. This intense pressure rise is accompanied by corresponding density gradients, particularly in the plateau region upstream of the central cavity, where compression stabilizes before further increasing inside the combustor zone. Although no fuel injection is modeled and the precise internal geometry remains idealized, the simulation indicates peak pressures within this cavity, underscoring the importance of understanding compressive loading and structural integrity in high-speed propulsion systems. Downstream, the nozzle expansion converts thermal and pressure energy into kinetic energy, leading to re-acceleration of the flow and a sharp pressure drop. These high-pressure regions correlate with significant thermal and mechanical stresses, which must be accounted for in future design and material selection efforts. It should be noted that the present simulation excludes combustion and employs an approximate geometry, serving as a first-order assessment of flow structure and pressure loading under rarefied, high-Mach conditions (Figs. 4, 5).

In Figs. 6 and 7, Q-criterion is used to visualize both oblique shock structures and vortex-dominated regions, offering vital insight into the flow physics that governs scramjet performance. In Fig. 6 the (curved) leading edge shock that engulfs the vehicle is seen to be followed by a shock system which originates on the vehicle upper and lower surface at the location of laminar-turbulent transition. Past that location a turbulent boundary layer develops and extends to the end of the vehicle, as indicated by the large-scale vortices contained underneath the secondary shock system. Analysis is underway to define the transition location on the basis of linear stability theory in which velocity slip and temperature jump are taken into account [17, 18]. Planar cuts highlight circular blue lines where oblique shocks form, while red areas represent coherent vortex cores. Three-dimensional iso-surfaces further reveal a primary oblique shock extending from the vehicle's leading edge and a secondary shock from the forward boundary of the engine duct both generating

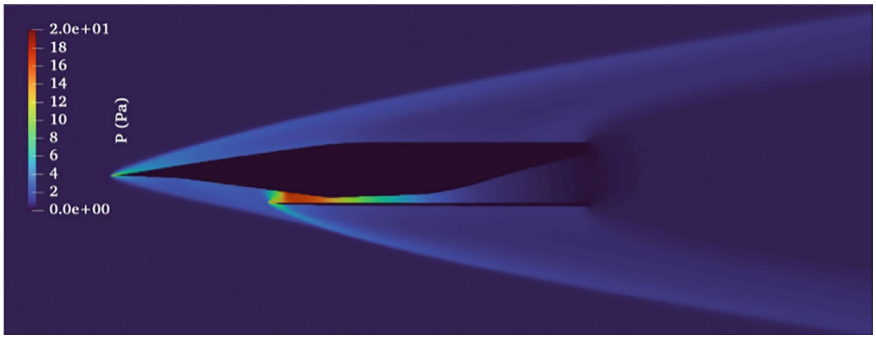

Fig. 4 Pressure contours around the vehicle and inside the engine

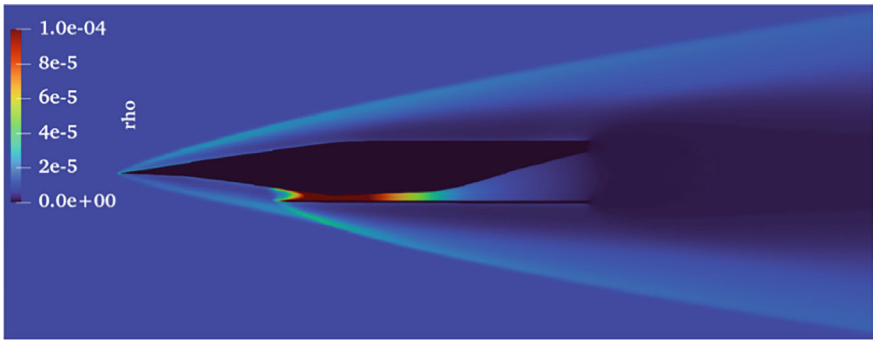

Fig. 5 Density contours around the vehicle and inside the engine

pressure gradients that influence heat transfer and structural loading. Multiple vortical structures also emerge from the vehicle's leading edge, underscoring the interplay between compressible flow features and the importance of precise geometric design to regulate shock-vortex interactions.

Further examination focuses on a major vortex at the ramp leading into the engine inlet. Although this vortex has the potential to disrupt inlet flow uniformity, the vehicle's lower-surface design confines these ramp-generated vortices, preserving favorable conditions for compression and combustion. The pronounced vorticity near the inlet highlights how minor adjustments in leading-edge geometry or ramp curvature can alter vortex formation and overall engine stability. Collectively, these findings underscore the complexity of hypersonic flow, where shocks and vortices interlink, and where meticulous external and internal geometry design is crucial for high-performance propulsion.

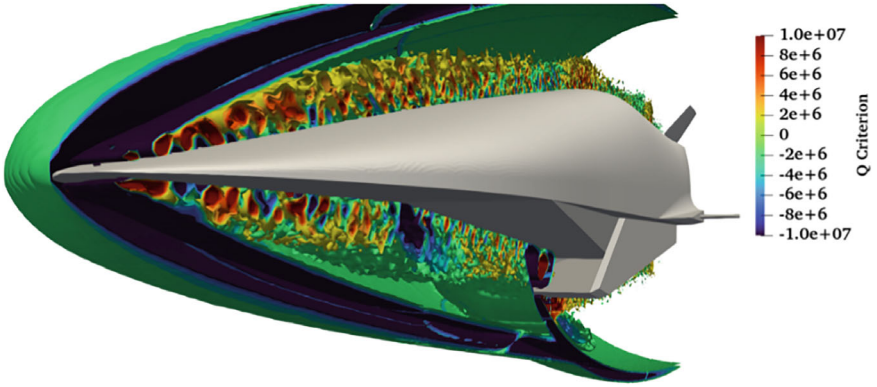

Fig. 6 Three-dimensional instantaneous Q-criterion iso-surfaces. The green–blue conical configuration corresponds to the primary oblique shock, whereas a secondary oblique shock emanates from the forward edge of the engine duct

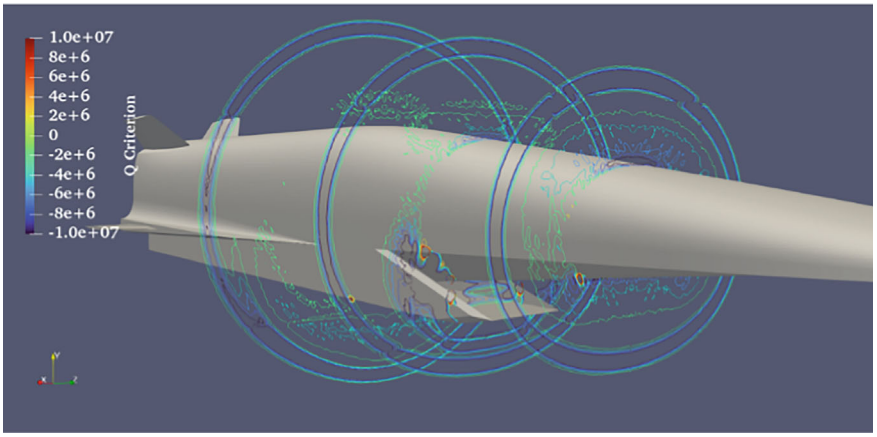

Fig. 7 Q-criterion contours depicted at multiple parallel planes to identify critical flow structures. The circular blue lines represent the locations of oblique shocks, whereas the red regions mark coherent vortex formations

4 Conclusions

This study presents a DSMC-based analysis of hypersonic flowfields around a scramjet-type vehicle, examining both external aerodynamics and internal flow behavior. Mach number contours reveal that oblique shocks at the nose and intake are essential for compressing incoming air to supersonic conditions, as required by scramjet propulsion. Although combustion is not modeled, pressure and density fields confirm effective airflow capture and highlight significant shock–boundary-layer interactions relevant to aerodynamic heating. Within the central cavity, density

gradients arise from shock convergence and viscous effects, emphasizing the importance of controlled internal flow. While fuel injection is not simulated, these flow features indicate where injection and mixing would be critical in future reactive models. Q-criterion analysis reveals shock–vortex interactions, showing that ramp-generated vortices can propagate upstream if not managed through careful design. Nozzle expansion downstream produces a drop in density and thermal energy, simulating momentum redistribution consistent with flow acceleration. Due to the absence of combustion, thrust and exit Mach number are not quantified. Nevertheless, the results demonstrate that inlet and nozzle geometry strongly influence shock structure and flow uniformity, with implications for managing thermal and mechanical loads. Future work will incorporate chemical reactions and energy exchange to enable realistic modeling of combustion dynamics, heat transfer, and propulsion performance.

References

1. Fry RS (2004) A century of ramjet propulsion technology evolution. J Propul Power 20(1):27–58
2. Jenkins DR (2007) X-15: extending the frontiers of flight. NASA
3. Heiser WH, Pratt DT (1994) Hypersonic airbreathing propulsion. AIAA Educ Ser
4. Barthelemy R (1989) The national aero-space plane program. In: AIAA maintainability of aerospace systems symposium, paper 5053
5. Voland RT, Huebner LD, McClinton CR (2006) X-43A hypersonic vehicle technology development. Acta Astronaut 59:181–191
6. Oppenheimer MW, Doman DB (2006) A hypersonic vehicle model developed with piston theory. In: AIAA atmospheric flight mechanics conference and exhibit, AIAA, p 6637
7. Rondeau CM, Jorris TR (2013) X-51A Scramjet demonstrator program: waverider ground and flight test. In: SFTE 44th International/SETP southwest flight test symposium, vol 28
8. Qi H, Li X, Yu C, Tong F (2021) Direct numerical simulation of hypersonic boundary layer transition over a lifting-body model HyTRV. Adv Aerodynamics 3(31):1–21
9. Li J, Jiang D, Geng X, Chen J (2021) Kinetic comparative study on aerodynamic characteristics of hypersonic reentry vehicle from near-continuous flow to free molecular flow. Adv Aerodynamics 3(10):1–10
10. Reji RV, Lal SA (2016) Simulations of hypersonic flow past a re-entry capsule using DSMC method. Front Heat Mass Transf 7(1):1–8. https://doi.org/10.5098/hmt.7.27
11. SECRET PROJECTS Homepage, https://secretprojects.co.uk/threads/darpa-boeing-x-51a-waverider.7406/page-11, last accessed 2024/02/28.
12. U.S. Standard Atmosphere, U.S. Government Printing Office, Washington D.C., NOAA-S/T 76-1562 (1976)
13. Plimpton SJ, Moore SG, Borner A, Stagg AK, Koehler TP, Torczynski JR, Gallis MA (2019) Direct simulation Monte Carlo on petaflop supercomputers and beyond. Phys Fluids 31(8)
14. Gallis MA, Torczynski JR (2011) Effect of collision-partner selection schemes on the accuracy and efficiency of the direct simulation Monte Carlo method. Phys Fluids 67(8)
15. Gallis, MA, Bitter N, Koehler T, Torczynski JR, Plimpton SJ, Papadakis G (2010) DSMC simulations of turbulent energy decay in the Taylor-Green vortex flow. In: SAND2017-9109C, Sandia National Lab, Albuquerque
16. Koura K, Matsumoto H (1991) Variable soft sphere molecular model for inverse-power-law or Lennard-Jones potential. Phys Fluids 3(10):2459–2465

17. Klothakis A, Sawant SS, Quintanilha H, Theofilis V, Levin DA (2021) Slip effects on the stability of supersonic laminar flat plate boundary layer. In: AIAA Scitech 2021 Forum, p 1659
18. Klothakis A, Quintanilha Jr H, Sawant SS, Protopapadakis E, Theofilis V, Levin DA, Linear stability analysis of hypersonic boundary layers computed by a kinetic approach: a semi-infinite flat plate at

Open Access This chapter is licensed under the terms of the Creative Commons Attribution 4.0 International License (http://creativecommons.org/licenses/by/4.0/), which permits use, sharing, adaptation, distribution and reproduction in any medium or format, as long as you give appropriate credit to the original author(s) and the source, provide a link to the Creative Commons license and indicate if changes were made.

The images or other third party material in this chapter are included in the chapter's Creative Commons license, unless indicated otherwise in a credit line to the material. If material is not included in the chapter's Creative Commons license and your intended use is not permitted by statutory regulation or exceeds the permitted use, you will need to obtain permission directly from the copyright holder.

Numerical Simulation of the Flow Field Around a Sounding Rocket for the PMWE Project

Miklas Schütte, Igor Hörner, Stefan Löhle, Stefanos Fasoulas, and Marcel Pfeiffer

Abstract Atmospheric in-situ measurements with sounding rockets provide high spatial resolution, but face aerodynamic influences. Correction factors from Direct Simulation Monte Carlo (DSMC) are employed to counter disturbances in the atomic oxygen measurements within the PMWE project. For the first time, the resolution of the simulation mesh resolves the sensor geometry and the correction factor is calculated solely from the number density of atomic oxygen. Correction factors vary from 2 (110 km) to 3 (85 km) and are about 80 % of total density correction due to separation effects. They are influenced mainly by free molecular effects and do not depend on the atomic oxygen inflow number density.

Keywords Sounding rocket · PMWE · DSMC · Atomic oxygen density measurement · Aerodynamic influences · Correction factor

1 Introduction

The polar mesosphere winter echoes (PMWE) are reflections of radar waves in the mesosphere/lower thermosphere (MLT) of the atmosphere that extends approximately between 60 and 110 km altitude. The goal of the PMWE-project is to explain their origin. For this purpose, sounding rockets with appropriate instrumentation were launched to conduct measurements in the MLT-region. The Institute of Space Systems (IRS) is involved in the project with the Flux-Φ(Phi)-Probe-Experiment (FIPEX) sensors. These are solid electrolyte sensors for the quantification of atomic oxygen [1–3].

The necessity for high spatial resolution requires in-situ measurement techniques. Sounding rockets are the only suitable carriers for the instruments, since the altitude range of interest is too high for balloons and too low for satellites [4]. However, due to the movement of the rocket at supersonic speed and the presence of the sensor, there are deviations between the measured variables and the value in the undisturbed

M. Schütte (✉) · I. Hörner · S. Löhle · S. Fasoulas · M. Pfeiffer
Institute of Space Systems, University of Stuttgart, Stuttgart, Germany
e-mail: schuettem@irs.uni-stuttgart.de

© The Author(s) 2026

M. Grabe et al. (eds.), *Rarefied Gas Dynamics*, Springer Aerospace Technology,
https://doi.org/10.1007/978-3-032-00094-1_19

atmosphere as a result of aerodynamic influences on the flow field [5, 6]. Therefore, it is of critical importance to understand the effects and to determine their influence.

This paper examines aerodynamic influences and provides correction factors for the measured atomic oxygen density n_O using numerical simulations. Future work will apply these factors to the measurements.

2 Methods

2.1 PMWE 2 Mission

On October 1st 2021 the second measurement campaign (PMWE-2) started from Andøya Space Center in Norway. The apogee of the suborbital flight was at an altitude of about 130 km [2]. Two payloads (FIONA and DUSTIN) equipped with several scientific instruments were used. FIONA carried three FIPEX sensor on its bottom deck and none on the front deck. DUSTIN was equipped with FIPEX sensors on both decks with the bottom deck being identical to the FIONA. Therefore, DUSTIN includes all geometrical information required for this study. The payload is depicted in Fig. 1. It is basically a long cylinder with a length of ≈ 2.7 m and a diameter of ≈ 36 cm. The measuring decks 1 and 2 are located at the respective ends. Three FIPEX sensors are attached to each deck. A detailed overview of the PMWE-2 mission with a focus on the FIPEX measurements is given in [2]. A correction of the measurement data, to take the aerodynamic influence into account, has not yet been part of the data analysis. The required correction factors are to be provided in the present work.

2.2 Correction Factor

The aerodynamic influences on the flow field are caused by compression and rarefaction effects, composition changes due to mass-dependent separation of species, chemical reactions at the surface and in the shock area, outgassing and desorption, and deviations from local thermodynamic equilibrium at high altitudes [7–9]. Due to theses effects above, the measured number density n_{exp} changes by a factor f_{aero} compared to the value of the undisturbed atmosphere n_∞ [5]:

$$n_{\text{exp}} = f_{\text{aero}} \cdot n_\infty \tag{1}$$

Fig. 1 Payload with measurement deck 1 (right) and deck 2 (left)

If the factor is known, it is possible to quantify the aerodynamic effects and to draw conclusion about the number density of atomic oxygen of the undisturbed atmosphere $n_{O,\infty}$ from the measurement data. This correction factor, determined through numerical simulation, describes the relationship between the local number density at the sensor position n and the undisturbed number density in the atmosphere n_∞ [10].

$$f_{\text{aero}} = \left(\frac{n}{n_\infty}\right)_{\text{sim}} \tag{2}$$

The factors are determined for several altitudes, because of the change in the aerodynamic conditions. In addition, the factor must be calculated for each sounding rocket project individually. This is due to the dependency of the aerodynamic influences on geometry, speed, angle of attack, atmospheric conditions, measurement principle and position on the payload [9].

The simulative investigation of the aerodynamic influences is complex, since the mean free path increases from a few millimeters at 80 km to several meters at 130 km. Thus, the aerodynamic conditions change from a continuum flow to a free molecular flow. Outside of the continuum regime conventional tools of computational fluid dynamics (CFD) are no longer usable. A common tool for the analysis of rarefied flows, is the direct simulation Monte Carlo (DSMC) method. This microscopic approach describes the movement and interactions of simulation particles, which represents multiple gas molecules or atoms [9]. In this work, the implemented DSMC method in the open source simulation program "PICLas" (Particle-In-Cell Las Vegas), which was and is being developed at IRS, is used for this purpose [11]. PICLas is extensively validated and verified for a wide range of applications [11, 12].

2.3 Calculation of the Correction Factor

The sensor measurements in the ram area are of particular interest for the experimental results, since they were found to reflect the actual variations better than the measurements in the wake area [4]. Therefore, the simulation focuses only on the flow around the measuring deck located in the ram area. The flow around deck 1 is simulated during the upleg only, and deck 2 only during the downleg. This approach significantly reduces the simulation area and minimizes the simulation effort.

For the first time, the simulation geometry includes the sensor itself, which is a small plate (see Fig. 2). The front 4 mm of this plate constitutes the sensitive measurement area. All calculated sensor values in the simulation (e.g. correction factors) are determined as area-averaged values in this area. In addition, the species-specific correction factor for atomic oxygen $n_O/n_{O,\infty}$ is determined. As a result, changes in composition (e.g. separation effects due to mass-dependent reflection) and the increase in number density on the sensor surface can be detected for the first time. Only wall

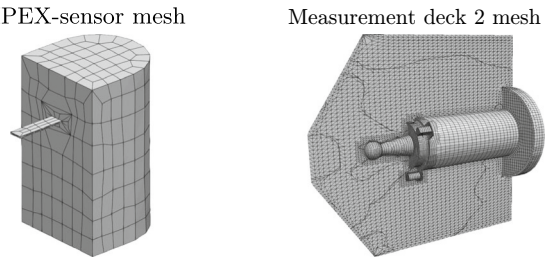

Fig. 2 Mesh of the FIPEX sensor and measurement deck 2

recombination, outgassing and desorption are not taken into account in the simulations. Previous studies only considered the total number density $n_t/n_{t,\infty}$, neglected the sensor geometry, and greatly simplified the overall payload geometry [4].

Simulation settings Since the FIPEX measurments (see [2]) change mainly in the range between 85 and 110 km, the simulation were chosen in the altitudes of 85, 90, 95, 100 and 110 km for the up- and downleg. The simulations employ a five-species model, which includes molecular and atomic nitrogen, molecular and atomic oxygen, and nitric oxide as a potential reaction product. The data for individual number densities and inflow temperatures are taken from the NRLMSISE-00 atmospheric model. For sufficient particle discretization in the DSMC simulation, the mean collision distance must be smaller than the mean free path [11]. Therefore, the particle weighting is between $1 \cdot 10^{10}$ at 110 km altitude and $2 \cdot 10^{11}$ at 90 km altitude. The nearest neighbor pairing algorithm and the octree method are used for particle pairing [13]. The time step was chosen to resolve the collision frequency to ensure a physically realistic simulation [14].

The velocity vector of the inflow $\vec{v}$ is inclined by the angle of attack relative to the center axis of the payload. Therefore, and because of the geometries of the measuring decks, no symmetry conditions can be applied and a complete 3D simulation is necessary. The magnitude of the inflow velocity and the angle of attack results from in-flight measurements. The velocities are between 600 and 1000 m/s. The angle of attack α varies between 5° and 10° for the upleg and between 20° and 30° for the downleg. The spin stabilization of 3 Hz [2] results in a maximum rotational velocity at the sensor position of only 2.17 m/s and is therefore negligible compared to the translational speed of the payload. In the simulation, the inflow direction is selected in such a way that the maximum correction factor occurs at one sensor, because the maximum correction factors for each height are required to correct the measured values. Section 3 summarizes the results for this sensor for the up- and downleg.

In a particle collision process, elastic collisions, relaxation of internal excitations and chemical reactions are considered. The collision cross-sections are calculated with the variable hard sphere model [14]. Chemical reactions are modeled using the total collision energy model. The FIPEX sensors and the rest of the payload surface are modeled as a diffuse reflecting wall. Catalytic surface reactions and electronic excitations are not considered in the simulations. The FIPEX sensors have a constant

wall temperature of 1000 K (due to sensor heating) and the remaining payload a temperature of 288.15 K.

Due to the fact that DSMC is a statistic approach, the results are subject to statistical noise [14]. The noise can be reduced by increasing the sample size. This can be done by increasing the number of simulation particles or by sampling over multiple iteration steps/time steps in the case of stationary problems [11]. Eventually, a trade-off between increasing the computing effort (computing time and memory requirements) and reducing the noise must be made. Even though we considered only atomic oxygen, which is only a fraction of the present particles, and the area of interest is small compared to the simulation area, we managed to reduce the noise on the sensor values to just a few percent on the correction factor $n_O/n_{O,\infty}$. This was achieved by meshing the selective sensor area as roughly as possible in order to have as many atomic oxygen simulation particles as possible available for sampling and by increasing the number of iterations. Only in the case of the lowest altitude of 85 km, the noise is larger, due to the small number of atomic oxygen particles in relation to the total number of simulation particles in the whole calculation area. Given the considerable complexity of the geometry and considering the correction factor for atomic oxygen, as well as the limited computational capacity, the noise impact on the factor is very small. The simulation time was between 6 and 13 h on 512 cores at the high performance computing center Stuttgart.

3 Results

3.1 Flow Field

Figure 3 shows the flowfield visualization around the ram oriented bottom deck on the downleg. At the highest altitude the flow is close to free molecular flow. As the payload moves downwards, the density increases and a compression shock forms. Due to the geometry of the payload, the compression shock is very close to the sensors. During the simulations no chemical reactions took place, since the velocities of the payload and the temperatures in the disturbed regions are too low.

3.2 Correction Factor

The maximum correction factors for atomic oxygen $n_O/n_{O,\infty}$ and the maximum correction factors from the total number density $n_t/n_{t,\infty}$ for the sensors are plotted in Fig. 4. The diagram illustrates that the decrease in the correction factor with increasing altitude is extremely small for the upleg and the downleg. The values are between approximately two and three. The same applies for the downleg. Another observation is that the correction factor for atomic oxygen $n_O/n_{O,\infty}$ at 90–110 km is

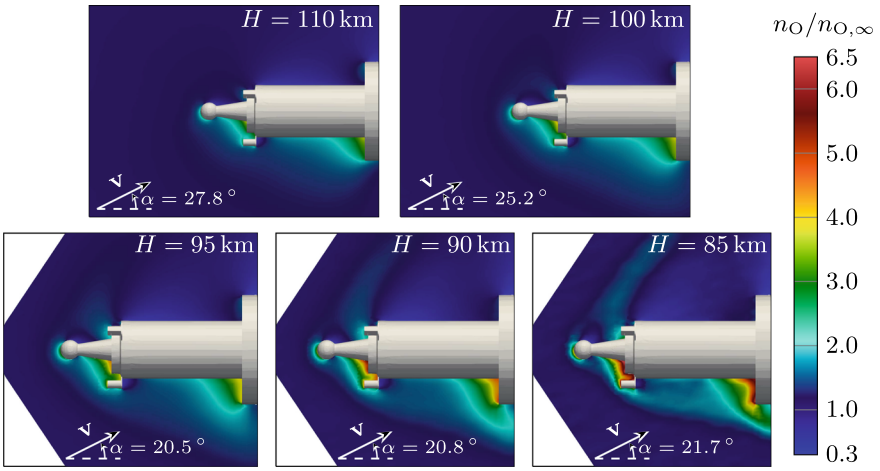

Fig. 3 Flow field around the payload on the downleg at altitudes 85–110 km

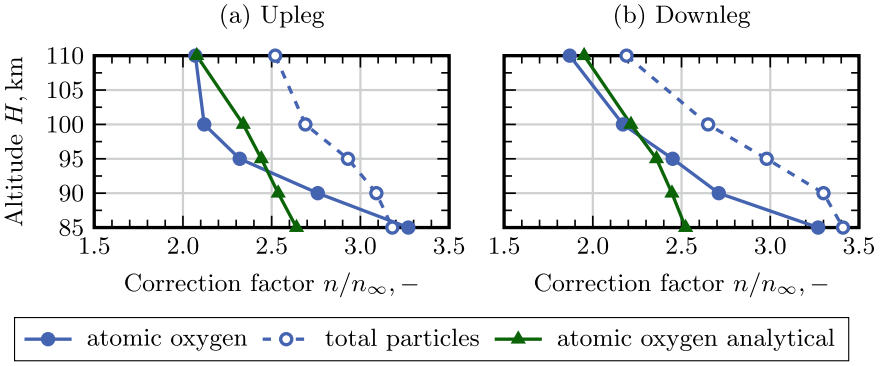

Fig. 4 Simulated correction factors of atomic oxygen $n_O/n_{O,\infty}$ and total particles $n_t/n_{t,\infty}$ as well as analytical determined atomic oxygen factor from Eq. 3

approximately 80 % of the total number density correction factor $n_t/n_{t,\infty}$. This variation is primarily attributed to separation effects, mainly caused by mass-dependent reflection. When comparing the atomic oxygen correction factors in the upleg and downleg, the upleg value at an altitude of 110 km is slightly larger. This difference results from the lower angle of attack in the upleg, which leads to a larger accumulation of particles on the surface and thus to a larger correction factor in this flow regime. At lower altitudes, the up- and downleg values are quite similar. Due to the geometry and angle of attack, the shock is positioned closer to the sensor during the downleg, resulting in a stronger influence on the correction factor compared to the upleg. However, the geometric influence of structures near the sensor increases in the upleg. Consequently, the values are similarly large in both the up- and downleg.

Analytical determination of the correction factor In a free molecular flow, there are no intermolecular collisions. Consequently, the gas reflected from the payload is superimposed on the surrounding gas. The number density for the particles adjacent to the surface n, at complete accommodation and diffuse reflection for a single species, is described as follows [14]:

$$\frac{n}{n_\infty} = \frac{1}{2}\left\{[1 + \mathrm{erf}\,(s\,\cos\theta)] \cdot \left[1 + \sqrt{\pi}\,s\,\cos\theta\sqrt{\frac{T_\infty}{T_\mathrm{w}}}\right] + \sqrt{\frac{T_\infty}{T_\mathrm{w}}}\,e^{-s^2\cos^2\theta}\right\} \quad (3)$$

The incident and the reflected components are included in n. The parameter n_∞ represents the number density of the inflow of this species, T_∞ is the temperature of the inflow, T_w is the wall temperature, θ describes the angle between the inflow and the surface normal and s is the velocity ratio between the body velocity and the most probable particle velocity of this species for a Maxwell distribution. The ratio n/n_∞ in Eq. 3 describes exactly the aerodynamic correction factor. Figure 4 shows the correction factor for atomic oxygen $n_\mathrm{O}/n_{\mathrm{O},\infty}$ at the sensor from the simulation compared to the analytically determined correction factor with Eq. 3. As can be seen, the simulation results agree well with the analytical results, especially at high altitudes. The effects that decisively influence the correction factor are consequently the accumulation of the particles on the surfaces and the separation due to mass-dependent reflection (free molecular effects). The increase in the factor with decreasing altitude is mainly due to increasing velocity and less to an influence from a shock wave. This is the result of the still rarefied flow and the generally low payload velocity. Additionally, due to the generally low angle of attacks, their influence is weak, especially compared to the velocity. The small deviations at high altitudes are due to geometry influences. The differences at low altitudes are due to the increasingly dense flow and the forming compression shock. This leads to a deviation in the Maxwell distribution in the inflow, which violates the assumptions behind Eq. 3. Furthermore, the equation does not account for nearby structures, causing a larger difference in the upleg than in the downleg. Another limitation arises when the sensor is blocked by the payload or impacted by scattered particles, causing the analytical correction factors to be invalid, even in free molecular flow. However, if it is known that the sensor is exposed to the free stream and surrounding geometries have minimal influence without doing a simulation, then the analytical equation is applicable in free molecular flow regime and can provide a good approximation for the correction factor.

4 Conclusion

As part of the PMWE project, the density of atomic oxygen was measured using FIPEX sensors on sounding rockets to study polar mesospheric winter echoes in the MLT region. Due to the intrusive measuring method, the measured values deviate

from the undisturbed atmosphere owing to aerodynamic influences. DSMC simulations were conducted at several altitudes in the up- and downleg of the trajectory, focusing on the payload side in the ram area.

The simulations have to be three-dimensional, because of the complex geometry and the angle of attack. The time step and the number of particles were chosen in such a way that the collision frequency and the mean free path are resolved. Additionally, the simulation was refined to the sensor level to capture accumulation and separation effects. Quantitative analysis determined correction factors for atomic oxygen, ranging from two and three. As a result of mass-dependent scattering at the sensor surface, the atomic oxygen correction factor is about 80 % of the total number density correction factor. The factor is primarily determined by free molecular effects and is largely independent of the atomic oxygen inflow number density. Despite the high detail in the simulation, additional effects such as wall recombination, outgassing, and desorption could further influence measurements.

It should be noted that quantitative and qualitative investigations of aerodynamic effects are necessary, as correction factors alone do not capture all aerodynamic influences. As a result, measurements may still be distorted. Qualitative analysis showed, that the upleg measurements are more influenced by geometry, than downleg measurements due to the complexity of the geometry.

Acknowledgements This work is funded by the Deutsche Forschungsgemeinschaft (DFG, German Research Foundation) – Project-ID 516238647 – SFB 1667 (ATLAS - Advancing Technologies of Very Low-Altitude Satellites). The authors also thank the High Performance Computing Center Stuttgart (HLRS) for granting the computational time that allowed the execution of the presented simulations.

References

1. Strelnikov B et al (2021) Sounding rocket project “PMWE” for investigation of polar mesosphere winter echoes. J Atmos Solar-Terrestrial Phys 218
2. Hoerner I et al (2022) atomic oxygen measurments on sounding rockets using solid electrolyte FIPEX sensors: first flight results from the PMWE mission. In: 25th ESA-PAC Symposium, Biarritz, France
3. Hoerner I et al (2025) Fast response solid electrolyte oxygen sensors with porous thin film electrodes. Rev Sci Inst 96(3):015002-1–015002-13
4. Eberhart M et al (2015) Measurement of atomic oxygen in the middle atmosphere using solid electrolyte sensors and catalytic probes. Atmos Meas Tech 8(8):3701–3714
5. Rapp M, Gumbel J, Lübken F-J (2001) Absolute density measurements in the middle atmosphere. Annales Geophysicae 19(5):571–580
6. Allen JB, Perl M, Hauser T (2006) Simulation of aerodynamic influences on rocket-mounted oxygen sensors. J Spacecr Rocket 43(6):1387–1394
7. Bird GA (1988) Aerodynamic effects on atmospheric composition measurements from rocket vehicles in the thermosphere. Planet Space Sci 36(9):921–926
8. Gumbel J, Rapp M, Unckell C (1999) Aerodynamic aspects of rocket-borne in situ studies. In: Kaldeich-Schürmann B (ed) European rocket and balloon programs and related research, vol 437. ESA Special Publication, pp 459–464

9. Gumbel J (2001) Aerodynamic influences on atmospheric in situ measurements from sounding rockets. J Geophys Res Space Phys 106(A6):10553–10563
10. Eberhart M et al (2019) Atomic oxygen number densities in the mesosphere–lower thermosphere region measured by solid electrolyte sensors on WADIS-2. Atmos Meas Tech 12(4):2445–2461
11. Fasoulas S et al (2019) Combining particle-in-cell and direct simulation Monte Carlo for the simulation of reactive plasma flows. Phys Fluids 31(7):072006-1– 072006-19
12. Nizenkov P et al (2016) Verification and validation of a parallel 3D direct simulation Monte Carlo solver for atmospheric entry applications. CEAS Space J 9
13. Pfeiffer M, Mirza A, Fasoulas S (2013) A grid-independent particle pairing strategy for DSMC. J Comput Phys 246:28–36
14. Bird GA (1994) Molecular gas dynamics and the direct simulation of gas flows, 2nd edn. Oxford Engineering Science Series

Open Access This chapter is licensed under the terms of the Creative Commons Attribution 4.0 International License (http://creativecommons.org/licenses/by/4.0/), which permits use, sharing, adaptation, distribution and reproduction in any medium or format, as long as you give appropriate credit to the original author(s) and the source, provide a link to the Creative Commons license and indicate if changes were made.

The images or other third party material in this chapter are included in the chapter's Creative Commons license, unless indicated otherwise in a credit line to the material. If material is not included in the chapter's Creative Commons license and your intended use is not permitted by statutory regulation or exceeds the permitted use, you will need to obtain permission directly from the copyright holder.

PICLas-Based Intake Simulation Activities for the Development of an ABEP Specular Intake

Nadine Barth, Jonathan Skalden, Konstantinos Papavramidis, Elizabeth Gutierrez, Franziska Tuttas, Marcel Pfeiffer, Raphael Tietz, Philipp Maier, and Georg Herdrich

Abstract Space missions in very low Earth orbit (VLEO) offer advanced capabilities for Earth observation, telecommunications, and security but are challenged by continuous orbit decay. Atmosphere-Breathing Electric Propulsion (ABEP), which uses atmospheric particles as propellant, provides a potential solution. Within the H2020 DISCOVERER, ESA ram-CLEP and ATLAS projects, IRS is developing a specular intake and helicon plasma thruster to advance ABEP systems. This study uses Direct Simulation Monte Carlo (DSMC) simulations to evaluate specular intake geometries, analyzing particle flux, pressure, mass flow rate, and collection efficiency. The results indicate that reducing the focal length of the parabolic intake significantly improves efficiency and mass flow rate, while increasing the discharge channel diameter proves more effective for achieving these high values as well. As pressure follows an opposing trend to efficiency, and reaching the ignition pressure is crucial, the optimal configuration among the investigated for balancing efficiency and pressure is a discharge channel diameter of 25 mm with a focal length of 3 mm.

Keywords ABEP · Intake · DSMC · Very low earth orbit

1 Introduction

Very Low Earth Orbit (VLEO) missions face significant atmospheric drag, necessitating efficient propulsion systems to maintain orbit and extend mission duration. Atmosphere-Breathing Electric Propulsion (ABEP) addresses this challenge by using residual atmospheric particles as propellant for an electric thruster.

The ABEP system, includes an intake that collects atmospheric particles and directs them into the discharge channel, where they are accelerated to generate thrust. This study focuses on the design and simulation of the ABEP intake system to optimize key parameters such as collection efficiency, pressure, and mass flow rate,

N. Barth · J. Skalden · K. Papavramidis · E. Gutierrez · F. Tuttas · M. Pfeiffer · R. Tietz · P. Maier · G. Herdrich (✉)
Institute of Space Systems, Stuttgart, Germany
e-mail: herdrich@irs.uni-stuttgart.de

© The Author(s) 2026

M. Grabe et al. (eds.), *Rarefied Gas Dynamics*, Springer Aerospace Technology,
https://doi.org/10.1007/978-3-032-00094-1_20

ensuring effective thruster operation while minimizing the intake's size and volume. Additional insights into ABEP and its platform design are available in Herdrich et al. [6, 7]. Related research on VLEO satellite operations is supported by the DFG-funded CRC 1667 ATLAS at the University of Stuttgart.

2 Related Work

In VLEO, the free molecular flow regime is dominated by infrequent collisions, making particle-wall interactions critical for intake design. These interactions, including absorption, scattering, and chemical reactions, are challenging to model due to limited data on surface properties such as finish, cleanliness, and adsorbed gas layers. This is particularly relevant in VLEO, where interactions with gases like atomic oxygen are significant. The Maxwell model, a simplified approach, distinguishes between specular and diffuse reflections [9], forming the basis for intake design classifications.

Romano [12] demonstrated through simulations that specular intake designs outperform diffuse ones, leading to further studies by Romano, Kun, and Herdrich [5, 6, 13]. The specular design uses the optical principles of a parabolic mirror, directing particles to the focal point of the paraboloid. Particles retain their tangential velocity while their normal velocity is reversed, assuming hyperthermal flow, which is less applicable in VLEO [1] but still provides a better performance than diffuse designs.

Figure 1 illustrates the functional principle of a parabolic intake based on specular reflection. This study evaluates three geometric modifications:

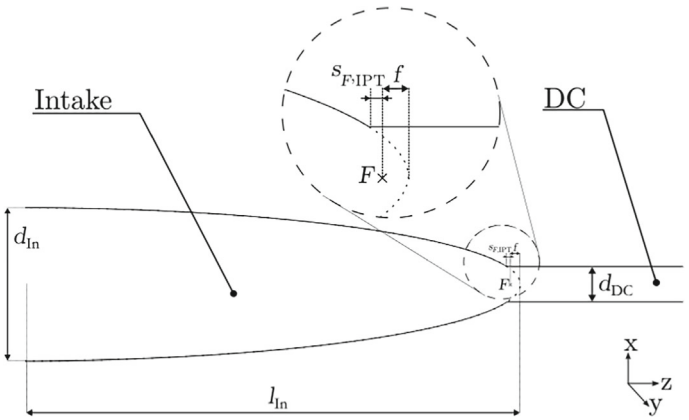

Fig. 1 Functional schematic of the parabolic intake, showing intake diameter d_{In}, intake length l_{In}, discharge channel diameter d_{DC}, and focal point position F inside the discharge channel with the focal length f and vertex-to-focal point distance $s_{F,\mathrm{IPT}}$

1. Intake Length (l_{In}): The intake length is varied between 500 mm, 1000 mm and 1500 mm.
2. DC diameter (d_{DC}): The diameter of the DC is scaled to 15 mm, 25 mm and 37 mm.
3. Focal length f: Focal lengths of 3.0 mm, 3.75 mm, and 5.5 mm are evaluated.

These variations influence intake diameter, intake area, and vertex-to-focal point distance $s_{F,\mathrm{IPT}}$.

The location of the focal point F relative to the DC is critical. Romano [12] tested three configurations: one in front of the DC intake vertex, one at the vertex, and one inside the DC. The most efficient setup was with F inside the DC, using a focal length f of 5.5 mm and a d_{DC} of 37 mm, achieving an $s_{F,\mathrm{IPT}}$ of 10 mm. Increasing $s_{F,\mathrm{IPT}}$ could further improve efficiency but would reduce intake area, limiting particle collection and pressure.

3 Methodology

In rarefied gas conditions, the Navier-Stokes equations are inapplicable, necessitating the use of the Direct Simulation Monte Carlo (DSMC) method for ABEP system simulations instead of continuum methods like Computational Fluid Dynamics (CFD). These simulations are conducted using the three-dimensional open-source particle code PICLas [4], which incorporates the DSMC method [2].

The simulations conducted in this work rely on atmospheric data provided by the NRLMSISE-00 model [10], a widely accepted standard in space research for modeling lower thermospheric conditions. Previous ABEP studies have used this model, including work by Romano [12] and Kun [5]. This study uses atmospheric data under low-activity conditions based on ISO-14222 [8] and ECSS [3] standards (F10.7 = 65, $\mathrm{A_P} = 0$). A fully specular intake material is assumed to focus on geometric and environmental factors. The effect of the specularity assumption of 100% is discussed in detail in [1, 12].

Simulations examine altitudes from 150 to 250 km. The lower limit of 150 km is selected to avoid increased drag, which raises thruster power demands and thermal loads [12]. While there is no strict upper limit, at higher altitudes it becomes increasingly difficult to collect enough particles to sustain thruster operation at a reasonable specific impulse, and the benefits of close proximity to the Earth's atmosphere are lost. Additionally, numerical resources are limited, so 250 km was chosen as the upper limit here. A minimum pressure of 0.1 Pa, sufficient to ignite the ABEP thruster IPT, is assumed based on experimental results from the University of Stuttgart [6]. However, it is possible that a lower threshold pressure may be required.

Rotational symmetry of the intake allows for 2D axisymmetrical simulations in PICLas. Results are averaged across the DC radius at a z-position 164 mm downstream of the intake-DC intersection, considering variations in altitude and geometry.

4 Simulation Results

4.1 Focal Length

The position of the focal point F significantly impacts performance. This study examines three focal lengths inside the DC for a DC diameter of 25 mm: $f = [3\,\text{mm}, 3.75\,\text{mm}, 5.5\,\text{mm}]$, corresponding to $s_{F,\text{IPT}} = [10.02\,\text{mm}, 6.67\,\text{mm}, 1.60\,\text{mm}]$. A focal length of 3 mm was chosen to match earlier IRS research on a DC37 configuration, while 3.75 mm was tested to evaluate the impact of a slightly larger intake area.

Figure 2 compares efficiency Fig. 2a and mean pressure Fig. 2b. Smaller focal lengths lead to higher efficiencies at all altitudes due to better particle focusing, with 5.5 mm performing worse than diffuse intake designs (46 % [11]). Even a 0.75 mm increase of the focal length significantly reduces efficiency. Ignition pressure is reached at similar altitudes for all focal lengths: 220 km for 3.0 mm and 3.75 mm, and 230 km for 5.5 mm. Despite small pressure losses, shorter focal lengths significantly improve efficiency, making 3 mm the optimal focal length for DC25.

4.2 DC Diameter

The comparison of DC diameters used a focal length of 5.5 mm for DC37, 3 mm for DC25, and 3 mm for DC15. A shorter focal length for DC15 was avoided as it reduced the intake area, limiting particle collection.

Figure 3a shows DC25 and DC37 achieving similar efficiencies, reaching up to 94 % for a 500 mm intake length. DC15 performs significantly worse, with its 3 mm focal length resulting in lower efficiencies than DC25's 5.5 mm focal length, even

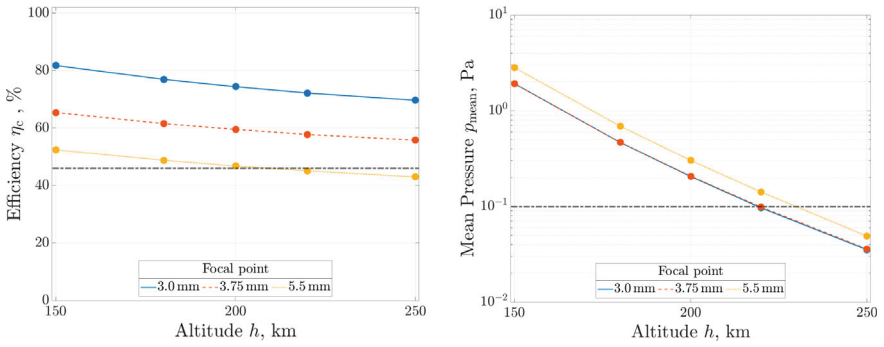

(a) Efficiency (b) Mean Pressure

Fig. 2 Efficiency and pressure levels for three different focal lengths at a DC diameter of 25 mm and a length of 1000 mm, with the black line showing the current efficiency limit for diffuse intakes (**a**) and the expected minimum pressure required for ignition of the thruster inside the DC (**b**)

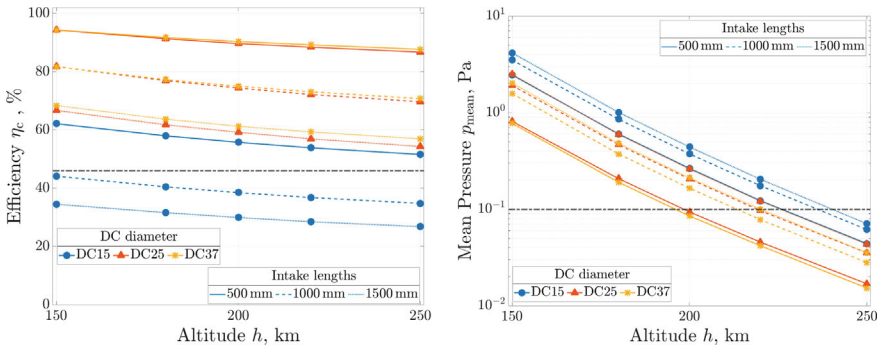

(a) Efficiency (b) Mean Pressure

Fig. 3 Efficiency and pressure levels for three different DC diameters and three different intake length over altitude, with the black line showing the current efficiency limit for diffuse intakes (**a**) and the expected minimum pressure required for ignition of the thruster inside the DC (**b**)

below diffuse designs. This highlights the need for shorter focal lengths for smaller DCs to increase $s_{F,\mathrm{IPT}}$ and outperform diffuse designs.

Figure 3b shows DC15 achieving the highest mean pressure across all intake lengths, while DC25 and DC37 show similar pressures, with DC25 slightly higher for longer intakes. As noted in [1], efficiency and pressure depend on the molecular speed ratio, with higher thermal velocities reducing particle focusing for longer intakes. DC37 excels at particle focusing, while DC25 produces more collisions, leading to higher pressure at longer intakes. Differences between DC25 and DC37 are attributed to slight variations in $s_{F,\mathrm{IPT}}$.

4.3 Comparison over Geometry

The previous results indicate a strong relationship between efficiency and $s_{F,\mathrm{IPT}}$ as the results for DC25 and DC37 were similar with comparable $s_{F,\mathrm{IPT}}$. Therefore Fig. 4a presents a comparison of all simulation results based on the vertex-to-focal point distance, $s_{F,\mathrm{IPT}}$, with error bars showing efficiency variations across altitudes. DC diameters are color-coded, and additional DC25 results for a 1000 mm intake length at $f = 3.75$ mm and $f = 5.5$ mm are included. For a given intake length, efficiency shows a linear dependency on $s_{F,\mathrm{IPT}}$, confirming that smaller focal lengths f, which increase $s_{F,\mathrm{IPT}}$, are essential for higher efficiency.

Efficiency is also analyzed as a function of intake area, which is influenced by all geometric factors. Figure 4b illustrates the results, with markers representing intake lengths and colors indicating DC diameters and focal lengths. A fitted curve demonstrates a linear relationship between efficiency and intake area across different configurations. The results indicate that DC37 consistently outperforms DC15

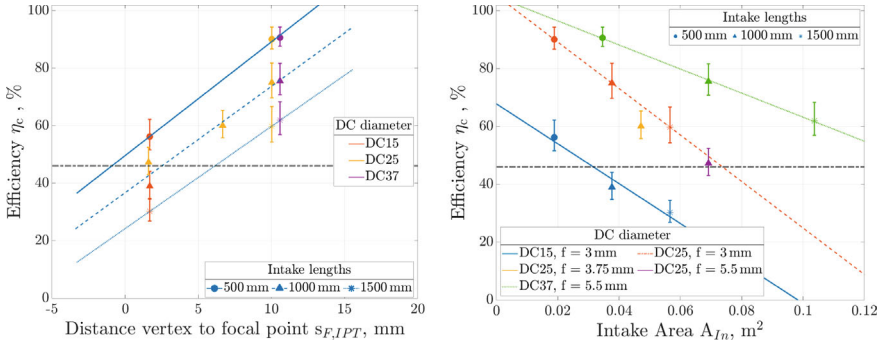

(a) Efficiency over $s_{F,\mathrm{IPT}}$ (b) Efficiency over intake area

Fig. 4 Efficiency for three different DC diameters with different focal lengths and three different intake length over $s_{F,\mathrm{IPT}}$ and intake area, with the black line showing the current efficiency limit for diffuse intakes

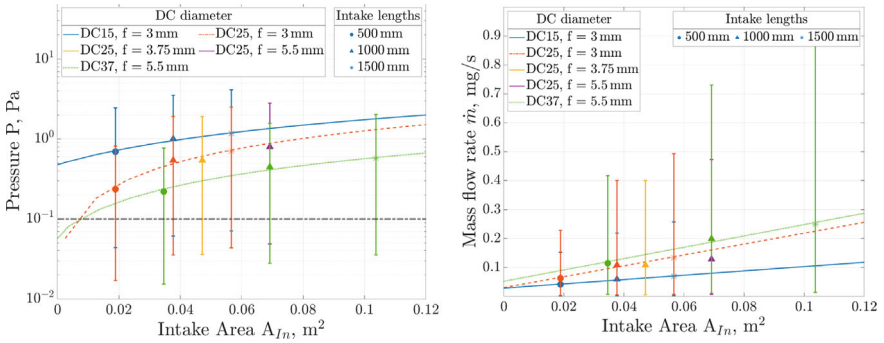

(a) Mean Pressure (b) Mass flow rate

Fig. 5 Pressure and mass flow rate for three different DC diameters and three different intake length over intake area

and DC25 in terms of efficiency. While DC25 achieves relatively high efficiency at smaller intake areas, its performance declines with longer intake lengths. This decline is expected, as focusing particles into a smaller discharge channel becomes more challenging with increased intake length. This effect is even more pronounced for DC15, where the non-optimal focal length further amplifies the limitations of the smaller discharge channel. Specular intakes outperform diffuse designs for smaller intake areas, but their advantage diminishes as intake area increases.

Efficiency alone, however, is not the sole consideration; sufficient pressure for thruster ignition must also be achieved. The ignition threshold in this study is set at 0.1 Pa, based on experimental results [6], though a lower threshold may be possible. Figure 5a shows the mean pressure in the DC, with a dotted line marking the 0.1 Pa ignition threshold. A linear fit indicates that pressure is highest for DC15 and lowest for DC37. Nonetheless, none of the configurations consistently meet the ignition

threshold across all altitudes, as error bars reveal instances where pressure falls below 0.1 Pa. The altitude at which ignition pressure is reached depends on the specific intake system. However, the results suggest that as the DC diameter decreases, the number of collected particles does not decrease proportionally, leading to a higher particle flux and, consequently, greater pressure.

Figure 5b presents the mass flow rate inside the DC, which shows a strong dependence on atmospheric conditions and altitude, as evidenced by the large error bars. Despite this variability, a clear linear trend in the mean mass flow rate across all altitudes is observed, suggesting that, for a given altitude, both mass flow rate and pressure scale linearly with the intake area. DC37 and DC25 have similar slopes for this linear relationship, while DC15 shows a less steep slope. This variation aligns with the previously discussed influence of focal length f and the resulting higher $s_{F,\mathrm{IPT}}$ values for DC25 and DC37, which improves their mass flow rate performance compared to DC15.

5 Conclusion

This simulative study of different ABEP intake geometries examines the impact of intake length, discharge channel diameter, and focal length on collection efficiency, pressure, and mass flow rates. Results indicate a linear relationship between the vertex-to-focal point distance ($s_{F,\mathrm{IPT}}$) and collection efficiency, with larger $s_{F,\mathrm{IPT}}$ resulting in higher efficiencies. For a 25 mm DC, a 3 mm focal length, resulting in $s_{F,\mathrm{IPT}} = 10$ mm, achieves efficiencies up to 94 % for a 500 mm intake length. In contrast, DC15 performs poorly due to its non-optimal larger focal length, highlighting the importance of small focal lengths for high efficiency.

Pressure within the DC is strongly influenced by geometry, with smaller DCs (e.g., DC15) producing higher pressures due to increased particle collisions but lower efficiencies, especially for longer intakes. This trade-off highlights the need to balance collection efficiency and pressure to optimize thruster performance.

Mass flow rate also has a linear dependency on intake area, mirroring the efficiency trend. DC37 and DC25 show similar slopes, while DC15 has a shallower slope due to its suboptimal focal length. Larger DC diameters, combined with optimal focal lengths, improve particle focusing, resulting in higher efficiencies and mass flow rates.

In conclusion, larger DC diameters and shorter focal lengths maximize efficiency and mass flow rates, while higher pressures are achieved with smaller DCs due to increased particle collisions. Among the configurations studied, a DC diameter of 25 mm with a 3 mm focal length offers the best balance between efficiency and pressure.

Acknowledgements This work is funded by the Deutsche Forschungsgemeinschaft project number 516238647-SFB1667/1, titled Advancing Technologies of Very Low Altitude Satellites (ATLAS). Additionally, partial support was provided by the Ram-CLEP project with the name “Technology

Enhancement of Atmosphere-Breathing Cathode-Less Electric Propulsion" funded by ESA under ITT AO/1-10597/20/NL/MG. The views and conclusions presented are solely those of the authors, and neither the Deutsche Forschungsgemeinschaft nor ESA assumes responsibility for any use of the information provided.

References

1. Barth N, Skalden J, Papavramidis K, Hild F, Pfeiffer M, Beyer J, Tietz R, Fasoulas S, Herdrich G (2025) Solar activity dependency of a specular intake for an abep system. J Electric Propulsion
2. Bird GA (1994) Molecular gas dynamics and the direct simulation of gas flows
3. ECSS-E-10-04C: space environment. Tech Rep, ESA Publications Division
4. Fasoulas S, Munz CD, Pfeiffer M, Beyer J, Binder T, Copplestone S, Mirza A, Nizenkov P, Ortwein P, Reschke W (2019) Combining particle-in-cell and direct simulation Monte Carlo for the simulation of reactive plasma flows. Phys Fluids 31(7)
5. Feng K (2023) Investigation of a novel atmosphere-breathing electric propulsion platform and intake
6. Herdrich G, Papavramidis K, Maier P, Skalden J, Hild F, Beyer J, Pfeiffer M, Fugmann M, Klinker S, Fasoulas S, Souhair N (2024) System design study of a VLEO satellite platform using the IRS RF helicon-based plasma thruster. Acta Astronautica 215:245–259
7. Herdrich G, Papavramidis K, Maier P, García-Almiñana D, Rodríguez Donaire S, Sureda Anfres M (2022) Platform and system design study of a VLEO satellite platform using the IRS rf helicon-based plasma thruster. In: Proceedings of the 73rd international astronautical congress, IAC-22-C4.9.1. International Astronautical Federation, pp 1–15
8. ISO-14222 (2013) Space environment (natural and artificial) earth upper atmosphere. Tech Rep
9. Livadiotti S, Crisp NH, Roberts PC, Worrall SD, Oiko VT, Edmondson S, Haigh SJ, Huyton C, Smith KL, Sinpetru LA, Holmes BE, Becedas J, Domínguez RM, Cañas V, Christensen S, Mølgaard A, Nielsen J, Bisgaard M, Chan YA, Herdrich GH, Romano F, Fasoulas S, Traub C, Garcia-Almiñana D, Rodriguez-Donaire S, Sureda M, Kataria D, Belkouchi B, Conte A, Perez JS, Villain R, Outlaw R (2020) A review of gas-surface interaction models for orbital aerodynamics applications. Progress Aerospace Sci 119
10. Picone J, Hedin A, Drob DP, Aikin A (2002) Nrlmsise-00 empirical model of the atmosphere: statistical comparisons and scientific issues. J Geophys Res Space Phys 107(A12): SIA–15
11. Romano F, Binder T, Herdrich G, Fasoulas S, Schönherr T (2015) Air-intake design investigation for an air-breathing electric propulsion system. Int Symp Space Technol Sci
12. Romano F, Espinosa-Orozco J, Pfeiffer M, Herdrich G, Crisp NH, Roberts P, Holmes B, Edmondson S, Haigh S, Livadiotti S, A MR (2021) Intake design for an atmosphere-breathing electric propulsion system (abep). Acta Astronautica 187:225–235
13. Romano F, Herdrich G, Chan YA, Crisp N, Roberts P, Holmes B, Edmondson S, Haigh S, Macario-Rojas A, Oiko V, Sinpetru L (2022) Design of an intake and a thruster for an atmosphere-breathing electric propulsion system. CEAS Space J 14(4):707–715

Open Access This chapter is licensed under the terms of the Creative Commons Attribution 4.0 International License (http://creativecommons.org/licenses/by/4.0/), which permits use, sharing, adaptation, distribution and reproduction in any medium or format, as long as you give appropriate credit to the original author(s) and the source, provide a link to the Creative Commons license and indicate if changes were made.

The images or other third party material in this chapter are included in the chapter's Creative Commons license, unless indicated otherwise in a credit line to the material. If material is not included in the chapter's Creative Commons license and your intended use is not permitted by statutory regulation or exceeds the permitted use, you will need to obtain permission directly from the copyright holder.

Effect of Gas-Surface Interactions on Very Low Earth Orbit Mission Operation

Sai Sudha Ramesh, Basman Elhadidi, Boo Cheong Khoo, and Wai Lee Chan

Abstract The recent surge in very low Earth orbit (VLEO) satellite operations necessitates the consideration of gas-surface interactions (GSI) to estimate the aerodynamic drag coefficient. This study utilizes the test particle Monte Carlo (TPMC) method to model the effects of GSI on orbital trajectories. The predominance of atomic oxygen (ATOX) in VLEO increases shear drag that is particularly adverse for VLEO satellite designs with large solar panels for power needs. Mitigation strategies include ATOX-resistant material coatings. This research explores drag reduction impacts on VLEO missions by using different reflective materials, which can be modeled in TPMC using GSI coefficients. Simulations indicate that specularly reflective material coatings on lateral surfaces can achieve approximately 10% thruster fuel savings and 40% longer mission operation windows, with room for improvement through optimization of mission phasing and sequencing.

Keywords Very low earth orbit · Gas-surface interactions · Test particle Monte Carlo · Satellite drag reduction · Satellite fuel efficiency

1 Introduction

The recent interest in very low Earth orbit (VLEO) satellite operations, typically defined by altitudes below 450 km [1], is primarily driven by the potential for improved image resolution, enhanced communication capabilities, reduced power requirements for data downlinking, and a lower risk of collision with space debris.

S. S. Ramesh (✉) · B. C. Khoo
Temasek Laboratories, National University of Singapore, Singapore, Singapore
e-mail: tslssr@nus.edu.sg

B. Elhadidi
School of Engineering and Digital Science, Nazarbayev University, Astana, Kazakhstan

W. L. Chan
Engineering Product Development, Singapore University of Technology and Design, Singapore, Singapore

© The Author(s) 2026

M. Grabe et al. (eds.), *Rarefied Gas Dynamics*, Springer Aerospace Technology,
https://doi.org/10.1007/978-3-032-00094-1_21

Despite the benefits of operating satellites in VLEO, a major challenge is compensating for the increased atmospheric drag, which can be up to 1000 times greater than in conventional low Earth orbits of 500 km and above. Consequently, accounting for aerodynamic drag effects is crucial in VLEO mission design and analysis.

A more rigorous approach for satellite aerodynamic analysis involves the Monte Carlo methods, which are better suited for the rarefied gas dynamics in VLEO operations. These methods account for the random thermal motion of particles through gas-surface interaction (GSI) models and consider multiple reflections from surfaces, such as antennas, solar panels, and deorbit devices [2]. Most common Monte Carlo methodologies are the test particle Monte Carlo (TPMC) and direct simulation Monte Carlo (DSMC) approaches, for which Jin et al. [2] have compared their computational efficiency and found that TPMC is 10,000 times more efficient than DSMC. This efficiency is due to DSMC's requirement for volume discretization, which TPMC does not need. However, a significant drawback of TPMC is its inability to handle intermolecular collisions, which may be prevalent at altitudes below 120 km [2]. Since typical orbits for VLEO satellites are projected to be sustained at above 200 km where free molecular flow assumption holds, this study chose to use TPMC to model the influence of gas-surface interactions (GSI) on orbital trajectories, thus implicitly opting for the computational efficiency of TPMC at the expense of the reasonable assumption of negligible intermolecular collisions.

In VLEO, the prevalence of atomic oxygen (ATOX) increases the randomness of scattered directions due to diffuse reflection, significantly contributing to shear along surfaces parallel to the incoming flow. This shear drag is particularly adverse for VLEO satellite designs with large solar panels to meet power requirements. The high concentration of atomic oxygen enhances sensitivity to gas-surface interactions, especially on elongated surfaces. A potential mitigation strategy involves applying ATOX-resistant material coatings, which can reduce drag by minimizing random reflections in the tangential direction and promoting more specular reflections. Such specularly reflective materials are suitable for orbit maintenance in VLEO [1, 3].

This study aims to compare the performance of two materials, one diffusive and one specular, using representative GSI coefficients across a range of pitch angles. The sensitivity of the drag coefficient, C_D, was analyzed over various altitudes and satellite orientations. A parametric representation of C_D variation based on satellite attitudes at a nominal altitude was incorporated into the General Mission Analysis Tool (GMAT) orbit propagator [4] to replace the traditional constant C_D value, which may not accurately predict fuel requirements. The advantage of each material type is then quantified in terms of thruster fuel requirements for a target duration in VLEO.

Accordingly, the remainder of the manuscript is organized into three sections. Section 2 presents the performance analysis of satellites using the two types of materials. Section 3 compares these materials in the context of orbit maintenance. The conclusions are presented in Sect. 4.

2 Material Performance in VLEO

The present study is based on the TPMC code that was developed by Los Alamos National Laboratory and openly available on GitHub repository [5]. The original code was modified to: (i) compute aerodynamic forces and moments; and (ii) evaluate the satellite surface pressure. The accuracy of the modified code has been verified in Reference [6]. The satellite model assumed for this study is shown in Fig. 1 at different orientations, based on a prototype of the Extremely Low Earth Orbit Imaging and Technology Explorer (ELITE) [7], a microsatellite developed by the Satellite Research Centre (SaRC) at Nanyang Technological University, Singapore, set to launch in 2026.

In this study, the interactions between impinging gas species and the satellite surface were modeled using the Cercignani–Lampis–Lord (CLL) model. This model can represent diffuse, quasi-specular, or specular reflections through the appropriate selection of two GSI parameters, namely α_n, which denotes normal energy accommodation coefficient, and σ_t, which represents tangential momentum accommodation coefficient. Since C_D depends on GSI coefficients, which determine the nature of particle reflections off the satellite surface and the resultant momentum exchange leading to aerodynamic drag, the assessment of satellite performance with GSI specifications for material coatings across various satellite attitudes is crucial. To this end, the current study considers single-axis pitch rotation to examine the impact of drag reduction on mission operations.

The thermospheric conditions for the performance analysis were derived from the NRLMSISE-00 model, based on data from March 13, 1989, during solar cycle 22 when solar activity was at its peak. Materials M1 and M2, corresponding to GSI parameters of $\{\alpha_n,\ \sigma_t\} = \{0.44,\ 0.25\}$ and $\{0.95,\ 0.78\}$, respectively, were considered. With a smaller σ_t, material M1 will lead to more specular reflections than material M2. Note that the GSI coefficients here were selected such that, under the assumption that $\alpha_n = \alpha_t$, σ_t is close to the surfaces with and without specularly reflective POSS-Novastrat coating in the study of the effects of ATOX scattering on drag reduction by Minton et al. [3]. The rationale for selecting these values is to understand their relative contributions to aerodynamic drag and their subsequent effects in mission analysis and operations.

Figure 2 compares the performances of the two materials M1 and M2 over a range of altitudes from 200–500 km and pitch angles 0° to −90°. A similar trend was

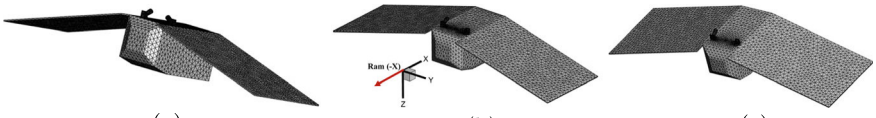

Fig. 1 Illustration of the VLEO satellite in this study modeled after ELITE [7] **a** pitch angle = −20°, **b** pitch angle = 0° and **c** pitch angle = 20°. All models have same coordinate system

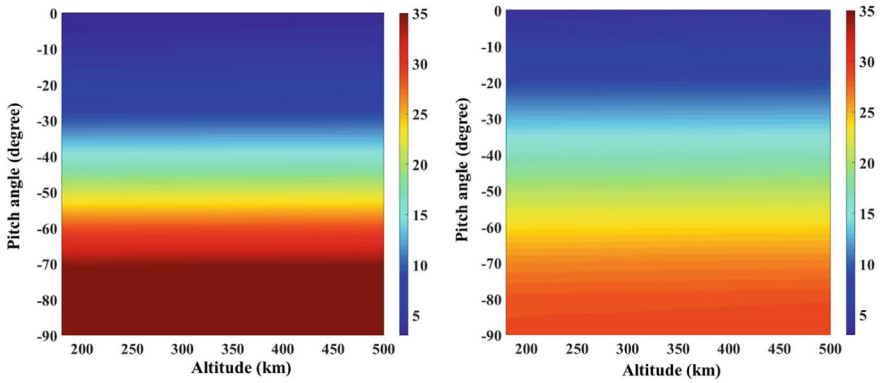

(a) Material M1 (b) Material M2

Fig. 2 C_D over a range of pitch angles and altitudes for **a** Material M1 (more specular) and **b** Material M2 (more diffusive) prescribed by GSI coefficients from Reference [3]

observed for pitch angles from 0° to 90° and so is not reported for brevity. The purpose of this analysis is to study the sensitivity of C_D to altitude and satellite orientations. Banded distributions can be observed for both materials across altitudes, indicating that C_D is insensitive to altitude variations. Conversely, there is higher sensitivity to pitch angle variations. Additionally, distinct bands are observed for M1 compared to M2, which may be attributed to less randomness in the tangential direction for the former.

Given the greater influence of pitch variations on C_D compared to altitudes as shown in Fig. 2, these variations can be approximated as a polynomial function of pitch angles at a specific altitude range. Doing so allows the incorporation of a varying C_D model with NASA GMAT [4] to assess the performance of the two materials in different mission scenarios. The parametric curves representing C_D variations for a mission scenario at a nominal altitude of 220 km for materials M1 and M2 are given in Eqs. (1) and (2), respectively:

$$C_D = 20.074\alpha^2 + 0.7143\alpha + 3.2005, \tag{1}$$

$$C_D = 258.2\alpha^4 - 263.5\alpha^3 + 106.33\alpha^2 - 1.2843\alpha + 3.6965, \tag{2}$$

where α denotes pitch angle in radians. The above equations will reasonably capture C_D variations within an altitude band of 200 to 265 km.

3 Numerical Simulation of VLEO Maintenance

The performances of the two materials were evaluated in the context of orbit maintenance, with the primary objective of quantifying thruster fuel savings and operational advantages resulting from reduced drag. The objective of this mission scenario is to

maintain an average altitude between approximately 200 km and 265 km for a duration of at least 100 days. To simulate a real mission, three operation modes are considered: OM1 for thruster operation; OM2 for nominal operation; and OM3 for attitude maneuver modes. OM1 involves the operation of an electric thruster with a specific impulse of 1200 s and a thrust output of 6 mN [8].

The thruster is activated for a specified duration, based on mission design, to maintain flight within the designated altitude band. OM2 represents the nominal operation mode, where the satellite's attitude is set with yaw, pitch, and roll angles at zero, providing the minimum drag configuration. OM3 involves attitude changes, with the pitch angle adjusting from 0° to 20° at a rate of 1°/min and maintained at 20° for a specified duration to perform mission operations.

Referring to Fig. 3, which compares C_D over pitch angles ranging from 0° to 20°, material M1, with its specularly reflective behavior, evidently has a significantly lower C_D than M2 by at least 13%. The reduced drag for M1 is attributed to its smaller σ_t, which results in a lower probability of particles contributing significantly along the flow direction, thereby reducing lateral shear. This behavior is depicted in Fig. 4 which assumes freestream velocity of 7772.5 m/s at an altitude of 220 km. The shear pressure along the solar panels is higher for M2, thus highlighting the effect of lateral shear, which leads to an increase in the drag coefficient. Interestingly, Fig. 4 also indicates that the normal pressure on the ram face of M1 is higher than M2, suggesting that specular reflection may not always be beneficial to drag reduction.

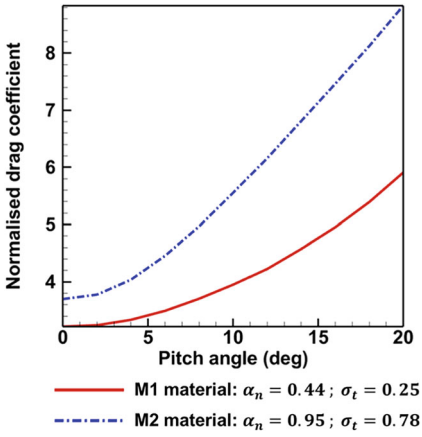

Fig. 3 C_D over a range of pitch angles for materials M1 and M2 for a nominal altitude of 220 km (altitude band between 200 km and 265 km)

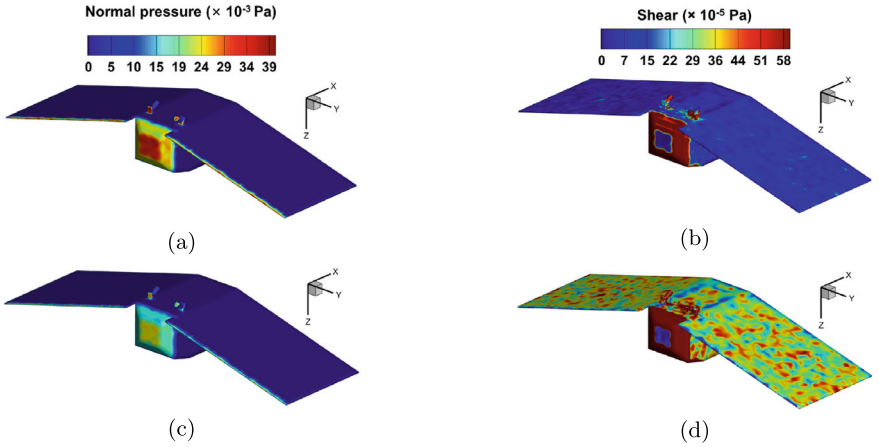

Fig. 4 Pressure distribution on satellite with materials **a**,**b** M1 and **c**, **d** M2

Table 1 presents the duration of different phases of mission operations associated with M1 and M2 to maintain VLEO flight between 200 and 265 km. The mission is divided into several phases, each consisting of a sequence of operation modes described earlier. For brevity, only the details for Phases 1 and 9 are presented (see Table 2). According to Table 1, Phase 1, with its mission sequence detailed in Table 2, is operated for 5 days and 2 days for M1 and M2, respectively. Although the current mission sequence is not optimized for M1 and M2, the mission duration and sequence for each phase were incrementally adjusted in small steps to ensure a sustained flight for 120 days. Consequently, this results in variations in the duration and phase sequences of M1 and M2.

Figure 5 compares the orbital trajectories associated with the two materials, with and without the inclusion of thruster firings. While thruster operation is essential for maintaining VLEO flight, it is advantageous to consider specularly reflective materials that reduce drag and fuel consumption compared to materials without AO-resistant coatings.

This is evident in Fig. 6, which shows that fuel depletion for M1 is approximately 10% lower than for M2 over a mission duration of 120 days. Clearly, material M1 is preferred over M2 for VLEO operations, as it aids in orbit maintenance without requiring extended thruster firing for drag compensation. Figure 6b compares the duration of mission operations for each mode, clearly demonstrating that M1 offers about a 27% reduction in thruster operation time compared to M2, ultimately allowing more time (over 40%) for nominal and attitude maneuver operations.

Table 1 Duration of different mission phases

Phase		1	2	3	4	5	6	7	8	9	10	11	12	13
Duration (days)	Material M1	5	5	20	20	8	25	8	3	32	–	–	–	–
	Material M2	2	3	20	15	12	2	10	10	10	7	8	22	12

Table 2 Duration of different operation modes in specific mission phases

Material M1	Phase 1	OM2(2)	OM1(1)	OM3(1)	OM1(1)	OM2(2)	OM3(1)
		OM2(2)	OM1(1)	OM3(1)	OM1(1)	OM2(1)	OM1(1)
	Phase 9	OM2(1) OM2(1)	OM1(3) OM1(1)	OM2(1) OM2(1)	OM1(2) OM1(2)	OM2(1)	OM1(2)
Material M2	Phase 1	OM2(2)	OM1(1)	OM3(1)	OM1(1)	OM2(2)	OM1(1)
		OM2(2)	OM1(1)	OM3(1)	OM1(1)	OM2(1)	OM1(1)
	Phase 9	OM2(2)	OM1(3)	OM2(1)	OM1(3)	OM2(1)	OM1(5)

Note Values inside parentheses indicate the number of orbital periods (approximately 5370 s) during which a particular operation mode is executed

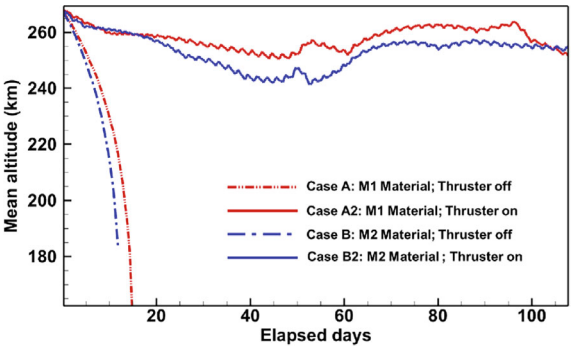

Fig. 5 Orbital trajectories in different scenarios

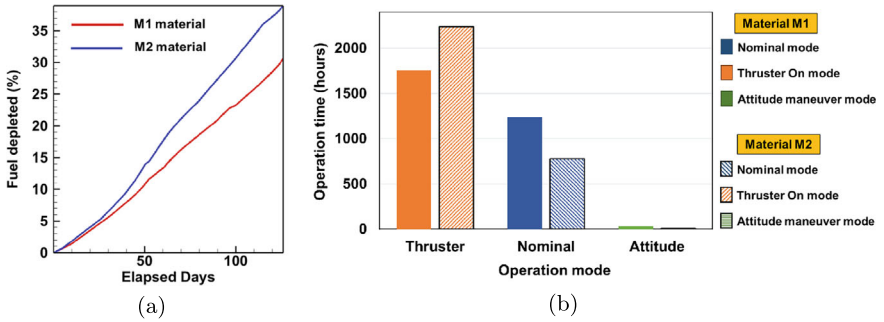

Fig. 6 Comparison of **a** percentage fuel depletion over mission and **b** duration of mission operation modes for materials M1 and M2

4 Conclusions

In this study, materials with different reflective characteristics were studied through prescription of gas-surface interaction coefficients. The reduction of drag for specularly reflective materials is attributed to a decrease in lateral shear that manifests prominently over areas that are parallel to the flow like the solar panels. However, specular reflections were also observed to increase normal pressure drag that acts along the ram face, suggesting that specularly reflective coating may not be suitable for application over all satellite surfaces. The variation of C_D was found to primarily depend on pitch variations, allowing a one-dimensional parametric representation of C_D that can be conveniently integrated with an orbit propagator. Simulations of mission scenarios with varying C_D for VLEO flight maintenance demonstrate that satellites with specularly reflective behavior can reduce drag and decrease thruster operations by 27% compared to those with diffusive materials, resulting in fuel savings of approximately 10%. In turn, this saving provides a 40% larger time window for scientific operations or small attitude maneuvers, thus benefiting the overall mission. Possible future studies include the exploration of selective specification of gas-surface interaction parameters on a satellite design, better characterization of gas-surface interaction coefficients, more robust incorporation of varying C_D model into an orbit propagator, and optimization of VLEO mission phasing and sequencing.

Acknowledgements This study is funded by the Office of Space Technology and Industry, Singapore, under the grant S21-19003-STDP. The computational work for this paper was performed on resources of the National Supercomputing Center, Singapore (https://www.nscc.sg).

References

1. Crisp N, Roberts P, Hanessian V, Sulliotti-Linner V, Herdrich G, García-Almiñana D, Kataria D, Seminari S (2022) A method for the experimental characterisation of novel drag-reducing materials for very low earth orbits using the satellite for orbital aerodynamics research (SOAR) mission. CEAS Space J 14:655–674
2. Jin X, Huang F, Cheng X, Wang Q, Wang B (2019) Monte Carlo simulation for aerodynamic coefficients of satellites in low-Earth orbit. Acta Astronaut 160:222–229
3. Minton T, Schwartzentruber T, Xu C (2021) On the utility of coated POSS-polyimides for vehicles in very low Earth orbit. ACS Appl Mater Interfaces 13:51673–51684
4. https://opensource.gsfc.nasa.gov/projects/GMAT/index.php
5. https://github.com/AndrewCWalker/impact-tpmc
6. Ramesh SS, Elhadidi B, Khoo BC, Chan WL (2025) Aerodynamic force and moment computations for very low Earth orbit satellites using a TPMC model. Acta Astronaut 228:88–100
7. Athreyas KN, Zhang X, Lim WS, Ramesh SS, Khoo BC, Chan WL (2024) Extremely low earth orbit imaging and technology explorer (ELITE): a very low earth orbit mission. In: 38th Small satellite conference, pp SSC24-II-03
8. Potrivitu G-C, Laterza M, Agarwal D, Sun X, Lim JWL (2024) Performance and plume characterization of the multi-stage ignition compact (MUSIC) hall effect thruster. In: 38th IEPC, pp IEPC-2024-586

Open Access This chapter is licensed under the terms of the Creative Commons Attribution 4.0 International License (http://creativecommons.org/licenses/by/4.0/), which permits use, sharing, adaptation, distribution and reproduction in any medium or format, as long as you give appropriate credit to the original author(s) and the source, provide a link to the Creative Commons license and indicate if changes were made.

The images or other third party material in this chapter are included in the chapter's Creative Commons license, unless indicated otherwise in a credit line to the material. If material is not included in the chapter's Creative Commons license and your intended use is not permitted by statutory regulation or exceeds the permitted use, you will need to obtain permission directly from the copyright holder.

Internal Flows in Vacuum Systems

Numerical Analysis of Rarefied Gas Flows Induced by Rotor-Stator Blades

Hiroshi Sugimoto, Ayako Miki, and Shogo Sugimoto

Abstract The unsteady gas flow in the two-dimensional model of the turbo-molecular pump is analyzed using the Boltzmann and BGK equations. The deterministic solver enables the visualization of instantaneous behavior in the time-periodic state induced by the rotor-stator system. A more straightforward explanation of the driving mechanism of the turbo-molecular pump is proposed, which leads to the alternative design of the pump. The combination of the traveling finite volume and the spherically designed grid enables the simulation of the full Boltzmann equation to be carried out by a personal computer.

Keywords Turbo-molecular pump · Moving boundary · Finite volume · Spherical design

1 Introduction

The turbo-molecular pump (TMP) may be the most common main pump. It has a high compression ratio and flow speed, and its easy handling is adequate for many laboratories and factories. Gaede proposed its original idea [1], but it made significant advances for practical usage after the improvement by Becker [2] at Pfeiffer Vacuum to have rotors and stators (both of them consist of many blades) stacked alternatively. Because the pressure inside TMP is low, we need the Boltzmann equation to analyze the behavior of the gas for its development and improvements. The problem here is that the direct numerical solution of the Boltzmann system used to be a challenging task due to its complex collision integral. The Direct Simulation Monte Carlo (DSMC) is one of the options [3, 4] to avoid this difficulty. However, the flow in TMP is time-dependent because the rotor blades rotate with a velocity close to

H. Sugimoto (✉) · A. Miki · S. Sugimoto
Department of Aeronautics and Astronautics, Kyoto University, Kyoto, Japan
e-mail: sugimoto.hiroshi.7s@kyoto-u.ac.jp

© The Author(s) 2026

M. Grabe et al. (eds.), *Rarefied Gas Dynamics*, Springer Aerospace Technology,
https://doi.org/10.1007/978-3-032-00094-1_22

sound speed; DSMC results are limited to time averages since present computational resources require some averaging process. Therefore, in the present study, we use our deterministic solver, Traveling Finite Volume method, to clarify the instantaneous flow field in the time-periodic behavior in TMP.

2 Numerical Model

We have to use the simplest model that can reproduce the gas flows in TMP since we do not yet have much information on the time variation of the rarefied gas in the device. Therefore, we throw away everything that is not essential and follow the model proposed by Sharipov [4]. Figure 1 presents our 2D model of TMP. The model consists of two arrays of slanted plates. The red plates, which are a substitute for the rotor of TMP, are slanted with θ_{R} and move in the direction of the yellow arrow with a constant speed v_R. The black plates at rest are substitutes for the stator. The plates are inversely slanted, and the angle is denoted by θ_{S}. The temperature of the plates is uniform at T_0. A rarefied gas with average number density n_0 fills the space between the plates. The regions between red plates are identified by part R, and those between black plates by part S. In the present study, two arrays share the same spacing (in the direction of plate motion) between the plates and the height of the slanted plates. They are denoted by, respectively, D and H. We define X_1 and X_2 axis as shown in the figure.

We numerically analyze the unsteady behavior of the gas under the following assumptions. (i) The gas behavior is periodic with period D in the X_1 direction, and (ii) the behavior is also periodic with period H in the X_2 direction. The latter assumption forces the pressure along the pump axis (i.e., along X_2 direction) periodic. Therefore, the analysis in the present paper targets only the open (or the maximum) flow rate of the device.

3 Governing Equations

The rarefied gas in the model obeys the Boltzmann equation

$$\frac{\partial F}{\partial t} + \boldsymbol{\xi} \cdot \frac{\partial F}{\partial \boldsymbol{X}} = J\,[F]\,, \tag{1}$$

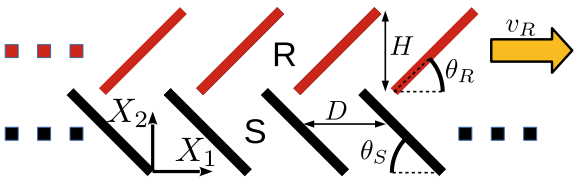

Fig. 1 2D model of the rotor-stator system. We assume periodicity both in X_1 and X_2 direction

where t is the time, $\boldsymbol{X}$ is the spatial coordinate, $\boldsymbol{\xi}$ is the molecular velocity, F is the velocity distribution function and $J[F]$ is the collision term. For the hard-sphere molecule with molecular mass m and diameter d_{m},

$$J_{\mathrm{HS}}[F] = \frac{d_{\mathrm{m}}^2}{2} \int_{\boldsymbol{\zeta}\in\mathbb{R}^3,\, \boldsymbol{\alpha}\in\mathbb{S}^2} \left[F\left(\boldsymbol{\xi}'\right) F\left(\boldsymbol{\zeta}'\right) - F(\boldsymbol{\xi}) F(\boldsymbol{\zeta})\right] |\boldsymbol{V}\cdot\boldsymbol{\alpha}| \mathrm{d}\Omega(\boldsymbol{\alpha})\, \mathrm{d}\boldsymbol{\zeta}, \quad (2)$$
$$\boldsymbol{V} = \boldsymbol{\zeta} - \boldsymbol{\xi},\ \boldsymbol{\xi}' = \boldsymbol{\xi} + (\boldsymbol{V}\cdot\boldsymbol{\alpha})\boldsymbol{\alpha},\ \boldsymbol{\zeta}' = \boldsymbol{\zeta} - (\boldsymbol{V}\cdot\boldsymbol{\alpha})\boldsymbol{\alpha},$$

where $\mathrm{d}\boldsymbol{\zeta} = \mathrm{d}\zeta_1 \mathrm{d}\zeta_2 \mathrm{d}\zeta_3$ and $\mathrm{d}\Omega(\boldsymbol{\alpha})$ is the solid angle element in the direction of $\boldsymbol{\alpha}$ on a unit sphere $\mathbb{S}^2$. Since the numerical simulation by J_{HS} requires a significant amount of computational resources, we mainly use the BGK model instead:

$$J_{\mathrm{BGK}}[F] = A_C n (F_E - F),\ F_E(n, \boldsymbol{v}, T; \boldsymbol{\xi}) = \frac{n}{(2\pi\kappa T/m)^{3/2}} \exp\left(-\frac{|\boldsymbol{\xi}-\boldsymbol{v}|^2}{2\kappa T/m}\right), \quad (3)$$

where A_C is a constant to give the collision frequency by $A_C n$, F_E is the Maxwellian belonging to number density n, flow velocity $\boldsymbol{v}$, and temperature T. The Boltzmann constant is denoted by κ. The values of n, $\boldsymbol{v}$, etc., are defined by the moments of F as

$$n = \int_{\boldsymbol{\xi}\in\mathbb{R}^3} F\, \mathrm{d}\boldsymbol{\xi} \quad n\boldsymbol{v} = \int_{\boldsymbol{\xi}\in\mathbb{R}^3} \boldsymbol{\xi} F\, \mathrm{d}\boldsymbol{\xi}, \quad p = \frac{1}{3}\int_{\boldsymbol{\xi}\in\mathbb{R}^3} |\boldsymbol{\xi}-\boldsymbol{v}|^2 F\, \mathrm{d}\boldsymbol{\xi} = \kappa n T. \quad (4)$$

The boundary condition on the solid wall (velocity $\boldsymbol{v}_w$, temperature T_0, and inward normal $\boldsymbol{n}_w$) is the diffuse reflection:

$$F((\boldsymbol{\xi}-\boldsymbol{v}_w)\cdot\boldsymbol{n}_w > 0) = F_E(\sigma_w, \boldsymbol{v}_w, T_0; \boldsymbol{\xi}) \quad (5)$$

where the number density σ_w is determined by the wall impermeability condition $(\boldsymbol{v}-\boldsymbol{v}_w)\cdot\boldsymbol{n}_w = 0$.

4 Method of Analysis

We use a deterministic numerical scheme that uses the spherical designed grid and the traveling finite volume method as in [5].

4.1 Spherical Designed Grid

The spherical design [6] is a set of points $\boldsymbol{a}_k$ $(1 \le k \le N_\Omega)$ on $\mathbb{S}^2$ arranged so that the average of a smooth function f on them approximates the average on $\mathbb{S}^2$:

$$\frac{1}{4\pi}\int_{\boldsymbol{a}\in\mathbb{S}^2} f\left(\boldsymbol{a}\right)\mathrm{d}\Omega\left(\boldsymbol{a}\right) \approx \frac{1}{N_\Omega}\sum_{k=1}^{N_\Omega} f\left(\boldsymbol{a}_k\right). \tag{6}$$

Equation (6) achieves the same accuracy of numerical integral of (4), which is essential for the BGK collision term (3), with a several orders small number of grid points $\boldsymbol{\xi}_{\ell,k} = \xi_\ell \boldsymbol{a}_k \ \left(1 \le \ell \le N_\xi\right)$ using the curvilinear coordinate $\mathrm{d}\boldsymbol{\xi} = \xi^2 \mathrm{d}\xi \mathrm{d}\Omega\left(\boldsymbol{a}\right)$ (cf. [5]). The impact is immense in the hard-sphere model J_{HS} since the four of the quintuple integral in (2), which is the reason for the dense computation, can be replaced by (6). The rest of the work is to carry out the one-dimensional numerical integral with some interpolation process and be carried out by personal computers.

4.2 Traveling Finite Volume Method

The traveling finite volume (TFV) method to solve the Boltzmann Eq. (1) is a finite volume method [7], with the only difference being the application of the characteristic coordinate (i.e., the motion path of the molecules) [5]. The TFV effectively avoids the numerical derivative across the discontinuity of F, a common feature of rarefied gas flows around convex bodies. See [5] for more details.

Before applying TFV, we reshape the parallelogram domains in Fig. 1 into rectangles in Fig. 2a by the appropriate linear transformation $\boldsymbol{Y} = \mathsf{A}\boldsymbol{X}$. The form of A depends on the size of rectangle. Examples for part R are

$$\mathsf{A} = \begin{pmatrix} 1 & -\cot\theta_{\mathsf{R}} & 0 \\ 0 & 1 & 0 \\ 0 & 0 & 1 \end{pmatrix} \text{(keep height), or } \begin{pmatrix} 1 & -\cot\theta_{\mathsf{R}} & 0 \\ 0 & \csc\theta_{\mathsf{R}} & 0 \\ 0 & 0 & 1 \end{pmatrix} \text{(keep edge length).}$$

LHS of (1) changes its form to $\dfrac{\partial F}{\partial t} + (\mathsf{A}\boldsymbol{\xi}) \cdot \dfrac{\partial F}{\partial \boldsymbol{Y}}$, but TFV is robust for this change since the molecular motion (i.e., the definition of the characteristics) can incorporate the matrix A in the form of $\mathsf{A}\boldsymbol{\xi}$. Then we introduce the moving frame $\boldsymbol{Y}'$ with

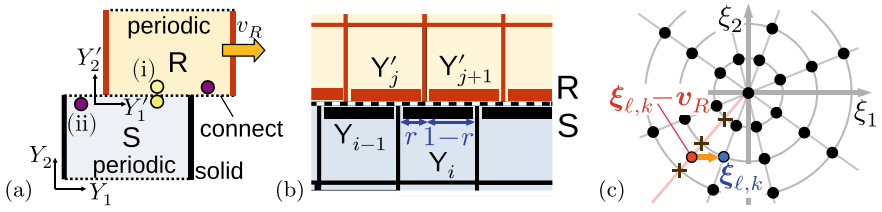

Fig. 2 **a** Moving frame in R, **b** ratio r among cell boundaries in R and S, and **c** a schematic of the interpolation process in $\boldsymbol{\xi}$-space to obtain the value at $\boldsymbol{\xi}_{\ell,k}$ in S, which corresponds $\boldsymbol{\xi}_{\ell,k} - \boldsymbol{v}_R$ in the moving frame in R. The set of grid points $\{\boldsymbol{\xi}_{\ell,k}\}$ in R are indicated by black points

speed $\boldsymbol{v}_R = (v_R, 0, 0)$. Part R rests in the moving frame, as part S does in the original frame. Therefore, we can calculate the gas flows in the model shown in Fig. 1 by investigating the gas in the regions at rest, only by introducing an appropriate coordinate transformation between R and S at their connection surfaces.

Figure 2b shows the boundaries of the finite volume cells between R and S parts. The boundaries in S (indicated by Y_{i-1} and Y_i in the figure) generally differs from those in R (Y'_j and Y'_{j+1}). When Y_i straddles Y'_j and Y'_{j+1} in the ratio $r : 1-r$, we apply

$$F_i = r\,F'_j + (1-r)\,F'_{j+1}\ \ (\mathsf{R} \to \mathsf{S})\,, \quad F'_j = (1-r)\,F_{i-1} + r\,F_i\ \ (\mathsf{S} \to \mathsf{R})\,. \tag{7}$$

We use the former to obtain the distribution function F_i in Y_i from F'_j and F'_{j+1} for molecules moving $\mathsf{R} \to \mathsf{S}$ with velocity $\boldsymbol{\xi}_{\ell,k}$, which belong to the grid points in S), and the latter vise versa. Since we use a moving frame in R, $\boldsymbol{\xi}_{\ell,k}$ in S maps to $\boldsymbol{\xi}_{\ell,k} - \boldsymbol{v}_R$ in R, and it does not fall onto the grid points $\boldsymbol{\xi}_{\ell,k}$ in R as shown in Fig. 2c. Thus we need an interpolation process: (i) we approximate F at all radii in the direction of $\boldsymbol{\xi}_{\ell,k} - \boldsymbol{v}_R$ [i.e., the points + in Fig. 2c], and (ii) interpolate the target value at $\boldsymbol{\xi}_{\ell,k} - \boldsymbol{v}_R$ from these points.

The pair of $\left(\mathsf{Y}_i, \mathsf{Y}'_j\right)$ along with the ratio r vary with time t. It is easy to calculate them if the corresponding cells are in touch as indicated (i) in Fig. 2a. In the case of (ii) there, the cell runs out of the range of the cells of the other region. We can find the corresponding cells even in these cases since we assume the periodicity in the X_1 direction. Since we choose the time step Δ_t evenly divides the wing time-period

$$T_C = D/v_R, \tag{8}$$

we only have to prepare T_C/Δ_t patterns of $\left(\mathsf{Y}_i, \mathsf{Y}'_j, r\right)$.

5 Results and Discussion

Firstly, we present the time evolution of the BGK solution at Knudsen number $\mathrm{Kn} = \ell_0/D = 1$ ($\ell_0 = 2c_0/\sqrt{\pi}A_C n_0$: reference mean free path, $c_0 = \sqrt{2\kappa T_0/m}$: most probable speed), wing speed $v_\mathrm{R} = 0.5c_0$, the wing angle $\theta = \theta_\mathrm{R} = \theta_\mathrm{S} = \pi/4$, and $\sqrt{2}H = D$. Figure 3a shows the time variation of the pump flow speed $-v_2$ of the gas. The black line plots the average $\overline{v}_2\,(t)$ in the gas defined by

$$\overline{h}\,(t) = \int_{\mathrm{gas}} h\,(X_1, X_2, t)\ \mathrm{d}X_1\mathrm{d}X_2 \Big/ \int_{\mathrm{gas}} \mathrm{d}X_1\mathrm{d}X_2 \tag{9}$$

versus the non-dimensional time t/t_0 ($t_0 = D/c_0$). The gas starts to move in the $-X_2$ direction right after the motion of the rotor at $t = 0$, then, $\bar{v}_2$ approaches a time-periodic state synchronous to the wing time-period T_C in a few periods. We

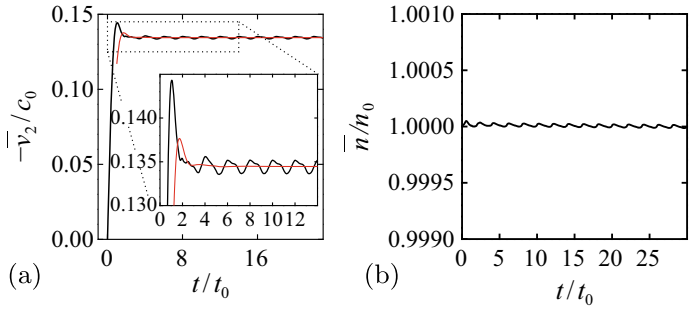

Fig. 3 Time evolution of the average **a** pump flow speed $\overline{v_2}\,(t)$ (black line) and **b** number density $\overline{n}/n_0$. The red line in **a** is the moving average $[\overline{v_2}]\,(t)$

confirm the approach to the quasi-steady state by introducing the moving average

$$\left[\,\overline{h}\,\right](t) = \frac{1}{T_C}\int_{t-T_C}^{t} \overline{h}\,(\tau)\;\mathrm{d}\tau. \tag{10}$$

The behavior of $-\,[\overline{v_2}]\,(t)$ [red line in Fig. 3a] indicates that several time-periods are sufficient to form the quasi-steady state. From the viewpoint of the numerical procedure, the approach to a steady state can be disturbed by the lack of mass conservation. However, this is not the case for the present result due to the superior conservative feature of the finite volume method; Fig. 3b shows the time variation of the average number density $\overline{n}$, which must be theoretically constant in this closed system. The value of $\overline{n}$ remains close to n_0, although it shows slight vibration resulting from calculating the time-integral of $J\,[F]$.

Figure 4 shows the time-periodic state's pressure (color) and flow velocity (arrows) distributions. The flow velocity distribution relative to the blade position remains almost unchanged despite the motion of the blades. The zero thickness of the blades and the large mean free path by $\mathrm{Kn} = 1$ can be the reason for the stable feature. Slight variation is discernible for the pressure field, but $\partial p/\partial X_1$ remains negative in R and positive in S throughout the period. Its size increases as the wing angle θ, as shown in Fig. 5a, which shows the distribution of p and $\boldsymbol{v}$ for $\theta = \pi/6$ and $\pi/3$. (The

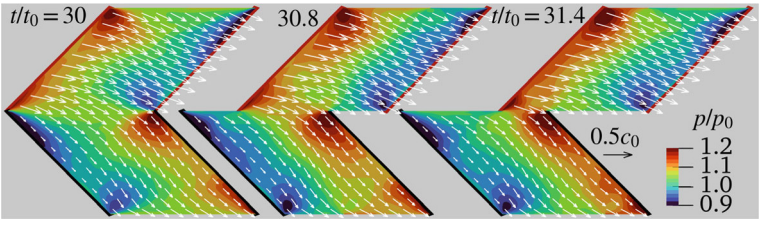

Fig. 4 Flow velocity and pressure field in the time-periodic state. The case for Fig. 3. $p_0 = \kappa n_0 T_0$

value of p for $\theta = \pi/3$ ranges in $0.8 \lesssim p/p_0 \lesssim 1.4$ and exceeds the color range of the figure). The flow speed $-[\overline{v_2}]$ at the quasi-steady state increases as θ, and takes its maximum value around $\theta \sim \pi/3$ (Fig. 5b).

The nonuniform pressure distribution results from the rotor's motion; the molecules entering R from S are more likely to collide with the wall at $-X_1$ side than at $+X_1$ side since walls in R move in the X_1 direction. Therefore, molecules accumulate near the wall at $-X_1$ side. This is the reason for the negative $\partial p/\partial X_1$ in R. On the contrary, the molecules entering S from R mainly collide with the $+X_1$ wall since the wall moves in the $-X_1$ direction relative to R. The positive $\partial p/\partial X_1$ in S shows it. The difference in the number of molecules colliding with the wall between two sides explains why TMP works. As shown in Fig. 6a, the wall surfaces with many molecules invariably face downward (i.e., $-X_2$ direction), and those with lesser molecules always face upward ($+X_2$ direction). As a result, the molecules move downward on average since diffusely reflected molecules must have a velocity normal to the wall, and $\cos\theta$ of the normal is its X_2 component.

The above explanation of the mechanism of TMP is more straightforward than those in the original work in [2]. It can explain the pressure distribution between the blades, giving the reason for the peak θ of the flow speed $-[\overline{v_2}]$ since $\cos\theta \to 0$ as $\theta \to \pi/2$. It also clarifies that the gas flow is a linear phenomenon despite the v_R of the commercial products being close to c_0. Our additional results (omitted here due to the limited space) show that $[\overline{v_2}] \propto v_R$ $(0 < v_R \lesssim c_0)$, as the early work [4]

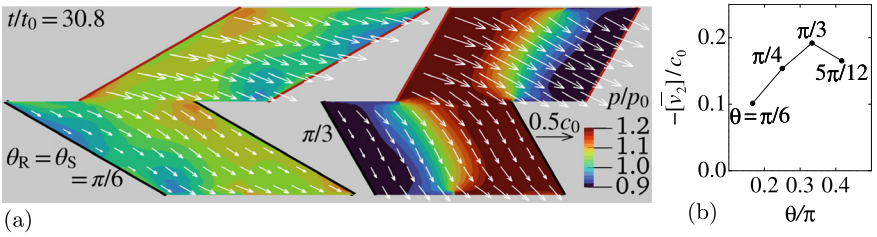

Fig. 5 Effect of the angle $\theta = \theta_R = \theta_S$ for $2H = D$, Kn $= 1$, and $v_R/c_0 = 0.5$,**a** te pressure and flow velocity distribution at $t/t_0 = 30.8$ for $\theta = \pi/6$ and $\pi/3$, **b** average flow speed $-\overline{v_2'}$ at time periodic state versus the angle of the wing $\theta = \theta_R = \theta_S$

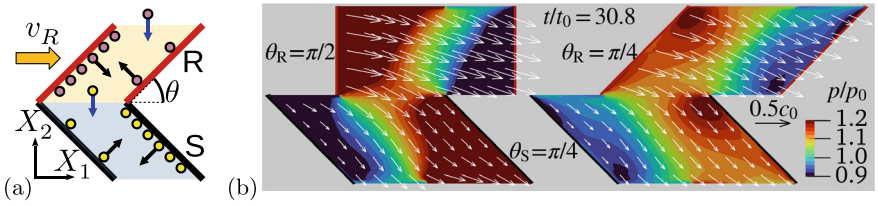

Fig. 6 **a** Driving mechanism of TMP, **b** alternative design of TMP. The distribution of p and $\boldsymbol{v}$ for $2H = D$, Kn $= 1$, and $v_R/c_0 = 0.5$, and $\theta_S = \pi/4$. Left is the case for $\theta_R = \pi/2$ and the right $\theta_R = \theta_S$

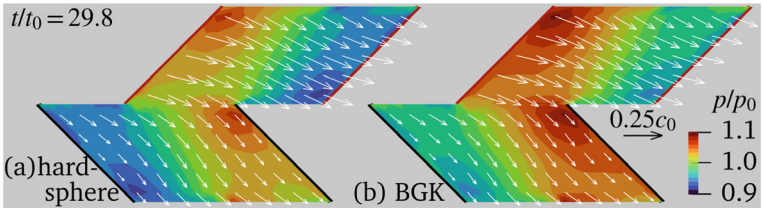

Fig. 7 Comparison between **a**the hard-sphere model and **b** the BGK model. $\theta = \pi/4$, $2H = D$, Kn $= 0.2$, and $v_R/c_0 = 0.25$

reports. Instead, we provide a result for a slightly different design of TMP in Fig. 6b, where the cases for $\theta_R = \pi/2$ and $\pi/4$ are compared. The standing plate of $\theta_R = \pi/2$ induces a greater pressure non-uniformity compared with the standard case $\theta_R = \theta_S$. The significant difference in the pressure (i.e., the number of molecules on the wall surface) results in a slightly stronger flow in the $-X_2$ direction. This result implies that the motion of the wall in the rotor is essential, but the wing-like shape is not.

Finally, we consider the dependency on the collision model. Figure 7 compares the results with J_{HS} in (a) and J_{BGK} in (b). The calculation of J_{HS} is heavy even with the spherical design (6) for unsteady 2D flows. Hence, we use coarser grids in both cases in Fig. 7. That is, each of R and S is divided into 10×5 finite volume cells, time step $\Delta_t/t_0 = 0.05$, and $N_\xi \times N_\Omega = 48 \times 94$, while these values are, respectively, 20×10 cells, time step 0.005, and $N_\xi \times N_\Omega = 48 \times 192$ in Figs 5a and 6b. The two models share the same qualitative feature of $\boldsymbol{v}$ and p distributions. The pressure variation for BGK is slightly larger than that for HS, while the flow speed $[\overline{v_2}]$ differs by only 1.2 %. We do not determine whether the reason is the difference in the collision term or the difference in the mean free path (cf. $\ell_0 = 1/\sqrt{2}\pi d_m^2 n_0$ for HS) at present since our additional calculation shows that $[\overline{v_2}]$ is insensitive to Kn. Reference [4] supports the insensitivity to Kn for the present problem. However, it further reports that the pressure ratio obtained by blocking the flow varies much for small Kn. This implies a possibility of a more significant impact on collision models in pressure-related problems, which should be addressed in future studies. We performed present computations by a computer with a 32-core CPU, and the simulation for period T_C requires 10 d for HS and 4 min for BGK.

6 Conclusion

We have visualized the unsteady behavior of the gas in the 2D model of TMP using the deterministic solver of the Boltzmann and BGK equations. The behavior of the gas obtained leads to a simple explanation of the driving mechanism of TMP, which helps explain various characteristics of TMP. Furthermore, the new explanation derives an alternative design of the pump. The qualitative feature of the gas flow is insensitive to the collision model, although the present results are limited to the case of open

flow of the pump device. The effect of the pressure load for various Kn, θ_*, ... will be reported in the forthcoming paper.

Acknowledgements This work is supported by JSPS grant-in-aid 24K07303.

References

1. Gaede W (1913) Die molekularluftpumpe. Annalen der Physik 346(7):337–380
2. Becker W (1966) The turbomolecular pump, its design, operation and theory; calculation of the pumping speed for various gases and their dependence on the forepump. Vacuum 16(11):625–632
3. Bird GA (2011) Effect of inlet guide vanes and sharp blades on the performance of a turbomolecular pump. J Vac Sci Technol A 29(1)
4. Sharipov F (2010) Numerical simulation of turbomolecular pump over a wide range of gas rarefaction. J Vac Sci Technol 28(6):1312–1315
5. Imazu R, Sugimoto H, Itou M (n.d.) Numerical study on the one-way flow between plates of different temperatures with periodic accommodation distribution. In: Proceedings of the 33rd International symposium on rarefied gas dynamics. Springer Nature, Cham (Submitted in this issue)
6. Womersley RS (2018) Efficient spherical designs with good geometric properties. Springer International Publishing, Cham, pp 1243–1285. https://doi.org/10.1007/978-3-319-72456-0_57
7. LeVeque RJ (2002) Finite volume methods for hyperbolic problems. In: Cambridge Texts in Applied Mathematics. Cambridge University Press, Cambridge

Open Access This chapter is licensed under the terms of the Creative Commons Attribution 4.0 International License (http://creativecommons.org/licenses/by/4.0/), which permits use, sharing, adaptation, distribution and reproduction in any medium or format, as long as you give appropriate credit to the original author(s) and the source, provide a link to the Creative Commons license and indicate if changes were made.

The images or other third party material in this chapter are included in the chapter's Creative Commons license, unless indicated otherwise in a credit line to the material. If material is not included in the chapter's Creative Commons license and your intended use is not permitted by statutory regulation or exceeds the permitted use, you will need to obtain permission directly from the copyright holder.

Micro-Tapered-Tubes Flow Analysis via DSMC and Experimental Methods

Christos Tantos, Foteini Litovoli, Franz Schweizer, Lucien Baldas, Juergen J. Brandner, Jan Gerrit Korvink, Thomas Giegerich, and Marcos Rojas-Cárdenas

Abstract A numerical and experimental analysis was performed on pressure-driven flows through micro-tapered tubes, which were fabricated using Two-Photon Polymerization additive manufacturing. Special emphasis was placed on the crucial role of uncertainties associated with the geometric size characterization. The constant volume technique was employed for experimental characterization, and nitrogen was used as the working gas. The DSMC method was utilized for the numerical part. The mass flow rate results show a good agreement between experiments and DSMC, within the numerical and experimental uncertainties. This study highlights the importance of DSMC as an effective tool for flow characterization in 3D microscale structures and of the TPP as a novel manufacturing technique for complex microfluidic devices working with rarefied gas flows.

Keywords Microfluidics · Tapered microchannels · DSMC · Two-photon-polymerization manufacturing

1 Introduction

The correct characterization and modeling of gas flows in microdevices enables the further development of micro-electro-mechanical systems (MEMS). As an extension of constant cross-section tubes and channels, tapered flow configurations are of

C. Tantos (✉) · F. Litovoli · T. Giegerich
Institute for Technical Physics (ITEP), Karlsruhe Institute of Technology (KIT), Karlsruhe, Germany
e-mail: christos.tantos@kit.edu

F. Schweizer · J. J. Brandner · J. G. Korvink
Institute of Microstructure Technology (IMT), Karlsruhe Institute of Technology (KIT), Karlsruhe, Germany

F. Schweizer · L. Baldas · M. Rojas-Cárdenas
Institut Clément Ader (ICA), Université de Toulouse, CNRS, INSA Toulouse, ISAE-SUPAERO, IMT Mines Albi, UT3, Toulouse, France

© The Author(s) 2026

M. Grabe et al. (eds.), *Rarefied Gas Dynamics*, Springer Aerospace Technology,
https://doi.org/10.1007/978-3-032-00094-1_23

increasing interest, because of their potential applications in various technological fields, including aerospace [1] and vacuum technologies [2].

Over the past decade, gas flow through tapered channels has become an increasingly attractive area of study for modelers in the rarefied gas dynamics community. These types of flow configurations have been studied throughout a wide range of gas rarefaction using mainly two different numerical approaches. The first approach, originally proposed in [3] for long tubes of variable radius, is based on mass conservation and its main advantage is that, as a 1D method, it allows fast calculations of the mass flow rate and pressure distribution along the flow direction. Due to its simplicity, this methodology has also been applied to analyze single gas flows through rectangular channels with variable cross-section [4]. Its effectiveness is well-established for channels with large length-to-radius ratios and relatively low variations of radius along the axis of the channel [5, 6]. The second approach is more computationally demanding and involves the complete solution of the flow field within the tapered channel using either Direct Simulation Monte Carlo (DSMC) or Discrete Velocity Method (DVM). Several studies in the literature have used the DSMC or DVM methods to investigate flows through diverging or converging channels, formed by parallel plates placed at a relative angle to each other [6–8]. To the best of our knowledge, most experimental studies on tapered micro-channels focus on planar geometries [1], with limited modeling of tapered tubes [5].

The scope of the present work is to study the computed and measured mass flow rates in pressure-driven flows through micro-tapered tubes manufactured via Two-photon-polymerization additive fabrication technique. Specific attention was given to the analysis of the crucial role of geometric size characterization. The paper is organized as follows. In Sect. 2, the experimental setup and the fabrication of the tapered channel are described. In Sect. 3, the simulated flow configuration and the numerical results are analyzed. In Sect. 4, the experimental and numerical results are presented and discussed, and in Sect. 5 the main conclusions are summarized.

2 Experimental Setup Methodology (Fabrication and the Characterization of the Tapered Channel)

The tapered channel structure was fabricated using Two-Photon-Polymerization (TPP), which is an additive manufacturing technique based on the local polymerization of a liquid photosensitive resin. This fabrication technique was previously utilized for the fabrication of straight microtubes for rarefied gas flows applications [9]. The working principle of the manufacturing technique is illustrated in Fig. 1a. After a droplet of resin (IP-Q, Nanoscribe GmbH) is deposited on a substrate, a femtosecond pulsed laser is focused and directed through the resin with controlled trajectory. The resin solidifies when the threshold of energy intensity is reached. This is only the case in the focus point of the laser, thus generating ellipsoidal voxels. The structure was fabricated by overlapping these ellipsoidal voxels with a slicing distance of 5

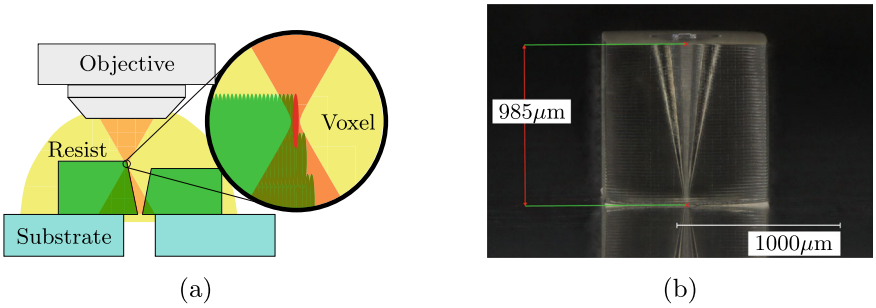

Fig. 1 **a** Schematic of the TPP process; **b** microscope image of the tapered channel

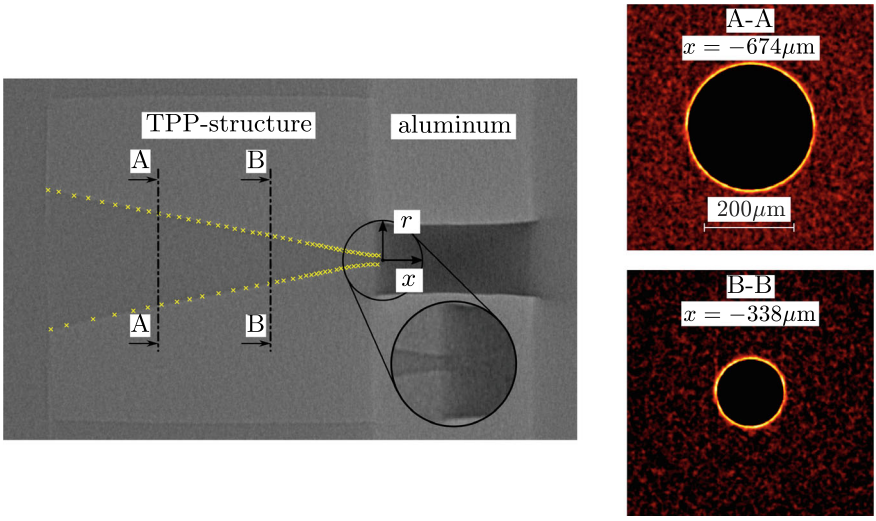

Fig. 2 Tomography image with radius measurement points and cross-sections. Not all measurement points are shown to avoid the overlapping of measurement markers

µm and a lateral hatching distance of 1 µm. After the printing process the sample was submerged in propylene glycol methylether acetate (PGMEA) for a total of 14 h to dissolve the uncured resin. Lastly the structure was rinsed in a solvent and left to dry at 7 °C for 30 min. The fabrication process therefore took approximately 15.5 h, including a printing time of 1 h.

As visible in Fig. 1b the tapered channel was written inside a polymer cube of roughly 1 mm × 1 mm × 1 mm. The structure was deposited on an aluminum substrate of the dimensions 25 mm × 25 mm × 0.5 mm. Furthermore the aluminum substrate encompasses a circular orifice of 200 µm in diameter. This orifice is aligned with the channel to enable the connection of the nozzle of the channel to the experimental setup (Fig. 2). The radius of the channel varies linearly from 215–14 µm over a length of 1012 µm. A high aspect ratio microtube with a circular cross-section,

Table 1 **a** Coefficient values of the polynomials for the radius function $R(x)$; **b** experimental campaign initial conditions

(a)

a_0	13.6 μm
a_1	0.01597
a_2	2.57822e-3 μm^{-1}
a_3	1.868179e-5 μm^{-2}
a_4	9.156089e-8 μm^{-3}
a_5	3.0165235e-10 μm^{-4}
a_6	6.5164167e-13 μm^{-5}
a_7	8.9978361e-16 μm^{-6}
a_8	7.6065986e-19 μm^{-7}
a_9	3.5761114e-22 μm^{-8}
a_{10}	7.150218e-26 μm^{-9}
b_0	111.1 μm
b_1	-6.83e-2
b_2	2.09e-4 μm^{-1}
b_3	-7.9e-08 μm^{-2}

(b)

	Converging		Diverging	
Case	P_A [Pa]	P_B [Pa]	P_A [Pa]	P_B [Pa]
1	210.0	10.0	10.0	206.4
2	303.3	103.2	104.3	304.3
3	409.0	209.0	205.1	401.4
4	505.0	209.0	305.3	505.3
5	604.0	404.0	405.5	599.6
6	705.1	505.1	504.8	700.4
7	800.2	600.2	602.4	802.4
8	902.2	702.2	703.6	901.0
9	1001.7	802.1	802.9	999.7
10	1104.2	904.2	902.6	1097.1
11	1202.4	1002.4	1001.6	1197.8
12	1298.9	1099.1	1101.0	1297.1

whose size varies, is thus obtained. Previous experimental investigations of tapered microchannels have mostly relied on standard planar micro-machining of silicon [1] or micro-milling of metals [10]. Owing to the limitations of these methods only rectangular cross-sections were investigated.

The geometry of the present channel was characterized using a EasyTom XL tomograph (RX Solutions). The resulting tomograms showed an isotropic pixel size of 2.77 μm and were analyzed to extract the internal geometry of the channel. The diameter variation along the length of the channel was measured on the symmetry plane of the channel (Fig. 2, left). The geometry measurement was performed via an edge detection algorithm. Since the nozzle geometry has a critical influence on the flow field, a higher number of measurements were obtained for this region. Furthermore, as it can be seen in Fig. 2 (right), the circularity of the tapered channel cross-section is of excellent quality. To smooth the measurement results, two polynomials were used: the $10th$ order polynomial for the tapered channel section ($R(x) = \sum_{i=0}^{10} a_i x^i$, $-1012\ \mu m \leq x \leq 0$) and a $3rd$ order polynomial for the section inside of the aluminum substrate ($R(x) = \sum_{j=0}^{3} b_j x^j$, $0 \leq x \leq 458\ \mu m$). The coefficients of the polynomials are given in Table 1a.

The flow properties of the channel structure were experimentally investigated utilizing the constant volume technique. This very well established technique relates pressure variation to mass variation in a constant volume [9, 11, 12]. The experimental methodology consisted in setting an initial pressure difference between inlet and outlet of the tapered channel and then allowing the thermodynamic system to relax to equilibrium. The mass flow rate generated through the channel creates a pressure

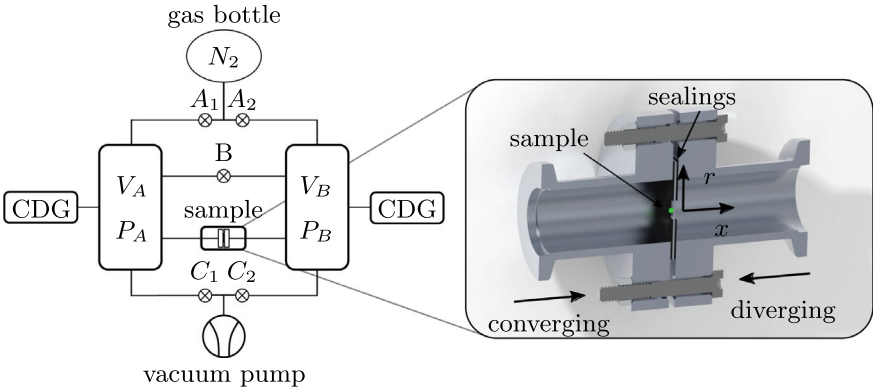

Fig. 3 Constant volume technique experimental setup and sample clamping technique

variation in the inlet and outlet tanks. The initial pressure conditions are specificied in Table 1b. Figure 3 shows a schematic of the used flow setup. The substrate of the flow sample was clamped in a casing using rubber seals. Furthermore the sample was connected to the two volumes V_A and V_B where the pressures P_A and P_B were acquired by Capacitance Diaphragm Gauges (CDG) with full ranges of 1333 Pa and an accuracy of 0.2% of reading. The average pressure and applied pressure difference in the setup could be controlled through the valves $A_{1,2}$ and $C_{1,2}$ which were connected to a pressurized nitrogen bottle and a vacuum pump. This setup allowed initial conditions $P_A > P_B$ for converging flow experiments and $P_A < P_B$ for diverging flow experiments.

The mass flow rate from the volumes and therefore through the sample can be calculated using the ideal gas law assuming isothermal conditions in the volumes $V_{A,B}$ as

$$\dot{m}_{A,B} = \frac{V_{A,B}}{R_g T_0} \frac{\mathrm{d}P_{A,B}}{\mathrm{d}t}, \tag{1}$$

with R_g and T_0 being the specific gas constant and the temperature in the experimental room. The uncertainty of the mass flow rate measurement was estimated to be roughly 3% following the propagation of uncertainty principle taking into account the uncertainty of the volume $V_{A,B}$, the temperature T_0 and pressure $P_{A,B}$ measurements. A more detailed description of the uncertainty estimation is outlined in [11]. The experiments were carried out in a temperature-controlled room ($T = 293.15\mathrm{K} \pm 0.5\mathrm{K}$), justifying the assumption of isothermal conditions in the volumes $V_{A,B}$. Details on the method can be found in [11, 12].

3 Numerical Modeling

The simulated flow setup includes the TPP structure (i.e., the tapered tube) and the substrate area (Fig. 4). The modeling domain corresponds to the physical domain extracted from tomography measurements. In the present model, the open borders (dashed lines) of the channel were maintained at different pressures (P_A and P_B). Two flow directions were considered: the converging flow with $P_A > P_B$ and the diverging flow with $P_A < P_B$, with the corresponding pressure ratio π defined as P_B/P_A and P_A/P_B respectively. In the modeling, the temperature of the solid walls and the gas at the open boundaries were maintained constant at $T_0 = 293.15$ K. Additionally, due to the axisymmetric nature of the flow, only a radial slice of the domain ($r > 0$) was considered. Thus, only two physical dimensions were taken into account, namely the $x-$ and $r-$ axis.

Based on the pressure values shown in Table 1b, the Knudsen number, calculated using the throat radius and the average pressure, ranges from 0.3 to 3.6. This suggests that the gas flow is in the transitional flow regime. In the present work, the Direct Simulation Monte Carlo method proposed by G. A. Bird [13] was applied to describe the flow behavior in the examined microstructure. Over the last few decades, it has evolved into a powerful and well-established numerical tool for studying phenomena over the whole range of the Knudsen number, making it well-suited for the flow problem addressed in this paper. For further details on the DSMC method the reader is referred to G. A. Bird's book [13]. In the present work, the effective collision scheme known as the No-Time-Counter (NTC) method, enhanced by the Variable Hard Sphere (VHS) model introduced by Bird, was used. The VHS model combines the simplicity of a hard-sphere scattering law with the flexibility of a variable collision cross-section, allowing for accurate representation of gas behavior under varying flow conditions. Based on the viscosity data for N_2 [14], the reference VHS diameter d_{ref} and the viscosity index ω for the examined flow conditions are taken as 4.11×10^{-10} m and 0.74 respectively. The gas-surface interaction was modeled based on the Diffuse-Specular model, in which a non-complete accommodation is assumed, while axisymmetric flow was also considered. By analyzing the available data in the literature on the accommodation coefficient α, it can be deduced that for typical technical surfaces without special treatment, a value between 0.9 and 1 is generally

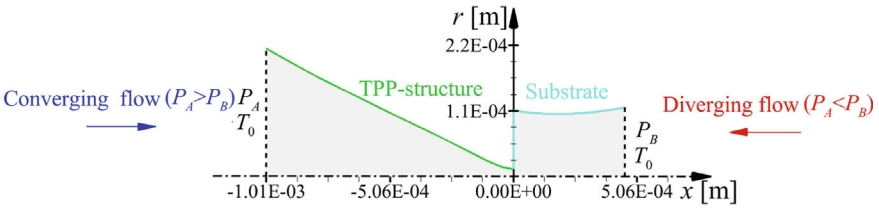

Fig. 4 Schematic view of the flow set-up considered in the present study. The gray area represents the computational domain

expected for N_2 [15, 16]. The computational grid consisted of 128,000 elements. The global cell size was $\Delta x = \Delta r = 1.34 \times 10^{-6}$ m, while in the region R = ($0 < r < 4 \times 10^{-5}$ m, -1.13×10^{-4} m $< x < 7.8 \times 10^{-5}$ m) the cell size was reduced three and six times in the $x-$ and $r-$ directions, respectively. It is noted that, cell size was chosen to be significantly smaller than the mean free path of the gas molecules. The number of DSMC particles varies from 33×10^6 to 40×10^6, with a minimum of at least 30 particles per cell. In order to maintain, as much as possible, uniform distributions of particles at each cell in the whole computational domain, the concept of the weighting factor widely applied in literature has been introduced. The time step Δt has been chosen to be sufficiently smaller (about 1/3) than the cell transversal time, defined as $\min(\Delta r, \Delta x)/u_0$ with u_0 being the most probable speed at reference temperature T_0 and Δr (or Δx) is the cell size in $r-$ (or $x-$) direction. The gas macroscopic quantities are obtained by time averaging over 10^7 time steps after the steady-state has been reached. In this type of pressure driven flows it is often essential to include two large reservoirs at the inlet and outlet of the channel to ensure the proper application of boundary conditions [5, 6, 8, 15]. For this specific setup, simulations using reservoirs up to eight times larger than the corresponding radius at the channel ends demonstrated no significant impact on the mass flow rate (within 1.5%). Consequently, the reservoirs are excluded from the configuration to save computational resources. The applied DSMC code has been successfully compared with results from kinetic models in [17].

4 Results and Discussion

In Fig. 5, a comparison between the DSMC data and the corresponding experimental ones is performed for both converging and diverging flow set-ups. The numerical and experimental data are in very good qualitative agreement for both configurations. As for the reference case, namely, $\alpha = 1$ and reference radius function $R(x)$ (see Table 1a), the comparison shows a consistent error of approximately 20%, which, while not negligible, is within an acceptable range given the geometrical fabrication complexity and the challenges associated with its experimental characterization. It is noted that, the DSMC results consistently underestimate the experimental results. To investigate and understand the sources of this deviation, we first examine the assumption of diffuse boundary conditions. For this purpose, we performed additional simulations assuming incomplete accommodation on the wall, with an accommodation coefficient $\alpha = 0.9$, which stands as the lowest expected value for the considered flow conditions. The corresponding results for $\alpha = 0.9$ are also shown in Fig. 5 for comparison purposes. As it is seen, a decrease in the accommodation coefficient of about 10% causes an increase in the mass flow rate about 10% bringing the DSMC data closer to the experimental ones. This can be considered the maximum uncertainty associated with the imposed pure diffuse boundary conditions.

Another important aspect that we investigated is the potential uncertainty related to the precise definition of the geometry, which remains challenging due to the small

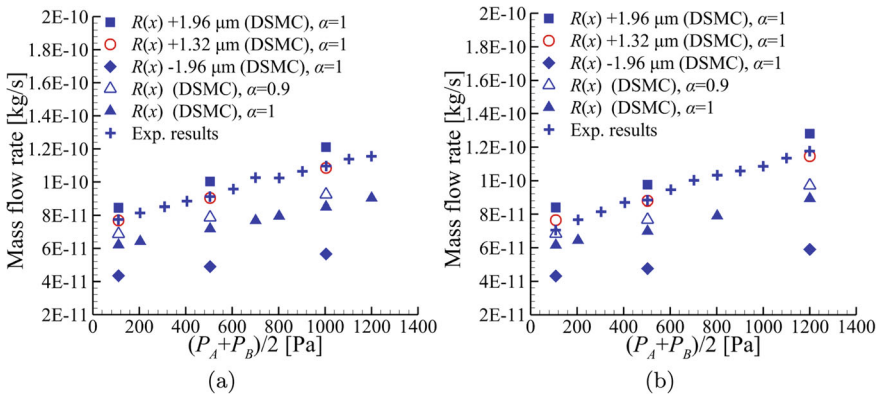

Fig. 5 Comparison of the mass flow rate between the DSMC and the experimental results for converging **a** and diverging **b** flow

scale of the channel. The uncertainty related to this measurement was estimated via a propagation of uncertainty principle. The radius measurement can be understood as a distance between two points. The position of either point has an uncertainty of $\pm dx/2$ (i.e. dx is the voxel size). Assuming both position measurements are not correlated, the uncertainty on the distance measurement is 1.96 μm corresponding to $\pm\sqrt{2}dx/2$. Additional simulations were performed by adding and subtracting 1.96 μm to the radius at each point in the flow direction, corresponding to the estimated uncertainty of the geometry measurement. As it is observed, the geometry uncertainties affect significantly the comparison between DSMC and experimental results. However, the experimental data are always within the two limits imposed by the DSMC simulations, with the experimental results showing better agreement with the larger radius geometry. Based on the above findings we can conclude that an acceptable agreement between the DSMC and experimental data is achieved, given the uncertainties associated with the geometry characterization and gas surface interaction modeling. Based on the mass flow rate data shown in Fig. 5, an attempt was made to estimate the potential radius increase required to obtain acceptable agreement between DSMC and experiments. Interpolation of the data showed that a uniform increase of 1.32 μm resulted in a very good agreement between the experimental and DSMC results with an average error over the entire pressure range of about 2%. This holds true for both examined flow configurations in a very consistent manner. For the sake of clarity and consistency, the corresponding results with $R(x)$+1.32 μm are also shown in Fig. 5. This level of agreement highlights the capability of such a kinetic modeling to complement experimental investigations, particularly in scenarios where the precise definition of the geometry is challenging due to the small scale of the channel.

Figure 6 shows indicative pressure and velocity contours for both converging and diverging flows for the case 1 of Table 1b. This case corresponds to the one with the largest inlet-to-outlet pressure ratio, namely $\pi \approx 0.05$. The velocity contours

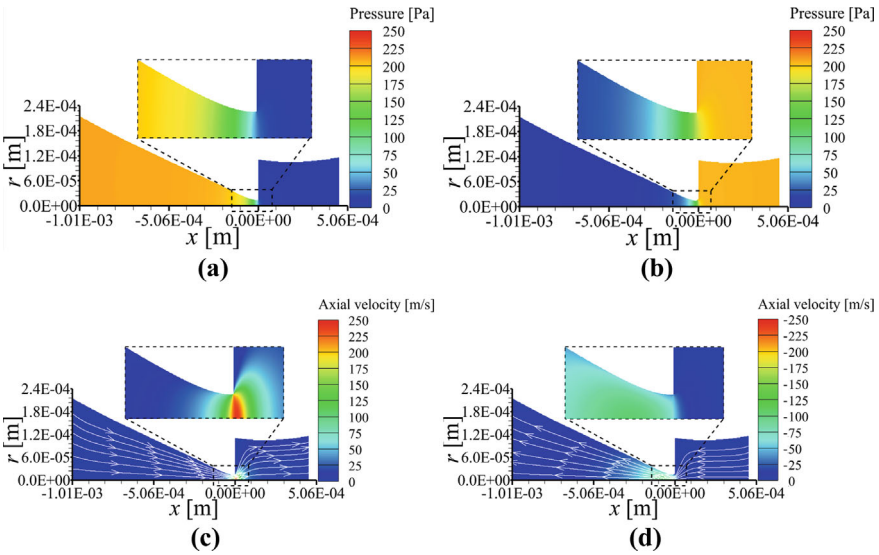

Fig. 6 Contours of pressure **a**, **b** and velocity **c**, **d** for converging **a**, **c** and diverging **b**, **d** flow, for case 1 ($\pi = 0.05$)

are overlaid by the velocity streamlines. The results show that for both pressure and axial velocity, the greatest variations are observed around the throat at $x = 0$. Similar qualitative behavior was observed for all the examined cases in Table 1b. It is observed that the radial pressure change is not very significant, whereas the radial velocity change is more pronounced, with the maximum values always occurring close to the axis of symmetry $r = 0$, a well-known behavior due to the wall friction effects.

In order to gain a better quantitative understanding of the changes in the macroscopic quantities, the axial distributions of velocity, temperature and pressure are shown in Fig. 7. Two cases are plotted, namely case 1 with $\pi \approx 0.05$ and 8 with $\pi \approx 0.8$, which correspond to high and low inlet-to-outlet pressure ratios, respectively. As can be seen, the velocity remains uniform and noticeably small far from the throat, while it shows strong variations in the throat region. By comparing the velocity profiles of cases 1 and 8, it can be easily deduced that the velocity is an increasing function of the pressure difference. The local Mach number always remains below 0.7 in converging flow direction and below 0.3 in diverging flow direction. In the converging direction, as the gas moves toward the throat, the decreasing area causes it to accelerate (due to the conservation of mass). In the diverging flow, however, the opposite occurs: the gas velocity reaches its maximum after the throat due to expansion effects, and then decreases due to the less resistance to the gas flow as a consequence of the increase in the area. As stated above, the gas flow accelerates as it passes through the narrow area at throat, which leads to an increase in kinetic energy, and part of this energy is extracted from the thermal energy, resulting in

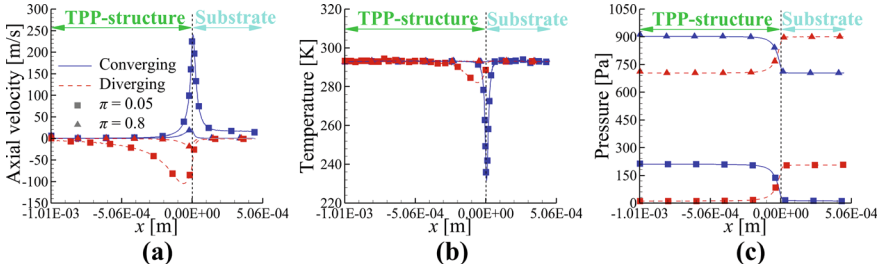

Fig. 7 Axial distributions of the axial velocity **a**, temperature **b** and pressure **c** at $r = 0$

a drop in temperature, as observed from the axial temperature distributions. It is noted that, as the inlet-to-outlet pressure drop decreases, the temperature of the gas flow approaches the wall temperature, and the flow shows isothermal characteristics. Finally, the axial pressure distributions show that the pressure remains uniform and close to its equilibrium values at the two entrances of the flow configuration, while a rapid change in pressure is observed near the throat, coinciding with the aforementioned increase in velocity.

5 Conclusions

This study presents, for the first time, a comparative analysis of experimental and numerical results for pressure-driven flows through micro-tapered tubes manufactured via two-photon-polymerization. The characterization of the flow is performed experimentally via the constant volume technique, as well as numerically via the DSMC method. A good comparison between the experimental and numerical data is observed, given all the uncertainties regarding the geometry characterization and the modeling assumptions which have been quantified in a detailed manner. This study shows that DSMC is a powerful tool for modeling rarefied gas flows in complex microstructures and for characterizing micro-device geometries in meso-scale configurations, where optical or X-ray measurements are challenging. In the future, we plan to extend both the experimental and numerical aspects of this analysis to more complex microstructures with varying cross-sections, relevant to aerospace and vacuum technologies.

Acknowledgements This work was carried out with the support of the Karlsruhe Nano Micro Facility (KNMFi, www.knmf.kit.edu), a Helmholtz Research Infrastructure at Karlsruhe Institute of Technology (KIT). The Research Federation FERMaT (FR 3089, Toulouse - France) is acknowledged for access to its Easy Tom XL X-ray tomograph. This work was supported by computational time granted from the National Infrastructures for Research and Technology S.A. (GRNET S.A.) in the National HPC facility - ARIS - under project ID pr015027-FUSFLOWSIM.

References

1. Alexeenko AA, Levin DA, Gimelshein SF, Collins RJ, Markelov GN (2002) Numerical simulation of high-temperature gas flows in a millimeter-scale thruster. J Thermophys Heat Transf 16. https://doi.org/10.2514/2.6667
2. López Quesada G, Tatsios G, Valougeorgis D, Rojas-Cárdenas M, Baldas L, Barrot C, Colin S (2020) Thermally driven pumps and diodes in multistage assemblies consisting of microchannels with converging, diverging and uniform rectangular cross sections. Microfluid Nanofluid 24:54 . https://doi.org/10.1007/s10404-020-02357-z
3. Sharipov F, Bertoldo G (2005) Rarefied gas flow through a long tube of variable radius. J Vac Sci Technol A 23:531–533. https://doi.org/10.1116/1.1897703
4. Graur I, Ho MT (2014) Rarefied gas flow through a long rectangular channel of variable cross section. Vacuum 101:328–332. https://doi.org/10.1016/j.vacuum.2013.07.047
5. Titarev VA, Shakhov EM, Utyuzhnikov SV (2014) Rarefied gas flow through a diverging conical pipe into vacuum. Vacuum 101:10–17. https://doi.org/10.1016/j.vacuum.2013.07.030
6. Tantos C, Litovoli F, Teichmann T, Sarris I, Day C (2024) Numerical study of rarefied gas flow in diverging channels of finite length at various pressure ratios. Fluids 9:78. https://doi.org/10.3390/fluids9030078
7. Ebrahimi A, Roohi E (2017) DSMC investigation of rarefied gas flow through diverging micro/nanochannels. Microfluid Nanofluid 21:18. https://doi.org/10.1007/s10404-017-1855-1
8. Sazhin O, Sazhin A (2023) Rarefied gas flow into vacuum through linearly diverging and converging channels. Int J Heat Mass Transf 203:123842. https://doi.org/10.1016/j.ijheatmasstransfer.2022.123842
9. Zhang D, López Quesada G, Bergdolt S, Hengsbach S, Bade K, Colin S, Rojas-Cárdenas M (2023) 3D micro-structures for rarefied gas flow applications manufactured via two-photon-polymerization. Vacuum 211:11915. https://doi.org/10.1016/j.vacuum.2023.111915
10. Graur I, Veltzke T, Méolans JG, Ho MT, Thöming J (2015) The gas flow diode effect: theoretical and experimental analysis of moderately rarefied gas flows through a microchannel with varying cross section. Microfluid Nanofluid 18:391–402. https://doi.org/10.1007/s10404-014-1445-4
11. Silva E, Deschamps CJ, Rojas-Cárdenas M, Barrot-Lattes C, Baldas L, Colin S (2018) A time-dependent method for the measurement of mass flow rate of gases in microchannels. Int J Heat Mass Transfer 120:422–434. https://doi.org/10.1016/j.ijheatmasstransfer.2017.11.147
12. Rojas-Cárdenas M, Silva E, Ho MT, Deschamps CJ, Graur I (2017) Time-dependent methodology for non-stationary mass flow rate measurements in a long micro-tube. Microfluid Nanofluid 21:86. https://doi.org/10.1007/s10404-017-1920-9
13. Bird GA (1994) Molecular gas dynamics and the direct simulation of gas flows. Clarendon Press, Oxford, Oxford Engineering Science Series
14. Boushehri A, Bzowski J, Kestin J, Mason EA (1987) Equilibrium and transport properties of eleven polyatomic gases at low density. J Phys Chem Ref Data 16:445-466. https://doi.org/10.1063/1.555800
15. Sharipov F (2016) Rarefied gas dynamics. Wiley-VCH Verlag GmbH & Co, KGaA, Weinheim, Germany
16. Yousefi-Nasab S, Safdari J, Karimi-Sabet J, Norouzi A, Amini E (2019) Determination of momentum accommodation coefficients and velocity distribution function for Noble gas-polymeric surface interactions using molecular dynamics simulation. Appl. Surf. Sci. 493:766–778. https://doi.org/10.1016/j.apsusc.2019.07.033
17. Tantos C, Varoutis S, Day C (2020) Deterministic and stochastic modeling of rarefied gas flows in fusion particle exhaust systems. J Vac Sci Technol B 38:064201. https://doi.org/10.1116/6.0000491

Open Access This chapter is licensed under the terms of the Creative Commons Attribution 4.0 International License (http://creativecommons.org/licenses/by/4.0/), which permits use, sharing, adaptation, distribution and reproduction in any medium or format, as long as you give appropriate credit to the original author(s) and the source, provide a link to the Creative Commons license and indicate if changes were made.

The images or other third party material in this chapter are included in the chapter's Creative Commons license, unless indicated otherwise in a credit line to the material. If material is not included in the chapter's Creative Commons license and your intended use is not permitted by statutory regulation or exceeds the permitted use, you will need to obtain permission directly from the copyright holder.

Analysis of Propellant Gas Suppression in Shattered Pellet Injector System of the ITER Experiment

Ákos Gyenge, Richárd László Csiszár, and Balázs Farkas

Abstract Plasma disruptions in tokamak fusion reactors like ITER threaten reactor equipment. To mitigate these events, a Shattered Pellet Injector (SPI) system using cryogenic solid pellets propelled by high-pressure gas was developed at the HUN-REN Centre for Energy Research. A suppressor system, consisting of multiple chambers and separators, was designed to capture the expelled gas. Computational Fluid Dynamics (CFD) simulations and experimental pressure measurements revealed that while CFD accurately predicts pressure peaks in the suppressor compartments, it struggles with gas expansion velocity. Experimental tests show gaps and leaks significantly influence pressure evolution. Findings indicate the suppressor retains some propellant gas but loses efficiency without a pellet. These insights help to develop disruption mitigation strategies for ITER.

Keywords Vacuum-expansion · CFD · Pressure measurement · Fusion technology

1 Introduction

In fusion reactors, such as the International Thermonuclear Experimental Reactor (ITER), plasma disruptions can occur when an instability grows to the point where the stored thermal and magnetic energy is rapidly discharged [3]. A shattered pellet injector (SPI) is planned to mitigate these disruptions and prevent them from damaging the device's plasma-facing wall. With this technique, a 28.5 mm-diameter, cylindrical cryogenic solid pellet is accelerated by a gas pulse and shattered on a plate near the plasma. The resulting fragments dilute and cool the plasma. An SPI injector

Á. Gyenge · R. L. Csiszár
HUN-REN Centre for Energy Research, Institute for Atomic Energy Research, Budapest, Hungary

Á. Gyenge (✉) · B. Farkas
Faculty of Mechanical Engineering, Department of Fluid Mechanics, Budapest University of Technology and Economics, Budapest, Hungary
e-mail: gyenge.akos@ek.hun-ren.hu

© The Author(s) 2026

M. Grabe et al. (eds.), *Rarefied Gas Dynamics*, Springer Aerospace Technology,
https://doi.org/10.1007/978-3-032-00094-1_24

was developed at the HUN-REN Centre for Energy Research in Budapest (CER) [7]. The solid protium, deuterium or noble gas pellets are propelled by high-pressure gas, which has a higher velocity than the pellet. For magnetohydrodynamic stability, it is disadvantageous if the gas reaches the plasma first. A gas suppressor was designed for the SPI system to prevent the propulsion gas from entering the reactor. To the authors' knowledge, this is the first operational evacuated gas suppressor for such cryogenic pellet injectors. The first half of the SPI test system is depicted in Fig. 1.

During operation, the suppressor volume is evacuated below 0.01 mbar absolute pressure before firing. Due to the low pressure, the gas in the suppressor system is initially considered slightly rarefied (Knudsen number with respect to pellet diameter is around 0.4). In the high-pressure zone, the Knudsen number is significantly lower; therefore, in the expanding gas, the continuum assumption holds. To investigate the developing flow field within the gas retention system and predict the amount of the propellant gas which could potentially reach the plasma, a series of CFD simulations were conducted. This research has two main objectives: first, to present an experimental study of a novel gas-retention system intended for use in fusion reactors; and second, to evaluate the suitability of commercial CFD tools for modelling the expansion of high-pressure gas into a slightly rarefied environment.

1.1 Eddy-Current Actuated Fast Valve

An eddy-current actuated fast valve was designed and built at EK-CER for with two adjustable launch parameters: the initial pressure (up to 100 bar) and the opening voltage (up to 1200 V) [4, 5]. The valve has view ports, where the piston movement is visually observed. The displacement is used as a boundary condition for CFD simulations.

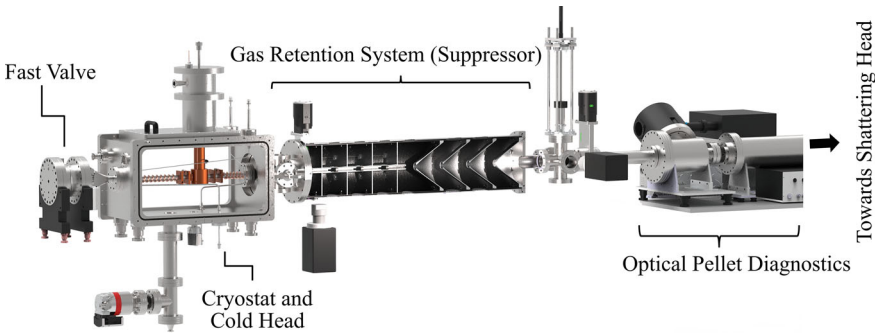

Fig. 1 First half of the Shattered Pellet Injector (SPI) system

1.2 The Suppressor System

In the CER SPI support laboratory, A suppressor model was built and instrumented with pressure sensors and cameras to validate the simulations experimentally. The suppressor is comprised of eight chambers, separated by flat and conical walls for optimal propellant recovery. The first half of the suppressor contains a guiding tube with rectangular cutouts for the gas to escape. The tubular duct serves two purposes: it guides the pellet, and holds the compartment separation plates, which are welded to it. Consequently, a small gap exists between the separator plate edge and the suppressor's inner cylindrical surface. The conical separators are held in place from the outside, allowing an airtight separation at the sides of the chambers.

Each chamber is equipped with a port for Keller M5-HB 0-3 bar fast pressure sensor. Only three pressure sensors are used at a time due to limitations in the data acquisition system. Sensors 1 and 9 are located on the base surfaces, 100 mm from the axis, while sensors 2–8 are placed on the cylindrical surface at 136, 266, 396, 526, 766, 906 and 1046 mm from the base, placing one sensor in each compartment. A close-up view of the suppressor and the pressure ports is presented in Fig. 2.

2 Simulations and Measurements on the Suppressor

2.1 CFD Simulations

A series of simulations was conducted on the SPI system with and without a pellet in ANSYS Fluent software. Although the presence of a slightly rarefied region would typically invoke the use of non-continuum modelling techniques, we chose to use this commercially available CFD solver for multiple reasons. Fluent is the designated tool for fluid dynamics simulations in the ITER project, making it important to assess its suitability for the present study. Secondly, the rarefied regime occurs only locally, just ahead of the expansion front, while the majority of the gas remains in the continuum

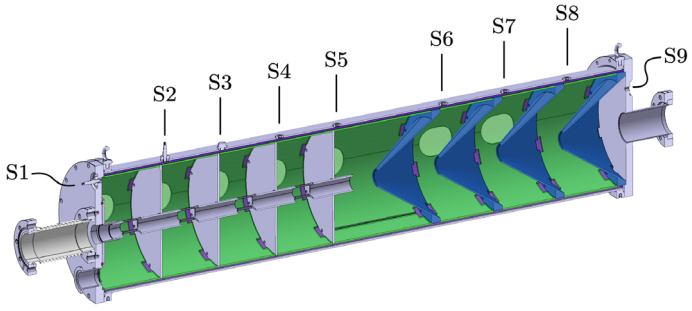

Fig. 2 Cross-section view of the suppressor and sensor locations

regime. If the expansion can be modelled with sufficient accuracy, Fluent can serve as a valid tool for simulating gas retention.

The system is modelled with a 2D axisymmetric geometry. The simulations contain two overset-mesh regions for modelling the valve head and pellet movement [6]. The domain consists of approximately 300 000 cells, all quadrilateral. An initial gap of 65 μ m is introduced at the valve head to maintain numerical stability and preserve a single computational domain. The mesh is refined in both the overset regions and the boundary layer. The simulations use laminar viscosity model. A density-based solver is utilized with implicit time stepping and AUSM+ convective flux, offering advantages in handling compressible flow and shock waves [2]. A time step of 100 ns is used. The zero-time step in the simulations corresponds to the moment when the valve head starts to move.

Due to the continuum assumption's failure at very low operating pressures, the simulations would not converge with the actual background pressure. We set the operating pressure to 1 mbar to overcome this issue. We conducted experiments both at 1 mbar and 1×10^{-3} mbar back pressure, and the pressure evolutions showed minimal deviation, therefore we consider the results of the CFD model applicable for comparison with high-vacuum cases as well.

The test shots were performed in multiple configurations, with or without pellets. For some of the shots, the suppressor internals (flat and conical deflector plates) were removed. The simulations reflected these setups. We conducted the mesh independence analysis using the method from [1]. The suppressor's performance was characterized by the gas retained at pellet exit (approximately 5 ms after launch), used as the representative variable. The analysis employed a fine grid (refinement factor 1.86) and a coarse grid (coarsening factor 1.43). The grid convergence index reached 29% and the total error relative to the fine and medium meshes was 10%. Therefore, we consider the results mesh-independent.

Figure 3 show Mach number and pressure contours for a simulation without pellet initially, right after valve closure, at $t = 1.5$ ms, when the gas starts to fill the suppressor volume and after 5 ms.

2.2 Measurements

A measurement grid, shown in Table 1, was established to ...evaluate the suppressor's performance under different valve pressures and opening voltages. The table lists the ejected gas quantity, expressed in bar-litres, a unit commonly used in fusion technology, for shots without pellets. The ejected gas quantities are even higher when a pellet is present due to shock wave interactions. The incoming gas creates a shock wave upon impact, which travels backward. At high valve pressures and opening voltages, these pressure waves can push the valve head back, causing it to reopen briefly and release additional gas.

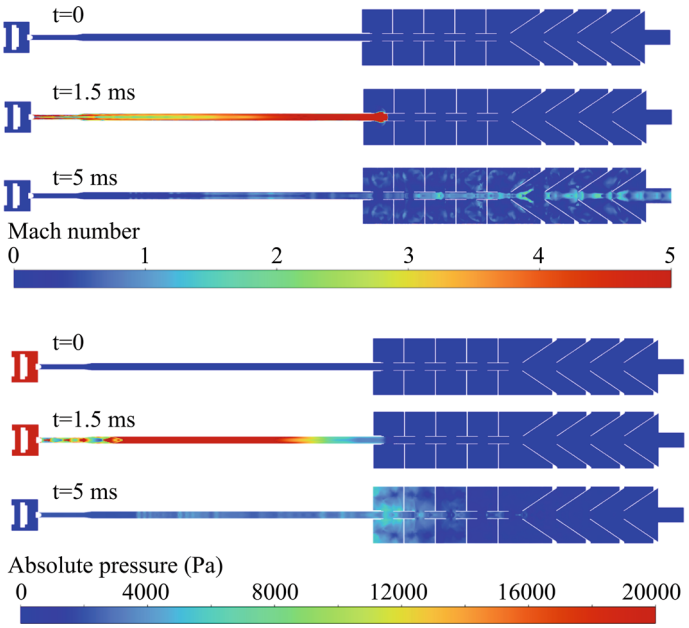

Fig. 3 Mach number and pressure contours initially, at valve closure (1.5 ms) and at 5 ms

Table 1 Test matrix

Valve pressure [bar]	Valve voltage [V]	Ejected gas [bar·litre]
100	900	3.2
100	1000	8.5
100	1100	19.5
80	900	4.8
80	1000	15
80	1100	31.5
60	900	8.7
60	1000	24.8
60	1100	21.8

As mentioned above, the suppressor internals are partially or fully removed for some launches. Only one pellet launch was successful with full suppressor internals, with shot number 1037. This launch was conducted with 80 bar valve pressure and 950 V opening voltage. The results from the whole test matrix are available for tests without pellet or suppressor internals, but those with the same launch parameters were selected for comparison.

3 Comparison of the Results

To compare CFD and measurements, pressure signals in the first, second and last compartments were used. Figure 4 shows the comparison of the aforementioned shot #1037 and the corresponding CFD simulation. In the latter, pressure rises later, especially in more downstream compartments, suggesting that the gas expansion velocity is not properly simulated. The rise and decay of the pressure in the case of the simulation is significantly slower than in the measurements. A probable explanation is the presence of gaps and leaks, which allow a larger mass flow rate between compartments in the actual setup leading to quicker pressure equalization than in the CFD, where the only way is in the central tube.

Figure 5 shows the comparison of simulation and measurements when no pellet is launched. When comparing the pellet-less measurements with simulations, we observe that the CFD simulation captures the pressure rise and peak value in compartment 1, but turbulent dissipation modelling is lacking; large vortices are present in the compartments, causing fluctuations and higher settling pressure in the end. The significant difference seen in Fig. 5 after 2.5 ms in the pressure at the second compartment can also be explained by the appearance of a large (unphysical) vortex in simulation.

In the absence of a pellet, the shape of the measured pressure signal is similar in compartment 1 but has a lower amplitude. The measured pressure in compartment 2 reaches a peak value similar to that of the tests with a pellet. Without a pellet, less gas enters the first few chambers, so we conclude that the gas retention is ineffective without a pellet. This is important since shadowgraph images show that some solid particles and gas (unclear if propellant or sublimated pellet material) precede

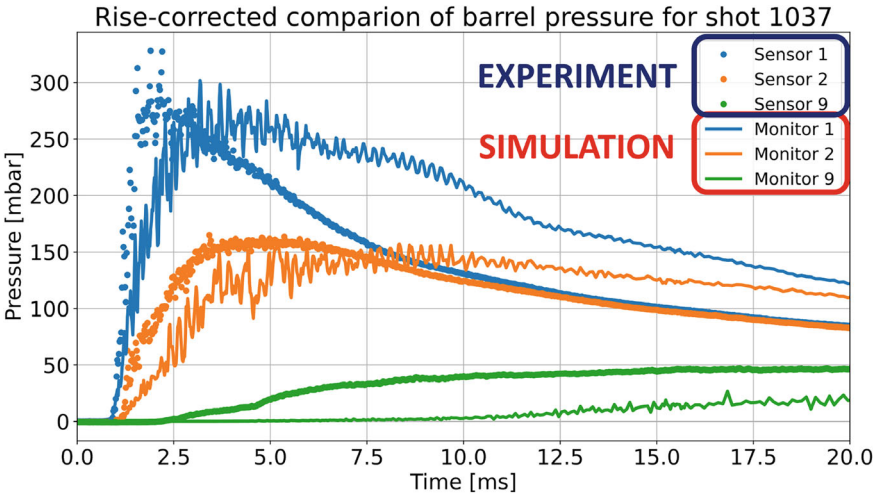

Fig. 4 Comparison of measurements and simulations with full suppressor internals and pellet

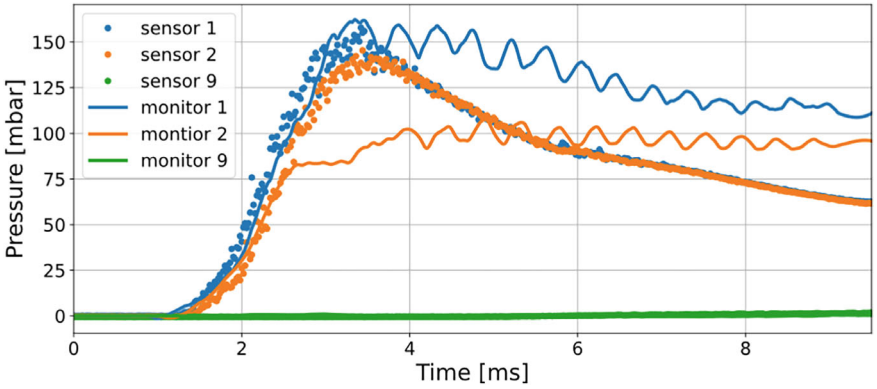

Fig. 5 Comparison of measurements and simulations with full suppressor internals without pellet

the pellet. The gas retention system is ineffective against this gas puff, and it will inevitably reach the reactor plasma before the pellet.

The comparison of measurements against simulation for shots without pellet and without suppressor internals (flat and conical deflector plates) is shown in Fig. 6. Here, the pressure reaches similar peaks as with the internals but lower than the cases that include a pellet. The oscillations seen in the pressure curves are due to the pressure waves travelling back and forth in the empty suppressor. The frequency is consistent with the speed of sound in hydrogen and the suppressor length. The wave amplitude and velocity are reproduced by CFD simulation with small errors.

From the results above, we can conclude that classical CFD tools cannot reproduce the expansion velocity of high-pressure gas puff into low vacuum in all cases. However, the simulation accurately predicts the pressure peaks occurring in the suppressor compartments. Therefore, it can be used to estimate the gas quantity.

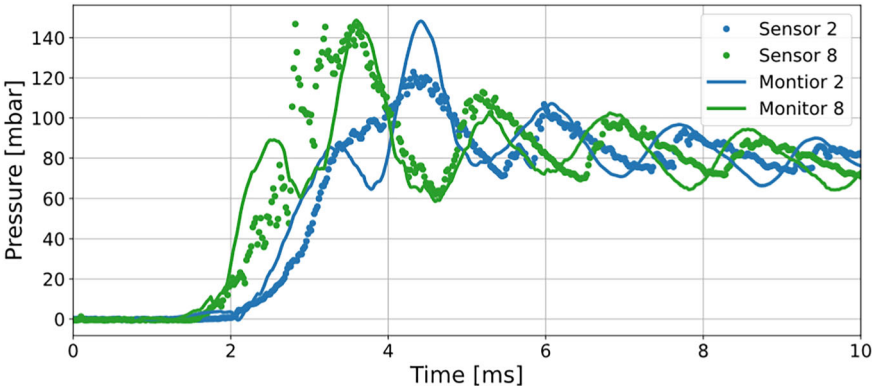

Fig. 6 Comparison of measurements and simulations without suppressor internals or pellet

Another finding of the analysis is that the setup's gaps and leaks significantly affect the pressure evolution. The effect of these gaps in the suppressor separators and around the pellet will be addressed in the future. Different shock-capturing methods can be tested to better model the gas expansion. However, despite the large difference in the operating pressure, the CFD simulations yield acceptable results in modelling the phenomenon. They can serve as preliminary tools for developing vacuum-suppressor systems.

Acknowledgements We acknowledge KIFÜ (Governmental Agency for IT Development, Hungary, https://ror.org/01s0v4q65) for awarding us access to the Komondor HPC facility based in Hungary. Project no. 2024-2.1.2-EKÖP-KDP-2024-00005 has been implemented with the support provided by the Ministry of Culture and Innovation of Hungary from the national research, development and innovation fund, financed under the EKÖP_KDP-24-1-BME-19 funding scheme.

References

1. ASME (2008) Procedure for estimation and reporting of uncertainty due to discretization in CFD applications. J Fluid Eng 130(7):078001. http://FluidsEngineering.asmedigitalcollection.asme.org/article.aspx?articleid=1434171
2. Liou MS (1996) A sequel to AUSM: AUSM+. J Comput Phys 129(2):364–382. https://linkinghub.elsevier.com/retrieve/pii/S0021999196902569
3. Meitner S, Baylor L, Commaux N, Shiraki D, Combs S, Bjorholm T, Ha T, McGinnis W (2017) Design and commissioning of a three-Barrel Shattered Pellet Injector for DIII-D Disruption Mitigation Studies. In: Fusion science and technology, pp 1–6. https://www.tandfonline.com/doi/full/10.1080/15361055.2017.1333854
4. Nagy D, Réfy D (2024) Eddy current actuated fast valve development for disruption mitigation applications. Fus Eng Des 202:114400. https://linkinghub.elsevier.com/retrieve/pii/S0920379624002539
5. Réfy D, Zoletnik S, Walcz E, Nagy D, Szepesi T, Vécsei M, Oravecz D, Katona I, Hegedüs S, Vavrik M, Jachmich S, Kruezi U (2023) Instrumented fast valve for the ITER DMS support laboratory test bench. Fus Eng Des 194:113893. https://linkinghub.elsevier.com/retrieve/pii/S0920379623004751
6. Steger JL, Benek JA (1987) On the use of composite grid schemes in computational aerodynamics. Comput Methods Appl Mechan Eng 64(1–3):301–320. https://linkinghub.elsevier.com/retrieve/pii/0045782587900454
7. Zoletnik S, Walcz E, Jachmich S, Kruezi U, Lehnen M, Anda G, Szabolics T, Szepesi T, Bartók G, Cseh G, Boros Z, Dunai D, Gárdonyi G, Hakl J, Hegedüs S, Katona I, Kovacs A, Kocsis G, Lengyel M, Mészáros S, Nagy D, Oravecz D, Poszovecz L, Réfy D, Vad K, Vécsei M (2023) Shattered pellet technology development in the ITER DMS test laboratory. Fus Eng Des 190:113701. https://linkinghub.elsevier.com/retrieve/pii/S0920379623002843

Open Access This chapter is licensed under the terms of the Creative Commons Attribution 4.0 International License (http://creativecommons.org/licenses/by/4.0/), which permits use, sharing, adaptation, distribution and reproduction in any medium or format, as long as you give appropriate credit to the original author(s) and the source, provide a link to the Creative Commons license and indicate if changes were made.

The images or other third party material in this chapter are included in the chapter's Creative Commons license, unless indicated otherwise in a credit line to the material. If material is not included in the chapter's Creative Commons license and your intended use is not permitted by statutory regulation or exceeds the permitted use, you will need to obtain permission directly from the copyright holder.

Kinetic Theory

From Kinetic Theory to Hyperbolic-Parabolic Fluid Systems of Equations

Vincent Giovangigli

Abstract Fluid systems of equations can be derived from the kinetic theory by using the Chapman-Enskog asymptotic method. We investigate the deep links between the hyperbolic-parabolic mathematical structure of such systems and the kinetic framework.

Keywords Fluid model · Hyperbolic-parabolic · Kinetic theory

1 Introduction

Fluids models can be derived from the kinetic theory of gases by using the Chapman-Enskog asymptotic method. As a representative example we consider in these notes the case of multicomponent flows with chemistry and transport. Such flows arise in various scientific and engineering applications like atmospheric reentry [1–3], crystal growth [4, 5], or combustion [6, 7].

2 Kinetic Derivation

2.1 Boltzmann Equations

Semiclassical Boltzmann equations in a mixture of polyatomic reactive gases may be written [3, 7–14]

$$\partial_t f_k + \boldsymbol{c}_k \cdot \nabla f_k + \boldsymbol{b}_k \cdot \nabla_{\boldsymbol{c}_k} f_k = \frac{1}{\epsilon} \mathcal{J}_k + \epsilon\, \mathcal{C}_k, \qquad k \in \mathfrak{S}, \tag{1}$$

V. Giovangigli (✉)
CMAP, CNRS, Ecole Polytechnique, Palaiseau Cedex, France
e-mail: vincent.giovangigli@polytechnique.edu
URL: https://cmap.polytechnique.fr/giovangi/

© The Author(s) 2026

M. Grabe et al. (eds.), *Rarefied Gas Dynamics*, Springer Aerospace Technology,
https://doi.org/10.1007/978-3-032-00094-1_25

where ∂_t denotes the time derivative, ∇ the space derivative, $\nabla_{\boldsymbol{c}_k}$ the derivative with respect to $\boldsymbol{c}_k$, $\mathfrak{S} = \{1, \ldots, \mathrm{N}\}$ the species indexing set, N the number of species, ϵ the Enskog expansion parameter, and for $k \in \mathfrak{S}$, f_k the distribution function, $\boldsymbol{c}_k$ the particle velocity, $\boldsymbol{b}_k$ the force per unit mass, $\mathcal{J}_k$ and $\mathcal{C}_k$ the scattering and reactive collision operators [3, 7]. The Maxwellian reaction regime with a scaling $\mathcal{O}(\epsilon)$ of chemistry terms is considered for simplicity and we refer to the literature for the tempered reaction regime $\mathcal{O}(\epsilon^0)$ or the kinetic equilibrium regime $\mathcal{O}(\epsilon^{-1})$ [7, 9, 14].

The distribution function of the kth species $f_k(t, \boldsymbol{x}, \boldsymbol{c}_k, \mathrm{K})$ depends on time t, spatial coordinate $\boldsymbol{x}$, particle velocity $\boldsymbol{c}_k = (c_{k1}, c_{k2}, c_{k3})^t$, quantum number K and $\mathfrak{Q}_k$ denotes the set of quantum energy states of the kth species. We denote by $\xi = (\xi_i)_{i\in\mathfrak{S}}$ any family of functions where $\xi_i = \xi_i(t, \boldsymbol{x}, \boldsymbol{c}_i, \mathrm{I})$ depends on t, $\boldsymbol{x}$, $\boldsymbol{c}_i$ and I, like the family of distribution functions $f = (f_i)_{i\in\mathfrak{S}}$. The scalar product between two families $\xi = (\xi_i)_{i\in\mathfrak{S}}$ and $\zeta = (\zeta_i)_{i\in\mathfrak{S}}$, where ξ is integrable as f, is defined by

$$\langle\!\langle \xi, \zeta \rangle\!\rangle = \sum_{\substack{i\in\mathfrak{S}\\ \mathrm{I}\in\mathfrak{Q}_i}} \int \xi_i(t, \boldsymbol{x}, \boldsymbol{c}_i, \mathrm{I})\zeta_i(t, \boldsymbol{x}, \boldsymbol{c}_i, \mathrm{I})\, d\boldsymbol{c}_i .$$

The collision terms $\mathcal{J}_k$ and $\mathcal{C}_k$ are conveniently written in terms of degeneracy averaged transition probabilities that satisfy reciprocity relations [3, 7–14]. The scattering source term may be written

$$\mathcal{J}_i(f) = \sum_{j\in\mathfrak{S}} \sum_{\substack{\mathrm{I}'\in\mathfrak{Q}_i\\ \mathrm{J},\mathrm{J}'\in\mathfrak{Q}_j}} \int \big(f_i' f_j' \tfrac{a_{i\mathrm{I}} a_{j\mathrm{J}}}{a_{i\mathrm{I}'} a_{j\mathrm{J}'}} - f_i f_j\big) W_{ij}^{\mathrm{IJ}\mathrm{I}'\mathrm{J}'} d\boldsymbol{c}_j d\boldsymbol{c}_i' d\boldsymbol{c}_j', \tag{2}$$

where $a_{i\mathrm{I}}$ is the degeneracy of the Ith energy state of the ith species, I and J the indices for the quantum states of the ith and jth species before collision, I′ and J′ the indices after collision, $W_{ij}^{\mathrm{IJ}\mathrm{I}'\mathrm{J}'}$ the transition probability for nonreactive collisions, $f_i' = f_i(t, \boldsymbol{x}, \boldsymbol{c}_i', \mathrm{I}')$ and $f_j' = f_j(t, \boldsymbol{x}, \boldsymbol{c}_j', \mathrm{J}')$ [7, 8, 13]. The transition probabilities satisfy the reciprocity relations $a_{i\mathrm{I}} a_{j\mathrm{J}} W_{ij}^{\mathrm{IJ}\mathrm{I}'\mathrm{J}'} = a_{i\mathrm{I}'} a_{j\mathrm{J}'} W_{ij}^{\mathrm{I}'\mathrm{J}'\mathrm{IJ}}$. The collisional invariants of the scattering operator $\mathcal{J} = (\mathcal{J}_i)_{i\in\mathfrak{S}}$ are given by $\psi^k = (\delta_{ik})_{i\in\mathfrak{S}}$, for $k \in \mathfrak{S} = \{1, \ldots, \mathrm{N}\}$, $\psi^{\mathrm{N}+l} = (m_i c_{il})_{i\in\mathfrak{S}}$, for $l \in \{1, 2, 3\}$, and $\psi^{\mathrm{N}+4} = (\frac{1}{2} m_i |\boldsymbol{c}_i|^2 + E_{i\mathrm{I}})_{i\in\mathfrak{S}}$ where δ_{ik} is the Kronecker symbol, m_i the mass of the ith species and $E_{i\mathrm{I}}$ the internal energy of the ith species in the Ith state. The corresponding fluid variables are $n_k = \langle\!\langle f, \psi^k \rangle\!\rangle, k \in \mathfrak{S}$, $\rho v_l = \langle\!\langle f, \psi^{\mathrm{N}+l} \rangle\!\rangle, l \in \{1, 2, 3\}$ and $\frac{1}{2}\rho|\boldsymbol{v}|^2 + \mathcal{E} = \langle\!\langle f, \psi^{\mathrm{N}+4} \rangle\!\rangle$ where n_k is the number density of the kth species, $\boldsymbol{v} = (v_1, v_2, v_3)^t$ the mixture mass velocity, and $\mathcal{E}$ the mixture internal energy par unit volume.

The chemical reactions are written in the molecular form

$$\sum_{i\in\mathfrak{F}^r} \mathfrak{M}_i \rightleftharpoons \sum_{k\in\mathfrak{B}^r} \mathfrak{M}_k, \qquad r \in \mathfrak{R}, \tag{3}$$

where $\mathfrak{M}_i$ is the symbol of the ith species, $\mathfrak{R} = \{1, \ldots, \mathrm{N}^r\}$ the set of reaction indices, N^r the number of reactions, $\mathfrak{F}^r$ and $\mathfrak{B}^r$ the indices for the reactants and products in the rth elementary reaction counted with their order of multiplicity. The letters $\mathfrak{F}^r$ and $\mathfrak{B}^r$ are mnemonics for the forward and backward directions. We denote by ν_{ir}^{f} and ν_{ir}^{b} the stoichiometric coefficients of the ith species in the rth reaction, i.e., the order of multiplicity of species i in $\mathfrak{F}^r$ and $\mathfrak{B}^r$, and we also denote by $_{F^r}$ and $_{B^r}$ the quantum states of reactants and products. For a given $i \in \mathfrak{S}$, $\mathfrak{F}_i^r$ denotes the set of reactant indices in which the index for the ith species has been removed once and we introduce a similar notation for $\mathfrak{B}_i^r$, $_{F_{\mathrm{I}}^r}$ and $_{B_{\mathrm{I}}^r}$. The reactive collision terms may be written $\mathcal{C}_i = \sum_{r\in\mathfrak{R}} \mathcal{C}_{ir}$ with [7]

$$\mathcal{C}_{ir} = \nu_{ir}^{\mathrm{f}} \sum_{F_I^r, B^r} \int \Big(\prod_{k\in\mathfrak{B}^r} f_k \frac{\prod_{k\in\mathfrak{B}^r}\beta_{k\mathrm{K}}}{\prod_{j\in\mathfrak{F}^r}\beta_{j\mathrm{J}}} - \prod_{j\in\mathfrak{F}^r} f_j\Big) \mathcal{W}^{F^r B^r}_{\mathfrak{F}^r \mathfrak{B}^r} \prod_{\substack{j\in\mathfrak{F}_i^r \\ k\in\mathfrak{B}^r}} d\boldsymbol{c}_j d\boldsymbol{c}_k$$

$$+\nu_{ir}^{\mathrm{b}} \sum_{F^r, B_I^r} \int \Big(\prod_{j\in\mathfrak{F}^r} f_j - \frac{\prod_{k\in\mathfrak{B}^r}\beta_{k\mathrm{K}}}{\prod_{j\in\mathfrak{F}^r}\beta_{j\mathrm{J}}} \prod_{k\in\mathfrak{B}^r} f_k\Big) \mathcal{W}^{F^r B^r}_{\mathfrak{F}^r \mathfrak{B}^r} \prod_{\substack{j\in\mathfrak{F}^r \\ k\in\mathfrak{B}_i^r}} d\boldsymbol{c}_j d\boldsymbol{c}_k, \tag{4}$$

where $\beta_i = h_{\mathrm{P}}/a_{i\mathrm{I}} m_i^3$, h_{P} is the Planck constant, and $\mathcal{W}^{F^r B^r}_{\mathfrak{F}^r \mathfrak{B}^r}$ are transition probabilities with the reciprocity relations $\mathcal{W}^{F^r B^r}_{\mathfrak{F}^r \mathfrak{B}^r} \prod_{k\in\mathfrak{B}^r}\beta_{k\mathrm{K}} = \mathcal{W}^{B^r F^r}_{\mathfrak{B}^r \mathfrak{F}^r} \prod_{j\in\mathfrak{F}^r}\beta_{j\mathrm{J}}$. All transition probabilities, species masses, internal energies, degeneracies, forces per unit mass, and chemical reactions details are assumed to be externally given in the model definition.

2.2 Kinetic Entropy

The kinetic entropy is defined by $\mathcal{S}^{\mathrm{kin}} = -k_{\mathrm{B}} \sum_{i\in\mathfrak{S},\mathrm{I}\in\mathfrak{Q}_i} \int f_i \big(\log(\beta_{i\mathrm{I}} f_i) - 1\big) d\boldsymbol{c}_i$ and satisfies the balance equation

$$\partial_t \mathcal{S}^{\mathrm{kin}} + \boldsymbol{\nabla}\cdot(\mathcal{S}^{\mathrm{kin}}\boldsymbol{v}) + \boldsymbol{\nabla}\cdot\boldsymbol{J}^{\mathrm{kin}} = \mathfrak{v}^{\mathcal{J}} + \mathfrak{v}^{\mathcal{C}}, \tag{5}$$

where $\boldsymbol{J}^{\mathrm{kin}} = -k_{\mathrm{B}} \sum_{i\in\mathfrak{S},\mathrm{I}\in\mathfrak{Q}_i} \int (\boldsymbol{c}_i - \boldsymbol{v}) f_i \big(\log(\beta_{i\mathrm{I}} f_i) - 1\big) d\boldsymbol{c}_i$ is the diffusive entropy flux, $\mathfrak{v}^{\mathcal{J}} = -k_{\mathrm{B}} \langle\!\langle \mathcal{J}, \log(\beta f)\rangle\!\rangle$ the scattering entropy production rate and $\mathfrak{v}^{\mathcal{C}} = -\sum_{r\in\mathfrak{R}} k_{\mathrm{B}} \langle\!\langle \mathcal{C}_r, \log(\beta f)\rangle\!\rangle$ the chemistry entropy production rate. Both entropy production rates $\mathfrak{v}^{\mathcal{J}}$ and $\mathfrak{v}^{\mathcal{C}}$ are nonnegative with

$$4\frac{\mathfrak{v}^{\mathcal{J}}}{k_{\mathrm{B}}} = \sum_{\substack{i,j\in\mathfrak{S}\\ \mathrm{I},\mathrm{I}'\in\mathfrak{Q}_i\\ \mathrm{J},\mathrm{J}'\in\mathfrak{Q}_j}} \int \big(f_i' f_j' \frac{a_{i\mathrm{I}} a_{j\mathrm{J}}}{a_{i\mathrm{I}'} a_{j\mathrm{J}'}} - f_i f_j\big) \log\big(\frac{f_i' f_j' a_{i\mathrm{I}} a_{j\mathrm{J}}}{f_i f_j a_{i\mathrm{I}'} a_{j\mathrm{J}'}}\big) W_{ij}^{\mathrm{I}\mathrm{J}\mathrm{I}'\mathrm{J}'} d\boldsymbol{c}_i d\boldsymbol{c}_j d\boldsymbol{c}_i' d\boldsymbol{c}_j',$$

$$\frac{\mathfrak{v}^{\mathcal{C}}}{k_{\mathrm{B}}} = \sum_{\substack{r\in\mathfrak{R}\\ F^r, B^r}} \int \Big(\prod_{k\in\mathfrak{B}^r} f_k \frac{\prod_{k\in\mathfrak{B}^r}\beta_{k\mathrm{K}}}{\prod_{j\in\mathfrak{F}^r}\beta_{j\mathrm{J}}} - \prod_{j\in\mathfrak{F}^r} f_j\Big) \log\Big(\frac{\prod_{k\in\mathfrak{B}^r}\beta_{k\mathrm{K}} f_k}{\prod_{j\in\mathfrak{F}^r}\beta_{j\mathrm{J}} f_j}\Big) \mathcal{W}_{\mathfrak{F}^r\mathfrak{B}^r}^{F^r B^r} \prod_{\substack{j\in\mathfrak{F}^r\\ k\in\mathfrak{B}^r}} d\boldsymbol{c}_j d\boldsymbol{c}_k.$$

2.3 Enskog Expansion

Application of the Chapman-Enskog method yields the fluid conservation equations, the thermochemistry properties, the transport fluxes, and the transport coefficients [3, 7–14]. The distributions are expanded as $f_k = f_k^0\big(1 + \epsilon\phi_k + \mathcal{O}(\epsilon^2)\big)$ for $k \in \mathfrak{S}$, and must satisfy the Enskog constraints $\langle\!\langle f - f^{(0)}, \psi^l\rangle\!\rangle = 0$ where ψ^l, $1 \le l \le \mathrm{N}+4$, are the collisional invariants.

The zeroth order distributions $f^{(0)} = (f_i^{(0)})_{i\in\mathfrak{S}}$ are found to be Maxwellians since $\mathcal{J}(f^{(0)}) = 0$ implies that $\log(\beta f^{(0)})$ is a collisional invariant and thus a linear combination of the ψ^l, $1 \le l \le \mathrm{N}+4$

$$f_i^{(0)}(t, \boldsymbol{x}, \mathrm{I}, \boldsymbol{c}_i) = \frac{1}{\beta_{i\mathrm{I}}} \frac{n_i}{Z_i} \exp\left\{-\frac{m_i}{2k_{\mathrm{B}}T}|\boldsymbol{c}_i - \boldsymbol{v}|^2 - \frac{E_{i\mathrm{I}}}{k_{\mathrm{B}}T}\right\}, \tag{6}$$

where $Z_i = Z_i^{\mathrm{tr}} Z_i^{\mathrm{int}}$, $Z_i^{\mathrm{tr}} = \big(\frac{2\pi m_i k_{\mathrm{B}} T}{h_{\mathrm{P}}{}^2}\big)^{3/2}$, $Z_i^{\mathrm{int}} = \sum_{\mathrm{I}\in\mathfrak{Q}_i} a_{i\mathrm{I}} \exp\big(-\frac{E_{i\mathrm{I}}}{k_{\mathrm{B}}T}\big)$, k_{B} is the Boltzmann constant and T the absolute temperature. The zeroth order equations are the Euler equations with the thermodynamic properties $p = \sum_{i\in\mathfrak{S}} n_i k_{\mathrm{B}} T$ and $\mathcal{E} = \sum_{i\in\mathfrak{S}} n_i \overline{E}_i$ where $\overline{E}_i = \frac{3}{2}k_{\mathrm{B}}T + \overline{E}_i^{\mathrm{int}}$ and $\overline{E}_i^{\mathrm{int}} = \sum_{\mathrm{I}\in\mathfrak{Q}_i} \frac{a_{i\mathrm{I}} E_{i\mathrm{I}}}{Z_i^{\mathrm{int}}} \exp\big(-\frac{E_{i\mathrm{I}}}{k_{\mathrm{B}}T}\big)$.

The linearized Boltzmann operator is in the form

$$\mathcal{I}_i^{\mathcal{J}}(\phi) = \sum_{j\in\mathfrak{S}} \sum_{\substack{\mathrm{I}'\in\mathfrak{Q}_i\\ \mathrm{J},\mathrm{J}'\in\mathfrak{Q}_j}} \int f_j^{(0)} (\phi_i + \phi_j - \phi_i' + \phi_j') W_{ij}^{\mathrm{I}\mathrm{J}\mathrm{I}'\mathrm{J}'} d\boldsymbol{c}_j d\boldsymbol{c}_i' d\boldsymbol{c}_j', \tag{7}$$

and the perturbations $\phi = (\phi_i)_{i\in\mathfrak{S}}$ satisfy the system of integral equations

$$\begin{cases} \mathcal{I}_i^{\mathcal{J}}(\phi) = -\Big(\partial_t \log f_i^{(0)} + \boldsymbol{c}_i \cdot \nabla \log f_i^{(0)}\Big) = \Psi_i, \qquad i \in \mathfrak{S} \\ \langle\!\langle f^{(0)}\phi, \psi^l\rangle\!\rangle = 0, \qquad 1 \le l \le \mathrm{N}+4. \end{cases} \tag{8}$$

The right hand sides Ψ_i may be decomposed in the form

$$\Psi_i = -\boldsymbol{\Psi}_i^{\eta} : \nabla \boldsymbol{v} - \tfrac{1}{3}\Psi_i^{\kappa} \nabla \cdot \boldsymbol{v} - \sum_{j\in\mathfrak{S}} \boldsymbol{\Psi}_i^{D_j} \cdot p\, \boldsymbol{d}_j - \boldsymbol{\Psi}_i^{\widehat{\lambda}} \cdot \nabla\Big(\frac{1}{k_{\mathrm{B}}T}\Big),$$

where $\boldsymbol{d}_j = (\nabla p_j - \rho_j \boldsymbol{b}_j)/p$ is the diffusion driving force of the jth species, p_j the partial pressure of the jth species and the expression of the coefficients $\boldsymbol{\Psi}_i^{\eta}$, Ψ_i^{κ}, $\boldsymbol{\Psi}_i^{D_j}$, $j \in \mathfrak{S}$, and $\boldsymbol{\Psi}_i^{\widehat{\lambda}}$ may be founded in the literature [7, 13].

The perturbed distribution functions are correspondingly decomposed as

$$\phi_i = -\boldsymbol{\phi}_i^{\eta} : \nabla \boldsymbol{v} - \tfrac{1}{3}\phi_i^{\kappa}\, \nabla \cdot \boldsymbol{v} - \sum_{j \in \mathfrak{S}} \boldsymbol{\phi}_i^{D_j} \cdot p\, \boldsymbol{d}_j - \boldsymbol{\phi}_i^{\widehat{\lambda}} \cdot \nabla\Big(\frac{1}{k_{\mathrm{B}} T}\Big),$$

and the equation for $\boldsymbol{\phi}^{\mu} = (\phi_i^{\mu})_{i \in \mathfrak{S}}$ is then $\mathcal{I}^{\mathcal{J}}(\boldsymbol{\phi}^{\mu}) = \Psi^{\mu}$ with the Enskog constraints $\langle\!\langle f^{(0)} \boldsymbol{\phi}^{\mu}, \psi^{l} \rangle\!\rangle = 0$, $1 \le l \le \mathrm{N} + 4$, for $\mu \in \{\kappa, \eta, \widehat{\lambda}\} \cup \{D_1, \ldots, D_{\mathrm{N}}\}$. The quantities $\boldsymbol{\phi}_i^{\eta}$ and $\boldsymbol{\Psi}^{\eta}$ are traceless symmetric second order tensors, $\boldsymbol{\phi}_i^{D_j}$ $\boldsymbol{\Psi}_i^{D_j}$, $\boldsymbol{\phi}_i^{\widehat{\lambda}}$ and $\boldsymbol{\Psi}_i^{\widehat{\lambda}}$, are vectors whereas ϕ_i^{κ} and Ψ^{κ} are scalars. It is established that $\langle\!\langle f^{(0)} \Psi^{\mu}, \psi^{l} \rangle\!\rangle = 0$ and the transport coefficients are typically given by $\mu = [\boldsymbol{\phi}^{\mu}, \boldsymbol{\phi}^{\mu}] = \langle\!\langle f^{(0)} \Psi^{\mu}, \boldsymbol{\phi}^{\mu} \rangle\!\rangle$. The bracket operator defined by $[\xi, \zeta] = \langle\!\langle f^{(0)} \xi, \mathcal{I}^{\mathcal{J}} \zeta \rangle\!\rangle$ is found to be symmetric $[\xi, \zeta] = [\zeta, \xi]$, positive semi-definite $[\xi, \xi] \ge 0$, and $[\xi, \xi] = 0$ if and only if ξ is a collisional invariant.

Substitution of the gradient decomposition of $\boldsymbol{\phi} = (\phi_i)_{i \in \mathfrak{S}}$ in the expressions of the species diffusion velocities $n_i \mathbf{V}_i = \sum_{\mathrm{I} \in \Omega_i} \int (\boldsymbol{c}_i - \boldsymbol{v}) f_i^{(0)} \phi_i d\boldsymbol{c}_i$, viscous tensor $\boldsymbol{\Pi} = \sum_{i \in \mathfrak{S}, \mathrm{I} \in \Omega_i} \int m_i (\boldsymbol{c}_i - \boldsymbol{v}) \otimes (\boldsymbol{c}_i - \boldsymbol{v}) f_i^{(0)} \phi_i d\boldsymbol{c}_i$, and heat flux $\boldsymbol{Q} = \sum_{i \in \mathfrak{S}, \mathrm{I} \in \Omega_i} \int \big(\frac{1}{2} m_i |\boldsymbol{c}_i - \boldsymbol{v}|^2 + E_{i1}\big)(\boldsymbol{c}_i - \boldsymbol{v}) f_i^{(0)} \phi_i d\boldsymbol{c}_i$ then yields the expressions of the fluxes in terms of macroscopic variable gradients as well as the expression of the transport coefficients.

3 Fluid Model

3.1 Governing Equations

The equations for conservation of species mass, momentum and energy derived from the kinetic theory are obtained in the form [7–14]

$$\partial_t \rho_k + \nabla \cdot (\rho_k \boldsymbol{v}) + \nabla \cdot (\rho_k \mathbf{V}_k) = m_k \omega_k, \qquad k \in \mathfrak{S}, \tag{9}$$

$$\partial_t (\rho \boldsymbol{v}) + \nabla \cdot (\rho \boldsymbol{v} \otimes \boldsymbol{v} + p \boldsymbol{I}) + \nabla \cdot \boldsymbol{\Pi} = \rho \boldsymbol{b}, \tag{10}$$

$$\partial_t (\mathcal{E} + \tfrac{1}{2} \rho \boldsymbol{v} \cdot \boldsymbol{v}) + \nabla \cdot \big((\mathcal{E} + \tfrac{1}{2} \rho \boldsymbol{v} \cdot \boldsymbol{v} + p) \boldsymbol{v}\big) + \nabla \cdot (\boldsymbol{Q} + \boldsymbol{\Pi} \cdot \boldsymbol{v}) = \rho \boldsymbol{v} \cdot \boldsymbol{b}, \tag{11}$$

where $\rho_k = m_k n_k$ denotes the mass density of the kth species, $\boldsymbol{v}$ the mass average flow velocity, $\mathbf{V}_k$ the diffusion velocity of the kth species, m_k the mass of the kth species, ω_k the molecular production rate of the kth species, $\rho = \sum_{k \in \mathfrak{S}} \rho_k$ the total mass density, p the pressure, $\boldsymbol{\Pi}$ the viscous tensor, $\boldsymbol{b}$ the specific force, $\mathcal{E}$ the internal energy per unit volume and $\boldsymbol{Q}$ the heat flux. The force acting on the species $\boldsymbol{b}$ has been assumed to be species independent for simplicity and the thermodynamic properties have been presented in Sect. 2.3.

The transport fluxes $\mathbf{V}_k$, $k \in \mathfrak{S}$, $\mathbf{\Pi}$, and $\boldsymbol{Q}$ due to fluid variable gradients are obtained in the form [7–13]

$$\mathbf{V}_k = -\textstyle\sum_{l\in\mathfrak{S}} D_{kl}\boldsymbol{d}_l - \theta_k \boldsymbol{\nabla} \log T, \qquad k \in \mathfrak{S}, \tag{12}$$

$$\mathbf{\Pi} = -\kappa(\boldsymbol{\nabla}\cdot\boldsymbol{v})\boldsymbol{I} - \eta\big(\boldsymbol{\nabla}\boldsymbol{v} + \boldsymbol{\nabla}\boldsymbol{v}^t - \tfrac{2}{3}(\boldsymbol{\nabla}\cdot\boldsymbol{v})\boldsymbol{I}\big), \tag{13}$$

$$\boldsymbol{Q} = -\widehat{\lambda}\,\boldsymbol{\nabla} T - p\textstyle\sum_{k\in\mathfrak{S}} \theta_k \boldsymbol{d}_k + \sum_{k\in\mathfrak{S}} h_k \rho_k \mathbf{V}_k, \tag{14}$$

where D_{kl}, $k, l \in \mathfrak{S}$, are the multicomponent diffusion coefficients, κ the volume viscosity, η the shear viscosity, $\widehat{\lambda}$ the partial thermal conductivity, θ_k, $k \in \mathfrak{S}$, the thermal diffusion coefficients, $h_k = (\frac{5}{2}k_{\mathrm{B}}T + \overline{E}_k^{\mathrm{int}})/m_k$ the enthalpy per unit mass of the kth species, θ_k, $k \in \mathfrak{S}$, the thermal diffusion coefficients, and ^{t} the transposition operator. The transport coefficients are further obtained in terms of the perturbed distributions

$$D_{ij} = \frac{p k_{\mathrm{B}} T}{3}[\phi^{D_i}, \phi^{D_j}], \quad \theta_i = -\frac{1}{3}[\phi^{D_i}, \phi^{\widehat{\lambda}}], \quad \widehat{\lambda} = \frac{1}{3k_{\mathrm{B}}T^2}[\phi^{\widehat{\lambda}}, \phi^{\widehat{\lambda}}], \tag{15}$$

$$\kappa = \frac{k_{\mathrm{B}} T}{9}[\phi^{\kappa}, \phi^{\kappa}], \quad \eta = \frac{k_{\mathrm{B}} T}{10}[\phi^{\eta}, \phi^{\eta}]. \tag{16}$$

The thermal diffusion ratios $\chi = (\chi_1, \ldots, \chi_{\mathrm{N}})^t$ introduced by Waldmann [8] are the unique solution of $D\chi = \theta$ with $\langle \chi, \mathbb{1}\rangle = 0$ where $\mathbb{1} = (1, \ldots, 1)^t$. The thermal conductivity λ is then given by $\lambda = \widehat{\lambda} - (p/T)\langle D\chi, \chi\rangle$ and both coefficients λ and χ may also be written in terms of bracket products [13]. The diffusion velocities and the heat flux may then be rewritten as [7, 8, 11–13]

$$\mathbf{V}_k = -\textstyle\sum_{l\in\mathfrak{S}} D_{kl}(\boldsymbol{d}_l + \chi_l \boldsymbol{\nabla} \log T), \quad k \in \mathfrak{S}, \tag{17}$$

$$\boldsymbol{Q} = -\lambda\,\boldsymbol{\nabla} T + p\textstyle\sum_{k\in\mathfrak{S}} \chi_k \mathbf{V}_k + \sum_{k\in\mathfrak{S}} h_k \rho_k \mathbf{V}_k, \tag{18}$$

and both formulations (12, 14) and (17, 18) may be used for applications. The mathematical structure and properties of the transport coefficients are then obtained from those of the bracket operator [13]. The diffusion matrix is symmetric $D = D^t$, positive semi-definite with nullspace $N(D) = \mathbb{R}\mathsf{y}$ and the thermal diffusion coefficients $\theta = (\theta_1, \ldots, \theta_{\mathrm{N}})^t$, are such that $\langle \theta, \mathsf{y}\rangle = 0$ where $\mathsf{y}_k = \rho_k/\rho$, $\mathsf{y} = (\mathsf{y}_1, \ldots, \mathsf{y}_{\mathrm{N}})^t$, and $\langle , \rangle$ denotes the scalar product. The thermal conductivity λ and the shear viscosity η are positive, and the volume viscosity κ is nonnegative.

The chemical production rates ω_k, $k \in \mathfrak{S}$, are obtained in the form

$$\omega_k = \textstyle\sum_{r\in\mathfrak{R}} (\nu_{kr}^{\mathrm{b}} - \nu_{kr}^{\mathrm{f}})\tau_r, \quad \tau_r = \mathcal{K}_r^{\mathrm{s}}\big(\exp\langle \mu, \nu_r^{\mathrm{f}}\rangle - \exp\langle \mu, \nu_r^{\mathrm{b}}\rangle\big), \tag{19}$$

where, for the rth reaction, τ_r is the rate of progress, $\mathcal{K}_r^{\mathrm{s}}$ the symmetric rate constant, $\nu_r^{\mathrm{f}} = (\nu_{1r}^{\mathrm{f}}, \ldots, \nu_{\mathrm{N}r}^{\mathrm{f}})^t$ and $\nu_r^{\mathrm{b}} = (\nu_{1r}^{\mathrm{b}}, \ldots, \nu_{\mathrm{N}r}^{\mathrm{b}})^t$ the reaction vectors, and $\mu = (\mu_1, \ldots, \mu_{\mathrm{N}})^t$, where $\mu_k = \log \frac{n_k}{Z_k}$ are the species chemical potentials. The expressions (19) are obtained from the kinetic reactive collision terms and the rate constants $\mathcal{K}_r^{\mathrm{s}}$ are averaged transition probabilities [7]

$$\mathcal{K}_r^{\mathrm{s}} = \sum_{F^r,B^r} \int \prod_{j\in\mathfrak{F}^r} \widetilde{f}_j^{(0)} \, \frac{\mathcal{W}_{\mathfrak{F}^r\mathfrak{B}^r}^{F^rB^r}}{\prod_{j\in\mathfrak{F}^r} \beta_{j\mathrm{J}}} \prod_{\substack{j\in\mathfrak{F}^r \\ k\in\mathfrak{B}^r}} d\boldsymbol{c}_j d\boldsymbol{c}_k,$$

where $\widetilde{f}_j^{(0)}$ denotes the reduced distribution $\widetilde{f}_j^{(0)} = f_j^{(0)}/n_j$. Decomposing the potentials as $\mu_k = -\log Z_k + \log n_k$, the rates of progress may be written $\tau_r = \mathcal{K}_r^{\mathrm{f}} \prod_{l\in\mathfrak{S}} n_l^{\nu_{lr}^{\mathrm{f}}} - \mathcal{K}_r^{\mathrm{b}} \prod_{l\in\mathfrak{S}} n_l^{\nu_{lr}^{\mathrm{b}}}$ with $\mathcal{K}_r^{\mathrm{f}} = \mathcal{K}_r^{\mathrm{s}} / \prod_{l\in\mathfrak{S}} Z_l^{\nu_{lr}^{\mathrm{f}}}$ and $\mathcal{K}_r^{\mathrm{b}} = \mathcal{K}_r^{\mathrm{s}} / \prod_{l\in\mathfrak{S}} Z_l^{\nu_{lr}^{\mathrm{b}}}$ and are thus compatible with the law of mass action. The equilibrium constant of the rth reaction is $\mathcal{K}_r^{\mathrm{e}}(T) = \prod_{l\in\mathfrak{S}} Z_l^{\nu_{lr}}$ and the reciprocity relations between the forward and backward constants $\mathcal{K}_r^{\mathrm{e}}(T) = \mathcal{K}_r^{\mathrm{f}}(T)/\mathcal{K}_r^{\mathrm{b}}(T)$ may be seen as Onsager relations for chemistry. The forward reaction constants $\mathcal{K}_r^{\mathrm{f}}$, $r \in \mathfrak{R}$, are often approximated with Arrhenius law.

3.2 Fluid Entropy

The fluid entropy $\mathcal{S}$ is the kinetic entropy evaluated with Maxwellian distributions $\mathcal{S} = \mathcal{S}^{\mathrm{kin}(0)}$ and is shown to be second order accurate $\mathcal{S}^{\mathrm{kin}} - \mathcal{S} = \mathcal{O}(\epsilon^2)$. This entropy reads $\mathcal{S} = \sum_{i\in\mathfrak{S}} n_i \overline{S}_i$ where the entropy per molecule of the ith species is $\overline{S}_i = \frac{5}{2} k_{\mathrm{B}} T + \overline{E}_i^{\mathrm{int}}/T - k_{\mathrm{B}} \log \frac{n_i}{Z_i}$. The Gibbs function per unit volume is given by $\mathcal{G} = \sum_{i\in\mathfrak{S}} n_i \overline{G}_i$ where $\overline{G}_i = k_{\mathrm{B}} T \log \frac{n_i}{Z_i} = k_{\mathrm{B}} T \mu_i$.

From the Gibbs relation $T\, \mathbb{D}\mathcal{S} = \mathbb{D}\mathcal{E} - \sum_{k\in\mathfrak{S}} \overline{G}_k \mathbb{D} n_k$, where $\mathbb{D}$ denotes the total derivative, the governing equation for $\mathcal{S}$ is in the form

$$\partial_t \mathcal{S} + \boldsymbol{\nabla}\cdot(\boldsymbol{v}\mathcal{S}) + \boldsymbol{\nabla}\cdot\Big(\frac{\boldsymbol{Q}}{T} - \sum_{k\in\mathfrak{S}} \frac{g_k \rho_k \mathbf{V}_k}{T}\Big) = \frac{\kappa}{T}(\boldsymbol{\nabla}\cdot\boldsymbol{v})^2 + \frac{\eta}{2T}\big|\Sigma\big|^2 + \frac{\lambda}{T^2}|\boldsymbol{\nabla} T|^2$$

$$+ \frac{p}{T} \sum_{k,l\in\mathfrak{S}} D_{kl}\big(\boldsymbol{d}_k + \chi_k \boldsymbol{\nabla}\log T\big)\cdot\big(\boldsymbol{d}_l + \chi_l \boldsymbol{\nabla}\log T\big) - k_{\mathrm{B}} \sum_{k\in\mathfrak{S}} \mu_k \omega_k, \tag{20}$$

where $\Sigma = \boldsymbol{\nabla}\boldsymbol{v} + \boldsymbol{\nabla}\boldsymbol{v}^t - \frac{2}{3}(\boldsymbol{\nabla}\cdot\boldsymbol{v})\, \boldsymbol{I}$ denotes of the rate of strain tensor. Since the thermal conductivity λ and the shear viscosity η are positive and the multicomponent diffusion matrix D is positive semidefinite we deduce that entropy production due to macroscopic gradients is nonnegative. On the other hand, the entropy production due to chemistry $-k_{\mathrm{B}} \sum_{k\in\mathfrak{S}} \mu_k \omega_k$ is such that

$$-\sum_{k\in\mathfrak{S}} \mu_k \omega_k = \sum_{r\in\mathfrak{R}} \mathcal{K}_r^{\mathrm{s}} \big(\langle \mu, \nu_r^{\mathrm{f}}\rangle - \langle \mu, \nu_r^{\mathrm{b}}\rangle\big) \, \big(\exp\langle \mu, \nu_r^{\mathrm{f}}\rangle - \exp\langle \mu, \nu_r^{\mathrm{b}}\rangle\big), \tag{21}$$

so that the rate of fluid entropy production (20) is a sum of nonnegative terms. Expanding in terms of ϵ the kinetic entropy production due to scattering yields

$\mathfrak{v}^{(-1)\mathcal{J}} = 0$, $\mathfrak{v}^{(0)\mathcal{J}} = 0$ and $\mathfrak{v}^{(1)\mathcal{J}} = k_{\mathrm{B}}[\phi, \phi]$ that coincides with fluid entropy production due to gradients. Similarly, expanding the kinetic entropy production due to reactive collisions yields $\mathfrak{v}^{(0)\mathcal{C}} = 0$ and $\mathfrak{v}^{(1)\mathcal{C}} = -k_{\mathrm{B}}\langle \mu, \omega \rangle$ that coincides with fluid entropy production due to chemistry. Denoting by $\mathcal{R}$ the linear space of chemical reactions $\mathcal{R} = \mathrm{span}\{\, \nu_r ;\ r \in \mathfrak{R} \,\}$ the expression (21) implies notably the following properties of chemical equilibrium

$$\langle \mu, \omega \rangle = 0 \iff \omega_k = 0,\ k \in \mathfrak{S} \iff \tau_r = 0,\ r \in \mathfrak{R} \iff \mu \in \mathcal{R}^{\perp}.$$

3.3 Vector Form

The governing equations for multicomponent fluids may finally be written in vector form $\partial_t \mathsf{u} + \sum_{i\in\mathfrak{D}} \partial_i \mathsf{F}_i + \sum_{i\in\mathfrak{D}} \partial_i \mathsf{F}_i^{\mathrm{diss}} = \Omega$ where u denotes the conservative variable $\mathsf{u} = \big(\rho_1, \dots, \rho_{\mathrm{N}}, \rho \boldsymbol{v}, \mathcal{E} + \frac{1}{2}\rho|\boldsymbol{v}|^2\big)^t$, $\mathfrak{D} = \{1, \dots, 3\}$ the set of direction indices, ∂_i the derivative in the ith direction, F_i and $\mathsf{F}_i^{\mathrm{diss}}$ the convective and dissipative fluxes in the ith direction, and Ω the source term given by

$$\begin{aligned}
\mathsf{F}_i &= \big(\rho_1 v_i, \dots, \rho_{\mathrm{N}} v_i,\ \rho \boldsymbol{v} v_i + p\boldsymbol{e}^i, (\mathcal{E} + p + \tfrac{1}{2}\rho|\boldsymbol{v}|^2) v_i\big)^t,\\
\mathsf{F}_i^{\mathrm{diss}} &= \big(\rho_1 \mathcal{V}_{1i}, \dots, \rho_{\mathrm{N}} \mathcal{V}_{\mathrm{N}i},\ \boldsymbol{\Pi}_i,\ Q_i + \boldsymbol{\Pi}_i \cdot \boldsymbol{v}\big)^t,\\
\Omega &= (m_1\omega_1, \dots, m_{\mathrm{N}}\omega_{\mathrm{N}}, \rho \boldsymbol{b}, \rho \boldsymbol{v} \cdot \boldsymbol{b})^t,
\end{aligned}$$

where $\boldsymbol{e}^i$, $1 \le i \le 3$, denote the standard basis vectors, $\boldsymbol{\Pi}_i = (\Pi_{1i}, \Pi_{2i}, \Pi_{3i})^t$ and $\boldsymbol{Q} = (Q_1, Q_2, Q_3)^t$. We may then use the—uniquely defined—dissipation matrices B_{ij} such that $\mathsf{F}_i^{\mathrm{diss}} = -\sum_{j\in\mathfrak{D}} \mathsf{B}_{ij}(\mathsf{u})\partial_j \mathsf{u}$ and the Jacobian matrices $\mathsf{A}_i = \partial_{\mathsf{u}} \mathsf{F}_i$ of the convective fluxes F_i in order to rewrite the governing equation as a second order system of partial differential equations.

4 Hyperbolic-Parabolic Structure

A essential step in order to investigate the mathematical structure and well posedness of a system of conservation laws is symmetrization [7, 15–17]. We discuss in this section the links between kinetic theory and symmetrization.

4.1 Entropy and Symmetrization

Using the conservative variable $\mathsf{u} = \big(\rho_1, \dots, \rho_{\mathrm{N}}, \rho \boldsymbol{v}, \mathcal{E} + \frac{1}{2}\rho|\boldsymbol{v}|^2\big)^t$, the vector notation of Sect. 3.3, the gradient decomposition of the dissipative fluxes $\mathsf{F}_i^{\mathrm{diss}} =$

$-\sum_{j\in\mathfrak{D}} \mathsf{B}_{ij}(\mathsf{u})\partial_j \mathsf{u}, i \in \mathfrak{D}$, involving the dissipation matrices $\mathsf{B}_{ij}, i, j \in \mathfrak{D}$, the Jacobian $\mathsf{A}_i(\mathsf{u}) = \partial_{\mathsf{u}}\mathsf{F}_i$ of the convective fluxes F_i, $i \in \mathfrak{D}$, and Ω the source term, the equations governing multicomponent flows read

$$\partial_t \mathsf{u} + \sum_{i\in\mathfrak{D}} \mathsf{A}_i(\mathsf{u})\partial_i \mathsf{u} = \sum_{i,j\in\mathfrak{D}} \partial_i\big(\mathsf{B}_{ij}(\mathsf{u})\partial_j \mathsf{u}\big) + \Omega(\mathsf{u}). \tag{22}$$

The system coefficients $\mathsf{A}_i(\mathsf{u})$, $i \in \mathfrak{D}$, $\mathsf{B}_{ij}(\mathsf{u})$, $i, j \in \mathfrak{D}$, and Ω are smooth functions of the conservative variable u on an open convex set $\mathcal{O}_{\mathsf{u}}$.

Symmetrization of the quasilinear system (22) may then be achieved by using a mathematical entropy σ compatible with convection, diffusion as well as source terms, that is, a smooth function satisfying (E_1)–(E_7) [7, 17]. Properties $(E_1)(E_2)$ of convective terms originate from the theory of hyperbolic systems [18, 19], properties $(E_3)(E_4)$ of dissipative terms from Kawashima [20], and properties (E_5)-(E_7) of source terms from Chen, Levermore and Liu [21] :

(E_1) $\partial^2_{\mathsf{u}}\sigma(\mathsf{u})$ is positive definite.
(E_2) $\partial_{\mathsf{u}}\sigma(\mathsf{u})\,\mathsf{A}_i(\mathsf{u}) = \partial_{\mathsf{u}}\mathsf{q}_i(\mathsf{u})$ where q_i is the ith entropy flux.
(E_3) $\big(\mathsf{B}_{ij}(\mathsf{u})\,\big(\partial^2_{\mathsf{u}}\sigma(\mathsf{u})\big)^{-1}\big)^t = \mathsf{B}_{ji}(\mathsf{u})\,\big(\partial^2_{\mathsf{u}}\sigma(\mathsf{u})\big)^{-1}$.
(E_4) $\sum_{i,j\in\mathfrak{D}} \mathsf{B}_{ij}(\mathsf{u})\,\big(\partial^2_{\mathsf{u}}\sigma(\mathsf{u})\big)^{-1} w_i w_j$ is positive semi-definite for $w \in \mathbb{R}^d$.
(E_5) There exists a fixed linear subspace $\mathfrak{E} \subset \mathbb{R}^{\mathsf{n}}$ such that $\Omega(\mathsf{u}) \in \mathfrak{E}^{\perp}$ and

$$\Omega(\mathsf{u}) = 0 \iff \big(\partial_{\mathsf{u}}\sigma(\mathsf{u})\big)^t \in \mathfrak{E} \iff \partial_{\mathsf{u}}\sigma(\mathsf{u})\;\Omega(\mathsf{u}) = 0.$$

(E_6) If $\Omega(\mathsf{u}) = 0$, $\partial_{\mathsf{u}}\Omega(\mathsf{u})\big(\partial^2_{\mathsf{u}}\sigma(\mathsf{u})\big)^{-1}$ is symmetric and $N\big(\partial_{\mathsf{u}}\Omega\,\big(\partial^2_{\mathsf{u}}\sigma\big)^{-1}\big) = \mathfrak{E}$.
(E_7) We have $\partial_{\mathsf{u}}\sigma(\mathsf{u})\,\Omega(\mathsf{u}) \le 0$.

The mathematical entropy balance is then in the form

$$\partial_t\sigma + \sum_{i\in\mathfrak{D}} \partial_i \mathsf{q}_i - \sum_{i,j\in\mathfrak{D}} \partial_i\langle \mathsf{v}, \widetilde{\mathsf{B}}_{ij}\partial_j \mathsf{v}\rangle = -\sum_{i,j\in\mathfrak{D}} \langle \partial_i \mathsf{v}, \widetilde{\mathsf{B}}_{ij}\partial_j \mathsf{v}\rangle + \langle \mathsf{v}, \widetilde{\Omega}\rangle,$$

and the entropic variable is defined by $\mathsf{v} = (\partial_{\mathsf{u}}\sigma)^t$. For multicomponent flows the mathematical entropy is taken to be $\sigma = -\mathcal{S}/k_{\mathrm{B}}$ and the entropic variable reads $\mathsf{v} = \frac{1}{k_{\mathrm{B}}T}\big(g_1 - \frac{1}{2}|\boldsymbol{v}|^2,\ \ldots,\ g_{\mathrm{N}} - \frac{1}{2}|\boldsymbol{v}|^2,\ \boldsymbol{v},\ -1\big)^t$ where $g_k = \overline{G}_k/m_k$, $k \in \mathfrak{S}$, are the species Gibbs functions per unit mass. The map $\mathsf{u} \mapsto \mathsf{v}$ is a smooth diffeomorphism from $\mathcal{O}_{\mathsf{u}}$ onto an open set $\mathcal{O}_{\mathsf{v}}$ and letting $\mathsf{u} = \mathsf{u}(\mathsf{v})$ in (22) yields the symmetrized equations

$$\widetilde{\mathsf{A}}_0(\mathsf{v})\partial_t \mathsf{v} + \sum_{i\in\mathfrak{D}} \widetilde{\mathsf{A}}_i(\mathsf{v})\partial_i \mathsf{v} = \sum_{i,j\in\mathfrak{D}} \partial_i\big(\widetilde{\mathsf{B}}_{ij}(\mathsf{v})\partial_j \mathsf{v}\big) + \widetilde{\Omega}(\mathsf{v}), \tag{23}$$

where $\widetilde{\mathsf{A}}_0 = \partial_{\mathsf{v}}\mathsf{u}\ \widetilde{\mathsf{A}}_i = \mathsf{A}_i\partial_{\mathsf{v}}\mathsf{u}$, $\widetilde{\mathsf{B}}_{ij} = \mathsf{B}_{ij}\partial_{\mathsf{v}}\mathsf{u}$, $\widetilde{\Omega} = \Omega$, and where :

(S_1) $\widetilde{\mathsf{A}}_0(\mathsf{v})$ symmetric positive definite.
(S_2) $\widetilde{\mathsf{A}}_i(\mathsf{v})$ symmetric.
(S_3) $\widetilde{\mathsf{B}}^t_{ij}(\mathsf{v}) = \widetilde{\mathsf{B}}_{ji}(\mathsf{v})$.
(S_4) $\sum_{i,j\in\mathfrak{D}} \widetilde{\mathsf{B}}_{ij}(\mathsf{v}) w_i w_j$ is positive semi-definite for $w \in \mathbb{R}^d$.
(S_5) There exits a fixed linear subspace $\mathfrak{E} \subset \mathbb{R}^{\mathsf{n}}$ with $\Omega(\mathsf{v}) \in \mathfrak{E}^\perp$ and

$$\Omega(\mathsf{v}) = 0 \iff \mathsf{v} \in \mathfrak{E} \iff \big\langle \mathsf{v}, \Omega(\mathsf{v}) \big\rangle = 0.$$

(S_6) If $\Omega(\mathsf{v}) = 0$ then $\partial_{\mathsf{v}}\Omega(\mathsf{v}) = \big(\partial_{\mathsf{v}}\Omega(\mathsf{v})\big)^t$ and $N\big(\partial_{\mathsf{v}}\Omega(\mathsf{v})\big) = \mathfrak{E}$.
(S_7) $\big\langle \mathsf{v}, \Omega(\mathsf{v}) \big\rangle \le 0$.

The existence of a mathematical entropy implies symmetrizability and symmetrizability with a change of variable $\mathsf{u} \to \mathsf{v}$ implies the existence of a mathematical entropy such that $\mathsf{v} = (\partial_{\mathsf{u}}\sigma)^t$ [7, 17–21]. The symmetrized system (23) finally reveals in particular the hyperbolic-parabolic structure and may also be used for stabilized finite element methods.

The fundamental links between kinetic theory and symmetrization may then be analyzed. Property (S_1) first results from the expression of Boltzmann entropy and Property (S_2)—or equivalently (E_2)—the existence of the entropy fluxes $\mathsf{q}_i = v_i\sigma$, $i \in \mathfrak{D}$, from the conservation of entropy by Euler equations that is itself a consequence of the kinetic entropy equation (5) at zeroth order. Property (S_3), the reciprocity relations $\widetilde{\mathsf{B}}^t_{ij} = \widetilde{\mathsf{B}}_{ji}$, $i, j \in \mathfrak{D}$, are consequences of the symmetry properties of the transport coefficients and thus of the bracket operator [7, 17]. Property (S_4), the positivity properties of the dissipation matrices, results from that of the bracket operator or equivalently from $\sum_{i,j\in\mathfrak{D}} \langle \partial_i \mathsf{v}, \widetilde{\mathsf{B}}_{ij}\partial_j \mathsf{v}\rangle = k_{\mathrm{B}}[\phi, \phi] = \mathfrak{v}^{(1)\mathcal{J}}$. The Properties ($S_5$) and ($S_7$) are consequences of the persistence of Boltzmann H theorem for reactive collisions at the fluid level (21) and we also have $\mathfrak{E}^\perp = M\mathcal{R} \times \{0\} \times \{0\}$ and $\langle \mathsf{v}, \widetilde{\Omega}\rangle = -\mathfrak{v}^{(1)\mathcal{C}}$ where $M = \mathrm{diag}(m_1, \dots, n_{\mathrm{N}})$. Finally Property ($S_6$) is a consequence of (19), and thus of the expression of kinetic reactive collision terms, that yields at chemical equilibrium the Jacobian $\partial_{\mathsf{v}}\widetilde{\Omega} = -\sum_{r\in\mathfrak{R}} \Lambda_r \nu'_r \otimes \nu'_r$ where $\nu'_r = (M\nu_r, 0, 0)^t$, and Λ_r are positive scalars [7]. All the symmetrization properties (S_1)–(S_7) may thus closely be related to the kinetic theory.

4.2 Well Posedness

The symmetrized entropic system may next be written in a normal form where hyperbolic and parabolic variables are split [7, 15–17, 20]. Introducing the partition $I = \{1\}$ and $II = \{2, \dots, \mathrm{N}+4\}$, the normal variable w is defined by $\mathsf{w} = (\mathsf{w}_I, \mathsf{w}_{II})^t$ with $\mathsf{w}_I = \rho$ and $\mathsf{w}_{II} = \frac{1}{k_{\mathrm{B}}T}\big(g_2 - g_1, \ \dots, \ g_{\mathrm{N}} - g_1, \ \boldsymbol{v}, \ -1\big)^t$. The equations in the w variable, obtained by the change of variable $\mathsf{v} = \mathsf{v}(\mathsf{w})$ and multiplying on the left by $\partial_{\mathsf{w}}\mathsf{v}^t$ in order to maintain symmetry, read

$$\overline{\mathsf{A}}_0(\mathsf{w})\partial_t \mathsf{w} + \sum_{i\in\mathfrak{D}} \overline{\mathsf{A}}_i(\mathsf{w})\partial_i \mathsf{w} = \sum_{i,j\in\mathfrak{D}} \partial_i\big(\overline{\mathsf{B}}_{ij}(\mathsf{w})\partial_j \mathsf{w}\big) + \overline{\Omega}(\mathsf{w}), \tag{24}$$

with $\overline{\mathsf{A}}_0 = (\partial_{\mathsf{w}}\mathsf{v})^t \widetilde{\mathsf{A}}_0\, \partial_{\mathsf{w}}\mathsf{v}$, $\overline{\mathsf{A}}_i = (\partial_{\mathsf{w}}\mathsf{v})^t \widetilde{\mathsf{A}}_i\, \partial_{\mathsf{w}}\mathsf{v}$, $\overline{\mathsf{B}}_{ij} = (\partial_{\mathsf{w}}\mathsf{v})^t \widetilde{\mathsf{B}}_{ij}\, \partial_{\mathsf{w}}\mathsf{v}$, $\overline{\Omega} = (\partial_{\mathsf{w}}\mathsf{v})^t \Omega$. The mathematical properties of the normal form (24) are by construction similar to that of the entropic form [7, 17] and we also have the block decompositions $\overline{A}_0 = \mathrm{diag}(\overline{A}_0^{I,I}, \overline{A}_0^{II,II})$ and $\overline{B}_{ij} = \mathrm{diag}(0, \overline{B}_{ij}^{II,II})$, and in addition the matrix $\overline{B}^{II,II} = \sum_{i,j\in\mathfrak{D}} \overline{B}_{ij}^{II,II} w_i w_j$ is positive definite for nonzero w. The resulting system (24) thus appears as a composite system symmetric-hyperbolic in the w_I variable and symmetric-strongly parabolic in the w_{II} variable. Symmetry is then a key point in order to derive a priori estimates that next yield local existence of solutions [15] as well as global solutions around constant equilibrium states and asymptotic stability [7, 16, 17]. There is also an important coupling stability condition between the hyperbolic and the parabolic operators, namely the Kawashima-Shizuta condition that yields strictly dissipative linearized normal form around equilibrium states [7, 17, 20]. A physical characterization of this coupling condition is that all waves associated with multicomponent Euler equations are damped by dissipative processes and this is again a consequence of the underlying physical framework [17].

4.3 Transport Coefficients

A major success of kinetic theory is to provide the transport coefficients (15, 16). A variational space is introduced for each coefficient μ and a Galerkin method is used in order to solve the corresponding system of Boltzmann linearized integral equations with the Enskog constraints [7, 8, 11–13]. This leads to linear systems with constraints and the mathematical properties of the transport linear systems may be extracted from the kinetic framework [7, 13].

Writing the linear system in the form $G\alpha = \beta$, the matrix G is either regular or its nullspace is one dimentional $N(G) = \mathbb{R}\mathcal{N}$ with a constraint $\langle \alpha, \mathcal{Z}\rangle = 0$ where $\langle \mathcal{N}, \mathcal{Z}\rangle \neq 0$. The transport coefficient is then typically given by the scalar product $\langle \alpha, \beta\rangle$. In the singular case, the matrix G is positive semidefinite, the nullspace $\mathbb{R}\mathcal{N}$ is associated with the collisional invariants in the variational approximation space and $\beta \in R(G)$. It is further possible to introduce the sparse transport matrix $db(G)$ constituted by diagonals of blocks of G. Assuming that the variational approximation space is perpendicular to the collisional invariants and orthogonal to constants, it can be shown [13] that $2db(G) - G$ and $db(G)$ are positive definite when $\mathrm{N} \geq 3$.

The solution of the transport linear system can then be obtained either from the symmetric positive definite system $(G + \mathcal{Z}\otimes\mathcal{Z})\alpha = \beta$ or from iterative techniques [22]. The iterative techniques may be generalized conjugate gradients using the very good preconditioning matrix $db(G)$ [13]. Stationary techniques may also be used with a splitting $G = M - L$ with $M = db(G)$, $T = M^{-1}L$ and $P = I - \mathcal{N}\otimes\mathcal{Z}/\langle \mathcal{N}, \mathcal{Z}\rangle$ that yield $\alpha = \sum_{0\leq j<\infty}(PT)^j P M^{-1} P^t \beta$. A key point is

then that the matrix $M + L = 2db(G) - G$ is positive definite but this is a consequence from Boltzmann linearized equations [13]. The kinetic theory thus provides the preconditioning matrix $db(G)$ for conjugate gradient methods and insures the convergence of the stationary algorithms [13, 22]

5 Conclusion

The close links between kinetic theory and the hyperbolic-parabolic structure of fluid systems of conservation laws has been discussed for multicomponent flows. A similar analysis may be obtained for other fluid systems like for instance for the relaxation of internal energy [23].

Only classical fluid systems have been intestigated in these notes by using the natural collisional invariants. For moment methods, however, such an ideal mathematical structure is not anymore guaranteed [24, 25]. More complex hyperbolic parabolic structure are also obtained for diffuse interface fluids with antisymmetric diffusion matrices arising from capillarity [26–28].

References

1. Anderson JD Jr (1989) Hypersonics and high temperature gas dynamics. McGraw-Hill Book Company, New-York
2. Capitelli M, Bruno D (2013) Fundamental aspects of plasma physics, transport, springer series on atomic, optical and plasma physics. Springer, New York. https://doi.org/10.1007/978-1-4419-8172-1
3. Nagnibeda E, Kustova E (2009) Non-equilibrium reacting gas flow. Springer, Berlin. https://doi.org/10.1007/978-3-642-01390-4
4. Kee RJ, Coltrin ME, Glarborg P (2003) Chemically reacting flow. Wiley, Hoboken. https://doi.org/10.1002/0471461296
5. Ern A, Giovangigli V, Smooke M (1996) Numerical study of a three-dimensional chemical vapor deposition reactor with detailed chemistry. J Comp Phys 126:21–39. https://doi.org/10.1006/jcph.1996.0117
6. Williams FA (1985) Combustion theory, 2nd edn. Co., Inc., Melo Park, The Benjamin/Cummings Pub. https://doi.org/10.1201/9780429494055
7. Giovangigli V (1999) Multicomponent flow modeling. Birkhaüser, Boston. https://doi.org/10.1007/978-1-4612-1580-6 Erratum at http://cmap.polytechnique.fr/ giovangi
8. Waldmann L (1958) Transporterscheinungen in Gasen von mittlerem Druck. Handbuch der Physik 12:295–514
9. Ludwig G, Heil M (1960) Boundary layer theory with dissociation and ionization, advances in applied mathematics. Academic Press, New York, vol VI, pp 39–118. https://doi.org/10.1016/S0065-2156(08)70110-8
10. Waldmann L, Trübenbacher E (1962) Formale Kinetische Theorie von Gasgemischen aus Anregbaren Molekülen. Zeitschr. Naturforschg. 17a:363–376. https://doi.org/10.1515/zna-1962-0501
11. Chapman S, Cowling TG (1970) The mathematical theory of non-uniform gases. Cambridge University Press, Cambridge

12. Ferziger JH, Kaper HG (1972) Mathematical theory of transport processes in Gases. North Holland Pub. Co., Amsterdam
13. Ern A, Giovangigli V (1994) Multicomponent transport algorithms lectures notes in physics, series monographs m24. Springer, Berlin. https://doi.org/10.1007/978-3-540-48650-3
14. Ern A, Giovangigli V (1998) The kinetic equilibrium regime. Physica-A 260:49–72. https://doi.org/10.1016/S0378-4371(98)00303-3
15. Giovangigli V, Massot M (1998) The local cauchy problem for multicomponent reactive flows in full vibrational nonequilibrium. Math Meth Appl Sci 21:1415–1439. https://doi.org/10.1002/(SICI)1099-1476(199810)21:15<1415::AID-MMA2>3.0.CO;2-D
16. Giovangigli V, Massot M (1998) Asymptotic stability of equilibrium states for multicomponent reactive flows, mathematical models & methods in applied. Science 8:251–297. https://doi.org/10.1142/S0218202598000123
17. Giovangigli V, Matuszewski L (2013) Mathematical modeling of supercritical multicomponent reactive fluids. Math Mod Meth App Sci 23:2193–2251. https://doi.org/10.1142/S0218202513500309
18. Godunov S (1961) An interesting class of quasilinear systems. Sov Math Dokl 2:947–949. https://doi.org/10.1016/j.jcp.2024.113521
19. Friedrichs KO, Lax PD (1971) Systems of conservation laws with a convex extension. Proc Nat Acad Sci USA 68:1686–1688. https://doi.org/10.1073/pnas.68.8.16
20. Kawashima S (1984) Systems of hyperbolic-parabolic composite type, with application to the equations of magnetohydrodynamics, Doctoral Thesis, Kyoto University. https://doi.org/10.14989/doctor.k3193
21. Chen GQ, Levermore CD, Liu TP (1994) Hyperbolic conservation laws with stiff relaxation terms and entropy. Comm Pure Appl Math 47:787–830. https://doi.org/10.1002/cpa.3160470602
22. Ern A, Giovangigli V (1995) Fast and accurate multicomponent property evaluations. J Comp Phys 120:105–116. https://doi.org/10.1006/jcph.1995.1151
23. Bruno D, Giovangigli V (2022) Internal energy relaxation processes and bulk viscosities in fluids. MDPI Fluids 7:356. https://doi.org/10.3390/fluids7110356
24. Struchtrup H (2005) Macroscopic transport equations for rarefied gas flows, interaction of mechanics and mathematics series. Springer, Heidelberg. https://doi.org/10.1007/3-540-32386-4
25. Torrilhon M (2016) Modeling nonequilibrium gas flow based on moment equations. Annu Rev Fluid Mech 48:429–458. https://doi.org/10.1146/annurev-fluid-122414-034259
26. Giovangigli V, Le Calvez Y, Nabet F (2023) Symmetrization and local existence of solutions for diffuse interface fluid models. J Math Fluid Mech 25:82. https://doi.org/10.1007/s00021-023-00825-4
27. Giovangigli V (2020) Kinetic derivation of diffuse-interface fluid models. Phys Rev E 102:012110. https://doi.org/10.1103/PhysRevE.102.012110
28. Giovangigli V (2021) Kinetic derivation of Cahn-Hilliard fluid models. Phys Rev E 104:054109. https://doi.org/10.1103/PhysRevE.104.054109

Open Access This chapter is licensed under the terms of the Creative Commons Attribution 4.0 International License (http://creativecommons.org/licenses/by/4.0/), which permits use, sharing, adaptation, distribution and reproduction in any medium or format, as long as you give appropriate credit to the original author(s) and the source, provide a link to the Creative Commons license and indicate if changes were made.

The images or other third party material in this chapter are included in the chapter's Creative Commons license, unless indicated otherwise in a credit line to the material. If material is not included in the chapter's Creative Commons license and your intended use is not permitted by statutory regulation or exceeds the permitted use, you will need to obtain permission directly from the copyright holder.

Relativistic Equilibrium Distribution of Rapidity: A Kinetic Theory Perspective

Guillermo Chacón-Acosta, Ana Laura García-Perciante, and Alma R. Méndez

Abstract The relativistic Boltzmann kinetic equation is reformulated using the rapidity variable, a Lorentz-invariant quantity with additive properties under boosts. From this, the equilibrium distribution function is obtained and its properties are explored, highlighting its applications and comparing its behavior with the usual Jüttner distribution function.

Keywords Relativistic kinetic theory · Jüttner distribution · Rapidity

1 Introduction

Historically, the Jüttner distribution function has been widely accepted as the equilibrium distribution for a relativistic gas given its compatibility with the principles of relativity, and statistical mechanics. However, the debate regarding whether this function corresponds to the correct relativistic generalization of the Maxwell-Boltzmann distribution has resurfaced, principally driven by a lack of detailed simulations and experimental evidence. Moreover, the so-called modified Jüttner distribution, which is characterized by a lower particle population in the high energy tail, has been proposed. This led to further questioning on the standard Jüttner distribution being the best description in some specific contexts.

In response to this debate, significant efforts have been made to validate either of the proposed distributions. Numerical simulations, in one [5], two [14] and three dimensions [9] strongly support Jüttner's distribution even under reference frame boosts. Also, theoretical studies confirm the Jüttner function as the equilibrium solution to the relativistic Boltzmann equation in collisionless systems, consistently with the H-theorem and thus ensuring a non-negative entropy production [4, 10]. However, additional studies revealed that the observed distribution could vary depending on specific modeling choices. For instance, the use of proper time as the temporal

G. Chacón-Acosta (✉) · A. L. García-Perciante · Alma R. Méndez
Departamento de Matemáticas Aplicadas y Sistemas, Universidad Autónoma Metropolitana Cuajimalpa, Cuajimalpa de Morelos, Ciudad de México, Mexico
e-mail: gchacon@cua.uam.mx

© The Author(s) 2026

M. Grabe et al. (eds.), *Rarefied Gas Dynamics*, Springer Aerospace Technology,
https://doi.org/10.1007/978-3-032-00094-1_26

variable leads to the modified Jüttner distribution, as shown in Refs. [8, 11]. The thermostatistical properties of this function, extended to any exponent of the relativistic energy, were studied in Ref. [1]. Also, a generalized distribution was found when the effects of a gravitational field are taken into account [16]. In this case a transition is encountered between a Jüttner function in the weak-field limit to a modified Jüttner in the strong field case. Recently, an alternative Lorentz invariant distribution has been derived by using the central limit theorem for the sum of the hyperbolic angles associated with Lorentz transformations [6, 7]. This variable, called rapidity, has the property of being additive under Lorentz boosts, as opposed to velocity. Rapidity is widely used to model high-energy experiments where relativistic effects primarily occur along the collision axis [17]. This approach offers intriguing perspectives but still lacks a direct kinetic justification.

The results mentioned above highlight the need for a more thorough theoretical understanding of statistical mechanics and kinetic theory in the relativistic regime. In this brief contribution, we address the kinetic theory derivation of the equilibrium distribution function in the rapidity variable. For this, we rewrite the relativistic Boltzmann equation in such variable and establish the equilibrium Jüttner distribution as the corresponding homogeneous solution. A qualitative analysis is carried out, aiming to provide new insights into its structure and behavior with increasing temperature. In particular, we seek to characterize the counterpart, in the rapidity framework, of the morphological transition to bimodality encountered in the Jüttner distribution [3, 13, 15]. This transition, which is interpreted as the threshold between non-relativistic and relativistic scenarios, reflects the increasing contribution of higher energy states as the system enters the relativistic domain. The rapidity distribution function is here found to retain its bell-shape throughout the transition with the hight of the single peak changing from increasing to decreasing at a critical temperature. This behavior may give additional insights into the transient regime.

The paper is organized as follows. Section 2 introduces the rapidity variable, discussing its definition and fundamental properties. In Sect. 3, we rewrite the relativistic Boltzmann equation in terms of the rapidity and derive the corresponding Jüttner equilibrium distribution. In Sect. 4, we analyze the implications of the bell-shaped rapidity distribution in the region where relativistic effects become relevant. Finally, in Sect. 5, we summarize and discuss our results and outline potential future research lines.

2 Rapidity as Relativistic Realization of Velocity

The one-dimensional Lorentz transformation of a particle's velocity v to a moving frame with relative velocity V is well known to be given by

$$v' = \frac{v + V}{1 + vV}, \tag{1}$$

where here and in what follows we consider natural units with $c = 1$. From this expression one can notice that $(v' - 1)/(v' + 1)$ does not depend on vV. Moreover, one can define a new variable, usually referred to as rapidity [17], as follows

$$y := \frac{1}{2} \ln \left(\frac{1 + v}{1 - v} \right), \tag{2}$$

such that y transforms in an additive fashion under Lorentz boosts. That is, if Y is the rapidity corresponding to the velocity V of the boost, one obtains $y' = y + Y$, which resembles a Galilean transformation. Moreover, Lorentz transformations can be parametrized in terms of rapidity by observing that $\cosh y$ reduces to the Lorentz factor γ and $\sinh y = \gamma V$. Consequently, the rapidity can be also written as $y = \operatorname{arctanh} V$ and is thus sometimes referred to as the hyperbolic angle in spacetime diagrams.

Rapidity is a fundamental concept in accelerator physics, mainly because collisions occur along a given axis in high-energy experiments [17]. For instance, the rapidity and angular differences between two events remain invariant under Lorentz boosts parallel to the beam axis, preserving the intrinsic symmetries of the system. This invariance simplifies the analysis and interpretation of collision data since it guarantees consistency regardless of the observer's reference frame. Experimental results are typically represented by histograms of rapidity distributions, which are often modeled with Gaussian profiles to provide the best fit to the observed data. These distributions are particularly helpful because they remain non-deformed with respect to the center-of-mass frame by boosts parallel to the collision axis.

Another interesting feature of rapidity is its behavior in the limiting cases. In the non-relativistic limit, where velocities are much smaller than the speed of light, one obtains $y \sim v$. For speeds close to the speed of light, it diverges as $y \sim \sqrt{2\,(\gamma - 1)}$, which coincides with the first approximation of the velocity in terms of γ. This divergence emphasizes its role in relativistic kinematics, where it provides a continuous and additive measure for relative motion. Therefore, the rapidity of a particle can be considered a relativistic realization of its velocity, which has advantages in describing high-speed dynamics.

Rapidity can also be expressed as a function of the four-momentum through the velocity in the boost direction, defined as $V = p_x/E$, as follows:

$$y = \frac{1}{2} \ln \left(\frac{E + p_x}{E - p_x} \right) = \ln \left(\frac{E + p_x}{m_T} \right). \tag{3}$$

Here E is the energy, $m_T^2 = E^2 - p_x^2 = m^2 + \mathbf{p}_T^2$ is the so-called transverse mass [17] and $\mathbf{p}_T$ is the momentum transverse to the direction of the boost. In these variables, momentum can be decomposed as $\mathbf{p} = p_x \hat{e}_x + \mathbf{p}_T$, with p_x being the longitudinal component of $\mathbf{p}$. For a free particle on the mass shell, i.e. satisfying $E^2 = \mathbf{p} \cdot \mathbf{p} + m^2$, the four-momentum has only three independent degrees of freedom. These can be conveniently parametrized by $(y, \mathbf{p}_T)$, where y replaces the longitudinal momentum

p_x. In this representation, E and p_x are directly expressed in terms of rapidity and transverse mass as:

$$E = m_T \cosh y, \quad p_x = m_T \sinh y. \tag{4}$$

This parametrization offers significant advantages in high-energy physics, particularly in collider experiments, where rapidity provides a natural measure for describing particle distributions due to its additive property under successive Lorentz transformations. Furthermore, using m_T and y highlights the separation between transverse and longitudinal dynamics, simplifying the analysis of processes involving boosts along a preferred direction.

3 Distribution Function of Rapidity from Relativistic Kinetic Theory

The covariant Boltzmann equation for the momentum distribution function $f(p)$ of a system of neutral relativistic particles in flat spacetime is given by [2]

$$p^\mu \frac{\partial f}{\partial x^\mu} = \int \frac{d^3 p_1}{E_1} d\Omega \, F \, \sigma \left(f_1' f' - f_1 f \right). \tag{5}$$

The integral on the right-hand side of Eq. (5) is the well-known collision term, accounting for interactions with particles of the system labeled with a subscript 1. Here $d^3 p_1 / E_1$ is the invariant line element, σ the interaction cross-section, $d\Omega$ the solid angle and $F = \sqrt{(p_1^\mu p_\mu)^2 - m^4}$ denotes the so-called invariant flux. Using Eq. (4) and the definitions of transverse mass and momentum, we can reformulate the Boltzmann equation (5) as a function of rapidity, as shown below

$$m_T \cosh y \frac{\partial f}{\partial t} + m_T \sinh y \frac{\partial f}{\partial x} + \mathbf{p}_T \cdot \nabla_T f = \int dy \, d^2 p_T \, d\Omega \, F \, \sigma \left(f_1' f' - f_1 f \right), \tag{6}$$

where ∇_T stands for the gradient in the direction orthogonal to the boost.

Following [2, 4], one can obtain the equilibrium distribution function f_{eq} by imposing the condition of zero entropy production. This leads to the fact that f_{eq} must depend only on the collisional invariants $\{1, p^\mu\}$ and remain invariant under Lorentz transformations. This, in turn, allows for evaluation in a convenient rest frame where $B^\mu \to (B, \mathbf{0})$, such that f_{eq} can be written as

$$f_{eq} = A \, e^{-B \, m_T \cosh y}, \tag{7}$$

where the coefficients A and B can be related to the physical moments of the distribution. Indeed, if N^μ and $T^{\mu\nu}$ are the particle four-flux and energy momentum tensor respectively, the following relations hold:

$$N^{\mu} = -A\frac{\partial \mathcal{I}}{\partial B_{\mu}}, \quad T^{\mu\nu} = A\frac{\partial^2 \mathcal{I}}{\partial B_{\mu}\partial B_{\nu}}, \tag{8}$$

where

$$\mathcal{I} = \int \frac{d^3p}{E} e^{-B^{\mu}p_{\mu}}.$$

In the frame here considered, $\mathcal{I}$ can be written in terms of $B = \sqrt{-B_{\mu}B^{\mu}}$ as follows

$$\mathcal{I} = \int dy\, d^2p_T e^{-Bm_T \cosh y} = \frac{4\pi m}{B} K_1(mB), \tag{9}$$

where and $K_i(z)$ is the modified Bessel function of the second kind. Aligning the rest frame with the fluid frame and using the definition of entropy flux, together with the Gibbs relation to express the energy density in terms of temperature [2, 4], leads to

$$A = \frac{nmB}{4\pi m^3 K_2(mB)}, \quad B = \frac{1}{T}, \tag{10}$$

where we also consider units in which the Boltzmann constant is $k_B = 1$. Accordingly, the equilibrium distribution function can be written as

$$f_{eq} = f_0 \frac{z}{K_2(z)} \exp\left(-z\mu \cosh y\right), \tag{11}$$

where $f_0 = n/4\pi m^3$. In Eq. (11) we have also introduced the relativistic factor $z = m/T$ and the fraction of the transverse mass $\mu = m_T/m$, such that the non-relativistic limit is characterized by $z \gg 1$ and $\mu \to 1$, additional to $y \ll 1$.

It is worth noticing that, by using the known physical moments given in Eq. (8), the resulting distribution should match the well-known Jüttner distribution, and thus Eq. (11) is indeed, the Jüttner distribution in terms of rapidity. When analyzed as a function of rapidity, transverse mass, and temperature, this distribution exhibits several interesting features. First, it is symmetric with respect to y, with a maximum at $y = 0$ for any positive value of z and μ. Moreover, as shown in Fig. 1, it resembles a gaussian-like bell-shaped curve in contrast with the unimodal to bimodal transition observed when expressed in terms of velocity. Furthermore, when analyzed as a function of temperature, the distribution exhibits a peak at a critical point, z_m, whose magnitude depends on the transverse mass, suggesting a possible correlation with the relativistic morphological transition between limiting cases. This feature is further discussed in the next section.

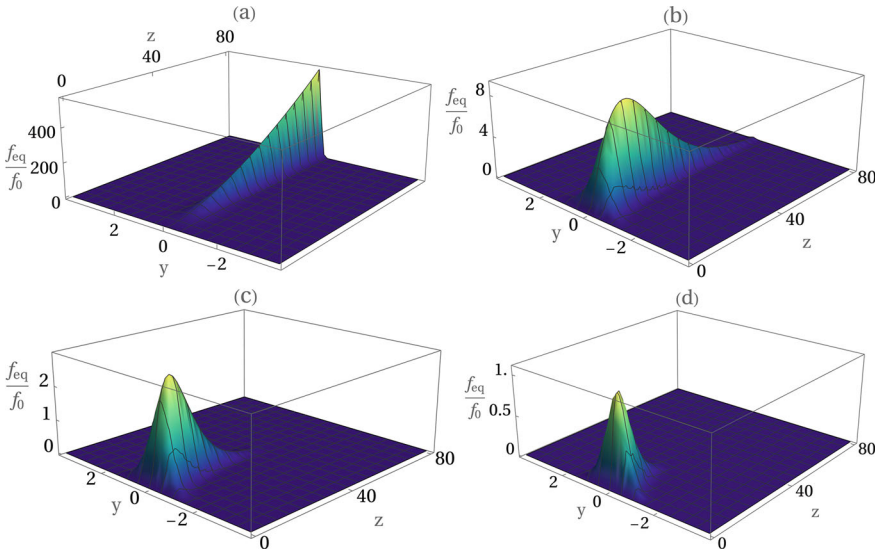

Fig. 1 Relativistic distributions of the rapidity for different values of the transverse mass fraction: **a** $\mu = 1.0$, **b** $\mu = 1.1$, **c** $\mu = 1.2$, **d** $\mu = 1.35$. We observe how z decreases with μ

4 Relation to the Relativistic Morphological Transition

As previously mentioned, the relativistic distribution exhibits a transition from unimodal to bimodal as the temperature increases. Moreover, relativistic effects are considered to become significant precisely at the critical temperature T_c of the transition, which depends on dimensionality and statistics [3, 13, 15].

In contrast, the distribution given in Eq. (11) does not show such a morphological transition. Instead, it has a single global maximum at $y = 0$, whose height depends on the temperature through the parameter z. As shown in Fig. 1, the behavior of $f_{eq}(y = 0)$ changes from increasing to decreasing at a critical value $z = z_m$ for each $\mu > 1$. However, in the non-relativistic regime, the distribution simplifies to $f_{eq} \sim \sqrt{2/\pi}\, z^{3/2} e^{-(y^2 z)/2}$ and thus diverges at $y = 0$, indicating the absence of a maximum temperature in this limit (see Fig. 1a). Thus the existence of the maximum temperature given by z_m appears to be an exclusive property for transverse masses $\mu \gtrsim 1$.

The behavior of the temperature corresponding to a maximum in $f_{eq}(y = 0)$ for $\mu > 1$ can be further assessed by inspection of Fig. 2, where z_m is shown for different values of μ. The red points correspond to the numerical values obtained by maximizing the distribution as a function of z for various values of μ, with the black curve corresponding to the interpolation of these points. The gray lines indicate the distribution contour lines as a function of (z_m, μ) for $y = 0$. Remarkably, for $\mu \simeq 1.36$ the inverse of the maximum temperature becomes close to the critical value of the relativistic transition, which in three dimensions corresponds to $z_c = 5$.

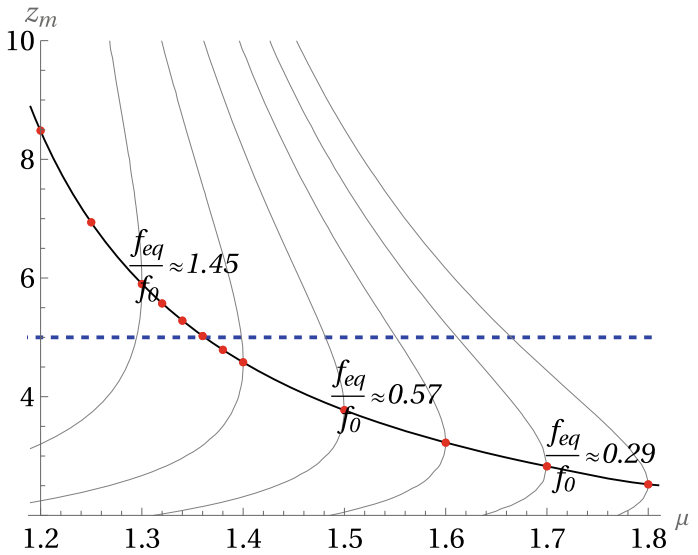

Fig. 2 Graph of z_m as a function of traverse mass fraction. The red dots are numerical values from the maximization of the distribution, the black curve is the interpolation, and the gray lines are the distribution contour lines for $y = 0$. The dashed blue line indicates the critical factor $z_c = 5$

Moreover, one finds that the level curve corresponding to $f_{eq}(y = 0)/f_0 \simeq 1$ in Fig. 2 passes through this region, suggesting that relativistic effects become important in this representation from these coincident values onwards.

5 Summary and Discussion

In this contribution, we established the rapidity distribution in an equilibrium configuration from the kinetic theory point of view and qualitatively analyzed its properties, principally in relation to the relativistic transition. The choice of the rapidity variable is mostly motivated by its additive property under Lorentz boosts, which results in its wide use in high-energy experiments [6, 7, 17]. To accomplish this task we reformulated the relativistic Boltzmann equation in terms of rapidity and transverse momentum, and solved it for the equilibrium case.

The resulting solution corresponds to the Jüttner distribution (Eq. 11) depending on rapidity, transverse mass fraction, and temperature. This distribution exhibits a bell-shaped profile for all temperatures, flattening in the ultra-relativistic regime and approximating a Gaussian in the non-relativistic limit. Interestingly, the peak of the distribution reaches a maximum at z_m depending on μ. This observation suggests a relation with the relativistic transition temperature, which has been previously

studied. It is important point out that in this contribution we focus on the non-quantum three-dimensional case in the comoving frame. However, it is very likely that the maximum temperature will also depend on frame velocity, statistics and dimensionality, similar to how the critical temperature of the relativistic transition described above behaves [3, 13, 15].

We found that the value of z_m for which the peak of the distribution reaches a maximum value is close to the critical value $z_c = 5$ of the relativistic transition [3, 13, 15], at approximately $\mu \simeq 1.36$. This suggests that z_m is the threshold between the ultra-relativistic (for $z < z_m$) and non-relativistic (for $z > z_m$) regimes. Thus, this approach offers an alternative perspective for studying the relativistic transition, in terms of the transverse mass and the maximum temperature, that may influence morphological transitions when analyzed in the original variables.

Future work could explore moments of rapidity to provide deeper insight into the relativistic transition. For instance, kurtosis may be relevant in the ultra-relativistic regime, where the distribution flattens. This analysis will follow from the transfer equation by integrating Eq. (5). Additionally, alternative distributions, like the modified Jüttner [1] or those derived from nonlinear Fokker-Planck equations in high-energy processes [12, 18], deserve further study as they differ from Jüttner distribution by energy functions, offering potentially valuable theoretical and experimental insights.

Acknowledgements We thank the organizers of the 33rd International Symposium on Rarefied Gas Dynamics for providing an excellent forum for scientific interaction.

References

1. Aragón-Muñoz L, Chacón-Acosta G (2018) J Phys: Conf Ser 1030:012004
2. Cercignani C, Kremer GM (2002) The relativistic Boltzmann equation: theory and applications. Birkhäuser Verlag
3. Chacón-Acosta G (2016) AIP Conf Proc 1786:070016
4. Chacón-Acosta G, Dagdug L, Morales-Técotl H (2010) Phys Rev E 81:021126
5. Cubero D, Casado-Pascual J, Dunkel J, Talkner P, Hänggi P (2007) Thermal equilibrium and statistical thermometers in special relativity. Phys Rev Lett 99:170601
6. Curado EMF, Cedeño CE, Soares ID, Tsallis C (2022) Chaos 32:103110
7. Curado EMF, Germani FTL, Soares ID (2016) Phys A 444:963–969
8. Dunkel J, Hänggi P (2009) Phys Rep 471:1–73
9. Dunkel J, Hänggi P, Hilbert S (2009) Nature Phys 5:741–747
10. García-Perciante AL, Méndez AR, Escobar-Aguilar E (2017) J Stat Phys 167:123–134
11. Ghodrat M, Montakhab A (2010) Phys Rev E 82:011110
12. Lavagnno A (2002) Phys A 305:2038–241
13. Mendoza M, Araújo NAM, Succi S, Herrmann HJ (2012) Sci Rep 2:611
14. Montakhab A, Ghodrat M, Barati M (2009) Statistical thermodynamics of a two-dimensional relativistic gas. Phys Rev E 79:031124
15. Montakhab A, Shahsavar L, Ghodrat M (2014) Phys A 412:32–38
16. Sánchez-Rey B, Chacón-Acosta G, Dagdug L, Cubero D (2013) Phys Rev E 87:052121
17. Torres-Rincon JM (2014) Hadronic transport coefficients from effective field theories. Springer
18. Wolschin G (2004) Phys Rev E 69:024906

Open Access This chapter is licensed under the terms of the Creative Commons Attribution 4.0 International License (http://creativecommons.org/licenses/by/4.0/), which permits use, sharing, adaptation, distribution and reproduction in any medium or format, as long as you give appropriate credit to the original author(s) and the source, provide a link to the Creative Commons license and indicate if changes were made.

The images or other third party material in this chapter are included in the chapter's Creative Commons license, unless indicated otherwise in a credit line to the material. If material is not included in the chapter's Creative Commons license and your intended use is not permitted by statutory regulation or exceeds the permitted use, you will need to obtain permission directly from the copyright holder.

Classical Trajectories Estimation of Transport Properties of N_2-O_2 Mixtures

Domenico Bruno and Aldo Frezzotti

Abstract Estimations of transport coefficients of N_2-O_2 mixtures are obtained by describing N_2-N_2, O_2-O_2 and N_2-O_2 binary collisions with three distinct Potential Energy Surfaces. Classical Trajectories are then used in combination with Monte Carlo and with non-equilibrium Direct Simulation Monte Carlo simulations to obtain transport coefficients of N_2-O_2 mixtures.

Keywords Air transport coefficients · Classical trajectories

1 Introduction

Elastic light scattering, or Rayleigh-Brillouin scattering (RBS), is currently employed for remote sensing of the atmosphere [29]. The current practice is to use the Tenti S6 model [7, 26] as line-shape model to interpret the experiments and extract the required gas temperature. It has been shown, however, that the Tenti S6 model fails to reproduce the RBS spectrum when the relaxation of internal degrees of freedom is slow enough that non-equilibrium models are required [10]. It is thus worth exploring more accurate theoretical tools to analyse Rayleigh-Brillouin scattering (RBS) experiments on air species. Direct Simulation Monte Carlo (DSMC) [6] is a natural choice since it solves the Boltzmann equation with no approximations. Phenomenological binary collision models [6] are replaced with Classical Trajectories (CT) calculations [15]. Simulations based on CT-DSMC techniques [19] benefit from the availability of accurate Potential Energy Surfaces (PES), describing the interaction of two colliding molecules. Here, attention is limited to PES's, describing N_2-N_2, O_2-O_2, and N_2-O_2 pairwise interactions between rigid, dumbbell-like molecules. The effects of vibrational excitations can, in fact, be neglected under the conditions

D. Bruno (✉)
National Research Council, Institute for Plasma Science and Technology, Bari, Italy
e-mail: domenico.bruno@cnr.it

A. Frezzotti
Department of Aerospace Science & Technology, Politecnico di Milano, Milan, Italy

© The Author(s) 2026

M. Grabe et al. (eds.), *Rarefied Gas Dynamics*, Springer Aerospace Technology,
https://doi.org/10.1007/978-3-032-00094-1_27

of RBS experiments conducted near room temperature. The considered PES's have been analyzed by computing transport coefficients by different methods, including Monte Carlo quadrature (CT-MC) applied to explicit expressions of transport coefficients [21] and non-equilibrium CT-DSMC simulations. The latter are, in general, more expensive than CT-MC estimations but provide values of transport coefficients that do not require higher order corrections [12]. Moreover, they can be used for complex gas mixtures when expressions of transport coefficients are not immediately available. The general form of the N_2-N_2, O_2-O_2, and N_2-O_2 PES's here used to estimate air transport coefficients is described in Sect. 2. Individual PES are described and discussed in Sects. 2.1–2.3. The results on air shear and bulk viscosity are given in Sect. 3.

2 Potential Energy Surfaces

The intermolecular potentials considered have the following general structure [2–4]:

$$V(R_{12},\theta_1,\theta_2,\phi) = \sum_{L_1,L_2,L} V^{L_1,L_2,L}(R_{12})\mathcal{Y}^{L,0}_{L_1,L_2}(\theta_1,\theta_2,\phi) \qquad (1)$$
$$L_1,\ L_2 = 0,1,2,\ldots,\quad |L_1-L_2| < L < L_1+L_2$$

where R_{12} is the distance between the molecular centers of mass, θ_1, θ_2 and ϕ are three angles that specify the relative orientation of molecular pairs (see Fig. 1). Potentials are expressed as superpositions of a finite number of terms, each resulting from the product of a radial function $V^{L_1,L_2,L}(R_{12})$ and a bipolar spherical harmonic function $\mathcal{Y}^{L,0}_{L_1,L_2}(\theta_1,\theta_2,\phi)$ [4]. In the expansion (1), the first term $V^{0,0,0}(R_{12})$ represents the isotropic contribution to the potential. The number of terms depends on interacting species, varying from 4 in the O_2-O_2 PES, to 6 in the N_2-O_2 PES. The form of the radial coefficients is described in Refs. [2–4] and it will not be given here, for brevity. However, it is important to mention that the adjustable parameters present in the radial functions have been determined from molecular beam scattering experimental data. Accordingly, parameters uncertainties are also provided in the case of O_2-O_2 and N_2-N_2 PES's, whereas no error intervals are given for the parameters that characterize N_2-O_2 PES.

The interpretation of parameters uncertainties requires some caution. Actually, an uncertainty quantification analysis, conducted within the present work, has shown that a considerable fraction of the PES parameters combinations, although compatible with the given error bounds, lead to strongly distorted and unrealistic PES's. Nevertheless, sensible variations, involving one or two parameters at a time, can be exploited to improve the predictions of transport coefficients, as shown in the following.

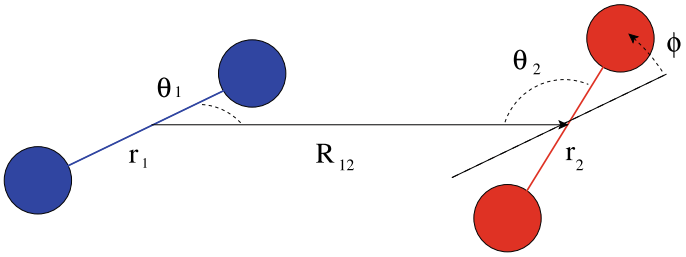

Fig. 1 Coordinates system describing the relative position and orientation of two interacting linear, rigid molecules

2.1 N_2-N_2 PES

The quality of N_2-N_2 PES [3] has been assessed by computing N_2 transport coefficients in the temperature range [250–600 K], by CT-MC simulations based on the expressions given in [21]. CT-MC estimations are compared with the reference experimental data from [20]. Figure 2 shows that the nominal PES, based on the central values of the confidence intervals of the parameters, underestimates both shear viscosity η_s and thermal conductivity λ. The agreement with experiments is improved by reducing the range of repulsive forces in the isotropic contribution of PES, $V^{0,0,0}(R_{12})$. Accordingly, the nominal value of the scale parameter R_m [4], 4.11Å, has been reduced to 4.065 Å, about half standard deviation below the central value. The correction makes the molecule "smaller" and increases η_s and λ. The accuracy of the corrected PES is comparable with that proposed in [15], which is probably the most accurate N_2-N_2 PES for low temperature applications.

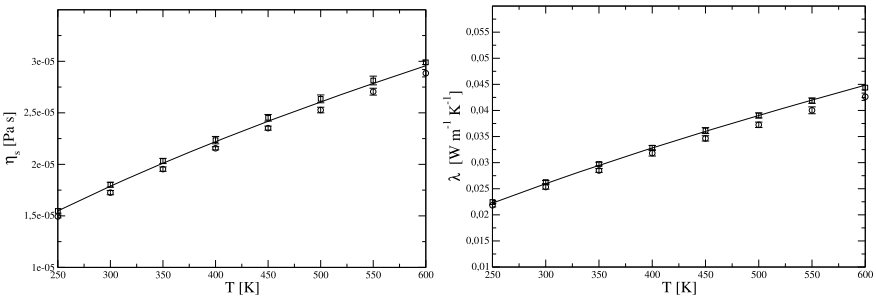

Fig. 2 *Left*—N_2 shear viscosity. Right—N_2 thermal conductivity. Solid lines: NIST data [20]; ○:N_2-N_2 PES with nominal parametes; □: modified N_2-N_2 PES

2.2 O_2-O_2 PES

A similar evaluation has been conducted for O_2-O_2 PES [4], extending a previous investigation [9] to include the effects of spin on molecular interaction. As shown in [4], spin coupling can be accounted for by introducing three separate PES's, describing singlet ($S = 0$), triplet ($S = 1$) and quintet ($S = 2$) states, being S the total spin. The weights associated with the three PES's are $\frac{1}{9}$, $\frac{3}{9}$, $\frac{5}{9}$, respectively [4]. Figure 3, presents the results of the shear viscosity and thermal conductivity obtained from the CT-MC simulations. As in the case of N_2, the nominal O_2-O_2 PES underestimates experimental η_s and λ. Moreover, spin corrections seem to have no effect on η_s and marginal effects on λ.

A closer inspection revealed that the transport properties are different for the three individual PES. However, their weighting compensates for the differences and returns values close to those obtained by the O_2-O_2 PES without spin corrections. As for N_2, the underestimation of the transport coefficients can be mitigated by reducing the effective range of molecular repulsive forces, in the isotropic term $V^{0,0,0}(R_{12})$. Since the deviation from the experimental data is greater than in the case of N_2-N_2 PES, the nominal value of the potential parameter R_m, 3.9 Å, has been reduced to 3.82 Å, about one standard deviation below the nominal value. As shown in Fig. 3, reducing R_m considerably improves the agreement with the experimental η_s, but it is not sufficient to reduce the deviation from the experimental λ by a comparable amount.

2.3 N_2-O_2 PES

The N_2-O_2 PES for the interaction between the N_2 and O_2 molecules is described in [3]. It shares its structure with N_2-N_2 and O_2-O_2 PES's, but no error intervals

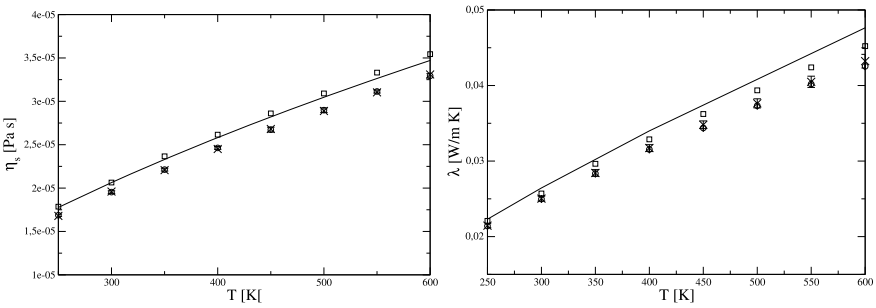

Fig. 3 *Left*—O_2 shear viscosity. *Right*—O_2 thermal conductivity. Solid lines: NIST data [20]; ○:O_2-O_2 PES with nominal parametes, no spin correction; X:PES with nominal parametes and spin correction; □: modified O_2-O_2 PES, with spin correction

are given for the parameters appearing in the radial function $V^{L_1,L_2,L}(R_{12})$. To the authors' knowledge, this particular PES has not yet been evaluated in regard to predictions of transport properties of N_2-O_2 mixtures. In addition to the shear and bulk viscosity estimations, described in Sect. 3, the quality of the PES has been evaluated by comparing data from binary diffusion coefficient data for equimolar mixtures N_2-O_2 [11] with CT-MC and CT-DSMC estimations. The latter have been obtained from equilibrium CT-DSMC simulations, in which the variance of molecular displacement from initial position, $< \Delta r^2 > (t)$, is recorded. The diffusion coefficient, D_{12}, is obtained by applying the Einstein relation [24]

$$D_{12} = \frac{1}{6}\frac{d}{dt} < \Delta r^2 > \tag{2}$$

after the slope of $< \Delta r^2 > (t)$ becomes constant (see Fig. 4). As shown in Fig. 4a, the agreement between the reference data, the estimations obtained by equilibrium CT-DSMC simulations, and the CT-MC direct evaluation of the orientation-averaged integral $\Omega^{(1,1)}_{(1,2)}$ [14] is very good, indicating that the PES describes the N_2-O_2 interactions well.

3 Estimation of Air Shear and Bulk Viscosities

Following Ref. [9], the shear viscosity η_s of N_2-O_2 mixtures was calculated by nonequilibrium CT-DSMC simulations of isothermal, uniform shear flows (USF). These are amenable to a spatially 0-dimensional problem in which the gas is subject to a velocity-dependent force field whose intensity is proportional to the imposed

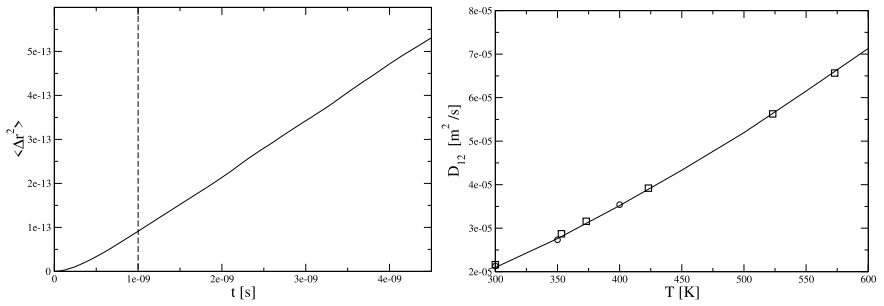

Fig. 4 *Left*—Time evolution of the variance of molecular displacements in an equimolar N_2-O_2 mixture at 1 bar and 300 K. The vertical dashed line, separates the initial, nearly collisionless regime, from the linear one, where Eq. (2) can be used to obtain D_{12}. *Right*—Temperature dependence of D_{12} in an equimolar N_2-O_2 mixture at 1 bar. Solid line: CT-MC estimation from $\Omega^{(1,1)}_{(1,2)}$; ∘: CT-DSMC estimation from Eq. (2); □: D_{12} data from Ref. [11]

shear rate α. A thermostat is also applied to contrast viscous heating and keep the desired temperature value.

The shear viscosity has been obtained by linear regression of shear stress data, computed for small values of α [9]. Since using the nominal PES's would have led to underestimation of η_s and masked the performance of the N_2-O_2 PES, the modified N_2-N_2 and O_2-O_2 PES's, discussed in Sects. 2.1 and 2.2, have been adopted in the comparisons with reference data.

The left panel of Fig. 5 shows the computed η_s as a function of the mixture temperature T, for two mixture compositions: $X_{O_2} = 0.21$ (air) and $X_{O_2} = 0.5$ (equimolar). In the first case η_s data lie slightly above the pure N_2 viscosity, computed by CT-MC. The point at $T = 300$ K is very close to NIST corresponding point. In the case of the equimolar mixture, the computed η_s data are slightly below the viscosity data from Ref. [11] but the overall agreement is good.

Bulk viscosity arises from the finite relaxation time of internal degrees of freedom [14]:

$$\eta_v = \frac{2c^{(i)}}{3c_V} p\tau^{(i)} \tag{3}$$

where $c^{(i)}, c_V$ are the internal and total specific heats (adimensional), p is the pressure and $\tau^{(i)}$ the relaxation time of the internal degrees of freedom:

$$\frac{dE^{(i)}}{dt} = \frac{E_\infty^{(i)} - E^{(i)}}{\tau^{(i)}} \tag{4}$$

where $E^{(i)}$ is the internal energy and $E_\infty^{(i)}$ is the internal energy at equilibrium.

For each gas mixture, the rotational relaxation time at temperature T_0 has been measured from the results of homogeneous (i.e. adiabatic) relaxation simulations where the starting conditions for translational and rotational temperatures are:

$$T_0^t = T_0 + \frac{\Delta T}{3}, \quad T_0^r = T_0 - \frac{\Delta T}{2} \tag{5}$$

The simulated relaxation of rotational energy is fitted with a simple exponential, as suggested by Eq. (4). Then an estimation of the true relaxation time is obtained using small ΔT's, of the order of 10–20 K. The results shown in Figs. 5 and 6 have been obtained using 2×10^6 molecules per simulation. The error bars are indicative of the run-to-run variation of the estimated relaxation times. The accuracy is not high, but sufficient to judge about the behavior of the quantities of interest. In variance with shear viscosity simulations, nominal PES parameters have been used for bulk viscosity estimations. In fact, the uncertainties of the anisotropic contributions of the PES are too large to obtain a reasonably precise estimate of η_v.

Figure 5 shows the results for air. The results of homogeneous relaxation are compared with values obtained from simulation of RBS spectra [10] with DSMC and to the values obtained by fitting the Tenti S6 model to experimental RBS spectra produced with two different driving laser wavelengths. We note that the experiment

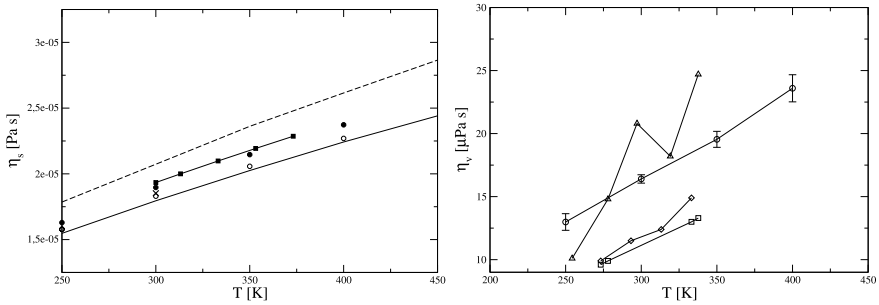

Fig. 5 *Left*—Shear viscosity of N_2-O_2 mixtures. Solid line: pure N_2; Dashed line: Pure O_2; ○: $X_{O_2} = 0.21$ from CT-DSMC simulations; ●: $X_{O_2} = 0.50$ from CT-DSMC simulations; cross: air viscosity from NIST [20]; ■: equimolar N_2-O_2 mixture viscosity data from [11]. *Right*—Bulk viscosity of air. ○: $X_{O_2} = 0.21$ from CT-DSMC simulations; □: DSMC estimations from RBS spectra [10]; ◇: Tenti S6 model estimations from RBS spectra (green light) [10]; △: Tenti S6 model estimations from RBS spectra (blue light) [10];

conducted with blue light is done under more rarefied conditions, where the accuracy of the Tenti S6 model is worse. The CT-DSMC estimations of η_v lie above the points obtained by fitting experimental RBS spectra to DSMC simulations of N_2-O_2 mixtures, based on VSS collision cross sections and Larsen-Borgnakke model for rotational-translational coupling [6]. Data obtained from Tenti S6 model and the same experimental RBS spectra are somehow closer to CT-DSMC estimations but the agreement is only qualitative. It is of some interest to consider bulk viscosity CT-DSMC estimations for pure N_2 and O_2, for which results from the literature are available. In Fig. 6 CT-DSMC results, obtained from homogeneous relaxation, are compared with the recommended values [27], to semiclassical calculations [5, 22, 28], and to experimental results [1, 17, 18, 23, 25]. Experimental results are mostly based on (old) ultrasound absorption measurements, they are available only at room temperature and show a large spread; semiclassical calculations report results for the first Chapman-Enskog approximation and therefore represent a lower bound; the recommendation in [27] is based on correlations obtained from the experimental measurements fitted to the temperature dependence obtained in the theoretical treatment of rotational relaxation of classical rigid rotors [8]. In the case of N_2, CT-DSMC points lie above all other data sets, suggesting that air bulk viscosity is also overestimated by the considered PES's. Oxygen CT-DSMC points are slightly below the recommended data from [27] but overestimate all other values, with the exception of Connor's measurement at $T = 300$ K.

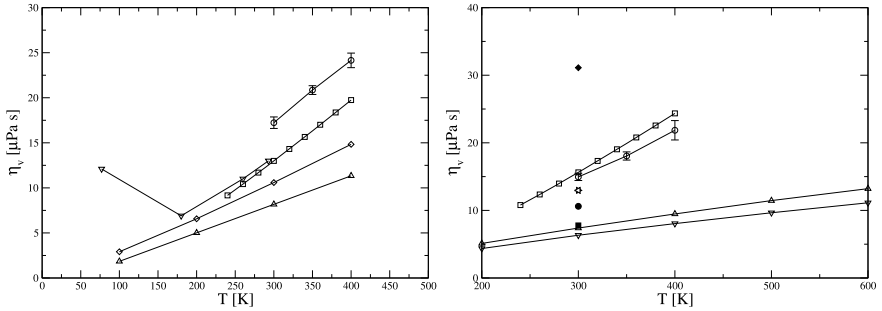

Fig. 6 *Left*—Bulk viscosity of pure N_2. ○: $X_{O_2} = 0.21$ from CT-DSMC simulations; □: from [27]; ◇: from [22]; △: from [5]; ▽: from [18]. *Right*—Bulk viscosity of pure O_2. ○: $X_{O_2} = 0.21$ from CT-DSMC simulations; □:from [27]; △, ▽: from [28]; ●: from [17]; ■: from [23]; ♦: from [13]; ►: from [25]; ◄: from [1]

4 Conclusions

Shear and bulk viscosity of N_2-O_2 mixtures have been computed assuming that N_2 and O_2 molecules behave as rigid dumbbell, interacting by three PES's, including isotropic and anisotropic contributions. Results, obtained by combining Classical Trajectories integration with Monte Carlo and Direct Simulation Monte Carlo, show that the nominal N_2 and O_2 PES's underestimate experimental pure gas shear viscosity and thermal conductivity. Modifying N_2 PES parameters within the given confidence intervals allows improving the agreement with experimental data but the modification on O_2 PES is not as effective. The N_2-O_2 PES seems to provide a good description of N_2 and O_2 coupling, based on CT-DSMC estimations of the binary diffusion coefficient. CT-DSMC estimations of the bulk viscosity of pure N_2, O_2 and air suggest that the nominal PES's overestimate experimental data.

The above considerations point at the necessity of replacing the N_2-N_2 and O_2-O_2 PES's analyzed here with the more accurate ones, respectively proposed in [15] for N_2, and in [16] for O_2.

References

1. Anderson W, Hornig D (1958) Technical Report 8. Brown University, Metcalf Research Laboratory
2. Aquilanti V, Bartolomei M, Cappelletti D, Carmona-Novillo E, Pirani F (2002) The N2–N2 system: an experimental potential energy surface and calculated rotovibrational levels of the molecular nitrogen dimer. J Chem Phys 117(2):615–627

3. Aquilanti V, Bartolomei M, Carmona-Novillo E, Pirani F (2003) The asymmetric dimer N2–O2: characterization of the potential energy surface and quantum mechanical calculation of rotovibrational levels. J Chem Phys 118(5):2214–2222
4. Aquilanti V, Ascenzi D, Bartolomei M, Cappelletti D, Cavalli S, de Castro Vitores M, Pirani F (1999) Molecular beam scattering of aligned oxygen molecules. The nature of the bond in the O2-O2 dimer. J Am Chem Soc 121(46):10794–10802
5. Billing G, Wang L (1992) Semiclassical calculations of transport coefficients and rotational relaxation of nitrogen at high temperatures. J Phys Chem 96:2572
6. Bird GA (1994) Molecular gas dynamics and the direct simulation of gas flows. Clarendon Press, Oxford
7. Boley C, Desai R, Tenti G (1972) Kinetic models and brillouin scattering in a molecular gas. Can J Phys 50:2158
8. Brau C, Jonkman R (1970) Classical theory of rotational relaxation in diatomic gases. J Chem Phys 52:477
9. Bruno D, Frezzotti A, Ghiroldi G (2015) Oxygen transport properties estimation by classical trajectory-direct simulation Monte Carlo. Phys Fluids 27(5)
10. Bruno D, Frezzotti A, Jamali SH, Van De Water W (2023) Finding the bulk viscosity of air from Rayleigh-Brillouin light scattering spectra. J Chem Phys 158(3):031101
11. Bzowski J, Kestin J, Mason EA, Uribe FJ (1990) Equilibrium and transport properties of gas mixtures at low density: eleven polyatomic gases and five noble gases. J Phys Chem Ref Data 19(5):1179–1232
12. Chapman S, Cowling TG (1990) The mathematical theory of non-uniform gases. Cambridge University Press, Cambridge
13. Connor J (1958) Ultrasonic dispersion in oxygen. J Acoust Soc 30:297
14. Ferziger JH, Kaper HG (1972) Mathematical theory of transport processes in gases. North Holland, Amsterdam
15. Hellmann R (2013) Ab initio potential energy surface for the nitrogen molecule pair and thermophysical properties of nitrogen gas. Molecul Phys 111(3):387–401
16. Hellmann R (2023) Ab initio potential energy surfaces for the O2–O2 system and derived thermophysical properties. J Chem Phys 159(10):104303
17. Holmes R, Jones G, Pusat N, Tempest W (1962) Rotational relaxation in helium + oxygen and helium + nitrogen mixtures. Trans Faraday Soc 58:2342–2347
18. van Houten H, Hermans L, Beenakker J (1985) A survey of experimental data related to the non-spherical interaction for simple classical linear molecules and their mixtures with noble gases. Physica 131A:64–103
19. Koura K (1997) 4 Carlo direct simulation of rotational relaxation of diatomic molecules using classical trajectory calculations: nitrogen shock wave. Phys Fluids 9(11):3543–3549
20. Lemmon EW, Jacobsen RT (2004) Viscosity and thermal conductivity equations for nitrogen, oxygen, argon, and air. Int J Thermophys 25(1):21–69
21. Taxman N (1958) Classical theory of transport phenomena in dilute polyatomic gases. Phys Rev 110(6):1235–1239
22. Nyeland C, Billing G (1988) Transport coefficients of diatomic gases: Internal-state analysis for rotational and vibrational degrees of freedom. J Phys Chem 92:1752
23. Parker J, Adams C, Stavseth R (1953) Absorption of sound in argon, nitrogen, and oxygen at low pressure. J Acoust Soc Am 25:263
24. Resibois P, DeLeener M (1977) Classical kinetic theory of fluids. Wiley, New York
25. Tempest W, Parbrook H (1957) The absorption of sound in argon, nitrogen and oxygen. Acta Acust 7:354–362
26. Tenti G, Boley C, Desai R (1974) On the kinetic model description of rayleigh-brillouin scattering from molecular gases. Can J Phys 52:285
27. Uribe F, Mason E, Kestin J (1989) A correlation scheme for the thermal conductivity of polyatomic gases at low density. Physica A 156:467–491
28. Wang L, Billing G (1993) Rotational relaxation and transport properties of oxygen by using the importance sampling method. J Phys Chem 97:2523

29. Witschas B, Lemmerz C, Reitebuch O (2014) Daytime measurements of atmospheric temperature profiles (2–15 km) by lidar utilizing rayleigh-brillouin scattering. Opt Lett 39:1972

Open Access This chapter is licensed under the terms of the Creative Commons Attribution 4.0 International License (http://creativecommons.org/licenses/by/4.0/), which permits use, sharing, adaptation, distribution and reproduction in any medium or format, as long as you give appropriate credit to the original author(s) and the source, provide a link to the Creative Commons license and indicate if changes were made.

The images or other third party material in this chapter are included in the chapter's Creative Commons license, unless indicated otherwise in a credit line to the material. If material is not included in the chapter's Creative Commons license and your intended use is not permitted by statutory regulation or exceeds the permitted use, you will need to obtain permission directly from the copyright holder.

Micro- and Nanoscale Flows

Uniform Flow Past a Circular Disk: Numerical Analysis and Modeling of Thermal Polarization

Takuma Tomita, Satoshi Taguchi, and Tetsuro Tsuji

Abstract In this paper, we investigate a slow rarefied gas flow past a circular disk with an emphasis on the thermal polarization effect. First, the behavior of the gas is numerically studied based on the Bhatnagar–Gross–Krook model of the Boltzmann equation and the diffuse reflection boundary condition, under the assumption that the system can be linearized. A key highlight of the numerical results is the localization of temperature variations near the edge of the disk in the near-continuum regime. Consistent with previous studies, we find that the temperature near the edge displays distinct behavior, differing from the classical kinetic boundary layer typically observed near smooth boundaries. Next, we explore the role of the free motion of gas molecules and construct a simplified toy model to interpret the above numerical results. The model demonstrates qualitative agreement with the numerical results, providing valuable insights into the observed phenomena.

Keywords Thermal polarization · Kinetic model · Edge effects

1 Introduction

When the mean free path of gas molecules is comparable to the characteristic length of a system, the continuum hypothesis and the assumption of local thermal equilibrium break down. Under such rarefied conditions, it is well-known that a non-uniform temperature distribution on a surface induces gas flow, even in the absence of external forces. Complementary to this phenomenon is thermal polarization [2], in which the gas temperature varies around a body in a flow, even when the surface of the body is maintained at the same temperature as the surrounding uniform flow. Thermal polarization is fundamentally a non-equilibrium effect and remains relevant even when the flow speed is sufficiently low for the system to be linearized, that is, when nonlinear effects such as viscous heating are negligible.

T. Tomita · S. Taguchi (✉) · T. Tsuji
Graduate School of Informatics, Kyoto University, Kyoto, Japan
e-mail: taguchi.satoshi.5a@kyoto-u.ac.jp

© The Author(s) 2026

M. Grabe et al. (eds.), *Rarefied Gas Dynamics*, Springer Aerospace Technology,
https://doi.org/10.1007/978-3-032-00094-1_28

From a theoretical perspective, these phenomena originate from the non-equilibrium velocity distribution of gas molecules. An important challenge in rarefied gas dynamics is bridging kinetic descriptions with macroscopic behavior. To this end, asymptotic expansion techniques have been widely used in the literature. In particular, with the aid of a systematic analysis of the kinetic boundary layer (Knudsen layer), Sone [4] classified various kinetic effects according to the orders of the Knudsen number Kn, which is defined as the ratio of the mean free path of gas molecules to the characteristic length of a system. For slow flows, which are of concern here, the zeroth order of Kn corresponds to the continuum theory, while the first, second, and higher orders account for non-equilibrium effects. This framework is known as generalized slip-flow theory.

However, the generalized slip-flow theory assumes that both boundary shapes and boundary conditions are smooth, making it inapplicable to flows around edge-shaped bodies. As reported in [6], a numerical study on thermal edge flow and radiometric flow in a two-dimensional setting revealed that macroscopic quantities exhibit anomalous behavior near an edge. Specifically, a fractional order of Kn was observed, which cannot be predicted by conventional slip-flow theory. It is worth noting that such non-smooth boundaries can be commonly encountered in modern applications, including micro gas pumps (Knudsen pumps) [8] and self-propelled particles (Janus particles) [1].

In this study, we extend the previous work [6] to a more realistic three-dimensional case by examining the thermal polarization effect induced by a slow uniform flow past a circular disk. The paper is divided into two main parts. In the first part, we numerically investigate the behavior of the gas based on a kinetic equation. In the second part, we construct a simplified toy model to qualitatively reproduce the numerical results and obtain an insight into the thermal polarization effect around the disk.

2 Numerical Analysis Based on a Kinetic Formulation

2.1 Problem and Formulation

Let us consider a situation where an infinitely thin circular disk is placed in a uniform flow at speed U. We take the radius of the disk L as the characteristic length of the system and introduce Cartesian coordinates Lx_i $(i = 1, 2, 3)$ in such a way that the origin is centered on the disk and the x_1-axis is perpendicular to the disk. The uniform flow is perpendicular to the disk, and the disk surface is maintained at a uniform temperature T_0. Far from the disk, the gas is in the equilibrium state with density ρ_0, flow velocity $(U, 0, 0)$, and temperature T_0. There is no external force acting on the gas. We investigate the steady behavior of the gas under the following assumptions: (i) The behavior of the gas is governed by the Bhatnagar–Gross–Krook (BGK) model of the Boltzmann equation; (ii) A gas molecule is diffusely reflected on the disk surface; (iii) The flow speed U is so small compared to the thermal speed

$(2RT_0)^{1/2}$ that the system can be linearized around the reference equilibrium state at rest with density ρ_0 and temperature T_0, where R is the specific gas constant.

Next, we formulate the problem. Let $(2RT_0)^{1/2}\boldsymbol{\zeta}$ be the molecular velocity and $\rho_0(2RT_0)^{3/2}(1+\phi(\boldsymbol{x},\boldsymbol{\zeta})E)$ be the velocity distribution function (VDF), where $E = E(\boldsymbol{\zeta}) := \pi^{-3/2}\exp(-\boldsymbol{\zeta}^2)$. In addition, we denote the mass density of the gas by $\rho_0(1+\omega(\boldsymbol{x}))$, the flow velocity by $(2RT_0)^{1/2}\boldsymbol{u}(\boldsymbol{x})$, and the temperature of the gas by $T_0(1+\tau(\boldsymbol{x}))$. These macroscopic quantities are related to $\phi(\boldsymbol{x},\boldsymbol{\zeta})$ through its moments with respect to $\boldsymbol{\zeta}$, as defined in (1c) below. The linearized BGK equation and its boundary conditions are summarized as follows (see §1.11 of [4]):

$$\boldsymbol{\zeta}\cdot\nabla_{\boldsymbol{x}}\phi = \frac{1}{\kappa}(\phi_e - \phi), \tag{1a}$$

$$\phi_e = \omega + 2\boldsymbol{\zeta}\cdot\boldsymbol{u} + (\boldsymbol{\zeta}^2 - \frac{3}{2})\tau, \tag{1b}$$

$$\omega = \int_{\mathbb{R}^3}\phi E\mathrm{d}\boldsymbol{\zeta}, \quad \boldsymbol{u} = \int_{\mathbb{R}^3}\boldsymbol{\zeta}\phi E\mathrm{d}\boldsymbol{\zeta}, \quad \tau = \frac{2}{3}\int_{\mathbb{R}^3}(\boldsymbol{\zeta}^2 - \frac{3}{2})\phi E\mathrm{d}\boldsymbol{\zeta}, \tag{1c}$$

$$\text{b.c.} \quad \phi \to \sigma_{\mathrm{w}}^{\pm}(\boldsymbol{x}), \quad \sigma_{\mathrm{w}}^{\pm}(\boldsymbol{x}) = 2\sqrt{\pi}\int_0^{\mp\infty}\zeta_1\left(\int_{-\infty}^{\infty}\int_{-\infty}^{\infty}\phi E\mathrm{d}\zeta_2\mathrm{d}\zeta_3\right)\mathrm{d}\zeta_1$$
$$(x_1 \to \pm 0,\ x_2^2 + x_3^2 < 1,\ \zeta_1 \gtrless 0), \tag{1d}$$

$$\text{b.c.} \quad \phi \to 2\zeta_1 u_\infty \quad (|\boldsymbol{x}| \to \infty). \tag{1e}$$

Here, κ in (1a) is the sole parameter of the system and is defined as $\kappa = (\sqrt{\pi}/2)\mathrm{Kn} = (\sqrt{\pi}/2)(\ell_0/L)$, where ℓ_0 represents the mean free path of the gas molecules in the reference equilibrium state at rest, while $\mathrm{Kn} = \ell_0/L$ is the Knudsen number of the system. The diffuse reflection boundary condition (1d) states that gas molecules are reflected on the surface according to the corresponding part of a stationary Maxwellian distribution, determined by the temperature of the disk surface and by the condition of no net flux across the boundary. This is also referred to as the complete accommodation condition. While more general boundary conditions incorporating accommodation coefficients are also used in the literature, we focus on the diffuse reflection condition for the sake of simplicity. Equation (1e) implies that ϕ approaches the uniform equilibrium state at infinity, where u_∞ denotes the non-dimensional speed of the uniform flow, defined by $u_\infty = U(2RT_0)^{-1/2}$. Note that $u_\infty \ll 1$ due to the above assumption (iii), and that $\phi, \omega, \boldsymbol{u}$, and τ linearly depend on u_∞.

In this study, we employ the BGK equation to simplify the analysis, although other models that yield more realistic Prandtl numbers could be used with additional computational effort.

2.2 Integral Equations

To balance accuracy and feasibility, our numerical analysis is fully based on the integral formulation of the BGK equation. The integral equation is briefly explained in this section, with further details deferred to a forthcoming paper.

The BGK equation (1a) is a transport equation, as its left-hand side represents the transport effect in the direction of the molecular velocity $\boldsymbol{\zeta}$. For a given $(\boldsymbol{x}, \boldsymbol{\zeta})$, the characteristic curve is the line passing through the point $\boldsymbol{x}$ and parallel to $\boldsymbol{\zeta}$. To derive the integral forms of the BGK equation (1a), we consider the following two cases separately. The first case arises when the disk is encountered while tracing the characteristic curve backward in the direction of $-\boldsymbol{\zeta}$ from the point $\boldsymbol{x}$. In this case, integrating (1a) along the characteristic curve gives

$$\phi(\boldsymbol{x}, \boldsymbol{\zeta}) = \frac{1}{\kappa|\boldsymbol{\zeta}|}\left[\int_0^{s_w} \exp(-\frac{s}{\kappa|\boldsymbol{\zeta}|})\phi_e(\boldsymbol{x} - \frac{\boldsymbol{\zeta}}{|\boldsymbol{\zeta}|}s, \boldsymbol{\zeta})\mathrm{d}s + \exp(-\frac{s_w}{\kappa|\boldsymbol{\zeta}|})\sigma_w^{\pm}(\boldsymbol{x}_*)\right]. \quad (2)$$

Here, the integral variable s represents the backward distance along the characteristic curve, s_w denotes the distance from $\boldsymbol{x}$ to the disk along this curve, and ϕ_e and $\sigma_w^{\pm}$ are given by (1b) (with (1c)) and (1d), respectively. The point $\boldsymbol{x}_* = \boldsymbol{x} - (\boldsymbol{\zeta}/|\boldsymbol{\zeta}|)s_w$ is the intersection of the characteristic curve with the disk. The plus-minus sign above σ_w indicates $+$ for $x_1 > 0$ and $-$ for $x_1 < 0$. Note that ϕ_e depends on ϕ through ω, $\boldsymbol{u}$ and τ, and that $\sigma_w^{\pm}$ also depends on ϕ. A similar comment applies to (3) below. The second case arises when the backward characteristic curve extends to infinity without intersecting the disk. In this case, the integral equation takes the form

$$\phi(\boldsymbol{x}, \boldsymbol{\zeta}) = \frac{1}{\kappa|\boldsymbol{\zeta}|}\int_0^{\infty} \exp(-\frac{s}{\kappa|\boldsymbol{\zeta}|})\phi_e(\boldsymbol{x} - \frac{\boldsymbol{\zeta}}{|\boldsymbol{\zeta}|}s, \boldsymbol{\zeta})\mathrm{d}s, \quad (3)$$

where ϕ_e is given by (1b) with (1c).

Equations (2) and (3) are solved by an iterative method similar to the one used in [7]. The discrepancy between (2) and (3), arising from distinct molecular trajectories, leads to discontinuities in ϕ (see, e.g., [5]). For an accurate analysis, these discontinuities were carefully taken into account in our numerical computations.

2.3 Numerical Results

First, let us examine the overall flow and temperature fields. In Fig. 1a, the flow velocity and the temperature fields around the disk are presented in the case of $\kappa = 0.5$. This figure shows the vectors of $\boldsymbol{u}/u_\infty$ and contours of τ/u_∞ in the region $-2 \le x_1 \le 2$, $-2 \le x_2 \le 2$ on the plane $x_3 = 0$. The cross-section of the disk, located at $x_1 = 0$,

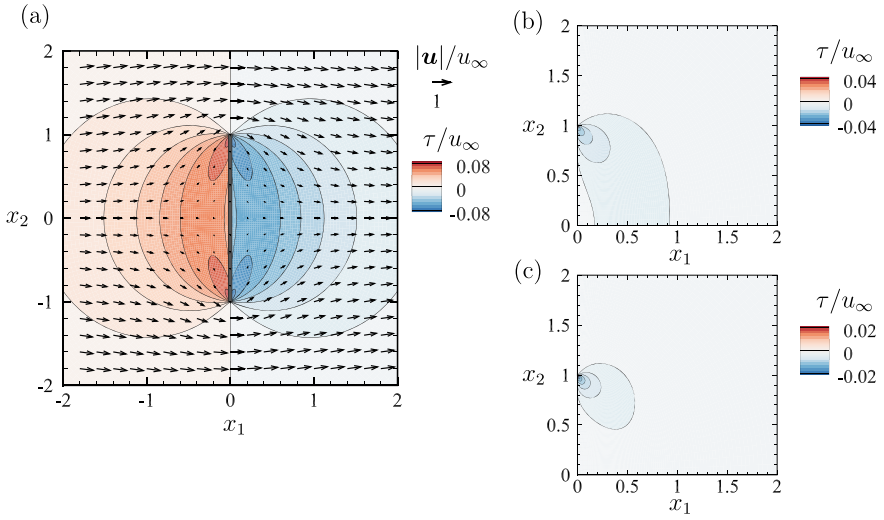

Fig. 1 **a** Flow velocity $\boldsymbol{u}/u_\infty$ (vector field) and temperature τ/u_∞ (contours) in the region $-2 \le x_1 \le 2$, $-2 \le x_2 \le 2$ on the plane $x_3 = 0$ for $\kappa = 0.5$. The thick line at the center of the figure indicates the cross-section of the disk. **b**, **c** Temperature distributions τ/u_∞ in the region $0 \le x_1 \le 2$, $0 \le x_2 \le 2$ on the plane $x_3 = 0$. **b** $\kappa = 0.1$, **c** 0.05

$-1 < x_2 < 1$, is also included and depicted as a thick segment for visibility. Owing to the axisymmetry of the system, the flow and temperature fields are symmetric with respect to the x_1 axis. In addition, τ is antisymmetric with respect to the x_2 axis in the figure. As shown, the flow is obstructed by the disk, and the gas temperature is higher than T_0 on the upstream side and lower on the downstream side, despite the fact that the disk surface is maintained at a uniform temperature T_0. This behavior exemplifies the thermal polarization effect.

Next, we examine how the temperature field depends on κ. In Fig. 1b, c, we present the contour plots of τ/u_∞ for (b) $\kappa = 0.1$ and (c) $\kappa = 0.05$. Considering the symmetric properties discussed earlier, only the region $0 \le x_1 \le 2$, $0 \le x_2 \le 2$ on the plane $x_3 = 0$ is shown. It is observed that the isothermal lines become increasingly concentrated near the edge of the disk located at $(x_1, x_2) = (0, 1)$ as κ decreases. This indicates that the thermal polarization effect becomes more localized near the edge with smaller values of κ.

To gain further insights, we analyze the relationship between τ and κ as follows. On the plane $x_3 = 0$, we select three points κ away from the edge: $(x_1, x_2) = (\kappa/\sqrt{2}, 1 + \kappa/\sqrt{2})$, $(\kappa, 1)$, $(\kappa/\sqrt{2}, 1 - \kappa/\sqrt{2})$, referred to as P, Q, and R, respectively (Fig. 2a). This scaling reflects the use of the mean free path ℓ_0 as the reference length, rather than L, in the region near the edge. Figure 2b shows the log-log plot of $|\tau/u_\infty|$ versus κ at these three points (red square for P, green triangle for Q, blue circle for R). The dashed line represents a slope of $\kappa^{1/2}$. The figure clearly shows that the magnitude of the perturbed temperature, $|\tau/u_\infty|$, decreases proportionally to

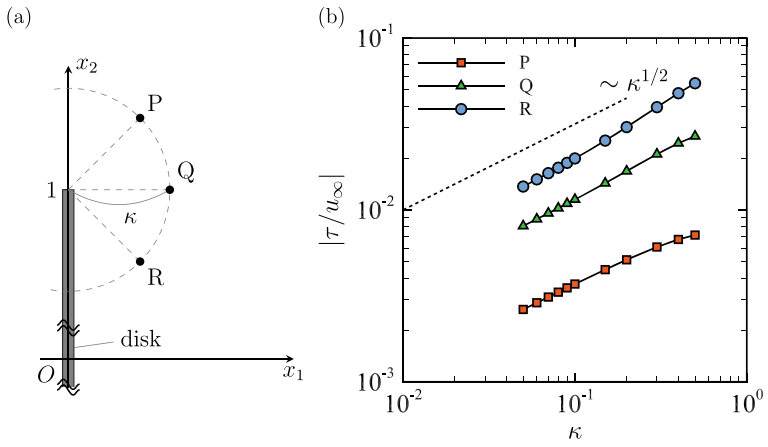

Fig. 2 **a** Three points located κ away from the edge: P$(\kappa/\sqrt{2}, 1+\kappa/\sqrt{2})$, Q$(\kappa, 1)$, R$(\kappa/\sqrt{2}, 1-\kappa/\sqrt{2})$. **b** Log-log plots of $|\tau/u_\infty|$ as a function of κ at these points: red squares for P, green triangles for Q, and blue circles for R. The dashed line indicates a slope of $\kappa^{1/2}$

$\kappa^{1/2}$ as $\kappa \to 0$ at all three points. As previously mentioned, such a fractional power behavior cannot be captured in the conventional framework of the generalized slip-flow theory, in which all quantities are expanded as a power series in the Knudsen numbers (i.e., the Hilbert expansion) [4].

3 Modeling of Thermal Polarization

In this section, we develop a toy model to qualitatively explain the thermal polarization effect around the disk. To this end, we focus on the role of the free motion of gas molecules. To better understand the significance of free motion, let us review the concept of thermal creep flow, which occurs near a wall with a non-uniform temperature distribution under rarefied conditions. It is well-known that the flow arises due to differences in the momentum of gas molecules reaching the wall. Specifically, molecules originating from the hotter side carry, on average, greater momentum than those from the colder side, while molecules are isotropically reflected off the wall due to diffuse reflection. Consequently, gas molecules impart a net momentum to the wall from the hotter side toward the colder side, inducing a counteracting gas flow from the colder side toward the hotter side. The critical point here is that this momentum exchange is enabled by the finite distance gas molecules travel after a molecular collision. (As the Knudsen number, $\mathrm{Kn} = \ell_0/L$, approaches zero, the free motion of molecules shrinks to a single point on the wall, where no temperature difference exists.) Through the construction of our toy model, we will see that the thermal polarization effect is closely connected to the free motion of molecules and that its mechanism is analogous to that of the thermal creep flow.

3.1 Modeling Method

We begin by interpreting the integral equations (2) and (3) from a physical perspective. If we make the change of integral variable $s = |\boldsymbol{\zeta}|t$ in (3), we obtain

$$\phi(\boldsymbol{x}, \boldsymbol{\zeta}) = \int_0^\infty \phi_e(\boldsymbol{x} - \boldsymbol{\zeta}t, \boldsymbol{\zeta}) f(t)\mathrm{d}t, \quad f(t) = \frac{1}{\kappa}\exp(-\frac{t}{\kappa}). \tag{4}$$

The new integral variable t represents the backward travel time of a molecule. Consequently, $\boldsymbol{x} - \boldsymbol{\zeta}t$ is the position of the molecule at time t before the present, and $\phi_e(\boldsymbol{x} - \boldsymbol{\zeta}t, \boldsymbol{\zeta})$ is the (perturbed) local Maxwellian at that location. Furthermore, $f(t)$ can be interpreted as the probability density function of an exponential distribution with the parameter $1/\kappa$. Therefore, the right-hand side of (4) represents the mean value of ϕ_e along the path of a molecule, weighted by an exponential distribution. In other words, ϕ_e encodes information about the molecular velocity at the moment of a molecular collision, and this information is transmitted via the free motion of the molecule. According to (4), the elapsed time since the most recent molecular collision follows an exponential distribution. Regarding (2), after changing the integral variable to $s = |\boldsymbol{\zeta}|t$ and performing a slight transformation of the second term, we obtain

$$\phi(\boldsymbol{x}, \boldsymbol{\zeta}) = \int_0^{s_\mathrm{w}/|\boldsymbol{\zeta}|} \phi_e(\boldsymbol{x} - \boldsymbol{\zeta}t, \boldsymbol{\zeta}) f(t)\mathrm{d}t + \int_{s_\mathrm{w}/|\boldsymbol{\zeta}|}^\infty \sigma_\mathrm{w}^\pm(\boldsymbol{x}_*) f(t)\mathrm{d}t. \tag{5}$$

In other words, if the path of the molecule intersects the disk during the backward tracing, the remaining contribution of ϕ_e must be replaced by $\sigma_\mathrm{w}^\pm(\boldsymbol{x}_*)$.

The set of equations (4) and (5) forms an implicit equation of ϕ, as the right-hand side also depends on ϕ through ϕ_e and $\sigma_\mathrm{w}^\pm$. To eliminate this dependence, we approximate ϕ_e and $\sigma_\mathrm{w}^\pm$ using a function independent of ϕ. Assuming a given density field $\omega_0(\boldsymbol{x})$, flow velocity field $\boldsymbol{u}_0(\boldsymbol{x})$, and temperature temperature field $\tau_0(\boldsymbol{x})$, the local Maxwellian $\phi_0(\boldsymbol{x}, \boldsymbol{\zeta}) = \omega_0(\boldsymbol{x}) + 2\boldsymbol{\zeta} \cdot \boldsymbol{u}_0(\boldsymbol{x}) + (\boldsymbol{\zeta}^2 - \frac{3}{2})\tau_0(\boldsymbol{x})$ can be used as a crude approximation of ϕ_e. Recall that molecular collisions dominate in the continuum regime. Taking this into account, we assume that $\omega_0(\boldsymbol{x}) = 0$, and $\boldsymbol{u}_0(\boldsymbol{x})$ and $\tau_0(\boldsymbol{x})$ satisfy the equations of continuum theory. The solution to the Stokes equation with no-slip boundary conditions can be found in [3]. In our problem setting, $\tau_0(\boldsymbol{x}) = 0$ serves as the trivial solution to the Laplace equation. In addition, the simplest way to approximate $\sigma_\mathrm{w}^\pm$ is to substitute ϕ_0 for ϕ in the definition of $\sigma_\mathrm{w}^\pm$ given in (1d). As a result, the integral on the right-hand side of (1d) becomes zero, causing the second term on the right-hand side of (5) to vanish.

After these manipulations, we obtain

$$\phi(\boldsymbol{x}, \boldsymbol{\zeta}) = \int_0^{s_B} \phi_0(\boldsymbol{x} - \boldsymbol{\zeta} t, \boldsymbol{\zeta}) f(t) \mathrm{d}t, \tag{6}$$

where $s_B = s_\mathrm{w}/|\boldsymbol{\zeta}|$ if the backward molecular path intersects the disk; otherwise, $s_B = \infty$. Since the right-hand side of (6) no longer depends on ϕ, the formula is significantly easier to compute than (4) and (5). Despite its simplicity, it retains the mathematical structure required to capture the effects of free molecular motion.

3.2 Computation of Thermal Polarization Using the Model

We are now ready to estimate the thermal polarization effect around the disk using the model. At this stage, analytical evaluation of the integrals in (6) and the third equation of (1c) is no longer feasible. Consequently, the results presented below are obtained through numerical computation. It is worth noting that the model (6) requires only a single set of numerical integrations without any iterative procedures. As a result, the computational costs are significantly lower compared to the numerical analysis discussed in Sect. 2.

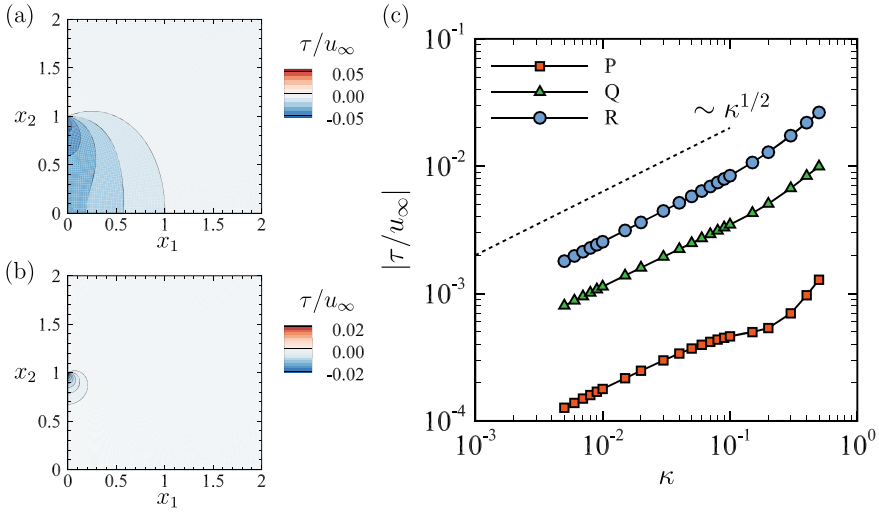

Fig. 3 **a**, **b** Temperature distribution obtained using (6). The values of τ/u_∞ are shown in the region $0 \le x_1 \le 2, 0 \le x_2 \le 2$ on the plane $x_3 = 0$. **a** $\kappa = 0.5$, **b** 0.1. **c** Log-log plots of $|\tau/u_\infty|$ as a function of κ at points P, Q, and R (Refer to the last paragraph in Sect. 2 and Fig. 2a). Red squares for P, green triangles for Q, and blue circles for R. The dashed line represents a slope of $\kappa^{1/2}$

In Fig. 3a, b, we present the spatial distributions of τ/u_∞ obtained using the model for (a) $\kappa = 0.5$ and (b) $\kappa = 0.1$. Only the region $0 \le x_1 \le 2, 0 \le x_2 \le 2$ on the plane $x_3 = 0$ is presented, consistent with Fig. 1b, c. From these figures, we can identify the localization of temperature variation as κ decreases. Furthermore, Fig. 3c shows the log-log plot of $|\tau/u_\infty|$ versus κ at the points P, Q, and R (refer to the last paragraph of Sect. 2.3 and Fig. 2a). Remarkably, Figs. 3c and 2b share a common feature: in both the results derived from the BGK equation and those from our toy model, $|\tau/u_\infty|$ decreases proportionally to $\kappa^{1/2}$ as κ approaches zero.

4 Conclusion

In this study, we investigated the steady behavior of a slow rarefied gas flow past a circular disk based on the linearized BGK equation and the diffuse reflection boundary condition. Our precise numerical analysis, in which the discontinuities in the VDF were fully accounted for, revealed the following key findings: (i) The temperature around the disk is higher on the upstream side and lower on the downstream side, demonstrating the thermal polarization effect; (ii) As κ decreases, temperature variation becomes increasingly localized near the edge of the disk; (iii) At points located κ away from the edge, the magnitude of the temperature decreases proportionally to $\kappa^{1/2}$ as $\kappa \to 0$.

Next, we proposed the formula (6) as a toy model. The temperature fields computed using this model showed good qualitative agreement with the numerical results based on the BGK equation, particularly regarding the three features discussed above. This suggests that the free motion of molecules plays a crucial role in the thermal polarization effect. Moreover, the computational cost of the model is significantly lower, making it an efficient tool for quickly exploring various kinetic effects.

Acknowledgements This work was supported by JSPS KAKENHI Grant Numbers JP20H02067, JP22K03924, JP22K18770, and JST SPRING Grant Number JPMJSP2110. Numerical computations were carried out using the supercomputer of ACCMS, Kyoto University.

References

1. Baier T, Tiwari S, Shrestha S, Klar A, Hardt S (2018) Thermophoresis of Janus particles at large Knudsen numbers. Phys Rev Fluids 3(9):094202
2. Bakanov SP, Vysotskij VV, Derjaguin BV, Roldughin VI (1983) Thermal polarization of bodies in the rarefied gas flow. J Non-Equilib Thermodyn 8(1):75–83
3. Happel J, Brenner H (1983) Low Reynolds number hydrodynamics: with special applications to particulate media. Springer, Netherlands
4. Sone Y (2007) Molecular gas dynamics: theory, techniques, and applications. Birkhäuser Boston

5. Sone Y, Takata S (1992) Discontinuity of the velocity distribution function in a rarefied gas around a convex body and the S layer at the bottom of the Knudsen layer. Trans Theory Statist Phys 21(4–6):501–530
6. Taguchi S, Aoki K (2012) Rarefied gas flow around a sharp edge induced by a temperature field. J Fluid Mechan 694:191–224
7. Taguchi S, Tsuji T, Kotera M (2020) Transient behaviour of a rarefied gas around a sphere caused by impulsive rotation. J Fluid Mechan 909:A6
8. Wang X, Su T, Zhang W, Zhang Z, Zhang S (2020) Knudsen pumps: a review. Microsyst Nanoeng 6(1):26

Open Access This chapter is licensed under the terms of the Creative Commons Attribution 4.0 International License (http://creativecommons.org/licenses/by/4.0/), which permits use, sharing, adaptation, distribution and reproduction in any medium or format, as long as you give appropriate credit to the original author(s) and the source, provide a link to the Creative Commons license and indicate if changes were made.

The images or other third party material in this chapter are included in the chapter's Creative Commons license, unless indicated otherwise in a credit line to the material. If material is not included in the chapter's Creative Commons license and your intended use is not permitted by statutory regulation or exceeds the permitted use, you will need to obtain permission directly from the copyright holder.

Modeling Transient Slip Behavior from Laminar to Molecular Flow

Rodion Groll

Abstract One of the greatest challenges of microfluid dynamics remains to describe the physical behavior in the transition region between the continuum and the free molecular regime. In this work, the non-dimensionalized relationship between mass flow and pressure drop in microchannels of different cross-sections is investigated. The flow resistance in microchannels is affected by increasing Knudsen numbers because the molecular wall collisions have an increasing influence. The reduced collision probabilities between the particles correspondingly reduce the influence of the effective viscosity of the fluid. In this work, approaches are investigated which have been able to predict the effective pressure difference specific permeation of a fluid as a function of the Knudsen number of an increasingly thinned gas flow. A further challenge is posed by the question of the origin of the local Knudsen minimum. This minimum of the non-dimensioned mass flow in the range Kn ≈ 1 is cancelled out in the range of free molecular flows by the increasing permeation. The model presented combines the effects of different scale ranges by superposition. The model data are compared with measured data and BGK simulation results in both the transient slip regime and the free molecular convection regime and show excellent agreement for both plane channel flows and pipe flows.

Keywords Scale-transitioning gas flow · Analytical modeling · Slip model · Knudsen flow

1 Introduction

This relationship of mass flow and pressure loss in microchannel flows is controlled on macroscopic scales by temperature or viscosity. When the Knudsen range is reached, the influence of molecular wall collisions increases significantly compared to inter-particle collisions, so that even at constant temperature the pressure loss varies with decreasing molecular number density. The hydraulic diameter of a plane

R. Groll (✉)
Center of Applied Space Technology and Microgravity, University of Bremen, Bremen, Germany
e-mail: groll@zarm.uni-bremen.de

© The Author(s) 2026

M. Grabe et al. (eds.), *Rarefied Gas Dynamics*, Springer Aerospace Technology,
https://doi.org/10.1007/978-3-032-00094-1_29

channel flow is described by the limit value of a channel flow with a rectangular cross-section, where the width w is considered to be much greater than the height h and is regarded as infinity. The hydraulic diameter of a flat channel flow corresponds to twice the channel height. In highly diluted gas flows, the no-slip condition known from laminar flows in fluid mechanics can no longer be fulfilled for higher Knudsen numbers. As a consequence, slip conditions are introduced for Kn > 0.01, for which it is known that they are no longer fulfilled at Kn < 1 at the latest. The laminar channel flow is described by a parabolic velocity profile. So, pressure gradient and mass flow are proportional as follows:

$$u_0(y) = \frac{1}{2\mu}\frac{dp}{dx}\left(y^2 - hy\right) \Rightarrow \dot{m}_0 = \int_0^h u_0 dy = \rho\frac{h^2}{12\mu}A\frac{dp}{dx};$$

$$\mu = \frac{5\pi}{32}\rho\lambda\bar{c}$$

Corresponding to the following relation the definition of the viscosity μ and the hydraulic diameter D_h (ratio between four-times the cross-sectional area A and the circumference/perimeter Γ) non-dimensional mass flow G is inversely proportional to the hydraulic Knudsen number $Kn_h = \lambda/D_h$ [16]:

$$G = -\frac{3}{D_h}\frac{\dot{m}_0}{A\frac{dp}{dx}}\frac{\sqrt{\pi}}{4}\bar{c} = \frac{1}{10\sqrt{\pi}}\frac{D_h}{\lambda} = \frac{Kn_h^{-1}}{10\sqrt{\pi}} \tag{1}$$

Thus, in this laminar description, a hyperbolic G-profile results, which deviates from the reference data in the said Knudsen range with increasing Knudsen numbers.

2 Slip Flow

First-Order Slip Model. *The higher mass flow in rarefied follows the. increasing velocity near the wall—so called velocity slip us.*

With the parabolic velocity profile the slip velocity generates an effective offset and mass flow follows (see Fig. 1 (right)):

$$A = wh \Rightarrow \dot{m} = \dot{m}_0 + \dot{m}_s = \rho\frac{wh^3}{12\mu}\frac{dp}{dx} + \rho u_s wh$$

The reality is anywhere between the ideal elastic and the purely diffusive reflection (see Fig. 1 (left and middle)). Based on the definitions of slip velocity $u_s = (u_\lambda + u_r)/2$ and rebound velocity $u_r = (1 - \sigma_v)u_\lambda + \sigma_v u_w$ the relative slip velocity $u_s - u_w$ is the average of impact u_λ and rebound velocity u_r. The rebound velocity depends on the weighting accommodation coefficient σ_v [14]. So, the effective model depends

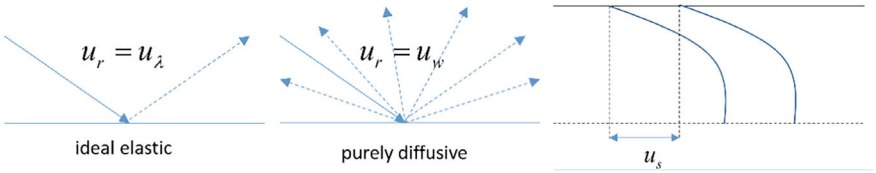

Fig. 1 Relation between averaged rebound velocity u_r, the averaging velocity from mean-free path-length distance u_λ and the velocity of the wall u_w (left and middle), Slip velocity shifts the velocity profile in channel flow and increases the effective volume flow (right)

on the velocity gradient at the wall. With the parabolic velocity profile slip velocity and mass flow follows neglecting wall velocity $u_w = 0$:

$$u_s = \frac{2-\sigma_v}{\sigma_v}\lambda \left.\frac{du}{dy}\right|_{y=0} = -\frac{2-\sigma_v}{\sigma_v}\frac{\lambda h}{2\mu}\frac{dp}{dx} \Rightarrow \frac{\dot{m}}{\dot{m}_0}$$
$$= \frac{\dot{m}_0 + \dot{m}_s}{\dot{m}_0} = 1 + 6\frac{2-\sigma_v}{\sigma_v}\frac{\lambda}{h}$$

With this linear slip velocity approximation, the corresponding non-dimensional parameter G is shifted by a constant depending on the accommodation coefficient σ_v.

$$-\frac{\dot{m}}{A\frac{dp}{dx}} = \left(1 + 6\frac{2-\sigma_v}{\sigma_v}\frac{\lambda}{h}\right)\rho\frac{h^2}{12\mu}; \mu = \frac{5\pi}{32}\rho\lambda\bar{c}$$
$$G = -\frac{3}{D_h}\frac{\dot{m}}{A\frac{dp}{dx}}\frac{\sqrt{\pi}}{4}\bar{c} = \frac{1}{10\sqrt{\pi}}\frac{D_h}{\lambda} + \frac{2-\sigma_v}{\sigma_v}\frac{6}{5\sqrt{\pi}} \quad (2)$$

Following this relation, the permeation is increasing with decreasing σ_v values. In the present example (Eq. 2), a superposition principle can be read off directly, whereby the effective permeation is represented as a summation of mass flows added to the laminar solution (Eq. 1), each of which is generated by different decoupled effects, as shown in Fig. 1.

Second-Order Slip Model. The second-order model describing the slip velocity (e.g., [1, 10]):

$$u_s = \frac{2-\sigma_v}{\sigma_v}\left(\lambda\left.\frac{du}{dy}\right|_{y=0} + \lambda^2\left.\frac{d^2u}{dy^2}\right|_{y=0}\right) = -\frac{2-\sigma_v}{\sigma_v}\left(\frac{\lambda h}{2\mu} - \frac{\lambda^2}{2\mu}\right)\frac{dp}{dx}$$

and the effective mass flow increases with this non-linear form:

$$\frac{\dot{m}}{\dot{m}_0} = \frac{\dot{m}_0 + \dot{m}_s}{\dot{m}_0} = 1 + 6\frac{2-\sigma_v}{\sigma_v}\frac{\lambda}{h}\left(1 - \frac{\lambda}{h}\right) = 1 + 12\frac{2-\sigma_v}{\sigma_v}\frac{\lambda}{D_h}\left(1 - 2\frac{\lambda}{D_h}\right)$$

With this second-order slip velocity approximation the corresponding non-dimensional parameter G is shifted by a linear function depending on the coefficient σ_v.

$$-\frac{\dot{m}}{A\frac{dp}{dx}} = \frac{\rho D_h^2}{48\mu} + \rho\frac{2-\sigma_v}{\sigma_v}\frac{\lambda D_h}{4\mu}\left(1-2\frac{\lambda}{D_h}\right)$$
$$\Rightarrow G = \frac{D_h}{10\sqrt{\pi}\lambda} + \frac{2-\sigma_v}{\sigma_v}\frac{6}{5\sqrt{\pi}}\left(1-2\frac{\lambda}{D_h}\right)$$

However, the second-order equation is also a superposition with a non-linear addition to the laminar solution. This non-linearity increases the error near in the region close to Kn = 1, the region where the mean-free path of molecules is similar to the channel height.

Slip Correction for higher Knudsen numbers. Analog algebraic approaches do not use accommodation coefficients. The non-dimensional mass flow is developed in a way analogue to second order with $h = D_h/2$. The results with the estimated coefficients of Cercignani and Daneri [3] ($C_1 = 1.1466$ and $C_2 = 0.2439$) as of Deissler [5] ($C_1 = 1$ and $C_2 = 9/32$) are shown in Fig. 2 (left). With accommodation coefficient depending "constants" the developed model can be approximated by the algebraic form $C_1 = 2/\sigma_v - 1$ and $C_2 = 1/2 - 1/\sigma_v$ (e.g., [1, 10]). So the non-dimensional mass flow G become independent from optimized constants:

$$G = \frac{1}{10\sqrt{\pi}}\frac{D_h}{\lambda} + \frac{6}{5\sqrt{\pi}}\left(C_1 + 4C_2\frac{\lambda}{D_h}\right) = \frac{Kn_h^{-1}}{10\sqrt{\pi}} + \frac{6}{5\sqrt{\pi}}\frac{2-\sigma_v}{\sigma_v}(1-2Kn_h)$$

Because of the increasing influence of wall collisions for $\lambda > 0.1$ h the effective mean-free path of molecules for characterizing the slip behavior is smaller than λ.

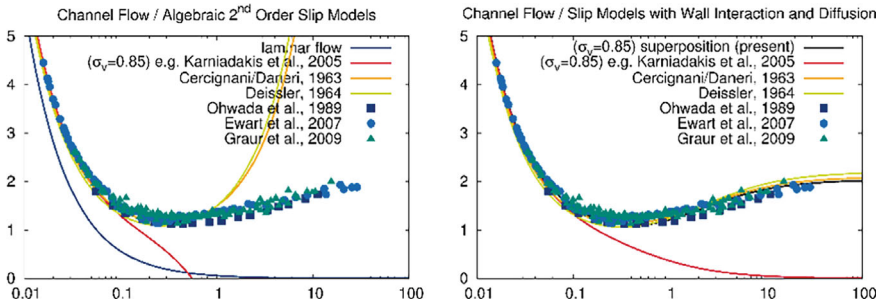

Fig. 2 Left: Non-dimensional mass flow [G] over hydraulic Knudsen number [Kn_h] increases unphysically by second-order optimized algebraic approaches for $Kn_h > 1$. [3, 5, 6, 8, 10, 12], right: Channel flow modeling non-dimensional mass flow [G] over hydraulic Knudsen number [Kn_h] including slip, wall-collision and free-molecular correction terms (Data: [3, 5, 6, 8, 10, 12])

With a model of the summarization of the wave numbers $1/\lambda_{\text{eff}} = 1/\lambda + 1/\text{h}$ (see e.g., [2, 4]). The effective Knudsen is decreased too.

$$Kn_{h,eff} = \frac{\lambda_{eff}}{D_h} = \frac{1}{\frac{D_h}{\lambda} + \frac{D_h}{h}} = \frac{1}{Kn_h^{-1} + 2} = \frac{Kn_h}{1 + 2Kn_h}$$

With the new-defined Knudsen number $\text{Kn}_{\text{h,eff}}$ the corrected transport results as follows:

$$\begin{aligned} G_{eff} &= \frac{Kn_h^{-1}}{10\sqrt{\pi}} + \frac{6}{5\sqrt{\pi}} \frac{2 - \sigma_v}{\sigma_v} \left(1 - 2Kn_{h,eff}\right) \\ &= \frac{Kn_h^{-1}}{10\sqrt{\pi}} + \frac{6}{5\sqrt{\pi}} \frac{2 - \sigma_v}{\sigma_v} \left(1 - \frac{2Kn_h}{1 + 2Kn_h}\right) \end{aligned}$$

3 Free-Molecular Flow

Depending on momentum conservation the free molecular mass flow is calculated by the definition of viscosity as follows (e.g., [9]):

$$\frac{\dot{m}_{FM}}{A} = \frac{\mu}{n\bar{c}} \frac{d}{dx}(n\bar{c}); \mu = \frac{5\pi}{32} \rho \lambda \bar{c} \Rightarrow -\frac{\dot{m}_{FM}}{A\frac{dp}{dx}} = \frac{5\lambda}{8\bar{c}} \frac{\gamma + 1}{\gamma}$$

Inserted to the definition of non-dimensional mass flow G the free-molecular approach results as follows.

$$G_{FM} = \frac{3}{D_h} \frac{\dot{m}_{FM}}{A\frac{dp}{dx}} \frac{\sqrt{\pi}}{4} \bar{c} = \frac{15\sqrt{\pi}}{32} \frac{\gamma + 1}{\gamma} \frac{\lambda}{D_h} = \frac{15\sqrt{\pi}}{32} \frac{\gamma + 1}{\gamma} Kn_h$$

With an effective, reduced mean-free path depending on characteristic geometric length proportional to hydraulic diameter $\text{l}_\alpha = \alpha \text{D}_\text{h}$ the summarization of wave numbers leads to $1/\lambda_{\text{FM,eff}} = 1/\lambda + \alpha/\text{D}_\text{h}$. The Knudsen number definition follows the effective Knudsen number describing free-molecular flows:

$$Kn_{FM,eff} = \frac{\lambda_{FM,eff}}{D_h} = \frac{1}{D_h\left(\frac{1}{\lambda} + \frac{\alpha}{D_h}\right)} = \frac{\frac{\lambda}{D_h}}{1 + \alpha\frac{\lambda}{D_h}} = \frac{Kn_h}{1 + \alpha Kn_h}$$

And the effective mass flow of free-molecular flows predicts the free molecular convection decreasing with smaller Knudsen numbers:

$$G_{FM,eff} = \frac{15\sqrt{\pi}}{32}\frac{\gamma+1}{\gamma}Kn_{h,eff} = \frac{15\sqrt{\pi}}{32}\frac{\gamma+1}{\gamma}\frac{Kn_h}{1+\alpha Kn_h}$$

Channel coefficient. Based on comparison of the limiting coefficients of (see [13, 15]):

$$\lim_{Kn_h\to\infty} G_{FM,eff} = \frac{2-\sigma_v}{\sigma_v}\frac{8}{3\sqrt{\pi}}$$

the equivalence approximation with the present study results the coefficient α and the effective free-molecular gas flow therefore (see [9]):

$$\frac{15\sqrt{\pi}}{32}\frac{\gamma+1}{\gamma}\alpha^{-1} = \frac{2-\sigma_v}{\sigma_v}\frac{8}{3\sqrt{\pi}} \Rightarrow \alpha = \frac{\sigma_v}{2-\sigma_v}\frac{45\pi}{256}\left(1+\frac{1}{\gamma}\right)$$

The effective molecular mass flow $G_{FM,eff}$ results with the implemented constant α as follows (see Fig. 2 (right)):

$$G_{FM,eff} = \frac{15\sqrt{\pi}}{32}\frac{\gamma+1}{\gamma}\frac{Kn_h}{1+\frac{\sigma_v}{2-\sigma_v}\frac{45\pi}{256}\left(1+\frac{1}{\gamma}\right)Kn_h}$$

4 Results

4.1 Channel Flow

Summarizing molecular free-flow solution to the slip solution $G_{tot} = G_{eff} + G_{FM,eff}$ the transition from laminar to free-molecular flow is modeled.

The closing result modeling this transient behavior of channel flows ($\sigma_v = 0.85$) is this explicit formulation describing the transient mass flow development by summarization (Eq. 3) of the components: the laminar, the slip and the free-molecular component (see Fig. 3 (left)):

$$G_{tot} = \frac{Kn_h^{-1}}{10\sqrt{\pi}} + \frac{2-\sigma_v}{\sigma_v}\frac{6}{5\sqrt{\pi}}\left(1-2\frac{Kn_h}{1+2Kn_h}\right) + \frac{\frac{15\sqrt{\pi}}{32}\frac{\gamma+1}{\gamma}Kn_h}{1+\frac{\sigma_v}{2-\sigma_v}\frac{45\pi}{256}\left(1+\frac{1}{\gamma}\right)Kn_h} \tag{3}$$

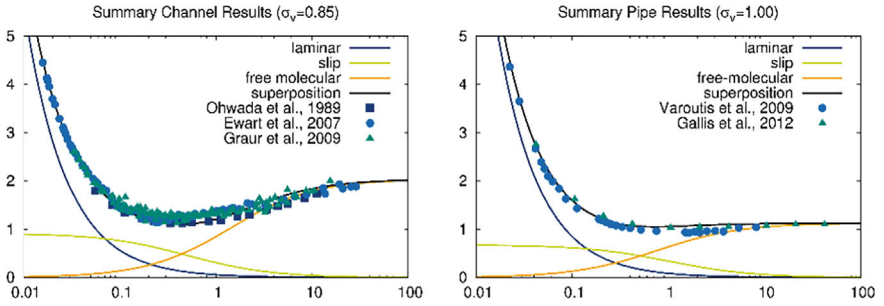

Fig. 3 Left: Channel flow modeling non-dimensional mass flow G depending on hydraulic Knudsen number (Kn_h) as superposition of laminar, slip and free-molecular component. [6, 8, 12], right: Pipe flow modeling non-dimensional mass flow G depending on hydraulic Knudsen number (Kn_h) as superposition of laminar, slip and free-molecular component [7, 17]

4.2 Pipe Flow

With the different form of the cross-sectional area of a pipe flow the definition of the circle area produces an equivalence of hydraulic diameter D_h and diameter d of the pipe. The solution of a laminar Hagen-Poiseuille flow produces a hyperbolic relation G_0 and the first-order slip model shifts the curve with a constant to G:

$$G_0 = \frac{3}{20\sqrt{\pi}} Kn_h^{-1} \Rightarrow G = \frac{3}{20\sqrt{\pi}} Kn_h^{-1} + \frac{2-\sigma_v}{\sigma_v} \frac{6}{5\sqrt{\pi}}$$

The second-order model transforms the curve with large differences in the Knudsen regime:

$$G = \frac{3}{20\sqrt{\pi}} Kn_h^{-1} + \frac{2-\sigma_v}{\sigma_v} \frac{6}{5\sqrt{\pi}} (1 - Kn_h)$$

For circular cross sections with an accommodation coefficient of $\sigma_v = 1.0$, the curves show a better fit in the slip regime. (Kn < 1) (e.g., [11]). With the Knudsen number correction of the slip component show as estimated a much better first-order approximation of the mass flow behavior in in slip regime for $\sigma_v = 1.0$. With substituted accommodation coefficients the wall-collision approximation of the second-order slip model produces analog with channel flow results also a decreasing curve with a limit G = 0 at infimum.

$$G_{eff} = \frac{3}{20\sqrt{\pi}} Kn_h^{-1} + \frac{6}{5\sqrt{\pi}} \left(1 - \frac{Kn_h}{1 + Kn_h}\right)$$

Also, for tubes the new model is the superposition (Eq. 4) of laminar flow, slip flow and molecular flow/diffusion.

$$G_{tot} = \frac{3}{20\sqrt{\pi}} Kn_h^{-1} + \frac{6}{5\sqrt{\pi}} \left(1 - \frac{Kn_h}{1 + Kn_h}\right) + \frac{15\sqrt{\pi}}{32} \left(1 - \frac{\left(1 + \frac{1}{\gamma}\right) Kn_h}{1 + \frac{15\pi}{64}\left(1 + \frac{1}{\gamma}\right) Kn_h}\right) \tag{4}$$

And also, this approximation matches with reference data in an excellent way as shown in Fig. 3 (right).

5 Conclusion

The results of this superposition model provide excellent results for the channel and pipe flow based on the hydraulic diameter and the corresponding Knudsen number. Except for minor adjustments to the accommodation coefficient in the slip regime, it can be concluded from the investigations presented that this method can be used to predict mass flows in microchannels independently of the shape of the cross-section in a Knudsen number-dependent manner.

Based on the modeling by three complementary causes, the previously only measured local Knudsen minimum can be quantitatively classified as a slip transition between continuum mechanical description and free molecular flow. In detail, the approaches can be summarized as follows. The slip and free-molecular flow effects follow the reflective and diffusive molecular rebound behavior and are modeled as an additional mass flow corresponding to an additional velocity profile. As shown many algebraic models show good results for $0.1 < \mathrm{Kn} < 1$, but they cannot model the behavior for $\mathrm{Kn} > 1$. For the wall collision effects, the influence of the slip flow decreases for higher Knudsen numbers ($\mathrm{Kn} > 1$). So, three mass flows are superimposed, two of which disappear for large Knudsen numbers and the third is so small even for large Knudsen numbers that it is negligible in other areas compared to the other values.

The strictly hyperbolic form of the laminar flow is supplemented by slip diffusion, which disappears for large Knudsen numbers and converges to a constant value for small Knudsen numbers. Relative to the laminar solution, this naturally disappears for small Knudsen numbers. The significance of the shape of the cross-sectional area on the model parameters in the slip regime could not be clarified conclusively. However, it is clear that concavely curved surfaces favor multiple collisions, which drastically reduces the effective free path length. This could be the starting point for further research. While the first two model components disappear for large Knudsen numbers, the third term, the free molecular diffusion, becomes dominant for the limiting range at $\mathrm{Kn} >> 1$.

References

1. Beskok A, Karniadakis GE (1999) A model for flows in channels, pipes and ducts at micro and nano scales. Microscale Thermophys Eng 3:43
2. Bird GA (1994) Molecular gas dynamics and the direct simulation of gas flows. Clarendon, Oxford
3. Cercignani C, Daneri A (1963) Flow of a rarefied gas between two parallel plates. J Appl Phys 34:3509
4. Chapman S, Cowling TG (1970) The mathematical theory of non-uniform gases. Cambridge University Press, Cambridge
5. Deissler RG (1964) An analysis of second-order slip flow and temperature-jump boundary conditions for rarefied gases. Int J Heat Mass Transf 7(6):681
6. Ewart T, Perrier P, Graur IA, Méolans JG (2007) Mass flow rate measurements in a microchannel, from hydrodynamic to near free molecular regimes. J Fluid Mech 584:337
7. Gallis MA, Torczynski JR (2012) Direct simulation Monte Carlo-based expressions for the gas mass flow rate and pressure profile in a microscale tube. Phys Fluids 24:012005
8. Graur IA, Perrier P, Ghozlani W, Méolans JG (2009) Measurements of tangential momentum accommodation coefficient for various gases in plane microchannel. Phys Fluids 21:102004
9. Groll R, Kunze S, Besser B (2020) Correction of second-order slip condition for higher Knudsen numbers by approximation of free-molecular diffusion. Phys Fluids 32:092008
10. Karniadakis GE, Beskok A, Aluru N (2005) Microflows and nanoflows: fundamentals and simulations. Springer, New York
11. Kunze S, Groll R, Besser B, Thöming J (2022) Molecular diameters of rarefied gases. Sci Rep 12:2057
12. Ohwada T, Sone Y, Aoki K (1989) Numerical analysis of the Poiseuille and thermal transpiration flows between two parallel plates on the basis of the Boltzmann equation for hard-sphere molecules. Phys Fluids A 1:2042
13. Perrier P, Graur IA, Ewart T, Meolans JG (2011) Mass flow rate measurements in microtubes: from hydrodynamic to near free molecular regime. Phys Fluids 23:042004
14. Schaaf SA, Chambre PL (1961) Rarefied gas dynamics. Princeton University Press, Princeton
15. Sharipov F, Seleznev V (1998) Data on internal rarefied gas flows. J Phys Chem Ref Data 27:657
16. Veltzke T (2013) On gaseous microflows under isothermal conditions. Universität Bremen. https://media.suub.uni-bremen.de/handle/elib/470
17. Varoutis S, Naris S, Hauer V, Day C, Valougeorgis D (2009) Computational and experimental study of gas flows through long channels of various cross sections in the whole range of the Knudsen number. J Vac Sci Technol A 27:89

Open Access This chapter is licensed under the terms of the Creative Commons Attribution 4.0 International License (http://creativecommons.org/licenses/by/4.0/), which permits use, sharing, adaptation, distribution and reproduction in any medium or format, as long as you give appropriate credit to the original author(s) and the source, provide a link to the Creative Commons license and indicate if changes were made.

The images or other third party material in this chapter are included in the chapter's Creative Commons license, unless indicated otherwise in a credit line to the material. If material is not included in the chapter's Creative Commons license and your intended use is not permitted by statutory regulation or exceeds the permitted use, you will need to obtain permission directly from the copyright holder.

A Meshless Approach to Study Rarefied Gas Flows in Lid-Driven Square Cavities

Himanshi, Anirudh Singh Rana, and Vinay Kumar Gupta

Abstract This paper investigates rarefied gas flows in a lid-driven square cavity using the method of fundamental solutions (MFS). Unlike traditional techniques requiring extensive computational resources and meshing for simulating rarefied gas flows in complex geometries, the MFS bypasses the need for mesh generation and offers a promising alternative. This research focuses on rarefied gas flows confined within an isothermal square cavity with single-sided and two-sided lid-driven configurations. The coupled constitutive relations (CCR) have been adopted in the present work to capture rarefaction effects.

1 Introduction

Gas flows in microchannels have gained importance with the miniaturization of devices like micro heat-exchangers, inkjet printheads, and micro pumps. In these systems, the Knudsen number (ratio of the molecular mean-free path to a characteristic length scale) becomes large and rarefaction effects come into play. While the Navier–Stokes–Fourier (NSF) equations are accurate for low Knudsen numbers, they fail at higher values, where effects like velocity slip and temperature jump dominate. The Boltzmann equation provides a comprehensive description in such cases but is computationally demanding. To bridge this gap, extended macroscopic transport equations have been derived from the Boltzmann equation such as those from the Chapman–Enskog technique [2] and moment methods like, Grad's moments approach [3] and regularized moment methods [4, 13]. More recently, Rana et al. [12] introduced a model to extend classical continuum theories which closes the mass, momentum, and energy balance equations with the coupled constitutive relations (CCR), and is therefore known as the CCR model.

Himanshi (✉) · V. K. Gupta
Department of Mathematics, Indian Institute of Technology Indore, Indore, India
e-mail: hkhungar@gmail.com

A. S. Rana
Department of Mathematics, Birla Institute of Technology and Science Pilani, Rajasthan, India

© The Author(s) 2026

M. Grabe et al. (eds.), *Rarefied Gas Dynamics*, Springer Aerospace Technology,
https://doi.org/10.1007/978-3-032-00094-1_30

Traditional methods like finite element and finite volume approaches, while precise, require substantial computational resources and complex meshing for 3D problems. In contrast, meshless methods, such as the method of fundamental solutions (MFS) offer a flexible and efficient alternative by superimposing Green's functions to approximate solutions to linear boundary value problems. The MFS has been successfully applied to rarefied gas flows [6–9, 11] due to its computational efficiency and straightforward implementation. Building on our earlier work [6], we extend the MFS framework based on the fundamental solutions of the CCR model in two dimensions to study the classic lid-driven cavity problem. The results are validated against the regularized 13-moment (R13) equations and direct simulation Monte Carlo (DSMC) data [10], and we further explore flow scenarios driven by the motion of two walls in both the same and opposite directions.

2 Problem Description and Mathematical Formulation

2.1 Problem Statement

We consider a monatomic rarefied gas contained within an isothermal square cavity of unit side length ($L = 1$). Three configurations are studied:

1. Single-sided lid-driven cavity, where the top wall moves at a constant (dimensionless) velocity $\boldsymbol{v}_w$ in the positive x-direction, while the other walls remain stationary (Fig. 1(a)).
2. Two-sided cavity with both top and bottom walls moving in the positive x-direction with the same velocity $\boldsymbol{v}_w$ (Fig. 1(b)).
3. Two-sided cavity with the top and bottom walls moving in opposite directions, each at speed $\boldsymbol{v}_w$ (Fig. 1(c)).

2.2 The Model and Numerical Technique

The complete CCR model includes the mass, momentum, and energy balance equations along with the coupled constitutive relations [12]. In the present work, we directly present the linearized CCR model in the steady state in order to avoid repetition. For details, the reader is referred to [6]. The steady-state linear dimensionless CCR model consists of the conservation laws

$$\nabla \cdot \boldsymbol{v} = 0, \quad \nabla p + \nabla \cdot \boldsymbol{\sigma} = \boldsymbol{0} \quad \text{and} \quad \nabla \cdot \boldsymbol{q} = 0 \tag{1}$$

closed with the relations

$$\boldsymbol{\sigma} = -2\mathrm{Kn}(\overline{\nabla \boldsymbol{v}} + \alpha_0 \overline{\nabla \boldsymbol{q}}) \quad \text{and} \quad \boldsymbol{q} = -\frac{5\mathrm{Kn}}{2\mathrm{Pr}}(\nabla T + \alpha_0 \nabla \cdot \boldsymbol{\sigma}). \tag{2}$$

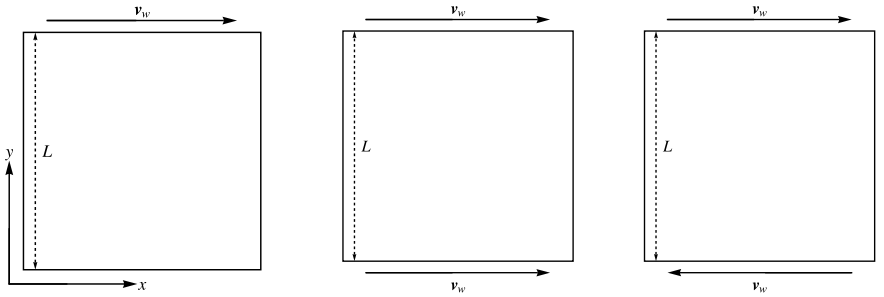

Fig. 1 Schematics of (**a**) single-sided lid-driven cavity, and two-sided lid-driven cavities with top and bottom walls moving in (**b**) same and (**c**) opposite directions

The variables $\boldsymbol{v}$, p, $\boldsymbol{q}$, T and $\boldsymbol{\sigma}$ denote the (dimensionless) velocity, pressure, heat flux, temperature and stress, respectively. Here, α_0 is the coupling coefficient, Kn is the Knudsen number, and Pr is the Prandtl number. The trace-free symmetric components of the velocity and heat flux gradients are represented by $\overline{\boldsymbol{\nabla v}}$ and $\overline{\boldsymbol{\nabla q}}$, respectively. In this study, $\alpha_0 = 2/5$ and $\mathrm{Pr} = 2/3$, corresponding to Maxwell molecules [12]. The thermodynamically-consistent boundary conditions associated with the CCR model read [6, 11]

$$\boldsymbol{v} \cdot \boldsymbol{n} - \boldsymbol{v}_w \cdot \boldsymbol{n} = 0, \tag{3}$$

$$\boldsymbol{q} \cdot \boldsymbol{n} = -1.3568(T + \alpha_0 \boldsymbol{n} \cdot \boldsymbol{\sigma} \cdot \boldsymbol{n}), \tag{4}$$

$$\boldsymbol{n} \cdot \boldsymbol{\sigma} \cdot \boldsymbol{t} = -0.7019(\boldsymbol{v} \cdot \boldsymbol{t} - \boldsymbol{v}_w \cdot \boldsymbol{t} + \alpha_0 \boldsymbol{q} \cdot \boldsymbol{t}), \tag{5}$$

where $\boldsymbol{v}_w$ is the wall velocity, $\boldsymbol{n}$ and $\boldsymbol{t}$ are the unit normal and tangent vectors at the boundary, respectively.

The fundamental solutions of the CCR model (1)–(2) in 2D have been determined in [6]. Implementation of the MFS for current problem involves the placement of source points outside the flow domain on a circular fictitious boundary, a schematic of which is illustrated in Fig. 2. A linear system is formed by evaluating the boundary conditions at each boundary node to calculate the unknowns (point force $\boldsymbol{f}_i = (f_{1_i}, f_{2_i})^{\mathsf{T}}$, and point heat source g_i) corresponding to i^{th} source point $\boldsymbol{x}_i^s$; see Refs. [6, 8] for details. The overall solution at a point in the domain having position $\boldsymbol{x}$ is given by superposition of the fundamental solutions which read [6]

$$\boldsymbol{v} = \sum_{i=1}^{N_s} \left[\frac{\boldsymbol{f}_i}{8\pi\,\mathrm{Kn}} \cdot \left(\frac{2\boldsymbol{r}_i \boldsymbol{r}_i}{r_i^2} - (2\ln r_i - 1)\boldsymbol{I} \right) + \frac{1}{4\pi} \frac{5\mathrm{Kn}}{\mathrm{Pr}} \alpha_0^2 \boldsymbol{f}_i \cdot \left(\frac{2\boldsymbol{r}_i \boldsymbol{r}_i}{r_i^4} - \frac{\boldsymbol{I}}{r_i^2} \right) \right], \tag{6}$$

$$p = \sum_{i=1}^{N_s} \frac{\boldsymbol{f}_i \cdot \boldsymbol{r}_i}{2\pi r_i^2}, \tag{7}$$

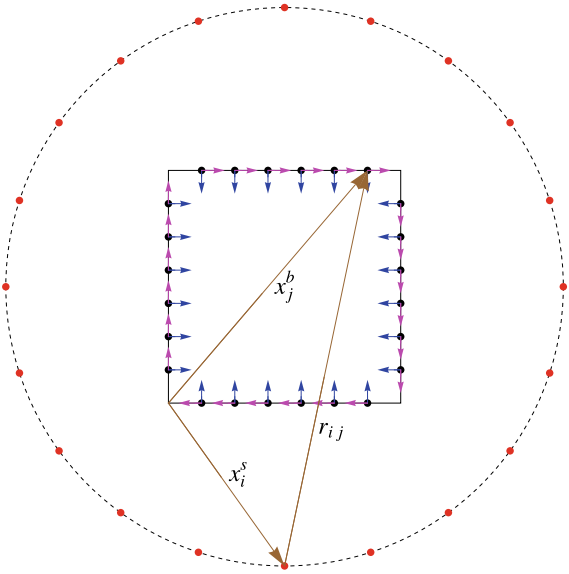

Fig. 2 Schematic of the distribution of collocation points (or boundary nodes) on the boundaries and source points outside the flow region for the problem described in Sect. 2.1. The magenta and blue arrows demonstrate the tangential and normal directions at each boundary node, respectively

$$\boldsymbol{\sigma} = \sum_{i=1}^{N_s} \frac{\boldsymbol{f}_i \cdot \boldsymbol{r}_i + 2\mathrm{Kn}\, g_i\, \alpha_0}{2\pi} \left(\frac{2\boldsymbol{r}_i \boldsymbol{r}_i}{r_i^4} - \frac{\boldsymbol{I}}{r_i^2} \right), \tag{8}$$

$$T = -\sum_{i=1}^{N_s} \frac{\mathrm{Pr}}{5\mathrm{Kn}} \frac{g_i\, \ln r_i}{\pi}, \tag{9}$$

$$\boldsymbol{q} = \sum_{i=1}^{N_s} \left[\frac{g_i}{2\pi} \frac{\boldsymbol{r}_i}{r_i^2} - \frac{1}{4\pi} \frac{5\mathrm{Kn}}{\mathrm{Pr}} \alpha_0 \boldsymbol{f}_i \cdot \left(\frac{2\boldsymbol{r}_i \boldsymbol{r}_i}{r_i^4} - \frac{\boldsymbol{I}}{r_i^2} \right) \right], \tag{10}$$

where $\boldsymbol{r}_i$ denotes the relative position vector of the i^{th} source point (having position $\boldsymbol{x}_i^s$) from any position $\boldsymbol{x}$ in the domain.

3 Results and Discussion

The results have been obtained by fixing an equal number of boundary nodes and source points, i.e., $N_b = N_s = 200$ and the cavity region $\{(x, y) : 0 \leq x \leq 1, 0 \leq y \leq 1\}$. The fictitious circular boundary on which the source points are placed is centered at $(0.5, 0.5)$ with radius $R_s = 2$.

3.1 Results for a Single-Sided Lid-Driven Cavity

The dimensionless velocity of the lid is fixed at $(v_x, v_y) = (1, 0)$. The results obtained from the MFS applied to the CCR model are validated against data from the DSMC method and R13 equations reported in [10]. The left panel of Fig. 3 illustrates the variation of the vertical velocity along the x-direction at fixed $y = 0.5$, i.e., the variation of $v_y(x, 0.5)$ along the horizontal centerline of the cavity for Kn $= 0.08$. Analogously, the right panel of Fig. 3 depicts the variation of the horizontal velocity $v_x(0.5, y)$ along the vertical centerline of the cavity for Kn $= 0.08$. It is evident that there is a good agreement among the results from the CCR model, DSMC method and R13 model in both panels. Small deviations near the corners are observed, likely due to the inability of the CCR model to capture Knudsen layers, which are more pronounced near solid boundaries.

Figure 4 further illustrates the variation of v_y along horizontal lines at $y = 0.1, 0.4$, and 0.8 (left panel) and v_x along vertical lines at $x = 0.1, 0.4$, and 0.8 (right panel). The increasing tendency of horizontal velocity component v_x with increase in y is due to the maximum horizontal velocity at lid, whereas the wave-like nature of the vertical velocity component v_y with variation in x is due to the formation of vortices which could be clearly depicted via velocity streamlines.

The left panel of Fig. 5 shows velocity streamlines over shear stress σ_{xy} contours for Kn $= 0.08$, indicating the clockwise vortex structure driven by the moving lid. The contours represent the distribution of shear stress σ_{xy} within the cavity induced due to velocity gradient. The right panel in Fig. 5 depicts the heat flux lines plotted over the temperature contours for Kn $= 0.08$. The second-order temperature-jump condition (4) causes cold and hot regions at the left and right corners near the moving

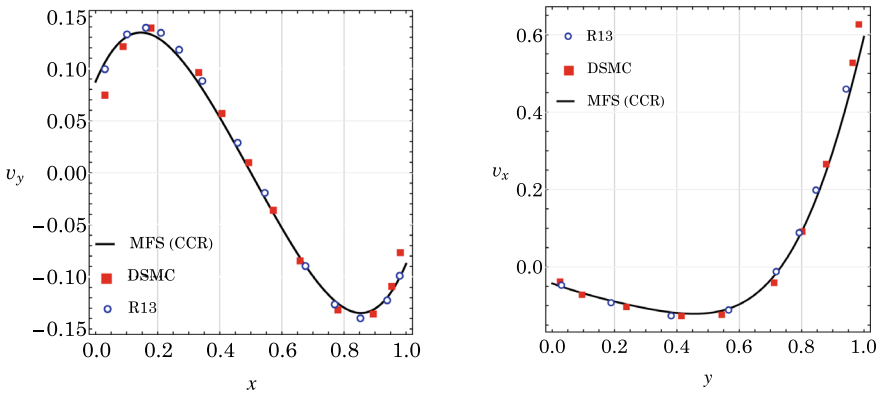

Fig. 3 Variation of v_y along the horizontal centerline (left) and variation of v_x along the vertical centerline (right) for Kn $= 0.08$. The solid black curve represents the results for the MFS applied to the CCR model, the red (square) and blue (circle) symbols denote the data from the DSMC method and R13 model, respectively, taken from Ref. [10]

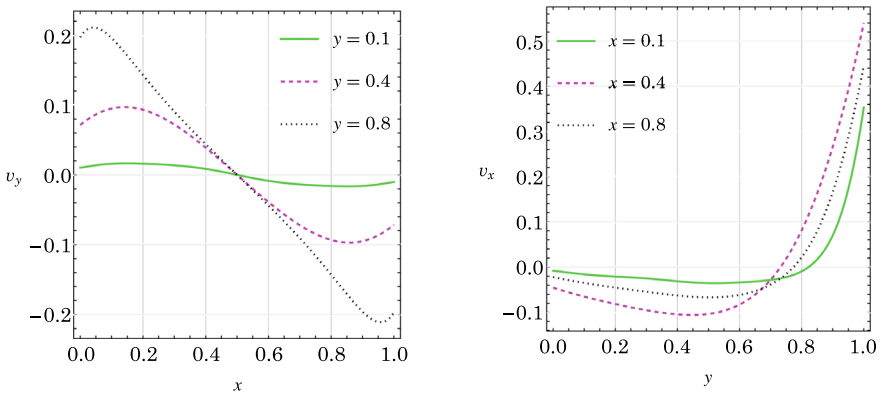

Fig. 4 Variation in v_y along different horizontal lines $y = 0.1, 0.4$ and 0.8 inside the cavity (left) and the variation of v_x along different vertical lines $x = 0.1, 0.4$ and 0.8 inside the cavity (right)

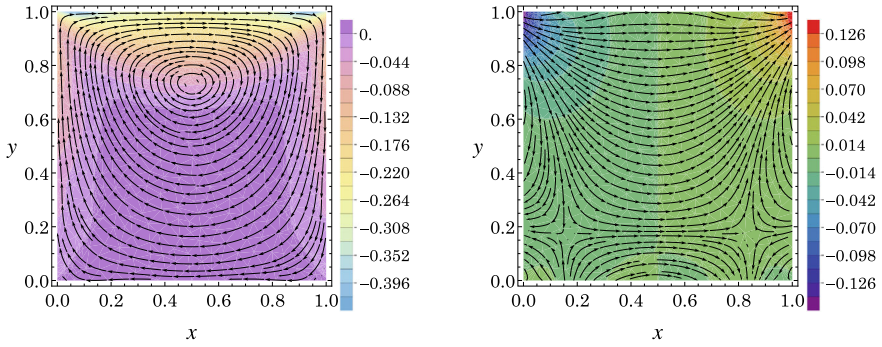

Fig. 5 Velocity streamlines plotted over shear stress contours (left) and heat flux lines plotted over temperature contours (right) for the case when top wall is moving in the positive x-direction

lid, respectively, as wall temperature is influenced by stress. Moreover, the coupling between stress and heat flux (substituting $(1)_2$ into $(2)_2$), gives

$$\boldsymbol{q} = -\frac{5\mathrm{Kn}}{2\mathrm{Pr}}(\boldsymbol{\nabla} T - \alpha_0 \boldsymbol{\nabla} p), \tag{11}$$

highlighting that heat flux depends on both temperature and pressure gradients. This relation introduces a competition between these gradients in determining the heat flow direction. In the present scenario, the pressure gradient dominates, leading to an anti-Fourier heat flow, as evidenced by the heat flux lines in the right panel of Fig. 5. This non-classical phenomenon, observed in microscale and rarefied gas flows, occurs when heat flows from cooler to warmer regions, opposite to the conventional Fourier law of heat conduction [1]. This phenomenon can be predicted well by the CCR model due to the relation (11). Although not shown here, the NSF model even

with second-order slip and jump conditions is unable to predict the anti-Fourier heat flow.

We also note that although the bulk flow and centerline velocity profiles agree closely with those in Ref. [10], significant differences appear in the temperature and heat-flux contours. The tilting and asymmetry reported in Ref. [10] arises due to fully non-linear equations, whereas the MFS framework employs the *linearized* CCR equations. The omission of non-linear convective enforces strictly symmetric fields. Such symmetric profiles are also seen in lid-driven cavity simulations for gas mixtures using linearized equations [5].

3.2 *Results for the Two-Sided Lid-Driven Cavity with Top and Bottom Walls Moving in the Same Direction*

In this subsection, we showcase the flow characteristics when the top and bottom walls are moving in the same direction with the same horizontal velocity v_x which is fixed as $v_x = 1$ for computational purpose. The left panel of Fig. 6 shows velocity streamlines superimposed on shear stress σ_{xy} contours for $\mathrm{Kn} = 0.1$. The flow pattern reveals two primary vortices, each occupying the upper and lower halves of the cavity, rotating in the same direction as the moving walls. The contours indicate that the shear stress magnitude is highest near the moving walls, with positive and negative values corresponding to the direction of the local velocity gradients. The heat flux lines plotted over the temperature contours for $\mathrm{Kn} = 0.1$ are illustrated in the right panel of Fig. 6. The temperature contours depict hot and cold regions near the corners associated with both top and bottom walls. As evident from the right panel, the heat flows from colder to hotter regions again depicting the anti-Fourier effect produced due to pressure gradients inside the cavity.

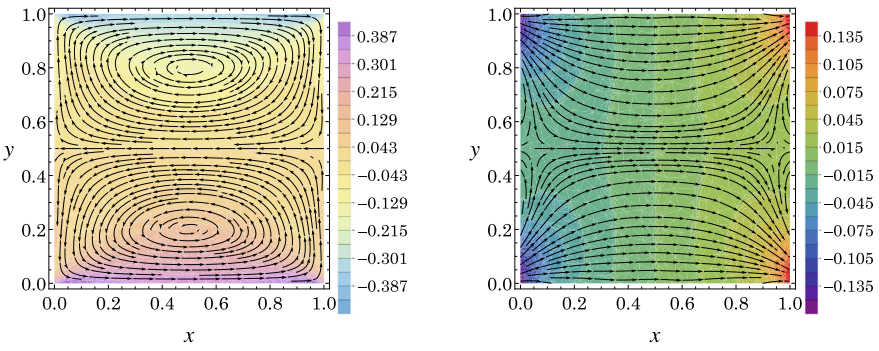

Fig. 6 Same as Fig. 5 but for the case when top and bottom walls are moving in same directions with the same speeds

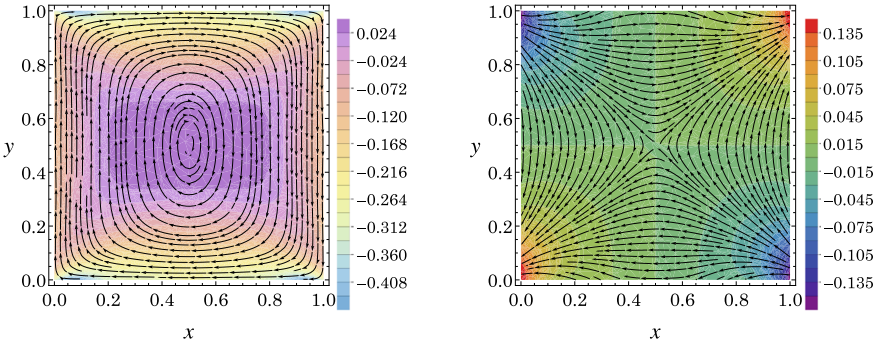

Fig. 7 Same as Fig. 5 but for the case when top and bottom walls are moving in opposite directions with the same speeds

3.3 Results for the Two-Sided Lid-Driven Cavity with Top and Bottom Walls Moving in Opposite Directions

In this case, the horizontal velocity is fixed as $v_x = 1$ and $v_x = -1$ for top and bottom walls, respectively, and the movement of walls leads to formation of a large vortex covering the entire cavity. As evident from the left panel of Fig. 7, the absolute value of shear stress is greatest near the corners of both top and bottom walls. In the present scenario, the hot and cold regions along the bottom walls are opposite as compared to the previous case (Sect. 3.2). However, the heat flux lines again depict the anti-Fourier effect.

References

1. Akhlaghi H, Roohi E, Stefanov S (2018) Ballistic and collisional flow contributions to anti-Fourier heat transfer in rarefied cavity flow. Sci Rep 8:13533
2. Chapman S, Cowling TG (1970) The mathematical theory of non-uniform gases. Cambridge University Press, Cambridge
3. Grad H (1949) On the kinetic theory of rarefied gases. Commun Pure Appl Math 2:331–407
4. Gu XJ, Emerson DR (2009) A high-order moment approach for capturing non-equilibrium phenomena in the transition regime. J Fluid Mech 636:177–216
5. Gupta VK (2015) Mathematical modeling of rarefied gas mixtures. Ph.D. thesis, RWTH Aachen University, Germany
6. Himanshi, Rana AS, Gupta VK (2023) Fundamental solutions of an extended hydrodynamic model in two dimensions: derivation, theory, and applications. Phys Rev E 108:015306
7. Himanshi, Rana AS, Gupta VK (2024) A viewpoint on thermally-induced transport in rarefied gases through the method of fundamental solutions. J Comput Theor Transp 53:279–301
8. Himanshi, Rana AS, Gupta VK (2025) Exploring external rarefied gas flows through the method of fundamental solutions. Phys Rev E 111:015101
9. Lockerby DA, Collyer B (2016) Fundamental solutions to moment equations for the simulation of microscale gas flows. J Fluid Mech 806:413–436

10. Rana A, Torrilhon M, Struchtrup H (2013) A robust numerical method for the R13 equations of rarefied gas dynamics: application to lid driven cavity. J Comput Phys 236:169–186
11. Rana AS, Saini S, Chakraborty S, Lockerby DA, Sprittles JE (2021) Efficient simulation of non-classical liquid-vapour phase-transition flows: a method of fundamental solutions. J Fluid Mech 919:A35
12. Rana AS, Gupta VK, Struchtrup H (2018) Coupled constitutive relations: a second law based higher-order closure for hydrodynamics. Proc Roy Soc A 474:20180323
13. Struchtrup H, Torrilhon M (2003) Regularization of Grad's 13 moment equations: derivation and linear analysis. Phys Fluids 15:2668–2680

Open Access This chapter is licensed under the terms of the Creative Commons Attribution 4.0 International License (http://creativecommons.org/licenses/by/4.0/), which permits use, sharing, adaptation, distribution and reproduction in any medium or format, as long as you give appropriate credit to the original author(s) and the source, provide a link to the Creative Commons license and indicate if changes were made.

The images or other third party material in this chapter are included in the chapter's Creative Commons license, unless indicated otherwise in a credit line to the material. If material is not included in the chapter's Creative Commons license and your intended use is not permitted by statutory regulation or exceeds the permitted use, you will need to obtain permission directly from the copyright holder.

Modelling of the Flow of a Thermal Binary Gas Mixture in a Microchannel with a Sinusoidal Varying Thickness

Cédric Croizet

Abstract Interest is significant in the ability to numerically predict the gas flows in microchannels. One of the reference methods used for this purpose is the DSMC method by Bird (Aktas et al., J Microelectromech S 10:538–549 (2001) [1]; Bird, Gas dynamics and the direct simulation of gas flows. Clarendon Press (1994) [2]). Although effective, this statistical method requires significant computational resources. A more economical alternative is to use an asymptotic model. We use this approach in the case of a planar microchannel whose thickness varies sinusoidally and whose wall temperature is a function of the longitudinal spatial variable. We are interested in the case of flows of a mixture of two inert gases with a low Mach number and a Knudsen number of the order of 10^{-1}. These flows correspond to the slip flow regime. As a consequence, the Navier-Stokes-Fourier equations remain valid, provided they are supplemented with slip conditions for velocity and temperature. The aim of this contribution is to study the effects of the channel cross-section function on the flow parameters.

1 Introduction

Miniaturization is a significant challenge in many industrial sectors. As a consequence, numerous applications and many devices involve channels whose size is typically in the micrometer range. For instance, microchannels are found in microturbines, micropumps, microheat exchangers, or microcooling systems. The existence of numerous and varied applications makes the study of gas flows in microchannels very practical and interesting. Several studies have been published discussing the theoretical, numerical, and experimental aspects of such flows [2, 5, 10–12, 15]. From a numerical standpoint, Bird's DSMC is relevant for simulating these flows but requires significant computational resources. Our approach is based on an asymptotic description of the flow that takes into account the main physical phenomena involved. This approach has already been applied in various cases: for a single gas [9,

C. Croizet (✉)
Sorbonne Université, CNRS, Institut Jean Le Rond d'Alembert, Paris, France
e-mail: cedric.croizet@sorbonne-universite.fr

© The Author(s) 2026

M. Grabe et al. (eds.), *Rarefied Gas Dynamics*, Springer Aerospace Technology,
https://doi.org/10.1007/978-3-032-00094-1_31

12], for mixtures in planar channels [4, 8, 10], and in axisymmetric channels [5, 6]. The Knudsen number, Kn, is equal to the ratio of the mean free path to the channel width. At standard conditions for temperature and pressure, the Knudsen number of gas flows in microchannels is of the order 10^{-1} [11, 12]. The Reynolds and Mach numbers are low. From a phenomenological standpoint, these values characterize flows in the weakly rarefied slip regime. As a consequence, the usual mass, momentum and energy balance equations (Navier-Stokes-Fourier equations) remain valid [3–5, 7, 10]. However, the usual no-slip boundary conditions are no longer valid and must be replaced with slip conditions involving coefficients determined from experimental measurement [11]. In this work, we set first order jump conditions for the temperatures and first order slip conditions for the velocities [12]. In order to take into account the interactions between the two gases, coupling terms are added to the momentum and energy equation.

In this contribution, we are interested in flows of a mixture of two compressible ideal gases in a two-dimensional microchannel. Our goal is to take into account small variations in the channel width and to observe their consequences on the flow. In a previous contribution [4], the case of weakly converging or diverging channels with straight walls was studied. In this contribution, the case of channels where the wall equation is a sinusoid is investigated (see Fig. 1). The gas flow can be induced by both a pressure gradient and a temperature gradient at the wall. Regarding the geometry of the channel, we formulate two hypotheses. Firstly, the aspect ratio of the channel, ϵ_1, is small: The channel length (L) is much greater than its width ($\bar{h}$). Secondly, we assume that the width of the channel varies slightly around its average value $\bar{h}$. Consequently, a second small parameter ϵ_2 is introduced to describe the local deviation of the channel width from its mean value $\bar{h}$. In addition, the walls are at rest and their temperature $\bar{T}_w$ depends on the longitudinal space variable $\bar{x}$. Finally,we assume that the flow is steady and symmetric with respect to the channel axis. The pressure and velocity of each gas are specific at the channel inlet. After a brief presentation, the model will be applied to a channel with sinusoidal walls.

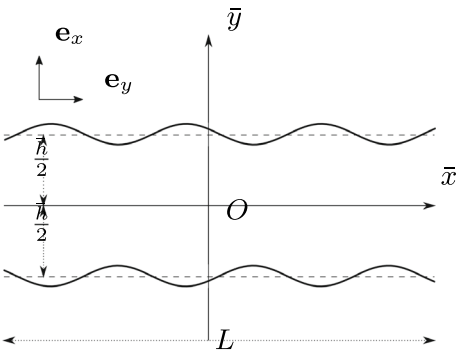

Fig. 1 Channel geometry

To focus our analysis on the effects of channel geometry, we consider an isothermal case. The solution of the first-order approximation is investigated.

2 Model Equations

We consider a two-dimensional channel, symmetric with respect to its longitudinal axis, of length $L = 20\,\mu\text{m}$. The $\bar{x}$-axis is parallel to the channel axis (see Fig. 1). Quantities with dimensions (except when they are constants) are denoted with a bar which is removed when referring to the corresponding dimensionless quantities. The walls equation is given by $\bar{y} = \pm \bar{H}(\bar{x})$.

The equations of motion are the Navier-Stokes-Fourier equations for a mixture of two ideal gases. The two gases (denoted with the subscripts "a" and "b") have constant heat capacities at constant pressure (c_{pa} and c_{pb}) and at constant volume (c_{va} and c_{vb}). We assume that the shear viscosities, μ_a and μ_b, and the thermal conductivities, κ_a and κ_b, depend only on the temperature and are such that the Prandtl numbers are constant. For the sake of conciseness, the model is not detailed here; a precise description can be found in [4, 10]. The velocity of the gas θ ($\theta = a, b$) is denoted: $\bar{\mathbf{u}}_\theta = \bar{u}_\theta(\bar{x}, \bar{y}, t)\,\mathbf{e}_x + \bar{v}_\theta(\bar{x}, \bar{y}, t)\,\mathbf{e}_y$, ρ_θ is the volumetric mass of the gas θ and r_θ its specific ideal gas constant. The boundary conditions are first-order slip conditions for the velocities and first order jump conditions for the temperature. For the gas θ at the upper wall $\bar{y} = \bar{H}(\bar{x})$, we have [11, 12]:

$$\bar{\mathbf{u}}_\theta(\bar{x}, \bar{y} = \bar{H}(\bar{x})) \cdot \tau = \left[\frac{\sigma_{p\theta}\,\bar{\mu}_\theta}{\bar{p}_\theta} \sqrt{2\, r_\theta\, \bar{T}_\theta}\, \bar{\nabla}(\bar{\mathbf{u}}_\theta \cdot \tau) \cdot \mathbf{n} + \frac{\sigma_{Ta} r_\theta \bar{\mu}_\theta}{\bar{p}_\theta}\, \bar{\nabla}(\bar{T}_\theta \cdot \tau) \right]_{\bar{y}=\bar{H}(\bar{x})}, \tag{1}$$

$$\bar{\mathbf{u}}_\theta(\bar{x}, \bar{y} = \bar{H}(\bar{x})) \cdot \mathbf{n} = 0\,, \tag{2}$$

$$\bar{T}_\theta(\bar{x}, \bar{y} = \bar{H}(\bar{x})) = \bar{T}_w + \left[\xi_{T\theta} \sqrt{2\, r_\theta\, \bar{T}_\theta}\, \bar{\nabla}(\bar{T}_\theta) \cdot \mathbf{n} \right]_{\bar{y}=\bar{H}(\bar{x})}, \tag{3}$$

where $\mathbf{n}$ and τ are the unit vectors respectively normal and tangential to the wall. The constant coefficients $\sigma_{p\theta}$, $\sigma_{T\theta}$ and $\xi_{T\theta}$ characterize the viscous and thermal slip of the species θ on the walls [13]. At the wall at $\bar{y} = -\bar{H}(\bar{x})$, analogous boundary conditions are set. Boundary conditions at the channel inlet and outlet will be specified further. To simplify the problem, we will analyze and compare the orders of magnitude of the different terms in the problem's equations in a dimensionless form. The length of the channel, L, is set as the longitudinal length scale. The channel width is characterized by the transversal length scale $\bar{h}$. Two small parameters are introduced: the aspect ratio of the channel, $\epsilon_1 = \bar{h}/L \ll 1$, and a second small parameter, ϵ_2, that characterizes the deviation of the local width of the channel from $\bar{h}$. We set $\bar{H}(\bar{x}) = \bar{h}\left[\frac{1}{2} + \epsilon_2 h(x)\right]$ with $h(x) = \sin\left(\frac{n\pi x}{L} + \lambda\right)$. Finally, U and V, T_c

(for the two species), $p_{\theta c}$ and $\rho_{\theta c}$ (with $p_{\theta c} = r_\theta \rho_{\theta c} T_c, \theta = a, b$) are set for the characteristic values of the axial and transversal velocities, the temperature, the pressure, and the volumetric mass, respectively. With these characteristic scales, we build the following dimensionless numbers:

$$\gamma_\theta = \frac{c_{p\theta}}{c_{v\theta}},\ Pr_\theta = \frac{\mu_\theta c_{p\theta}}{\kappa_\theta},\ Re_\theta = \frac{\rho_{\theta c}\, U\, \bar{h}}{\mu_{\theta c}},$$
$$Ma_\theta = \frac{U}{\sqrt{\gamma_\theta\, r_\theta\, T_c}},\ Kn_\theta = \sqrt{\frac{\gamma_\theta\, \pi}{2}}\, \frac{Ma_\theta}{Re_\theta},$$

where μ_θ and κ_θ are proportional to $T_\theta^{\omega_\theta}$ since Pr_θ is constant. The Principle of Least Degeneracy applied to the mass balance equation implies that $U = \epsilon_1 V$. In the momentum balance projected in the main direction of the flow $(O, \mathbf{e_x})$, the pressure gradient appears as the driving force. We also recall that we are interested in flows at Mach and Reynolds numbers small or of order unity. To determine the degeneracies that correspond to the physics of our problem, we set $Re_a = R_a \epsilon_1^\alpha$ and $Ma_a = M_a \epsilon_1^\beta$, where R_a and M_a are of order one. From the dimensionless balance of momentum and energy, we have $\alpha = \beta = 1$. This case corresponds to Mach and Reynolds numbers of order ϵ_1. As a consequence we have $Kn_\theta = O(1), \theta = a, b$. At the first approximation order in ϵ_1, we have for the gas a:

$$\frac{\partial}{\partial x}(\rho_a\, u_a) + \frac{\partial}{\partial y}(\rho_a\, v_a) = 0 \tag{4}$$

$$-\frac{1}{\gamma_a M_a^2}\frac{\partial p_a}{\partial y} = 0 \tag{5}$$

$$\frac{1}{\gamma_a M_a^2}\frac{\partial p_a}{\partial x} = \frac{1}{R_a}\frac{\partial}{\partial y}\left(\mu_a \frac{\partial u_a}{\partial y}\right)$$
$$+F_{ab}\frac{\rho_{bc}}{\rho_{ac}}\left(\frac{\mu_{ac}}{\mu_{bc}}\right)^{\frac{1}{2}} \frac{R_a}{\gamma_a M_a^2}\frac{p_a\, p_b}{\sqrt{\mu_a \mu_b}}\left(\frac{T_b}{T_a}\right)^{\frac{1}{2}}(u_b - u_a) \tag{6}$$

$$\frac{\gamma_a}{R_a\, Pr_a}\frac{\partial}{\partial y}\left(\kappa_a \frac{\partial T_a}{\partial y}\right) + G_{ab}\frac{R_a}{\gamma_a M_a^2}\frac{\rho_b\, p_a}{\sqrt{\mu_a\, \mu_b}}\sqrt{\frac{T_b}{T_a}}\,(T_b - T_a) = 0, \tag{7}$$

where F_{ab} and G_{ab} depend on the gas properties and are explicitely given in [4]. From Eq. (5) and the analogous equation for gas b, it is obvious that p_a and p_b depend only on x. The equations for the gas b are obtained by exchanging a and b in Eqs. (4) to (7). At the same approximation order, the temperature jump at the upper wall is written as:

$$T_\theta\left(x, \frac{1}{2} + \epsilon_2 h(x)\right) = T_w(x) - \frac{\sqrt{2\,\gamma_\theta} M_\theta}{R_\theta}\xi_{\theta T}\frac{\mu_\theta\sqrt{T_\theta}}{p_\theta}\frac{\partial T_\theta}{\partial y}\left(x, \frac{1}{2} + \epsilon_2 h(x)\right) \tag{8}$$

If we assume that the flow is in thermal equilibrium, meaning both gases are at the same temperature, Eq. (7) with the wall condition (8) implies that the two gases are at the wall temperature : $T_a(x, y) = T_w(x) = T_b(x, y) = T(x)$. Consequently, the dimensionless velocity conditions at the upper wall are:

$$u_\theta\left(x, \frac{1}{2} + \epsilon_2 h(x)\right) = -\frac{K_\theta\,[T]^{\omega_\theta+\frac{1}{2}}}{p_\theta}\frac{\partial u_\theta}{\partial y}\left(x, \frac{1}{2} + \epsilon_2 h(x)\right) + \frac{\sigma_{\theta T}}{R_\theta}\frac{[T]^{\omega_\theta}}{p_\theta}\frac{dT}{dx} \tag{9}$$

$$v_\theta\left(x, \frac{1}{2} + \epsilon_2 h(x)\right) - \epsilon_2\frac{dh}{dx}(x)\,u_\theta\left(x, \frac{1}{2} + \epsilon_2 h(x)\right) = 0 \tag{10}$$

where: $K_\theta = \sigma_{\theta\,p}\sqrt{2\gamma_\theta}\,M_\theta/R_\theta$. At this approximation order, we have a set of six equations derived from the mass and momentum balance of the two gases. With the ideal gas law for the two species, we have: $p_a(x) = \rho_a(x)\,T(x)$ and $p_b(x) = \rho_b(x)\,T(x)$ and the problem is reduced to:

$$\frac{\partial}{\partial x}(\rho_a u_a) + \frac{\partial}{\partial y}(\rho_a v_a) = 0, \quad \frac{\partial}{\partial x}(\rho_b u_b) + \frac{\partial}{\partial y}(\rho_b v_b) = 0, \tag{11}$$

$$\begin{aligned} \tfrac{\partial^2 u_a}{\partial y^2} - \frac{B_a}{A_a}p_a\,p_b(u_a - u_b) &= \frac{1}{A_a}\frac{dp_a}{dx}, \\ \tfrac{\partial^2 u_b}{\partial y^2} + \frac{B_b}{A_b}p_a\,p_b(u_a - u_b) &= \frac{1}{A_b}\frac{dp_b}{dx}, \end{aligned} \tag{12}$$

where $A_\theta(x)$ and $B_\theta(x)$ $(\theta = a, b)$ are given in [4]. From the longitudinal momentum equations (12), an explicit expression of the longitudinal component of the velocities at the first approximation order is obtained. So, by using the conservation of mass in its global form and introducing the mass flow rates of each gas, it is straightforward to obtain two coupled ordinary differential equations of the first order for the pressures [4]:

$$X_a\frac{dp_a}{dx} + X_b\frac{dp_b}{dx} = S_a\,, \qquad Y_a\frac{dp_a}{dx} + Y_b\frac{dp_b}{dx} = S_b\,. \tag{13}$$

For the sake of conciseness, the detailed expressions of X_θ and Y_θ $(\theta = a, b)$, are not explicitly given here.

3 Numerical Solution

In order to solve Eq. (13), we need to impose the wall temperature and boundary conditions at the inlet and at the outlet of the channel. Given the form of the equations, we set the pressures at the inlet for each gas, as well as the constant mass flow rates $\bar{Q}_{ma}$ and $\bar{Q}_{mb}$, of each gas. The two Eq. (13) are solved with MATLAB ; a fourth order Runge-Kutta method with variable stepsizes is used.

Table 1 Physical properties of the gases [2]

	Argon	Neon
Molecular mass (kg)	$66.3\ 10^{-27}$	$33.5\ 10^{-27}$
Molecular diameter (m)	$4.11\ 10^{-10}$	$2.72\ 10^{-10}$
γ	5/3	5/3
μ_{VSS} (Pa.s)	$2.117\ 10^{-5}$	$2.975\ 10^{-5}$
α	1.40	1.31
ω	0.81	0.66

Although the model is capable of addressing problems involving arbitrary temperature distributions along the walls, an isothermal case ($T = 300$ K) is considered here in order to isolate and analyze the effect of the channel geometry. We consider the case of a mixture of Argon (a) and Neon (b) (Table 1). From a geometric point of view, the walls are sinusoidal curves chosen such that the length of the channel is equal to a quarter of the sinusoid period. We set: $\epsilon_2 = 10^{-1}$, $h_2(x) = \sin(\frac{\pi x}{2})$, and $h_2(x) = \sin(\frac{\pi x}{2} + \pi)$. In the first case, a converging channel is built with an inlet half-width of 0.5 μm and an outlet half-width of 0.4 μm. In the second case, a diverging channel is constructed with an inlet half-width of 0.5 μm and an outlet half-width of 0.6 μm. A third geometry is considered: a channel with straight walls and a constant half-width of 0.5 μm. In addition, we set: $\bar{p}_a(-L/2) = 3.533\ 10^4$ Pa, $\bar{p}_b(-L/2) = 1.514\ 10^4$ Pa, $\bar{Q}_{ma} = 2.248\ 10^{-6}$ kg m^{-1} s^{-1} and $\bar{Q}_{mb} = 0.485\ 10^{-6}$ kg m^{-1} s^{-1}. For each of the three geometries, the evolution of the pressures along the channel axis is plotted in Fig. 2a. We observe that the results are very similar to those obtained in the case of channels with straight walls [4], with inlet and outlet half-widths identical to those of the channels studied in this contribution and with identical boundary conditions. The channel geometry influences the pressure of the two gases: When the channel width at the outlet increases, the outlet pressures increase. The profiles of the longitudinal component of the velocity at the channel outlet are plotted in Fig. 2b. At the channel outlet, the slip velocity of Argon is smaller than the slip

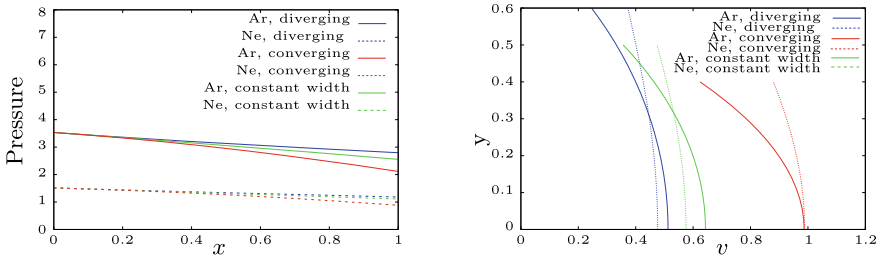

Fig. 2 Dimensionless pressures along the channel axis for $T = 300$ K and different channel shapes: converging channel $\bar{h} = 0.4$ μm, straight channel $\bar{h} = 0.5$ μm, diverging channel $\bar{h} = 0.6$ μm (**a**), dimensionless axial velocities (**b**)

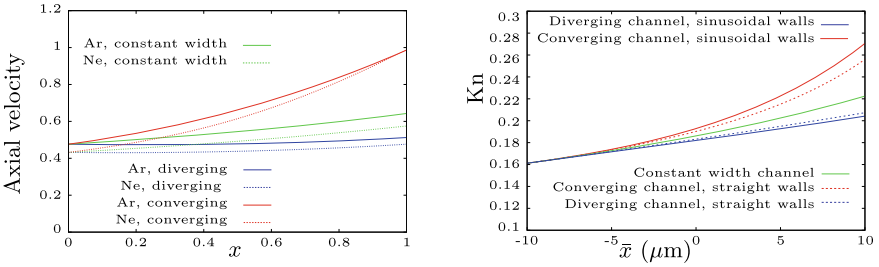

Fig. 3 Dimensionless axial velocity along the channel axis for $T = 300\,\mathrm{K}$ and different channel shapes: converging channel $\bar{h} = 0.4\ \mu\mathrm{m}$, constant width channel $\bar{h} = 0.5\ \mu\mathrm{m}$, diverging channel $\bar{h} = 0.6\ \mu\mathrm{m}$ (**a**), Knudsen number (**b**)

velocity of Neon. On the other hand, when the channel width at the outlet increases the axial velocity at the channel outlet decreases.

For the three geometries, the evolution of the value of the longitudinal component of the velocity along the channel axis is plotted in Fig. 3a. For the two gases, we observe that the axial velocity increases along the channel axis. Its value for Neon is smaller than for Argon. Moreover, when the channel width at the outlet increases, the axial velocity decreases. These observations are consistent with what has been observed in the case of straight walls [4]. In Fig. 3b the evolution of the Knudsen number of the mixture along the channel axis is plotted for the constant width channel, the diverging channels with straight and sinusoidal walls and the converging channels with straight and sinusoidal walls.

The expression of the Knudsen number of the mixture is given in [5, 14] for instance. Whether for sinusoidal or straight walls, the results are quite similar: the Knudsen number increases along the channel axis and, at the outlet, it increases as the channel thickness decreases. This behavior seems to be amplified by the sinusoidal walls: in this case, the difference between the Knudsen number values at the outlet is greater than in the case of straight walls. In Fig. 4a, we plot the molar fraction of Argon along the channel axis in the five cases. It is slightly affected by the shape

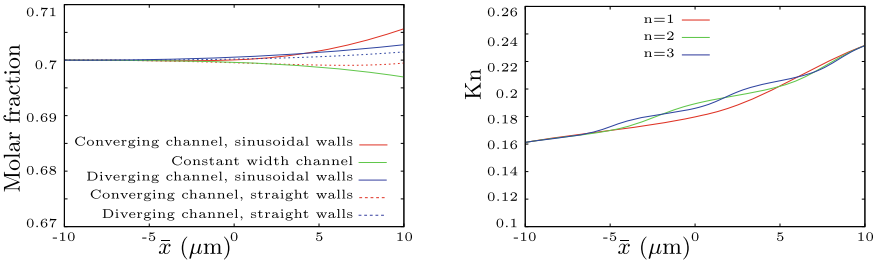

Fig. 4 Molar fraction of Argon along the channel axis: converging channel $\bar{h} = 0.4\ \mu\mathrm{m}$, straight channel $\bar{h} = 0.5\ \mu\mathrm{m}$, diverging channel $\bar{h} = 0.6\ \mu\mathrm{m}$ (**a**), molar fraction of Argon along the channel axis for $n = 1$, $n = 2$ and $n = 3$ (**b**)

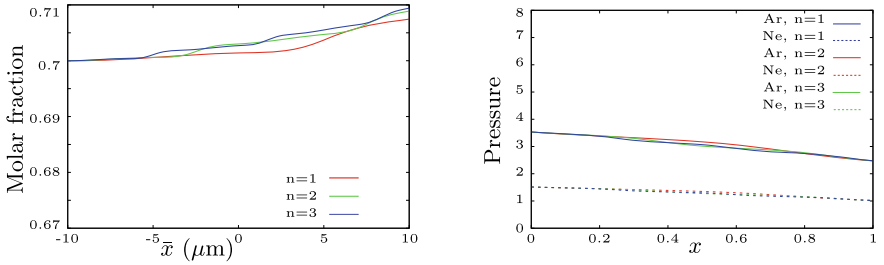

Fig. 5 Molar fraction of Argon along the channel axis for different channel shapes: $n = 1$, $n = 2$ and $n = 3$ (**a**), dimensionless pressures along the channel axis for different channel shapes: $n = 1$, $n = 2$ and $n = 3$ (**b**)

of the wall as it varies by less than one percent; however, this variation seems more noticeable in the case of sinusoidal walls. It follows that the molar diffusion is weak, and thus the flow is dominated by the pressure gradient. It follows that the flow is close to Poiseuille flow with slip boundary conditions; the pressure decreases along the channel (Fig. 2a) as a consequence of the viscous dissipation.

We now consider the case where the wall equation is of the form $h_2(x) = \sin(2n\pi x)$ with $\epsilon_2 = 10^{-1}$ and n an integer. In Figs. 4b, 5a, b, we depict the Knudsen number, the molar fraction of Argon, and the pressures along the channel axis, respectively, for $n = 1$, 2, and 3. It is observed that in this isothermal case, the Knudsen number increases along the channel axis. The effects of the variation in the channel thickness are local and the Knudsen number at the outlet is approximately equal in the three considered cases. The geometry has a rather weak influence on the molar fraction of Argon. Its variation is lower than 1.5 %, but its value at the outlet increases when n increases. The pressures decrease along the channel axis and the outlet pressures are very close in the three considered cases.

4 Conclusion

This contribution deals with a microchannel with a sinusoidal-shaped wall. From the Navier-Stokes-Fourier equations for each gas, we derived an asymptotic model. The case of converging and diverging channels has been investigated. At the first approximation order, the channel geometry has an influence on the flow: quantitative differences are observed between the case of a channel with straight walls and that of a channel with sinusoidal walls. In the case of channels with identical width at the inlet and at the outlet, the molar fraction of Argon at the outlet increases with the number of period n of the sine function.

References

1. Aktas O, Aluru NR, Ravaioli U (2001) Application of a parallel DSMC technique to predict flow characteristics in microfluidic filters. J Microelectromech S 10:538–549
2. Bird GA (1994) Gas dynamics and the direct simulation of gas flows. Clarendon Press
3. Chapman S, Cowling TG (1952) The mathematical theory of non-uniform gases. C. U. P
4. Croizet C, Gatignol R (2024) Asymptotic modelling of the flow of a thermal binary gas mixture in a microchannel with variable width. AIP Conf Proc 2996(1):100002. https://doi.org/10.1063/5.0187532
5. Croizet C, Gatignol R (2019) Asymptotic modelling of thermal binary gas flows in circular micro-channels. Microfluid. Nanofluidics 23(7):94. https://doi.org/10.1007/s10404-019-2260-8
6. Croizet C, Gatignol R (2019) Molecular mass effect on the flow of a thermal binary gas mixture in a circular micro channel. AIP Conf Proc 2132(1):160002. https://aip.scitation.org/doi/abs/10.1063/1.5119649
7. Elizarova TG, Graur IA, Lengrand JC (2001) Two-fluid computational model for a binary gas mixture. Eur J Mech B-Fluids 3:351–369
8. Gatignol R, Croizet C (2014) Asymptotic modelling of the flow of a thermal binary gas mixture in a microchannel. AIP Conf Proc 1628(1):807–814. https://aip.scitation.org/doi/abs/10.1063/1.4902676
9. Gatignol R, Croizet C (2011) Asymptotic modelling of the flows in micro-channel by using macroscopic balance equation. AIP Conf Proc 1333(1):730–735. https://aip.scitation.org/doi/abs/10.1063/1.3562733
10. Gatignol R, Croizet C (2017) Asymptotic modeling of thermal binary monatomic gas flows in plane microchannels—comparison with DSMC simulations. Phys Fluids 29(4):042001. http://dx.doi.org/10.1063/1.4979683
11. Kandlikar S, Garimella S, Li D, Colin S, King M (2005) Transfer and fluid flow in minichannels and microchannels. Elsevier
12. Karniadakis G, Beskok A (2006) Microflows–fundamentals and simulation. Springer
13. Sharipov F, Seleznev V (1998) Data on internal rarefied gas flows. J Phys Chem Ref Data 27:657–706
14. Sharipov F, Kalempa D (2002) Gaseous mixture flow through a long tube at arbitrary knudsen numbers. J Vac Sci Technol A 20(3):814–822
15. Silva E, Deschamps CJ, Rojas-Cárdenas M, Barrot-Lattes C, Baldas L, Colin S (2018) A time-dependent method for the measurement of mass flow rate of gases in microchannels. Int J Heat Mass Transf 120:422–434

Open Access This chapter is licensed under the terms of the Creative Commons Attribution 4.0 International License (http://creativecommons.org/licenses/by/4.0/), which permits use, sharing, adaptation, distribution and reproduction in any medium or format, as long as you give appropriate credit to the original author(s) and the source, provide a link to the Creative Commons license and indicate if changes were made.

The images or other third party material in this chapter are included in the chapter's Creative Commons license, unless indicated otherwise in a credit line to the material. If material is not included in the chapter's Creative Commons license and your intended use is not permitted by statutory regulation or exceeds the permitted use, you will need to obtain permission directly from the copyright holder.

Moment Methods

Spatially Adaptive Moment Model Using Padded Buffer Cell for Linear Hierarchical Moment Equations

Rik Verbiest and Julian Koellermeier

Abstract The need for spatial adaptivity in simulations of rarefied gases arises because different subdomains within a rarefied gas domain often require varying levels of modeling complexity. Different moment models are effective at describing rarefied flows with respective degrees of complexity in each subdomain. However, currently there is no operational spatially adaptive method to efficiently couple moment models in a single simulation. This paper presents a Spatially Adaptive Moment Model (SAMM) for simulating linear hierarchical moment models. A padded buffer cell approach is proposed to couple these varying-order moment models. Numerical shock tube simulations demonstrate that the proposed model achieves accurate results comparable to a high-order model while providing a computational speedup corresponding to the reduction of variables.

Keywords Moment models · Rarefied gases · Adaptive simulation

1 Introduction

Many complex gas flows are characterized by the presence of both rarefied and continuum regimes. Examples are high-altitude flights and atmospheric reentry flights [8, 12, 16], in which the mean free path varies in time and space. While in domains of small Knudsen number, standard fluid dynamics models yield sufficient accuracy, the nonequilibrium effects in domains of large Knudsen number need models beyond the standard fluid solvers [14]. Particle simulations such as DSMC [1] have become the main computational tool for simulating large Knudsen number rarefied gas flows, but result in prohibitively large computational effort for more moderate Knudsen numbers [7].

R. Verbiest (✉) · J. Koellermeier
Bernoulli Institute, University of Groningen, Groningen, The Netherlands
e-mail: r.verbiest@rug.nl

J. Koellermeier
Department of Mathematics, Computer Science and Statistics, Ghent University, Gent, Belgium

© The Author(s) 2026

M. Grabe et al. (eds.), *Rarefied Gas Dynamics*, Springer Aerospace Technology,
https://doi.org/10.1007/978-3-032-00094-1_32

Moment models for kinetic equations have proven to be a powerful modeling technique for the simulation of rarefied gases with moderate Knudsen numbers [3, 15]. Moment models achieve increasing accuracy by successively including more variables and evolution equations. A moment model is characterized by its order. A higher order moment model is often more accurate but computationally more expensive than a lower order moment model as more variables are included in the model. Moment models are ideally suited for spatial adaptivity because they are hierarchical, which simplifies the coupling considerably. However, there is no spatially adaptive scheme for moment models, yet.

The goal of this paper is to construct a spatially adaptive numerical scheme for the simulation of linear hierarchical moment models. We introduce the first spatially adaptive moment model simulations using a domain decomposition approach with padded buffer cells at the interfaces between two models with a different number of moments. The proposed model is called the Spatially Adaptive Moment Model using Padded Buffer Cell (SAMM-PBC). We investigated the precision using a shock tube test case.

2 Moment Equations: Hermite Spectral Method

For simplicity, we consider the 1D spatial space and leave the extension to higher dimensions to future work. The motion of gas particles is described by the 1D Boltzmann transport equation

$$\partial_t f(t,x,c) + c\partial_x f(t,x,c) = S(f) \,, \tag{1}$$

with particle distribution $f(t,x,c)$, spatial position $x \in \Omega \subseteq \mathbb{R}$, microscopic velocity $c \in \mathbb{R}$ and collision operator $S(f)$. The non-linear Hyperbolic Moment Equations (HME) [2] are obtained by expanding $f(t,x,c)$ in a truncated expansion of order $M \in \mathbb{N}$ in the Hermite polynomials $\Phi_i^{u,T}\left(\frac{c-u}{\sqrt{T}}\right)$ [6], i.e.,

$$f(t,x,c) = \sum_{i=0}^{M} m_i(t,x)\Phi_i^{u,T}\left(\frac{c-u}{\sqrt{T}}\right) \,, \tag{2}$$

with velocity u, temperature T and density ϱ. The moment equations are then obtained by projecting (1) onto test functions up to a desired order. We consider the linearized version of the HME model (that is, linearized around $u_0 \approx 0$ and $T_0 \approx 1$), called the Hermite Spectral Method (HSM) [5, 10]. In the HSM, the evolution of the expansion coefficients $\mathbf{w}_M = (m_0, m_1, \ldots, m_M)^T \in \mathbb{R}^{M+1}$ is governed by the linear hyperbolic PDE

$$\frac{\partial \mathbf{w}_M}{\partial t} + A_M \frac{\partial \mathbf{w}_M}{\partial x} = S(\mathbf{w}_M) \,, \tag{3}$$

with constant system matrix

$$A_M = \begin{pmatrix} & 1 & & \\ 1 & & \ddots & \\ & \ddots & & M \\ & & 1 & \end{pmatrix} \in \mathbb{R}^{(M+1)\times(M+1)} ,$$

and where the right-hand side collision term $S(\mathbf{w}_M)$ is given by the simple BGK model $S(\mathbf{w}_M) = -\frac{1}{\tau}(0, 0, 0, m_3, \ldots, m_M)^T \in \mathbb{R}^{M+1}$ with constant relaxation time $\tau \in \mathbb{R}^+$ in this paper.

3 Spatially Adaptive Simulation of Moment Models

Equation (3) is discretized in Ω with grid size Δx, producing semi-discretized cell-averaged moment vectors $w_i \in \mathbb{R}^{M+1}$ in cells $\mathcal{C}_i = [x_{i-\frac{1}{2}}, x_{i+\frac{1}{2}}]$ with equidistant cell centers x_i and cell interfaces $x_{i\pm\frac{1}{2}} = x_i \pm \frac{\Delta x}{2}$, $i = 1, 2, \ldots, N_x$, and discretized in time with time step Δt, yielding the fully discretized cell-averaged moment vectors $w_i^n \in \mathbb{R}^{M+1}$ at discrete times t_n, $n = 0, 1, \ldots, N_t$. For the numerical simulation of (3), we use a finite volume scheme with the Polynomial Viscosity Method (PVM) [4] notation due to its generality and due to its applicability to nonconservative systems. The PVM reads

$$w_i^{n+1} = w_i^n - \frac{\Delta t}{\Delta x}\left(D^+_{i-\frac{1}{2}} + D^-_{i+\frac{1}{2}}\right) - \Delta t S(w_i^n) , \tag{4}$$

with fluctuations $D^\pm_{i+1/2} = A^\pm_\Phi(w_i, w_{i+1})$ given by

$$A^\pm_\Phi(w_L, w_R) = \frac{1}{2}\left(A_\Phi(w_L, w_R)\cdot(w_R - w_L) \pm Q_\Phi \cdot (w_R - w_L)\right) , \tag{5}$$

with generalized Roe linearization $A_\Phi = A_\Phi(w_L, w_R)$ given by

$$A_\Phi(w_L, w_R)\cdot(w_R - w_L) = \int_0^1 A(\Phi(s; w_L, w_R))\frac{\partial \Phi}{\partial s}(s; w_L, w_R) ds , \tag{6}$$

and where the numerical viscosity matrix $Q_\Phi = Q_\Phi(w_L, w_R) = P(A_\Phi(w_L, w_R))$ is a function $P(\cdot)$ of the generalized Roe matrix $A_\Phi(w_L, w_R)$. The Lax-Friedrichs flux [11] is chosen, which is equivalent to $Q_\Phi = \frac{\Delta x}{\Delta t} I$, where I is the identity matrix. Here, $\Phi(s; w_L, w_R)$ denotes a path connecting the left and right states at the cell interface, such that $\Phi(0; w_L, w_R) = w_L$ and $\Phi(1; w_L, w_R) = w_R$. Note that the expression (4) is written in nonconservative form for generality.

3.1 Domain Decomposition

The proposed spatially adaptive simulation of moment models consists of two steps: (1) domain decomposition into subdomains, each modeled by a moment model of a certain order, and (2) coupling of the different order moment models at their interfaces. We consider a decomposition into two domains that is performed in some time step during the computation. For now, the time index will be dropped to simplify notation. Assume that the domain interface is given by $x_{I+\frac{1}{2}} \in \Omega$, so that for $x < x_{I+\frac{1}{2}}$, an Mth order moment model is used, while for $x \geq x_{I+\frac{1}{2}}$, an $(M+1)$th order moment model is used. The situation is sketched in Fig. 1. The spatial domain Ω is divided into two subdomains $\Omega_M = \{x : x \in \Omega, x < x_{I+\frac{1}{2}}\}$ and $\Omega_{M+1} = \{x : x \in \Omega, x \geq x_{I+\frac{1}{2}}\}$. In each cell $\mathcal{C}_l \subset \Omega_M$ of the left subdomain, the moment vector $w_l \in \mathbb{R}^{M+1}$ contains the moments $m_{l,0}$ to $m_{l,M}$, while in each cell $\mathcal{C}_r \subset \Omega_{M+1}$ of the right subdomain, the moment vector $w_r \in \mathbb{R}^{M+2}$ contains the moments $m_{r,0}$ to $m_{r,M+1}$:

$$w_l = (m_{l,0}, \ldots, m_{l,M})^T,\ \mathcal{C}_l \subset \Omega_M\ ,\ \text{and}\ w_r = (m_{r,0}, \ldots, m_{r,M+1})^T,\ \mathcal{C}_r \subset \Omega_{M+1}\ .$$

The generalization towards more domains or an arbitrary difference in the number of moments is straightforward and follows directly from the presented analysis.

3.2 Spatially Adaptive Moment Model Using Padded Buffer Cell (SAMM-PBC)

We have $\mathcal{C}_I \subset \Omega_M$, so that $w_I \in \mathbb{R}^{M+1}$, and $\mathcal{C}_{I+1} \subset \Omega_{M+1}$, so that $w_{I+1} \in \mathbb{R}^{M+2}$. The difficulty is the computation of the flux at the boundary interface between the cells $\mathcal{C}_I$ and $\mathcal{C}_{I+1}$. We propose padded buffer cells to couple different order moment models at the boundary interface. The padded buffer cell locally uses the cell $\mathcal{C}_I$ as a buffer cell and pads it with certain values for the missing moments. Padding can be understood as increasing the size of the shorter moment vector by adding the additional last moments. In this example, this leads to the situation illustrated in Fig. 2. The moment vector w_I is padded with a last moment $\widetilde{m}_{I,M+1}$. The choice of $\widetilde{m}_{I,M+1}$ determines how the two moment models are coupled and should represent the physics of the system. We will define the new padded moment vector as $\widetilde{w}_I :=$

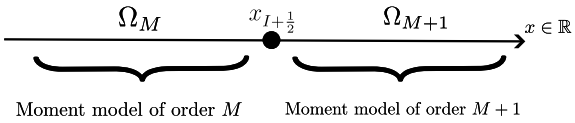

Fig. 1 The domain is split into two subdomains Ω_M and Ω_{M+1} in which a moment model of order M and $M+1$ is used, respectively

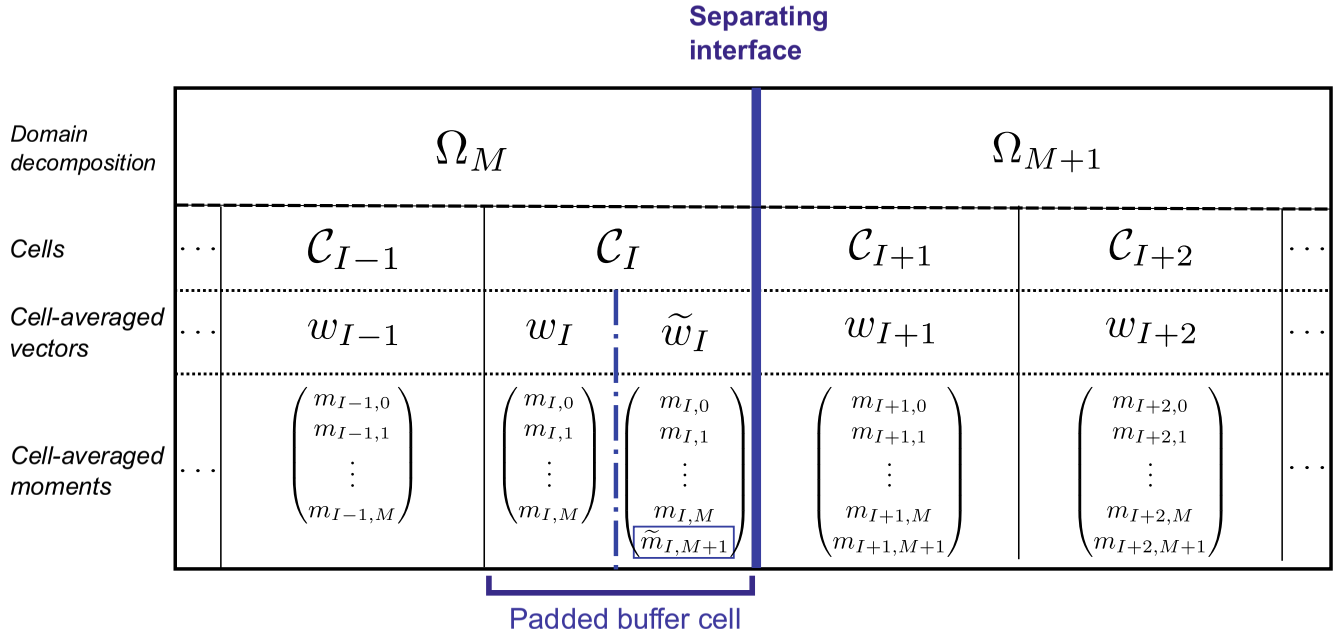

Fig. 2 Padded buffer cell with added last moment $\widetilde{m}_{I,M+1}$ for the coupling of Ω_M and Ω_{M+1}.

$(m_{I,0}, m_{I,1}, \ldots, m_{I,M}, \widetilde{m}_{I,M+1})^T \in \mathbb{R}^{M+2}$. The still to be defined padded moment $\widetilde{m}_{I,M+1}$ is solely used to compute the flux at the boundary interface between the cells $\mathcal{C}_I$ and $\mathcal{C}_{I+1}$; all other fluxes are between cells with the same number of moments, which predefines the moment model for the flux computation at those cells. The new padded moment vector in the padded buffer cell can then be inserted in the relevant PVM equations (4). We will call the resulting finite volume method the Spatially Adaptive Moment Model using Padded Buffer Cell (SAMM-PBC).

The SAMM-PBC introduced here takes the same fluctuation-differencing form as (4). We assume that the domain decomposition is performed after collecting the cell averages at time t_n but before computing the cell averages at time t_{n+1} using the PVM formula (4). The Mth order and the $(M+1)$th order HSM moment equations (3) read

$$\frac{\partial \mathbf{w}_M}{\partial t} + A_M \frac{\partial \mathbf{w}_M}{\partial x} = S(\mathbf{w}_M) \ , \quad \text{and} \quad \frac{\partial \mathbf{w}_{M+1}}{\partial t} + A_{M+1} \frac{\partial \mathbf{w}_{M+1}}{\partial x} = S(\mathbf{w}_{M+1}) \ , \tag{7}$$

respectively, with $\mathbf{w}_M \in \mathbb{R}^{M+1}$, $A_M \in \mathbb{R}^{(M+1)\times(M+1)}$, $\mathbf{w}_{M+1} \in \mathbb{R}^{M+2}$ and $A_{M+1} \in \mathbb{R}^{(M+2)\times(M+2)}$. To compute the flux across the interface between $\mathcal{C}_I$ and $\mathcal{C}_{I+1}$, the generalized Roe linearization (6) needs to be computed:

$$A_\Phi(\widetilde{w}_I^n, w_{I+1}^n) \cdot (w_{I+1}^n - \widetilde{w}_I^n) = \int_0^1 \widetilde{A}(\Phi(s; \widetilde{w}_I^n, w_{I+1}^n)) \frac{\partial \Phi}{\partial s}(s; \widetilde{w}_I^n, w_{I+1}^n) ds \ , \tag{8}$$

with padded moment vector $\widetilde{w}_I^n := (m_{I,0}^n, m_{I,1}^n, \ldots, m_{I,M}^n, \widetilde{m}_{I,M+1}^n)^T \in \mathbb{R}^{M+2}$, padded with the still to be defined last moment $\widetilde{m}_{I,M+1}^n$. The interface transport matrix $\widetilde{A}(\Phi(s; \widetilde{w}_I^n, w_{I+1}^n)) \in \mathbb{R}^{(M+2)\times(M+2)}$ models propagation of information between $\widetilde{w}_I^n$ and w_{I+1}^n along the path $\Phi(s; \widetilde{w}_I^n, w_{I+1}^n)$. Using the constant matrix $\widetilde{A} = A_{M+1}$ to be consistent with the higher order model, the integral along the path does not need to be evaluated. The fluctuation $D_{I-1/2}^+ \in \mathbb{R}^{M+2}$ needs to implement a boundary condition for the added moment $\widetilde{m}_{I,M+1}^n$, while the fluctuation $D_{I-1/2}^- \in \mathbb{R}^{M+1}$ uses w_I^n instead of the padded moment vector $\widetilde{w}_I^n$, i.e.,

$$D_{I-\frac{1}{2}}^- = A_\Phi^-(w_{I-1}^n, w_I^n) \ , \qquad D_{I-\frac{1}{2}}^+ = \begin{pmatrix} A_\Phi^+(w_{I-1}^n, w_I^n) \\ a_{\text{bound}} \end{pmatrix} \ , \ \text{with} \tag{9}$$

$$A_\Phi^\pm(w_{I-1}^n, w_I^n) = \frac{1}{2}(A_M(w_I^n - w_{I-1}^n) \pm Q_M(w_I^n - w_{I-1}^n)) \ , \tag{10}$$

and where a_{bound} is some interface boundary condition for the padded moment $\widetilde{m}_{I,M+1}^n$, which originates from the fact that there is an artificial boundary for the padded moment. We propose $a_{\text{bound}} = a_{M+1} \cdot (\widetilde{w}_I^n - \widetilde{w}_{I-1}^n)$, where we defined $\widetilde{w}_{I-1}^n := (m_{I-1,0}, m_{I-1,1}, \ldots, m_{I-1,M}, \widetilde{m}_{I,M+1})^T \in \mathbb{R}^{M+2}$ and where $a_{M+1} \in \mathbb{R}^{1\times(M+2)}$ is the last row of A_{M+1}. The Roe linearizations at the remaining

interfaces are simply given by

$$A_\Phi(w_i, w_{i+1})(w_{i+1} - w_i) = A_M(w_{i+1} - w_i)\ , \quad i = 1, \ldots, I-2\ , \tag{11}$$
$$A_\Phi(w_i, w_{i+1})(w_{i+1} - w_i) = A_{M+1}(w_{i+1} - w_i)\ , \quad i = I+1, \ldots, N_x - 1. \tag{12}$$

The numerical viscosity matrix Q_Φ can then be computed by using $Q_\Phi(w_L, w_R) = P(A_\Phi(w_L, w_R))$ at all interfaces. Expressions (8), (9) (11) and (12) can be readily inserted into the PVM equations (4), yielding the SAMM-PBC.

4 Numerical Simulation

We consider a 1D shock tube test case with initial conditions

$$(\varrho, u, T)^T(0, x) = \begin{cases} (3 + 0.2x, 0, 1)^T, & x \le 0, \\ (1, 0, 1)^T, & x > 0, \end{cases}\ , \quad m_i(0, x) = 0\ , \quad i > 2\ ,$$

requiring high accuracy because of the density discontinuity at $x = 0$ [9, 13], and a small linear density profile in the left subdomain, modelled with sufficient accuracy by a lower order model. The relaxation time is $\tau = 1$. The 1D HSM (3) is simulated on the interval $\Omega = [-2, 1]$, that is decomposed into $\Omega_M = [-2, -1]$ and $\Omega_{M+2} = [-1, 1]$, using three different models:

1. **SAMM-PBC46**: The SAMM-PBC proposed in this paper, using $M = 4$ moments in Ω_M and $M + 2 = 6$ moments in Ω_{M+2}.
2. **HSM4**: the lower order moment model with $M = 4$ moments in Ω.
3. **HSM6**: the higher order moment model with $M + 2 = 6$ moments in Ω.

The order of the moment models was chosen based on the observation that the expansions had converged sufficiently well for these orders in the corresponding subdomains. The derivation of suitable domain decomposition criteria is ongoing work. Note that we use a difference of two moments between the lower order model HSM4 and the higher order model HSM6 instead of only one moment difference that was used in Sect. 3 to simplify the notation in the description of the method. The initial values for the higher order moments are zero, such that the only logical initial choice for the two padded moments in the SAMM-PBC46 is to set them to zero. The goal of this test case is to verify whether the SAMM-PBC46 yields comparable results to the higher order model HSM6 while realizing a computational speedup. Note that the expected speedup cannot exceed some theoretical bound based on the domain decomposition and number of moments.

The spatial grid is composed of $N_x = 300$ equally sized cells. The end time of the simulation is $t_{end} = 0.3$ with a fixed time step of $\Delta t = 6.7 \times 10^{-4}$ based on the CFL condition and the stable integration of the relaxation term. Outflow boundary conditions are implemented by zero-order extrapolation in the ghost cells.

The numerical results are shown in Fig. 3. For each of the variables ϱ (Fig. 3a), u (Fig. 3b) and T (Fig. 3c), the results for SAMM-PBC46, HSM4, and HSM6 are shown. Our new SAMM-PBC46 and the higher order model HSM6 yield nearly identical results and cannot be visually distinguished, apart from a small bump in velocity and temperature at the boundary interface $x = -1$. This small bump is a result of the coupling of two different order models and should be reduced as much as possible by using appropriate padded values in the buffer cell. The difference between the lower order model HSM4 and the other two models is significant. These observations are confirmed in Fig. 3d, which shows the relative 2-norm difference of HSM4 and SAMM-PBC46 with respect to HSM6 for different relaxation times. The greater the non-equilibrium in the gas, the greater the gain achieved by using the adaptive scheme compared to the low-order scheme. The speedup of SAMM-PBC46 compared to HSM6 was $\approx 19\%$. We can conclude that for this specific test case, SAMM-PBC46 yields nearly identical accuracy as HSM6, while realizing a speedup of 19 percent. We note that only a small part of the domain ($\approx 33\%$) uses HSM4, for which this speedup is significant.

5 Conclusion

We introduced a proof-of-concept for the spatially adaptive simulation of a 1D linear moment model with space-dependent order. A lower order and a higher order moment model are coupled at their boundary interface using a buffer cell in which the moment vector is padded with additional moments. Due to the structure of hierarchical moment models, an efficient implementation is possible. Numerical simulations of a shock tube with a small linear density profile in a subdomain using the spatially adaptive model yielded accurate results, compared with a high order model, while realizing a significant speedup. This paper serves as an introduction to adaptive simulation of moment models. Future extensions could include time adaptive domain decomposition, multiple domains, and the extension to non-linear systems.

References

1. Bird GA (1994) Molecular gas dynamics and the direct simulation of gas flows. Oxford University Press, Oxford. https://doi.org/10.1093/oso/9780198561958.001.0001
2. Cai Z, Fan Y, Li R (2013) Globally hyperbolic regularization of grad's moment system in one-dimensional space. Commun Math Sci 11:547–571
3. Cai Z, Fan Y, Li R (2015) A framework on moment model reduction for kinetic equation. SIAM J Appl Math 75(5):2001–2023. https://doi.org/10.1137/14100110X
4. Castro Díaz MJ, Fernández-Nieto E (2012) A class of computationally fast first order finite volume solvers: PVM methods. SIAM J Sci Comput 34(4):A2173–A2196. https://doi.org/10.1137/100795280

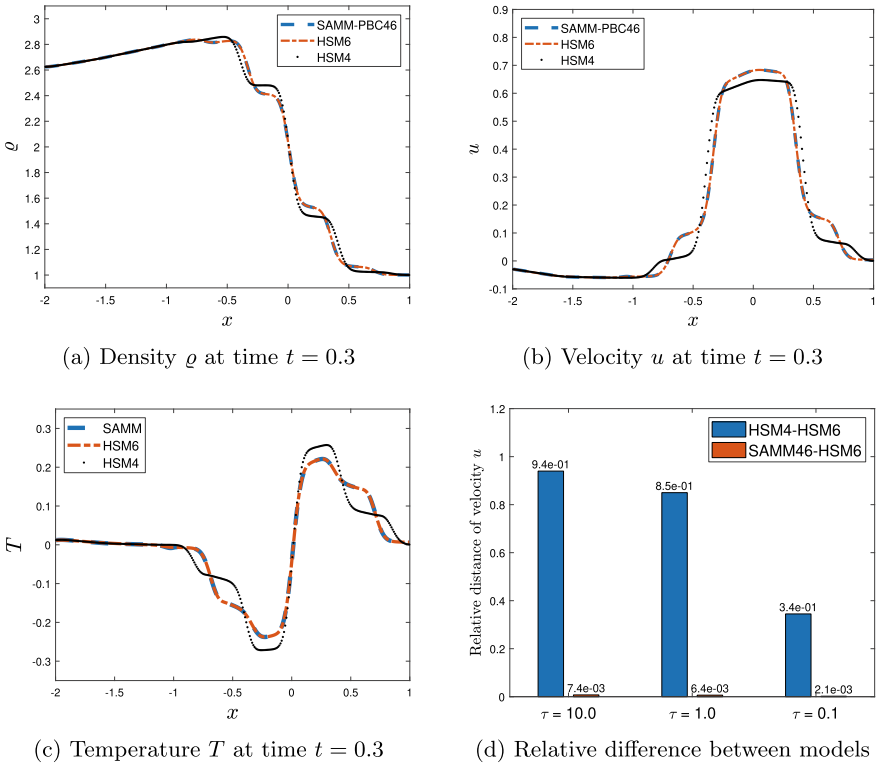

(a) Density ϱ at time $t = 0.3$

(b) Velocity u at time $t = 0.3$

(c) Temperature T at time $t = 0.3$

(d) Relative difference between models

Fig. 3 Numerical results for 1D shock tube test case for HSM4 (black dotted), HSM6 (orange dash-dotted) and SAMM-PBC46 (blue dashed). (**a**) density ϱ. (**b**) velocity u. (**c**) Temperature T. (**d**) relative difference of velocity u of SAMM-PBC46 and HSM4 with respect to HSM6 for varying Knudsen number τ.

5. Fan Y, Koellermeier J (2020) Accelerating the convergence of the moment method for the Boltzmann equation using filters. J Sci Comput 84(1):1. https://doi.org/10.1007/s10915-020-01251-8
6. Grad H (1949) On the kinetic theory of rarefied gases. Commun Pure Appl Math 2(4):331–407. https://doi.org/10.1002/cpa.3160020403
7. Hash D, Hassan H (1997) Two-dimensional coupling issues of hybrid DSMC/Navier-Stokes solvers. In: 32nd thermophysics conference. Fluid dynamics and co-located conferences, AIAA. https://doi.org/10.2514/6.1997-2507
8. Ivanov MS, Gimelshein SF (1998) Computational hypersonic rarefied flows. Annu Rev Fluid Mech 30:469–505. https://www.annualreviews.org/content/journals/10.1146/annurev.fluid.30.1.469
9. Koellermeier J (2019) Error estimators for adaptive simulation of rarefied gases using hyperbolic moment models. AIP Conf Proc 2132(1):120004. https://doi.org/10.1063/1.5119617
10. Koellermeier J, Samaey G (2021) Projective integration schemes for hyperbolic moment equations. Kinet Relat Models 14(2):353–387. https://www.aimsciences.org/article/doi/10.3934/krm.2021008
11. Lax PD (1954) Weak solutions of nonlinear hyperbolic equations and their numerical computation. Commun Pure Appl Math 7(1):159–193. https://doi.org/10.1002/cpa.3160070112

12. Li ZH, Zhang HX (2009) Gas-kinetic numerical studies of three-dimensional complex flows on spacecraft re-entry. J Comput Phys 228(4):1116–1138. https://www.sciencedirect.com/science/article/pii/S0021999108005408
13. Rovenskaya O, Croce G (2014) Application a hybrid solver to gas flow through a slit at arbitrary pressure ratio. Vacuum 109:266–274
14. Struchtrup H (2005) Macroscopic transport equations for rarefied gas flows-approximation methods in kinetic theory. Springer, Berlin
15. Torrilhon M (2016) Modeling nonequilibrium gas flow based on moment equations. Annu Rev Fluid Mech 48(48):429–458. https://www.annualreviews.org/content/journals/10.1146/annurev-fluid-122414-034259
16. Tsien HS (1946) Superaerodynamics, mechanics of rarefied gases. J Astronaut Sci 13(12):653–664. https://doi.org/10.2514/8.11476

Open Access This chapter is licensed under the terms of the Creative Commons Attribution 4.0 International License (http://creativecommons.org/licenses/by/4.0/), which permits use, sharing, adaptation, distribution and reproduction in any medium or format, as long as you give appropriate credit to the original author(s) and the source, provide a link to the Creative Commons license and indicate if changes were made.

The images or other third party material in this chapter are included in the chapter's Creative Commons license, unless indicated otherwise in a credit line to the material. If material is not included in the chapter's Creative Commons license and your intended use is not permitted by statutory regulation or exceeds the permitted use, you will need to obtain permission directly from the copyright holder.

Application of Regularized 13-Moment Equations to Continuum–Rarefied Gas Flow Over Aerospike Blunt Body

Satyvir Singh and Manuel Torrilhon

Abstract The accurate modeling of continuum-rarefied gas flows is crucial for understanding non-equilibrium phenomena in aerospace applications, particularly for high-speed vehicles encountering rarefied flow conditions. Traditional Navier–Stokes-Fourier equations fail to capture these effects, while kinetic approaches like the Boltzmann equation are computationally prohibitive. The regularized 13-moment (R13) equations offer a promising alternative by bridging the gap between continuum and rarefied regimes with improved accuracy and computational efficiency. This study investigates the application of the R13 equations to simulate gas flow over aerospike blunt bodies, a geometry known for its aerodynamic and thermal efficiency in high-speed conditions. The R13 framework effectively captures non-equilibrium phenomena, which are critical in transitional flow regimes. For numerical simulations, a two-dimensional modal discontinuous Galerkin method is developed to solve the R13 equations. Key flow characteristics, such as shock wave interactions, rarefaction effects, and aerodynamics coefficients, are analysed to assess the performance of the R13 model. The findings demonstrate the capability of the R13 equations to accurately predict flow behavior across a wide range of Knudsen numbers while maintaining computational efficiency.

Keywords R13 equations · Continuum-rarefied · Discontinuous galerkin method · Aerospike body

1 Introduction

Aerospace applications, particularly in hypersonic flight and spacecraft re-entry, often involve gas flows that span multiple regimes, from continuum to rarefied [1]. Understanding and accurately modeling these flows is critical for aerodynamic performance and thermal protection system design [2]. Hypersonic flows over blunt bodies generate strong shocks and significant non-equilibrium effects, such as velocity

S. Singh (✉) · M. Torrilhon
Applied and Computational Mathematics, RWTH Aachen University, Aachen, Germany
e-mail: singh@acom.rwth-aachen.de

© The Author(s) 2026

M. Grabe et al. (eds.), *Rarefied Gas Dynamics*, Springer Aerospace Technology,
https://doi.org/10.1007/978-3-032-00094-1_33

slip and temperature jump, which traditional continuum-based models like Navier-Stokes equations cannot resolve adequately [3]. These effects become pronounced in transitional flow regimes, where the continuum assumption breaks down. Aerospike blunt bodies are an advanced aerodynamic design aimed at reducing drag and heat flux by modifying shock-wave behavior and redistributing pressure loads [4]. Their potential to enhance efficiency in high-speed vehicles makes them a key area of research. However, simulating the flow physics around these configurations remains complex due to the interplay of continuum and rarefied dynamics.

Traditional macroscopic models struggle in non-equilibrium regimes, necessitating approaches rooted in kinetic theory. The moment-based methods derive macroscopic equations by averaging the Boltzmann equation [5], enabling better representation of rarefied flows. Compared to direct simulation Monte Carlo (DSMC) methods [1], which are computationally expensive for near-continuum flows, moment methods provide a more efficient and deterministic alternative. A versatile framework for deriving evolution equations for macroscopic quantities from the Boltzmann equations is offered by moment approaches. By anticipating higher-order rarefaction effects, these methods generally close the gap between fluid dynamics and kinetic gas theory in extreme non-equilibrium situations.

In 1949, Grad brought moment method into kinetic theory using a Hilbert expansion of the distribution function in Hermite polynomials [6]. The field equations based on Grad's 13-moment methods use an extended set of variables to describe the state of a gas, starting with the fluid dynamic quantities-density, velocity, and temperature including higher-order moments of the distribution function. Interestingly, Grad's 13-moment equations were an initial step, but they suffered from instabilities, especially in strong non-equilibrium conditions [7]. The regularized 13-moment (R13), derived from the Boltzmann equation using moment closure techniques, extend the classical Grad-13 moment equations by incorporating regularization terms to ensure hyperbolicity and stability [8]. These equations are well-suited for capturing non-equilibrium effects, such as heat flux and stress anisotropy, which are critical in rarefied gas dynamics. A comprehensive summary of the applied numerical methods for solving Grad's system can be found in the study of Torrilhon [9]. The R13 model has been successfully applied to various benchmark problems, but its potential in addressing the aerodynamic challenges of high-speed vehicles, particularly those with complex geometries like aerospike blunt bodies, remains underexplored.

Aerospike blunt bodies are known for their drag reduction and enhanced heat management, critical for high-speed and space applications [10]. Their unique flow features, including detached shock waves and complex interactions in the wake region, require advanced modeling techniques. Few studies leverage moment-based methods to explore the continuum-rarefied regime, leaving a gap this study aims to address [11]. This study aims to investigate the application of the R13 equations to simulate continuum-rarefied gas flows over aerospike blunt bodies. The focus is on assessing the model's capability to predict flow phenomena across different regimes, and exploring its computational efficiency for practical engineering applications. By leveraging the R13 equations, this work seeks to enhance the understanding of non-equilibrium effects in supersonic flows.

The remainder of the study is structured as follows: Sect. 2 introduces the mathematical formulation for two-dimensional R13 moment equations. Section 3 discusses the employed numerical solver. Section 4 presents simulation results and provides a detailed description of continuum-rarefied gas flow over an aerospace blunt body. Finally, Sect. 5 gives the concluding remarks and outlook for the future work.

2 Two-Dimensional Regularized 13-Moment Equations

In this study, we performed the numerical simulations for the two-dimensional regularized 13-moment (R13) equations in continuum-rarefied gas flows. The two-dimensional R13 equations are derived by Torrilhon [12] in conservative form as

$$\frac{\partial \mathbf{U}(W)}{\partial t} + \nabla \cdot \mathbf{F}(\mathbf{U}) = \mathbf{P}(\mathbf{U}), \tag{1}$$

with nine independent variables $W = \{\rho, v_x, v_y, p, p_x, p_y, \sigma, q_x, q_y\}$. Here, ρ is mass density; v_x, v_y are velocity components; p is the pressure; p_x, p_y are the directional pressure; σ is the shear stress; and q_x, q_y are the components of heat flux vector in $x-$ and $y-$ directions. Pressure tensor (p_{ij}) is related with stress tensor σ_{ij} by the mathematical expression $p_{ij} = p\delta_{ij} + \sigma_{ij}$. In Eq. (1), $\mathbf{U}$ is the vector of conservative variables, $\mathbf{F} = (F, G)$ is the vector of flux functions, and $\mathbf{P}$ is the vector of production terms, which are defined as follows:

$$\mathbf{U} = \begin{bmatrix} \rho \\ \rho v_x \\ \rho v_y \\ \rho v^2 + 3p \\ \rho v_x^2 + p_x \\ \rho v_y^2 + p_y \\ \rho v_x v_y + \sigma \\ \rho v_x v_x^2 + 3\rho v_x + 2(p_x v_x + \sigma v_y) + 2q_x \\ \rho v_y v_y^2 + 3\rho v_y + 2(p_y v_y + \sigma v_x) + 2q_y \end{bmatrix}, \quad \mathbf{P} = -\frac{p}{\mu} \begin{bmatrix} 0 \\ 0 \\ 0 \\ 0 \\ p_x - p \\ p_y - p \\ \sigma \\ \sigma v_y + (p_x - p)v_x + q_x \\ \sigma v_x + (p_y - p)v_y + q_y \end{bmatrix}$$

$$F = \begin{bmatrix} \rho v_x \\ \rho v_x^2 + p_x \\ \rho v_x v_y + \sigma \\ \rho v_x v^2 + 2(p_x v_x + 2\sigma v_y) + 3p v_x + 2q_x \\ \rho v_x^3 + 3p_x v_x + \frac{6}{5} q_x + m_{xxx} \\ \rho v_x v_y^2 + p_y v_x + 2\sigma v_y + \frac{2}{5} q_x + m_{xyy} \\ \rho v_y v_x^2 + p_x v_y + 2\sigma v_x + \frac{2}{5} q_y + m_{xxy} \\ (pv^2 + 3p + 4p_x)v_x^2 + (7\theta + v^2)p_x + 4\sigma v_x v_y + \frac{32}{5} q_x v_x + \frac{4}{5} q_y v_y - 2\theta p + \hat{R}_{xx} \\ (\rho v^2 + 3p + 2(p_x + p_y))v_x v_y + (7\theta + 3v^2)\sigma + \frac{14}{5}(q_x v_y + q_y v_x) + \hat{R}_{xy} \end{bmatrix}$$

$$G = \begin{bmatrix} \rho v_y \\ \rho v_x v_y + \sigma \\ \rho v_y^2 + p_y \\ \rho v_y v^2 + 2(p_y v_y + 2\sigma v_x) + 3p v_y + 2q_y \\ \rho v_y v_x^2 + p_x v_y + 2\sigma v_x + \frac{2}{5} q_x + m_{yxx} \\ \rho v_y^3 + 3p_y v_y + \frac{6}{5} q_y + m_{yyy} \\ \rho v_x v_y^2 + p_y v_x + 2\sigma v_y + \frac{2}{5} q_y + m_{xyy} \\ (\rho v^2 + 3p + 2(p_x + p_y)) v_x v_y + (7\theta + 3v^2)\sigma + \frac{14}{5}(q_x v_y + q_y v_x) + \hat{R}_{xy} \\ (p v^2 + 3p + 4p_y) v_y^2 + (7\theta + v^2) p_y + 4\sigma v_x v_y + \frac{32}{5} q_y v_y + \frac{4}{5} q_x v_x - 2\theta p + \hat{R}_{yy} \end{bmatrix}$$

Here, $p = \rho\theta$, and μ is the shear viscosity. The terms m_{ijk} and R_{ij} represent higher-order moments introduced to regularize Grad's original equations. Their definitions are derived from a Chapman–Enskog expansion around the Grad 13-moment approximation, as established by Struchtrup and Torrilhon [8, 12]. These regularization terms enhance the stability of the stress and heat flux equations and improve the model's accuracy across the continuum to rarefied flow regimes. These higher moments are connected by the relationship: $\hat{R}_{ij} = m_{ijk} v_k + R_{ij}$. For two-dimensional R13 equations, m_{ijk} and R_{ij} are defined by

$$\begin{bmatrix} m_{xxx} \\ m_{xxy} \\ m_{xyy} \\ m_{yyy} \end{bmatrix} = -2\frac{\mu}{p}\theta \begin{bmatrix} \frac{3}{5}\left(\frac{\partial p_x}{\partial x} - \frac{\partial p}{\partial x}\right) - \frac{2}{5}\frac{\partial \sigma}{\partial y} \\ \frac{1}{3}\frac{\partial p_x}{\partial y} - \frac{1}{5}\frac{\partial p}{\partial y} + \frac{8}{15}\frac{\partial \sigma}{\partial x} - \frac{2}{15}\frac{\partial p_y}{\partial y} \\ \frac{1}{3}\frac{\partial p_y}{\partial x} - \frac{1}{5}\frac{\partial p}{\partial x} + \frac{8}{15}\frac{\partial \sigma}{\partial y} - \frac{2}{15}\frac{\partial p_x}{\partial x} \\ \frac{3}{5}\left(\frac{\partial p_y}{\partial y} - \frac{\partial p}{\partial y}\right) - \frac{2}{5}\frac{\partial \sigma}{\partial x} \end{bmatrix},$$

$$\begin{bmatrix} R_{xx} \\ R_{xy} \\ R_{yy} \end{bmatrix} = -2\frac{\mu}{p}\theta \begin{bmatrix} \frac{5}{3}\frac{\partial q_x}{\partial x} + \frac{2}{3}\frac{\partial q_y}{\partial y} \\ \frac{1}{2}\left(\frac{\partial q_y}{\partial x} + \frac{\partial q_x}{\partial y}\right) \\ \frac{5}{3}\frac{\partial q_y}{\partial y} + \frac{2}{3}\frac{\partial q_x}{\partial x} \end{bmatrix}.$$

3 Numerical Solver and Validation

In this study, a modal discontinuous Galerkin method is developed to solve the two-dimensional R13 equations in the continuum-rarefied regime. The domain is discretized using non-overlapping triangular elements with Dubiner modal basis functions [3]. Gauss-Legendre quadrature is used for volume and flux integration, and the local Lax–Friedrichs (LLF) scheme computes the interface fluxes. Time advancement is performed using a third-order strong stability-preserving Runge-Kutta method. To ensure physical consistency, a positivity-preserving limiter [3] is applied to avoid non-physical values such as negative density or pressure.

To validate the R13-based computational model, we compare it with classical NSF results and experimental data for a one-dimensional normal shock in argon gas. Figure 1a shows that at $Ma = 3.8$, the R13 model matches the experimental density profile from Alsmeyer [13] more closely than the NSF model, accurately capturing the shock structure. Figure 1b presents the inverse density thickness $1/\delta$ over a range of Mach numbers, where R13 results show good agreement with experiments from Alsmeyer and Camac [14], while NSF consistently overpredicts the thickness. These comparisons demonstrate the superior accuracy of R13 in capturing non-equilibrium effects in the transitional regime (Fig. 2).

4 Results and Discussion

In this section, we present the numerical results of the R13 equations for supersonic gas flow over an aerospike blunt body in the continuum–rarefied regime. The computational domain is discretized using 30,739 non-overlapping triangular elements, as shown in Fig. 1, with mesh refinement near the wall to accurately resolve the boundary layer and shock structures. For the aerospike configuration, a geometric ratio of $d/D = 0.2$ and $L/D = 1.5$ is employed, where d is the aero-disk diameter, D is the diameter of the blunt body (used as the reference length), and L is the spike length. The outer boundary of the domain is treated as a far-field inflow, while the inner boundaries representing the solid surface are imposed with no-slip and isothermal wall conditions. The free-stream conditions are specified as Mach number $Ma = 2.0$, angle of attack $AoA = 0°$, temperature $T_\infty = 26.6$. The wall temperature is fixed as $T_w = 26.6$. Simulations are conducted for three Knudsen numbers: $Kn = 0.0001$, 0.001, and 0.01, capturing the transition from near-continuum to rarefied regimes. The corresponding Reynolds numbers, based

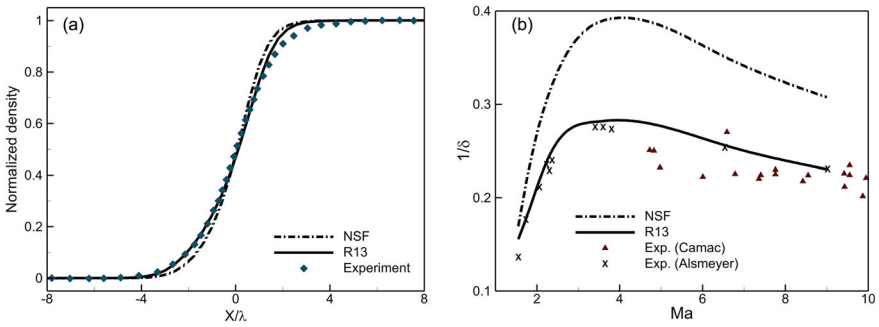

Fig. 1 Comparison of **a** normalized density profiles at $Ma = 3.8$, and **b** inverse density thickness versus Mach number for NSF, R13, and experimental data. Results are validated against experimental data from Alsmeyer [13] and Camac [14] for argon gas in a one-dimensional shock structure problem

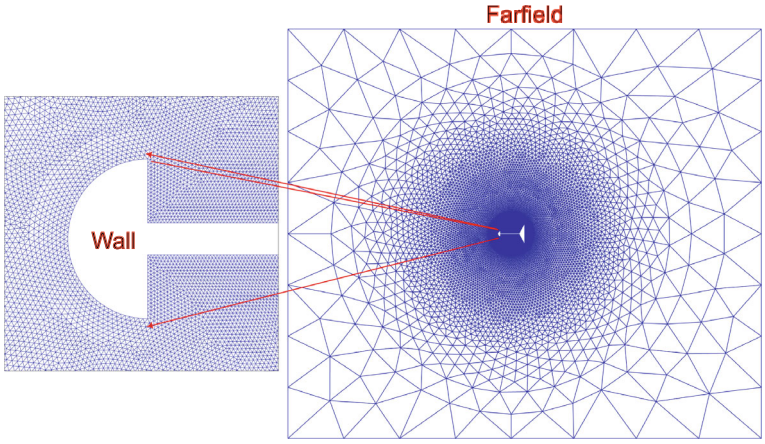

Fig. 2 Computational domain and boundary conditions

on the reference length D, are $Re = 19412$, 1941.2, and 194.12, respectively. The working gas is monatomic argon, selected for its well-characterized thermophysical properties, making it suitable for rarefied flow studies.

Figure 3 presents the contours of density, Mach number, and temperature for supersonic flow over an aerospike blunt body at three different Knudsen numbers ($Kn = 0.0001, 0.001, 0.01$), illustrating the transition from continuum to rarefied regimes. At $Kn = 0.0001$, the flow exhibits continuum-like behavior with a well-defined bow shock, resulting in sharp increases in density and temperature and a distinct deceleration in Mach number near the spike. As Kn increases, the shock structure becomes increasingly diffused due to non-equilibrium effects, leading to lower post-shock density and temperature values, and smoother Mach number transitions. At $Kn = 0.01$, significant rarefaction effects emerge, weakening the compression and thermal gradients, and revealing broader, non-equilibrium shock layers. The temperature fields particularly demonstrate reduced heat conduction and less pronounced heating in the stagnation region. Across all cases, the aerospike effectively modifies the flow structure by increasing the shock stand-off distance and redistributing the compression away from the main body, thereby reducing aerodynamic heating and drag.

Figure 4 shows the effect of the Knudsen number (Kn) on the computed drag coefficient for supersonic gas flow over an aerospike blunt body, highlighting the transition from continuum to rarefied flow regimes. At low Kn values ($\text{Kn} < 0.001$), corresponding to the continuum regime, the drag coefficient is highest due to significant collisional interactions and strong shock waves, resulting in pronounced viscous and pressure drag. As Kn increases into the transitional regime ($0.001 \leq \text{Kn} \leq 0.01$), non-equilibrium effects such as velocity and temperature slip reduce momentum transfer and weaken shock structures, leading to a sharp decline in drag. In the rarefied

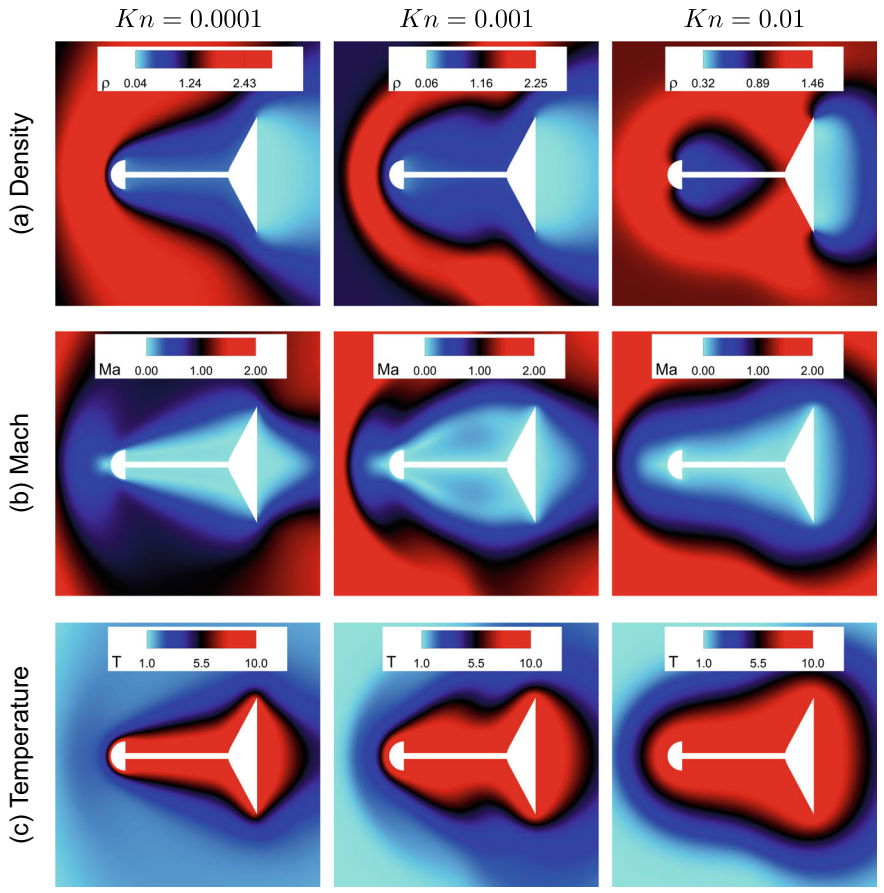

Fig. 3 Contours of **a** density, **b** Mach, and **c** temperature obtained for the supersonic gas flow over an aerospike blunt body with three Knudsen numbers ($Kn = 0.0001, 0.001,$ and 0.01)

regime (Kn $>$ 0.01), the drag coefficient stabilizes at a lower value as free-molecular effects dominate, and collisional drag mechanisms become negligible.

5 Concluding Remarks

This study demonstrates the capability of the R13 equations to effectively model continuum-rarefied gas flows over an aerospike blunt body. By employing a two-dimensional modal discontinuous Galerkin method, the R13 framework accurately captures key non-equilibrium phenomena-such as stress anisotropy, heat flux effects, and rarefaction-induced deviations from classical behavior-across a range of Knudsen

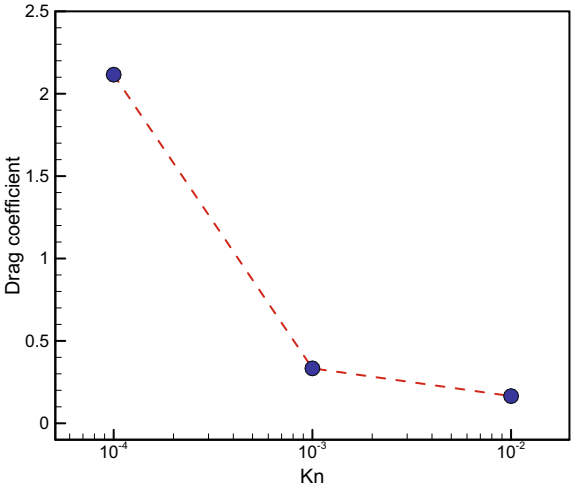

Fig. 4 Knudsen number effect on computed drag coefficient for the supersonic gas flow over an aerospike blunt body

numbers. Despite enforcing no-slip and isothermal boundary conditions at the wall, the model successfully reveals critical transitions in flow structure and aerodynamic performance from the continuum to the rarefied regime. The results confirm that the aerospike configuration substantially reduces drag and thermal loads, particularly in near-continuum conditions.

In addition to physical accuracy, the R13-DG approach exhibits favorable computational efficiency. While it incurs higher costs than classical NSF solvers, it remains significantly more efficient than particle-based methods such as DSMC and Fokker-Planck in transitional flow regimes. Its high-order accuracy and deterministic formulation make it a promising and practical alternative for simulating non-equilibrium gas dynamics in complex aerospace configurations.

References

1. Bird GA (1994) Molecular gas dynamics and the direct simulation of gas flows. Oxford University Press, Oxford
2. Reese JM, Gallis, Michael A, Lockerby, Duncan A (2003) New directions in fluid dynamics: non-equilibrium aerodynamic and microsystem flows. Philos Trans R Soc A 361:2967–298
3. Singh S, Karchani A, Chourushi T, Myong RS (2022) A three-dimensional modal discontinuous Galerkin method for the second-order Boltzmann-Curtiss-based constitutive model of rarefied and microscale gas flows. J Comput Phys 457:111052
4. Chinnappan AK, Malaikannan G, Kumar R (2017) Insights into flow and heat transfer aspects of hypersonic rarefied flow over a blunt body with aerospike using direct simulation Monte-Carlo approach. Aerosp Sci Technol 66:119–128
5. Boltzmann L (1872) Weitere Studien uber das Wa rmegleichgewicht unter Gasmolekulen. Wien
6. Grad H (1949) On the kinetic theory of rarefied gases. Commun Pure Appl Math 2:331–407

7. Singh S, Song H, Torrilhon M (2024) Modal discontinuous Galerkin simulations for Grad's 13 moment equations: application to Riemann problem in continuum-rarefied flow regime. J Comput Theor Transp 398–422
8. Struchtrup H, Torrilhon M (2003) Regularization of Grad's 13 moment equations: derivation and linear analysis. Phys Fluids 15:2668–2680
9. Torrilhon M (2016) Modeling nonequilibrium gas flow based on moment equations. Annu Rev Fluid Mech 48:429–458
10. Wood CJ (1962) Hypersonic flow over spiked cones. J Fluid Mech 12(48):614–624
11. Chourushi T, Singh S, Vishnu AS, Myong RS (2024) Numerical simulations of rarefied gas flow over an aero-spiked hypersonic blunt body using the second-order Boltzmann-Curtiss constitutive model. AIP Conf Proc 2996:140001
12. Torrilhon M (2006) Two-dimensional bulk microflow simulations based on regularized Grad's 13-moment equations. Multiscale Model Sim 5:695–728
13. Alsmeyer H (1976) Density profiles in argon and nitrogen shock waves measured by the absorption of an electron beam. J Fluid Mech 74:497–513
14. Camac M (1965) Argon shock structure. In: Proceedings of the fourth international symposium on rarefied gas dynamics, vol 1, p 240

Open Access This chapter is licensed under the terms of the Creative Commons Attribution 4.0 International License (http://creativecommons.org/licenses/by/4.0/), which permits use, sharing, adaptation, distribution and reproduction in any medium or format, as long as you give appropriate credit to the original author(s) and the source, provide a link to the Creative Commons license and indicate if changes were made.

The images or other third party material in this chapter are included in the chapter's Creative Commons license, unless indicated otherwise in a credit line to the material. If material is not included in the chapter's Creative Commons license and your intended use is not permitted by statutory regulation or exceeds the permitted use, you will need to obtain permission directly from the copyright holder.

Suitability of Moment Methods to Model the Ion Dynamics in a Low-Temperature Plasma

Anatole Berger, Nicolas Lequette, Thierry Magin, Anne Bourdon, and Alejandro Alvarez Laguna

Abstract We present a study of the suitability of several moment methods to capture the ion dynamics in a bounded non-equilibrium low-temperature plasma between two electrically-floating walls under different pressure regimes. We use a set of kinetic simulations in order to study the properties of one-dimensional five-moment (1D 5M) closures. We discuss on the advantages and disadvantages of some of the most common moment methods: Grad's closure, the quadrature method of moments (QMOM), the extended QMOM (EQMOM) and maximum entropy. For this study, we analyse the capability of each closure to capture the dynamics of the closing flux and its ability to retrieve the distribution function. The results show that the accuracy of each model largely depends on the pressure regime. In general, all the considered methods behave rather fine at high pressure and exhibit different challenges in order to represent the low-pressure regime.

Keywords Plasma discharge · Ions · Moment methods · Grad · QMOM · EQMOM · Maximum entropy · Particle-in-cell

1 Introduction

Low-temperature plasmas are fundamental to a wide number of industrial applications, from plasma etching for microelectronics [6, 20] and electric propulsion [11] to biomedical applications [9]. These plasmas are characterized by a large temperature difference between the heavy species (ions and neutral atoms or molecules) and electrons. The former are close to room temperature, while the latter are usually several eVs (or tens of thousands of Kelvin). Low-temperature plasmas are weakly

A. Berger (✉) · N. Lequette · A. Bourdon · A. Alvarez Laguna
Laboratoire de Physique des Plasmas, Centre National de la Recherche Scientifique, Sorbonne Université, École Polytechnique, Institut Polytechnique de Paris, Palaiseau, France
e-mail: anatole.berger@lpp.polytechnique.fr

T. Magin
Aeronautics and Aerospace Department, von Karman Institute for Fluid Dynamics, Sint-Genesius-Rode, Belgium

© The Author(s) 2026

M. Grabe et al. (eds.), *Rarefied Gas Dynamics*, Springer Aerospace Technology,
https://doi.org/10.1007/978-3-032-00094-1_34

ionized, with an ionization degree often much below the percent (usually around 10^{-4}). Furthermore, depending on the application, we deal with pressures ranging from a few tenths of Pascals up to atmospheric or higher pressures.

The charged species of low-temperature plasmas are often out of equilibrium [13] due to the presence of strong electric fields, gradients, and collisions with the neutral species. In this non-equilibrium regime, kinetic simulations are very computationally expensive (especially at higher pressures), whereas fluid models are less accurate because of the conditions far from the continuum regime. As a result, different moment methods (see e.g. [22] for a recent review on general applications of moment models) have been proposed in the low-temperature plasma literature. These include Grad [2, 16, 26], maximum entropy [3, 4], anisotropic Gaussian closures [14, 15], and the quadrature-based methods of moments (QMOM) [24]. Despite these efforts, the comparison with kinetic simulations that are representative of a bounded low-temperature plasma is still a challenge due to the presence of strong electric fields in the plasma sheath [1, 23]. In this paper, we study some of the most common moment closures in order to represent the ion dynamics and distribution functions of low-temperature plasmas, with realistic collision cross sections in a wide range of pressures and collisional regimes. In this paper, we assess the suitability of these models whereas in a future work, we will present non-linear numerical solutions of the moment models.

2 Kinetic Simulations of a Low-Temperature Bounded Plasma at Different Pressures

We study a one-dimensional bounded argon plasma between two electrically-floating walls, similar to the numerical set-up explained by Tavant et al. [25]. We consider a one-dimensional domain of 10 cm and neutral gas pressures that vary from 0.05 to 100 mTorr (0.0067–13 Pa). We use an in-house Particle-In-Cell (PIC) code with Monte Carlo collisions for the charged species, i.e., singly-charged ions and electrons [18]. The cross sections are taken from the LxCat data-base [21], considering ion isotropic elastic scattering and charge exchange. The neutral gas background is considered to be at rest with a Maxwellian distribution at room temperature (300 K). Therefore, in these simulations, only the charged particles (ions and electrons) are simulated, and their dynamics are coupled with Poisson's equation. We impose the ionization, proportional to the local plasma density, as proposed by Tavant et al. [25], in order to have a steady-state solution with an average ion density of 10^{15} m^{-3}. The ions are injected with the neutral distribution whereas the electrons are injected with a Maxwellian distribution at 5 eV. Note that although the simulation domain is one-dimensional, the three velocity directions are considered in the kinetic model. In this work, we focus on the ion dynamics and therefore only ion data will be presented.

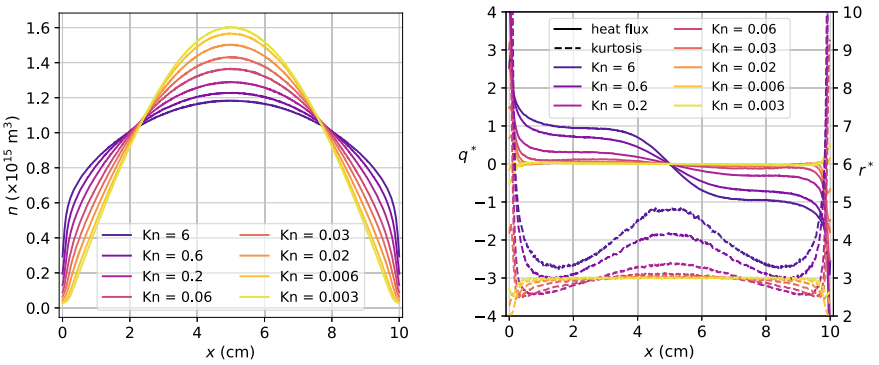

Fig. 1 Ion density profile (left), and normalized heat-flux and kurtosis profiles (right) for different pressure regimes. The right plot is zoomed in, but the moments reach higher values at the wall (namely, 6 for the heat-flux and 60 for the kurtosis in the most extreme cases). The Knudsen number refers to the ion-neutral collisions

We define the characteristic ion-neutral Knudsen number as

$$\mathrm{Kn} = \frac{l_{\mathrm{ig}}}{L}\,, \tag{1}$$

with the domain length L and the ion-neutral mean-free-path $l_{\mathrm{ig}} = (\sigma_{\mathrm{ig}}^0 n_{\mathrm{g}})^{-1}$ where $\sigma_{\mathrm{ig}}^0 = 10^{-18}$ m^2 is the ion-neutral characteristic cross section, and n_{g} the atomic argon density, which is constant in this study and varies depending on the pressure, following an ideal perfect gas law. Note that in these kinetic simulations, the ion-ion and ion-electron collisions are neglected as they are much less frequent than the ion-neutral collisions. Therefore, the ion-neutral Knudsen of Eq. (1) does not necessarily quantify the tendency to thermodynamic equilibrium of the ion population.

The considered system is one-dimensional in space and, therefore, we are interested in the ion dynamics in the x direction. Nevertheless, the system is simulated with a kinetic model that simulates the three velocity components. Because of the studied geometry, the impact of the transverse velocity of the ions on the dynamics is very reduced: e.g., the transverse mean velocity is zero and the transverse temperature is nearly the constant gas temperature in the whole domain at all considered pressures. As a result, we can simplify the kinetic problem by considering that the distribution function along the transverse direction is nearly at equilibrium and perform the integration of the distribution function in the perpendicular direction in order to reduce the problem to 1D-1V, as follows,

$$f_x^{\mathrm{1D}}(v_x) = \int_{\mathbb{R}^2} f^{\mathrm{3D}}(\vec{v})\,\mathrm{d}v_y\,\mathrm{d}v_z\,. \tag{2}$$

Similarly, the considered moments will be only along the x direction, as follows,

$$M_x^{(k)} = \int_{\mathbb{R}^3} \psi_k(v_x) f^{3D}(\vec{v})\, \mathrm{d}^3\vec{v} = \int_{\mathbb{R}} \psi_k(v_x) f_x^{1D}(v_x)\, \mathrm{d}v_x\,. \tag{3}$$

where $\psi_k(v_x)$ is a monomial in the x component of the velocity, that depends on the moment considered.

In the rest of the article, we will denote f the 1D VDF and drop the x subindex for the velocity and VDF. We define the following moments that are relevant to the discussion of the 1D 5-moment model, referred to as number density, drift velocity, pressure, heat flux, kurtosis, and kurtosis flux, as follows,

$$n = \int_{\mathbb{R}^3} f^{3\mathrm{D}}(\vec{v})\, \mathrm{d}^3v = \int_{-\infty}^{\infty} f(v)\, \mathrm{d}v\,, \quad nu = \int_{-\infty}^{\infty} vf\, \mathrm{d}v, \quad p = m\int_{-\infty}^{\infty} (v-u)^2 f\, \mathrm{d}v\,,$$

$$q = m\int_{-\infty}^{\infty} (v-u)^3 f\, \mathrm{d}v, \quad r = m\int_{-\infty}^{\infty} (v-u)^4 f\, \mathrm{d}v\,, \quad s = m\int_{-\infty}^{\infty} (v-u)^5 f\, \mathrm{d}v\,,$$

where m is the ion mass. Note that, as explained above, the moments are along the x direction, and therefore the high order moments written in the tensorial notation correspond to: $u \equiv u_x$, $p \equiv p_{xx}$, $q \equiv Q_{xxx}$, etc. In the following, we will use the normalized higher-order centered moments, defined as,

$$q^* = \frac{q}{\rho v_{\mathrm{th}}^3}, \qquad r^* = \frac{r}{\rho v_{\mathrm{th}}^4} \quad \text{and} \quad s^* = \frac{s}{\rho v_{\mathrm{th}}^5}\,, \tag{4}$$

where the mass density is $\rho = mn$ and the thermal speed is $v_{\mathrm{th}} = \sqrt{p/\rho}$.

The number density profile of the particle-in-cell simulations at different pressures is shown on the left panel of Fig. 1. In all cases, it has a dome-like shape with a maximum in the center and approaches zero at the wall since the charged particles are created in the bulk by ionization and then lost at the floating wall. The density profile flattens for decreasing pressures. This figure clearly illustrates the effect of the ion-neutral collisions in the transport of charged species of a bounded plasma.

The right panel of Fig. 1 shows the profiles of the normalized heat flux and kurtosis, as computed with the results of the particle-in-cell simulations. At high-pressure, both the heat-flux and the kurtosis are mostly at equilibrium in the whole domain, except in the sheath (i.e., close to the boundary). At low pressure, they are out-of-equilibrium in all the domain and increase sharply in the sheath, to reach very high values.

In the left panel of Fig. 2, we present the heat flux and kurtosis profiles in the realizability phase space. In this plot, we draw the boundary of the realizability domain (the black solid line in figure) that separates realizable and unrealizable velocity distribution functions (VDFs). Any physical VDF (positive definite integrable function) lies above this curve. Similarly, we present the Junk line, that is relevant for the

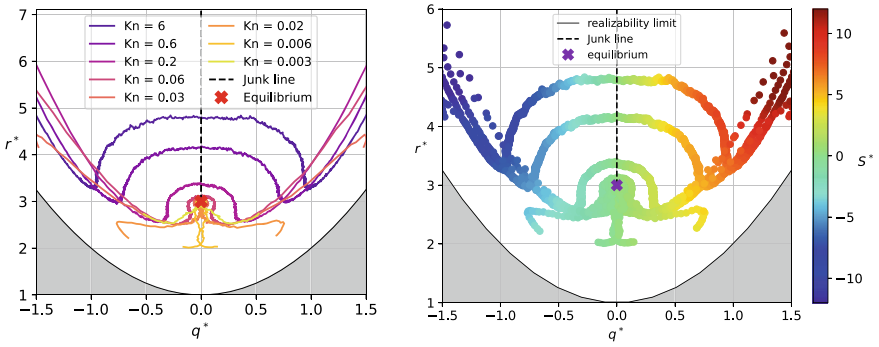

Fig. 2 (Left) high-order moment evolution in the realizability space for different pressure level. (Right) variation of the kurtosis-flux in this same space. The plots are zoomed in around the equilibrium. The grey area is the non-realizable zone in which no physical VDF exists with the corresponding heat-flux and kurtosis

discussion of maximum entropy and EQMOM closures. Note that the low-pressure simulations cross the Junk line.

We can then plot the variation of the normalized kurtosis-flux (the fifth order moment) in this space. This is shown on the right plot of Fig. 2. This plot shows an interesting trend. First, the behaviour of the fifth order moment seems to be similar in all the studied pressure regimes. As seen in the right panel of the figure, the fifth order moment seems to have a dependence on the normalized heat flux that is nearly linear and that it seems to be the same and independent of the background pressure. This is an interesting finding as it can provide guidelines in order to choose a closure model, as it will be shown in the next section. In addition, as the fifth order moment seems to have a behavior that can be determined by the previous moments (mainly on the heat-flux), it strongly motivates one to consider the kurtosis-flux as the closing flux and hence to consider five-moment (5M) models.

3 Comparison of Different Moment Closures for Ions in Low-Temperature Plasmas

In this section, we will first review some of the most common one-dimensional 5M closures: Grad, QMOM, EQMOM and maximum entropy. A discussion on these methods for 1D shocks can be found in Ref. [17]. Secondly, we will assess their suitability for capturing the ion properties as observed in the kinetic simulations. We base our assessment on a comparison of the closing flux (including their realizability) and the reconstructed VDF. We underline that in this work we do not implement a numerical solver of the moment closures, which is left to a future work. Instead, we

take the first five moments (up to order four) of the kinetic simulation, as show in the previous section, and we use them to study the above-mentioned properties of the closures.

3.1 One-Dimensional 5M-Closures

We will consider four of the most common closures, namely, Grad [12], the hyperbolic quadrature method of moment (HyQMOM) [10], the extended quadrature method of moment (EQMOM) or bi-Maxwellian closure [7], and maximum entropy (Max. Entr.) [8, 19] , with five moments. The expression of the VDF for each closure is

$$
\begin{aligned}
f^{\mathrm{1D}}_{\mathrm{Grad}}(c) &= \frac{\rho\, \mathrm{e}^{-c^2/2}}{\sqrt{2\pi k_{\mathrm{B}} T}} \left(1 - \frac{q^*}{6}\left(3c - c^3\right) + \frac{r^* - 3}{6}\left(3 - 6c^2 + c^4\right)\right) , \\
f^{\mathrm{1D}}_{\mathrm{HyQMOM}}(c) &= \rho_0 \delta(c) + \rho_1 \delta(c - c_1) + \rho_2 \delta(c - c_2) , \\
f^{\mathrm{1D}}_{\mathrm{EQMOM}}(c) &= \frac{\rho_1\, \mathrm{e}^{-(c-c_1)^2/2}}{\sqrt{2\pi k_{\mathrm{B}} T_0}} + \frac{\rho_2\, \mathrm{e}^{-(c-c_2)^2/2}}{\sqrt{2\pi k_{\mathrm{B}} T_0}} , \\
f^{\mathrm{1D}}_{\mathrm{Max.Ent.}}(c) &= \exp\left(k_0 + k_1 c + k_2 c^2 + k_3 c^3 + k_4 c^4\right) .
\end{aligned}
$$

where c is the peculiar velocity along the x direction normalized to the thermal speed, i.e., $c \equiv v_x / v_{\mathrm{th}}$ (the x index is dropped for the sake of simplicity), normalized to the thermal speed, ρ, ρ_1 and ρ_2 are densities, $T = p/(nk_B)$ and T_0 are temperatures, k_{B} is the Boltzmann constant, $k_0, \cdots, k_4$ are some non-dimensional coefficients that are function of the accessible moments and are computed numerically by solving an optimization problem, and $\delta(c)$ are Dirac delta distributions.

3.2 Closing Flux

The closure of a 1D 5M model is completely characterized by the dependency of the kurtosis-flux on the heat-flux and the kurtosis. In Fig. 3, we present s^* in the realizability space for the four considered closures. This can be compare to Fig. 2, where the kurtosis-flux from the kinetic simulations was presented. At high pressures ($\mathrm{Kn} < 0.2$) the kinetic data are close to the equilibrium and the four closures resemble the PIC results. Alternatively, at low-pressures ($\mathrm{Kn} \geq 0.2$), the kinetic simulations cross the Junk line at the center of the domain. This line is singular in the EQMOM and maximum entropy closures so this may be an issue for these closures. Furthermore, the kurtosis-flux does not have the right trend as compared to the kinetic solutions around this line (it diverges while it is zero in the kinetic data). Grad's closure and HyQMOM have, on the other hand, a more similar behavior. In particular, HyQMOM

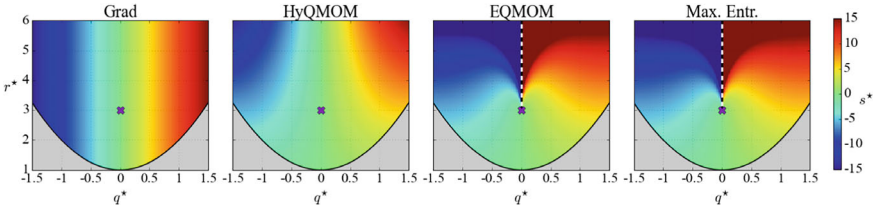

Fig. 3 Value of the kurtosis-flux in the realizability space for the different closures considered. The violet cross represent the equilibrium, the grey area is the non-realizable zone and the dashed line is the Junk line. The colorbar is cut-off at 25 because the kurtosis-flux diverges around the Junk line for EQMOM and Maximum entropy

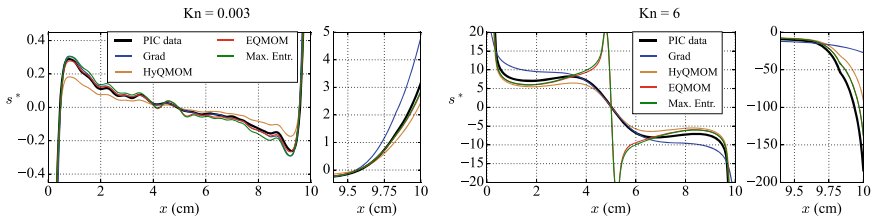

Fig. 4 Kurtosis-flux profile as directly computed from the VDF of PIC data and from the previous moments using the 4 closures considered in this study at two different pressures. The right panel in each subfigure show a zoom of the region close to the wall, i.e., the sheath region

closure seems to match the best the behavior at low pressure, as the closing flux takes into account the dependency on the kurtosis (as seen in the kinetic solutions) while Grad's closing depends only on the heat-flux.

Figure 4 shows kurtosis-flux profiles for two pressures, high pressure (Kn = 0.003) and low pressure (Kn = 6). We plot the kurtosis-flux directly taken from the PIC data, as well as the kurtosis-flux computed from the heat-flux and kurtosis of the PIC data using the 4 closures introduced in this section. At high pressure, in the bulk (and pre-sheath, i.e., $x \in [0.5,\ 9.5]$ cm) all closures but HyQMOM have similar and very good accuracy. The latter is less accurate but still follows the right trend. The sheath region is shown in the right panel of each subfigure of Fig. 4. In this region, Maximum entropy and EQMOM capture the kinetic solution and HyQMOM provides a less accurate approximation, while Grad becomes far from the kinetic solution. At low pressure (Kn = 0.6), HyQMOM becomes the best approximation of the flux in the all domain. Maximum entropy and EQMOM are accurate in the sheath and in a large part of the bulk but diverge in the center (because of the crossing of the Junk line). Grad is the less accurate, in particular in the sheath region. Overall, each closure has its own domains and regimes of accuracy, maximum entropy and EQMOM being extremely similar.

3.3 VDF Reconstruction from the Moments

We will now study the accuracy of the considered closures to recover the VDF of the kinetic solutions from its moments. Grad's VDF reconstruction is straightforward since its expression as a function of the moment is analytical. For HyQMOM and EQMOM, the link between the moments and the parameters of the VDF can be reduced to a single polynomial equation, that is solved using Brent algorithm [5]. For maximum entropy, there is no known simplification, and the total system of five equations is solved using Newton-Raphson algorithm.

At high pressure in the bulk, the kinetic VDF is mostly Maxwellian, so the reconstruction from the moments is almost exact and equivalent for all closures but HyQMOM. HyQMOM VDF being a sum of Dirac delta distributions, it will not be a continuous function, which is a major drawback for the physical consistency and for the computation of the collisional processes.

In Fig. 5, we present some cases with non-Maxwellian VDF: at high pressure in the sheath (left plot), at low pressure in the center (center plot) and at low pressure in the sheath (right plot). For each case, a Maxwellian with the same first three moments is also shown as a reference. Despite having an almost identical closing flux, maximum entropy and EQMOM have very different VDF reconstructions. The former is extremely accurate in the high-pressure regime and manages to recover an almost exact VDF in all the domain, even in the sheath as can be seen in the left plot. It is also the most accurate (and smoothest) in most of the domain in the low pressure regime except around the center of the domain (close to the Junk line), otherwise it only struggles to catch the stiffness of the PIC VDF in the sheath at very low pressure. EQMOM being a sum of two Gaussians, its VDF will be less smooth. Indeed, as can be seen in the right plot, its only way to create a large skewness is by increasing the space between the two Gaussians, leading to two distinct populations in extreme cases, which is not representative of what happens to the kinetic VDF. Finally, Grad is a small improvement from a Maxwellian for small perturbations but becomes unpractical for large deviations as its tail can become negative (as can be seen on the right plot).

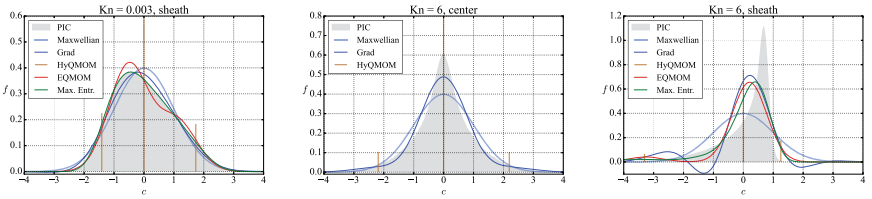

Fig. 5 Comparison of the VDF reconstructed from the first five moments with different closures. The HyQMOM VDF being a sum of Dirac delta distributions, it is represented with vertical lines with heights corresponding to the weights of each Dirac. In the center plot, there is no fit for EQMOM and Maximum entropy since the moment set is on the Junk line

4 Conclusion and Discussion

We studied the suitability of several one-dimensional moment models for ions in a one-dimensional bounded low-temperature plasma. We have used for this study kinetic simulations under a wide pressure range, considering realistic collisional processes, including elastic isotropic scattering and charge-exchange collisions. We used the first five moments of the kinetic simulations in order to analyze the behavior of the closures with these accessible moments. We summarize here our conclusions:

- The study of the fifth-order moment, as seen from the kinetic data, in the 5M realizability space, suggests that there is a mapping between this moment and the normalized heat flux and kurtosis. This mapping seems to be unique, independent of the pressure conditions. This leads us to believe that a 5M closure is a sound choice for this problem.
- When compared to the different considered closures, we observe that the maximum-entropy and EQMOM closures are able to capture the closing flux with a high degree of accuracy at high pressure. At low-pressure, the kinetic solutions lie on the Junk-line in the center of the domain, which hinders the suitability of maximum-entropy and EQMOM. Nevertheless, maximum-entropy, EQMOM, and HyQMOM capture the closing flux in the sheath with remarkable accuracy.
- The reconstructed VDFs at the wall are particularly important in order to study wall physical processes, e.g., etching rates for microelectronics applications. Maximum-entropy and EQMOM are able to capture this VDF at the high-pressure regime. However, none of the considered closures provide a satisfactory approximation at low-pressure.

This study will be continued with the numerical resolution of the moment equations, which will be presented in a separate paper. The current analysis shows that a unique model able to capture all the pressure regimes is a challenge. Also, the model should be simple enough in order to include the collisional processes in a realistic manner. One possible solution could be the consideration of a hierarchy with higher number of moments, which can help to solve some of the shown limitations.

One example of these limitations is the singular behaviour of EQMOM along the Junk line, which might be solved by considering a larger number of moments. The usual EQMOM considers a sum of Gaussians with a single temperature because the moment inversion algorithm (often based on the Wheeler algorithm) requires this assumption in order to invert the problem in a computationally efficiently manner. A possible alternative that would solve this singular behaviour could be to consider two different temperatures for the Gaussians, which would require a 6M model. However, this would come with an increase of the computational cost.

Alternatively, the limitations associated to the Junk line for maximum-entropy models in the center of the domain at low pressure might be more challenging to solve by increasing the number of moments. By observing the VDF at the center of the simulation at low pressure, we can note that it decays as an exponential with $-|v|$ in the exponent and hence it has symmetric heavy tails (positive excess kurtosis).

However, the symmetric maximum entropy leading-order terms at $v \to \infty$ are by construction of order $-v^{2n}$ inside the exponential (for $n \geq 1$). As a result, even with an increased number of moments, the maximum-entropy will have problems to capture the decay as seen in the simulations and therefore the Junk line will still be a problem in the center of the domain at low pressures.

Acknowledgements This work is part of a PhD funded by the Institut Polytechnique de Paris (IPP) and the EUR PlasmaScience. The authors would like to thank Clinton Groth, whose course on the moment methods and discussions greatly helped realizing this study.

References

1. Alvarez Laguna A, Pichard T, Magin T, Chabert P, Bourdon A, Massot M (2020) An asymptotic preserving well-balanced scheme for the isothermal fluid equations in low-temperature plasmas at low-pressure. J Comput Phys 419:109634
2. Alvarez Laguna A, Esteves B, Bourdon A, Chabert P (2022) A regularized high-order moment model to capture non-Maxwellian electron energy distribution function effects in partially ionized plasmas. Phys Plasmas 29(8):083507. https://doi.org/10.1063/5.0095019
3. Boccelli S, Giroux F, Magin TE, Groth CPT, McDonald JG (2020) A 14-moment maximum-entropy description of electrons in crossed electric and magnetic fields. Phys Plasmas 27(12):123506. https://doi.org/10.1063/5.0025651
4. Boccelli S, McDonald JG, Magin TE (2022) 14-moment maximum-entropy modeling of collisionless ions for Hall thruster discharges. Phys Plasmas 29(8):083903. https://doi.org/10.1063/5.0100092
5. Brent RP (1973) Algorithms for minimization without derivatives. Prentice-Hall
6. Chabert P, Braithwaite N (2011) Physics of radio-frequency plasmas. Cambridge University Press
7. Chalons C, Fox R, Massot M (2010) A multi-gaussian quadrature method of moments for gas-particle flows in a les framework. In: Proceedings of the summer program, pp 347–358
8. Dreyer W (1987) Maximisation of the entropy in non-equilibrium. J Phys A: Math General 20(18):6505. https://dx.doi.org/10.1088/0305-4470/20/18/047
9. Duchesne C, Banzet S, Lataillade J, Rousseau A, Frescaline N (2019) Cold atmospheric plasma modulates endothelial nitric oxide synthase signalling and enhances burn wound neovascularisation. J Pathol 249
10. Fox RO, Laurent F, Vié A (2018) Conditional hyperbolic quadrature method of moments for kinetic equations. J Comput Phys 365:269–293. https://www.sciencedirect.com/science/article/pii/S0021999118301852
11. Goebel D, Katz I (2008) Fundamentals of electric propulsion: ion and hall thrusters. In: JPL space science and technology series. Wiley. https://books.google.fr/books?id=P5OGFXcBKcwC
12. Grad H (1949) On the kinetic theory of rarefied gases. Commun Pure Appl Math 2(4):331–407. https://onlinelibrary.wiley.com/doi/abs/10.1002/cpa.3160020403
13. Kolobov V, Godyak V (2019) Electron kinetics in low-temperature plasmas. Phys Plasmas 26(6):060601. https://doi.org/10.1063/1.5093199
14. Kuldinow DA, Yamashita Y, Mansour AR, Hara K (2024) Ten-moment fluid model with heat flux closure for gasdynamic flows. J Comput Phys 508:113030. https://www.sciencedirect.com/science/article/pii/S0021999124002791
15. Kuldinow D, Yamashita Y, Hara K (2024) Ten-moment fluid model for low-temperature magnetized plasmas. Phys Plasmas 31:3

16. Laguna AA, Esteves B, Raimbault JL, Bourdon A, Chabert P (2023) Discussion on the transport processes in electrons with non-maxwellian energy distribution function in partially-ionized plasmas. Plasma Phys Controlled Fusion 65(5):054002
17. Laplante J, Groth CPT (2016) Comparison of maximum entropy and quadrature-based moment closures for shock transitions prediction in one-dimensional gaskinetic theory. AIP Conf Proc 1786(1):140010. https://doi.org/10.1063/1.4967641
18. Lequette N, Alvarez Laguna A, Chabert P, Bourdon A, Esteves B (2024) Pic fluid hybrid simulation of a discharge for electric propulsion. In: Proceedings of the 38th international electric propulsion conference, Toulouse, France, pp 2024–686
19. Levermore CD (1996) Moment closure hierarchies for kinetic theories. J Statist Phys 83(5–6):1021–1065
20. Lieberman MA, Lichtenberg A (2005) Principles of plasma discharges and materials processing, 2nd edn. Wiley-Interscience
21. Phelps Database (2021) www.lxcat.net, retrieved on 14 Apr 2021
22. Pichard T (2023) Some recent advances on the method of moments in kinetic theory. ESAIM ProcS 75:86–95
23. Sahu R, Mansour AR, Hara K (2020) Full fluid moment model for low temperature magnetized plasmas. Phys Plasmas 27(11):113505
24. Taunay PYC, Mueller ME (2023) Quadrature-based moment methods for kinetic plasma simulations. J Comput Phys 473:111700. https://www.sciencedirect.com/science/article/pii/S002199912200763X
25. Tavant A, Lucken R, Bourdon A, Chabert P (2019) Non-isothermal sheath model for low pressure plasmas. Plasma Sources Sci Technol 28(7):075007. https://dx.doi.org/10.1088/1361-6595/ab279b
26. Zhdanov V, Tirskii G (2003) The use of the moment method to derive the gas and plasma transport equations with transport coefficients in higher-order approximations. J Appl Math Mechan 67(3):365–388. https://www.sciencedirect.com/science/article/pii/S0021892803900219

Open Access This chapter is licensed under the terms of the Creative Commons Attribution 4.0 International License (http://creativecommons.org/licenses/by/4.0/), which permits use, sharing, adaptation, distribution and reproduction in any medium or format, as long as you give appropriate credit to the original author(s) and the source, provide a link to the Creative Commons license and indicate if changes were made.

The images or other third party material in this chapter are included in the chapter's Creative Commons license, unless indicated otherwise in a credit line to the material. If material is not included in the chapter's Creative Commons license and your intended use is not permitted by statutory regulation or exceeds the permitted use, you will need to obtain permission directly from the copyright holder.

A Study on Gramian Closures in Bimodal Phenomena

Eda Yilmaz, Georgii Oblapenko, and Manuel Torrilhon

Abstract This work analyzes the prediction quality of Gramian closures using a strongly bimodal distribution modeled as the superposition of two Gaussian functions. In [1], a new class of hyperbolic closures based on orthogonal polynomials named Gramian and extended Gramian closures has been introduced. These new closures are compared with Grad and the maximum entropy closures in terms of approximation quality. Numerical experiments show that the extended Gramian closure achieves competitive accuracy with the maximum entropy approach, particularly for even-order moments.

Keywords Kinetic theory of gases · Moment methods · Non-linear closures

1 Introduction

Capturing the dynamics of non-equilibrium gas flows requires models that go beyond classical continuum formulations. In such regimes, traditional continuum laws such as Navier-Stokes and Fourier fail to provide accurate results. As continuum assumptions break down, it becomes necessary to model gas behavior at the kinetic level, where individual molecular motion is considered. Kinetic theory provides a microscopic description of gas behavior by modeling the time evolution of the particle distribution function governed by the Boltzmann equation.

Despite providing a detailed description of microscopic gas dynamics, the Boltzmann equation remains computationally taxing due to its high dimensionality and the complexity of the collision operator. A widely used simplification technique is the method of moments, which projects the Boltzmann equation onto a finite set of macroscopic quantities such as density, momentum, and energy. However, this process generates an infinite hierarchy of moment equations, as the evolution of each moment depends on higher-order ones. In order to close this set of equations,

E. Yilmaz (✉) · G. Oblapenko · M. Torrilhon
Applied and Computational Mathematics (ACoM), RWTH Aachen University, Aachen, Germany
e-mail: yilmaz@acom.rwth-aachen.de

© The Author(s) 2026

M. Grabe et al. (eds.), *Rarefied Gas Dynamics*, Springer Aerospace Technology,
https://doi.org/10.1007/978-3-032-00094-1_35

information of the next moment needs to be defined based on the given set of lower moments, which is called a closure relation.

Over the past decades, many closure strategies have been proposed. One well-known classical technique is constructed by Grad [2] for closing the moment system (2) by expanding the distribution function as a series. In this approach, the distribution function is expressed as a weighted sum of Hermite polynomials based on equilibrium. The coefficients of the series represent the parameters of the ansatz. Grad's closure is a well-known and widely used classical method, but it loses hyperbolicity under non-equilibrium conditions. Another approach is centered on entropy and provides a nonlinear closure that maximizes entropy under the constraints of given moments [3, 4]. This method guarantees hyperbolicity and leads to a system of equations in conservative form, making it attractive for modeling non-equilibrium flows. However, the maximum entropy closure may not produce a valid distribution for all moment sets, and the resulting fluxes often lack closed form expressions, making the method computationally intensive and limited to lower order systems.

Quadrature-based methods offer another direction. McGraw [5] first introduced such an approach for modeling aerosol dynamics, and it was later extended in various contexts [6–9]. However, classical quadrature-based closures often result in non-hyperbolic systems, which can lead to nonphysical shock formations. More recently, the Hyperbolic Quadrature Method of Moments (HyQMOM) [6] has been proposed. This method relies on orthogonal polynomials and provides a solution to the moment closure problem without reconstructing the underlying probability distribution function.

This work builds upon [1] by introducing a new benchmark test problem. Specifically, we examine a strongly bimodal distribution constructed as a superposition of two Gaussians with distinct velocities. We evaluate the performance of Gramian and extended Gramian closures in predicting the $(M+1)^{\text{th}}$ moment based on n lower-order moments, and compare their accuracy against those of Grad's and maximum entropy closures.

The remainder of the paper starts with a brief overview of moment closure problem, including the one-dimensional kinetic transport equation and its associated moment system. In addition, the relation of orthogonal polynomial with Gramian matrix is also introduced. Section 3 summarizes the various closure strategies used in this work. Then, in Sect. 4, details of the numerical procedure used to evaluate the accuracy of each closure, based on reference moments computed from a bimodal distribution are presented. Lastly, the bimodal test case is defined and numerical results comparing the relative errors of each closure method across a range of velocity values and moment orders are drawn.

2 Moment Closures

We focus on the solution of the one-dimensional kinetic transport equation

$$\partial_t f + c\partial_x f = S(f) \qquad (x, t, c) \in \Omega \times [0, T] \times \mathbb{R}, \tag{1}$$

where $f(x, t, c)$ represents the particle distribution over space $\mathbb{R}$ and time $[0, T]$. The variable c represents particle velocity at each point (x, t), and $S(f)$ denotes the collision operator.

The distribution function $f : \mathbb{R} \to \mathbb{R}^+$, defined by $c \mapsto f(c)$, is a key component in the formulation of moment equations. The moments of a distribution on the real line are defined as $u_k = \int_{\mathbb{R}} c^k f(c)dc$, where $f(c)$ satisfies the usual requirements of, e.g., positivity and integrability. The set of moments $u := \{u_k\}_{k=0,1,..,M}$ up to a given order M are the only information available about the distribution, while $f(c)$ is generally unknown. When the distribution function depends on space and time, moments also vary respectively. The process of multiplying the kinetic transport equation by successive powers of c and integrating over the velocity space generates a system of partial differential equations. The system of moment equations has the following form

$$\begin{aligned} \partial_t u_0 + \partial_x u_1 &= s_0 \\ \partial_t u_1 + \partial_x u_2 &= s_1 \\ &\vdots \\ \partial_t u_M + \partial_x u_{M+1} &= s_M \end{aligned} \tag{2}$$

where the s_k are the moments of the collision operator $S(f)$. It is important to highlight that this system follows a cascading structure, where the equation for the n^{th}-order moment depends on the next higher-order moment. The closure relation for u_{M+1} must be defined to complete the system.

Definition 1 A prediction of the next moment based on a set of given moments in the form $u_{M+1} = \mathcal{C}(u_0, u_1, \cdots, u_M)$, where $\mathcal{C} : \mathcal{R} \to \mathbb{R}$ is a smooth function, is called a *moment closure*.

Orthogonal Polynomials

A scalar product defined using a distribution function $f(c)$ is given by $\langle v, w\rangle_f = \int_{\mathbb{R}} v(c)w(c)f(c)dc$. This inner product can be used to define orthogonal polynomials $p_k \in \mathbb{P}_k$, which satisfy the orthogonality condition $\langle p_k, p_l\rangle_f = 0$ for $k \neq l$. Here, $\mathbb{P}_k$ represents the space of univariate polynomials with degree at most k, and monic polynomials are considered. Recent work replaces Gram-Schmidt orthogonalization with a Gramian matrix to determine the orthogonal polynomials $\{p_k\}$.

Definition 2 Let the moments $\{u_k\}_{k=0,\dots,2n} \subset \mathcal{R}$ of a distribution be given and finite. Then the matrix $G_n = \{\langle c^i, c^j \rangle_f\}_{i,j=0,\dots,n}$ is called the monomial-based *Gramian matrix* of order $n \in \mathbb{N}$.

In the classical book [10, Sect. 2.2], the explicit representation of the orthogonal polynomial p_n is defined by

$$p_n(c) = \frac{1}{\det G_{n-1}} \det \begin{pmatrix} & & u_n \\ & G_{n-1} & \vdots \\ & & u_{2n-1} \\ 1, & c, \cdots, & c^{n-1} \quad c^n \end{pmatrix}. \tag{3}$$

For simplicity, the determinant of Schur complement is used and Eq. (3) is written in the following form

$$p_n(c) = c^n - (1, c, \cdots, c^{n-1}) G_{n-1}^{-1} u_{n,2n-1} \tag{4}$$

where we used the abbreviation $u_{k,l} := (u_k, u_{k+1}, \dots, u_l)^\mathsf{T} \in \mathbb{R}^{l-k+1}$ for $k \le l$ for the vector $u_{n,2n-1} \in \mathbb{R}^n$.

3 Closure Techniques

The choice of closure plays a key role in the accuracy and stability of moment methods. In this study, we investigate two recently developed closures, Gramian and extended Gramian closures, and compare them with classical approaches such as Grad's method and the maximum entropy closure. Gramian closures are based on orthogonal polynomials derived from the Gramian matrix and provide explicit expressions for the next higher moment. The extended version introduces an additional parameter χ, which allows adjusting certain mathematical properties of the closure.

The mathematical properties of these closures vary depending on whether the number of moments M is even or odd. For even values of M, the extended Gramian closure satisfies strict hyperbolicity over a broad range of parameters, ensures gauge invariance for a specific choice, and preserves equilibrium. In contrast, for odd M, equilibrium preservation is no longer possible. The standard Gramian closure in this case is only weakly hyperbolic, while the extended version offers improved behavior near equilibrium and achieves gauge invariance under certain conditions.

Even Gramian Closure

Let $M \in \mathbb{N}$ be even and $n = \frac{M}{2}$. The condition $\int_{\mathbb{R}} p_n(c) c^{n+1} f(c) dc = 0$ defines the relation $\mathbf{u_{2n+1}} = \mathbf{u_{n+1,2n}^T G_{n-1}^{-1} u_{n,2n-1}}$ between $u_{M+1} = u_{2n+1}$ and $\{u_k\}_{k=0,1,..,M}$, which we call *Gramian moment closure*. The closure relation arises directly by inserting the polynomial in (4) into the integral condition.

Extended Even Gramian Closure
Let $M \in \mathbb{N}$ be even and $n = \frac{M}{2}$. For an arbitrary $\chi \in \mathbb{R}$, the relation

$$u_{2n+1} = u_{n+1,2n}^T G_{n-1}^{-1} u_{n,2n-1} + \chi \frac{n+1}{n} \frac{u_{2n} - u_{n,2n-1}^T G_{n-1}^{-1} u_{n,2n-1}}{u_{2n-2} - u_{n-1,2n-3}^T G_{n-2}^{-1} u_{n-1,2n-3}} \left(u_{2n-1} - u_{n,2n-2}^T G_{n-2}^{-1} u_{n-1,2n-3}\right)$$

between $u_{M+1} = u_{2n+1}$ and $\{u_k\}_{k=0,1,\ldots,M}$, which we call *extended Gramian moment closure* for even M.

Odd Gramian Closure
Let $M \in \mathbb{N}$ be odd and $n = \frac{M+1}{2}$. The condition $\int_{\mathbb{R}} p_n(c) c^n f(c) dc = 0$ defines the relation $u_{2n} = u_{n,2n-1}^T G_{n-1}^{-1} u_{n,2n-1}$ between $u_{M+1} = u_{2n}$ and $\{u_k\}_{k=0,1,..,M}$, which we call *Gramian moment closure* for odd M.

Extended odd Gramian Closure
Let $M \in \mathbb{N}$ be odd and $n = \frac{M+1}{2}$. The relation

$$u_{2n} = u_{n+1,2n-1}^T G_{n-2}^{-1} u_{n-1,2n-3} + \chi \frac{(u_{2n-1} - u_{n,2n-2}^T G_{n-2}^{-1} u_{n-1,2n-3})^2}{u_{2n-2} - u_{n-1,2n-3}^T G_{n-2}^{-1} u_{n-1,2n-3}}$$

between $u_{M+1} = u_{2n}$ and $\{u_k\}_{k=0,1,\ldots,M}$, which we call *extended Gramian moment closure* for odd M.

4 Computation Procedure

In this work, dimensionless moments scaled by density, temperature, and shifted by velocity are considered. First, we evaluate reference moment values $\{u_k^{(\text{reference})}\}_{k=0,1,\ldots,M+1}$ with the bimodal distribution function as defined below. Using the first M reference moment values, the next higher moment is calculated by different closure methods. This can be achieved by applying a reconstructed distribution, as is done in the Grad and maximum entropy closures, or through a direct approach, which is the case for all Gramian closures. For the maximum entropy closure, we compute point values of $\boldsymbol{f} \in \mathbb{R}^{N_c}$ on a discrete velocity grid $\{c_j\}_{j=1,\ldots,N_c}$ on a finite domain $[c_{\min}, c_{\max}]$. To improve the convergence behavior, the logarithm is modified by writing $-f \log(f + \varepsilon)$ where $\varepsilon = 10^{-8}$. It is important to mention that this method allows handling odd cases when the maximum entropy distribution fails to be integrable. We define the relative error as the measure of the difference between the reference moment value $u_{M+1}^{(\text{reference})}$ and the predicted moment u_{closure} obtained by the closure method. It is formulated as

$$e_{\text{rel}}(u_{\text{closure}}) = \left| \frac{u_{\text{closure}} - u_{M+1}^{(\text{reference})}}{u_{M+1}^{(\text{reference})}} \right|.$$

5 Bimodal Distribution

The following superposition of Maxwellian type distribution functions

$$f_{\mathrm{BM}}(c) = f^{(\mathrm{eq})}(\rho_1, v_1, \theta_1, c) + f^{(\mathrm{eq})}(\rho_2, v_2, \theta_2, c),$$

where $f^{(\mathrm{eq})}$represents the equilibrium distribution characterized by densities (ρ_i), velocities (v_i), and temperatures (θ_i) for $i = 1, 2$, is considered as a bimodal test problem. We fix the parameters $\rho_1 = 0.4$, $v_1 = 0$, $\theta_1 = 1 = \theta_2$, $\rho_2 = 0.6$, and using the distribution function f_{BM} we calculate the first M moments for each v_2 value between 0.5 and 4 with step size 0.05. For the maximum entropy closure, the computational domain is taken with $c \in [-4, 6]$ with 1000 grid points. The resulting distributions are shown in Fig. 1. The distribution function for the velocity $v_2 = 0.5$ is actually very close to equilibrium, but it goes into non-equilibrium states as v_2 increases and two peaks slowly begin to form.

The relative error of the next moment is plotted in Fig. 2. As expected, close to equilibrium the relative error of Grad's closure results goes down to zero. Furthermore, around equilibrium, compared to other methods Grad's closure mostly gives better results, yet maximum entropy is also competitive. The disadvantage of Grad's closure is loss of hyperbolicity in non-equilibrium processes, which limits its use even though the relative error may be performing well.

The error curve of the maximum entropy closure shows a strongly nonlinear behavior including singularities where the error actually vanishes. Similar behavior is visible in the other examples below. A general explanation of this behavior is difficult and out of the scope of this paper. Close to equilibrium, for small v_2 the maximum

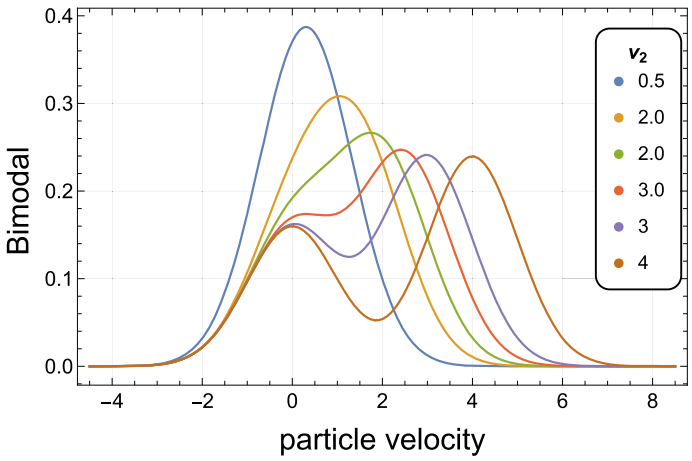

Fig. 1 The bimodal distribution $f_{BM}(c)$ is shown with varying values of v_2, while other parameters are kept fixed

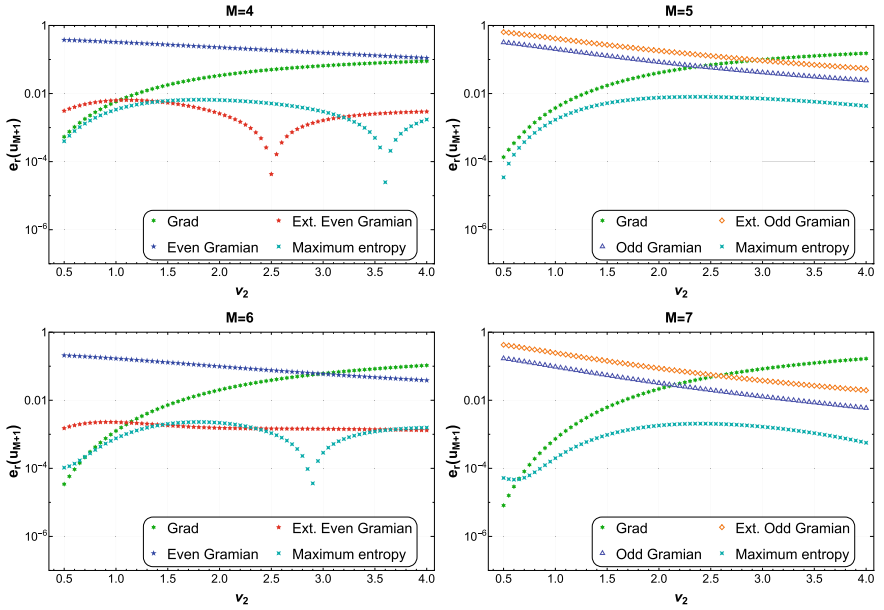

Fig. 2 Relative error $e_r(u_{M+1})$ of the next higher moment for a range velocity shifts in the bimodal test case. The left part of the figure shows the relative error for even number of moments $M = 4, 6$ while the right one shows odd cases $M = 5, 7$. Different plot markers with colors represent the closure. Note, that the Gramian and extended Gramian closure are defined in the even and odd case differently

entropy closure should show vanishing errors. For larger moment orders $M = 6, 7$ the calculation of the maximum entropy distribution becomes significantly more difficult and numerical errors prevent the approximation from becoming better in proximity to equilibrium. Some of the error curves show sharp spikes at different points due to the error briefly passing through zero as parameters change, which is difficult to explain. These rare cases are considered outliers, and the main focus is placed on the overall behavior of the error. However, overall the maximum entropy approach mostly provides better relative errors compared to the other closure methods. For the new closures the extended Gramian closure in the even case performs best, even comparable to maximum entropy. Surprisingly, that closure even mimics the nonlinear behavior of the maximum entropy error. In the even cases, the impact of gauge-invariance between the extended Gramian and simple Gramian closures can be observed. For the odd case, surprisingly, the simple Gramian closure is slightly better than the extended version and it is not clear what causes this. The closures for odd values of M demonstrate relatively large errors, yet still show decay, despite the absence of equilibrium preservation. Although the significant errors in the odd-order case can be attributed to the absence of equilibrium preservation, additional research is required, and this will be explored in future studies. Odd Gramian and extended odd Gramian relative errors are not as good as maximum entropy or Grad close to

equilibrium states, but when two peaks begin to form in the distribution function their relative errors become clearly better than Grad's closure.

6 Conclusion

In this work, we examined the predictive accuracy of various moment closure techniques, namely Grad, maximum entropy, Gramian, and extended Gramian closures, using a highly non-equilibrium bimodal distribution as a benchmark test case. The outcomes of our numerical investigation demonstrate that the extended Gramian closure exhibits performance comparable to the maximum entropy closure, especially in predicting even-order moments. Moreover, unlike maximum entropy methods, Gramian-based closures provide explicit and computationally efficient expressions for the higher-order moments without requiring iterative optimization or function reconstruction. This highlights their potential for scalable implementation in complex flow simulations where computational efficiency and robustness are critical. Future work will explore extensions to multidimensional settings and incorporate realistic collision models to further assess the applicability of these closures in kinetic theory.

References

1. Yilmaz E, Oblapenko G, Torrilhon M (2024) On nonlinear closures for moment equations based on orthogonal polynomials. arXiv preprint, arXiv:2407.05894v2. https://doi.org/10.48550/arXiv.2407.05894
2. Grad H (1949) On the kinetic theory of rarefied gases. Commun Pure Appl Math 2(4):331–407. Wiley Online Library
3. Levermore CD (1997) Entropy-based moment closures for kinetic equations. Transp Theor Statist Phys 26(4–5):591–606
4. Dreyer W (1987) Maximisation of the entropy in non-equilibrium. J Phys A: Math Gener 20(18):6505. https://doi.org/10.1088/0305-4470/20/18/047
5. McGraw R (1997) Description of aerosol dynamics by the quadrature method of moments. Aerosol Sci Technol 27(2):255–265
6. Fox RO, Laurent F (2022) Hyperbolic quadrature method of moments for the one-dimensional kinetic equation. SIAM J Appl Math 82:750–771
7. Kah D, Chalons C, ve Massot M (2010) Beyond pressureless gas dynamics: quadrature-based velocity moment models. Commun Math Sci (submitted)
8. Fox RO (2008) A quadrature-based third-order moment method for dilute gas-particle flows. J Comput Phys 227(12):6313–6350
9. Huang Q, Li S, Yong W-A (2020) Stability analysis of quadrature-based moment methods for kinetic equations. SIAM J Appl Math 80(1):206–231
10. Szegö G (1939) Orthogonal polynomials. AMS, Providence
11. Struchtrup H (2005) Macroscopic transport equations for rarefied gas flows. Springer
12. Torrilhon M (2016) Modeling nonequilibrium gas flow based on moment equations. Ann Rev Fluid Mechan 48:429–458
13. Aheizer N, Krein M (1962) Some questions in the theory of moments. Translations of Mathematical Monographs, American Mathematical Society, vol 2

14. Gautschi W (1996) Orthogonal polynomials: applications and computation. Acta Numerica 5:45–119
15. Hamburger HL (1944) Hermitian transformations of deficiency-index (1,1), Jacobi matrices and undetermined moment problems. Am J Math 66(4):489–522

Open Access This chapter is licensed under the terms of the Creative Commons Attribution 4.0 International License (http://creativecommons.org/licenses/by/4.0/), which permits use, sharing, adaptation, distribution and reproduction in any medium or format, as long as you give appropriate credit to the original author(s) and the source, provide a link to the Creative Commons license and indicate if changes were made.

The images or other third party material in this chapter are included in the chapter's Creative Commons license, unless indicated otherwise in a credit line to the material. If material is not included in the chapter's Creative Commons license and your intended use is not permitted by statutory regulation or exceeds the permitted use, you will need to obtain permission directly from the copyright holder.

Numerical Study of Grad-14 and 17 Moment Equations for Rarefied Polyatomic Gases

Hang Song, Satyvir Singh, and Manuel Torrilhon

Abstract The Grad-type moment equations provide an extended hydrodynamic framework for describing the non-equilibrium behavior of rarefied polyatomic gases beyond the classical Navier-Stokes-Fourier equations. In this study, we present a numerical investigation of Grad-14 and Grad-17 moment equations to analyze their accuracy and applicability in capturing rarefaction effects, translational-rotational energy exchange, and non-equilibrium transport phenomena. The numerical scheme employs a high-order nodal discontinuous Galerkin method to solve the Grad-type equations for rarefied polyatomic flows. The results are compared with solutions from the direct simulation Monte Carlo (DSMC) method and experimental data to assess the predictive capability of the moment approach. Our analysis demonstrates that the Grad formulation offers superior accuracy over the Navier-Stokes-Fourier equations in capturing non-equilibrium phenomena at Mach numbers up to 1.6, particularly under strong velocity/temperature gradient conditions. Nevertheless, persistent non-physical sub-shock formations emerge as a critical limitation at Mach 2.0. Additionally, the study highlights the limitations of moment closure assumptions and their implications for extending higher-order moment theories to polyatomic gases.

Keywords Polyatomic gas · Moment equations · Grad's closure · Shock wave

1 Introduction

Gaseous systems exhibiting non-equilibrium behavior hold critical significance across diverse technical disciplines, particularly when encountered in rarefied environments or under extreme velocity and thermal gradients. Such deviations from thermodynamic equilibrium emerge when molecular velocity distributions substantially depart from Maxwellian statistics, a characteristic feature observed in microscale fluid dynamics and vacuum-based gas transport applications. For polyatomic gas molecules, additional complexities arise from their internal degrees of freedom

H. Song · S. Singh (✉) · M. Torrilhon
Applied and Computational Mathematics, RWTH Aachen University, Aachen, Germany
e-mail: singh@acom.rwth-aachen.de

© The Author(s) 2026

M. Grabe et al. (eds.), *Rarefied Gas Dynamics*, Springer Aerospace Technology,
https://doi.org/10.1007/978-3-032-00094-1_36

including rotational and vibrational excitations, which significantly influence energy redistribution mechanisms and relaxation dynamics during molecular collisions [1].

In non-equilibrium gas flows, the Knudsen number (Kn) is an essential parameter for evaluating the influence of non-equilibrium effects on flow dynamics [2]. This dimensionless quantity is defined as the ratio of the mean free path of gas molecules (λ) to a characteristic length scale (L) of the system: $\mathrm{Kn} = \lambda/L$. Based on the Kn number, gas flows are divided into four regimes: continuum ($\mathrm{Kn} \lesssim 0.001$), slip ($0.001 \lesssim \mathrm{Kn} \lesssim 0.01$), transition ($0.01 \lesssim \mathrm{Kn} \lesssim 10$), and free molecular ($\mathrm{Kn} \gtrsim 10$) [3]. At higher Knudsen numbers, the lack of sufficient particle collisions becomes the primary factor for significant non-equilibrium effects, which are further exacerbated as the Mach number increases. This results in considerable challenges in modeling such gas flows both theoretically and computationally.

The Boltzmann transport equation (BTE) remains fundamental for modeling non-equilibrium gas flows where continuum assumptions fail. It characterizes gas behavior through a velocity distribution function tracking particle motions in space-time. While macroscopic models like the Euler or Navier-Stokes-Fourier (NSF) equations offer computational efficiency in transition regimes, their accuracy diminishes with increasing Knudsen number. Grad's pioneering work introduced moment-based formulations into kinetic theory through Hermite polynomial expansions of the distribution function, subsequently enabling the gas state description via extended variable sets in field equations [4]. This framework extends beyond traditional fluid dynamic variables to systematically incorporate higher-order moments of the distribution function. The Grad-14 (G14) moment equations with a Boltzmann collision operator in the continuous internal energy setting were developed to describe polyatomic gases with temperature-dependent specific heats or thermally perfect (non-polytropic) gases [5]. A macroscopic system of Grad-17 (G17) moment equations and its transport coefficients has been derived through analysis of the BTE based on a continuous internal energy variable for modeling polyatomic gases with constant specific heats [6].

This study investigates non-equilibrium flow simulations of polyatomic gases through the G14 and G17 moment equations, focusing on elucidating complex shock phenomena under low non-equilibrium conditions ($\mathrm{Ma} \leq 2.0$), where both translational and rotational energies are explicitly considered while vibrational energy remains excluded from the analysis. The objective is to evaluate the effect of Grad models when predicting non-equilibrium phenomena in high-speed flows. By analyzing one-dimensional shock structures, the study will validate the Grad models through comparison with DSMC results. The remainder of the paper is structured as follows: Sect. 2 introduces the mathematical formulation for polyatomic gases, including various Grad-type moment equations. Section 3 discusses the employed numerical solver. Section 4 presents numerical results and provides a detailed description of non-equilibrium flow simulations in polyatomic gases. Finally, Sect. 5 gives the concluding remarks and outlook for the future work.

2 Mathematical Formulation

The BTE for polyatomic gases extends the classical kinetic equation to incorporate additional internal energy modes inherent in molecular structures with multiple atoms. Unlike monatomic gases (with purely translational motion), polyatomic systems exhibit rotational and vibrational energy states due to intramolecular configurations. A continuous parameter $I \in \mathbb{R}_+$ is employed, termed "microscopic internal energy", to collectively model non-translational energy states, acting as a lumped descriptor for internal degrees of freedom. The present study exclusively considers rotational energy in the analysis.

The macroscopic state of a rarefied polyatomic gas is statistically characterized by a non-negative distribution function: $f(\mathbf{x}, \mathbf{v}, I, t) \geq 0$, in which spatial coordinates $\mathbf{x} \in \mathbb{R}^3$, molecular velocity $\mathbf{v} \in \mathbb{R}^3$, internal energy $I \in \mathbb{R}_+$, and time$t \in \mathbb{R}_+$. The BTE governs its spatiotemporal evolution as Eq. 1. The bilinear collision operator $R[f]$ acts exclusively on $\mathbf{v}$ and I, preserving conservation laws through its integral structure.

$$\left(\frac{\partial}{\partial t} + \mathbf{v} \cdot \nabla_{\mathbf{x}}\right) f = R[f](\mathbf{v}, I). \tag{1}$$

2.1 Moment Methods

The moment equations governing polyatomic gases originate from the BTE, establishing a system of conservation laws that describe macroscopic quantities and higher-order moments. For polyatomic gases, these conservation relations exhibit increased complexity due to the necessity of incorporating internal degrees of freedom beyond translational motion. In kinetic theory, the moments are mathematically constructed through phase space integration of the distribution function. Specifically, a seris of vaiables are defined: mass density (ρ), flow velocity (u_i), dynamic pressure (p), average pressure ($\overline{p}$), pressure difference ($p_{\text{diff}} = p - \overline{p}$), pressure tensor ($p_{ij}$), stress tensor ($\sigma_{ij}$), translational heat flux (q_i), rotational heat flux (s_i), and total heat flux ($q_i^{\text{tot}} = q_i + s_i$).

$$\begin{pmatrix} \rho \\ \rho u_i \\ p \\ \overline{p} \\ p_{\text{diff}} \\ p_{ij} \\ \sigma_{ij} \\ q_i \\ s_i \\ q_i^{\text{tot}} \end{pmatrix} = \int_{\mathbb{R}^3 \times R_+} \begin{pmatrix} m \\ m v_i \\ \frac{1}{3} m c^2 \\ \frac{2}{\delta+3}\left(\frac{1}{2} m c^2 + I\right) \\ \frac{1}{3} m c^2 - \frac{2}{\delta+3}\left(\frac{1}{2} m c^2 + I\right) \\ m c_i c_j \\ m c_i c_j - \frac{1}{3} m c^2 \delta_{ij} \\ \frac{1}{2} m c^2 c_i \\ I c_i \\ \frac{1}{2} m c^2 c_i + I c_i \end{pmatrix} f \, d\mathbf{v} \, dI, \quad i, j \in \{1, 2, 3\}.$$

Here, $\mathbf{c} = \mathbf{v} - \mathbf{u}$ is the thermal velocity of the gas molecule, and $\delta > 0$ represents the internal degrees of freedom, δ_{ij} is the Kronecker delta. Proceeding with the methodology, the BTE (1) for polyatomic gases is integrated using the moments specified in the list, yielding the fundamental conservation principles for the associated densities. The system can be formulated in the conservative form Eq. (2) as

$$\frac{\partial \mathbf{U}}{\partial t} + \nabla \cdot \mathbf{F}(\mathbf{U}) = \mathbf{S}(\mathbf{U}), \tag{2}$$

where $\mathbf{U}$ represents the vector of conserved quantities, $\mathbf{F}(\mathbf{U})$ denotes the flux tensor, and $\mathbf{S}(\mathbf{U})$ characterizes the source terms.

2.2 Grad-17 Moment Equations

Based on the theory of Grad moment equations, the heat flux of translation energy (q) and rotation energy (s) are analyzed separately in G17 equations. For polyatomic gas, the difference between kinetic pressure (p) and average pressure ($\overline{p}$) cannot be neglected. The equation of kinetic pressure and heat flux are added to the system, the set of primitive variables $W = \{\rho, u_i, \overline{p}, p_{ij}, q_i, s_i\}^{\mathsf{T}}$ is applied. In three-dimensional simulations, this system contains 17 independent variables: ρ (1 scalar), u_i (3 vector components), $\overline{p}$ (1 scalar), p_{ij} (6 independent components of symmetric tensor), q_i (3 vector components), and s_i (3 vector components). G17 equations are shown as Eq. (3) [6].

$$\mathbf{U} = \begin{pmatrix} \rho \\ \rho u_i \\ \rho|u|^2 + (\delta+3)\overline{p} \\ \rho u_i u_j + p_{ij} \\ (\rho|u|^2 + 3p)u_i + 2p_{ij}u_j + 2q_i \\ 2s_i + (\delta+3)\overline{p}u_i - 3pu_i \end{pmatrix},$$

$$\mathbf{F}(\mathbf{U}) = \begin{pmatrix} \rho u_k \\ \rho u_i u_k + p_{ik} \\ (\rho|u|^2 + (\delta+3)\overline{p})u_k + 2p_{jk}u_j + 2q_k + 2s_k \\ \rho u_i u_j u_k + u_i p_{jk} + u_j p_{ki} + u_k p_{ij} + \frac{2}{5}(q_i\delta_{jk} + q_j\delta_{ik} + q_k\delta_{ij}) \\ \quad (\rho|u|^2 + 3p)u_i u_k + 2u_i u_j p_{jk} + 2u_j u_k p_{ij} + |u|^2 p_{ik} + 2u_i q_k + 2u_k q_i \\ \qquad + \frac{4}{5}(u_i q_k + u_k q_i + u_j q_j \delta_{ik}) + 7\frac{\overline{p}}{\rho}p_{ik} - 5\frac{\overline{p}^2}{\rho}\delta_{ik} + 3\frac{\overline{p}}{\rho}p\delta_{ik} \\ \frac{\overline{p}}{\rho}(\delta p_{ik} - \delta p + \delta p\delta_{ik} - 3p\delta_{ik} + 3\overline{p}\delta_{ik}) \\ \qquad + 2u_i s_k + 2u_k s_i + u_i u_k((\delta+3)\overline{p} - 3p) \end{pmatrix}, \tag{3}$$

$$\mathbf{S}(\mathbf{U}) = \begin{pmatrix} 0 \\ 0 \\ 0 \\ -\frac{\overline{p}}{\mu}(p_{ij} - p\delta_{ij}) - \frac{\overline{p}}{\mu_b}\frac{2\delta}{3\delta+9}(p-\overline{p})\delta_{ij} \\ -\frac{\overline{p}}{\mu}(2u_j p_{ij} - 2pu_i) - \frac{\overline{p}}{\mu_b}\frac{2\delta}{3\delta+9}(p-\overline{p})(5u_i) - \frac{\overline{p}}{\mu}(2P_q^{(0)}q_i + 2P_q^{(1)}s_i) \\ -\frac{\overline{p}}{\mu}(2P_s^{(0)}s_i + 2P_s^{(1)}q_i) + \frac{\overline{p}}{\mu_b}\frac{2\delta}{3\delta+9}(p-\overline{p})(3u_i) \end{pmatrix}.$$

The coefficients $P_q^{(0)}$, $P_q^{(1)}$, $P_s^{(0)}$, $P_s^{(1)}$ of source terms depend on the collision model applied in the simulation. Their relationship with Pr number is shown as Eq. (4).

$$\mathrm{Pr} = \frac{\delta + 5}{2} \frac{2(P_q^{(0)} P_s^{(0)} - P_q^{(1)} P_s^{(1)})}{5(P_s^{(0)} - P_s^{(1)}) + \delta(P_q^{(0)} - P_q^{(1)})} \tag{4}$$

In this study, the default values are $P_q^{(0)} = \frac{2}{3}$, $P_s^{(0)} = 1$, $P_q^{(1)} = P_s^{(1)} = 0$ which are obtained through BGK model. The default parameters yield $\delta = 2$ for diatomic gases and $\mathrm{Pr} = 14/19$, demonstrating close agreement with both DSMC simulations and experimental measurements of nitrogen.

2.3 Grad-14 Moment Equations and NSF Equations

It is also possible to avoid using an independent equation of heat flux of rotational energy. However, the difference of average pressure and kinetic pressure is still significant. An additional equation is contained in the system compared with Grad-13 moment equations. The set of primitive variables is $W = \{\rho, u_i, \overline{p}, p_{ij}, q_i^{\mathrm{tot}}\}^T$. The G14 equations are shown in [7]. The mathematical expression for these heat fluxes are then combined into a single equation representing the total energy heat flux.

The NSF equations emerge as a limiting regime of the G14/G17 moment equations under near-equilibrium conditions, achieved through appropriate closure relations. In this framework, the gas resides near thermodynamic equilibrium, resulting in small deviations of higher-order moments (e.g., stress tensor and heat flux) that scale linearly with the gradients of conserved variables (velocity and temperature). For polyatomic gases, the shear stress tensor and heat flux can be respectively expressed as $\tau_{ij} = \mu_b \frac{\partial u_j}{\partial x_j}\delta_{ik} + \mu\left(\frac{\partial u_i}{\partial x_k} + \frac{\partial u_k}{\partial x_i} - \frac{2}{3}\frac{\partial u_j}{\partial x_j}\delta_{ik}\right)$ and $q_i = \lambda \frac{\partial T}{\partial x_i}$.

3 Employed Numerical Solver

The discontinuous Galerkin (DG) method is a variant of the finite element approach, which allows it to efficiently handle complex geometries and irregular meshes [8]. The DG method excels in solving problems with discontinuous solutions, making it particularly well-suited for fluid dynamics and other fields requiring high-precision numerical simulations. The numerical method employed in this research is the nodal DG spectral element method (DGSEM), which is a combination of the DG method and the spectral element method. DGSEM provides higher accuracy, fewer degrees of freedom, and better numerical stability, making it particularly suitable for complex flows and situations requiring high-order solutions. The foundation of this work

is Trixi.jl, a numerical framework centered on conservation laws that incorporates error-based and CFL-based adaptive step size control [9]. The approximation of the function on each element is based on the third-order Lobatto-Legendre basis.

4 Numerical Results and Discussion

The one-dimensional steady shock problem is a fundamental issue in fluid dynamics, involving the steady propagation of a shock wave in one-dimensional flow. In this scenario, the properties of the gas, contains density, pressure, velocity, and temperature, undergo discontinuous changes across the shock, while the shock wave propagates at a constant speed. The left inflow boundary condition and initial state for $x < 0$ are rigorously prescribed to replicate the pre-shock gas properties governed by the Rankine-Hugoniot relations, while the right outflow boundary condition and initial state for $x > 0$ are systematically configured to enforce the post-shock thermodynamic state through strict conservation of Rankine-Hugoniot jump conditions.

In this section, the research gas is nitrogen, of which the rotational energy cannot be ignored. The mean free path of pre-shock region (left side) is 1 mm and the temperature is 273.15K, and the reference values are provided by Bird [10]. Three inflow Mach numbers Ma = 1.2, 1.6, and 2.0 were discussed. Except for the Euler, NSF, G14 and G17 equations, the particle method DSMC is also applied to verify the effect. Two popular collision models of DSMC, the variable hard sphere (VHS) and the variable soft sphere (VSS) are employed in the validation.

As shown in Fig. 1, the G14 and G17 equations provide a more accurate description of density, velocity, and average pressure compared to the NSF equations at inflow Ma $= 1.2, 1.6$. Nonlinear processes become more significant as Mach number of inflow increasing, causing the constitutive relations between fluxes and spatial derivatives to break down. It is evident that the NSF equations deviate more from the DSMC results in the regions $-8 < x/\lambda < -6$ and $2 < x/\lambda < 4$ compared to the G14 and G17 equations at inflow Ma $= 1.6$. For Ma $= 2.0$, a small sub-shock appears near the pre-shock region ($x/\lambda \approx -5$) because of the symmetric hyperbolicity, leading to inaccuracies in the G14 and G17 equation simulations. The largest deviation of propagation speeds of G14 and G17 equations from bulk velocity are $2.032\sqrt{p/\rho}$ and $2.130\sqrt{p/\rho}$, which are 1.72 and 1.8 times that of the sound speed of polyatomic gas [11]. Mathematically, the polyatomic gas flow at Ma > 1.8 cannot be simulated accurately through G14 and G17 equations. The discrepancies between the NSF equations and DSMC are also significant, highlighting that the strong non-equilibrium effects caused by inflow at Ma > 2.0 cannot be precisely captured by either the NSF equations or the Grad moment equations.

In Fig. 2, both the G14 and G17 equations demonstrate good agreement with the DSMC results regarding pressure difference and stress at Mach numbers of 1.2 and 1.6, whereas the NSF equations are inadequate. This discrepancy arises because, when the high-speed airflow passes through a shock wave, the molecular translational energy increases rapidly, leading to a sharp rise in kinetic pressure.

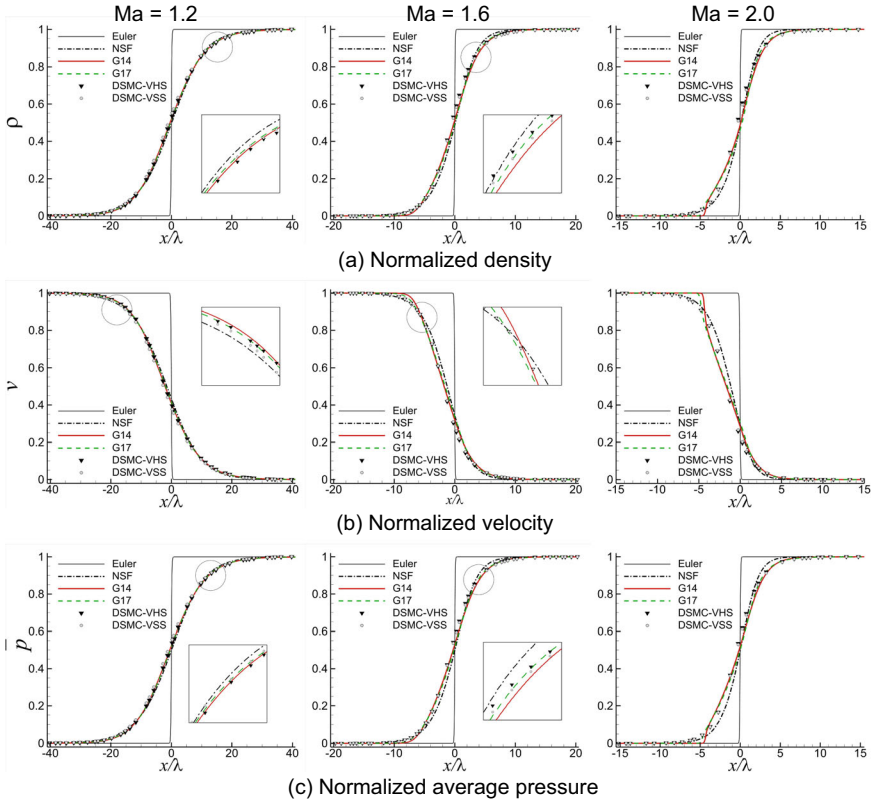

Fig. 1 1D shock structure problem: profiles of normalized density (ρ), normalized velocity (v), normalized average pressure ($\overline{p}$) at Ma = 1.2, 1.6 and 2.0

However, the response of rotational energy is slower, resulting in a difference between kinetic pressure (p) and average pressure ($\overline{p}$). Except for the region of sub-shock at Ma $= 2.0$, the agreements are also acceptable. The simulations of heat flux by both Grad moment equations and the NSF equations are not ideal at Ma $= 1.6, 2.0$, which means the calculation of third-order terms are not satisfactory. It is necessary to adjust the coefficients in the source terms of G17 equations to quantify model-form errors and establish baseline performance before pursuing more complex moment system extensions. This parametric study will inform the development of higher-order Grad models while maintaining computational tractability, which will be addressed in subsequent research.

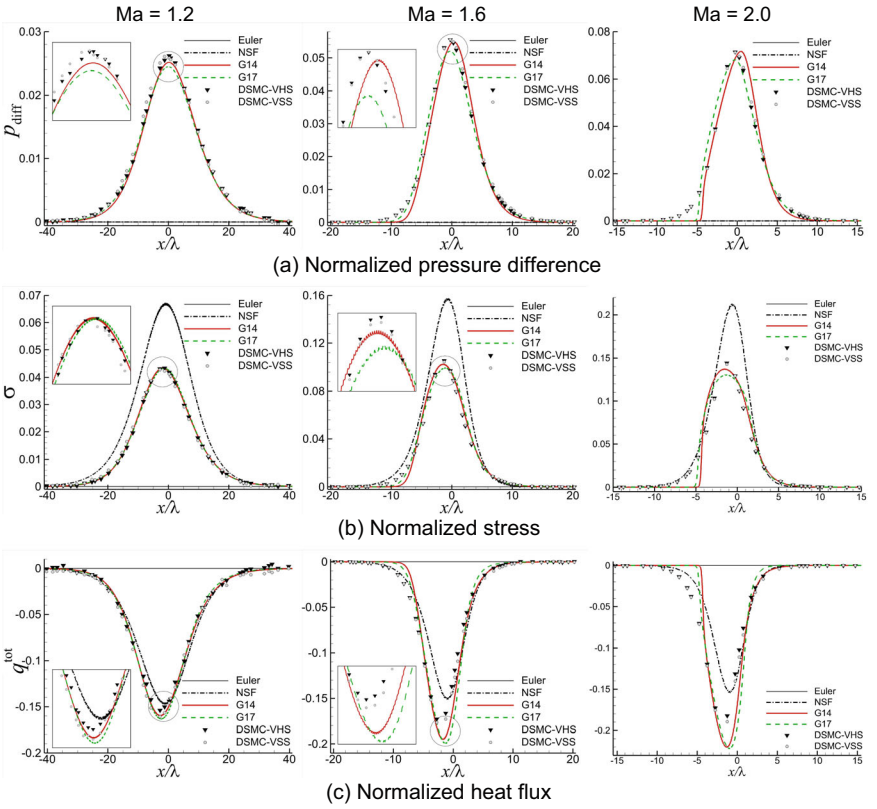

Fig. 2 1D shock structure problem: profiles of normalized pressure difference (p_{diff}), normalized stress (σ), normalized heat flux of total energy (q^{tot}) at Ma = 1.2, 1.6 and 2.0

5 Conclusion

In this research, the non-equilibrium processes are simulated using polyatomic G14 and G17 moment equations through a one-dimensional shock wave. A solver based on the DGSEM is employed, forming the foundation for high-order Grad moment equations and regularized equation systems. It was found that the Grad models, particularly the G17 model, offer superior accuracy in predicting non-equilibrium effects compared to traditional Euler and NSF models. These results were validated through comparisons with DSMC data, highlighting the Grad models' ability to resolve shock thickness, stress, and heat flux in high-speed flows, where non-equilibrium phenomena are significant. Nevertheless, the persistence of hyperbolicity-induced sub-shocks remains an unresolved challenge in the current framework, necessitating the systematic investigation through regularization techniques in forthcoming research initiatives.

References

1. Vincenti WG, Kruger CH, Teichmann T (1966) Introduction to physical gas dynamics. Phys Today 19(10):95
2. Struchtrup H (2005) Macroscopic transport equations for rarefied gas flows. In: Macroscopic transport equations for rarefied gas flows. Interaction of mechanics and mathematics. Springer, Berlin, pp 159–186
3. Torrilhon M (2016) Modeling nonequilibrium gas flow based on moment equations. Ann Rev Fluid Mechan 48(1):429–458
4. Grad H (1952) The profile of a steady plane shock wave. Commun Pure Appl Math 5:257
5. Pavi'c-Čoli'c M, Simi'c S (2022) Kinetic description of polyatomic gases with temperature-dependent specific heats. Phys Rev Fluids 7:083401
6. Djordji'c V, Oblapenko G, Pavi'c-Čoli'c M, Torrilhon M (2023) Boltzmann collision operator for polyatomic gases in agreement with experimental data and DSMC method. Continuum Mech Thermodyn 35:103–119
7. Pavić-Čolić M, Simić S (2014) Moment equations for polyatomic gases. Acta Appl Math 132:469–482
8. Singh S, Karchani A, Myong RS (2022) A three-dimensional modal discontinuous Galerkin method for the second-order Boltzmann-Curtiss-based constitutive model of rarefied and microscale gas flows. J Comput Phys 457:111052
9. Schlottke-Lakemper M et al (2021) A purely hyperbolic discontinuous Galerkin approach for self-gravitating gas dynamics. J Comput Phys 442:110467
10. Bird G (1970) Direct simulation and the Boltzmann equation. Phys Fluids 13:2676–2681
11. Song H, Singh S, Torrilhon M (2025) Non-equilibrium flow simulations based on Grad-14 and Grad-17 moment equations for polytropic gases. Phys Fluids 37(3)

Open Access This chapter is licensed under the terms of the Creative Commons Attribution 4.0 International License (http://creativecommons.org/licenses/by/4.0/), which permits use, sharing, adaptation, distribution and reproduction in any medium or format, as long as you give appropriate credit to the original author(s) and the source, provide a link to the Creative Commons license and indicate if changes were made.

The images or other third party material in this chapter are included in the chapter's Creative Commons license, unless indicated otherwise in a credit line to the material. If material is not included in the chapter's Creative Commons license and your intended use is not permitted by statutory regulation or exceeds the permitted use, you will need to obtain permission directly from the copyright holder.

Numerical Methods for Kinetic Equations

Adaptation of the Unified Gas-Kinetic Scheme to ES-BGK Models

Céline Baranger, Alexis Coëpeau, and Luc Mieussens

Abstract The Unified Gas-Kinetic Scheme stands out from traditional deterministic numerical approaches to gas dynamics by enabling the resolution of flow regimes ranging from rarefied to continuum, within a simulation time independent of the regime. Its effectiveness in solving complex flows has primarily been demonstrated with Shakhov or Rykov models. Here, we propose to examine in detail the applicability of UGKS to ES-BGK models, extending its application from the monoatomic framework to the polyatomic framework by using recent ES-BGK models that take into account rotational and vibrational energy modes.

Keywords Gas dynamics · UGKS · ES-BGK models

1 Introduction

The Ellipsoidal-Statistical BGK (ES-BGK) model [5] is an alternative modelling of the Boltzmann equation, developed to enable faster numerical simulations of transport phenomena within a monoatomic gas in a transitional state between rarefied and continuous regimes. This model retains the same fundamental properties as the Boltzmann equation since it ensures the positivity of the mass distribution, has the same collisions invariants, satisfies the H-Theorem [1], and is able to recover a Prandtl number of 2/3 for monoatomic gases. It has also been extended to polyatomic gases [1] and has undergone various modifications, such as capturing rotational and vibrational energy relaxation processes [4, 7].

For a long time, these kinetic models were only solved numerically using methods that were extremely time-consuming as the density of the resolved flow increased. However, since 2010, Kun Xu et al. have been developing a unified method known

C. Baranger · A. Coëpeau
CEA-CESTA, Le Barp Cedex, France

A. Coëpeau (✉) · L. Mieussens
University of Bordeaux, CNRS, Bordeaux INP, IMB, Talence, France
e-mail: alexis.coepeau@u-bordeaux.fr

© The Author(s) 2026

M. Grabe et al. (eds.), *Rarefied Gas Dynamics*, Springer Aerospace Technology,
https://doi.org/10.1007/978-3-032-00094-1_37

as the "Unified Gas-Kinetic Scheme" [10]. This singular method allows the accurate resolution of all ranges of flows with a computational cost independent of the rarefaction of the gas.

The UGKS scheme has only been applied to the monoatomic ES-BGK model [3, 6]. Here, we propose to extend it to phenomena typical of diatomic models, such as internal energy storage, as described by Andriès et al. [1].

2 The Ellipsoidal-Statistical BGK Model for Polyatomic Gases

To describe the dynamics of a polyatomic gas, it is customary to use a microscopic distribution of mass F defined over the phase space $(t, \mathbf{x}, \mathbf{v}, I) \in \mathbb{R}^+ \times \mathbb{R}^3 \times \mathbb{R}^3 \times \mathbb{R}^+$ such that, at any time $t \in \mathbb{R}^+$, $F(t, \mathbf{x}, \mathbf{v}, I)\, d\mathbf{x}\, d\mathbf{v} dI$ represents the mass of gas in the volume $d\mathbf{x}\, d\mathbf{v} dI$ centred at the spatial point $\mathbf{x}$, the particle velocity $\mathbf{v}$ and the internal energy $\epsilon(I) = I^{2/\delta}$. The number of internal degrees of freedom δ is typically set to 2 for diatomic molecules at sufficiently low temperature to enable only the rotational mode of energy.

The densities of mass ρ, momentum $\rho\mathbf{u}$ (where $\mathbf{u}$ is the macroscopic flow velocity), and total energy E, which are macroscopic quantities depending on space and time only, are recovered as velocity and internal energy moments of the microscopic distribution:

$$\rho = \langle\langle F \rangle\rangle, \quad \rho\mathbf{u} = \langle\langle \mathbf{v} F \rangle\rangle, \quad E = \left\langle\left\langle \frac{1}{2}|\mathbf{v}|^2 F + \epsilon(I) F \right\rangle\right\rangle, \tag{1}$$

with $\langle\langle \phi \rangle\rangle = \int_{\mathbb{R}^3} \int_{\mathbb{R}^+} \phi dI d\mathbf{v}$ for any distribution $\phi(\mathbf{v}, I)$. We also define for further needs: $\langle \psi \rangle = \int_{\mathbb{R}^3} \psi d\mathbf{v}$ for any distribution $\psi(\mathbf{v})$. Moreover, additional quantities, such as the modal temperatures, can be derived as follows:

$$E_c = \frac{1}{2}\rho|\mathbf{u}|^2, \quad E_{tr} = \frac{3}{2}\rho R_s T_{tr}, \quad E_{int} = \frac{\delta}{2}\rho R_s T_{int}\ . \tag{2}$$

In these expressions, R_s is the specific constant of the gas. The subscripts tr and int refer to the translational and internal modes of energy. Finally, T_{eq} is the equilibrium temperature associated with both translational and internal modes.

The distribution F is governed by the following equation [1]:

$$\partial_t F + \mathbf{v} \cdot \nabla_{\mathbf{x}} F = \frac{1}{\tau}(G[F] - F), \tag{3}$$

where the anisotropic equilibrium state G is defined as the product of G_{tr} and G_{int}, expressed as follows:

$$G_{\mathrm{tr}}(\mathbf{v}) = \frac{\rho}{\sqrt{\det(2\pi\,\mathsf{T})}} \exp\left(-\frac{1}{2}(\mathbf{v}-\mathbf{u})\cdot\mathsf{T}^{-1}\cdot(\mathbf{v}-\mathbf{u})\right), \tag{4}$$

$$G_{\mathrm{int}}(I) = \frac{\Lambda_\delta}{(R_{\mathrm{s}}T_{\mathrm{int}}^{\mathrm{rel}})^{\delta/2}} \exp\left(-\frac{\epsilon(I)}{R_{\mathrm{s}}T_{\mathrm{int}}^{\mathrm{rel}}}\right) . \tag{5}$$

Here, $\Lambda_\delta^{-1} = \int_{\mathbb{R}^+} e^{-\epsilon(I)} dI$ is constant and $T_{\mathrm{int}}^{\mathrm{rel}}$ is the relaxation internal temperature. The relaxation temperature tensor $\mathsf{T}/R_{\mathrm{s}}$ is related to the anisotropic tensor of temperature Θ/R_{s}, and the relaxation translational temperature $T_{\mathrm{tr}}^{\mathrm{rel}}$ by the following expressions:

$$\begin{aligned}
\mathsf{T} &= R_{\mathrm{s}}T_{\mathrm{tr}}^{\mathrm{rel}} + \left(1-\frac{1}{\mathrm{Pr}}\right)[\Theta - R_{\mathrm{s}}T_{\mathrm{tr}}],\\
\Theta &= \frac{1}{\rho}\langle\langle(\mathbf{v}-\mathbf{u})\otimes(\mathbf{v}-\mathbf{u})F\rangle\rangle,\\
T_{\mathrm{tr}}^{\mathrm{rel}} &= T_{\mathrm{tr}} + \frac{1}{Z_{\mathrm{int}}}(T_{\mathrm{eq}}-T_{\mathrm{tr}}), \quad T_{\mathrm{int}}^{\mathrm{rel}} = T_{\mathrm{int}} + \frac{1}{Z_{\mathrm{int}}}(T_{\mathrm{eq}}-T_{\mathrm{int}}) .
\end{aligned}$$

In these relations, Pr denotes the Prandtl number, and Z_{int} corresponds to the average number of collisions required to realise an energy exchange between equilibrium and internal modes. Finally, the characteristic relaxation time τ is related to the fluid viscosity μ and the pressure $p = \rho R_{\mathrm{s}}T_{\mathrm{tr}}$ by $\tau = \frac{\mu}{\mathrm{Pr}\,p}$.

With parameters $2/3 \leq \mathrm{Pr}$ and $1 < Z_{\mathrm{int}}$, this model has been proven in [1] to conserve mass, momentum, and total energy, satisfy the H-theorem, give the correct Prandtl number, and admit the Maxwell-Boltzmann distribution $M(\mathbf{v}, I)$ below as full equilibrium:

$$M(\mathbf{v}, I) = \frac{\rho}{(2\pi R_{\mathrm{s}}T_{\mathrm{eq}})^{3/2}} \exp\left(-\frac{|\mathbf{v}-\mathbf{u}|^2}{2R_{\mathrm{s}}T_{\mathrm{eq}}}\right) \frac{\Lambda_\delta}{(R_{\mathrm{s}}T_{\mathrm{eq}})^{\delta/2}} \exp\left(-\frac{\epsilon(I)}{R_{\mathrm{s}}T_{\mathrm{eq}}}\right) . \tag{6}$$

3 The Unified-Gas Kinetic Scheme (UGKS)

The numerical method will be presented in a 1D spatial framework for simplicity, although it can be extended to 2D or 3D. We begin by outlining the framework before constructing the UGKS for the ES-BGK model introduced by [1].

3.1 A Discrete-Velocity-Model Finite-Volume Framework

The ES-BGK model is an integro-differential equation expressed in a advection-relaxation form, which makes the finite volume framework intrinsically well suited.

In this context, all phases of the equation will be discretised. In that sense, the time space $\mathbb{R}^+$ and the physical space $\mathbb{R}$ are divided into intervals $([t^n, t^{n+1}])_{n\in\mathbb{N}}$ and $([x_{i-\frac{1}{2}}, x_{i+\frac{1}{2}}])_{i\in\mathbb{Z}}$, respectively. For simplicity, the spatial interval length will be constant, denoted as $\Delta x = x_{i+\frac{1}{2}} - x_{i-\frac{1}{2}}$. Finally, following the methodology of Discrete Velocity Models (DVM), we consider a finite velocity set $\mathcal{V} \subset \mathbb{R}^3$ and a quadrature rule $\langle\rangle_{\mathcal{V}}$ that enables the computation of the moments of the set of microscopic distributions.

We introduce the distribution families $(F^n_{i,k}(\cdot))_{n\in\mathbb{N},i\in\mathbb{Z},k\leq|\mathcal{V}|}$ and $(G^n_{i,k}(\cdot))_{n\in\mathbb{N},i\in\mathbb{Z},k\leq|\mathcal{V}|}$ defined as the mean value of F and G on a spatial cell $[x_{i-\frac{1}{2}}, x_{i+\frac{1}{2}}]$ at time t^n, and velocity near $\mathbf{v}_k$. All of these considerations lead to the classical finite volume formulation:

$$F^{n+1}_{i,k}(I) - F^n_{i,k}(I) = -\frac{\Delta t}{\Delta x}\left[\phi^n_{i+\frac{1}{2},k} - \phi^n_{i-\frac{1}{2},k}\right](I) + \int_{t^n}^{t^{n+1}}\int_{x_{i-\frac{1}{2}}}^{x_{i+\frac{1}{2}}} \frac{G-F}{\tau}(t, x, \mathbf{v}_k, I)dxdt, \tag{7}$$

$$\phi^n_{i+\frac{1}{2},k}(I) = \frac{1}{\Delta t}\int_{t^n}^{t^{n+1}} \mathbf{v}_k F(t, x_{i+\frac{1}{2}}, \mathbf{v}_k, I)dt\ . \tag{8}$$

Finally, for further needs, we also introduce the moments $(\mathbf{W}^n_i)_{n\in\mathbb{N},i\in\mathbb{Z}}$ of $(F^n_{i,k}(\cdot))_{n\in\mathbb{N},i\in\mathbb{Z},k\leq|\mathcal{V}|}$, where $\langle\langle\cdot\rangle\rangle_{\mathcal{V}}$ combines a continuous integration over the internal energy phase and the chosen quadrature rule on the velocity phase:

$$\mathbf{W}^n_i = \left\langle\left\langle \mathbf{m}_k(I)F^n_{i,k}(I)\right\rangle\right\rangle_{\mathcal{V}}, \quad \mathbf{m}_k(I) = (1\ \ \mathbf{v}_k\ \ \mathbf{v}_k\otimes\mathbf{v}_k\ \ \epsilon(I))^T\ . \tag{9}$$

3.2 The Construction of the UGKS

A Second Order Multi-scale Formulation of the Flux Part of the Numerical Scheme The key idea of the UGKS [10] is to use the characteristics method on the entire model Eq. (3) to express the evolution of the distribution F at cell interface position. Assuming τ is constant over $[t^n, t]$, we get:

$$F(t, \mathbf{x}_{i+\frac{1}{2}}, \mathbf{v}_k, I) = \exp\left(-\frac{t-t^n}{\tau}\right)F(t^n, \mathbf{x}_{i+\frac{1}{2}} - \mathbf{v}_k(t-t^n), \mathbf{v}_k, I) + \int_{t^n}^{t}\exp\left(-\frac{t-s}{\tau}\right)\frac{1}{\tau}G(s, \mathbf{x}_{i+\frac{1}{2}} - \mathbf{v}_k(t-s), \mathbf{v}_k, I)ds\ . \tag{10}$$

For accuracy, the continuous distributions F and G are approximated using linear reconstructions based on discretised distributions $(F^n_{i,k}(\cdot))$ and $(G^n_{i,k}(\cdot))$. Classically [10], reconstructions for F and G are performed at each cell interface involving

discrete approximations of partial derivatives $\overline{\partial_x F}$, $\overline{G}$, $\overline{\partial_x G}$, and $\overline{\partial_t G}$. The construction of $\overline{\partial_x F}$, moments $\mathbf{W}^n_{i+\frac{1}{2}}$, and the term $\overline{G}$ is standard [10].

A Major Replacement in the Discrete Derivative Terms The key idea employed here to ensure the proper behaviour of the scheme is to replace the Gaussian derivatives with those of the corresponding Maxwellian distribution.

First, note that the derivatives of G and M are close to within a error of the order of τ. This is a classical result from Chapman-Enskog analysis (see, e.g., [1]). Thus, for a large time step $\Delta t \gg \tau$, the average time derivative of G closely matches that of M, with an error depending on $\tau \ll \Delta t$.

Second, the discrete time derivative contribution in the numerical fluxes is mainly important in the continuum regime. An approximation of $O(\tau)$ on the derivative of equilibrium would not break down the Navier-Stokes asymptotic since it is a convenient replacement in the Chapmann-Enskog expansion.

The last and deeper reason is stability. In the continuum regime, numerical fluxes achieve a second-order time scheme by approximating indirectly the equilibrium at $t^n + \Delta t/2$. This approach resembles a forward Euler method based on the time derivative at t^n. However, since the relaxation time of the Gaussian state G toward the Maxwellian M scales with τ, using a time step $\Delta t/2 \gg \tau$ may over-relax G, potentially leading to negative distribution values

Finally, this approach was used for the monoatomic ES-BGK model in [3] and for the Shakhov model in [11]. Since the terms $\overline{\partial_x M}$ an $\overline{\partial_t M}$ are classic in the UGKS framework [10], their constructions are not presented here.

Conclusion on the Flux Part of the Scheme Injecting the reconstructions in the numerical flux definition (8) leads to expression of the numerical flux ϕ :

$$\begin{aligned}\phi^n_{i+\frac{1}{2},k}(I) = q_1 \overline{G}^n_{i+\frac{1}{2},k}(I) + q_2 v_{kx} \overline{\partial_x M}^n_{i+\frac{1}{2},k}(I) + q_3 \overline{\partial_t M}^n_{i+\frac{1}{2},k}(I) \\ + q_4 \overline{F}^n_{i+\frac{1}{2},k}(I) + q_5 v_{kx} \overline{\partial_x F}^n_{i+\frac{1}{2},k}(I) \,. \end{aligned} \tag{11}$$

The coefficients $(q_i)_{1\le i\le 5}$ determine the behaviour of the scheme and depend locally on Δt and $\tau^n_{i+\frac{1}{2}}$ [10].

Relaxation Part of the Scheme A Crank-Nicolson based approximation is used for the relaxation part [10]. The numerical scheme is therefore:

$$\begin{aligned} F^{n+1}_{i,k}(I) = F^n_{i,k}(I) - \frac{\Delta t}{\Delta x}\left[\phi^n_{i+\frac{1}{2},k} - \phi^n_{i-\frac{1}{2},k}\right](I) \\ + \frac{\Delta t}{2}\left[\left(\frac{G-F}{\tau}\right)^n_{i,k} + \left(\frac{G-F}{\tau}\right)^{n+1}_{i,k}\right](I) \,. \end{aligned} \tag{12}$$

Classically, the equilibrium state at time t^{n+1} is computed based on the moments of F, which are obtained from the moments of the microscopic scheme (12) [6, 10].

This accurate technique could lead to a non-symmetric positive-definite tensor Θ and could compromise the calculation of an equilibrium G^{n+1}. This is why we instead use a backward Euler relaxation term for the macroscopic scheme:

$$\mathbf{W}_i^{n+1} = \mathbf{W}_i^n - \frac{\Delta t}{\Delta x}\left[\mathbf{\Phi}^n_{i+\frac{1}{2}} - \mathbf{\Phi}^n_{i-\frac{1}{2}}\right] + \Delta t \left(\frac{\mathbf{V}-\mathbf{W}}{\tau}\right)_i^{n+1}, \tag{13}$$

$$\mathbf{\Phi} = \langle\langle \mathbf{m}\phi\rangle\rangle_{\mathcal{V}}, \quad \mathbf{V} = \langle\langle \mathbf{m}G\rangle\rangle_{\mathcal{V}}\ . \tag{14}$$

4 Numerical Results

To assess the effectiveness of incorporating the collision process into the characteristic method (10) used to define numerical fluxes, we introduce the KO2 scheme, which is formulated without these relaxation effects. This scheme is obtained from (11) by fixing $q_{1,2,3}$ to 0, and q_4 and q_5 to 1 and $-\Delta t/2$, respectively.

For faster simulations, these numerical schemes are combined with the reduced distribution technique: by integrating with respect to the energy variable I as well as the velocity components v_z and/or v_y in 1D and 2D problems, it permits to reduce the computational cost, without any approximation (see [1]).

4.1 Couette Flow

In the Couette configuration, the gas flows between two parallel, isothermal, infinite plates separated by a distance L. One plate is stationary, while the other moves with a finite velocity u_w in the y-direction. Under the continuum approximation, with no slip boundary conditions, the compressible Navier-Stokes-Fourier equations (CNS) yield to:

$$u_y(x) = \frac{x}{L}u_\mathrm{w}, \quad T(x) = T_\mathrm{w} + \frac{1}{2}\frac{\mathrm{Pr}}{c_\mathrm{p}}\frac{x(L-x)}{L^2}u_\mathrm{w}^2, \quad p(x) = cst\ . \tag{15}$$

The Knudsen number of the flow is here defined as: $\mathrm{Kn} = \lambda/L$, where λ is the mean free path, that can be defined as $\lambda = \tau v_\mathrm{th}$ at the boundary, where $v_\mathrm{th} = \sqrt{R_\mathrm{s}T_\mathrm{w}}$ is the thermal velocity at the wall temperature T_w. Simulations are conducted in near continuum regime, at different Knudsen numbers by varying the initial mass density of the flow.

The parameters defining the gas are taken constant as follows: the specific constant R_s is $296.8\,\mathrm{J\,kg^{-1}\,K^{-1}}$, the viscosity μ is $1.656\times10^{-5}\,\mathrm{Pa\,s}$, the Prandtl number Pr is 0.71, the degree of freedom number δ is 2.0, and the average number Z_int is set

to 5.0. Furthermore, the boundary walls are separated by a distance $L = 1\,\mathrm{m}$, are maintained at 273 K and the wall velocity u_w is set to $300\,\mathrm{m\,s^{-1}}$.

The spatial domain is discretised exclusively in the x-direction using 25 uniform cells. The velocity grid is Cartesian, defined over the range $[\pm 1200] \times [-1200, +1500]\,\mathrm{m\,s^{-1}}$, with 50 velocity points in both the x- and y-directions.

Figure 1 presents comparisons of the UGKS and KO2 schemes with the CNS solutions at different Knudsen numbers. Simulations with the KO2 scheme and a finer mesh have been conducted to highlight the deviation of the CNS solution from the rarefied flow solutions caused by the boundary conditions.

First, Fig. 1 illustrates that both UGKS and KO2 can capture near-continuum flows. However, UGKS achieves higher accuracy on a same mesh, while KO2 requires a significantly finer mesh to match UGKS accuracy. Additionally, as the Knudsen number decreases, predictions deviate only for KO2.

Second, using the temperature Eq. (15), the Prandtl number can be roughly evaluated through a parabolic regression using the least squares method. The estimations on Fig. 1 shows the excellent capability of UGKS to simulate a correct Prandtl number for a given mesh, compared to the KO2 scheme.

4.2 Flow Passing a Flat Plate

This second case reproduces the experiment conducted by [8], where a flat plate is immersed in a supersonic near-continuum nitrogen cold flow. The internal energy of the gas is entirely associated with the rotational mode. Therefore, the ES-BGK model from [1] with parameter $\delta = 2$ is appropriate.

The gas is modelled according to the VSS model, with parameters taken from [2]. The spatial domain is meshed using a 2D structured mesh all around the plate. The velocity grid is bounded within $[-1200, 2200] \times [-1700, 1500]\,\mathrm{m\,s^{-1}}$ and discretised with 25 points in both x- and y-directions.

Comparisons between the simulation and experimental measurements of rotational temperature, taken at 5 and 20 mm from the stagnation point on vertical lines, are presented in Fig. 2. The shapes of the rotational temperature are well reproduced, although some discrepancies arise due to uncertainties in modelling the real relaxation processes involved. To align the relaxation processes used by Bird [2] or Mathiaud et al. [7], a simple adjustment of Z_{int} can be achieved as $Z'_{\mathrm{int}} = \tau_C Z_{\mathrm{int}}/\tau$ or $Z''_{\mathrm{int}} = \frac{3}{5}\tau_C Z_{\mathrm{int}}/\tau$, respectively, where τ_C is the mean collision time defined in the VSS model [2]. These modifications significantly influence the profiles of rotational temperature, as illustrated in Fig. 2, even though the results are in a general good agreement with the experimental measurements.

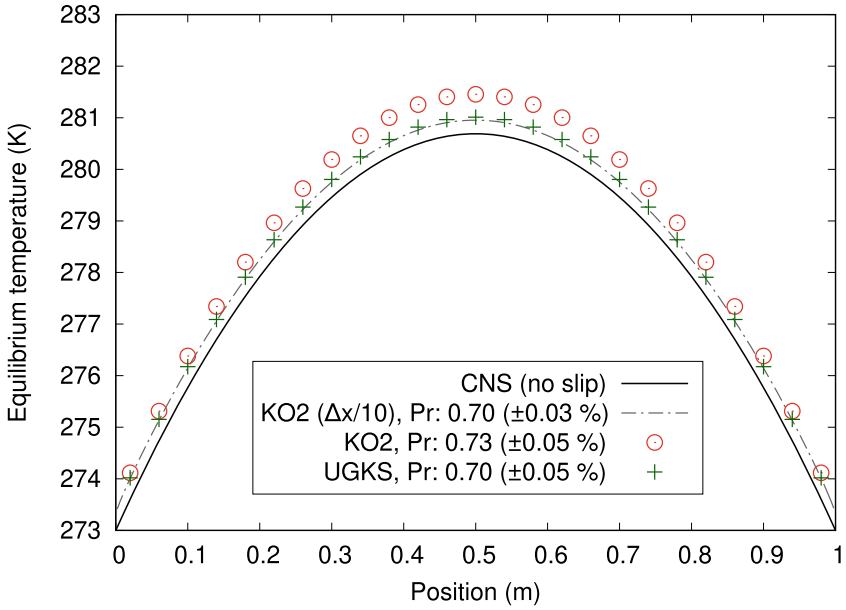

(a) $Kn = 9.0 \times 10^{-3}$,

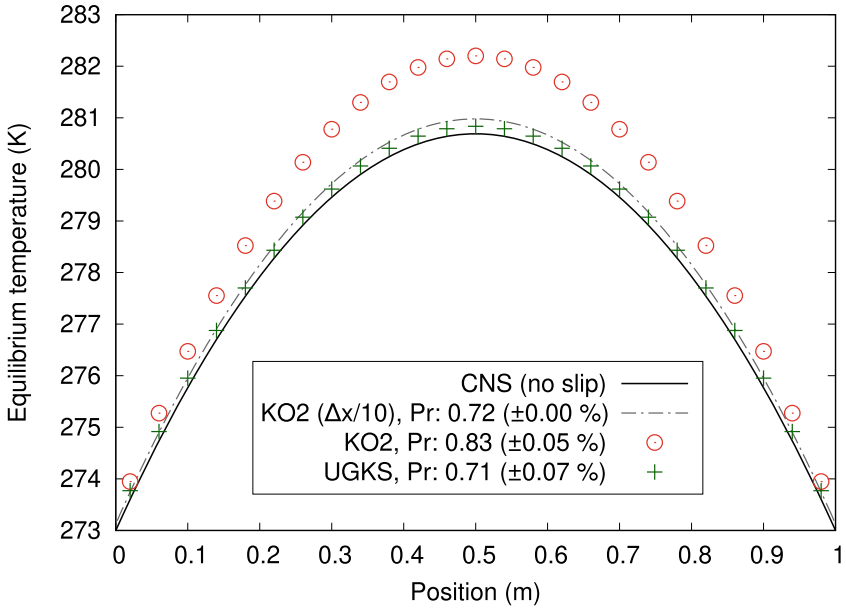

(b) $Kn = 2.2 \times 10^{-3}$,

Fig. 1 Comparison of UGKS and KO2 schemes with CNS solution in 1D Couette flow

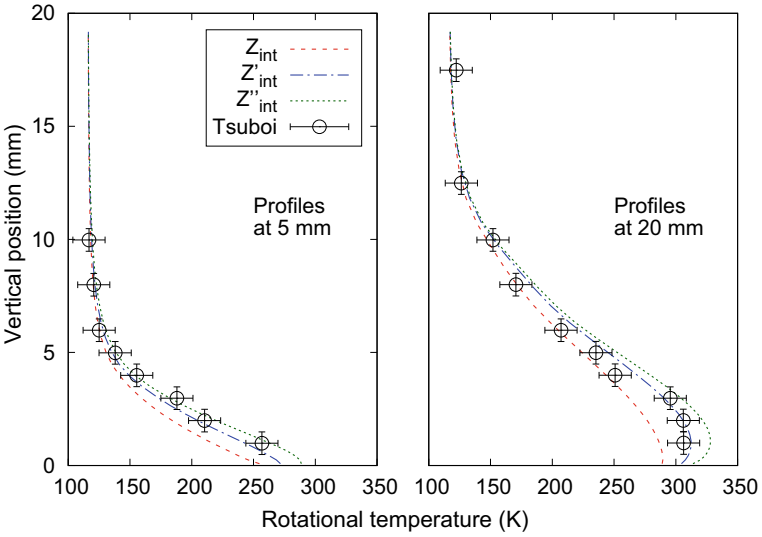

Fig. 2 Comparison of rotational temperature predictions between ES-BGK models at 5 and 20 mm after the stagnation point (*Diffuse wall reflection*)

5 Conclusion

We proposed an extension of the Unified Gas-Kinetic Scheme (UGKS) to an ES-BGK model that accounts for internal energy modes. This adaptation extends the UGKS-ES-BGK framework from monoatomic to diatomic gases using techniques similar to those applied in extending UGKS-BGK to Shakhov and Rykov models. The method shows good agreements both for a 1D viscous-driven flow and an experimental 2D hypersonic flow. Consequently, future work will address the incorporation of vibrational effects within the framework of ES-BGK models.

References

1. Andriès P, Le Tallec P, Perlat J-P, Perthame B (2000) The Gaussian-BGK model of Boltzmann equation with small Prandtl number. Eur J Mechan B/Fluids 19(6):813–830
2. Bird GA (1994) Molecular gas dynamics and the direct simulation of gas flows. Oxford Science Publications, Oxford
3. Chen S, Xu K, Cai Q (2015) A comparison and unification of ellipsoidal statistical and Shakhov BGK models. Adv Appl Math Mechan 7(2):245–266
4. Dauvois Y, Mathiaud J, Mieussens L (2021) An ES-BGK model for polyatomic gases in rotational and vibrational nonequilibrium. Eur J Mechan B/Fluids 88:1–16
5. Holway LH (1965) Kinetic theory of shock structure using an ellipsoidal distribution function. Rarefied Gas Dyn 1:193–215

6. Liu S, Zhong C (2014) Investigation of the kinetic model equations. Phys Rev E 89(3):033306–033322
7. Mathiaud J, Mieussens L, Pfeiffer M (2022) An ES-BGK model for diatomic gases with correct relaxation rates for internal energies. Eur J Mechan B/Fluids 96:65–77
8. Tsuboi N, Matsumoto Y (2005) Experimental and numerical study of hypersonic rarefied gas flow over flat plates. AIAA J 43(6):1243–1255
9. Xu K (2021) A Unified Computational Fluid Dynamics Framework from Rarefied to Continuum Regimes. Cambridge University Press, Cambridge
10. Xu K, Huang J-C (2010) A unified gas-kinetic scheme for continuum and rarefied flows. J Comput Phys 229(20):7747–7764
11. Xu K, Huang J-C (2011) An improved unified gas-kinetic scheme and the study of shock structures. IMA J Appl Math 76(5):698–711

Open Access This chapter is licensed under the terms of the Creative Commons Attribution 4.0 International License (http://creativecommons.org/licenses/by/4.0/), which permits use, sharing, adaptation, distribution and reproduction in any medium or format, as long as you give appropriate credit to the original author(s) and the source, provide a link to the Creative Commons license and indicate if changes were made.

The images or other third party material in this chapter are included in the chapter's Creative Commons license, unless indicated otherwise in a credit line to the material. If material is not included in the chapter's Creative Commons license and your intended use is not permitted by statutory regulation or exceeds the permitted use, you will need to obtain permission directly from the copyright holder.

Spatially-Parallel Collision Scheme for Implementing Direct Simulation Monte Carlo in Field-Programmable Gate Arrays

Saleen Bhattarai, Sean O' Byrne, Edwin Peters, and David Petty

Abstract Direct simulation Monte Carlo is a numerical method to simulate gas flows, leveraging some embarrassingly parallel steps like random number generation, advection, and sampling. Field-programmable gate arrays—devices with reconfigurable logic—are well suited for these tasks. Efficiently parallelising the commonly used no-time-counter collision evaluation scheme on these devices, however, introduces challenges, particularly repeated particle selections and race conditions during simultaneous post-collision velocity updates. These issues reduce the collision frequency and compromise accuracy. We address this with a modified scheme that splits and shuffles particle indices within a cell, enabling fine-grained, highly parallel collision evaluations without repeated particles or pairs and a preservation of collision frequency while still realising coarse-grained cell-based spatial parallelism within the programmable logic of a single device. We demonstrate the method on a one-dimensional heat transfer problem, achieving accurate results comparable to standard no-time-counter-based implementations.

Keywords DSMC · Spatial parallelism · FPGA acceleration

S. Bhattarai (✉) · E. Peters · D. Petty
The University of New South Wales Canberra, Campbell, ACT, Australia
e-mail: saleen.bhattarai@unsw.edu.au

E. Peters
e-mail: edwin.peters@unsw.edu.au

D. Petty
e-mail: d.petty@unsw.edu.au

S. O' Byrne
The Australian National University, Acton, ACT, Australia
e-mail: sean.obyrne@anu.edu.au

© The Author(s) 2026

M. Grabe et al. (eds.), *Rarefied Gas Dynamics*, Springer Aerospace Technology,
https://doi.org/10.1007/978-3-032-00094-1_38

1 Introduction

Direct simulation Monte Carlo (DSMC) [4] is a stochastic particle-based algorithm for simulating rarefied gas flows. It has a wide range of applications from hypersonics [10] to micro-scale flows [9]. Advancements in hardware have enabled large-scale DSMC simulations, often leveraging heterogeneous architectures that combine CPUs and GPUs for efficient parallelisation [7], but at the cost of using more computational resources than continuum methods [10].

In contrast, field-programmable gate arrays (FPGAs) offer reconfigurable logic that can be tailored to specific tasks, allowing custom-width data pathways, continuous data flow every clock cycle without the overhead of operating systems and fixed-width buses, and potential for parallelism. This degree of control can provide higher power efficiency and better performance than CPUs or GPUs [11]. The limited size of current FPGAs may make them impractical for large-scale DSMC simulations. However, micro-scale flows, where the bulk velocity is low and only a few particles and collision cells are needed – yet demand significant ensemble averaging – are therefore more suitable for FPGA implementation.

A critical step in DSMC involves simulating binary collisions. While CPUs or GPUs manage collision schemes through serialised steps, attempting parallel collision evaluation on FPGAs can lead to race conditions. This paper presents a novel method to eliminate these issues, ensuring accurate and efficient FPGA-based parallel collision evaluations. Traditional DSMC codes use message passing interface (MPI) for spatial parallelism, partitioning the domain into large subdomains across ranks that each still perform collision tests in a loop (possibly via threads). In contrast, our FPGA scheme instantiates one collision kernel per cell (multiple of which can fit inside a single FPGA chip) and further replicates pair-test/velocity-update logic within each kernel so that all collisions in a cell execute truly concurrently on-chip.

2 Spatial Parallelism and the DSMC Algorithm

FPGAs excel as computational accelerators due to inherent parallelism, offering both task and spatial parallelism. Task parallelism allows different algorithm stages to be executed in a pipelined manner, reducing the overall runtime. Spatial parallelism enables replication of a task multiple times at different locations within the FPGA, maximising computational throughput. These methods rely on FPGA resources such as look-up tables (LUT), flip flops (FF), block RAMs (BRAM), and digital signal processor (DSP) blocks.

The DSMC algorithm uses collision cells to locally evaluate binary elastic collisions. Thus, an ideal FPGA implementation of the DSMC algorithm would include a collision kernel for each cell that is spatially replicated within the resource constraints of the FPGA logic. This would be equivalent to performing a domain decomposition at the collision cell level. We aim to go a step further by proposing a spatially parallel

evaluation of all collisions within a single collision cell every time step. Details on the FPGA implementation can be found in [3].

The DSMC algorithm [4] has three major phases: advection of particles, simulating particle collisions, and sampling of macroscopic variables from the particle velocity distribution within a cell. The advection and sampling phases are embarrassingly parallel over all particles due to the particle-specific independence in the nature of these calculations. On the contrary, the collision phase is evaluated stochastically in DSMC and is not embarrassingly parallel. The process has two stages: first, potential collision partners within a collision cell are identified using the no-time-counter (NTC) method [4], followed by collision testing and updating the post-collision velocities for the accepted pairs.

3 Limitations Preventing Spatial Parallelism on FPGAs

In many parallel implementations of the NTC method, potential collision pairs are generated randomly. This means that either the same pair (type A) or the same particle (type B) can be selected multiple times. Previous studies [1] have tried to quantify the effects of successive type A pairs in DSMC simulations showing that their presence tends to reduce the collision frequency affecting the distribution of properties of the particles in the collision cells. Alternative methods [8] have been proposed to avoid the generation of such pairs.

Type B pairs are permissible in conventional hardware (CPUs or GPUs) with sequential calculation of collisions as subsequent interactions will use the correct intermediate particle dynamics. This is because even if the same particle is selected twice and accepted both times, the post-collision velocity updates happen at different times. Spatially parallel evaluation of these collisions (involving both type A and B pairs) presents a race condition where multiple post-collision velocity updates may occur simultaneously. This prevents the implementation of a completely spatially parallel version of the collision kernel using the NTC method on an FPGA. An earlier attempt [3] at spatially parallelising the collisions achieved this by generating unique pairs. However, until now, no attempt has been made to discuss the validity of results obtained from computing DSMC with spatial parallelism that involves an absence of type B pairs.

4 Methodology for Resolving the Limitations

An early collision scheme for vectorised DSMC implemented on the Cray supercomputer [2] tackled a similar problem. The scheme avoided race conditions by employing fixed collision pairs followed by a lengthening of the local particle index array with a simple pairing strategy based on a cyclically selected first particle paired with another offset by a fixed gap. Our approach to resolve the limitations highlighted

in the previous section is also to deterministically select collision pairs, particularly in a way that prevents the occurrence of successive type A pairs. However, unlike a simple cyclical pairing strategy of [2], pseudo-randomness is introduced into the simulation in a post-collision step by shuffling the particles referenced by the local particle indices. Lastly, batched repetitions of the entire set of collisions are performed to introduce type B pairs into the simulation. The algorithm (termed as half-split-shuffle or HSS) is as follows:

1. Generate a local particle index list for each collision cell every time step.
2. Pair the particles referenced by the first half of the index list with the second half. All pairings are unique and without any type A or type B pairs. Thus, the number of potential collision pairs per batch is given by:

$$N_{\text{sel}} \leq 0.5 N_{\text{p}} \tag{1}$$

3. Collide all N_{sel} pairs at once using the following probability:

$$P_{\text{col, }ab} = \frac{1}{N_{\text{batch}}} N_{\text{x}} N_{\text{eff}} (\sigma c_r)_{ab} \frac{\Delta t}{V_{\text{cell}}} \tag{2}$$

$$N_{\text{x}} = \begin{cases} N_{\text{p}}, & \text{when } N_{\text{p}} \text{ is odd} \\ N_{\text{p}} - 1, & \text{when } N_{\text{p}} \text{ is even} \end{cases} \tag{3}$$

where N_{batch} = number of batched repetitions, N_{eff} = number of molecules represented by a simulated particle, $(\sigma c_r)_{ab}$ = product between collision cross section (σ) and relative velocity (c_r) of particles (a, b), Δt = time step, and V_{cell} = volume of the cell. Collision occurs if $P_{\text{col, }ab} \geq R$ where R is a uniformly distributed random number between 0 and 1.
4. Calculate and update the post-collision velocities (V'_a, V'_b) of all colliding pairs in parallel using the following equations in a step termed a batch:

$$V'_{rab} = V_{rab} \, [\cos\chi, \ \sin\chi\cos\phi, \ \sin\chi\sin\phi], \tag{4}$$

$$V'_a \text{ or } V'_b = V_{\text{CM}} \pm V'_{rab}/2, \tag{5}$$

where V_{CM} = centre-of-mass velocity of the pairs and $(\chi, \ \phi)$ = scattering angles obtained using different Rs.
5. Shuffle the local particle index list using a Fisher-Yates algorithm [6].
6. Repeat steps 3 and 4 for a specified number of batches (N_{batch}).

Compared to the earlier scheme, the proposed HSS method applies a more robust shuffle to ensure randomness across batches. By design, it eliminates type A pairs (equivalent to generating unique pairs i.e. selecting two without replacement from a pool of N_{p} particles) and remains highly spatially parallelisable, with minimal FPGA resource usage because it does not require any complex logic to keep track of type A and type B pairs. The proposed method also ensures that type B pairs, while being eliminated from a single batch to allow effective spatial parallelism, are still

introduced through batched repetitions. A consequence of this method is that there is a requirement to ensure that $P_{\text{col, }ab} \leq 1$ by appropriately choosing Δt and V_{cell}.

To analyse the proposed method, we compare its results against an implementation of the standard NTC algorithm for a benchmark Fourier heat transfer problem as outlined in [1]. We consider Argon gas (molecule mass $m = 6.63 \times 10^{-26}$ kg, molecule diameter $d = 3.66 \times 10^{-10}$ m, initial temperature $T = 273$ K, and initial density $\rho = 1.78$ kg/m^3) with a hard-sphere collision model. The length of the domain is 10^{-3} m in the y-direction bounded by two thermal walls with perfect accommodation: a hot wall at the top and a cold wall at the bottom with a temperature difference of 100 K each with an area A. The walls are separated (Knudsen number 0.024) by a varying number of collision cells N_{c}. We observe the distribution of the temperature and the number of accepted collisions in the domain. We also calculate the wall heat flux q by tracking the change in kinetic energy of molecules impacting the wall as follows:

$$q = \frac{m N_{\text{eff}}}{A \Delta t} \sum \left({v_{\text{i}}}^2 - {v_{\text{r}}}^2 \right), \ \text{W/m}^2 \tag{6}$$

In addition, we consider the effects of the proposed HSS technique compared to the NTC method on more subtle parameters like the probability distribution of the relative velocity of accepted collisions. Finally, we observe the effects of the number of batched repetitions on our simulation results.

The method was implemented on a Versal VPK120 FPGA (containing approximately 10^6 LUTs, 2×10^6 FFs, 4000 DSPs, and 1350 BRAMs) using the Vitis HLS 2023.4 tool. Each collision kernel consumed 7093 LUTs (0.79 %), 3601 FFs (0.20 %), 49 DSPs (1.23 %), and 7 BRAMs (0.52 %). It is evident that DSPs are the constraining resource which limits theoretical scalability to 81 collision kernels. In order to prevent routing congestion in the FPGA, a total of 50 collision kernels were implemented. All results obtained using the current method were obtained from this implementation. It should be noted that for obtaining the results for cases with $N_{\text{c}} > 50$, the computation was carried out in groups of 50 cells at a time.

5 Results and Discussion

A detailed comparison between the results obtained for the Fourier heat transfer problem using the NTC and the current method is shown in Fig. 1. Qualitative agreement between the temperature profiles obtained using the two methods is shown in Fig. 1a. The degree of agreement between the two results is supported by the maximum normalised difference in the temperature profile being less than 0.005 as shown in Fig. 1b, implying that these different collision evaluation techniques yield nominally equivalent macroscopic temperature profiles.

Moving from temperature to collision rate, Fig. 1c depicts the distribution of accepted collisions normalised by half the average number of particles in the cell (see Eq. 1). The figure shows that despite testing a larger but deterministic number

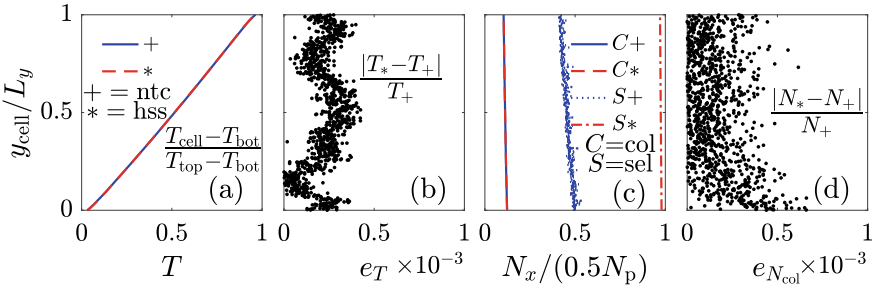

Fig. 1 Results: Fourier heat transfer problem for N_{p}=20, N_{c}=1000, $\Delta t/\tau$=10: **a** temperature, **b** difference in the temperature, **c** number of pair selections (sel) and accepted collisions (col), **d** difference in the accepted collisions

of potential collision pairs than the NTC method, the HSS method is able to replicate the number of accepted collisions, suggesting a preservation of collision frequency. Fig. 1d shows the normalised difference in the accepted collision distribution between the two methods with the maximum being less than 0.007, once again, showing that both methods are in close agreement with each other.

Fig. 2a illustrates the probability distribution of relative velocities of accepted collision pairs across several batches of simulations compared with the theoretical values and the results obtained using the NTC method. Each theoretical curve is constructed at a specific y-location using the value of temperature obtained at that location from Fig.1a using the following relation [5]:

$$P_{\text{col, accept}}\,(c_r) = 2\left(\frac{m_r}{2K_BT}\right)^2 c_r^3\,\exp\left(-\frac{m_r c_r^2}{2K_BT}\right) \tag{7}$$

where m_r = the reduced mass of the pair and K_B = Boltzmann's constant. Each curve represents the probability distribution function $P(c_r)$ of relative velocities of accepted collision pairs in different y-locations (different colours) and for different numbers of batched evaluations (different line styles). The figure shows that as N_{batch} increases, the obtained distributions tend to converge towards the theoretical curve, highlighting the accuracy of the batched repetition approach. Fig. 2b shows the normalised mean error (with respect to the theoretical curve) as a function of the batch number. The plot indicates asymptotic convergence towards the theoretical result with increasing N_{batch}. The results from Figs. 1, 2a, b collectively highlight the reliability of using batched repetitions to capture both macroscopic and microscopic properties of the problem.

Figure 2c shows how the value of the wall heat flux (normalised by the values obtained in similar conditions using the NTC method) converges as N_{batch} is increased for different choices of N_{c}. The value of wall heat flux obtained from the HSS method converges to within a single percentage point of the value obtained from NTC after performing just two batched repetitions. It is interesting to note that

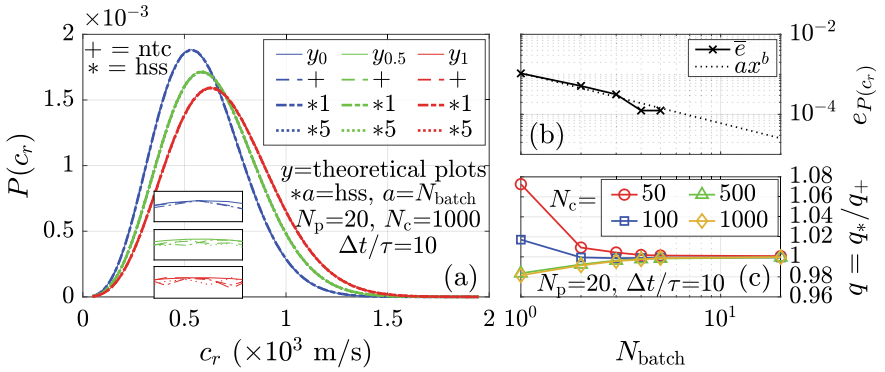

Fig. 2 **a** Distribution of the relative velocities of accepted collision pairs with batched repetitions, **b** error as a function of the batch number, **c** convergence in the value of wall heat flux with increasing batches

there is a large deviation in the results when performing only a single batch. This is explained by the deviation in the probability distributions for $N_{\text{batch}} = 1$ compared to the theoretical and NTC curves in Fig. 2a. The wall heat flux is a computationally sensitive quantity that directly depends on the number of particles, and their associated energy, that reach the wall. A small deviation in the distribution of the relative velocities of accepted collisions implies a small bias towards accepting pairs whose relative velocities only lie within a specific range. These biases are amplified when updating the post-collision velocities and materially alter the number of particles, and their associated energy, which interact with the bounding walls. As a consequence, the value of the wall heat flux is affected to a higher degree than the calculated temperature profile.

The reason why the probability distribution is different for a single batched HSS result compared to the same from NTC is because, by design, a single batch can never contain type B pairs to prevent race conditions as discussed earlier. This can be illustrated by keeping track of potential collision pairs as N_{batch} is increased and comparing that with the same from the NTC method. This has been demonstrated in Fig. 3. The graphs represent the distribution of the probability that a pair (a, b) is selected. Each box represents a pair chosen once or more during the simulation, while its colour represents the probability of that pair being selected. The lower plots represent the method of choosing pairs randomly with no restriction on either repeated particles or repeated pairs (equivalent to NTC). The upper plots represent the method of selecting unique pairs (equivalent to HSS). For a single repetition ($N_{\text{batch}} = 1$), we find that the lower plot will likely have boxes adjacent to each other or boxes sharing rows or columns, which represent type B pairs. The upper plots, for a single repetition, will never have such occurrences. This difference is enough to bias the pair selection such that it can affect the wall heat flux. The heat flux value obtained by HSS converges to the NTC value by introducing type B pairs with several repetitions of HSS. A key point to note here is that after the second set of repetitions,

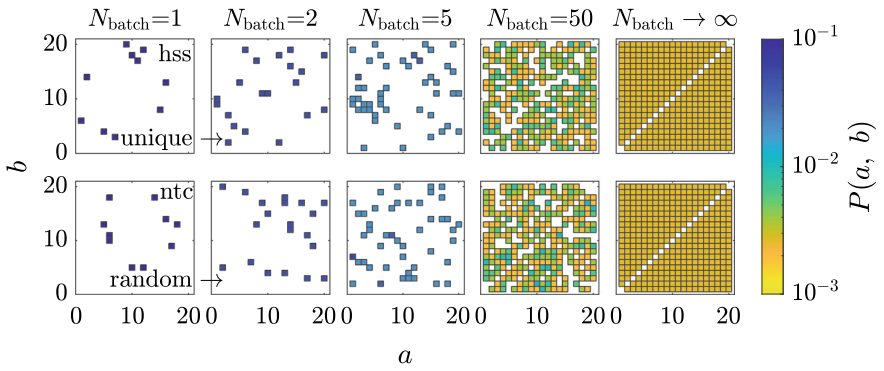

Fig. 3 Comparison of collision pair selection schemes ($N_{\text{p}} = 20$, $N_{\text{sel}} = 0.5N_{\text{p}}$)

the behaviour of both methods (in regard to the pair selection pattern) is no different from one another. The number of batches required to achieve this convergence is much less that the number of accepted collisions that must be sequentially calculated using NTC. The probability of a pair being selected by the HSS method becomes equivalent to any other pair in the limit of infinite batching.

6 Conclusion

This paper has presented a spatially-parallel collision scheme for implementing DSMC on FPGAs. The proposed HSS method addresses the limitations preventing parallel evaluation of collisions on an FPGA by eliminating type A pairs and introducing type B pairs through batched repetitions. The scheme preserves macroscopic and microscopic properties of interest in DSMC simulations as verified through a benchmark Fourier heat transfer problem. Results indicate that the temperature distribution and the number of accepted collisions obtained using this method agree closely with those obtained using the NTC method. The distribution of the relative velocities of accepted collision pairs converges towards theoretical values as the number of batches increases. While performing only a single batch results in significant deviations in the wall heat flux due to the absence of type B pairs, convergence to within 1% of the NTC values is achieved after just two batched repetitions. This is supported by an analysis of the probability distribution of potential collision pair selection which shows that the behaviour of both methods, with the pattern in which particle pairs are selected, becomes indistinguishable after the second set of repetitions. By combining an intra-cell fine-grained FPGA parallelism with a coarse-grained cell-based collision kernel hardware replication, this method opens new opportunities for accelerating micro-scale flow simulations with a small number of particles and collision cells. Future work will focus on quantifying the performance and energy efficiency benefits of this implementation against CPUs and GPUs.

Acknowledgements This work was supported by the Air Force Office of Scientific Research (23IOA106). We would like to thank Prof. Andrew Lambert and Dr. Jong-Leng Liow for their contributions to the discussion phase of this work.

References

1. Akhlaghi H, Roohi E, Stefanov S (2018) On the consequences of successively repeated collisions in no-time-counter collision scheme in DSMC. Comput Fluids 161:23–32
2. Baganoff D, McDonald JD (1990) A collision-selection rule for a particle simulation method suited to vector computers. Phys Fluids 2(7):1248–1259
3. Bhattarai S, Petty D, O'Byrne S, Peters E (2024) Parallel implementation of direct simulation monte carlo using field-programmable gate arrays. In: Australasian fluid mechanics conference. AFMS, Canberra
4. Bird GA (2013) The DSMC method, 2nd edn. CreateSpace, US
5. Boyd ID, Schwartzentruber TE (2017) Nonequilibrium gas dynamics and molecular simulation. Cambridge University Press, pp 323–328
6. Fisher RA, Yates F (1948) Statistical tables for biological, agricultural and medical research. Oliver & Boyd, 3 edn, pp 26–27
7. Hagleitner C, Diamantopoulos D, Ringlein B, Evangelinos C, Johns C, Chang RN, D'Amora B, Kahle JA, Sexton J, Johnston M, Pyzer-Knapp E, Ward C (2021) Heterogeneous computing systems for complex scientific discovery workflows. In: Design, automation and test in Europe conference and Exhibition. IEEE, Grenoble
8. Javani M, Roohi E, Stefanov S (2024) Symmetrized generalized and simplified Bernoulli-trials collision schemes in DSMC. Comput Fluids 272:106188
9. Mirnezhad N, Amiri-Jaghargh A, Qaderi A (2022) DSMC analysis of flow in Knudsen pumps with square-shaped wall roughness. AUT J Mech Eng 6(1):77–93
10. Plimpton SJ, Moore SG, Borner A, Stagg AK, Koehler TP, Torczynski JR, Gallis MA (2019) Direct simulation Monte Carlo on petaflop supercomputers and beyond. Phys Fluids 31(8):086101
11. Thomas DB, Howes L, Luk W (2009) A comparison of CPUs, GPUs, FPGAs, and massively parallel processor arrays for random number generation. International symposium on field programmable gate arrays. ACM, Monterey, pp 63–72

Open Access This chapter is licensed under the terms of the Creative Commons Attribution 4.0 International License (http://creativecommons.org/licenses/by/4.0/), which permits use, sharing, adaptation, distribution and reproduction in any medium or format, as long as you give appropriate credit to the original author(s) and the source, provide a link to the Creative Commons license and indicate if changes were made.

The images or other third party material in this chapter are included in the chapter's Creative Commons license, unless indicated otherwise in a credit line to the material. If material is not included in the chapter's Creative Commons license and your intended use is not permitted by statutory regulation or exceeds the permitted use, you will need to obtain permission directly from the copyright holder.

Higher-Order Meshfree Methods for BGK Equations with Moving Boundaries

Klaas Willems, Sudarshan Tiwari, and Axel Klar

Abstract We present a numerical method for simulating mixtures of rarefied gases that interact with moving boundaries and rigid bodies. The gas mixture is described by the general consistent BGK model for gas mixtures (Bobylev et al. in Kinetic Related Models 11(6):1377–1393, 2018) [1]. The BGK equations are solved using an Arbitrary Lagrangian-Eulerian method, in which grid points move with the local mean velocity of the gas (Tiwari et al. in J Comput Phys 458, 2022) [2]. The main advantage of the moving grid is that the algorithm can deal well with cases where the domain boundaries are time-dependent and the simulation domain contains rigid objects. Due to the irregular nature of the grid, we use a novel MUSCL-like Moving Least Squares Method (MLS) spatial discretization coupled with a second-order IMEX method. To avoid spurious oscillations at discontinuities, we use the so-called MOOD algorithm (Clain et al. in J Comput Phys 230(10):4028–4050, 2011) [3]. As a proof-of-concept, we apply the algorithm to Sod's shock tube and a moving boundary problem.

Keywords Multi-species BGK · Meshfree methods · MOOD

1 Introduction

In recent years, moving boundary problems for rarefied gas dynamics have been extensively investigated in connection with Micro-Electro-Mechanical-Systems (MEMS) [4]. In these applications, a low-Mach flow interacts with a small electronic sensor such as an accelerometer or micro engine. Because the mean free path of the gas is on the order of magnitude of the size of the MEMS, a kinetic description of the gas is required. Historically, simulations of rarefied flows were performed

K. Willems (✉) · S. Tiwari · A. Klar
Department of Mathematics, Rheinland-Pfälzische Universität Kaiserslautern-Landau, Kaiserslautern, Germany
e-mail: klaas.willems@math.rptu.de
URL: https://math.rptu.de/en/wgs/techno

© The Author(s) 2026

M. Grabe et al. (eds.), *Rarefied Gas Dynamics*, Springer Aerospace Technology,
https://doi.org/10.1007/978-3-032-00094-1_39

with Direct Simulation Monte Carlo (DSMC). However, due to the transient, low-Mach nature of the flow, DSMC is not well-suited for these problems [2]. Another approach to modelling these problems is through deterministic methods in which the Boltzmann equation is replaced by the more simple BGK model. Several numerical methods for the BGK-equation adapted to moving boundaries have been presented, such as a semi-Lagrangian method [5] and a finite volume method [6]. See latter reference for a overview. In this text, we present a Lagrangian method in which the grid points move with the mean velocity of the gas. This method is easily extendable to higher dimensions and can keep track of the gas-obstacle boundary exactly.

This text is organised as follows. In Sect. 2, we introduce the model. In Sect. 3, we discuss the space, velocity and time discretization. Finally, in Sect. 4, we validate the method on two numerical examples.

2 The Multi-Species BGK Model

We consider a mixture of rarefied gases described by the general consistent BGK model from [1]. Each kinetic equation in said model describes the evolution of the population $f_s(x, v, t)$ of gas species s as a function of space $x \in \mathbb{R}^3$, microscopic velocity $v \in \mathbb{R}^3$, and time $t \in \mathbb{R}^+$

$$\frac{\partial f_s}{\partial t} + v \cdot \nabla_x f_s = \frac{1}{\tau} \sum_{k=1}^{L} \nu_{sk}(n_s M_{sk} - f_s), \quad s = 1 \dots L \,. \tag{1}$$

The parameters $\nu_{sk} = \lambda_{sk} n_k$ are collision frequencies, and τ is the mean free path. The Maxwellians M_{sk} are defined as follows,

$$M_{sk} = \frac{1}{(2\pi RT_{sk})^{3/2}} \exp \frac{|v - u_{sk}|^2}{2RT_{sk}}, \tag{2}$$

in which the pseudo-velocities u_{sk} and temperatures T_{sk} are defined such that the BGK relaxation operators have the same collision invariants as the associated multi-species Boltzmann collision operator. We define the number density n_s, mean velocity u_s and temperature T_s for species s as

$$n_s = \langle 1, f_s \rangle, \quad n_s u_s = \langle v, f_s \rangle, \quad 3n_s RT_s = \langle |v - u_s|^2, f_s \rangle. \tag{3}$$

The macroscopic values for the whole mixture can then be obtained from

$$n = \sum_{s=1}^{L} n_s, \quad u = \frac{1}{\rho} \sum_{s=1}^{L} \rho_s u_s, \quad 3nRT = 3 \sum_{s=1}^{L} n_s T_s + \sum_{s=1}^{L} n_s |u_s - u|^2. \tag{4}$$

The model features the same structure as the corresponding Boltzmann equations and fulfils all consistency requirements concerning conservation laws, equilibria and H-theorem. The hydrodynamical limits of this BGK model were formally derived in [7].

We intend to solve (1) in complex geometries with moving boundaries, while avoiding cumbersome algorithms such as a cut-cell method [6]. To this end, we write (1) in 'Lagrangian' form

$$\frac{\mathrm{d}x}{\mathrm{d}t} = u \tag{5}$$

$$\frac{\mathrm{d}f_s}{\mathrm{d}t} = -(v-u)\cdot\nabla_x f_s + \frac{1}{\tau}\sum_{k=1}^{L}\nu_{sk}(n_s M_{sk} - f_s), \quad s = 1\ldots L\,. \tag{6}$$

In other words, we move grid points with the mean macroscopic velocity of the gas mixture. To account for this motion, the population density is advected with velocity $v-u$. In the following section, we discretize the equation on a moving irregular grid. For the purpose of this paper, we limit ourselves to 1D examples. To avoid the large time complexity associated with the full three-dimensional velocity field, we reduce the dimension of the equation using a Chu-reduction [8].

Remark 1 By moving the grid points with the mean velocity of the gas, the grid may become distorted throughout the simulation, leading to large discretization errors. A particle management algorithm is run periodically to avoid gaps in the grid or clustering of points. This algorithm uses a background grid to remove points where the point density is higher and adds points where the the point density is low [2].

Remark 2 This method only concerns the advection term in the BGK equation and is thus applicable to any BGK-type equation. For an overview of multi-species BGK-type equations, see for example [9].

3 Discretization Scheme

3.1 MUSCL-Like Spatial Discretization

The main difficulty associated with the Lagrangian form of the multi-species BGK equations is that the grid moves. One option to solve the equations is to use a finite volume method for moving unstructured grids [10]. However, for simplicity, we restrict ourselves to finite difference methods. Due to the unstructured nature of the grid, we cannot rely on classical finite difference schemes. Instead, we use the so-called Generalised Finite Difference Method (GFDM), which relies on a Moving Least Squares Approximation (MLS) [11]. MLS uses a Taylor expansion around a central point $f_s(x_i, v, t) \approx f_i$

$$f_j = f_i + \Delta x_{ij} \frac{\partial f_i}{\partial x} + \frac{\Delta x_{ij}^2}{2} \frac{\partial^2 f_i}{\partial x^2} + e_{ij}, \quad j \in \mathcal{C}_i, \tag{7}$$

where $\Delta x_{ij} = x_j - x_i$, and $\mathcal{C}_i$ is the set of all points that are within some distance of x_i. The spatial derivatives are then obtained by minimizing the $\mathcal{L}^2$ norm of the errors e_{ij} with respect to a weight function. One then obtains a result of the form

$$\frac{\partial f_i}{\partial x} \approx \sum_{j \in \mathcal{C}_i} \alpha_{ij} (f_j - f_i), \tag{8}$$

$$\frac{\partial^2 f_i}{\partial x^2} \approx \sum_{j \in \mathcal{C}_i} \beta_{ij} (f_j - f_i), \tag{9}$$

which can then be substituted into equation (6). To obtain a stable discretization, upwinding is required. Thus, the choice of stencil C_{ij} should depend on the velocity v. On the other hand, a central stencil is preferred due to significantly lower cost: the coefficients α_{ij} can only be computed once and can be reused for each velocity v. The novel MUSCL-like method achieves a stable discretization using central stencils and is based on the first-order positive method from [12]. We write the spatial derivative as

$$\frac{\partial f_i}{\partial x} \approx 2 \sum_{j \in \mathcal{C}_i} \alpha_{ij} (f_{ij} - f_i), \tag{10}$$

where f_{ij} is an approximation for the midpoint between x_i and x_j. The midpoint f_{ij} is reconstructed using a Taylor expansion from point x_i or x_j depending of the velocity

$$f_{ij} = \begin{cases} f_i + \frac{\Delta x_{ij}}{2} \sum_{k \in C_i} \alpha_{ik} (f_k - f_i) + \frac{\Delta x_{ij}^2}{8} \sum_{k \in C_i} \beta_{ik} (f_k - f_i) & \text{if } (v - u) \Delta x_{ij} > 0, \\ f_j - \frac{\Delta x_{ij}}{2} \sum_{k \in C_j} \alpha_{jk} (f_k - f_j) + \frac{\Delta x_{ij}^2}{8} \sum_{k \in C_j} \beta_{jk} (f_k - f_j) & \text{else.} \end{cases} \tag{11}$$

Upwinding is thus obtained by selecting the midpoint; the stencil is purely central. The scheme above is of second-order, or one order lower than the order of the Taylor expansion. Note that the extension to higher orders is straightforward. First, one should solve the least squares problem to a higher-order Taylor expansion, analogous to (7). Using the coefficients from the least squares problem, one can then do a higher-order reconstruction of the midpoint.

3.2 Velocity Discretization

For simplicity, we use a uniform zero-centered velocity discretization $[-v_{max}, v_{max}]$. All continuous inner products are approximated using the midpoint rule. Schemes that use this type of velocity discretization are referred to as discrete velocity models.

Remark 3 Due to the finite-difference nature of the spatial discretization, the discrete velocity model, and the non-conservative flux in (6), this algorithm is not conservative.

3.3 Time Discretization

We use the ARS222 IMEX Runge-Kutta scheme from [] for time integration of (6). The advection term is time-integrated using the explicit RK method. BGK-collision terms must be treated implicitly as in [13]. This avoids a time restriction due to the (possibly) stiff term, and ensures that the scheme is asymptotic preserving, i.e., in the limit for $\tau \to 0$, the numerical solution tends to the solution of the hydrodynamical limit. The explicit scheme of the IMEX method is used to time integrate the evolution equation for the position of the grid points (5).
Although the combination of an IMEX scheme and the MUSCL-like discretization is stable, it is possible to show that it is not positive. As a result, the algorithm will yield spurious oscillations at discontinuities. To avoid this, we use the so-called Multidimensional Optimal Order Detection (MOOD) method [3]. In the most basic version of MOOD, one checks if the numerical solution satisfies the local discrete maximum property (DMP)

$$\min_{j \in C_i}(f_i, f_j) \leq f_i^* \leq \max_{j \in C_i}(f_i, f_j). \tag{12}$$

If the proposed numerical solution does not satisfy the DMP property, the solution is recomputed using a lower-order method. In our case, we use the first-order positive method from [12], combined with a forward Euler time integration scheme. We apply MOOD on the numerical solution after every explicit RK stage f_i^* to avoid spurious oscillations due to the linear transport step. To avoid loss of accuracy at extrema, we relax criterion (12) with the so-called u2 detection criterion from [14].

4 Numerical Examples

4.1 Multi-Species Shock Tube

We consider the multi-species shock tube from Section 6.3 in [13]. We assume a spatial domain $[-1, 1]$ with diffusive reflective boundary conditions. The velocity domain is truncated to $[-15, 15]$. The numerical solutions are computed with $N_x = 200$ spatial grid points and $N_v = 50$ velocity grid points until the final time $t_f = 0.2$. We set the CFL number to 0.5 and set $\tau = 10^{-5}$. We compare three spatial discretisation methods: the second-order MUSCL-like scheme from 3.1 with and

without MOOD, and a second-order meshless WENO method from [2]. All simulations are performed with the second-order IMEX ARS(2, 2, 2) time integration scheme. The density and temperature are shown in Fig. 1. The meshless MUSCL scheme without MOOD yields significant oscillations. Adding MOOD at the kinetic level removes the oscillations and results in sharp discontinuities. The meshless WENO scheme is a bit more diffusive than the MUSCL scheme.

4.2 Single Species Moving Plate Problem

As a final test, we consider the single species slider problem from [2]. This test illustrates the flexibility of meshless schemes when it comes to moving boundaries. A schematic of the test problem is provided in Fig. 2. A moving plate separates two chambers filled with Argon gas ($R_s = 208, \tau = 5.398 \times 10^{-4}$). Initially, the plate is at rest in the centre of the domain. We take as initial data of the gas in the left and right chamber Maxwellians with density $\rho_0 = 6.87 \times 10^{-7}$, velocity $U_0 = 0$, and temperature $T_0 = 270$. The density of the plate is ten times the density of the gas. The temperature of the walls of the left and right gas chambers are set to T_0 and $T_w = 330$ respectively. Due to the higher temperature of the walls of the right gas chamber, the pressure will increase, pushing the moving plate to a new equilibrium position. The motion of the plate is described by Newton's equation of motion. In the one-dimensional setting, the force that the gas applies to the moving plate is given by

$$F = \left(\psi_{left} - \psi_{right}\right) A$$
$$\psi_i = \int (v - U_w)^2 f \, dv,$$

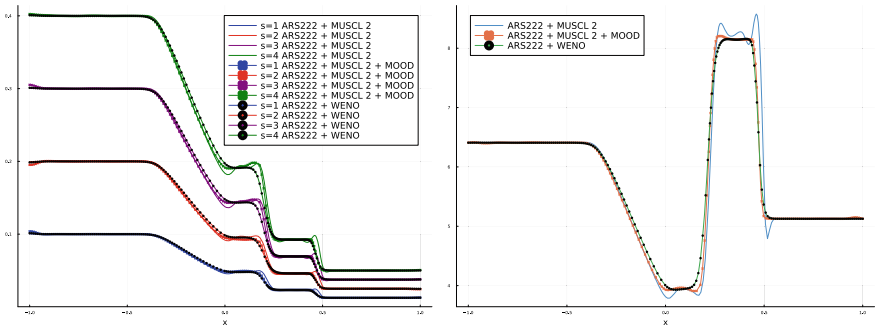

Density ρ_s. Temperature of the first gas species T_1.

Fig. 1 Density and temperature for the multi-species shock tube

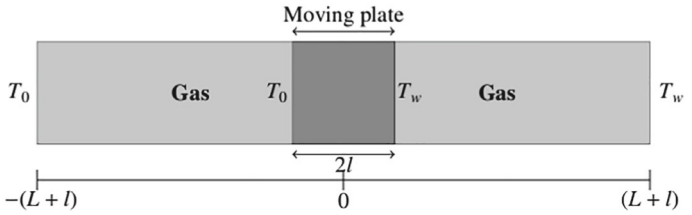

Fig. 2 Schematic of moving plate problem with $L = 1$ and $l = 0.1$ [2]

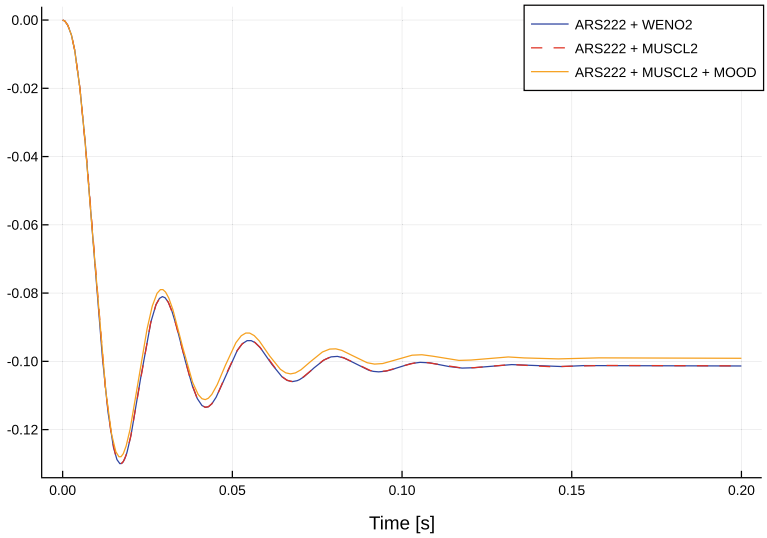

Fig. 3 The position of the centre of mass of the moving plate

where $A = 1$ is the surface area of the plate and U_w the velocity of the plate. This problem is often used as a benchmark because the equilibrium position of the slider can be computed explicitly from

$$x_{eq} = L\frac{T_0 - T_w}{T_0 + T_w} = -0.1.$$

The spatial domain and velocity domain $[-1600, 1600]$ are discretized using $N_x = 200$ and $N_v = 30$ points respectively. We perform the simulation up to time $t_f = 0.2$ with CFL $= 0.5$ using the same algorithms as in Sect. 4.1. The position of the centre of mass of the moving plate is plotted as a function of time in Fig. 3. The meshless WENO and MUSCL methods yield very comparable results. The main takeaway from this test is that no additional algorithms are required to deal with the moving boundary compared to the shock tube simulation. Due to the moving points and the particle management algorithm (see remark 1), the grid automatically adapts to the boundary.

5 Conclusion

We have presented a meshless scheme for linear hyperbolic equations on unstructured grids and applied it to the Lagrangian form of the multi-species BGK model. The numerical scheme uses a central stencil, which allows for the reuse of the stencil coefficients for each kinetic velocity. The MUSCL-like reconstruction at the stencil midpoints dynamically selects the upwind direction for each kinetic velocity and ensures the stability of the scheme. The meshless scheme is coupled with an IMEX time discretization scheme and a MOOD algorithm to avoid spurious oscillations at discontinuities. As a proof-of-concept, we have applied the algorithm to two test cases: a multi-species shock tube and the moving slider problem. In the former test case, the new MUSCL scheme with MOOD yields sharper discontinuities and no oscillations than the meshless WENO scheme from [2]. The latter test case illustrates the flexibility of meshless schemes when the domain contains moving boundaries. In future work, we intend to extend the scheme to fourth order and investigate the stability and conservation properties. In addition, we will extend the scheme to 2D and attempt simulations of more complex geometries.

References

1. Bobylev AV, Bisi M, Groppi M, Spiga G, Potapenko IF (2018) A general consistent BGK model for gas mixtures. Kinetic Related Models 11(6):1377–1393. https://doi.org/10.3934/krm.2018054
2. Tiwari S, Klar A, Russo G (2022) A meshfree arbitrary Lagrangian-Eulerian method for the BGK model of the Boltzmann equation with moving boundaries. J Computat Phys 458. https://doi.org/10.1016/j.jcp.2022.111088
3. Clain S, Diot S, Loubère R (201) A high-order finite volume method for systems of conservation laws—Multi-dimensional Optimal Order Detection (MOOD). J Comput Phys 230(10):4028–4050. https://doi.org/10.1016/j.jcp.2011.02.026
4. Karniadakis G, Beskok A, Aluru N (2005) Microflows and nano-flows: fundamentals ans simulations, Springer, New York. https://link.springer.com/book/10.1007/0-387-28676-4
5. Russo G, Filbet F (2009) Semilagrangian schemes applied to moving boundary problems for the BGK model of rarefied gas dynamics. Kinetic and Related Models 2:231–250. http://aimsciences.org//article/doi/10.3934/krm.2009.2.231
6. Déchristé G, Mieussens L (2016) A Cartesian cut cell method for rarefied flow simulations around moving obstacles. J Comput Phys 314:012030. https://doi.org/10.1016/j.jcp.2016.03.024
7. Bisi M, Groppi M, Martalò G (2021) Macroscopic equations for inert gas mixtures in different hydrodynamic regimes. J Phys A: Math Theoret 54(8):085201. https://iopscience.iop.org/article/10.1088/1751-8121/abbd1b
8. Chu CK Kinetic-theoretic description of the formation of a shock wave. In: The physics of fluids https://pubs.aip.org/aip/pfl/article-abstract/8/1/12/957838/Kinetic-Theoretic-Description-of-the-Formation-of?redirectedFrom=fulltext
9. Brull S, Pavan V, Schneider J (2012) Derivation of BGK model for mixtures. Eur J Mech B&Fluids, 33:74–86. https://linkinghub.elsevier.com/retrieve/pii/S0997754611001324
10. Boscheri W (2017) High order direct arbitrary-lagrangian–eulerian (ALE) finite volume schemes for hyperbolic systems on unstructured meshes. Arch Comput Methods Eng 751–801. https://doi.org/10.1007/s11831-016-9188-x

11. Lancaster P, Salkauskas K (1981) Surfaces generated by moving least squares methods. Math Comput 37:141–158. https://www.ams.org/journals/mcom/1981-37-155/S0025-5718-1981-0616367-1/
12. Chandrashekar P A positive meshless method for hyperbolic equations. https://www.researchgate.net/publication/277759856_A_positive_meshless_method_for_hyperbolic_equations
13. Cho SY, Boscarino S, Groppi M, Russo G Conservative semi-lagrangian schemes for a general consistent BGK model for inert gas mixtures. https://dx.doi.org/10.4310/CMS.2022.v20.n3.a4
14. Diot S, Clain S, Loubère R (2012) Improved detection criteria for the multi-dimensional optimal order detection (MOOD) on unstructured meshes with very high-order polynomials. Comput Fluids 64:43–63. https://doi.org/10.1016/j.compfluid.2012.05.004
15. Déchristé G, Mieussens L (2012) Numerical simulation of micro flows with moving obstacles. J Phys: Conf Ser 362:465–488. https://iopscience.iop.org/article/10.1088/1742-6596/362/1/012030
16. Ascher UM, Ruuth SJ, Spiteri RJ (1997) Implicit-explicit Runge-Kutta methods for time-dependent partial differential equations. Appl Numer Math 25(2–3):151–167. https://doi.org/10.1016/S0168-9274(97)00056-1

Open Access

Open Access This chapter is licensed under the terms of the Creative Commons Attribution 4.0 International License (http://creativecommons.org/licenses/by/4.0/), which permits use, sharing, adaptation, distribution and reproduction in any medium or format, as long as you give appropriate credit to the original author(s) and the source, provide a link to the Creative Commons license and indicate if changes were made.

The images or other third party material in this chapter are included in the chapter's Creative Commons license, unless indicated otherwise in a credit line to the material. If material is not included in the chapter's Creative Commons license and your intended use is not permitted by statutory regulation or exceeds the permitted use, you will need to obtain permission directly from the copyright holder.

Comparison of Stochastic BGK and FP Methods for the Simulation of Non-Equilibrium Multi-species Molecular Gas Flows

Franziska Tuttas and Marcel Pfeiffer

Abstract Due to limited possibilities of experimental investigations for non-equilibrium gas flows, numerical results are of highest interest. Although the well-established Direct Simulation Monte Carlo (DSMC) method achieves highly accurate solutions, the computational requirements increase excessively for lower Knudsen regimes. Computationally more efficient simulations can be achieved with stochastic continuum-based methods using either the Bhatnagar-Gross-Krook (BGK) or the Fokker-Planck (FP) approximations where, instead of particle collisions, particle relaxation processes are considered. This paper explains the implementation of different stochastic BGK and FP methods in the open-source particle code PICLas for multi-species molecular gas flows. For verification, the results of different test cases are compared.

Keywords DSMC · BGK · Fokker-Planck · Multi-species · Mixture

1 Introduction

Looking at multi-scale flow problems across a wide range of Knudsen numbers, the well-established Direct Simulation Monte Carlo (DSMC) method [1] achieves highly accurate solutions. However, the computational requirements increase excessively for lower Knudsen regimes, making it computationally infeasible for many practical applications. A possible solution is a coupling of the DSMC method with continuum-based methods, leading to reduced computational costs. Using the same particle approach for simplicity of the coupling, different stochastic particle-based methods such as the Bhatnagar-Gross-Krook (BGK) [2–4] and the Fokker-Planck (FP) [5–10] approximations for the Boltzmann collision integral can be used for this purpose. The advantage of these methods in the computational efficiency in transition and continuum regimes, as they consider relaxation processes of the particles instead of binary particle collisions.

F. Tuttas (✉) · M. Pfeiffer
Institute of Space Systems, University of Stuttgart, Stuttgart, Germany
e-mail: tuttasf@irs.uni-stuttgart.de

© The Author(s) 2026

M. Grabe et al. (eds.), *Rarefied Gas Dynamics*, Springer Aerospace Technology,
https://doi.org/10.1007/978-3-032-00094-1_40

In this paper, the implementation of different stochastic BGK and FP methods for multi-species molecular gas flows in the open-source particle code PICLas [11, 12] is explained. First, the different models are presented, including an Ellipsoidal Statistical BGK (ESBGK) model [3], a Shakhov BGK model (SBGK) [4], and an Ellipsoidal Statistical Fokker-Planck (ESFP) model [7]. The focus of this paper lies in the differences between the models and their implementation in PICLas, mainly regarding the relaxation and sampling of the particle velocities. The relaxation of internal energies are described through Landau-Teller equations as shown in Hild et al. [13], which is the same for all models and thus is not presented any further here. The energy and momentum conservation scheme is discussed briefly, which is crucial for the stability of the simulations. To assess the accuracy of the different models, the results of two supersonic Couette flow test cases are compared to DSMC reference solutions.

2 BGK Method

The BGK operator approximates the Boltzmann collision integral by a relaxation process of a particle distribution function $f_s(\mathbf{x}, \mathbf{v}, t)$ of a species s at position $\mathbf{x}$ and with velocity $\mathbf{v}$ towards a target distribution f_s^t [2], using the relaxation frequency ν:

$$\partial_t f_s + \mathbf{v}\partial_{\mathbf{x}} f_s = \nu(f_s^t - f_s). \tag{1}$$

For atomic species, the target distribution function only consists of a translational part $f_s^{t,\mathrm{tr}}(\mathbf{v})$, whereas for molecular species, the distribution function can be separated into a translational, a rotational, and a vibrational part as demonstrated in [14, 15]. Both the ESBGK [3] and the SBGK [4] models use one relaxation term per species, produce the Maxwellian distribution in the equilibrium state, and fulfill the indifferentiability principle, yielding same outcomes for one species or two identical species. While there the H theorem is proven for the ESBGK model, there is no general proof for the SBGK model. Furthermore, the positivity of SBGK target distribution function $f_s^{\mathrm{SBGK,tr}}$ cannot be guaranteed.

2.1 ESBGK Mixture Model

The ESBGK model presented here combines different models of Mathiaud et al. [14], Pfeiffer [16] and Brull [17, 18] into a mixture model that allows for non-equilibrium effects in the internal degrees of freedom. It is already discussed in greater detail in [13]. Instead of a Maxwellian target distribution, the correct Prandtl number is achieved by using an anisotropic Gaussian distribution [3]:

$$f_s^{\mathrm{ESBGK,tr}} = \frac{n_s}{\sqrt{\det 2\pi \mathbf{A}_s}} \exp\left[-\frac{1}{2}\mathbf{c}^{\mathrm{T}}\mathbf{A}_s^{-1}\mathbf{c}\right]. \tag{2}$$

The anisotropic matrix $\mathbf{A}_s$ is defined as

$$\mathbf{A}_s = \frac{k_{\mathrm{B}}T_{\mathrm{tr,rel}}}{m_s}\mathbf{I} - \frac{1-\alpha Pr}{\alpha Pr}\left(\frac{T_{\mathrm{tr,rel}}}{T_{\mathrm{tr}}}\boldsymbol{\Theta} - \frac{k_{\mathrm{B}}}{m_s}T_{\mathrm{tr,rel}}\mathbf{I}\right) \tag{3}$$

with the identity matrix $\mathbf{I}$, and the symmetric stress tensor $\boldsymbol{\Theta}$, calculated with the pressure tensor $\mathbf{P}$, and the mass density ρ:

$$\boldsymbol{\Theta} = \frac{\mathbf{P}}{\rho} = \frac{1}{\rho}\sum_{s=1}^{M} m_s \int \mathbf{c}\mathbf{c}^{\mathrm{T}} f_s \,\mathrm{d}\mathbf{v} \tag{4}$$

$T_{\mathrm{tr,rel}}$ is the translational relaxation temperature, defined according to [13, 14]. The parameter α is a model variable that depends on mass fraction, density fraction and internal degrees of freedom [18]:

$$\alpha = m\frac{\sum_{s=1}^{M}\frac{n_s}{m_s}\left(5+\xi_{\mathrm{vib},s}+\xi_{\mathrm{rot},s}\right)}{\sum_{s=1}^{M} n_s\left(5+\xi_{\mathrm{vib},s}+\xi_{\mathrm{rot},s}\right)} \tag{5}$$

The relaxation frequency ν_{ESBGK} of the model is defined as

$$\nu_{\mathrm{ESBGK}} = \frac{nk_{\mathrm{B}}T_{\mathrm{tr}}}{\mu}\alpha Pr \tag{6}$$

with the viscosity of the mixture μ and the translational temperature T_{tr}. Pr is the targeted Prandtl number of the gas mixture, which is calculated using collision integrals [19]. For molecular species, the rotational and vibrational components of the distribution function are taken directly from [14]. The relaxation temperatures are chosen to match the Landau-Teller relaxation. For more details, the reader is referred to [13].

2.2 Shakhov BGK Mixture Model

In the SBGK model, the heat flux is modified to produce the correct Prandtl number [4]. Thus, the target distribution function for a mixture model reads

$$f_s^{\mathrm{SBGK,tr}} = f_s^{\mathrm{M}}\left[1 + (1-\alpha Pr)\frac{\mathbf{c}^{\mathrm{T}}\mathbf{q}/m_s}{5n\left(k_{\mathrm{B}}T_{\mathrm{tr}}/m_s\right)^2}\left(\frac{|\mathbf{c}|^2}{2k_{\mathrm{B}}T_{\mathrm{tr}}/m_s} - \frac{5}{2}\right)\right] \tag{7}$$

with the heat flux vector

$$\mathbf{q} = \sum_{s=1}^{M} m_s \int \mathbf{c} \, |\mathbf{c}|^2 \, f_s \, \mathrm{d}\mathbf{v} \tag{8}$$

and the Maxwellian distribution f_s^{M}. The relaxation frequency ν_{SBGK} of the model is defined as

$$\nu_{\mathrm{SBGK}} = \frac{n k_{\mathrm{B}} T_{\mathrm{tr}}}{\mu}. \tag{9}$$

For molecular species, the rotational and vibrational components of the distribution function are defined similar as for the ESBGK model (see Sect. 2.1).

3 FP Method

The FP operator approximates the Boltzmann collision term by using a drift vector $\mathbf{a} = a_i$ and a diffusion matrix $\mathbf{D}_s = D_{ij,s}$ [5]:

$$\partial_t f_s + \mathbf{v} \partial_{\mathbf{x}} f_s = -\sum_{i=1}^{3} \frac{\partial}{\partial v_i} (a_i f_s) + \sum_{i=1}^{3} \sum_{j=1}^{3} \frac{\partial^2}{\partial v_i \partial v_j} (D_{ij,s} f_s). \tag{10}$$

For molecular species, the internal energies are handled following the BGK approach presented in Sect. 2. In this paper, the ESFP model [7] for molecular gas mixtures is presented and compared to the BGK models. Same as the ESBGK model, it fulfills the H theorem.

3.1 ESFP Mixture Model

The ESFP mixture model modifies the diffusion matrix $\mathbf{D}_s$ to correct the Prandtl number of the Standard FP model [7]:

$$\mathbf{D}_s^{\mathrm{ESFP}} = \nu_{\mathrm{ESFP}} \left((1 - \chi_s) \frac{k_{\mathrm{B}} T_{\mathrm{tr}}}{m_s} \mathbf{I} + \chi_s \boldsymbol{\Theta} \right). \tag{11}$$

$\mathbf{D}_s$ is a convex combination of the stress tensor $\boldsymbol{\Theta}$ and its equilibrium value $(k_{\mathrm{B}} T_{\mathrm{tr}}/m_s)\mathbf{I}$ for a species s with a parameter χ_s including $\lambda_{\max}$ as the (positive) maximum eigenvalue of $\boldsymbol{\Theta}$, so that $\mathbf{D}_s$ remains strictly definite positive:

$$\chi_s = \max \left(1 - \frac{3}{2Pr}, -\frac{k_{\mathrm{B}} T_{\mathrm{tr}}/m_s}{\lambda_{\max} - k_{\mathrm{B}} T_{\mathrm{tr}}/m_s} \right). \tag{12}$$

The drift vector is defined similar to the Standard FP model:

$$\mathbf{a}^{\mathrm{ESFP}} = -\nu_{\mathrm{ESFP}}\mathbf{c}. \tag{13}$$

The relaxation frequency ν_{ESFP} of the model is defined as

$$\nu_{\mathrm{ESFP}} = \frac{nk_{\mathrm{B}}T_{\mathrm{tr}}}{3\mu}Pr. \tag{14}$$

4 Implementation

All the particle methods presented in this paper are implemented in the open-source code PICLas [11]. The different implementations of the models for the translational relaxation of the particles and the sampling of the new velocities are discussed. In addition, the basic energy and momentum conservation scheme is described (for details see [13]). For details on the rotational and vibrational relaxations, the reader is also referred to [13].

4.1 Relaxation and Sampling of Particle Velocities

For the BGK models, all particles in a cell relax with a probability P in each time step Δt towards the specified target distribution function $f_s^{\mathrm{ESBGK,tr}}$ or $f_s^{\mathrm{SBGK,tr}}$:

$$P = 1 - \exp\left[-\nu\Delta t\right], \quad \nu = \nu_{\mathrm{ESBGK}}, \nu_{\mathrm{SBGK}}. \tag{15}$$

The relaxation frequency ν is calculated in each cell and time step using collision integrals [19], as described in [13]. If a uniform random number is smaller than the probability, the particle considered relaxes and its new velocity is sampled from the target distribution function of the used method.

For the ESBGK method, the transformation matrix $\mathbf{S}_s$ [20] with $\mathbf{A}_s = \mathbf{S}_s\mathbf{S}_s^{\mathrm{T}}$ is approximated and used to transform a random Maxwellian vector $\mathbf{r}_p$ for a particle p to a velocity vector from the ESBGK target distribution:

$$\mathbf{v}_{p,\mathrm{ESBGK}}^{*} = \mathbf{u} + \mathbf{S}_s\mathbf{r}_p, \tag{16}$$

$$\mathbf{S}_s = \sqrt{\frac{k_{\mathrm{B}}T_{\mathrm{tr,rel}}}{m_s}}\left[\mathbf{I} - \frac{1-\alpha Pr}{2\alpha Pr}\left(\frac{m}{k_{\mathrm{B}}T_{\mathrm{tr}}}\boldsymbol{\Theta} - \mathbf{I}\right)\right]. \tag{17}$$

The superscript * marks a parameter after relaxation, but before energy and momentum conservation.

For the SBGK method, however, an analytical expression for a similar vector transformation is not available, which is why an acceptance-rejection (AR) algorithm [21] is used. Hereby, an envelope function $g_s(\mathbf{r}_p)$ is defined. For the presented

particle SBGK method, good results are found by choosing

$$g_s(\mathbf{r}_p) = A_s f_s^{\mathrm{SBGK,tr}}(\mathbf{r}_p) \tag{18}$$

$$A_s = 1 + 10\frac{\max(\mathbf{q}/m_s)}{(k_\mathrm{B}T_\mathrm{tr}/m_s)^{3/2}} \tag{19}$$

as envelope function and

$$P_s^{\mathrm{SBGK,AR}}(\mathbf{r}_p) = 1 + (1 - Pr)\frac{\mathbf{r}_p^\mathrm{T}\mathbf{q}/m_s}{5n(k_\mathrm{B}T_\mathrm{tr}/m_s)^{3/2}}\left(\frac{|\mathbf{r}_p|^2}{2} - \frac{5}{2}\right) \tag{20}$$

as acceptance probability. A normal distributed vector $\mathbf{r}_p$ is accepted if a uniform random number $r < P_s^{\mathrm{SBGK,AR}}(\mathbf{r}_p)/A_s$. The new velocity is then calculated with

$$\mathbf{v}^*_{p,\mathrm{SBGK}} = \mathbf{r}_p\sqrt{\frac{k_\mathrm{B}T_\mathrm{tr,rel}}{m_s}}. \tag{21}$$

For a detailed description of the different BGK sampling options, the reader is referred to [12], in which also alternative methods for sampling are described.

The ESFP model relaxes each particle according to the Ornstein-Uhlenbeck process [22] with the following stochastic differential equation to solve the corresponding FP Eq. (10):

$$\mathrm{d}\mathbf{c} = \mathbf{a}\,\mathrm{d}t + \sqrt{2}\mathbf{D}^{1/2}\,\mathrm{d}\mathbf{w} \tag{22}$$

d$\mathbf{w}$ is the standard three-dimensional Wiener process [7]. Using an exact time integration [5], the new particle velocity for the ESFP model is calculated by

$$\mathbf{v}^*_{p,\mathrm{ESFP}} = \mathbf{u} + \mathbf{c}_p\exp\left(-\nu_\mathrm{ESFP}\Delta t\right) + \frac{\left(\mathbf{D}_s^\mathrm{ESFP}\right)^{1/2}}{\sqrt{\nu_\mathrm{ESFP}}}\sqrt{1 - \exp\left(-2\nu_\mathrm{ESFP}\Delta t\right)}\cdot\mathbf{r}_p \tag{23}$$

with $\mathbf{c}_p$ being the thermal particle velocity before relaxation.

4.2 Energy and Momentum Conservation

Due to the stochastic approach with particles, an energy and momentum conservation scheme needs to be established even though the presented BGK and FP models are in general both momentum and energy conserving. The reason for this lies in the random choice of the new states of the particles from the distribution functions as described in Sect. 4.1, whereby the conservation of energy and momentum is not automatically given. Thus, a large number of particles would be needed for stable simulation results

if no additional energy and momentum conservation step would be implemented. In general, the chosen conservation scheme is based on the work in [16, 23] and extended to polyatomic molecules and mixtures of different gas species in [13]. The main idea is to distribute the energy difference between the old energy and the new energy from the sampling evenly according to the respective degrees of freedom to the translational energy of all particles in the cell and the internal energies of the respective relaxing particles within the cell [16]. More details on the implementation can be found in [13].

5 Simulation Results for Supersonic Couette Flows

The different multi-species BGK and FP implementations are verified and compared with a test case of two one-dimensional supersonic Couette flows. Simulating a 50%-50% N_2-He mixture first, the initial particle density is $n_0 = 1.3 \times 10^{20}\mathrm{m}^{-3}$, leading to a Knudsen number of $Kn_{\mathrm{VHS}} = 0.0112$ with a characteristic length of $L = 1\mathrm{m}$. As second case, an air mixture with N, O, N_2, O_2, and NO, with $n_0 = 1.25 \times 10^{20}\mathrm{m}^{-3}$ and a corresponding Knudsen number of $Kn_{\mathrm{VHS}} = 0.0126$ is simulated in order to test the models with a more complicated case of multiple molecular species in a mixture. The velocity and temperature of the gas are initialized at $v_0 = 0\mathrm{ms}^{-1}$ and $T_0 = 273\mathrm{K}$ in both cases. The boundaries in y direction have a velocity of $v_{\mathrm{wall},1} = 350\mathrm{ms}^{-1}$ and $v_{\mathrm{wall},2} = -350\mathrm{ms}^{-1}$, respectively, assuming diffuse reflection and complete thermal accommodation at a constant wall temperature of $T_{\mathrm{wall}} = 273\mathrm{K}$. The time steps and particle weighting factors are chosen so that the mean free path and the collision frequency are resolved. The VHS model is used [1], and the parameters for a collision pair of unlike species are determined as an average (referred to as collision-averaged).

The translational temperature results in comparison for the different methods are shown in Fig. 1. While there is very good agreement for the ESBGK and SBGK

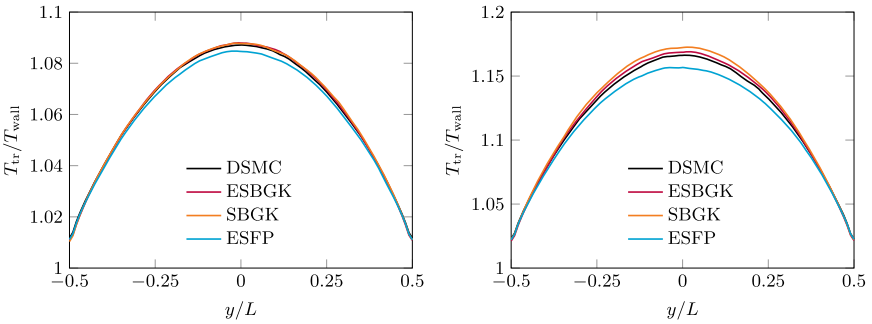

(a) N_2-He mixture (b) Air mixture

Fig. 1 Translational temperature for the ESBGK (purple), SBGK (orange), and ESFP (blue) models as well as the DSMC result (black) as reference

models compared to the DSMC reference solution, the ESFP model shows deviations in the peak temperature. Similar results for a comparable Knudsen number are shown in [24] for a single-species ESFP model, which is why the deviations are attributed to the model itself rather than the mixture modeling. The results for the rotational temperatures are similar due to the thermal equilibrium in the Couette flow.

6 Conclusion

Different continuum-based particle methods, namely an ESBGK model, a Shakhov BGK model, and an ESFP model are proposed. Aiming for solutions of multi-scale problems, the handling of molecular gas mixture flows is implemented in the open-source particle code PICLas. Two different supersonic Couette flows with molecular gas mixtures indicate overall very good agreement of the results between both the BGK models and the DSMC method, whereas small deviations occur for the ESFP model. In future work, the implementation of chemical reactions into all the different models is envisioned.

Acknowledgements This project has received funding from the European Research Council (ERC) under the European Union's Horizon 2020 research and innovation programme (grant agreement No. 899981 MEDUSA).

References

1. Bird GA (1994) Molecular gas dynamics and the direct simulation of gas flows. Oxford University Press, New York
2. Bhatnagar PL, Gross EP, Krook M (1954) A model for collision processes in gases. I. Small amplitude processes in charged and neutral one-component systems. Phys Rev 94(3):511–525
3. Holway HL Jr (1966) New statistical models for kinetic theory: methods of construction. Phys Fluids 9:1658–1673
4. Shakhov EM (1968) Generalization of the Krook kinetic relaxation equation. Fluid Dyn 33:95–96
5. Jenny P, Torrilhon M, Heinz S (2010) A solution algorithm for the fluid dynamic equations based on a stochastic model for molecular motion. J Comput Phys 229(4):1077–1098
6. Pfeiffer M, Gorji MH (2017) Adaptive particle-cell algorithm for Fokker-Planck based rarefied gas flow simulations. Comput Phys Commun 213:1–8
7. Mathiaud J, Mieussens L (2016) A Fokker-Planck model of the Boltzmann equation with correct Prandtl number. J Stat Phys 162:397–414
8. Gorji MH, Jenny P (2010) An efficient particle Fokker-Planck algorithm for rarefied gas flows. J Comput Phys 262:325–343
9. Kim S, Jun E (2025) A particle Fokker-Planck method for rarefied gas flows of monatomic mixtures. Phys Fluids 37:016104
10. Hepp C, Grabe M, Hannemann K (2020) A kinetic Fokker-Planck approach for modeling variable hard-sphere gas mixtures. AIP Advances 10:085219

11. Fasoulas S, Munz C-D, Pfeiffer M, Beyer J, Binder T, Copplestone S, Mirza A, Nizenkov P, Ortwein P, Reschke W (2019) Combining particle-in-cell and direct simulation Monte Carlo for the simulation of reactive plasma flows. Phys Fluids 31:072006
12. Pfeiffer M (2018) Particle-based fluid dynamics: comparison of different Bhatnagar-Gross-Krook models and the direct simulation Monte Carlo method for hypersonic flows. Phys Fluids 30:106106
13. Hild F, Pfeiffer M (2024) Multi-species modeling in the particle-based ellipsoidal statistical Bhatnagar-Gross-Krook method including internal degrees of freedom. J Comput Phys 514:113226
14. Mathiaud J, Mieussens L, Pfeiffer M (2022) An ES-BGK model for diatomic gases with correct relaxation rates for internal energies. Eur J Mech B/Fluids 96:65–77
15. Dauvois Y, Mathiaud J, Mieussens L (2021) An ES-BGK model for polyatomic gases in rotational and vibrational nonequilibrium. Eur J of Mech B/Fluids 88:1–16
16. Pfeiffer M (2018) Extending the particle ellipsoidal statistical Bhatnagar-Gross-Krook method to diatomic molecules including quantized vibrational energies. Phys Fluids 30:116103
17. Brull S (2014) An ellipsoidal statistical model for gas mixtures. Commun Math Sci 13:1–13
18. Brull S (2021) An ellipsoidal statistical model for a monoatomic and a polyatomic gas mixture. Commun Math Sci 19(8):2177–2194
19. Hirschfelder JO, Curtiss CF, Bird RB (1964) The molecular theory of gases and liquids. Wiley-Interscience
20. Gallis MA, Torczynski JR (2000) The application of the BGK model in particle simulations. In: 34th thermophysics conference, American institute of aeronautics and astronautics, Denver, Colorado, USA
21. Garcia AL, Aldr BJ (1998) Generation of the Chapman-Enskog distribution. J Comput Phys 140:66–70
22. Uhlenbeck GE, Ornstein LS (1930) On the theory of the Brownian motion. Phys Rev 36:823–841
23. Burt JM, Boyd ID (2006) Evaluation of a particle method for the ellipsoidal statistical bhatnagar-gross-krook equation. In: 44th AIAA aerospace sciences meeting and exhibit
24. Jun E, Pfeiffer M, Mieussens L, Gorji MH (2019) Comparative study between cubic and ellipsoidal Fokker-Planck kinetic models. AIAAJ 57(6):2524–2533

Open Access This chapter is licensed under the terms of the Creative Commons Attribution 4.0 International License (http://creativecommons.org/licenses/by/4.0/), which permits use, sharing, adaptation, distribution and reproduction in any medium or format, as long as you give appropriate credit to the original author(s) and the source, provide a link to the Creative Commons license and indicate if changes were made.

The images or other third party material in this chapter are included in the chapter's Creative Commons license, unless indicated otherwise in a credit line to the material. If material is not included in the chapter's Creative Commons license and your intended use is not permitted by statutory regulation or exceeds the permitted use, you will need to obtain permission directly from the copyright holder.

Molecular-Level Simulations of Turbulent Couette Flow Over Rough Surfaces

Ryan M. McMullen, Timothy P. Koehler, and Michael A. Gallis

Abstract We report flow statistics from simulations using the direct simulation Monte Carlo method for turbulent Couette flow where the lower wall is replaced by an idealized rough surface. We focus on conditions yielding a modest global Reynolds number, supersonic Mach number, and a global Knudsen number in the near-continuum regime, allowing for comparison with direct numerical simulation of the Navier-Stokes equations for the same conditions. While we observe discrepancies on the order of a few percent, we find the overall level of agreement between macroscopic and molecular-level descriptions of turbulent flow encouraging.

Keywords DSMC · Turbulence · Rough surfaces · TPS materials

1 Introduction

Thermal-protection-system (TPS) materials used to coat the surfaces of reentry vehicles are often rough and permeable. This surface layer has the potential to significantly modify the turbulent boundary layer over the vehicle and thereby alter the aerothermal loading, which could in turn compromise vehicle performance [1]. Consequently, the ability to make accurate predictions about turbulent flows over TPS materials is of great interest. However, the length scales of common TPS materials can be on the order of the gas-molecular mean free path [2], which itself may not be small compared to other characteristic flow length scales. Therefore, the validity of predictions from conventional continuum computational fluid dynamics needs to be assessed in the context of flow over reentry vehicles coated with TPS materials.

On the other hand, the direct simulation Monte Carlo (DSMC) method of molecular gas dynamics is suitable for a wider range of flow physics, including situations in which noncontinuum and nonequilibrium effects are important [3]. DSMC simulates gas flows by tracking large numbers of computational particles (each of which in turn represents a large number of real gas molecules) that move, collide with

R. M. McMullen (✉) · T. P. Koehler · M. A. Gallis
Engineering Sciences Center, Sandia National Laboratories, Albuquerque, NM, USA
e-mail: rmmcmul@sandia.gov

© The Author(s) 2026

M. Grabe et al. (eds.), *Rarefied Gas Dynamics*, Springer Aerospace Technology,
https://doi.org/10.1007/978-3-032-00094-1_41

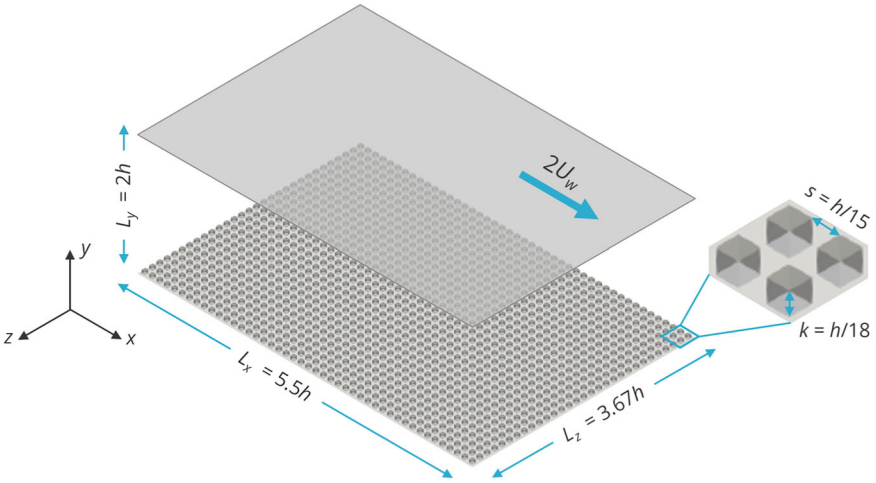

Fig. 1 Configuration for turbulent Couette flow over a rough wall with cubical roughness elements

each other, and reflect from solid surfaces just like real gas molecules do. Although DSMC is a molecular-level method and thus computationally intense, algorithmic and computing-power advances have recently made DSMC simulations of near-continuum turbulent flows computationally feasible. DSMC has now been shown to be able to simulate turbulent flows accurately, reproducing known features of decaying turbulence [4] and self-sustaining wall-bounded turbulence [5]. Furthermore, DSMC inherently includes noncontinuum effects, such as Knudsen layers adjacent to solid surfaces and molecular thermal fluctuations, which become significant in the dissipation range of the turbulent energy cascade [6–8].

With these capabilities, DSMC should be well suited for performing high-fidelity simulations of turbulent flows over complex TPS-like rough and permeable surfaces. However, the ability of DSMC to simulate turbulent flow over rough surfaces has not yet been verified. Therefore, we herein compare DSMC simulations of turbulent Couette flow over an idealized and canonical rough surface consisting of regularly spaced cubical roughness elements to direct numerical simulation of the Navier-Stokes (NS) equations. The flow conditions and surface geometry have been chosen such that good agreement between the two methods is anticipated.

2 Rough-Wall Simulations

2.1 Flow Configuration

Figure 1 shows a schematic diagram of the flow configuration. x, y, and z are the streamwise, wall-normal, and spanwise directions, respectively. The velocity components corresponding to these directions are denoted u, v, w, respectively. The domain extent is $(L_x, L_y, L_z) = (5.5h, 2h, 3.67h)$, where $h = 500\,\mu\text{m}$ is the channel half-height. The boundary conditions are periodic in the x and z directions, and all solid surfaces are fully accommodating. The lower wall is roughened with cubical roughness elements of height $k = h/18$, which are separated by a distance $s = h/15$.

The global Reynolds number is $\text{Re} = \rho_0 U_\text{w} h/\mu_\text{w} = 2790$, where $\rho_0 = 0.345$ kg m^{-3} is the volume-averaged density, $U_\text{w} = 461.85$ m s^{-1} is half the velocity difference between the walls, and $\mu_\text{w} = 2.86 \times 10^{-5}$ Pa s is the value of the dynamic viscosity at the constant wall temperature $T_\text{w} = 273.15$ K. The global Mach number is $\text{Ma} = U_\text{w}/a_\text{w} = 1.5$, where $a_\text{w} = \sqrt{\gamma k_\text{B} T_\text{w}/m} = 307.9$ m s^{-1} is the sound speed at T_w, $\gamma = 5/3$ is the specific heat ratio, k_B is the Boltzmann constant, and $m = 6.63 \times 10^{-26}$ kg is the molecular mass. The global Knudsen number is $\text{Kn} = \lambda_0/h = \sqrt{\pi\gamma/2}\,\text{Ma}/\text{Re} = 8.7 \times 10^{-4}$, where λ_0 is the molecular mean-free path at ρ_0 and T_w. Velocities and lengths nondimensionalized by U_w and h, respectively, are referred to as being in outer units or as outer-scaled. Velocities and lengths nondimensionalized by the friction velocity $u_\tau = \sqrt{\tau_\text{w}/\rho_\text{w}}$ and viscous length scale $\mu_\text{w}/\rho_\text{w} u_\tau$, respectively, are referred to as being in inner units or as inner-scaled and are denoted with a superscript "+".

2.2 Numerical Details

The DSMC simulations are performed using Sandia's open-source massively parallel code SPARTA [9]. The domain is divided into $N_x \times N_y \times N_z = 2141 \times 823 \times 1475$ uniform cells. For the conditions considered herein, this cell size yields a mean collision separation comparable to λ_0, such that any potential shocks are well resolved. On average, each cell contains 30 particles, giving approximately 73 billion particles total. The time step is 9.12 ps, which is less than 1% of the mean collision time. Particle-particle collisions are performed using hard-sphere interactions, which produces a viscosity temperature dependence of the form $\mu(T) = \mu_\text{w}\sqrt{T/T_\text{w}}$ [3]. The simulation was performed on the Los Alamos National Laboratories Crossroads supercomputer and was run to approximately 77×10^6 time steps, corresponding to a dimensionless stopping time of $tU_\text{w}/h \approx 650$.

A cut-cell method is used to conform the mesh to the rough lower surface [9]. In this approach, a closed three-dimensional structure represented by triangular surface elements is embedded in the Cartesian grid. The surface elements intersecting a given grid cell cut the portion of its volume accessible to particles, and the reduced

volume for each cut cell is then calculated and taken into account when performing particle-particle collisions.

Macroscopic quantities of interest are obtained by averaging over the particles contained within each cell. However, since each simulated particle represents $O(10^5)$ real molecules, the statistical variations arising from thermal molecular fluctuations are drastically overestimated [3], often resulting in an unacceptably low signal-to-noise ratio. A common technique to mitigate this effect is to additionally perform temporal averages within the cells. Ideally, an averaging time that gives acceptable noise reduction is still much smaller than any macroscopic flow timescale, though this is not always possible. Here, we found that averaging over 10^3 consecutive time steps, which is less than 1% of the turnover time h/U_w and less than 10% of the viscous time $\mu_\mathrm{w}/\tau_\mathrm{w}$, reduced noise acceptably without significantly smearing out the turbulent structures.

The initial condition for the simulation is the incompressible laminar smooth-wall solution $u = U_\mathrm{w}(y/h + 1)$ plus a sinusoidal perturbation with amplitude sufficient to trigger transition to turbulence. Turbulence statistics are collected for $tU_\mathrm{w}/h \geq 200$ to allow the flow to reach statistically steady state, which is confirmed by examination of the skin friction shown in Fig. 2. Subsequently, DSMC realizations were collected every 10^6 time steps (every $8.4\,tU_\mathrm{w}/h$).

Companion direct numerical simulation (DNS) of the NS equations for the same flow conditions was performed using the Sandia-developed finite-volume code SPARC [10]. The DNS is performed using a grid of $N_x \times N_y \times N_z = 495 \times 278 \times 330$. Uniform grid spacing is used in the homogeneous wall-parallel directions, resulting in $\Delta x^+ = \Delta z^+ = 2.3$. The grid in the wall-normal direction is uniform within the cubical roughness elements, with $\Delta y_r^+ = 0.42$. Above the roughness elements, the grid is stretched using a hyperbolic tangent distribution, such that the resolution at the channel center is $\Delta y_c^+ = 3.8$. Likewise, the grid is stretched moving from the top wall toward the channel center, with a near-wall resolution of $\Delta y_\mathrm{w}^+ = 0.45$. Time is advanced using a fourth-order explicit Runge-Kutta scheme with a Courant-Friedrichs-Lewy number of 0.5 to determine the time step. The present simulation thus has resolutions comparable to other DNS studies of compressible turbulent Couette flow [11]. The initial condition for the NS simulation is identical to the one used for the DSMC simulation. For $tU_\mathrm{w}/h \geq 200$, statistics were collected every turnover time h/U_w up to the simulation stopping time of $tU_\mathrm{w}/h \approx 3700$.

2.3 Results

First, we compare the DSMC and NS wall skin friction τ_w (drag per unit plan area). Figure 2 shows the DSMC and NS values of the top- and bottom-wall skin friction nondimensionalized by the laminar value $\mu_\mathrm{w}U_\mathrm{w}/h$. Both agree almost exactly for early times $tU_\mathrm{w}/h \lesssim 50$ corresponding to breakdown of the deterministic initial condition into turbulence. The flow reaches statistically steady state at $tU_\mathrm{w}/h \approx 200$, after which the DSMC and NS wall shear stress have very similar mean values (10.6

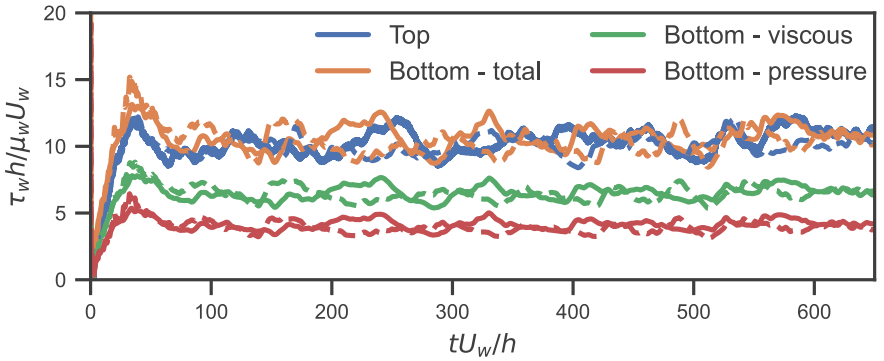

Fig. 2 Comparison of top- and bottom-wall skin friction for DSMC (solid lines) and NS (dashed lines). Also shown is the decomposition of bottom-wall skin friction into viscous- and pressure-drag contributions

and 10.1, respectively) but different time histories due to the chaotic nature of turbulent flows. The slight discrepancy of $\sim 5\%$ between the mean values can possibly be attributed to the relatively short record length of DSMC simulation compared to that of the NS simulation.

Note that both the top (smooth) and bottom (rough) walls are guaranteed to have the same mean skin friction since the mean momentum balance for Couette flow states that the total (viscous plus turbulent) shear stress is a constant (equal to τ_w) across the entire channel. However, this does not mean that the rough wall has no effect on the drag. Indeed, NS simulations for the same Re and Ma in which both walls are smooth (not shown in Fig. 2) yield a mean dimensionless skin friction value of 9.23, so that the rough wall increases drag by $\sim 10\%$.

While the top-wall skin friction is entirely due to viscous drag (shear stress), the skin friction on the roughened bottom wall is comprised of both pressure drag (normal stress) and viscous drag on the cubical roughness elements. Each of these contributions to the bottom-wall skin friction is also shown in Fig. 2, where once again the DSMC and NS results are found to be in good agreement. Pressure drag comprises 39% and 38% of the total bottom-wall skin friction for the DSMC and NS simulations, respectively. This implies that the flow falls into the so-called "transitionally rough" regime [12], in which both viscous and pressure drag are both significant.

Next, we compare the DSMC and NS mean density and velocity profiles, which are shown in Fig. 3. For reference, profiles for a smooth-wall NS simulation with the same Re and Ma are also shown (black lines). The location of the tops of the cubical roughness elements is indicated by the vertical gray lines. The agreement between the rough-wall DSMC and NS density profiles shown in the left panel of Fig. 3 is excellent, and both are in good agreement with the smooth-wall density profile, except in the vicinity of the rough wall, which causes the density to rise more abruptly. This level of agreement between the rough-wall DSMC and NS density

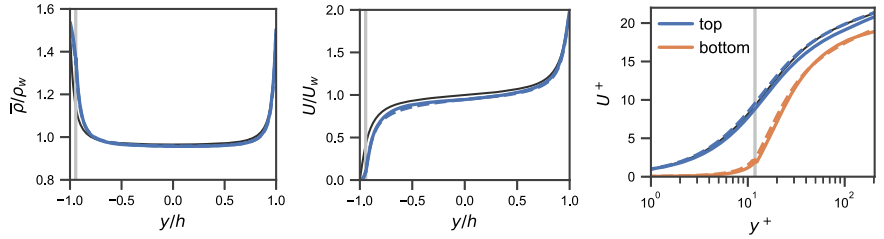

Fig. 3 Comparison of DSMC (solid lines) and NS (dashed lines) mean density (left), outer-scaled mean velocity (middle), and inner-scaled velocity (right) profiles. The vertical gray line indicates the location of the top of the roughness elements. The thin black line is a smooth-wall NS simulation for the same Re and Ma

profiles is unsurprising given that the density fluctuations for the present Ma are relatively small.

The outer-scaled mean velocity profiles are plotted in the middle panel of Fig. 3. Overall the DSMC and NS velocity profiles agree fairly well, and both deviate significantly from the smooth-wall velocity profile across the majority of the channel. The minor discrepancies between the rough-wall DSMC and NS profiles can again likely be attributed to the limited number of DSMC samples. More significant discrepancies are apparent in the upper-half inner-scaled profiles shown in the right panel of Fig. 3. However, most of this discrepancy arises from the aforementioned difference in the mean value of the skin friction τ_w, which in turn results in a different value of the friction velocity u_τ used to normalize the inner-scaled velocity profiles. Note that the NS upper-half inner-scaled velocity profile collapses onto the smooth-wall velocity profile, indicating that significant roughness effects are confined to the lower half of the channel. In other words, the primary effect of the rough bottom wall on the flow near the smooth upper wall is a modification of the boundary condition by adjusting τ_w (and hence u_τ).

Thus far we have examined spatially averaged quantities (skin friction, mean velocity profiles). Now, we turn our attention to comparison of the structure of the turbulent fluctuations, quantified via the (density-weighted) premultiplied velocity spectra, e.g., $k_x k_z E_{\rho uu}$, which describe how the kinetic energy associated with turbulent fluctuations is distributed in scale (Fourier) space, and where k_x and k_z are the streamwise and spanwise wavenumbers, respectively. Premultiplication by $k_x k_z$ ensures that equal volumes in scale space correspond to equal energy when plotted on logarithmic axes. The velocity spectra plotted as functions of streamwise and spanwise wavelengths $\lambda_x = 2\pi/k_x$ and $\lambda_z = 2\pi/k_z$, respectively, are shown in Fig. 4 for the plane immediately above the roughness elements, $y/h = -0.94$. Because the DSMC simulation has a higher spatial resolution than the NS simulation, smaller wavelengths are resolved in the DSMC spectra. Accordingly, the region containing the wavelengths in the NS simulation are indicated by the cyan rectangle. Also, small wavelengths in the DSMC simulation are dominated by thermal fluctuations, which are absent from the NS simulation [8]. Otherwise, the DSMC and NS spectra agree

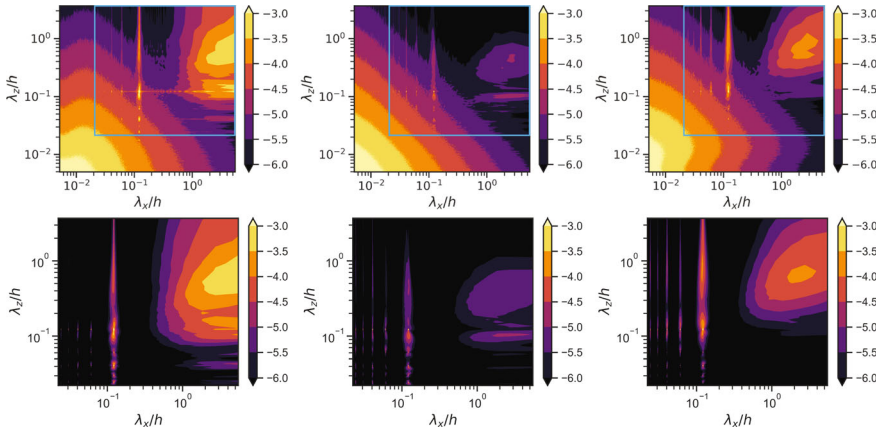

Fig. 4 Comparison of DSMC (top) and NS (bottom) velocity spectra in the plane $y/h = -0.94$ (immediately above the roughness elements). Left column: $k_x k_z E_{\rho uu}$. Center column: $k_x k_z E_{\rho vv}$. Right column: $k_x k_z E_{\rho ww}$. The blue interior of the cyan rectangles indicate the wavenumbers included in the NS simulations

very well in both shape and magnitude, indicating that both simulations capture the same turbulence structures.

For both simulations, the most energetic structures in Fig. 4 correspond to long streamwise wavelengths, $\lambda_x > h$, and spanwise wavelengths $\lambda_z \sim h$, consistent with large streaky structures commonly observed in turbulent Couette flow [11]. The other most prominent feature in the spectra is the strong peak located at $\lambda_x = \lambda_z = 0.12h$, which corresponds to the periodicity of the roughness elements, $k + s$. Several harmonics and subharmonics of this wavelength are also visible. Note also that the roughness introduces "side bands" of energetic streaky structures in the u and v spectra with $\lambda_x > h$ and $\lambda_z \approx k + s$, which are the spectral signature of intense narrow streaks corresponding to fluid being accelerated between columns of roughness elements.

3 Summary and Conclusions

We compared statistical quantities from DSMC and NS simulations of turbulent Couette flow with a rough wall. The simulations agree well for the skin friction, mean density and velocity profiles, and velocity spectra. The minor discrepancies (on the order of a few percent) in these quantities can reasonably be attributed to the relatively limited number of samples available for calculating statistics from the DSMC simulation. Nonetheless, we find the overall level of agreement between macroscopic (NS) and molecular-level (DSMC) descriptions of turbulent flow encouraging.

This successful demonstration of DSMC's capability to reproduce rough-wall turbulence effects in the near-continuum regime sets the stage for DSMC simulations of turbulent flow over realistic TPS materials having mean-free-path-scale features, for which the NS equations may not be accurate. Additionally, recent efforts have aimed at improving SPARTA's ablation modeling capability [13], so future work incorporating the effects of ablation on the overlying turbulent flow would be of great technological interest.

Acknowledgements Sandia National Laboratories is a multi-mission laboratory managed and operated by National Technology & Engineering Solutions of Sandia, LLC (NTESS), a wholly owned subsidiary of Honeywell International Inc., for the U.S. Department of Energy's National Nuclear Security Administration (DOE/NNSA) under contract DE-NA0003525. This written work is authored by an employee of NTESS. The employee, not NTESS, owns the right, title and interest in and to the written work and is responsible for its contents. Any subjective views or opinions that might be expressed in the written work do not necessarily represent the views of the U.S. Government. The publisher acknowledges that the U.S. Government retains a nonexclusive, paid-up, irrevocable, world-wide license to publish or reproduce the published form of this written work or allow others to do so, for U.S. Government purposes. The DOE will provide public access to results of federally sponsored research in accordance with the DOE Public Access Plan [14]. The authors thank L. J. DeChant for helpful discussions about this work.

References

1. NASA identifies cause of artemis i orion heat shield char loss. https://www.nasa.gov/missions/artemis/nasa-identifies-cause-of-artemis-i-orion-heat-shield-char-loss/, Accessed: 19 Dec 2024
2. Borner A, Panerai F, Mansour NN (2017) High temperature permeability of fibrous materials using direct simulation monte carlo. Int J Heat Mass Transfer 106:1318–1326
3. Bird GA (1994) Molecular gas dynamics and the direct simulation of gas flows. Oxford University Press, Oxford
4. Gallis M, Bitter N, Koehler T, Torczynski J, Plimpton S, Papadakis G (2017) Molecular-level simulations of turbulence and its decay. Phys Rev Lett 118(6):064501
5. Gallis MA, Torczynski JR, Bitter NP, Koehler TP, Plimpton SJ, Papadakis G (2018) Gas-kinetic simulation of sustained turbulence in minimal Couette flow. Phys Rev Fluids 3(7):071402
6. Bandak D, Goldenfeld N, Mailybaev AA, Eyink G (2022) Dissipation-range fluid turbulence and thermal noise. Phys Rev E 105(6):065113
7. Bell JB, Nonaka A, Garcia AL, Eyink G (2022) Thermal fluctuations in the dissipation range of homogeneous isotropic turbulence. J Fluid Mech 939:A12
8. McMullen RM, Krygier MC, Torczynski JR, Gallis MA (2022) Navier-Stokes equations do not describe the smallest scales of turbulence in gases. Phys Rev Lett 128(11):114501
9. Plimpton S, Moore S, Borner A, Stagg A, Koehler T, Torczynski J, Gallis M (2019) Direct simulation Monte Carlo on petaflop supercomputers and beyond. Phys Fluids 31(8)
10. Howard M, Bradley A, Bova SW, Overfelt J, Wagnild R, Dinzl D, Hoemmen M, Klinvex A (2017) Towards performance portability in a compressible CFD code. In: 23rd AIAA computational fluid dynamics conference, p 4407
11. Yao J, Hussain F (2023) Study of compressible turbulent plane Couette flows via direct numerical simulation. J Fluid Mech 964:A29
12. Jiménez J (2004) Turbulent flows over rough walls. Annu Rev Fluid Mech 36(1):173–196

13. Hong AY, Gallis MA, Moore SG, Plimpton SJ (2024) Toward physically realistic ablation modeling in direct simulation Monte Carlo. Phys Fluids 36(12):126132
14. https://www.energy.gov/doe-public-access-plan

Open Access This chapter is licensed under the terms of the Creative Commons Attribution 4.0 International License (http://creativecommons.org/licenses/by/4.0/), which permits use, sharing, adaptation, distribution and reproduction in any medium or format, as long as you give appropriate credit to the original author(s) and the source, provide a link to the Creative Commons license and indicate if changes were made.

The images or other third party material in this chapter are included in the chapter's Creative Commons license, unless indicated otherwise in a credit line to the material. If material is not included in the chapter's Creative Commons license and your intended use is not permitted by statutory regulation or exceeds the permitted use, you will need to obtain permission directly from the copyright holder.

Simulation of Multi-species Kinetic Instabilities with the Numerical Flow Iteration

Rostislav-Paul Wilhelm and Manuel Torrilhon

Abstract Kinetic instabilities are one of the most challenging aspects in computational plasma physics. Accurately capturing their onset and evolution requires fine resolution of the high-dimensional distribution functions of each relevant species, which quickly becomes computationally prohibitively expensive. Additionally, plasma dynamics is an inherently multi-scale phenomenon due to the vast separation of scales between heavy ions and light-weight electrons. In previous work the *Numerical Flow Iteration* (NuFI) was suggested as a high-fidelity alternative with reduced memory complexity making it an interesting candidate to simulate complicated kinetic instabilities. In this work we extend NuFI to non-periodic boundary conditions and demonstrate how it is possible to reduce the computational complexity to allow for longer simulation periods.

Keywords Computational plasma physics · Kinetic theory · Numerical methods

1 Introduction

In many applications such as ion thrusters or nuclear fusion devices it is relevant to fundamentally understand how instabilities in a plasma are triggered and how they evolve over time. This often requires modelling the plasma evolution through the (collisionless) Vlasov equation [1]

$$\partial_t f^\alpha + v \cdot \nabla_x f^\alpha + F^\alpha \cdot \nabla_v f^\alpha = 0. \tag{1}$$

R.-P. Wilhelm (✉)
Centre for Mathematical Plasma Astrophysics, KU Leuven, Leuven, Belgium
e-mail: paul.wilhelm@kuleuven.be

R.-P. Wilhelm · M. Torrilhon
Institute for Applied and Computational Mathematics, RWTH Aachen University, Aachen, Germany

© The Author(s) 2026

M. Grabe et al. (eds.), *Rarefied Gas Dynamics*, Springer Aerospace Technology,
https://doi.org/10.1007/978-3-032-00094-1_42

where f^α is the probability distribution of the species α in the up to six-dimensional phase-space. To discuss the fundamental methodical issues we restrict ourselves to the electro-static case, i.e., where the forces reduce to the self-induced electric field force $F^\alpha = \frac{q_\alpha}{m_\alpha} E$ computed through

$$-\Delta_x \varphi = \rho = \sum_\alpha q_\alpha \int_{\mathbb{R}^3} f_\alpha \mathrm{d}v, \tag{2}$$

$$E = -\nabla_x \varphi. \tag{3}$$

This coupling yields the (non-linear) Vlasov–Poisson system.[1]

Due to the high-dimensionality of the problem it is already challenging to handle by itself even on modern large-scale supercomputers. In addition f is notoriously known for its turbulent behaviour and development of fine scale structures, which are relevant for the plasma dynamics and, in particular, are crucial to capture the onset of kinetic instabilities. Additionally, the problem is naturally multi-scale due to the large difference in mass between electrons and ion-species, however, in-situ and numerical measurements suggest that each stage of the cascade can have a non-negligible effect on the global dynamics [2, 3].

We argue that many problems of "classical Vlasov solvers" stem from trying to directly discretize the complicated and high-dimensional distribution functions. Thus NuFI arises from a change of paradigm: Instead of a direct discretization of f^α we approximate the characteristics. This is possible in an efficient way as they can be reconstructed on-the-fly using operator-splitting and only requires knowledge of the past electric fields at the cost of increasing the computational complexity from linear to quadratic in the number of time-steps [4]. Previous publications discussed the efficient implementation of NuFI for single- and multi-species simulations in the electro-static limit with periodic boundary conditions [4–6]. This work demonstrates how NuFI can be extended to non-periodic boundary conditions and showcases a prototype implementation of a restart to reduce the computational complexity. In Sect. 2 we give a brief introduction to NuFI followed, including multi- species simulations and handling of non-periodic boundary conditions. In Sect. 3 we discuss a restart procedure for NuFI and discuss its impact on accuracy and computational time. In Sect. 4 we showcase how NuFI can be applied by simulating an ion-acoustic shock with non-periodic boundaries.

2 Simulation of Kinetic Plasma Dynamics with NuFI

Before moving on to the main focus of this work, we want to briefly recap the ideas of the Numerical Flow Iteration (NuFI). The underlying idea of NuFI is to approximate the flow-map of the Vlasov–Poisson equation instead of directly solving for the

[1] The normalization of units is discussed in Appendix 5.

distribution function f^α. The solution of (1) can be written as

$$f^\alpha(t, x, v) = f_0^\alpha(\Phi_t^{0,\alpha}(x, v)), \tag{4}$$

where the *backward flow* $s \mapsto \Phi_t^{s,\alpha}(x, v) = (\hat{x}_\alpha(s), \hat{v}_\alpha(s))$ is the solution to

$$\begin{aligned} \tfrac{\mathrm{d}}{\mathrm{d}s}\hat{x}^\alpha(s) &= -\hat{v}^\alpha(s), & \hat{x}^\alpha(t) &= x, \\ \tfrac{\mathrm{d}}{\mathrm{d}s}\hat{v}^\alpha(s) &= -\tfrac{q_\alpha}{m_\alpha} E\left(s, \hat{x}^\alpha(s)\right), & \hat{v}^\alpha(t) &= v. \end{aligned} \tag{5}$$

To solve (5) numerically we use the Störmer–Verlet time-integration method: Starting from $\hat{x}_n^h = x$ and $\hat{v}_n^h = v$ at the time-step $t = t_n$ compute

$$\hat{v}_{i-1/2}^{h,\alpha} = \hat{v}_i^{h,\alpha} - \tfrac{\Delta t}{2}\tfrac{q_\alpha}{m_\alpha} E(t_i, \hat{x}_i^{h,\alpha}), \tag{6}$$

$$\hat{x}_{i-1}^{h,\alpha} = \hat{x}_i^{h,\alpha} - \hat{v}_{i-1/2}^{h,\alpha}, \tag{7}$$

$$\hat{v}_{i-1}^{h,\alpha} = \hat{v}_{i-1/2}^{h,\alpha} - \tfrac{\Delta t}{2}\tfrac{q_\alpha}{m_\alpha} E(t_{i-1}, \hat{x}_{i-1}^{h,\alpha}) \tag{8}$$

for $i = 0, ..., n$. Now

$$f^\alpha(t, x, v) = f_0^\alpha(\hat{x}_0^{h,\alpha}, \hat{v}_0^{h,\alpha}) + \mathcal{O}\left(\Delta t^2\right). \tag{9}$$

Note that to compute ρ via (2) we can skip the first half-step (6) as it can be recast as a transformation of the respective integral with functional determinant 1. With this we can state the full NuFI algorithm. Note that we only write it out for $d = 1$ but extending to $d = 2, 3$ is trivial [4].

Algorithm 1 Solving the Vlasov–Poisson system in $d = 1$.

function NuFI(f_0^e, f_0^i, N_t, Δt, N_x, N_v)
  Allocate a array C for the coefficients of φ ($N_t N_x$ floats).
  for $n = 0, ..., N_t$ **do**
    for $k = 0, ..., N_x$ **do**
      $\rho_k^e, \rho_k^i = 0.$
      for $l = 0, ..., N_v$ **do**
        Evaluate $\tilde{f}_e = f^e(t_n, x_k, v_l)$ and $\tilde{f}_i = f^i(t_n, x_k, v_l)$ using (9).
        $\rho_k^e \mathrel{+}= h_v \tilde{f}_e$ and $\rho_k^i \mathrel{+}= h_v \tilde{f}_i$.
      end for
      $\rho_k = q_i \rho_k^i + q_e \rho_k^e$.
    end for
    Solve the Poisson's equation via FFT to obtain $\varphi_0, ..., \varphi_{N_x}$ from $\rho_0, ..., \rho_{N_x}$.
    Interpolate $\varphi_0, ..., \varphi_{N_x}$ and store the coefficients of $\varphi_{\Delta t,h}$ in the B-Spline basis.
  end for
end function

A detailed derivation and discussion of the algorithm can be found in Kirchhart and Wilhelm's previous work [4]. The extension to multiple species and adaptive integration (instead of the mid-point integration rule used above) was presented in Wilhelm et al. [5]. A convergence analysis and accuracy comparisons to Particle-In-Cell (PIC) and semi-Lagrangian approaches was also carried out in previous works [4–6].

2.1 Handling of Boundary Conditions

In the following we list how common boundary conditions can be handled with the NuFI

- **Periodic boundary**: When the characteristic hits a periodic boundary, let it re-enter on the opposite side and continue the backwards-tracing as before.
- **In-Flow boundary**: When the characteristic hits a in-flow boundary stop the back-tracing procedure and return the value of f prescribed at the respective boundary (instead of f_0).
- **Open boundary**: No additional implementation is required for this case as we move backwards along the characteristics and thus we are not interested in characteristics leaving the domain, i. e., they are naturally accounted for.
- **Reflective boundary**: For perfect reflection it is sufficient to reflect the characteristic analogous to a reflection of a particle. If a temperature is prescribed at a wall, this is analogous to prescribing a Maxwellian as boundary value.

3 Restarting NuFI

The improved accuracy and low-memory consumption of NuFI comes at cost of having to evaluate the entire characteristic map backwards until the initial data is reached, thus the computational complexity of NuFI is quadratic, not linear, in the total number of time-steps [4, 5]. To elevate this limiting factor, in particular, considering that we are interested in kinetic instabilities and turbulence which can take substantial time periods to develop it is of interest to restart NuFI after a fixed number of time-steps throughout a longer simulation.

A simple, yet effective approach is to store values of $f^\alpha(t,\cdot,\cdot)$ on a (regular) grid with $N_x^r \times N_v^r$ degrees of freedom in phase-space every $n_r \gg 1$ time-steps and evaluating in between the grid-points using linear interpolation.

Remark 1 This naive approach only works for lower-dimensional simulations as otherwise the memory-requirement would grow too large same as for any classical approach directly approximating the distribution function. A more efficient approach would be adaptive or sparse meshes such as they are discussed in e.g. Gerhard et al. [7]. However, this is a prototype implementation to demonstrate the feasibility

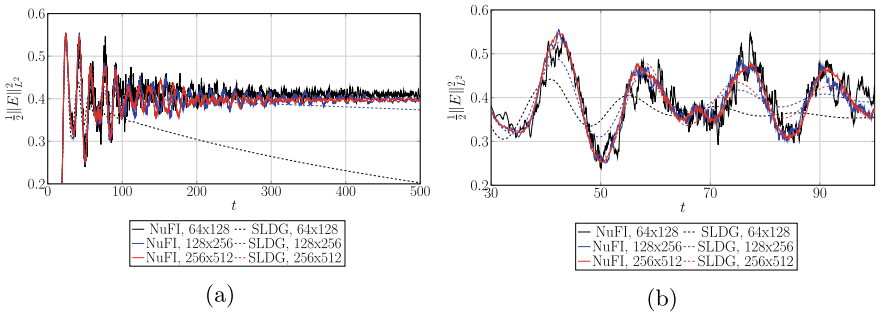

Fig. 1 A comparison of the electric energy in a two stream instability simulation between NuFI and SLDG. NuFI uses the restart procedure discussed in Sect. 3 with $n_r = 200$ and $N_x^r = N_v^r = 1024$

of restarting NuFI and therefore we kept it simple. Additionally, this type of storage is easy to compress using low-rank tensor-based approaches as was discussed in Kormann's work [8].

In the following we compare simulation results of NuFI with SLDG (Semi-Lagrangian Discontinuous Galerkin) [9]. To this end we consider the *two stream instability* benchmark, which is known as a notoriously complicated kinetic instability [4]. In Fig. 1 we compare the evolution of the electric energy over time until $T = 500$. Figure 1b zooms in on the electric energy after the kinetic instability saturates at which point the electric energy starts periodically oscillating around a fixed level. While NuFI captures this effect even with low resolution until $t = 100$, but SLDG requires a four times finer resolution to capture the oscillation even at early times. At later stages the electric energy essentially "flat-lines" and starts decreasing (the faster the lower the resolution), which is a consequence of numerical diffusion.

We also checked how restarting NuFI with above method influences its conservation properties, see Fig. 2. As expected some of the conservation properties are no longer fulfilled exactly by the restarted NuFI approach: There is a relative deviation of up to 1% for the entropy and of up to 4% for the L^2-norm until $T = 500$. The conservation of total energy seems to be broken during the first restart, when the total energy increases by roughly 1% but remains (essentially) constant afterwards. However, these drifts are still substantially lower than for SLDG with the same resolution. The error in entropy conservation is at 7% and the error in the L^2-norm exceeds 14%. Therefore we can conclude that even if NuFI looses its exact conservation properties through a this restart procedure the overall accuracy and conservation properties still substantially exceed those of SLDG.

Finally let us remark that the restart procedure indeed reduced the computational complexity back to linear for NuFI. Therefore in the case of the simulations run for Fig. 2 we observed a speed-up of a factor 35, i. e., a simulation until $T = 500$ would take 2240 s without restart, while with restart it only takes 64 s. SLDG requires for a simulation with same grid resolution roughly 20 s, i. e., is roughly 3 times faster.

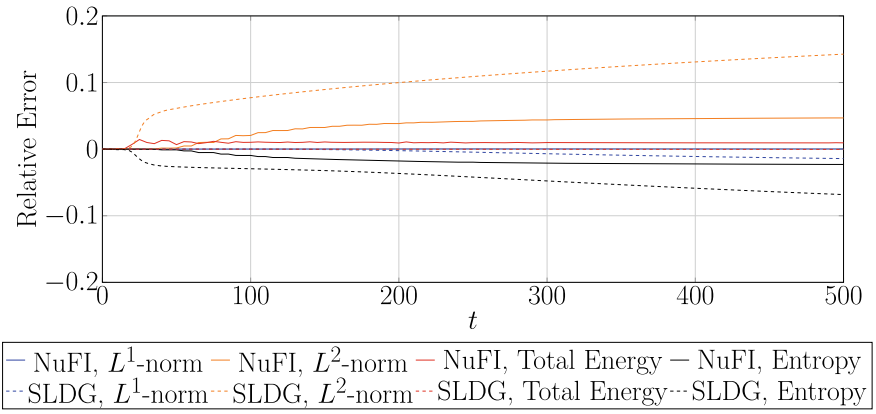

Fig. 2 Compared are the relative errors in L^1-, L^2-norm as well as total energy and entropy between NuFI and SLDG. Both approaches used a resolution of $N_x = N_v = 64$ and $\Delta t = \frac{1}{16}$ and NuFI was restarted every $n_r = 200$ time-steps on a uniform grid with $N_x^r = N_v^r = 1024$ grid points

However, when accounting for the better accuracy and conservation properties of NuFI we argue that it is worthwhile to use NuFI.[2]

4 Ion-Acoustic Shock with Reflecting Wall

After establishing in theory how NuFI can be used run simulations of the Vlasov–Poisson system with a range of boundary conditions and how it is possible to improve the computational complexity enabling longer simulations, we want to showcase some results obtained in a setting with non-periodic boundary conditions. The simulation setup is inspired by the setup used by Liseykina et al. in their work, however, with some slight modifications[3] [10].

We again restrict ourselves to $d = 1$ with only electro-static forces. This time we consider both electrons and ions (Hydrogen-ions), where we set the realistic mass ratio of $M_r = 1836$, i.e., $m_e = 1$ and $m_i = 1836$. The physical domain is from $x_{\min} = -L$ to $x_{\max} = 0$ with $L \gg 1$. The ions and electrons are initialized with unperturbed Maxwellian velocity distributions, where the ion distribution is centred around a drift speed $u_s > 0$. The right boundary is set to be a perfectly reflecting wall for both electrons and ions. The left boundary is an open boundary for particles leaving the domain and for particles entering the domain prescribes an

[2] All of the above simulations were carried out on a local workstation using a Intel(R) Xeon(R) E-2276M CPU @ 2.80GHz with 6 physical cores.

[3] Our initial goal to reproduce the results from Liseykina's work failed due to a unclear parameter choices in their work. Still we believe that the setup presented there is an interesting setup to verify a Vlasov solver in non-periodic boundary conditions.

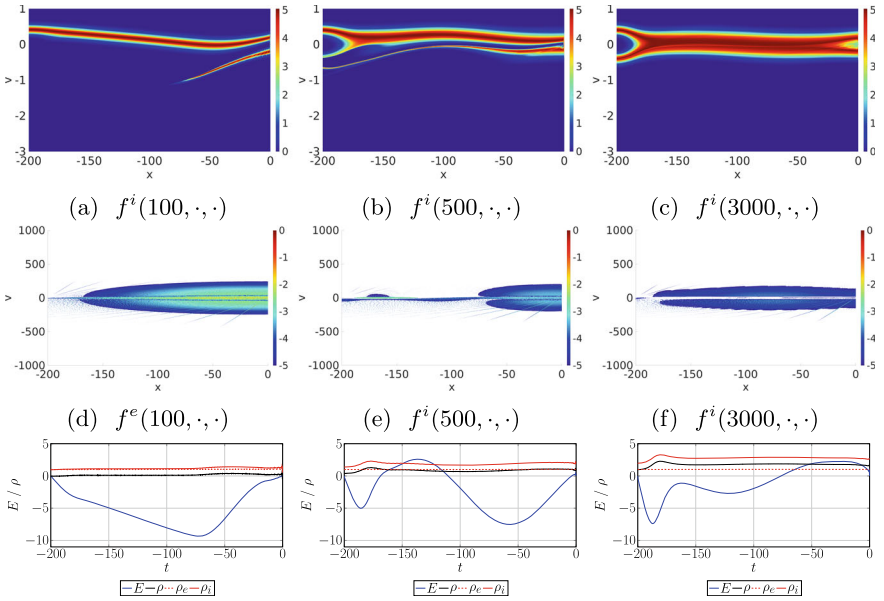

Fig. 3 Simulation of setup described in Sect. 4. Top row are the ion distribution functions at $t = 100, 500, 3000$. The middle row shows the absolute distance between electron distribution function and the Maxwellian distribution. The bottom row shows the electric field, the total charge density as well as the charge densities of the electrons and ions

in-flow with the same Maxwellian as the initial condition for the particle species. Both boundaries are set to be perfectly conducting, i.e., for the Poisson equation we set zero Neumann-boundary conditions.

Following the suggestions of Liseykina et al. in the $u_s = 0.4$ case we chose $T_e = 11475 \gg T_i = 10$ and $L = 200$. We simulate with NuFI choosing $N_x = 1024$, adaptive integration in velocity with at least $N_v = 64$ cells and a time-integration step of $\Delta t = \frac{1}{10}$. To restart NuFI we use $n_r = 200$ and $N_x^r = N_v^r = 1024$.

In Fig. 3 we display the distribution functions as well as the electric field and charge densities at the times $t = 100, 500, 3000$. To be better able to identify the shock in the electron distribution function we show the (absolute) distance between f^e and the Maxwellian (with T_e and m_e from the initial data) in a logarithmic scale. The reflected ion population moving from right to left induces a shock in the electrons, which initially also moves from right to left. When the reflected ion population reaches the left boundary a vortex starts forming.[4]

Another big vortex forms at the right boundary and grows with time. Additionally smaller vortices also form in the ion distribution in the middle and move to the left finally uniting with the stationary vortex at the left boundary.

[4] The vortex at the left boundary is a boundary effect and could be avoided by choosing L even larger. As we are only interested in triggering the shock this setup is sufficient.

5 Conclusion

In this work we discussed how the Numerical Flow Iteration (NuFI) can be extended to handle multi-species Vlasov simulations with non-periodic boundary conditions and additionally we showed that NuFI can be restarted while still remaining more accurate than other semi-Lagrangian approaches with the same resolution. Finally we successfully applied the resulting algorithm to a simulation of an ion-acoustic shock caused by an ion-population being reflected at a wall.

Acknowledgements Special thanks goes to Jan Eifert who assisted in the initial implementation of the Dirichlet extension to NuFI's codebase. Furthermore we want to acknowledge the support of from the German national high performance computing organisation (NHR) funded by the Federal Ministry of Education and Research as well as the state governments and by the Deutsche Forschungsgemeinschaft (DFG, German Research Foundation)—333849990/GRK2379 (IRTG Hierarchical and Hybrid Approaches in Modern Inverse Problems).

Normalization of Units

To normalize the quantities in our work we follow Arber and Vann: The spatial length are given in Debye length $\lambda_D = \sqrt{(\epsilon_0 k_B T_e)/(n_0 e^2)}$ (n_0 is the equilibrium number density), velocities are given in the thermal speed $v_{th} = \sqrt{(k_B T_e)/(m_e)}$, time is given in ω_p^{-1} and the electric field is in[11] $(m_e v_{th}^2)/(e\lambda_D)$.

References

1. Chen F (2015) Introduction to plasma physics and controlled fusion. Springer Cham. https://doi.org/10.1007/978-3-319-22309-4
2. Lapenta G et al (2022) Do we need to consider electrons' kinetic effects to properly model a planetary magnetosphere: the case of mercury. Space Phys, J Geophys Res. https://doi.org/10.1029/2021JA030241
3. Verscharen D et al (2019) The multi-scale nature of the solar wind. Living Rev Sol Phys. https://doi.org/10.1007/s41116-019-0021-0
4. Kirchhart M et al (2024) The Numerical flow iteration for the Vlasov-Poisson equation. SIAM J Sci Comp. https://doi.org/10.1137/23M154710X
5. Wilhelm R-P, Eifert J et al (2024) High fidelity simulations of the multi- species Vlasov equation in the electro-static, collisional-less limit. J Plasma Phys Contr Fusion. https://doi.org/10.1088/1361-6587/ad9fdb
6. Wilhelm R-P et al (2023) Introduction to the numerical flow iteration for the Vlasov-Poisson equation. Pro Appl Math Mech. https://doi.org/10.1002/pamm.202300162
7. Gerhard N et al (2022) A wavelet-free approach for multiresolution-based grid adaptation for conservation laws, communications on applied mathematics and computation. https://doi.org/10.1007/s42967-020-00101-6
8. Kormann K (2015) A Semi-Lagrangian Vlasov Solver in Tensor Train Format. SIAM Journal on Scientific Computing. https://doi.org/10.1137/140971270

9. Einkemmer L (2016) High performance computing aspects of a dimension independent semi-Lagrangian discontinuous Galerkin code. Comput Phys Commun. https://doi.org/10.1016/j.cpc.2016.01.012
10. Liseykina TV et al (2015) Ion-acoustic shocks with reflected ions: modelling and particle-in-cell simulations. J Plasma Phys. https://doi.org/10.1017/S002237781500077X
11. Arber T et al (2002) A critical comparison of Eulerian-grid-based Vlasov solvers. J Comput Phys. https://doi.org/10.1006/jcph.2002.7098

Open Access This chapter is licensed under the terms of the Creative Commons Attribution 4.0 International License (http://creativecommons.org/licenses/by/4.0/), which permits use, sharing, adaptation, distribution and reproduction in any medium or format, as long as you give appropriate credit to the original author(s) and the source, provide a link to the Creative Commons license and indicate if changes were made.

The images or other third party material in this chapter are included in the chapter's Creative Commons license, unless indicated otherwise in a credit line to the material. If material is not included in the chapter's Creative Commons license and your intended use is not permitted by statutory regulation or exceeds the permitted use, you will need to obtain permission directly from the copyright holder.

A Novel Splitting Method for Vlasov-Ampère

James A. Rossmanith and Christine Vaughan

Abstract Vlasov equations model the dynamics of plasma in the collisionless regime. A standard approach for numerically solving the Vlasov equation is to operator split the spatial and velocity derivative terms, allowing simpler time-stepping schemes to be applied to each piece separately (known as the Cheng-Knorr method). One disadvantage of such an operator split method is that the order of accuracy of fluid moments (e.g., mass, momentum, and energy) is restricted by the order of the operator splitting (second-order accuracy in the Cheng-Knorr case). In this work, we develop a novel approach that first represents the particle density function on a velocity mesh with a local fluid approximation in each discrete velocity band and then introduces an operator splitting that splits the inter-velocity band coupling terms from the dynamics within the discrete velocity band. The advantage is that the inter-velocity band coupling terms are only needed to achieve consistency of the full distribution functions, but the local fluid models within each band are sufficient to achieve high-order accuracy on global moments such as mass, momentum, and energy. The resulting scheme is verified on several standard Vlasov-Poisson test cases.

1 Introduction

Plasma is a highly energetic state of matter where electrons have dissociated from their nuclei, creating a mixture of charged particles that interact through electromagnetic forces and particle-particle collisions. In the collisionless approximation, the plasma can be modeled via the celebrated Vlasov equation. In particular, we are concerned here with the (non-dimensionalized) single-species (i.e., streaming electrons with stationary neutralizing background ions) Vlasov-Ampère system [5] in 1D1V:

J. A. Rossmanith (✉)
Department of Mathematics, Iowa State University, Ames, IA, USA
e-mail: rossmani@iastate.edu

C. Vaughan
Physicians Health Plan, Lansing, MI, USA

© The Author(s) 2026

M. Grabe et al. (eds.), *Rarefied Gas Dynamics*, Springer Aerospace Technology,
https://doi.org/10.1007/978-3-032-00094-1_43

$$f_{,t} + v f_{,x} - E(t,x) f_{,v} = 0, \quad E_{,t} = \mathbb{M}_1(t,x) - J_0, \tag{1}$$

$$\mathbb{M}_1(t,x) = \int_{-\infty}^{\infty} v f(t,x,v)\, dv, \quad J_0 = \frac{1}{b-a} \int_a^b \mathbb{M}_1(t=0,x)\, dx, \tag{2}$$

where $t \in \mathbb{R}_{\geq 0}$ is time, $x \in [a,b]$ is the spatial coordinate, $v \in \mathbb{R}$ is the velocity coordinate, $f(t,x,v) : \mathbb{R}_{\geq 0} \times [a,b] \times \mathbb{R} \mapsto \mathbb{R}_{\geq 0}$ is the particle density function (PDF) describing the distribution of electrons in phase space, $E(t,x) : \mathbb{R}_{\geq 0} \times [a,b] \mapsto \mathbb{R}$ is the electric field, $\mathbb{M}_1(t,x) : \mathbb{R}_{\geq 0} \times [a,b] \mapsto \mathbb{R}$ is the electron momentum density, and $J_0 \in \mathbb{R}$ is the stationary background ion momentum density. The initial electric field can be computed from the Gauss' law:

$$E_{,x} = \rho_0 - \rho(t,x), \ \rho(t,x) = \int_{-\infty}^{\infty} f(t,x,v)\, dv, \ \rho_0 = \frac{1}{b-a} \int_a^b \rho(t=0,x)\, dx, \tag{3}$$

where $\rho(t,x) : \mathbb{R}_{\geq 0} \times [a,b] \mapsto \mathbb{R}_{\geq 0}$ is the electron mass density and $\rho_0 \in \mathbb{R}$ is the stationary background ion mass density.

A standard approach for numerically solving the Vlasov equation is to operator split the spatial and velocity derivative terms, allowing simpler time-stepping schemes to be applied to each piece separately (known as the Cheng-Knorr method [1]):

$$\textbf{Problem A:} \quad f_{,t} + v f_{,x} = 0, \quad E_{,t} = \mathbb{M}_1(t,x) - J_0; \tag{4}$$

$$\textbf{Problem B:} \quad f_{,t} - E f_{,v} = 0. \tag{5}$$

One disadvantage of such an operator split method is that the order of accuracy of fluid moments (e.g., mass, momentum, and energy) is restricted by the order of the operator splitting (second-order accuracy in the Cheng-Knorr [1] case, which is based on Strang operator splitting [10].)

2 A Novel Operator Splitting Method

We develop in this work a novel operator splitting approach for the Vlasov-Ampère system (1)–(2). We begin by discretizing the truncated velocity space, $v \in [V_{\min}, V_{\max}]$, into non-overlapping *velocity bands* each of width and center:

$$\Delta v = (V_{\max} - V_{\min})/N_v, \quad v_j = V_{\min} + \left(j - \frac{1}{2}\right) \Delta v \quad \text{for} \quad j = 1, \ldots, N_v. \tag{6}$$

where $V_{\max}$ is the maximum of velocity domain, $V_{\min}$ is the minimum velocity, and N_v is the number of velocity layers. Within each velocity layer, we define the *local*

fluid moments as,

$$\mathbb{M}_{\ell}^{(j)} = \int_{v_{j-\frac{1}{2}}}^{v_{j+\frac{1}{2}}} v^{\ell} f(t,x,v)\, dv, \quad \ell = 0,1,2,3,4, \tag{7}$$

where $v_{j\pm\frac{1}{2}} = v_j \pm \Delta v/2$. Theoretically, we can take as many local fluid moments as desired; in the current work, we restrict ourselves to five (e.g., $\ell = 0,1,2,3,4$). In practice, at least the first three moments should be included (mass, momentum, energy) to guarantee high-order accuracy on the lowest-order statistics. The more moments included, the more computationally complex the system in each velocity band will be. Five moments were chosen to balance accuracy and computational complexity. We then take Vlasov equation (1), multiply by v^{ℓ}, and integrate over each discrete velocity band, which, after integration by parts in velocity, becomes the following expression:

$$\mathbb{M}_{\ell,t}^{(j)} + \mathbb{M}_{\ell+1,x}^{(j)} - \left[E v^{\ell} f\right]_{v_{j-\frac{1}{2}}}^{v_{j+\frac{1}{2}}} = -\ell \mathbb{M}_{\ell-1}^{(j)} E, \tag{8}$$

for $j = 1,\ldots,N_v$ and $\ell = 0,1,2,3,4$. We note that the global moments (e.g., mass, momentum, and energy) can be directly computed from the local moments:

$$\mathbb{M}_{\ell} = \sum_{j=1}^{N_v} \mathbb{M}_{\ell}^{(j)}, \quad \text{for} \quad \ell = 0,1,2,3,4. \tag{9}$$

In each velocity band, we arrive at the following system of local moments:

$$\underline{\mathbb{M}}_{,t}^{(j)} + \underline{\underline{A}}^{(j)}\, \underline{\mathbb{M}}_{,x}^{(j)} = -E\underline{S}^{(j)} + E\underline{S}_{+}^{(j)} f\big|_{v_{j+\frac{1}{2}}} - E\underline{S}_{-}^{(j)} f\big|_{v_{j-\frac{1}{2}}}, \tag{10}$$

where

$$\underline{\mathbb{M}}^{(j)} = \begin{bmatrix} \mathbb{M}_0^{(j)} \\ \mathbb{M}_1^{(j)} \\ \mathbb{M}_2^{(j)} \\ \mathbb{M}_3^{(j)} \\ \mathbb{M}_4^{(j)} \end{bmatrix}, \ \underline{\underline{A}}^{(j)} = \begin{bmatrix} 0 & 1 & 0 & 0 & 0 \\ 0 & 0 & 1 & 0 & 0 \\ 0 & 0 & 0 & 1 & 0 \\ 0 & 0 & 0 & 0 & 1 \\ A_{51} & A_{52} & A_{53} & A_{54} & A_{55} \end{bmatrix}, \ \underline{S}^{(j)} = \begin{bmatrix} 0 \\ \mathbb{M}_0^{(j)} \\ 2\mathbb{M}_1^{(j)} \\ 3\mathbb{M}_2^{(j)} \\ 4\mathbb{M}_3^{(j)} \end{bmatrix}, \ \underline{S}_{\pm}^{(j)} = \begin{bmatrix} 1 \\ v_{j\pm\frac{1}{2}} \\ v_{j\pm\frac{1}{2}}^2 \\ v_{j\pm\frac{1}{2}}^3 \\ v_{j\pm\frac{1}{2}}^4 \end{bmatrix}, \tag{11}$$

where

$$A_{51} = \frac{5\Delta v^4 v_j}{336} - \frac{5\Delta v^2 v_j^3}{18} + v_j^5, \quad A_{52} = \frac{-5\Delta v^4}{336} + \frac{5\Delta v^2 v_j^2}{6} - 5v_j^4,$$
$$A_{53} = \frac{-5\Delta v^2 v_j}{6} + 10v_j^3, \quad A_{54} = \left(\frac{5}{18}\right)\left(\Delta v^2 - 36v_j^2\right), \quad A_{55} = 5v_j. \tag{12}$$

It can readily be shown that $\underline{\underline{A}}^{(j)}$ is fully diagonalizable with only real eigenvalues. For a full derivation, please see Vaughan [11].

We note that the first three terms in equation (10) are entirely local to the j^{th} velocity band, and only the final two terms in (10) are responsible for coupling the j^{th} band to the $j+1$ and $j-1$ bands. This suggests a new operator-splitting approach:

$$\textbf{Problem A:} \quad \underline{\mathbb{M}}_{,t}^{(j)} = E\underline{S}_{+}^{(j)} f\Big|_{v_{j+\frac{1}{2}}} - E\underline{S}_{-}^{(j)} f\Big|_{v_{j-\frac{1}{2}}}; \tag{13}$$

$$\textbf{Problem B:} \quad \underline{\mathbb{M}}_{,t}^{(j)} + \underline{\underline{A}}^{(j)}\,\underline{\mathbb{M}}_{,x}^{(j)} = -E\underline{S}^{(j)}, \quad E_{,t} = \mathbb{M}_1(t,x) - J_0. \tag{14}$$

Just as in Cheng and Knorr [1], we introduce Strang operator splitting [10]: we will solve **Problem A** on a half time step, $\frac{\Delta t}{2}$, followed by solving **Problem B** on a full time step, Δt, and then finally again solving **Problem A** on a half time.

Proposition 1 *Under the assumption that the distribution function, f, is zero at $v = V_{min}$ and $v = V_{max}$, the operator splitting technique shown in (13) and (14) clearly introduces an $\mathcal{O}\left(\Delta t^2\right)$ splitting error into the accuracy of the PDF, f, but there is no operator splitting error in the global moments: $\mathbb{M}_0, \ldots, \mathbb{M}_4$.*

Proof The global moments, $\mathbb{M}_0, \mathbb{M}_1, \mathbb{M}_2, \mathbb{M}_3, \mathbb{M}_4$, as defined by (9) remain constant during **Problem A**, since $\underline{S}_{+}^{(j)} = \underline{S}_{-}^{(j+1)}$ for all j, and summing over j in (13) results in a telescoping series such that the only remaining terms involve f at $v = V_{\text{min}}$ and $v = V_{\text{max}}$, which we assume are zero. □

3 Numerical Method

We discretize (13)–(14) using the Lax-Wendroff discontinuous Galerkin (LxW-DG) as described in Johnson et al. [4], which is based on previous versions of the LxW-DG work of Qiu et al. [7] and Gassner et al. [2]. The method allows us to discretize in space and time with piecewise polynomials of degree M_{O} (i.e., $\mathcal{P}^{M_{\text{O}}}$), which in the case of smooth solutions results in errors of size $\mathcal{O}\left(\Delta t^{M_{\text{O}}+1} + \Delta x^{M_{\text{O}}+1}\right)$. We omit the details of this here and instead refer the reader to Johnson et al. [4].

The novel aspect of this work is the introduction of **Problem A** (13); and, as such, we include details here on how this equation is solved numerically. If $E \geq 0$,

we construct the following Taylor expansion comparing moments at $t = t^n$ and $t = t^n + \Delta t$ (see Vaughan [11]):

$$\underline{\underline{\mathbb{M}}}^{(j)}(t^n + \Delta t) = \underline{\underline{\mathbb{M}}}^{(j)} - \Delta t \left(\underline{S}_+^{(j)} E \beta_+^{(j)} - \underline{S}_-^{(j)} E \beta_+^{(j-1)} \right) + \mathcal{O}(\Delta t^5), \tag{15}$$

where

$$\begin{aligned} \beta_+^{(j)} &= \left(1 - \frac{5\kappa}{2} + \frac{25\kappa^2}{6} - \frac{125\kappa^3}{24}\right) \alpha_+^{(j)} + \left(\frac{\kappa}{2} - \frac{5\kappa^2}{3} + \frac{25\kappa^3}{8}\right) \alpha_+^{(j-1)} \\ &+ \left(\frac{\kappa^2}{6} - \frac{5\kappa^3}{8}\right) \alpha_+^{(j-2)} + \left(\frac{\kappa^3}{24}\right) \alpha_+^{(j-3)}, \; \kappa = \frac{5E\Delta t}{\Delta v}, \; \alpha_+^{(j)} = \underline{N}_+^{(j)} \cdot \underline{\underline{\mathbb{M}}}^{(j)}, \end{aligned} \tag{16}$$

where $\underline{N}_+^{(j)}$ is an interpolated vector describing the distribution function at the upper interface of the velocity band j. There is a similar formula for $E \leq 0$ [11].

We define on each element, Gauss-Legendre quadrature points, ξ_m, for $m = 1, 2, \ldots, M_{\mathrm{O}}$. We also define the Legendre polynomials $\psi_k(\xi)$ for $k = 1, 2, \ldots, M_{\mathrm{O}}$. Putting all the pieces together, we find that

$$\underline{\mathbb{M}}_k^{(j)}(t^n + \Delta t) = \underline{\mathbb{M}}_k^{(j)}(t^n) - \Delta t \left(\underline{\gamma}_k^{(j+\frac{1}{2})} - \underline{\gamma}_k^{(j-\frac{1}{2})} \right) + \mathcal{O}(\Delta t^5), \tag{17}$$

where

$$\underline{\gamma}_k^{(j\pm\frac{1}{2})} = \underline{S}_\pm^{(j)} \left[\frac{1}{2} \sum_{m=1}^{M_{\mathrm{O}}} \omega_m \psi_\ell(\xi_m) \beta_m^{(j\pm\frac{1}{2})} \right], \tag{18}$$

where

$$\beta_m^{(j-\frac{1}{2})} = \min(E(\xi_m), 0)\, \beta_-^{(j-1)} + \max(E(\xi_m), 0)\, \beta_+^{(j)}, \tag{19}$$

$$\beta_m^{(j+\frac{1}{2})} = \min(E(\xi_m), 0)\, \beta_-^{(j)} + \max(E(\xi_m), 0)\, \beta_+^{(j+1)}. \tag{20}$$

4 Numerical Examples

In this section we discuss the examples used to test the velocity-banded quadrature-based moment closure. We begin with a forced problem, using the method of manufactured solutions. We used this example to perform a convergence test to show the method converges up to fourth order in space and time. We also show that error in space and time as well as round-off error dominate the error over that produced by the discretization of the velocity space. Next, we show the results from the weak Landau damping problem, the strong Landau damping problem, and two-stream instability. Finally, we show the results from a plasma sheath example.

Table 1 Relative L^2 errors for the forced manufactured problem with 200 bands for the Vlasov-Ampère equation with the $\mathcal{P}^1$ (Columns 2 and 3), $\mathcal{P}^2$ (Columns 4 and 5), and $\mathcal{P}^3$ (Columns 6 and 7) Lax-Wendroff DG schemes

N	e_N ($M_\mathrm{O}=1$)	$\log_2 \frac{\mathrm{e}_{N/2}}{\mathrm{e}_N}$	e_N ($M_\mathrm{O}=2$)	$\log_2 \frac{\mathrm{e}_{N/2}}{\mathrm{e}_N}$	e_N ($M_\mathrm{O}=3$)	$\log_2 \frac{\mathrm{e}_{N/2}}{\mathrm{e}_N}$
20	5.203e−02	–	2.995e−03	–	1.144e−04	–
40	1.454e−02	1.840	4.075e−04	2.878	7.829e−06	3.869
80	3.890e−03	1.902	4.964e−05	3.037	4.927e−07	3.990
160	9.943e−04	1.968	6.170e−06	3.008	3.098e−08	3.991
320	2.502e−04	1.991	7.715e−07	3.000	2.335e−09	3.730

Here N refers to the number of spatial elements, $\Delta x = 2\pi/N$, and $\Delta t = \mathrm{CFL} \times \Delta x / V_{\max}$, where $V_{\max} = 4$ and $\mathrm{CFL} = 0.09$

4.1 Manufactured Solution

Consider the forced Vlasov-Poisson equation:

$$f_{,t} + v f_{,x} + E f_{,v} = \psi(t,x,v), \quad E_{,x} = \sqrt{\pi} - \int_{-\infty}^{\infty} f(t,x,v)\, dv, \tag{21}$$

on the domain $(t,x,v) \in [0,0.1] \times [-\pi,\pi] \times [-4,4]$ with periodic boundary conditions in x. The forced exact solution is given by [8]:

$$f(t,x,v) = (2 - \cos(2x - 2\pi t))\, e^{-\frac{(4v-1)^2}{4}}, \; E(t,x) = \frac{\sqrt{\pi}}{4} \sin(2x - 2\pi t), \tag{22}$$

$$\psi(t,x,v) = \frac{1}{2} S e^{-\frac{1}{4}(4v-1)^2} \left[\left(2\sqrt{\pi} + 1\right)\left(4v - 2\sqrt{\pi}\right) - \sqrt{\pi}\,(4v-1)\, C \right], \tag{23}$$

where $S := \sin(2x - 2\pi t)$ and $C := \cos(2x - 2\pi t)$. A convergence table for 3 different polynomial orders are shown in Table 1. In the convergence study, we are decreasing Δx and Δt (both are proportional to $1/N$), but fixing Δv (i.e., the number of velocity bands).

4.2 Weak and Strong Landau Damping

Landau damping is a well-studied problem both numerically and analytically [1, 3], and the damping effect of the L_2 norm of the electric field is well-established and has been rigorously studied by Mouhot and Villani [6]. This work earned Villani the 2010 Fields Medal. Given that the Landau damping problem is so well-studied, it is a

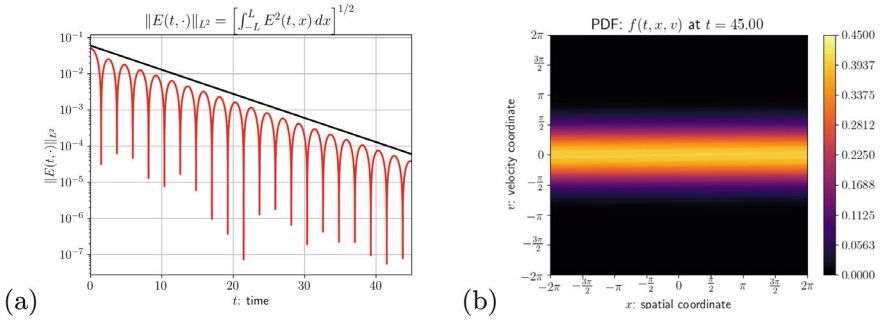

Fig. 1 Weak Landau damping problem. Panel **a** shows the exponential decay of the L_2-norm of the electric field and the line $0.06e^{\gamma t}$ with the numerically computed decay rate $\gamma = -0.1536$, and Panel **b** shows the reconstructed PDF

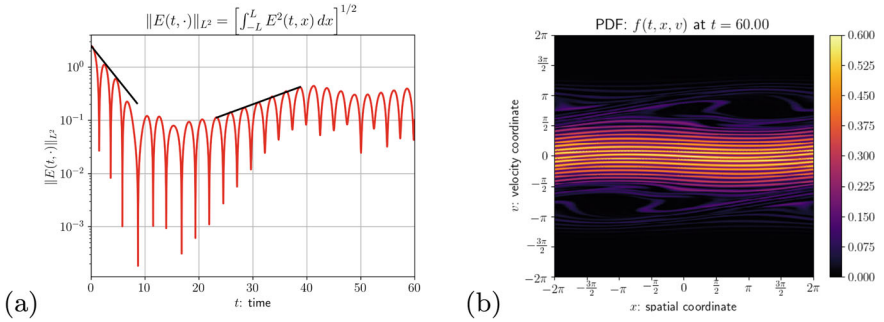

Fig. 2 Strong Landau damping problem. Panel (a) shows the initial exponential decay of the L_2-norm of the electric field ($\gamma_1 = -0.2918$) followed by exponential growth due to nonlinear effects ($\gamma_2 = 0.08584$), and Panel (b) shows the reconstructed PDF

favorite test example to study methods for plasma dynamics. The initial distribution function for the weak Landau damping problem is,

$$f(t=0,x,v) = (1+\alpha\cos(kx))\,\frac{1}{\sqrt{2\pi}}e^{-\frac{v^2}{2}}, \tag{24}$$

with $\alpha = 0.01$ (weak) or $\alpha = 0.5$ (strong) and $k = 0.5$ on the domain $(x,v) \in [-2\pi, 2\pi] \times [-2\pi, 2\pi]$.

The weak Landau simulation was run to $t = 45$ with 40 cells in space and 80 bands in velocity. The simulation results are presented in Fig. 1. Panel (a) shows the damping of the L_2 norm of the electric field over time. Panel (b) shows the reconstructed distribution function at the final time. These results closely match those from the literature.

The strong Landau simulation was run to $t = 60$ with 40 cells in space and 80 bands in velocity. The simulation results are presented in Fig. 2. Panel (a) shows the

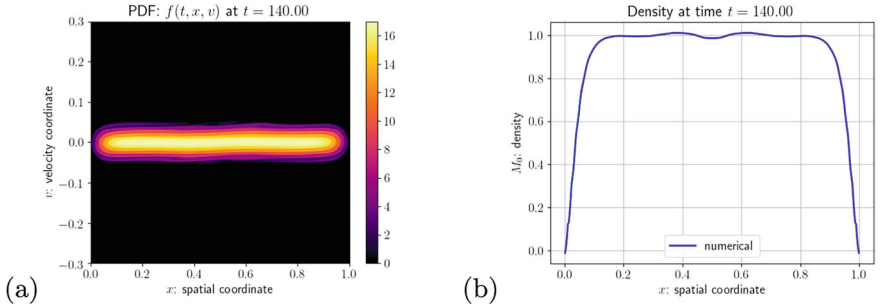

Fig. 3 Plasma sheath problem. Panel **a** shows the PDF, and Panel **b** shows the density

damping and growth of the L_2 norm of the electric field over time. Panel (b) shows the reconstructed distribution function at the final time. These results closely match those from the literature.

4.3 Plasma Sheath

The plasma sheath problem is a classic example where the distribution function represents the electrons inside the region, $0 \leq x \leq L$. We use a zero-inflow boundary condition, assuming no electrons can enter the domain. The initial condition is given by

$$f(0, x, v) = \frac{\rho_0}{\sqrt{2\pi\theta_0}} e^{-\frac{v^2}{2\theta_0}}. \tag{25}$$

The problem is solved on the domain $(t, x, v) \in [0, 140] \times [0, 1] \times [-0.2, 0.2]$. The setup shown here is identical to that in Seal [9].

Figure 3 displays the results of the simulation with 80 grid cells in space and 80 bands in velocity. Panel (a) shows the PDF and Panel (b) shows the density at $t = 140$, where a plasma sheath has formed due to the net positive charge, keeping the electrons from leaving the domain. These results match those found in literature (e.g., Figure 20(b) of Seal [9]).

5 Conclusions

In this work, a novel discontinuous Galerkin scheme for the Vlasov-Ampère system was developed. The scheme uses a spectral element moment-closure that results in a series of fluid models in each velocity band. Strang operator splitting is introduced to decouple these local fluid models and their inter-velocity coupling term. The coupling terms do not directly affect the global moments (e.g., mass, momentum, and energy);

thus, high-order accuracy is achieved on the global moments. The scheme was tested on several numerical examples.

Acknowledgements We would like to thank the anonymous referees for their thoughtful comments and suggestions that helped to improve this paper. This research was partially funded by NSF Grants DMS–2012699 and DMS–2410538.

References

1. Cheng C, Knorr G (1976) The integration of the Vlasov equation in configuration space. J Comput Phys 22:330–351
2. Gassner G, Dumbser M, Hindenlang F, Munz C-D (2011) Explicit one-step time discretizations for discontinuous Galerkin and finite volume schemes based on local predictors. J Comput Phys 230:4232–4247
3. Heath RE, Gamba IM, Morrison PJ, Michler C (2012) A discontinuous Galerkin method for the Vlasov-Poisson system. J Comput Phys 231:1140–1174
4. Johnson ER, Rossmanith JA, Vaughan C (2023) Positivity-preserving Lax-Wendroff discontinuous Galerkin schemes for quadrature-based moment-closure approximations of kinetic models. J Sci Comput 95
5. Landau L (1946) On the vibrations of the electronic plasma. J Phys (USSR) 10:25–34
6. Mouhot C, Villani C (2010) Landau damping. J Math Phys 51
7. Qiu J, Dumbser M, Shu C-W (2005) The discontinuous Galerkin method with Lax-Wendroff type time discretizations. Comput Methods Appl Mech Engr 194:4528–4543
8. Rossmanith JA, Seal DC (2011) A positivity-preserving high-order semi-Lagrangian discontinuous Galerkin scheme for the Vlasov-Poisson equations. J Comput Phys 230:6203–6232
9. Seal DC (2012) Discontinuous Galerkin methods for vlasov models of plasma. PhD thesis, University of Wisconsin. https://www.proquest.com/pqdtglobal/docview/1022644798/
10. Strang G (1968) On the construction and comparison of difference schemes. SIAM J Numer Anal 5:506–517
11. Vaughan C (2021) Spectral element moment-closure methods for kinetic Vlasov models of plasma. PhD thesis, Iowa State University. https://www.proquest.com/pqdtglobal/docview/2572602286/

Open Access This chapter is licensed under the terms of the Creative Commons Attribution 4.0 International License (http://creativecommons.org/licenses/by/4.0/), which permits use, sharing, adaptation, distribution and reproduction in any medium or format, as long as you give appropriate credit to the original author(s) and the source, provide a link to the Creative Commons license and indicate if changes were made.

The images or other third party material in this chapter are included in the chapter's Creative Commons license, unless indicated otherwise in a credit line to the material. If material is not included in the chapter's Creative Commons license and your intended use is not permitted by statutory regulation or exceeds the permitted use, you will need to obtain permission directly from the copyright holder.

Modeling Gap Closure Within Vaporizing Transmission Lines of Pulsed Power Machines Using Particle-in-Cell Direct Simulation Monte Carlo (PIC-DSMC)

Grace Kirk, Georgii Oblapenko, David Sirajuddin, Christopher Moore, David Goldstein, and Philip Varghese

Abstract We use a hybrid PIC-DSMC approach for modeling gap closure and examine the effectiveness of the novel variable weight DSMC method Event Splitting for this problem. Event Splitting has been shown to decrease computational costs and simulation noise in 0-D and 1-D electrical breakdown simulations by modeling all collision outcomes with the probability of each event reflected in post-collision macroparticle weights. Gap closure occurs in high-energy vacuum diodes where vaporized diode material creates a quasineutral plasma capable of disrupting the current. We examine the framework of our reduced surrogate simulation for reaching a fully closed gap and provide a discussion of the physics present during wave propagation across the domain as the quasineutral plasma evolves. Our results show that due to a lack of a more robust merging scheme, event splitting provides little benefit for the gap closure simulations considered in the present work.

Keywords PIC · DSMC · Event splitting · Gap closure

G. Kirk (✉) · D. Goldstein · P. Varghese
ASE-EM Department, The University of Texas at Austin, Austin, TX, USA
e-mail: grace.kirk@utexas.edu

G. Oblapenko
Applied and Computational Mathematics, RWTH Aachen, Aachen, Germany

G. Kirk · D. Goldstein · P. Varghese
Oden Institute for Computational Engineering and Sciences, The University of Texas at Austin, Austin, TX, USA

D. Sirajuddin · C. Moore
Sandia National Laboratories, Albuquerque, NM, USA

© The Author(s) 2026

M. Grabe et al. (eds.), *Rarefied Gas Dynamics*, Springer Aerospace Technology,
https://doi.org/10.1007/978-3-032-00094-1_44

1 Introduction

1.1 Gap Closure

Gap closure is a phenomenon associated with the high-energy physics of vacuum diodes. "Closing the gap" describes the formation and expansion of a quasineutral plasma between the anode and the cathode [6]. In a terawatt pulsed-power accelerator, the combination of resistive heating from mega-ampere currents and the energy deposition from relativistic electrons impacting the anode lead to vaporizing diode surfaces during operation. Vaporized particles diffuse into the vacuum, where they are ionized by collisions with electrons. This causes the number density of ions to increase, which slows the electrons, resulting in a build-up of charge density capable of screening the externally applied electric field to near zero. Once the expanding plasma fills the entire gap, the lack of gradients in the electric potential will stop electron acceleration, effectively terminating the discharge [12]. Increasing simulation fidelity of gap closure physics is needed to develop predictive modeling capabilities for pulsed power engineering needs.

1.2 Modeling Methods

Although not the usual application of these methods, modeling gap closure requires the hybrid coupling of PIC and DSMC to capture proper ionization rates, particle accelerations, and electrostatic field variations while still maintaining the coupling between the collision and field solver.

Particle-in-Cell (PIC) is a particle approach focused on modeling ideal plasma dynamics with either electrostatic or electromagnetic fields. For our code the domain is discretized using an Eulerian focus that allows electrostatic information to be interpolated from the grid nodes to the particles, accelerating the computational macroparticles and then interpolating charges back to the grid to solve Poisson's equation for the new electric field [3].

$$\nabla^2 \Phi = \frac{\rho}{\varepsilon_0} = \frac{e(n_i - n_e)}{\varepsilon_0} \tag{1}$$

Here Φ is the electric potential, ρ is the charge density, ε_0 is the permittivity of free space, and n_i and n_e are the number densities of ions and electrons, respectively.

Direct Simulation Monte Carlo (DSMC) is a kinetic method that leverages first principle equations of motion and statistical collision ensembles to solve the Boltzmann equation [2] that describes the evolution of the particle velocity distribution function f in physical and velocity space:

$$\frac{\partial f}{\partial t} + \boldsymbol{v} \cdot \nabla_x f + \boldsymbol{a} \cdot \nabla_v f = \left(\frac{\partial f}{\partial t}\right)_{coll} \tag{2}$$

where $\boldsymbol{v}$ is the velocity, $\boldsymbol{a}$ is the acceleration, and the effect of collisions is represented by $\left(\frac{\partial f}{\partial t}\right)_{coll}$.

Event Splitting (ES) is a novel numerical method that realizes all collisional outcomes with macroparticle weights commensurate with the event probabilities – essentially every possible outcome is modeled. This method has been proven to reduce noise with fewer macroparticles than standard DSMC when applied to plasma flows. This can result in lower computational costs since rare events are simulated more efficiently [8–10]. However, a consequence of this method is an explosion of macroparticle number due to the frequent particle splitting: every collision pair produces additional particles whereas standard DSMC follows the accept-reject method. In this work, we mitigate costly exponential growth using the octree merging method, which periodically collapses the particle distribution function into a much smaller set of particles while preserving mass, momentum, angular momentum, and energy [7].

2 Simulation Setup

Our goal is not to create a self-consistent diode gap closure simulation but rather to exercise novel approaches (e.g. ES) to see if they could benefit such simulations. Towards that end, we design a surrogate simulation that produces gap closure so that we can grade these techniques on our problem of interest. Our "bare bones" simulation has a monoenergetic beam of neutrals and electrons fluxing into a vacuum while an external electric field is applied.

The focus of our study was on gap closure within the pulsed-power machine Saturn at Sandia National Labs. Specifically, we study its last millimeter of circuitry where there is a field of 4×10^8 V/m [11]. In these conditions, electrons are shot across the gap with relativistic velocities, while neutrals (accumulating to densities on the order of 10^{25} particles/m^3) passively diffuse into the vacuum, resulting in extremely steep density gradients. To reduce the high computational costs in terms of spatial discretization and time steps required as well as avoid relativistic effects, we scaled the problem down to a smaller domain (gap length L) and lower applied voltage while maintaining the original environment through a base Knudsen number ($Kn = \lambda_{MFP}/L = 0.02$) and electric field ($\nabla\Phi = V/L = 400$ MV/m) [11].

Within our simulation, we control these two properties – loosely, as this is a very dynamic environment – with the fluxes of neutrals and electrons and the chosen gap length. We further simplify the problem by using argon as our neutral of choice for its monoatomic structure (breakdown of a molecule would result in several species) and well documented cross-sections. Its flux ($\Gamma_{\mathrm{Ar}} = n_{\mathrm{Ar}} v_{\mathrm{Ar}}$) was chosen such that the collisionality was high enough for breakdown of the injected material to occur. To maintain a realistic electron flux we used the Child-Langmuir space-charge limit law.

$$J = \frac{4\varepsilon_0}{9}\sqrt{\frac{2e}{m_e}}\frac{V^{\frac{3}{2}}}{L^2} \tag{3}$$

Here, e is the electron charge, m_e is the electron mass, V is the applied voltage, and L the gap length [5]. A second-order finite difference scheme was used for the field solver, with linear basis functions for interpolation of the charge density and electrostatic forces. The velocity Verlet time integrator was used.

The necessary resolution for the temporal and spatial scales are determined by the plasma frequency ω_{pe} and Debye length λ_D for electrons and the mean free path λ_{MFP} and mean time between collisions τ for argon.

$$\Delta t_e \approx \frac{1}{\omega_{pe}} = \sqrt{\frac{m_e\varepsilon_0}{n_e e^2}}, \tag{4}$$

$$\Delta t_{\mathrm{Ar}} \approx \tau = \frac{1}{n_{\mathrm{Ar}}\sigma_i v_{\mathrm{Ar}}} \approx \frac{1}{\Gamma_{\mathrm{Ar}}\sigma_i} \tag{5}$$

$$\Delta\lambda_e \approx \lambda_D = \sqrt{\frac{\varepsilon_0 k_B T_e}{n_e e^2}}, \tag{6}$$

$$\Delta\lambda_{\mathrm{Ar}} \approx \lambda_{MFP} = \frac{1}{n_{\mathrm{Ar}}\sigma_{iz}} \tag{7}$$

The number densities of electrons and argon are denoted by n_e and n_{Ar}, respectively. T_e is the temperature of electrons, k_B is Boltzmann's constant, and σ_{iz} represents the ionization cross-section. Cross-sections for Ar-Ar and Ar-e collisions were determined using the Variable Hard Sphere (VHS) model and the IST-LISBON database, respectively [1, 2].

When selecting flux values, it was critical to assess their influence on the required spatial and temporal resolution and whether such demands were computationally feasible. In typical gap closure scenarios, it is impractical to fully resolve the smallest Debye length and mean free path (nm scale), particularly near the cathode surface. Fortunately, the most extreme gradients are highly localized near the cathode wall, where vaporized material is rapidly ablated and diffused into the domain. In this small region, the Debye length and mean free path were under-resolved with our uniform mesh by factors of approximately 370% and 850%, respectively. Despite this, we maintain stable and physically accurate solutions (e.g., consistent expansion velocities). In the bulk plasma away from the cathode, these scales were substantially better resolved, with the Debye length and mean free path orders of magnitude larger. Any numerical grid heating that arose was confined to a narrow region near the cathode, and affected particles quickly migrated to areas with higher spatial resolution. A more detailed discussion can be found in the thesis by Grace Kirk [4].

Ultimately we identified a "Goldilocks zone" of gap length and simulation parameters (Table 1) that balanced computational constraints with the physical fidelity required for studying gap closure. Achieving this involved applying standard

Table 1 Final parameters used for simulating gap closure

Parameter	Value	Units
Neutral flux	1.5×10^{29}	$m^{-2}\ s^{-1}$
Electron flux	1.0×10^{29}	$m^{-2}\ s^{-1}$
Macroparticles per cell	250:500	–
Wall temperature	3000	K
Neutral initial velocity	9.82×10^{3}	$m\ s^{-1}$
Electron initial velocity	0	$m\ s^{-1}$
Voltage	2000	V
Domain length	5.0×10^{-6}	m
Cells	500	–
Time step size	1.0×10^{-16}	s
Number of time steps	30×10^{6}	–

PIC-DSMC resolution Eqs. (4–7) alongside iterative trial-and-error adjustments to mitigate numerical grid heating and preserve accuracy.

3 Results and Discussion

The following results are broken down into several significant phases (Table 2) and are graphically represented by the number density of individual species and the electric field (Fig. 1). Attaining these results of full gap closure took about three days using sequential computing on a workstation.

As seen in the top left pane of Fig. 1, the electrons fill the entire gap with a wide density distribution, whereas argon lags significantly behind. As the collisionality increases near the right side from the continuous argon injection, the electron density spread narrows (from having a range of $10^{20} : 10^{23}$ to $5 \times 10^{21} : 5 \times 10^{22}$ m^{-3}) and the number of ions increases. The electrons begin to be slowed by increased collisions and a growing attraction to the denser ion region. The slowed electrons

Table 2 Gap closure phases and their descriptions

Phase	Description
Pre-ionization ($T \approx 9$ ps)	Flux of neutrals and electrons off one of the diode surfaces
Initial ionization ($T \approx 1$ ns)	Significant ionization of neutral argon leading to ion creation
Steady quasineutral expansion ($T \approx 2$ ns)	Plasma expansion continues
Gap closure ($T \approx 2.7$ ns)	The plasma fills the gap

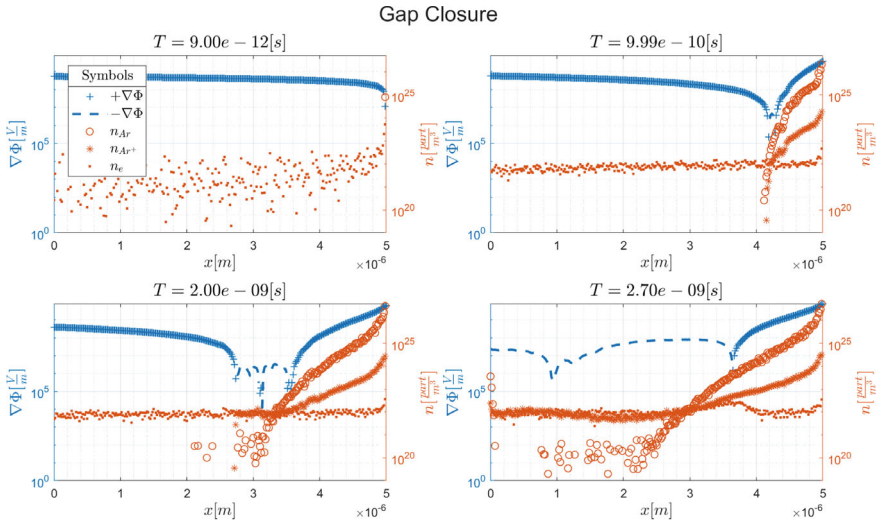

Fig. 1 Gap Closure Phases: Pre-Ionization (Top Left): steady electric field with an electron beam; Significant Ionization (Top Right): electric field varies from increase in charged particles; Steady Quasineutral Expansion (Bottom Left): larger regions of electric field screening by plasma growth; Closure (Bottom Right): field reversal with the plasma filling entire gap. Note log scales used for y-axis where the $-$ and $+$ signs denote positive and negative electric field

will then neutralize or even reverse the electric field (depending on local electron densities). The continual diffusion and ionization of neutrals acts as fuel to the plasma, expanding it further across the gap until it fills the full gap, reversing most of the electric field. This then quickly leads to an interruption of the current as there is no continuous direction of the field for electrons to follow.

Our simulations show in full kinetic detail that while plasma expansion has steady growth (a representative expansion velocity can be calculated), its advancing front is complicated, exhibiting "sloshing and spillage". For our case this was between 0.35 and 0.99 ns; in a larger scale simulation this would occur very quickly, possibly numerous times, and would go relatively unnoticed. Essentially some ions travel too far ahead of the quasineutral region during their creation and expansion and are then aggressively drawn back to the cathode by a very strong positive field. This can be imagined as a glass of water jerked too quickly where the spilled water represents ions, and gravity plays the role of the electric field. While this instability lasts briefly, it can irreparably destabilize the simulation as seen in the graphs titled "ES on" in Fig. 2. This highlights one of many challenges in faithfully simulating a system having both complicated dynamics and disparate scales such as a closing diode.

When testing Event Splitting for Gap Closure, we saw that it failed to maintain a stable solution. In the above figure, we can see, as denoted by the black arrows, the sloshing motion of the ions clearly shown in the "ES Off" results. When ES is on, we see a blow-out effect of the ions where they reach unreasonable velocities,

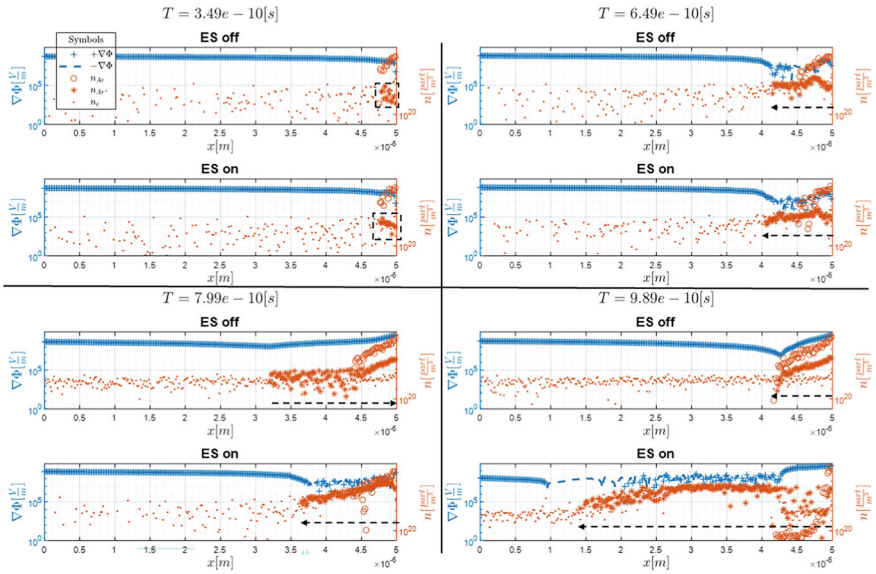

Fig. 2 Ion instability: comparison of results with and without event splitting (ES) where dashed lines/arrows denote regions of interest and general ion motion

beyond what would be expected from predicted field effects. We believe that they could be artificially accelerated by numerical grid heating arising from distortion of the distribution functions by excessive merging, which pushes an unsteady and barely resolved solution into instability. However, to Event Splitting's credit, we do see reduced noise in early formation of ions when comparing the ES on vs ES off solutions highlighted by the dashed box in the top left panel of Fig. 2.

4 Conclusions

The purpose of this paper was to describe our creation of a model capable of simulating full gap closure as well as examine the feasibility of a novel numerical method for reducing computational costs. This was done using a 1-D PIC-DSMC code with numerous simplifying assumptions, as the goal was to simply test these methods under representative conditions.

The extreme gradients in particle density and electrostatic properties associated with gap closure make it far too computationally expensive to fully resolve the maximal spatial and temporal requirements across the full domain. To reach gap closure, we required a reduced domain that maintained the desired physical properties by preservation of the Knudsen number and electric field.

Event Splitting improves the noise levels when compared to standard DSMC for the same macroparticle counts given a fully resolved simulation domain, i.e. adequate temporal and spatial resolutions. For an extremely unsteady and marginally unresolved simulation, however, event splitting creates so many particles, which then need to be merged so frequently, that the distribution function is greatly distorted. This then creates a heightened sensitivity to DSMC noise fluctuations which leads to numerical instabilities. For the simulation conditions of the gap closure problem examined in this work we found no benefit from the use of the Event Splitting.

Future work could include developing merge schemes that preserve more details of the distribution function. This would enable more robust use of ES and on a broader set of problems including the gap closure problem in this work. Additionally, mixed strategies could be considered, e.g. employing ES for some collisions, while using conventional DSMC for others, or using an adaptive spatial grid for the DSMC and PIC solvers. These pose their own challenges of particle tracking and preserving higher moments of the distribution functions while merging particles (merging will be required regardless of the method). Ultimately, finding a balance between simulation fidelity and computational cost will be required to simulate these detailed physics processes on real-world systems (e.g., simulations of the Saturn accelerator). Strategies such as those explored in this work are among a growing set of techniques that can play such a role.

Acknowledgements This work was supported in part by Sandia National Laboratories. Sandia National Laboratories is a multimission laboratory managed and operated by National Technology and Engineering Solutions of Sandia, LLC., a wholly owned subsidiary of Honeywell International, Inc., for the U.S. Department of Energy's National Nuclear Security Administration under contract DE-NA0003525.

References

1. Alves LL (2014) The IST-LISBON database on LXCat. J Phys: Conf Ser 565(1)
2. Bird GA (1994) Molecular gas dynamics and the direct simulation of gas flows. Oxford University Press. https://doi.org/10.1093/oso/9780198561958.001.0001
3. Birdsall CK, Langdon AB (2018) Plasma physics via computer simulation. CRC Press. https://doi.org/10.1201/9781315275048
4. Kirk G, Oblapenko G, Sirajuddin D, Moore C, Goldstein D, Varghese P (2023) Modeling gap closure within vaporizing transmission lines of pulsed power machines using particle-in-cell direct simulation Monte Carlo (PIC-DSMC). Master's thesis, University of Texas at Austin, Austin, TX. https://repositories.lib.utexas.edu/items/3c50abed-c1a3-4218-bb5e-cee6630df771/full
5. Langmuir I (1913) The effect of space charge and residual gases on thermionic currents in high vacuum. Phys. Rev. 2(6):450. https://doi.org/10.1103/PhysRev.2.450
6. Latham RV (1995) High voltage vacuum insulation: basic concepts and technological practice. Elsevier
7. Martin RS, Cambier JL (2016) Octree particle management for DSMC and PIC simulations. J Comput Phys 327:943. https://doi.org/10.1016/j.jcp.2016.01.020

8. Oblapenko G, Goldstein D, Varghese P, Moore C (2022) Hedging direct simulation monte carlo bets via event splitting. J Comput Phys 466:111390. https://doi.org/10.1016/j.jcp.2022.111390
9. Oblapenko G, Goldstein DB, Varghese P, Moore C (2022) Improving PIC-DSMC simulations of electrical breakdown via event splitting. AIAA SciTech 2022 Forum. https://doi.org/10.2514/6.2022-2152
10. Oblapenko G, Goldstein D, Varghese P, Moore C (2022) Improving PIC-DSMC simulations of RF plasmas via event splitting. 9th European conference for aero-nautics and aerospace sciences (EUCASS) 2022
11. Renk T, Struve K, Hustel B, Ulmen B (2023) Development of saturn transmission line circuit modeling: from bertha origins to CASTLE modeling of original and replacement hardware performance as part of saturn recap program. SAND2023-10990
12. Roy A, Menon R, Mitra S, Kumar S, Sharma V, Nagesh KV, Mittal KC, Chakravarthy DP (2009) Plasma expansion and fast gap closure in a high power electron beam diode. Phys. Plasmas 16(5):053103. https://doi.org/10.1063/1.3129802

Open Access This chapter is licensed under the terms of the Creative Commons Attribution 4.0 International License (http://creativecommons.org/licenses/by/4.0/), which permits use, sharing, adaptation, distribution and reproduction in any medium or format, as long as you give appropriate credit to the original author(s) and the source, provide a link to the Creative Commons license and indicate if changes were made.

The images or other third party material in this chapter are included in the chapter's Creative Commons license, unless indicated otherwise in a credit line to the material. If material is not included in the chapter's Creative Commons license and your intended use is not permitted by statutory regulation or exceeds the permitted use, you will need to obtain permission directly from the copyright holder.

Evaporation Simulations in High Pressure Environments with a Multi-species Enskog-Vlasov Solver

Raphael Tietz, Rolf Stierle, Stefanos Fasoulas, and Marcel Pfeiffer

Abstract This paper presents a novel multi-species Enskog-Vlasov solver designed to simulate mixtures with different particle diameters and masses and their evaporation coefficients. Traditional combustion engines face efficiency deficits due to suboptimal two-phase mixing of liquid fuel droplets and air. Recent approaches suggest heating fuel droplets above their critical temperature to achieve single-phase mixing, but accurate evaporation coefficients for high-pressure and high-temperature conditions are lacking. The proposed solver closes the gap to other EV solvers which are only capable of solving single-species simulations or multi-species simulations with equal particle diameter and masses. The solver is validated against existing single-species solvers and SAFT-VRQ Mie model. The results show good agreement with reference data, demonstrating the solver's capability to replicate multi-species simulations and determine evaporation and condensation coefficients.

Keywords Enskog-Vlasov equation · DSMC · Evaporation · Multi-species · Combustion engines · SAFT-VRQ mie

1 Introduction

The ongoing climate crisis requires a transition from traditional combustion engines to electric alternatives. However, this transition is not always feasible like in aviation or nautical applications. A mayor problem with combustion engines is their efficiency deficit, in part due to suboptimal two-phase mixing of liquid fuel droplets and air.

R. Tietz (✉) · S. Fasoulas · M. Pfeiffer
University of Stuttgart, Institute of Space Systems, Stuttgart, Germany
e-mail: rtietz@irs.uni-stuttgart.de
URL: https://www.irs.uni-stuttgart.de/en/research/space-transport-technology/numerical-modeling-and-simulations/mehrphasen/

R. Stierle
Institute of Thermodynamics and Thermal Process Engineering, University of Stuttgart, Stuttgart, Germany

© The Author(s) 2026

M. Grabe et al. (eds.), *Rarefied Gas Dynamics*, Springer Aerospace Technology,
https://doi.org/10.1007/978-3-032-00094-1_45

Recent research by Lamanna et al. [1] proposes an innovative approach to address this inefficiency by heating fuel droplets above their critical temperature so that the liquid phase disappears, allowing for more efficient and simpler single-phase mixing. However, their model relies on evaporation coefficients to model the heating process of the cold fuel droplet, until it reaches super-critical state. But they are not available for high pressure and high temperature conditions as they appear in combustion engines. This paper presents a novel multi-species Enskog-Vlasov (EV) solver and simulations designed to obtain accurate evaporation coefficients at distinct temperatures and pressures. The composition of the liquid and vapor phase of these simulations are then compared with results of the SAFT-VRQ Mie model to validate their accuracy and potential application in improving the efficiency of combustion engines. This model and evaporation studies may also be of interest in other disciplines, such as the development of new combustors for rocket engines, where higher pressures lead to higher thrust.

To date, only single-species EV solvers or multi-species EV solvers with equal particle diameters and masses of all species have been developed [2, 3]. This work goes a step further and presents a multi-species EV solver capable of simulating mixtures with different particle diameters and masses.

2 Numerical Modeling

In this work the Enskog-Vlasov equation is solved for a multi-species gas mixture. The Enskog-Vlasov equation [4] is an extension of Boltzmann's equation that describes the evolution of the distribution function $f(\underline{x}, \underline{v}, t)$ in dense gases and fluids and is given by:

$$\frac{\partial f}{\partial t} + \left\langle \underline{v} \cdot \frac{\partial f}{\partial \underline{x}} \right\rangle + \left\langle \frac{\underline{F}}{m} \cdot \frac{\partial f}{\partial \underline{v}} \right\rangle = C_E(f, f), \tag{1}$$

where t is the time, $\underline{x}$ and $\underline{v}$ are the position and velocity vectors, respectively, m is the particle mass, $\underline{F}$ is the mean-field force, and $C_E(f, f)$ is the Enskog collision integral [5].

The interaction potential of the particles is described by the Sutherland potential $\phi(r)$, which is split at its most negative position. The inner part, the hard sphere part, is modeled by the collision operator $C_E(f, f)$, while the attractive tail is modeled by the Vlasov integral and coupled in by the mean-field force $\underline{F}$.

$$\phi(r) = \begin{cases} +\infty & r < d \\ -\phi_d \left(\frac{r}{d}\right)^{-\gamma} & r \geq d \end{cases}, \tag{2}$$

$$\underline{F} = \int\limits_{|\underline{x}_1 - \underline{x}| > d} \frac{d\phi}{dr} \frac{\underline{x}_1 - \underline{x}}{|\underline{x}_1 - \underline{x}|} n(\underline{x}_1) d\underline{x}_1, \tag{3}$$

where r is the radius, ϕ_d is the depth of the potential well, d is the particle diameter, and γ is the power of the potential. The mean-field force $\underline{F}$ is calculated by integrating the gradient of the potential over the particle distribution $n(\underline{x}_1)$, if the distance between $\underline{x}_1$ and $\underline{x}$ is greater than d.

The collision integral $C_E(f, f)$ reads as follows:

$$C_E(f,f) = d^2 \int_{\mathcal{S}} \int_{\mathbb{R}^3} R(\langle \underline{c_r} \cdot \underline{k} \rangle) \cdot \begin{bmatrix} Y(n(\underline{x} - \frac{d\underline{k}}{2}))\, f(\underline{x}, \underline{v}')\, f(\underline{x} - d\underline{k}, \underline{v}'_*) \ldots \\ -Y(n(\underline{x} + \frac{d\underline{k}}{2}))\, f(\underline{x}, \underline{v})\, f(\underline{x} + d\underline{k}, \underline{v}_*) \end{bmatrix} d^3\underline{v}_*\, d^2\underline{k}, \tag{4}$$

where c_r is the relative velocity of the colliding particles and $\underline{k}$ is the unit vector through the position of both particles. $\underline{v}$ and $\underline{v}_*$ are the pre-collision velocities of the first and second particles, and $\underline{v}'$ and $\underline{v}'_*$ are the post-collision velocities of them. Y is the pair correlation function at contact.

The Enskog collision integral includes several additional effects compared to the Boltzmann integral. First, colliding particles are only allowed to collide if they are moving toward another due to the Ramp function $R(\langle \underline{c_r} \cdot \underline{k} \rangle) = \mathbf{max}\left(\langle \underline{c_r} \cdot \underline{k} \rangle, 0\right)$ to model the correct virial. Second, the collision distance, which is equal to the particle diameter, is not neglected, which leads to a non-locality of the collisions. Third, the collision frequency is increased by the pair correlation function at contact Y due to higher number densities near the particles in dense media, where usually the Carnahan and Starling equation of state (EOS) for a single-species Sutherland fluid [6] is used to derive it.

3 Multi-species Enskog-Vlasov DSMC

The multi-species EV solver is based on the single-species solvers of Montanero et al. [7] and Frezzotti et al. [8]. They developed a single-species DSMC-like solver for the EV equation. The main idea is to divide the collision procedure into several passes, one for each species of the second collision particle, since this must be known before pairing. The pair correlation function Y is changed to one based on the BMCSL EOS [9], which is a multi-species extension of the Carnahan and Starling EOS. Finally, the calculation of post-collision velocities and sampling must be adjusted to allow for different particle masses and diameters.

4 Results

The solver was tested against the simulations of Ohashi et al. [2] to demonstrate the capability of the solver to replicate state-of-the-art results. They performed similar simulations as required for this work, but the only difference between the two species is their respective ϕ_d. The interspecies attraction is calculated via the Lorentz-Berthelot combining rule. The simulations are conducted with an argon-neon mixture with equal particle diameters d and masses m. The critical temperature of neon $T_{c,Ne}$ is lower than in reality by a factor of about 4 to minimize perturbations of the liquid phase by dissolved neon. The simulations are performed with varying amounts of neon in the simulation domain, resulting in varying pressures and a constant temperature of $0.633T_{c,Ar}$. The number density profiles are shown in Fig. 1 and follow the expected trend.

The evaporation and condensation coefficients (σ_e and σ_c) are calculated using the following formulas:

$$\sigma_e = \frac{J_{evap}}{J_{evap} + J_{refl}} \quad \text{and} \quad \sigma_c = \frac{J_{cond}}{J_{cond} + J_{refl}}, \tag{5}$$

where J_{evap} and J_{cond} are the particle flux from the liquid to the gas phase and vice versa, and J_{refl} is the particle flux of particles reflected at the interface according to [10]. The evaporation and condensation coefficients shown in Fig. 2 are in good agreement with the reference. This shows the ability of the solver to reproduce state-of-the-art multi-species simulations with equal masses and diameters of all species.

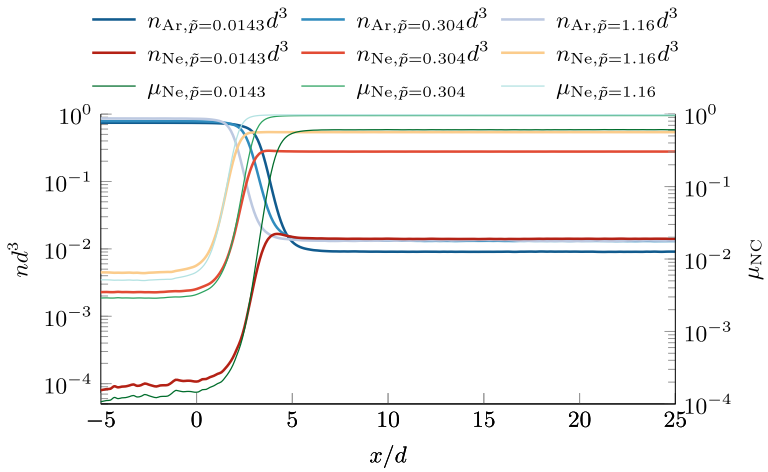

Fig. 1 Argon and neon number density profiles and neon mole fractions of cases 1, 5 and 8 of Ohashi et al. [2]

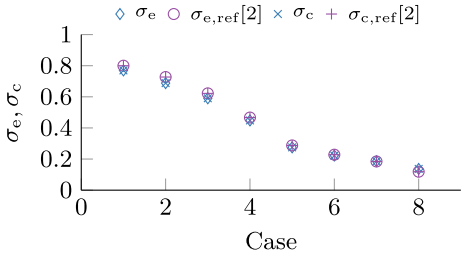

Fig. 2 Evaporation and condensation coefficients compared to Ohashi et al. [2]

Table 1 Particle Diameters of the subsequent simulations

T/T_c	d_{Ar}/Å	d_{Ne}/Å
0.633	3.3322	2.5898
0.767	3.2270	2.5663
0.900	3.1418	2.5489

To demonstrate the full multi-species capability of the solver, vapor and liquid phase densities are compared with SAFT-VRQ Mie model [11, 12]. This is a sophisticated EOS capable of describing the vapor-liquid equilibrium of mixtures and their composition by simplified Mie interaction potentials. For this comparison, the critical temperature of neon is raised to its correct value and the particle diameters are fitted to external data: The argon diameter is fitted to single species results of the SAFT-VRQ Mie EOS by replicating the correct liquid density, and the neon diameter is fitted to NIST pressure data [13]. The diameters are listed in Table 1.

The simulations are executed at three different temperatures 0.633, 0.767, and $0.900T_{c,Ar}$ and the pressure is varied by different amounts of neon in the domain.

The simulation domain was initialized with pure argon in the liquid phase with a number density of $2 \cdot 10^{28} \frac{1}{m^3}$ and a length of 25.538Å. On the right boundary a surface flux of neon was applied with a neon pressure of 0, 1, 10, 50 and 100bar. The part of the computational domain what is still empty, was initialized with neon at the same pressure. The left boundary is a symmetric boundary with a thermostatted region next to it to counteract evaporation heat losses tuned to the temperature of the simulation.

The results are depicted in Fig. 3 and show that more neon is dissolved in the liquid phase due to the higher neon attraction, smaller particle diameter, and higher simulated temperatures. Especially at the higher temperatures the amount of neon disturbs the liquid phase due to a high neon mole fraction in it. For the highest pressure case at the highest temperature no stable liquid phase formed. The agglomeration of neon atoms at the gas-liquid interface region can also be observed in the results of other work.

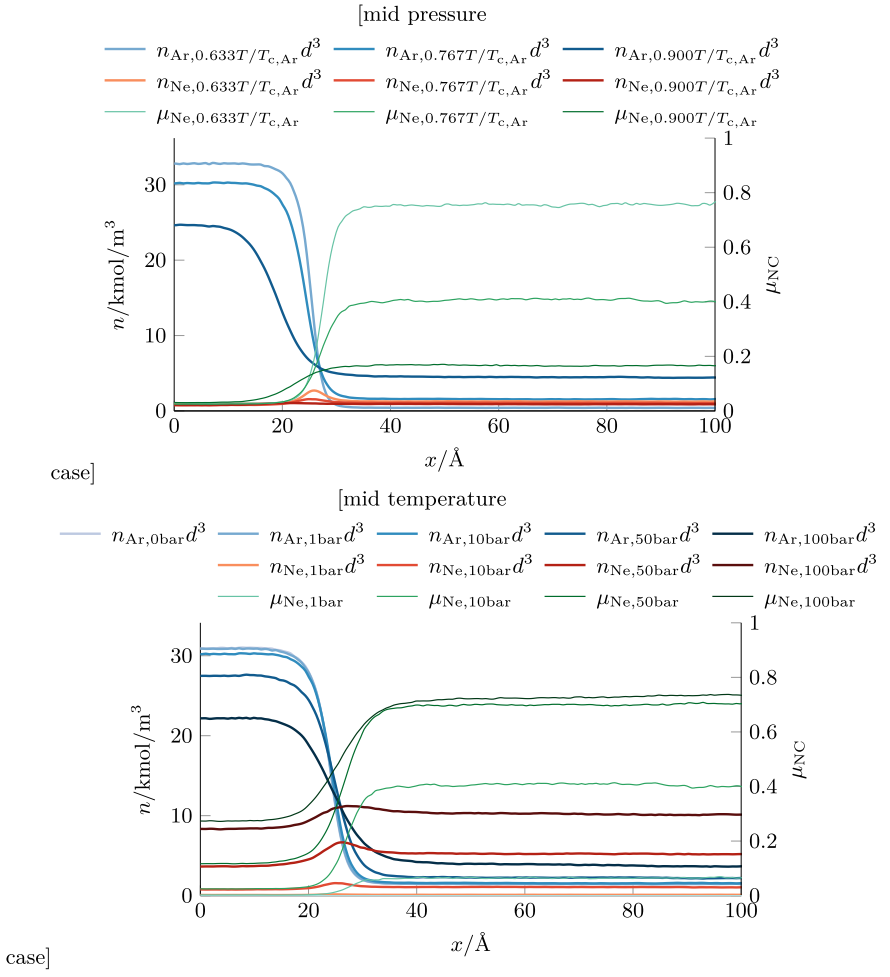

Fig. 3 Number density profiles and neon mole fractions with different particle diameters and masses of the species

The equilibrium compositions of the liquid and gaseous phases are compared with results of the SAFT-VRQ Mie model [11, 12] in Fig. 4. The results of both methods are in reasonable agreement to each other. The deviations may be due to the different interaction potentials used – Sutherland vs. Mie potential. The higher the temperature or pressure the higher are the deviations. Therefore, the particles come closer in those circumstances and this is the point where the used interaction potentials have their highest differences. The results indicate that the presented multi-species EV solver is able to simulate mixtures with different particle diameters and masses.

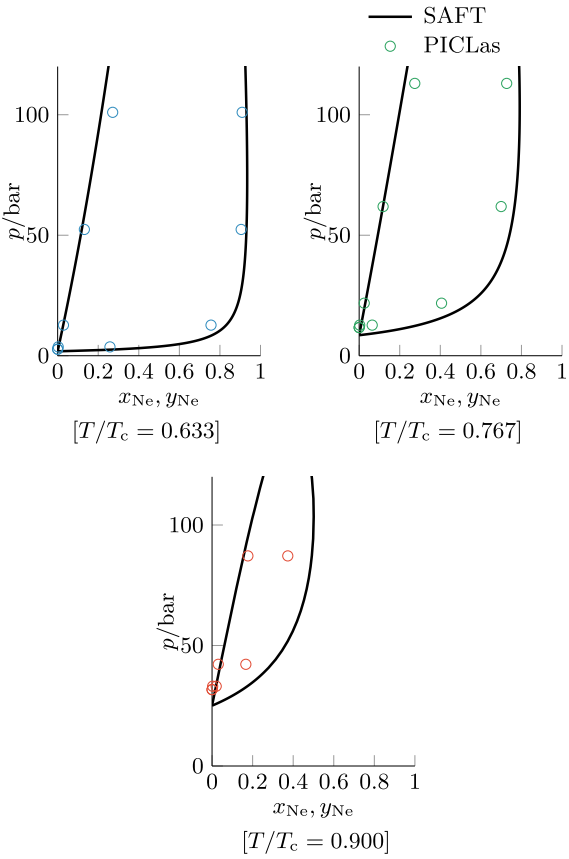

Fig. 4 Enskog-Vlasov result compared to SAFT-VRQ Mie [11, 12]

With this knowledge the solver can be used to sample the evaporation coefficients. The same sampling technique for the evaporation coefficients as in the simulations before was used and are shown in Fig. 5. The coefficients follow the expected trend. For higher pressures Ohashi et al. [2] observed a decrease of the evaporation coefficient. This is due to the higher number density of the gas phase leading to a higher number of collisions and therefore a lower probability of evaporation. Frezzotti et al. [8] observed a decrease in the evaporation coefficient with increasing temperature. This trend continues with higher temperatures.

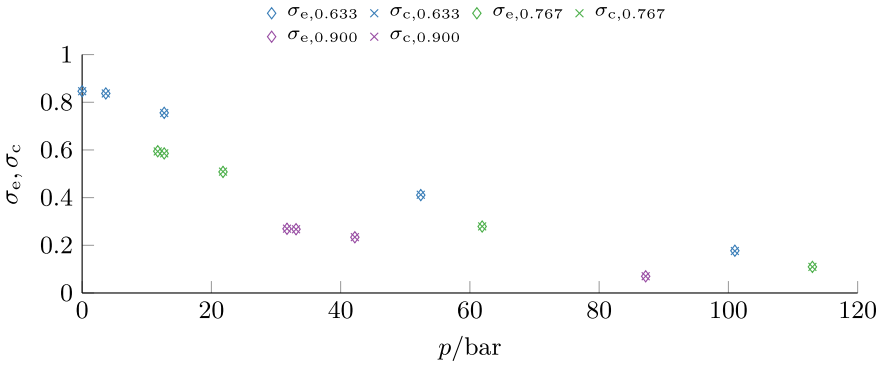

Fig. 5 Evaporation and condensation coefficients

5 Conclusion

In this paper, we present a novel multi-species EV solver designed to simulate evaporation in high-pressure environments. This solver simulates mixtures with different particle diameters and masses, filling the gap in existing models. The solver has been validated against single-species EV solvers and SAFT-VRQ Mie model, showing good agreement with reference data of Ohashi et al. [2]. The results demonstrate the ability of the solver to reproduce multi-species simulations and to determine evaporation and condensation coefficients. In the future this novel EV solver can be used in non-equilibrium simulations to demonstrate its capabilities in such scenarios.

These results have significant implications for improving the efficiency of internal combustion engines and reducing emissions. Future work will focus on further validation and application of the solver to real-world scenarios, as well as exploring its potential in other areas requiring accurate evaporation modeling.

References

1. Lamanna G, Steinhausen C, Weigand B (2023) On the role of trancritical evaporation in controlling the transition from two-phase to single-phase mixing. In: ILASS Europe 2023, 32nd European conference on liquid atomization and spray systems
2. Ohashi K, Kobayashi K, Fujii H, Watanabe M (2020) Evaporation coefficient and condensation coefficient of vapor under high gas pressure conditions. Sci Rep 10(1):8143. https://doi.org/10.1038/s41598-020-64905-5
3. Frezzotti A, Gibelli L, Lockerby DA, Sprittles JE (2018) Mean-field kinetic theory approach to evaporation of a binary liquid into vacuum. Phys Rev Fluids 3(5):054,001. https://doi.org/10.1103/PhysRevFluids.3.054001
4. Grmela M (1971) Kinetic equation approach to phase transitions. J Statist Phys 3(3):347–364. https://doi.org/10.1007/BF01011389
5. Enskog D (1922) Kinetische Theorie der Wärmeleitung: reibung und Selbst-diffusion in Gewissen verdichteten gasen und flüssigkeiten. Almqvist & Wiksells boktryckeri-a.-b

6. Carnahan NF, Starling KE (1969) Equation of state for nonattracting rigid spheres. J Chem Phys 51(2):635–636. https://doi.org/10.1063/1.1672048
7. Montanero JM, Santos A (1997) Simulation of the Enskog equation à la Bird. Phys Fluids 9(7):2057–2060. https://doi.org/10.1063/1.869325
8. Frezzotti A, Gibelli L, Lorenzani S (2005) Mean field kinetic theory description of evaporation of a fluid into vacuum. Phys Fluids **17**(1), 012,102. https://doi.org/10.1063/1.1824111
9. Yau DHL, Chan KY, Henderson D (1997) Pair correlation functions for a hard sphere mixture in the colloidal limit. Molecular Physics 91(6):1137–1142. https://doi.org/10.1080/002689797170860
10. Ishiyama T, Yano T, Fujikawa S (2004) Molecular dynamics study of kinetic boundary condition at an interface between argon vapor and its condensed phase. Phys Fluids 16(8):2899–2906. https://doi.org/10.1063/1.1763936
11. Aasen A, Hammer M, Ervik Å, Müller EA, Wilhelmsen Ø (2019) Equation of state and force fields for feynman–hibbs-corrected mie fluids. i. application to pure helium, neon, hydrogen, and deuterium. J Chem Phys 151(6):064,508 https://doi.org/10.1063/1.5111364
12. Aasen A, Hammer M, Müller EA, Wilhelmsen Ø (2020) Equation of state and force fields for feynman–hibbs-corrected mie fluids. ii. application to mixtures of helium, neon, hydrogen, and deuterium. J Chem Phys 152(7):074,507. https://doi.org/10.1063/1.5136079
13. Acree Jr, WE, Chickos JS (2000) NIST chemistry webbook: NIST standard reference database number 69. Nat Inst Stand Technol Gaithersburg MD, 20899 (2000). https://doi.org/10.18434/T4D303

Open Access This chapter is licensed under the terms of the Creative Commons Attribution 4.0 International License (http://creativecommons.org/licenses/by/4.0/), which permits use, sharing, adaptation, distribution and reproduction in any medium or format, as long as you give appropriate credit to the original author(s) and the source, provide a link to the Creative Commons license and indicate if changes were made.

The images or other third party material in this chapter are included in the chapter's Creative Commons license, unless indicated otherwise in a credit line to the material. If material is not included in the chapter's Creative Commons license and your intended use is not permitted by statutory regulation or exceeds the permitted use, you will need to obtain permission directly from the copyright holder.

Combining Stochastic Particle BGK and Discrete Velocity Method for Efficient Multiscale Simulations

Félix Garmirian and Marcel Pfeiffer

Abstract The Bhatnagar-Gross-Krook (BGK) equation is widely used as an efficient model for flow simulations in transitional Knudsen number regimes. The two main types of solvers based on the BGK model, the deterministic discrete velocity methods (DVM) and the stochastic particle-based BGK solvers, each come with specific disadvantages such as six-dimensional discretization or statistical noise. This work introduces a coupling in velocity space between both approaches, creating a flexible noise-reduced method capable of accelerating the resolution of multiscale problems. The method is verified on test cases, showing improved efficiency compared to the pure DVM or the pure particle-based solver.

Keywords Stochastic particle BGK · Discrete velocity method · Velocity-space coupling · Multiscale methods

While the discrete simulation Monte Carlo (DSMC) method [4] has become the standard for rarefied gas simulations, it still suffers from a decreasing efficiency in the transition regime, where the Knudsen number is still too high to enable valid Navier-Stokes simulations. In such conditions, where the low mean-free path and large collision frequency would require computationally expensive DSMC simulations, the use of the BGK model [3] has proven to be efficient [10, 17].

Indeed, BGK solvers can avoid the physics-based restrictions of DSMC, and with the right integration method, even the relaxation frequency of this model does not need to be resolved. Several methods that capitalize on these advantages have been developed, based either on the discrete velocity method (DVM) [9, 10, 14, 19], or on a stochastic particle-based approach (SPBGK) similar to DSMC [7, 18], all able to reach at least second-order accuracy in time and space. While the particle-based solvers retain some of the flexibility of DSMC when it comes to boundary interaction, chemical reactions or supersonic flows, the DVMs have the benefit of noise-free results due to their fully deterministic nature, making them particularly useful for unsteady low-Mach number flows where DSMC results with a high signal-to-noise ratio are hardly achievable.

F. Garmirian (✉) · M. Pfeiffer
Institute of Space Systems, University of Stuttgart, Stuttgart, Germany
e-mail: garmirianf@irs.uni-stuttgart.de

© The Author(s) 2026

M. Grabe et al. (eds.), *Rarefied Gas Dynamics*, Springer Aerospace Technology,
https://doi.org/10.1007/978-3-032-00094-1_46

In order to develop a method that would profit from the advantages of the BGK model in all flow regimes, both approaches, particle-based and DVM, have been implemented in the open-source kinetic suite PICLas [6]. The stochastic and deterministic solvers are then coupled in velocity space, with the goal of using a limited range and resolution for the DVM velocity discretization while stochastic particles make up for the rest of the distribution function. A similar coupling in the context of DSMC has been investigated in the past [15, 16], but with the opposite decomposition, using a deterministic solver to better resolve the distribution tails. Another type of stochastic/deterministic hybrid BGK method has also been developed [5], in which the velocities of particles representing the deviation from equilibrium have to lie on DVM grid points.

With the coupling described in this paper, the aim is to reduce the statistical noise produced by the stochastic particle-based approach, while avoiding the increase in memory and CPU cost for 3D supersonic flows associated with DVM. This first-order SPBGK/DVM coupling could also be extended to a second-order method by using the same second-order integration for both components, as the boundary between stochastic particles and the deterministic solver is fixed throughout the simulation, what could be an advantage over other noise-reduced particle methods [1, 12, 13].

1 The Bhatnagar-Gross-Krook Model

The BGK equation [3] is an approximation of the Boltzmann equation, where the collision integral is replaced by a relaxation of the velocity distribution function $f(\mathbf{x}, \mathbf{v}, t)$ towards a target distribution f^t at the frequency $\nu = 1/\tau$:

$$\frac{\partial f}{\partial t} + \mathbf{v} \cdot \frac{\partial f}{\partial \mathbf{x}} = -\nu(f - f^t) \,, \tag{1}$$

with position $\mathbf{x}$, velocity $\mathbf{v}$ and time t. Using the equilibrium Maxwell distribution as target results in a fixed Prandtl number $\mathrm{Pr} = 1$, several corrected models have therefore been developed to account for thermal and viscous effects at the same time [11, 17]. In this paper, the ellipsoidal statistical BGK (ESBGK) model is preferred for its positivity because it satisfies Boltzmann's H-theorem [2, 11].

In the ESBGK model, the relaxation frequency and target distribution are defined as

$$\nu = \mathrm{Pr}\frac{n k_\mathrm{B} T}{\mu}, \quad f^{\mathrm{ES}} = \frac{n}{\sqrt{\det(2\pi \mathsf{A})}} \exp\left[-\frac{\mathbf{c}^T \mathsf{A}^{-1} \mathbf{c}}{2}\right] , \tag{2}$$

with particle density n, particle mass m, temperature T, viscosity μ and Boltzmann constant k_B. The matrix A is constructed from the pressure tensor P:

$$\mathsf{A} = \frac{k_\mathrm{B} T}{m \mathrm{Pr}} \mathsf{Id} + \left(1 - \frac{1}{\mathrm{Pr}}\right) \frac{\mathsf{P}}{nm} \,, \tag{3}$$

where Id is the identity matrix and $\mathsf{P} = \int m\mathbf{c}\mathbf{c}^T f d\mathbf{v}$.

Most numerical methods that use the BGK model to simulate rarefied gas flows are based either on the stochastic particle-based approach [8] or on the deterministic DVM [14]. The first one uses the same representation of the distribution function by simulation particles as DSMC. It also shares with DSMC the particle movement step, differing only in the collision step, replaced by a resampling of some particles from the chosen target distribution. The DVM approach, on the other hand, consists in a deterministic discretization of the velocity space into an appropriate grid. The BGK equation is then solved for each phase space point, usually with a finite volume scheme.

2 Stochastic Particle/DVM Coupling

One major disadvantage of discrete velocity methods for practical use is that, along the usual space mesh and time steps, a velocity grid must be constructed. The dimension of this grid depends of course on the problem considered, exponentially increasing the computational cost when going from 1D to 3D. Besides, even though many types of adapted grids have been developed to reduce the number of velocities, selecting the resolution and the bounds of the velocity grid for maximum accuracy still remains a challenge, especially in strong non-equilibrium conditions where the shape of the distribution function is unknown.

On the other hand, particle-based methods are more flexible, as their Monte-Carlo approach leads to cost increasing only as the square root of the dimension. The particle velocities are only limited by computer precision, enabling in theory a more accurate representation of non-equilibrium distribution tails. However, these stochastic methods introduce statistical noise, particularly problematic in the low-Mach number regime where the signal-to-noise ratio is low.

We therefore choose to couple DVM and SPBGK in velocity space, using DVM for the velocities closer to the mean velocity, where most of the density is located, and SPBGK for high-velocity particles making up the distribution tails. The cost of SPBGK is thus concentrated in the parts of the distribution that determine the non-equilibrium effects hard to capture with DVM, and the central DVM grid greatly reduces the number of particles needed to achieve low-noise results.

2.1 Velocity Space Decomposition

The coupling is done by splitting the velocity space into two regions, $\mathcal{V}_{\text{DVM}}$ and $\mathcal{V}_{\text{part}}$, delimited by velocity bounds $\mathbf{v}_{\min}$ and $\mathbf{v}_{\max}$ between which a DVM grid with evenly spaced points is constructed. Such a decomposition can be seen in two dimensions on Fig. 1. The distribution function is then separated according to this decomposition:

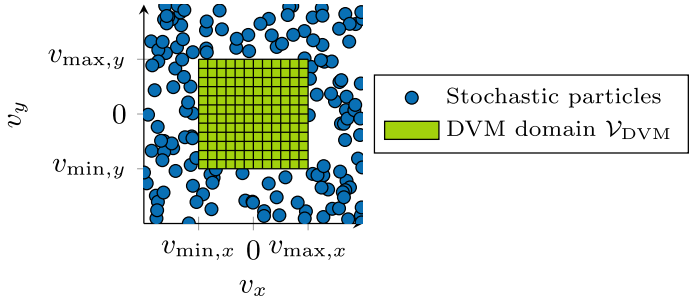

Fig. 1 Example of a decomposition of the 2D velocity space in DVM and SPBGK regions

$$f(\mathbf{v}) = f^{\mathrm{DVM}}(\mathbf{v}) + f^{\mathrm{part}}(\mathbf{v}) \quad \text{with} \quad \mathrm{supp}(f^{\mathrm{DVM}}) = \mathcal{V}_{\mathrm{DVM}} = [\mathbf{v}_{\min}, \mathbf{v}_{\max}], \tag{4}$$

meaning that the DVM representation f^{DVM} is limited to the central velocity grid while stochastic particles f^{part} can exist in the whole domain. The relaxation algorithm is however constructed so that the density represented by particles that fall inside the DVM domain will automatically pass from f^{part} to f^{DVM} for the next time step.

In this first approach, the BGK equation is solved using a first-order splitting of the advection and relaxation terms. For the advection, both parts of the distribution are evolved using their corresponding methods, i.e. particles are moved according to their velocity:

$$f^{\mathrm{part}}(\mathbf{x}, \mathbf{v}, t + \Delta t) = f^{\mathrm{part}}(\mathbf{x} - \mathbf{v}\Delta t, \mathbf{v}, t), \tag{5}$$

while, for the DVM part, a simple first-order upwind finite volume scheme is applied to solve:

$$\frac{\partial f^{\mathrm{DVM}}}{\partial t} + \mathbf{v} \cdot \frac{\partial f^{\mathrm{DVM}}}{\partial \mathbf{x}} = 0. \tag{6}$$

For the relaxation, the moments of the total distribution $f = f^{\mathrm{DVM}} + f^{\mathrm{part}}$ are then computed and the target distribution $f^{\mathrm{ES}}(\mathbf{x}, \mathbf{v})$ is constructed at each point of the DVM grid ($\mathbf{v} \in \mathcal{V}_{\mathrm{DVM}}$). The relaxation term can be integrated exactly:

$$\frac{\partial f}{\partial t} = \nu \left(f^{\mathrm{ES}} - f \right) \implies f(t + \Delta t) = \gamma\ f(t) + (1 - \gamma)\ f^{\mathrm{ES}}, \qquad \gamma = \exp(-\nu \Delta t). \tag{7}$$

The relaxation step is first applied to the limited DVM domain:

$$\forall \mathbf{v} \in \mathcal{V}_{\mathrm{DVM}}, \quad f^{\mathrm{DVM}}(\mathbf{x}, \mathbf{v}, t + \Delta t) = \gamma\ f^{\mathrm{DVM}}(\mathbf{x}, \mathbf{v}, t) + (1 - \gamma)\ f^{\mathrm{ES}}(\mathbf{x}, \mathbf{v}). \tag{8}$$

Note that, although the BGK collision operator is conservative, this DVM step is not. Indeed, f^{ES} is calculated from the total moments, and can therefore already include

the density represented by particles with an initial velocity outside of the $\mathcal{V}_{\mathrm{DVM}}$ but relaxing into it.

Finally, some particles are randomly picked to relax with probability $1-\gamma$, their velocity is resampled from f^{ES}, but they are then deleted if their new velocity falls inside $\mathcal{V}_{\mathrm{DVM}}$, as this part of the distribution has already been handled with (8). With $\mathbb{1}$ the indicator function, this can be written as:

$$f^{\mathrm{part}}(\mathbf{x},\mathbf{v},t+\Delta t)=\gamma\ f^{\mathrm{part}}(\mathbf{x},\mathbf{v},t)+(1-\gamma)\ \mathbb{1}_{\mathbb{R}^3\setminus\mathcal{V}_{\mathrm{DVM}}}\ f^{\mathrm{ES}}(\mathbf{x},\mathbf{v}), \tag{9}$$

which, combined with (8), corresponds to the full relaxation step (7).

2.2 Conservation of Moments

For the output of results, and for the calculation of f^{ES} as previously mentioned, the moments of the total distribution function have to be computed. To this end, the conservative moments of f^{part} and f^{DVM} are simply summed together, accounting for all discretization points, i.e. particles and DVM grid points.

However, as the selection and resampling process for the relaxation of particles involves random numbers, the density of deleted particles can differ from the one added to the DVM domain. To enforce mass conservation, the density of the particles resampled from f^{ES} that do not fall inside $\mathcal{V}_{\mathrm{DVM}}$ is adjusted to:

$$n_{\mathrm{resampled}}=n(f_{\mathrm{old}})-n(f_{\mathrm{new}}^{\mathrm{DVM}})-n(\gamma f_{\mathrm{old}}^{\mathrm{part}}), \tag{10}$$

where old and new refer to the state before and after the relaxation step. Besides, as this calculated density $n_{\mathrm{resampled}}$ can sometimes be negative due to the numerical error associated with a very low density outside $\mathcal{V}_{\mathrm{DVM}}$ or a too low number of relaxing particles, it is set to zero in such cases. Mass conservation is instead enforced by slightly rescaling the whole DVM distribution.

For momentum and temperature, conservation is enforced by computing their deviation on the total distribution, and applying a similar velocity rescaling as Gallis and Torczynski [8] to the particles only.

2.3 Boundary Conditions

While immobile specular boundaries do not require any special treatment, as reflected velocities stay in the same domain as incoming ones, the coupling of velocities through a diffusive wall's Maxwell distribution needs to be addressed. First, the outgoing DVM flux at each diffusive boundary is computed and summed with the flux of particles hitting the same boundary. Those particles are deleted, and new ones are sampled from the wall distribution function, with a density corresponding to the

outgoing flux. To prevent an always increasing number of particles in the simulation domain, new incoming particles with a velocity inside $\mathcal{V}_{\text{DVM}}$ are deleted, and replaced by an incoming DVM flux with the same density.

3 Results

3.1 Sod Shock Tube

The first test case is the Sod shock tube, with argon at an initial density of $n_\text{l} = 1.294 \times 10^{21}$ m^{-3} on the left part of the domain and $n_\text{r} = 1.618 \times 10^{20}$ m^{-3} on the right, with temperatures $T_\text{l} = 273$ K and $T_\text{r} = 218.4$ K. The flow is thus in the transition regime ($10^{-3} < \text{Kn} < 10^{-2}$). The simulation is run on a 500 cells mesh, with a time step of $\Delta t = 10^{-6}$ s. Figure 2 shows the temperature profiles at the beginning and at the end of the simulation, for a noisy pure SPBGK simulation and for a coupled SPBGK/DVM simulation. Results are compared to a DSMC reference that used around 10^6 particles per cell to lower the noise level. Both the pure SPBGK and the coupled solver are initialized using around 300 000 particles to represent the total density. The DVM domain for the SPBGK/DVM coupling consists of 15 Gauss-Hermite points between -1500 and 1500 m/s. As the coupled simulation runs, the number of particles decreases down to zero in a few hundred time steps, because all the density they represent is passed to the DVM domain that encompasses most of the distribution function. The statistical noise is thus clearly reduced while maintaining very good accuracy.

3.2 Couette Flow

In order to evaluate the efficiency of the coupled method, two Couette flows are simulated, one with a Knudsen number of Kn = 0.01 between plates moving in

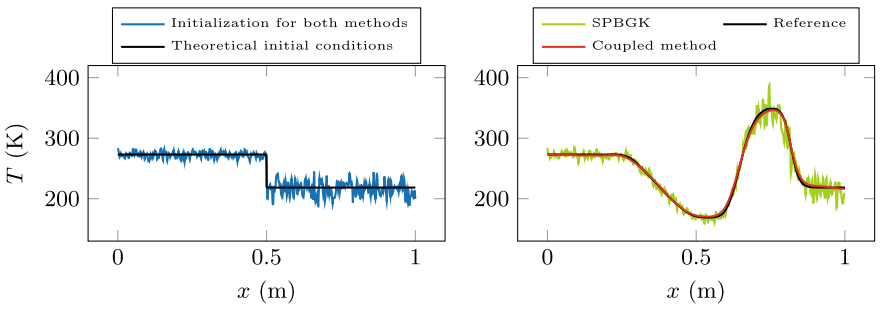

Fig. 2 Temperature profiles of the Sod shock tube test case. Left: initial conditions. Right: Profile after $t = 7 \times 10^{-4}$ s

opposite directions at ± 50 m/s, the other with Kn $= 0.1$ and wall velocities of ± 500 m/s resulting in a supersonic flow with Mach number Ma $\simeq 1.6$. Both cases are run using argon gas with a time step of $\Delta t = 10^{-6}$ s.

For the first case, shown on the left of Fig. 3, a 2D DVM velocity grid of 15×15 equally spaced points between -1500 and 1500 m/s is constructed. The coupled simulation is initialized with all the density as stochastic particles, which, as the simulation runs, are deleted as they fall inside the DVM domain. The simulation runs until the relative variation of the maximum temperature stays under 10^{-6}. With 440 initial particles per cell, this resulted in the coupled simulation taking 158 min on 5 CPU cores. As the limited velocity grid alone already allows for accurate results in this case, the pure DVM simulation only lasted 52 min. However, this was much more efficient than the pure SPBGK simulation initialized with the same number of particles, which needed 198 min to reach steady state, plus another 75 min to produce time-averaged results, still much noisier than the instantaneous results of the coupled simulation.

The second case (right part of Fig. 3) is less costly for pure particle methods as the high gradients in the flow macroscopic values lead to a higher signal-to-noise ratio. Using a converged SPBGK simulation as reference, the coupled solver with a 25×25 grid limited to $\mathcal{V}_{\text{DVM}} = [-900, 900]^2$ m/s, along with 10 to 100 particles per cell at steady state, results in a L^2 error of less than 1.5 K in the temperature profile. However, as the velocities span a larger range and because the non-equilibrium effects are more pronounced, a pure DVM simulation with the same 25×25 grid is inaccurate, and a 51×51 velocity grid between -3000 and 3000 m/s was required to reach the same accuracy. The coupled representation compensates the DVM limitations with a few high-velocity particles, thus greatly reducing the memory usage when compared to pure DVM.

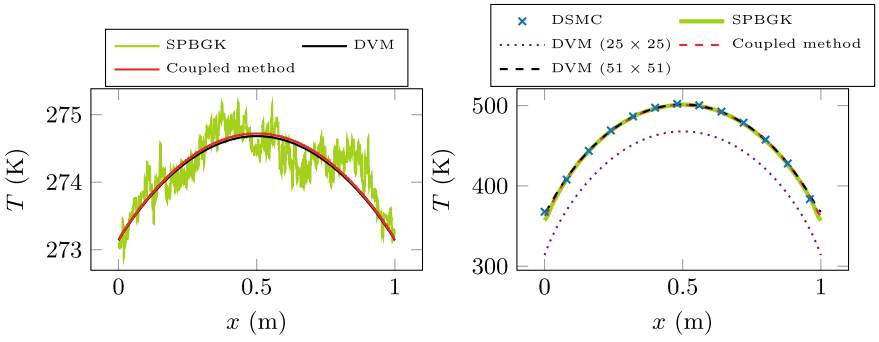

Fig. 3 Temperature profile of the Couette flows. Left: low-Mach number flow. Right: supersonic flow

4 Conclusion

A coupling of SPBGK and DVM in velocity space has been developed and evaluated on two common test cases, showing improved efficiency on one or the other parent method depending on the flow regime. This coupled method would therefore be interesting for multiscale simulations, where the flow goes from one regime to another, in terms of rarefaction or Mach number. Future work would include the extension of the method to second order in time and space, and the development of a better strategy for velocity domain decomposition, perhaps using a spherical boundary for the DVM domain. It would then be interesting to compare the resulting method to other noise-reduced particle methods.

Acknowledgements This project has received funding from the European Research Council (ERC) under the European Union's Horizon 2020 research and innovation programme (grant agreement No. 899981 MEDUSA).

References

1. Al-Mohssen HA, Hadjiconstantinou NG (2010) Low-variance direct Monte Carlo simulations using importance weights. ESAIM: Mathematical Modelling Numer Anal 44(5):1069–1083
2. Andries P, Le Tallec P, Perlat JP, Perthame B (2000) The Gaussian-BGK model of Boltzmann equation with small Prandtl number. Eur J Mech - B/Fluids 19(6):813–830
3. Bhatnagar PL, Gross EP, Krook M (1954) A model for collision processes in gases. I. Small amplitude processes in charged and neutral one-component systems. Phys Rev 94(3):511–525
4. Bird GA (1994) Molecular gas dynamics and the direct simulation of gas flows. Oxford University Press, Oxford, New York, Oxford Engineering Science Series
5. Dimarco G, Pareschi L (2008) Hybrid multiscale methods II. Kinetic equations. Multiscale Modeling Simulat 6(4):1169–1197
6. Fasoulas S, Munz CD, Pfeiffer M, Beyer J, Binder T, Copplestone S, Mirza A, Nizenkov P, Ortwein P, Reschke W (2019) Combining particle-in-cell and direct simulation Monte Carlo for the simulation of reactive plasma flows. Phys Fluids 31(7):072006
7. Fei F, Zhang J, Li J, Liu Z (2020) A unified stochastic particle Bhatnagar-Gross-Krook method for multiscale gas flows. J Comput Phys 400:108972
8. Gallis MA, Torczynski JR (2011) Investigation of the ellipsoidal-statistical Bhatnagar-Gross-Krook kinetic model applied to gas-phase transport of heat and tangential momentum between parallel walls. Phys Fluids 23(3):030601
9. Garmirian F, Pfeiffer M (2025) Implementation of asymptotic preserving discrete velocity methods into the simulation code PICLas. Comput Phys Commun p 109648
10. Guo Z, Xu K (2021) Progress of discrete unified gas-kinetic scheme for multiscale flows. Adv Aerodynam 3(1):6
11. Holway LH Jr (1966) New statistical models for kinetic theory: methods of construction. Phys Fluids 9(9):1658–1673
12. Homolle TMM, Hadjiconstantinou NG (2007) A low-variance deviational simulation Monte Carlo for the Boltzmann equation. J Comput Phys 226(2):2341–2358
13. Liu C, Zhu Y, Xu K (2020) Unified gas-kinetic wave-particle methods I: continuum and rarefied gas flow. J Comput Phys 401:108977
14. Mieussens L (2000) Discrete velocity model and implicit scheme for the BGK equation of rarefied gas dynamics. Math Models Methods in Appl Sci 10(08):1121–1149

15. Oblapenko G, Goldstein D, Varghese P, Moore C (2020) A velocity space hybridization-based Boltzmann equation solver. J Comput Phys 408:109302
16. Pan TJ, Stephani KA (2016) Investigation of velocity-space coupling approach in DSMC for tail-driven processes. In: 30th international symposium on rarefied gas dynamics. Victoria, BC, Canada, p 050017
17. Pfeiffer M (2018) Particle-based fluid dynamics: comparison of different Bhatnagar-Gross-Krook models and the direct simulation Monte Carlo method for hypersonic flows. Phys Fluids 30(10):106106
18. Pfeiffer M, Garmirian F, Gorji MH (2022) Exponential Bhatnagar-Gross-Krook integrator for multiscale particle-based kinetic simulations. Phys Rev E 106(2):025303
19. Xu K, Huang JC (2010) A unified gas-kinetic scheme for continuum and rarefied flows. J Comput Phys 229(20):7747–7764

Open Access This chapter is licensed under the terms of the Creative Commons Attribution 4.0 International License (http://creativecommons.org/licenses/by/4.0/), which permits use, sharing, adaptation, distribution and reproduction in any medium or format, as long as you give appropriate credit to the original author(s) and the source, provide a link to the Creative Commons license and indicate if changes were made.

The images or other third party material in this chapter are included in the chapter's Creative Commons license, unless indicated otherwise in a credit line to the material. If material is not included in the chapter's Creative Commons license and your intended use is not permitted by statutory regulation or exceeds the permitted use, you will need to obtain permission directly from the copyright holder.

An Improved Particle Scheme for Solving Fokker-Planck Models of the Boltzmann Equation

Tobias Ott, Hossein Gorji, and Marcel Pfeiffer

Abstract This paper presents an improved particle scheme for solving Fokker-Planck models of the Boltzmann equation. The proposed method employs a second-order Strang splitting scheme for accurate time integration. Element-wise basis functions are chosen for spatial discretization, and the moments of the distribution function are calculated by projection onto these basis functions. The method is validated using a 1D Couette flow test case, demonstrating its temporal and spatial convergence properties. The results show that the proposed scheme provides accurate solutions for the Boltzmann equation with the Ellipsoidal-Statistical Fokker-Planck collision operator.

Keywords Particle methods · Boltzmann equation · Fokker-planck

1 Introduction

Numerical simulation proves to be especially important for non-equilibrium flows, where conducting experiments is often prohibitively expensive or not feasible at all. Traditionally, the Direct Simulation Monte Carlo (DSMC) method [1] has been the standard approach for the numerical solution of problems in this flow regime. However, a significant limitation of the DSMC method is its requirement to resolve the mean collision frequency and the mean free path, constraints that become particularly restrictive in denser flow regimes. To circumvent this limitation, the Boltzmann collision integral is often replaced by approximations such as the Fokker-Planck (FP) equation. Recently, more advanced FP models, such as the ellipsoidal statistical FP model [2] or the cubic FP model [3], have been developed that reproduce the correct

T. Ott (✉) · M. Pfeiffer
Institute of Space Systems, University of Stuttgart, Stuttgart, Germany
e-mail: ottt@irs.uni-stuttgart.de

H. Gorji
Laboratory for Computational Engineering, Empa, Swiss Federal Laboratories for Materials Science and Technology, Dübendorf, Switzerland

© The Author(s) 2026

M. Grabe et al. (eds.), *Rarefied Gas Dynamics*, Springer Aerospace Technology,
https://doi.org/10.1007/978-3-032-00094-1_47

relaxation rates for the pressure tensor and the heat flow and thus reproduce the correct Prandtl number. In theory, these advanced models are applicable to a wide range of flow phenomena from rarefied flows to flows near thermal equilibrium. However, due to the accuracy of the numerical methods, fine temporal and spatial discretization is required. In this work, we introduce a new particle scheme for solving the Boltzmann equation with the Ellipsoidal Statistical Fokker-Planck (ESFP) collision operator. First, we present the theoretical background of the ESFP model and the particle-based method. Then, we describe the time integration and spatial discretization methods used in the scheme. Finally, we validate the method using a 1D Couette flow test case and compare its accuracy and convergence properties with standard methods.

2 Theory

The behavior of monatomic gases can be described by the Boltzmann equation

$$\frac{\partial f}{\partial t} + v_i \cdot \frac{\partial f}{\partial x_i} = \left.\frac{\partial f}{\partial t}\right|_{\text{coll}}, \tag{1}$$

where $f = f(\mathbf{x}, \mathbf{v}, t)$ is the distribution function in phase space spanned by the position $\mathbf{x}$ and the velocity $\mathbf{v}$ at time t. The collision term $\left.\frac{\partial f}{\partial t}\right|_{\text{coll}}$ describes the interaction between particles and can be approximated by the Fokker-Planck operator:

$$\left.\frac{\partial f}{\partial t}\right|_{\text{coll}} = \frac{\partial}{\partial v_i}\left(a_i(\mathbf{x}, t) f(\mathbf{x}, \mathbf{v}, t)\right) + \frac{\partial^2}{\partial v_i \partial v_j}\left(D_{ij}(\mathbf{x}, t) f(\mathbf{x}, \mathbf{v}, t)\right). \tag{2}$$

In this paper, we will focus on the ESFP model by Mathiaud and Mieussens [2], where the coefficients a_i and D_{ij} are given by

$$a_i = \frac{1}{\tau}\left(v_i - u_i\right), \quad D_{ij} = \frac{1}{\tau}\left((1-\nu)\frac{\mathrm{Tr}(\Sigma)}{3}\delta_{ij} + \nu\Sigma_{ij}\right). \tag{3}$$

Here, τ is the relaxation time and ν is the anisotropy parameter given as a function of the Prandtl number Pr by

$$\tau = \frac{3}{Pr}\frac{\mu}{p}, \quad \nu = 1 - \frac{3}{2}\frac{1}{Pr}. \tag{4}$$

Additionally, we require the zeroth, first, and second moments of the distribution function which are the number density n, the velocity $\mathbf{u}$, and the covariance matrix Σ respectively:

$$n(\mathbf{x},t)=\int f\mathrm{d}\mathbf{v},\quad \mathbf{u}(\mathbf{x},t)=\frac{1}{n}\int \mathbf{v}f\mathrm{d}\mathbf{v},\quad \Sigma(\mathbf{x},t)=\frac{1}{n}\int (\mathbf{v}-\mathbf{u})\,(\mathbf{v}-\mathbf{u})^T\,f\mathrm{d}\mathbf{v}. \tag{5}$$

Using the mass density $\rho = m_s n$ with the mass of the species m_s and the Boltzmann constant k_B, the temperature and pressure can be calculated as

$$T=\frac{m_s}{k_B}\frac{\mathrm{Tr}(\Sigma)}{3},\quad p=nk_\mathrm{B}T. \tag{6}$$

The dynamic viscosity μ needed to calculate the relaxation time is assumed to follow the power law:

$$\mu=\mu_{\mathrm{ref,s}}\left(\frac{T}{T_{\mathrm{ref,s}}}\right)^{\omega_\mathrm{s}}, \tag{7}$$

with the reference viscosity given as a function of the reference temperature $T_{\mathrm{ref,s}}$, the power law exponent ω_s and the mass m_s and the diameter of the species d_s by [4]

$$\mu_{\mathrm{ref,s}}=\frac{30\sqrt{m_\mathrm{s}k_\mathrm{B}T_{\mathrm{ref,s}}}}{4\sqrt{\pi}(5-2\omega_\mathrm{s})(7-2\omega_\mathrm{s})d_\mathrm{s}^2}. \tag{8}$$

3 Implementation

We use a particle-based method to solve the Boltzmann equation with the ESFP collision operator. For this, we can write

$$f(\mathbf{x},\mathbf{v},t)=\int\int f(\mathbf{x}_p,\mathbf{v}_p,t)\delta(\mathbf{x}-\mathbf{X}_k)\delta(\mathbf{v}-\mathbf{V}_k)\mathrm{d}\mathbf{X}_k\mathrm{d}\mathbf{V}_k. \tag{9}$$

This integral can be solved approximately by Monte Carlo integration. If we assume that the samples are distributed according to the distribution function f, the approximate integral is given as a sum over the particles:

$$f(\mathbf{x},\mathbf{v},t)\approx\frac{N}{N_p}\sum_{k=1}^{N_p}\delta(\mathbf{x}-\mathbf{X}_k)\delta(\mathbf{v}-\mathbf{V}_k), \tag{10}$$

where $N=\int\int f\,\mathrm{d}\mathbf{x}\mathrm{d}\mathbf{v}$ is the number of physical particles, N_p is the number of simulation particles, and $\mathbf{x}_p$ and $\mathbf{v}_p$ are the position and velocity of particle p, respectively.

3.1 Time Integration

The solution of the Boltzmann Equation (1) can be described by the *flow* φ given as

$$\varphi(t,\, f_0(\mathbf{x}, \mathbf{v})) = f(\mathbf{x}, \mathbf{v}, t), \quad \text{with} \quad f(\mathbf{x}, \mathbf{v}, 0) = f_0(\mathbf{x}, \mathbf{v}). \tag{11}$$

We can split the Boltzmann equation into two equations, one describing the movement of particles and one describing the collision term:

$$\frac{\partial f}{\partial t} = -v_i \frac{\partial f}{\partial x_i} \quad \text{and} \quad \frac{\partial f}{\partial t} = \left.\frac{\partial f}{\partial t}\right|_{\text{coll}}. \tag{12}$$

The solutions of these equations can also be described by their flows $\varphi_t^M(f_0) = \varphi^M(t,\, f_0)$ and $\varphi_t^C(f_0) = \varphi^C(t,\, f_0)$, respectively. Using a composition of these flows, the second order Strang splitting scheme [5] can be written as:

$$\varphi(\Delta t,\, f_0) = \left(\varphi^M_{\Delta t/2} \circ \varphi^C_{\Delta t} \circ \varphi^M_{\Delta t/2}\right)(f_0(\mathbf{x}, \mathbf{v})). \tag{13}$$

The movement flow φ_t^M can be solved exactly by simply pushing the particles along their velocity vector:

$$f(\mathbf{x}, \mathbf{v}, \Delta t) = f(\mathbf{x} - \mathbf{v}\Delta t, \mathbf{v}, 0), \quad \rightarrow \quad \mathbf{X}_k(\Delta t) = \mathbf{X}_k(0) + \mathbf{V}_k \Delta t. \tag{14}$$

For the collision flow φ_t^C, we must solve the ESFP operator (2, 3). To do this, we can first rewrite the ESFP operator as a stochastic differential equation:

$$\mathrm{d}\mathbf{V}_k = \mathbf{a}(\mathbf{X}_k, t)\mathrm{d}t + \sqrt{2}\mathbf{D}^{1/2}(\mathbf{X}_k, t)\mathrm{d}\mathbf{W}, \tag{15}$$

where $\mathbf{D}^{1/2}(\mathbf{X}_k, t)$ is the Cholesky decomposition of the diffusion matrix $\mathbf{D}(\mathbf{X}_k, t)$ and $\mathbf{W}_k$ is a Wiener process. A standard approach to solve this equation is to assume that the stochastic term is constant [6, 7] which can then be easily solved to get

$$\mathbf{V}_k(\Delta t) = (\mathbf{V}_k(0) - \mathbf{u})e^{-\Delta t/\tau} + \sqrt{1 - e^{-2\Delta t/\tau}}\mathbf{D}^{1/2}(\mathbf{X}_p, 0)\xi. \tag{16}$$

Here, ξ is a random normal vector with zero mean and unit variance. For the ESFP operator, however, the equation can be solved exactly by [6]

$$\begin{aligned}\mathbf{V}_k(\Delta t) = {} & (\mathbf{V}_k(0) - \mathbf{u})e^{-\Delta t/\tau} \\ & + \left(\left(1 - e^{-3\Delta t/(\tau Pr)}\right)\frac{\mathrm{Tr}(\Sigma)}{3}\mathbf{I} + \left(e^{-3\Delta t/(\tau Pr)} - e^{-2\Delta t/\tau}\right)\Sigma\right)^{1/2}\xi.\end{aligned} \tag{17}$$

All macroscopic values must be evaluated at the position of the particle $\mathbf{X}_i$. For example, the velocity and covariance matrix are given by $\mathbf{u}(\mathbf{X}_i, 0)$ and $\Sigma(\mathbf{X}_i, 0)$, respectively.

3.2 Deposition and Interpolation

In each time step, the particles must be deposited onto the grid to calculate the moments. In this work, we first choose an element-wise basis to represent the moments M,

$$M(\mathbf{x}, t) \approx M^E(\mathbf{x}, t) = \sum_j \hat{M}_i^E(t)\phi_j^E(\mathbf{x}), \tag{18}$$

with the degrees of freedom $\hat{M}_j^E(t)$ and the basis functions $\phi_j^E(\mathbf{x})$. This choice allows for element-local deposition at the cost of allowing for discontinuities at the element interfaces. The unknown degrees of freedom $\hat{M}_j^E(t)$ can be calculated by projecting the moments onto each basis function ϕ_i^E, specifically by solving

$$\int \phi_i^E(\mathbf{x})M(\mathbf{x}, t)\mathrm{d}\mathbf{x} \overset{!}{=} \int \phi_i^E(\mathbf{x})M^E(\mathbf{x}, t)\mathrm{d}\mathbf{x} = \sum_j \hat{M}_j^E(t) \int \phi_i^E(\mathbf{x})\phi_j^E(\mathbf{x})\mathrm{d}\mathbf{x}. \tag{19}$$

By using orthogonal basis functions, the projection matrix becomes diagonal and the degrees of freedom can be calculated without the need to solve a system of equations. Although any polynomial degree can be used, in this work we limit ourselves to constant and linear basis functions.

Another approach to achieve a higher accuracy when using the constant basis is the stochastic interpolation scheme proposed by Fei et al. [8], where the moments for a particle i are evaluated at a random position $\mathbf{x}_i^*$ within half the element size of the particle position $\mathbf{X}_i$:

$$x_{i,j}^* = X_{i,j} + R_j \Delta x_j, \quad R_j \sim \mathcal{U}(-0.5, 0.5). \tag{20}$$

3.3 Momentum and Energy Conservation

After the relaxation, the particle velocities are updated to enforce conservation of momentum and energy:

$$\mathbf{V}_i = \mathbf{u}_{\text{old}} + \sqrt{\frac{\text{Tr}(\Sigma_{\text{old}})}{\text{Tr}(\Sigma_{\text{new}})}}(\mathbf{V}_{i,\text{new}} - \mathbf{u}_{\text{new}}). \tag{21}$$

In this equation, the subscripts old and new denote the values before and after the relaxation step, respectively. Note that this conservation step is always done on the constant basis, as the linear basis would require the solution of a coupled system of all particles in each element.

4 Results

The time integration methods and spatial discretization methods are compared using a simple 1D Couette flow. In this test case, two parallel plates are placed at a distance of $L = 1\,\mathrm{m}$. The two plates are moving in opposite directions with a velocity of $|v_y| = 500\,\mathrm{m\,s^{-1}}$ in the y direction. The interaction between the particles and the plates is assumed to be fully diffuse with a constant plate temperature of $T_w = 273\,\mathrm{K}$. Argon gas, with properties listed in Table 1, is used as the working fluid. The simulations are initialized with a uniform number density of $n = 1.37 \times 10^{20}\,\mathrm{m^{-3}}$ leading to a Knudsen number of approximately $\mathrm{Kn} \approx 0.01$. In all simulations, a total of $N_p = 137000$ particles are simulated.

4.1 Temporal Convergence

In order to test the temporal convergence of the schemes, the simulation is performed with different time steps, varying from $\Delta t = 2.5 \times 10^{-6}\mathrm{s}$ to $\Delta t = 1.6 \times 10^{-4}\,\mathrm{s}$. In all temporal convergence tests, the spatial discretization is kept constant with $N_e = 64$ elements and the linear basis. Figure 1a shows the simulated temperature profile of the two different time integration schemes simulated with $\Delta t = 2 \times 10^{-5}\,\mathrm{s}$. As a reference solution, the simulation results with a very small time step, $\Delta t = 1 \times 10^{-6}\,\mathrm{s}$, are used. We see that the result of the method using the exact integration of the collision term is in much better agreement with the reference solution than that of the standard approach.

In order to further investigate the temporal convergence of the two methods, the L_2-error can be plotted over the different time steps. The L_2-error is given by

$$L_2 = \sqrt{\frac{1}{N_e} \sum_{i=1}^{N_e} \left(T_i - T_{\mathrm{ref,i}}\right)^2}, \tag{22}$$

Table 1 Species-specific parameters used for all simulations

Species	d_s / m	$T_\mathrm{ref,s}$ / K	ω_s	m_s / kg
Ar	4.05×10^{-10}	273	0.77	6.63×10^{-26}

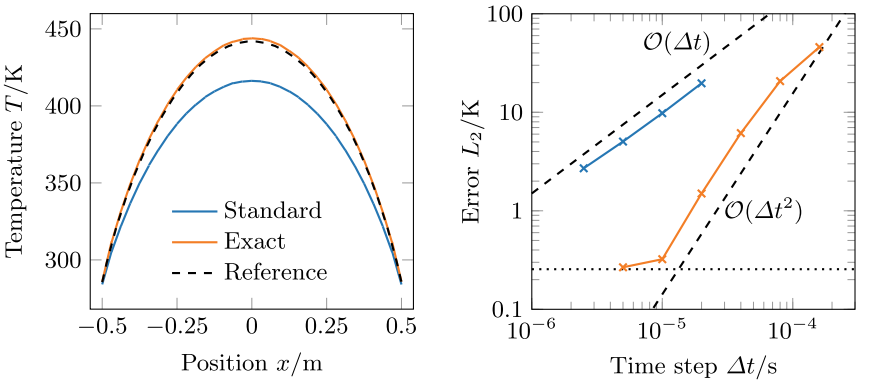

(a) Results with $\Delta t = 2 \times 10^{-5}$ s. (b) Convergence for varying time steps.

Fig. 1 Comparison of the exact integration of the collision operator against the standard approach that assumes a constant diffusion matrix. The dotted line on the right plot shows the estimated bias of the temperature

where T_i and $T_{ref,i}$ are the temperatures of the current simulation and the reference solution evaluated at the center of element i respectively. Figure 1b shows the error L_2 for the two different time integration schemes. It can be seen that, while both methods theoretically use a second-order splitting scheme, only the method using the exact integration of the collision term shows a second-order convergence rate. The standard approach only shows a first-order convergence rate because of the first-order time integration of the collision term. For the smallest time step used in the exact integration of the collision term, the method does not exhibit second-order convergence. This is because the numerical error caused by the finite number of particles dominates at this time step, making the time integration error negligible in comparison. The approach used to calculate the moments on the grid gives a biased estimate of the covariance matrix, see Eq. (5), and thus leads to a biased estimate of the temperature. An estimate of the bias is drawn in Fig. 1b as a dotted line. The error is approximated by assuming a constant temperature T_{ref} and a constant number density, which leads to $N_{\text{DOF}} = N_p/(2N_e)$ particles on average per degree of freedom. Then, the bias can be calculated by using Bessel's correction:

$$\Delta T_{bias} \approx T_{\text{ref}} \left(\frac{N_{\text{DOF}}}{N_{\text{DOF}} - 1} - 1 \right). \tag{23}$$

4.2 Spatial Convergence

The convergence behavior for the different spatial interpolation schemes is tested by varying the number of elements from $N_e = 2$ to $N_e = 128$. During these tests, the

time step is kept constant at $\Delta t = 5 \times 10^{-6}$ s and the exact integration of the collision term is used. In Fig. 2, the simulation results of the spatial discretization methods are plotted when simulated using 16 elements. As with the previous example, a very fine discretization is chosen as the reference solution. In this case, the reference solution is simulated with 128 elements and a linear basis. While the constant basis exhibits a large temperature error especially in the center of the channel, the linear basis shows a near perfect agreement with the reference solution.

As for the temporal convergence, the L_2-error can be plotted over the different discretization levels. Figure 2b shows the L_2-error over the number of elements for the different discretization methods. We see that, at a given number of elements, the absolute error of the linear basis is lowest and the error of the constant basis without stochastic interpolation is highest. Interestingly, all methods appear to converge with a second-order convergence rate when the number of elements is greater than $N_e = 8$. Unfortunately, when using the linear basis, the spatial discretization error is found to be of the order of error due to the biased temperature estimate, even when only 32 elements are used. Thus, the convergence rate of the linear basis is limited by the biased estimate of the temperature. The estimate bias shown as a dotted line in Fig. 2b is calculated in the same way as for the temporal convergence. Since the number of degrees of freedom depends on the the number of elements, this bias is not constant. Also, no results could be obtained for the linear basis with fewer than 8 elements, as the stochastic noise would lead to negative pressures. The reason for this is that the orthogonal linear basis functions are not strictly positive. This can lead to negative densities as well as negative eigenvalues of the covariance matrix, which in turn leads to negative pressures.

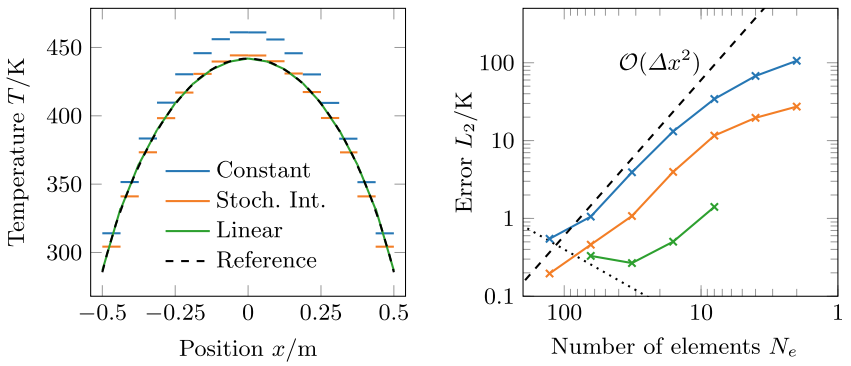

(a) Results with 16 elements.

(b) Convergence when varying the number of elements.

Fig. 2 Comparison of the deposition and interpolation schemes using a constant basis, a constant basis with stochastic interpolation and the linear basis. The dotted line on the right plot shows the estimated bias of the temperature for the linear basis

5 Conclusion

This paper presented an improved particle scheme for solving Fokker-Planck models of the Boltzmann equation. The simulation results of a 1D Couette flow showed that the Strang splitting as well as using linear basis functions provide accurate solutions for the Boltzmann equation with the Ellipsoidal-Statistical Fokker-Planck collision operator. Future work will focus on the possibility to limit the linear basis functions to avoid negative pressures. Additionally, further investigation will be done on extending the method to other Fokker-Planck operators and exploring higher-order spatial and temporal discretizations.

Acknowledgements This project has received funding from the European Research Council (ERC) under the European Union's Horizon 2020 research and innovation program (grant agreement No. 899981 MEDUSA).

References

1. Bird GA (1994) Molecular gas dynamics and the direct simulation of gas flows. Oxford University Press, New York
2. Mathiaud J, Mieussens L (2016) A Fokker–Planck model of the Boltzmann equation with correct Prandtl number. J Statist Phys 162(2):397–414
3. Gorji MH, Jenny P (2014) An efficient particle Fokker-Planck algorithm for rarefied gas flows. J Computat Phys 262:325–342
4. Burt JM, Boyd ID (2006) Evaluation of a particle method for the ellipsoidal statistical Bhatnagar-gross-Krook equation. In: 44th AIAA aerospace sciences meeting and exhibit
5. Strang G (1968) On the construction and comparison of difference schemes. J Numer Anal 5(3):506–517
6. Jiang Y, Gao Z, Lee C-H (2018) Particle simulation of nonequilibrium gas flows based on ellipsoidal statistical Fokker-Planck model. Comput Fluids 170:106–120
7. Jun E, Pfeiffer M, Mieussens L, Gorji MH (2019) Comparative study between cubic and ellipsoidal Fokker-Planck kinetic models. AIAA J 57:2524–2533
8. Fei F, Ma Y, Wu J, Zang J (2021) An efficient algorithm of the unified stochastic particle Bhatnagar-Gross-Krook method for the simulation of multi-scale gas flows. Adv Aerodynam 1–16

Open Access This chapter is licensed under the terms of the Creative Commons Attribution 4.0 International License (http://creativecommons.org/licenses/by/4.0/), which permits use, sharing, adaptation, distribution and reproduction in any medium or format, as long as you give appropriate credit to the original author(s) and the source, provide a link to the Creative Commons license and indicate if changes were made.

The images or other third party material in this chapter are included in the chapter's Creative Commons license, unless indicated otherwise in a credit line to the material. If material is not included in the chapter's Creative Commons license and your intended use is not permitted by statutory regulation or exceeds the permitted use, you will need to obtain permission directly from the copyright holder.

Impact of Entropy in Shock Recovery Through Fokker-Planck Kinetics

Veronica Montanaro, Lukas Netterdon, Manuel Torrilhon, and Hossein Gorji

Abstract While numerical methods based on the Boltzmann equation are often computationally demanding in near-continuum regime, Fokker-Planck approximations can offer efficient alternative. However, existing Fokker-Planck models remain largely heuristic and often lack global accuracy across diverse kinetic regimes, from micro-nano fluidics to the hypersonic setups. We propose a systematic recipe to construct Fokker-Planck models with special emphasis on the role of entropy and its evolution. We make the case that the Fisher entropic constraint is a key to build viable Fokker-Planck models, particularly for resolving physically accurate shock profiles. Our arguments are supported by numerical tests on a two-dimensional shock problem.

Keywords Fokker-Planck equation · Entropy · Langevin dynamics

1 Introduction

Efficient and accurate simulations of rarefied gas flows, which occur in micro-nano geometries and/or atmospheric reentry flights, remain an active area of research. This is mainly due to the limitations of conventional hydrodynamic equations, such as the Navier-Stokes-Fourier system, which often fail to provide a satisfactory macroscopic description. The Boltzmann equation is, on the other hand, the cornerstone of gas kinetics across the whole range of rarefactions [1]. Despite its mathematically rich structure and physically accurate descriptions, the numerical solution of the Boltzmann equation remains by far computationally expensive. A particle based variant

V. Montanaro · H. Gorji (✉)
Computational Engineering Laboratory, Empa, Switzerland
e-mail: mohammadhossein.gorji@empa.ch

V. Montanaro
Institute of Mathematics, EPFL, Switzerland

L. Netterdon · M. Torrilhon
Applied and Computational Mathematics, RWTH Aachen University, Aachen, Germany

© The Author(s) 2026

M. Grabe et al. (eds.), *Rarefied Gas Dynamics*, Springer Aerospace Technology,
https://doi.org/10.1007/978-3-032-00094-1_48

of the Boltzmann equation, provided by Direct Simulation Monte-Carlo (DSMC) [2] is often the method of choice, especially when practical rarefied gas settings are considered. Despite the Monte-Carlo basis of DSMC, which makes it efficient in terms of scaling with respect to the dimension, it may suffer from high computational costs in transitional regime. This is mainly due to the sharp increase in the time complexity entailed in resolving binary collisions, besides sample complexity arising in low signal-to-noise ratio regime [3, 4].

Simplified kinetic models surged as a viable tool to study different aspects of the Boltzmann equation and corresponding physical processes. Simplified collision operators such as linearized Boltzmann [5], BGK [6], and Fokker-Planck [7, 8] were introduced and studied as an alternative to solution algorithms focusing on the Boltzmann equation. Development of such models can also be of interest in broader communities concerned with micro-macro couplings [9].

Kinetic equations are inherently high-dimensional and therefore their computational complexity and memory requirements can become a limiting factor as richer processes are considered. However, they can be reset in the Monte-Carlo framework, in the same fashion as DSMC, to leverage favourable scaling while avoiding the stringent requirement of resolving collisional scales. This was the main motivation behind Fokker-Planck (FP) based particle algorithms targetting rarefied gas flow simulations. Nevertheless, one should note that these approaches do not provide a direct remedy to the sample complexity problem encountered in the low Mach regime [10, 11].

Historically, the FP equation has been studied as diffusive limit of Boltzmann kinetics [8]. Modern approaches were built on and enriched this asymptotic result, in order to improve the accuracy of FP based rarefied gas simulations. Most notably, Linear-FP [12], Cubic-FP [13], ES-FP [14], and EFP [15] were proposed. To a large degree, the modeling rational behind these approaches remain heuristic. Having these models in hand, the aim of the current study is to propose a methodology which can bring together flexibility of nonlinear-drift models and favourable entropy aspect of the Linear-FP model. The focus of the work remains at the modeling front, and we leave the more advanced algorithmic aspects including high-order time integration to separate studies.

2 Background on Fokker-Planck Models

Physically motivated derivation of FP has been pursued from different perspectives. For example, the Hamiltonian dynamics can be projected onto a resolved particle leading to the Generalised Langevin Equation, as performed in the Mori-Zwanzig formalism [16]. Alternatively, in the Kramers-Moyal expansion, the FP equation can be derived after keeping the first and second order terms [17]. No matter which path is taken, the appeal of the FP equation seems to be in its expressive power to describe complex distributions.

For our purpose, the FP equation remains an approximation of the Boltzmann equation and therefore we do not intend to pursue a first-principled derivation of FP. Instead, we postulate a flexible FP model and impose the desired properties on its structure. Yet note that the resulting model only weakly correspond to the collision dynamic underlying the Boltzmann equation, as it approximates the latter in the statistical sense. In other words, we do not attempt to recover the path of a sample particle in the FP model. This weak approximation enables us to replace collisions with stochastic paths governed by Langevin dynamics.

The FP model should be designed to ensure that (certain) non-equilibrium moments relax at rates similar to those in the Boltzmann equation. This design choice of the model is motivated by the fact that the quantities of interest in rarefied gas flow simulations can be described as macroscopic moments. Furthermore, the model should obey the entropy law, specifically with the same H-functional as in the Boltzmann equation. Besides the theoretical appeal of an entropy law (rooted in stability of the governing equation), it has been suggested that imposing certain dynamics on the entropy offers physically more accurate results, especially in shock related problems [15, 18, 19].

The main objective behind FP models is to approximate the collision operator, $S^{Boltz}[f]$, governed by the Boltzmann equation

$$\partial_t f + \nabla_{x_i}(v_i f) = S^{Boltz}[f], \tag{1}$$

with a FP one

$$S^{FP}[f] = -\nabla_{v_i}(A_i[f]f) + \Delta_{v_i v_j}(D_{ij}[f]f)\,. \tag{2}$$

Note that $f(v; x, t) : \mathbb{R}^6 \times \mathbb{R}^+ \to \mathbb{R}^{\geq 0}$ is the (normalized) density of probability of observing a particle with velocity near $v \in \mathbb{R}^3$, at position $x \in \mathbb{R}^3$ and time $t \in \mathbb{R}^+$. The drift, $A : f \mapsto A[f] \in \mathbb{R}^3$, and diffusion, $D : f \mapsto D[f] \in S^3_+$ with S^3_+ being the set of 3×3 positive semi-definite matrices with component values in $\mathbb{R}^3$, are model unknowns. Note that throughout this manuscript, we employ the index summation convention.

The path taken by the Cubic-FP model was to introduce enough degrees of freedom in the drift functional, such that the FP operator fulfills

$$\langle S^{FP}[f]H_\alpha(v)\rangle_f \stackrel{!}{=} \langle S^{Boltz}[f]H_\alpha(v)\rangle_f \tag{3}$$

for $H_\alpha(v) \in \{1, v, v \otimes v, v\|v\|^2\}$, where $\langle . \rangle_f$ is shorthand for the integration, i.e., $\langle g \rangle_f = \int_{\mathbb{R}^3} gf \; dv$. Despite the fact that introducing higher order terms in $A[f]$ leads to fulfillment of the constraint (3), it turns out the specific form of the entropy relaxation is crucial for accuracy of the model in shock structure problems [15]. Upon close inspection of the Linear-FP model, we observe that the entropy functional

$$\mathcal{H}[f] = \langle \log f - 1 \rangle_f \tag{4}$$

follows specific dynamics. In particular, we get

$$\partial_t \mathcal{H}[f] = -D[f] \overbrace{\left\langle \nabla_{v_i} \log \frac{f}{f_{eq}} \nabla_{v_i} \log \frac{f}{f_{eq}} \right\rangle_f}^{=:I[f|f_{eq}]} , \tag{5}$$

where f_{eq} is the equilibrium density and $D_{ij} = D\delta_{ij}$. Note that the term $I[f|f_{eq}]$ is the Fisher information, which has rich physical interpretations [20], and we refer to Eq. (5) as the Fisher entropic constraint.

3 Problem Statement and Main Idea

Motivated by flexibility of the Cubic-FP model, we propose a modeling approach where moment constraints (3) along with the Fisher entropic constraint (5) are fulfilled. We construct the model as an expansion around the linear one, with the time scale $\tau > 0$. Therefore, we set

$$A[f] = -\frac{1}{\tau} v_i' + A^{ho}[f] \tag{6}$$

where $v' = v - U$, $U = \langle v \rangle_f$, and

$$D_{ij}[f] = \frac{1}{3\tau} \langle v_l' v_l' \rangle_f \delta_{ij} =: D\delta_{ij} , \tag{7}$$

with δ_{ij} as the Kronecker delta. Direct computation shows that the Fisher entropic constraint can be translated into

$$\langle \nabla_{v_i} A_i^{ho}[f] \rangle_f = 0 . \tag{8}$$

This is an interesting result since it allows us to embed the entropy constraint given by Eq. (5) into the high-order terms of the drift. Considering the moment constraints for momentum, pressure tensor, and heat-fluxes, besides Eq. (8), we follow a polynomial expansion of the drift

$$A_i^{ho}[f](v) = c_i^{(0)} + c_{ij}^{(1)} v_j' + 2c_j^{(2)} v_i' v_j' + c_i^{(2)} \|v'\|^2 + c^{(3)} v_i' \|v\|^2 + c^{(4)} v_i' \|v'\|^4 , \tag{9}$$

where the 11 coefficients $\{c^{(0)}, c^{(1)}, c^{(2)}, c^{(3)}\}$ depend on f (through its moments), ensuring the moment consistency relations together with the entropy constraint. The coefficient $c^{(4)} < 0$, $|c^{(4)}| \ll 1$ is introduced for the stability of the drift, guaranteeing that $A_i \to -\infty$ as $\|v\| \to \infty$. Besides $c^{(0)}$, that can be found based on momentum conservation and $c^{(4)}$, which is set as a stabilizer, the 10 remaining coefficients (six

components in $c^{(1)}$, three components in $c^{(2)}$ and one in $c^{(3)}$) can be computed from a 10×10 linear system via plugging the ansatz (9) into the constraints (3) and (8). We refer to the model with coefficients described above as Fisher Entropic FP (FE-FP) model. Some remarks are in order.

1. The model coefficients can be found from the linear system where the explicit knowledge of f is not required. The system is comprised of the moments which can be computed from particle ensemble.
2. In comparison to EFP [15], which only ensures $\partial_t \mathcal{H} \leq 0$, the introduced model fulfills a stronger constraint on the entropy evolution given by Eq. (5).
3. The time scale τ which controls the rate of entropy decay via

$$\partial_t \mathcal{H} = -\frac{1}{3\tau} \langle v_i' v_i' \rangle_f \left\langle \nabla_{v_j} \log \frac{f}{f_{eq}} \nabla_{v_j} \log \frac{f}{f_{eq}} \right\rangle_f , \tag{10}$$

remains a free parameter and can be adjusted either from physical considerations or empirically based on model performance. Following the first path, it is straightforward to find $\tau = 2\mu/p$ (where μ is the viscosity and p is the pressure) leads to entropy relaxation rate of the FE-FP consistent with the Botlzmann equation, for anisotropic Gaussian initial distribution. f_G. Note that this time scale is similar to the one obtained in the linear drift model.

4 Overview of Numerics

Similar to DSMC, a particle-based Monte-Carlo approach is employed to solve the FP model. However, instead of free flight and collisions, the particle trajectories follow the Langevin equations

$$dM_i = A_i[f](M)\, dt + \sqrt{2D[f]}\, dW_i \quad \text{and} \quad dX_i = M_i\, dt, \tag{11}$$

where $M(t), X(t) \in \mathbb{R}^3$ are random variables corresponding to the particle velocity and position, respectively. The term dW denotes Wiener process with zero mean and variance dt. It follows from classic arguments that the density of the random variables, which evolve according to the Langevin equations given above, coincides with the solution of the FP equation with drift A and diffusion D [17].

Time integration of the Langevin system of the form given above requires a spatio-temporal discretization, since the coefficients depend on the macroscopic quantities through f. For simplicity, we focus on the first-order Euler-Maruyama scheme, similar to [15]. The algorithm then proceeds for each time steps, according to the following steps.

1. Estimate moments from the particle ensemble and solve for $\{c^{(0)}, c^{(1)}, ..., c^{(4)}\}$.
2. Compute the drift and diffusion, Eqs. (9) and (7).
3. Update particles velocities and positions, Eq.(11).

4. Apply the boundary conditions (similar to DSMC).
5. Output macroscopic quantities of interest.

5 Shock Results

We test the FE-FP model in supersonic flow of argon (with hard sphere molecular model and the mass $m = 66.3 \times 10^{-27}$ kg) over an infinitely thin vertical plate of length $l = 0.1828$ m. The chosen setup is the one appearing in [15], in order to highlight the deficiency of previous FP models in capturing shock structure. The vertical plate is placed at the center of a rectangular domain of $2.5l \times 1.5l$. The number density $n = 10^{20}\ 1/m^3$, and temperature $T_0 = 273$ K (similar to the isothermal plate). The flow enters the domain from the left boundary. The simulation employs 3×10^6 number of particles, 120×120 computational cells, and time-step size $\Delta t = 1.5978 \times 10^{-6}$ s. After 2′000 initial time-steps, 5′000 steps are used for time averaging.

We run the simulation with different value of the Mach number of the upstream flow Ma $= [4, 5, 6, 7]$, using the DSMC results as the benchmark. The Mach contour is compared with respect to both DSMC and Cubic-FP results, as shown in Fig. 1. Excellent agreement is observed between FE-FP and DSMC for all the range of Mach numbers, while the Cubic-FP exhibits diffused shock profile increasing proportionally with Ma. To gain further insight into the deviations between considered models, temperature profiles at $y = 1.875l$ are depicted as shown in Fig. 2. The agreement with the DSMC solution is further confirmed there.

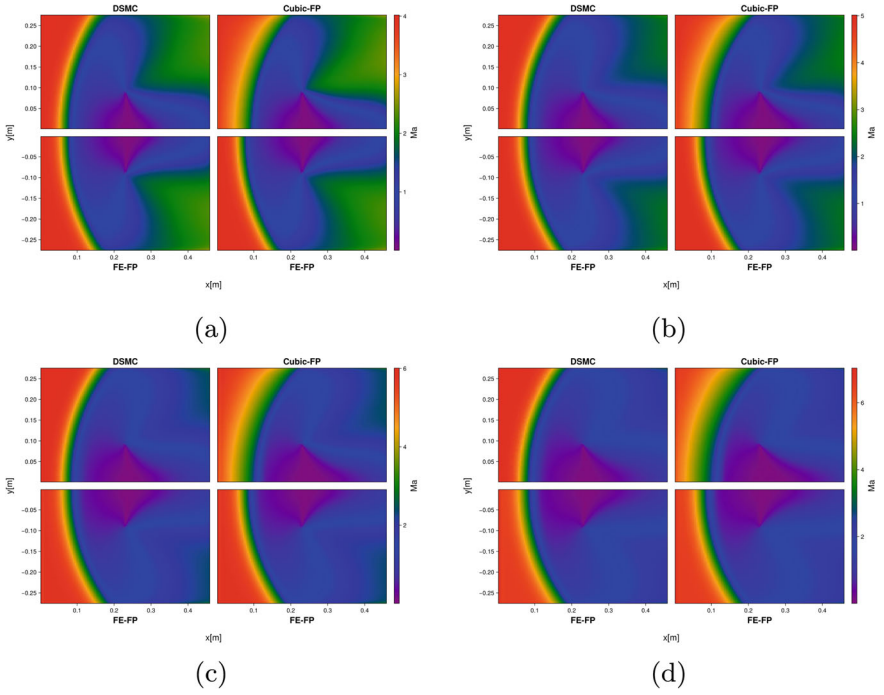

Fig. 1 Mach contours for a flow of argon over a vertical plate; Results for **a** Ma = 4, **b** Ma = 5, **c** Ma = 6, and **d** Ma = 7; DSMC and Cubic-FP results are shown on top and compared with respect to the FE-FP results at the bottom

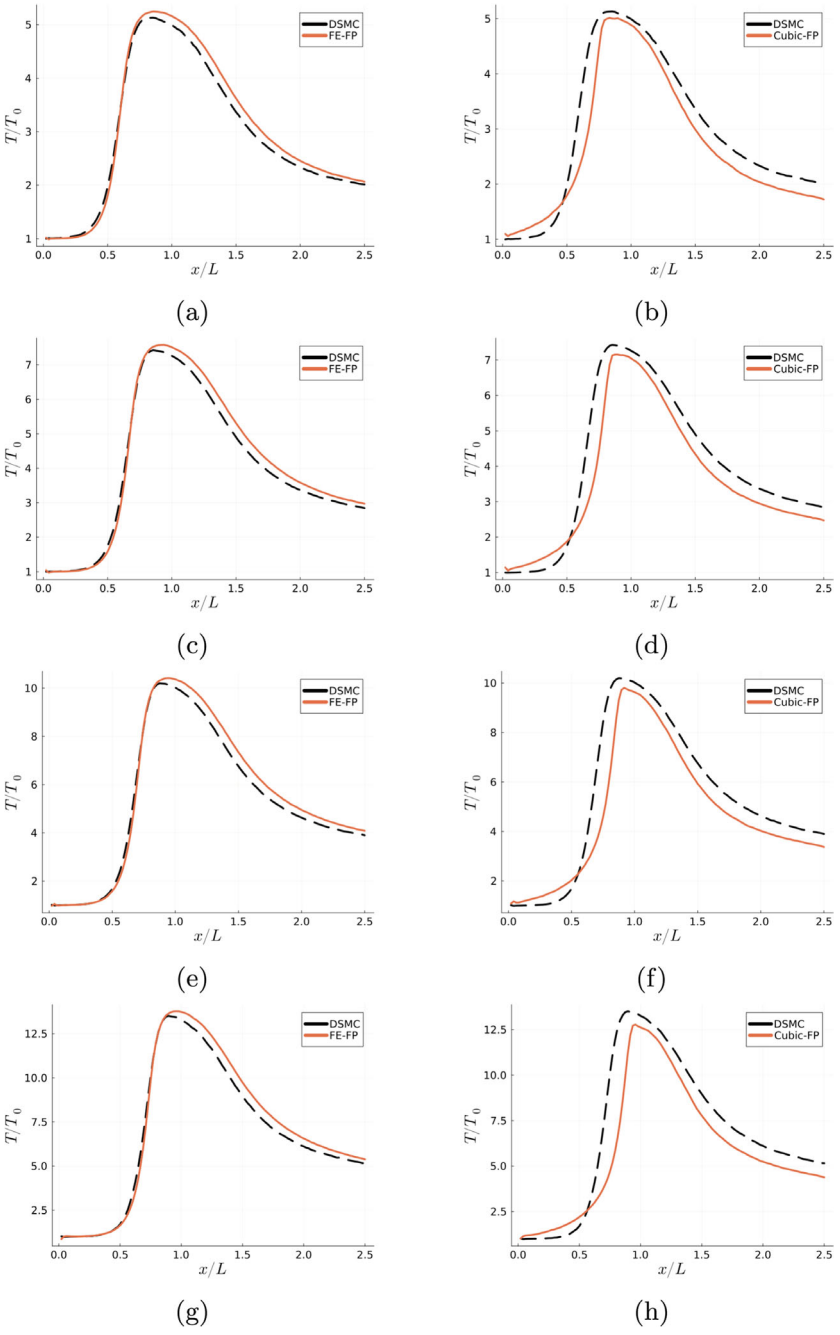

Fig. 2 Normalized temperature profiles along $y = 1.875l$; **a** and **b** Ma $= 4$, **c** and **d** Ma $= 5$, **e** and **f** Ma $= 6$, **g** and **h** Ma $= 7$; The left column compares the DSMC reference solution with the FE-FP model, while the right column shows comparisons with the Cubic-FP model

6 Conclusion

In this study, we developed a systematic approach to derive Fokker-Planck (FP) models that preserve the Fisher-entropic property. Our framework integrates the flexibility of the Cubic-FP model with the favorable entropy treatment of the Linear-FP model. This combination led to the formulation of the FE-FP model, which accurately captures shock structures given an appropriate choice of the time scale governing the entropy rate. Future works will include more extensive investigation of the FE-FP model in different benchmark problems, along with a further characterization of the time scale's role in model accuracy.

Acknowledgements This work was supported by Swiss National Science Foundation under grant number 217408, and by the Deutsche Forschungsgemeinschaft (DFG, German Research Foundation)—SPP 2410 "Hyperbolic Balance Laws in Fluid Mechanics: Complexity, Scales, Randomness (CoScaRa)" within the Project 525660607 "Model Cascades for Stochastic Particle Simulations of Rarefied Polyatomic Gases".

References

1. Carlo C (1988) The boltzmann equation. Springer, New York
2. Bird GA (1994) Molecular gas dynamics and the direct simulation of gas flows. Oxford University Press
3. Baker LL, Hadjiconstantinou NG (2005) Variance reduction for Monte Carlo solutions of the Boltzmann equation. Phys Fluids 17(5)
4. Garcia Alejandro L, Wolfgang W (2000) Time step truncation error in direct simulation Monte Carlo. Phys Fluids 12(10):2621–2633
5. Gross EP, Atlee Jackson E (1959) Kinetic models and the linearized Boltzmann equation. Phys Fluids 2(4):432–441
6. Shakhov EM (1968) Generalization of the Krook kinetic relaxation equation. Fluid Dynam 3(5):95–96
7. Pawula RF (1967) Approximation of the linear Boltzmann equation by the Fokker-Planck equation. Phys Rev 162(1):186
8. Lebowitz JL, Frisch HL, Helfand E (1960) Nonequilibrium distribution functions in a fluid. Phys Fluids 3(3):325–338
9. Sadr M, Hadjiconstantinou NG, Hossein Gorji M (2024) Wasserstein-penalized Entropy closure: a use case for stochastic particle methods. J Comput Phys 511(2024):113066
10. Gorji MH, Andric N, Jenny P (2015) Variance reduction for Fokker-Planck based particle Monte Carlo schemes. J Comput Phys 295:644–664
11. Collyer Benjamin S, Colm C, Lockerby Duncan A (2016) Importance sampling variance reduction for the Fokker-Planck rarefied gas particle method. J Comput Phys 325:116–128
12. Patrick J, Manuel T, Stefan H (2010) A solution algorithm for the fluid dynamic equations based on a stochastic model for molecular motion. J Comput Phys 229(4):1077–1098
13. Gorji MH, Torrilhon M, Jenny P (2011) Fokker-Planck model for computational studies of monatomic rarefied gas flows. J Fluid Mech 680:574–601
14. Mathiaud J, Mieussens L (2016) A Fokker-Planck model of the Boltzmann equation with correct Prandtl number. J Stat Phys 162:397–414
15. Gorji MH, Torrilhon M (2021) Entropic Fokker-Planck kinetic model. J Comput Phys 430:110034

16. Chorin Alexandre J, Hald Ole H, Raz Kupferman (2000) Optimal prediction and the Mori-Zwanzig representation of irreversible processes. Proc the Nat Acad Sci 97(7):2968–2973
17. Risken H (1996) The Fokker-Planck equation
18. Jun E, Pfeiffer M, Mieussens L, Hossein Gorji M (2019) Comparative study between cubic and ellipsoidal Fokker-Planck kinetic models. AIAA J 57(6):2524–2533
19. Kim S, Gorji H, Jun E (2023) Critical assessment of various particle Fokker–Planck models for monatomic rarefied gas flows. Phys Fluids 35(4)
20. Frieden BR (1990) Fisher information, disorder, and the equilibrium distributions of physics. Phys Rev A 41(8):4265

Open Access This chapter is licensed under the terms of the Creative Commons Attribution 4.0 International License (http://creativecommons.org/licenses/by/4.0/), which permits use, sharing, adaptation, distribution and reproduction in any medium or format, as long as you give appropriate credit to the original author(s) and the source, provide a link to the Creative Commons license and indicate if changes were made.

The images or other third party material in this chapter are included in the chapter's Creative Commons license, unless indicated otherwise in a credit line to the material. If material is not included in the chapter's Creative Commons license and your intended use is not permitted by statutory regulation or exceeds the permitted use, you will need to obtain permission directly from the copyright holder.

A Coupled Semi-Lagrangian/Finite Volume Scheme to Deal with Close-Packing Limit in Thick Sprays

Christophe Buet, Bruno Després, and Victor Fournet

Abstract This work is dedicated to the numerical discretization of a thick spray model. We present a coupled method combining a Finite Volume scheme for the fluid phase, and a semi-Lagrangian scheme for the dispersed phase. We also present two methods for taking into account the close-packing limit of the particles in the model.

Keywords Fluid-kinetic system · Numerical method · Vlasov equation

1 Introduction

In this work, we are interested in the numerical simulation of dense suspensions of particles within a carrying fluid. The starting point of this work is the following fluid kinetic system

C. Buet · V. Fournet (✉)
CEA, DAM, DIF, Arpajon, France
e-mail: victor.fournet@sorbonne-universite.fr

C. Buet
e-mail: christophe.buet@cea.fr

C. Buet
Universite Paris-Saclay, CEA DAM DIF, Laboratoire en Informatique Haute Performance pour le Calcul et la simulation, Arpajon, France

B. Després · V. Fournet
Laboratoire Jacques Louis Lions, Sorbonne Universite, Paris, France
e-mail: despres@ann.jussieu.fr

© The Author(s) 2026

M. Grabe et al. (eds.), *Rarefied Gas Dynamics*, Springer Aerospace Technology,
https://doi.org/10.1007/978-3-032-00094-1_49

$$\begin{cases} \partial_t(\alpha\varrho) + \nabla_x \cdot (\alpha\varrho\mathbf{u}) = 0 \\ \partial_t(\alpha\varrho\mathbf{u}) + \nabla_x \cdot (\alpha\varrho\mathbf{u}\otimes\mathbf{u}) + \alpha\nabla_x p = D_\star \displaystyle\int_{\mathbb{R}^3} (\mathbf{v}-\mathbf{u}) f \,\mathrm{d}v \\ \partial_t f + \mathbf{v}\cdot\nabla_x f + \nabla_v \cdot (\Gamma f) = 0 \\ \alpha = 1 - m_\star \displaystyle\int_{\mathbb{R}^3} f \,\mathrm{d}v \\ m_\star \Gamma = -m_\star \nabla_x p - D_\star(\mathbf{v}-\mathbf{u}). \end{cases} \tag{1}$$

The first two equations are modified isentropic Euler equations, where the fluid is described by its volume fraction $\alpha(t,\mathbf{x})$, its density $\varrho(t,\mathbf{x})$ and its velocity $\mathbf{u}(t,\mathbf{x})$. We moreover assume that this fluid is ideal and barotropic, with a pressure law $p(\rho)$. The particle are described by a distribution function $f(t,\mathbf{x},\mathbf{v})$ which evolves according to the third equation of (1). The coupling between the two phases is done not only through a linear drag force, where $D_\star > 0$ is a (constant) drag coefficient, but also through the volume fraction of the fluid α in the fluid equations and through the presence of the pressure gradient $-\nabla_x p$ in the force field of the Vlasov equation. The system (1) is a prototype for describing dense flow of particles within a carrying gas, it is sometimes refered to as a thick spray model [9]. In this work, we only consider the case where $p(\varrho) = \varrho^\gamma$, where $\gamma > 1$ is the adiabatic index. We place ourselves in a system of unit where the density of particles is 1, so that the coefficient $m_\star$ is an adimensional volume. Traditionaly, the numerical discretization of this kind of fluid-particle coupling is done with a Particle-In-Cell (PIC) method for the Vlasov equation [1, 7]. The PIC method has the primary advantage of only discretizing the physical space x and not the velocity space v. This drastically reduces the computational cost of a direct discretization of the Vlasov equation. Indeed, the primary computational challenge comes from the fact that the distribution function f lives in an up to six-dimensional phase space. However, particle methods are known to suffer from numerical noise that decreases very slowly, as the square root of the number of particles. They are also known to be highly sensitive to sampling errors. Recently, especially in the plasma physics community, Eulerian methods for the Vlasov equation have been developed with remarkable success [4, 5, 10–12, 14, 19]. Due to the substantial increase in computational power, 4D simulation can now be performed routinely on high performance computing (HPC) systems.

In this work, we present a numerical method for the discretization of thick sprays, based on semi-Lagrangian method for the Vlasov equation, and a Finite Volume method for the fluid phase [2, 3]. A point of interest in this work is to take into account the *close-packing limit* in the system, characterized by a state where the particle density reaches a maximum.

1.1 Close-Packing Limit

By close-packing limit, we refer to the configuration where the maximal density for the particles is reached, which typically corresponds to the case where the particles are packed on top of each other. The close-packing of particles is a part of a larger family of congestion phenomena in fluid equations. The study of such phenomena represents a prolific area of the literature, see [6, 8, 15, 17, 18] and the references therein. The system (1) does not take into account the modelling of close-packing limit. We would like to modify the model (1) so that, given a lower bound $0 \leq \alpha_\star < 1$ and assuming that the initial data verifies $\alpha(t = 0, \cdot) > \alpha_\star$, the solutions preserve the bound $\alpha(t, \cdot) > \alpha_\star$ for all $t > 0$. A priori, the system (1) does not verify this property. In the literature, multiple ways to model the close-packing limit can be found. For instance, a possible way [1, 3] to modify the Vlasov equation is to add a pressure term in the force field: $m_\star \Gamma = D_\star(\mathbf{u} - \mathbf{v}) - m_\star \nabla_x p - \frac{1}{1-\alpha}\nabla_x \pi(\alpha)$, The function $\pi : [0, \alpha_\star) \to [0, +\infty)$ is required to satisfy $\pi(0) = 0$ and $\lim_{\alpha \to \alpha_\star} \pi(\alpha) = +\infty$. Another possibility, found for instance in [13] is to modify the free transport operator directly: $\partial_t f + \nabla_x \cdot (\mathbf{v} f - \pi(\alpha)\nabla_v f) + \nabla_v \cdot (\Gamma f) = 0$. Our first proposition to implement close-packing effects in the model (1) is to modify Vlasov equation $\partial_t f + \nabla_x \cdot (\mathbf{v} f - \nabla_x \pi f) + \nabla_v \cdot (\Gamma f) = 0$.

In the literature [8], it is common to give a formula for π, which is mainly of empirical nature. A typical formula is

$$\pi(\alpha) = \varepsilon \left(\alpha_f\right)^\beta (\alpha_\star - \alpha_f)^{-\beta}, \quad \beta > 1. \tag{2}$$

The coefficient $\varepsilon > 0$ is usually taken small. Its role is to make π negligible when α_f is not very close to $\alpha_\star$. The coefficient $\beta > 1$ is given empirically. This kind of expression for π corresponds to so-called *soft congestion models* [8]. The idea is that the singular pressure π acts as a barrier that prevents the particle volume fraction from becoming too big. When $\varepsilon \to 0$, the singular pressure π tends to a limit pressure π_∞ such that $(\alpha - \alpha_\star)\pi_\infty = 0$, $\alpha \geq \alpha_\star$, $\pi_\infty \geq 0$, and the corresponding models that use this type of pressure are known as *hard congestion models* [8]. The link between the hard and soft models is interesting from a numerical point of view. The hard limit is difficult to handle because of the sharp unknown interface between the free domain (where $\pi_\infty = 0$) and the congested domain. One can instead use the soft model with small ε to approximate the hard model [6]. In this work, we only consider the case $\varepsilon > 0$. Our second proposition to take into account the close packing limit is purely of numerical nature. The idea is to introduce a correction procedure in the numerical scheme that imposes the bound $\alpha \geq \alpha_\star$. The correction procedure we propose is inspired by works done in [15, 16, 18] on the modeling of crowd motion. To finish this section, let us write the two systems that we will study. We rewrite the fluid phase in terms of the conserved variables $n := \alpha\varrho$, $\mathbf{q} := \alpha\varrho\mathbf{u} + m_\star \int_{\mathbf{R}^3} \mathbf{v} f \, \mathrm{d}v$,. The original system without packing pressure π is

$$\begin{cases} \partial_t n + \nabla_x \cdot \left(\mathbf{q} - m_\star \int \mathbf{v} f \, \mathrm{d}v\right) = 0 \\ \partial_t \mathbf{q} + \nabla_x \cdot \left(\dfrac{\left(\mathbf{q} - m_\star \int \mathbf{v} f \, \mathrm{d}v\right)^{\otimes 2}}{n} + m_\star \int \mathbf{v} \otimes \mathbf{v} f \, \mathrm{d}v \right) + \nabla_x p \left(\dfrac{n}{\alpha}\right) = 0 \\ \partial_t f + \nabla_x \cdot (\mathbf{v} f) + \nabla_v \cdot (\Gamma f) = 0 \\ \alpha = 1 - m_\star \displaystyle\int_{\mathbf{R}^3} f \, \mathrm{d}v \\ m_\star \Gamma = -m_\star \nabla_x p - D_\star (\mathbf{v} - \mathbf{u}), \end{cases} \tag{3}$$

that we will refer to as the "original model". Then, we have the system with added packing pressure

$$\begin{cases} \partial_t n + \nabla_x \cdot \left(\mathbf{q} - m_\star \int \mathbf{v} f \, \mathrm{d}v\right) = 0 \\ \partial_t \mathbf{q} + \nabla_x \cdot \left(\dfrac{\left(\mathbf{q} - m_\star \int \mathbf{v} f \, \mathrm{d}v\right)^{\otimes 2}}{n} + m_\star \int \mathbf{v} \otimes \mathbf{v} f \, \mathrm{d}v - m_\star \partial_x \pi \int f v \, \mathrm{d}v \right) + \nabla_x p \left(\dfrac{n}{\alpha}\right) = 0 \\ \partial_t f + \nabla_x \cdot [(\mathbf{v} - \nabla_x \pi(\alpha)) f] + \nabla_v \cdot (\Gamma f) = 0 \\ \alpha = 1 - m_\star \displaystyle\int_{\mathbf{R}^3} f \, \mathrm{d}v \\ m_\star \Gamma = -m_\star \nabla_x p - D_\star (\mathbf{v} - \mathbf{u}) \\ \pi(\alpha) = \varepsilon \left(\dfrac{\alpha_f}{\alpha_\star - \alpha_f} \right)^\beta, \quad \beta > 1, \end{cases} \tag{4}$$

and we will refer to it as the "soft model".

2 Numerical Methods

In this work, the systems (3) and (4) are discretized by combining classical methods. We use an appropriate time-splitting where the fluid phase is discretized using a Finite Volume scheme with Rusanov flux. The Vlasov equation is discretized using a conservative semi-Lagrangian scheme, the PFC scheme [11].

Correction procedure. The spirit of the correction procedure is to compare α_i^k with $\alpha_\star$ and check if $\alpha_i^k \geq \alpha_\star$. In this work, $\alpha_\star$ is the same in all the cells, but one could easily extend this work to a non-homogenous packing limit. Assume that $\alpha_i^k < \alpha_\star$, this means that the particle volume fraction in the cell i, $m_\star \Delta v \sum_j f_{i,j}^k$ is too big, and one has to redistribute the mass in the cells around the cell i. Taking inspiration from [15], we propose to redistribute the mass with a stochastic algorithm. Starting from the saturated cell, we initiate a random walk. When the walk encounters a cell which is not saturated, it get rids of as much mass as it can. Then the random walk continues, until the exceeding mass has been completely redistributed.

3 Numerical Results

In this section, we present several numerical results to validate our methods.

3.1 Collision of Two Pack of Particles

In this test, we consider the case with a gas initially at rest, with two clouds of particles going into the middle of the domain. The initial condition for the gas is a gas at rest with constant density and pressure $(\varrho_0, u_0, p_0)(x) = (1, 0, 1)$, with $\gamma = 1.4$. The initial condition for the particles is

$$f_0(x, v) = \frac{1}{\sqrt{2\pi\sigma_v}} e^{-\frac{(v-6)^2}{2\sigma_v^2}} \frac{1}{\sqrt{2\pi\sigma_x}} e^{\frac{(x-2.6)^2}{2\sigma_x^2}} \mathbf{1}_{v>0}(v) + \frac{1}{\sqrt{2\pi\sigma_v}} e^{-\frac{(v+6)^2}{2\sigma_v^2}} \frac{1}{\sqrt{2\pi\sigma_x}} e^{\frac{(x-3.4)^2}{2\sigma_x^2}} \mathbf{1}_{v<0}(v). \tag{5}$$

with $\sigma_x = \sigma_v = 0.1$. It corresponds to two clouds of particles with opposite velocities. The drag coefficient is $D_\star = 1$, and $m_\star = 0.32$, $N_x = N_v = 200$. Moreover, $\alpha_\star = 0.4$. The computational domain is $[0, 6] \times [-10, 10]$ with periodic boundary conditions on both dimensions, and discretization parameters $N_x = N_v = 200$.

The results are visible in Fig. 1 with the system (3) and in Fig. 2 with the system (4).

Initially, the two particle clouds move toward each other, the particle volume fraction increases until reaching the close-packing limit, $\alpha_\star$. This collision compresses the gas, causing a sharp rise in fluid density in the congested zone. Over time, some particles begin to penetrate this dense layer, reducing both the particle concentration and gas density as the congestion dissipates.

3.2 Shock Wave Passing Through a Layer of Particles

In this test, we examine the interaction between a shock wave and a stationary particle cloud. The gas is initialized as:

$$(\varrho_0, u_0, p_0)(x) = \begin{cases} (0.54, 1.54, 1.54^\gamma) & \text{for } x < 0.2 \\ (1, 0, 1) & \text{for } x > 0.2. \end{cases}$$

where $\gamma = 1.4$. Immediately after the shock front, there is a cloud of particles at equilibrium, with an initial distribution function given by

$$f_0(x, v) = \frac{1}{\sqrt{2\pi\sigma_x}} e^{-\frac{(x-3)^2}{\sigma_x}} \frac{1}{\sqrt{2\pi\sigma_v}} e^{-\frac{v^2}{\sigma_v}}, \tag{6}$$

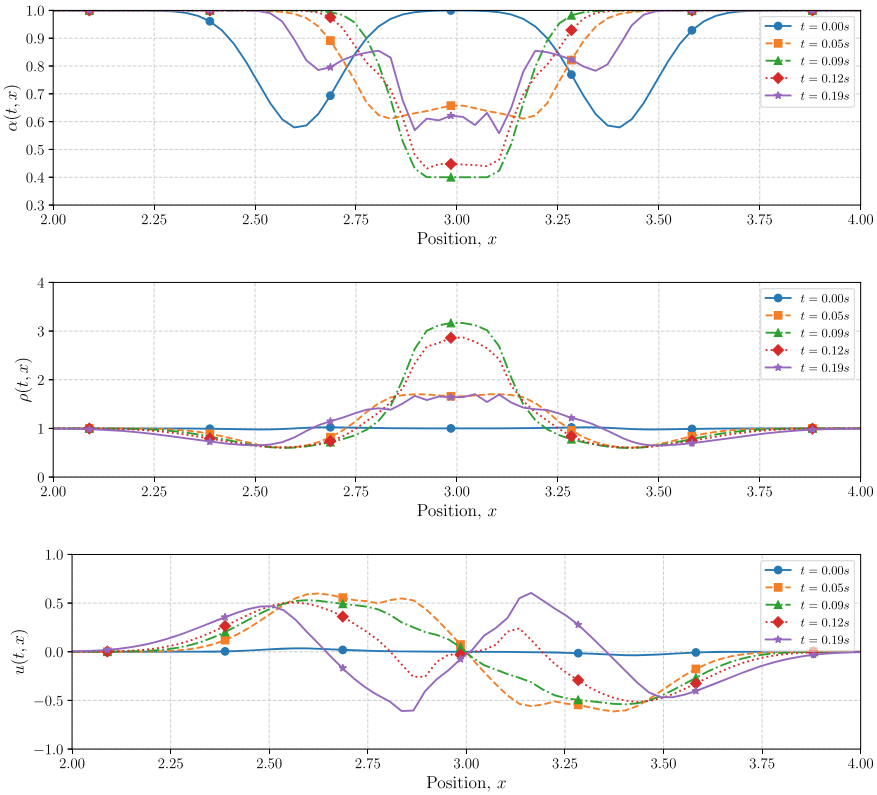

Fig. 1 Collision with the original model (3) with the PFC scheme

where $\sigma_x = \sigma_v = 0.1$. The computational domain is $[0, 6] \times [-10, 10]$. Other parameters include a drag coefficient $D_\star = 1$, $m_\star = 0.32$, $\alpha_\star = 0.4$, and discretization parameters $N_x = N_v = 200$. The results for the PFC scheme are shown in Fig. 3 for system (3) and in Fig. 4 for system (4). Initially, we observe that the shock wave compresses and pushes the particle cloud forward. This interaction causes a noticeable increase in the gas density on the left side of the particle cloud, as particles concentrate and reach the close-packing limit. At $t = 0.38$, the fluid volume fraction reaches the close-packing limit $\alpha_\star$, marking the peak compression phase in the congested region. Due to drag effects and the pressure of the gas, the gas shock transfers momentum to the particles, accelerating them in the shock's direction. This momentum transfer results in particle movement and spreading of the initial particle distribution as the shock front propagates. As particles disperse following the shock passage, the gas density and particle volume fraction start to decline, gradually returning to equilibrium. The density profile residual perturbations as the particles and gas adjust post-shock.

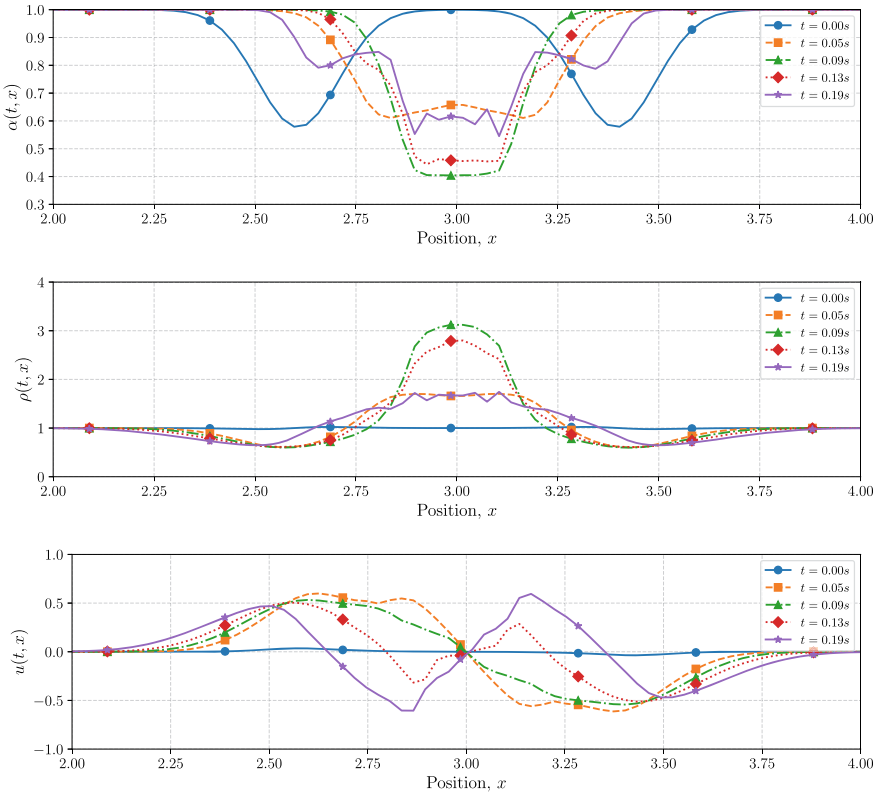

Fig. 2 Collision with the soft-congested model (4) with $\varepsilon = 10^{-6}$ with the PFC scheme

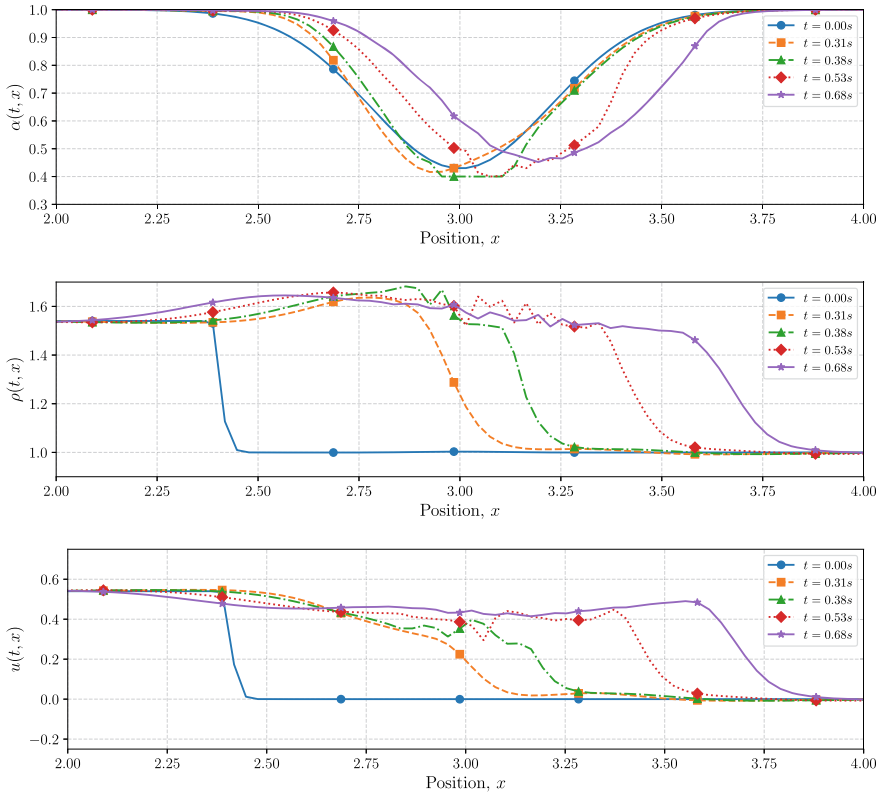

Fig. 3 Shock with the original model with the PFC scheme

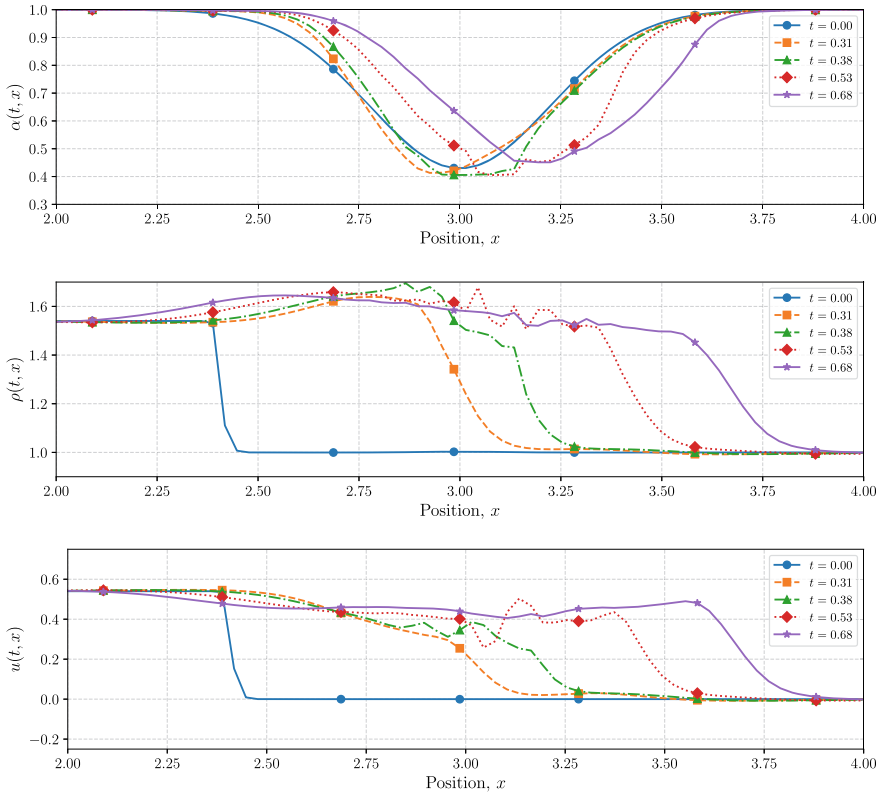

Fig. 4 Shock with the soft-congested model with $\varepsilon = 10^{-6}$ with the PFC scheme

References

1. Andrews M, O'Rourke P (1996) The multiphase particle-in-cell (mp-pic) method for dense particulate flows. Int J Multiphase Flow 22(2):379–402. https://www.sciencedirect.com/science/article/pii/0301932295000720
2. Bernard-Champmartin A, Braeunig J, Fochesato C, Goudon T (2016) A semi-lagrangian approach for dilute non-collisional fluid-particle flows. Commun Comput Phys 19(3):801–840
3. Berthelin F, Goudon T, Minjeaud S (2016) Multifluid flows: a kinetic approach. J Sci Comput 66(2):792–824
4. Besse N, Sonnendrücker E (2003) Semi-lagrangian schemes for the vlasov equation on an unstructured mesh of phase space. J Comput Phys 191:341–376
5. Cheng CZ, Knorr G (1976) The integration of the vlasov equation in configuration space. J Comput Phys 22(3):330–351
6. Degond P, Hua J, Navoret L (2010) Numerical simulations of the euler system with congestion constraint. J Comput Phys
7. Dukowicz JK (1980) A particle-fluid numerical model for liquid sprays. J Comput Phys 35(2):229–253
8. EDP J (ed) (2018) An overview on congestion phenomena in fluid equations
9. Ertzbischoff L, Han-Kwan D (2023) On well-posedness for thick spray equations, arxiv

10. Filbet F, Russo G (2003) High order numerical methods for the space non-homogeneous Boltzmann equation. J Comput Phys 186:457–480
11. Filbet F, Sonnendrücker E, Bertrand P (2001) Conservative numerical schemes for the vlasov equation. J Comput Phys 172:166–187
12. Filbet F, Sonnendrücker E, Bertrand P (2001) Conservative numerical schemes for the vlasov equation. J Comput Phys 172(1):166–187
13. Fox RO, Posey JW, Houim RW, Laurent F (2024) A kinetic-based model for polydisperse, high-speed, fluid-particle flows. Int J Multiphase Flow 171:104–698
14. Mangeney A, Califano F, Cavazzoni C, Travnicek P (2002) A numerical scheme for the integrations of the vlasov-maxwell system of equations. J Comput Phys 179:495–538
15. Maury B, Roudneff-Chupin A, Santambrogio F, Venel J (2011) Handling congestion in crowd motion modeling. Netw Heterogeneous Media
16. Maury B, Roudneff-Chupin A, Santambrogio F (2010) A macroscopic crowd motion model of gradient flow type. Math Models Methods Appl Sci
17. Perrin C, Zatorska E (2015) Free/congested two-phase model from weak solutions to multi-dimensional compressible navier-stokes equations. Commun Partial Diff Eq (2015)
18. Santambrogio F (2018) Crowd motion and evolution pdes under density constraints. ESAIM: Proceedings Surveys 64:137–157
19. Umeda T (2008) A conservative and non-oscillatory scheme for vlasov code simulations. Earth Planet SP 60:773–779

Open Access This chapter is licensed under the terms of the Creative Commons Attribution 4.0 International License (http://creativecommons.org/licenses/by/4.0/), which permits use, sharing, adaptation, distribution and reproduction in any medium or format, as long as you give appropriate credit to the original author(s) and the source, provide a link to the Creative Commons license and indicate if changes were made.

The images or other third party material in this chapter are included in the chapter's Creative Commons license, unless indicated otherwise in a credit line to the material. If material is not included in the chapter's Creative Commons license and your intended use is not permitted by statutory regulation or exceeds the permitted use, you will need to obtain permission directly from the copyright holder.

Numerical Methods for Non-equilibrium Flows

Effect of Scaled Angle on Unsteadiness Characteristics of Large Separation Bubbles in High Speed Flows

Irmak T. Karpuzcu, Deborah A. Levin, and Vassilis Theofilis

Abstract In this work, high-speed flows at moderate Reynolds numbers over compression ramps with large scaled angles were computed using the Direct Simulation Monte Carlo (DSMC) method. The free-stream conditions and ramp angles were selected to ensure that the resulting scaled angles were large, leading to correspondingly large separation bubbles. The study revealed that once the separation bubble reached a certain size, further decreasing the wall temperature and increasing the free-stream speed and physical ramp angle destabilized the flow, and resulted in the formation of secondary recirculation regions. Moreover, configurations that had secondary recirculation regions were found to exhibit unsteady behavior. This unsteadiness in the near-reattachment region was particularly pronounced across all cases.

Keywords Direct simulation monte carlo · High speed flows · Unsteadiness · Shock boundary layer interactions

1 Problem Definition and Motivation

Compression ramps are representative of many components widely used in high-speed aircraft, such as inlets, swept wings, and control surfaces. At supersonic and hypersonic speeds, these components generate complex flow structures, beginning with a leading-edge shock. As the flow moves downstream, the compression corner produces a compression shock, and the interaction of this shock with the incoming boundary layer typically results in boundary layer separation. This separation gives rise to a separation bubble, which is enclosed by the separated shear layer, the separation shock, and, farther downstream, a reattachment shock. The interactions among

I. T. Karpuzcu (✉) · D. A. Levin
University of Illinois, Urbana-Champaign, IL, USA
e-mail: itk3@illinois.edu

V. Theofilis
Center for High-Speed Flow, Faculty of Aerospace Engineering, Technion—Israel Institute of Technology, Haifa, Israel

© The Author(s) 2026

M. Grabe et al. (eds.), *Rarefied Gas Dynamics*, Springer Aerospace Technology,
https://doi.org/10.1007/978-3-032-00094-1_50

these flow structures can be classified into several types of Edney interactions [5], where each different type of interaction can cause different flow responses in terms of separation length, unsteadiness, and surface properties. It has been established that these interactions are also prone to generating unsteadiness [3, 4, 7].

One of the strong theoretical approaches to simulate such flows over compression ramps is triple deck theory [2, 12]. It assumes three decks or length scales to describe the flow where in each deck the importance of viscous and inviscid forces interchange. Three decks of the triple deck theory consists of a lower, main and an upper deck characterized by the dominant flow mechanisms such as viscous forces in the lower deck, a combination of viscous and inviscid forces in the main deck and the inviscid and irrotational forces in the upper deck. The lengths of these decks are determined by the scalings given Refs. [2, 12]. These lengths scale with $\mathrm{Re}^{-\frac{5}{8}}$ in the lower, $\mathrm{Re}^{-\frac{1}{2}}$ in the main and $\mathrm{Re}^{-\frac{3}{8}}$ in the upper deck, which also relates to the classical boundary layer theory. Triple deck theory has been used to predict surface parameters such as skin friction and pressure distributions over a flat plate and compression ramp walls. Moreover, a scaled angle parameter that uses the ratio of momentum viscous and inviscid forces is defined as [11, 14];

$$\alpha = \alpha^* \frac{Re^{\frac{1}{4}}}{0.332^{\frac{1}{2}} C^{\frac{1}{4}} (M_\infty^2 - 1)^{\frac{1}{4}}}, \qquad C = \frac{\mu_w T_\infty}{\mu_\infty T_w} \tag{1}$$

where α^* is the angle of the ramp in radians, subscript w denotes values at the wall, and ∞ at the freestream. The experiments of Egorov et al. [6] have been compared with triple deck theory to explain many flow characteristics such as the appearance of the secondary recirculation regions and the three dimensionality of the flow.

Our previous work on a 42° angle configuration demonstrated that the base flow is steady, with a large single recirculation bubble present in the flow [8]. A BiGlobal linear stability analysis revealed that this flow exhibits a growing mode in the spanwise direction as was confirmed by a three-dimensional spanwise-periodic DSMC computations. Interestingly, this unstable mode originates at the leading edge, rather than from the conventional modes typically associated with the separation bubble. Recognizing that this 42° angle case is critically stable, we modified one parameter from this case—hereafter referred to as the base configuration—and investigated the effects of wall temperature, free-stream velocity, and physical ramp angle. In our follow-up study, we established the relationship between the scaled angle and the emergence of secondary recirculation regions, as well as the dependence of separation length and recirculation strength on these parameters [10].

In this work, we further investigate the relation between the scaled angle and the unsteadiness of the flowfields. We use direct simulation Monte Carlo (DSMC) to compute the flowfields [1]. DSMC provides high-fidelity simulations for shock-dominated flowfields, such as the compression ramp flow cases considered in this study. It effectively resolves high-gradient regions, including shocks and shear layers, where continuum breakdown occurs, without introducing numerical viscosity. Furthermore, DSMC's inherent time accuracy is crucial for capturing the unsteady

Table 1 Free stream conditions for each configuration and corresponding scaled angles

	Base	Tw175	M6	CR45
Ramp angle°	42	42	42	45
Free stream velocity (m/s)	432	432	864	432
Reynolds number	11.2×10^3	11.2×10^3	22.4×10^3	11.2×10^3
Mach number	3.0	3.0	6.0	3.0
Wall temperature (K)	275	175	275	275
Scaled angle	8.60	8.45	7.07	9.22

flow characteristics typical of these flowfields. Moreover, even though the free stream conditions are continuum-like, continuum breakdown[1] occurs within the shock and shear layers of the considered flows. Therefore a kinetic method must to be used.

2 Relation Between Unsteadiness and Scaled Angle

We utilized our in-house code SUGAR [13] in this work using the free stream conditions given in Table 1. Note that the base configuration of 42° angle given in column 1 is stable and steady in 2D. In all configurations isothermal walls are used with the given wall temperatures. The free stream flow consists of molecular nitrogen (N_2) and to capture viscosity temperature dependence Variable Hard Sphere (VHS) model is used with the molecular diameter $4.17 \times 10^{-10} m$ and viscosity coefficient of 0.255. Internal modes of N_2 molecule are modeled with rigid rotor and simple harmonic oscillator models however due to the low temperature there was no effect of the internal modes on the flow conditions considered in this work. For each case, 1.1 million sampling cells are used with at least 150 simulation particles in each sampling cell giving total number of simulation particles of 200 million. SUGAR employs adaptive mesh refinement and ensures that at least 20 particles are present in each collision cell per time step.

Streamwise velocity contours with streamlines for each configuration are shown in Fig. 1 to describe the overall flowfield characteristics. As mentioned before, the base configuration is steady with a single recirculation region occupying most of the flat plate and ramp surface. Increasing the free stream velocity results in three recirculation regions in the separation bubble as well as a better defined reattachment shock. A similar result is observed when decreasing the wall temperature to 175K however there are two recirculation regions for this case, which means the effect is weaker compared to the free stream velocity. Lastly, increasing the ramp angle, the CR45 case, also results in a secondary recirculation region, however it is very small and contained at the corner location of the flow.

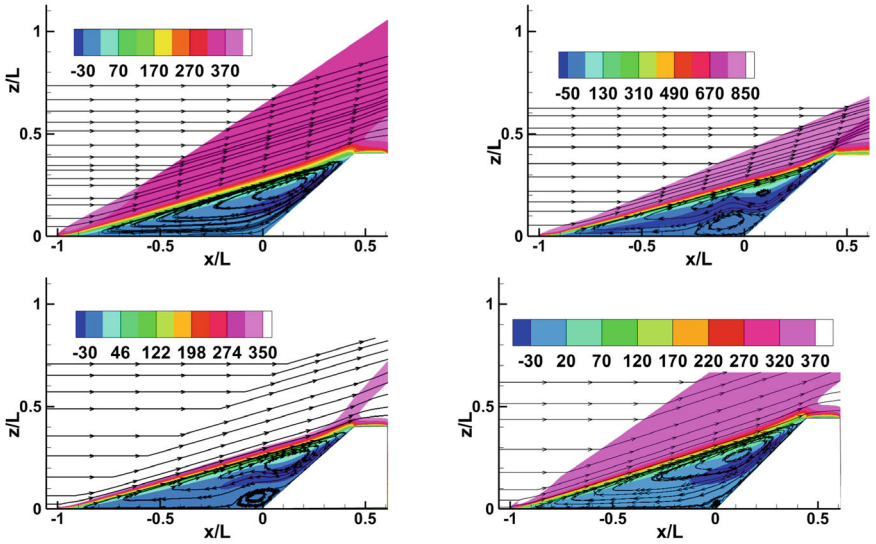

Fig. 1 Streamwise velocity, V_x (m/s), contours with streamlines. Top left: base case, top right: M6 case, bottom left: Tw175 case and bottom right: CR45 case

Next, we investigate the correlation between recirculation strength Δv [15]—defined as the ratio of the maximum reverse streamwise velocity in the separation bubble to the free-stream velocity—scaled angle, and unsteadiness characteristics. Figure 2 shows that, as the scaled angle increases, recirculation strength generally follows an increasing trend, with portions of the case results taken from earlier work [9, 10]. However, for similar scaled angle values, variations in recirculation strength are observed.

More notably, configurations with secondary recirculation regions are consistently unsteady, as indicated by the rectangular symbols in Fig. 2. These findings suggest that scaled angle alone may not fully capture the characteristics of separation bubbles at large scaled angle values. One possible reason is that the scaled angle formulation assumes a developed boundary layer, whereas the configurations in this study experience separation near the leading edge. In such cases, traditional length scalings, such as the full flat plate length, may not be appropriate and a physics-informed length, such as the boundary layer thickness prior to separation, might be more suitable.

To further investigate the unsteadiness in the flowfields, numerical probe data instantaneous pressure was taken from several locations of the separation bubble and important flow structures such as the separation and reattachment shock. It was seen that the strongest unsteadiness occurs near the reattachment location where the reattachment shock interacts with the shear layer and an immediate expansion occurs right after the reattachment. Power spectral densities (PSDs) of the mean subtracted pressure taken from the probes located near the reattachment shock foot for each case are shown in Fig. 3. It can be seen that a low frequency broadband is present for

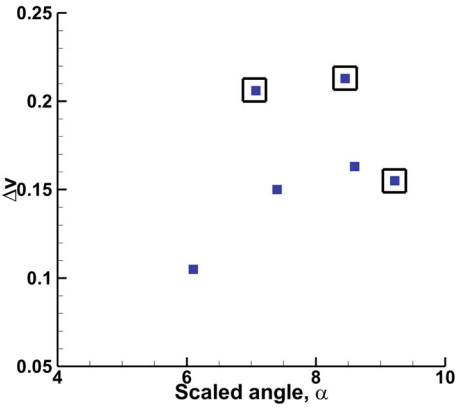

Fig. 2 Recirculation strength comparison with scaled angle. Squares indicate unsteady cases

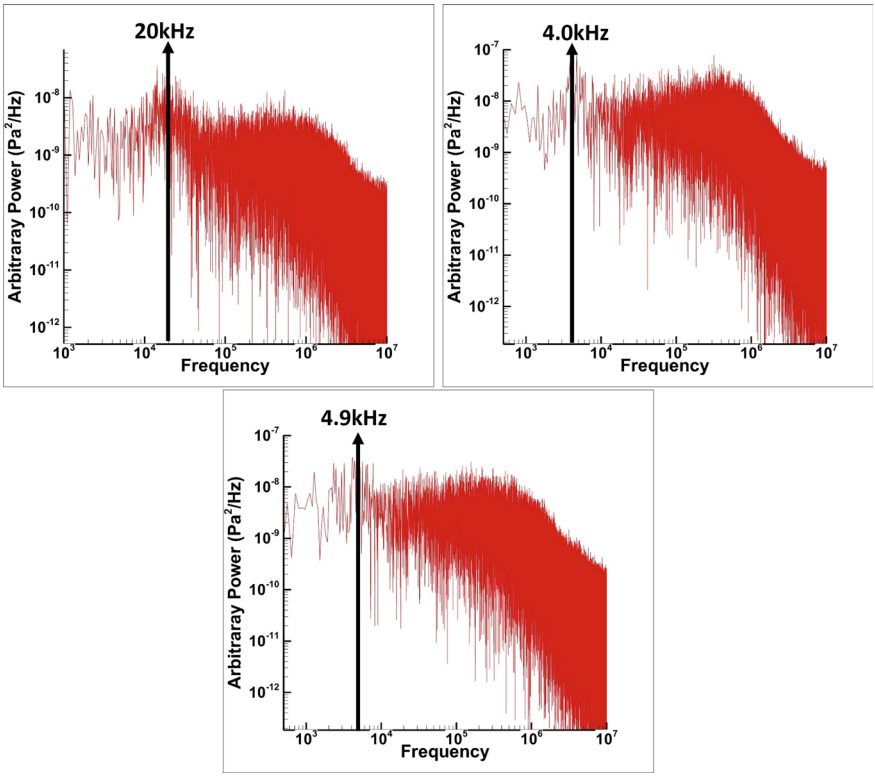

Fig. 3 Power spectral density calculated for the probe located near the reattachment for all cases. Top left: M6 case, top right: Tw175 case, and bottom: CR45 case. The arrows indicate the center of the low frequency broadband regions of the dominant frequencies

all configurations with considerably higher power peaks than the expected thermal fluctuations in the MHz range. Similar peak frequencies around 4–5 kHz are observed for Tw175 and CR45 configurations whereas a higher 20kHz band is present for the M6 configuration. This might be partly related to the fact that M6 case has twice the free stream speeds of the other cases as well as having a higher free stream Mach number that creates more complex shock interactions. These results show that the flowfields reported in this work apart from the baseline case have unsteady flow features, that needs to be investigated in more detail in a future work.

3 Summary

In this study, compression ramps with large scaled angles were simulated using DSMC in supersonic and hypersonic flows. It was shown that varying parameters such as free-stream speed, wall temperature, and ramp angle—despite producing similar scaled angle values—resulted in vastly different flowfields. Using the base configuration from Karpuzcu et al. [8], the two-dimensional base flows were found to exhibit multiple recirculation regions and unsteadiness characterized by different frequency components.

Future work will employ data-driven methods, such as Spectral Proper Orthogonal Decomposition (SPOD) and Dynamic Mode Decomposition (DMD), to investigate the unsteadiness in greater detail and extract coherent structures within these stochastic flowfields.

Acknowledgements The research conducted in this work is supported by the Office of Naval Research under Grant No. N000141202195 titled "Multi-scale modelling of unsteady shock-boundary layer hypersonic flow instabilities," with Dr. Eric Marineau as the Program Officer. This research is also supported by NSF TACC Frontera supercomputer with the project number CTS23002.

References

1. Bird GA (1994) Molecular gas dynamics and the direct simulation of gas flows. Clarendon, Oxford, England, U.K
2. Cassel KW, Ruban AI, Walker JDA (1995) An instability in supersonic boundary-layer flow over a compression ramp. J Fluid Mech 300:265–285
3. Clemens NT, Narayanaswamy V (2014) Low-frequency unsteadiness of shock wave/turbulent boundary layer interactions. Ann Rev Fluid Mech 46(1):469–492
4. Dolling DS (2001) Fifty years of shock-wave/boundary-layer interaction research: what next? AIAA J 39(8):1517–1531
5. Edney B (1968) Anomalous heat transfer and pressure distributions on blunt bodies at hypersonic speeds in the presence of an impinging shock. Aeronautical Research Institute of Sweden, Report 115 (1968)

6. Egorov I, Neiland V, Shredchenko V (2011) Three-dimensional flow structures at supersonic flow over the compression ramp. In: 49th AIAA aerospace sciences meeting including the new horizons forum and aerospace exposition. No. AIAA 2011-730
7. Gaitonde DV (2015) Progress in shock wave/boundary layer interactions. Progress in Aerospace Sciences 72: 80–99. Celebrating 60 Years of the Air Force Office of Scientific Research (AFOSR): A Review of Hypersonic Aerothermodynamics
8. Karpuzcu IT, Theofilis V, Levin DA (2024) On linear stability of supersonic flow over a short compression corner at large ramp angles. https://doi.org/10.48550/arXiv.2405.06775
9. Karpuzcu IT, Levin DA, Cerulus N, Theofilis V (2023) On the unsteadiness and three dimensionality of a laminar separation bubble for a supersonic flow over a compression corner. AIAA Paper 2023-0679
10. Karpuzcu IT, Levin DA, Theofilis V (2024) Effect of the scaled angle on the stability of a large separation bubble. AIAA Paper 2024-1359
11. Neiland VY (1969) Theory of laminar boundary layer separation in supersonic flow. Fluid Dynamics 4(4):33–35
12. Rizzetta D, Burggraf O, Jenson R (1978) Triple-deck solutions for viscous supersonic and hypersonic flow past corners. J Fluid Mech 89(3):535–552
13. Sawant SS, Tumuklu O, Jambunathan R, Levin DA (2018) Application of adaptively refined unstructured grids in DSMC to shock wave simulations. Comput Fluids 170:197–212
14. Stewartson K (1970) On laminar boundary layers near corners. Quarterly J Mech Appl Math 23(2):137–152
15. Theofilis V, Hein S, Dallmann U (2000) On the origins of unsteadiness and three-dimensionality in a laminar separation bubble. Philosophical Trans Royal Soc London 358:3229–3324

Open Access This chapter is licensed under the terms of the Creative Commons Attribution 4.0 International License (http://creativecommons.org/licenses/by/4.0/), which permits use, sharing, adaptation, distribution and reproduction in any medium or format, as long as you give appropriate credit to the original author(s) and the source, provide a link to the Creative Commons license and indicate if changes were made.

The images or other third party material in this chapter are included in the chapter's Creative Commons license, unless indicated otherwise in a credit line to the material. If material is not included in the chapter's Creative Commons license and your intended use is not permitted by statutory regulation or exceeds the permitted use, you will need to obtain permission directly from the copyright holder.

Vibronic Modelling in Direct Simulation Monte Carlo

Clément H. B. Civrais, Marcel Pfeiffer, Craig White, and René Steijl

Abstract The traditional methods for modelling the electronic excitation in direct simulation Monte Carlo (DSMC) simulations treat each internal mode individually and disregard any interaction between modes. To address this, a vibronic model was developed by Civrais et al. (Phys. Fluids 36:086112, 2024) allowing each electronic excited state to excite its unique vibrational quantum levels. This work expands on previous work by providing complementary physical insights into the modelling of the vibrational quantum levels of electronic states. The fundamental differences between the uncoupled and coupled approaches in terms of the internal energies and distribution functions are outlined. Then, the scalability of the vibronic model against the traditional approach is demonstrated for elementary operations. It is shown that the coupled approach demonstrates a comparable runtime as the uncoupled approach. Finally, the traditional uncoupled and coupled approaches are applied to the modelling of the electronic excited states on the forebody of the Space Shuttle at an altitude of 99.49 km, demonstrating the inaccuracy of the traditional assumption of the electronic excited states being distributed according to the Boltzmann statistics. It is also shown that the population of the electronic excited states and their vibrational quantum levels strongly deviate between the two approaches, suggesting a significant impact on the line intensity of molecular species' absorption spectrum.

Keywords Electronic excited states · Scalability · Space shuttle · DSMC

C. H. B. Civrais
Present institution: Center for Hypersonics and Entry Systems Studies, University of Illinois at Urbana-Champaign, Urbana, USA

C. H. B. Civrais (✉) · C. White · R. Steijl
James Watt School of Engineering University of Glasgow, Glasgow, UK
e-mail: ccivrais@uci.edu

M. Pfeiffer
Institute of Space Systems University of Stuttgart, Stuttgart, Germany

© The Author(s) 2026

M. Grabe et al. (eds.), *Rarefied Gas Dynamics*, Springer Aerospace Technology,
https://doi.org/10.1007/978-3-032-00094-1_51

1 Introduction

Modelling the electronic excited states remains a critical challenge for numerous aerothermodynamics applications. For instance, in hypersonic reentries [14], ionisation reactions and radiation are predominantly governed by the excitation of the electronic states. Furthermore, state-of-the-art chemistry calculations have demonstrated that chemical reactions not only occur from ground electronic states but also electronic excited states [12, 13]. In the context of the development of versatile numerical platforms [18, 21], it is important to allow for consistent modelling of thermodynamic and transport properties to ensure accuracy and global stability.

Over the past few decades, the direct simulation Monte Carlo (DSMC) method has emerged as a standard approach for simulating rarefied non-equilibrium flows [3]. One reason for this is the relatively simple implementation of the method, along with the various physical and chemical models that can be implemented. This adaptability enables the DSMC method to simulate complex thermal and chemical non-equilibrium effects in a flow [6, 9, 10]. Beyond its successful application in reproducing experimental measurements of typical hypersonic flows [11], recent studies have also demonstrated the successful applications of the DSMC method to combustion applications [20].

In the DSMC community, three methods have been developed to model the electronic excitation in flows [4, 14, 15]. A common aspect of all methods is that each internal mode, i.e. rotational, vibrational, and electronic, is regarded separately. However, real-gas effects involve adiabatic and non-adiabatic interactions between the internal modes. This becomes particularly significant in the analysis of molecular radiation, where achieving the correct distribution of vibrational and electronic excitation energy is crucial. In recent years, coupling of the DSMC method with radiation transport solvers has emerged for such investigations [1, 2, 18]. While in the DSMC method, the internal modes are treated separately and any interaction between modes is neglected, radiation solvers adopt a more detailed description of the internal modes in which all types of interactions between the internal modes are modelled. To perform such coupling, assumptions are made to transfer uncoupled information from DSMC into the coupled models of radiation solvers [1, 2, 14, 18].

This issue was partially addressed by Civrais et al. [5] with the development of a model for coupling the electronic and vibrational modes of molecular species in DSMC. The derivation and implementation of the vibronic model were verified for a series of adiabatic reactor simulations. In the present article, complementary studies are conducted to provide further physical insights into the modelling of the vibrational quantum levels of the electronic excited states. This work intends to demonstrate the scalability of the vibronic model against the traditional approach for elementary operations such as the initialisation of the particles in the domain and the collision routine. Additionally, it aims to compare the two approaches to the modelling of the electronic excited states of N_2 for a non-reactive air mixture about the forebody of the Space Shuttle at an altitude of 99.49 km [17].

2 Mathematical Description

2.1 Uncoupled Approach

The traditional approach [19] models the vibrational excitation using the harmonic oscillator (HO) model, where the vibrational energy is expressed as

$$\epsilon_j = hc\omega_{e,0}\left(j + \frac{1}{2}\right), \tag{1}$$

where h is the Planck constant, c the speed of light in vacuum, and $\omega_{e,0}$ is the harmonic oscillator spectroscopic constant of the ground electronic state. All spectroscopic constants presented in this article are extracted from the National Institute of Standards and Technology (NIST) database [16].

The harmonic oscillator model allows an infinite number of vibrational quantum levels, with each level being non-degenerate, i.e. $g_v = 1$. While more detailed approaches for modelling the vibrational energy of molecular species exist [7, 8], this article focuses on evaluating the coupled approach against the traditional approach for modelling the vibrational mode, i.e. Equation (1). Consequently, these more detailed approaches are not considered in this study.

Additionally, the energies associated to each electronic state are calculated as,

$$\epsilon_i = hc\kappa_{e,i}, \tag{2}$$

where $\kappa_{e,i}$ is the electronic transition of state i. Note that all electronic states have a distinct degeneracy corresponding to their electronic configuration [16].

In the uncoupled approach, each internal mode is treated separately and any interaction between modes is neglected. Therefore, each electronic excited state can only excite the same set of vibrational levels as the ground electronic state. The joint distribution function for the vibrational-electronic mode is given by the product of each individual distribution function which yields,

$$f_{i,j} = f_i \times f_j = \frac{g_i e^{-\frac{\varepsilon_i}{kT}}}{\sum\limits_{i\in\mathscr{I}} g_i e^{-\frac{\varepsilon_i}{kT}}} \times \frac{e^{-\frac{\varepsilon_j}{kT}}}{\sum\limits_{j\in\mathscr{J}} e^{-\frac{\varepsilon_j}{kT}}} = \frac{g_i e^{-\frac{\varepsilon_i}{kT}}}{Q_e} \times \frac{e^{-\frac{\varepsilon_j}{kT}}}{Q_v}, \tag{3}$$

where g_i is the degeneracy of the electronic state, $\mathscr{I}$ is the ensemble of electronic quantum levels, $\mathscr{J}$ is the ensemble of vibrational quantum levels of the ground electronic state, T is the temperature, Q_v is the vibrational partition function and Q_e is the electronic partition function.

2.2 Coupled Approach

The coupled approach assumes a coupling between the vibrational and electronic modes. Specifically, each electronic excited state has a unique set of vibrational levels described by

$$\epsilon_{i,j} = hc\kappa_{e,i} + hc\omega_{e,i}\left(j + \frac{1}{2}\right) - hc\omega_{e,i}\chi_{e,i}\left(j + \frac{1}{2}\right)^2, \tag{4}$$

where $\kappa_{e,i}$, $\omega_{e,i}$ and $\omega_{e,i}\chi_{e,i}$ are the spectroscopic constants of electronic state i.

Considering an electronic state i, the maximum vibrational quantum level permissible is determined as the vibrational quantum immediately before the dissociation energy of electronic state i, i.e. $\epsilon_{i,j} < \epsilon_{d,i}$. For some electronic configurations, all the vibrational quantum levels lie below the corresponding dissociation energy. In this particular scenario, the maximum vibrational quantum level is determined as the last vibrational quantum level before the gradient $\partial\epsilon_{i,j}/\partial j$ changes sign.

Since the electronic excited states allow for vibrational excitation, the corresponding distribution function for the vibronic mode consists of a two-dimensional Boltzmann distribution such that,

$$f_{i,j} = \frac{g_i e^{-\frac{\varepsilon_{i,j}}{kT}}}{\sum\limits_{i\in\mathscr{I}}\sum\limits_{j\in\mathscr{J}_i} g_i e^{-\frac{\varepsilon_{i,j}}{kT}}} = \frac{g_i e^{-\frac{\varepsilon_{i,j}}{kT}}}{Q_{ve}}, \tag{5}$$

where $\mathscr{J}_i$ is the set of vibrational quantum levels of electronic state i and Q_{ve} is the partition function of the vibronic mode.

As shown by Eqs. (3) and (5), the two approaches yield distinct distribution functions. In the uncoupled approach, the vibrational and electronic quantum levels are distributed through two one-dimensional distribution functions. In contrast, the coupled approach distributes the two modes on a two-dimensional distribution function that accounts for the coupling between the vibrational and electronic modes. As a result, the coupled approach defines a unique partition function for the vibronic mode which imposes the definition of a vibronic temperature, i.e. T_{ve}.

This contrasts with the traditional uncoupled approach which requires separate internal temperatures for each mode, i.e. T_v and T_e. The vibronic temperature must be used with caution to avoid misleading interpretations. Specifically, it describes a mean excitation of the vibrational-electronic mode. Since the electronic mode admits a set of vibrational levels the vibrational-electronic temperature cannot reflect the vibrational excitation of each electronic excited state but, rather, a mean excitation of the electronic excited states and their corresponding vibrational quantum levels. While it may serve the purpose of a verification exercise to verify the implementation of the model in thermal equilibrium conditions, for any non-equilibrium conditions, the vibronic temperature carries minimal physical insights. It is recommended that the local distribution functions rather than the vibronic temperature be evaluated.

3 Scalability

In the present section, the two approaches are compared on the scalability of the initialisation and collision routines. The test case involves an adiabatic reactor represented by a single cubic cell with a side length of 1.88×10^{-4} m filled with a number of DSMC simulator particles ranging between 10^4 and 2×10^6 with periodic boundaries at an equilibrium temperature of 20, 000 K. The scalability of the two approaches is monitored and depicted in Fig. 1. The ratio between the two approaches is included for reference.

Figure 1a shows that the coupled approach requires a slightly larger runtime of the initialisation routine in comparison to the uncoupled approach. For the uncoupled approach, the distribution function simplifies to an analytical expression from which the vibrational quantum level is sampled. In contrast, the electronic quantum level is sampled from a Boltzmann distribution using an acceptance-rejection scheme. The coupled approach requires sampling the vibrational and electronic quantum levels from a two-dimensional distribution function using an acceptance-rejection scheme [5]. This difference in the sampling schemes for the initialisation routine is responsible for the slight increase in the computational expense depicted in Fig. 1a.

Figure 1b shows that the coupled approach requires a similar runtime of $100\Delta t$ to the uncoupled approach as shown with a quasi-constant ratio of 1 for the range of particles considered. For the two approaches, the post-collision quantum levels are sampled from a combined distribution function of the translational and an internal mode of the colliding particle. Thus, the two approaches utilise similar sampling techniques and only differ in the description of the distribution function.

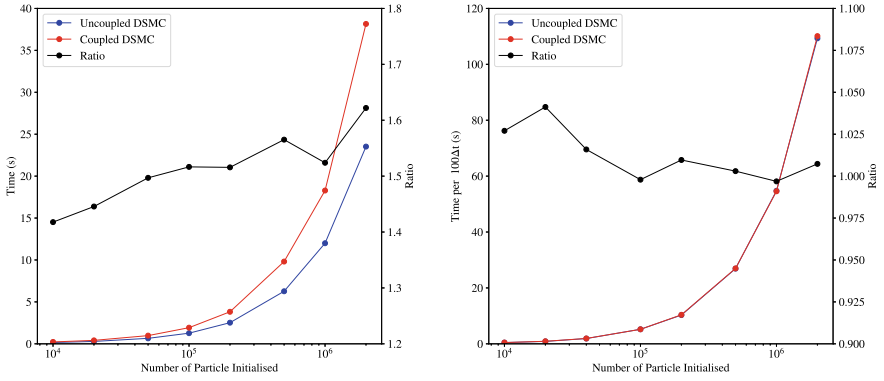

(a) Initialisation routine.

(b) Runtime for 100Δt.

Fig. 1 Scalability of the coupled approach

4 Space Shuttle Forebody at 99.49 Km

In the present section, the uncoupled and coupled approaches are compared on the modelling of the electronic excited states of N_2 for a non-reactive air mixture about the forebody of the Space Shuttle at an altitude of 99.49 km. The freestream conditions are extracted from Moss and Bird [17].

The main objective of this section is to compare the two approaches for the distribution of the internal quantum levels measured by the DSMC method and to assess the assumption that the internal quantum levels are distributed according to the Boltzmann distribution. For both approaches, the vibrational and electronic density functions are calculated with the local internal temperatures, namely $f = f_i(T_e) f_j(T_v)$ for the uncoupled approach and $f = f_{i,j}(T_{ve})$ for the coupled approach.

The computational domain extends to a length of 1.5 m upstream of the stagnation point. The freestream mean free path is approximately $\lambda_\infty = 0.133$ m resulting in a Knudsen number based on the nose radius of about $Kn = 0.098$. The mesh is refined near the stagnation point to ensure the cell size, Δx, remains smaller than the local mean free path, λ, resulting in a total number of 15, 625 cells. The time step is carefully chosen to resolve the collision frequency which results in $\Delta t = 1 \times 10^{-8}$ s. Intermolecular collisions are computed with the VHS model for a reference temperature of $T_{ref} = 273$ K. For the uncoupled approach, a finite probability of $P_r = 0.2$, $P_v = 0.02$, and $P_e = 0.002$ are, respectively, considered for rotational, vibrational, and electronic relaxation. To reproduce the typical relaxation behaviour of the uncoupled approach, a finite probability of $P_r = 0.2$, $P_1 = 0.02$, and $P_2 = 0.1$ for a particle to undergo rotational relaxation, pure vibrational excitation/de-excitation, and electronic and vibrational excitation/de-excitation, respectively, is applied [5]. The gas-surface interactions are fully diffusive with a wall temperature $T_w = 800$ K. To maintain a minimal number of 100 particles per cell throughout, the numerical mesh is populated with a total number of 1.53×10^7 DSMC particles at steady state.

Figure 2 shows the distribution functions probed at four stations along the stagnation streamline. It is shown that the DSMC measurements of the distribution function at about 1 m to the stagnation point are similar to that of the distribution function located at 0.25 m to the stagnation point. This suggests that post-shock information is carried upstream of the shock wave. This phenomenon is attributed to high Knudsen number regimes in which the degree of rarefaction is sufficient for a particle to collide with the surface of the body and travel backwards without undergoing sufficient collisions with any other particles to de-excite and return to an equilibrium distribution. This non-equilibrium effect is characterised by a strong deviation from a Maxwell velocity distribution [1, 14, 15].

Additionally, Fig. 2 indicates a strong deviation between the two approaches in the DSMC measurements. For all locations, the two approaches appear to present similar distributions for the first few quantum levels where the two approaches differ in the tail. This deviation is the result of the difference in the description of the vibrational quantum between the two approaches. Specifically, the traditional approach assumes

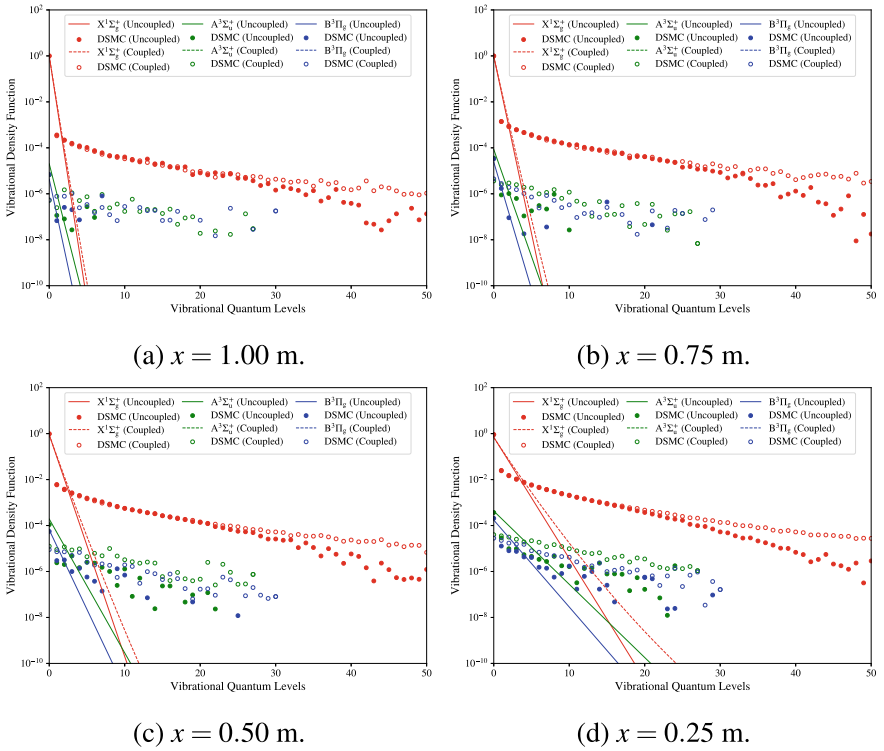

(a) $x = 1.00$ m. (b) $x = 0.75$ m.

(c) $x = 0.50$ m. (d) $x = 0.25$ m.

Fig. 2 Vibrational density function of the first three electronic states of N_2 at four locations along the stagnation streamline

that each electronic state excites the same set of infinite vibrational quantum levels as the ground state, whereas the coupled approach models the vibrational excitation of the electronic states with a state-specific set of vibrational quantum levels.

Furthermore, Fig. 2 shows that the DSMC measurements largely deviate from the traditional assumption of the quantum levels being distributed according to the Boltzmann distribution. The derivation of the Boltzmann distribution imposes the system to be in thermal equilibrium which is not applicable in such an application. In light of these results, when coupling a DSMC and a radiation solver, the authors recommend transferring the local distribution function rather than the mean internal temperatures. While this recommendation does not fully address the limitations in modelling all the interactions between internal modes, it can at least carry more accurate and meaningful information between solvers.

5 Conclusion

The merits of the recently developed coupled approach for modelling the vibrational quantum levels of the electronic states are discussed. The scalability of the initialisation and collision routines of the coupled approach is assessed against the uncoupled approach. Additionally, the coupled approach is applied to a non-reactive air mixture past the Space Shuttle at an altitude of about 99.49 km to assess the traditional assumption made to transfer uncoupled information from the DSMC method to radiation solvers.

The scalability study indicates that the coupled approach has similar computational requirements to the uncoupled approach. The initialisation routine presents a slight increase in the computation expenses due to the sampling on a two-dimensional distribution function. However, the coupled approach demonstrates comparable runtime per 100 iterations to the uncoupled approach.

The STS-II study demonstrates that the traditional assumption of the vibrational and electronic quantum levels being Boltzmann distributed is invalid. This discrepancy is attributed to non-equilibrium effects in high Knudsen number regimes. The authors recommend taking advantage of the DSMC method by measuring the local distribution functions rather than the internal temperatures and transferring this measurement to radiation solvers.

In the present article, chemical reactions have been neglected; however, it is evident that they play a significant part in aerothermodynamic applications. Therefore, further investigations must be carried out to integrate the contribution of the electronic excited states to the reaction rates. Given the limited data available on chemical reactions involving electronic excited states, one may benefit from the quantum-kinetic (QK) chemistry model which solely relies on the collision properties of the colliding partners.

Acknowledgements This work was initiated during a secondment at the University of Stuttgart. The lead author gratefully acknowledges scholarship funding from the James Watt School of Engineering through the Jim Gatheral Travel Grant 2023.

References

1. Beyer J, Nizenkov P, Fasoulas S, Pfeiffer M (2024) Simulation of radiating non-equilibrium flows around a capsule entering Titan's atmosphere. In: AIP conference proceedings, vol 2996, issue 1, p 200002
2. Beyer J, Pfeiffer M, Fasoulas S (2022) Non-equilibrium radiation modeling in a gas kinetic simulation code. J Quantitative Spectrosc Radiative Transfer 280:108083
3. Bird GA (1994) Molecular gas dynamics and the direct simulation of gas flows. Oxford University Press Inc
4. Burt JM, Josyula E (2017) Direct simulation Monte Carlo modeling of gas electronic excitation for hypersonic sensing. J Thermophysics Heat Transfer 31(4):858–870

5. Civrais CHB, Pfeiffer M, White C, Steijl R (2024) Modelling of the electronic excited states in high-temperature flows. Phys Fluids 36(8):086112
6. Civrais CHB, Pfeiffer M, White C, Steijl R (2025) Development and validation of the vibronic QK model for oxygen dissociation reactions. In: 3rd international conference on flight vehicles, aerothermodynamics and re-entry (FAR), Arcachon
7. Civrais CHB, White C, Steijl R (2022) Vibrational modeling with an anharmonic oscillator model in direct simulation Monte Carlo. J Thermophysics Heat Transfer 37(3):534–548
8. Civrais CHB, White C, Steijl R (2023) Extension of the normal shock wave relations for calorically imperfect gas. Shock Waves 33:533–551
9. Civrais CHB, White C, Steijl R (2024) Quantum kinetics chemistry models with an anharmonic oscillator model. Model derivation and limitations. Phys Fluids 36(8):086120
10. Civrais CHB, White C, Steijl R (2024) Quantum kinetics chemistry models with an anharmonic oscillator model. Model extension and validation. Phys Fluids 36(11):116128
11. Gimelshein SF, Wysong IJ (2019) Nonequilibrium air flow predictions with a high-fidelity direct simulation Monte Carlo approach. Phys Rev Fluids 4(3):033405
12. Grover MS, Bisek NJ, Valentini P (2025) Direct simulation Monte Carlo of hypervelocity experiments. In: AIAA SCITECH 2025 Forum. Orlando, FL, AIAA Paper 2025-0209
13. Jo SM, Venturi S, Kim JG, Panesi M (2023) Rovibrational internal energy transfer and dissociation of high-temperature oxygen mixture. J Chem Phys 158(6):064305
14. Li Z, Ozawa T, Sohn I, Levin DA (2011) Modeling of electronic excitation and radiation in non-continuum hypersonic reentry flows. Phys Fluids 23(6):066102
15. Liechty DS, Lewis MJ (2014) Extension of the quantum-kinetic model to lunar and Mars return physics. Phys Fluids 26(2):027106
16. Linstrom PJ, Mallard WG (2024) NIST Chemistry WebBook, NIST Standard Reference Database Number 69. National Institute of Standards and Technology. Retrieved 30 Jan 2024
17. Moss JN, Bird GA (2003) Direct simulation of transitional flow for hypersonic reentry conditions. J Spacecraft Rockets 40(5):830–843
18. Pfeiffer M, Beyer J, Vaubaillon J, Matlovič P, Tóth J, Fasoulas S, Löhle S (2024) Numerical simulation of an iron meteoroid entering into Earth's atmosphere using DSMC and a radiation solver with comparison to ground testing data. Icarus 407:115768
19. Pfeiffer M, Nizenkov P, Mirza A, Fasoulas S (2016) Direct simulation Monte Carlo modeling of relaxation processes in polyatomic gases. Phys Fluids 28(2):027103
20. Trivedi S, Cant RS, Harvey JK (2021) Molecular level simulations of combustion processes using the DSMC method. Combustion Theory Modelling 25(2):351–363
21. Vasileiadis N, White C (2024) hybridDCFoam: a coupled DSMC/Navier–Stokes–Fourier solver for steady-state multiscale rarefied gas flows. Adv Eng Softw 193:103669

Open Access This chapter is licensed under the terms of the Creative Commons Attribution 4.0 International License (http://creativecommons.org/licenses/by/4.0/), which permits use, sharing, adaptation, distribution and reproduction in any medium or format, as long as you give appropriate credit to the original author(s) and the source, provide a link to the Creative Commons license and indicate if changes were made.

The images or other third party material in this chapter are included in the chapter's Creative Commons license, unless indicated otherwise in a credit line to the material. If material is not included in the chapter's Creative Commons license and your intended use is not permitted by statutory regulation or exceeds the permitted use, you will need to obtain permission directly from the copyright holder.

A Non-negative Least Squares-Based Approach for Moment-Preserving Particle Merging

Georgii Oblapenko

Abstract In the present work, a novel particle merging scheme is proposed for PIC-DSMC simulations, based on the solution of a Non-negative Least Squares problem. The merging algorithm conserves arbitrary moments of the velocity distribution function, and a collision rate-conserving version of the algorithm is presented as well. Numerical simulations show excellent performance of the merging algorithm in terms of accuracy.

Keywords DSMC · Particle merging · Non-negative least squares

1 Introduction

Rarefied gas flows arise in a variety of engineering applications, such as aerospace engineering, semiconductor manufacturing, and nanotechnology applications [17]. Their non-equilibrium nature precludes the use of traditional continuum-based computational fluid dynamics approaches for their simulation and necessitates the use of either higher-order moment equations [18], or of kinetic solvers, such as the Direct Simulation Monte Carlo (DSMC) method [3]. The DSMC method has established itself as one of the main tools for rarefied gas dynamics simulations. In its standard formulation, the DSMC approach assumes that each computational particle represents a fixed number of actual particles. This causes issues in simulating flows with large density gradients and/or trace chemical species, as resolving the low populations requires a large number of simulation particles.

To resolve this issue, variable-weight DSMC approaches have been suggested, where the weight of the computational particles are not fixed [2, 5, 16]. The drawback is that, during collisions, particles have to be split, leading to an exponential growth in the number of particles if left unchecked. The growth becomes even more rapid if modern collision schemes with improved resolution of low-probability events are used [2, 14]. Therefore, particle merging is required, i.e. a procedure that reduces

G. Oblapenko (✉)
Applied and Computational Mathematics, RWTH Aachen, Schinkelstrasse 2, Aachen, Germany
e-mail: oblapenko@acom.rwth-aachen.de

© The Author(s) 2026

M. Grabe et al. (eds.), *Rarefied Gas Dynamics*, Springer Aerospace Technology,
https://doi.org/10.1007/978-3-032-00094-1_52

the number of particles in a simulation. This inherently incurs an information loss and may lead to significant numerical errors. Multiple merging algorithms have been developed [6, 12, 15, 19] in an attempt to reduce this error and improve the efficiency of the merging procedure. They frequently rely on a "divide-and-conquer" strategy: the particles chosen for merging are grouped into smaller sets in velocity space, and in each of these subsets all the particles are replaced by a very small number (usually 1 or 2) of particles. The advantage of such an approach is that it is possible to compute the weights, positions, and velocities of the post-merge particles in each subset analytically. However, the analytical merging of particles is restricted to conservation of lower-order moments of particle distribution, as conservation of higher-order moments requires solving of systems of non-linear equations. In addition, it is in general not possible to guarantee that post-merge particles will not end up outside of the physical domain or that their velocities will not exceed the velocities of the original set of particles. Therefore, it is of interest to design merging schemes that can ensure conservation of higher-order moments and constraint satisfaction [10]. The recent scheme of Gonoskov [7] is an example of a moment-preserving merging scheme that has also been successfully coupled with the octree grouping approach [8]. In this work we investigate an alternative moment-preserving merging scheme based on solution of a non-negative least squares problem and apply it to simulation of two model spatially homogeneous problems. In addition, a rate-preserving version of the scheme is formulated for plasma simulations. We compare the results with those obtained by the octree merging scheme and show that the new scheme leads to lower bias in the numerical solution.

2 Particle Merging

We consider a set of particles $\mathcal{P}_N = \{(w^{(i)}, v_x^{(i)}, v_y^{(i)}, v_z^{(i)})\}_{i=1}^N$, where each particle is characterized by its non-negative computational weight $w^{(i)} \geq 0$ and the 3 velocity components $v_x^{(i)}, v_y^{(i)}, v_z^{(i)}$. In the present work we disregard the particle positions and focus only on preservation of velocity moments. Merging of particles corresponds to computation of a new set of particles $\hat{\mathcal{P}}_M = \{(\hat{w}^{(i)}, \hat{v}_x^{(i)}, \hat{v}_y^{(i)}, \hat{v}_z^{(i)})\}_{i=1}^M$, $M < N$.

We are interested in conserving central moments, but since we assume Galilean invariance, once can always compute the mean velocities $\overline{v}_x, \overline{v}_y, \overline{v}_z$, subtract them from the velocities of $\mathcal{P}_N$, merge down the particles, and add the mean velocity components to the post-merge particles $\hat{\mathcal{P}}_M$. Therefore, we assume that $\overline{v}_x = \overline{v}_y = \overline{v}_z = 0$ and focus on the non-central moments

$$M_{jkl}(\mathcal{P}) = \frac{1}{\sum_i w^{(i)}} \sum_i w^{(i)} \left(v_x^{(i)}\right)^j \left(v_y^{(i)}\right)^k \left(v_z^{(i)}\right)^l. \tag{1}$$

We are interested in developing a merging approach that can conserve not only the basic invariants of mass, momentum, and energy, but also certain higher-order moments M_{jkl} of prescribed order j, k, l.

2.1 Non-negative Least Squares Merging

Now we consider an alternative merging algorithm, based on the non-negative least squares approach. Let us consider the definition (1) for a set of moments $(M_{j_1k_1l_1}, \ldots, M_{j_Lk_Ll_L})$ in matrix form:

$$\mathbf{V}\mathbf{w} = \mathbf{M}, \tag{2}$$

where the matrices and vectors $\mathbf{V} \in \mathbb{R}^{L\times N}$, $\mathbf{w} \in \mathbb{R}^N$, $\mathbf{M} \in \mathbb{R}^L$ are defined as

$$\mathbf{V} = \begin{pmatrix} \left(v_x^{(1)}\right)^{j_1}\left(v_y^{(1)}\right)^{k_1}\left(v_z^{(1)}\right)^{l_1} & \ldots & \left(v_x^{(N)}\right)^{j_1}\left(v_y^{(N)}\right)^{k_1}\left(v_z^{(N)}\right)^{l_1} \\ & \ddots & \\ \left(v_x^{(1)}\right)^{j_L}\left(v_y^{(1)}\right)^{k_L}\left(v_z^{(1)}\right)^{l_L} & \ldots & \left(v_x^{(N)}\right)^{j_L}\left(v_y^{(N)}\right)^{k_L}\left(v_z^{(N)}\right)^{l_L} \end{pmatrix}, \tag{3}$$

$$\mathbf{w} = \left(w^{(1)} \ldots w^{(N)}\right)^{\mathrm{T}}, \quad \mathbf{M} = \left(M_{j_1k_1l_1} \ldots M_{j_Lk_Ll_L}\right)^{\mathrm{T}}. \tag{4}$$

We can switch our point of view and consider (2) not as a definition (i.e. given particle velocities and weights, one can compute the moments), but as a system of linear equations for $\mathbf{w}$, i.e. the particle weights: given a set of moments and particle velocities, one can compute the weights. Depending on the number of particle velocities and moments, this system is be either under- ($N > L$), well- ($N = L$, or over-determined ($N < L$). We consider the under-determined case ($N > L$), that is, we have more unknown particle weights than moments. However, we augment the system with the requirement that $w_i \geq 0$. This leads to a non-negative least squares (NNLS) problem [11]. One property of solutions of under-determined NNLS problems is their sparsity: it is highly likely that some entries of the solution vector $\mathbf{w}$ will be 0. We can leverage this sparsity property of NNLS solutions in order to use the NNLS algorithm as a merging method:

1. Given a set of particles $\mathcal{P}_N$, we compute the matrix $\mathbf{V}$ and vector $\mathbf{M}$, as defined by (3)–(4)
2. Next, we solve system (2) for $\mathbf{w}'$ using the NNLS method
3. We replace the original set of particles $\mathcal{P}_N$ with new particles, by taking the velocities from the original set of velocities used to construct $\mathbf{V}$ and new weights from the solution vector $\mathbf{w}$, skipping creation of particles whose weights are equal to 0.

Thus one can can conserve any velocity and spatial moments (not considered in the present work, but incorporating them only means adding additional rows to $\mathbf{V}$ and

M), and also has full control over the post-merge velocities and spatial locations of the particles, since they are explicitly used to construct **V**. However, the existence of a solution is not guaranteed. In addition, we have no control of the number of non-zero weights, although in practice it is usually equal to L. The algorithm conserves mass, momentum, and energy, as long as the moments M_{000}, M_{100}, M_{010}, M_{001}, M_{200}, M_{020}, M_{002} are conserved; therefore, these are always included in the set of conserved moments.

To increase the chances of finding a solution, we compute the velocities defined by the second-order moments: $v_{x,M_2} = \sqrt{M_{200}}, v_{y,M_2} = \sqrt{M_{020}}, v_{z,M_2} = \sqrt{M_{020}}$. We then augment the matrix **V** with additional columns computed using new velocities with a magnitude of $\alpha v_{i,M_2}, i = x, y, z$, where $\alpha \in [0, 1]$ is a user-defined multiplier, with the velocity signs chosen so that these additional velocities cover all octants in velocity space. In the present work, 16 additional columns are added to **V** in this manner: 8 with $\alpha = 1$ and 8 with $\alpha = 0.5$. An additional constraint is added that the velocities of these points do not exceed the minimum and maximum velocities in the corresponding directions. This has been found to improve the stability of the algorithm, but a more detailed investigation of the optimal choice of additional velocities is left for future work. If on a given timestep the NNLS merging approach fails to produce a sparse solution to the linear system (2), one can switch to an alternative merging approach.

We also consider conservation of inter-species collision rates. This is complicated by the fact that collision rates depend on the relative velocity of the colliding particles g, i.e. on both species' VDFs. However, for the specific case of electron-neutral collisions in a plasma, one can use the common assumption that the electron velocities are significantly higher than those of the neutrals:

$$v_{\mathrm{e}} \gg v_{\mathrm{n}}, \tag{5}$$

where v_{e} is the velocity of electrons, and v_{n} is the velocity of the neutrals. Using this assumption, one can approximate an electron-neutral collision rate k as

$$k(g) = \frac{1}{w_{\mathrm{e}} w_{\mathrm{n}}} \sum_i \sum_j w_{\mathrm{e}}^{(i)} w_{\mathrm{n}}^{(j)} |v_{\mathrm{e}}^{(i)} - v_{\mathrm{n}}^{(j)}| \sigma(|v_{\mathrm{e}}^{(i)} - v_{\mathrm{n}}^{(j)}|) \approx \frac{1}{w_{\mathrm{e}}} \sum_i w_{\mathrm{e}}^{(i)} |v_{\mathrm{e}}^{(i)}| \sigma(|v_{\mathrm{e}}^{(i)}|). \tag{6}$$

Here $\sigma(g)$ is the cross-section of the process for which the rate is being calculated. With this assumption, the approximate rate becomes a function of the electron VDF only, and can thus be conserved when merging the electron particles by adding the following row to matrix **V**:

$$\left(|v_{\mathrm{e}}^{(i)}| \sigma(|v_{\mathrm{e}}^{(i)}|) \ldots |v_{\mathrm{e}}^{(N)}| \sigma(|v_{\mathrm{e}}^{(N)}|)\right) \tag{7}$$

and the corresponding entry to the right-hand side vector **M**:

$$\sum_i w_{\mathfrak{e}}^{(i)} |v_{\mathfrak{e}}^{(i)}| \sigma(|v_{\mathfrak{e}}^{(i)}|). \tag{8}$$

This procedure can be carried out for multiple different processes, such as elastic scattering, electron-impact electronic excitation, electron-impact ionization, etc.

3 Numerical Results

The octree merging and NNLS-based merging approaches were implemented in Merzbild.jl, a DSMC code implemented in the Julia programming language. The code and the input files used to produce the results for the present work are publicly available on Github [13]. As a baseline merging approach, the octree binning algorithm [12] was used.

3.1 BKW Relaxation

We first consider the BKW relaxation problem [4, 9], as we can compare the numerical solutions to the analytical solution. The problem is initialized by evaluating the velocity distribution function on a 32^3 velocity grid and converting the points on the grid with their associated VDF values to variable-weight particles. For NNLS merging, different numbers of conserved central moments were considered, with **all** mixed moments of order up to $L_{m,1}$ conserved (that is, all moments $M_{j_i k_i l_i}$ such that $j_i + k_i + l_i \leq L_{m,1}$), and additional conservation of moments $M_{j_i 00}$, $M_{0 j_i 0}$, $M_{0 j_i 0}$, where $L_{m,1} < j_i \leq L_{m,2}$. The target number of particles for the octree merging algorithm was chosen to be similar to that of the post-merge particles obtained via the NNLS merging. 400 simulations were performed for 500 timesteps each for each set of merging settings and then averaged, to reduce the impact of stochastic noise on the analysis of the results.

As an error metric, we consider the bias of the ensemble-averaged solution w.r.t. the analytical solution:

$$\mathcal{B}\left(\hat{M}^{2l}\right) = \sqrt{\frac{1}{N_t} \sum_{t_i} \left(\overline{\hat{M}^{2l}}(t_i) - \hat{M}_{an}^{2l}(t_i)\right)^2}. \tag{9}$$

Here $\hat{M}^{2l}$ is the total moment of order $2l$ (the moment of the particle speed of order $2l$), N_t is the number of timesteps over which the bias is computed, t_i is the time at timestep i, $\overline{\hat{M}^{2l}}$ is the ensemble average of the computed moments, and $\hat{M}_{an}^{2l}$ is the analytical value of the moment.

Figure 1 shows the ensemble-averaged evolution of the 4-th total moment of the BKW distribution for different merging algorithms and different numbers of particles

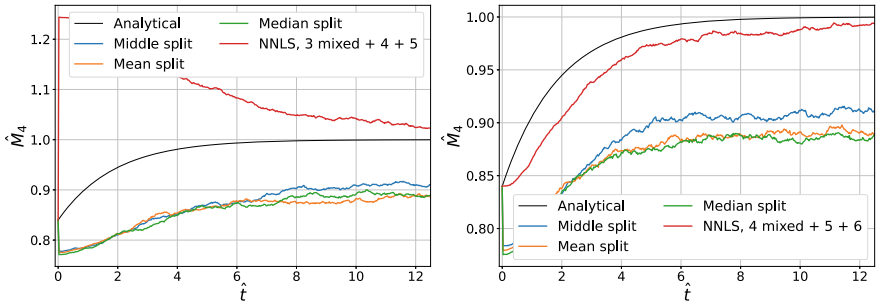

Fig. 1 Evolution of the 4-th total moment of the BKW distribution, 50:30 merge (left) and 75:50 merge (right)

considered. The N:M numbers on the legend denote the threshold number of particles N (if it is exceeded, particle merging is performed) and target post-merge number of particles M. The "middle split", "mean split", and "median split" are different versions of the octree merging algorithm with different splitting of the bins for refinement: either along the middle of the bean (regardless of the particles' velocities), along the mean velocity of the particles in the bin, or along the median velocity of the particles in the bin. On the left subplot, we see significant deviations from the analytical solution, and both the octree merging and NNLS-based merging algorithms exhibit a large jump at $t = 0$, as the very finely sampled distribution is merged down to only a few dozen particles. On the right subplot, the octree merging algorithm exhibits similar behaviour, although the error is somewhat lower, as the number of particles is increased. The NNLS merging algorithm however now conserves a sufficient number of moments to be able to preserve the 4-th total moment during merging—no jump can be seen at $t = 0$, and the solution in general is much closer to the analytical one.

Figure 2 shows the bias in the 4-th total moment of the BKW distribution as a function of the time-averaged number of particles $\overline{N}_p$. We see that all versions of the octree merging exhibit a significantly higher bias than the proposed moment-preserving approach, requiring at least 5 times as many particles to achieve a similar level of solution bias. Out of all the octree bin splitting strategies, the "middle split" performs the best, due to it avoiding any bias induced by the distribution of particles in phase space.

3.2 0-D Ionization

Next, we consider a spatially homogeneous ionization in an argon plasma driven by a constant electric field of 400 Tn. Only electron-neutral elastic scattering and electron-impact ionization were accounted for, with isotropic scattering, and the collision cross-sections taken from the IST-Lisbon database [1]. After an initial burn-in time,

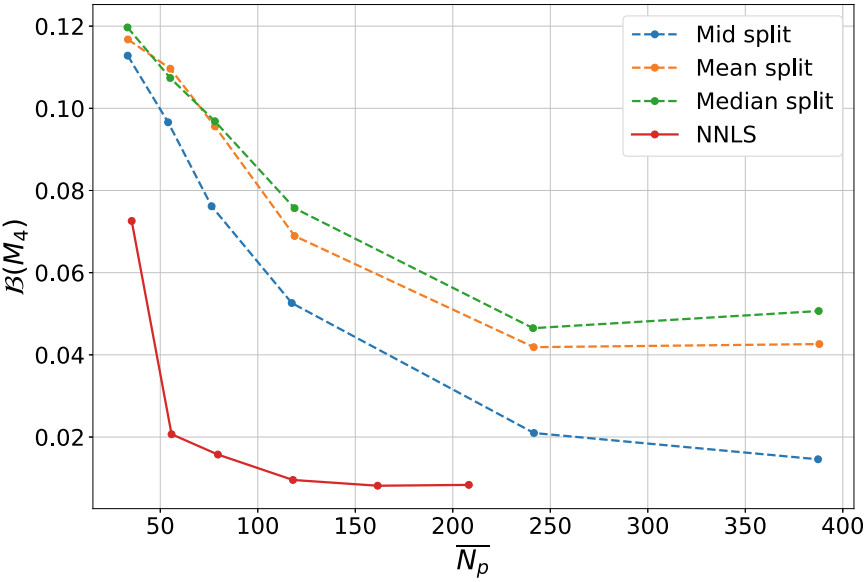

Fig. 2 Bias in the 4-th total moment of the BKW distribution as a function of the average number of particles

the system reaches a quasi-steady state, characterized by a constant ionization rate coefficient. The event-splitting scheme was used for collisions [14]. We analyze the bias introduced into the ionization rate coefficient in the first 100 timesteps after merging of the electron VDF is performed (averaged over all merging events). Since the system is driven by an external force, it has time to "recover" between merging events, and thus the bias immediately after merging has been performed is a better metric to compare the error introduced by the different merging approaches.

Figure 3 shows the average bias in the ionization rate coefficient immediately after merging events. Two versions of the NNLS merging approach were considered: with and without preservation of approximate electron-neutral collision rates (red and black lines, correspondingly). We see that for low numbers of particles, the NNLS-based approaches outperform the octree merging approach. The addition of the approximate rate preservation constraints also reduces the bias; however, as more and more moments are conserved in the NNLS merging algorithm (corresponding to a larger average number of particles $\overline{N_p}$), the difference between the rate preserving and non-rate preserving formulations becomes negligible, as the high-velocity tails of the electron VDF are sufficiently well-preserved during merging when $\overline{N_p}$ is sufficiently large.

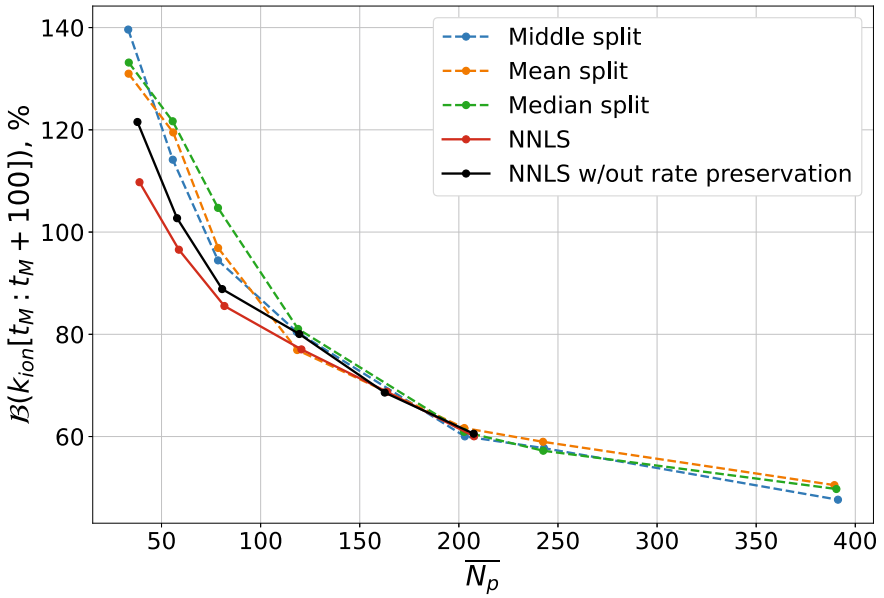

Fig. 3 Average Bias in the ionization rate coefficient in the first 100 timesteps after merging events as a function of the average number of particles

4 Conclusions

A novel moment-preserving particle merging approach based on the solution of a non-negative least-squares problem has been developed, along with an approximate rate-conserving version for plasmas. It has been shown to noticeably reduce the merging-induced the bias in higher-order moments of the velocity distribution function, as well as provide a better representation of the ionization rate coefficient for low numbers of computational particles.

Future planned extensions to the work include coupling the NNLS approach with the octree merging algorithm [12] for a greater degree of adaptivity, and consideration of spatial moments for inhomogeneous problems.

Acknowledgements This work has been supported by the German Research Foundation within the research unit SFB 1481.

References

1. Alves L (2014) The IST-LISBON database on LXCat. J Phys Conf Ser 565:012007 (IOP Publishing)
2. Araki SJ, Martin RS (2020) Interspecies fractional collisions. Phys Plasmas 27(3)

3. Bird GA (1994) Molecular gas dynamics and the direct simulation of gas flows. Clarendon, Oxford, England, UK
4. Bobylev AV (1976) One class of invariant solutions of the Boltzmann equation. In: Akademiia Nauk SSSR Doklady. vol 231, pp 571–574
5. Boyd ID (1996) Conservative species weighting scheme for the direct simulation Monte Carlo method. J Thermophysics Heat Transfer 10(4):579–585
6. Chen Z, Chen Z, Wang Y, Xu J, Chen Z, Jiang W, Wang H, Zhang Y (202) Stochastic weighted particle control for electrostatic particle-in-cell Monte Carlo collision simulations in an axisymmetric coordinate system. In: Computer physics communications, p 109390
7. Gonoskov A (2022) Agnostic conservative down-sampling for optimizing statistical representations and PIC simulations. In: Computer physics communications, vol 271, p 108200
8. Huerta C, Eckhardt D, Martin R (2024) In-situ, conservative particle merging with octree sorting. In: AIP conference proceedings, vol 2996. AIP Publishing
9. Krook M, Wu TT (1977) Exact solutions of the Boltzmann equation. Phys Fluids 20(10):1589–1595
10. Lama S, Zweck J, Goeckner M (2020) A higher order moment preserving reduction scheme for the stochastic weighted particle method. SIAM J Sci Comput 42(5):A2889–A2909
11. Lawson CL, Hanson RJ (1995) Solving least squares problems. SIAM
12. Martin RS, Cambier JL (2016) Octree particle management for DSMC and PIC simulations. J Comput Phys 327:943–966
13. Oblapenko G (2024) Merzbild.jl: A Julia DSMC code. https://github.com/merzbild/Merzbild.jl
14. Oblapenko G, Goldstein D, Varghese P, Moore C (2022) Hedging direct simulation Monte Carlo bets via event splitting. J Comput Phys 466:111390
15. Rjasanow S, Schreiber T, Wagner W (1998) Reduction of the number of particles in the stochastic weighted particle method for the Boltzmann equation. J Comput Phys 145(1):382–405
16. Rjasanow S, Wagner W (1996) A stochastic weighted particle method for the Boltzmann equation. J Comput Phys 124(2):243–253
17. Shen C (2006) Rarefied gas dynamics: fundamentals, simulations and micro flows. Springer Science & Business Media
18. Torrilhon M (2016) Modeling nonequilibrium gas flow based on moment equations. Annu Rev Fluid Mech 48:429–458
19. Vranic M, Grismayer T, Martins JL, Fonseca RA, Silva LO (2015) Particle merging algorithm for PIC codes. Comput Phys Commun 191:65–73

Open Access This chapter is licensed under the terms of the Creative Commons Attribution 4.0 International License (http://creativecommons.org/licenses/by/4.0/), which permits use, sharing, adaptation, distribution and reproduction in any medium or format, as long as you give appropriate credit to the original author(s) and the source, provide a link to the Creative Commons license and indicate if changes were made.

The images or other third party material in this chapter are included in the chapter's Creative Commons license, unless indicated otherwise in a credit line to the material. If material is not included in the chapter's Creative Commons license and your intended use is not permitted by statutory regulation or exceeds the permitted use, you will need to obtain permission directly from the copyright holder.

Data-Driven Extraction of 3D Orthogonal Velocity Distribution Modes from 1D DSMC Shocks

Robert S. Martin

Abstract This work investigates the structure of 3D particle velocity distribution functions (VDFs) within 1D normal shock waves. To explore the potential to extend continuum Boltzmann reduced order models previously studied only for a subset of homogeneous relaxation problems, low-rank modal structures are extracted from normalized Mach 2 and Mach 8 shock structure solutions. Because full 1D shock structure solutions are not readily available, cell-based continuum VDFs are instead sampled from highly resolved Direct Simulation Monte Carlo (DSMC) results. Normalized heat fluxes for Mach 2 and Mach 8 shocks are compared with expansion in terms of the Sonine polynomials traditionally used in Chapman-Enskog expansions. The viability of adapting the resulting data-driven modes for development of spatially inhomogeneous Boltzmann-ROMs and potential for other future algorithmic hybridization are also discussed.

Keywords Direct Simulation Monte Carlo · Proper Orthogonal Decomposition (POD) · Data-driven · Boltzmann Equation · Shock structure

1 Introduction

In Ref. [1], three orders of magnitude speedup relative to a nodal discontinuous Galerkin method for a class of 0D homogeneous relaxation solutions to the Boltzmann equation using a projective Reduced Order Model (ROM) was achieved. However, since the modes used to construct the ROM were extracted using singular values of solution vectors from randomly sampled trajectories of nearby initial conditions, extending this approach to spatially inhomogeneous flows would require a large database of spatially inhomogeneous solution trajectories. Such solution databases would quickly become prohibitively large and expensive to compute with direct

DISTRIBUTION STATEMENT A. Approved for public release. Distribution is unlimited.

R. S. Martin (✉)
DEVCOM Army Research Laboratory, Army Research Office, Research Triangle Park, NC, USA
e-mail: robert.s.martin163.civ@army.mil

© The Author(s) 2026

M. Grabe et al. (eds.), *Rarefied Gas Dynamics*, Springer Aerospace Technology,
https://doi.org/10.1007/978-3-032-00094-1_53

Boltzmann solvers, especially for higher spatial dimension problems. Instead, this work explores extracting such mode structures from 1D DSMC solutions to the Boltzmann equation. The work of Ref. [10] was extended in the 32nd symposium with streaming proper orthogonal decomposition (POD) based on Ref. [7] to extract dominant spatial modes of cell based density fields from transient particle simulations. In theory, such streaming POD could be used to similarly extract other observables of the flow such as VDF densities. In an operator split implementation of a Boltzmann solver, the multi-dimensional advection schemes could be coupled with a precomputed ROM for homogeneous collisional relaxation in each cell if a low-rank structure can be identified in the VDF space. This is not particularly distinct from the mindset of perturbation solutions used in moment-methods. The low-rank assumption in this case is equivalent to an expectation that the flow is sufficiently collisional as to be dominated by the equilibrium distribution and a sequence of perturbations. In this case, that sequence is simply data-driven and extracted from stochastic particle simulation rather than functional forms preselected for analytical convenience.

As with spatial cells, there is an inherent tradeoff between cell size and statistical noise. Because such high-dimensional noise is generally orthogonal to itself, the noise rejection properties of streaming POD are particularly useful. However, as VDFs exponentially decay in unbounded velocity domains, the large dynamic range in density makes retention of statistically significant correlations in distribution tails challenging. This work represents a first cut at exploring these issues in the relatively simplified restricted configuration of 1D shock structures.

2 Method

The structure of 1D normal shock-waves, as in Ref. [3], was an early application of the DSMC method. Following the basic DSMC formulation presented in [4], Mach 2 and Mach 8 stationary Xe gas shock-wave cases were setup with the parameters defined in Table 2 of the Appendix within the Thermophysics Universal Research Framework (TURF) [2, 8] previously shown to compare favorably to DS1V results.[1] Additional details of the setup and numerical parameters are provided in Appendix A.1. The solution was allowed to evolve $50\,\mu s$ with a time-step of 10 ns to establish a steady state. No shock stabilization technique was applied though the drift is expected to be negligible with high particle counts of $\tilde{1}6.4$ and 24.0 million computational particles for the Mach 2 and Mach 8 cases respectively. After an initial $50\,\mu$s transient, VDF sampling began. The solution was run for an additional $50\,\mu s$ with particle distributions sampled to the mesh every $1\,\mu$s (100 iterations) though full output of all VDFs was only performed at 16, 33, $50\,\mu$s after restart due to the relatively large output files. The steps between sampling were selected to ensure that samples of the low

[1] Note equivalent results would be expected using DS1V. TURF was only used for convenience due to preexisting data structures and I/O functionality for continuum VDF data requiring only minimal modification of sampling procedures.

speed particles in the stationary reference frame were not overly correlated due to the same slow particle residing in the same spatial cell for multiple time-steps, although any potential impact of such correlations are outside the scope of this work. Samples were accumulated for the full time from restart with time averaging performed in post processing.

Accumulating VDF solutions to a static mesh induces a few challenges. First, the change in mean velocity and temperature through the shock generally demand a relatively large velocity space mesh. With the idea that the extracted basis functions might serve as modes for a future POD Boltzmann ROM, the need to minimize the VDF mesh dimension further directly impacts the viability of preprocessing the ROM collision integrals. For this reason, the continuum VDF mesh followed the normalization used in Ref. [1]. To ensure that all of the initial conditions converged to the same equilibrium VDF, the VDF initial conditions were normalized to a standard, zero-drift Maxwellian with non-dimensional temperature of 0.1. Prior to sampling in the particle VDF in each spatial cell, the instantaneous particle temperature and mean velocity were used to similarly transform the particle VDF. While the initial results used the same 41^3 of ± 3 dimensionless velocity mesh as the 0D cases, this mesh was shifted in the shock normal direction to -4.317 to 1.683 normalized velocity units to account for the heavy backscattered VDF tail observed in the Mach 8 case, similar to tail distributions noted in Figs. 12.40 & 12.44 of Ref. [4].

To construct data-driven reduced order models (ROMs) as described in Ref. [5], a common approach is to first build a more efficient linear basis for representing the solutions. In the case of collision integrals, $\partial f/\partial t|_{\text{collision}}$, this corresponds to a truncated singular value decomposition (SVD) based compressed representation referred to as POD. Whereas POD is most commonly used to represent spatial "snapshot" vectors across time sequences, the same philosophy can be ascribed to a velocity space basis across spatial cells for a steady-state problem like the shock structure calculation. A modified "streaming" version of POD derived as a subset of the dynamic mode decomposition algorithm of Ref. [7] was used to extract the mode structures. Additional algorithmic details are provided in Appendix A.2. For the results presented, a maximum rank of 35 with periodic re-compression to 25 was used. The modes were also processed sequentially from upstream to downstream. These sizes and order were selected arbitrarily to appear sufficient capture a dominant low-rank structure and subsequent noise floor in combination with the sampling procedure described. Further optimization and the impact of truncation making long range correlations undetectable are left to future work.

Though full distribution POD modes were also computed, this paper focuses only on the δf results corresponding to a modal expansion around the equilibrium solution $\delta f = f - f_0$. The equilibrium Maxwellian is subtracted from each VDF prior to constructing the modes. This corresponds to the more stable solution in the previous 0D ROM results and also mitigates the issue that the dominant 0-mode was the spatial mean VDF rather than Maxwellian. In particular, the non-Maxwellian 0-mode caused a heavy upstream tail in the 0-mode and significant residual downstream mode amplitudes in the Mach 8 case. By focusing on δf-modes only, the amplitudes also correspond to the degree of non-equilibrium captured in the low-rank approximation.

Table 1 Mode energy preserved relative δf^2 of meshed VDF. Top-25 mode and further truncated fraction provided

Sampling Duration	16 μs	33 μs	50 μs
Mach 2 (Top-3)	48.9% (40.4%)	64.1% (58.8%)	72.2% (67.6%)
Mach 8 (Top-7)	99.27% (99.15%)	99.64% (99.58%)	99.76% (99.72%)

The non-equilibrium portion of the shock structure solutions are then approximated by parametric loops starting and ending at the origin of the r-dimensional space.

3 Results

Figure 1 shows results for the δf VDF modes for the Mach 2 and Mach 8 Xenon test cases respectively. The figures provide 2D summed distributions of 3D orthonormal POD modes in one of the two equivalent transverse velocity directions. The figures also provide projection of the 1D shock structure solutions into the i-th discrete POD mode amplitudes, $a_i(x_j) = \phi_i \cdot f(x_j)$. The corresponding VDF energy spectra, and a comparison of the non-dimensionalized heat-flux constructed by discretely summing the VDF representation with $\mathcal{C}^2\mathcal{C}_x$ normalized velocity in the transformed coordinate mesh. Table 1 shows the fraction of non-equilibrium δf^2 energy retained by the POD expansions.

Though a larger fraction of the energy is retained in the Mach 8 case compared to the Mach 2 case, this is because the non-equilibrium signal exceeds the noise floor of the VDF distribution more significantly in the Mach 8 case. By comparing the energy spectra across sampling durations in Fig. 1, it can be seen that the significant modes are quite stable across sampling durations while the noise floor in the higher modes progressively decreases with additional sampling time. This is particularly apparent as the third mode emerges from the noise floor only after 33 μs of sampling for the Mach 2 case. A significant fraction of the truncated energy in both cases is the result of truncating noise that approximates an infinite dimensional white spectra. While the fraction of energy retained is significantly higher in the Mach 8 case, the noise floor falls at a similar absolute magnitude of for both cases because a similar number of particles are sampled onto the same VDF mesh.

Sonine polynomials from Chapman-Enskog theory (Appendix A.3) were used to compare the estimated normalized heat-flux from both the analytical perturbative expansion and POD to the full-VDF based heat flux in Fig. 1. While the POD and full-VDF heat fluxes agree well, the Sonine expansion in 25 modes severely amplifies the VDF noise due to mode amplitudes being biased to amplify noise in the high velocity region of the VDF. Interestingly, if the full mesh VDF is first projected into the first

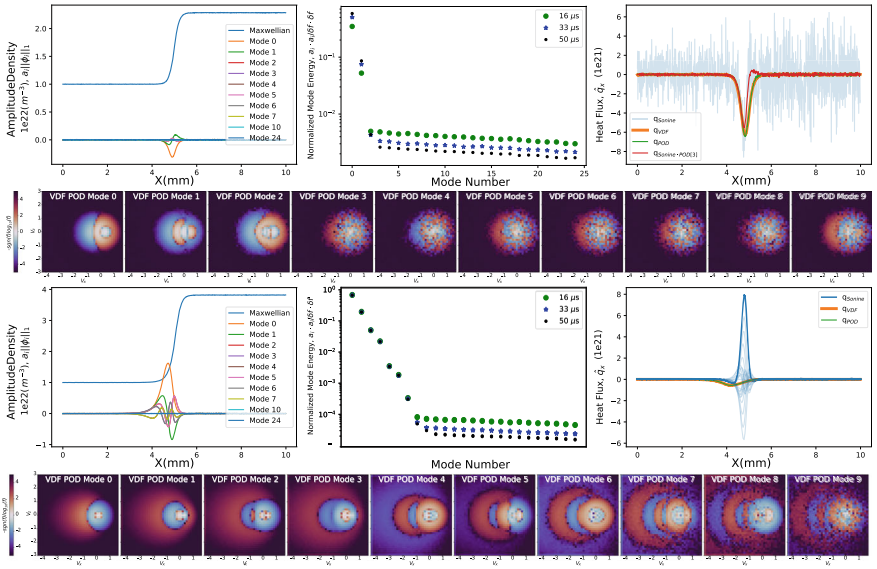

Fig. 1 Mach 2 (top) and Mach 8 (bottom) results: relative mode amplitudes (upper left), mode energy spectrum (upper middle), non-dimensionalized heat flux, $\hat{q}$ (upper right), and 2D summation of top-10 mode basis functions by energy (lower)

3 POD modes and then expanded in Sonine polynomials, this noise is significantly suppressed due to the global averaging that contributes to the POD mode smoothness deep into the tail of the distribution. A noticeable discrepancy remains between this projected Sonine expansion and the POD solution that cannot be attributed to the POD projection as the 3-Mode POD heat flux is indistinguishable from the 25-Mode POD on this scale. This discrepancy also corresponds to the region of highest discrepancy in Navier-Stokes solutions to the shock structure and may be the result of a breakdown of the assumption of small perturbation in this VDF tail region. For Mach 8, the heat-flux comparisons again matched well between the full VDF and POD projection. However, while the noise is significantly reduced for this case, the Sonine basis resulted in divergent heat flux. As additional Sonine basis functions are progressively added, the downstream heat flux resulted in oscillations with progressively higher mode counts. This is likely due to the alternating polynomial sign of the Sonine weighting amplified by the very heavy tails of the Mach 8 distributions. However, further investigations into this phenomena are beyond the scope of this work.

The rapid decay of the energy spectra in both cases is the hallmark of a problem amenable to construction of efficient low-Rank ROMs. This is noteworthy as "advection" dominated ROMs are challenging due to the *Kolmogorov n-width* problem [12]. Though not traditional advection, the equilibrium VDF does translate and scale relative to a fixed VDF mesh through the shock-wave. By first applying the affine transformation to the particle distribution that removes these drift and temperature variations, the anticipated low-Rank structure in the perturbative expansions

underpinning Chapman-Enskog theory [13] is recovered. This suggests an alternative route for ROM construction for problems previously tackled with similar perturbative expansions that falls between linear projection and fully nonlinear neural network methods. Such transformations can inherit the benefits of improved interpretability and closed form construction while expanding the applicability of an otherwise linear low-rank basis.

4 Conclusion and Future Work

The rapid mode decay suggests a few-mode perturbative expansion based ROM may provide reasonable shock structures calculations. While expected for the Mach 2 case where fluid solutions retain reasonable accuracy, low rank structure of Mach 8 results is more compelling evidence that a linear POD-Galerkin ROM may be feasible for the family of 1D shock structures. The first 3 significant modes in Mach 2 and 7–8 in Mach 8 are likely sufficient for single Mach input. However, initial attempts at projecting the Mach 2 modes into the Mach 8 basis results in significant residuals due to the heavy tails throughout the Mach 8 basis. Each basis is therefore insufficient for flows in the other condition. While 10–11 concatenated modes would still be quite low-rank, the overall rank needed to represent a family of intermediate Mach shock structure solutions within this finite Mach number range requires further exploration. The selection of sufficient intermediate conditions to accurately build such a basis also remains unexplored.

For some moderate Mach range, full 1D ROMs should next be constructed. This will require coupling the 0D Boltzmann ROM for collisional relaxation with some collisionless transport method. Due to the imposed translational invariance in the VDF ROM basis, it would be particularly interesting to apply this ROM to non-stationary solutions where long DSMC sampling used to construct modes would be challenging to converge. Though the transport portion could use particles methods like DSMC, development of a fluid based moment-method in the data-driven basis may be considerably more efficient. However, if coarsely resolved particle transport is sufficient to project and denoise VDF solutions back into the ROM basis, a hybrid algorithm may have additional advantages such as simpler integration of boundary conditions or domain decomposed coupling with traditional DSMC or deviational particle flow regions.

The low rank structure of the solutions also has interesting implications for the analysis of other learned closure models [6, 11]. Relatively few linearly independent non-equilibrium observables are sufficient to uniquely specify an entire VDF approximation for these problems. Once reconstructed, any other observable function of the VDF such as moments and transport fluxes could then be approximated with bounded approximation error. This low rank structure likely underpins the observed successes in more general learned closures.

Beyond 1D, using VDF transformation that align to the dominant eigenvectors of the particle covariance, as in presentation [9], rather than isotropic temperature

would be a relatively straightforward extension to multiple dimensions. Whether this results in emergence of a similar low-Rank structure is much less clear. The Kolmogorov n-Width problem may re-emerge for multi-parametric solution families like oblique or curved shocks. Similar issues should be expected for solid interfaces if the surface VDF discontinuity is significant. The closer the flow conforms to assumptions underpinning continuum Navier-Stokes solutions, the more likely that the perturbation expansion logic will translate into a similar low-Rank structure. This makes these ROMs likely to be most useful in extending the domain of validity of near equilibrium fluid solutions into non-equilibrium flows. Whether fully nonlinear mode compression becomes practically necessary as the degree of non-equilibrium increases is an interesting question, but in all these cases, these low rank structures are likely to remain useful in analyzing the accuracy and model capacity requirements of more complex methods.

Appendix A.1 Test Case Setup Details

See Table 2.

Standard VHS parameters, T_{ref}=273 K, α=0.35, and d_{ref}=5.74E-10 were used with a 1E7 macroparticle weight. The solution was initialized in a 1000 cell (1 cm) long 1D domain with 1 mm^2 cross section as a discontinuity at the center of the domain given the pre-shock (0) and post-shock (f) states.

Appendix A.2 Streaming POD

Consider the data block $\mathbf{X} \in \mathcal{R}^{n\times m}$ representing the full time-averaged meshed VDF solutions where n is the state dimension of the VDF mesh time averaged solutions (41^3) and m is the number of VDFs (1000). The matrix $\mathbf{X}$ can be replaced with a low-rank approximation truncating to the first $r \ll m$ largest singular values as $\tilde{\mathbf{X}} = \tilde{\mathbf{U}}\tilde{\Sigma}\tilde{\mathbf{V}}^*$ where $\tilde{\mathbf{U}}$ is $n \times r$, $\tilde{\Sigma}$ is $r \times r$ leading singular values, and $\tilde{\mathbf{V}}$ is the $r \times m$

Table 2 Xenon shock initial conditions

Case	Mach 2	Mach 8
Density, n_0(m^{-3})	1.0E22	1.0E22
Density, n_f(m^{-3})	2.2857E22	3.8209E22
Temp., T_0 (K)	293.0	293.0
Temp., T_f (K)	608.891	6115.517
Velocity, v_0(m/s)	351.71	1406.84
Velocity, v_f(m/s)	153.873	368.196

amplitudes for the r modes in each $m = 1000$ cells. While $\mathbf{X}$ is not unmanageably large at 551mb for this simple 1D problem in double precision, following Ref. [7], a streaming version of the POD portion of the dynamic mode decomposition algorithm can be adapted that avoids both storing the large matrix and solving large eigenvalue problems. In this case, $\tilde{\mathbf{U}}$ can be built progressively by appending appending orthogonal projections of solution vectors, $e = x_i - (\mathbf{U}\mathbf{U}^T)x_i$, equivalent to the Gram-Schmidt basis that would be constructed if the full $\mathbf{X}$ were available. This basis is allowed to grow and the outer product of the low-rank approximated vectors $\tilde{x}_i = \mathbf{U}^T x_i$ are accumulated in an $r \times r$ matrix $\mathbf{G}$ by padding $\mathbf{G}$ with 0s every time r is increased. Because the particle noise results in large residuals, the rank grows with each snapshot, x_i, added. When the rank exceeds some $r > r_{max}$, the $\mathbf{G}$ matrix can be used to re-compress the solutions by solving an $r \times r$ eigenvalue problem for the r_{min} leading eigenvectors $\tilde{\mathbf{V}}$ of $\mathbf{G}$ as $\tilde{\tilde{\mathbf{G}}} = \tilde{\mathbf{V}}^T \tilde{\mathbf{G}} \tilde{\mathbf{V}}$ and $\tilde{\tilde{\mathbf{U}}} = \tilde{\mathbf{V}}^T \tilde{\mathbf{U}}$. This periodic re-compression preserves a computational cost proportional to the square of r_{max} which remains relatively tractable for low-rank problems.

Appendix A.3 Sonine Polynomial Expansion

This appendix reviews construction of a Sonine polynomial basis derived from the descriptions provided in Ref. [13]. Starting from the perturbative expansion of the VDF, $f = f_0(1 + \Phi_1 + \Phi_2 + \dots)$, the perturbation, Φ, follows the functional form in Eq. 1. The forms of A_i and B_{ij} that respect the symmetries and invariances of the collision operator is are then shown in Eq. 2. Due to the symmetric nature of the 1D flow, only A_x for q_x and B_{xx} for τ_{xx} are therefore nonzero.

$$\Phi_1 = -\frac{1}{n}\left[\sqrt{2kT/m}A_j \frac{\partial}{\partial x_i}(\ln T) + B_{jk}\frac{\partial \bar{c}_j}{\partial x_k}\right] \tag{1}$$

$$A_i = A(\mathcal{C}, T)\mathcal{C}_i, \quad B_{ij} = B(\mathcal{C}, T)\left(\mathcal{C}_i\mathcal{C}_j - \tfrac{1}{3}\mathcal{C}^2\right) \tag{2}$$

$$S_m^{(n)} = \sum_{p=0}^{n} \frac{(m+n)!}{(m+p)!p!(n-p)!}(-x)^p = L_n^m \tag{3}$$

$$\begin{aligned} f &= f_0(1 + A_x + B_{xx}) \\ &= f_0\left(\begin{array}{l} 1 + \sum_{r=0}^{\infty} a_r S_{3/2}^{(r)}[\mathcal{C}^2]\mathcal{C}_x + \\ \sum_{r=1}^{\infty} b_r S_{5/2}^{(r-1)}[\mathcal{C}^2]\left(\mathcal{C}_x\mathcal{C}_x - \frac{1}{3}\mathcal{C}^2\right) \end{array}\right) \end{aligned} \tag{4}$$

The use of Sonine polynomials, $S_m^{(n)}$ for expanding A_i and B_{ij} was developed to leverage orthogonality that enables rapid convergence of the evaluation of transport properties. Sonine terminology has since been supplanted by 'associated Laguerre polynomials', L_n^m, where the subscript and superscript have been exchanged as shown in Eq. 3.

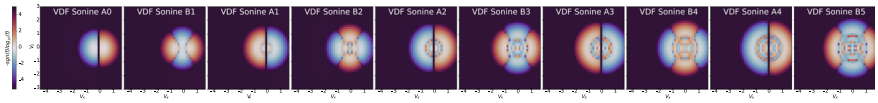

Fig. 2 2D summation of first 5 Sonine mode basis functions for A_x and B_{xx} modes

This gives perturbed distribution function, Eq. 1, in terms of the Sonine series expanded around the equilibrium distribution, f_0, shown in Eq. 4. For the 1D flow, the distribution function can then be expanded as a power series in terms of coefficients a_i and b_i and orthogonal mode shapes $f_0^{1/2} S_{3/2}^{(r)} \mathcal{C}_x$ and $f_0^{1/2} S_{5/2}^{(r-1)} \left(\mathcal{C}_x \mathcal{C}_x - \frac{1}{3} \mathcal{C}^2 \right)$ as shown in Fig. 2 where the mode normalization can be absorbed into the series coefficients, a_r and b_r.

References

1. Alekseenko A, Martin RS, Wood A (2022) Fast evaluation of the Boltzmann collision operator using data driven reduced order models. J Comput Phys 470:111526
2. Araki S, Martin RS, Bilyeu DL, Brieda L, Hill C, Choi M (2022) Current capabilities of AFRLś spacecraft simulation tool. In: 37th international electric propulsion conference, Boston, MA
3. Bird GA (1970) Aspects of the structure of strong shock waves. Phys Fluids 13(5):1172–1177
4. Bird G (1994) Molecular gas dynamics and the direct simulation of gas flows. Oxford University Press
5. Brunton SL, Kutz JN (2022) Data-driven science and engineering, 2nd edn. Cambridge University Press
6. Garg G, Mankodi TK, Esmaeilifar E, Myong RS (2024) Neural network-based finite volume method and direct simulation Monte Carlo solutions of non-equilibrium shock flow guided by nonlinear coupled constitutive relations. Phys Fluids 36(10):106113. https://doi.org/10.1063/5.0223654
7. Hemati MS, Williams MO, Rowley CW (2014) Dynamic mode decomposition for large and streaming datasets. Phys Fluids 26(11):111701
8. Martin R, Koo J (2015) Thermophysics universal research framework—infrastructure release. Air Force Research Laboratory (AFRL/RQRS), Version 1.0.0 edn. aFRL-RQ-ED-OT-2015-108
9. Martin RS (2013) Multidimensional effects on conservative particle merging. In: DSMC, Santa Fe, NM, aFRL-RQ-ED-VG-2013-241
10. Martin RS, Eckhardt D (2019) Denoising quasi-steady state particle simulations. In: 31st rarefied gas dynamics, AIP conference proceedings, vol 2132, issue 1, p 090010
11. Nair AS, Sirignano J, Panesi M, MacArt JF (2023) Deep learning closure of the Navier–Stokes equations for transition-continuum flows. AIAA J 61(12):5484–5497. https://doi.org/10.2514/1.J062935
12. Peherstorfer B (2022) Breaking the Kolmogorov barrier with nonlinear model reduction. Notices of the American Mathematical Society
13. Vincenti W, Kruger Jr C (2022) Introduction to physical gas dynamics. Krieger Publishing Company

Open Access This chapter is licensed under the terms of the Creative Commons Attribution 4.0 International License (http://creativecommons.org/licenses/by/4.0/), which permits use, sharing, adaptation, distribution and reproduction in any medium or format, as long as you give appropriate credit to the original author(s) and the source, provide a link to the Creative Commons license and indicate if changes were made.

The images or other third party material in this chapter are included in the chapter's Creative Commons license, unless indicated otherwise in a credit line to the material. If material is not included in the chapter's Creative Commons license and your intended use is not permitted by statutory regulation or exceeds the permitted use, you will need to obtain permission directly from the copyright holder.

Numerical Study on the One-Way Flow Between Plates of Different Temperatures with Periodic Distribution of Accommodation Coefficient

Ryuichiro Imazu, Hiroshi Sugimoto, and Maika Itou

Abstract This research numerically explores the feasibility of a one-way flow between two finite-sized planar plates, each with a different uniform temperature. In the case of infinite plates, a periodic distribution of the accommodation coefficient enables a one-way flow. An actual plate inevitably has its edges, and in the rarefied gas, the edge in a non-uniform temperature field induces localized fast flow—thermal edge flow. The present results show that the one-way flow by the distribution of the accommodation coefficient is also possible for finite-sized plates as well as infinite plates. The one-way flow survives under strong thermal edge flow vortices. We also report the optimal aspect ratio between the plate spacing and the period length of the distribution that maximizes the one-way flow as a function of the Knudsen number.

Keywords Thermal transpiration flow · Thermal edge flow · Knudsen pump

1 Introduction

The temperature field plays a pivotal role in various phenomena in rarefied gas. We have long observed various gas flows around stationary bodies solely due to the interaction of gaseous temperature and the surface. With recent advances in microdevices, numerous researchers have worked vigorously on developing devices such as micropumps and gas mixture separation that utilize these phenomena. The concept underlying these devices is thermal transpiration flow, where the cold gas adjacent to the solid wall moves toward the hot gas part along the wall. Some devices induce this by varying the temperature of the wall, and some use the geometrical shapes and arrangement of the hot/cold parts, sometimes accompanied by the distribution of the accommodation coefficient. One of the authors recently found a possibility of a similar flow in an elementary geometry—a channel between two flat plates—by the

R. Imazu · H. Sugimoto (✉) · M. Itou
Department of Aeronautics and Astronautics, Kyoto University, Kyoto, Japan
e-mail: sugimoto.hiroshi.7s@kyoto-u.ac.jp

© The Author(s) 2026

M. Grabe et al. (eds.), *Rarefied Gas Dynamics*, Springer Aerospace Technology,
https://doi.org/10.1007/978-3-032-00094-1_54

numerical simulation [5]. The one-way flow through the channel occurs if one of the plates is heated and both plates have a periodic distribution of the accommodation coefficient. The simple structure and the separation of hot and cold parts enhance easy fabrication of the device.

At the same time, the flow speed is slower than other standard thermal transpiration flows. Actual plates must have their edges due to their finite size, and the edges most likely induce strong localized gas flow—the thermal edge flow [4]—which may disrupt the structure of the weak one-way flow. Therefore, we numerically analyze the one-way flow induced by the periodic distribution of the accommodation coefficient using the finite-sized plates to evaluate its feasibility in real devices.

2 Problem Setups

The basic 2D geometry that induces the one-way flow in [5] is shown in Fig. 1a. A rarefied gas fills the gap of height D between a heated plate (uniform temperature T_1) and an unheated plate (uniformly T_0). Both plates have a periodic distribution of the accommodation coefficient, which varies alternately between 1 (i.e., diffuse reflection) and some $\alpha(< 1)$ at a distance of L. In this setup, the gas flows along the plate if the distributions of the accommodation coefficient on two plates have a phase difference Λ. To account for the geometry's periodicity, we perform our calculation in the green region in the figure.

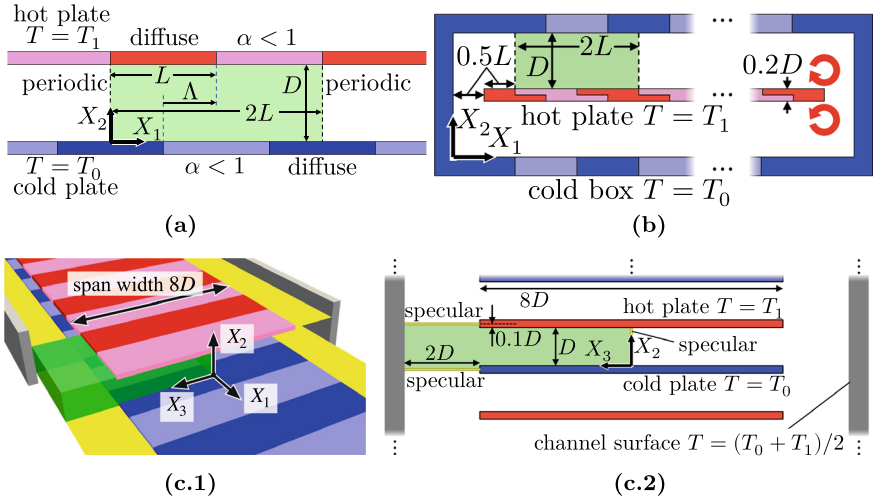

Fig. 1 Setups of the problems. **a** The basic setup in [5]. **b** Streamwise edge setup. **c.1** Spanwise edge setup. **c.2** A cross-sectional view of **(c.1)** on the X_2X_3 plane

We introduce the ends of the plate to confirm the feasibility of the one-way flow by finite-sized plates. In the 2D model shown in Fig. 1b, a heated plate of thickness $0.2D$ is confined in an unheated box of $7.5L \times 2.2D$ to make a closed loop. The upper and lower channels correspond to the units, one shown in green and lined up to induce counterclockwise flow, but we have two ends of the heated plate. We assume the accommodation coefficient around the edge is unity. Therefore, the two edges induce the thermal edge vortices [4] (indicated by the red circle arrows in the figure). We simulate the rarefied gas flow to see if a one-way flow can go through thermal edge vortices.

We also have the edges in the spanwise direction for actual finite-sized plates. In response, we consider a spanwise edge setup Fig. 1c.1. The setup requires 3D simulation. Considering the periodicity in X_1 and the symmetry in X_3 of the geometry, we calculate the gas flows in the green region in the figure. A cross-sectional view of this on the X_1X_2 plane is the same as in Fig. 1a, and that on the X_2X_3 plane is shown in Fig. 1c.2. A vertical array of plates (thickness $0.2D$) of finite span width $8D$ is put in a diffusely reflecting channel $-6D < X_3 < 6D$, whose surface temperature is $(T_0 + T_1)/2$. The temperatures of the array plates are alternately set to T_0 and T_1. For the sake of simplicity, we assume the flow is symmetric at $X_2 = -0.1D$ and $1.1D$. We observe if the one-way flow in the central part of the plate survives the disturbance of thermal edge vortices on the edges in the spanwise direction.

3 Governing Equation

The governing equation is the BGK model:

$$\left.\begin{aligned} &\frac{\partial F}{\partial t} + \xi \cdot \frac{\partial F}{\partial \boldsymbol{X}} = J\,[F], \qquad J\,[F] = A_C n\,(F_E - F)\,, \\ &F_E\,(n, \boldsymbol{v}, T; \boldsymbol{\xi}) = \frac{n}{(2\pi\kappa T/m)^{3/2}} \exp\left(\frac{-\mid \boldsymbol{\xi} - \boldsymbol{v} \mid^2}{2\kappa T/m}\right). \end{aligned}\right\} \tag{1}$$

Here, t is the time, $\boldsymbol{X}$ is the Cartesian coordinate, $\boldsymbol{\xi}$ is the molecular velocity, $F(t, \boldsymbol{X}, \boldsymbol{\xi})$ is the velocity distribution function, m is the molecular mass, κ is the Boltzmann constant, J is the collision term, and A_C is a constant whose products with the number density n equals the collision frequency. F_E is the equilibrium distribution determined by n, the flow velocity $\boldsymbol{v}$, and the temperature T of the gas. The distribution function F defines them through

$$\left.\begin{aligned} n &= \int_{|\boldsymbol{\xi}|<\infty} F\,\mathrm{d}\boldsymbol{\xi}, \qquad n\boldsymbol{v} = \int_{|\boldsymbol{\xi}|<\infty} \xi F\,\mathrm{d}\boldsymbol{\xi}, \\ \frac{3}{2}\kappa n T &= \int_{|\boldsymbol{\xi}|<\infty} \frac{m}{2} \mid \boldsymbol{\xi} - \boldsymbol{v} \mid^2 F\,\mathrm{d}\boldsymbol{\xi}, \qquad p = \kappa n T, \end{aligned}\right\} \tag{2}$$

where p is the pressure. The boundary condition is the Maxwell condition

$$F\left(t, \boldsymbol{X}_w, \boldsymbol{\xi} \cdot \boldsymbol{n}_w > 0\right) = \alpha F_E\left(\sigma_w, \boldsymbol{0}, T_w; \boldsymbol{\xi}\right) + (1-\alpha) F\left(t, \boldsymbol{X}_w, \boldsymbol{\xi} - 2\left(\boldsymbol{\xi} \cdot \boldsymbol{n}_w\right) \boldsymbol{n}_w\right),$$

$$\sigma_w = -\sqrt{\frac{2\pi}{\kappa T_w / m}} \int_{\boldsymbol{\zeta} \cdot \boldsymbol{n}_w < 0} \boldsymbol{\zeta} \cdot \boldsymbol{n}_w F\left(t, \boldsymbol{X}_w, \boldsymbol{\zeta}\right) \mathrm{d}\boldsymbol{\zeta},$$

where T_w is the wall temperature, $\boldsymbol{n}_w$ is the unit normal directed to the gas, and α is the accommodation coefficient. The case $\alpha = 1$ is the diffuse reflection, and $\alpha = 0$ is the symmetry condition. The mean free path l_0, the most probable speed of molecule c_0, and the corresponding Knudsen number Kn at the reference stationary state (number density n_0 and temperature T_0) are expressed by

$$c_0 = \sqrt{\frac{2\kappa T_0}{m}}, \qquad l_0 = \frac{2c_0}{\sqrt{\pi} A_C n_0}, \quad \mathrm{Kn} = \frac{l_0}{D}.$$

4 Method of Analysis

We use a deterministic numerical scheme that uses the *spherical designed grid* and the *traveling finite volume (TFV) method* [2]. The *spherical design* [6] is a set of points $\boldsymbol{a}_k$ $(k = 1, 2, \ldots, N_\Omega)$ arranged nearly uniformly on a unit sphere $\mathbb{S}^2$. The points $\boldsymbol{a}_k$ are selected so that the average value of arbitrary t-th order polynomial $P_{\mathrm{t}}(\boldsymbol{x})$ on these points is the average of $P_{\mathrm{t}}(\boldsymbol{x})$ on $\mathbb{S}^2$. An example is shown in Fig. 2a. Then, we approximate the integral of $f(\boldsymbol{x})$ on $\mathbb{S}^2$, thus the integrals in (2) by, e.g.,

$$n = \int_{\boldsymbol{a} \in \mathbb{S}^2} \left[\int_0^\infty F\left(\xi \boldsymbol{a}\right) \xi^2 \mathrm{d}\xi \right] \mathrm{d}\Omega\left(\boldsymbol{a}\right) \sim \frac{4\pi}{N_\Omega} \sum_{k=1}^{N_\Omega} \int_0^\infty F\left(\xi \boldsymbol{a}_k\right) \xi^2 \mathrm{d}\xi. \tag{3}$$

Therefore, we define discretized molecular velocity

$$\xi_j \boldsymbol{a}_k \qquad \left(j = 1, 2, \ldots, N_\xi,\ k = 1, 2, \ldots, N_\Omega\right) \tag{4}$$

in the simulation. This grid gives exceptionally accurate results compared to the standard rectangular grid, shown in Fig. 2b. For a fixed error size, the spherical designed grid (indicated in red) requires a smaller number of the grid points $N_\sharp = N_\xi N_\Omega$ by few orders compared with the rectangular grid (indicated in black). Since the computational resources—the memory size and computational time—are closely related to $N_\sharp$, the present method is much faster than the standard rectangular grid. The spherical designed grid enables us to carry out 3D flow simulation by personal computers.

The *traveling finite volume method* is a numerical method for the Boltzmann equation (1) with nearly complete conservation of mass, momentum, and energy. To

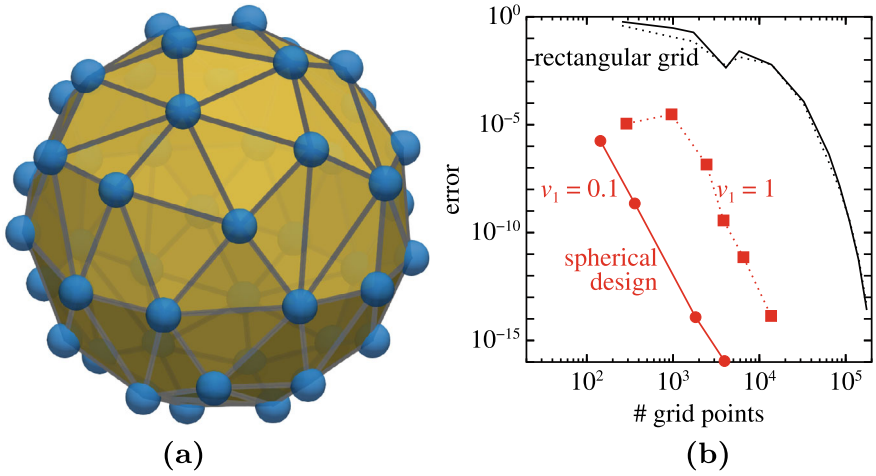

Fig. 2 **a** An example of the spherical design [6]. The case for $N_\Omega = 48$ and t = 9. **b** The errors in the numerical integration of $\int \Phi(\boldsymbol{\xi})\, \mathrm{d}\boldsymbol{\xi} = 1$ $\left[\Phi(\boldsymbol{\xi}) = a\left(1 + \frac{7}{5}|\boldsymbol{\xi} - \boldsymbol{v}^2|\right) \exp\left(-\frac{7}{5}|\boldsymbol{\xi} - \boldsymbol{v}|^2\right), \boldsymbol{v} = (v_1, 0, 0)\right]$. Solid line: $v_1 = 0.1$ and dotted line: $v_1 = 1$. Black: The Simpson's formula and uniform rectangular grid for $\boldsymbol{\xi}$. Red: The spherical designed grid

this end, we replace $(t, \boldsymbol{X})$ with the characteristic coordinate $(t, \boldsymbol{\chi} + \boldsymbol{\xi} t)$. Then we have

$$\left(\frac{\partial G}{\partial t}\right)_{\boldsymbol{\chi}, \boldsymbol{\xi}: \text{fix}} = J[G], \qquad G(t, \boldsymbol{\chi}, \boldsymbol{\xi}) = F(t, \boldsymbol{\chi} + \boldsymbol{\xi} t, \boldsymbol{\xi}). \tag{5}$$

We apply the finite volume method [1] for $\boldsymbol{\chi}$-space. During the time step Δ_t, the finite volume cells travels in $\boldsymbol{X}$-space with each molecular velocity (4). Therefore, we also prepare fixed finite volume cells in $\boldsymbol{X}$-space, and reconstruct the $\boldsymbol{X}$-cell data from the $\boldsymbol{\chi}$-cell data at every time step. By repeating the reconstruction and time advance by the finite volume scheme, we obtain the time evolution of $\boldsymbol{X}$-cell data by (1). The advantage of the present method is (i) we do not need numerical flux by (5) because it is essentially a bundle of ordinary differential equations (i.e., we do not have the CFL condition), and (ii) we do not need the numerical derivative across the discontinuity [3] of the velocity distribution function because the solution of the ordinary differential equation (5) is continuous in t.

5 Results and Discussion

5.1 *Infinite Plates Problem*

First, we show the present result in Fig. 3a. The parameters are mostly common to [5]: $\Lambda/L = 0.5$, $\alpha = 0.5$, $\mathrm{Kn} = 0.5$, and $L/D = 1$. We choose vanishingly small temperature difference, $T_1/T_0 - 1 = \varepsilon = 10^{-4}$, because (i) the gas flow obtained in [5] is roughly proportional to ε, (ii) small ε is easy for future experimental verification, and (iii) the present TFV method becomes accurate for small variation of the flow field. The reference number density n_0 is the average number density in the region. The white lines are the streamlines obtained as the contour of the stream function Ψ defined by

$$\Psi(X_1, X_2) = \frac{1}{n_0 c_0 D} \int_0^{X_2} [n v_1](X_1, y)\, \mathrm{d}y.$$

Despite the differences in the molecular models and temperature setup from Ref. [5] (which employs the hard-sphere model and $T_1/T_0 = 3$), temperature and flow velocity distribution show no qualitative difference: the temperature of the gas close to the diffuse section approaches that of the wall, resulting in a vortex flow near the discontinuity of the accommodation coefficient. Some streamlines connect the vortices and go through between the plates. Thus, Fig. 3a clearly shows that the one-way flow also exists in the BGK model, just as in the hard-sphere molecules.

The nondimensional mass flux through the channel $Q = \Psi(X_1, D)$ does not depend on X_1 in the steady state. Figure 4 shows Q/ε versus Kn for several aspect ratios L/D. For a fixed value of L/D, Q takes its maximum value at some Kn. For $L/D \lesssim 1$, the Knudsen number is close to 0.5. Reference [5] also reports the same Knudsen number $\mathrm{Kn} \sim 0.5$ for hard-sphere molecules for $L/D = 1$. For larger L/D, Q takes a maximum at higher Knudsen numbers. The maximum value of Q varies with L/D: it takes a maximum at $L/D \sim 2$ or 4. The flow field at $L/D = 2$ and $\mathrm{Kn} = 1$ is shown in Fig. 3b. The meandering of the streamlines becomes gentler compared with $L/D = 1$ in Fig. 3a. Therefore, unless otherwise stated, we consider the case with $\mathrm{Kn} \sim 1$ and $L/D = 2$ in the subsequent calculations.

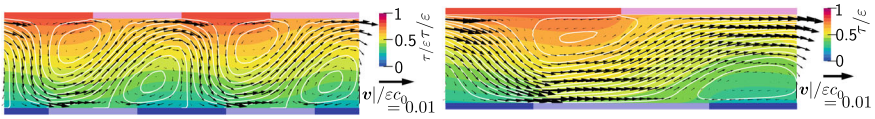

Fig. 3 Temperature and flow velocity distributions for the basic setup. $\Lambda/L = 0.5$, $\alpha = 0.5$ and $T_1/T_0 - 1 = \varepsilon = 10^{-4}$. Colors show the temperature (T/T_0 or $\tau = T/T_0 - 1$), arrows show the flow velocity, and white lines show the streamlines. **a** The case for $\mathrm{Kn} = 0.5$ and $L/D = 1$: the same as Fig. 15 of [5] except the value of T_1/T_0. **b** The case for $\mathrm{Kn} = 1$ and $L/D = 2$

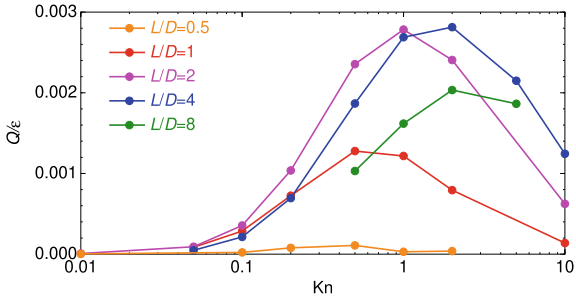

Fig. 4 Nondimensional mass flux versus Kn for several aspect ratios for the basic setup with $\Lambda/L = 0.5$, $\alpha = 0.5$ and $\varepsilon = 10^{-4}$

5.2 *Effect of Streamwise Edge*

Figure 5 shows the flow fields in the streamwise edge setup (Fig. 1b). We find four strong vortices around $X_1/L \sim 0.5$ and 7. The direction of the flow coincides with those by the thermal edge flow in Fig. 1b. Despite these strong vortices, we observe one-way flows similar to that in Fig. 3b in the central part of the upper and lower channels; the flow image in the upper channel is reversed in the X_1 direction, which accords with the distribution of the accommodation coefficient. The non-dimensional mass flux Q in the upper channel in $1 < X_1/L < 6.5$ is approximately $-2.1\varepsilon \times 10^{-3}$, which is of the same order of magnitude as that observed in Fig. 3b ($2.8\varepsilon \times 10^{-3}$). To summarize, we have confirmed that the plate edge in the streamwise direction disturbs only slightly the one-way flow induced by the distribution of the accommodation coefficient.

5.3 *Effect of Spanwise Edge*

Figure 6 shows the flow velocity and temperature field projections for the spanwise edge setup (Fig. 1c.1) in several cross-sections. Figure 7 presents some of the cross-section images separately. Panel (a) is the image at $X_1 = 0$. The thermal edge flow induced by the edges forms a strong vortex; however, the vortex flow does not pen-

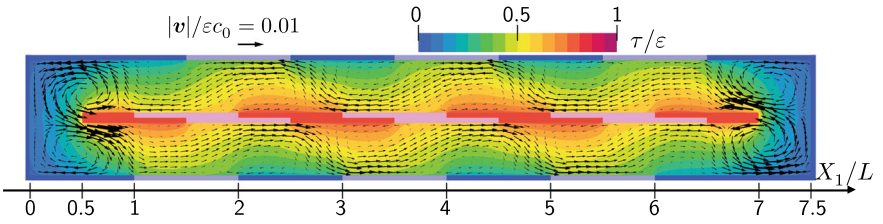

Fig. 5 Temperature and flow velocity distribution for the spanwise edge setup (Fig. 1b). Each unit corresponds to $\Lambda/L = 0.5$, $\alpha = 0.5$, $\varepsilon = 10^{-4}$, Kn = 1 and $L/D = 2$ shown in Fig. 3b

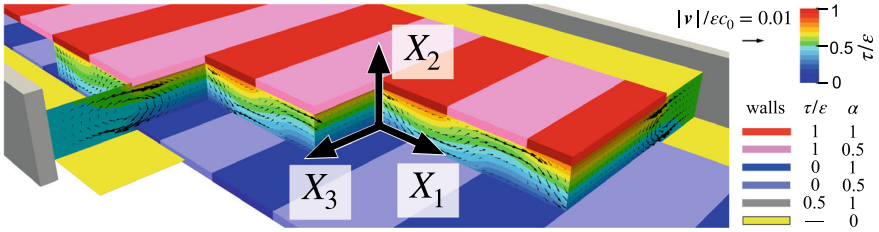

Fig. 6 Projections of the flow velocity and temperature distribution for the spanwise edge setup (Fig. 1c.1) on several cross-sections. The plates correspond to the basic setup Fig. 1a for $\Lambda/L = 0.5$, $\alpha = 0.5$, $\varepsilon = 10^{-4}$, Kn $= 0.5$ and $L/D = 2$

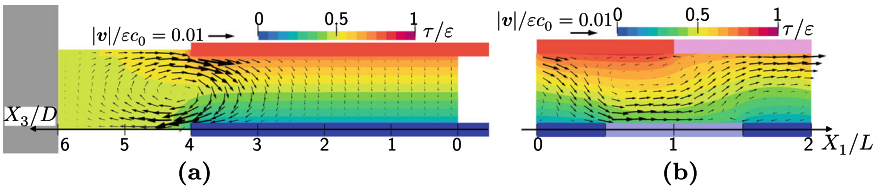

Fig. 7 Projections of the flow velocity and temperature distributions for the spanwise edge setup (Fig. 1c.1) on two cross-sections. The parameters are the same as in Fig. 6. **a** The spanwise cross-section $X_1 = 0$. **b** The streamwise cross-section at the center of the plates $X_3 = 0$

etrate the gap between hot and cold plates. The cross-section image at $X_3 = 0$ is panel (b). The one-way flow similar to that in Fig. 3b occurs here. To summarize, the spanwise edge induces a strong thermal edge vortex but does not stop the one-way flow at the central part. Therefore, we can expect the occurrence of the one-way flow if the plate has a sufficiently large width in the spanwise direction.

6 Summary

We report numerical research results on the feasibility of the one-way flow [5] between flat plates of different temperatures induced by the periodic distribution of the accommodation coefficient. The BGK model gives almost the same qualitative results as the hard-sphere molecules. The nondimensional mass flux (i.e., the flow speed) through the gap reaches its maximum value when the period of the accommodation coefficient distribution is 4–8 times the distance between the plates. The mean free path of the molecule should ideally be the same as the plate distance. We also investigate the effects of the finite size of real plates. Although the edges of the plates induce strong thermal edge flow and vortices, their effects are confined to some narrow areas around the edge. A sufficient width of the one-way flow device can weaken the influence of thermal edge flow. To summarize, the one-way flow between the flat plates with the periodic distribution of the accommodation

coefficient in real devices is highly feasible, judging from the analysis based on the Maxwellian boundary condition.

Acknowledgements This work is supported by the JSPS grant-in-aid 24K07303.

References

1. LeVeque RJ (2002) Finite volume methods for hyperbolic problems. Cambridge texts in applied mathematics. Cambridge University Press, Cambridge
2. Morikawa Y, Sugimoto H (2021) A new fast numerical method for rarefied gas simulation by spherically designed grid and traveling finite volume (in Japanese). In: Nagare, vol 40, pp 394–397
3. Sone Y (2007) Molecular gas dynamics. Birkhäuser
4. Sone Y, Yoshimoto M (1997) Demonstration of a rarefied gas flow induced near the edge of a uniformly heated plate. Phys Fluids 9(11):3530–3534. https://doi.org/10.1063/1.869461
5. Sugimoto S, Sugimoto H (2022) Thermal transpiration flows induced by differences in accommodation coefficients. Phys Fluids 34(4):042005. https://doi.org/10.1063/5.0084455
6. Womersley RS (2018) Efficient spherical designs with good geometric properties. Springer International Publishing, Cham, pp 1243–1285. https://doi.org/10.1007/978-3-319-72456-0_57

Open Access This chapter is licensed under the terms of the Creative Commons Attribution 4.0 International License (http://creativecommons.org/licenses/by/4.0/), which permits use, sharing, adaptation, distribution and reproduction in any medium or format, as long as you give appropriate credit to the original author(s) and the source, provide a link to the Creative Commons license and indicate if changes were made.

The images or other third party material in this chapter are included in the chapter's Creative Commons license, unless indicated otherwise in a credit line to the material. If material is not included in the chapter's Creative Commons license and your intended use is not permitted by statutory regulation or exceeds the permitted use, you will need to obtain permission directly from the copyright holder.

Simulation of the Neutral Gas Flow Within an Electric Thruster by the Kinetic Fokker-Planck Method and Comparison with Force Balance Measurements

Jens Schmidt and Leo Basov

Abstract This study investigates the neutral gas flow in the DEEVA electric thruster, developed within DLR. The thruster uses electron-cyclotron-resonance (ECR) discharge and a magnetic nozzle to accelerate plasma, supporting noble and reactive gases as propellants. Simulations using the Fokker-Planck method in SPARTA were conducted for argon and xenon at different flow rates to understand asymmetries in the neutral gas plume. Results showed that the original injector design caused plume asymmetry due to pressure gradients, while a refined injector produced a symmetric plume. Experimental cold gas thrust measurements partially matched simulation results and analytical models, though deviations occurred for xenon at higher flow rates. Findings support injector optimization and provide initial conditions for plasma simulations, improving discharge modeling and thruster performance. Future work will focus on density measurements and studies with diatomic propellants.

Keywords Rarefied gas dynamics · Fokker-Planck-method · DSMC · Electric propulsion

1 Introduction

Within the German Aerospace Center's (DLR) *Decentralized Energy supplied Electric Propulsion* (DEEP) project, a microwave-heated electric thruster is developed [4]. The plasma is created using an electron-cyclotron-resonance (ECR) discharge and accelerated using a magnetic nozzle. This allows the usage of different propellants such as noble gases but will also allow the use of reactive gases like air. As a first step to calculate the plasma properties and understand the neutral gas distri-

J. Schmidt (✉) · L. Basov
German Aerospace Center, Institute of Aerodynamics and Flow Technology, Göttingen, Germany
e-mail: jens.schmidt@dlr.de

L. Basov
Applied and Computational Mathematics, RWTH Aachen, Aachen, Germany

© The Author(s) 2026

M. Grabe et al. (eds.), *Rarefied Gas Dynamics*, Springer Aerospace Technology,
https://doi.org/10.1007/978-3-032-00094-1_55

bution within the discharge tube, a Fokker-Planck simulation of the the neutral gas flow is performed. This is motivated by an observed asymmetry of the plasma plume during operation which can not be explained by any effects on the charged particles. Since the power coupling efficiency of the ECR discharge and the confinement of the plasma depend highly on the local number density, the channel flow and the plume of the thruster should initially be simulated for neutral gas. Therefore a simulation was performed to understand the neutral gas distribution and how the injector design will influence it. In addition, simulations are performed with a different injector design. The simulations are performed for argon and xenon to understand the influence of the molecular weight on the neutral gas distribution. To validate the results of the simulation, the thrust is calculated from the flow and compared with experimental measurements of the cold gas thrust as well as estimates from an analytical model. The simulation is performed for argon and xenon at three different volume flow rates of $\dot{V} = 1, 10, 45$ sccm which are representative for the thruster operation and ignition.

2 Description of the DEEVA Thruster

The DEEVA (DLR Electrodeless ECR Via magnetic nozzle Acceleration) thruster, as shown schematically in Fig. 1 consists of 4 major components: the gas injector, the discharge tube, the slotted antenna and the magnet system. The neutral gas is injected into the discharge tube by the gas injector and then ionized due to the microwaves emitted by the two slits of the slotted antenna. Due do the magnetic field, the electrons perform circular motions around the magnetic field line. The electrons can be heated in resonance if they are excited at the same frequency at which they are gyrating around the magnetic field lines, which is dependent on the local magnetic field strength. The thruster is usually operated at a frequency of $f = 2.4 - 2.5\,\mathrm{GHz}$ leading to a necessary magnetic field strength of $B = 0.875\,\mathrm{T}$.

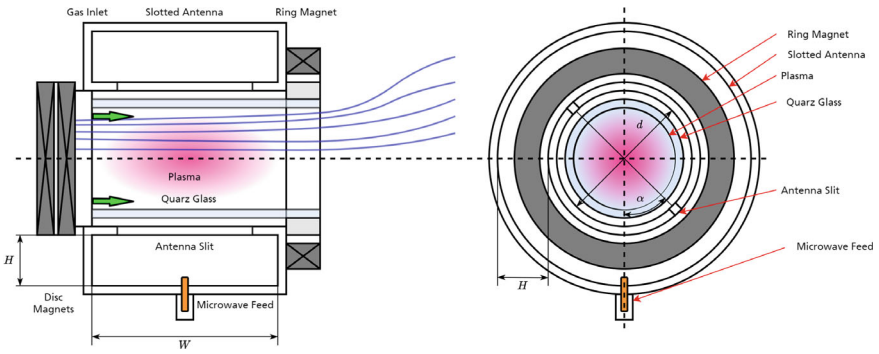

Fig. 1 Scheme of the DEEVA thruster as seen from the side (left) and front (right)

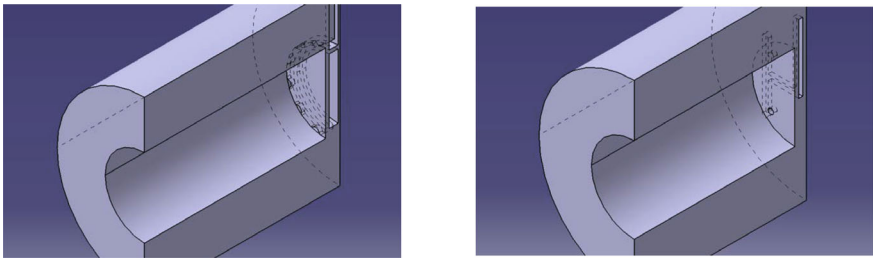

(a) Old gas injector geometry (b) New gas injector geometry

Fig. 2 CAD model of the simulated geometries for the old (left) and new (right) gas injector design and discharge channel

Due to the magnetic field configuration, the plasma is then confined to reduce wall losses and expanded along the divergent magnetic field lines utilizing the field of the magnetic nozzle. Since the electric field strength of the microwave is stronger at the outer edge of the discharge tube closer to the slits, the number density of the neutral gas at the outer edge of the tube should be higher. In addition, the neutral gas distribution should be symmetric to not introduce any asymmetries into the plasma plume. This can be ensured by a proper design of the neutral gas injection which is studied numerically and experimentally. For this study, two injector geometries were compared numerically, both shown in Fig. 2, furthermore referred to as 'old' and 'new'. In the 'old' injector geometry, the gas is fed from the top and flows along the outer radius to the injector holes as seen in Fig. 2a. In the 'new' geometry, the gas first flows from the top to the center and then is spread radially in the four injector openings, resulting in a more equal pressure distribution.

3 Numerical Method

The simulations were performed using the kinetic cubic Fokker-Planck (FP) model [2]. The method is being continuously developed at DLR Göttigen as an extension to the open-source DSMC code SPARTA by Sandia National Labs [1, 3]. It is important to note that this is an extension of the code, not the DSMC method. Unlike Direct-Simulation Monte Carlo (DMSC), the FP method does not resolve the particle-particle interactions of the Boltzmann collision operator directly. Rather it uses a continuous stochastic process which leads to the computational cost being independent of the Knudsen number Kn. This allows the method to be computationally more efficient than DSMC in areas of low Kn numbers like in the inflow structure used in the thruster under investigation. The signal-to-noise ratio of both methods should be similar, as the noise scales with the inverse of the square root of the particle number. The FP method is necessary, as there is a strong pressure (and density) gradient within the discharge channel due to the gas injection at almost

Table 1 Boundary conditions and species properties from bird [1]

Boundary	Condition		
1–4	Outflow		
5–7	Inflow		
8	Wall (Diffuse Reflection with $T_w = 273.15$ K)		
Gas	m/kg	d_{ref}/m	ω
Argon	$6.63 \cdot 10^{-26}$	$3.657 \cdot 10^{-10}$	0.81
Xenon	$218.0 \cdot 10^{-27}$	$5.74 \cdot 10^{-10}$	0.85

atmospheric pressure and the expansion into high vacuum. The Knudsen number is $Kn \approx 10^{-5}$ in the discharge tube, and $Kn \approx 1$ in the plume, therefore there is a transition from a collisional into the collisionless regime, which makes a method necessary which is able to work in both regimes. The simulation was performed for Argon and Xenon as a neutral gas at different given volume flow rates $\dot{V}$ representing different operational points. The volume flow rates used were 1 sccm, 10 sccm and 45 sccm. The simulation was performed using only one half of the geometry to save computational time, since the geometry is symmetric along the middle axis. The downstream boundaries as well as the outside of the simulation domain were defined as outflow. The inflow in the injector was calculated using the given volume flow and calculating the number density in the inlet surface for a assumed temperature of $T = 300$ K. Variable hard sphere (VHS) parameters of the used species required for the simulation as well as the boundary conditions are given in Table 1. The resulting thrust force can be found by integrating over the local density $\rho(\vec{x})$ and velocity $\vec{v}(\vec{x})$ at the position $\vec{x}$ of the inlet and outlet of the control volume shown in Fig. 3 by

$$F = \oiint \rho(\vec{x})\vec{v}(\vec{x})\vec{v}(\vec{x})dS = \dot{m} \oiint \vec{v}(\vec{x})dS \tag{1}$$

to consider non-uniformities of the flow that might occur due to an asymmetry of the gas injection.

4 Experimental Setup

To confirm the numerical results, cold gas thrust measurements of the DEEVA thruster with argon and xenon were performed using DLRs DEPB thrust balance within the STG-MT vacuum chamber, which has previously been tested with other thrusters[5]. The thrust balance features quartz glass rods as load-bearing springs to minimizhe thermal drift, a Sartorius® WZA224-N load cell for precision, and an eddy current brake to dampen oscillations. The calibration is performed using fine

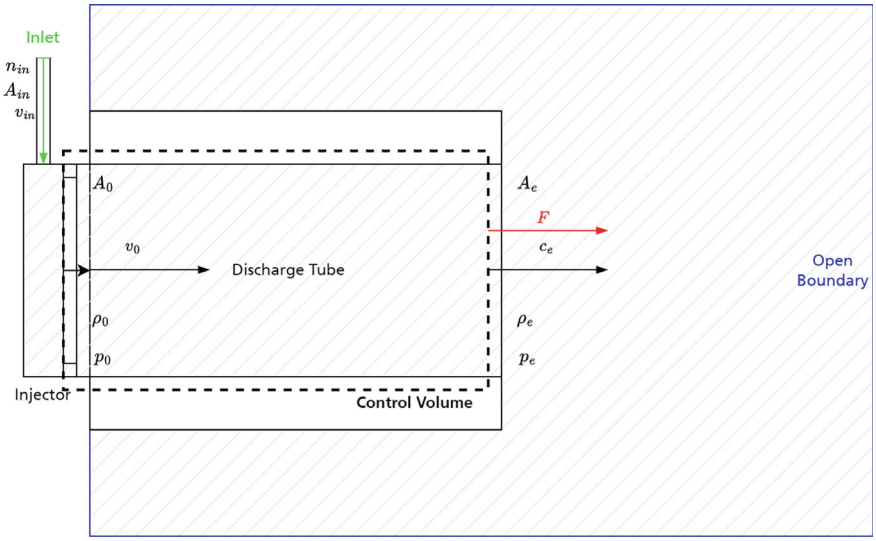

Fig. 3 Control volume used for the simulation and calculation of the thrust and boundaries. Boundary 4 is not shown. The area filled with hatches indicates the simulation domain

weights to ensure accurate and repeatable thrust measurements. This will lead to further understand the influence of the injector geometry and assist in optimization of the neutral flow injection into the discharge channel.

5 Analytical Model

The thrust is calculated with the analytical model under the assumption that the flow in the tube is subsonic. The exit velocity c_e can then be calculated from the isentropic relation

$$c_e = \sqrt{2c_p(T_e - T_0)} = \sqrt{\frac{\kappa}{\kappa - 1}(1 - (p_a/p_0)^{\frac{\kappa-1}{\kappa}}} \tag{2}$$

In which the isentropic coefficient was assumed to be a constant at $\kappa = 1.67$ for noble gases, the reservoir pressure was assumed to be $p_0 = 150000$ Pa and the ambient pressure was assumed to be $p_a = 0.001$ Pa, while the gas in the reservoir is assumed to be at room temperature of $T_0 = 300$ K. The thrust can then be calculated from

$$F = \dot{m} c_e \tag{3}$$

While this model is very simple, it can give a first-order estimate of the expected neutral gas thrust. The mass flow $\dot{m} = \rho \dot{V}$ was calculated from the volume flow $\dot{V}$ under the assumption of a ideal gas at a temperature of $T_0 = 300$ K to calculate the density.

6 Results

The simulation revealed details about the neutral gas flow within the discharge tube. As it can be seen for the results with the old geometry, in Fig. 4b, there is a pressure gradient in the gas injector as the gas flow is injected from the top and distributing within the radial channel. Since the pressure is higher at the top inlet ports, the flow velocity and density in the ports is also significantly higher. Due to the collisions downstream in the discharge channel, there is also a gradient in the exiting neutral gas plume, resulting in the observed asymmetry of the plume. With the new injector geometry and a central feeding of the gas into the discharge channel, the plume is symmetric (Fig. 5). In addition, it was observed for both the simulation results and the experimental measurements, that the cold gas thrust increases with the volume flow rate. The comparison of these results for argon and xenon with the analytical model are shown in Fig. 6, where the cold gas thrust F as calculated from the analytical model (circles), the measured experimental results (diamonds) and the calculated numerical results (squares) are shown. As it can be seen for argon in Fig. 6a, the agreement between the analytical model and the experimental and simulated results is quite good for argon and within the measurement uncertainty of the thrust measurements. For xenon, there are more differences observed. The analytical model increases linear with the volume flow rate, while for the experiment and simulation a logarithmic behaviour is observed. The results from the simulation and the experiment are within the measurement uncertainty for the lower flow rates but disagree for a very high flow rate. For the analytical model by the linear behaviour and the one-dimensional calculation not modelling all physics correctly. For the lower flow rates, this difference is significant enough. The disagreement between experiment and simulation for the higher flow rate can not be explained at the moment, except that Xenon at low temperatures due to the expansion might not be modelled correctly (Fig. 7).

7 Conclusion

Within this work, the neutral gas flow within an electric thruster was simulated using the Fokker-Planck-method extension in SPARTA. Comparative measurements of the cold gas thrust were performed for argon and xenon. The results will allow to improve the design of the gas injector and the modelling of the plasma discharge itself, since the structure of the magnetic field and microwave radiation are known from independent measurements and simulations. Therefore, the knowledge of the local number density can directly assist in the improvement of the simple discharge models. Additionally, the results for the inflow from the injector can be used as an initial condition for particle-in-cell simulations. In addition, it was observed that the improved gas injector will produce a homogeneous distribution of the neutral gas in the plume. The comparison with the experimental results showed good agreement within the mea-

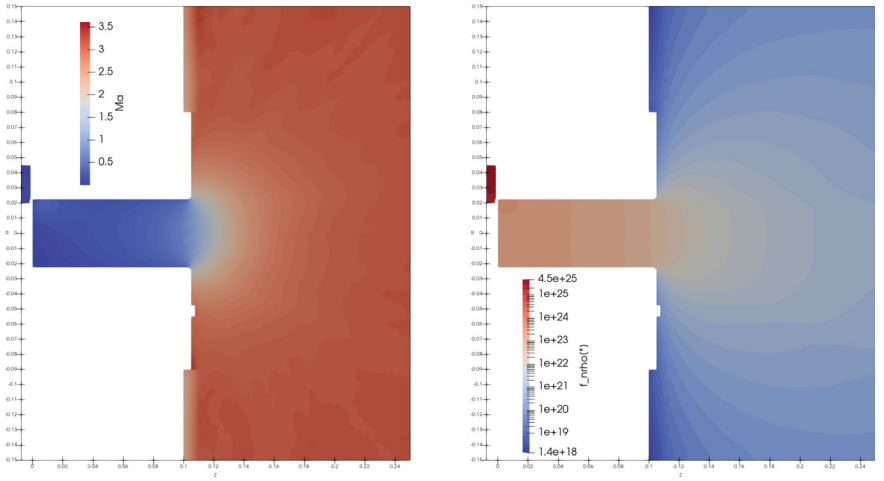

(a) Mach number Ma (b) Number Density n

Fig. 4 Mach number and number density in the old geometry for argon at a flowrate of $\dot{V} = 1$ sccm

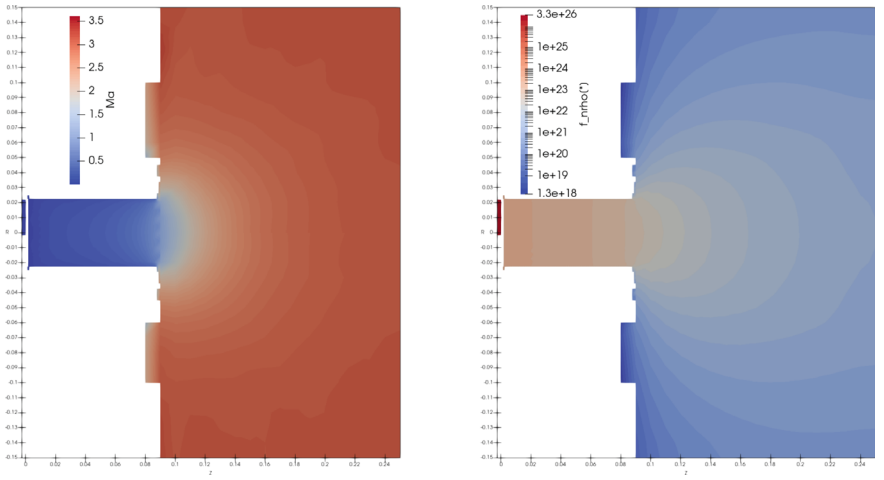

(a) Mach Number Ma (b) Number density n

Fig. 5 Mach number and number density in the new geometry for argon at a flowrate of $\dot{V} = 1$ sccm

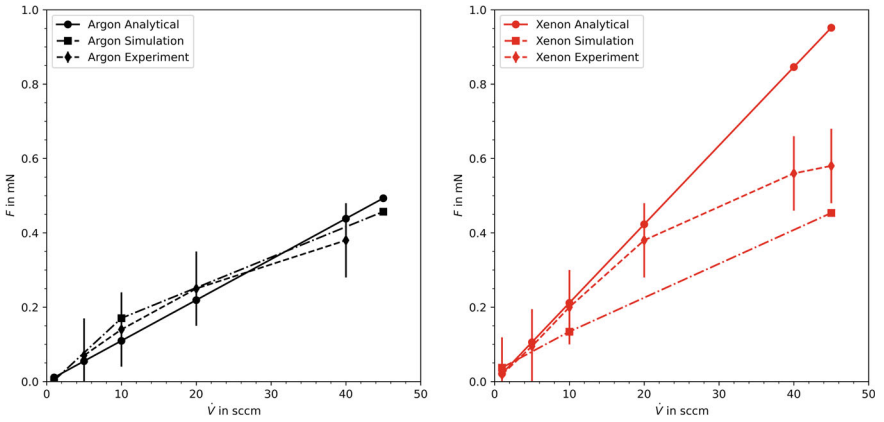

(a) Results for Argon (b) Results for Xenon

Fig. 6 Comparison of the cold gas thrust measurements (diamonds) with the analytical model (circles) and the numerical results (squares)

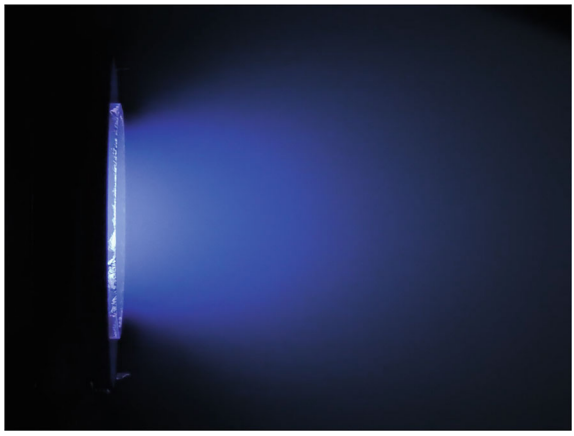

Fig. 7 Thruster plume during operation with argon at a volume flow rate of 2 sccm and a microwave power of $P_{MW} = 60$ W

surement uncertainty of the thrust balance for for argon, but disagreement for xenon. In future, the number density in the plume should be measured using a Patterson probe to understand the neutral gas distribution and compare it with the simulation results. In addition, more operation points shall be studied at a lower measurement uncertainty and for diatomic or multispecies propellants.

References

1. Bird GA (1994) Molecular gas dynamics and the direct simulation of gas flows. Oxford University Press
2. Gorji MH, Torrilhon M, Jenny P (2011) Fokker-Planck model for computational studies of monatomic rarefied gas flows. J Fluid Mech 680:574–601
3. Plimpton SJ, Moore SG, Borner A, Stagg AK, Koehler TP, Torczynski JR, Gallis MA (2019) Direct simulation Monte Carlo on petaflop supercomputers and beyond. Phys Fluids 31(8):086101
4. Schmidt J, Simon J, Grabe M (2022) The DEEP thruster concept. In: IEPC (ed) 37th international electric propulsion conference, Boston, pp 1–9. https://elib.dlr.de/148314/
5. Schmidt J, Simon J, Neumann A (2023) Thrust measurements of the RIT-10 thruster with a new type of thrust balance. Int J Energetic Mater Chem Propulsion 22(4) (Begel House Inc)

Open Access This chapter is licensed under the terms of the Creative Commons Attribution 4.0 International License (http://creativecommons.org/licenses/by/4.0/), which permits use, sharing, adaptation, distribution and reproduction in any medium or format, as long as you give appropriate credit to the original author(s) and the source, provide a link to the Creative Commons license and indicate if changes were made.

The images or other third party material in this chapter are included in the chapter's Creative Commons license, unless indicated otherwise in a credit line to the material. If material is not included in the chapter's Creative Commons license and your intended use is not permitted by statutory regulation or exceeds the permitted use, you will need to obtain permission directly from the copyright holder.

DSMC: A Statistical Mechanics Perspective

Alejandro L. Garcia

Abstract This paper presents a perspective in which Direct Simulation Monte Carlo (DSMC) is viewed not in its traditional role as an algorithm for solving the Boltzmann equation but as a numerical method for statistical mechanics. First, analytical techniques such as the collision virial and Green-Kubo relations, commonly used in molecular dynamics, are used to study the numerical properties of the DSMC algorithm. The stochastic aspect of DSMC, which is often viewed as unwanted numerical noise, is shown to be a useful feature for problems in statistical physics, such as Brownian motion and thermodynamic fluctuations. Finally, it is argued that fundamental results from statistical mechanics can provide guardrails when applying machine learning to DSMC.

Keywords Direct simulation Monte Carlo · Statistical mechanics · Molecular dynamics · Kinetic theory · Fluctuations

1 MD and DSMC—Brothers Separated at Birth

Three scientific eras dawned in the middle of the last century: the atomic age, the space age, and the age of the computer. Numerical algorithms were developed for the study of fluids under extreme conditions, such as nuclear explosions and orbital reentry, that were beyond the realm of conventional laboratory experiments. An early example is the Metropolis Monte Carlo method, which in 1953 showed that a particle representation could be used to map phase space and using statistical mechanics extract a fluid's thermodynamic properties, such as the equation of state [39]. It was closely followed by molecular dynamics (MD), introduced in 1959 by Alder and Wainwright, which uses a similar particle representation but includes dynamics, allowing it to measure transport properties such as viscosity [1].

A. L. Garcia (✉)
San Jose State University, San Jose, CA, USA
e-mail: Alejandro.Garcia@sjsu.edu
URL: http://www.algarcia.org

© The Author(s) 2026

M. Grabe et al. (eds.), *Rarefied Gas Dynamics*, Springer Aerospace Technology,
https://doi.org/10.1007/978-3-032-00094-1_56

In 1963, Graeme Bird submitted to *Physics of Fluids* a paper entitled "Approach to Translational Equilibrium in a Rigid Sphere Gas." In this article he introduced a stochastic collision algorithm that would become the cornerstone of Direct Simulation Monte Carlo (DSMC). The paper was rejected (G.A. Bird, personal communication). The referee had failed to recognize that DSMC differed significantly from MD; after revising it to explain these differences, Bird's paper was accepted [12].

DSMC went on to become the dominant numerical method in aerospace engineering for rarefied gas dynamics while MD established popularity in the field of statistical mechanics for the simulation of microscopic systems. For many years, these communities remained separate, yet recently they have found common interests in topics such as nanofluidics and granular flows. This paper presents several short stories in which DSMC is used by researchers, such as myself, whose background is in statistical mechanics and molecular dynamics. As we shall see, by approaching DSMC from an unconventional perspective, a number of new avenues are opened. This narrative is intentionally personal, since Graeme Bird, to whom this paper is dedicated, was a colleague and friend for nearly 30 years. In the interest of space, a summary of the DSMC algorithm is omitted; see [4] for an introduction and [14, 15, 20] for full treatments.

2 But Why Ideal Gas Law?

In 1989 I joined the faculty at San Jose State University, located in Silicon Valley. About that time I met Berni Alder and started working with him at the nearby Livermore Lab. Alder took an immediate interest in DSMC and we eventually published 16 papers together, most of them on ways to extend the DSMC algorithm. Yet when I first explained DSMC to Berni, he was puzzled and asked "But why does it give the ideal gas law?" Graeme Bird did not address this question in his books on DSMC [13–15] since he always viewed the algorithm as numerically solving the Boltzmann equation, a perspective that was reinforced by a proof by Wagner [48].

In their seminal MD simulations Alder and Wainwright [2] measured the equation of state for hard spheres (mass m, diameter d) as

$$p = nkT + \tfrac{1}{3} m \Gamma \Theta \tag{1}$$

where p, n, T are pressure, number density, and temperature; k is the Boltzmann constant. The collision rate is Γ and

$$\Theta = \langle \Delta \mathbf{v}_\alpha \cdot \mathbf{r}_{\alpha\beta} \rangle \geq 0 \tag{2}$$

is the virial. For a collision between particles α and β, $\Delta \mathbf{v}_\alpha$ is the change in velocity for particle α and $\mathbf{r}_{\alpha\beta} = \mathbf{r}_\alpha - \mathbf{r}_\beta$ is their separation. The virial is an average over collisions and depends on the particle diameter since $|\mathbf{r}_{\alpha\beta}| = d$. In (1) the pressure is the sum of translational and collisional contributions to momentum transfer.

In DSMC collisions occur within cells and the probability of a collision is *independent* of the positions of the particles, so $\langle \mathbf{r}_{\alpha\beta} \rangle = 0$ and $\langle \Delta \mathbf{v}_\alpha \cdot \mathbf{r}_{\alpha\beta} \rangle = \langle \Delta \mathbf{v}_\alpha \rangle \cdot \langle \mathbf{r}_{\alpha\beta} \rangle = 0$ so $\Theta = 0$. Since the virial contribution is zero, the equation of state for DSMC is the ideal gas law. Note that Wagner's proof is for infinitesimal collision cells yet we have the ideal gas law even for finite cell size due to symmetry in the selection of collision partners in DSMC.

Alder found this unsatisfactory, so, together with Frank Alexander, we formulated the Consistent Boltzmann Algorithm (CBA) [5]. It is identical to DSMC except that collisions change both the velocities *and* the positions of colliding particles. Specifically, after computing the post-collision velocities the positions are shifted as

$$\mathbf{r}_\alpha \Rightarrow \mathbf{r}_\alpha + d\,\hat{\mathbf{a}}_\alpha \quad ; \quad \mathbf{r}_\beta \Rightarrow \mathbf{r}_\beta - d\,\hat{\mathbf{a}}_\alpha \tag{3}$$

where $\hat{\mathbf{a}}_\alpha = \Delta \mathbf{v}_\alpha / |\Delta \mathbf{v}_\alpha|$ is a unit vector in the direction of the apse line (line between centers) for a hard sphere collision with this change in velocity. Simulations verified that CBA gives the correct pressure and reasonably accurate transport coefficients up to moderately high densities.

The Consistent Universal Boltzmann Algorithm (CUBA) makes the post-collision displacement a function of density and temperature, which allows one to choose the desired equation of state [6, 34]. For example, by choosing the van der Waals equation, we were able to simulate the condensation of vapor into liquid droplets. However, for simulating liquids, we found that CUBA was not competitive with MD in terms of computational cost.

Today, the most popular variants of DSMC for dense gases are based on the Enskog equation [27, 40]. Instead of using a CBA displacement, the correct virial Θ can be obtained by using a collision probability that depends on both the relative velocity and the relative position for a collision pair [25]. In other words, the Enskog perspective is that particle positions affect collisions, while in CBA, collisions affect particle positions.

3 A Lesson on Transport from Molecular Dynamics

In his first book, Graeme Bird said of DSMC, "the results are remarkably insensitive …and no deleterious effects are generally present …if the cell size approaches the mean free path or if the time step approaches the mean collision time" [13]. Nevertheless, the demonstration program in this book for the Rayleigh problem sets the collision cell size to half a mean free path and the time step to a fifth of a mean free collision time.

A common way of quantifying the error due to cell size and time step is to measure viscosity or thermal conductivity and, at low Knudsen number, compare with Chapman-Enskog theory. These transport coefficients can be obtained by measuring the momentum (or heat) flux in a DSMC simulation with a linear velocity (or temperature) gradient [19]. From the perspective of non-equilibrium thermodynamics,

the transport coefficient is an Onsager coefficient that relates the thermodynamic flux to the thermodynamic force due to the gradient [24, 41].

Yet in the early days of molecular dynamics, such non-equilibrium measurements were not feasible since simulations were limited to a few hundred particles. Instead, transport properties were measured in simulations of equilibrium systems using results from statistical mechanics.

The basic idea is to apply the fluctuation-dissipation theorem, which connects statistical fluctuations to the rate of dissipation. The best known example is Brownian motion in which the mobility, μ, of a particle is obtained from measuring the variance of its position in time as

$$\mu = \frac{1}{6kT} \lim_{t\to\infty} \frac{\langle |\mathbf{r}(t) - \mathbf{r}(0)|^2 \rangle}{t} \tag{4}$$

By contrast, a non-equilibrium measurement obtains the mobility $\mu = v_T/F_{ext}$ from the terminal velocity, v_T, for the particle under an external force of magnitude F_{ext}.

Using Einstein-Helfand theory one can measure the viscosity of a fluid from molecular trajectories as [3]

$$\eta = \frac{1}{2VkT} \lim_{t\to\infty} \frac{\langle [G(t) - G(0)]^2 \rangle}{t} \qquad \text{with} \qquad G(t) = m \sum_{i=1}^{N} \dot{x}_i(t) y_i(t) \tag{5}$$

where N is the number of molecules, V is the system volume, x_i, y_i are components of $\mathbf{r}_i$, and $\dot{x} \equiv dx/dt$. This allows us to measure the viscosity (and other transport coefficients) from *equilibrium* simulations. A related approach uses the off-diagonal stress tensor component,

$$J(t) = \dot{G}(t) = m \sum_{i=1}^{N} \dot{x}_i(t)\dot{y}_i(t) + \frac{1}{2} \sum_{i=1}^{N} \sum_{i=j}^{N} F_{ij}^{x}(y_i - y_j) \tag{6}$$

where $\mathbf{F}_{ij}$ is the force between molecules. Our previous result now takes the more familiar form from Green-Kubo theory,

$$\eta = \frac{1}{VkT} \int_0^\infty \langle J(t) J(0) \rangle \, dt \tag{7}$$

Notice from (6) that J is the sum of a kinetic (ballistic) contribution and a contribution due to the transfer of momentum by intermolecular forces.

For hard sphere collisions Wainwright wrote [49]

$$J(t) = m \sum_{i=1}^{N} \dot{x}_i(t)\dot{y}_i(t) + \sum_{c}^{\text{collisions}} \frac{m}{d^2} (\Delta \mathbf{v}_\alpha \cdot \mathbf{r}_{\alpha\beta})(x_\alpha - x_\beta)(y_\alpha - y_\beta)\delta(t - t_c) \tag{8}$$

where t_c is the time of a collision. He was able to evaluate (7) and express it as the sum of three contributions, $\eta = \eta^{\mathrm{K}} + \eta^{\mathrm{K}\times\mathrm{C}} + \eta^{\mathrm{C}}$. The kinetic contribution η^{K} is precisely the Chapman-Enskog viscosity. The cross term $\eta^{\mathrm{K}\times\mathrm{C}}$ and the collision term η^{C} are dense gas corrections.

In DSMC, the collision term η^{C} is *not* zero due to the finite distance between the collision partners (i.e., the finite collision cell size). Unlike the equation of state contribution due to the virial (see (2)), this contribution to the viscosity does not average to zero over DSMC collisions within a cell. In fact, following a similar analysis as Wainwright one finds

$$\eta^{\mathrm{C}} = \frac{m^2\Gamma}{2kT}\left\langle (y_\alpha - y_\beta)^2\right\rangle\left\langle (\Delta\dot{x}_\alpha - \Delta\dot{x}_\beta)^2\right\rangle \tag{9}$$

For cubic collision cells of size ℓ the average $\left\langle (y_\alpha - y_\beta)^2\right\rangle = \ell^2/6$; at equilibrium $\left\langle (\Delta\dot{x}_\alpha - \Delta\dot{x}_\beta)^2\right\rangle = 4kT/3m$. In DSMC the cross term $\eta^{\mathrm{K}\times\mathrm{C}}$ is zero and so the hard sphere viscosity is [7]

$$\eta = \eta^{\mathrm{K}} + \eta^{\mathrm{C}} = \frac{5}{16d^2}\sqrt{\frac{mkT}{\pi}}\left(1 + \frac{16}{45\pi}\frac{\ell^2}{\lambda^2}\right) \tag{10}$$

where λ is the mean free path. Note that the error goes as ℓ^2; for a cell size of one mean free path the viscosity deviates from its Chapmann-Enskog value by 11%. A similar analysis (with a similar result) may be applied to obtain the error in thermal conductivity due to finite cell size. Finally, this approach also gives the error in the transport coefficients due to a finite time step τ; in DSMC this error goes as τ^2 [31, 33].

In his last book Bird wrote "(In) early DSMC programs …the mean spacing between collision pairs was too large in comparison with the mean free path and this led to the introduction of sub-cells …(and) an option to select the collision pairs from the nearest-neighbour pairs within the cell" [15]. He also mentions that "The time step is set to a specified small fraction of the sampled mean collision time." A challenge for modern DSMC codes is to minimize the distance between colliding particles and to minimize the time between ballistic movement steps while avoiding unphysical bias errors (see Sect. 5).

4 Fluctuations—One Man's Garbage …

My introduction to DSMC came in 1983 as I was finishing my doctoral studies at The University of Texas at Austin in what is now The Ilya Prigogine Center for Studies in Statistical Mechanics and Complex Systems. At that time there were theoretical results, confirmed by light scattering experiments, indicating that hydrodynamic

fluctuations had weak, long-ranged correlations in non-equilibrium systems (e.g., under a temperature gradient).

In his first book, Bird describes fluctuations in DSMC as an unavoidable annoyance but that with a sufficiently large sample size the desired mean value can be measured to the desired accuracy [13]. One commonly held misconception was that these fluctuations came from the Monte Carlo nature of the collision algorithm in DSMC. Yet the very same fluctuations are also found in molecular dynamics, which has deterministic dynamics.

Due to computer memory constraints, the number of particles (or "simulators") in a DSMC calculation is typically a small fraction of the number of physical molecules. For example, at standard temperature and pressure, the mean free path in air is roughly 60 nanometers and a cubic mean free path contains about 6000 molecules. In contrast, a typical DSMC simulation uses 20 particles per cubic mean free path, that is, each DSMC particle represents $F_N = 300$ physical molecules. This number scales as the Knudsen number so it is much higher for rarefied flows.

Statistical mechanics gives us the standard deviation of hydrodynamic variables, allowing us to estimate the expected statistical standard error in particle simulations [35]. For example, in a cell with N_c particles, the variance in each component of fluid velocity is $\langle \delta u_x^2 \rangle = kT/mN_c$ [36]. For both MD and DSMC the fractional error in estimating u_x from S independent statistical samples is

$$E = \frac{\sqrt{\langle \delta u_x^2 \rangle}/\sqrt{S}}{|u_x|} \approx \frac{1}{\sqrt{SN_c}} \frac{1}{\mathrm{Ma}} \tag{11}$$

where Ma is the Mach number of the flow. This result illustrates why nanofluidic flows, in which $\mathrm{Ma} \ll 1$, are much harder to measure in DSMC compared to hypersonic flows. In DSMC N_c is smaller than the number of physical molecules by a factor of F_N, the variance in fluid velocity increases by the same factor.

After accounting for this amplification factor, we find that hydrodynamic fluctuations in DSMC are physically correct [30] and yield hydrodynamic information. For example, from the time correlation of density fluctuations one may measure the sound speed and viscosity from the location and width of the Brillouin peak, mimicking the technique used by light scattering [10, 21]. This dynamic structure factor is a useful way to compare DSMC models (e.g. internal energy relaxation) with laboratory measurements and theoretical predictions [22].

The first numerical observations of long-ranged correlations of hydrodynamic fluctuations were made using DSMC for systems with a temperature gradient [37] and a velocity gradient [29]. The "giant fluctuation" phenomenon, first reported in diffusive mixing experiments [46], is due to such non-equilibrium correlations for fluctuations of concentration and fluid velocity, as confirmed by DSMC [26]. Most recently DSMC simulations have been used to study the impact of thermal fluctuations on turbulence [28, 38]. They confirm theoretical predictions [9] and numerical fluctuating hydrodynamic observations [11] that molecular fluctuations *dominate* the turbulent energy cascade at the Kolmogorov length scale.

Bird wrote in his last book, "While the fluctuations are unphysical when F_N is large, they are physically realistic …(with) a one-to-one correspondence between real and simulated molecules. This is another instance of DSMC going beyond the Boltzmann equation because fluctuations are neglected in the Boltzmann model." His last three papers were on Brownian motion [16–18].

5 Exorcising the Demons

In 1887 Maxwell presented a thought experiment, "…conceive of a being whose faculties are so sharpened that he can follow every molecule in its course …so as to allow only the swifter molecules to pass from (chamber) A to B, and only the slower molecules to pass from B to A. He will thus, without expenditure of work, raise the temperature of B and lower that of A, in contradiction to the second law of thermodynamics." The DSMC algorithm has full information and control of the particle's dynamics and modern implementations have many complex stages. How can we be sure that we do not have a Maxwell demon hiding in our simulations? In other words, how do we test that our simulations satisfy the Second Law of Thermodynamics? Boltzmann's H-theorem is not helpful, since, due to fluctuations, it only applies in the limit $N \to \infty$.

Consider an isolated system with microstate dynamics [44]

$$\dot{p}_i = \sum_{j}^{\text{states}} (p_j W_{ji} - p_i W_{ij}) \tag{12}$$

where p_i is the probability of state i and W_{ij} is the transition rate from i to j. At equilibrium $\dot{p}_i = 0$. If $W_{ij} = W_{ji}$, then we have *microscopic reversibility*. At equilibrium we have *detailed balance* ($p_j W_{ji} = p_i W_{ij}$) and *ergodicity* ($p_i = p_j$) if and only if we have microscopic reversibility. Finally, the dynamics satisfies the Second Law ($\dot{S} = -k \sum_j \dot{p}_j \ln p_j \geq 0$) if and only if we have ergodicity [44].

Detailed balance is a necessary condition for microscopic reversibility, which is a sufficient condition for the dynamics to obey the Second Law. Yet, it is not uncommon to find DSMC implementations that do *not* satisfy detailed balance. For example, some of the early surface scattering models were ad hoc empirical fits to experimental data, which led Cercignani and Lampis to formulate a model that imposed detailed balance [23]. Many implementations of inflow/outflow boundaries also fail to satisfy detailed balance [45]. If machine learning methods are used to handle some elements in a DSMC calculation, such as chemical reactions and internal degrees of freedom, we may not know if detailed balance is satisfied [8]. And even when the algorithm in a DSMC code is theoretically sound, there is always the possibility that the implementation has a 'bug' (coding error).

In testing for the presence of Maxwell demons in a DSMC code, equilibrium hydrodynamic fluctuations can serve as a coal mine canary. For example, at equilib-

rium, the number of particles in each cell is independently Poisson distributed, and this result is independent of the collision model, boundary conditions, etc. Statistical mechanics provides further relations for the variances and correlations of fluid velocity, temperature, internal energy, and other variables [32, 36]. While this is a necessary but not sufficient statistical test, it is a sensitive one that can reveal malevolent problems. Ensuring the correctness of simulation data is increasingly important as we enter the age of artificial intelligence. Given the AI systems' voracious appetite for such data, we must avoid having machines learn the wrong lessons.

6 Concluding Remarks

Graeme Bird and Berni Alder met for the first time at the 22nd Rarefied Gas Dynamics Symposium in Sydney, Australia, nearly 40 years after their original publications on DSMC and MD. In the 25 years since that meeting, we find increasing cooperation between the two algorithms' communities. One example is the study of rotational relaxation using all-atom molecular dynamics simulations combined with DSMC [47]. Yet perhaps the best example is the shared heritage of LAMPPS [43] and SPARTA [42], two of the most widely used codes for molecular dynamics and direct simulation Monte Carlo. Although separated at birth, MD and DSMC are now the patriarchs overseeing a large family of particle-based fluid algorithms.

Acknowledgements The author acknowledges support from the US Department of Energy, Office of Science, Office of Advanced Scientific Computing Research, Applied Mathematics Program under contract no. DE-AC02-05CH11231.

References

1. Alder BJ, Wainwright TE (1959) Studies in molecular dynamics. i. General method. J Chem Phys 31(2):459–466
2. Alder BJ, Wainwright TE (1960) Studies in molecular dynamics. ii. Behavior of a small number of elastic spheres. J Chem Phys 33(5):1439–1451
3. Alder B, Gass D, Wainwright T (1970) Studies in molecular dynamics. viii. The transport coefficients for a hard-sphere fluid. J Chem Phys 53(10):3813–3826
4. Alexander FJ, Garcia AL (1997) The direct simulation Monte Carlo method. Comput Phys 11(6):588–593
5. Alexander FJ, Garcia AL, Alder BJ (1995) A consistent Boltzmann algorithm. Phys Rev Lett 74(26):5212
6. Alexander FJ, Garcia AL, Alder BJ (1997) The consistent Boltzmann algorithm for the van der Waals equation of state. Phys A Statistical Mech Appl 240(1–2):196–201
7. Alexander FJ, Garcia AL, Alder BJ (1998) Cell size dependence of transport coefficients in stochastic particle algorithms. Phys Fluids 10(6):1540–1542
8. Ball ND, MacArt JF, Sirignano J (2024) Online optimisation of machine learning collision models to accelerate direct molecular simulation of rarefied gas flows. arXiv preprint arXiv:2411.13423

9. Bandak D, Goldenfeld N, Mailybaev AA, Eyink G (2022) Dissipation-range fluid turbulence and thermal noise. Phys Rev E 105(6):065113
10. Baras F, Mansour MM, Garcia A, Mareschal M (1995) Particle simulation of complex flows in dilute systems. J Comput Phys 119(1):94–104
11. Bell JB, Nonaka A, Garcia AL, Eyink G (2022) Thermal fluctuations in the dissipation range of homogeneous isotropic turbulence. J Fluid Mech 939:A12
12. Bird G (1963) Approach to translational equilibrium in a rigid sphere gas. Phys Fluids 6:1518–1519
13. Bird G (1976) Molecular gas dynamics. Oxford engineering science series, Clarendon Press. https://books.google.com/books?id=OAgpAQAAMAAJ
14. Bird G (1994) Molecular gas dynamics and the direct simulation of gas flows. No. v. 1 in molecular gas dynamics and the direct simulation of gas flows. Clarendon Press. https://books.google.com/books?id=Bya5QgAACAAJ
15. Bird G (2013) The DSMC method. CreateSpace Independent Publishing Platform. https://books.google.com/books?id=0YdnngEACAAJ
16. Bird G (2015) The rate of energy transfer from air as an initially stationary particle acquires Brownian motion. Nano Energy 11:463–470
17. Bird G (2016) Brownian relaxation of an inelastic sphere in air. Phys Fluids 28(6)
18. Bird G (2017) The possibility of harvesting useful energy from the thermal motion of air molecules. NanoWorld J 3(1):18–22
19. Bird G, Gallis M, Torczynski J, Rader D (2009) Accuracy and efficiency of the sophisticated direct simulation Monte Carlo algorithm for simulating noncontinuum gas flows. Phys Fluids 21(1)
20. Boyd I, Schwartzentruber T (2017) Nonequilibrium gas dynamics and molecular simulation. Cambridge Aerospace Series. Cambridge University Press. https://books.google.com/books?id=8PdFDgAAQBAJ
21. Bruno D, Frezzotti A, Ghiroldi GP (2017) Rayleigh-Brillouin scattering in molecular oxygen by CT-DSMC simulations. Eur J Mech-B/Fluids 64:8–16
22. Bruno D, Giovangigli V (2022) Internal energy relaxation processes and bulk viscosities in fluids. Fluids 7(11):356
23. Cercignani C, Lampis M (1971) Kinetic models for gas-surface interactions. Transport Theory Statistical Phys 1(2):101–114
24. De Groot S, Mazur P (2013) Non-equilibrium thermodynamics. Dover Books on Physics, Dover Publications. https://books.google.com/books?id=mfFyG9jfaMYC
25. Donev A, Alder BJ, Garcia AL (2008) Stochastic hard-sphere dynamics for hydrodynamics of nonideal fluids. Phys Rev Lett 101(7):075902
26. Donev A, Bell JB, de La Fuente A, Garcia AL (2011) Diffusive transport by thermal velocity fluctuations. Phys Rev Lett 106(20):204501
27. Frezzotti A (1997) A particle scheme for the numerical solution of the enskog equation. Phys Fluids 9(5):1329–1335
28. Gallis M, Bitter N, Koehler T, Torczynski J, Plimpton S, Papadakis G (2017) Molecular-level simulations of turbulence and its decay. Phys Rev Lett 118(6):064501
29. Garcia A, Mansour MM, Lie G, Clementi E (1987) Hydrodynamic fluctuations in a dilute gas under shear. Phys Rev A 36(9):4348
30. Garcia A, Penland C (1991) Fluctuating hydrodynamics and principal oscillation pattern analysis. J Statistical Phys 64:1121–1132
31. Garcia A, Wagner W (2000) Time step truncation error in direct simulation Monte Carlo. Phys Fluids 12(10):2621–2633
32. Garcia A (2007) Estimating hydrodynamic quantities in the presence of microscopic fluctuations. Commun Appl Math Comput Sci 1(1):53–78
33. Hadjiconstantinou NG (2000) Analysis of discretization in the direct simulation Monte Carlo. Phys Fluids 12(10):2634–2638
34. Hadjiconstantinou NG, Garcia AL, Alder BJ (2000) The surface properties of a van der Waals fluid. Phys A Statistical Mech Appl 281(1–4):337–347

35. Hadjiconstantinou NG, Garcia AL, Bazant MZ, He G (2003) Statistical error in particle simulations of hydrodynamic phenomena. J Comput Phys 187(1):274–297
36. Landau LD, Lifshitz EM (2013) Statistical physics, vol 5. Elsevier
37. Mansour MM, Garcia AL, Lie GC, Clementi E (1987) Fluctuating hydrodynamics in a dilute gas. Phys Rev Lett 58(9):874
38. McMullen RM, Krygier MC, Torczynski JR, Gallis MA (2022) Navier-stokes equations do not describe the smallest scales of turbulence in gases. Phys Rev Lett 128(11):114501
39. Metropolis N, Rosenbluth AW, Rosenbluth MN, Teller AH, Teller E (1953) Equation of state calculations by fast computing machines. J Chem Phys 21(6):1087–1092
40. Montanero JM, Santos A (1997) Simulation of the enskog equation a la bird. Phys Fluids 9(7):2057–2060
41. Öttinger H (2005) Beyond equilibrium thermodynamics. Wiley. https://books.google.com/books?id=Prh9moT1WzMC
42. Plimpton SJ, Moore S, Borner A, Stagg A, Koehler T, Torczynski J, Gallis M (2019) Direct simulation Monte Carlo on petaflop supercomputers and beyond. Phys Fluids 31(8)
43. Thompson AP, Aktulga HM, Berger R, Bolintineanu DS, Brown WM, Crozier PS, In't Veld PJ, Kohlmeyer A, Moore SG, Nguyen TD et al (2022) Lammps—a flexible simulation tool for particle-based materials modeling at the atomic, meso, and continuum scales. Comput Phys Commun 271:108171
44. Thomsen JS (1953) Logical relations among the principles of statistical mechanics and thermodynamics. Phys Rev 91(5):1263
45. Tysanner MW, Garcia AL (2005) Non-equilibrium behaviour of equilibrium reservoirs in molecular simulations. Int J Numerical Methods Fluids 48(12):1337–1349
46. Vailati A, Giglio M (1997) Giant fluctuations in a free diffusion process. Nature 390(6657):262–265
47. Valentini P, Zhang C, Schwartzentruber TE (2012) Molecular dynamics simulation of rotational relaxation in nitrogen: implications for rotational collision number models. Phys Fluids 24(10)
48. Wagner W (1992) A convergence proof for bird's direct simulation Monte Carlo method for the Boltzmann equation. J Statistical Phys 66:1011–1044
49. Wainwright T (1964) Calculation of hard-sphere viscosity by means of correlation functions. J Chem Phys 40(10):2932–2937

Open Access This chapter is licensed under the terms of the Creative Commons Attribution 4.0 International License (http://creativecommons.org/licenses/by/4.0/), which permits use, sharing, adaptation, distribution and reproduction in any medium or format, as long as you give appropriate credit to the original author(s) and the source, provide a link to the Creative Commons license and indicate if changes were made.

The images or other third party material in this chapter are included in the chapter's Creative Commons license, unless indicated otherwise in a credit line to the material. If material is not included in the chapter's Creative Commons license and your intended use is not permitted by statutory regulation or exceeds the permitted use, you will need to obtain permission directly from the copyright holder.

Ab Initio-Based Collision Model for High-Temperature Molecular Gas Flows

Ashirbad Mallick and Tapan K. Mankodi

Abstract The present work focuses on a new ab initio-based collision model for calculating collision cross-sections from the data generated using the quasi-classical trajectory (QCT) method. A large number of trajectories were run on state-of-the-art potential energy surfaces to get the collision cross-section data. The model is expected to be better than the existing phenomenological collision models and produce more realistic results for studying re-entry flows. The new model is employed in the in-house direct simulation Monte Carlo (DSMC) code and used to study the effect of the collision models on Couette flow simulations and steady shock structure flow. The results are compared with those employing the widely used variable hard sphere (VHS) model.

Keywords Ab initio model · Re-entry flows · Direct simulation Monte Carlo

1 Introduction

The flow physics of re-entry of a space vehicle travelling at hypersonic speeds, especially at rarefied conditions, requires the study of the inelastic energy exchange, chemical and ionisation reactions that occur near the vehicle's surface. Analysis of such non-equilibrium flow involves studying the basic process of collision. Such rarefied flows are often studied using a widely used method known as the direct simulation Monte Carlo (DSMC) [2] method. Traditionally, the DSMC algorithm employs phenomenological collision models to estimate cross-sections and post-collision velocities. Such models are developed to obtain accurate relations of various transport properties as a function of temperature. However, the range over which such models can accurately predict the transport properties is often limited. In addition, phenomenological models usually rely on experimental values of transport properties that are often difficult to estimate at extremely high temperatures.

A. Mallick (✉) · T. K. Mankodi
Department of Mechanical Engineering, Indian Institute of Technology Guwahati, Guwahati, Assam, India
e-mail: m.ashirbad@iitg.ac.in

© The Author(s) 2026

M. Grabe et al. (eds.), *Rarefied Gas Dynamics*, Springer Aerospace Technology,
https://doi.org/10.1007/978-3-032-00094-1_57

2 Ab Initio-Based Collision Cross-Section Model

A new ab initio-based collision model has been proposed as a part of the present work to estimate the cross-section more appropriately. These collision cross-section values are found using quasi-classical trajectory (QCT) [1, 11] simulations, which use highly accurate CASSCF-CASPT2-based potential energy surfaces (PES) [10]. The QCT cross-section data were already computed and taken from the supplementary material of [6]. The QCT code developed for calculating the cross-sections has been validated extensively in previous reports [7, 8] on dissociation cross-sections for various colliding species.

It was observed that the total collision cross-sections from the QCT method [6] were invariant with the rotational quantum levels since they did not affect the scattering angle distributions at a given vibrational level. However, the effect of vibrational quantum levels on the collision cross-section was significant. Such effects have generally been ignored in the phenomenological models that are employed in DSMC.

The collision cross-section in the new ab initio-based collision model is a function of the relative speed as well as the vibrational levels of the molecule(s), which can be described for an atom-molecule collision using a simple fit given as (for atom-molecule interaction):

$$\sigma_{ab-initio} = (pv_1 + q)V_R{}^{(lv_1+m)} \tag{1}$$

and molecule-molecule interaction as

$$\sigma_{ab-initio} = (a(v_2 + v_3) + bv_2v_3 + c)V_R{}^{d(v_2+v_3)+ev_2v_3+f} \tag{2}$$

where v_1, v_2 and v_3 are the vibrational levels of the molecules, V_R is the relative velocity, and, $p, q, l, m, a, b, c, d, e$ and f are model parameters.

Figure 1 shows the comparison of the fitting function of the new model with the data obtained from the QCT simulations for $O_2 - O$, $N_2 - O$, $O_2 - O_2$ and $N_2 - N_2$ at various combinations of vibrational quantum levels. It is clear from the figure that the above expression of the fit is a close match with the collision cross-section data for different atom-molecule and molecule-molecule interactions from the QCT data [6].

The ab initio-based collision model was implemented in the in-house DSMC code. This was used to study the flow physics in the planar Couette flow problem and the effect of non-equilibrium on the shock structure profiles for nitrogen gas at various Mach numbers. The results obtained from the simulation employing the ab initio-based collision model were compared with those employing the extensively used VHS model [2]. In all these simulations, N_2 was used as the gas medium.

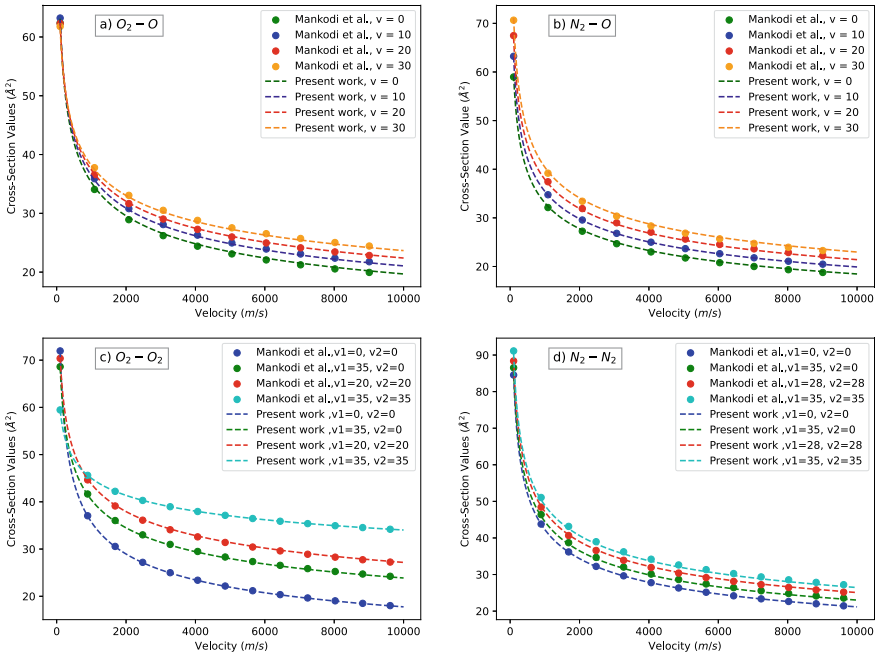

Fig. 1 Collision cross-section area comparison by using the ab initio-based model with the QCT computed data for the cases of **a**) $O_2 - O$, **b**) $N_2 - O$, **c**) $O_2 - O_2$ and **d**) $N_2 - N_2$

3 Couette Flow

The ab initio-based model was used to study Couette flow with nitrogen gas (N_2) flowing in a planar channel. The DSMC simulations employing the traditional VHS and ab initio-based collision models were carried out with the constant parameter Larsen-Borgnakke model ($Z_R = 5$ and $Z_V = 50$) [3] for handling rotational and vibrational relaxation. The walls in the horizontal channel were separated by 1 m ($L = 1$ m). The lower wall was assumed to be stationary, and the upper wall was made to move at a velocity of 300 m/s. The translational temperature of the lower and upper walls was kept at 2000 K and 3000 K, respectively [5]. The values of the translational (T_{trans}) and the vibrational (T_{vib}) temperatures differed for the upper and lower walls, resulting in a non-equilibrium boundary condition. The vibrational temperatures at the lower and upper walls were 3000 K and 2000 K, respectively. It was assumed that the rotational temperatures were in equilibrium with the translational temperatures at the wall.

Figure 2 shows the variation of normalised translational temperature, vibrational temperature and the horizontal velocity component along the channel height obtained from the DSMC simulations employing the two collision models. It can be inferred from the figures that a good agreement at most regions (central core) of the plots

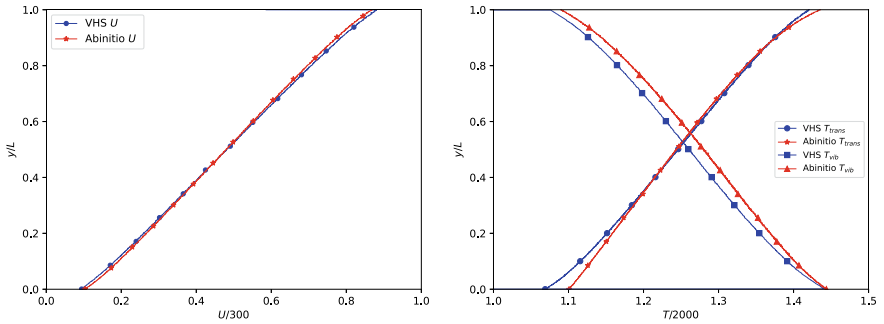

Fig. 2 Comparison of the horizontal component of velocity (left) and translation temperature and vibrational temperature (right) in Couette flow problem employing the VHS and ab initio-based collision model

can be seen for T_{trans}, T_{vib} and U predicted by the ab initio and the VHS models. However, we see significant differences in the temperature profiles in the regions closer to the lower and upper walls. The effect of the ab initio-based cross-section is more prominent in the temperature jump values compared to the velocity slip. At the lower wall, the temperature jump in the translational temperature is higher in the simulation employing the ab initio-based collision model than that obtained from the VHS model. The vibrational temperature at the lower wall is higher than the translational temperature, leading to a high degree of non-equilibrium. This results in a viscosity lower than that estimated by the VHS model [9]. In contrast, at the upper wall, the vibrational temperature is less than the translational temperature, leading to higher viscous effects as predicted by the cross-section data, leading to more collisions and a lower translational temperature jump.

4 Shock Structures in Nitrogen Gas

In addition to the Couette flow problem, simulations were conducted to study the interplay between non-equilibrium and collision models on the Mach 15 nitrogen shock structure. The driven and driver conditions for the Mach 15 shock structure were calculated using the Rankine-Hugoniot relations for vibrationally active diatomic gases, as shown in Table 1.

DSMC simulations were run for two models of the Larsen-Borgnakke inelastic collision model: (a) constant parameters ($Z_R = 5$ and $Z_V = 50$), and (b) temperature-dependent model [4]. The latter allows us to understand the combined effect of the elastic collision and inelastic energy models on the shock structure and the vibrational relaxation [12]. Figure 3 shows various temperature (translational, rotational and vibrational) profiles across the shock structure employing the two collision mod-

Table 1 Driver and driven conditions calculated using the Rankine-Hugoniot relations

Upstream		Downstream	
p_1	1.0 Pa	p_2	274.11 Pa
T_1	273.15 K	T_2	9907.03 K
U_1	5054.40 m/s	U_2	672.17 m/s

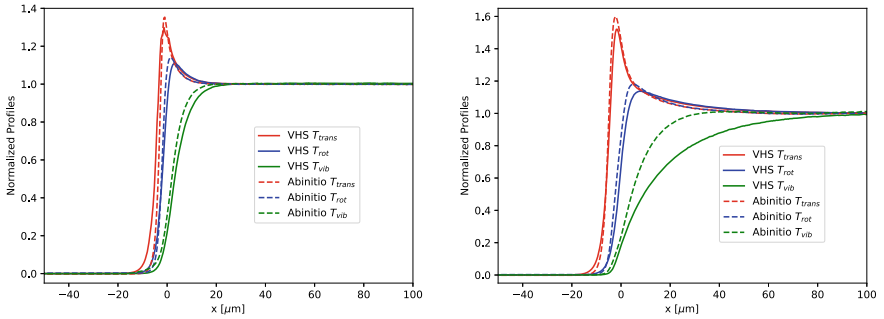

Fig. 3 Comparison of temperature profiles obtained from DSMC simulations with the VHS and ab initio-based collision models and employing constant parameters LB model (left) and temperature-dependent LB model (right)

els, the constant parameter LB model and the temperature-dependent LB model, respectively. It is clear from the temperature profiles that the peak translational temperature was higher for the shock structure obtained from the DSMC simulation employing the ab initio-based model compared to those obtained from the simulations employing the VHS model. In addition, the shock structures obtained using the ab initio-based collision model were much steeper and narrower than those obtained using the VHS model. This effect is even more pronounced in the case of simulation employing the temperature-dependent LB model. This is attributed to the vibrational favouring when calculating the collision cross-section using the ab initio-based collision model.

Higher vibrational levels in the ab initio-based collision model lead to higher collision cross-section values. This leads to more collisions and higher translational temperatures in the shock structure. The higher amount of collisions also results in more inelastic collisions, leading to higher values of rotational and vibrational temperatures. This also leads to faster relaxation, resulting in a narrower shock structure. This is even more pronounced in the case of simulations employing the temperature-dependent LB model. Higher translational temperatures in the simulation using the ab initio-based collision model lead to lower rotational (Z_{rot}) and vibrational (Z_{vib}) relaxation numbers compared to those calculated in the VHS model. This further leads to faster relaxation in the shock structure in the simulation employing the ab initio-based collision model compared to the VHS model. The difference in the shock structure profile can also be attributed to the phenomenological nature of the

VHS model, rendering an inaccurate viscosity-temperature relation, especially at high temperatures and higher degrees of non-equilibrium.

5 Conclusion

The present work introduces a new ab initio-based collision model which employs collision cross-section data computed using the QCT method. According to this model, the collision cross-section is a function of vibrational levels in addition to the relative velocity of the colliding particles. The in-house DSMC code employed the new model for simulating planar Couette flow with non-equilibrium boundary conditions and nitrogen shock structures at high Mach numbers. The results were compared with those obtained using the phenomenological VHS model. Contrasting temperature jump conditions at the lower and upper walls were observed from the two models, pointing to the contrasting effect of different kinds of non-equilibrium conditions on collision cross-section and viscous effects. In the case of the shock structure study, it was found that the profiles obtained from the simulation employing the ab initio-based collision model were narrower with a higher peak temperature and faster translational-rotational and translational-vibrational relaxation compared to those obtained using the VHS model. The interplay between the chemistry modelling and collision model will be investigated for the re-entry flows as part of future work. In addition, the work will be extended to study hypersonic flow past re-entry vehicles with realistic ambient conditions at various altitudes.

References

1. Bender JD, Nompelis I, Valentini P, Doraiswamy S, Schwartzentruber TE, Candler GV, Paukk Y, Yang KR, Varga Z, Truhlar DG (2014) Quasiclassical trajectory analysis of the N_2+N_2 reaction using a new ab initio potential energy surface. In: 11th AIAA/ASME joint thermophysics and heat transfer conference, p 2964
2. Bird GA (1994) Molecular gas dynamics and the direct simulation of gas flows (Clarendon Press; Oxford University Press)
3. Borgnakke C, Larsen PS (1975) Statistical collision model for Monte Carlo simulation of polyatomic gas mixture. J Comput Phys 18(4):405–420
4. Boyd ID, Schwartzentruber TE (2017) Nonequilibrium gas dynamics and molecular simulation, vol 42. Cambridge University Press
5. Casseau V, Palharini RC, Scanlon TJ, Brown RE (2016) A two-temperature open-source CFD model for hypersonic reacting flows, part one: zero-dimensional analysis. Aerospace 3(4):34
6. Mankodi TK, Bhandarkar UV, Myong R (2020) Collision cross sections and nonequilibrium viscosity coefficients of N_2 and O_2 based on molecular dynamics. Phys Fluids 32(3)
7. Mankodi TK, Bhandarkar UV, Puranik BP (2017) An ab initio chemical reaction model for the direct simulation Monte Carlo study of non-equilibrium nitrogen flows. J Chem Phys 147(8):084305
8. Mankodi TK, Bhandarkar UV, Puranik BP (2018) Dissociation cross-sections for high energy O_2–O_2 collisions. J Chem Phys 148(14)

9. Nidharia M, Mane S, Mankodi TK (2024) Ab initio-based two-temperature transport property model for hypersonic non-equilibrium flows. Phys Fluids 36(12)
10. Paukku Y, Yang KR, Varga Z, Truhlar DG (2013) Global ab initio ground-state potential energy surface of N_4. J Chem Phys 139(4)
11. Truhlar DG, Muckerman JT (1979) Reactive scattering cross sections iii: quasiclassical and semiclassical methods. In: Atom-molecule collision theory. Springer, Heidelberg, pp 505–566
12. Valentini P, Zhang C, Schwartzentruber TE (2012) Molecular dynamics simulation of rotational relaxation in nitrogen: implications for rotational collision number models. Phys Fluids 24(10)

Open Access This chapter is licensed under the terms of the Creative Commons Attribution 4.0 International License (http://creativecommons.org/licenses/by/4.0/), which permits use, sharing, adaptation, distribution and reproduction in any medium or format, as long as you give appropriate credit to the original author(s) and the source, provide a link to the Creative Commons license and indicate if changes were made.

The images or other third party material in this chapter are included in the chapter's Creative Commons license, unless indicated otherwise in a credit line to the material. If material is not included in the chapter's Creative Commons license and your intended use is not permitted by statutory regulation or exceeds the permitted use, you will need to obtain permission directly from the copyright holder.

Impact of Electronic State-Specific Modeling on High-Enthalpy Nitrogen Flows

Yuzhe Zhang, Qizhen Hong, Xiaoyong Wang, Chao Yang, and Quanhua Sun

Abstract An electronic state-to-state (StS) approach is developed to numerically simulate the nonequilibrium radiative metric measured in experiments conducted at the Electric Arc Shock Tube (EAST) facility. The present StS model solves for the electronic states of strong radiators by integrating a collisional-radiative model into the master equations, while considering both rotational nonequilibrium and vibrational nonequilibrium under a multi-temperature assumption. The StS results for radiation behind the shock waves are compared with predictions from the four-temperature quasi-steady-state (4T-QSS) model. It is found that the StS model accurately predicts the spectrally-integrated radiance in the Vis/NIR range for experimental shot 40, but it overestimates both the peak and post-peak values in the UV range for shot 37. Moreover, both the StS and 4T-QSS models exhibit discrepancies when compared to the experimental nonequilibrium radiative metrics for both shots. The analysis of electronic state populations of N_2 reveals a post-shock region where the QSS assumption breaks down, and the populations deviate notably from the Boltzmann distribution until reaching equilibrium.

Keywords High-enthalpy flows · State-to-state modeling · Quasi-steady-state · Nonequilibrium radiation

Y. Zhang · Q. Hong (✉) · X. Wang · Q. Sun
State Key Laboratory of High Temperature Gas Dynamics, Institute of Mechanics, Chinese Academy of Science, Beijing, China
e-mail: hongqizhen@imech.ac.cn

Q. Sun
e-mail: qsun@imech.ac.cn

Y. Zhang · Q. Sun
School of Engineering Science, University of Chinese Academy of Sciences, Beijing, China

C. Yang
Wide Range Flight Engineering Science and Application Center, Institute of Mechanics, Chinese Academy of Science, Beijing, China

© The Author(s) 2026

M. Grabe et al. (eds.), *Rarefied Gas Dynamics*, Springer Aerospace Technology,
https://doi.org/10.1007/978-3-032-00094-1_58

1 Introduction

In hypersonic flows, intense shock waves convert kinetic energy into thermal energy, resulting in very high gas temperatures within the shock layer. This gas environment is characterized by significant thermochemical nonequilibrium phenomena occurring simultaneously [13], including internal energy excitation promoting the population of elevated internal energy levels and chemical reactions (e.g., dissociation and ionization) leading to the emergence of atoms and free electrons. To numerically simulate the physicochemical processes described above, the multi-temperature model, particularly the two-temperature (2T: translational-rotational and vibrational-electron-electronic temperatures) model, has been widely employed to calculate high-enthalpy flowfields. Additionally, a quasi-steady-state (QSS) approximation is commonly used to estimate the populations of molecular excited states, which are crucial for accurately predicting spectral features and radiative intensity [11]. In our previous work [18], we conducted a comprehensive assessment of the performance of both the 2T and four-temperature (4T: translational, rotational, vibrational, and electron-electronic temperatures) models for high-enthalpy shock-heated nitrogen flows, using various modeling parameters. It was found that the 4T model provides better accuracy in predicting experimental temperatures compared to the 2T model. Despite this advantage, discrepancies persisted between the calculations and experimental nonequilibrium radiative metrics when using the 4T-QSS model, even after incorporating various modeling options. This situation motivates the present study to explore the impact of more detailed modeling on the prediction of high-temperature radiation.

As pointed out by several studies [6, 8–10], the QSS assumption lacks sufficient accuracy due to the decoupling of molecular excited state population calculations from the flowfield solution process. The QSS assumption approximates the net population rate of molecular states as zero, which becomes invalid under conditions of significant thermochemical nonequilibrium. To address this limitation, the theoretically more accurate state-to-state (StS) model has been used instead to directly track the population of internal energy states by solving the master equations [1, 7, 9, 10]. Notably, the vibrational StS model, incorporating first-principle-calculated vibrational StS kinetics, has been shown to accurately predict post-shock vibrational temperatures in undiluted oxygen [17], and the vibrational-electronic StS model has proven effective in accurately predicting radiative intensities across both infrared and ultraviolet spectral ranges in shock-heated CO flows [2]. Therefore, this study aims to evaluate the impact of electronic state-specific modeling on predicting high-temperature nitrogen radiation and to quantify the discrepancies introduced by the QSS assumption. The organization of this paper is as follows: Sect. 2 describes the thermochemistry models. In Sect. 3, post-shock simulations are performed using the present electronic StS model, with the calculated radiative properties compared to experimental data [3] and the 4T-QSS results. To further evaluate the impact of electronic state-specific modeling, the electronic state populations of N_2 calculated from both the StS model and the QSS assumption are compared. Conclusions are drawn in the last section.

Table 1 Rate parameters for the electron impact excitation of atomic N

i	Reaction	A (cm^3/mol/s)	n	E (K)	T_c	Ref.
1	$N(^4S^o) + e^- \leftrightarrow N(^2D^o) + e^-$	1.05E+15	0.20	27669	T_{ee}	[13]
2	$N(^4S^o) + e^- \leftrightarrow N(^2P^o) + e^-$	3.05E+14	0.21	41500	T_{ee}	[13]
3	$N(^2D^o) + e^- \leftrightarrow N(^2P^o) + e^-$	2.70E+14	0.27	13831	T_{ee}	[13]

The rate coefficient is expressed in the generalized Arrhenius form, $k_f(T_c) = AT_c^n \exp(-E/T_c)$, where T_c represents the controlling temperature

2 Thermochemistry Modeling

To simulate the high-enthalpy nitrogen shock-heated flows, we solve the one-dimensional Euler equations using the electronic StS (collisional-radiative, CR) model in the Poshax3 code [16]. In the electronic StS model, five species of N_2, N_2^+, N, N^+, and e^- are considered, and the relevant electronic states of strong radiators are treated as distinct pseudo-species in master equations, i.e., $N_2(X^1\Sigma_g^+, A^3\Sigma_u^+, B^3\Pi_g, C^3\Pi_u)$, $N_2^+(X^2\Sigma_g^+, A^2\Pi_u, B^2\Sigma_u^+, C^2\Sigma_u^+)$, and $N(^4S^o, {}^2D^o, {}^2P^o)$. The other electronic states of N_2, N_2^+, and N are assumed to follow the Maxwell-Boltzmann distribution referencing the nearest lower pseudo-species under the electronâĽ“electronic temperature T_{ee}, e.g., the number density of $N_2(b'^1\Sigma_u^+)$ (the upper state of the Birge-Hopfield 2 band) is derived from the population of $N_2(C^3\Pi_u)$. In contrast, for N^+ and e^-, only the ground electronic state is considered due to their negligible contribution to radiation. Overall, the StS model incorporates 13 electronic states from different species and accounts for 57 state-specific reactions in the master equations. The rate coefficients for these reactions are inherited from the CR model presented in our previous work [18], except that we now incorporate three additional electron impact excitation reactions for atomic N (Table 1) to predict the non-Boltzmann populations of excited N species. Heavy-particle impact excitations of N are neglected, as their rate coefficients are much smaller than those of electron-atom collisions [13], and predissociation of $N_2(C^3\Pi_u)$ is also excluded due to significant uncertainties in the rate coefficients at high temperatures (above 10,000 K). Moreover, rotational and vibrational nonequilibrium are accounted for by employing the relaxation times proposed by Park [14] and Kim and Jo [12] in the present work, respectively. The modified Marrone-Treanor (MMT) model [4], which accounts for non-Boltzmann distribution effects on dissociation rates and vibrational energy removal, is employed to address the vibration-dissociation coupling. As demonstrated in our previous work [18], the MMT model provides more accurate predictions than the Park and Marrone-Treanor models for both experimental temperatures and nonequilibrium radiative metrics.

Additionally, we conduct 4T-QSS simulations for comparison. Details of the 4T-QSS model can be found in Ref. [18], except that the CR model used in the QSS analysis is now the same as that of the present StS model.

Table 2 EAST shot conditions (shock-tube diameter 10.16 cm) and investigated spectral ranges

Shot No.	Velocity (km/s)	Pressure (Torr)	Range (nm)	Major features
37	7.15	0.2	UV 200–360	$N_2(2^+)$, $N_2^+(1^-)$
40	6.88	0.2	Vis/NIR 480–900	$N_2(1^+)$

3 Results

The aforementioned electronic state-specific modeling is applied to nitrogen shock-heated flows corresponding to two different shots (see Table 2) in EAST experiments (campaign 62). The nonequilibrium radiative metric, defined as the average radiance within ± 2 cm of the peak [3], is calculated based on the StS and 4T-QSS results, respectively. Radiative spectrum calculations are conducted with the open-source code Photaura [16], and further details, along with modifications to the code, can be found in Ref. [18]. Figure 1 shows the nonequilibrium radiative metric in the UV and Vis/NIR ranges for shots 37 and 40, respectively. In both shots, deviations between the predictions and measurements are observed for the detailed spectrum. Specifically, in the UV spectrum for shot 37, the present StS model shows a slightly better agreement with the experimental peaks of the 2nd Positive band of N_2 compared to the 4T-QSS model. However, significant discrepancies exist concerning the 1st Negative band of N_2^+ (peak at about 330.8 and 358.2 nm), which suggests that the population of $N_2^+(B^2\Sigma_u^+)$ (upper state of this band) is significantly underestimated. Additionally, the large discrepancies observed around 350 nm might also be due to CN contamination present in the experiment [5]. In the Vis/NIR spectrum for shot 40, both models underestimate the radiative intensity of the 1st Positive band of N_2, primarily due to an underestimation of the $N_2(B^3\Pi)$ (upper state of this band), while overestimating the intensity contributed by atomic N (with several Ritz wavelengths marked in the plot). A similar underestimation of the 1st Positive band of N_2 was recently observed using the vibronic state-specific model proposed by Pereira et al. [15], whereas their predictions were an order of magnitude further lower than the present StS results.

Although varying degrees of discrepancies persist in the detailed spectra, the present StS model performs better in predicting the spectrally-integrated radiance versus position. Spatial radiance is the integral of spectral intensity over considered wavelengths, representing the total radiation from both discrete and continuous emissions by atomic or molecular radiators. Note that the computed values have been spatially adjusted to ensure that the point where the radiance begins to rise abruptly aligns with the measured values [15], since the exact position of the shock wave cannot be directly determined from the spectra obtained in the EAST experiments. As shown in Fig. 2, the StS results agree well with experimental data in the Vis/NIR range for shot 40, although it still overestimates both the peak and post-peak values in the UV range for shot 37. In contrast, the 4T-QSS model performs slightly better in shot 37, while it underestimates the peak values in shot 40. The spatial radiance

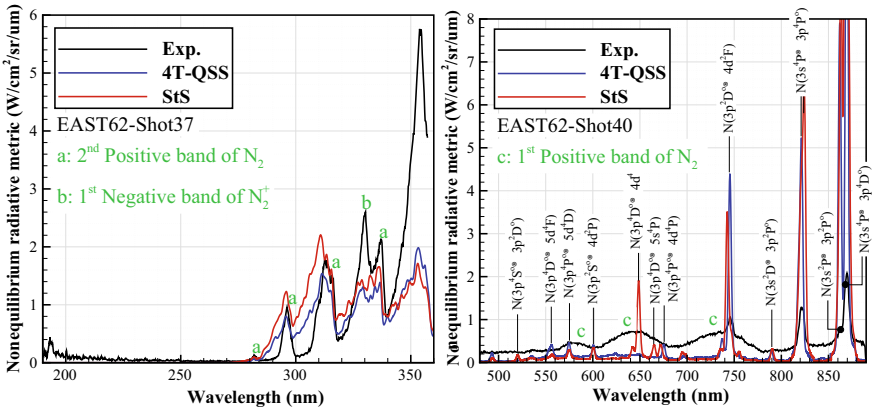

(a) EAST62-shot 37 (b) EAST62-shot 40

Fig. 1 Comparison of the nonequilibrium radiative metrics between the StS and 4T-QSS result for shots 37 and 40, respectively

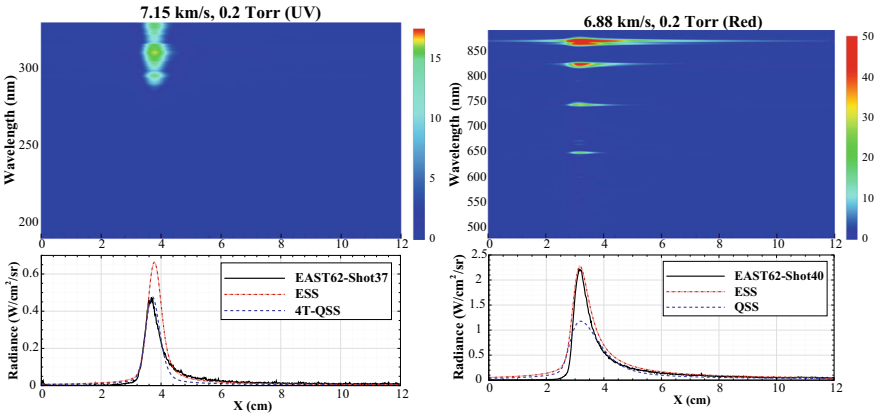

(a) EAST62-shot 37 (b) EAST62-shot 40

Fig. 2 The StS 3D spectral intensity maps (radiance versus position and wavelength) and spectrally-integrated radiance versus position for the UV range (over 199.05–329.99 nm) for shot 37 and the Vis/NIR range (over 480.04–889.86 nm) for shot 40

clearly illustrates the nonequilibrium overshoot behind the shock wave and the subsequent relaxation toward equilibrium, as also seen in the calculated 3D spectral intensity maps. The persistent discrepancies between the StS calculations and experimental data in both the nonequilibrium radiative metric and spatial radiance indicate that the currently adopted StS kinetics may lack sufficient detail and accuracy for the investigated temperature ranges (additionally, as noted by Pereira et al. [15], the shock tube-related phenomena, such as the absorption of radiation emitted by the driver gas, may also contribute to these discrepancies). While state-of-the-art values

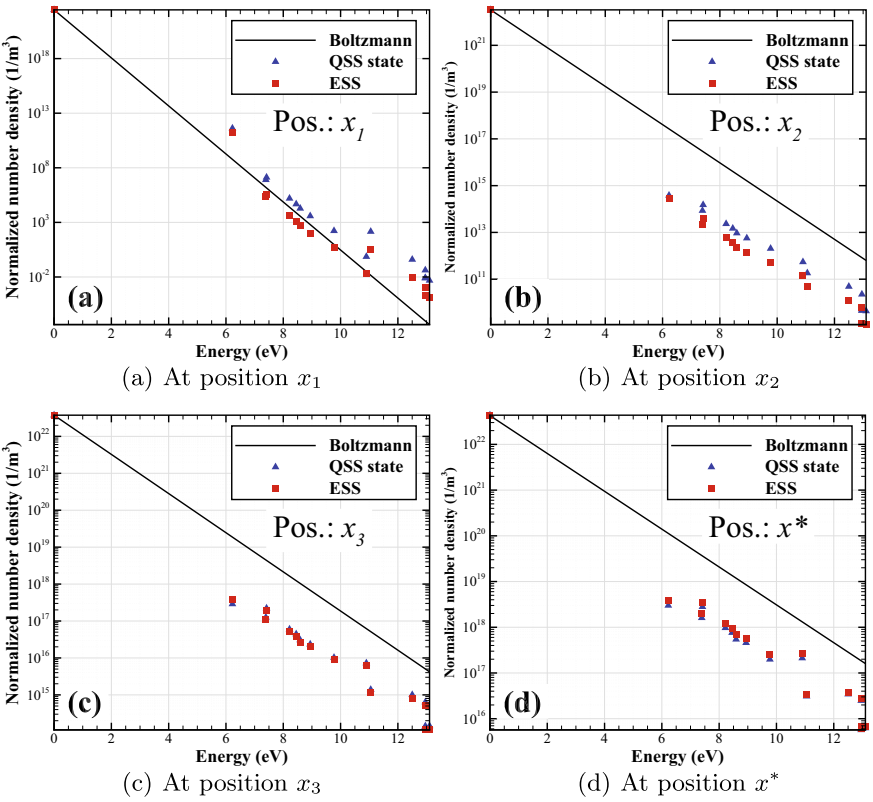

Fig. 3 Comparison of the normalized population distribution (the ratio of number density to degeneracy) of the electronic states of N_2 at different positions (see text) for shot 37, where x^* represents the position of the peak T_{ee}

are used herein for the StS rate coefficients available in the literature, many relevant rate coefficients remain unavailable and exhibit (significant) uncertainties. Therefore, uncertainty quantification of the StS rate coefficients is ongoing, with the aim of improving specifically the accuracy of the most relevant rate coefficients through *ab initio* calculations.

To further investigate the impact of electronic state-specific modeling, we quantify the discrepancies introduced by the QSS assumption. While widely used to estimate internal state populations quickly, the QSS assumption approximates the net population rates of excited states as being much smaller than both the sum of incoming rates and the sum of outgoing rates [13], which may become invalid under significant thermochemical nonequilibrium conditions. For a fair comparison, the QSS populations (unrelated to the aforementioned 4T-QSS results) are derived from macroscopic quantities obtained from the StS results and compared to the StS populations. Figure 3 shows the populations of N_2 at various post-shock locations, including x_i ($i = 1, 2, 3,$

representing three spatial positions at equal intervals between the shock front and x^*) and x^* (the position of the peak T_{ee}). For reference, the Boltzmann distributions at the local T_{ee} are also presented. At position x_1, near the shock front where internal energy states remain largely unexcited, the QSS populations of all excited electronic states are systematically higher than the StS populations. This discrepancy arises because electronic energy excitation processes dominate in this region, causing the sum of incoming rates to become the dominant term in the net population rate, thereby leading to the breakdown of the QSS assumption. The dominance of electronic energy excitation also reflects on the overpopulation effect for both QSS and StS populations when compared to the Boltzmann distribution, especially for states above $N_2(C^3\Pi_u)$ (around 11.05 eV). As the flow moves downstream to position x_2, the difference between QSS and StS populations persists but with a slight reduction, and both models predict excited state populations lower than the Boltzmann distribution. This underpopulation effect is attributed to the significant dissociation and ionization of electronic excited states at position x_2, where elevated controlling temperatures enhance these processes, thereby accelerating reaction rates and significantly depleting the excited states (more energetically favorable for reaction) of N_2. As the vibrational and electron-electronic temperatures (thus the controlling temperatures for reactions) increase while the flow approaches position x^*, the incoming rates of excited states by energy excitation and the outgoing rates by dissociation and ionization become more balanced. This dynamic interplay facilitates the establishment of QSS conditions, as illustrated by the population distributions observed at positions x_3 (panel c) and x^* (panel d), while both QSS and StS populations remain lower than the Boltzmann distribution.

4 Conclusion

This paper presented an electronic StS approach, with incorporating both rotational and vibrational nonequilibrium, for simulating nitrogen shock-heated flows and radiation. It was found that the StS model accurately predicts the spatial radiance in the Vis/NIR range for EAST shot 40 while it overestimates both the peak and post-peak values in the UV range for shot 37. Additionally, the StS model showed slightly better agreement with the experimental radiative peaks (in nonequilibrium radiative metric) of the 2nd Positive band of N_2 compared to the 4T-QSS model for shot 37. In the Vis/NIR spectrum for shot 40, both models underestimated the radiative intensity of the 1st Positive band of N_2 while overestimating the intensity contributed by atomic N. The persisted discrepancies between the electronic state-specific modeling and experimental data indicate the need for a comprehensive uncertainty analysis of the StS kinetic mechanisms in future work. Furthermore, based on the StS results, the populations of N_2 were obtained using the QSS assumption and compared with those derived directly from the StS results. The comparison revealed that differences between the StS and QSS models mainly occur in the region behind the shock front, where electronic energy excitation processes dominate, causing the sum of incom-

ing rates to become the dominant term in the net population rate and leading to the breakdown of the QSS assumption. However, as the flow approaches and moves beyond the peak T_{ee} position, the QSS assumption generally holds as the incoming and outgoing rates of electronic excited states become more balanced.

Acknowledgements This study was supported by the Strategic Priority Research Program of the Chinese Academy of Sciences (grant number XDB0620201).

References

1. Aiken TT, Boyd ID (2024) Collisional-radiative modeling of shock-heated nitrogen mixtures. J Appl Phys 135(9)
2. Aliat A, Chikhaoui A, Kustova E (2003) Nonequilibrium kinetics of a radiative co flow behind a shock wave. Phys Rev E 68(5):056306
3. Brandis AM, Cruden BA (2018) Shock tube radiation measurements in nitrogen. In: 2018 joint thermophysics and heat transfer conference, p 3437
4. Chaudhry RS, Boyd ID, Candler GV (2020) Vehicle-scale simulations of hypersonic flows using the MMT chemical kinetics model. In: AIAA aviation 2020 forum, p 3272
5. Glenn AB, Varley O, Collen P, McGilvray M (2024) Radiation measurements of shockwaves in synthetic air and pure nitrogen. In: AIAA SCITECH 2024 forum, p 0226
6. Hao J, Wang J, Lee C (2017) State-specific simulation of oxygen vibrational excitation and dissociation behind a normal shock. Chem Phys Lett 681:69–74
7. Hong Q, Wang X, Hu Y, Lin X, Sun Q (2020) Rebuilding experimental nonequilibrium radiation in shock-heated Martian-like mixture flows using electronic state-to-state approach. Int J Modern Phys B 34(14n16):2040084
8. Istomin V, Kustova E, Prutko K (2024) Different approaches for simulating heat and radiative fluxes in planetary entry problems. In: AIP conference proceedings, vol 2996. AIP Publishing
9. Jo SM, Munafò A, Panesi M (2024) Self-consistent flow-radiation coupling for hypersonic atmospheric entry. In: AIAA SCITECH 2024 forum, p 1686
10. Johnston CO, Panesi M (2018) Impact of state-specific flowfield modeling on atomic nitrogen radiation. Phys Rev Fluids 3(1):013402
11. Johnston CO (2006) Nonequilibrium shock-layer radiative heating for Earth and Titan entry. Ph.D. thesis, Virginia Polytechnic Institute and State University
12. Kim JG, Jo SM (2021) Modification of chemical-kinetic parameters for 11-air species in re-entry flows. Int J Heat Mass Transfer 169:120950
13. Park C (1989) Nonequilibrium hypersonic aerothermodynamics. Wiley, New York
14. Park C (2004) Rotational relaxation of N_2 behind a strong shock wave. J Thermophysics Heat Transfer 18(4):527–533
15. Pereira É, Loureiro J, da Silva ML (2023) Vibronic state-specific modelling of high-speed nitrogen shocked flows. Part ii: shock tube simulations. arXiv preprint arXiv:2308.05164
16. Potter D (2011) Modelling of radiating shock layers for atmospheric entry at Earth and Mars. Ph.D. thesis, School of Mechanical and Mining Engineering, The University of Queensland
17. Wang X, Hong Q, Yang C, Sun Q (2023) Uncertainty quantification in state-specific modeling of thermal relaxation and dissociation of oxygen. AIAA J 61(6):2734–2738
18. Zhang Y, Hong Q, Wang X, Yang C, Sun Q (2024) Assessment of thermochemical models on nonequilibrium flowfield and radiation in shock-heated nitrogen. Comput Fluids 289:106533

Open Access This chapter is licensed under the terms of the Creative Commons Attribution 4.0 International License (http://creativecommons.org/licenses/by/4.0/), which permits use, sharing, adaptation, distribution and reproduction in any medium or format, as long as you give appropriate credit to the original author(s) and the source, provide a link to the Creative Commons license and indicate if changes were made.

The images or other third party material in this chapter are included in the chapter's Creative Commons license, unless indicated otherwise in a credit line to the material. If material is not included in the chapter's Creative Commons license and your intended use is not permitted by statutory regulation or exceeds the permitted use, you will need to obtain permission directly from the copyright holder.

Exploitation of Continuum and Kinetic Theory Approaches for the Simulation of Particle Beam Experiments

Surya Kiran Peravali, Amit K. Samanta, Muhamed Amin, Philipp Neumann, Jochen Küpper, and Michael Breuer

Abstract X-ray free-electron lasers (XFELs) promise to allow for atomically resolved imaging of isolated nanoparticles through single-particle diffractive imaging (SPI) [1]. Achieving this requires nanoparticle beams with controlled dimensions, typically generated using aerosol injectors operating under varying gas-flow conditions. Numerical simulations play a vital role in understanding and optimizing these injection systems. We present a multi-scale simulation framework that models gas dynamics across continuum-, transition-, and free-molecular-flow regimes as well as particle translation. Leveraging computational fluid dynamics (CFD), direct simulation Monte Carlo (DSMC), and corresponding hybrid methods, the framework provides a foundation for improving aerosol-injection techniques. It was validated against experiments over wide temperature (4–300 K) and size (10–300 nm) ranges.

Keywords DSMC · Nanoparticle injection · Continuum assumption · Transition regime · Rarefied flow · single-particle imaging · Particle injection

S. K. Peravali · M. Breuer
Professur für Strömungsmechanik, Helmut-Schmidt-Universität/Universität der Bundeswehr Hamburg, Hamburg, Germany

S. K. Peravali (✉) · A. K. Samanta · J. Küpper
Center for Free-Electron Laser Science CFEL, Deutsches Elektronen-Synchrotron DESY, Hamburg, Germany
e-mail: peravals@hsu-hh.de

A. K. Samanta · J. Küpper
Center of Ultrafast Imaging, Universität Hamburg, Hamburg, Germany

J. Küpper
Department of Physics, Universität Hamburg, Hamburg, Germany

M. Amin
Laboratory of Computational Biology, National Heart, Lung and Blood Institute, National Institutes of Health, Bethesda, MD, USA

P. Neumann
Department of Informatics, High Performance Computing & Data Science, Universität Hamburg, Hamburg, Germany

Deutsches Elektronen-Synchrotron DESY, Hamburg, Germany

© The Author(s) 2026

M. Grabe et al. (eds.), *Rarefied Gas Dynamics*, Springer Aerospace Technology,
https://doi.org/10.1007/978-3-032-00094-1_59

1 Introduction

X-ray free-electron lasers (XFELs) have revolutionized structural biology and material sciences by enabling high-resolution imaging of nanoscale objects and their ultrafast dynamics. The technique of single-particle diffractive imaging (SPI) leverages intense, femtosecond XFEL pulses to capture atomically resolved structures of isolated nanoparticles without requiring large, highly ordered crystals [1, 2]. This opens new avenues for studying the structure and dynamics of complex systems, including biomolecules, viruses, and nanomaterials.

A critical requirement for successful SPI experiments is the ability to deliver well-focused nanoparticle beams with controlled dimensions and minimal divergence. To achieve this objective, aerodynamic lens stacks (ALS) [3–5] and cryogenically cooled buffer-gas cells (BGC) [6] are employed as particle injection systems. These injectors utilize gas dynamics to guide particles from an ambient-pressure environment into the high-vacuum chamber. However, optimizing these processes to produce particle beams with the desired properties remains a significant challenge.

Numerical simulations play an indispensable role in addressing this bottleneck, providing insights into the complex interplay of gas dynamics and particle behavior across various flow regimes. From continuum to free-molecular flows, simulations allow researchers to predict particle trajectories and evaluate injector performance under a wide range of operating conditions. Recent advancements in computational modeling techniques, such as computational fluid dynamics (CFD), the direct simulation Monte Carlo (DSMC) method, and hybrid CFD-DSMC approaches, have significantly enhanced our ability to simulate gas-particle interactions with high accuracy.

In this study, we present a multi-scale numerical framework designed to model the transport of nanoparticles in gas flows under diverse experimental conditions. This framework integrates CFD, DSMC, and hybrid methodologies to capture the carrier gas dynamics and particle migration over a broad spectrum of temperatures (4–300 K) and particle sizes (10–300 nm). By incorporating various force models influencing particle trajectories, the framework provides a comprehensive tool for simulating and optimizing nanoparticle injection systems.

The proposed methodologies were validated against experimental data, demonstrating their applicability and reliability for SPI experiments. Additionally, we discuss benchmark results and highlight potential areas for future improvements, including refinements in drag force models and coupling techniques. This work aims to bridge the gap between simulation and experiment, offering a pathway toward more efficient and precise nanoparticle injection systems for XFEL applications.

2 Methodology

This study investigates the gas-particle dynamics in different aerosol injectors using a two-step approach. First, the steady-state flow field is computed, followed by particle trajectory calculations based on interpolated flow quantities and the corresponding forces on the particles. A decoupled approach is adopted as the particle volume fraction is low, ensuring a negligible effect of the particles on the gas flow.

For continuum and slip regimes ($Kn < 0.1$), the flow field is predicted using `rhoCentralFoam`, a compressible CFD-solver in OpenFOAM [7]. For rarefied regimes ($Kn > 0.1$), the DSMC method implemented in SPARTA [8] is employed to capture molecular-scale effects. To address flows in the transition regime between these two cases, a one-way coupled hybrid CFD-DSMC approach is utilized. The coupling is based on a continuum-breakdown criterion, defined as the maximum of the global Knudsen number and Boyd's gradient-based local Knudsen numbers—calculated from density, temperature, and velocity fields – enabling efficient domain decomposition and accurate multiscale resolution of the flow field [9, 10]. In the DSMC domain, molecular collisions are modeled using the Variable Hard Sphere (VHS) model, while internal energy exchange is handled via the Larsen–Borgnakke (LB) model with constant relaxation. For nitrogen, a rotational relaxation number of 0.2 is used, whereas for helium it is set to zero, consistent with its monoatomic nature. Vibrational and chemical reaction modes are assumed to be frozen in the present study. The numerical parameters for the VHS and LB models are taken from standard literature sources [11].

Particle transport is modeled using the Langevin equation, incorporating drag ($\mathbf{F}_{\text{drag}}$) and Brownian motion forces ($\mathbf{F}_b$) [12]. The governing equation reads

$$\frac{d}{dt}\left(m_p\,\mathbf{u}_p\right) = \mathbf{F}_{\text{drag}} + \mathbf{F}_b\ , \tag{1}$$

with the mass of the particle m_p, the particle velocity vector $\mathbf{u}_p$, and the time t. Drag models incorporate Stokes-Cunningham corrections for slip-flow regimes [13] and molecular drag models for rarefied conditions [14, 15], with parameters optimized for accuracy across varying flow conditions. The Brownian motion is modeled using a Gaussian white-noise approach [12, 16]. A detailed assessment of the applicability and accuracy of these drag models across different Knudsen and Mach number regimes, including corrections for high rarefaction, has been provided in an earlier work [10], where their influence on particle dynamics in hybrid simulations was systematically evaluated.

This integrated multi-scale simulation methodology, combining hybrid CFD-DSMC gas flow predictions—was previously validated for gas-only nozzle flows [9] and for full gas-particle simulations in ALS-relevant configurations [10], demonstrating both accuracy and computational efficiency. The complete hybrid framework, including the coupling strategy and selection criteria for numerical parameters such

as CFD discretization schemes, DSMC cell size, number of particles per cell, and sampling strategies, is detailed in these studies [9, 10].

3 Results and Discussion

The behavior of nanoparticle beams was analyzed for three distinct cases: (1) an aerodynamic lens system (ALS), (2) a buffer-gas cell (BGC), and (3) the combined BGC-ALS system. Simulation results were compared to experimental data to evaluate beam widths and focal positions for each case. This comparison highlights the influence of aerodynamic focusing and gas-particle collisions on beam shaping and focusing efficiency and it validates the accuracy of the numerical framework developed in this work.

3.1 Case I: Aerodynamic-Lens-Stack Injector at Room Temperature

The aerodynamic lens stack (ALS) is composed of a series of orifices that focus particle beams by accelerating and concentrating them into a narrow stream. Particles are transferred into the gas phase, collimated, and subsequently extracted into a vacuum. The ALS design used in this study follows the configuration previously described in Worbs [5].

Figure 1 illustrates the flow field for nitrogen at room temperature, and corresponding particle trajectories for 69 nm-diameter polystyrene particles at an inlet pressure of $p_{in} = 50$ Pa. The hybrid-CFD-DSMC method predicted the flow field, represented by the axial velocity (v_z) along the main flow direction, while particle trajectories were computed using the Stokes-Cunningham drag model combined with Brownian forces. At the ALS exit ($z = 0$), the gas expands at supersonic speeds into the vacuum chamber ($z > 0$). The simulated particle trajectories converge to a minimum beam width within the vacuum chamber.

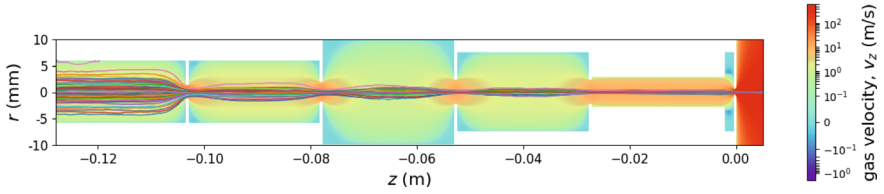

Fig. 1 Simulated trajectories of 69 nm-diameter polystyrene particles (colored lines) passing through the ALS. The axial velocity of the gas-flow field at $p_{in} = 50$ Pa is illustrated on a logarithmic colorscale

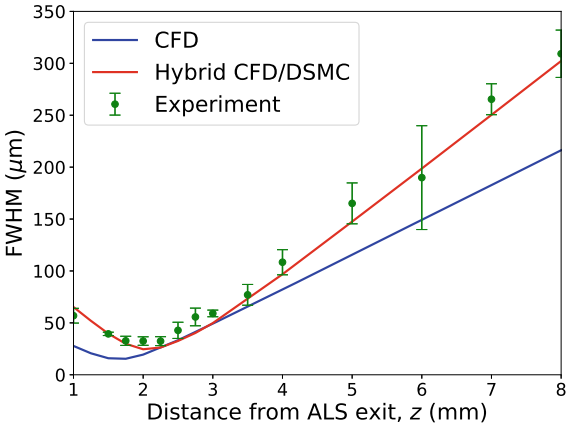

Fig. 2 Simulated evolution of the particle beam size (FWHM) for 69 nm-diameter polystyrene spheres at an inlet pressure of $p_{in} = 50$ Pa, compared to experimental data [17]

Beam widths were measured at positions starting from $z = 1$ mm, where the particle beam exhibits a Gaussian-like distribution [17]. The beam width, defined by the full-width at half-maximum (FWHM[1]), was compared with experimental data in Fig. 2. The hybrid CFD/DSMC simulations accurately capture the focusing-defocusing behavior and focus position, showing excellent agreement with experimental results, and they perform better than pure CFD simulations.

3.2 *Case II: Cryogenic Buffer-Gas Cell*

The cryogenic buffer-gas cell (BGC) was designed to rapidly cool nanoparticles, such as biomolecules and proteins, below their glass-temperature at ~133 K within nano- or microseconds [6]. This shockfreezing process is sufficiently fast to preserve the biomolecules structural integrity. The cooled particles are extracted into a collimated particle stream under high-vacuum conditions. In this injector, cold helium gas, down to 4 K, serves as the carrier gas.

Figure 3a illustrates the helium flow field within the cryogenic buffer-gas cell (BGC)—simulated using the hybrid CFD-DSMC methodology for a helium inlet flow rate of 25 ml_n/min. The flow is visualized by streamlines, colored according to the Mach-number magnitude. Helium entered the BGC through the inlet located at the top of the thin inlet disk on the left side of the main cell. Particles of 220 nm diameter were injected through a capillary transport tube [6], passed through the BGC starting from outlet 1, and were eventually extracted through outlet 2. Molecular-drag-force models [14, 15] were applied to predict the particle behavior under these conditions.

[1] Difference between two points on the curve where the value is half of the max. value.

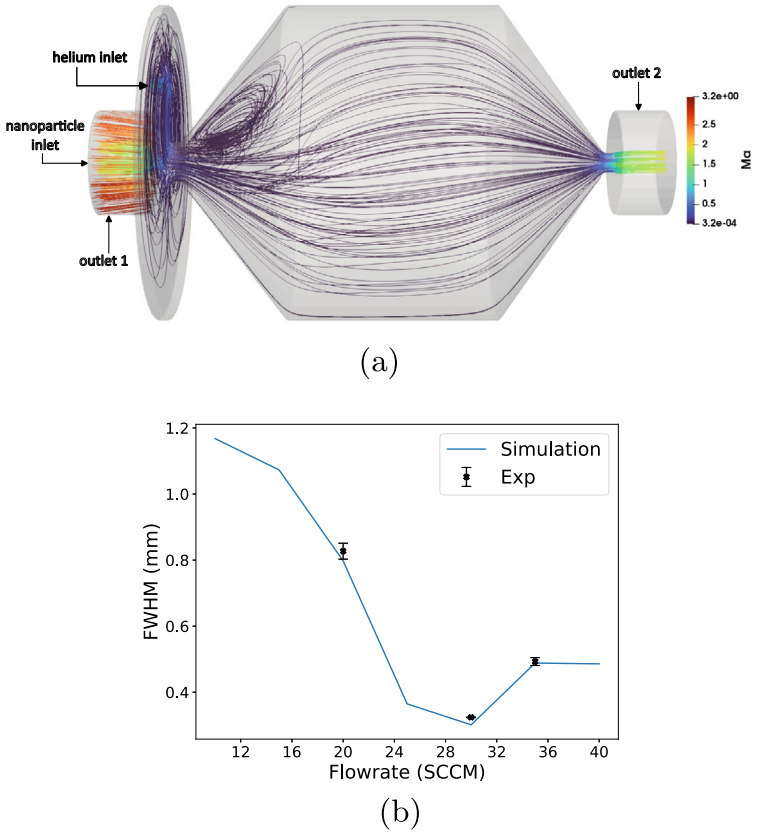

Fig. 3 **a** Streamlines of the flow field inside the cryogenic buffer-gas cell, colored by the Mach-number magnitude, as simulated using the hybrid DSMC/CFD method. **b** Predicted particle beam widths (blue spheres) for 220 nm-diameter polystyrene spheres as a function of the helium flow rate, compared to experimental data (black x-cross and error bars) [6]

Figure 3b shows the particle beam widths (FWHM) of 220 nm polystyrene particles measured 10 mm downstream of outlet 2 as a function of the helium flow rate, capturing the effects of varying pressures and velocities. The simulation results align well with experimental data [6], accurately reproducing the observed trends.

3.3 Case III: Aerodynamic Lens with Cryogenic Cooling

Delivering smaller particles with diameters less than 20 nm, e.g., proteins, still poses a challenge due to their low inertia and high diffusivity. These particles tend to

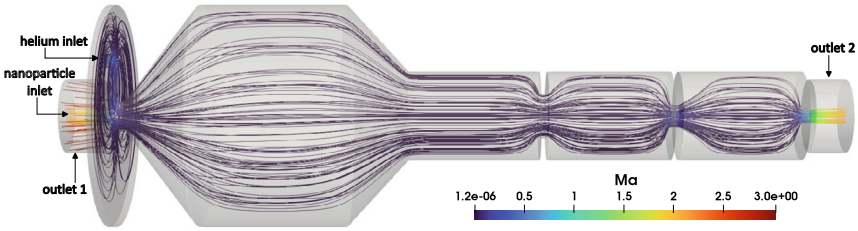

Fig. 4 Streamlines of the flow field through the combined setup of BGC and ALS, colored by the Mach-number magnitude, as simulated using the hybrid DSMC/CFD method

closely follow the gas streamlines, resulting in only limited focusing. Furthermore, their motion is strongly influenced by Brownian dynamics, leading to substantial diffusivity. This behavior not only widens the particle beam, but also causes significant particle losses, making it even more difficult to produce well-collimated particle streams for SPI experiments. One effective strategy to address these challenges involves reducing the carrier-gas temperature, which enhances the injection of small particles [17]. Further experimental progress was demonstrated for the focusing of particles smaller than 100 nm by combining an ALS with the BGC.

Figure 4 depicts the helium flow field within the BGC-ALS system, simulated using the hybrid CFD-DSMC methodology at a helium inlet flow rate of 15 ml_n/min. The flow field is represented by streamlines, with colors indicating the Mach-number magnitude. Helium enters the system through the inlet on the upper side of the thin inlet disk at the left of the main cell. Particles of 88 nm diameter were introduced through outlet 1 via a capillary transport tube [17], traversed the BGC-ALS system, and were subsequently extracted through outlet 2. Particle trajectories were computed using molecular-drag-force models [14, 15], ensuring accurate predictions of particle dynamics under these conditions.

Figure 5 presents the evolution of particle beam widths (FWHM) at various distances downstream of the BGC-ALS exit (final lens) for helium flow rates of 10 ml_n/min and 15 ml_n/min. The beam widths are compared with experimental measurements taken 6, 8, and 10 mm downstream the exit [17]. The simulation results show very good agreement with the experimental data, accurately capturing the particle beam focusing behavior.

4 Conclusions

The behavior of nanoparticle beams in the multi-scale regime was investigated for three configurations: An aerodynamic-lens-stack system (ALS), a buffer-gas cell (BGC), and the combined buffer-gas cell and the aerodynamic-lens-stack system (BGC-ALS). The simulation results for beam widths and focus positions were com-

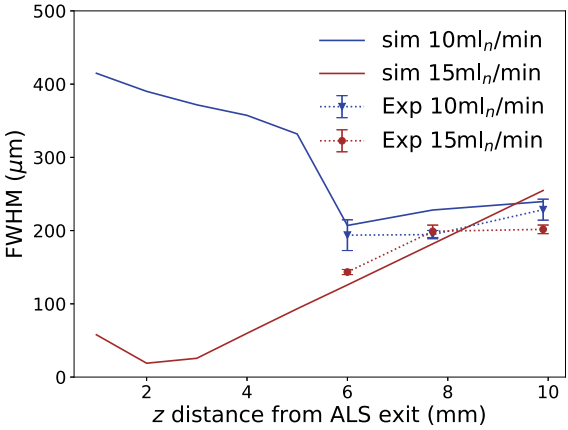

Fig. 5 Simulated evolution of the particle beam size (FWHM) for 88 nm-diameter polystyrene spheres at different flow rates of helium, compared to experimental data [17]

pared with experimental data, showing good agreement and thus validating the accuracy of the developed numerical framework.

The results highlight the strengths and limitations of each configuration. The ALS effectively focuses nanoparticle beams at low pressures, while the BGC enables controlled cooling and collimation of the particles. The BGC-ALS combination demonstrates superior performance by leveraging the strengths of both systems, achieving enhanced beam quality and improved focus.

The numerical framework developed in this study provides a robust tool for modeling and optimizing nanoparticle injection systems, offering insights into their design and performance under various operation conditions. Future work will extend the framework to include more complex particle interactions and it will incorporate machine-learning techniques for further optimization.

Acknowledgements This work was supported by the HELMHOLTZ Data Science Graduate School for the Structure of Matter (DASHH, HIDSS-0002), by the Helmut-Schmidt University Hamburg, and by Deutsches Elektronen-Synchtrotron (DESY@HGF).
We also acknowledge dtec.bw – Digitalization and Technology Research Center of the Bundeswehr (project hpc.bw) for provision of computational resources on HSUper. dtec.bw is funded by the European Union—NextGenerationEU.

References

1. Neutze R, Wouts R, Van der Spoel D, Weckert E, Hajdu J (2000) Potential for biomolecular imaging with femtosecond X-ray pulses. Nature 406:752–757. https://doi.org/10.1038/35021099
2. Spence J, Chapman N (2014) The birth of a new field. Philos Trans R Soc Lond B Biol Sci 369:1647. https://doi.org/10.1098/rstb.2013.0309
3. Roth N, Horke DA, Lübke J, Samanta AK, Estillore AD, Worbs L, Pohlman N, Ayyer K, Morgan A, Fleckenstein H, Domaracky M, Erk B, Passow C, Correa J, Yefanov O, Barty A,

Bajt S, Kirian RA, Chapman HN, Küpper J (2024) New aerodynamic lens injector for single particle diffractive imaging. Nucl Instrum Methods Phys Res A 1058:168820. https://doi.org/10.1016/j.nima.2023.168820
4. Roth N, Awel S, Horke DA, Küpper J (2018) Optimizing aerodynamic lenses for single-particle imaging. J Aerosol Sci 124:17–29. https://doi.org/10.1016/j.jaerosci.2018.06.010
5. Worbs L, Roth N, Lübke J, Estillore AD, Xavier PL, Samanta AK, Küpper J (2021) Optimizing the geometry of aerodynamic-lens stack injectors for single-particle diffractive imaging. J Appl Cryst 54(6):1730–1737
6. Samanta AK, Amin M, Estillore AD, Worbs L, Horke DA, Küpper J (2020) Controlled beams of shock-frozen, isolated, biological and artificial nanoparticles. Structural Dyn 7(2):024304. https://doi.org/10.1063/4.0000004
7. OpenFOAM—The open source CFD toolbox. https://www.openfoam.com
8. SPARTA—Stochastic parallel rarefied-gas time-accurate analyzer. https://www.sparta.github.io
9. Peravali SK, Jafari V, Samanta AK, Amin M, Neumann P, Küpper J, Breuer M (2024) Accuracy and performance evaluation of low density internal and external flow predictions using CFD and DSMC. Comput Fluids 279:106346. https://doi.org/10.1016/j.compfluid.2024.106346
10. Peravali SK, Samanta AK, Amin M, Neumann P, Küpper J, Breuer M (2025) An improved simulation methodology for nanoparticle injection through aerodynamic lens systems. Phys Fluids 37:033380. https://doi.org/10.1063/5.0260295
11. Bird GA (1994) Molecular gas dynamics and the direct simulation of gas flows. Clarendon Press, Oxford
12. Welker S, Amin M, Küpper J (2022) CMInject: Python framework for numerical simulation of nanoparticle injection pipelines. Comput Phys Commun 270:108138. https://doi.org/10.1016/j.cpc.2021.108138
13. Cunningham E, Larmor J (1910) On the velocity of steady fall of spherical particles through a fluid medium. Proc R Soc Lond A 83:357–365
14. Epstein PS (1924) On the resistance experienced by spheres in their motion through gases. Phys Rev 23:710–723
15. Baines MJ, Williams IP, Asebiomo AS, Agacy RL (1965) Resistance to the motion of a small sphere moving through a gas. Mon Not R Astron Soc 130:63–74. https://doi.org/10.1093/mnras/130.1.63
16. Li A, Ahmadi G (1992) Dispersion and deposition of spherical particles from point sources in a turbulent channel flow. Aerosol Sci Techn 16:209
17. Worbs L (2022) Toward cryogenic beams of nanoparticles and proteins. Ph.D. thesis, Universität Hamburg, Hamburg, Germany

Open Access This chapter is licensed under the terms of the Creative Commons Attribution 4.0 International License (http://creativecommons.org/licenses/by/4.0/), which permits use, sharing, adaptation, distribution and reproduction in any medium or format, as long as you give appropriate credit to the original author(s) and the source, provide a link to the Creative Commons license and indicate if changes were made.

The images or other third party material in this chapter are included in the chapter's Creative Commons license, unless indicated otherwise in a credit line to the material. If material is not included in the chapter's Creative Commons license and your intended use is not permitted by statutory regulation or exceeds the permitted use, you will need to obtain permission directly from the copyright holder.

Calibration of the Larsen-Borgnakke Model for NO-O Vibrational Relaxation

Shubham Thirani, Deborah A. Levin, and Ingrid J. Wysong

Abstract Modeling of Nitric Oxide (NO) vibrational states in hypersonic reentry flows is necessary to interpret emission and absorption spectra. To that end, the vibrational relaxation number, Z_v^C, is an important parameter in the Larsen-Borgnakke (LB) model which is used to express vibrational relaxation rates for collisions. In this work, we use rates obtained from Quasi-Classical Trajectory (QCT) calculations of Andrienko et al. [2] for the NO-O vibrational relaxation process to arrive at a new fit for the Z_v^C parameter. This new fit for Z_v^C is implemented in Direct Simulation Monte Carlo (DSMC) calculations for the case of hypersonic flow over a cylinder where the effect of the new fit on NO macroparameters and vibrational state populations is studied.

Keywords Larsen-Borgnakke · Vibrational relaxation · Nitric oxide infrared emission

1 Introduction

NO emission measurements in the infrared (IR) region from hypersonic ground testing facilities [4, 5] may provide important information about non-equilibrium flow chemistry. A fundamental aspect related to the modeling of NO vibrational states in the ground electronic state is the modeling of relaxation mechanisms for the vibrational energy mode of NO. In this work, we focus our efforts on the vibrational relaxation number, Z_v^C, used to model the NO-O vibrational relaxation process. Based on the continuum approach, Z_v^C is defined as the ratio of the vibrational relaxation time constant, τ_v, and the mean collision time, τ_c, that is,

S. Thirani (✉) · D. A. Levin
Department of Aerospace Engineering, University of Illinois Urbana-Champaign, Urbana, IL, USA
e-mail: thirani2@illinois.edu

I. J. Wysong
AFRL Retired, Seattle, WA, USA

© The Author(s) 2026

M. Grabe et al. (eds.), *Rarefied Gas Dynamics*, Springer Aerospace Technology,
https://doi.org/10.1007/978-3-032-00094-1_60

$$Z_v^C := \frac{\tau_v}{\tau_c}\,, \tag{1}$$

where the superscript C emphasizes the connection with continuum approaches. In this work, we obtain a new fit for the Z_v^C parameter while using vibrational state-to-state rates obtained from QCT calculations of Andrienko et al. [2] for the NO-O collisional mechanism and assess its impact on flow macroparameters and IR emission spectra in the expansion regions of the flowfield.

2 Isothermal Bath Calculations

The LB model [11] defines the probabilities for energy transfer from the translational mode to internal energy modes during inelastic binary collisions. In their DSMC work Gimelshein and Wysong [8] discuss why even though it may be important to use a state-to-state model for vibrational relaxation in O_2 or N_2 collisions, the LB model works very well for the vibrational relaxation of NO. Since NO relaxation is a rapid process mediated by attractive forces, the final vibrational level tends to be independent of the initial vibrational level. Gimelshein and Wysong [8] modeled the NO-O vibrational relaxation process using the calibrated fit for the Z_v^C parameter developed by Kulakhmetov et al. [10] for the O_2-O vibrational relaxation process as,

$$Z_v^C = \begin{cases} 52.46 + 0.04911 T_T - 3.128 \times 10^{-5} T_T^2 & \text{if } T_T \leq 1000 \text{ K} \\ \exp\left[5.228 - 0.1405 \ln(T_T)\right] & \text{if } T_T > 1000 \text{ K}, \end{cases} \tag{2}$$

where T_T is the local translational temperature. Following the framework described by Kulakhmetov et al. [10], 0-D thermal relaxation studies for constant rotranslational temperatures, T_{RT}, and variable vibrational temperatures, T_V, were performed for the NO-O non-reacting vibrational relaxation process to obtain τ_v assuming that the vibrational relaxation process proceeds only through the following mechanism,

$$\mathrm{NO}(x) + \mathrm{O} \leftrightarrow \mathrm{NO}(y) + \mathrm{O}, \quad x, y \in [0, 48] \text{ and } x \neq y\,, \tag{3}$$

where x and y represent different NO vibrational levels. The forward and backward mechanisms described in Eq. 3 generate a set of coupled first order differential equations, termed the master equations, which can be solved to track the evolution of the NO vibrational state populations with time. The forward rates were obtained from Ref. [2] and detailed mass balance was employed to obtain the backward rates. The 0-D simulations were initialized with a mixture of NO and O at a total number density of 10^{21} m^{-3} and equal mole fractions.

Assuming a Landau-Teller form for vibrational relaxation, the evolution of the relaxation parameter, Λ, was obtained as a function of time from the solution of the master equation, where

$$\Lambda(t, T_{RT}) = \exp\left(-\frac{1}{\tau_v}\right) = \frac{\overline{E_v(t)} - E_{eq,v}(T_{RT})}{E_v^o - E_{eq,v}(T_{RT})} \tag{4}$$

and t is the instantaneous time, $\overline{E_v(t)}$ is the average vibrational energy at time t, $E_{eq,v}(T_{RT})$ is the vibrational energy at thermal equilibrium with temperature T_{RT}, and E_v^o is the initial vibrational energy. Furthermore, the instantaneous vibrational temperature, T_V, was evaluated using the partition functions as

$$\overline{E_v}(t) = \frac{\Sigma_v E_v(v) \exp\left(-\frac{E_v(v)}{k_B T_V}\right)}{\Sigma_v \exp\left(-\frac{E_v(v)}{k_B T_V}\right)} \tag{5}$$

where k_B is Boltzmann's constant. We use Eq. 5 to calculate E_v^o using the T_V value at $t = 0$ and $E_{eq,v}(T_{RT})$ by assigning $T_V = T_{RT}$. The vibrational energy of the v^{th} vibrational state, $E_v(v)$, is expressed as

$$E_v(v) = \omega_e(v + 0.5) - \omega_e x_e(v + 0.5)^2 + \omega_e y_e(v + 0.5)^3 \tag{6}$$

where ω_e is the vibrational frequency, and x_e and y_e are the first and second anharmonicity constants [9].

Figure 1 presents the results of the 0-D simulations initialized with the different T_{RT} values given in the figure where all cases had an initial T_V of 500 K. Given the definition of τ_v in Eq. 4, the projections of the intersection points of the $\Lambda = 1/e$ line with the Λ curves on the t axis gives the τ_v value for each 0-D thermal relaxation case. Furthermore, τ_c may be written as [3, 8],

$$\tau_c = \frac{1}{2\sqrt{\pi} d^2 \sqrt{2k_B T_{RT}/m_R} (T_{\text{ref}}/T_{RT})^{\omega - 0.5}}, \tag{7}$$

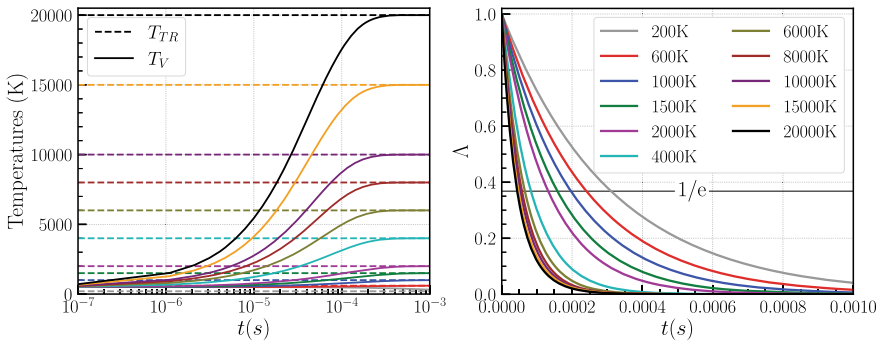

(a) Evolution of T_V with time (b) Evolution of Λ with time

Fig. 1 Evolution of **a** T_V and **b** Λ with time for different initial T_{RT}

where d, ω and T_{ref} are the variable hard sphere (VHS) diameter, exponent and reference temperature, respectively, and m_R is the reduced mass for the NO-O collision pair. The values of τ_v derived from Fig. 1b and Eqs. 1 and 7 are then used to calculate Z_v^C.

The variation of the product of the partial pressure of the target molecule, p_{xx}, and τ_v with respect to different initial T_{RT} is shown in Fig. 2a where xx refers to NO (green and blue curves) and O_2 (red curve) using the results of Kulakhmetov et al. [10] for the O_2-O mixture. The relaxation times derived here follow trends noted by Torres and Schwartzentruber [13] for comparisons of their NO+O vibrational relaxation times with rates previously available in literature. Figure 2b illustrates the variation in Z_v^C with respect to different initial T_{RT} values with blue and red squares indicating our current calculations and the calculations performed by Kulakhmetov et al. [10], respectively. The red curve is generated using the fit for Z_v^C defined in Eq. 2 and the dashed purple curve represents the new fit based on our current solutions of the master equation, that is,

$$Z_v^C = 21.084 + \frac{3476.852}{122.958 + (T_{RT}/408.665)^3} \,. \tag{8}$$

The 0-D solutions indicate that NO-O collisions experience faster vibrational relaxation compared to those of O_2-O, consistent with QCT simulations [2, 10].

To test our implementation of Eq. 8 in the DSMC solver, we performed 0-D DSMC simulations (see Fig. 2a) that can be compared with the master equation results. We also implemented the correction proposed by Gimelshein et al. [7] to resolve the inconsistency between the continuum and discrete [3] definitions of the vibrational relaxation number. The results from 0-D DSMC simulations show a close match with the master equation results demonstrating the consistent implementation of the new fit in the DSMC solver.

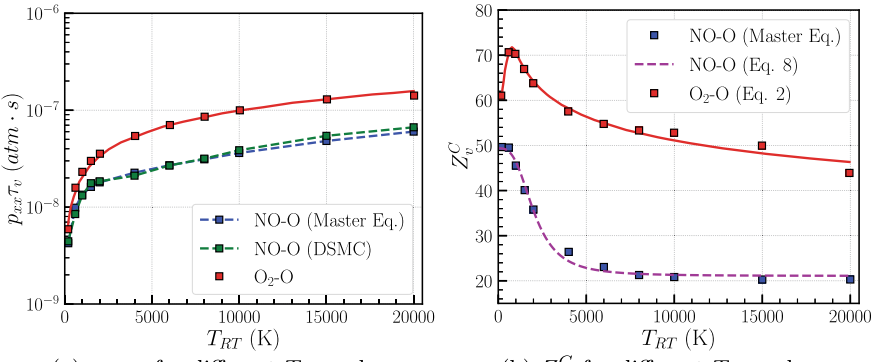

(a) $p_{xx}\tau_v$ for different T_{RT} values (b) Z_v^C for different T_{RT} values

Fig. 2 Variation of $p_{xx}\tau_v$ and Z_v^C as a function of T_{RT} for NO-O and O_2-O collisions. Note that pressure is varied with T_{RT} for the same mole fraction of NO or O_2 for all cases considered

3 Impact on Emission Spectra

To assess the impact of faster NO-O vibrational relaxation times predicted by the fit for Z_v^C described in Eq. 8, we simulate a hypersonic flow over a cylinder as shown in Fig. 3. Table 1 presents the freestream conditions, which are based on the work of Yanes et al. [15], and DSMC computational parameters. Knudsen number is defined as the ratio of the freestream mean free path and the radius of the cylinder and FNum is the number of physical molecules represented by a simulated molecule. The cylinder is modeled as an isothermal wall at 300 K and has a diameter of 31.75 mm. The domain has a total of 1.84×10^8 simulation particles, with at least 200 particles in each collision cell. A five species air mixture with 19 chemical reactions [8] were modeled in the DSMC simulations. A high fidelity non-equilibrium model that uses the Bias model [8] to account for vibrational favoring in dissociation reactions was used. Furthermore, the high fidelity model used discrete vibrational energy levels so as to model internal modes more accurately. The forced harmonic oscillator [1]

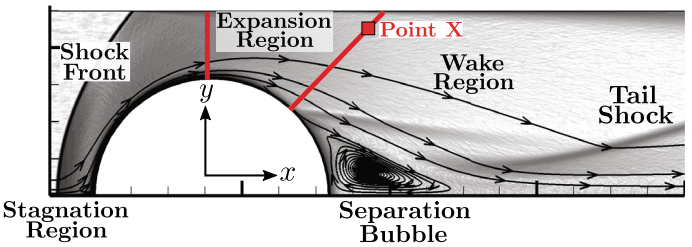

Fig. 3 Schematic showing important flow features for hypersonic flow over a cylinder

Table 1 Freestream conditions and DSMC computational parameters

Parameter	Value
Velocity (m/s)	3950
Temperature (K)	752
Mach Number	7.2
Number density (m^{-3})	7.233×10^{22}
Mean free path (m)	2.092×10^{-5}
Knudsen number	1.318×10^{-3}
Reynolds number** (m^{-1})	4.152×10^5
Sampling cell size (m)	1.0×10^{-4}
Number of time steps sampled	50, 000
Time step (s)	1.0×10^{-9}
FNum	3.0×10^{11}
Domain size ($x \times y$)	10×2.5 cm

*Reynolds number based on freestream viscosity computed using the VHS model [3] parameters given by Gimelshein and Wysong [8]

model was used to calculate vibrational relaxation rates for O_2 and N_2 for collisional processes involving all species present in the flow, and energy redistribution after a reaction was performed using the LB [11] model. We consider the two sets of rates described in Eqs. 2 and 8 to model the NO-O vibrational relaxation mechanism.

Flowfield macroparameters are extracted along the vertical line at the shoulder and the 45° line in the expansion region (red lines in Fig. 3). We are not showing comparisons of solutions in the stagnation region and along the wake line since both sets of Z_v^C give similar predictions in these regions. Figure 4 shows the temperatures and NO mole fractions along the vertical and 45° lines with solutions from the Z_v^C fits given by Eqs. 2 and 8 denoted as 'Old Z_v^C' and 'New Z_v^C', respectively. We note that there are negligible differences in the bulk temperatures with the use of the new Z_v^C fit which is expected as the bulk temperatures are dominated by contributions from N_2 molecules which have mole fractions in the range of $0.67 - 0.78$ throughout the domain. Furthermore, even though there are negligible differences in NO mole fraction values, the calculation performed with the new Z_v^C fit predicts NO vibrational temperatures ∼300 K and ∼400 K lower than those computed with the old Z_v^C fit along the vertical and 45° lines respectively. This difference in solutions is small near the cylinder wall and peaks at the domain boundary.

Figure 5a presents NO vibrational level populations at a point 17 mm from the cylinder wall, Point X in Fig. 3, which is characterized by a ∼400 K difference in NO vibrational temperatures predicted by the two sets of Z_v^C. The distributions marked as 'DSMC' are obtained by sampling and binning NO simulation particles over the discrete vibrational energy levels directly from the DSMC simulations once the flowfield is fully developed. It is to be noted that though the sampling process involved gathering statistics for higher vibrational states we are reporting distributions only up to a vibrational level of six due to the higher statistical noise associated with the higher states. The population distributions marked as 'Boltz, NO T_v' are the Boltzmann population distributions evaluated at the NO vibrational temperature at Point X. As can be seen, the population distributions obtained with the DSMC sampling procedure are similar to those obtained using the Boltzmann population distribution

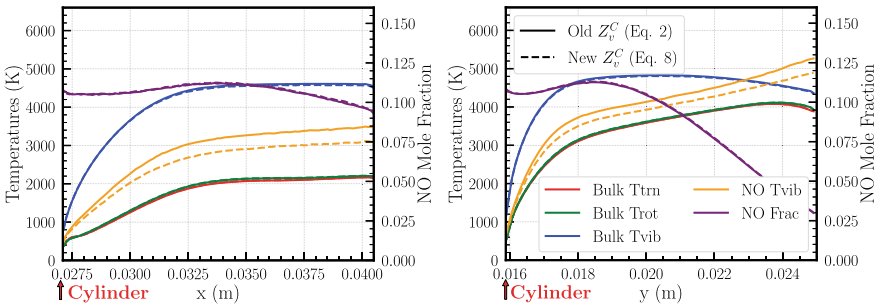

(a) Vertical line (b) 45° line

Fig. 4 Comparison of bulk temperatures, NO vibrational temperatures and NO mole fractions obtained by the two sets of Z_v^C approximations

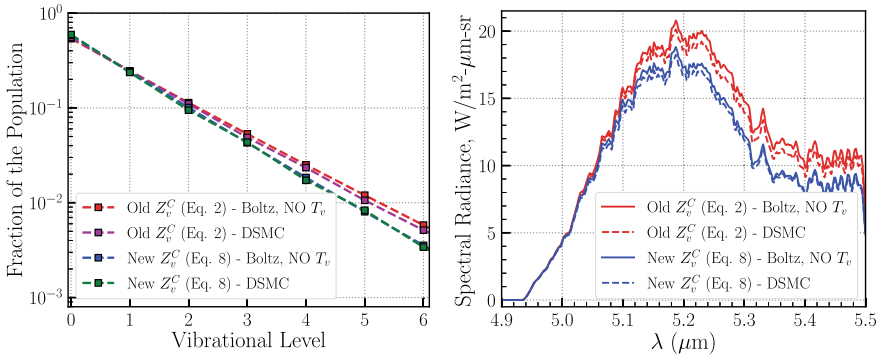

(a) NO Vibrational Level Populations (b) NO absolute spectral radiance

Fig. 5 NO **a** vibrational level populations and **b** absolute spectral radiance computed at Point X along the 45° line

function for both sets of Z_v^C considered in this work. We also note that the population distributions are noticeably different between the two sets of Z_v^C considered with the larger slope for the distribution predicted using the 'New Z_v^C' fit signifying lower NO vibrational temperatures as compared to that predicted using the 'Old Z_v^C' fit.

We used a modified version of the Nonequilibrium Radiative Transport and Spectra Program (NEQAIR) [6, 14], which computes emission and absorption intensities for relevant IR transitions based on user-specified vibrational state populations, to compute emission spectra. Figure 5b presents absolute spectral radiance calculated along a line-of-sight with constant flow properties passing through Point X and along the spanwise direction with a path length of 95.25 mm. The translational, rotational and vibrational temperatures of NO at Point X are provided as input to NEQAIR along with NO vibrational state populations shown in Fig. 5a. A Smeared Gaussian lineshape [6] was used to model the instrument lineshape in NEQAIR which was also used by Thirani et al. [12] to model NO IR emission spectra in the NASA Electric Arc Shock Tube facility.

We observe that the set of spectra generated using flowfield solutions predicted by the 'New Z_v^C' fit have lower radiance values as compared to those generated using flowfield solutions predicted by the 'Old Z_v^C' fit. This is a direct result of lower NO vibrational temperature values predicted by the 'New Z_v^C' fit. Furthermore, since the spectra generated using the 'Boltz, NO T_v' populations are similar to those generated with 'DSMC' populations, reasonable estimates of emission spectra can be obtained while using the Boltzmann distribution evaluated at NO vibrational temperature for flowfields similar to that considered in this work. This does, however, necessitate an accurate estimate of the vibrational temperature.

4 Conclusion

A new fit for the vibrational relaxation number, Z_v^C, for NO-O vibrational state-to-state collisions was obtained in this work and its impact was evaluated for a hypersonic flow over a cylinder. We observed that the faster relaxation rates led to only negligible differences in the bulk temperatures and NO mole fractions while leading to lower NO vibrational temperatures in regions where the flow is expanding. Furthermore, the maximum difference in NO vibrational temperatures between the two set rates was ∼400 K. This difference in NO vibrational temperatures is reflected in absolute radiance values for the IR emission spectra which can be generated using the Boltzmann population distribution computed using an accurate estimate of NO vibrational temperatures.

Acknowledgements The research is supported by the Air Force Office of Scientific Research through AFOSR Grant No. FA9550-19-1-0342 and computational resources are provided by the National Science Foundation's ACCESS program with the project number TG-PHY210065. The authors are thankful to Dr. Daniil Andrienko and Alexander Fangman for providing the QCT rates for NO-O vibrational relaxation mechanisms. The authors are also thankful to Dr. Sergey F. Gimelshein for help with running the 0-D thermal relaxation bath cases in the DSMC solver.

References

1. Adamovich IV, Macheret SO, Rich JW, Treanor CE (1996) Vibrational energy transfer rates using a forced harmonic oscillator model. J Thermophysics Heat Transfer 12(1):57–65
2. Andrienko DA, Boyd ID (2018) State-resolved characterization of nitric oxide formation in shock flows. AIAA SciTech 2018 forum
3. Bird GA (1994) Molecular gas dynamics and the direct simulation of gas flows. Clarendon, Oxford, England, UK
4. Chang E, Streicher JW, Krish A, Hanson RK (2022) High-temperature infrared-based diagnostic for nitric oxide using tunable diode laser absorption spectroscopy. AIAA SciTech 2022 Forum
5. Cruden BA, Tibere-Inglesse AC (2024) Radiative emission in incident air shocks from 3–7 km/s. AIAA Aviation Forum and Ascend 2024
6. Cruden BA, Brandis AM (2014) Updates to the neqair radiation solver. In: 6th international workshop on radiation of high temperature gases in atmospheric entry. St. Andrews, Scotland
7. Gimelshein NE, Gimelshein SF, Levin DA (2002) Vibrational relaxation rates in the direct simulation Monte Carlo method. Phys Fluids 14(12):4452–4455
8. Gimelshein SF, Wysong IJ (2019) Nonequilibrium air flow predictions with a high-fidelity direct simulation Monte Carlo approach. Phys Rev Fluids 4(3):033405
9. Herzberg G (1950) Molecular spectra and molecular structure 1. Spectra of diatomic molecules. D. Van Nostrand Company, New York
10. Kulakhmetov MF, Sebastiao IB, Alexeenko A (2016) Adapting vibrational relaxation models in DSMC and CFD to ab-initio calculations. In: 46th AIAA thermophysics conference
11. Larsen PS, Borgnakke C (1975) Statistical collision model for Monte Carlo simulation of polyatomic gas mixture. J Comput Phys 18(4):405–420
12. Thirani S, Karpuzcu IT, Levin DA (2024) Experimental validation of modeling efforts to estimate nitric oxide emission in high Mach number flows. AIAA Scitech 2024 Forum

13. Torres E, Schwartzentruber TE (2025) Characteristic vibrational and rotational relaxation times for air species from first-principles calculations. J Thermophysics Heat Transfer 0(0):1–27
14. Whiting EE, Park C, Liu Y, Arnold JO, Paterson JA (1996) Neqair 96 user manual. Tech rep, NASA Ames Research Center, Moffett Field, CA
15. Yanes NJ, Austin JM (2019) Nitric oxide spectroscopic measurements in a hypervelocity stagnation flow. In: AIAA Paper 2019–0794

Open Access This chapter is licensed under the terms of the Creative Commons Attribution 4.0 International License (http://creativecommons.org/licenses/by/4.0/), which permits use, sharing, adaptation, distribution and reproduction in any medium or format, as long as you give appropriate credit to the original author(s) and the source, provide a link to the Creative Commons license and indicate if changes were made.

The images or other third party material in this chapter are included in the chapter's Creative Commons license, unless indicated otherwise in a credit line to the material. If material is not included in the chapter's Creative Commons license and your intended use is not permitted by statutory regulation or exceeds the permitted use, you will need to obtain permission directly from the copyright holder.

Adaptive Particle Discretization Methods for Multiscale Non-equilibrium Flows

Simone Lauterbach, Stefanos Fasoulas, and Marcel Pfeiffer

Abstract Highly accurate simulation results for complex flow fields with strong nonequilibrium and noncontinuum effects, such as present during atmospheric entry processes, can be obtained by the Direct Simulation Monte Carlo (DSMC) method. However its use is limited by the increasing computational cost in denser regions. In these cases, efficiency-increasing methods are required. Alternative particle methods, such as Fokker-Planck (FP) or Bhatnagar-Gross-Krook (BGK) can achieve similar accuracy to DSMC in regions with lower Knudsen numbers, but with a lower computational demand. Additionally, these methods allow for a straightforward coupling to DSMC. Several optimization techniques have been implemented in the simulation code PICLas, including adaptive particle weights and a mesh refinement. In addition, various equilibrium breakdown criteria have been implemented for an efficient coupling between DSMC and other particle-based methods. All implemented adaption techniques are evaluated in terms of their accuracy and efficiency, in comparison to a non-adapted DSMC simulation.

Keywords DSMC · BGK · FP · Adaptive methods · Efficiency increase

1 Introduction

The efficient treatment of multiscale flows poses a significant challenge for many applications in the field of aerospace science. During the atmospheric entry process, the spacecraft enters the atmosphere in the rarefied regime, with a fast transition into denser regions at lower altitudes. Additionally, while the free-stream of the flow on the vehicle can be well in the continuum regime, rarefaction effects can become important in the wake of the flow. The Direct Simulation Monte Carlo (DSMC) method can accurately treat non-equilibrium effects, but has a too high computational demand for the transitional and continuum regime [1]. Alternative particle-based continuum methods, such as the Bhatnagar-Gross-Krook (BGK) method [2] and the Fokker-

S. Lauterbach (✉) · S. Fasoulas · M. Pfeiffer
University of Stuttgart, Stuttgart, Germany
e-mail: lauterbachs@irs.uni-stuttgart.de

© The Author(s) 2026

M. Grabe et al. (eds.), *Rarefied Gas Dynamics*, Springer Aerospace Technology,
https://doi.org/10.1007/978-3-032-00094-1_61

Planck (FP) [3, 4] method have gained importance in the recent years. These methods have less stringent constraints on the temporal and spatial discretization, as the mean collision time and the mean free path do not need to be resolved. At the same time, the methods have a similar accuracy compared to DSMC in the transition regime and a straightforward coupling to DSMC is possible, as the numerical algorithm for the methods differs only in the collision treatment. Therefore, interface regions are not required in the coupling procedure.

Apart from the use of alternative numerical methods, the efficiency of the particle methods can be further improved by a meaningful choice of the underlying simulation set-up. Parameters, such as the particle weight or the cell size, can be optimized in such a way that a higher discretization and thus a higher computational effort is used only in the regions of interest, while still ensuring physical validity throughout the simulation domain.

Several adaptive procedures for all particle-based methods have been implemented in the open-source gas and plasma simulation tool PICLas [5], including an automatic adaption of the particle weight per cell and an anisotropic refinement of the mesh by the use of virtual subcells. Furthermore, various continuum breakdown criteria have been implemented to allow for an efficient coupling between DSMC and other available particle methods.

The implemented methods are presented in the following in more detail.

2 Numerical Methods

The Boltzmann equation is the basis for the description of the microscopic gas state and the change in the particle distribution function $f(\mathbf{x}, \mathbf{v}, t)$ in dependence of the particle positions $\mathbf{x}$, velocities $\mathbf{v}$ and the time t, together with the collision term $\frac{\partial f}{\partial t}|_{\text{Coll}}$. External forces are neglected in this equation:

$$\frac{\partial f}{\partial t} + \mathbf{v} \cdot \nabla_{\mathbf{x}} f = \frac{\partial f}{\partial t}|_{\text{Coll}} \tag{1}$$

An analytical solution of the Boltzmann equation is not possible, therefore particle methods are used to approximate the Boltzmann collision integral. The physical gas flow is represented by the movement and collision of weighted simulation particles. Particle motion and interactions are treated independent of each other, with the motion step following Newton's laws. The particle methods in PICLas are all of stochastic nature, but differ in the collision treatment. In a DSMC simulation, binary particle pairs are determined, for which a collision probability is calculated and compared with a random number in order to decide whether an interaction takes place. In the BGK method, the Boltzmann collision integral is approximated by the relaxation towards a target distribution function f^t, chosen in a way to achieve the correct Prandtl number:

$$\frac{\partial f}{\partial t}|_{\text{Coll}} = \nu(f^t - f) \tag{2}$$

The FP approach approximates the Boltzmann equation by a Fokker-Planck equation, in dependence of a drift A_i and a diffusion term D_{ij}:

$$\frac{\partial f}{\partial t}|_{\text{Coll}} = -\sum_{i=1}^{3} \frac{\partial}{\partial v_i}(A_i f) + \frac{1}{2}\sum_{i=1}^{3}\sum_{j=1}^{3} \frac{\partial^2}{\partial v_i \partial v_j}(D_{ij} f) \tag{3}$$

2.1 Coupled Particle-Methods

As the algorithms of the particle methods in PICLas differ only in the approximation of the Boltzmann collision integral, a coupling of the methods can be performed directly by a cell-local switch of the collision routine. The particles carry all information through the simulation domain, therefore no data exchange or interface region is necessary between the methods. The coupling strongly depends on a meaningful continuum breakdown criterion for an optimal compromise between accuracy and efficiency. In PICLas, multiple coupling parameter can be employed individually or in combination with each other. The simulations are in all cases initialized with the more efficient BGK or FP method. Afterwards, the domain division is updated dynamically throughout the simulation to capture emerging non-equilibrium regions by the more accurate DSMC method.

The most simple criterion in PICLas is a density threshold, above which the more efficient particle method is employed. In a slightly more sophisticated setup, the global Knudsen number Kn_{G} of each cell can be calculated from the mean free path λ_c and a characteristic length L:

$$Kn_{\text{G}} = \frac{\lambda_c}{L} \tag{4}$$

If Kn_{G} exceeds a given value in a simulation cell, the DSMC method is used, while the remaining part of the simulation domain is treated by the BGK or FP method. Both the density threshold and the global Knudsen number typically lead to similar predictions of non-equilibrium without a significant increase in computational demand. However, both criteria are not representative of local effects of non-equilibrium and the definition of the macroscopic length scale in the global Knudsen number remains somewhat arbitrary.

A more suitable estimator for local continuum breakdown is the gradient-length-local Knudsen number Kn_{L} as defined by Burt and Boyd [6]. Here, continuum breakdown is defined to occur if the gradients of the flow variables Q are large:

$$Kn_{\text{L}} = \frac{\lambda_c}{Q}\left|\frac{\text{d}Q}{\text{d}x}\right| \tag{5}$$

In PICLas, the maximum value for the density, velocity and temperature gradients are used. However, a disadvantage of this criterion is the increase in the computational demand due to the gradient calculations.

An alternative parameter, that is also representative of local effects of non-equilibrium, is the simplified Chapman-Enskog parameter. Continuum breakdown is defined to occur if the maximum value of the normalized heat flux vector and shear stress tensor exceed a given threshold [7]:

$$B = \max(\left|q_i^*\right|, \left|\tau_{ij}^*\right|) \tag{6}$$

In addition to the above defined breakdown parameter, an estimator for thermal non-equilibrium is used in the simulation of di- and poly-atomic species:

$$\Delta T = \sqrt{\frac{(T_{x,y,z} - T_{\mathrm{tot}})^2 + \xi_{\mathrm{R}}(T_{\mathrm{R}} - T_{\mathrm{tot}})^2 + \xi_{\mathrm{V}}(T_{\mathrm{V}} - T_{\mathrm{tot}})^2}{(3 + \xi_{\mathrm{R}} + \xi_{\mathrm{V}})T_{\mathrm{tot}}^2}} \tag{7}$$

2.2 Adaptive Particle Weights

Preliminary simulation results can be used to automatically determine the optimal particle weight per simulation cell in PICLas. The adaption aligns the particle weight with the number density in the cell, while also ensuring that the necessary particle discretization is met throughout the simulation domain. To avoid jumps in the particle weights between neighboring cells, an averaging filter is used on the initial weight distribution.

When a particle moves to a new cell with a lower weight, it is cloned with a probability, based on the weighting factor before and after the particle movement step, w_{old} and w_{new}:

$$P_{\mathrm{clone}} = \frac{w_{\mathrm{old}}}{w_{\mathrm{new}}} - \mathrm{INT}\left(\frac{w_{\mathrm{old}}}{w_{\mathrm{new}}}\right) \tag{8}$$

Clones are introduced over the course of multiple time steps and are inserted in random order to promote collisions between nearly created clones and other particles. To avoid unphysical effects, such as the Avalanche phenomenon [8], more than one clone per particle is not allowed.

If a particle moves to a cell with a higher weight, the deletion probability is calculated from the respective cloning probability for the opposite moving direction:

$$P_{\mathrm{delete}} = 1 - P_{\mathrm{clone}} \tag{9}$$

The deletion rate per time step is restricted to half of the particle flux to a new cell, in order to limit the loss of information.

In the calculation of the collision probability, an average weighting factor is used for particles with different weights. Energy and momentum are not conserved in each collision but on average over many collisions.

2.3 Anisotropic Mesh Adaption

Coarse simulation meshes in PICLas can be handled dynamically by an automatized cell refinement. Virtual subcells are introduced to reduce the separation distance between collision partners for DSMC and to improve the spatial resolution of the moment estimators for BGK and FP. In contrast to adaptive remeshing, the virtual subcells are considered only for the collision and relaxation step, which reduces the overall memory requirement.

Mesh cells undergo refinement if the local mean free path in the cell for DSMC or the gradients of the density, velocity and temperature for BGK and FP exceed a predefined threshold. In contrast to an Octree refinement [9], the implemented mesh adaption is not recursive and allows to re-use the virtual subcell structure for a given number of iterations. Thus, the overall computational demand of the method is reduced. The number of virtual subcells per mesh cell is calculated from the number of simulation particles in the cell and a predefined minimum particle number:

$$N_{\text{cell}} = \text{INT}\left[\left(\frac{N_{\text{part}}}{N_{\text{min}}}\right)^{1/3}\right] \tag{10}$$

For BGK and FP, a minimum number of 12 particles per cell has proven to result in meaningful macroscopic coefficients.

As the particle methods in PICLas make use of unstructured meshes, the virtual subcells are defined around equally spaced interpolation points in the the $[-1, 1]^3$ reference space. Particles are first mapped to the reference space by a Jacobian mapping, in which all subcell and position operations are performed. This mapping allows for a more efficient handling of the mesh adaption, as the calculation of particle distances would otherwise be costly, especially for larger numbers of interpolation points per cell.

To ensure that the minimum requirement of simulation particles per cell is met, the subcells can be merged along a space-filling Peano curve. This cell merge is of particular importance in BGK or FP simulations to achieve qualitatively good results. The Peano curve initially connects the cells in planar slices and only after the slices are merged completely, the third dimension is taken into account. A favored direction, which is only dissolved in the last step, emerges naturally from this procedure. In the current implementation, the merge order is based on the relative size of the directional temperature gradient, such that the cells along the direction of the highest gradient are always merged last. In addition, the merge procedure along the Peano curve can be used to generate an anisotropic refinement in contrast to the isotropic Octree scheme.

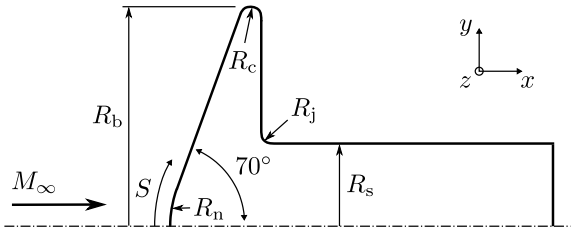

Fig. 1 Schematic representation of the simulated 70° blunted cone that is taken as input for PICLas. Simulated is the inflow of molecular nitrogen, with an angle $\alpha = 0°$

3 Hypersonic Flow Around a 70° Blunted Cone

As a test case for the adaptive methods, the hypersonic flow of nitrogen around a 70° blunted cone, as illustrated in Fig. 1, is chosen. To allow for a comparison to experimental heat flux values, the free-stream conditions are chosen according to [10], with $v_\infty = 1633.8$ m/s, $T_\infty = 15.29$ K and $n_\infty = 1.002 \times 10^{-22}\,\mathrm{m}^3/\mathrm{s}$. The flow case has a Mach number of $M_\infty = 20$ and a Knudsen number $K_n = 0.005$. For the surface, full thermal accommodation is assumed, with a constant wall temperature of $T_\mathrm{w} = 300$ K. To reduce the overall computational effort, the symmetric flow on the cone is made use of in a 2D-axisymmetric simulation setup. First, a highly resolved and non-adapted reference DSMC simulation is performed, with a time step $\Delta t = 2 \times 10^{-9}$ s and weighting factor $\omega = 1 \times 10^9$. The test case is further evaluated by ESFP, ESBGK and the respective coupled simulations with DSMC. Here, the same time step as for the DSMC case is used. However, the simulation cases are initialized with a higher weighting factor $\omega = 1 \times 10^{11}$. The coupling of DSMC with ESBGK or ESFP is performed based on the local Knudsen number. As a threshold, $Kn_\mathrm{L} = 0.1$ was chosen, above which the DSMC method is utilized.

This value has proven to still produce good results, but no longer led to a significant reduction in the computational effort. In addition, the newly implemented automatic determination of the particle weights and the automatic gradient-based mesh refinement is employed for these simulation cases.

The accuracy of the adapted simulation cases is evaluated by comparing the results to the non-adapted simulations, as well as to the reference DSMC simulation and experimental values. In Fig. 2 the heat flux values for the various ESBGK and ESFP simulation cases are compared. The non-adapted ESBGK result overestimates the heat flux at the front of the cone, while good agreement can be observed for both the adapted ESBGK and ESBGK-DSMC simulation with the DSMC results and the experimental values. As for the ESBGK cases, the non-adapted ESFP simulation overestimates the heat flux at the front significantly. The use of the adaptive methods in both the ESFP and the coupled ESFP-DSMC simulations led to an increase in the accuracy, however the heat flux values still are still not in perfect agreement with the DSMC results.

To evaluate the efficiency of the various methods, the computational time and the required number of simulation particles for a resolved simulation are compared in Table 1. The simulation time for the non-adapted DSMC method is utilized as

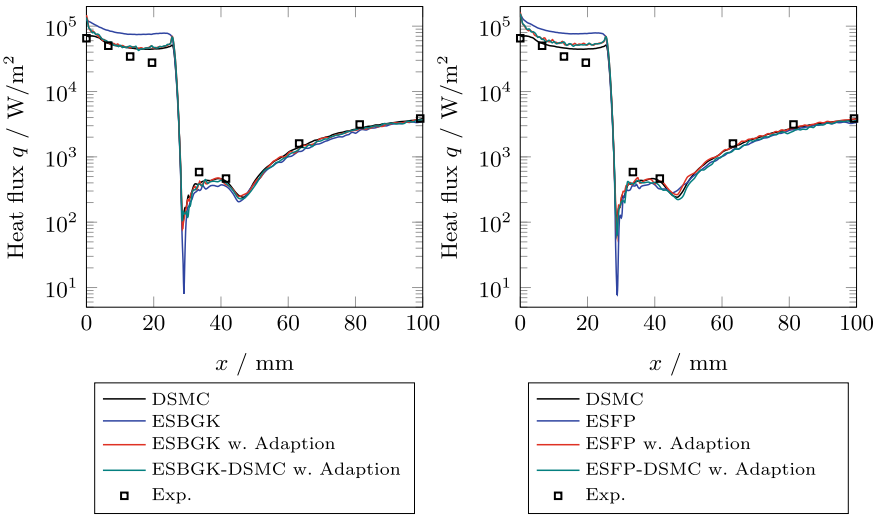

Fig. 2 Comparison of the measured and calculated heat flux over the length of the surface for the flow around the 70° blunted cone

Table 1 Comparison of the total simulation particle number and the required computational time for the different methods

	N_{part}	CPU h_{DSMC}/CPU h
DSMC	$1.24 \times 10^{+8}$	1
ESBGK	$1.81 \times 10^{+6}$	223.5
ESBGK w. adaption	$1.01 \times 10^{+6}$	242.9
ESBGK-DSMC w. adaption	$1.00 \times 10^{+6}$	252.3
ESFP	$1.81 \times 10^{+6}$	258.7
ESFP w. adaption	$9.96 \times 10^{+5}$	232.5
ESFP-DSMC w. adaption	$9.98 \times 10^{+5}$	264.4

a reference point. While a large particle number was required to achieve properly resolved DSMC results, approximately two order of magnitudes fewer particles could be employed in the ESBGK and ESFP simulations. These methods are not based on binary particle collisions and therefore do not require the resolution of the mean free path. With this lower particle number, the computational effort could be significantly reduced in comparison to the DSMC reference. With adaptive particle weights, the simulations showed a further increase in efficiency when compared to the non-adapted ESBGK and ESFP simulation.

Overall, the adapted ESBGK and ESBGK-DSMC showed the best performance in the test case, with a good overall agreement to the reference DSMC results, but a significantly reduced computational effort.

4 Conclusion

Several adaptive procedures for the particle methods are implemented into PICLas, including an anisotropic refinement of the simulation mesh and an automatized determination of the optimal particle weight for each cell. In addition, the coupling between different particle methods is extended from a density-based criterion by multiple, more sophisticated continuum-breakdown criteria.

The implementation and functionality of the adaptive methods are verified by the simulation of the hypersonic flow of nitrogen around a 70° blunted cone. The application of the adaptive methods allowed for a significant reduction of the computational time, while ensuring good overall agreement to experimental heat flux values.

In future work, the adaptive weighting scheme will be extended for the handling of trace species, especially for chemical reactions. In addition, the efficiency of the mesh adaption process will be further increased, in such a way, that the optimal number of subcells is directly calculated at the start of the simulation, without the need for a cell merging process.

Acknowledgements The authors gratefully acknowledge funding provided by Airbus Defence and Space and by ArianeGroup. This project has received funding from the European Research Council (ERC) under the European Union's Horizon 2020 research and innovation programme (grant agreement No. 899981 MEDUSA).

References

1. Bird G (1994) Molecular gas dynamics and the direct simulation of gas flows. Oxford University Press
2. Bhatnagar P, Gross E, Krook M (1954) A model for collision processes in gases. I. Small amplitude processes in charged and neutral one-component systems. Phys Rev 94:511
3. Gorji M, Jenny P (2014) An efficient particle Fokker-Planck algorithm for rarefied gas flows. J Comput Phys 262:325–343
4. Pfeiffer M, Gorji M (2017) Adaptive particle–cell algorithm for Fokker-Planck based rarefied gas flow simulations. Comput Phys Commun 213:1–8
5. Fasoulas S, Munz C, Pfeiffer M, Beyer J, Binder T, Copplestone S, Mirza A, Nizenkov P, Ortwein P, Reschke W (2019) Combining particle-in-cell and direct simulation Monte Carlo for the simulation of reactive plasma flows. Phys Fluids 31
6. Burt J, Boyd I (2009) A hybrid particle approach for continuum and rarefied flow simulation. J Comput Phys 228:460–475
7. Garcia A, Alder B (1998) Generation of the Chapman-Enskog distribution. J Comput Phys 140:66–70
8. Galitzine C, Boyd I (2015) An adaptive procedure for the numerical parameters of a particle simulation. J Comput Phys 281:449–472
9. Pfeiffer M, Mirza A, Fasoulas S (2013) A grid-independent particle pairing strategy for DSMC. J Comput Phys 246:28–36
10. Allegre J, Bisch D, Lengrand J (1997) Experimental rarefied heat transfer at hypersonic conditions over 70-degree blunted cone. J Spacecraft Rockets 34:724–728

Open Access This chapter is licensed under the terms of the Creative Commons Attribution 4.0 International License (http://creativecommons.org/licenses/by/4.0/), which permits use, sharing, adaptation, distribution and reproduction in any medium or format, as long as you give appropriate credit to the original author(s) and the source, provide a link to the Creative Commons license and indicate if changes were made.

The images or other third party material in this chapter are included in the chapter's Creative Commons license, unless indicated otherwise in a credit line to the material. If material is not included in the chapter's Creative Commons license and your intended use is not permitted by statutory regulation or exceeds the permitted use, you will need to obtain permission directly from the copyright holder.

An Effective Temperature Formulation for Predicting State-Specific Reaction Rates and Simulating One-Dimensional Hydrogen-Air Detonations in DSMC

Shrey Trivedi, Ahren W. Jasper, John K. Harvey, and Jacqueline H. Chen

Abstract In this paper, simulations of hydrogen-air detonations are performed in the continuum regime using Direct Simulation Monte Carlo (DSMC). Continuum codes assuming thermal equilibrium or even with a multi-temperature approach may be inadequate for simulating conditions with strong thermal and chemical non-equilibrium, and hence DSMC is utilized here. There are two aspects of this study: (1) One-dimensional (1-D) detonation waves are simulated in the continuum regime, under near-equilibrium conditions using the established TCE model and (2) a novel Effective Temperature (T_{eff}) formulation accounting for vibrational non-equilibrium, based on the equipartition principle, is tested in DSMC. For detonation analysis, a preheated case at Mach number M = 3.0, with reactants at an initial temperature of 900 K and initial pressure of 0.3 atm is simulated. The results are compared with the Zel'dovich-von Neumann-Döring (ZND) solution obtained from the Shock and Detonation (SDT) toolbox. It is found that DSMC results in a robust and steady detonation structure and shows excellent agreement with the ZND solution. For conditions with non-equilibrium effects, reaction rates specific to individual ro-vibrational states need to be incorporated. To this effect, the use of T_{eff} within the TCE model results in good agreement of state-specific reaction rates with those obtained from the Quasi-Classical Trajectory (QCT) calculations.

Keywords DSMC · 1D detonation · Hydrogen-air reacting flows

S. Trivedi (✉) · J. H. Chen
Sandia National Laboratories, Livermore, CA, USA
e-mail: strived@sandia.gov

A. W. Jasper
Argonne National Laboratories, Lemont, IL, USA

J. K. Harvey
University of Cambridge, Cambridge, UK

© The Author(s) 2026

M. Grabe et al. (eds.), *Rarefied Gas Dynamics*, Springer Aerospace Technology,
https://doi.org/10.1007/978-3-032-00094-1_62

1 Introduction

The Direct Simulation Monte Carlo (DSMC) method proposed by Bird [2] has been used extensively for solving rarefied flow problems in the upper atmosphere. However, DSMC is also well-suited for combustion problems with significant non-equilibrium effects or when molecular transport is not adequately treated, for example, in Scramjets or Rotating Detonation Engines. In DSMC, the motion of molecules is solved in a time-accurate manner in two phases, namely a move phase and a collision phase [1]. These are carried out in alternate time steps. In the move phase, the particles move in a straight line unless hitting a surface or leaving the domain. In the collision phase, the sample colliding partners are appropriately selected and their interaction is treated through collision models. These two phases effectively solve the Boltzmann equation. However, the DSMC time step and cell size must be comparable to the mean collision time and the mean free path respectively. This makes DSMC computationally expensive.

The objective of this paper is to present hydrogen-air detonation using DSMC in the continuum regime. To the best of our knowledge, no such analysis has been performed within the framework of DSMC. Combustion studies using DSMC are rare [16–18]. Furthermore, DSMC analyses of flows in the continuum or near-continuum regime are also limited [20, 21]. Some preliminary hydrogen-oxygen detonation studies exist [3, 7, 25] utilizing a less detailed reaction mechanism. The hydrogen-oxygen system has a lower activation energy, making it easier to ignite, and it has a more steady detonation structure. Detonations show rapid discontinuous changes, and the effect of non-equilibrium can be prominent. It has been shown, for example, that the non-equilibrium effects can change the ignition delay time in Scramjets [8]. DSMC can account for molecular phenomena such as transport processes, internal energy relaxation, and chemical reactions, directly through molecular collisions. With accurate molecular data based on first principles, DSMC is a robust tool to gain insights into the fundamental problem of reacting flows under non-equilibrium conditions.

In cases of non-equilibrium, collisional cross sections can be evaluated from ab-initio data or using models based on molecular dynamics [16]. Models based on Quasi-Classical Trajectory (QCT) calculations are being developed for internal energy relaxation and dissociation reactions [9, 11, 15, 24]. However, these calculations require potential surfaces for each of the collision pairs which are yet ready for all of the reactions describing hydrogen-air chemistry. To this effect, a simpler effective temperature model is presented in this paper, based on the equipartition principle [10], to account for the vibrational non-equilibrium. For treating collisions between particles, the Variable Soft Sphere (VSS) model [5] is used in this analysis. For post-collisional redistribution of total energy, the Larsen-Borgnakke [4] model is commonly utilized and is used here. The open access code SPARTA [14] is employed in this analysis.

2 Effective Temperature Formulation

Effective temperature models approximate rate constants for non-thermal reactions using a single effective temperature. Here, the non-thermal rate constant k^* for a bimolecular reaction with a distinct reactant vibrational energy E_{vib}, reactant rotational temperature T_{rot}, and relative translational temperature T_{trans} is evaluated from the thermal rate constant k as follows

$$k^*(E_{vib}, T_{rot}, T_{trans}) \sim k(T_{eff}). \tag{1}$$

Here, $k(T)$ is the known thermal rate constant fit to an Arrhenius expression. It can be obtained either from experimental evaluations or from QCT calculations. The effective temperature formulation used in this study was validated for similar reactions in recent work [10] and uses the equipartition principle to evaluate T_{eff} as

$$T_{eff} = (T_{vib}n_{vib} + T_{rot}n_{rot}/2 + T_{trans}n_{trans}/2)/(n_{vib} + n_{rot}/2 + n_{trans}/2) \tag{2}$$

The variable n_x is the number of modes of type x. For example, for H + O_2, $n_{vib} = 1$, $n_{rot} = 2$, and $n_{trans} = 3$.

In DSMC since the simulation proceeds through the particle energies in different modes, i.e., E_{trans}, E_{vib}, and E_{rot}. To convert the collision energy, for example, E_{vib} to T_{vib}, the following expressions is used.

$$T_{vib} = E_{vib}/k_B n_{vib} \tag{3}$$

Note that the temperature in DSMC is evaluated from the energy of a collision pair, and not the cell-averaged values. Finally, the total collision energy (TCE) model is used to evaluate the reaction probabilities. The default TCE models only makes use of the translational temperature in evaluating the reaction probabilities. However, the implementation of effective temperature in DSMC is achieved by replacing the translational temperature in the default TCE model with the effective temperature T_{eff} (Eq. 2).

3 Results

3.1 Reaction Rates Using Effective Temperature Formulation

Reaction 1: H + O_2 → OH + O The reaction H + O_2 → O + OH is well known to be an important chain branching reaction in the hydrogen-air reaction mechanism. There are many Potential Energy Surfaces (PES) for this reaction in the literature [23]. For this analysis, the PES from the reference [10] is chosen. Validation of this PES is

provided through the comparison of the predicted thermal rate from QCT calculations with an experimental recommendation from Varga et al. [22]. Results from an earlier set of QCT calculations from Miller et al. [13] is also provided. The cross-sections obtained from the QCT calculations are integrated over all vibrational and rotational levels to calculate the equilibrium reaction rates. These integrated rates and the experimental results are shown in Fig. 1.

A good agreement can be observed for all cases, with current QCT giving a slightly better agreement with the experiments. Note that experimental results are limited to ~3000 K whereas the temperature of interest for non-equilibrium conditions could exceed that value. Under such conditions, QCT can be utilized to evaluate reaction rates, especially when the effect of other internal modes (rotational and vibrational) needs to be taken into account. The integrated reaction rates from the current QCT calculations can be fitted to a thermal rate constant 5.078e–13 (T / 300 K) 1.635exp (– 2458 K / T) cm^3/s.

Next, vibrational states were included in the analysis to account for the non-thermal state with vibrational non-equilibrium. In the most detailed scheme, the vibrational and rotational quantum numbers of $O_2(\nu, j)$ as well as the translational temperatures of O_2 and H should be used (with T_{trans} for the reaction to be the arithmetic average of the two translational temperatures of the reactants). In this analysis, the rovibrational coupling has been ignored, and the rotational temperature is assumed to be equilibrated with translational temperature. The trans-rotational temperature is simply referred to as T in the rest of the analysis. In summary, we use ν, and T or equivalently E_{vib}, and T.

The results for T = 4000 K and E_{vib} corresponding to ν = 0 – 9 are shown in Fig. 2a. Note that O_2 has bound states up to ν = 41. The dot symbols in this figure show the reaction rates directly from QCT. The dashed line shows the effective temperature model based on the mean vibrational temperature (Eq. 3) plugged simply into the Arrhenius formulation. The orange line shows the reaction rates from DSMC, obtained by using T_{eff} within the TCE model. The effective temperature model stays in good agreement with the QCT results. DSMC performs well at lower vibrational energy, but degrades slightly as Evib exceeds 10 kcal/mol. However, the values remain within a factor of 2–3 from the QCT results which can be considered a good

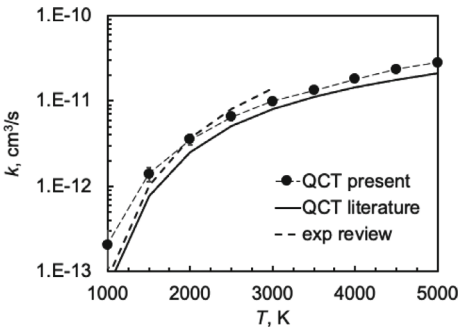

Fig. 1 Reaction rates obtained from the QCT calculations for reaction H + $O_2 \rightarrow$ OH + O from this work (solid dots), and Miller et al. [13] (solid line). The dashed line represents the measurements from Varga et al. [22]

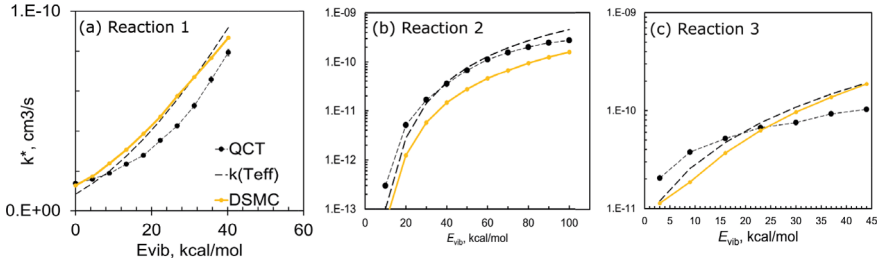

Fig. 2 Reaction rates for the reactions **a** $H + O_2 \rightarrow OH + O$, **b** $H_2O + H \rightarrow H_2 + OH$, and **c** $O_2 + H \rightarrow H_2 + O_2$, with vibrational non-equilibrium. Black dots show results from QCT calculations, black dashed line shows the Arrhenius formulation with the effective temperature model, orange dashed lines show the DSMC results using T_{eff} in the TCE model

agreement. This is also consistent with the findings of a previous analysis of CH_4 based reactions in Ref. [10].

Reaction 2 and 3 Results for the reaction $H_2O + H \rightarrow H_2 + OH$ are shown in Fig. 2b. For this reaction, T = 1000 K. The $n_{vib} = 3$ for H_2O. This can be accounted for in SPARTA through a separate file containing information about the different vibrational modes. For this reaction, the T_{eff} plugged into the Arrhenius form matches closely with the QCT results, whereas the DSMC results are slightly underpredicted for the entire range of the E_{vib} considered. Nevertheless, the results from the effective temperature model remain well within an order of magnitudefrom QCT.

The reaction rates for another reaction, $HO_2 + H \rightarrow H_2 + O_2$, are shown in Fig. 2c. In this case, the results from the T_{eff} model are underpredicted compared to QCT for lower vibrational energies, and overpredicted for higher vibrational energy, matching only at $E_{vib} \sim 20$ kcal/mol. Once again, the rates differ by a factor of two to three.

These results demonstrate that the effective temperature model adequately captures the reaction rates of the hydrogen-air reactions. Although the rates from the T_{eff} model differ slightly, this is acceptable since the uncertainly in the experimental results can be of an order of magnitude or higher in the range that is relevant to combustion/detonation. In the future, reaction rates at more values of temperature, and at a higher range of Evib will be tested.

3.2 1D Detonation Using T_{eff}

A quasi one-dimensional (1D) hydrogen-air detonation wave was simulated by setting a domain with $L_x >> L_y, L_z$, with L_x set equal to 50 mm. The domain had an inflow of an unburnt hydrogen-air stoichiometric mixture at Mach number M = 3.0. The reactants are at T = 900 K and P = 0.3 atm. A temperature and pressure discontinuity was initialized close to the middle of the domain. At $24.6 < x < 25.0$ mm,

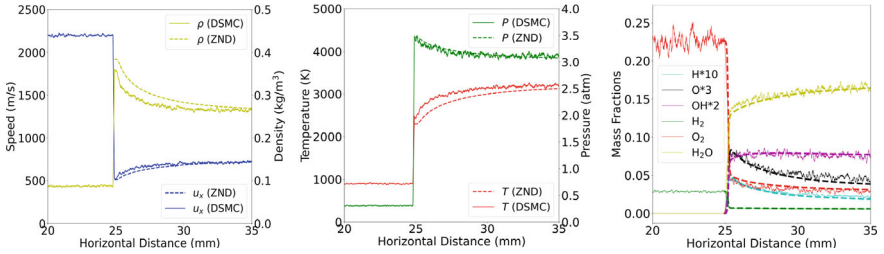

Fig. 3 Temperature, pressure, density, velocity, and species mass fractions from the 1D hydrogen-air detonation using the T_{eff} model. Solid lines show the results for DSMC whereas the dashed lines correspond to the equilibrium ZND solution

the pressure and temperature values were set corresponding to the post-shock values of the hydrogen-air mixture at M = 3.0. This region mimics the induction zone in a detonation wave, in which the pressure and temperature remain constant for a short period. At x > 25.0 mm, the temperature and pressure were set corresponding to the post-detonation values obtained by solving the so-called equilibrium ZND model using the Shock and Detonation Toolbox (SDT) [12]. The gas in the region was the combustion exhaust, i.e., H_2O and N_2. More details on this setup can be found in the reference [19], along with the results from the default TCE model. Note that the given conditions correspond to a slightly overdriven detonation wave. A 9-species 21-reaction mechanism of Burke et al. [6] was used to describe the chemistry.

The profiles for temperature, pressure, density, velocity, and species mass fractions are shown in Fig. 3. The dashed lines in this figure show the profiles from the equilibrium ZND solution. The figure shows that the profiles from the effective temperature model closely match ZND solution. This is not unexpected since this case is close to equilibrium (see Sect. 2). Nevertheless, it confirms that the effective temperature model is implemented correctly and is able to reproduce the expected results for this case. In future, cases with higher degrees of non-equilibrium will be tested with this model. The induction zone length (abbreviated as L_{ind}) from the default TCE model and the one using T_{eff} is shown in Table 1. The value of L_{ind} is evaluated by calculating the distance between the peak pressure and the peak thermicity. However, computing thermicity requires calculation of gradients, and hence can be noisy for individual snapshots. Thus, time-averaging was performed

Table 1 Comparison of induction zone length between DSMC and the ZND solution from the default TCE model and one using effective temperature T_{eff}

Case	L_{ind} DSMC (mm)	L_{ind} ZND (mm)	Percentage diff. (%)
Default TCE	0.275	0.295	7.0
T_{rff}	0.285	0.295	3.6

between t = 15 μs and 30 μs and L_{ind} is based on time-averaged thermicity. The value of L_{ind} in both cases is very close to its ZND counterpart for both cases.

4 Conclusions

This paper demonstrates simulating hydrogen-air detonations in the continuum region using DSMC. The results from DSMC are compared with the equilibrium ZND solution. It is shown that the default TCE model captures the temperature, pressure, density, velocity, and species mass fraction profiles accurately. Even though rapid changes occur across the detonation front that result in non-equilibrium effects inherent to these problems, the effects of non-equilibrium do not appear to be significant in this case, and the DSMC results match closely with the equilibrium ZND solutions.

For cases with higher degree of non-equilibrium, reaction models accounting for vibrational energy becomes important (assuming the rotational temperature quickly equilibrates with the translational temperature). To this effect, an effective temperature (T_{eff}) model based on the equipartition of energy is proposed [10]. The DSMC implementation of it involves using the TCE model but using T_{eff} instead of translational temperature. The reaction rates from quasi-classical trajectory (QCT) calculations accounting for individual vibrational levels is compared with those obtained from the T_{eff} model, and a good agreement is obtained for select reactions with differences of the order of two to three. This is acceptable since combustion reactions often have an order of magnitude or more uncertainty. Finally, a 1D detonation wave is simulated with the T_{eff} model, with results matching closely with those from the ZND model.

This paper sets the framework for simulating hydrogen-air detonations with higher degree of non-equilibrium in the continuum regime. Since DSMC can account for transport properties, internal energy exchange, and chemical reactions at a molecular level, it is well-suited for detonation reacting flow problems where rapid changes occur and non-equilibrium can play an important role. Currently, DSMC is limited by the availability and accuracy of relevant molecular data. However, it should be acknowledged this method is still in early stages of development for combustion studies.

Acknowledgements The work is supported by the US Department of Energy, Office of Basic Energy Sciences, Division of Chemical Sciences, Geosciences, and Biosciences. Sandia National Laboratories is a multimission laboratory managed and operated by National Technology and Engineering Solutions of Sandia, LLC., a wholly owned subsidiary of Honeywell International, Inc., for the U.S. Department of Energy's National Nuclear Security Administration under contract DE-NA-0 0 03525. The computational resources were provided by National Energy Research Scientific Computing Center (NERSC) and Oak Ridge Leadership Computing Facility (OLCF).

References

1. Babinsky H, Harvey JK (2011) Shock wave-boundary-layer interactions, vol 32. Cambridge University Press
2. Bird GA (1994) Molecular gas dynamics and the direct simulation of gas flows. Oxford University Press
3. Bondar YA, Maruta K, Ivanov MS (2011) Hydrogen-oxygen detonation study by the DSMC method. In: AIP conference proceedings, vol 1333. American Institute of Physics, pp 1209–1214
4. Borgnakke C, Larsen PS (1975) Statistical collision model for Monte Carlo simulation of polyatomic gas mixture. J Comput Phys 18(4):405–420
5. Boyd ID, Schwartzentruber TE (2017) Nonequilibrium gas dynamics and molecular simulation, vol 42. Cambridge University Press
6. Burke MP, Chaos M, Ju Y, Dryer FL, Klippenstein SJ (2012) Comprehensive H_2/O_2 kinetic model for high-pressure combustion. Int J Chem Kinet 44(7):444–474
7. Chou CH, Pan KL (2024) Computational investigation of chemical and non-equilibrium effects on the Richtmyer-Meshkov instability. Proc Combust Inst 40(1):105335
8. Fiévet R, Voelkel S, Koo H, Raman V, Varghese PL (2017) Effect of thermal nonequilibrium on ignition in scramjet combustors. Proc Combust Inst 36(2):2901–2910
9. Gimelshein S, Wysong I (2017) DSMC modeling of flows with recombination reactions. Phys Fluids 29(6):067106
10. Jasper AW, Sivaramakrishnan R, Klippenstein SJ (2019) Nonthermal rate constants for ch4* + x → ch3 + hx, x = h, o, oh, and o2. J Chem Phys 150(11):114112
11. Kulakhmetov M, Gallis M, Alexeenko A (2016) Ab initio-informed maximum entropy modeling of rovibrational relaxation and state-specific dissociation with application to the O_2 + O system. J Chem Phys 144(17):174302
12. Lawson J, Shepherd J (2021) https://shepherd.caltech.edu/EDL/PublicResources/sdt/
13. Miller JA, Garrett BC (1997) Quantifying the non-RRKM effect in the H + O2 ⇄ OH + O reaction. Int J Chem Kinet 29(4):275–287
14. Plimpton SJ, Gallis MA. Sparta. http://sparta.sandia.gov
15. Sebastião IB, Kulakhmetov M, Alexeenko A (2017) DSMC study of oxygen shockwaves based on high-fidelity vibrational relaxation and dissociation models. Phys Fluids 29(1):017102
16. Sebastião IB, Qiao L, Alexeenko A (2018) Direct simulation Monte Carlo modeling of H_2-O_2 deflagration waves. Combust Flame 198:40–53
17. Trivedi S, Cant RS, Harvey JK (2021) Molecular level simulations of combustion processes using the DSMC method. Combust Theory Modell 25(2):351–363
18. Trivedi S, Harvey JK, Stewart Cant R (2022) Molecular level simulations of hydrogen-air flame at high pressures. Proc Combust Inst
19. Trivedi S, Salinas JS, Harvey JK, Poludnenko AY, Chen JH (2025) Simulations of hydrogen-air detonations using Direct Simulation Monte Carlo: *under review*. Combust Flame
20. Trivedi S, Salinas JS, Lee M, Desai S, Gallis MA, Harvey JK, Chen J. Comparison of DSMC and multi-temperature simulations of thermal nonequilibrium in a supersonic Kelvin-Helmholtz shear layer. AIAA SCITECH 2024 Forum
21. Valentini P, Grover MS, Verhoff AM, Bisek NJ (2023) Near-continuum, hypersonic oxygen flow over a double cone simulated by direct simulation monte carlo informed from quantum chemistry. J Fluid Mech 966:A32
22. Varga T, Olm C, Nagy T, Zsély IG, Valkó E, Pálvölgyi R, Curran HJ, Turányi T (2016) Development of a joint hydrogen and syngas combustion mechanism based on an optimization approach. Int J Chem Kinet 48(8):407–422
23. Voelkel S, Raman V, Varghese P (2016) Effect of thermal nonequilibrium on reactions in hydrogen combustion. Shock Waves 26(5):539–549

24. Wysong I, Gimelshein S, Bondar Y, Ivanov M (2014) Comparison of direct simulation Monte Carlo chemistry and vibrational models applied to oxygen shock measurements. Phys Fluids 26(4):043101
25. Yang C, Huang H, Sun Q (2019) A microscopic study of one-dimensional H_2-O_2 detonation using DSMC method. In: AIP conference proceedings, vol 2132. AIP Publishing LLC, p 070013

Open Access This chapter is licensed under the terms of the Creative Commons Attribution 4.0 International License (http://creativecommons.org/licenses/by/4.0/), which permits use, sharing, adaptation, distribution and reproduction in any medium or format, as long as you give appropriate credit to the original author(s) and the source, provide a link to the Creative Commons license and indicate if changes were made.

The images or other third party material in this chapter are included in the chapter's Creative Commons license, unless indicated otherwise in a credit line to the material. If material is not included in the chapter's Creative Commons license and your intended use is not permitted by statutory regulation or exceeds the permitted use, you will need to obtain permission directly from the copyright holder.

Plasma Flows and Processes

Effect of Microwave Coupling and Magnetic Field Topology on Electron Temperature and Thrust on the Example of Two Electric Propulsion Concepts

C. E. Schäfer, J. Schmidt, F. Plettenberg, M. Grabe, Y. A. Chan, J. Martinez-Schramm, K. Bräumer, K. Holste, and P. J. Klar

Abstract Electric propulsion concepts involving electron cyclotron resonance excitation for plasma generation eliminate the need for electrodes inside the plasma. Concepts, employing magnetic nozzles to accelerate the entire plasma for thrust production, remove the necessity for a neutralizer. Two thruster concepts realizing such plasma production and acceleration are investigated: the well-known MINOTOR thruster prototype of ONERA and a new prototype under development at DLR called DEEVA. It is assumed that converging parts in the magnetic field lines along the plume direction lead to the weaker performance of the DEEVA prototype compared to the MINOTOR prototype. This study investigates the effects of magnetic field configurations on the DEEVA prototype, examining both a converging-diverging character and a strictly diverging configuration of the DEEVA magnetic field topology. The effects of these magnetic field variations are compared with the MINOTOR prototype using Langmuir probe measurements and thrust balance measurements. By observing trends resulting from operational variations of the prototypes - such as changes in input power, frequency settings, and volume flow - we can infer the influence of the magnetic field topology on plasma parameters and thrust. Potential improvements for thruster development are discussed based on the measured magnetic field topologies.

Keywords Electric propulsion · ECRT · Magnetic nozzle · Langmuir probe · Thrust balance

C. E. Schäfer (✉)
Propulsion Department, OHB System AG, Bremen, Germany
e-mail: clara.schaefer@ohb.de

J. Schmidt · F. Plettenberg · M. Grabe · Y. A. Chan · J. Martinez-Schramm
Spacecraft Department, German Aerospace Center, Göttingen, Germany

K. Bräumer · K. Holste · P. J. Klar
Institute of Experimental Physics I, Justus Liebig University, Giessen, Germany

© The Author(s) 2026

M. Grabe et al. (eds.), *Rarefied Gas Dynamics*, Springer Aerospace Technology,
https://doi.org/10.1007/978-3-032-00094-1_63

1 Introduction

Typical issues with ion thruster technologies include electrode and grid erosion, along with the requirement for additional neutralizer devices [3]. Using electron cyclotron resonance (ECR) excitation for plasma generation, which eliminates the need for electrodes, offers a promising solution. Additionally, employing a magnetic nozzle (MN) to accelerate the entire plasma for thrust production removes the need for a neutralizer. The effects of electrodeless microwave coupling on plasma properties, combined with the magnetic field topology of a new thruster that achieves electrodeless plasma production and acceleration, are currently unknown. This study aims to fill this knowledge gap by comparing two thruster concepts. We examine the DEEVA (*DLR Electrodeless ECR Via microwave plasma Accelerator*) thruster, developed by the German Aerospace Center, which uses ECR for plasma production and a magnetic nozzle for acceleration. This is compared with a prototype of the well-known MINOTOR (*Magnetic Nozzle Electron Cyclotron Resonance Thruster*) concept, developed by the Office national d'études et de recherches aérospatiales (ONERA) [8]. Both prototypes employ a magnetic nozzle, are of similar size, and are designed to operate within a similar frequency and power range. However, they differ in terms of the concept employed for microwave coupling into the plasma as well as in the arrangement of the permanent magnets delivering the magnetic field topology. Comparing both thrusters under the same operating conditions (same power, volume flow and frequency setting) allows us to carry out detailed studies of the impact of the microwave coupling method and the magnetic field topology on plasma parameters.

As former studies have shown, the magnetic field topology of the DEEVA prototype includes a converging part in the magnetic field lines between the ECR zone and the thruster exit plane [11]. This is assumed to be the reason for the DEEVA prototype's performance not yet being comparable to the MINOTOR prototype [10, 11]. To investigate this assumption, we vary the magnetic field topology of DEEVA by realigning the permanent magnets. In one configuration, the disc magnets and the ring magnet are aligned in an attracting manner. This setup, referred to as *DEEVA-attractive*, was investigated in earlier studies [10, 11]. The second magnetic field setup aligns the magnets in a repulsive manner, and is therefore denoted as *DEEVA-repulsive*. In the repulsive configuration, a strictly diverging magnetic field character is expected. Previous studies have shown a correlation between electron temperature and ion energy for both the MINOTOR and DEEVA prototypes [5, 10]. This correlation is based on the assumption of an ambipolar electric field in the magnetic nozzle due to electron dynamics. Analyzing data from different diagnostic methods and directly comparing the plasma parameters of both thrusters enables us to assess the impact of different magnetic field configurations on performance.

2 Methods and Experimental Set Up

The experiments are conducted in the vacuum facility *Simulationsanlage für Treibstrahlen Göttingen - Miniatur Triebwerke* (STG-MT) at the DLR in Göttingen. The chamber has a length of 1 m and a diameter of 1.1 m. It is equipped with two backing pumps, a rotary vane pump, and a roots pump yielding a base pressure of 10^{-3} mbar. For lower pressure ranges a turbomolecular pump is added allowing pressure ranges of 10^{-6} mbar and background pressures during thruster operation in the range of 10^{-5} mbar. For the operation of the thrusters, we use the microwave signal generator KU-SG 2.45-250A of the company Kuhne Elecronics GmbH as well as the Bronkhorst mass control unit (MCU) for maximum 50 sccm air. The gases in use are xenon, in case of MINOTOR, and argon, in case of DEEVA. The mapping of each thruster is performed as follows: For all operation points the plasma is measured with Langmuir probe (LP) in $d = 100 \pm 0.5$ cm distance to the thruster exit. The thrust is investigated by means of thrust balance (TB) measurements. Multiple measurements performed at the same thruster setting using both the LP and the TB yield the experimental uncertainty in the results.

The operating principle of both the ECR thrusters with MN is the ionization of the propellant via ECR and the acceleration by a divergent magnetic field [2, 8, 14]. The prototypes are described in various publications [9, 10]. In presence of a magnetic field, charged particles (electrons and ions) are trapped along the magnetic field lines in such a way that they are circulating (gyrating) around the field lines, due to Lorentz forces [14]. If an electromagnetic wave with that cyclotron frequency is applied, the electron is resonantly accelerated by the electric field of the wave. It absorbs the energy of the electromagnetic wave, gains kinetic energy and increases the impact ionization process rate [2, 14]. Given the magnetic field of 87.5 mT, one comes to a microwave frequency of 2.45 GHz for resonant excitation. The acceleration of the produced ions is due to the gradient in the magnetic field strength. The magnetic moment μ of the charged particles (forming due to the gyration of the particles about the magnetic field lines) and the mass of the particle m, can be used to formulate an acceleration ($\dot{v}_{||}$) opposite to the gradient direction $\nabla_{||} B$ [6, 14]:

$$m\dot{v}_{||} = -\mu \nabla_{||} B. \tag{1}$$

The electrons therefore experience a force in opposite direction of the gradient in magnetic field strength, leading to a charge separation and the build up of an ambipolar electric field. It is a well-established assumption of MN's, that this electrostatic field converts the thermal energy motion of the electrons into ion kinetic energy. Therefore the electron dynamics plays a crucial role in configuring the electrostatic field in the plume, responsible for ion acceleration and ultimately thrust generation [4].

The magnetic field plays a crucial role in the functioning of the thruster, more specifically in the generation and acceleration of the quasi-neutral plasma. For this reason, the thruster's magnetic field is measured in three spatial directions using a

3D Hall probe from the company Projekt Elektronik GmbH. The range of the probe in use is ±200 mT and the linearity error is given as ±0.1 mT. In addition to the downstream measurements, the magnetic field in the vicinity of the ECR zone is also measured. This is possible by moving the probe in all three spatial directions (x, y, z) with linear stages. We will present results in the x, y plane after confirming rotational symmetry.

One of the most technically simple, yet difficult to interpret, diagnostics tools is the Langmuir probe (LP) [14]. A single electrode probe is introduced into the plasma and the voltage U is varied with respect to a reference potential. The current-voltage characteristic obtained, delivers a set of plasma parameters. For this study the crucial electron energy distribution function EEDF ($f(E)$)—based on the second derivative of the measured current voltage characteristic $\frac{\mathrm{d}^2 I_\mathrm{e}}{\mathrm{d}U^2}$ is determined [1]. By taking the moment of the distribution function we obtain the electron temperature T_e of the plasma:

$$T_\mathrm{e} = \frac{2}{3n_\mathrm{e}} \int_0^\infty f(E)\, E\, \mathrm{d}E. \tag{2}$$

The thrust balance DEPB (*DLR Electric Propulsion Thrust Balance*) used in this investigation is described in Refs. [7] and [13]. It is an inverted double pendulum, consisting of two pendulums connected by a plate with a given stiffness and elasticity. The TB consists of an aluminium table, casing and eight quartz-glass rods used as flexible bearings for the thruster table. To dampen possible high frequency oscillations an eddy current brake is built in. A micrometer-screw is used to establish the connection between the moving thrust balance table and the Sartorius® WZA224 load cell [13]. An accuracy of 0.2 mN and a repeatability of 0.1 mN for the DEPB are given [12]. In our study, multiple measurements are conducted for each operation point of the thruster to determine the mean thrust based on delta measurements. A "delta measurement" involves running the thruster for several minutes and then switching it off. The resulting step change in the force measurement curve is identified as the produced thrust. This process is repeated multiple times, and the thrust values are averaged. The standard deviation of these values is represented as error bars in the following.

3 Magnetic Field and Plasma Characteristics

The three magnetic field configurations can be seen in Fig. 1. The ECR zones, where a magnetic field strength of $|\vec{B}| = 87.5$ mT is achieved, is marked by a white line for all three configurations. For all three set ups, $x = 0$ marks the thruster exit plane. As one can see in case of MINOTOR the ECR condition is achieved close to the back plate. The magnetic field then decreases fast, leading to a high gradient in magnetic field strength. In case of DEEVA-attractive, a diverging-converging-diverging character

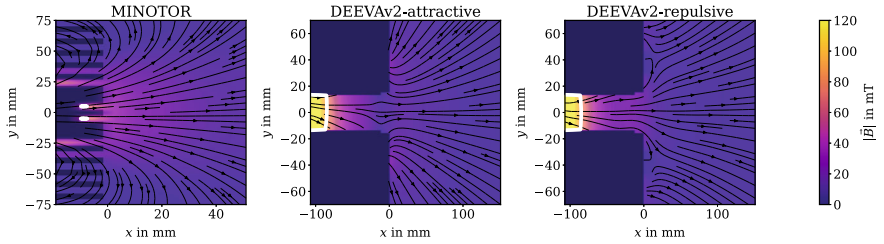

Fig. 1 Magnetic field configurations of the ECR thrusters. **a** MINOTOR is pictured on the left, dark area at $x < 0$ marks the mask where the probe could not access the thruster. $x = 0$ marks the thruster exit plane. The white dots mark the magnetic field strength of $|\vec{B}| = 87.5\,\mathrm{mT}$, the ECR zone. DEEVA in the center is shown in attractive configuration (**b**). On the right DEEVA is shown in repulsive configuration (**c**). Again, the dark area at $x < 0$ marks the mask where the probe could not access the slotted antenna. $x = 0$ marks the thruster exit plane and the white line $|\vec{B}| = 87.5\,\mathrm{mT}$, therefore the ECR zone

of the magnetic field can be observed. Since the converging part could lead to a reflection of particles, it is decided to test a different magnetic field configuration; the DEEVA-repulsive configuration is depicted in Fig. 1 on the right. Here we see again, the ECR condition is fulfilled in the back of the thruster vessel, near to the gas inlet. In contrast to DEEVA-attractive, we observe in this configuration a strictly diverging character of the magnetic field lines.

The effect of magnetic field topologies on the electron temperature with changes in operational points is shown in Fig. 2. On the left, we see the input power variation. The center plot shows the frequency variation, and the right plot depicts the variation in volume flow. The electron temperature for the MINOTOR prototype is higher across all operational parameter variations. For the two DEEVA configurations, DEEVA-attractive and DEEVA-repulsive, the repulsive configuration shows higher values in both power and frequency variations. For power variation, there is not a significant change in electron temperature for all prototypes. However, for frequency variation, higher values are observed around the design frequency of 2450 MHz for MINOTOR (a) and DEEVA-repulsive (c). In contrast, DEEVA-attractive (b) shows little change with frequency variation. For all three prototypes, electron temperature decreases with increasing volume flow. The values for the DEEVA-attractive configuration are the lowest, while those for the MINOTOR are the highest.

As shown in Fig. 3, the overall thrust for the MINOTOR prototype is higher, reaching up to $T_\mathrm{T} = 1.7\,\mathrm{mN}$. In contrast, the thrust values for both magnetic field topologies of the DEEVA thruster do not exceed 0.3 mN. There is no significant difference in thrust between the two DEEVA configurations. We observe an increase in thrust for all three prototypes with increasing input power. For MINOTOR, there is a clear optimum at 2450 MHz. DEEVA-attractive also shows an optimum at this frequency. DEEVA-repulsive operates at a constant thrust value over a broader frequency range. For volume flow variation, thrust decreases with increasing volume flow for all prototypes. However, DEEVA-attractive shows a slight increase in thrust around 2 sccm before decreasing as well.

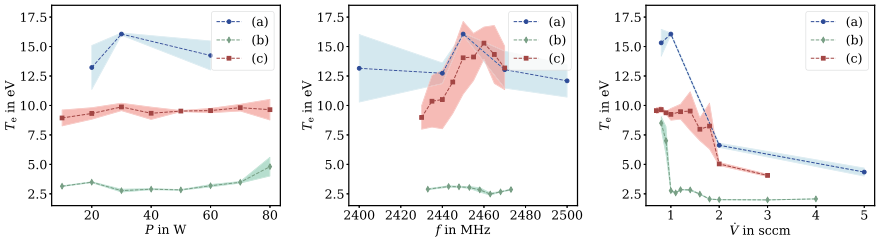

Fig. 2 Comparison between the determined electron temperatures T_e for the MINOTOR (**a**), DEEVA-attractive (**b**) and DEEVA-repulsive (**c**) configurations. The plot on the left shows power variations at a frequency set of 2450 MHz and a volume flow of 1 sccm of argon (in case of DEEVA) and xenon (in case of MINOTOR). The center plot depicts frequency variation at power input of 30 W and a volume flow of 1 sccm. The right plot shows the volume flow variation (of again argon, in case of DEEVA; and xenon, in case of MINOTOR) at the constant frequency 2450 MHz and input power of 30 W. The filled space shows the standard deviation of the resulting values from multiple measurements

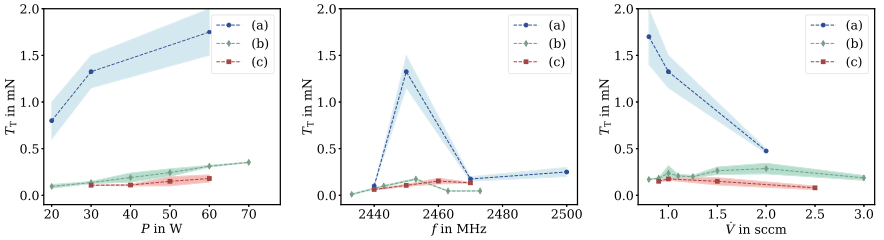

Fig. 3 Comparison between the determined thrust T_T for the MINOTOR (**a**), DEEVA-attractive (**b**) and DEEVA-repulsive (**c**) configurations. The plot on the left shows power variations at a frequency set of 2450 MHz and a volume flow of 1 sccm of argon (in case of DEEVA) and xenon (in case of MINOTOR). The center plot depicts frequency variation at power input of 30 W and a volume flow of 1 sccm. The right plot shows the volume flow variation (of again argon, in case of DEEVA; and xenon, in case of MINOTOR) at the constant frequency 2450 MHz and input power of 30 W. The filled space shows the standard deviation of the resulting values from multiple measurements

4 Discussion

First and foremost, it is important to note that MINOTOR is operated with xenon, while both DEEVA configurations are operated with argon. This choice is based on preliminary measurements showing significantly higher ion energies when DEEVA attractive is operated with argon [10]. This comparative study must be considered in light of this difference. Xenon is heavier than argon, and thus, the same ion energy results in higher thrust for xenon. Measurements of the magnetic field topologies revealed that the DEEVA-repulsive configuration indeed achieves a strictly diverging magnetic field. The higher gradient observed after the thruster exit in MINOTOR should result in greater electron acceleration (see Eq. 1). With the changes in magnetic field topology in the DEEVA-repulsive case, aiming for high gradients while avoiding

excessive convergence in magnetic field lines, we achieve higher electron temperatures compared to the attractive configuration, and they are almost comparable to those of the MINOTOR prototype.

We can consider possible explanations for our findings that the determined thrust is not significantly higher in the DEEVA-repulsive configuration compared to the DEEVA-attractive configuration and not as high as in the MINOTOR case, despite the higher electron temperatures suggesting otherwise. Firstly, the ion energies must be investigated and correlated with the electron temperatures presented in this study. Secondly, the ion current, which determines the total number of ions ejected from the thruster need to be determined. The third explanation involves thrust generated by neutral gas. Alongside investigating ion energy and ion current to determine thrust production, it's crucial to consider the effects of neutral gas on thrust. As reported in Ref. [15], thrust calculated using probe measurements underestimates total thrust. By comparing calculated thrust with thrust balance results, we can estimate the efficiency of the magnetic nozzle designs employed in this study.

Due to the early development stage of the new DEEVA thruster, it is uncertain whether it can achieve performance levels comparable to the optimized MINOTOR thruster in the future. However, the DEEVA concept introduces electrodeless microwave coupling into the plasma and electrodeless acceleration with a magnetic nozzle, potentially paving the way for long-term space missions employing ECR thrusters.

References

1. Demidov V, Ratynskaia S, Rypdal K (2002) Electric probes for plasmas: the link between theory and instrument. Rev Sci Instrum 73(10):3409–3439
2. Goebel D, Katz I (2008) Fundamentals of electric propulsion: ion and Hall thrusters, vol 1. Wiley
3. Holste K, Dietz P, Scharmann S, Keil K, Henning T, Zschätzsch D, Reitemeyer M, Nauschütt B, Kiefer F, Kunze F et al (2020) Ion thrusters for electric propulsion: Scientific issues developing a niche technology into a game changer. Rev Sci Instrum 91(6):061101
4. Kim J, Chung KJ, Takahashi K, Merino M, Ahedo E (2022) Kinetic electron cooling in magnetic nozzle: experiments and modeling. Plasma Sources Sci Technol
5. Lafleur T, Cannat F, Jarrige J, Elias P, Packan D (2015) Electron dynamics and ion acceleration in expanding-plasma thrusters. Plasma Sources Sci Technol 24(6):065013
6. Longmier B, Bering E, Carter M, Cassady L, Chancery W, Díaz FC, Glover T, Hershkowitz N, Ilin A, McCaskill G et al (2011) Ambipolar ion acceleration in an expanding magnetic nozzle. Plasma Sources Sci Technol 20(1):015007
7. Neumann A, Simon J, Schmidt J (2021) Thrust measurement and thrust balance development at dlr's electric propulsion test facility. EPJ Techn Instrum 8(1):17
8. Packan D, Elias P, Jarrige J, Vialis T, Correyero S, Peterschmitt S, Porto J, Merino M, Sánchez-Villar A, Ahedo E et al (2019) H2020 minotor: magnetic nozzle electron cyclotron resonance thruster. In: 36th international electric propulsion conference
9. Peterschmitt S, Packan D (2019) Comparison of waveguide coupled and coaxial coupled ecra magnetic nozzle thruster using a thrust balance. In: IEPC 2019

10. Schaefer C, Schmidt J, Plettenberg F, Chan Y, Grabe M, Marinez-Schramm J, Holste K, Klar PJ (2024) Comparative study of electron temperature and ion energy in two different magnetic nozzle thruster designs. In: 39th international electric propulsion conference
11. Schaefer C, Schmidt J, Plettenberg F, Chan Y, Grabe M, Marinez-Schramm Heinz TJ, Holste K, Klar PJ (2024) Investigation of the correlation between microwave coupling and ion energy on the example of two thruster concepts. In: Space propulsion conference
12. Schmidt J (2023) DLR electric propulsion balance documentation
13. Schmidt J, Simon J, Neumann A (2022) Thrust measurements of the rit-10 thruster with dlr's new depb thrust balance. In: 8th international conference on space propulsion, pp 1–7
14. Stroth U (2011) Plasmaphysik. Springer
15. Vialis T, Jarrige J, Aanesland A, Packan D (2018) Direct thrust measurement of an electron cyclotron resonance plasma thruster. J Propuls Power 34(5):1323–1333

Open Access This chapter is licensed under the terms of the Creative Commons Attribution 4.0 International License (http://creativecommons.org/licenses/by/4.0/), which permits use, sharing, adaptation, distribution and reproduction in any medium or format, as long as you give appropriate credit to the original author(s) and the source, provide a link to the Creative Commons license and indicate if changes were made.

The images or other third party material in this chapter are included in the chapter's Creative Commons license, unless indicated otherwise in a credit line to the material. If material is not included in the chapter's Creative Commons license and your intended use is not permitted by statutory regulation or exceeds the permitted use, you will need to obtain permission directly from the copyright holder.

Spatially Resolved Collisional-Radiative Model for a Rarefied Plasma Plume

Bruno Fontaine, Federico Bariselli, Pietro Parodi, Pedro Jorge, Damien Le Quang, and Thierry Magin

Abstract The VKI DRAG-ON facility was designed to replicate Very Low Earth Orbit flow conditions, to study Air-Breathing Electric Propulsion intakes and gas-surface interaction physics. Its Particle Flow Generator produces a low-density, low-temperature argon plasma plume. This study investigates the flow's thermochemical non-equilibrium by comparing synthetic spectra from Collisional-Radiative modeling to Optical Emission Spectroscopy measurements. A Lagrangian reactor approach is used to account for the reacting species advection. The results also show how the assumption on the Electron Energy Distribution Function shape can affect the diagnostics. Model-experiment comparisons reveal potential for plasma diagnostics and suggest targeted chemical model refinements. The results also show how the assumption on the Electron Energy Distribution Function shape can affect the diagnostics.

Keywords Optical emission spectroscopy · Lagrangian reactor

B. Fontaine (✉) · F. Bariselli · P. Parodi · P. Jorge · D. Le Quang · T. Magin
Aeronautics and Aerospace Department, von Karman Institute for Fluid Dynamics, Sint-Genesius-Rode, Belgium
e-mail: bruno.fontaine@vki.ac.be

B. Fontaine · T. Magin
Aéro-Thermo-Mécanique, Université Libre de Bruxelles, Brussels, Belgium

B. Fontaine
Aérospatiale et Mécanique, Université de Liège, Liège, Belgium

P. Parodi
Department of Mathematics, KU Leuven, Leuven, Belgium

P. Jorge
Materials and Chemistry, Vrije Universiteit Brussel, Brussels, Belgium

© The Author(s) 2026

M. Grabe et al. (eds.), *Rarefied Gas Dynamics*, Springer Aerospace Technology,
https://doi.org/10.1007/978-3-032-00094-1_64

1 Introduction

The VKI DRAG-ON facility, commissioned in 2023, was designed to replicate the Very Low Earth Orbit (VLEO) flow conditions to study Air-Breathing Electric Propulsion (ABEP) [1] intakes and gas-surface interaction physics [7]. It operates in free molecular flow conditions, at pressures of the order of 10^{-5} mbar, using a LTA-100 Particle Flow Generator (PFG) from ThrustMe [12] to generate a partially ionized argon or oxygen plume with ion speeds of 6–10 km/s.

Since ion beams interact with walls through sheath potentials, as opposed to the mostly neutral flow at VLEO, corrections for wall effects require knowledge of the electron temperature and density. Characterizing these parameters is therefore essential for extrapolation to flight conditions. Optical Emission Spectroscopy (OES) is of particular interest for its simple setup and non-invasive nature. It provides line-of-sight (LoS) integrated emission intensities, which can be used to infer plasma parameters such as electron temperature and density [2, 9]. Their relation to the emission line intensities is established through a Collisional-Radiative (CR) model, describing the chemical reactions and radiative processes. The CR model depends on the Electron Energy Distribution Function (EEDF) shape, which is often assumed to be Maxwellian. Other EEDF shapes can however be appropriate in some cases, including low-density plasmas [5, 6].

CR models are usually applied in a 0-D, Quasi-Steady-State (QSS) approach. However, for flows where chemical and flow timescales are comparable, the advection of the reacting species should be considered. A Lagrangian reactor approach provides an efficient alternative to a full flow-chemistry coupling, by transporting a thermochemical reactor along pre-computed streamlines without detailed chemistry, then recomputing the gas composition at each position [3].

In this study, we aim to advance the understanding of the non-equilibrium plasma dynamics in the VKI DRAG-ON facility by comparing spatially resolved OES measurements to predictions from a spatially resolved CR model using a Lagrangian reactor approach, for the PFG running with argon gas. We aim to identify the key factors influencing the model results and discrepancies with the experiment, such as electron temperature and density at the outlet of the PFG and the EEDF shape. In Sect. 2 we detail the experimental setup and OES data processing, in Sect. 3 we describe the modeling approach, and finally in Sect. 4 we compare results to assess model sensitivity and fidelity.

2 Optical Emission Spectroscopy

The DRAG-ON facility consists of two vacuum chambers linked by a duct that serves as test section for ABEP intake systems. Each chamber is equipped with a rotary vane mechanical pump and a turbomolecular pump, achieving an ultimate pressure of

10^{-8} mbar (when no gas is fed to the PFG). Each chamber is instrumented with hot-cathode and cold-cathode pressure gauges, and the main chamber has side windows for optical access. The PFG is aligned with the center axis of the main chamber (0.9 m length, 0.61 m diameter), and operated at 3 sccm argon flow, 60 W RF-power, 1 A focusing coil current, and floating electrode bias. During operation, the chamber pressure was 2.7×10^{-5} mbar.

Figure 1 shows the OES setup. The light emitted by the plasma is collected with a 12 mm reflective collimator (RC12SMA-P01, ThorLabs) mounted on a 2-D motorized motion stage with 0.03 mm positioning accuracy. A 1 m optical fiber (MS53L01, ThorLabs) conducts the light to the high-sensitivity spectrometer (Maya2000Pro, OceanOptics) with a 600–1000 nm range, a circular aperture 50 μm in diameter, a blazed grating with 600 lines/mm, and a Hamamatsu S11510 CCD detector. The spectrometer was calibrated in wavelengths by the manufacturer. Relative intensity calibration was performed by replicating the setup in front of a black body source (R1500T, AMATEK Land) at 1723 K.

Spatial emission measurements were conducted by moving the optics relative to the plume's axis at the PFG outlet. Scans were performed at axial positions $x = 14$, 21, 28, and 35 mm, with a transverse step size of 5 mm up to $z = \pm20$ mm, and a step of 10 mm beyond. The OceanView software was used for data acquisition. At each measurement point, 25 scans were performed for averaging, with 400 ms integration time each, with dark current correction.

Figure 2 shows a typical spectrum, with background subtracted and setup spectral response correction. The emission lines are identified to argon transitions (red labels, with levels indexed by energy starting from the ground state Ar(0)). They are integrated spectrally for comparison to the CR model results. To reduce noise, they are fitted to a Gaussian, typical for instrumental broadening [2].

Figure 3 shows the intensity spatial profiles for the 811 nm line. Others have similar profiles. The results show good symmetry and repeatability across campaigns. The uncertainty level, including fitting error and calibration noise, is small (average standard deviation of 3% and maximum of 10% for all lines, at all positions). The size of the window is a limitation of the current setup, as it prevents measurements far from the centerline, preventing Abel inversion.

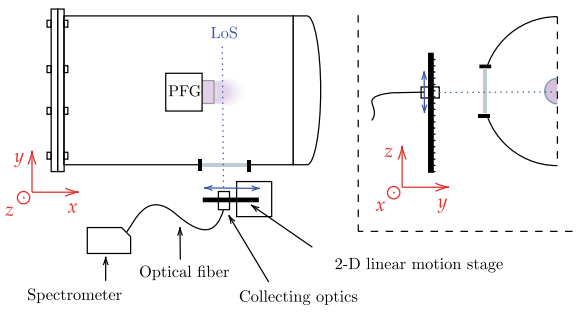

Fig. 1 Schematic experimental setup top view (*left*) and front view (*right*)

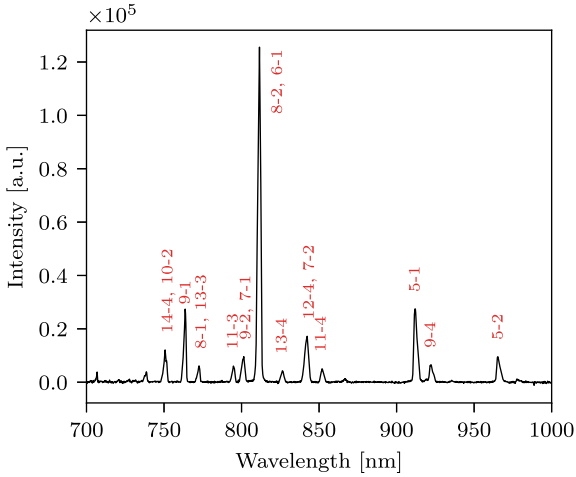

Fig. 2 Typical argon spectrum, at $x = 14$ mm and $z = 0$ mm

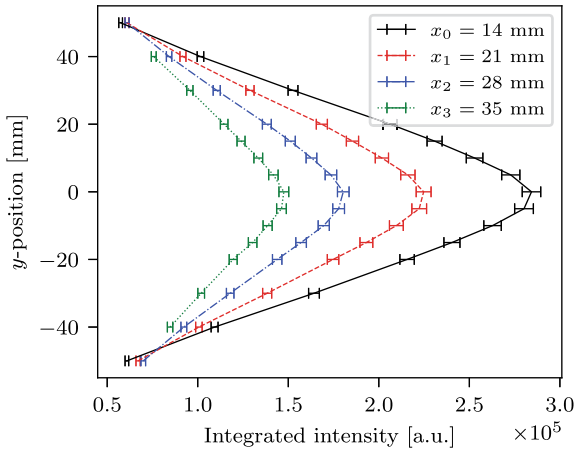

Fig. 3 Vertical intensity profiles (LoS integrated) for the line at 811 nm

3 Plume Model

The model predicts the intensity of emission lines by coupling a flow model with a Collisional-Radiative (CR) model using a Lagrangian reactor approach.

The governing equation for species conservation along streamlines is [3]:

$$\frac{\mathrm{d}Y_i}{\mathrm{d}s} = \frac{\dot{\omega}_i}{\rho U}, \quad \forall i \in \mathcal{S}, \tag{1}$$

where $\mathcal{S}$ is the set of species (here pseudo-species representing the excited states of argon), s (m) the curvilinear coordinate along the streamline, $Y_i = \rho_i/\rho$ (–) the mass fraction of species i, ρ (kg/m^3) the total mass density, U (m/s) the flow velocity

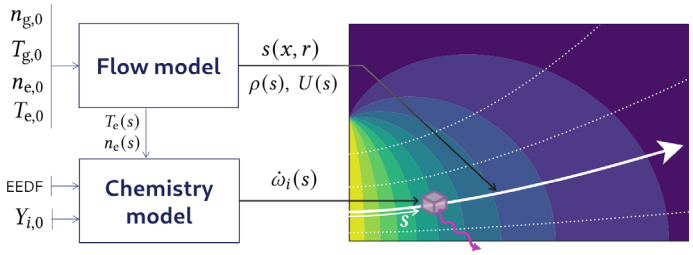

Fig. 4 Modeling approach and input parameters.

norm, and $\dot{\omega}_i$ (kg/(m^{3}s)) the net chemical production rate of species i. The approach (Fig. 4) requires a *flow model*, which takes as inputs the conditions inside the PFG $n_{g,0}$, $T_{g,0}$, $n_{e,0}$ and $T_{e,0}$ respectively the neutral density, neutral temperature, electron density and electron temperature. Through the flow model, these inputs fix the streamlines and flow conditions along them. A *chemistry model* then recomputes the species concentrations according to Eq. (1) with a Lagrangian reactor advected along the streamlines starting from an initial distribution $Y_{i,0}$, with local reaction rates depending on the local electron temperature, electron density and shape of the EEDF.

Flow model: The plume is modeled as a collisionless thermal expansion of neutral argon, with analytical velocity and density fields [4], interacting with a field of hot electrons. The electron temperature and density fields were computed with a Particle-in-Cell (PIC) simulation of DRAG-ON [10], with uniform outlet conditions $T_{e,0} = 5$ eV and $n_{e,0} = 2 \times 10^{15}$ m^{-3}. For the purpose of this study, the results were extrapolated to different outlet conditions with a linear scaling.

CR model: It includes the 31 first energy levels of argon, extracted from the NIST Atomic Spectral Database (ASD) [8]. Neglecting heavy interactions and assuming the plasma to be optically thin, the reactions included in the model are electron impact excitation/de-excitation and spontaneous radiative decay:

$$\mathrm{Ar}(l) + \mathrm{e}^- \underset{K_{ul}}{\overset{K_{lu}}{\rightleftharpoons}} \mathrm{Ar}(u) + \mathrm{e}^-, \quad \mathrm{Ar}(u) \xrightarrow{A_{ul}} \mathrm{Ar}(l) + h\nu,$$

where $u > l$ are respectively the upper and lower states. Rate coefficients for radiative decay A_{ul} (s^{-1}) are extracted from NIST-ASD, selecting all allowed transitions involving levels in $\mathcal{S}$ with an experimentally observed wavelength and a known A_{ul} (77 reactions). Electron-impact rates K_{lu} (m^3/s) are computed as a weighted integral of cross sections with the EEDF, using cross sections from [13] (465 reactions). The integrals are pre-fitted to a modified Arrhenius form for efficiency. The de-excitation coefficients K_{ul} are computed with the principle of detailed balance. Finally, the net production rate for each level i is:

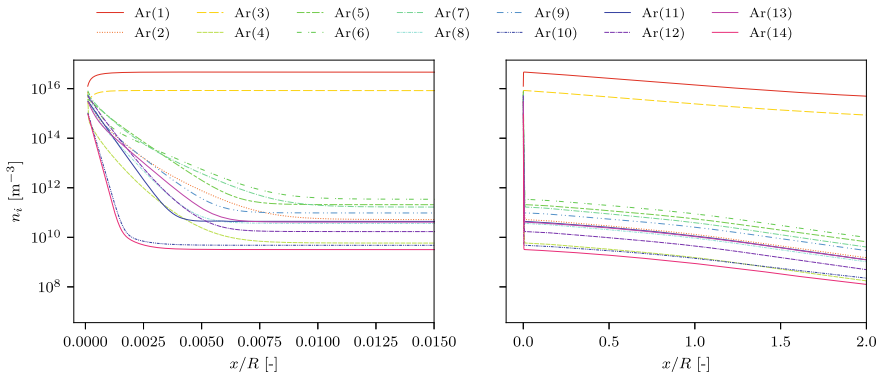

Fig. 5 Evolution of the densities of the 14 first excited states (centerline), with $n_{g,0} = 10^{19}$ m^{-3}, $T_{g,0} = 500$ K, $n_{e,0} = 5 \times 10^{14}$ m^{-3}, $T_{e,0} = 10$ eV, Maxwellian EEDF

$$\dot{\omega}_i/M = \sum_{i<j} A_{ji} n_j - \sum_{i>j} A_{ij} n_i + \sum_{j \neq i} K_{ji} n_e n_j - \sum_{j \neq i} K_{ij} n_e n_i. \tag{2}$$

with $M = 6.63 \times 10^{-26}$ kg the atomic mass of argon.

Solving Eq. (1) along a streamline gives the evolution of excited-state populations. Figure 5 shows results for the centerline, for typical input parameters. The initial conditions are chosen as a Boltzmann distribution at $0.2 \times T_{e,0}$ to start from a high state of excitation, as expected in the PFG ionization chamber.

We identify two main regions in the flow. First is a radiative length scale ($s/R < 0.015$), where the highly excited configuration from the PFG quickly decays, except for Ar(1) and Ar(3), the known argon metastables. After that, the flow appears to be chemically frozen, with a constant distribution of excited states along the streamline. For other plasma conditions than shown in Fig. 5, we also note a reactive length scale in-between these two regions, of varying length depending on the T_e and n_e distributions.

4 Comparison of Model and Experiment

In this section, we reconstruct the experimental results from the model results. A comparison criterion is defined to perform a sensitivity analysis on the inputs.

The line intensities for each transition considered are predicted in the model from the rate coefficient A_{ul} and the number density of the upper excited state n_u, with $I_{ul}(x, r) \propto A_{ul} n_u(x, r)/\lambda_{ul}$. For lines involving multiple transitions, contributions are summed. LoS-integrated model intensities are generated for the positions $x_i \in \mathcal{X}$ (axial positions with experimental data) by applying the forward Abel transform, assuming axisymmetry and the medium to be optically thin. OES intensities being

relative, we normalize them with

$$\hat{I}_l^m(x,z) = \frac{I_l^m(x,z)}{\frac{1}{N_c}\sum_{x_i\in\mathcal{X}}\sum_{k\in\mathcal{L}} I_k^m(x_i,0)}, \tag{3}$$

where $m \in \{\text{OES,CR}\}$, l is the line index in set $\mathcal{L}$ of 12 identified lines, and $N_c = \sum_{\mathcal{X}}\sum_{\mathcal{L}} 1$ is the total number of intensity values measured on the centerline.

A comparison criterion ξ (–) is defined to quantify the discrepancy between the OES and model results:

$$\xi = \sqrt{\frac{1}{N}\sum_{l\in\mathcal{L}}\sum_{x_i\in\mathcal{X}}\sum_{z_j\in\mathcal{Z}_i}\frac{\left(\hat{I}_l^{\text{OES}}(x_i,z_j) - \hat{I}_l^{\text{CR}}(x_i,z_j)\right)^2}{\left(\hat{I}_l^{\text{OES}}(x_0,0)\right)^2}}, \tag{4}$$

with $\mathcal{Z}_i$ the set of z positions in the scan at x_i, and $N = \sum_{\mathcal{L}}\sum_{\mathcal{X}}\sum_{\mathcal{Z}_i} 1$ is the total number compared values. The resulting comparison criterion ξ is a function of the model parameters only, and equals zero for a perfect match.

A sensitivity analysis was performed on ξ with small perturbations to identify key parameters. The initial conditions $Y_{i,0}$ were parametrized using a Boltzmann distribution at $2 \times T_{\text{el},0}$. The neutral density in the PFG $n_{\text{g},0}$ is fixed as it only affects absolute intensities. The model showed low sensitivity to T_g ($\leq$1% variation between 300 and 600 K) or to $T_{\text{el},0}$ ($\leq$7% between 1 and 15 eV, likely damped by the rapid radiative decay). However, higher sensitivity was found for the parameters governing electron impact excitation rates (EEDF shape, $T_{\text{e},0}$, $n_{\text{e},0}$). We therefore performed a mapping with respect to these parameters. The tested EEDF shapes were chosen to have very different tails (power-law for Kappa [11], exponential for Maxwellian, super-exponential for Druyvesteyn [5]).

Figure 6 shows ξ maps over ($T_{\text{e},0}$, $n_{\text{e},0}$) for each EEDF. These maps could in principle reveal whether one EEDF shape leads to better agreement with the experiment.

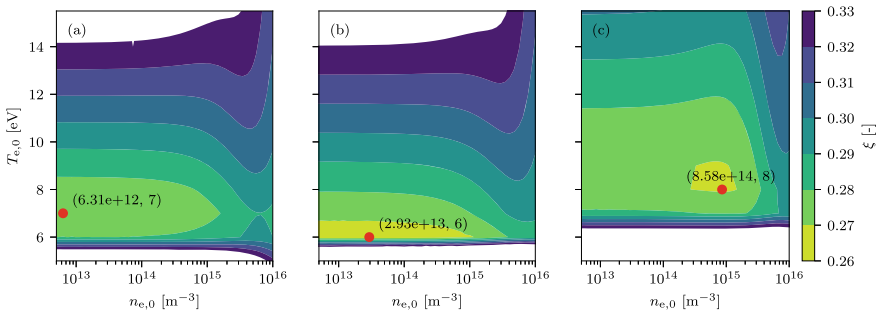

Fig. 6 Mapping of $\xi(n_{\text{e},0}, T_{\text{e},0})$ for each EEDF, with **a** Maxwellian, **b** Druyvesteyn and **c** Kappa ($\kappa = 2$), and location of minimum discrepancy ξ^* at $(T^*_{\text{e},0}, n^*_{\text{e},0})$

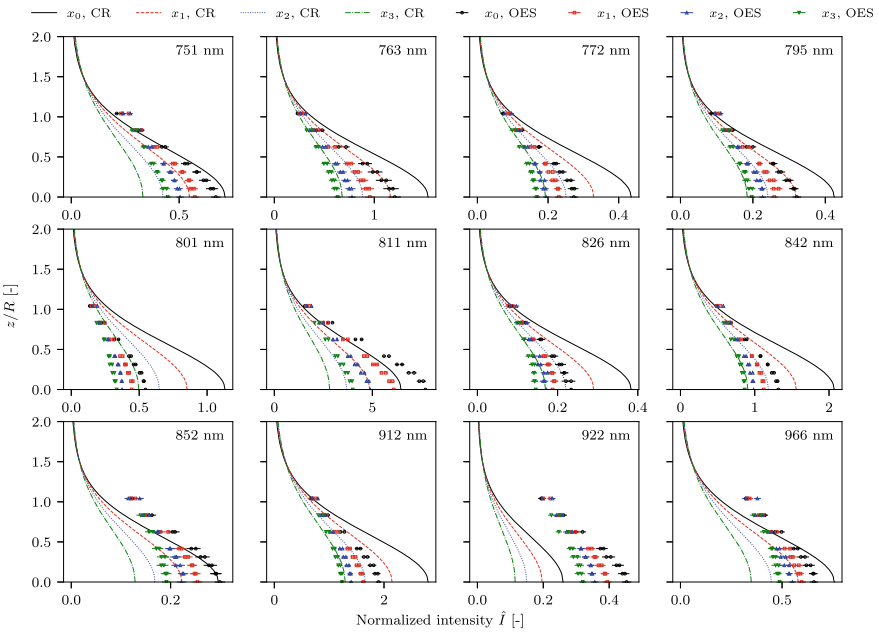

Fig. 7 Comparison of OES and model normalized intensity profiles for all lines, for a Maxwellian EEDF, $T^*_{e,0} = 10$ eV, $n^*_{e,0} = 3\times10^{15}$ m^{-3}, $T^*_{el,0} = 2$ eV, and $T^*_{g,0} = 500$ K

Here, however, all three yield similar minimum ξ^*. Nonetheless, the ξ contours differ depending on the choice of EEDF, and so does the location of the minimum discrepancy. In particular, we note that a less populated tail leads to a higher sensitivity on T_e. This can also be said for the sensitivity on n_e, although the sensitivity on this parameter remains relatively low for all EEDF shapes.

The obtained estimates of the electron temperature $T^*_{e,0}$, identified in Fig. 6, align well with invasive measurements [7]. This supports the potential for non-invasive diagnostics in DRAG-ON for the electron temperature. For the electron density, the optimal n^*_e are scattered across several orders of magnitude depending on the choice of EEDF shape. The diagnostics of this plasma parameter is therefore not conclusive at this stage because of the low sensitivity of xi on n_e and the correlation between n^*_e and the unknown EEDF shape. Figure 7 shows a visual comparison of OES and CR normalized intensities for a Maxwellian distribution at the minimum discrepancy. It shows reasonable agreement, given the large model uncertainties, with Einstein coefficients uncertainties reaching 50% [8] and cross sections varying widely across databases, but shows further model refinenements could be incorporated to reduce discrepancies.

5 Conclusions and Future Work

This study advances the understanding of non-equilibrium plasma dynamics in the VKI DRAG-ON facility by comparing the first spatially resolved OES measurements in the facility to a CR model using a Lagrangian reactor approach. A promising first problem inversion identified an electron temperature in the expected range, demonstrating the potential of our approach for non-invasive diagnostics in DRAG-ON, which could ultimately be applied during ABEP intake tests or gas-surface interaction studies. Remaining discrepancies between model and experiment suggest future model improvements such as extended PIC databases for different PFG conditions and inclusion of radiation trapping by metastable states. Particular attention should also be given to assumptions on the EEDF. While the EEDF shape had little impact on the extracted electron temperature under the present test conditions, it did affect the sensitivity of the model to the electron temperature and density, suggesting that it remains a critical parameter for plasma diagnostics. Langmuir probe measurements or Boltzmann equation simulations could provide alternatives to the analytical shapes used here. Future work will also focus on plasma diagnostics by problem inversion with uncertainty quantification tools.

Acknowledgements Bruno Fontaine is a F.R.S.-FNRS Research Fellow.

References

1. Andreussi T et al (2022) The AETHER project: development of air-breathing electric propulsion for VLEO missions. CEAS Space J 14(4):717–740
2. Bariselli F et al (2022) Characterization of an Air-Xenon operated electric thruster plume through optical emission spectroscopy. In: 9th international workshop on radiation of high temperature gases for space missions. Azores, Portugal
3. Boccelli S et al (2019) Lagrangian diffusive reactor for detailed thermochemical computations of plasma flows. Plasma Sources Sci Technol 28(6):065002
4. Cai C, Boyd ID (2007) Collisionless gas expanding into vacuum. J Spacecr Rockets 44(6):1326–1330
5. Druyvesteyn MJ, Penning FM (1940) The mechanism of electrical discharges in gases of low pressure. Rev Modern Phys 12(2):87–174
6. Gudmundsson JT (2001) On the effect of the electron energy distribution on the plasma parameters of an argon discharge: a global (volume-averaged) model study. Plasma Sources Sci Technol 10(1):76–81
7. Jorge PDC et al (2025) Relevance of an RF plasma source to satellite material testing in VLEO conditions. Under review at CEAS Space Journal (preprint available on Research Square)
8. Kramida A et al (2022) NIST atomic spectra database
9. Lee D et al (2022) Two-dimensional electron temperature and density profiles of Hall thruster plume plasmas using tomographically reconstructed optical emission spectroscopy. Plasma Sources Sci Technol 31(12):125004
10. Parodi P et al (2024) Particle-in-cell simulation of the VKI DRAG-ON facility. In: AIAA SciTech forum

11. Pierrard V, Lazar M (2010) Kappa distributions: theory and applications in space plasmas. Solar Phys 267(1):153–174
12. Rafalkyi D, Dudin S (2024) RF plasma flow generator for LEO environment simulation: use cases. In: 38th international electric propulsion conference
13. Zatsarinny O, Wang Y, Bartschat K (2014) Electron-impact excitation of argon at intermediate energies. Phys Rev A 89(2)

Open Access This chapter is licensed under the terms of the Creative Commons Attribution 4.0 International License (http://creativecommons.org/licenses/by/4.0/), which permits use, sharing, adaptation, distribution and reproduction in any medium or format, as long as you give appropriate credit to the original author(s) and the source, provide a link to the Creative Commons license and indicate if changes were made.

The images or other third party material in this chapter are included in the chapter's Creative Commons license, unless indicated otherwise in a credit line to the material. If material is not included in the chapter's Creative Commons license and your intended use is not permitted by statutory regulation or exceeds the permitted use, you will need to obtain permission directly from the copyright holder.

Evaluation of the Ambipolar Diffusion Approximation Using an Eulerian Boltzmann-Poisson-BGK Solver

Marisa Petrusky and Iain D. Boyd

Abstract Because first principles modeling of a weakly ionized gas is computationally expensive, the ambipolar diffusion approximation is often invoked. This approximation assumes the ionized gas undergoes ideal ambipolar diffusion, and is conventionally considered valid if the electron Debye length is orders of magnitude smaller than the neutral mean free path. However, this criterion is not intrinsic to ambipolar diffusion theory. An improved set of criteria for evaluating the validity of the ambipolar diffusion approximation is proposed, then verified with theory and simulation. An Eulerian Boltzmann-Poisson-BGK solver, which circumvents consideration of statistical noise present in particle methods, is used to simulate an unsteady expanding weakly ionized gas undergoing ideal ambipolar diffusion. Potential consequences of incorrectly applying the ambipolar diffusion approximation are demonstrated and discussed.

Keywords Weakly ionized gas · Plasma · Ambipolar diffusion approximation · Boltzmann solver

1 Introduction

The presence of charged particles in rarefied gas flows warrants careful consideration of modeling methods. All charged particles exert electrostatic forces on each other, and if a sufficient degree of charge separation occurs bulk electric fields form. First principles modeling of electrostatic effects requires solving Maxwell's equations in addition to treating electrons as an independent species. The latter is computationally expensive as electrons' lightweight mass necessitates a significantly smaller simulation time step for propagation. To simplify calculations the ambipolar diffusion approximation is often invoked. The approximation assumes positive ions and electrons travel at the same bulk velocity. In particle-based kinetic methods such as

M. Petrusky (✉) · I. D. Boyd
Ann and H.J. Smead Department of Aerospace Engineering Sciences, University of Colorado Boulder, Boulder, CO, USA
e-mail: marisa.petrusky@colorado.edu

© The Author(s) 2026

M. Grabe et al. (eds.), *Rarefied Gas Dynamics*, Springer Aerospace Technology,
https://doi.org/10.1007/978-3-032-00094-1_65

direct simulation Monte Carlo (DSMC) [2], the approximation is typically enforced by transporting electrons with the corresponding ion they were created with [1], or by propagating electrons at the mean ion velocity [4]. In computational fluid dynamics (CFD) codes, the approximation is enforced by setting the electron flux equal to the ion flux in each fluid element [10]. The validity of the ambipolar diffusion approximation is typically assessed by checking whether the electron Debye length $\lambda_{D,e}$ is much less than the neutral mean free path λ_n, where the full definition of the Debye length λ_D is given by

$$\lambda_D = \sqrt{\frac{\epsilon_0 k_B / e^2}{n_e / T_e + \sum_i z_i^2 n_i / T_i}} \tag{1}$$

where subscripts e and i denote electron and ionic species properties. ϵ_0 is the permittivity of free space, k_B is the Boltzmann constant, e is the elementary charge, n is number density, T is translational temperature, and z is the charge number. If the motion of ions is negligible compared to electrons, the ion term can be neglected, and Eq. 1 defines the electron Debye length, $\lambda_{D,e}$.

Despite its near ubiquitous use in both kinetic and continuum simulation of rarefied flows, the criterion $\lambda_{D,e} \ll \lambda_n$ is not intrinsic to ambipolar diffusion theory and thus may be insufficient justification for the approximation. It may also falsely predict when electrostatic interactions are negligible. In this study, a new set of criteria is proposed for assessing the validity of the ambipolar diffusion approximation in continuum flows. These criteria are verified through a series of unsteady weakly ionized gas simulations using a Boltzmann-Poisson-BGK solver, which circumvents consideration of statistical noise present in particle simulations. A case is tested where $\lambda_{D,e} \ll \lambda_n$ is violated. Additionally, simulation results with the ambipolar diffusion approximation and with direct electric field modeling are compared to assess how well the ambipolar diffusion approximation captures ideal ambipolar diffusion.

2 Review of the Derivation of Ambipolar Diffusion

The ambipolar diffusion approximation is based on, but not strictly interchangeable with, the phenomena of ambipolar diffusion. In a weakly ionized plasma, fast electrons will separate from ions, leading to a negative charge deficit. To remain quasineutral the plasma develops an electric field within itself to slow electrons and accelerate ions such that they diffuse at the same rate and have the same bulk velocity. From the fluid equations of motion for a single species plasma one can derive the ambipolar electric field $\mathbf{E}_a$

$$\mathbf{E}_a \equiv \frac{D_i - D_e}{\mu_i + \mu_e} \frac{\nabla n}{n} \tag{2}$$

$$\mu_j \equiv \frac{|q_j|}{m_j \nu_{j,n}} \tag{3}$$

$$D_j \equiv \frac{k_B T_j}{m_j \nu_{j,n}} \tag{4}$$

where the subscript j denotes either species quantities, n is the quasineutral plasma density, m_j is the mass, q_j is electrical charge, and $\nu_{j,n}$ is the collision frequency with neutrals. The mobility and Einstein relation charged species diffusion coefficients are μ_j and D_j, respectively [6].

Several assumptions are made throughout this derivation. By starting from the fluid equations the flow is implied to be under continuum conditions. Second, the gas must be sufficiently weakly ionized such that charged particles primarily collide with neutrals rather than each other. This ensures particles diffuse in a random-walk manner consistent with Fick's Law, rather than the collective and often oscillatory motion of strongly and fully ionized plasmas. Finally, the weakly ionized gas must be a "plasma" by the following definition:

1. $\lambda_D \ll L$, where L is the characteristic size of the system
2. $N_D \gg 1$, where N_D is the number of plasma particles within a radius of λ_D
3. $\omega\tau > 1$, where ω is the frequency of typical plasma oscillations, and τ is the mean time between collisions between plasma particles and neutrals

Most critical to this study is the first item, known as quasineutrality. Plasmas are able to shield out charge disturbances, such that far from the disturbance, the plasma is charge neutral. While "charge neutral" refers to the net charge of an ionized gas being exactly zero at a point, "quasineutral" refers to the plasma as a whole being sufficiently close to charge neutral, such that $n_i \simeq n_e$. Therefore, it is possible that within a quasineutral plasma at length scales $\sim \lambda_D$, local charge neutrality may not be maintained.

3 Methodology

An Eulerian grid-based Boltzmann-Poisson-BGK solver (known as DK) is used for this study [8]. A detailed explanation of the solver, as well as citations to previous work, can be found in [5]. To investigate charged species diffusion with as few external variables as possible a simplified weakly ionized gas expansion setup is designed in one physical dimension and one velocity dimension (1D1V). A uniform background neutral gas is initialized inside a periodic domain of length $L = 1.0$ m, and an ionization fraction is imposed at the center of the domain from $0.25L \leq x \leq 0.75L$. Both the neutral and the ionized gas are at thermodynamic equilibrium at 500 K. At time $t = 0$, the ionized gas expands into the background neutral gas. Each simulation is allowed to run until a sufficient number of collisions have occurred such that any ambipolar fields have time to form. The number of normalized collision times is given by $n_{coll} = t/\tau_{j,n}$, where $\tau_{j,n}$ refers to the average time between collisions

between a particle of type j and a neutral. Argon is used as the test gas. No ionization or recombination is allowed.

Both hard sphere and variable hard sphere collision models [2] are tested, and simulations are run with and without Coulomb and charge exchange (CEX) collisions. The final conclusions made in this study are invariant of collision model and the addition of Coulomb and CEX collisions. The plots shown in the following section are from simulations with hard sphere collisions with only momentum exchange (MEX) collisions between charged particles and neutrals. This represents the closest possible simulation setup to ideal ambipolar diffusion. The configuration space grids ensure at least 4 points per λ_i and at least 32 points per $\lambda_{D,e}$. Velocity space is discretized with 256 points. These grids ensure sufficient resolution of derived electrostatic properties [5].

4 Results

Results presented here are assessed in terms of the following. First, given a set of flow conditions, one must know whether ambipolar diffusion is expected. The Phelps diffusion length ratios [11] were derived to determine charged species diffusion type in gas discharge vessels where the diffusion length Λ is calculated from the length of the domain. Its ratio with the ion mean free path (Λ/λ_i) determines degree of ionized gas collisionality, and its ratio with the electron Debye length ($\Lambda/\lambda_{D,e}$) determines how well the ionized gas behaves like a plasma (i.e. a restatement of quasineutrality). The ionized gas expansion setup relaxes several assumptions of Phelps' derivation. Thus, a comprehensive set of simulations are run testing multiple diffusion length ratios, which ultimately found the Phelps ratios can successfully predict charged species diffusion type for the setup described above. In this setup, ratios of $\Lambda/\lambda_{D,e} \geq 100$ and $\Lambda/\lambda_i \geq 100$ are predicative of ambipolar diffusion, and ratios of $\Lambda/\lambda_{D,e} \leq 1$ and $\Lambda/\lambda_i \geq 10$ are predicative of free diffusion. Results are also assessed in terms of normalized charge separation ($= |n_i - n_e|/n_i$), which measures local charge neutrality. For the purposes of this study, local charge neutrality is considered achieved when the normalized charge separation value is below 0.01 in a given cell.

4.1 Time Evolution of Ambipolar Diffusion

Ambipolar diffusion theory suggests time must elapse between the start of diffusion and the point when local charge neutrality is established everywhere. During this time the electric field described by Eq. 2 establishes itself the moment charge neutrality is violated, decaying as the plasma neutralizes itself, becoming zero when local charge neutrality is restored everywhere.

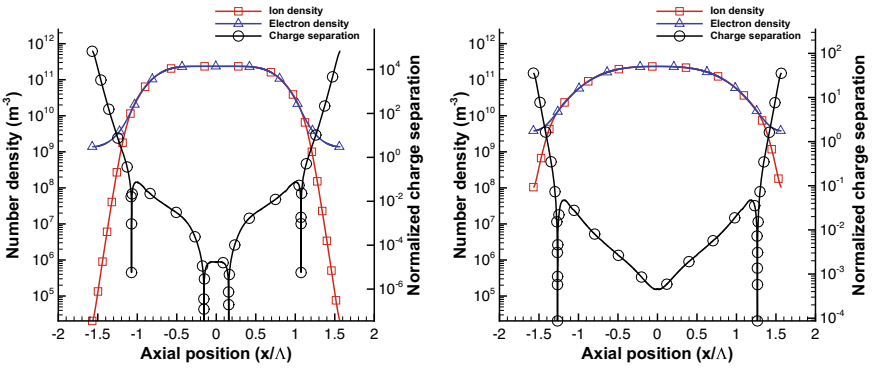

(a) $t = 2 \times 10^{-4}$ s $\approx 16\tau_{i,n} \approx 4283\tau_{e,n}$ (b) $t = 4 \times 10^{-4}$ s $\approx 32\tau_{i,n} \approx 8566\tau_{e,n}$

Fig. 1 Number density and normalized charge separation profiles during ambipolar diffusion at midpoint and end of simulation ($\Lambda/\lambda_i = 100$, $\Lambda/\lambda_{D,e} = 100$)

Figure 1 shows the time evolution of ion and electron number density and normalized charge separation profiles for a plasma undergoing ambipolar diffusion. The initial number densities of the background and ionized gas were $n_n = 6.12 \times 10^{20}$ m^{-3} and $n_i = n_e = 2.35 \times 10^{11}$ m^{-3}, corresponding to $\Lambda/\lambda_i = 100$ and $\Lambda/\lambda_{D,e} = 100$. It is evident that the rate at which local charge neutrality is achieved everywhere occurs on the order of tens of ion collision times and thousands of electron collision times. At the end of the simulation (Fig. 1b) local charge neutrality is approximately achieved everywhere except at the far boundaries of the simulation ($|x/\Lambda| > 1.25$). Thus, the ambipolar diffusion approximation would only be valid in this simulation at the given point in time for $|x/\Lambda| < 1.25$. Ultimately, unsteady simulations with processes that occur on time scales on the order of collision times should be mindful of the time dependence of ambipolar diffusion, especially when using the ambipolar diffusion approximation.

4.2 Electron Debye Length Versus the Mean Free Path

As previously discussed, the criterion of the electron Debye length being orders of magnitude smaller than the neutral mean free path is not inherent to the ambipolar diffusion derivation, nor is it consistent with the Phelps diffusion length criteria for ambipolar diffusion. One could alternatively take the limit as $\lambda_n \to \infty$, in which case the plasma is not collisional with neutrals, and the charged species are in the ion inertia regime.

This is confirmed with simulation results in Fig. 2a and b . A simulation case is set up with a Λ/λ_i ratio of 10,000 and a $\Lambda/\lambda_{D,e}$ ratio of 100, corresponding to $n_n = 6.12 \times 10^{22}$ m^{-3} and $n_i = n_e = 2.35 \times 10^{11}$ m^{-3}. The hard sphere collision

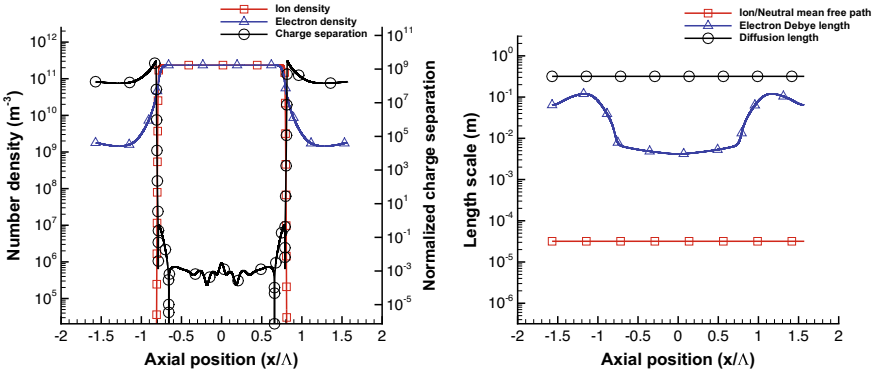

(a) Number density and charge separation profiles.

(b) Characteristic length scales for evaluating ambipolar diffusion.

Fig. 2 Number density (left) and characteristic length scale profiles (right) for ambipolar diffusion case where $\Lambda/\lambda_{D,e} = 100$, $\Lambda/\lambda_i = 10,000$, but $\lambda_{D,e} \gg \lambda_n$, at $t = 4 \times 10^{-5}$ s $\approx 323\tau_{i,n} \approx 37,418\tau_{e,n}$

model ensures the neutral mean free path is identical to the ion mean free path. This case violates the conventional criterion for the validity of the ambipolar diffusion approximation by two orders of magnitude. Figure 2a shows the number density and charge separation profiles, while Fig. 2b compares relevant length scales. At all points in the flow, $\lambda_{D,e} > \lambda_i$ by at least two orders of magnitude. However, at the points where $\Lambda/\lambda_{D,e} = 100$ ($|x/\Lambda| < 0.8$), local charge neutrality is achieved, indicating ambipolar diffusion is occurring. Thus, the Phelps criteria for charged species diffusion is a more accurate predictor of ambipolar diffusion than $\lambda_{D,e} \ll \lambda_n$.

4.3 Comparison with Kinetic Simulations Invoking the Ambipolar Diffusion Approximation

To assess the validity of the ambipolar diffusion approximation as it pertains to capturing actual ambipolar diffusion, an ambipolar diffusion case ($\Lambda/\lambda_i = 100$, $\Lambda/\lambda_{D,e} = 10,000, n_n = 6.12 \times 10^{20}$ m$^{-3}, n_i = n_e = 2.35 \times 10^{15}$) is run using both the DK solver and the Stochastic PArallel Rarefied-gas Time-accurate Analyzer (SPARTA) DSMC code [12], the latter of which implements the ambipolar diffusion approximation such that local charge neutrality is always guaranteed. Each SPARTA run follows the same simulation initialization conditions described in Sect. 3, with the exception of the grid points per Debye length and velocity space requirements. The SPARTA results shown are time averaged over 1000 runs, and use a particle weight of 10^6. By simulating only one physical grid cell in the perpendicular directions SPARTA can be run in 1D with three velocity dimensions. It is permissible to

compare 1D1V DK to 1D3V SPARTA if the flow does not have significant energy transfer between translational energy modes. This is confirmed by benchmarking a 1D1V and 1D3V DK simulation.

Figure 3a demonstrates that even for a plasma well into the ambipolar diffusion regime the approximation does not capture the same number density profiles as DK's direct electric field modeling. This is best understood by looking at the axial velocity profiles for both codes (Fig. 3b). When the ambipolar diffusion approximation is implemented the shared axial velocity profile for ions and electrons averages to zero across the domain, in part because no ambipolar particles have traveled past $|x/\Lambda| > 0.9$. Meanwhile, the DK ion and electron velocity profiles begin to linearly increase from $0.6 < |x/\Lambda| < 1.5$ before dropping off towards the boundaries of the domain. At the beginning of the simulation, the fastest electrons would have escaped from the center of the domain. Once the ambipolar field establishes itself, any electrons leaving the center of the domain will do so at the ambipolar diffusion rate with a proportional number of ions. However, the formation of an electric field will also allow the fastest ions to accelerate to the boundaries. Only a small portion of ions will do this, as the peak ion axial velocity corresponds with a number density of around 10^{10} m^{-3}. In spite of this, the ion acceleration mechanism allows just enough ions to catch up with electrons to allow the domain to achieve local charge neutrality and equalize charged species bulk velocities sooner.

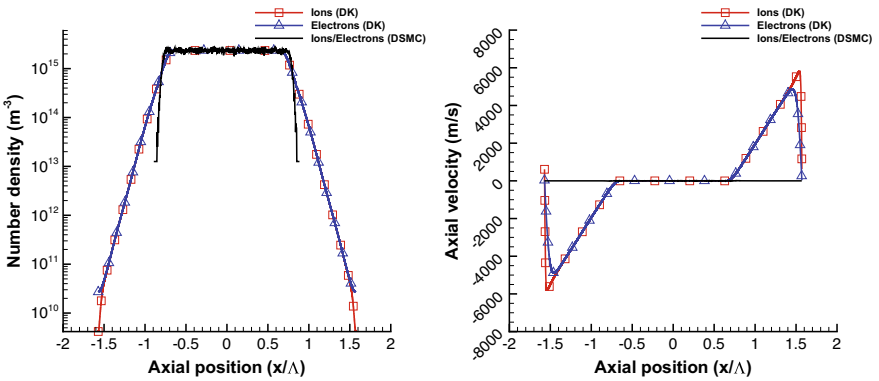

(a) Number density profiles for charged species and SPARTA ambipolar diffusion approximation plasma particles.

(b) Axial velocity profiles for DK charged species and DSMC ambipolar diffusion approximation plasma particles.

Fig. 3 Number density (left) and axial velocity profiles (right) for ambipolar diffusion approximation (DSMC) versus direct electric field modeling (DK) for ambipolar diffusion case with $(\Lambda/\lambda_i = 100, \Lambda/\lambda_{D,e} = 10,000)$ at $t = 5 \times 10^{-5}$ s $\approx 4\tau_{i,n} \approx 755\tau_{e,n}$.

5 Conclusions

Altogether, for a weakly ionized gas flow in the continuum regime, the ambipolar diffusion approximation can be justified if the following conditions hold:

1. The gas meets the three fundamental criteria for a plasma,
2. Charged particles primarily collide with neutrals rather than each other,
3. The ratio between the electron Debye length and the diffusion length scale (proportional to the characteristic length scale of the problem) has a ratio of at least $\Lambda/\lambda_{D,e} = 100$, and
4. The flow has had sufficient time for the ambipolar field to restore local charge neutrality (generally, on the order of many ion collision times).

These criteria do not guarantee results obtained with the ambipolar diffusion approximation will be identical to those from direct electric field modeling, particularly in unsteady flows. They also require confidence in plasma properties a priori, especially in the electron number density distributions used to calculate the Debye length, which are heavily influenced by electrostatic effects. Overall, these criteria represent a significant improvement from the conventional criterion used to justify the ambipolar diffusion approximation: $\lambda_{D,e} \ll \lambda_n$. During free diffusion, ions and electrons should be simulated as their own separate species. If the flow is within the transition regime between free and ambipolar diffusion direct electric field modeling is recommended as charged species diffusion dynamics cannot readily be predicted.

Whether the ambipolar diffusion approximation is valid under non-continuum conditions requires further investigation. Because the derivation of ambipolar diffusion begins with the fluid equations of motion, a breakdown of continuum behavior may result in irregularities in the plasma diffusion which might make the ambipolar diffusion approximation invalid. This has been investigated recently in hypersonic flows with particle-based methods [7, 9] and fluid codes [3] and will be investigated with the DK solver in upcoming studies.

References

1. Bird GA (1986) Direct simulation of typical AOTV entry flows. In: AIAA/ASME 4th joint thermophysics and heat transfer conference. AIAA, Boston. https://doi.org/10.2514/6.1986-1310
2. Bird GA (1994) Molecular gas dynamics and the direct simulation of gas flows. Clarendon Press, Oxford
3. Blanco A, Josyula E (2020) Numerical modeling of hypersonic weakly ionized external flowfields with Poisson's equation. AIAA J 58(8). https://doi.org/10.2514/1.J059307
4. Boyd ID (1997) Monte Carlo simulation of nonequilibrium flow in a low-power hydrogen arcjet. Phys Fluids 9:3086–3095. https://doi.org/10.1063/1.869474
5. Chan WR, Boyd ID (2022) Enabling direct kinetic simulation of dense plasma plume expansion for laser ablation plasma thrusters. J Electr Propuls 1(26). https://doi.org/10.1007/s44205-022-00030-x

6. Chen FF (2016) Introduction to plasma physics and controlled fusion, 3rd edn. Springer International Publishing Switzerland, Cham
7. Farbar ED, Boyd ID (2010) Modeling of the plasma generated in a rarefied hypersonic shock layer. Phys Fluids 22(10):106101. https://doi.org/10.1063/1.3500680
8. Hara K (2015) Development of grid-based direct kinetic method and hybrid kinetic-continuum modeling of hall thruster discharge plasmas. Dissertation, University of Michigan
9. Kaplan CR, Oran ES (2022) Analysis of the ambipolar diffusion approximation in hypersonic ionizing reentry flows. J Thermophys Heat Trans 36(3). https://doi.org/10.2514/1.T6416
10. Lee JH (1984) Basic governing equations for the flight regimes of aeroassisted orbital transfer vehicles. In: AIAA 19th thermophysics conference. AIAA, Snowmass. https://doi.org/10.2514/6.1984-1729
11. Phelps AV (1990) The diffusion of charged particles in collisional plasmas: free and ambipolar diffusion at low and moderate pressures. J Res Natl Inst Stand Technol 95(407):407–431. https://doi.org/10.6028/jres.095.035
12. Plimpton S, Moore S, Borner A, Stagg A, Koehler T, Torcyznski J, Gallis M (2019) Direct simulation Monte Carlo on petaflop supercomputers and beyond. Phys Fluids 31:086101. https://doi.org/10.1063/1.5108534

Open Access This chapter is licensed under the terms of the Creative Commons Attribution 4.0 International License (http://creativecommons.org/licenses/by/4.0/), which permits use, sharing, adaptation, distribution and reproduction in any medium or format, as long as you give appropriate credit to the original author(s) and the source, provide a link to the Creative Commons license and indicate if changes were made.

The images or other third party material in this chapter are included in the chapter's Creative Commons license, unless indicated otherwise in a credit line to the material. If material is not included in the chapter's Creative Commons license and your intended use is not permitted by statutory regulation or exceeds the permitted use, you will need to obtain permission directly from the copyright holder.

A Structure-Preserving Solver for Particle-Wave Interaction in Non-uniform Magnetized Plasmas

Kun Huang, Irene M. Gamba, and Chi-Wang Shu

Abstract We present a struture-preserving solver for particle-wave interaction in magnetized plasmas. The solver combines a conservative local discontinuous Galerkin (LDG) scheme for the interaction part with a trajectory averaging method for the Hamiltonian flow part. The proposed LDG scheme is an extension of the conservative scheme we developed in 2023. The trajectory averaging method significantly reduces computational cost by taking advantage of the multiscale feature of this system. By introducing a novel concept "trajectory bundle", we transform a continuous topological problem into a discrete graph theory problem. Numerical examples for a non-uniform magnetized plasma in an infinitely long symmetric cylinder is presented. It is verified that the connection-proportion algorithm allows to distinguish different trajectory bundles, and the proposed DG scheme rigorously preserves all the conservation laws.

Keywords Quasilinear theory · Discontinuous Galerkin method · Hamiltonian dynamics · Multiscale method

1 Introduction

The interaction between charged particles and waves is a critical aspect of plasma behavior, which occurs across multiple time scales. In order to simulate the waves within reasonable computational cost, waves are modeled as quasi-particles (plasmons) under WKB approximation [4], which have Hamiltonian equations of motion in the phase space. At the same time, their interaction with particles are modeled by the quasilinear theory [6, 10], which renders an additional collision-like operator: the quasilinear interaction operator.

K. Huang (✉) · I. M. Gamba
The University of Texas at Austin, Austin, TX, USA
e-mail: k_huang@utexas.edu

C.-W. Shu
Brown University, Providence, RI, USA

© The Author(s) 2026

M. Grabe et al. (eds.), *Rarefied Gas Dynamics*, Springer Aerospace Technology,
https://doi.org/10.1007/978-3-032-00094-1_66

As an approximation of the Vlasov-Maxwell system, our kinetic system of electrons and plasmons inherits the conservation properties, which relies on the delicate structure of the "collision" operators and the Poisson bracket. The goal of this paper is to develop numerical solvers that preserve the structure of the underlying physical systems.

The only precedent work on structure-preserving schemes for quasilinear theory is our paper [8] in 2023, where a continuous Galerkin method was adapted to discretize the diffusion operator for electrons. We generalize the idea and propose a novel discontinuous Galerkin version for quasilinear theory.

The trajectory-averaging technique [3] has been successful in tackling problems with simple advection field lines. For more complicated problems, there is the ray-tracing method [1], where sample trajectories are calculated with the Hamilton's equation, and numerical averaging is performed on these trajectories. However, such approach is expensive, not conservative, and not compatible with finite element or finite difference solvers. To tackle these problems, instead of discretizing the averaging operator directly, we propose a structure-preserving method based on the discretization of untraditional test spaces.

This paper is organized as follows. In Sect. 2 we describe the set up of the problem. After that we derive the weak form of trajectory-averaged equation and the connection-proportion algorithm in Sect. 3. The conservative LDG method for quasilinear theory will be introduced in Sect. 5. Section 6 contains the numerical results.

2 The Kinetic System for Particles and Plasmons

Consider an infinitely long cylinder $\Omega_x = (0, R) \times (0, 2\pi) \times \mathbb{R}_z$. At any given location $(r, \phi, z) \in \Omega_x$, there is a set of local orthonormal basis $(\mathbf{e}_z, \mathbf{e}_r, \mathbf{e}_\phi)$. Suppose a plasma is confined in the cylinder, embedded in a magnetic field along the z-axis, $\mathbf{B}(\mathbf{x}) = B(r)\mathbf{e}_z$.

We focus on the (z, ϕ)-symmetric case for simplicity, which means any function $g(\mathbf{x})$ depend only on r.

The momentum $\mathbf{p}$ of a particle at (r, ϕ, z) can be decomposed as $\mathbf{p} = p_z\mathbf{e}_z + p_r\mathbf{e}_\mathbf{r} + p_\phi\mathbf{e}_\phi \in \mathbb{R}^3_p$. Define $p_\parallel = \frac{\mathbf{B}}{|\mathbf{B}|} \cdot \mathbf{p}$ and $p_\perp = \left|\left(I - \frac{\mathbf{B}}{|\mathbf{B}|} \otimes \frac{\mathbf{B}}{|\mathbf{B}|}\right) \cdot \mathbf{p}\right|$. Then for highly magnetized plasma, averaging over the fast gyro-motion renders a particle probability density function independent of azimuthal angle φ, i.e. $f(\mathbf{p}, \mathbf{x}, t) = f(p_\parallel, p_\perp, r, t)$. The momentum $\mathbf{k}$ of a plasmon (the wave vector of a wave packet) can also be decomposed as $\mathbf{k} = k_z\mathbf{e}_z + k_r\mathbf{e}_\mathbf{r} + k_\phi\mathbf{e}_\phi \in \mathbb{R}^3_k$. Let us define $q_\phi = k_\phi \cdot r$, then (k_r, q_ϕ, k_z) and (r, ϕ, z) are a set of canonical coordinates. Given (z, ϕ)-symmetry, the plasmon probability density function can be written as $N(\mathbf{k}, \mathbf{x}, t) = N(k_r, q_\phi, k_z, r, t)$.

The following system governs the evolution of the particle and plasmon probability density functions:

$$\begin{cases} \partial_t f + v_z \partial_z f &= \nabla_p \cdot (D[N] \cdot \nabla_p f), \\ \partial_t N + \{\omega, N\} &= \Gamma[f] N. \end{cases} \tag{1}$$

The advection term $v_z \partial_z f$ comes from the gyro-averaged Vlasov equation, it vanishes since f does not depend on z. The Poisson bracket $\{\omega, N\} = \frac{\partial N}{\partial r}\frac{\partial \omega}{\partial k_r} - \frac{\partial \omega}{\partial r}\frac{\partial N}{\partial k_r}$ is a result of WKB approximation. Let us denote it as $\mathcal{T}N$, then obviously the operator $\mathcal{T}$ is anti-symmetric. The quasilinear diffusion term and the reaction term accounts for particle-plasmon interaction [4].

Testing the equations with $\varphi(\mathbf{p}, \mathbf{x})$ and $\eta(\mathbf{k}, \mathbf{x})$, we obtain the following weak form:

$$\iint_{px} \varphi \partial_t f + \iint_{kx} \eta \partial_t N = \iint_{kx} N \mathcal{T} \eta + \iiint_{pkx} (\eta \mathcal{L} E - \omega \mathcal{L} \varphi)\, \mathcal{L} f N \mathcal{B}, \tag{2}$$

where $\mathcal{E}(\mathbf{p})$ is the kinetic energy of a single particle,

$$\mathcal{E}(\mathbf{p}) = \gamma(\mathbf{p}) mc^2 = \sqrt{m^2 c^4 + p^2 c^2},$$

the directional differential operator $\mathcal{L}$ is defined as,

$$\mathcal{L} g := k_\parallel \frac{\partial E}{\partial p_\perp} \frac{p}{p_\perp} \frac{\partial g}{\partial p_\parallel} + \left(\omega - k_\parallel \frac{\partial E}{\partial p_\parallel}\right) \frac{p}{p_\perp} \frac{\partial g}{\partial p_\perp}, \tag{3}$$

and the emission/absorption kernel $\mathcal{B}$ reads,

$$\mathcal{B}(\mathbf{p}, \mathbf{k}, \mathbf{x}) := \sum_l \frac{1}{\omega^2(\mathbf{k}, \mathbf{x})} U_l(\mathbf{p}, \mathbf{k}, \mathbf{x}) \delta(\omega(\mathbf{k}, \mathbf{x}) - k_\parallel v_\parallel - l\omega_c(\mathbf{x})/\gamma(\mathbf{p})). \tag{4}$$

The dispersion relation $\omega(\mathbf{k}, \mathbf{x})$ is determined by the electron density $n_e(\mathbf{x})$. For details we refer the readers to the appendix of [8].

Theorem 1 *(unconditional conservation [8])*
If $f(\mathbf{p}, \mathbf{x}, t)$ and $N(\mathbf{k}, \mathbf{x}, t)$ solve Eq. (1) with emission/absorption kernel replaced by $\mathcal{B}_\varepsilon$, then for any $\mathcal{B}_\varepsilon$ we have the following conservation laws:

$$\begin{aligned} \partial_t \mathcal{M}_{tot} &= \partial_t \left((f, 1)_{px} + (N, 0)_{kx} \right) = 0, \\ \partial_t \mathcal{P}_{z,tot} &= \partial_t \left((f, p_z)_{px} + (N, k_z)_{kx} \right) = 0, \\ \partial_t \mathcal{E}_{tot} &= \partial_t \left((f, \mathcal{E})_{px} + (N, \omega)_{kx} \right) = 0. \end{aligned}$$

3 Trajectory Average

As can be observed in Eq. (1), there are three different time scales associated with the model, τ_{diff}, τ_{adv} and τ_{reac}. According to Kiramov and Breizman [9], the advection process is much faster than the other two, $\tau_{\text{adv}} \ll \tau_{\text{diff}} \sim \tau_{\text{reac}}$. In practice, particle-wave interaction is of interest, rather than plasmon advection. Hence it is reasonable to eliminate the Poisson bracket term through trajectory averaging.

Consider the Liouville-reaction equation

$$\frac{\partial N(k,x,t)}{\partial t} + \frac{1}{\varepsilon}\{N(k,x,t), H(k,x)\} = \Gamma(k,x,t)N(k,x,t). \tag{5}$$

We define the advection operator $\mathcal{T}$ as follows,

$$\mathcal{T}g := \nabla_k H \cdot \nabla_x g - \nabla_x H \cdot \nabla_k g. \tag{6}$$

Denoting the orthogonal projection from $L^2(\Omega_b)$ onto $L^2(\Omega_b) \cap \ker\mathcal{T}$ as $\mathcal{P}$, we have $\mathcal{P}u \in L^2(\Omega_b) \cap \ker\mathcal{T}$, and $(\mathcal{P}u, \eta)_{\Omega_b} = (u, \eta)_{\Omega_b}$ for any $\eta \in L^2(\Omega_b) \cap \ker\mathcal{T}$. According to [3], the lowest order approximation N_0 satisfies

$$\partial_t N_0 = \mathcal{P}(\Gamma N_0). \tag{7}$$

We call $\mathcal{P}$ the trajectorial averaging operator, and Eq. (7) is the averaged equation. The weak form of the averaged problem can be stated as follows:

Find an $N_0 \in L^2(\Omega_b) \cap \ker\mathcal{T}$ such that

$$(\partial_t N_0, \eta)_{\Omega_b} = (\Gamma N_0, \eta)_{\Omega_b}, \tag{8}$$

for any $\eta \in L^2(\Omega_b) \cap \ker\mathcal{T}$.

Since $\tau_{\text{adv}} \ll \tau_{\text{diff}}$, the diffusion equation for particle probability density function in (1) can be approximated with

$$\partial_t f = \nabla_p \cdot (D[N_0] \cdot \nabla_p f)$$

Testing the averaged system with $\varphi(\mathbf{p}, \mathbf{x}) \in \mathcal{G} = H^1(\mathbb{R}^3_p) \otimes L^2(\Omega_x)$ and $\eta(\mathbf{k}, \mathbf{x}) \in \mathcal{N} = \ker\mathcal{T} \cap L^2(\mathbb{R}^3_k \times \Omega_x)$ yields

$$\iint_{px} \varphi \partial_t f + \iint_{kx} \eta \partial_t N = \iiint_{pkx} (\eta\mathcal{L}E - \omega\mathcal{L}\varphi)\,\mathcal{L}f\,N\mathcal{B}, \tag{9}$$

where we have used N instead of N_0. It can be verified that the unconditional conservation property is preserved even after trajectorial average.

4 Trajectory Bundle: Definition and Construction

To discretize Eq. (9), it is necessary to construct a series of finite dimensional spaces approximating the test space $\ker\mathcal{T} \cap L^2(\mathbb{R}^3_k \times \Omega_x)$. Hence in this section we introduce the concept of trajectory bundle, and propose the connection-proportion algorithm to construct basis functions.

For details, we refer the readers to [7].

5 The Conservative Scheme Based on LDG Method

As has been proved in Theorem 1, the averaged system admits three conservation laws. In this section, we seek for a discretization that preserves all of them rigorously. The idea here is analogous to the one introduced in our previous work [8]: to replace some quantities with their projection in the test spaces. In what follows, we generalize the idea from continuous Galerkin method to local discontinuous Galerkin method.

As has been discussed in [2], the LDG weak form can also be written in bilinear form using discrete gradient operator ∇_h:

$$(\partial_t f, \varphi)_\Omega + (\nabla_h f, D \cdot \nabla_h \varphi)_\Omega = 0$$

The test space for particle probability density function, $\mathcal{G}_h$, consists of discontinuous piecewise polynomials. The test space for plasmon probability density function, $\mathcal{N}_h$, consists of indicator functions of trajectory bundles.

5.1 The Conservative Scheme

Recall the definition of directional differential operator

$$\mathcal{L}g := k_\parallel \frac{\partial E}{\partial p_\perp} \frac{p}{p_\perp} \frac{\partial g}{\partial p_\parallel} + \left(\omega - k_\parallel \frac{\partial E}{\partial p_\parallel}\right) \frac{p}{p_\perp} \frac{\partial g}{\partial p_\perp}.$$

We propose a discretized operator as follows,

$$\mathcal{L}_h g_h := k_{\parallel,h} \left(\partial_{\perp,h} E_h\right) \cdot \frac{p}{p_\perp} \left(\partial_{\parallel,h} g_h\right) + \left(\omega_h - k_{\parallel,h} \left(\partial_{\parallel,h} E_h\right)\right) \frac{p}{p_\perp} \left(\partial_{\perp,h} g_h\right), \quad (10)$$

where $k_{\parallel,h} := \Pi_{kx,h} k_\parallel$, $\omega_h := \Pi_{kx,h}\omega$, $E_h := \Pi_{px,h} E$, $\partial_{\parallel,h} g_h := \frac{\mathbf{B}}{|\mathbf{B}|} \cdot \nabla_{p,h} g_h$, $\partial_{\perp,h} g_h := \left|\left(I - \frac{\mathbf{B}}{|\mathbf{B}|} \otimes \frac{\mathbf{B}}{|\mathbf{B}|}\right) \cdot \nabla_{p,h} g_h\right|$, and the discrete gradient operator $\nabla_{p,h}$ is defined in [5].

Based on the above discrete operator $\mathcal{L}_h$, we propose an unconditionally conservative semi-discrete weak form [7].

Theorem 2 *If $f_h(t) \in \mathcal{G}_h$ and $N_h(t) \in \mathcal{N}_h$ satisfy that*

$$\iint\limits_{px} \varphi_h \partial_t f_h + \iint\limits_{kx} \eta_h \partial_t N_h = \iiint\limits_{pkx} N_h \mathcal{B}_\varepsilon \left(\eta_h \mathcal{L}_h E_h - \omega_h \mathcal{L}_h \varphi_h\right) \mathcal{L}_h f_h, \tag{11}$$

for any $\varphi_h(t) \in \mathcal{G}_h$ and $\eta_h(t) \in \mathcal{N}_h$, then we have discrete conservation laws:

$$\begin{aligned}
\partial_t \mathcal{M}_{tot}^h &:= \partial_t \left((f_h, 1)_{px} + (N_h, 0)_{kx}\right) = 0. \\
\partial_t \mathcal{P}_{z,tot}^h &:= \partial_t \left((f_h, \Pi_{px,h} p_z)_{px} + (N_h, \Pi_{kx,h} k_z)_{kx}\right) = O(e^{-L^2}), \\
\partial_t \mathcal{E}_{tot}^h &:= \partial_t \left((f_h, \Pi_{px,h} E)_{px} + (N_h, \Pi_{kx,h} \omega)_{kx}\right) = 0.
\end{aligned}$$

6 Numerical Results

Analogous to [8], only anomalous Doppler resonance with $l = 1$ is considered. For dispersion relation $\omega(\mathbf{k}, \mathbf{x})$ we take the lowest branch.

Consider a magnetized plasma with non-uniform electron density $n_e(r) = n_0 \left[1 - \left(\frac{r}{R_{max}}\right)^2\right]$, embedded in a uniform external magnetic field $\mathbf{B}(r) = B_0 \mathbf{e}_z$.

Analogous to [8], we only compute the "bump" part of electron probability density function $f(\mathbf{p}, \mathbf{x}, t)$, which takes the following initial configuration:

$$f(p_\parallel, p_\perp, r)\big|_{t=0} = \left[10^{-5} \frac{1}{\sqrt{\pi}} \exp\left(-\left(\frac{p_\parallel}{m_e c} - 20\right)^2 - \left(\frac{p_\perp}{m_e c}\right)^2\right)\right] \frac{n_0}{m_e^3 c^3} \left(\frac{1}{R_{max}}\right)^3.$$

Meanwhile, the plasmon probability density function $N(\mathbf{k}, \mathbf{x}, t)$ is initialized as follows:

$$N\left(r, k_r, q_\phi, k_z\right)\big|_{t=0} = 10^{-5} \frac{n_0 m c^2}{(\omega_0/c)^3} \frac{1}{\hbar \omega_0} \left(\frac{1}{R_{max}}\right)^3.$$

Trajectory bundles As shown in Fig. 1, the triangular partition of the (r, k_r)-domain is done by dividing every rectangular mesh into two. The connection-proportion algorithm successfully distinguishes different trajectory bundles in the inverse image of the same box(in this case, interval).

Electron pdf In the first row of Fig. 2 we show the evolution of electron probability density function $f(p_\parallel, p_\perp, r, t)$ at $r = \frac{31 R_{max}}{40}$. In the second row of Fig. 2 the electron probability density function at the same time point $t = 3 \times 10^6 \frac{1}{2\pi\omega_0}$ in different positions is presented.

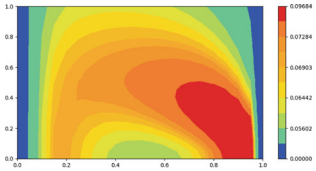

(a) $\omega(r, k_r; q_\phi, k_z)/\omega_0$ at $(q_\phi, k_z) = (\frac{9\omega_0}{80c}, \frac{9\omega_0 R_{max}}{80c})$

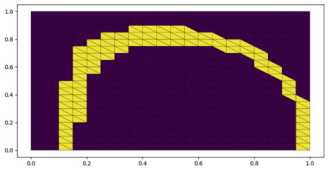

(b) The minimal triangle cover of S_{11}

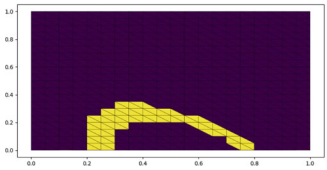

(c) The minimal triangle cover of S_{12}

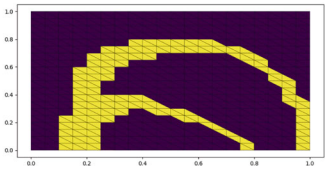

(d) The minimal triangle cover of S_{13}

Fig. 1 Trajectory bundles and their minimal triangle covers. The x-axis represents r/R_{max}, and the y-axis represents $k_r c/\omega_0$. Since the Hamiltonian is symmetric for $\pm k_r$, we only plot half of the domain. Note that S_{11} and S_{12} are two trajectory bundles generated by the same Hamiltonian range interval. And S_{13} is not a single strip because it contains a saddle point

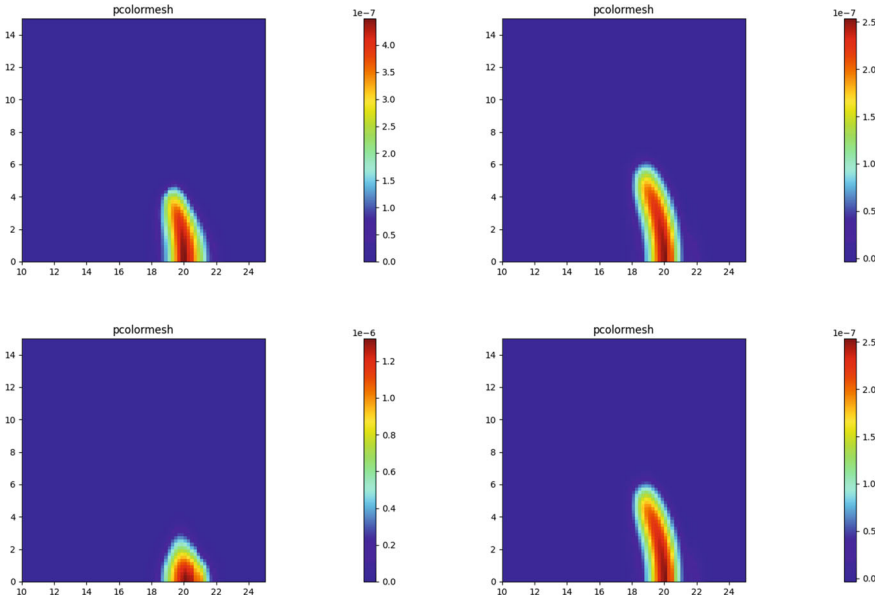

Fig. 2 Electron distribution

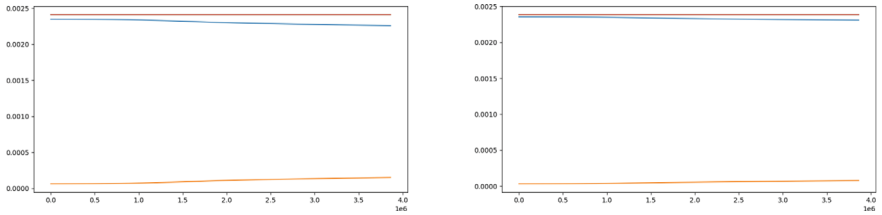

(a) Momentum evolution. (b) Energy evolution.

Fig. 3 Conservation laws

Conservation verification For the evolution of the electron-plasmon system momentum and energy, see Fig. 3. With $T_{max} = 3.86 \times 10^6 \frac{1}{2\pi\omega_0}$, we have the following relative errors: $e_{rel}(\mathcal{M}_{tot,h}) = 4.6 \times 10^{-16}$, $e_{rel}(\mathcal{P}_{\|,tot,h}) = 1.8 \times 10^{-14}$ and $e_{rel}(\mathcal{E}_{tot,h}) = 5.5 \times 10^{-16}$.

7 Conclusion

In this paper, we introduced a structure-preserving solver for particle-wave interaction in a cylinder with radially non-uniform plasma density. We preserve all the conservation laws during "collision" by adopting the unconditionally conservative weak form. For the fast periodic advection of plasmons in the phase space, we proposed a novel averaging method, which significantly reduces the computational cost without violating the Hamiltonian structure. All these properties have been verified by numerical experiments, where we observe different diffusion rate in different positions.

In the future, we plan to extend the solver for more sophisticated models, enabling the full-scale simulation of runaway electrons.

Acknowledgements The authors thank and gratefully acknowledge the support from the Oden Institute of Computational Engineering and Sciences and the University of Texas Austin. This project was supported by funding from NSF DMS: 2009736, NSF grant DMS-2309249 and DOE DE-SC0016283 project Simulation Center for Runaway Electron Avoidance and Mitigation.

References

1. Aleynikov P, Breizman B (2015) Stability analysis of runaway-driven waves in a tokamak. Nuclear Fusion 55(4):043014
2. Arnold DN, Brezzi F, Cockburn B, Marini LD (2002) Unified analysis of discontinuous galerkin methods for elliptic problems. SIAM J Numer Anal 39(5):1749–1779

3. Bostan M (2010) Transport equations with disparate advection fields. Application to the gyrokinetic models in plasma physics. J Differ Eq 249(7):1620–1663
4. Breizman BN, Aleynikov P, Hollmann EM, Lehnen M (2019) Physics of runaway electrons in tokamaks. Nuclear Fusion 59(8):083001
5. Di Pietro DA, Ern A (2011) Mathematical aspects of discontinuous Galerkin methods, vol 69. Springer Science & Business Media
6. Drummond W, Pines D (1962) Non-linear stability of plasma oscillations
7. Huang K (2023) A numerical and analytical study of kinetic models for particle-wave interaction in plasmas. Ph.D. thesis
8. Huang K, Abdelmalik M, Breizman B, Gamba IM (2023) A conservative galerkin solver for the quasilinear diffusion model in magnetized plasmas. J Comput Phys 488:112220
9. Kiramov D, Breizman B (2021) Reduced quasilinear treatment of energetic electron instabilities in nonuniform plasmas. In: APS division of plasma physics meeting abstracts, vol 2021, pp JP11–068
10. Vedenov A, Velikhov E, Sagdeev R (1961) Nonlinear oscillations of rarified plasma. Nuclear Fusion 1(2):82

Open Access This chapter is licensed under the terms of the Creative Commons Attribution 4.0 International License (http://creativecommons.org/licenses/by/4.0/), which permits use, sharing, adaptation, distribution and reproduction in any medium or format, as long as you give appropriate credit to the original author(s) and the source, provide a link to the Creative Commons license and indicate if changes were made.

The images or other third party material in this chapter are included in the chapter's Creative Commons license, unless indicated otherwise in a credit line to the material. If material is not included in the chapter's Creative Commons license and your intended use is not permitted by statutory regulation or exceeds the permitted use, you will need to obtain permission directly from the copyright holder.

Potential Fluctuations of Emissive Sheaths in Collisional Boundary Layer Plasmas Using a Kinetic Approach

Davut Vatansever and Deborah A. Levin

Abstract Emissive plasma sheaths are subject to various instabilities, including two-stream (TS) and self-spike (SS) oscillations, both of which play critical roles in the sheath dynamics. This study extends our previous work by examining the effects of these instabilities on potential field fluctuations and the electron velocity distribution functions (EVDFs) in boundary layer plasmas. Using a fully kinetic PIC-DSMC approach, we demonstrate that the TS instability induces strong oscillations in the sheath potential, exceeding the sheath potential by up to tenfold in large domains. In contrast, the SS instability produces sawtooth oscillations with instantaneous, non-amplifying disturbances. Additionally, the TS instability significantly alters the EVDFs, creating highly non-Maxwellian distributions, while the SS instability causes instantaneous shifts in the EVDF peaks during SS ejections.

1 Introduction

Emissive plasma sheaths are subject to various instabilities, including two-stream (TS) electron instability, self-spike (SS) oscillations, electrostatic instabilities, and gradient-driven instabilities. The TS instability arises in the presence of counter-streaming electron populations [3, 6]. It can be triggered by variations in the domain length, plasma density, electron temperature, or potential bias [7]. The SS instability occurs in the presence of significant charge-exchange (CEX) collisions within the sheath. These collisions lead to oscillations in the virtual cathode (VC), which manifest as spikes in the plasma sheath [1]. Our simulations demonstrate the occurrence of TS and SS instabilities, both independently and simultaneously. When a sufficiently long domain size (30 λ_D) with collisions is considered, interactions between the SS and TS instabilities are observed, where the latter dominates due to stronger

D. Vatansever (✉) · D. A. Levin
Department of Aerospace Engineering, University of Illinois Urbana-Champaign, Urbana, IL, USA
e-mail: davutv2@illinois.edu

D. A. Levin
e-mail: deblevin@illinois.edu

© The Author(s) 2026

M. Grabe et al. (eds.), *Rarefied Gas Dynamics*, Springer Aerospace Technology,
https://doi.org/10.1007/978-3-032-00094-1_67

and more frequent fluctuations. These interactions result in the weakening of the SS spikes due to strong fluctuations induced by the TS instability.

In our previous work [8], we explored the mechanisms behind the development of TS and SS instabilities, characterized the wave-number frequency spectrum of their oscillations, and analyzed the interaction between these two instabilities. In the present study, we focus on the effects of these instabilities on potential field fluctuations and electron velocity distribution functions (EVDFs), probed both inside and outside the VC region in a boundary layer plasma. This work is an extension to our results where we revealed that the TS instability induces significantly larger potential fluctuations compared to the SS instability (sawtooth oscillations), for which the fluctuations are instantaneous at spike times and not amplifying.

2 Numerical Method and Simulation Cases

1D3V simulations were conducted with our fully kinetic GPU-based solver, CHAOS [5]. CHAOS incorporates fully kinetic particle approaches, namely the Particle-In-Cell (PIC) and Direct Simulation Monte Carlo (DSMC) methods, which together allow for the self-consistent calculation of the electric field at each time step while accurately capturing collisions between heavy charged particles and neutrals. The PIC module determines the spatial distribution of the electric field by solving Poisson's equation,

$$\nabla^2 \phi = \frac{e(n_i - n_e - n_{ee})}{\epsilon_0} \tag{1}$$

$$E = -\nabla \phi \tag{2}$$

where ϕ is electric potential, ϵ is permittivity of free space in vacuum, e is elementary charge, E is electric field which accelerates charged species, n_i, n_e, and n_{ee} are number density of ions, plasma electrons and wall emitted electrons, respectively. The DSMC approach is used to model ion-neutral and neutral-neutral collisions in the presence of neutrals in addition to plasma. By coupling the DSMC and PIC modules, the solver simulates CEX collisions and analyzes their impact on the electric field. The presence of neutrals leads to significant alterations in the sheath structure, as CEX ions are generated and become trapped within the VC formed by strong electron emission from the wall.

Figure 1a and b illustrate the emissive sheath structure in a hypersonic boundary layer plasma and the corresponding computational setup. The near-wall region, spanning only tens of Debye lengths, is simulated by placing an electron-emitting wall at z = 0 and injecting plasma from z = L. The wall is biased at 0 V, with Dirichlet boundary conditions of 2V is applied at z = L.

A Maxwellian argon plasma with a temperature of 0.5 eV flows into the domain from z = L, into a vacuum for the collisionless cases and into a Maxwellian neutral

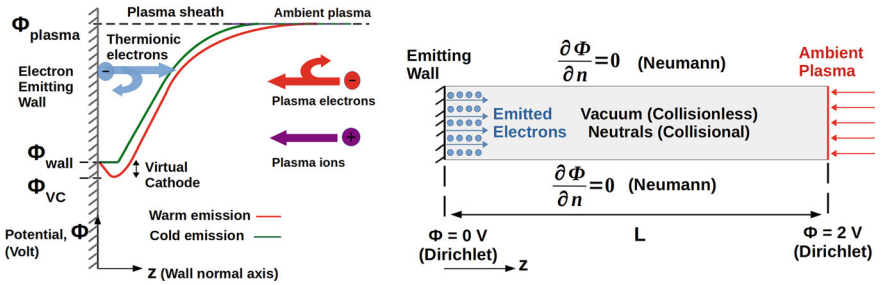

(a) A SCL emissive sheath structure. (b) Computational domain.

Fig. 1 Emissive sheath structure and computational setup for simulations

Table 1 Conditions for different sheath simulation cases

Case	Collisions	Domain length (mm)	Neutral density	Neutral temperature
1A	Off	$0.4 = 15\,\lambda_D$	–	–
2A	Off	$0.8 = 30\,\lambda_D$	–	–
3A	Off	$1.6 = 60\,\lambda_D$	–	–
1B	On	$0.4 = 15\,\lambda_D$	1×10^{19} m^{-3}	300 K
2B	On	$0.4 = 15\,\lambda_D$	1×10^{20} m^{-3}	300 K
3B	On	$0.4 = 15\,\lambda_D$	1×10^{20} m^{-3}	2000 K
2C	On	$0.8 = 30\,\lambda_D$	1×10^{20} m^{-3}	300 K

background for the collisional cases. Warm electrons, emitted from the wall at z = 0, are continuously injected with a half-Maxwellian distribution corresponding to a temperature of 0.17 eV. The plasma density is 8×10^{16} m^{-3}, with equal ion and electron densities. Plasma ions have a bulk speed of 8 km/s, equivalent to the ram speed of a hypersonic vehicle [2]. Wall-emitted electron density is set to ten times that of the plasma electrons to form a space-charge limited sheath [3], which includes the VC region as shown in Fig. 1a. The full descriptions of the PIC and DSMC methods implemented in CHAOS can be found in [4, 5], while the specific computational parameters used in this study are detailed in [8].

Seven plasma sheath cases, summarized in Table 1, were analyzed to study the effects of domain length, collisionality, neutral density, and temperature. The collisionless cases (1A, 2A, 3A) used domain lengths of 0.4, 0.8, and 1.6 mm to explore the impact of domain size on TS instabilities. The collisional cases (1B, 2B, 3B, 2C) included varying neutral densities of 10^{19} and 10^{20} m^{-3}, with neutral temperatures of 300 K (0.026 eV) and 2000 K (0.17 eV) for the high-density scenario. Cases 1B, 2B, and 3B focus on the shortest domain length (0.4 mm) to isolate SS instability from TS effects, while case 2C demonstrates their combined impact. The present study considers only ion-neutral collisions, as their mean free paths are significantly

shorter than those of other relevant collision processes, namely, Coulomb collisions and electron-neutral collisions, under the conditions investigated [8].

3 Potential Fluctuations Created by Two-Stream Instability

Large-amplitude plasma oscillations develop early in simulations when the domain size is sufficiently large to support long-wavelength disturbances, as in cases 2A and 3A. Figure 2 shows time snapshots of the velocity phase space of plasma and emitted electrons in case 3A, represented by red and blue dots, respectively. At 0.125 μs, plasma and emitted electron streams begin to occupy the domain and interact. A distinct shear layer forms between the emitted and plasma electrons, leading to disturbances in the plasma electron phase space. At initial times up to 0.175 μs, as seen from the top row, the mixing of the two populations is minimal, and their phase spaces remain largely separable.

By 0.5 μs, the two populations have fully mixed, as shown in the bottom-left frame of the figure. Beyond this time, large-amplitude plasma oscillations becomes apparent. The bottom row illustrates the continued evolution and mixing, with increasingly complex phase space structures emerging over time. These fluctuations in the phase space also generate large potential fluctuations, further amplifying the dynamic behavior of the sheath.

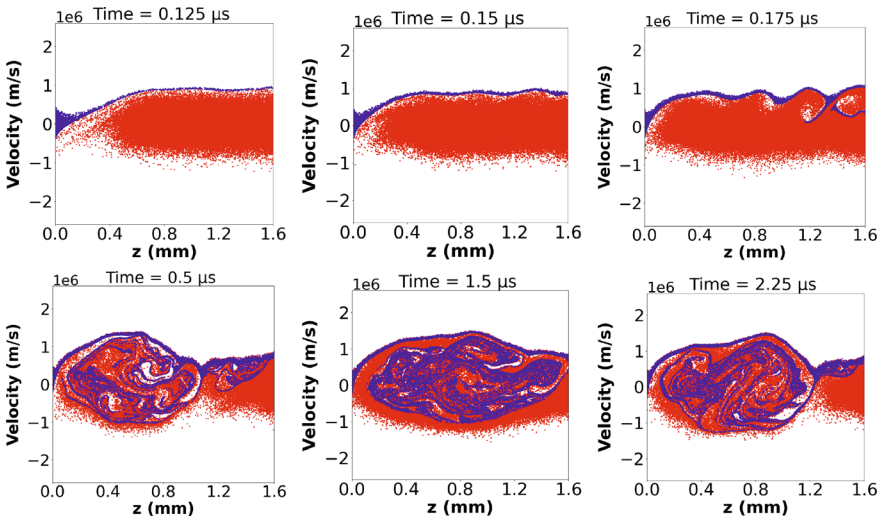

Fig. 2 Time snapshots of velocity phase spaces of plasma (red) and emitted (blue) electrons from 0.1 μs to 2.25 μs for Case 3A, where L = 60 λ_D

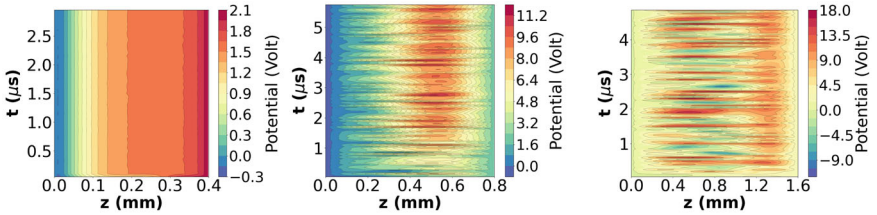

(a) Case 1A. (b) Case 2A. (c) Case 3A.

Fig. 3 Spatio-temporal fluctuations in electric potential field for the cases 1A (15 λ_D), 2A (30 λ_D), and 3A (60 λ_D). The case with the shortest domain length reaches a quasi-steady state. In contrast, strong periodic oscillations are observed for cases 2A and 3A

Figure 3 shows the time evolution of the spatial distribution of the electric potential field for the three collisionless cases simulated. Development of the TS instability with increased domain length causes spatio-temporal fluctuations in the electric potential. Note that for all the three cases, the wall is negatively biased at 0 V with respect to the plasma potential of 2 V. Case 1A with a 15 λ_D length domain is at quasi-steady state and does not exhibit temporal and spatial oscillations. As the length of the domain is increased from 15 λ_D to 30 λ_D, strong periodic oscillations can be observed in the downstream region, especially after 1 μs. In case 1A, the potential monotonically increases from the dip of the VC to the plasma boundary on the right hand side (from – 0.2 to 2 V). However, the development of the TS instability creates electron turbulences and disrupts the monotonically increasing profile observed in case 1A. For case 2A, the figure shows that the time-varying potential always remains above the plasma potential in the downstream between 0.4 mm $<$ z $<$ 0.8 mm. As the domain length is further increased, we start to see even stronger spatio-temporal fluctuations in the plasma field. Due to increased electron mixing in case 3A, even negative potential values can be observed in the downstream region. The strength of the oscillations is higher in this case with the plasma potential oscillating between – 10 and 18 V in comparison to the fluctuations between – 0.2 and 11 V in the case 2A. The presence of periodic structures can be observed in these two unstable cases. For example in case 3A, starting from 0.5 μs, nine different peaks can be observed in the z-t domain of the plasma potential. It is also noticeable that the potential fluctuations are weaker in the VC, z $<$ 0.03 mm, for both cases.

4 Potential Fluctuations Created by Self-spike Instability

In this section, we examine the impact of ion-neutral collisions on the plasma sheath potential fluctuations caused by the trapping of slow CEX ions within the VC. In our published work [8], we explained the detailed transient CEX entrapment and SS ejection processes. The periodic ejections of CEX ions from the VC induce sawtooth

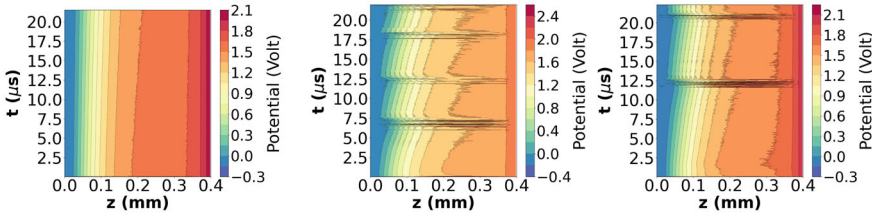

(a) Case 1B. (b) Case 2B. (c) Case 3B.

Fig. 4 Sawtooth fluctuations in electric potential field for the collisional cases 1B, 2B, and 3B

oscillations in the potential field, significantly influencing the sheath dynamics. The ejection of trapped ions from the VC occurs with different periodicities depending on the neutral temperature and density, leading to varying fluctuation patterns in the potential field.

Figure 4a shows that the potential field for case 1B exhibits no spikes due to its low collisionality, as the neutral density is an order of magnitude lower than in the other collisional cases. However, a subtle spatio-temporal gradient in the potential field can still be observed in case 1B compared to the collisionless case 1A (Fig. 3a). In contrast, sawtooth oscillations are clearly visible in the potential fields for cases 2B and 3B, as shown in Fig. 4b and c, respectively. These oscillations arise from the higher collisionality and increased CEX ion generation. In case 2B, the colder neutral temperature (300 K) results in slower CEX ion velocities, causing more ions to become trapped in the VC compared to case 3B, where the neutral temperature is 2,000 K. This difference in ion behavior produces distinct periodic spike patterns in the potential field, with spike periods of approximately 5 μs for case 2B and 8 μs for case 3B.

5 The Effect of Instabilities on EVDFs

First, we analyze the effect of the TS instability on the EVDFs. In general, fluctuations caused by the TS instability in the VC region are less significant than those observed in the region downstream of the VC. VC region is dominated by the more populous space charged thermionic electron causing the EVDF to largely reflect thermionic electron behavior. Hence, the EVDFs probed in the VC shows similar behavior for all cases, except during a SS time. However, in the region downstream of the VC where there is a large population of plasma electrons, the EVDFs can be seen to have large TS fluctuations even at earlier times.

The top row of Fig. 5 shows that at 0.1 μs there are two peaks in the EVDF for each case corresponding to thermionic and plasma electrons. As the time progresses to 1.5 μs, the EVDF of the short domain case 2B remains almost constant whereas additional peaks occur for the 30 λ_D cases of 2A and 2C. This is due to electron

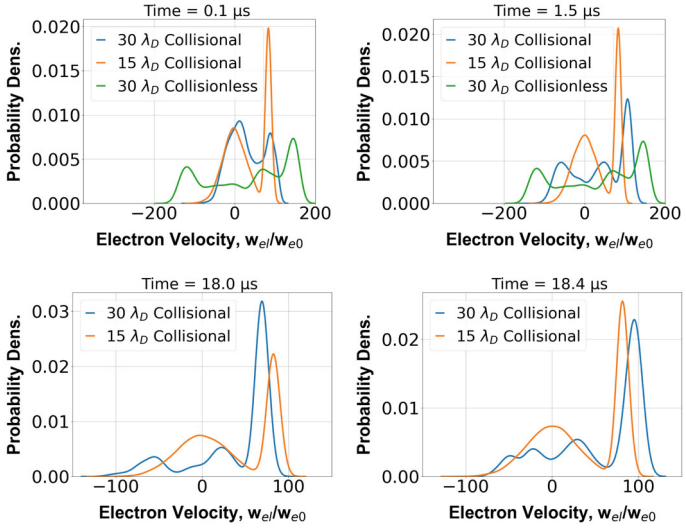

Fig. 5 Comparison of EVDFs in the downstream region of $0.3 < z < 0.4$ mm for long (30 λ_D) and short (15 λ_D) collisional (2C and 2B) and the long (30 λ_D) collisionless (2A) cases

mixing caused by the TS instability in the 30 λ_D cases. The top row of the figure shows that the EVDFs of the cases 2A and 2C become highly non-Maxwellian and their distributions differ from each other. However, it is difficult to attribute this difference to the CEX collisions and SS instability because the TS electron instability is more dominant in this region as well as the fact that in this region the ions are not trapped. At longer times, as seen from the bottom row of Fig. 5, the EVDF of case 2C shows highly non-Maxwellian distribution due to electron mixing process while that of case 2B has still a bimodal distribution.

Next, we present the effect of the SS instability by comparing the short domain cases 1A and 2B. The EVDFs from cases 1A and 2B for long times in both the VC (top row of Fig. 6) and downstream regions (bottom row of Fig. 6) are presented. In the VC region, the EVDFs of both cases look similar, with the difference that the EVDF of case 2B at 4μs starts to deviate from earlier times due to accumulation of trapped CEX ions in the VC. For times up to 4μs, EVDFs of cases 1A and 2B show similar bimodal distributions. In the VC, the peak of the EVDF differs due to the oscillations triggered by the SS for case 2B as shown in the top row of Fig. 6. Within the downstream region, despite maintaining a bimodal distribution, the EVDF of case 2B undergoes alterations in both peak widths and heights as shown in the bottom row of Fig. 6. These changes are observed specifically during the occurrence of a SS, with the most significant shift observed in the second peak, corresponding to emitted electrons.

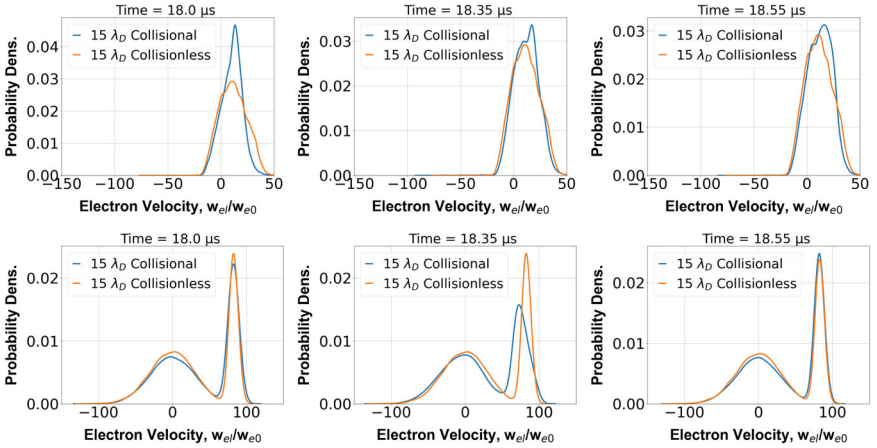

Fig. 6 Comparison of EVDFs during spike times. Top and bottom rows are in the VC and the downstream region of $0.3 < z < 0.4$ mm, respectively for the 15 λ_D length collisional (2B) versus collisionless (1A) cases

6 Conclusion

The plasmadynamics of an emitting electron wall for conditions similar to the near-wall region of a hypersonic boundary layer have been predicted using a fully kinetic PIC-DSMC approach. The TS instability in the sheath leads to stronger oscillations in the potential field, with fluctuations far exceeding the sheath potential. In sufficiently large plasma domains (60 λ_D), the potential in the sheath can oscillate up to 10 times the sheath potential, demonstrating the considerable influence of TS instability on sheath dynamics. For the SS instability, the potential field exhibits sawtooth oscillations, with disturbances occurring instantaneously and not resulting in amplified fluctuations following the SS ejection. We also show that both instabilities significantly impact the EVDFs: the TS instability results in highly non-Maxwellian distributions, while the SS instability causes instantaneous shifts in the EVDF peaks within the VC and bulk plasma regions during SS ejection.

Acknowledgements This project is supported by the Lockheed Martin Corporation, LMC Reference : S20-002-001/UIUC Grant C0764. We thank NCSA for providing us with the computational resources on Delta petascale computing facility.

References

1. Campanell MD, Umansky MV (2017) Improved understanding of the hot cathode current modes and mode transitions. Plasma Sources Sci Technol 26(12):124002. https://doi.org/10.1088/1361-6595/aa97a9

2. Hanquist KM, Hara K, Boyd ID (2017) Detailed modeling of electron emission for transpiration cooling of hypersonic vehicles. J Appl Phys 121(5):053302
3. Hara K, Hanquist K (2018) Test cases for grid-based direct kinetic modeling of plasma flows. Plasma Sources Sci Technol 27(6):065004. https://doi.org/10.1088/1361-6595/aac6b9
4. Jambunathan R, Levin DA (2017) Advanced parallelization strategies using hybrid MPI-CUDA octree DSMC method for modeling flow through porous media. Comput Fluids 149:70–87
5. Jambunathan R, Levin DA (2018) Chaos: an octree-based PIC-DSMC code for modeling of electron kinetic properties in a plasma plume using MPI-CUDA parallelization. J Comput Phys 373:571–604
6. Sydorenko D, Smolyakov A, Kaganovich I, Raitses Y (2007) Effects of non-maxwellian electron velocity distribution function on two-stream instability in low-pressure discharges. Phys Plasmas 14(1):013508. https://doi.org/10.1063/1.2435315
7. Thorne KS, Blandford RD (2017) Modern classical physics: optics, fluids, plasmas, elasticity, relativity, and statistical physics. Princeton University Press, New Jersey
8. Vatansever D, Nuwal N, Levin DA (2024) Numerical investigations of spatiotemporal dynamics of space-charge limited collisional sheaths. Phys Plasmas 31(9):093508. https://doi.org/10.1063/5.0216487

Open Access This chapter is licensed under the terms of the Creative Commons Attribution 4.0 International License (http://creativecommons.org/licenses/by/4.0/), which permits use, sharing, adaptation, distribution and reproduction in any medium or format, as long as you give appropriate credit to the original author(s) and the source, provide a link to the Creative Commons license and indicate if changes were made.

The images or other third party material in this chapter are included in the chapter's Creative Commons license, unless indicated otherwise in a credit line to the material. If material is not included in the chapter's Creative Commons license and your intended use is not permitted by statutory regulation or exceeds the permitted use, you will need to obtain permission directly from the copyright holder.

Challenges Using Rarefied Atmospheric Gases as Propellant for an RAM-EP System

Jana Zorn, Ole Forchheim, Kristof Holste, and Peter J. Klar

Abstract Many challenges have to be faced in order to develop an air-breathing electric propulsion system using a radio frequency ion thruster (RIT). The underlying assumptions of gas-surface-interactions for DSMC simulations of the intake give a wide spread of results in operating points available for the thruster. Thus, it is necessary to replicate the VLEO conditions experimentally in the future. Furthermore, precise experimental characterization of the propulsion system using atmospheric propellants is essential for mission success, although this also presents significant challenges. The background pressure of the test facility can cause an overestimation of the measured atomic-to-molecular ratio by a factor of 10. The sputtering of the beam dump can cause a back-streaming of carbon particles to the thruster of approx. 3.4×10^{13} particles/(s mA). Moreover, the reactive propellant causes significant material degradation of all materials in direct contact with the plasma.

Keywords ABEP · RAM-EP · Challenges · RIT · RF-neutralizer · Air · Air-breathing

1 Introduction

Air-breathing electric propulsion systems (ABEP, or RAM-EP) are receiving considerable attention recently. They shall provide a cheap and sustainable tool for long-term missions in the very low earth orbit (VLEO). An intake system collects the residual atmospheric gas present in VLEO. Since density and composition of the atmosphere serving as propellant strongly fluctuate with orbit and sun activity it is very challenging to design an intake that always guarantees a sufficient mass flow to the thruster and thus a constant drag compensation [1]. As a consequence of the significant fluctuations in atmospheric conditions, the thruster must be capable of maintaining optimal performance across a wide range of mass flows while operating within a constrained power envelope, ensuring consistent thrust delivery [1].

J. Zorn (✉) · O. Forchheim · K. Holste · P. J. Klar
Justus Liebig University, Giessen, Germany
e-mail: jana.zorn@physik.uni-giessen.de

© The Author(s) 2026

M. Grabe et al. (eds.), *Rarefied Gas Dynamics*, Springer Aerospace Technology,
https://doi.org/10.1007/978-3-032-00094-1_68

Thus, the thruster system must be characterized with high precision for all possible conditions. However, achieving this required precision in terrestrial experimental environments is a significant challenge. For example, the various chemical interactions and sputtering processes between materials that are in direct contact with the atmospheric plasma can change the performance significantly. Furthermore, charge exchange processes and other facility effects impact the experimental data and can cause unreliable results.

2 Intake Design

Designing a functional intake system to collect enough residual gas for the propulsion system is quite challenging due to the strong fluctuations of the atmospheric conditions. An important unknown is the gas-surface interaction (GSI) between the intake material and the residual gas at a velocity of approximately 8 km/s. Especially the interaction between atomic oxygen and surface material of the intake is not well investigated yet. Atomic oxygen can get physically adsorbed or react chemically and thus change the surface significantly, resulting in varying GSI (diffuse, specular, or Cercignani-Lampis-Lord (CLL) model). The scattering process is significantly influenced by the material, surface smoothness, projectile type, velocity and angle of incidence [9]. It primarily determines the performance for a chosen configuration of the intake system, as can be seen in the results of a DSMC simulation in Fig. 1. As experimentally shown, the scattering of an atomic oxygen beam with 8 km/s hitting various materials is most likely described with the CLL model [8]. Most importantly, scattering processes of atomic oxygen and molecular nitrogen with intake materials and their surfaces must be studied under VLEO conditions, in order to develop a reliable intake system. None of the attempts reported so far have been able to meet all VLEO requirements [1]. The beam typically consists of ions instead of neutrals in most terrestrial approaches [5, 11]. The replication of atmospheric conditions in a laboratory setting to accurately investigate the GSI remains a major challenge.

3 Propulsion System

A further crucial, yet demanding aspect of an ABEP system is the propulsion system itself, which is primarily composed of a thruster and a neutralizer. Both devices need to be well characterized in order to deliver thrusts larger than the drag acting on the satellite. However, testing light molecular propellants leads to several challenges that need to be considered for obtaining reliable results.

Experimental setup: Several diagnostics are installed in the test facility “Obelix” (Fig. 2). The vacuum chamber has a volume of 4800 L and is equipped with one turbomolecular pump and one cryogenic pump. A base pressure in the low 10^{-7} mbar range

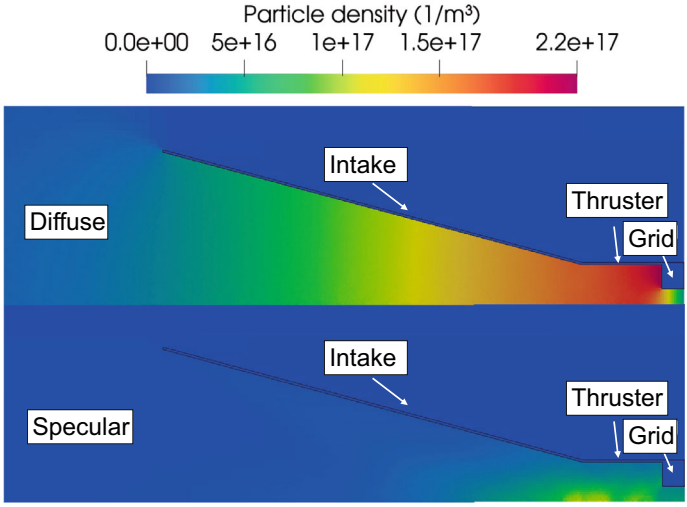

Fig. 1 Intake simulation assuming two different gas-surface interactions (GSI)

can be reached, enabling a pressure during the experiments in the mid 10^{-6} mbar range. At the end of the chamber a mass spectrometry setup is installed consisting of a double-focusing electromagnet. A Faraday cup at the end of the magnet is used for ion detection. Two additional turbo-molecular pumps with a total pumping speed of 66 L/s are attached to the mass spectrometry setup. A RIT-10 with a 10 cm diameter discharge vessel and a three grid system was employed as thruster. A radio frequency neutralizer (RFN) is employed in addition to the RIT-10. A graphite plate with an orifice of 6 mm and a thickness of 1 mm is used as ion catcher. A second ion catcher is positioned in close proximity to the gas inlet, consisting of nine thin tungsten wires (0.3 mm in diameter) of varying lengths. To measure beam dump sputtering a witness plate is installed in the facility. It is placed 31.5 cm behind the thrusters exit plane and 13.5 cm away from the center line of the beam. It consists of a 94 mm^2 small piece of silicon wafer, from which 26 mm^2 are covered with tape. This yields a total collection area of 68 mm^2, where sputtered material may be deposited.

Influence of background pressure: When performing any kind of beam diagnostics it is of great importance to keep the pressure inside the test facility as low as possible to avoid misleading results [3, 13]. To study the effect of the background pressure on the beam composition, the thruster was kept stable in one operating point at 8 sccm nitrogen and 100 mA of beam current. The pressure in the main facility was kept constant in the medium 10^{-6} mbar range during the experiment, while the background pressure in the beam line towards the detector (see Fig. 2) was changed between 5×10^{-6} mbar and 7×10^{-5} mbar. The measured atomic-to-molecular ratio for different background pressures at the detector behind the analyzing magnet is shown in Fig. 3. The atomic-to-molecular ratio increases by almost a decade

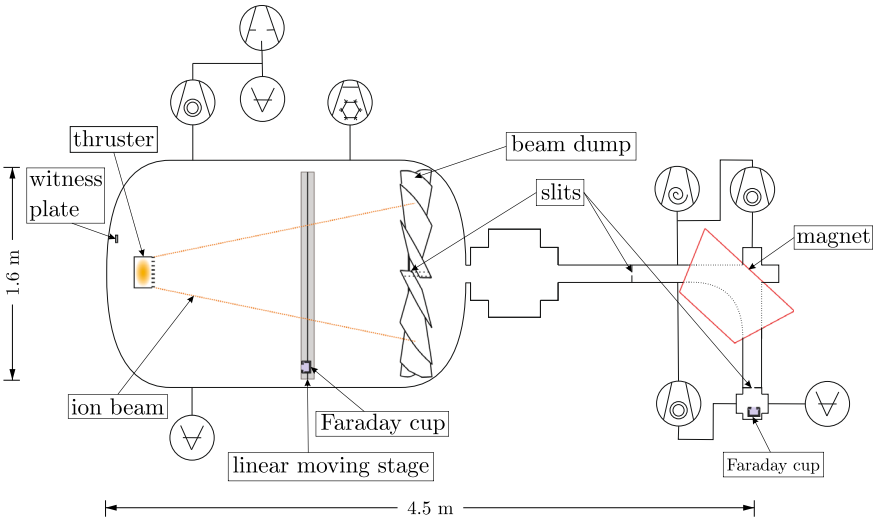

Fig. 2 Schematic drawing of the test facility "Obelix" with diagnostics.

from 0.3 % to 2.5 % going to higher pressures. The cause of this phenomenon can be attributed to scatter and charge exchange processes along the beam path. An elevated background pressure increases the likelihood of these processes occurring. Thus, a correction of the measured data is needed when limited in pumping speed. The correction for scattering and CEX losses can be calculated using

$$\left(\frac{N^+}{N_2^+}\right)_{corr} = \frac{1}{1 - n \cdot \sigma \cdot z} \cdot \left(\frac{N^+}{N_2^+}\right)_{measure} . \tag{1}$$

n is the neutral particle density in the detector line or facility, σ is the cross-section for CEX ($2.48 \times 10^{-19}\,m^2$ for N_2^+-N_2 and $5.44 \times 10^{-20}\,m^2$ for N^+-N_2 [10]) or scattering between the different species and z is the length of the detector line or

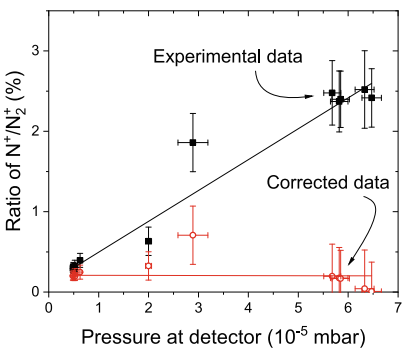

Fig. 3 Measured ratio of N^+/N_2^+ in the plume for different pressures (black squares) and corrected values (red circles)

the facility. For simplicity, the cross sections for scattering are for neutral atoms and molecules. Furthermore, it was assumed that the background gas only consists of molecular nitrogen. The cross section for scattering was calculated with the geometrical cross section using the molecular and atomic radii ($4.16 \times 10^{-19}\,m^2$ for N_2-N_2 and $2.01 \times 10^{-19}\,m^2$ for N-N_2) [2, 4].

The corrected data tends towards a constant ratio, in this case 0.22 % for all background pressures. The deviation of the corrected and the measured data increases strongly when increasing the pressure in the region of the detector. A linear fit to the deviation, followed by calculation of the pressure for a deviation of 0 %, yields a result of 2.7×10^{-6} mbar. Thus, at pressures below 3×10^{-6} mbar, the beam composition measured at the end of the beam line agrees with that right after the grid, i.e., scattering and CEX along the beam path are negligible. Nevertheless, a correction of the measured data, independent of the diagnostics, will be necessary at higher pressures. Both CEX and collisions must be taken into account for the correction, as both have a non-negligible impact on the data reliability.

Beam dump sputtering: Another challenge for precisely characterizing an EP thruster using atmospheric propellants are increased sputtering effects inside the facility that can disturb or falsify measurements. Mostly graphite beam dumps are used at the end of test chambers to reduce sputtering effects by ion beams. However, since the energy threshold for sputtering is very low for all materials when sputtered by oxygen or nitrogen (maximum threshold is 52 eV for C [7]) there is a significant amount of back-streaming of sputtered material towards the thruster, the diagnostics, and the pumps, as was already demonstrated for xenon as propellant [6]. Back-streaming conductive material towards the thruster can cause a conductive layer inside the discharge vessel. Thus, a fraction of the power used for driving the rf coil of the RIT will be lost in this thin layer due to eddy current losses and will not be available to generate and excite the plasma. The efficiency will be significantly reduced, contingent on layer thickness.

To measure the back-streaming flux of graphite particles towards the thruster a small piece of silicon wafer is used, as shown in Fig. 2. The RIT-10 was used for a total of 55 h working at different operating points with both gases and an extraction voltage on the first grid of 1400 V, extracting beam currents between 10 and 150 mA. After the test, the layer thickness on the witness plate was measured and investigated with SEM and EDX. The layer thickness was determined to 77 nm and a very smooth surface layer has formed, with only some minor defects. The EDX measurement yields several elements in the deposited layer. Most of the found elements was silicon from the wafer (68 %), but also a lot of carbon from the beam dump (19 %), some oxygen (5 %) and also some iron from the facility (2 %) and alumina from the diagnostics (1 %). To calculate the back-streaming flux to the thruster some simplifications are made. To derive the particle number on the witness plate, a face-centered unit cell of the sputtered material (closed pacing of spheres) was assumed. With the radius of a carbon atom (70 pm) [2], the volume of the unit cell was calculated to $V_{\text{unitcell}} = 7.8 \times 10^{-21}\,mm^3$. The probe volume, consisting of the open area times the layer thickness, is $V_{\text{probe}} = 5.2 \times 10^{-3}\,mm^3$. Assuming 4 atoms per unit cell, the

number of particles on the probe was calculated to $N_{\text{probe}} = 2.7 \times 10^{18}$. The sputter yield for oxygen atoms at 1400 eV on a carbon target is $Y_{\text{oxygen}} = 0.69$, for nitrogen it is $Y_{\text{nitrogen}} = 0.63$ [7]. A mean sputter yield of $Y_{\text{mean}} = 0.66$ is assumed. Taking into account the total duration of the experiment and all the beam currents extracted, it can be calculated that $N_{\text{ext}} = 1.3 \times 10^{23}$ particles hit the beam dump. Thus, a total of $N_{\text{sputter}} = 8.7 \times 10^{22}$ sputtered carbon particles leaving the beam dump. To calculate the theoretical number on the sample, the angle Θ between the surface normal and the sample and the solid angle $\mathrm{d}\Omega$ are required. In a very simplified calculation, it is also assumed that all incident particles hit a very small surface element of the beam dump at normal incident. Thus, the divergence of the beam and CEX processes, as well as collisions with the background gas, are neglected. Θ can be determined via the tangent of the distances of the sample to the beam dump to $\Theta = 17\,^{\circ}$. With the Lambert's cosine law,

$$N_{\text{theo}} = N_{\text{sputter}} \cos(\Theta) \frac{A_{\text{witness}}}{l^2}, \tag{2}$$

where l is the distance between the probe and the center of the beam dump, the theoretical particle density on the witness plate can be calculated to $N_{\text{theo}} = 5.7 \times 10^{18}$ particles on the witness plate.

The difference of a factor two between the calculated particle number from the measurement and the calculated particle number from the theoretical estimation can be explained by all the simplifications made. Nevertheless, it shows that this simple theoretical estimate at least can be used to determine the correct order of magnitude of the back-streaming of carbon atoms from the beam dump forwards the thruster. Subsequently the anticipated particle flux onto the thruster can be calculated using $\Theta = 0\,^{\circ}$. Thus, a particle flux of 3.4×10^{15} particles/s from the beam dump back to the thruster is obtained. If we now consider that the average extracted particle flux from the thruster in the experiment was 6.4×10^{17} particles/s, it indicates that 0.5 % of the extracted particle flux returns to the thruster as sputtered carbon atoms. The dependence between extracted current and back-sputtering carbon to the thruster is shown in Fig. 4 for oxygen as well as nitrogen. Due to the higher sputter yield the back-streaming for oxygen is slightly larger than for nitrogen. Up to 3.4×10^{13} carbon particles/(s mA) are deposited onto the thruster.

Material durability: The materials of the thruster and neutralizer, which are in direct contact with the plasma, are also exposed to corrosive and erosive effects. The ion catcher material inside an RF neutralizer can experience significantly erosion effects in the presence of an elevated electron temperature [12]. The ion catcher is negatively biased to actively attract ions so that an equal amount of negative charges can be extracted through the orifice. The choice of ion catcher material is crucial for the lifetime of the ABEP system. Tungsten and carbon have the highest sputter threshold for nitrogen and oxygen. Consequently, both materials were subjected to testing within the RF neutralizer under these very challenging conditions imposed by oxygen and nitrogen. After testing the neutralizer at different operating points for 13 h using oxygen and 8.5 h using nitrogen, the catcher materials were subjected to a

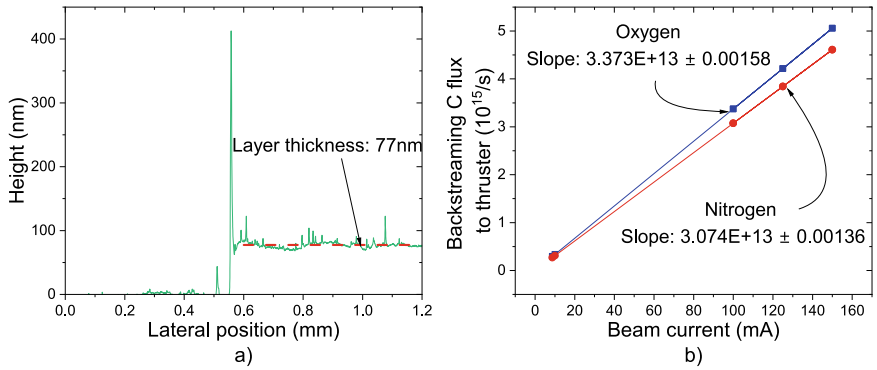

Fig. 4 Layer thickness of the back sputtered graphite. Calculated back-streaming of the sputtered beam dump to the thruster for oxygen and nitrogen

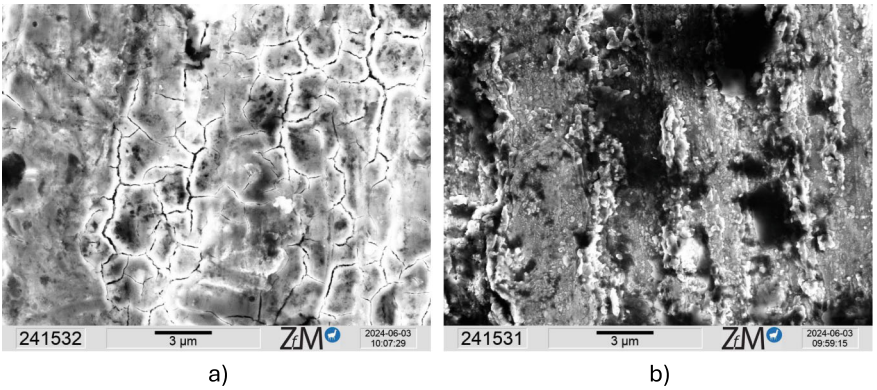

Fig. 5 SEM images of tungsten wires **a** pristine state, **b** after use in O_2 plasma

series of evaluations utilizing SEM and EDX. It is evident that both materials experienced significant damage as a result of exposure to oxygen and nitrogen plasma. The surface of both materials has undergone a significant degree of roughening following the exposure period, with tungsten exhibiting a particularly pronounced alteration (Fig. 5). A large amount of tungsten was found on the graphite plate, on both the SEM and EDX measurements. In addition, carbon was found on the tungsten wires. This indicates a high sputter rate of both materials during the experiments, which leads to the assumption of a high electron temperature of the plasma inside the RF neutralizer in combination with the varying negative catcher potential. Furthermore, non-conductive layers were found on the surface of the tungsten wires, indicating a tungsten-oxide layer that formed during the experiment. This non-conductive oxide layer leads to a smaller effective catcher area, leading to smaller extraction currents for the same operating point. These material issues need to be solved in order to guarantee quasi-neutrality on the satellite.

4 Conclusion

The design of the intake is of critical importance, as its configuration is contingent upon the poorly understood GSI that are present in VLEO. On-ground experiments are inevitable to accurately validate intake simulations. To accurately measure the performance of the thruster system, regardless of whether it is the neutralizer or the thruster, the background pressure of the test facility must be below 3×10^{-6} mbar to get reliable and accurate results. Due to the low sputter thresholds for atmospheric gases, the back-streaming of carbon onto the thruster with approximately 0.5 % of the extracted beam current is a huge challenge. Conductive layers form in the discharge vessel and disturb the inductive power coupling between rf-coil and plasma. Furthermore, sputtering and degradation of materials in direct contact with the plasma (e.g. grids or ion catcher) can shorten the mission lifetime.

References

1. Andreussi T, Ferrato E, Giannetti V (2022) A review of air-breathing electric propulsion: from mission studies to technology verification. J Electr Propuls 1(1)
2. Cordero B, Gómez V, Platero-Prats AE, Revés M, Echeverría J, Cremades E, Barragán F, Alvarez S (2008) Covalent radii revisited. Dalton Trans 21:2832
3. Désangles V, Packan D, Jarrige J, Peterschmitt S, Dietz P, Scharmann S, Holste K, Klar PJ (2023) ECRA thruster advances: 30 W and 200 W prototypes latest performances. J Electr Propuls 2(1)
4. Ismail AF (2015) Gas separation membranes. Springer International Publishing AG, Cham (description based on publisher supplied metadata and other sources)
5. Jorge P, Magin T, Hubin A, Le Quang D (2022) Modeling and simulation of VKI's new low density facility
6. Lim G, Tran H, Levin DA, Chew HB, Nishii K (2024) Kinetic simulation of carbon sputtering by a gridded ion thruster with a molecular dynamics based model. In: Proceedings of the 38th international electric propulsion conference
7. Matsunami N, Yamamura Y, Itikawa Y, Itoh N, Kazumata Y, Miyagawa S, Morita K, Shimizu R, Tawara H (1984) Energy dependence of the ion-induced sputtering yields of monatomic solids. Atomic Data Nuclear Data Tables 31(1):1–80
8. Minton TK, Schwartzentruber TE, Xu C (2021) On the utility of coated POSS-polyimides for vehicles in very low earth orbit. ACS Appl Mater Interf 13(43):51673–51684
9. Murray VJ, Pilinski MD, Smoll EJ, Qian M, Minton TK, Madzunkov SM, Darrach MR (2017) Gas-surface scattering dynamics applied to concentration of gases for mass spectrometry in tenuous atmospheres. J Phys Chem C 121(14):7903–7922
10. Phelps AV (1991) Cross sections and swarm coefficients for nitrogen ions and neutrals in N2 and argon ions and neutrals in Ar for energies from 0.1 eV to 10 keV. J Phys Chem Refer Data 20(3):557–573
11. Rafalskyi D, Dudin S (2024) RF plasma flow generator for LEO environment simulation: use cases. In: IEPC-2024-337, international electric propulsion conference (IEPC), Toulouse, France

12. Tisaev M, Karadag B, Ferrato E, Andreussi T, Lucca Fabris A (2024) Development and standalone testing of the air-breathing Microwave Plasma CAThode (AMPCAT). Acta Astronaut 214:722–736
13. Walker MLR, Victor AL, Hofer RR, Gallimore AD (2005) Effect of backpressure on ion current density measurements in hall thruster plumes. J Propuls Power 21(3):408–415

Open Access This chapter is licensed under the terms of the Creative Commons Attribution 4.0 International License (http://creativecommons.org/licenses/by/4.0/), which permits use, sharing, adaptation, distribution and reproduction in any medium or format, as long as you give appropriate credit to the original author(s) and the source, provide a link to the Creative Commons license and indicate if changes were made.

The images or other third party material in this chapter are included in the chapter's Creative Commons license, unless indicated otherwise in a credit line to the material. If material is not included in the chapter's Creative Commons license and your intended use is not permitted by statutory regulation or exceeds the permitted use, you will need to obtain permission directly from the copyright holder.

Astronomical Line Polarization Through Gas Transport

Boy Lankhaar

Abstract Magnetic fields are critical to the dynamics of the interstellar medium (ISM), influencing star formation and interstellar gas dynamics. This paper explores a novel way to probe magnetic fields through molecular line polarization mechanism, that is based on the experimentally well-established Senftleben-Beenakker (SB) effect. In molecular line polarization through SB effects, gaseous transport processes such as viscous strain and thermal gradients, cause molecules to align through directional collisions, subsequently polarizing their emission lines. This polarization mechanism differs from the Goldreich-Kylafis (GK) effect, as it is not dependent on optical depth nor non-thermal excitation. We derive a theoretical framework to model molecular alignment due to the SB effect. We discuss the applicability of SB polarization as a tool to trace magnetic fields in turbulent media and accretion disks.

1 Introduction

Magnetic fields permeate the interstellar medium, shaping astrophysical dynamics. This work focuses on molecular interstellar media, that exist in gas condensations with densities of 100 to 10^9 cm^{-3}, and temperatures ranging from 10 to 1000 Kelvin. Although ionization fractions are low, collisional coupling transfers magnetic influence to neutral gas, significantly affecting dynamics, as magnetic energy can rival or exceed turbulent and thermal energy densities. Thus, measuring magnetic fields in molecular media is crucial for a comprehensive understanding of interstellar processes.

Magnetic fields in molecular media can be indicated through the observation of molecular line polarization. Molecular line emission is polarized to degrees of some per cents and is observable in the strongest emission lines. The origin of molecular line polarization is commonly attributed to the Goldreich-Kylafis (GK) effect [7]. The GK effect explains this polarization as arising from molecular excitation in an

B. Lankhaar (✉)
Department of Space, Earth and Environment, Onsala Space Observatory, Chalmers University of Technology, Onsala, Sweden
e-mail: lankhaar@chalmers.se

© The Author(s) 2026

M. Grabe et al. (eds.), *Rarefied Gas Dynamics*, Springer Aerospace Technology,
https://doi.org/10.1007/978-3-032-00094-1_69

anisotropic medium, where the anisotropic radiation field aligns molecules. Molecular alignment is initially oriented in the direction of the radiation field anisotropy, but due to the precession of the molecule around the magnetic field, the alignment is re-oriented to the magnetic field direction. When magnetic precession is faster than other molecular interactions, emission polarizes parallel or perpendicular to the magnetic field. The GK effect is effective at near-unity optical depth and low gas densities, when radiative excitation dominates over collisions. The GK effect has been leveraged to trace magnetic fields towards (high-mass) star-forming regions, protoplanetary disks, the circumstellar envelopes of evolved stars, and molecular clouds in external galaxies.

Molecular alignment and subsequent line polarization can be induced not only by radiative processes but also by collisions [16, 25]. This study explores additional conditions under which directional collisions induce molecular alignment in an interstellar gas. To this end, we consider the experimentally well-established and characterized Senftleben-Beenakker (SB) effect [3, 23]. In the SB effect, fluids, that are under the influence of a magnetic field, acquire anisotropic transport properties. The anisotropies in the transport processes are the consequence of the molecular constituents of the fluid aligning along the transport direction, through directional collisions between particles that have anisotropic potential. The magnetic field impacts this process, as particles also precess around it. If this precession is fast compared to the collision time, then the alignment will be re-oriented to the magnetic field. In this way, molecular alignment along the magnetic field direction is retained, while it is effectively quenched in other cases. The resulting anisotropic transport coefficients, that are a function of the magnetic field strength divided by the pressure (i.e., the magnetic precession frequency divided by the collision frequency), have been well-characterized through experimental means for hydrodynamical transport tensors such as the viscosity tensor [13], and the thermal conductivity tensor [12], for a wide variety of molecules (for a full review, see [4, 21]). While tensor-anisotropies under magnetic fields is interesting from a fluid-dynamical perspective, their measurements have also served as experimental benchmarks for the testing of collisional modeling, specifically their dependence on the (anisotropic) intermolecular potential energy surfaces [10]. The large body of experimental and theoretical literature on the SB effect has been condensed in the monographs of Ref. [21].

Given the low densities of interstellar gas, where magnetic precession rates typically exceed collision rates [17], SB effects should be prevalent. Effectively, this means that under the influence of gaseous viscous strains, or thermal gradients, the molecular constituents of the gas should acquire alignment, leading to the polarization of their spectral lines. This paper investigates the conditions under which SB effects significantly and detectably polarize molecular emission. Molecular emission polarized through SB effects provides for a robust polarization mechanism that, in contrast to the GK effect, is not dependent on line optical depth, and does not require non-thermal excitation of the molecules. The molecular line polarization due to SB effects can be used as a robust tracer of the ambient interstellar magnetic field. In addition, it may also be possible to relate the line polarization due to SB effects to fluid dynamical properties of interstellar gases that cannot be measured otherwise.

This paper is built up as follows. In Sect. 2 we review the theory of alignment and polarization of molecules and their spectral lines. In Sect. 3, we discuss astrophysical processes conducive to SB effects and identify regions in the interstellar medium where anisotropic transport phenomena lead to significantly polarized line emission. Section 4 highlights potential limitations and model deficiencies. We conclude in Sect. 5.

2 Polarization and Alignment Due to the SB Effect

Due to the Senftleben-Beenakker (SB) effect, gas transport coefficients, of e.g. thermal transport or viscous strain, become anisotropic under the influence a magnetic field. The anisotropic transport properties are the result of alignment manifesting in the molecular constituents. Therefore, it is implicit in the theory of the SB effect, that a fluid also becomes birefringent under the effect of a directional flow. Leveraging this insight, Hess [8, 9] discussed the possibility to characterize the SB effect through experimental polarization observations, and in-so-doing derived the proper kinetic theory, starting from the Waldmann-Snider equations, of the alignment of molecules under directional flows.

We briefly revise concepts from the description of quantum molecular alignment, that are commonly applied to transfer of polarized line radiation in astrophysical gases. We assume that a molecule, with eigenstates of definite (total) angular momentum, j, precesses fast around a magnetic field, $\boldsymbol{B}$, which determines its symmetry axis: its eigenstates can be accurately described by the total angular momentum and its projection onto the magnetic field direction, $|jm\rangle$. We describe the molecular population in terms of its irreducible density matrix operator elements, $\hat{\rho}_{jk} = \sum_m \left[C^{j\ j\ k}_{m\ -m\ 0} \right]^2 |jm\rangle \langle jm|$, where the symbol $C^{j\ j\ k}_{m\ -m\ 0}$ is a Clebsch-Gordan coefficient. The rank of the irreducible tensor element, k, runs from 0 to $2j$. The $k = 0$ element is related to the total population of the quantum state j, while for $k > 0$, the elements of k which are even are commonly referred to as alignment elements, and those for which k is odd are referred to as the orientation elements. We note the expectation value of irreducible density matrix operator as $\rho_{jk} = \langle \hat{\rho}_{jk} \rangle$. The relative alignment and orientation of a specific quantum level we denote by $\sigma_{jk} = \rho_{jk}/\rho_{j0}$. Alignment is present in a population of molecules if their magnetic sublevels are populated unequally, but symmetrically, for levels with equal absolute projection, $|m|$. Orientation is present in a population of molecules if there is an imbalance between the population of magnetic sublevels of equal absolute projection $|m|$. Both alignment and orientation can be produced through collisions, yet in gaseous transport, alignment elements are more potently excited and accordingly have more effect on the transport properties [21]. Thus in the following, we set population elements, ρ_{jk}, of uneven k to zero: our molecules are aligned but not oriented.

We now discuss the transfer of radiation through an aligned molecular medium. We describe the propagation of radiation, with spectral energy flux density, $I_\nu(\hat{k})$ at

frequency ν, in the direction $\hat{k}$. Since alignment of the molecules is with respect to the magnetic field direction, it is most advantageous to denote the transfer of radiation in the two polarization modes parallel and perpendicular to the magnetic field rejection onto the propagation direction, $\hat{e}_\parallel$ and $\hat{e}_\perp = \hat{k} \times \hat{e}_\parallel$. For brevity, we denote these $I_\parallel$ and $I_\perp$, dropping in the notation the dependence on frequency and direction. We are interested in the production of polarization, $p_l = [I_\parallel - I_\perp]/[I_\parallel + I_\perp]$, by the molecular medium. We consider the transfer of radiation at radio-to-millimeter frequencies, where radiation scattering is negligible, and astronomical observations of molecules are commonly made. In the optically thin limit, the polarization fraction of a transition between quantum states $j \to j-1$, that characterizes astrophysically common diatomic molecules, can be related to the degree of molecular alignment, and tends to [16, 19], $p_l \simeq -\frac{3}{4\sqrt{5}}\sqrt{\frac{(j+1)(2j+3)}{j(2j-1)}}\sigma_{j2}\ \sin^2\theta$, where $\cos\theta = \hat{k}\cdot\hat{b}$ is the projection of the radiation direction onto the magnetic field direction.

Reference [9] modeled the population of magnetic sublevels within a level j, which he denotes $N_{jm} = \langle |jm\rangle \langle jm| \rangle$, under the influence of a viscous strain. We restate equation (22) of Ref. [9] in terms of the relative alignment of the molecular quantum level, under the influence of a viscous strain $\sigma_{j2} = \sqrt{\frac{6j(j+1)}{(2j-1)(2j+3)}}\left[\frac{\eta}{p_0}\frac{\omega_{T\eta}}{\omega_\eta}\left(\hat{b}\cdot\overline{\nabla \boldsymbol{v}^T}\hat{b}\right)\right]$, where η and p_0 are the dynamical viscosity and pressure, and $\overline{\nabla \boldsymbol{v}^T}$ is the traceless symmetric part of the strain-rate tensor. The ratio $\omega_{T\eta}/\omega_\eta$ is a measure for the anisotropy of the interaction potential of the molecular collision complex. We can now derive the expected linear polarization fraction of an optically thin $j \to j-1$ transition, that is the result of the viscous strain in the gas that it traces, $p_l^\eta = -\frac{3}{4}\sqrt{\frac{6}{5}}\frac{j+1}{2j-1}\left[\frac{\eta}{p_0}\frac{\omega_{T\eta}}{\omega_\eta}\left(\hat{b}\cdot\overline{\nabla \boldsymbol{v}^T}\hat{b}\right)\right]\sin^2\theta$. In this way, we have related the polarization degree of line radiation that emerges from astrophysical gas, to the viscous strain in the direction of the magnetic field that this gas is under.

3 Astrophysical Conditions Leading to Viscous Polarization

Viscous dissipation of MHD turbulence. Turbulence is ubiquitous in the interstellar medium, and spans eight orders of magnitude from its driving scale to the viscous scale, where dissipation occurs. Given the complexity of turbulence, we take an order-of-magnitude approach to estimate its effects on molecular alignment and polarization. To estimate the polarization fraction due to turbulent strains, we focus on dissipation at the viscous scale, as at these scales, the internal states of the gaseous particles become excited. The dynamical viscosity scales as $\eta \sim \rho c_\mathrm{s} \ell_\mathrm{mfp}$, with the gas density, ρ, the sound velocity c_s and the mean-free-path of the molecular gas constituents, ℓ_mfp. The pressure scales as $p_0 \sim \rho c_\mathrm{s}^2$. Thus, the fraction $\frac{\eta}{p_0} \sim \frac{\ell_\mathrm{mfp}}{c_\mathrm{s}}$. Now, we specialize the viscous strain term, $\hat{b}\cdot\overline{\nabla \boldsymbol{v}^T}\hat{b}$, to a turbulent medium. At first glance, one would expect this term to average out to 0 in the case of isotropic turbulence; after all, the directional strain-rate of circular eddies averages to zero. However,

it is well established that turbulence in the interstellar medium is magnetized, and therefore is anisotropic. Eddies are elongated in the direction along the magnetic field, $\ell_\parallel > \ell_\perp$, and their relative elongation increases going to lower scales. While the precise scaling relations are still under debate, a common result is the scaling of $\ell_\parallel \sim \ell_\perp^{2/3} L_{\rm inj}$ [2]. Thus, with such elongated eddies, the highest rate-of-strain, and thus the strongest alignment, is expected perpendicular to the magnetic field direction: $\hat{b} \cdot \overline{\nabla \boldsymbol{v}^T} \hat{b} \simeq -\frac{1}{2}\frac{v_\eta}{\ell_\eta}$, where v_η and ℓ_η are the expected velocity and dimension at the viscous scale. We estimate this fraction by order-of-magnitude. We assume that turbulence in the interstellar medium follows roughly two scaling regimes: above the sonic scale, turbulence follows a Burgers scaling, while below the sonic scale, we assume that turbulence follows a Kolmogorov scaling [22]. Adopting these scalings and extrapolating to the sonic scale, we find that the strain at the viscous scale can be expressed as $\frac{v_\eta}{\ell_\eta} \sim \frac{[\ell_\eta/\ell_{\rm s}]^{1/3} c_{\rm s}}{\ell_{\rm mfp}^{3/4} \ell_{\rm s}^{1/4}} \sim c_s [\ell_{\rm mfp} \ell_{\rm s}]^{-1/2}$. Now we can proceed to make an estimate for the polarization fraction that is due to anisotropic turbulent viscous dissipation. First for a general $j \to j-1$, transition, we find $p_l^{\eta,{\rm turb}} \sim \frac{3}{8}\sqrt{\frac{6}{5}}\frac{j+1}{2j-1}\frac{\omega_{T\eta}}{\omega_\eta}\sqrt{\frac{\ell_{\rm mfp}}{\ell_{\rm s}}}$. Now, specializing in $j = 1$, adopting $\omega_{\eta T}/\omega_\eta \sim 0.1$ [9], and using typical values from Ref. [22]: $\ell_{\rm mfp} \sim 10^{13}$ cm and $\ell_{\rm s} \sim 10^{17}$ cm, we obtain $p_l^{\eta,{\rm turb}} \sim 0.1\%$. Since $p_l^{\eta,{\rm turb}} \propto \ell_{\rm mfp}^{1/2}$, denser regions with shorter mean free paths should exhibit greater angular momentum polarization. Notably, such regions are also more influenced by gravitational forces, which can further enhance directional alignment, as we will explore in the next section.

In principle, all constituents of the interstellar medium should be impacted by turbulent angular momentum polarization, and exhibit polarization degrees of the order 0.1%. However, modern telescopes are sensitive to these low degrees of polarization only for those species that are associated with brightest emission lines, such as CO. We expect this polarization mechanism to be dominant when molecular lines are thermally excited, at densities above the critical density, when collisional transitions occur frequently with respect to the Einstein A-coefficient of the transition under investigation. For subthermally excited molecules, alternative polarization effects such as through the GK effect [7] likely dominate.

Viscous dissipation in the α-disk. The α-disk model was introduced by Ref. [24] as a theoretical model of an accretion disk around a compact object. In the α-disk, the transport of angular momentum, thus facilitating accretion, is due to so-called turbulent viscosity. Whereas for regular microscopic kinematic viscosity, $\nu \sim c_s \ell_{\rm mfp}$, turbulence can enhance this viscosity, when describing global processes that do not resolve the eddy-like motions that cause strains on smaller scales. In an accretion disk, the effective turbulent kinematic viscosity is thus parameterized according to its typical velocities and dimensions, as $\nu = \alpha c_s H$, where H is the disk scale height and $\alpha \leq 1$.

We restate the estimate of the polarization fraction due to viscous strain, putting in the proper relations according to α-disk theory of a thin accretion disk. For the ratio between the viscosity and the pressure, we put $\eta/p_0 \sim \nu/c_s \sim \alpha H/c_s$. Furthermore,

in a thin disk, we have $H \sim c_s/\Omega_K$, where $\Omega_K = \sqrt{GM/R^3}$ is the Keplerian rate of rotation at radial distance R, around a compact object of mass M (G is the gravitational constant). We let the velocity field be fully Keplerian: $\left(\hat{b} \cdot \overline{\nabla \boldsymbol{v}^T} \hat{b}\right) \sim \Omega_K$. Then, the line polarization fraction of a $j \rightarrow j-1$ transition due to viscous strain in an α-disk is, $p_l^\alpha \sim -\frac{3}{4}\sqrt{\frac{6}{5}}\frac{j+1}{2j-1}\frac{\omega_{T\eta}}{\omega_\eta}\alpha$. This leaves us with a rather simple relation between the α-parameter, that is a proxy for the disk activity, and the polarization fraction for molecular lines excited in them. For a typical molecule possessing a dipole, we have $\omega_{\eta T}/\omega_\eta \sim 0.1$ for collisions with its main collision partner H_2. Typical estimates place α in the range $\sim 10^{-2} - 0.6$ [1]. Thus, for a $1 \rightarrow 0$ transition, we have $p_l^\alpha = 1.6\alpha$. For the most active accretion disks, $p_l^\alpha = 10\%$, while typical disks of $\alpha \sim 0.1$ yield polarization fractions $p_l^\alpha \sim 0.2\%$.

Protoplanetary disks. A protoplanetary disk forms around a low-mass protostar at the late stages of its formation. The physical conditions, dynamics, evolution and chemistry of the disk determine the environment where planets form. While α-disk prescriptions were popular in early modeling of protoplanetary disks, it is now believed that accretion processes in protoplanetary disks are mainly due to the launching of magnetically driven winds [20], even though the magnetic fields that would drive such winds have not been directly measured [15, 27]. The low levels of turbulence that have been observed towards a variety of protoplanetary disks [5] put stringent upper limits on the $\alpha \lesssim 10^{-2}$, making viscosity subdominant as an agent of angular momentum transport. Concurrently, it also puts an upper limit on the predicted angular momentum polarization due to viscous strain in an alpha disk, and constrains $p_l^\alpha \lesssim 0.1\%$. There have been deep observations to probe the polarized emission from protoplanetary disk molecules, which have yielded marginal detections of the polarized emission at the level of some percents for ^{12}CO and its main isotopologue ^{13}CO [26]. If real, such high polarization fractions cannot be the product of the angular momentum polarization due to SB effects, but instead are likely due to GK effects [17, 18].

Active Galactic Nuclei (AGN). Accretion disks around AGN are crucial for feeding supermassive black holes and influencing galaxy evolution. As an example of an AGN disk, we turn to the closeby active galaxy NGC 1068. While it has been attempted to fit the accretion disk of NGC 1068 to the mold of an α-disk, the α-disk model proved inconsistent as it implied strong gravitational instabilities. In an attempt to supersede the simple α-disk prescription, models that include gas clumpiness are favored [14]. At any rate, high-resolution ALMA observations show intricate dynamics towards the nuclear region of NGC 1068, with a flip in rotation direction in the inner disk [11]. Such dynamics are associated with very high degrees of shearing, that should be reflected in the angular momentum polarization of the molecular constituents. The site of the rotation flip should be associated with high polarization degrees of several per cents due to SB polarization in the thermal lines. SB polarization through gaseous transport should be dominant in dense gas where GK polarization is quenched through

collisions. In this way, resolved polarization observations of thermal lines would offer a unique view of the magnetic fields of in the highly dynamic nuclear gas.

NGC 1068 belongs to a class of active galaxies that hosts strong water megamaser emissions. NGC 1068 is the first galaxy where water megamasers have been found to have polarized emission [6], which has lead to interesting constraints on the accretion dynamics in the innermost regions and its relation to magnetic fields. Water masers should be polarized to degrees $p_l^{\mathrm{H_2O}} \sim 3\% \left[\frac{\alpha}{0.1}\right] \left[\frac{\omega_{\eta T}/\omega_\eta}{0.1}\right] \left[\frac{\tau_{\mathrm{m}}}{10}\right]$, adopting representative values for α and $\omega_{\eta T}/\omega_\eta$ and the maser optical depth, τ_{m}. This mechanism of polarization is about as effective as through anisotropic pumping [19].

4 Model Assumptions and Parameters

We examined molecular alignment in astrophysical transport processes and its observability through polarized molecular line emission. Molecular alignment is a prerequisite for the Senftleben-Beenakker (SB) effect, where anisotropic transport coefficients arise under a magnetic field. This effect is well understood both experimentally and theoretically, emerging naturally from the Boltzmann transport equations when applied to rotating molecules. The specialization of these equations to rotational states, known as the Waldmann-Snider equations, requires assumptions for solvability. Typically, a near-equilibrium molecular distribution is assumed, with first-order corrections accounting for gas strains and thermal gradients. Anisotropic transport effects arise when molecular rotation interacts with a magnetic field, but the equilibrium assumption weakens as the Knudsen number increases. Experiments have validated SB effects, particularly by measuring anisotropic transport coefficients at moderately low Knudsen numbers [12, 13]. Reference [9] introduced polarization spectroscopy as a tool for characterizing SB effects, laying the theoretical foundation that this work builds upon. The degree of polarization can be linked to the Knudsen number: $\frac{\eta}{p_0}\bar{\nabla}\boldsymbol{v}^T \sim \mathcal{M}\frac{\ell_{\mathrm{mfp}}}{L} \sim \mathcal{M}$ Kn. The moderate polarization fractions that we predict puts Kn $\lesssim 1$, supporting the validity of our approach. However, since SB effects emerge at viscous scales, direct observations are beyond current telescope capabilities, and our estimates rely on extrapolation. If an observational experiment can be set up that pristinely traces SB polarization in a spectral line, this would yield a direct probing of gas motions at viscous scales.

Another key quantity in polarization estimates is the ratio $\omega_{\eta T}/\omega_\eta$, which strongly depends on the molecular species. Although the interstellar medium (ISM) is composed almost entirely of H2, its symmetric structure and high rotational constant make it difficult to observe. Radio astronomers therefore rely on tracer species like CO (with typical abundances of $\sim 10^{-4}$) to characterize the molecular ISM. This means that when considering the ratio $\omega_{\eta T}/\omega_\eta$, the relevant collision-complex is the one between the tracer species and H_2. While collisions between ISM molecules and H_2 are under active and ongoing investigation, the properties that are commonly extracted from these collision complexes are the state-to-state collisional transition

rate coefficients. While the collision-complex anisotropy is an extremely relevant variable to these calculations, it's representation in the $\omega_{\eta T}/\omega_{\eta}$ factor is not commonly extracted and reported from the calculations. As such, no modern theoretical constraints on $\omega_{\eta T}/\omega_{\eta}$ for different ISM species exist. Similarly, experimental efforts have not been directed to constrain the transport properties of different molecules embedded in H_2 gases, as experimentalists have directed most of their attention to pure gases [21]. This leaves the ratio $\omega_{\eta T}/\omega_{\eta}$ largely unconstrained.

5 Conclusion

We have introduced a novel mechanism for molecular line polarization in astrophysical environments, through the theoretically and experimentally well established Senftleben-Beenakker (SB) effect. SB effects show that molecules that constitute a gas that is under viscous strains or thermal gradients, align themselves along the direction of gaseous transport. In environments such as interstellar media, due to the presence of magnetic fields, alignment is re-oriented to the magnetic field, and thus spectral emission from aligned molecules carries information on the magnetic field. In contrast to other mechanisms of interstellar molecular line polarization, such as through the Goldreich-Kylafis (GK) effect, line polarization due to SB effects does not require molecules to be excited subthermally, or excited under the influence of an anisotropic radiation field. Rather, line polarization due to SB effects require some gas strain to be present to be operative. Exploratory calculations suggest that gas strains due to turbulent dissipation can lead to polarization fractions of a fraction of a per cent, while the gas strain that is present in viscously evolving accretion disks can lead to molecular line polarization of some percents.

References

1. Balbus SA, Hawley JF (1998) Instability, turbulence, and enhanced transport in accretion disks. Rev Mod Phys 70(1):1
2. Beattie JR et al (2024) Magnetized compressible turbulence with a fluctuation dynamo and reynolds numbers over a million. arXiv preprint arXiv:2405.16626
3. Beenakker JJ, Scoles G, Knaap HF, Jonkman R (1962) The influence of a magnetic field on the transport properties of diatomic molecules in the gaseous state. Phys Lett 2
4. Beenakker J, McCourt F (1970) Magnetic and electric effects on transport properties. Annu Rev Astron Astrophys 21(1):47–72
5. Flaherty KM et al (2018) Turbulence in the TW Hya disk. Astrophys J 856(2):117
6. Gallimore JF, Impellizzeri CV, Aghelpasand S, Gao F, Hostetter V, Lankhaar B (2024) The discovery of polarized water vapor megamaser emission in a molecular accretion disk. Astrophys J Lett 975(1):L9
7. Goldreich P, Kylafis ND (1981) On mapping the magnetic field direction in molecular clouds by polarization measurements. Astrophys J 243:L75–L78
8. Hess S (1969) Flow birefringence of polyatomic gases. Phys Lett A 30(4):239–240

9. Hess S (1973) Flow-birefringence in gases an example of the kinetic theory based on the boltzmann-equation for rotating particles. In: The Boltzmann equation: theories and applications. Springer
10. Hutson JM, McCourt FR (1984) Close-coupling calculations of transport and relaxation cross sections for H_2 in Ar. J Chem Phys 80(3):1135–1149
11. Impellizzeri CV et al (2019) Counter-rotation and high-velocity outflow in the parsec-scale molecular torus of NGC 1068. Astrophys J Lett 884(2):L28
12. Knaap H, Beenakker J (1967) Heat conductivity and viscosity of a gas of non-spherical molecules in a magnetic field. Physica 33(3):643–670
13. Korving J et al (1967) The influence of a magnetic field on the transport properties of gases of polyatomic molecules: part I, viscosity. Physica 36(2):177–197
14. Kumar P (1999) The structure of the central disk of NGC 1068: a clumpy disk model. Astrophys J 519(2):599
15. Lankhaar B, Teague R (2023) Three-dimensional magnetic field imaging of protoplanetary disks using Zeeman broadening and linear polarization observations. Astron Astrophys 678:A17
16. Lankhaar B, Vlemmings W (2020) Collisional polarization of molecular ions: a signpost of ambipolar diffusion. Astron Astrophys 638:L7
17. Lankhaar B, Vlemmings W (2020) Portal: three-dimensional polarized (sub)millimeter line radiative transfer. Astron Astrophys 636:A14
18. Lankhaar B, Vlemmings W, Bjerkeli P (2022) Tracing the large-scale magnetic field morphology in protoplanetary disks using molecular line polarization. Astron Astrophys 657:A106
19. Lankhaar B et al (2024) Maser polarization through anisotropic pumping. Astron Astrophys 683:A117
20. Lesur GR (2021) Systematic description of wind-driven protoplanetary discs. Astron Astrophys 650:A35
21. McCourt FR, Beenakker JJ, Kohler WE, Kuscer I (1991) Nonequilibrium phenomena in polyatomic gases: dilute gases. Oxford University Press
22. McKee CF, Ostriker EC (2007) Theory of star formation. Annu Rev Astron Astrophys 45(1):565–687
23. Senftleben H (1930) Einfluss eines magnetfieldes auf das wärmeleitungsvermögen fon paramagnetischen gasen. Phys Z 31:822
24. Shakura N, Sunyaev R (1976) A theory of the instability of disk accretion on to black holes and the variability of binary X-ray sources, galactic nuclei and quasars. Mon Not R Astron Soc 175(3):613–632
25. Sinha M, Caldwell C, Zare R (1974) Alignment of molecules in gaseous transport: alkali dimers in supersonic nozzle beams. J Chem Phys 61(2):491–503
26. Teague R et al (2021) Discovery of molecular-line polarization in the disk of TW Hya. Astrophys J 922(2):139
27. Vlemmings W, Lankhaar B et al (2019) Stringent limits on the magnetic field strength in the disc of TW Hya-ALMA observations of CN polarisation. Astron Astrophys 624:L7

Open Access This chapter is licensed under the terms of the Creative Commons Attribution 4.0 International License (http://creativecommons.org/licenses/by/4.0/), which permits use, sharing, adaptation, distribution and reproduction in any medium or format, as long as you give appropriate credit to the original author(s) and the source, provide a link to the Creative Commons license and indicate if changes were made.

The images or other third party material in this chapter are included in the chapter's Creative Commons license, unless indicated otherwise in a credit line to the material. If material is not included in the chapter's Creative Commons license and your intended use is not permitted by statutory regulation or exceeds the permitted use, you will need to obtain permission directly from the copyright holder.